ASME
SETTING THE STANDARD

Journal of Engineering for Gas Turbines and Power

Published Quarterly by ASME

VOLUME 129 • NUMBER 2 • APRIL 2007

Transactions of the ASME, Journal of Engineering for Gas Turbines and Power (ISSN 0742-4795) is published quarterly (Jan., April, July, Oct.) by The American Society of Mechanical Engineers, Three Park Avenue, New York, NY 10016. Periodicals postage paid at New York, NY and additional mailing offices. POSTMASTER: Send address changes to Transactions of the ASME, Journal of Engineering for Gas Turbines and Power, c/o THE AMERICAN SOCIETY OF MECHANICAL ENGINEERS, 22 Law Drive, Box 2300, Fairfield, NJ 07007-2300.
CHANGES OF ADDRESS must be received at Society headquarters seven weeks before they are to be effective. Please send old label and new address.
STATEMENT from By-Laws. The Society shall not be responsible for statements or opinions advanced in papers or ... printed in its publications (B7.1, par. 3).

TECHNICAL PAPERS

(Contents continued on inside back cover)

This journal is printed on acid-free paper, which exceeds the ANSI Z39.48-1992 specification for permanence of paper and library materials. ♾™
♻ 85% recycled content, including 10% post-consumer fibers.

(Contents continued)

Journal of Engineering for Gas Turbines and Power APRIL 2007

Volume 129, Number 2

Gas Turbines: Controls, Diagnostics, and Instrumentation

Gas Turbines: Cycle Innovations

Gas Turbines: Heat Transfer

Gas Turbines: Industrial and Cogeneration

Microturbines & Small Turbomachinery

Gas Turbines: Structures and Dynamics

Fuels and Combustion Technologies (FACT)

(Contents continued on facing page)

Journal of Engineering for Gas Turbines and Power APRIL 2007

Volume 129, Number 2

Internal Combustion Engines

TECHNICAL BRIEF

The ASME Journal of Engineering for Gas Turbines and Power is abstracted and indexed in the following:

AESIS (Australia's Geoscience, Minerals, & Petroleum Database), Applied Science & Technology Index, Aquatic Sciences and Fisheries Abstracts, Civil Engineering Abstracts, Compendex (The electronic equivalent of Engineering Index), Computer & Information Systems Abstracts, Corrosion Abstracts, Current Contents, Engineered Materials Abstracts, Engineering Index, Enviroline (The electronic equivalent of Environment Abstracts), Environment Abstracts, Environmental Science and Pollution Management, Fluidex, INSPEC, Mechanical & Transportation Engineering Abstracts, Mechanical Engineering Abstracts, METADEX (The electronic equivalent of Metals Abstracts and Alloys Index), Pollution Abstracts, Referativnyi Zhurnal, Science Citation Index, SciSearch (The electronic equivalent of Science Citation Index), Shock and Vibration Digest

Rayleigh-Bénard Convection in Open and Closed Rotating Cavities

Martin P. King
Abdus Salam International Centre for Theoretical Physics, Strada Costiera 11, Trieste, Italy

Michael Wilson

J. Michael Owen
e-mail: ensjmo@bath.ac.uk

Department of Mechanical Engineering, University of Bath, Bath BA2 7AY, UK

Buoyancy effects can be significant in the rotating annular cavities found between compressor discs in gas-turbine engines, where Rayleigh numbers above 10^{12} are common. In some engines, the cavity is "closed" so that the air is confined between four rotating surfaces: two discs and inner and outer cylinders. In most engines, however, the cavity is "open" and there is an axial throughflow of cooling air at the center. For open rotating cavities, a review of the published evidence suggests a Rayleigh–Bénard type of flow structure, in which, at the larger radii, there are pairs of cyclonic and anti-cyclonic vortices. The toroidal circulation created by the axial throughflow is usually restricted to the smaller radii in the cavity. For a closed rotating annulus, solution of the unsteady Navier–Stokes equations, for Rayleigh numbers up to 10^9, show Rayleigh–Bénard convection similar to that found in stationary enclosures. The computed streamlines in the r-θ plane show pairs of cyclonic and anti-cyclonic vortices; but, at the larger Rayleigh numbers, the computed isotherms suggest that the flow in the annulus is thermally mixed. At the higher Rayleigh numbers, the computed instantaneous Nusselt numbers are unsteady and tend to oscillate with time. The computed time-averaged Nusselt numbers are in good agreement with the correlations for Rayleigh–Bénard convection in a stationary enclosure, but they are significantly higher than the published empirical correlations for a closed rotating annulus. [DOI: 10.1115/1.2432898]

Keywords: Rayleigh–Bénard convection, rotating cavities

1 Introduction

Buoyancy-induced flow occurs in the rotating annular cavities found between the compressor disks in gas-turbine engines. In some engines the cavity is *closed*, and the trapped air is confined between four rotating surfaces: two disks and an inner and outer cylindrical surface. In most engines, however, the cavity is *open*, as shown in Fig. 1, and there is an axial throughflow of cooling air in the clearance between the center of the discs and a rotating shaft. (Although the shaft usually rotates at a different angular speed from that of the discs, in this paper it is assumed to have the same speed, Ω.) Figure 2 shows a schematic diagram of the open and closed rotating cavities that are the subject of this paper.

Rayleigh–Bénard convection can occur in the fluid enclosed between two, stationary, horizontal plates, the lower of which is heated. The buoyancy-induced flow structure (see Refs. [1–3]) comprises a parallel array of contrarotating vortices with horizontal axes, as shown in Fig. 3. King and Wilson [4] showed that a similar flow structure can occur in a rotating annulus, where the outer cylindrical surface is heated. In this case, where the centripetal acceleration, $\Omega^2 r$, is much greater than the gravitational acceleration, g, the axes of the counter-rotating vortices in the annulus are in the axial direction. (In an engine, $\Omega^2 r/g$ is typically of the order of 10^4, and Rayleigh numbers are usually greater than 10^{12}.)

This paper considers the occurrence of Rayleigh–Bénard convection, and related buoyancy-induced flow, in both open and closed rotating cavities. Section 2 presents the linear equations for rotating fluids, and Sec. 3 reviews some relevant published work. Section 4 describes the governing equations and computational methods that are used to produce the computed flow structures and Nusselt numbers that are presented in Sec. 5 for a closed cavity. The principal conclusions are summarized in Sec. 6.

2 Linear Equations for Rotating Fluids

Consider a frame of reference, rotating with angular speed Ω about an axis located at point 0. In cylindrical-polar coordinates, u, v, and w are the components of velocity in the r, θ, z directions.

The so-called linear equations are a simplified form of the Navier–Stokes equations when the nonlinear inertial terms are negligibly small compared with the Coriolis acceleration. Strictly, the linear equations are only valid when $|u|$ and $|v|$ are much smaller than Ωr. There are, however, many flows where the equations give good predictions of experimental measurements even when $|u|$ and $|v|$ are of similar magnitude to Ωr (see Refs. [5,6]). The equations developed below are based on those derived by Farthing et al. [7]; they are used here to show their relevance to Rayleigh–Bénard flow.

For steady flow, the continuity equation and the inviscid linear equations (which, in meteorology, are referred to as the *geostrophic equations*) can be expressed as

$$\partial_r(\rho r u) + \partial_\theta(\rho v) + \partial_z(\rho r w) = 0 \tag{1}$$

$$2\Omega v = \frac{1}{\rho}\partial_r p - \Omega^2 r \tag{2a}$$

$$2\Omega u = -\frac{1}{\rho r}\partial_\theta p \tag{2b}$$

$$0 = \frac{1}{\rho}\partial_z p \tag{2c}$$

Equations (1) and (2) lead to the result that

Contributed by the Internal Gas Turbine Institute (IGTI) of ASME for publication in the JOURNAL OF ENGINEERING FOR GAS TURBINES AND POWER. Manuscript received October 31, 2005; final manuscript received November 15, 2005. Review conducted by Dilip R. Ballal. Paper presented at the ASME Turbo Expo 2005: Land, Sea and Air (GT2005), Reno, Nevada, June 6–9, 2005, Paper No. GT2005-68948.

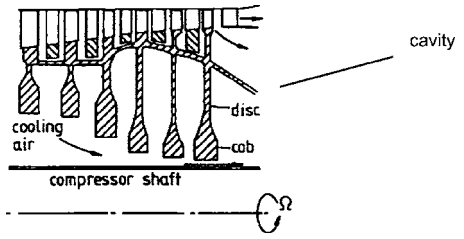

Fig. 1 Simplified diagram of high-pressure compressor rotor with axial throughflow

$$\partial_z(\rho w) = \frac{\Omega}{2}\partial_\theta \rho \tag{3}$$

For incompressible or axisymmetric flow (where $\partial_{\theta\rho}$ is zero) it follows that ρw is invariant with z. This result, often referred to as the Taylor–Proudman theorem, means that u and v are also invariant with z. Two important consequences should be noted: (i) rotation tends to create two-dimensional (2D) stratified flow, reducing circulation; (ii) radial flow can only occur if $\partial_\theta p \neq 0$. (As shown in Ref. [6], for source-sink flow in a rotating cavity, radial flow is confined to Ekman layers on the discs and there is virtually no flow in the inviscid core of fluid between these layers.)

For incompressible flow, equation (2*a*) can be written as

$$2\Omega v = \frac{1}{\rho}\partial_r P \tag{4}$$

where P is the so-called *reduced pressure* defined by

$$P = p - \frac{1}{2}\rho\Omega^2 r^2 \tag{5}$$

For cyclonic circulation, where $v > 0$, the pressure increases radially. As the pressure at the center of the circulation is lower than that at the outside, cyclonic circulation is associated with low pressure (as in the earth's atmosphere); conversely, anti-cyclonic circulation is associated with high pressure.

In a rotating cavity, Rayleigh–Bénard convection is always associated with an *even* number of vortices; in a stationary enclosure, the number may be odd or even. These cyclonic and anti-cyclonic pairs of vortices create the circumferential pressure gradient that is needed to produce the radial convection of fluid in the rotating cavity. The above results apply to inviscid flow: viscosity tends to reduce the circulation, and heat transfer to the cylindrical surfaces of a rotating cavity occurs in the boundary layers on these surfaces.

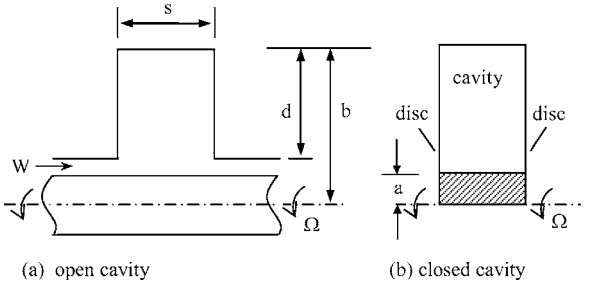

Fig. 2 Schematic diagram of open and closed rotating cavities

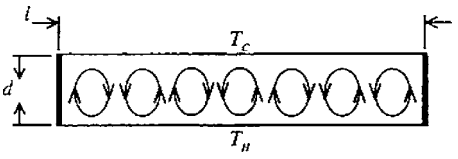

Fig. 3 Rayleigh–Bénard convection in a horizontal stationary enclosure

3 Review of Previous Work

The definition of symbols is given in the Nomenclature.

3.1 Open Rotating Cavities. The Sussex Group [7–12] made measurements and computations for a rotating cavity with an axial throughflow of cooling air for $a/b \approx 0.1$. There was no central shaft, and either the discs or the shroud (the outer cylindrical surface) were heated.

Farthing et al. [7] carried out flow visualization and laser-Doppler anemometry (LDA) studies in both isothermal and heated cavities. For the isothermal case, the axial throughflow was seen to generate a powerful toroidal vortex, in cavities with large gap ratios ($G > 0.4$), the strength of which decreased as the rotational speed increased. Depending on the values of G and Ro, the Rossby number, axisymmetric and nonaxisymmetric vortex breakdown [13] was observed in the central jet. When one or both of the disks were heated, the flow in the cavity became nonaxisymmetric, and cyclonic and anti-cyclonic circulation was observed. The core of fluid between the discs precessed at an angular speed (Ω_c say) slightly less than that of the discs. The ratio of Ω_c/Ω decreased as the temperature difference between the discs and the cooling air increased.

For the case of $G = 0.138$, with both discs heated to the same (radially increasing) temperature, Farthing et al. [8] correlated the Nusselt number, Nu_1, by

$$\mathrm{Nu}_1 = 0.0054\,\mathrm{Re}_z\mathrm{Gr}_1^{0.25} \tag{6}$$

The correlations for natural convection [14] from a heated vertical plate in air (where the centripetal acceleration $\Omega^2 r$ in the definition of Gr_1 is replaced by the gravitational acceleration g, and $(b-r)$ is replaced by the vertical height) are

$$\mathrm{Nu}_1 = 0.36\,\mathrm{Gr}_1^{0.25} \quad \text{for laminar flow} \tag{7a}$$

$$\mathrm{Nu}_1 = 0.022\,\mathrm{Gr}_1^{0.4} \quad \text{for turbulent flow} \tag{7b}$$

For the vertical plate, transition from laminar to turbulent flow occurs at $\mathrm{Gr}_1 \approx 10^9$. For the rotating cavity, Farthing et al. found no evidence of transition even for $\mathrm{Gr}_1 > 10^{11}$, which suggested that the flow might be laminar even at very large values of the Grashof number.

As part of a major European research project [internal cooling air systems in gas turbines (ICAS-GT)] Owen and Powell [15] made measurements in an open cavity, where $a/b = 0.4$ and $G = 0.2$, in which one of the discs was heated. LDA and heat transfer measurements were made for $1.4 \times 10^3 < \mathrm{Re}_z < 5 \times 10^4$ and $4 \times 10^5 < \mathrm{Re}_\phi < 3.2 \times 10^6$. Spectral analysis of the LDA measurements revealed a multi-cell structure comprising one, two or three pairs of vortices. As found in the experiments of Farthing et al., the core of fluid between the discs precessed at an angular speed, Ω_c, less than that of the discs, and Ω_c/Ω decreased as the temperature of the heated disk increased. At the smaller values of Re_z, the measured Nusselt numbers were consistent with buoyancy-induced flow; at the larger values of Re_z, the effect of the axial throughflow became dominant.

Complementary computational research, conducted as part of ICAS-GT, was reported by Smout et al. [16]. Three-dimensional, unsteady, turbulent computations for the open rotating cavity at low values of Re_z produced a multi-cell structure and the computed Nusselt numbers were consistent with the measurements made by Owen and Powell.

Tian et al. [17] computed the flow and heat transfer in a rotating cavity based on the geometry of Farthing et al. Their 3D, steady, turbulent computations showed that the flow structure comprised two parts: Rayleigh–Bénard convection at the larger radii, and forced convection in the central region. The computations suggested that there is a critical Rayleigh number above which the

flow becomes unstable and time dependent.

Johnson et al. [18] investigated the stability characteristics of variable-density swirling flow in rotating cavities. Using a narrow-gap approximation for inviscid flow, they produced criteria for the necessary and sufficient conditions for stability. When the rotating surfaces are colder than the "cooling air" (such as at takeoff in an aeroengine) the flow is stably stratified: the axial throughflow cannot penetrate very far into the cavity and the resulting convective heat transfer is relatively low. Conversely, when the rotating surfaces are hotter than the air (at cruise and landing), the flow is unstable, the axial flow can readily enter the cavity, and the heat transfer is increased as a consequence. (For these unstable conditions, flow visualization revealed "multi-lobe secondary flows" rotating inside the cavities of a compressor drum.)

3.2 Closed Rotating Cavities. The Aachen group [19–22] made measurements and computations for a sealed annulus where the heat flow could be either axial (from a hot disk to a cold one) or radial (from a hot outer cylindrical surface to a cold inner one). The subscripts 2 and 3 are used below for axial and radial heat transfer, respectively. In both cases, the Nusselt numbers represent the ratio of (axial or radial) convection to conduction in the annulus. The Nusselt numbers are spatially and time averaged values.

For $G=0.5$, $a/b=0.52$, $2\times10^8<\mathrm{Ra}_2<5\times10^{10}$, the Nusselt number for the axial case was correlated by

$$\mathrm{Nu}_2 = 0.346\,\mathrm{Ra}_2^{0.124} \tag{8}$$

For the radial case, three different geometries were tested for $10^7<\mathrm{Ra}_3<10^{12}$, and the correlations are given below.

Geometry A (axisymmetric annulus with $G=0.34$, $a/b=0.35$)

$$\mathrm{Nu}_{3,A} = 0.266\,\mathrm{Ra}_3^{0.228} \tag{9a}$$

Geometry B (axisymmetric annulus with $G=0.5$, $a/b=0.52$)

$$\mathrm{Nu}_{3,B} = 0.317\,\mathrm{Ra}_3^{0.211} \tag{9b}$$

Geometry C (annulus with 45 deg segments with $G=0.5$, $a/b=0.52$)

$$\mathrm{Nu}_{3,C} = 0.365\,\mathrm{Ra}_3^{0.213} \tag{9c}$$

From the definitions of Ra_3 and Re_3 it follows that

$$\mathrm{Ra}_3 = (s/r_m)\mathrm{Pr}\,\beta\Delta T\,\mathrm{Re}_3^2 \tag{10}$$

where

$$\mathrm{Re}_3 = \Omega r_m s/\nu \tag{11}$$

Therefore the Rayleigh number depends on both the rotational Reynolds number, Re_3, and the buoyancy parameter, $\beta\Delta T$. Coriolis forces increase as Ω increases, and the results of Sec. 2 suggest that circulation inside the annulus should be reduced as Ω, and hence Re_3, increases. In the experiments, for a given value of Ra_3, $\mathrm{Re}_{3,B}$ was greater than $\mathrm{Re}_{3,A}$. Consequently, $\mathrm{Nu}_{3,B}<\mathrm{Nu}_{3,A}$, although the differences were relatively small.

As shown in Sec. 2, radial flow can only occur in the inviscid core of fluid if $\partial_\theta p\neq 0$. For annuli A and B, this pressure gradient is created by pairs of cyclonic and anti-cyclonic vortices. In annulus C, the radial walls in the cavity allow a pressure gradient to exist without the need for vortex pairs. Bohn et al. [20] found that, in annulus C, there was anti-cyclonic circulation, with an isothermal core, in each of the eight segments. This circulation provided enhanced convection so that, for a given value of Ra_3, the Nusselt numbers in annulus C were slightly greater than those in either A or B.

For Rayleigh–Bénard convection in stationary, horizontal enclosures, King [23] used dimensional and physical arguments to show that $\mathrm{Nu}_3=A_1\mathrm{Ra}^{a1}+A_2\mathrm{Ra}^{a2}+\ldots$, where A_1, A_2, a_1, and a_2 are constants. Niemela et al. [24] correlated Nu_3 for low and high Rayleigh numbers, and Grossman and Lohse [3] produced the semi-empirical result

$$\mathrm{Nu}_3 = 0.27\,\mathrm{Ra}^{1/4} + 0.038\mathrm{Ra}^{1/3} \tag{12}$$

Holland et al. [25] obtained the correlation, for $\mathrm{Pr}=0.7$

$$\mathrm{Nu}_3 = 1 + 1.44\,\max\{1-1708/\mathrm{Ra},0\} + \max\{(\mathrm{Ra}/5830)^{1/3}-1,0\} \tag{13}$$

King and Wilson [4] solved the unsteady 2D laminar equations (see Sec. 4) for an annulus (with the outer surface heated) in which the gravitational acceleration, g, was replaced by a *constant* centripetal acceleration ($\Omega^2 b$). Their computed streamlines showed the vortex structure associated with Rayleigh–Bénard convection. The computed Nusselt numbers, for $10^4<\mathrm{Ra}<10^9$ and $a/b=0.5$ and 0.7, were in good agreement with the above correlations for a stationary enclosure.

4 Governing Equations and Computational Methods

The unsteady Navier–Stokes equations are expressed, using dimensionless variables, in vorticity-streamfunction and velocity–vorticity formulations for the 2D and 3D computations, respectively. Derivations, from the original primitive-variables forms of the equations using Boussinesq approximations and suitable substitutions, are given by Lewis [26] and King [23].

The 2D dimensionless equations in cylindrical polar coordinates and in a rotating frame of reference for radial–tangential (r-θ) flow in streamfunction-vorticity form are

$$\bar{\omega} = \nabla^2\bar{\psi} \tag{14}$$

$$\frac{1}{\mathrm{Pr}}\left[\partial_{\bar{t}}\bar{\omega} + \frac{1}{\bar{r}}J(\bar{\omega},\bar{\psi})\right] + \frac{2\mathrm{Ra}_\phi}{\bar{r}\mathrm{Re}_\phi\mathrm{Pr}}J(\bar{T},\bar{\psi}) + \mathrm{Ra}_\phi\partial_\theta\bar{T} = \nabla^2\bar{\omega} \tag{15}$$

$$\partial_{\bar{t}}\bar{T} + \frac{1}{\bar{r}}J(\bar{T},\bar{\psi}) = \nabla^2\bar{T} \tag{16}$$

where the Jacobian operator is given by $J(A,B)=\partial_{\bar{r}}A\,\partial_\theta B - \partial_{\bar{r}}B\,\partial_\theta A$ and $\bar{t},\bar{T},\bar{\omega}$, and $\bar{\psi}$ are the nondimensional time (or Fourier number), temperature, vorticity and streamfunction, respectively.

The vorticity-velocity formulation for the dimensionless 3D equations are

$$\frac{1}{\mathrm{Pr}}\left[\partial_{\bar{t}}A + (\underline{\bar{u}}\,.\,\nabla)A - A\partial_{\bar{r}}\bar{u} - \frac{B}{\bar{r}}\partial_\theta\bar{u} - C\partial_{\bar{z}}\bar{u}\right]$$

$$- 2\mathrm{Re}_\phi\partial_{\bar{z}}\bar{u} + \frac{2\mathrm{Ra}_\phi}{\mathrm{Re}_\phi\mathrm{Pr}}(\bar{T}\partial_{\bar{z}}\bar{u} + \bar{u}\partial_{\bar{z}}\bar{T})$$

$$= \nabla^2 A - \frac{2}{\bar{r}^2}\partial_\theta B - \frac{A}{\bar{r}^2} \tag{17}$$

$$\frac{1}{\mathrm{Pr}}\left[\partial_{\bar{t}}B + (\underline{\bar{u}}\,.\,\nabla)B - A\left(\partial_{\bar{r}}\bar{v} - \frac{\bar{v}}{\bar{r}}\right) - \frac{B}{\bar{r}}(\bar{u} + \partial_\theta\bar{v}) - C\partial_{\bar{z}}\bar{v}\right]$$

$$- 2\mathrm{Re}_\phi\partial_{\bar{z}}\bar{v} + \frac{2\mathrm{Ra}_\phi}{\mathrm{Re}_\phi\mathrm{Pr}}(\bar{T}\partial_{\bar{z}}\bar{v} + \bar{v}\partial_{\bar{z}}\bar{T})$$

$$+ \bar{r}\mathrm{Ra}_\phi\partial_{\bar{z}}\bar{T} = \nabla^2 B + \frac{2}{\bar{r}^2}\partial_\theta A - \frac{B}{\bar{r}^2} \tag{18}$$

$$\frac{1}{\mathrm{Pr}}\left[\partial_{\bar{t}}C + (\underline{\bar{u}}\,.\,\nabla)C - A\partial_{\bar{r}}\bar{w} - \frac{B}{\bar{r}}\partial_\theta\bar{w} - C\partial_{\bar{z}}\bar{w}\right]$$

$$- 2\mathrm{Re}_\phi\partial_{\bar{z}}\bar{w} + \frac{2\mathrm{Ra}_\phi}{\mathrm{Re}_\phi\mathrm{Pr}}\left(\bar{T}\partial_{\bar{z}}\bar{w} - \bar{u}\partial_{\bar{r}}\bar{T} - \frac{\bar{v}}{\bar{r}}\partial_\theta\bar{T}\right)$$

$$-Ra_{\phi}\partial_{\theta}\bar{T} = \nabla^2 C \tag{19}$$

where A, B, and C are the components of vorticity and $\bar{u}, \bar{v}, \bar{w}$ the nondimensional velocities in the r, θ, and z directions, respectively. The Poisson equations for velocity are derived using the curl of the vorticity and the continuity equation. The velocity expressed in terms of vorticity is then given by

$$\nabla^2 \bar{w} = \frac{1}{\bar{r}}\partial_{\theta}A - \partial_{\bar{r}}B - \frac{B}{\bar{r}} \tag{20}$$

$$\nabla^2 \bar{v} + \frac{2}{\bar{r}}\partial_{\bar{r}}\bar{v} + \frac{\bar{v}}{\bar{r}^2} = \partial_{\bar{r}}C + \frac{2C}{\bar{r}} - \partial_{\bar{z}}A \tag{21}$$

$$\nabla^2 \bar{u} + \frac{2}{\bar{r}}\partial_{\bar{r}}\bar{u} + \frac{\bar{u}}{\bar{r}^2} = \partial_{\bar{z}}B = \frac{1}{\bar{r}}\partial_{\theta}C - \frac{1}{\bar{r}}\partial_{\theta}C - \frac{2}{\bar{r}}\partial_{\bar{z}}\bar{w} \tag{22}$$

The energy equation is

$$\partial_{\bar{t}}\bar{T} + (\bar{u} \,.\, \nabla)\bar{T} = \nabla^2 \bar{T} \tag{23}$$

The boundary conditions for the various dimensionless variables are such that there are no-slip velocity conditions, adiabatic side discs, $\bar{T}=1$ on the outer cylinder, and $\bar{T}=0$ on the inner cylinder. The computations were started from solid-body rotation and a conduction profile in temperature; the unstable flows develop through either numerical rounding errors or an imposed artificial disturbance.

The equations were solved using second-order-accurate finite-difference approximations in space on collocated uniform curvilinear grids for the 2D equations and on staggered grids for the 3D equations. The Arakawa [27] formulation was used to treat the nonlinear terms in the 2D equations. Time-stepping was based on the Du- Fort–Frankel method where values of a dependent variable at the present time step were exchanged for averages of new and previous time-step values. Equations (14) and (20)–(22) are boundary value problems within each time step. To accelerate convergence, they were solved using a V-cycling multigrid routine, incorporating a Gauss–Seidel line relaxation scheme.

The computed Nusselt numbers were based on the ratio of radial convection, at $\bar{r}=1$, to 1D radial conduction in the annulus. The local Nusselt number, Nu_3, was therefore defined as

$$\mathrm{Nu}_3 = \ln(b/a)(\partial_{\bar{r}}\bar{T})_{\bar{r}=1} \tag{24}$$

and the global, or spatially averaged, Nusselt number, $\mathrm{Nu}_{3,\mathrm{av}}$, was obtained by integrating Nu_3 over the area of the outer cylindrical surface.

Various grid and time-step resolutions were used to ensure numerical stability. For the 2D computations, the finest grid resolution was 96×192 (in r-θ) and the smallest time step was 2×10^{-8}; for the 3D computations, they were $32\times32\times128$ (in r-z-θ) and 5×10^{-8}, respectively.

5 Computed Flow in Closed Cavities

5.1 Flow Structure. The results discussed below were obtained by solving the equations given in Sec. 4 for $\mathrm{Pr}=0.7$ and $a/b=0.5$. Limitations in available computing power meant that computations were not practical for Rayleigh numbers greater than 10^9 for 2D flow and 10^6 for 3D flow.

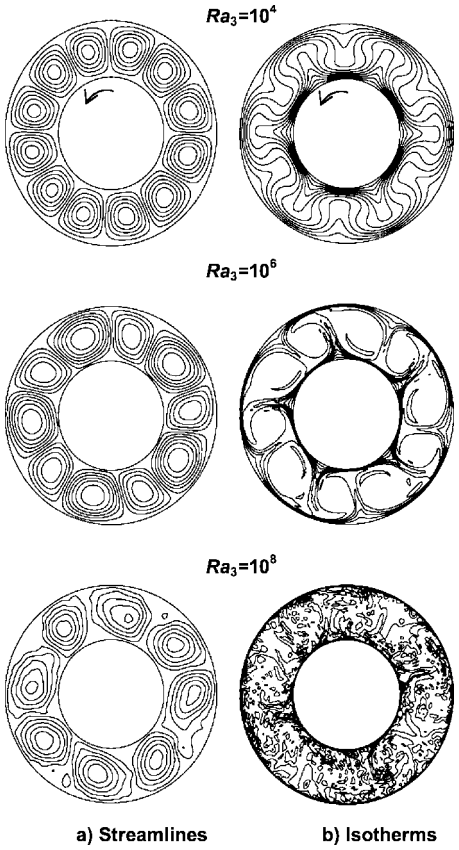

Fig. 4 Computed 2D streamlines and isotherms for $a/b=0.5$

The values of $\beta\Delta T$ used in the computations were chosen to match those in the experiments of Bohn et al. It was assumed that $\beta\Delta T = 1.1\mathrm{Ra}_3^{-0.114}$; as $\mathrm{Ra}_3 \propto \beta\Delta T\,\mathrm{Re}_3^2$, $\beta\Delta T$ varied between 0.44 and 0.1, and Re_3 between 128 and 1.5×10^5 for the range of Rayleigh numbers used in the computations. (As shown in Sec. 2, increasing Ω—and hence increasing Re_3—tends to reduce the circulation in the annulus. As found in the Aachen experiments, for a given value of Ra_3, increasing Re_3 tends to reduce the Nusselt number.)

Figure 4 shows the 2D computations of the instantaneous streamlines and isotherms; the values of $\bar{t}$ are given in Table 1. Although the streamlines show clear evidence of Rayleigh–Bénard convection, the isotherms show a more complicated picture. For $\mathrm{Ra}_3=10^4$, the isotherms show a series of lobes; for $\mathrm{Ra}_3=10^6$, the vortex pairs are clearly visible and their cores appear to be virtually isothermal; for $\mathrm{Ra}_3=10^8$, despite the vortex flow seen in the streamlines, the isotherms suggest that thermal mixing has occurred. Reasons for this mixing are discussed below.

Two-dimensional computations were conducted for $10^{3.5} \le \mathrm{Ra}_3 \le 10^9$, and Table 1 shows the number of pairs of vortices, n, that were observed for each value of Ra_3. The fact that n can vary from 4 to 6 in what appears to be a random fashion suggests that

Table 1 Number of pairs of observable vortices, n, in annulus for $a/b=0.5$

Ra_3	$10^{3.5}$	10^4	$10^{4.5}$	10^5	$10^{5.5}$	10^6	$10^{6.5}$	10^7	$10^{7.5}$	10^8	$10^{8.5}$	10^9
$\bar{t}$	2.5	0.25	0.25	0.2	0.2	0.15	0.04	0.015	0.003	0.01	0.003	0.0015
n(streamlines)	5	6	5	6	5	5	5	5	5	4	6	5
n(isotherms)	5	6	5	6	5	5	5	5	5	—	—	—

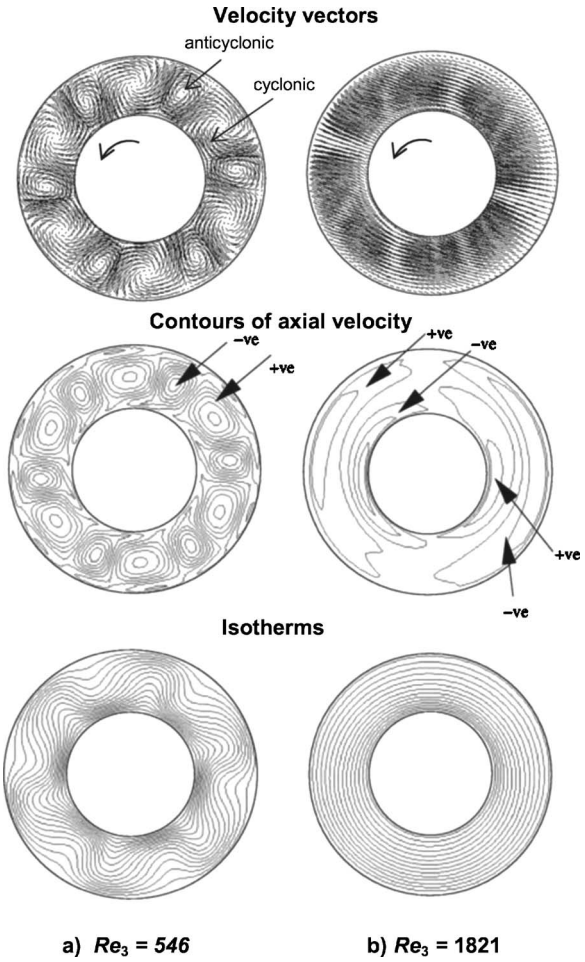

Fig. 5 Computed 3D flow structure at $\bar{z}=0.25$ and for $Ra_3=10^{3.9}$, $a/b=0.5$, $G=0.5$

n is time dependent. (The computations of Lewis [26] for a rotating annulus also showed that the number of vortex pairs could change with time.) The flow *vacillates*, and it is this vacillation that is thought to be responsible for the lack of coherence in the isotherms for $Ra_3 \geq 10^8$: the constantly changing flow structure acts as an effective thermal-mixing device. (*Vacillation* is used to mean an unsteadiness in the flow structure; this includes *structural vacillation* in which the number of vortices can change with time.)

The phenomenon of coherent flow structures and thermal mixing was also seen, above a critical Rayleigh number, in computations in a stationary annulus [23]. The measurements of Niemela et al. [24] for Rayleigh–Bénard flow in a stationary enclosure confirmed that large-scale coherent flow structures with thermal mixing could occur for Rayleigh numbers up to 10^{17}. This suggests that the phenomenon is physical.

Figure 5 shows the 3D computations of the instantaneous flow structure in an annulus with a gap ratio of $G=0.5$ for $Ra_3=10^{3.9}$ and $Re_3=546$ and 1821. For $Re_3=546$, the velocity vectors, at $z/s=0.25$ in the r-θ plane, show a similar structure to the 2D computations for $Ra_3=10^4$ in Fig. 4.

In the 3D computations for $Re_3=546$, the contours of axial velocity show that there is axial flow away from the discs (+ve) in the cyclonic (low pressure) vortices, and flow towards the disc (−ve) in the anti-cyclonic vortices. (This can be seen more clearly in the results for $Re_3=546$ than for $Re_3=1821$.) The isotherms show a lobe-type of structure similar to that shown in the 2D computations in Fig. 4.

For $Re_3=1821$, the 3D flow structure in Fig. 5 is far less clear but, for the reason stated above, increasing Re_3 reduces the circulation, and the circular isotherms show that conduction dominates over convection.

5.2 Nusselt Numbers. Figure 6 shows the computed variation of $Nu_{3,av}$, the global Nusselt number, with time $\bar{t}$ for $Ra_3=10^4$, 10^6, and 10^8. For stably stratified flow, where only conduction occurs, $Nu_{3,av}=1$, which is the case as $\bar{t}\rightarrow 0$. For $Ra_3=10^4$, the flow becomes unstable (that is, Rayleigh–Bénard convection occurs) for $\bar{t}>0.1$, and $Nu_{3,av}$ increases to a constant value of approximately 2.5. For $Ra_3=10^6$, however, $Nu_{3,av}$ never achieves a steady value: for $\bar{t}>0.1$, periodic oscillations occur and $7<Nu_{3,av}<9$. For $Ra_3=10^8$, the oscillations are aperiodic, and $30<Nu_{3,av}<40$. The oscillations in $Nu_{3,av}$ are attributed to the vacillating flow structure discussed above.

Figure 7 shows the variation of $\overline{Nu}_{3,av}$, the computed time-average global Nusselt number, with Ra_3. The computed Nusselt numbers are in good agreement with the correlations for a stationary enclosure but differ significantly from those for a rotating annulus.

King [23] conducted 3D laminar computations, for $Ra_3 \leq 10^6$, and the computed Nusselt numbers were in good agreement with the correlations for a stationary enclosure. Limitations in computing power meant that it was not possible to compute $\overline{Nu}_{3,av}$ at values of Ra_3 high enough to make comparisons with the empirical correlations for the rotating annulus. It is possible that 3D computations, with an appropriate turbulence model, could produce better agreement with the correlations for the rotating annulus, but that is beyond the scope of this paper. (It should be noted that Sun et al. [28] achieved good agreement with the results of Bohn et al. using a 3D compressible time-accurate code with a low-Mach-number preconditioner.)

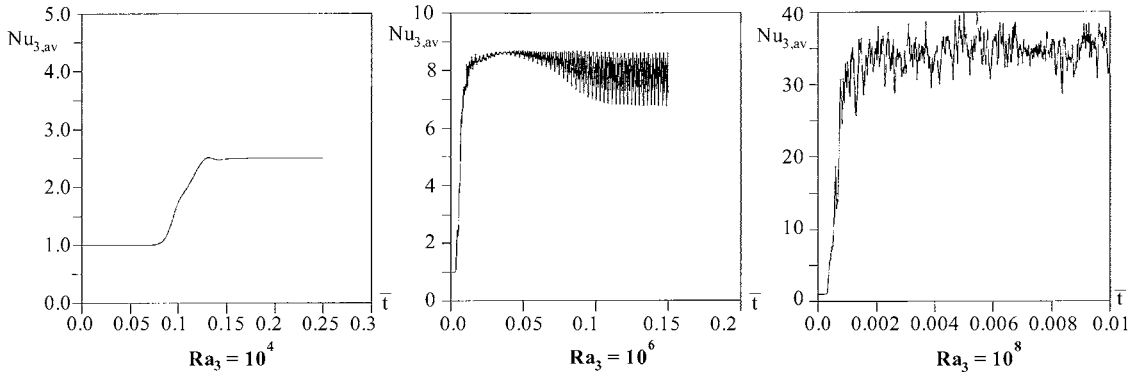

Fig. 6 2D computations of variation of $Nu_{3,av}$ with $\bar{t}$ for $a/b=0.5$

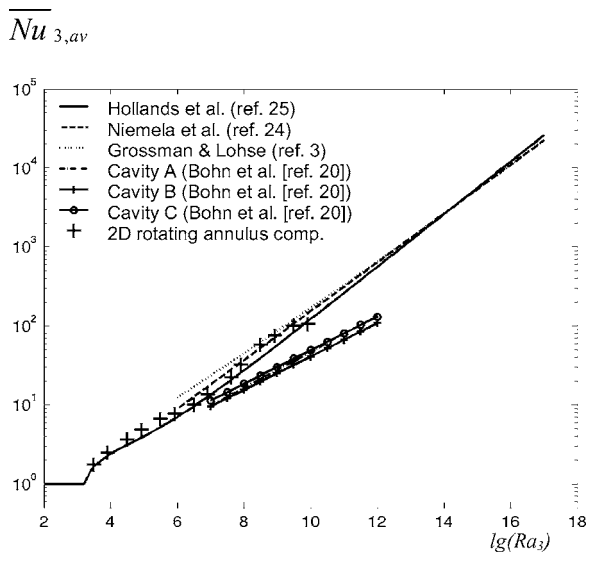

Fig. 7 2D computations of variation of $\overline{Nu}_{3,av}$ with Ra_3 for $a/b=0.5$

Heating the disks, or the outer surfaces, of a rotating cavity can produce buoyancy-induced flow. For the case of an open rotating cavity with an axial throughflow of cooling air, previously published work shows that a complex flow structure occurs: cyclonic and anti-cyclonic vortex pairs are created at large radii and the toroidal circulation induced by the throughflow is confined to the smaller radii.

For a closed rotating cavity (or sealed annulus), where the outer cylindrical surface is hotter than the inner one, the computed flow structure is similar to the Rayleigh–Bénard convection that occurs in stationary horizontal enclosures. Two-dimensional unsteady solutions of the Navier–Stokes equations, for rotational Rayleigh numbers up to 10^9 in a cavity with $a/b=0.5$, show that cyclonic and anti-cyclonic vortex pairs are created in the r-θ plane. For large Rayleigh numbers, the computed streamlines show clear evidence of vortex pairs, whereas the thermal contours suggest that the flow in the annulus is thermally mixed. This result, which has also been observed in stationary enclosures, is thought to be caused by vacillation in the flow structure.

The computed instantaneous Nusselt numbers also show unsteady behavior at the higher Rayleigh numbers. The time-averaged Nusselt numbers are in good agreement with the correlations for Rayleigh–Bénard convection in stationary enclosures, but they are significantly higher than the empirical correlations for a closed rotating annulus. The reason for this overprediction is not understood, but it is possible that the use of an appropriate turbulence model may produce better agreement between the computations and measurements for the rotating annulus.

Acknowledgment

The authors wish to thank Sarah Fuge for typing this paper, and we thank the reviewers for their constructive comments.

Nomenclature

a,b = inner, outer radius of cavity
A,B,C = components of vorticity in r, θ, z directions
d = vertical height of stationary enclosure; radial height of annulus
g = gravitational acceleration
G = s/b, gap ratio
Gr_1 = $\Omega^2 r(b-r)^3\beta\Delta T/v^2$, Grashof number for open cavity
k = thermal conductivity
l = horizontal length of stationary enclosure
L = characteristic length
$\dot{m}$ = mass flow rate
n = number of vortex pairs
Nu_1 = $q(b-r)/k\Delta T$, Nusselt number for open cavity
$\mathrm{Nu}_{2,av}$ = $q_{av}s/k\Delta T$, average Nusselt number for annulus (axial heat flow)
Nu_3 = q/q_{cond}, local Nusselt number for annulus (radial heat flow) or stationary enclosure
$\underline{\mathrm{Nu}}_{3,av}$ = global-average of Nu_3
$\overline{\mathrm{Nu}}_{3,av}$ = time average of $\mathrm{Nu}_{3,av}$
Pr = ν/α, Prandtl number
q = heat flux
r = radius
$\bar{r}$ = r/b, nondimensional radius
r_m = $\frac{1}{2}(a+b)$, mean radius of annulus
Ra = $gd^3\beta\Delta T/v\alpha$, Rayleigh number for stationary enclosure
Ra_2 = $\Omega^2 r_m s^3\beta\Delta T/\nu\alpha$, Rayleigh number for annulus (axial heat flow)
Ra_3 = $\Omega^2 r_m d^3\beta\Delta T/v\alpha$, Rayleigh number for annulus (radial heat flow)
Ra_ϕ = $\Omega^2 b^4\beta\Delta T/\nu\alpha$, rotational Rayleigh number
Re_3 = $\Omega r_m s/v$, rotational Reynolds number for annulus
Re_z = WL/ν, axial Reynolds number
Re_ϕ = $\Omega b^2/\nu$, rotational Reynolds number
Ro = $W/\Omega a$, Rossby number
s = axial gap between disks
t = time
$\bar{t}$ = $\alpha t/b^2$, nondimensional time (Fourier number)
T = absolute temperature
$\bar{T}$ = $(T-T_c)/(T_H-T_c)$, nondimensional temperature
u,v,w = radial, tangential and axial components of velocity in a rotating frame of reference
$\bar{u},\bar{v},\bar{w}$ = values of u,v,w normalized with respect to Ωb
W = bulk-average axial velocity
z = axial distance from left-hand disk
$\bar{z}$ = z/s, nondimensional axial distance
α = thermal diffusivity
β = T_{ref}^{-1}, volume expansion coefficient
ΔT = (T_H-T_c) temperature difference
μ = dynamic viscosity
ν = kinematic viscosity
ρ = density
Ω = angular speed of cavity
Ω_c = angular speed of fluid core
ω = vorticity
$\bar{\omega}$ = $\omega b^2/\alpha$, nondimensional vorticity
ψ = streamfunction in r-θ plane
$\bar{\psi}$ = ψ/α nondimensional streamfunction

Subscripts

av = average value
C = cold surface
cond = conduction
H = hot surface
I = inlet value
ref = reference value

References

[1] Koschmieder, E. L., 1993, *Bénard Cells and Taylor Vortices*, Cambridge University Press, Cambridge, UK.
[2] Siggia, E. D., 1994, "High Rayleigh Number Convection," Annu. Rev. Fluid Mech., **26**, pp. 137–168.
[3] Grossman, S., and Lohse, D., 2000, "Scaling in Thermal Convection: A Uni-

fying Theory," J. Fluid Mech., **407**, pp. 27–56.
[4] King, M. P., and Wilson, M., 2002, "Free Convective Heat Transfer Within Rotating Annuli," *Proceedings 12th International Heat Transfer Conference*, Vol. 2, Grenoble, France, pp. 465–470.
[5] Owen, J. M., and Rogers, R. H., 1989, "Flow and Heat Transfer in Rotating-Disc Systems," *Rotor-Stator Systems*, Vol. 1, Research Studies Press, Taunton, UK.
[6] Owen, J. M., and Rogers, R. H., 1995, "Flow and Heat Transfer in Rotating-disc Systems," *Rotating Cavities*, Vol. 2, Research Studies Press, Taunton, UK.
[7] Farthing, P. R., Long, C. A., Owen, J. M., and Pincombe, J. R., 1992, "Rotating Cavity With Axial Throughflow of Cooling Air: Flow Structure," J. Turbomach., **114**, pp. 237–246.
[8] Farthing, P. R., Long, C. A., Owen, J. M., and Pincombe, J. R., 1992, "Rotating Cavity With Axial Throughflow of Cooling Air: Heat Transfer," J. Turbomach., **114**, pp. 229–236.
[9] Long, C. A., 1994, "Disk Heat Transfer in a Rotating Cavity With an Axial Throughflow of Cooling Air," Int. J. Heat Fluid Flow, **15**, pp. 307–316.
[10] Long, C. A., and Tucker, P. G., 1994, "Shroud Heat Transfer Measurements From a Rotating Cavity With an Axial Throughflow of Air," J. Turbomach., **116**, pp. 525–534.
[11] Long, C. A., and Tucker, P. G., 1994, "Numerical Computation of Laminar Flow in a Heated Rotating Cavity With an Axial Throughflow of Air," Int. J. Numer. Methods Heat Fluid Flow, **4**, pp. 347–365.
[12] Long, C. A., Morse, A. P., and Tucker, P. G., 1997, "Measurement and Computation of Heat Transfer in High Pressure Compressor Drum Geometries With Axial Throughflow," J. Turbomach., **119**, pp. 51–60.
[13] Owen, J. M., and Pincombe, J. R., 1979, "Vortex breakdown in a rotating cylindrical cavity," J. Fluid Mech., **90**, pp. 109–127.
[14] Jaluria, Y., 1980, "Natural Convection Heat and Mass Transfer," Pergamon, London.
[15] Owen, J. M., and Powell, J., 2004, "Buoyancy-Induced Flow in a Heated Rotating Cavity," ASME J. Eng. Gas Turbines Power, **128**, pp. 128–134.
[16] Smout, P. D., Chew, J. W., and Childs, P. R. N., 2002, "ICAS-GT: A European Collaborative Research Programme on Internal Cooling Air Systems for Gas Turbines," ASME Paper No. GT-2002-30479.
[17] Tian, S., Tao, Z., Ding, S., and Xu, G., 2004, "Investigation of Flow and Heat Transfer in a Rotating Cavity With Axial Throughflow of Cooling Air," ASME Paper No. GT2004-53525.
[18] Johnson, B. V., Lin, J. D., Daniels, W. A., and Paolillo, R., 2004, "Flow Characteristics and Stability Analysis of Variable-Density Rotating Flows in Compressor-Disk Cavities," ASME Paper No. GT2004-54279.
[19] Bohn, D., Dibelius, G. H., Deuker, E., and Emunds, R., 1994, "Flow Pattern and Heat Transfer in a Closed Rotating Annulus," J. Turbomach., **116**, pp. 542–547.
[20] Bohn, D., Deuker, E., Emunds, R., and Gorzelitz, V., 1995, "Experimental and Theoretical Investigations of Heat Transfer in Closed Gas Filled Rotating Annuli," J. Turbomach., **117**, pp. 175–183.
[21] Bohn, D., Edmunds, R., Gorzelitz, V., and Kruger, U., 1996, "Experimental and Theoretical Investigations of Heat Transfer in Closed Gas-Filled Rotating Annuli II," J. Turbomach., **118**, pp. 11–19.
[22] Bohn, D., and Gier, J., 1998, "The Effect of Turbulence on the Heat Transfer in Closed Gas-Filled Rotating Annuli," J. Turbomach., **120**, pp. 824–830.
[23] King, M. P., 2003. "Convective Heat Transfer in a Rotating Annulus," Ph.D. thesis, University of Bath, Bath, UK.
[24] Niemela, J. J., Skrbek, L., Sreenivasan, K. R., and Donnelly, R. J., 2000, "Turbulent Convection at Very High Rayleigh Numbers," Nature (London), **404**, pp. 837–840.
[25] Hollands, K. G. T., Raithby, G. D., and Konicek, L., 1975, "Correlation Equations for Free Convection Heat Transfer in Horizontal Layers of Air and Water," Int. J. Heat Mass Transfer, **18**, pp. 879–884.
[26] Lewis, T., 1999, "Numerical Simulation of Buoyancy-Induced Flow in a Sealed Rotating Cavity," Ph.D. thesis, University Bath, Bath, UK.
[27] Arakawa, A., 1996, "Computational Design for Long-Term Numerical Integration of the Equations of Fluid Motion: Two-Dimensional Incompressible Flow. Part 1," Comput. Phys., **1**, pp. 119–143.
[28] Sun, X., Kifoil, A., Chew, J. W., and Hills, N. J., 2004, "Numerical Simulation of Natural Convection in Stationary and Rotating Cavities," ASME Paper No. GT2004-53528.

Components Map Generation of Gas Turbine Engine Using Genetic Algorithms and Engine Performance Deck Data

Changduk Kong
e-mail: cdgong@mail.chosun.ac.kr

Jayoung Ki
e-mail: kjy2568110@nate.com

Department of Aerospace Engineering,
Chosun University,
#375 Seosuk-dong, Dong-gu,
Kwangju, Republic of Korea

In order to estimate the gas turbine engine performance precisely, the component maps containing their own performance characteristics should be used. Because the components map is an engine manufacturer's propriety obtained from many experimental tests with high cost, they are not provided to the customer generally. Some scaling methods for gas turbine component maps using experimental data or data partially given by engine manufacturers had been proposed in a previous study. Among them the map generation method using experimental data and genetic algorithms had showed the possibility of composing the component maps from some random test data. However not only does this method need more experimental data to obtain more realistic component maps but it also requires some more calculation time to treat the additional random test data by the component map generation program. Moreover some unnecessary test data may introduced to generate inaccuracy in component maps. The map generation method called the system identification method using partially given data from the engine manufacturer (Kong and Ki, 2003, ASME J. Eng. Gas Turbines Power, ***125****, 958–979) can improve the traditional scaling methods by multiplying the scaling factors at design point to off-design point data of the original performance maps, but some reference map data at off-design points should be needed. In this study a component map generation method, which may identify the component map conversely from some calculation results of a performance deck provided by the engine manufacturer using the genetic algorithms, was newly proposed to overcome the previous difficulties. As a demonstration example for this study, the PW206C turbo shaft engine for the tilt rotor type smart unmanned aerial vehicle which has been developed by Korea Aerospace Research Institute was used. In order to verify the proposed method, steady-state performance analysis results using the newly generated component maps were compared with them performed by the Estimated Engine Performance Program deck provided by the engine manufacturer. The performance results using the identified maps were also compared with them using the traditional scaling method. In this investigation, it was found that the newly proposed map generation method would be more effective than the traditional scaling method and the methods explained above.* [DOI: 10.1115/1.2436561]

Introduction

Generally, it must be agreed that not only will performance simulation of the gas turbine reduce the risk as well as the cost at the engine development phase but will also monitor the engine health for optimal maintenance in the operation phase.

The purpose of performance simulation is to estimate precisely the engine performance at various operational conditions using each component performance characteristic and thermodynamic relationship. Therefore, the correct engine performance simulation should satisfy the constraint that "each component's performance of the engine should follow its component's performance map." In other words, it is a very important condition for performance simulation that component maps to express precisely their characteristics should be obtained.

Generally, in order to simulate performance similar to a real engine, major component maps should be used through their component rig tests. However, component maps of most commercial engines are not released even to the purchaser because those are treated by the manufacturer's important propriety. Therefore most research engineers, who are studying the performance simulation of the gas turbine, use the scaled maps based on the design point from the known and limited component maps. But the scaling method is only available if it may use very similar maps to the real engine. If similar maps were not used to simulate the engine, the simulated performance may be very different from the real engine performance at off-design conditions.

In order to overcome the above mentioned difficulties, Kong and Ki [1] proposed a map generation method called the system identification method using partially given operation performance data from the engine manufacturer, and they could improve the traditional scaling methods by multiplying the scaling factors at design point to off-design point data of the original performance maps. However this technique has a limitation on generation of component maps for the engine performance simulation at various operational conditions. In addition to this, recently Kong et al. proposed a new map generation method obtained by applying genetic algorithms to some random test data, and therefore he had showed a possibility of composing the component maps from some random performance data [2].

When the engine customer purchases the engine, most engine makers provide a performance deck which can calculate only the engine performance output with input data but cannot see the

Contributed by the International Gas Turbine Institute of ASME for publication in the JOURNAL OF ENGINEERING FOR GAS TURBINES AND POWER. Manuscript received June 10, 2006; final manuscript received July 24, 2006. Review conducted by Dilip R. Ballal. Paper presented at the ASME Turbo Expo 2006: Land, Sea and Air (GT2006), Barcelona, Spain, May 8–11, 2006. Paper No. GT2006-90975.

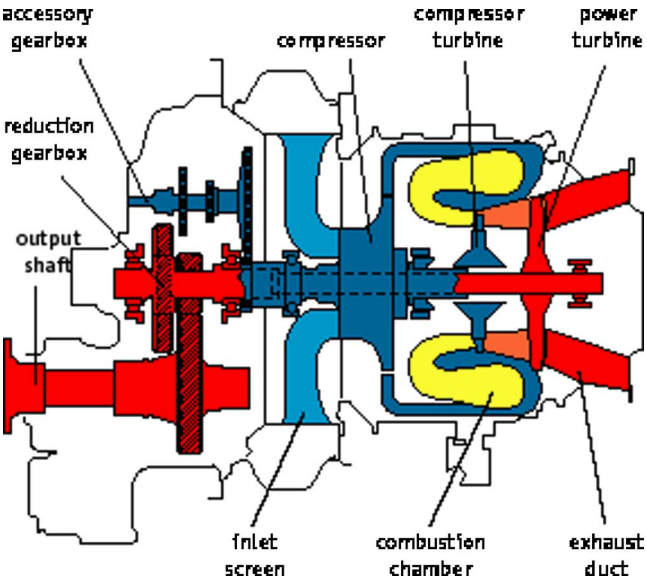

Fig. 1 Engine schematic diagram of PW206C turbo shaft engine

context of the program. In such cases, because sufficient performance data cannot be obtained if the performance deck would only be used, the user must develop a performance simulation program. Therefore, a component map generation method, which may identify a component map conversely from a performance deck provided by the engine manufacturer, is proposed in this study. Because this method can generate the component maps with engine manufacturer's partial performance data, maps similar to real engine maps may be obtained.

As a demonstration example for this study, the PW206C turbo shaft engine for the tilt rotor type Smart unmanned aerial vehicle (UAV) which has been developed by Korea Aerospace Research Institute (KARI) was used, and genetic algorithms (GAS) were used for identification of the component maps. Because each component's efficiency might not be found from analysis results of the performance deck, it was assumed by the proper value obtained from similar engine component data.

In order to evaluate the newly proposed map generation technique, the engine performance analysis results using the component maps obtained from the present method were compared with the analysis results using the traditional scaling method. As the engine performance analysis tool for evaluation of the proposed method, the commercial engine performance program GASTURB 9.0 was utilized [3].

Engine Specification

As previously mentioned, the PW206C turbo shaft engine is used to demonstrate the newly proposed component map generation method, because it was selected as a power plant for the tilt rotor type Smart UAV which has been developed by KARI. Its performance deck was provided by the manufacturer PWC. Figure 1 shows a schematic layout of this engine.

It was constructed with the gas generator composed of single stage centrifugal compressor, reverse flow annular type combustion chamber, and single stage compressor turbine, and the power section composed of single stage free power turbine, exhaust duct, reduction gear box, and output drive shaft.

The System Integration Group of the Smart UAV Project Center of KARI provided the operating flight range requirement for the propulsion system (see Table 1).

Table 2 shows the design performance data at maximum takeoff condition, which was provided by the engine manufacturer [4].

Table 1 Operating range of propulsion system required by System Integration Group of Smart UAV of KARI

Gas generator (rpm)	65–100%
Altitude (ft)	0–15000
Flight mach no.	0–0.4

Compressor Map Generation Using Gas

The GA is an adaptive heuristic search algorithm based on the evolutionary ideas of natural selection and genetics. As such it represents an intelligent exploitation of a random search used to solve optimization problems. Although the GA is randomized, it exploits historical information to direct the search into a better performance region within the search space. The basic technique of the GA is designed to simulate a required process for evolution in natural systems. In particular, the GA follows the principle of "survival of the fittest," which was first proposed by Charles Darwin. In other words, competition among individuals in scanty resource circumstances results in the survival of the fittest individual dominating over the weaker ones.

The GA simulates the survival of the fittest among individuals over consecutive generations for solving a problem. Each generation consists of a population of character strings that may be analogous to the chromosome. Each individual represents a point in a search space and a possible solution. The individuals in the population are then made to go through a process of evolution.

The GA is based on an analogy with genetic structure and behavior of chromosomes within a population of individuals using the following fundamental principles [5]:

1. Individuals in a population compete for resources and mates;
2. More successful individuals in each "competition" will produce more offspring than the poorly performing individual;
3. Genes, from "good" individuals propagate throughout the population so that a good pair will produce better offspring than their parents sometimes; and
4. Thus each successive generation will be suited more to its environment.

In this study, the compressor map is identified from the performance deck data using the genetic algorithms characteristics mentioned above. The characteristic map for the compressor can be expressed as the related functions such as the engine rotational speed, the pressure ratio, the mass flow function, and the isentropic efficiency. The mass flow parameter and the pressure ratio for constructing the component map can be calculated from the EEPP deck of the PW206C turbo shaft engine, and these component parameters can be corrected to the standard atmospheric condi-

Table 2 Design performance data provided by engine manufacturer

Variable	Values
Atmospheric condition	Sea level static standard condition
Mass flow rate (lbm/s)	4.418
Fuel flow rate (lbm/s)	0.087
Compressor pressure ratio	7.912
Turbine inlet temperature (R)	2258
Shaft horse power (hp)	560.8
SFC (lbm/hp h)	0.556
Gas generator rotational speed (100% rpm)	58900
Propeller rotational speed (100% rpm)	6120

tion. Here the mass flow function (MFP_N) may become a function of the pressure ratio (PR) and the rotational speed (N) as follows

$$MFP_N = aPR^3 + bPR^2 + cPR + d \quad (1)$$

Because the isentropic efficiency might not be found from analysis results of the performance deck, it was assumed as the proper value obtained from similar engine component data.

According to the proposed scheme in the present study, first the known compressor map similar to the study map at each rotational speed is scaled by the mass flow parameter, and the pressure ratio at each observed rotational speed obtained from the performance deck. The reason why the scaling is first performed with the known map is because it is much faster to obtain the unknown coefficients a, b, c, and d of Eq. (1) using the GAs through a rough design of the compressor map.

In the next step, two point data among the roughly scaled map and some data obtained from the performance deck are used as the reference data for the object function of the GAs.

In the present study, a simple GA is applied to find the unknown coefficients a, b, c, and d. After constructing n number of data sets from Eq. (1) through calculation at various conditions, the absolute value of the following object function is minimized

$$\text{Objetfuc} = \sqrt{\frac{\sum_{i=1}^{n} \text{error}_i^2}{n}} \quad (2)$$

where the "error" is defined as a percentage error about arbitrary a, b, c, and d, respectively. In this study, three reference data sets were used by function of the mass flow parameter and the compressor pressure ratio.

In the GAs, individuals are considered at two levels such as the phenotypic level and the genotypic level. An individual's phenotype is its value in the domain over which the objective function is defined, constituting a candidate setting for the decision variables of the problem. On the other hand, an individual's genotype is a representation of its phenotype at a lower level, analogous to the genetic sequences contained in biological chromosomes, which the computer stores and the GA manipulates. The phenotype is therefore encoded in the genotype, as a real encoding in this study. The random initialization is applied to produce the initial population, and in this study 1000 populations and four chromosomes were used. Individuals are evaluated via the objective function which defines the problem. The fitness of each individual is normalized by using the scaling windows scheme. Selection, crossover, and mutation are used to obtain the genetic operator for reproduction. Selection is the process of choosing individuals to participate in the production of offspring proportionally to their fitness. In this study, the gradient-like selection scheme is used, and the modified simple crossover technique is used to crossover operation. In mutation operation, the dynamic mutation method is applied. The crossover rate and the mutation rate were 0.9 and 0.1 in this study, respectively [6].

Figure 2 shows the calculation structure of the GAs applied to the present study [6].

Table 3 shows the reference data sets, which were obtained from EEPP and the scaled maps, for the 100% compressor rotational speed line.

Figure 3 and Table 4 shows that three mass flow parameter (mfp) values obtained by the GAs were almost the same as the reference data. Furthermore it shows that the absolute value of the object function error is finally converged to 0.583.

In this calculation, it was assumed that the number of generation is 600, and the range of unknown coefficients is from −1200 to 1200. The coefficients a,b,c,d were obtained at 70%, 80%, 90%, and 100% rpm, respectively, as shown in Table 5.

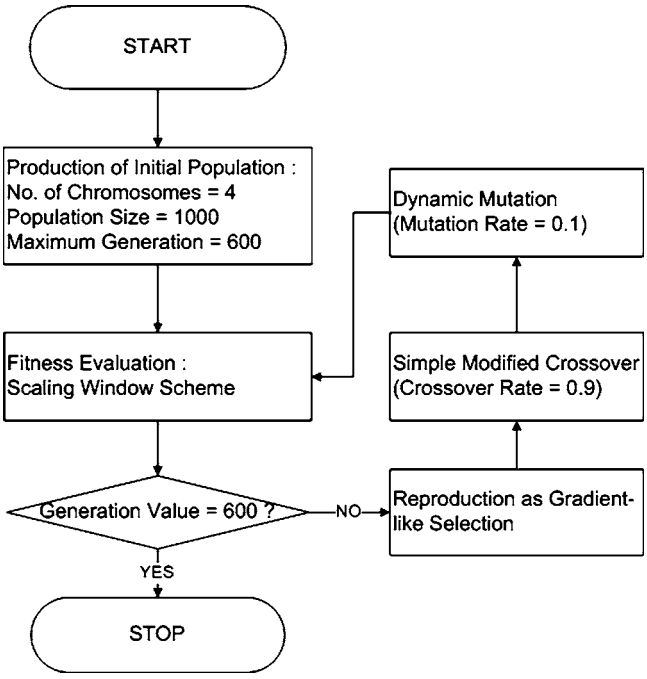

Fig. 2 Flow chart of genetic algorithms applied to the present study

Therefore the compressor map generated is finally derived as shown in Fig. 4.

Performance Analysis for Evaluation of the Generated Map

In order to evaluate the proposed component map generation scheme, steady-state performance analysis of the PW206C engine was performed at various operational conditions such as rotational speeds of the gas generator, altitudes, and flight Mach numbers using the commercial performance program GASTURB 9.0.

In this analysis, there are two calculations such as the result using the compressor map shown in Fig. 4 that is obtained from the present study and the result using the map by the traditional scaling method based on the design point performance data. These two calculation results were compared with some performance parameters such as mass flow rate, fuel flow rate, and shaft horse power of the performance deck "EEPP."

Because of the limited information by the performance deck, the component map of NASAGV61 for the compressor turbine and the map of NASAGV68 for the power turbine provided by the GASTURB for the compressor turbine and the power turbine were used by scaling [3].

Figure 5 shows the performance analysis results with varying gas generator rotational speed at sea level static condition.

According to performance analysis comparison results at each rotational speed of the gas generator, when the scaled compressor map provided by GASTURB is used, if the calculation point is far

Table 3 Reference data sets used for 100% compressor rotational speed

Data set No.	mfp	CPR	Obtained from
1	4.42	7.912	EEPP
2	4.30	7.965	Scaled Map
3	5.06	4.234	Scaled Map

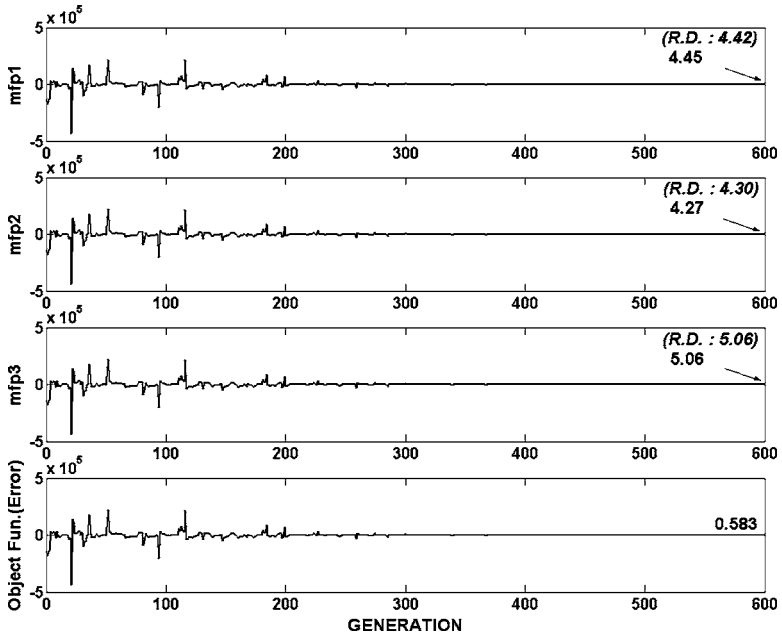

Fig. 3 MFP value and convergence of object function in growth of generation

away from the design point the error of the performance analysis results increases. This shows that the well-known traditional scaling method might be used very limitedly.

However the performance analysis results using the compressor map generated by the present study are well agreed on with the EEPP results at even far away off—design points from the design point.

Figure 6 shows the performance analysis results with varying altitude at 100% rpm and Mach number 0.

As shown in Fig. 6, the error of the performance analysis results using the scaled compressor map provided by GASTURB is greatly reduced relatively to the part load performance analysis results. The major reason for the error reduction might be that the analysis was performed at a design point operation region such as 100% gas generator rpm and static flight condition with only altitude variation. However the performance analysis results using the compressor map generated by the present study is much closer to the EEPP results compared to those using the scaled compressor map provided by GASTURB.

Table 4 Errors between reference data and GAs data

Data set No.	Reference (mfp)	Obtained by GAs	Error (%)
1	4.42	4.45	0.679
2	4.30	4.27	0.697
3	5.06	5.06	0
Objectfuc	—	—	0.583

Table 5 Unknown coefficients obtained by GAs

%RPM	*a*	*b*	*c*	*d*
60	−5.628	59.151	−205.21	240.498
70	−13.675	160.731	−626.19	815.302
80	−17.90	219.90	−895.80	1119.0
90	−15.00	187.60	−777.30	1077.40
100	−6.186	77.442	−322.41	454.25

Figure 7 shows the performance analysis results with varying flight Mach number at 100% rpm and 25,000 ft.

As shown in Fig. 7, both of the errors of the performance analysis results using the scaled compressor map provided by GASTURB and those using the compressor map generated by the present study are increasing at off-design points such as far away from the design point flight Mach number and altitude. However it is confirmed that the proposed scheme for the compressor map can reduce the error of the performance analysis results relatively to the traditional scaling map.

In the above investigation, the performance analysis results using both maps generated by the traditional scaling scheme and the newly proposed scheme in this study are the same as those of the performance deck, EEPP at the design point such as the 100% gas generator rpm and sea level static ISA condition. However when

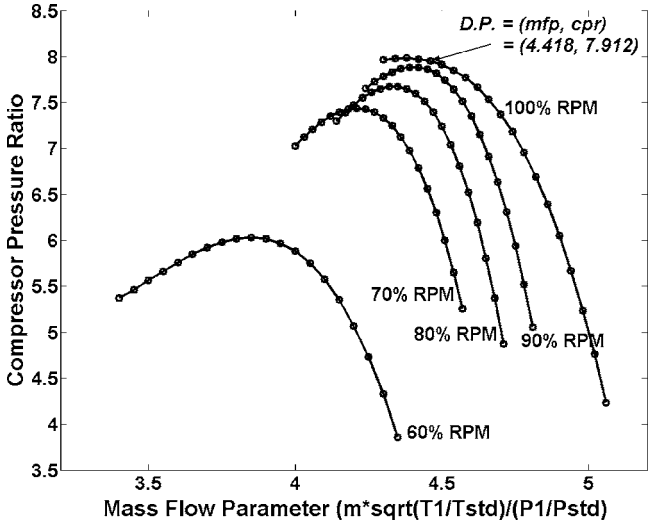

Fig. 4 Compressor map generated by GAs and some data from EEPP

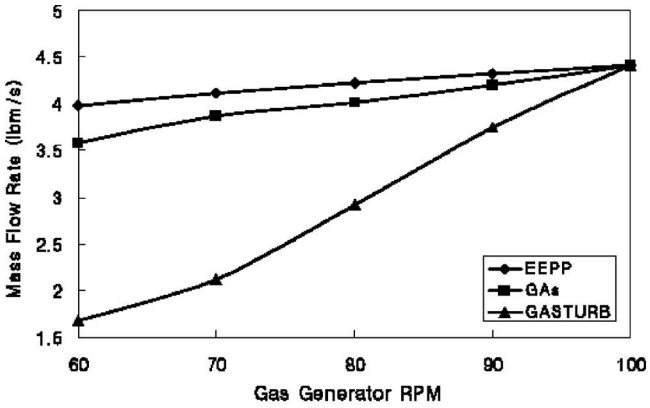

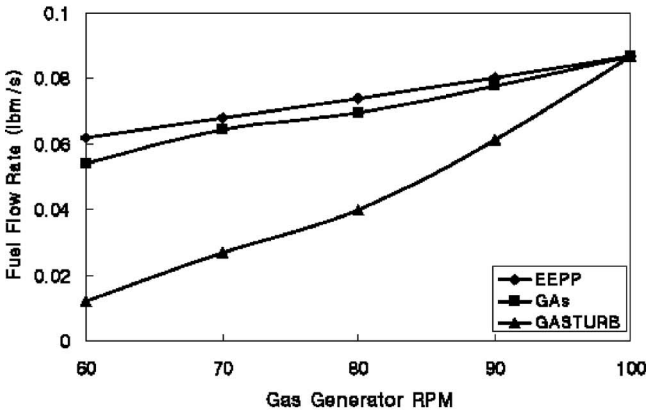

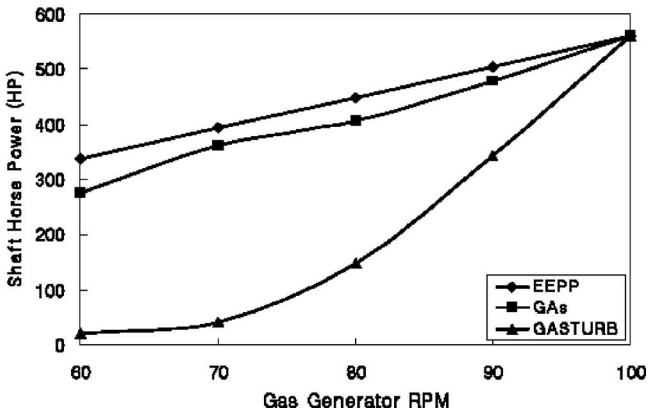

Fig. 5 Performance analysis results with varying gas generator rotational speed at sea level static standard atmospheric condition

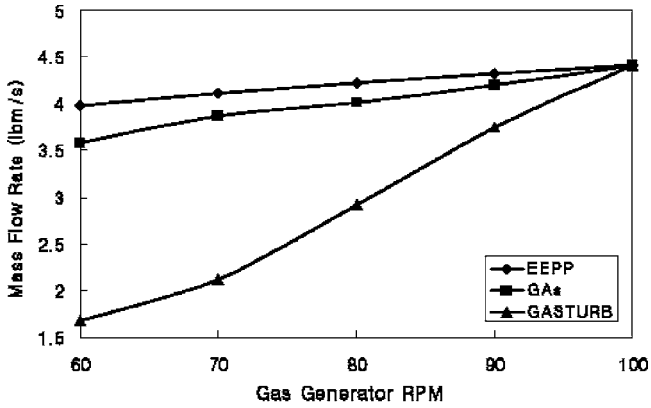

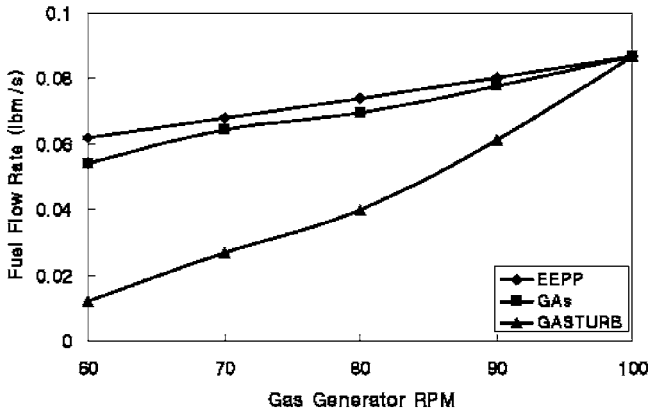

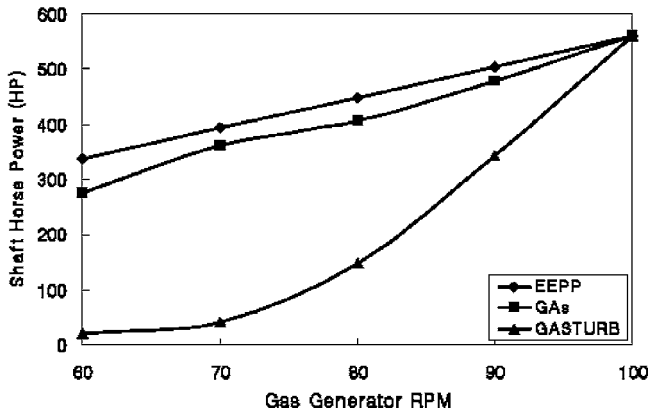

Fig. 6 Performance analysis results with varying altitude at 100% rpm and static standard atmospheric condition

the performance analysis is performed at remove operation conditions from the design point, in the case of use of the component map by the traditional scaling method, the error of the performance analysis results is greatly increased. On the other hand, if in the case of use of the compressor map generated by the proposed GAs scheme, the performance analysis results are closely met with those by the performance deck, EEPP. In other words, through this study, the availability of the proposed map generation method using the GAs can be confirmed.

Conclusion

A component map generation method, which can identify the component map conversely from performance calculation results of the performance deck EEPP provided by engine manufacture PWC, was proposed in this study.

The genetic algorithm was utilized to generate a compressor component map which might be available for searching the optimal target value from random space.

In order to obtain the precise component map, it is very important to build the object function. More precise results need more reference data, but this requires more time for calculation. Moreover because some data that can be taken from the performance deck at each gas generator rotational speed are greatly limited, additional reference data scaled from similar class engines were used.

By comparing the performance analysis results using the compressor map generated by the present study with those using the scaled compressor map provided by GASTURB, it is found that the component map obtained by the newly proposed present method can reduce the error of the performance analysis results.

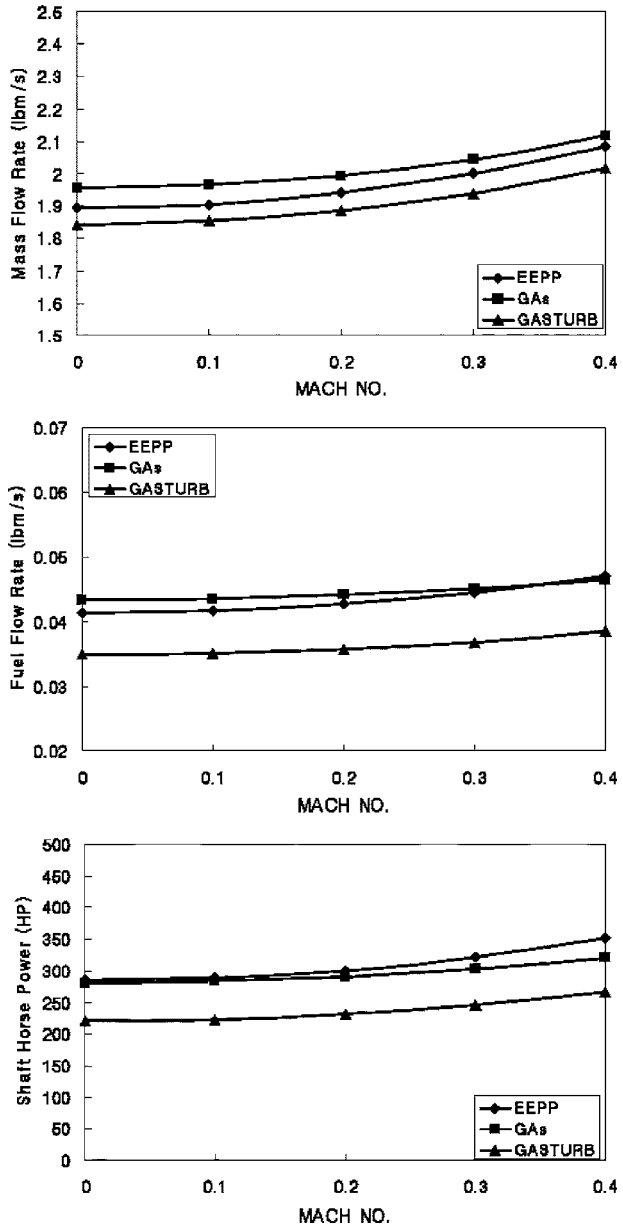

Fig. 7 Performance analysis results with varying flight Mach number at 100% rpm and 25,000 ft standard atmospheric condition

If the component maps for the compressor turbine and the power turbine may be generated with the same scheme as the compressor map presented in this study, the error of the performance analysis results may be further reduced. Moreover because the accuracy of the component map depends on available reference data, a criterion for selection of the useful reference data must be additionally found in the near future.

Acknowledgment

This study was supported by research funds from Chosun University, 2006.

Nomenclature

CPR = compressor pressure ratio
EEPP = engine estimated performance program
GAs = genetic algorithms
N = percentage nondimensional rotational speed
Objectfun = object function of genetic algorithms
PR = pressure ratio
rpm = revolution per minute
UAV = unmanned aerial vehicle
$a,b,c,d,$ = unknown coefficients of a function
error = percentage error for unknown coefficient
mfp = mass flow parameter
n = number of data sets

References

[1] Kong, C., and Ki, J., 2003, "A New Scaling Method for Component Maps of Gas Turbine Using System Identification," ASME J. Eng. Gas Turbines Power, **125**, pp. 958–979.
[2] Kong, C., Kho, S., and Ki, J., 2004, "Component Map Generation of a Gas Turbine Using Genetic Algorithms," ASME Paper No. GT2004-53736.
[3] Kurzke, J., 2001, "Manual GASTURB 9.0 for Windows—A Program to Calculate Design and Off-design Performance of Gas Turbines," Technical Report, Dachau, Germany.
[4] *EEPP (Estimated Engine Performance Program) Manual*, Pratt & Whitney, Canada.
[5] Moon, B. L., 2001, *Genetic Algorithms*, Dasung Press, Seoul, Korea.
[6] Jin, G. G., 2000, *Genetic Algorithms and Their Applications*, Kyowoo Press, Seoul, Korea.

Zixiang Sun
Fluids Research Centre,
School of Engineering,
University of Surrey,
Guildford, Surrey, GU2 7XH, UK
e-mail: Zixiang.Sun@surrey.ac.uk

Klas Lindblad
Volvo Aero Corporation,
Dept 7161,
SE-461 81 Trollhättan, Sweden
e-mail: Klas.Lindblad@volvo.com

John W. Chew
Fluids Research Centre,
School of Engineering,
University of Surrey,
Guildford, Surrey, GU2 7XH, UK
e-mail: J.Chew@surrey.ac.uk

Colin Young
Rolls-Royce plc,
PO Box 31,
Derby, DE24 8BJ, UK
e-mail: colin.young@rolls-royce.com

LES and RANS Investigations Into Buoyancy-Affected Convection in a Rotating Cavity With a Central Axial Throughflow

The buoyancy-affected flow in rotating disk cavities, such as occurs in compressor disk stacks, is known to be complex and difficult to predict. In the present work, large eddy simulation (LES) and unsteady Reynolds-averaged Navier-Stokes (RANS) solutions are compared to other workers' measurements from an engine representative test rig. The Smagorinsky-Lilly model was employed in the LES simulations, and the RNG k-ε turbulence model was used in the RANS modeling. Three test cases were investigated in a range of Grashof number $\mathrm{Gr}=1.87$ *to* 7.41×10^8 *and buoyancy number* $\mathrm{Bo}=1.65$ *to 11.5. Consistent with experimental observation, strong unsteadiness was clearly observed in the results of both models; however, the LES results exhibited a finer flow structure than the RANS solution. The LES model also achieved significantly better agreement with velocity and heat transfer measurements than the RANS model. Also, temperature contours obtained from the LES results have a finer structure than the tangential velocity contours. Based on the results obtained in this work, further application of LES to flows of industrial complexity is recommended.* [DOI: 10.1115/1.2364192]

1 Introduction

In order to achieve further improvements in turbomachinery internal air system design and component temperature prediction, an accurate knowledge of the flow and heat transfer behavior of the system is essential. Computational fluid dynamics (CFD) is now commonly used to support the design of many elements of the internal air system, but the prediction of buoyancy-affected flow in high-pressure compressor disk cavities has proven particularly difficult. Recognizing the need for progress in this area, experimental and computational research studies of convection in rotating cavities have been included in the European Union (EU) sponsored ICAS-GT (internal cooling air systems for gas turbines) and ICAS-GT2 research. Most of the work described here was undertaken as part of the ICAS-GT2 research program and arose from the recognition that LES methods may have distinct advantages over RANS methods for this problem, which is known to give rise to large scale unsteady flow structures. In LES the larger turbulent eddies are simulated, with smaller (subgrid scale) eddies being modeled. The subgrid scale modeling is dependent on the mesh size and (unlike RANS models) is designed to allow development of the larger resolved eddies that interact with the mean flow.

A number of relevant experimental studies have been reported using various experimental techniques, such as velocity measurement, heat transfer, and/or flow visualization. The geometries considered in the experiments include simply enclosed rotating cavities (for example, [1]), the idealized plane disc with an axial throughflow [2–4], as well as geometries that are more representative of engines [5–9]. Typically, the cavity flows were found to be highly three-dimensional (3D) and unsteady, with various flow structures, such as "radial arms," penetrating the cavities. Strong dependency on rotational speed, axial throughflow strength, and temperature gradients has also been identified. The disk heat transfer regimes can be broadly divided into three regimes: buoyancy dominated, axial throughflow dominated, and transitional. Heat transfer correlations are often related to rotational Rayleigh or Grashof numbers, through analogy to results for free convection in gravitational fields. Dependencies on Reynolds number and Rossby number ($\mathrm{Ro}=W/a\Omega$ where W is the axial throughflow bulk velocity and $a\Omega$ is the disk speed at the inner radius) have also been identified. In accordance with mixed convection under gravity, different regimes have been associated with different ranges of a buoyancy number ($\mathrm{Bo}=\mathrm{Ro}/[\beta\Delta T]^{0.5}$, where ΔT is the driving temperature difference and β is the coefficient of thermal expansion). The experimental correlations are inevitably based on particular geometries and consequently often display significant scatter. In these difficult experiments, measurement uncertainty can also be significant.

A number of numerical simulations have also been reported. For low rotational Grashof number convection in a sealed cavity with different uniform disk temperatures, Chew [10] found that an axisymmetric, steady, laminar flow model gave good agreement with heat transfer measurements. Bohn et al. [11,12] reported that laminar steady models gave "quite good" agreement with measurements for axially heated sealed rotating cavities at higher Grashof number, and also noted the tendency of the flow to become unsteady with radial heating. It is now widely accepted that negative radial density gradients cause flow unsteadiness analogous to Rayleigh-Benard convection under gravity. Long and Tucker [13] obtained laminar unsteady CFD solutions for a heated cavity with axial throughflow and claimed reasonable accord with an earlier experimental correlation for disk surface heat transfer. However, limitations of the laminar model were also recognized. Iacovides and Chew [14] applied a steady, axisymmetric RANS model to the high Rossby number "throughflow-dominated" regime and concluded that the calculated disk heat transfer was comparable to measured data, but firm conclusions could not be drawn due to experimental and modeling uncertainties. Other studies (for example, [15,16]) have been reported using conventional k-ε turbulence models in unsteady 3D simulations, but the

Contributed by the International Gas Turbine Institute (IGTI) of ASME for publication in the JOURNAL OF ENGINEERING FOR GAS TURBINES AND POWER. Manuscript received October 1, 2005; final manuscript received February 1, 2006. IGTI Review Chair: R. S. Abhari. Paper presented at the ASME Turbo Expo 2006: Land, Sea and Air (GT2006), Barcelona, Spain, May 8–11, 2006, Paper No. GT2006-90251.

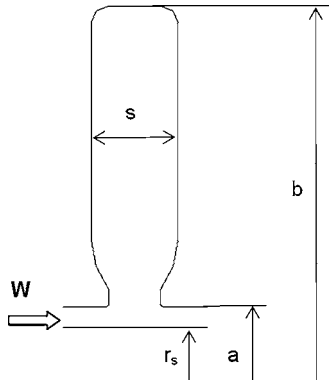

Fig. 1 Schematic illustration of the rotating cavity

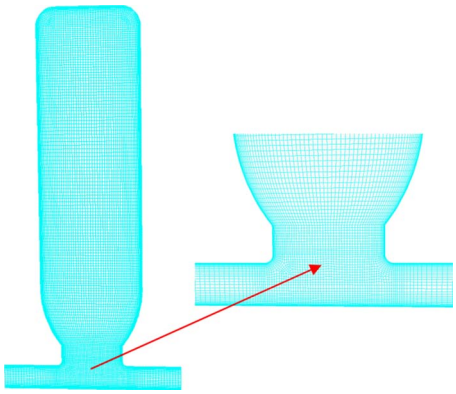

Fig. 2 Sectional view of the 120 deg mesh

information available in the open literature is limited. Wong's comparisons [16] with heat transfer measurements gave mixed results. In a recent publication, King et al. [17] applied a two-dimensional, unsteady, laminar CFD model to Rayleigh-Benard convection in a sealed cavity. The calculated heat transfer was higher than Bohn et al.'s [1] experimental correlation.

As a precursor to the present work, Sun et al. [18] studied high Rayleigh number free convection under gravity in a stationary cube and under centripetal force in a rotating cavity. Somewhat surprisingly, laminar, unsteady three-dimensional CFD models were found to give excellent agreement with accepted empirical correlations for the stationary cube, and with Bohn et al.'s sealed rotating cavity results. Large-scale flow structures were found at all conditions considered. Although the solutions showed turbulent characteristics, the smallest (Kolmogorov) turbulent length scales were not fully resolved, indicating that these calculations could be classed as large eddy simulations with the numerical viscosity contributing to turbulence energy dissipation. As the laminar unsteady/LES model would be unlikely to be suitable for modeling cavities with a central axial throughflow, the Smagorinsky-Lilly model was used in the present LES study. The results obtained are compared to both experimental data and with RANS solutions. The configuration studied experimentally by Long et al. [19] was selected for this study, as it was considered to be reasonably representative of engine operating conditions, and shroud heat transfer and cavity velocity measurements were available. As far as the authors are aware, this is the first application of LES to the problem of buoyancy affected rotating cavity flow with axial throughflow.

2 Model Definition

2.1 Geometry and Meshing. The geometry considered in this work is based on the rig described by Long et al. [19]. A detailed description of the test rig and experiments performed can be found in the thesis by Alexiou [20]. This test rig included a stack of model compressor disks forming four rotating cavities. The third cavity was selected for detailed investigation and is illustrated schematically in Fig. 1. The ratio of the inner and outer radii is $a/b=0.319$. The gap ratio between the cavity width s and the outer radius b of the cavity is $G=s/b=0.195$. A stationary shaft, radius $r_s=0.886a$ formed the inboard flow boundary. During the experiments, the disks and connecting cavity shroud were rotated at a constant speed, and heating was applied to the outer surface of the rotor.

The computational meshes were generated in GAMBIT [21] by first defining a 2D mesh in the plane of Fig. 1 and then extruding this circumferentially. Following Sun et al. [18], sector models were generated instead of a full 360 deg cavity to reduce computing requirements. Three sector models, with arc lengths of 45, 90, and 120 deg, as well as a full 360 deg model were generated. The mesh sizes for these models were constructed from 1.36, 3.24, 4.07, and 12.2 million hexahedral cells, respectively. Mesh spacing was such that the value of the mean dimensionless near-wall distance (y^+) was 0.6–1.0 in the LES calculations. The number of mesh cells in the wall boundary is typically 20. The expansion ratio of the boundary mesh cells is 1.1. Such a mesh resolution may be regarded as adequate from a general consideration of LES practice. Supporting evidence is also given by the mesh independence investigation conducted in the authors' previous study [18] for high Rayleigh number free convection under gravity in a stationary cube and under centripetal force in a rotating cavity, although mesh independence has not been demonstrated in the present investigation. A sectional view of the 120 deg mesh, which has 250 equally spaced points in the circumferential direction, is shown in Fig. 2.

2.2 Boundary Conditions and CFD Modeling. The FLUENT CFD code version 6.1 [22] was used in all the calculations presented here. The domain boundary was divided into rotating surfaces, stationary surfaces, inlet, and exit and circumferentially periodic sections, and appropriate conditions were imposed. The inlet mass flow rate and the outlet static pressure were defined in accordance with experimental data. In FLUENT LES computations, the stochastic velocity components of the inflow are accounted for by superposing random perturbations on individual velocity components, which are obtained in terms of the assigned turbulence intensity, mean flow velocity, and the Gaussian random function. In recognition of the strong mixing effects between the central axial throughflow and swirl flow in the upstream cavities, the inlet turbulence intensity was set to 20%. For two LES cases discussed later (tests 33 and 34), the inlet mean swirl velocity was specified from the tangential velocity profile at outlet obtained from a steady, axisymmetric RANS simulation of an annular pipe flow with similar geometry. For a third case (test 50), the preswirl was simply defined consistent with "solid-body" rotation at rotor speed, as this was thought to be a fair approximation to the steady RANS solution. No-slip conditions were imposed on all solid boundaries. Rotor temperatures were specified from interpolation of thermocouple measurements for the corresponding experiment, and the shaft was assumed to be adiabatic.

The LES models used the classic Smagorinsky-Lilly subgrid scale model [23,24]. It is generally thought that the model parameter C_s needs to be tuned from case to case. According to Sagaut [25], the model constant C_s represents a relationship between the mixing length associated with the subgrid scales and filtering cutoff length and may vary from 0.10 to 0.33. The theoretical value of C_s is 0.18 for isotropic, homogeneous turbulence. For the inertial subrange of an isotropic, homogeneous turbulence, Lilly [24] further derived a value of 0.23 for the constant C_s. Therefore, the constant $C_s=0.23$ was adopted after some initial experimentation. In the near-wall regions, the FLUENT LES model is reported to assume linear profiles when y^+ values are small (as is the case

Table 1 Three test cases investigated in the study

Test case	Re_z	Re_ϕ	Ro	Gr	Bo
33	4.41×10^4	1.04×10^6	1.46	2.32×10^8	3.0
34	4.35×10^4	1.99×10^6	0.75	7.41×10^8	1.65
50	1.53×10^5	1.03×10^6	5.05	1.87×10^8	11.5
50* (CFD)	1.53×10^5	1.29×10^6	4.04	2.92×10^8	9.21

here).

To compare to the LES simulations, a RANS calculation using the same mesh was also conducted. The RANS turbulence model employed in this calculation was a two-layer RNG k-ε/k-l model [26,22]. This model is appropriate for the fine near-wall mesh spacing used here and had been found to perform similarly to other two-equation RANS models for this class of flow.

An implicit pressure correction solution algorithm was employed, with second-order temporal and spatial discretization for both the LES and RANS solutions. Central spatial differencing was used for the LES calculations, and upstream differencing for the RANS calculations. The time step was set to 1.0 ms (corresponding, for example, to 0.02 times the revolution time $(2\pi/\Omega)$ for test 33). Solutions were obtained in the frame of reference rotating with the rotor; thus, relative velocities were smaller than they would have been in the absolute frame. Unsteady simulations were started from "part-converged" steady-state RANS solutions.

2.3 Flow Conditions. The three experimental test cases considered, tests 33, 34, and 50, are summarized in Table 1, with appropriate nondimensional parameters. The test cases were selected to cover most of the experimental range for the Buoyancy number with the rotational speeds being relatively low to minimize the mesh resolution requirements. The shroud Grashof number in Table 1 is defined as $Gr=\Omega^2\beta\Delta Tb(s/2)^3/\nu^2$, where ΔT is the shroud to inlet air temperature difference, and ν denotes kinematic viscosity. The Rossby number Ro and the buoyancy number Bo are as previously defined. Axial and rotational Reynolds numbers ($Re_z=Wl/\nu$, and $Re_\phi=\Omega b^2/\nu$, where l is the inlet hydraulic diameter) are also given for reference. Note that in the test 50 calculations, the operating pressure was set to a higher value in the CFD than in the corresponding experiment, resulting in $Gr=2.92\times10^8$ and Bo=9.21, whereas $Re_z=1.53\times10^5$ remained unchanged. Based on the results of other work and experimental evidence in this parameter range, it is judged that the higher operating pressure should not radically affect the Shroud Nusselt number predictions.

With regard to the computation speed, typically for a 120 deg model with a mesh of 4×10^6 cells, each time step takes ~4 min in CPU time when performed on a PC cluster with 20 2 GHz processors using low latency Myrinet networking. More powerful PC clusters and supercomputers will shorten the computation time.

3 Results

LES results are presented first, in the following three subsections. RANS and LES models are then compared in the section "Comparison of LES and RANS Models."

3.1 Shroud Heat Transfer. In the experimental investigation, heat fluxes were estimated from thermocouple measurements at the midaxial position on the shroud. Shroud heat transfer was therefore selected for initial evaluation and comparison of results. Figure 3 shows a time history for the calculated circumferentially averaged midshroud heat flux. This is typical of the LES results. Considerable variations occur even after circumferential averaging, and this indicates the presence of large-scale rotating structures in the flow. (Henceforth, the term average is used to refer to a circumferential average.) Note that the shroud Nusselt number used here is defined as

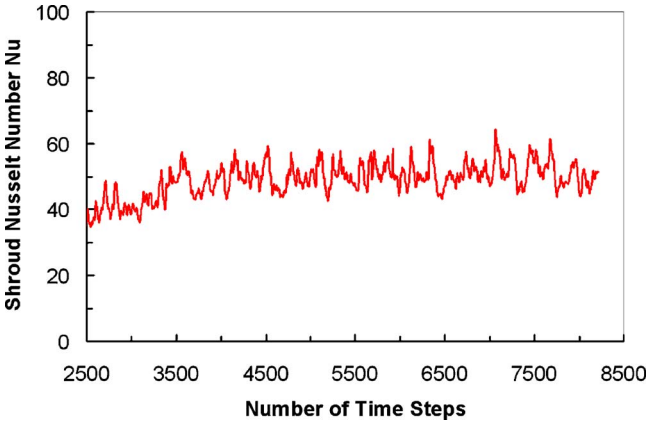

Fig. 3 Time history of shroud Nusselt number, LES, test 34, 120 deg model, $Gr=7.41\times10^8$, Bo=1.65

$$\mathrm{Nu}=\frac{q(s/2)}{k\Delta T} \tag{1}$$

where q is shroud heat flux.

Sensitivity to the angular extent of sector used in the model was examined for test 33, and results are shown in Fig. 4, which also presented the corresponding experimental data. The CFD results in Fig. 4 (and elsewhere when time-mean values are presented) are obtained from time averages of the monitored circumferentially averaged shroud heat flux data, typically based on 5000 time steps in the later part of the simulation, for which the time mean value had stabilized. (Henceforth, the term mean is used to denote the time average of the circumferential average monitors). For convection in a sealed rotating cavity, Sun et al. [18] showed that there was little difference in computed mean heat transfer between 45 deg sector and full 360 deg models. In the present results, some sensitivity is apparent, although there is little change in results obtained using the 120 and 360 deg models. The trend can be explained by the fact that the periodic conditions limit the appearance of larger flow structures, consequently reducing the heat transfer on the shroud. All further calculations reported here were conducted using the 120 deg sector model.

Underprediction of the shroud heat transfer is obvious in Fig. 4. Further comparisons are shown in Figs. 5 and 6. The experimental

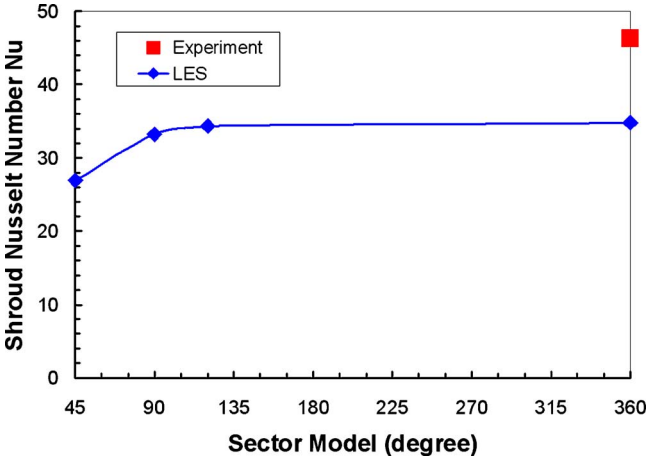

Fig. 4 Shroud mean Nusselt number for test 33 with sector and full annulus models, $Gr=2.32\times10^8$, Bo=3.0

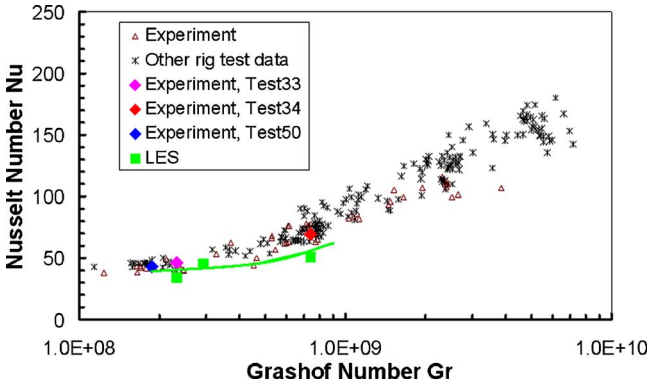

Fig. 5 Comparison of shroud mean Nusselt number between CFD and experiment, Nu versus Gr

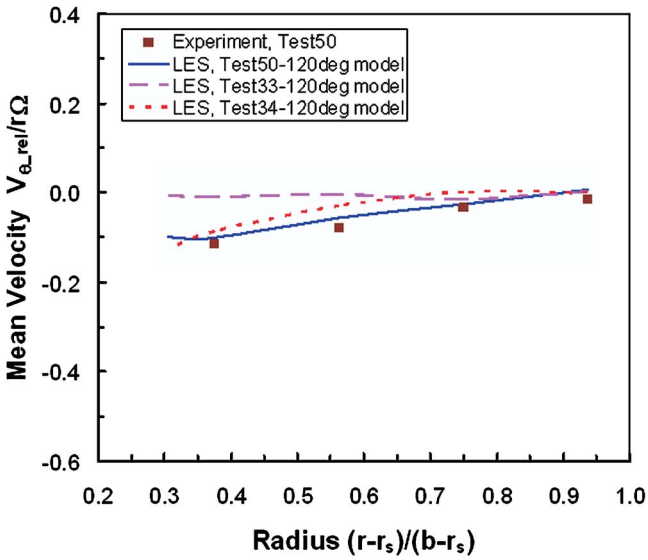

Fig. 7 Comparison of mean relative tangential velocity profiles on the midaxial plane

data presented in these figures and the choice of parameters are from Long and Tucker [7] and Long et al. [19]. In Ref. [19], accuracy of the shroud heat transfer results is estimated as approximately ±1% to ±6%, based on uncertainty in measured surface temperatures of ±0.2 K. For test 50, the displacement between the test and CFD 50* on the abscissae is due to a higher value of pressure used in the calculations, as explained above. Noting the experimental trends of shroud Nusselt number at these Grashof and buoyancy numbers, this is unlikely to have a serious effect on the conclusions drawn here. Tests 33 and 34 are at relatively low buoyancy numbers. Test 50 is at a higher buoyancy number, where the axial throughflow is relatively stronger. The difference in heat transfer between the LES calculations and the measurements is between −25% and 6%. For tests 33 and 34, LES underpredicts the heat transfer, whereas for test 50 the difference may well be within experimental uncertainty. Experimental trends are followed by the model predictions reasonably well, as far as can be deduced from this limited number of tests. Also, considering that these results may be sensitive to the near-wall LES modeling and the assumed boundary conditions, the degree of agreement achieved is considered encouraging.

3.2 Mean Velocity and Turbulence Characteristics. Experimental velocity measurements from this test rig have been reported by Alexiou [27]. These show that the mean flow is almost in "solid-body" rotation in the outer part of the cavity when buoyancy number is small. This behavior is captured in the present LES calculations for tests 33 and 34, as shown in Fig. 7. Here, the time mean and circumferentially averaged relative tangential velocity at the midaxial position divided by the disk speed is plotted against nondimensional radial position. A direct comparison of the tangential velocity profile with measurement for the test case test 50, for which Bo=11.5, is also given in this figure. It can be seen that the LES predictions are in good agreement with the measured data.

As previously noted, the predicted flow and heat transfer is essentially three-dimensional and unsteady, as observed in experiment. Although the existence of large-scale unsteady structures is widely accepted, the degree of turbulence that is present is less well established. Indeed, it has been hypothesized that regions of laminar flow may occur. Monitoring point histories of temperature and relative tangential velocity at the domain central point (CP) are shown in Figs. 8 and 9. Corresponding normalized turbulence energy spectra are shown in Figs. 10 and 11. The data shown are for test 34. Figures 10 and 11 include a −5/3 trend line to allow comparison to the expected trend for isotropic turbulence in the inertial subrange as observed in many experiments (see, for example, [28]). Clear irregular fluctuations can be seen in Figs. 8 and 9. The corresponding spectra in Figs. 10 and 11 show that the resolved turbulence energy spectra have regions where the slope is −5/3. Qualitatively, the spectra have the expected properties with

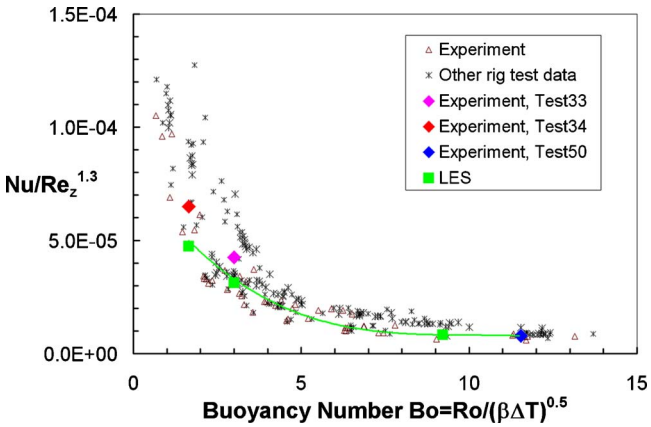

Fig. 6 Comparison of shroud mean heat transfer between CFD and experiment, Nu versus Bo

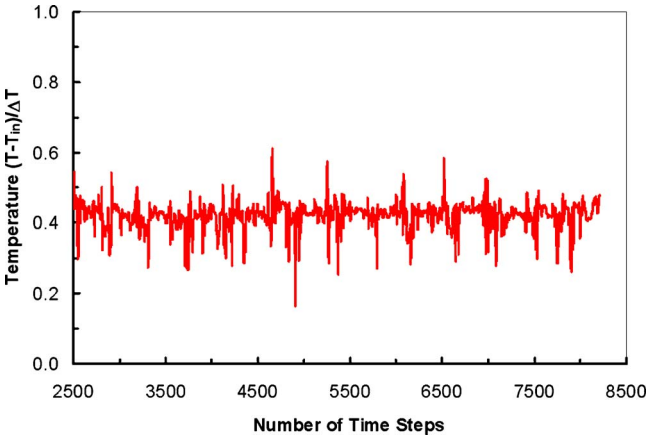

Fig. 8 Time history of temperature at the central point, LES, test 34, 120 deg model, Gr=7.41×10^8, Bo=1.65

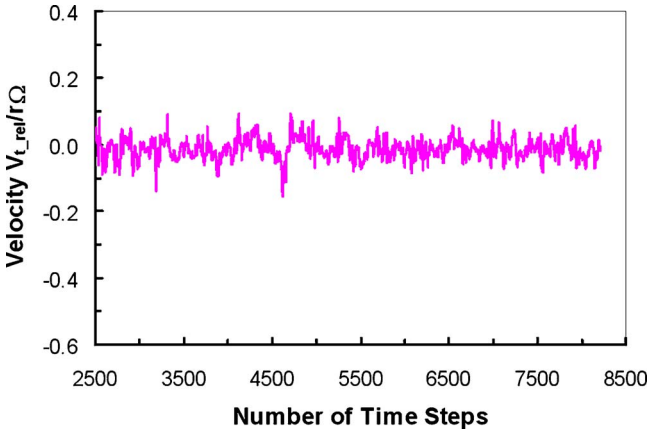

Fig. 9 Time history of relative tangential velocity at the domain central point, LES, test 34, 120 deg model, Gr=7.41×10^8, Bo=1.65

foreshortening of the −5/3 region at high frequencies due to dissipation associated with the sub-grid-scale turbulent viscosity and (possibly) numerical diffusion.

3.3 Flow Structures. Large-scale flow structures are revealed by instantaneous, midaxial contour plots of static temperature $(T-T_{in})/\Delta T$, relative tangential velocity $V_{t\_rel}/r\Omega$ and radial velocity $V_r/b\Omega$ in Figs. 12–14. The colder central throughflow can clearly be seen in Fig. 12. It may also be observed that hot and cold radial "arms" or "plumes" penetrate the cavity. Test 34, with the highest Grashof number and lowest buoyancy number, shows the strongest cold plume emanating from the throughflow jet. The flow structures for this case are possibly less ordered than at lower Grashof number. CFD 50*, corresponding to Test 50, with the highest buoyancy number, exhibits the sharpest definition of the jet boundary and has a generally cooler core flow within the cavity.

The instantaneous velocity contours in Figs. 13 and 14 show larger flow structures compared to those from the instantaneous temperature contours in Fig. 12. King et al. [17] noted even more pronounced differences between velocity and temperature contours in some of their 2D laminar-sealed cavity simulations, and

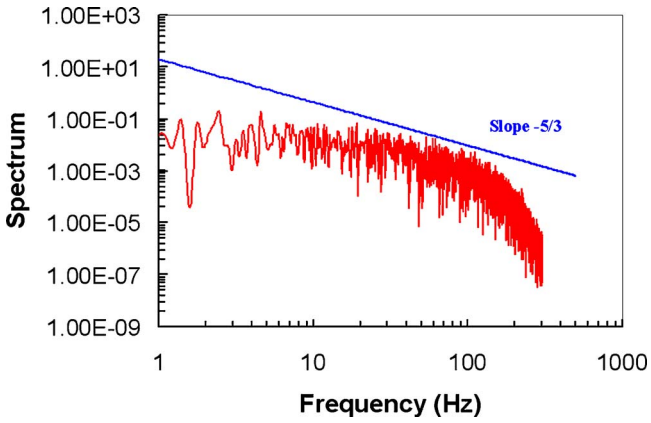

Fig. 10 Temperature fluctuation spectrum at the domain central point, LES, test 34, 120 deg model, Gr=7.41×10^8, Bo=1.65

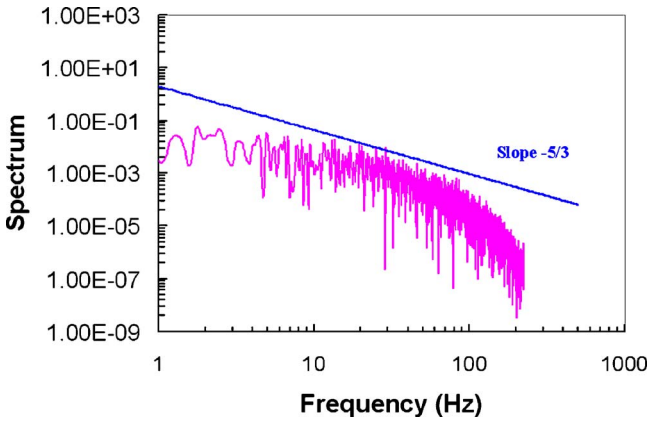

Fig. 11 Relative tangential velocity spectrum at the domain central point, LES, test 34, 120 deg model, Gr=7.41×10^8, Bo=1.65

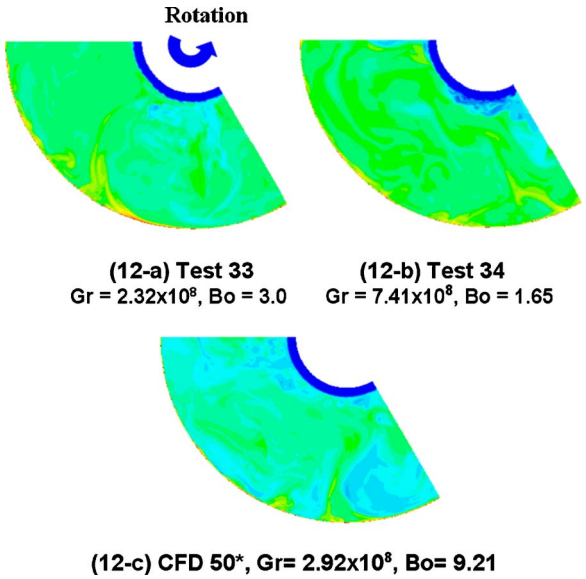

Fig. 12 Instantaneous temperature contours on the midaxial plane

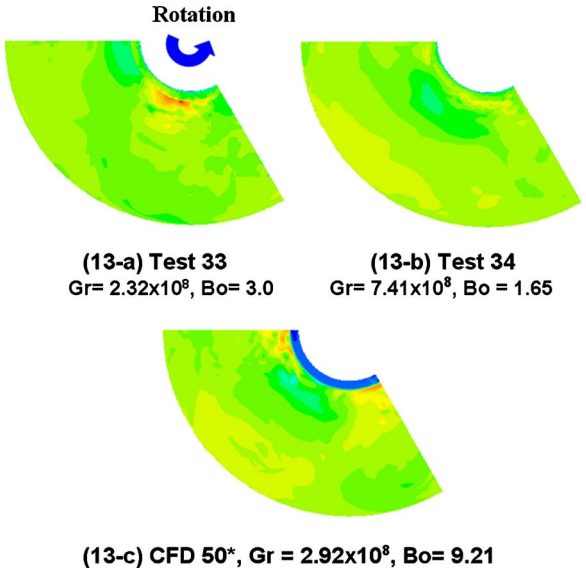

Fig. 13 Instantaneous relative tangential velocity contours on the midaxial plane

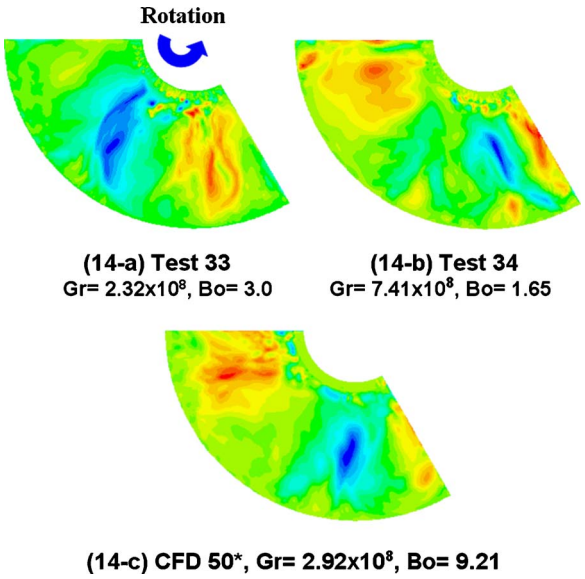

Fig. 14 Instantaneous radial velocity contours on the midaxial plane

attributed this to vacillation of the flow structure. Examination of transient behavior does confirm that the flow structure is continually changing.

3.4 Comparison of LES and RANS Models. For comparison to the LES results, an unsteady RANS calculation for test 50 was conducted using the RNG k-ε model with the 120 deg sector model and same mesh as for the LES calculation. As shown in Fig. 15, it was found that the RANS calculation gave much poorer predictions in terms of shroud heat transfer and tangential velocity profiles. The amplitude of shroud heat transfer fluctuations is also weaker in the RANS calculation. A further RANS calculation, using a coarser, 2×10^6 cell mesh for the full 360 deg domain, also gave similar results.

Comparison of the RANS prediction of turbulence viscosity to the LES sub-grid-scale turbulence viscosity at the cavity midaxial position shows the former to be around two orders of magnitude larger, as might be expected. This, of course, affects the mean flow field and its fluctuations, as confirmed by the center point tangential velocity results in Fig. 16. At first sight, the normalized turbulence energy spectra from the two calculations are perhaps surprisingly similar. Note, however, that it is difficult to identify clear trends from these data; longer simulation times are really required to reduce the statistical scatter and aliasing. This does of course raise interesting questions regarding the relationship between unsteady RANS calculations and LES as often practiced. In this case, the basic instability of a rotating flow with a negative radial density gradient makes some unsteadiness in the RANS solution inevitable, and the energy contained in large-scale fluctuations, must presumably be convected away or dissipated. The subgrid turbulence time scale in the LES calculation is given by L_{sgs}^2/ν_{sgs}, where L_{sgs} and ν_{sgs} denote the subgrid length and the subgrid turbulence kinematic viscosity, respectively. The subgrid turbulence time scale is of order 10 ms at the cavity center point, which is consistent with dissipation of turbulence energy (and departure from the $-5/3$ slope in Fig. 16) for frequencies greater than 100 Hz. The turbulence time scale for the RANS solution at the cavity center is ~3 ms. This corresponds to a frequency of ~300 Hz, and, compared to the LES result, gives a less convincing representation of the large scale turbulence.

Differences between large-scale flow structures presented in the LES and RANS results are more obvious in the instantaneous, midaxial plane temperature and velocity contours. For the RANS calculations, these are given in Fig. 17, which should be compared to Figs. 12–14. In the case of the RANS results, the structures appear sharper and better defined.

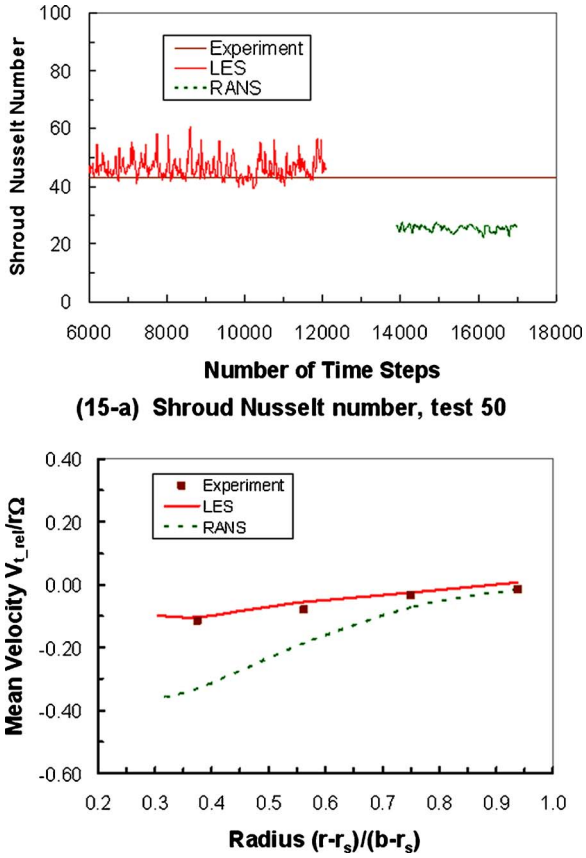

Fig. 15 Comparison of flow and heat transfer between LES, RANS, and measurement

4 Conclusions

Large eddy simulations of flow and heat transfer in a heated rotating cavity with a central axial throughflow have been obtained and compared to the available experimental data and unsteady RANS model calculations. The results of the LES models are very encouraging in that they were clearly in better agreement with the measured data than those obtained using a k-ϵ model. In the LES study, shroud heat transfer predictions were within 25% of measurements, and good agreement with tangential velocity measurements was demonstrated. However, the LES calculations are computationally demanding, to the extent that the present investigation was limited to just three experimental conditions. Further work is recommended, including investigation of more experimental conditions and careful consideration of the near-wall LES modeling and interaction of the flow in the central jet with the main cavity flow. As recent calculations on the UK national HPCx computing facility show, the capability for LES calculations is advancing rapidly and further development and application of LES for this class of problem is to be expected.

Both LES and RANS models reveal large-scale flow structures. These are better defined for the RANS calculations, and there is a higher level of fluctuation in the LES. Temperature contours from the LES results show a finer structure than the corresponding velocity contours. For both RANS and LES models, results from a 120 deg sector model gave very similar mean flow quantities to those obtained from a full 360 deg model. For smaller sector arc lengths, the suppression of the larger structures by the periodic boundary condition does affect the mean flow and heat transfer.

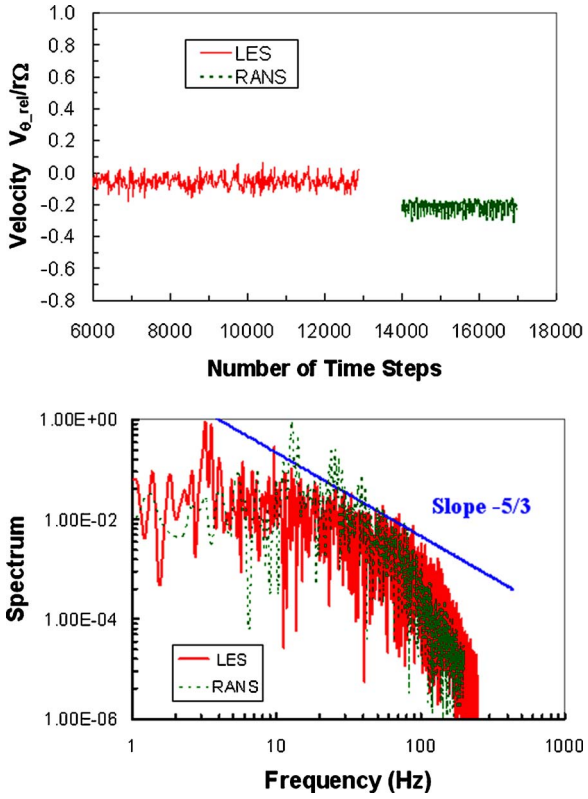

Fig. 16 Comparison of RANS and LES velocity predictions, test 50

From a more general point of view, it may be observed that the current study adds to the growing evidence that LES can be of use in flows of industrial complexity and offer advantages in terms of accuracy over unsteady RANS models. A review of progress in this area is beyond the scope of this paper, but examples may be found in the open literature. Further turbomachinery applications of LES are given by Viswanathan and Tafti [29], who illustrate LES applications for turbine blade internal cooling, and Sarkar and Voke [30], who show LES calculations for flow over a low-pressure turbine blade.

Acknowledgment

Most of this research was conducted within the EU project on Internal Cooling Air Systems for Gas Turbines 2 (ICAS-GT2). Funding from the industrial partners and the EU is gratefully acknowledged, as well as the experimental data from the University of Sussex. Thanks also go to Rolls-Royce plc and the Engineering and Physical Sciences Research Council UK Applied Aerodynamics Consortium for high-power computing for supporting the 360 deg model LES solution. Technical discussions with and comments from all of the ICAS-GT2 partners are also gratefully acknowledged, with particular thanks to Dr. Nick Hills, Professor Alan Robins, Professor Peter Voke and all colleagues at the TF-SUTC at the University of Surrey, and staff at Fluent Europe.

Nomenclature

a = inner radius of cavity
b = outer radius of cavity
Bo = buoyancy number $=\mathrm{Ro}/(\beta\Delta T)^{0.5}$
Cp = specific heat at constant pressure
G = gap ratio of cavity $=s/b$
Gr = shroud Grashof number $=\Omega^2\beta\Delta T b(s/2)^3/\nu^2$
l = hydraulic diameter of annular inlet
Nu = shroud Nusselt number $=q(s/2)/\kappa\Delta T$

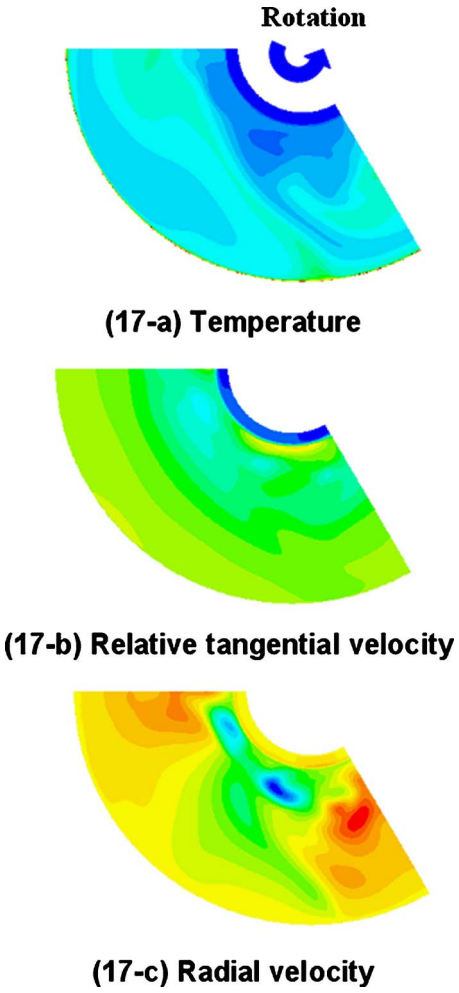

Fig. 17 Instantaneous temperature and velocity contours on the midaxial plane, test 50, RANS calculation

Pr = Prandtl number $=\mu Cp/\kappa$
q = shroud heat flux
r = radius
r_s = shaft radius
Ra = Rayleigh number = Pr Gr
Re_z = axial through flow Reynolds number $=\rho \mathrm{W} l/\mu$
Re_ϕ = rotational Reynolds number $=\rho\Omega b^2/\mu$
Ro = Rossby number $=W/a\Omega$
s = cavity width
T = temperature
T_{in} = cooling air temperature at inlet
T_{sh} = shroud wall temperature
W = bulk velocity
y^+ = normalized wall distance $=\rho \mathrm{u}_\tau \mathrm{y}/\mu$

Greek Symbols

β = coefficient of thermal expansion
ΔT = temperature difference between shroud and cooling air
κ = thermal conductivity
μ = dynamic viscosity
ν = kinematic viscosity $=\mu/\rho$
ρ = density
τ = stress tensor or wall friction stress
Ω = angular velocity of rotor

References

[1] Bohn, D., Deuker, E., Emunds, R., and Gorzelitz, V., 1995, "Experimental and

Theoretical Investigations of Heat Transfer in Closed Gas-Filled Rotating Annuli," ASME J. Turbomach., **117**, pp. 175–183.
[2] Farthing, P. R., Long, C. A., Owen, J. M., and Pincombe, J. R., 1992, "Rotating Cavity With Axial Throughflow of Cooling Air: Heat Transfer," ASME J. Turbomach., **114**, pp. 229–236.
[3] Kim, S. Y., Han, J. C., Morrison, G. L., and Elovic, E., 1993, "Influence of Surface Heating Condition on Local Heat Transfer in Enclosed Rotating Disks With Axial Throughflow," ASME Paper No. 93-GT-258.
[4] Bohn, D. E., Deutsch, G. N., Simon, B., and Burkhardt, C., 2000, "Flow Visualisation in a Rotating Cavity With Axial Throughflow," ASME Paper No. 2000-GT-280.
[5] Burkhardt, C., Mayer, A., and Reile, E., 1993, "Transient Thermal Behavior of a Compressor Rotor With Axial Cooling Air Flow and Co-rotating or Contra-rotating Shaft," AGARD CP527, pp. 21.1–21.9.
[6] Alexiou, A., Hills, N. J., Long, C. A., Turner, A. B., and Millward, J. A., 2000, "Heat Transfer in High-Pressure Compressor Gas Turbine Internal Air Systems: A Rotating Disc-Cone Cavity With Axial Throughflow," Exp. Heat Transfer, **13**, pp. 299–328.
[7] Long, C. A., and Tucker, P. G., 1994, "Shroud Heat Transfer Measurements From a Rotating Cavity With an Axial Throughflow of Air," ASME J. Turbomach., **116**, pp. 525–534.
[8] Owen, J. M., and Powell, J., 2004, "Buoyancy-Induced Flow in a Heated Rotating Cavity," ASME Paper No. GT2004-53210.
[9] Lin, J. D., Paolillo, R., Johnson, B. V., and Daniels, W., 2004, "Flow Characteristics and Stability Analysis of Variable-Density Rotating Flows in Compressor Disk Cavities," ASME Paper No. GT2004-54279.
[10] Chew, J. W., 1985, "Computation of Convective Laminar Flow in Rotating Cavities," J. Fluid Mech., **153**, pp. 339–360.
[11] Bohn, D., Dibelius, G. H., Deuker, E., and Emunds, R., 1994, "Flow Pattern and Heat Transfer in a Closed Rotating Annulus," ASME J. Turbomach., **116**, pp. 542–547.
[12] Bohn, D., Emunds, R., Gorzelitz, V., and Kruger, U., 1996, "Experimental and Theoretical Investigations of Heat Transfer in Closed Gas-Filled Rotating Annuli. II," ASME J. Turbomach., **118**, pp. 11–19.
[13] Long, C. A., and Tucker, P. G., 1994, "Numerical Computation of Laminar Flow in a Heated Rotating Cavity With an Axial Throughflow of Air," Int. J. Numer. Methods Heat Fluid Flow, **4**, pp. 347–365.
[14] Iacovides, H., and Chew, J. W., 1993, "The Computation of Convective Heat Transfer in Rotating Cavities," Int. J. Heat Fluid Flow, **14**, pp. 146–154.
[15] Smout, P. D., Chew, J. W., and Childs, P. R. N., 2002, "ICAS-GT: A European Collaborative Research Programme on Internal Cooling Air Systems for Gas Turbines," ASME Paper No. GT-2002-30479.
[16] Wong, L.-S., 2002, "Flow and Heat Transfer in Rotationally Induced Buoyancy Flow," D. Phil. thesis, University of Sussex.
[17] King, M. P., Wilson, M., and Owen, J. M., 2005, "Rayleigh-Benard Convection in Open and Closed Rotating Cavities," ASME Paper No. GT2005-68948.
[18] Sun, Z., Kilfoil, A., Chew, W. J., and Hills, N. J., 2004, "Numerical Simulation of Natural Convection in Stationary and Rotating Cavities," ASME Paper No. GT2004-53528.
[19] Long, C. A., Alexiou, A., and Smout, P. D., 2003, "Heat Transfer in H.P. Compressor Gas Turbine Internal Air Systems: Measurements From the Peripheral Shroud of a Rotating Cavity With Axial Throughflow," HEFAT2003, 2nd Intl. Conf. on Heat Transfer, Fluid Mechanics, and Thermodynamics, Paper No. LC1.
[20] Alexiou, A., 2000, "Flow and Heat Transfer in Gas Turbine H.P. Compressor Internal Air Systems," D.Phil. thesis, School of Engineering, University of Sussex.
[21] FLUENT Inc, http://www.FLUENT.com, Gambit User's Guide.
[22] FLUENT Inc, http://www.FLUENT.com, Fluent User's Guide.
[23] Smagorinsky, L., 1963, "General Circulation Experiments With the Primitive Subgrid-Scale Eddy Viscosity Model," Mon. Weather Rev., **91**, pp. 99–164.
[24] Lilly, D. K., 1966, "On the Application of the Eddy Viscosity Concept on the Inertial Subrange of Turbulence," NCAR Manuscript 123.
[25] Sagaut, P., 2002, *Large Eddy Simulation for Incompressible Flows*, Springer-Verlag, Heidelberg.
[26] Yakhot, A., Orszag, S. A., Yakhot, V., and Isreali, M., 1989, "Renormalization Group Formulation of Large-Eddy Simulation," J. Sci. Comput., **4**, pp. 139–158.
[27] Alexiou, A., 2002, "ICAS-GT2 Year 1 Progress Report. Work Package 2: Rotating Cavity Flow and Heat Transfer Experimental Investigation," Sussex research report.
[28] Pope, S. B., 2000, *Turbulent Flow*, Cambridge University Press, Cambridge, England.
[29] Viswanathan, A. K., and Tafti, D. K., 2005, "Large Eddy Simulation in a Duct With Rounded Skewed Ribs," ASME Paper No. GT2005-68117.
[30] Sarkar, S., and Voke, P. R., 2005, "Large-Eddy Simulation of Unsteady Pressure Over a LP Turbine Blade due to Interactions of Passing Wakes and Inflexional Boundary Layer," ASME Paper No. GT2005-6886.

A. G. Straatman
Department of Mechanical and Materials Engineering,
The University of Western Ontario,
London, Ontario, N6A 5B9 Canada
and Thermalcentric Inc., London, Ontario, Canada

N. C. Gallego
Metals and Ceramics Division,
Oak Ridge National Laboratory,
Oak Ridge, TN 37831

Q. Yu

B. E. Thompson

Thermalcentric Inc.,
London, Ontario, N6G 4K1 Canada

Characterization of Porous Carbon Foam as a Material for Compact Recuperators

Experiments are presented to quantify the convective heat transfer and hydrodynamic loss that is obtained by forcing water through blocks of porous carbon foam (PCF) heated from one side. The experiments were conducted in a small-scale water tunnel instrumented to measure the pressure drop and temperature rise of the water passing through the blocks and the base temperature and heat flux into the foam block. In comparison to similar porosity aluminum foam, the present results indicate that the pressure drop across the porous carbon foam is higher due to the large hydrodynamic loss associated with the cell windows connecting the pores, but the heat transfer performance suggests that there may be a significant advantage to using PCF over aluminum foam for extended surface convection elements in recuperators and electronic cooling devices. [DOI: 10.1115/1.2436562]

Introduction

Cast or foamed materials, such as porous carbon foam, typically have an open, interconnected void structure that enables fluid exposure to internal surface area and, thus, the potential for significant convective heat transfer. Therefore, such materials have the potential for wide application in energy exchange and heat recovery. Porous carbon foam (PCF) is produced by a process of foaming, carbonization, and subsequent graphitization of a carbon-based precursor material. PCF has a high effective (stagnant) conductivity (40–160 W/m K) [1] due to the high material conductivity of the graphitized carbon material (800–1900 W/m K). In comparison, similar porosity aluminum foams have effective conductivities of 2–26 W/m K, resulting from material conductivities of 140–237 W/m K (for various aluminum alloys) [2]. The high conductivity of the graphitized solid enables PCF to readily entrain heat into the solid structure of the foam to be swept away by passing fluid. Another significant advantage of PCF over aluminum or other metal foams is the high internal surface area that results from the foaming process. The internal surface area, which can be as high as 5000–50,000 m^2/m^3, serves to reduce the convective resistance thereby fostering energy exchange at the pore level. It is this combination of high material conductivity and high internal surface area that makes PCF attractive as a heat transfer material for both single and multiphase applications.

Although data is available quantifying the convective heat transfer in open cell metal foams (see, for example, [3–5]), there is relatively little information available on the fundamental characterization of porous carbon foam. Gallego and Klett [6] provided some of the first data on the pressure drop and heat transfer for PCF. Their study provides estimates of the influence of configuration on the heat transfer and pressure drop, but not enough detail was provided to assess the influence of porosity, pore diameter, and Reynolds number. Yu et al. [7] proposed a sphere-centered unit-cube geometry model to characterize the internal structure of PCF. The unit-cube model provides expressions for the internal and external surface area, and the effective (or stagnant) conductivity as a function of the porosity and the void diameter. Straatman et al. [8] recently considered the convective enhancement obtained by bonding a layer of PCF to a metal substrate and subjecting the layer to parallel airflow. Convective enhancements of 30–10% over that obtained from the flat plate alone were observed over the range of Reynolds numbers 150,000–500,000. The enhancements in this case were due to natural infiltration of air into the foam resulting in exposure to the internal surface area of the foam. For cases where the air is forced directly into the foam, the surface area exposure is much higher, and thus, convective heat transfer enhancement is expected to be much more significant.

The purpose of the present work is to further explore the heat transfer and pressure drop obtained when passing fluid through the internal structure of PCF. The motivation for this work is to develop expressions describing the pressure drop and pore-level heat transfer such that PCF can be considered in design applications such as recuperators and electronic heat sinks. Experiments are described that establish the flow and convective heat transfer obtained by forcing water through PCF specimens of different porosity and pore diameter. Results are presented to show the hydrodynamic and thermal performance of the PCF specimens, and a formulation is presented that produces universal results for the Nusselt number. The present results are also compared to similar results for aluminum foams. Though experiments using a gas would be more directly relevant for recuperator applications, the present experiments still effectively show the difference in thermal and hydraulic performance of available PCFs.

Carbon Foam Specimens

Three different PCF specimens have been considered in the present work. The geometric properties and effective thermal conductivities of the specimens are summarized in Table 1. Scanning electron microscope (SEM) images of the foam specimens are given in Fig. 1. On the basis of the large pore diameter and high effective conductivity, the tabulated data indicates that the POCO^{TM} foam has the best combination of properties for convective heat transfer. Conversely, the 218-3 foam appears to have the poorest combination of geometric and thermal properties. The images in Fig. 1 indicate that there are also significant differences between the foams in terms of the size of the cell windows connecting the pores. The cell windows provide the interconnectivity

Contributed by the International Gas Turbine Institute of ASME for publication in the JOURNAL OF ENGINEERING FOR GAS TURBINES AND POWER. Manuscript received June 12, 2006; final manuscript received June 28, 2006. Review conducted by Lee Langston. Paper presented at the ASME Turbo Expo 2006: Land, Sea and Air (GT2006), Barcelona, Spain, May 8–11, 2006. Paper No. 90598

Table 1 Summary of properties for the carbon foam specimens tested

Specimen	Porosity (%)	Average void diameter (μm)	β[a] (m^2/m^3)	k_{eff} (W/m K)
219-3	86	350	6850	72
218-3	88	400	5640	61
POCO™	82	500	5240	120

[a]As obtained from the unit-cube geometry model [7].

between the voids and thus afford access to the internal surface area of the foam. From the point of view of heat transfer, it is best to have small cell windows to maximize the internal surface area available for convection. However, from the point of view of flow into the foam, small cell windows will lead to much higher pressure drops due to the hydrodynamic loss associated with rapid contraction/expansion through the cell windows. Thus, the most *open* foam will undoubtedly yield the lowest pressure drop; however, it may not necessary yield the highest convective heat transfer because of the lower internal surface area. Something the SEM images do not show, because of the high magnification, is the small porosity gradient that can occur in the foaming process. The gradient is due to gravity and is typically only in the foaming (vertical) direction; however, the images in Fig. 1 clearly show lateral nonuniformity, particularly in the 219-3 foam. For the present experiments, test specimens were machined such that the (gravity) gradient was aligned with the vertical coordinate of the channel. Samples of foam were cut such that the nominal plan dimensions were 50×50 mm, and the nominal thickness was 6 mm, to minimize gradient effects. Approximately 0.2 mm was added to each nominal dimension so that the foam specimens could be pressed into the test section to avoid fluid bypass.

Experiments

Experiments have been conducted in a small-scale test rig to measure the heat transfer and pressure drop obtained by passing water through specimens of PCF. The test setup, shown in Fig. 2, consists of a channel with a water inlet and outlet, a heating element, and instrumentation to measure the flow rate, the heat input, the fluid pressure drop and temperature across the foam specimen (from position 1 to 2), and the base temperature of the heating element. The flow channel was 50 mm wide by 6 mm high. Foam specimens, described in the previous section, were pressed into the test section of the channel. As shown in Fig. 2, the upper 50×50 mm surface of the foam was pressed against the heating element and the lower surface was pressed against a phenolic composite wall, which was insulated to avoid heat loss. As such, the foam specimens represent 50×50 mm cross section extended surfaces heated from one side.

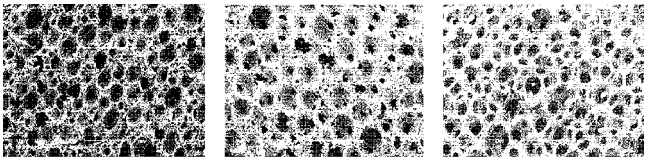

Fig. 1 Scanning electron microscope images of the porous carbon foam specimens tested

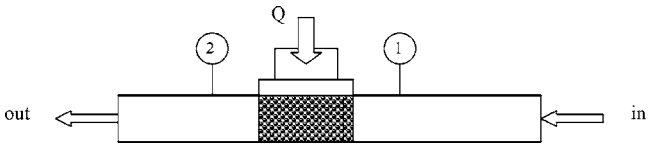

Fig. 2 Schematic of experimental setup showing the position and orientation of the carbon foam, the fluid inlet and outlet, and the heat input

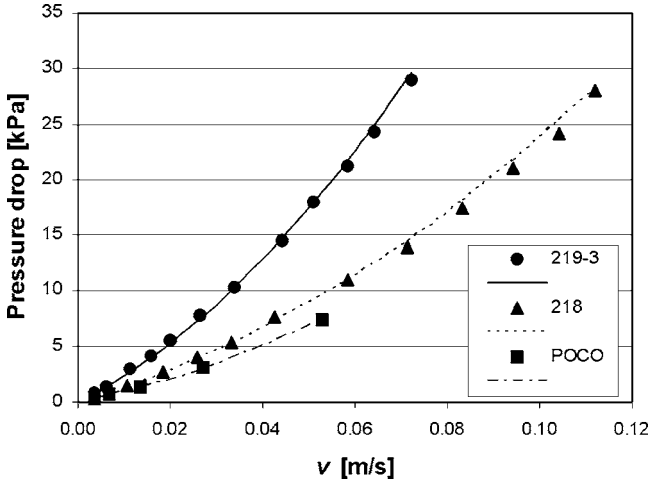

Fig. 3 Plot showing the pressure drop as a function of Reynolds number for the three foam specimens considered. The symbols are measured data and the curves are generated from Eq. (1), with the values of permeability and form drag summarized in Table 2.

The specimens were subjected to a range of water flow rates and power densities to quantify variations of pressure drop and heat transfer on the foam structure, characterized by porosity ε and void diameter D_p. For each foam specimen, tests were initially run without heating to establish the pressure drop as a function of flow for ambient (cold) conditions. The pressures were monitored very carefully to ensure that the reported results were for steady-state conditions. The tests were then repeated for several power densities to establish the heat transfer under different flow conditions.

Results and Discussion

The pressure data are used to obtain permeability and form drag coefficients so that the classical Darcy-Forchheimer law for porous media can be used to describe pressure losses

$$\frac{\Delta P}{L} = \frac{\mu}{K} v + \frac{c_f}{\sqrt{K}} \rho v^2 \tag{1}$$

Here, ΔP is the pressure drop across the foam specimen, L is the length of the specimen along the flow direction (50 mm in the present work), v is the filter (or average channel) velocity, and K and c_f are the permeability and Forchheimer (form drag) coefficient. The permeability and form drag coefficients are evaluated simultaneously by considering the whole flow range at the tested conditions.

Results for the pressure drop as a function of v are shown in Fig. 3 for the three foam specimens considered. Figure 3 shows measured pressure drops in symbolic form and curves generated using Eq. (1) with the permeability and form drag coefficients established and shown in Table 2. It is clear from Fig. 3 and Table 2 that the permeability and, thus, the pressure drop is very different for the three specimens tested, with the 219-3 foam having the highest fluid pressure drop and POCO having the lowest. As suggested in the previous section, the pressure drop is strongly affected by the pore diameter and perhaps more importantly, the size of the cell windows connecting the pores, due to the hydrodynamic loss associated with the sudden contraction/expansion. Al-

Table 2 Summary of permeability and Forchheimer coefficients for the carbon foam specimens tested

Specimen	Permeability K (m^2)	Forchheimer coefficient c_f
219-3	2.41×10^{-10}	0.7444
218-3	4.46×10^{-10}	0.4548
POCO	6.13×10^{-10}	0.4457

though the results show the expected trend, it is difficult based on the present result to assess the impact of pore diameter and cell window size separately.

The results for pressure drop can be compared, in terms of permeability, to similar results obtained for aluminum foams. Boomsma and Poulikakos [4] evaluated the permeability of 6101 aluminum alloy foams with and without compression. The uncompressed foam had porosities in the range of 92–93% and internal surface areas of 820–2700 m^2/m^3, whereas the compressed foams had porosities in the range of 66–88% and internal areas two to four times higher than those noted above. In comparison to the POCO foam, which has the lowest pressure drop among the foams tested herein, similar-porosity 6101 compressed aluminum foam has a permeability approximately three times higher, indicating that it is much easier to pass a fluid through the aluminum foam. This is largely due to the difference between the internal structures of the aluminum and PCF foams. The aluminum foam is comprised of thin fused strands and large open cell windows, but relatively little internal surface area. The PCF is comprised of spherical voids and small(er) cell windows, but a larger amount of internal surface area. Since the low permeability of the current PCF is due to the large hydraulic loss associated with the cell windows that link the spherical voids, it is of interest to modify the foaming process for PCF to provide larger and smoother cell windows to lower the hydraulic loss.

Heat transfer results were obtained by considering several different heat inputs for a particular fixed flow rate, and then repeating the process for several different flow rates. Since the temperature of the heater base was a consequence of the particular flow/heating condition, it is not possible to plot the heat input as a function of velocity for a given temperature difference between the fluid inlet and the heater base. Instead, the measured heat input and temperature difference were used to calculate the thermal resistance for a given flow rate

$$R = \frac{1}{n}\sum_{i=1}^{n}\frac{\Delta T_i}{Q_i} \tag{2}$$

in degrees Kelvin per watt, where ΔT is the temperature difference between the heater base and the fluid inlet, Q is the heat input in watts, and n is the number of heating conditions for the flow rate under consideration. Because the thermal resistance is a function of the Reynolds and Prandtl numbers, it is essentially constant for all of the heating conditions at a given flow rate. Figure 4 shows the results of thermal resistance as a function of filter velocity for all of the conditions considered. The plot indicates that the POCO foam has the lowest thermal resistance followed by 218-3 and 219-3. Figure 4 is important because it alludes to the difference in thermal effectiveness of equal-sized PCF specimens of different geometric and thermal properties. Figure 4 does not, however, provide universal information about the foam specimens that can be used in design applications. The required information can be generated from the data shown in Fig. 4, but care must be taken to ensure that the scaled data is universally applicable.

The heat transfer data are used to form the Nusselt number, which is obtained by

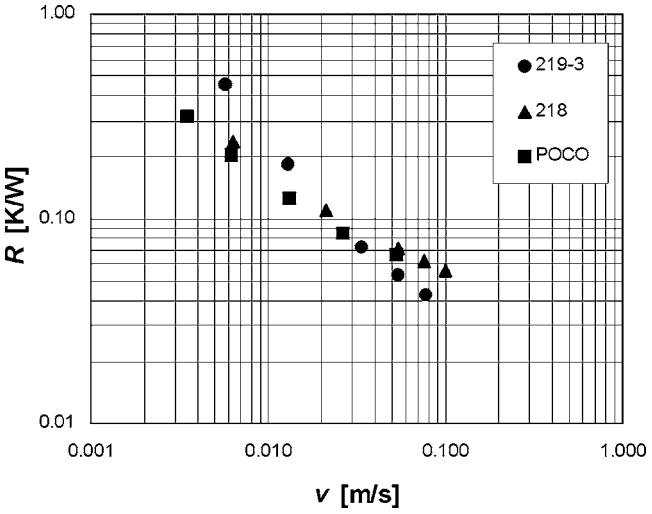

Fig. 4 Plot showing the thermal resistance as a function of the filter velocity v for the foam specimens tested

$$\mathrm{Nu} = \frac{h_{sf}D}{k_{fa}} = \frac{D}{k_{fa}A}\frac{q_{\mathrm{avg}}}{\Delta T} \tag{3}$$

where h_{sf} is the heat transfer coefficient at the pore level, D is a length scale, q_{avg} is the heat transfer obtained from the power applied to the heater (and from an energy balance on the fluid), k_{fa} is the thermal conductivity of the fluid evaluated at the average fluid temperature, A is an area, and ΔT is a temperature difference (either the mean temperature difference between the heated base and the fluid inlet or the log-mean temperature difference). As suggested, the length and area scales can be based on different variables and the virtues of those mentioned will be discussed in terms of the current results. In the present treatment, the length scale D is based on either the equivalent particle diameter of the foam D_e or the hydraulic diameter of the channel. The equivalent particle diameter is the solid particle diameter that preserves the interior surface area of a single spherical void and is obtained using $D_e = 6(1-\varepsilon)/\beta$ (see [7]). The hydraulic diameter is obtained as $D_{\mathrm{hyd}} = 4A_{\mathrm{chan}}/P$, where A_{chan} is the cross-sectional area of the channel and P is the wetted perimeter. The area in Eq. (2) is either the effective heat transfer surface area or the heated base area of the foam sample. The effective surface area is obtained as $A_{\mathrm{eff}} = \eta A_f + \varepsilon A_b$, where η is the equivalent microfin efficiency of the foam obtained using the Taylor model [9], A_f is the interior wall surface area of the foam specimen obtained from $A_f = \beta V$, where β is the area factor [7] and V is the volume of the specimen, and A_b is the heated based area of the foam; $A_b = 50\times50 = 2500$ mm^2 for the present case.

The thermal performance of the foam specimens is shown in terms of the Nusselt number in Figs. 5 and 6; the Reynolds number is defined as $\mathrm{Re} = \rho v D/\mu$, where ρ is the density of the fluid, v is the channel bulk velocity, and μ is the dynamic viscosity of the fluid. Figure 5 follows the approach described by Boomsma et al. [5] wherein the Nusselt number is devised using the hydraulic diameter D_{hyd}, the heated base area A_b, and the temperature difference between the heated base and the fluid inlet and plotted as a function of the filter velocity. In Fig. 6, the Nusselt number is formulated using the equivalent particle diameter D_e, the effective area A_{eff} and the log-mean temperature difference, and is plotted as a function of the Reynolds number based on D_e. Although the figures produce a similar picture in terms of the thermal performance of the foam specimens, care must be taken in interpreting the utility of the different formulations. Because of the method used to produce Fig. 5, the resulting Nusselt number cannot be considered constant and there is an inherent difficulty with ex-

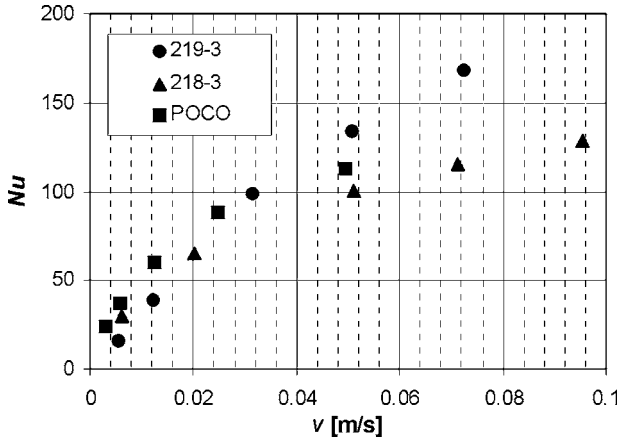

Fig. 5 Plot showing the Nusselt number (based on D_{hyd} and A_b) as a function of the filter velocity v

tending the results to different sized foam blocks. For example, doubling the foam thickness while maintaining the heated base area increases the hydraulic diameter and thus reduces the convective coefficient. This leads to the prediction that for a given base area and temperature difference, the heat transfer is reduced with increasing foam thickness. Consider also the effect of increasing the heated length of the foam while maintaining the thickness (and hydraulic diameter). In this case, the Nusselt number remains constant and the heated base area increases linearly with increased length. For a given temperature difference, this suggests that the heat transfer increases linearly with increased heated path length, which is also not physically correct. Thus, the formulation adopted from Boomsma et al. [5] and used to produce Fig. 5 does not characterize the results in a universally applicable way.

The formulation used to produce Fig. 6 removes the dependence of the Nusselt number on the physical dimensions of the foam blocks tested and does, therefore, provide universal results. For example, increasing the thickness of the foam increases the internal surface area, but reduces the equivalent micro-fin efficiency. Thus, using the effective surface area A_{eff} in Eq. (3) removes the dependence of the Nusselt number on the thickness of foam used. The dependence of the Nusselt number on the heated length is also removed by using the log-mean temperature difference. As such, the Nusselt number values presented in Fig. 6 can be considered constant for the given flow condition. Another advantage of this formulation is that the Nusselt and Reynolds numbers are formed in terms of the equivalent particle diameter, which characterizes the internal structure of the foam.

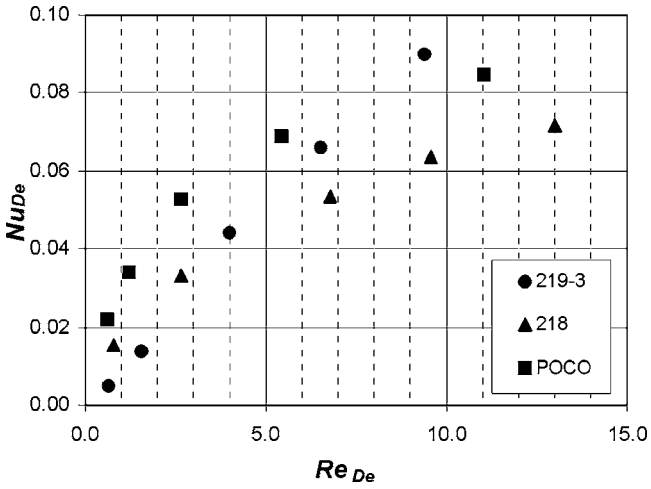

Fig. 6 Plot showing the Nusselt number as a function of Re (based on D_e and A_{eff}) for the three foams considered

Turning now to the thermal performance of the different foams, Figs. 5 and 6 both show POCO to be the superior foam followed by 219-3 and 218-3. Differences between the foams can be reconciled by considering the properties listed in Table 1 and the SEM images given in Fig. 1. The 219-3 and 218-3 foams have a similar effective conductivity, but 219-3 has significantly more internal surface area and thus a better capacity to remove energy that is conducted in. POCO foam has a substantially higher effective conductivity than 219-3 and thus a higher microfin efficiency. In this case, the thermal performance of POCO is considerably higher despite its smaller internal surface area. On the basis of the present measurements, and considering both the hydrodynamic and thermal characteristics, the POCO foam is considered to perform best.

Comparisons to the measured performance of 6010 aluminum foam [5] can be made by considering the data in Fig. 6. The comparisons, which are not shown explicitly in this paper, indicate that POCO foam is slightly better than compressed aluminum in terms of thermal performance. However, since the data in [5] is presented in terms of the scales used in Fig. 5, it is important to consider how proper scaling will influence the comparison. The heat transfer measurements in Boomsma et al. [5] were conducted on 2 mm thick compressed aluminum foam specimens (of 40 $\times$ 40 mm cross section). Thus, the fin efficiency was likely quite high over the full range of Re considered. However, because of the low effective conductivity of aluminum, the fin efficiency would drop considerably with increased thickness and thus, the heat transfer effectiveness of the thicker specimen would be poor. Since the effective conductivity of PCF is 5–20 times higher than that for aluminum foam, the heat transfer effectiveness would remain high for much thicker extended surfaces. Thus, if similar thickness specimens were considered, the heat transfer performance of PCF would be many times higher than that of the aluminum. This is perhaps one of the most important merits of PCF and forms the motivation for pursuing PCF as a convective enhancement material in energy exchange and electronics applications.

Conclusions

Measurements of the pressure drop and heat transfer obtained by forcing water through blocks of porous carbon foam are reported. The pressure drop is seen to be a function of the pore diameter and porosity, but also strongly affected by the size of the cell windows connecting the spherical pores. This is due to the large hydrodynamic loss associated with the fluid contracting/expanding through the windows. The heat transfer was seen to be a function of the effective conductivity and the internal surface area, as might be expected. A comparison of two different sets of scaling parameters showed the importance of including geometric and thermal parameters in the formation of the Nusselt number. Of the specimens tested, the POCO foam offers the best combination of hydrodynamic and thermal performance. The present results suggest that there may be a significant advantage for using PCF as an extended surface convective enhancement material in energy exchange and electronic cooling applications.

Acknowledgment

This work has been sponsored by the Advanced Automotive Materials Program, DOE Office of FreedomCAR and Vehicle Technology Program, under Contract No. DE-AC05-00OR22725 with UT-Battelle, LLC, and by the Natural Science and Engineering Research Council of Canada (NSERC).

References

[1] Klett, W. J., Hardy, R., Romine, E., Walls, C., and Burchell, T., 2000, "High-

Thermal Conductivity, Mesophase-Pitch-Derived Carbon Foam: Effect of Precursor on Structure and Properties," Carbon, **38**, pp. 953–973.
[2] Paek, W. J., Kang, H. B., Kim, Y. S., and Hyum, M. J., 2000, "Effective Thermal Conductivity and Permeability of Aluminum Foam Materials," Int. J. Thermophys., **21**(2), pp. 453–464.
[3] Calmidi, V. V., and Mahajan, R. L., 2000, "Forced Convection in High Conductivity Metal Foams," ASME J. Heat Transfer, **122**, pp. 557–565.
[4] Boomsma, K., and Poulikakos, D., 2002, "The Effects of Compression and Pore Size Variations on the Liquid Flow Characteristics in Metal Foams," ASME J. Fluids Eng., **124**, pp. 263–272.
[5] Boomsma, K., Poulikakos, D., and Zwick, F., 2003, "Metal Foams as Compact High Performance Heat Exchangers," Mech. Mater., **35**, pp. 1161–1176.
[6] Gallego, C. N., and Klett, W. J., 2003, "Carbon Foams for Thermal Management," Carbon, **41**, pp. 1461–1466.
[7] Yu, Q., Thompson, B. E., and Straatman, A. G., 2006, "A Unit-Cube Based Model for Heat Transfer and Pressure Drop in Porous Carbon Foam," ASME J. Heat Transfer, **128**(4), pp. 352–360.
[8] Straatman, A. G., Gallego, N. C., Thompson, B. E., and Hangan, H., 2006, "Thermal Characterization of Porous Carbon Foam—Convection in Parallel Flow," Int. J. Heat Mass Transfer, **49**, pp. 1991–1998.
[9] Taylor, G. I., 1971, "A Model for the Boundary Condition of a Porous Material. Part 1," J. Fluid Mech., **49**, pp. 319–326.

Multifunctional Energy System (MES) With Multifossil Fuels and Multiproducts

Hongguang Jin[1]
e-mail: hgjin@mail.etp.ac.cn

Wei Han[2]
e-mail: hanwei@mail.etp.ac.cn

Lin Gao[2]
e-mail: gaolin@china.com

Institute of Engineering Thermophysics,
Chinese Academy of Sciences,
Beijing 100080, China

A new kind of multifunctional energy system (MES) with multifossil fuels and multiproducts is proposed in this paper. This new system consumes coal and natural gas as fuel simultaneously, and cogenerates methanol and power. Coal and natural gas are utilized synthetically based on the method of dual-fuel reforming, which integrates the methane/steam reforming and the combustion of coal. During the dual-fuel reforming process, combustion of coal provides high-temperature thermal energy to methane/steam reforming reaction to product syngas. Then, the chemical energy of syngas is used efficiently since the new system integrates the chemical process and power plant. In this manner, the energy including both chemical energy of fuels and thermal energy can be used more effectively from the viewpoint of the whole system. As a result, the total energy efficiency of this new system was about 60–66%. Compared with the conventional systems, the new system provides an energy savings of about 8–15%. The results obtained here indicate that this new system may provide a new way to utilize coal and natural gas more efficiently and economically. [DOI: 10.1115/1.2432895]

1 Introduction

The world energy demand has increased steadily and will continue to increase in the future [1], and fossil fuel (coal, natural gas, and oil) will continue to be the main energy source. Coal is overwhelmingly abundant, and will play an extremely important role in the future of energy [2,3]. Gasification of coal has been considered as a promising and effective technology to utilize coal more efficiently [4]. Syngas as the product of gasification can be used for power generation through a combine cycle and chemical products synthesis (methanol and DME). Recently, many demonstration plants of integrated gassification combined cycle (IGCC) and methanol plants based on coal have begun to operate throughout the world [5]. One of the disadvantages of gasification of coal is that it requires a complex system, which includes a gasifier, cleanup unit and air separation unit. Another disadvantage is the high investment; for example the investment ($/kW) of an IGCC plant is about double that of a combined cycle plant, which limited the application of IGCC in large scale. Poly generation systems were considered as a better way to convert syngas to power and methanol with high efficiency and its energy saving ratio can reach 4–15% [6–10].

Natural gas is another major fossil fuel for power and chemical production. In a combined cycle, natural gas is directly burned in the combustion chamber, and the exergy destruction of combustion accounts for about half of total exergy destruction of the cycle [11,12]. In a chemical process, natural gas has to first be transformed into syngas, which is the raw and processed material to synthesize chemical products, through methane/steam reforming reaction [13,14]. During the reforming process, a part of natural gas (NG) (about 30% of the total NG input) has to be burned to provide higher temperature thermal energy (above 900°C) to the methane/steam reforming reaction. Obviously, the combustion of natural gas will cause great exergy destruction.

The objectives of this paper are: (1) to propose a new approach to utilize coal and natural gas synthetically and efficiently from the viewpoint of energy level; (2) to disclose the features in the dual fuel reforming process; and (3) to synthesize a novel energy system with coal and natural gas as fuel.

2 New Multifunctional Energy System

2.1 Conceptual Design of the Multifunctional Energy System. Figure 1 illustrates the schematic of the multifunctional energy system (MES) according to two basic concepts:

1. To combine the utilization processes of NG and coal to produce cleaning syngas; and
2. To integrate the chemical process and power plant to use the syngas efficiently.

Figure 1 shows the concept process of the new MES system. The figure enclosed by the dashed line illustrates the new approach of synthetic utilization of coal and natural gas. The methane/steam reforming process and the burning coal is integrated. The high-temperature thermal energy from burning coal is provided to the reforming reaction as the driving force. Since two different fossil fuels are consumed simultaneously, the new method is called dual fuel reforming in this paper.

Methane/steam reforming is widely used by the chemical industry, and it is a major method to produce syngas from natural gas. The process is based on two independent equilibrium-limited reactions, as follows

$$CH_4 + H_2O \rightarrow 3H_2 + CO \quad \Delta H^0_{298} = 206 \text{ kJ/mol} \tag{1}$$

$$CO + H_2O \rightarrow CO_2 + H_2 \quad \Delta H^0_{298} = -41 \text{ kJ/mol} \tag{2}$$

Reaction (1) is an endothermic steam reforming reaction, and the typical reaction temperature is around 900°C. The second one, often known as the water-gas shift reaction, is a lightly exothermic reaction. As a whole, the reforming of methane by steam will absorb a large amount of thermal energy at high temperature.

The conventional methane/steam reforming method, commonly used in the chemical industry, only consumes natural gas. There-

[1]Corresponding author.
[2]Also at the Graduate School of the Chinese Academy of Sciences, Beijing 100080, China.

Contributed by the International Gas Turbine Institute (IGTI) of ASME for publication in the JOURNAL OF ENGINEERING FOR GAS TURBINES AND POWER. Manuscript received May 14, 2006; final manuscript received September 6, 2006. Review conducted by Umberto Desideri. Paper presented at the ASME Turbo Expo 2006: Land, Sea and Air (GT2006), Barcelona, Spain, May 8–11, 2006, Paper No. GT2006-90977.

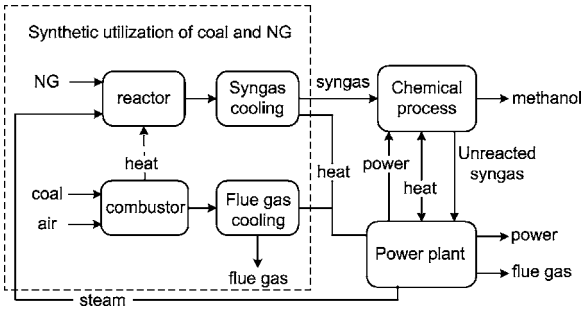

Fig. 1 Schematic of the multifunctional energy system

fore, the natural gas may be divided into two streams: one stream (nearly 70%), as reactant natural gas, is reformed by steam in the reactor to produce syngas. The other stream, acting as fuel natural gas, is burned to provide high-temperature thermal energy to the reforming reaction. During the combustion, about 30% of the chemical exergy of the fuel natural gas is destructed and the other part is transformed into thermal exergy. In the dual fuel reforming, the thermal energy absorbed by the reforming reaction comes from the burning of coal, instead of the burning of natural gas in the conventional method. All of the natural gas acts as reactant and most of the chemical exergy of natural gas is transformed into the chemical exergy of syngas without exergy destruction, which means that the chemical energy of natural gas is used more efficiently in the new method. With the same natural gas input, the dual fuel reforming can generate syngas more than the conventional methane/steam reforming, but the dual fuel reforming has to consume additional coal. It means that the coal has been changed into clean syngas indirectly only through burning. Here it refers that the utilization of coal in the new method as indirect gasification.

Since the combustion of coal is substituted for the combustion of NG in the dual fuel reforming process, the high-temperature corrosion and fouling in the dual fuel reformer should have been taken into account. The technologies, such as the treatment of coal to remove most of the components of sulfur, ash, and alkali metals and the proper combustion system to minimize the corrosion and fouling, should have been investigated further.

For a long time, the chemical process and power plant have developed independently. Currently, both of them have met obstructions that restrict their further development for higher performance. On one hand the chemical process has focused on the high yields of chemical products, but the efficient utilization of chemical energy and thermal energy has not been taken into consideration. A chemical plant, especially the chemical plant based on coal, has a captive power plant (steam cycle) to provide steam and power to some special chemical processes, such as syngas compress, reforming, and distillation processes. In the captive power plant, since coal is burned directly, much chemical exergy (about 30%) of coal is destructed. At the same time, purge gas, which is unsuitable for chemical synthesis, is discharged to the atmosphere from the chemical process. In addition, plenty of high-temperature thermal energy might be released in some chemical processes, such as syngas cooling and synthesis processes, but the thermal energy usually is used to generate midpressure saturated steam regardless of the big temperature difference, which causes large exergy destruction. On the other hand the power plant puts emphasis on the transition of thermal energy to power. All of the chemical energy of fuel is transformed into thermal energy through combustion, in which a large amount of the chemical exergy of fossil fuel (20–30%) is destructed. Even though the thermal energy has been used more and more efficiently, the performance of the current power plant is unsatisfied. Cascade utilization of the chemical energy of fuel becomes a potential to improve the performance of power plant further.

When the chemical process and power plant are integrated, the obstructions of both systems might be overcome simultaneously. Figure 1 also shows the concept of integration of chemical process and power plant. The fuel (syngas) can be used for chemical synthesis first, in which the active components of the syngas are converted to chemical products with lower energy consumption. The inactive components (unreacted syngas) are discharged form the chemical process and provided to the power plant as fuel to generate power efficiently. The thermal energy released from the chemical process can be recovered by the power plant to generate the proper pressure steam. The exergy destruction during the heat exchange process might be obviously decreased. The power plant also provides the proper pressure steam and power to the chemical process and meets the needs of the chemical process. In other words, the chemical energy of fuel and thermal energy can be used efficiently by the integration of chemical process and power plant.

2.2 Configuration of MES System. Figure 2 shows a flow chart of the novel multifunctional energy system (MES). This system is mainly comprised of several subsystems including the dual fuel reformer (a); the methanol synthesis and purification ($c1-c2$) and ($d-f$); and the heat recovery and the power generation ($b1-b3$) and ($g-k$). The reformer (a) is comprised of reaction tubes and a hearth. The catalyst of the methane/steam reforming is stored inside of the tubes and the reforming reaction also takes place here. The coal is burned with the preheated air in the hearth

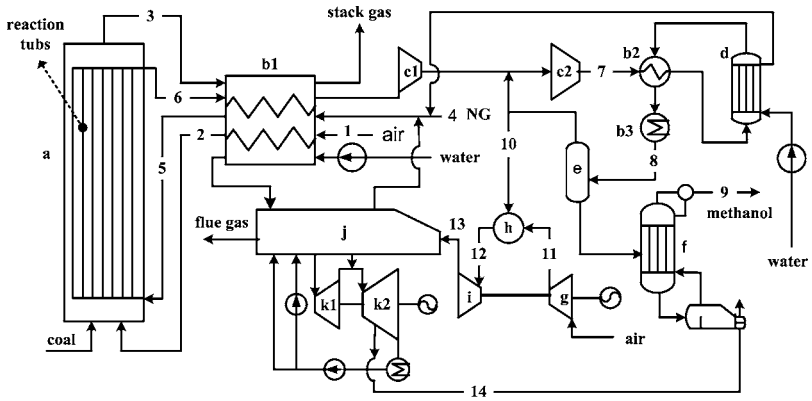

a:dual fuel reformer b1-b3:heat exchanger c1,c2:syngas compressor d:synthesizer e:separator
f:distilation unit g:air compressor h:combustion- chamber i:gas turbine j:HRSG k1-k2:steam turbine

Fig. 2 Configuration of MES system

(outside of the tubes), which provides high-temperature thermal energy to the reforming reaction. The stack gases are discharged to atmosphere after the heat recovery in the heat exchanger ($b1$). The mixture of the natural gas and the middle pressure steam extracted from the heat recovery steam generator (HRSG) (j) and synthesizer (d) enter the reaction tubes of the dual fuel reformer after being preheated in the heat exchanger ($b1$), and at the reactor the natural gas and steam are converted into syngas. The syngas is compressed in the syngas compressor ($c1$) after cooling in the heat exchanger. Then it is mixed with circulating syngas from the separator (e). Finally the syngas is compressed in the syngas compressor ($c2$) to the pressure of methanol synthesis. After being preheated by the heat exchanger ($b2$), the high-pressure syngas enters the methanol synthesizer (d) to synthesize methanol, and the heat emitted from the methanol synthesis is recovered to generate saturated steam. The products of methanol synthesis are cooled, and raw methanol is separated in the separator (e). The raw methanol is refined to high purity methanol in the distillation unit, which is a tricolumn refiner. The unreacted syngas from the separator (e) is divided into two streams: one stream acts as the circulating syngas for methanol synthesis and the other steam is sent to the gas turbine as fuel. The steam used in the distillation is extracted from the low-pressure steam turbine ($k2$).

Based on the new method (dual fuel reforming), possible schemes of difference multifunctional energy systems such as integration of hydrogen and power or DME and power can be synthesized further.

2.3 Reference Systems Description. As the energy system proposed in this paper has multiinput of fossil fuels and multioutput of products, we estimated the performance of the MES system based on the comparison of reference systems, which included the IGCC for power generation, the methanol synthesis based on coal (MSC), the combined cycle (CC), and the methanol synthesis based on natural gas (MSN). The IGCC is assumed as integration of Texaco's gasification process, gas cleanup and heat recovery system with a gas turbine generator, a heat recovery steam generator (HRSG), and the steam turbine generator. The thermal efficiency of the IGCC is 43.1%. The MSC is composed of Texaco's gasification process and gas cleanup system with a methanol synthesis process of Japan Petroleum Institute (JPI) [13]. Usually, the MSC system also includes a captive power plant, which is a coal fired power plant, to provide steam and power to the chemical processes. The energy consumption of MSC system is 45 GJ/t CH_4O [9]. In the CC, the turbine inlet temperature (TIT) and pressure ratio of compressor are, respectively, 1308°C and 15.0. The HRSG of the combined cycle works at two pressure levels and the thermal efficiency of the CC is 54.2%. The MSN system is composed of methane/steam reforming process and JPI's methanol synthesis process, and the energy consumption is 32.2 GJ/t CH_4O. The main assumptions during the simulation of MES and reference systems are presented in Table 1.

Table 1 Main assumptions of evaluation

Chemical process	
Synthesis pressure of methanol (MPa)	10
Synthesis temperature of methanol (°C)	270
Pressure loss of synthesizer (%)	5
Pressure loss of heat exchangers (%)	3
Pressure loss of reformer of cold side (%)	10
Pressure loss of reformer of hot side (%)	1
Isentropic syngas compressor	0.75
Reforming temperature (°C)	950
Reforming pressure (MPa)	2
Steam to methane ratio	3
Surplus air ratio of coal combustion	1.22
Power plant	
Pressure ratio of compressor	15
Turbine inlet temperature (°C)	1308
Pressure loss of heat exchangers (%)	3
Isentropic efficiency of air compressor	0.88
Isentropic efficiency of gas turbine	0.89
Isentropic efficiency of pump	0.8
Pinch point in HRSG (°C)	10
Approach point in HRSG (°C)	30
Pressure loss of HRSG (gas-side) (%)	3
Pressure loss of HRSG (steam, water)	10
Condensation pressure, (MPa)	0.0085

3 Evaluation of MES System

3.1 Simulation and Results. We assumed that the reference systems produce the same quantities of power and methanol as the proposed system, and the fuel thermal input (lower heating value (LHV)) ratio of methane to coal is equal to each system. The energy saving ratio (ESR) was used as a criterion and the definition was

$$\mathrm{ESR} = \frac{Q_{\mathrm{ref}} - Q_{\mathrm{MES}}}{Q_{\mathrm{ref}}} \times 100\%$$

where Q_{ref} was the sum of the fuel thermal input of coal and natural gas consumed by the reference system; and Q_{MES} was the sum of fuel thermal input of coal and natural gas consumed by the proposed system.

Based on the above assumptions, the system was studied by

Table 2 Parameters of main points of MES system

				CH_4	C_2H_6	CH_4O	CO	CO_2	H_2	H_2O	O_2	N_2
Point	G (kg/s)	p (MPa)	T (°C)	Percent molar composition (%)								
1	62.8	0.103	25	—	—	—	—	—	—	1.0	20.8	78.2
2	62.8	0.102	512	—	—	—	—	—	—	1.0	20.8	78.2
3	68.3	0.1	950	—	—	—	—	16.3	—	3.6	3.7	76.4
4	6.4	2.58	25	90.0	10.0	—	—	—	—	—	—	—
5	28.1	2.32	500	20.9	2.3	—	—	—	—	76.8	—	—
6	28.1	2.09	950	1.1	—	—	11.7	4.5	51.6	31.1	—	—
7	41.7	10.5	92.7	5.1	—	0.2	4.7	2.8	87.1	0.1	—	—
8	41.7	9.8	38	5.6	—	5.2	1.5	1.7	84.5	1.5	—	—
9	11.6	0.11	66.6	—	—	99.9	—	—	—	0.1	—	—
10	1.7	9.8	38	6.0	—	0.3	1.6	1.8	90.2	0.1	—	—
11	95.5	1.49	25	—	—	—	—	—	—	1.0	20.8	78.2
12	97.3	1.46	1308	—	—	—	—	1.1	—	12.1	12.8	74.0
13	117.8	0.105	551	—	—	—	—	1.0	—	10.1	14.1	74.8
14	9.5	0.55	158.5	—	—	—	—	—	—	100	—	—

Table 3 Results for MES and reference systems (MW)

Items	MES	Reference systems			
		IGCC	MSC	CC	MSN
Natural gas	314.7			85.6	275.2
Coal	158.6	42.9	138.9		
Methanol	230.3		60.3		170.0
Power	63.96	18.5		46.4	−0.93
Efficiency, %	62.2	43.1	43.4	54.2	61.4

means of the commercial software Aspen. Pressure, temperature, mass flow, and composition of the main points in Fig. 2 are listed in Table 2.

The energy balance results and the overall efficiency of the MES system are reported in Table 3. The overall efficiency is defined as the ratio of products' energy (no matter electricity and chemical products) to the lower heating value of the consumed fossil fuel. The fuel thermal input ratio of natural gas to coal was nearly 2 and the overall efficiency of the MES system reached 62.2%. The ESR of the proposed system was 12.8%, when the preheated temperature of air for burning of coal was 512°C. The temperature of stack gas at the outlet of the reformer was 950°C, and the circulating ratio of unreacted syngas was 4.0.

Table 4 shows the exergy distributions of the MES system and the reference systems, based on the simulation of the MES system. To produce the same quantities of methanol (258.48 MW) and power (63.96 MW), the reference systems consumed 48.48 MW natural gas (exergy) and 23.4 MW coal (exergy) more than those in the MES system. In other words, the MES system would result in saving about 12.8% natural gas and coal compared to the reference systems.

3.2 Exergy Presentation on EUD. Since the MES system involves chemical and thermal processes, the conventional exergy analysis is not enough to reveal the internal phenomena of energy conversion in those processes, because the conventional method mainly focuses on the exergy difference between output and input of a process. The energy-utilization diagram (EUD) methodology [15,16] considers an energy transformation between an energy-donating process and an energy-accepting process, and focuses graphically on the energy level difference in a pair of energy donor and energy acceptor and the variations of both energy level and energy quantity are graphically shown with $A-\Delta H$ coordinates. The energy level A is an intensive parameter and a ratio of exergy change to energy change of a process ($A=\Delta E/\Delta H=1-T_0\Delta S/\Delta H$). The change of energy quantity (ΔH) refers to any kind of energy changes, such as thermal energy, power consumption, or generation, and energy change in chemical reaction etc. In order to reveal the internal phenomenon and the fundamental features, we adopted the graphical exergy methodology of EUD to analyze the process of dual fuel reforming.

3.3 Significant Role of Dual Fuel Reforming in the MES System. In MES system the syngas is produced by the new method of dual fuel reforming. In contrast, in the reference systems the syngas is produced by the conventional methods of methane/steam reforming and coal gasification. As Table 4 shows, the exergy destruction during the syngas producing process in the MES system is 19.87 MW (28.5%) lower than that of the reference systems.

Figure 3(*a*) a shows the exergy-destruction distribution of dual fuel reforming. The oxidation of coal with air acts as an energy donating reaction (curve of A_{ed}), and the methane/steam reforming process acts as an energy accepting reaction (curve of A_{ea4}). Three feed streams, air (curve of A_{ea1}), coal (curve of A_{ea2}), and a mixture of methane and steam (curve of A_{ea3}) acts as the energy acceptors which are preheated to the specific combustion or reforming temperature. The results show that the exergy destruction of the dual fuel reforming process is equivalent to the area between the curves of the energy donor (curve of A_{ed}) and the energy acceptors (curves of A_{ea1}–A_{ea4}) giving to 49.97 MW.

Figure 3(*b*) shows the exergy-destruction distribution of gasification of coal and conventional methane/steam reforming. The curve of A_{ed1} represents the process of oxidation of natural gas with air in the methane/steam reformer, which acts as an energy donating reaction, and the methane/steam reforming (curve of A_{ea4}) acts as an energy accepting reaction. The energy acceptors also include three streams of air (curve of A_{ea1}), natural gas (curve of A_{ea2}) and a mixture of methane and steam (curve of A_{ea3}), which are preheated to the temperature of combustion or reforming. The exergy destruction of the conventional methane/steam reforming is 46.64 MW. The curve of A_{ed2} represents the partial oxidation of coal in the gasifier, which acts as an energy donating reaction, and the energy acceptors included gasification reaction (curve of A_{ea8}) and three streams of oxygen (curve of A_{ea5}), coal (curve of A_{ea6}), and water (curve of A_{ea7}), which are preheated to the specific gasification temperature of 1200°C. The exergy destruction of the coal gasification is 23.2 MW.

Comparing Figs. 3(*a*) and 3(*b*), we can find that the utilization of coal and natural gas is obviously different. As the coal-gasification process needs pure oxygen as an oxidant, the energy level of the partial oxidation of coal (curve of A_{ed2} in Fig. 3(*b*)) is higher than that of the oxidation of coal with air (curve of A_{ed} in Fig. 3(*a*)) in the dual fuel reforming process. On the other hand, the thermal energy exchanged between the energy donor and the energy acceptor in the dual fuel reforming process (158.6 MW) is also lower than that of the reference methods (199.7 MW). Af-

Table 4 Exergy distributions of MES system and reference systems

Exergy (MW)	MES	IGCC	MSC	CC	MSN	Total of ref
Natural gas input	330.62			89.94	289.16	379.1
Coal input	159.50	43.17	139.73			182.9
Syngas production	49.97	6.58	16.62	—	46.64	69.84
Air separation	—	1.17	3.10	—	—	4.27
Shift reaction	—	—	2.25	—	—	2.25
Cleanup unit	—	0.43	6.08	—	—	6.51
Combustion	31.15	7.63	11.06	27.86	—	46.55
Heat exchangers	44.73	2.59	12.31	5.48	31.83	52.21
Synthesizer	4.71	—	2.36	—	3.49	5.85
Distillation unit	5.01	—	3.35	—	5.31	8.66
Power subsystem	22.25	4.25	1.65	8.41	8.10	22.41
Flue gas	9.86	2.02	4.29	1.76	3.96	12.03
Purge gas	—	—	8.98	—	—	8.98
Methanol output	258.48		67.68		190.80	258.48
Power output	63.96	18.50	—	46.43	−0.97	63.96
Total	490.12	43.17	139.73	89.94	289.16	562.0

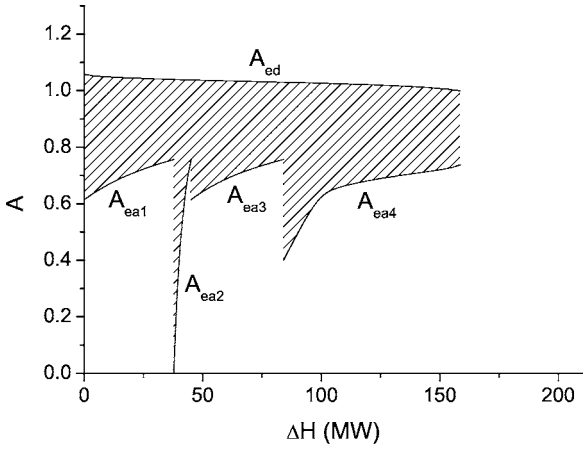

(*a*)

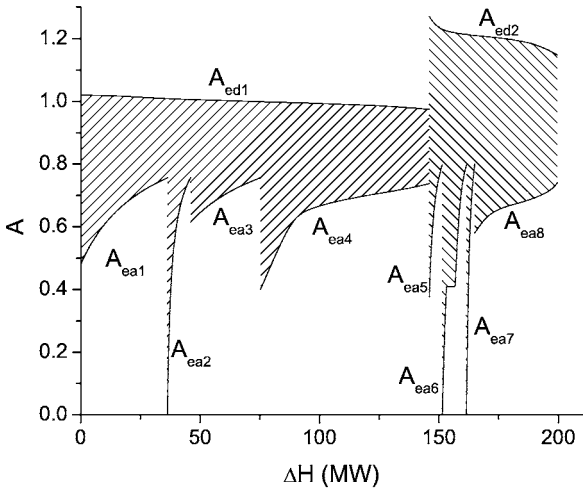

(*b*)

Fig. 3 (*a*) EUD for dual fuel reforming; and (*b*) EUD for reference methods

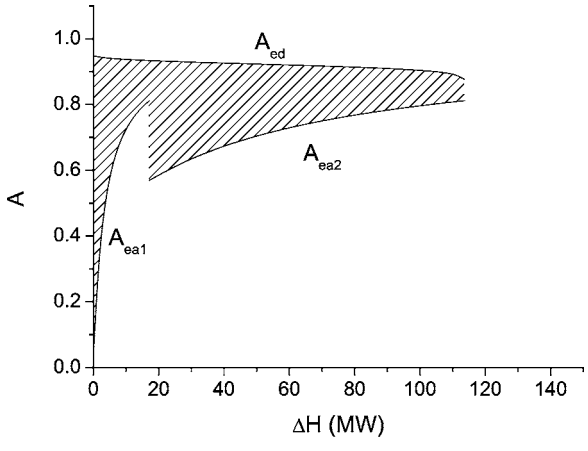

(*a*)

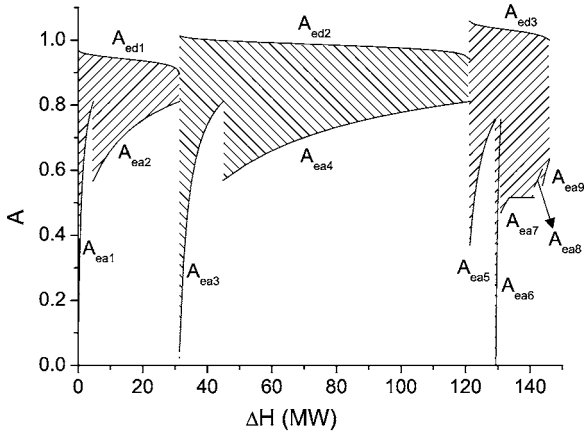

(*b*)

Fig. 4 (*a*) EUD for combustion of unreacted syngas in MES system; and (*b*) EUD for combustion in reference systems

fected by the two factors above, the exergy destruction of dual fuel reforming (the shaded area in Figs. 3(*a*) and 3(*b*)) is decreased. Because coal and natural gas are utilized in an efficient way, the performance of dual fuel reforming was superior to that of conventional methods.

In the methanol synthesis plant based on coal, the surplus CO in syngas has to be converted to CO_2 through a shift reaction, which will cause the exergy destruction of 2.25 MW, as shown in Table 4. Then the CO_2 is separated from the products of shift reaction, which causes the exergy be destructed by 6.51 MW. The conventional gasification of coal needs O_2 of 95% as an oxidant and the exergy destruction during the process of oxygen generation is 4.27 MW. In the MES system, coal is combusted with air in the dual fuel reformer and the air separation unit is not required. The exergy destruction of air separation unit (4.27 MW) is not included in the MES system. In addition, the syngas produced by the dual fuel reforming is clean and suitable for methanol synthesis and the processes of shift and cleanup are also unnecessary for the MES system. Without the shift, air separation, and cleanup processes, the exergy destruction in these processes (13.03 MW) is avoided in the MES system.

3.4 Integration of Chemical Process and Power Generation System. The proposed system integrates the thermal cycle and the methanol synthesis system. Since the syngas and thermal energy can be exchanged between the two sides, there exists a big potential to utilize the syngas and thermal energy more efficiently. From Table 4 we can see that the exergy destruction of combustion in the MES system was decreased by 15.4 MW (33%) compared with the reference systems. In the MES system, the combustion takes place in the thermal cycle, in which a part of the unreacted syngas is burned in the combustor of the gas turbine and the exergy destruction is 31.15 MW. In IGCC and CC, the fuels burned in the combustor of the gas turbines, respectively, are cleaned syngas and natural gas, and the exergy destruction are, respectively, 7.63 MW and 27.86 MW. In methanol synthesis system based on coal (MSC), a captive power plant (coal fired power plant) is necessary to provide power, steam, and thermal energy for the chemical process. In the captive power plant the coal is burned with air in the boiler and the exergy destruction is 11.06 MW. Figures 4(*a*) and 4(*b*), respectively, show the combustion in the MES system and the reference systems.

Figure 4(*a*) is the EUD diagram for the combustion of unreacted syngas in the combustor of the gas turbine in the MES system. The oxidation of unreacted syngas acts as an energy donating reaction (curve of A_{ed}), and heating processes of two streams (the curve of A_{ea1} represents the preheating process of the unreacted syngas and the curve of A_{ea2} represents the preheating process of the air for combustion) act as energy acceptors, which are preheated to the specific combustion temperature of 1308 °C. Figure 4(*b*) gives the EUD diagram for combustion in the reference systems. Curves of A_{ed1} and A_{ed2}, respectively, represent the oxidation reaction of cleaned syngas in IGCC and natural gas in CC, and the heating processes of four streams (curves of A_{ea1}–

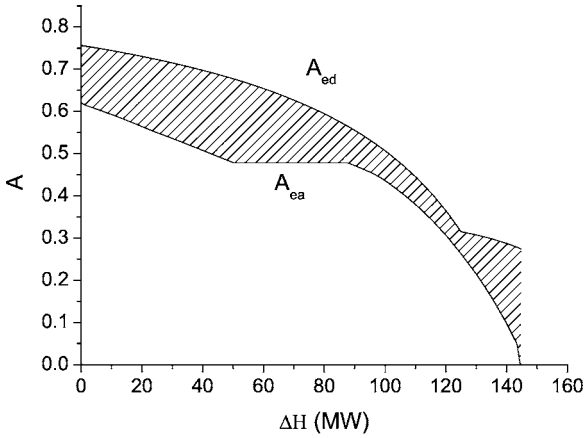

(*a*)

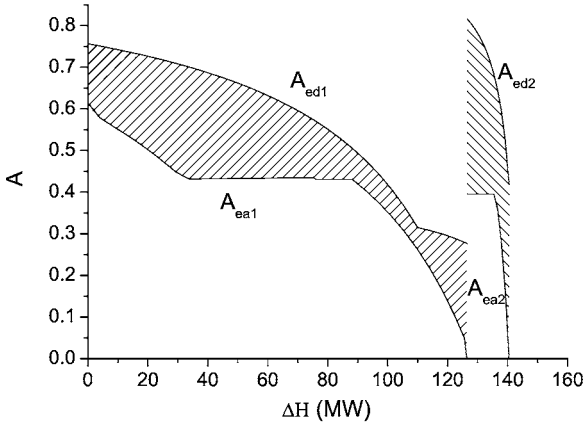

(*b*)

Fig. 5 (*a*) EUD for heat exchange of chemical subsystem in MES system; and (*b*) EUD for heat exchange of chemical subsystem in reference systems

A_{ea4}, respectively, represent the preheating processes of the syngas, combustion air of syngas, natural gas, and combustion air of natural gas) act as energy acceptors, which are preheated to the combustion temperature of 1308°C. Curves of A_{ed3} and A_{ea5}–A_{ea9} present the processes of burning of coal in the captive power plant of the MSC system. The oxidation of coal with air in the boiler (curve of A_{ed3}) acts as a donating reaction and heating processes of five steams (curves of A_{ea5}–A_{ea9}) act as the energy acceptors: the preheating of air and coal, the evaporation of water, the superheating of steam, and the reheating of steam.

Since the components of the unreacted syngas burned in MES system are mainly hydrogen and carbon monoxide, the energy level of oxidation of unreacted syngas (curve of A_{ed} in Fig. 4(*a*)) in the MES system is lower than that of oxidation of natural gas (curve of A_{ed2} in Fig. 4(*b*)) in the combined cycle. Along with the decrement of energy level of donators, the exergy destruction of the combustion of the unreacted syngas is also decreased by 4.34 MW more than that of the combustion of natural gas. The combustion of coal in the boiler also causes a large amount of exergy destruction (11.06 MW) in the MSC system. Since the MES system integrates the methanol synthesis system and power plant, the captive power plant (coal fired power plant) used in the MSC system is unnecessary in the MES system. As a result, the total exergy destruction of the combustion (area of shadow in Fig. 4(*a*)) in the MES system is smaller than that (area shaded in Fig. 4(*b*)) in the reference systems.

In the methanol synthesis system some of the unreacted syngas, called purge gas, is removed from the synthesizer, because the components of purge gas are not suitable for the methanol synthesis. In the MSC system, the purge gas is discharged into the atmosphere after burning, which causes the exergy loss of 8.98 MW (about 6.4 percentage points of input coal) as shown in Table 4. In the MES system, the unreacted syngas is used efficiently by recovering the purge gas and sending it to the power subsystem of the MES system to generate power.

Table 5 Cost of dual fuel reformer and reference reformer or gasifier

	Dual fuel reformer	Conventional reformer	Gasifier, cleanup unit, and ASU
Base specific cost (M$/MW)	0.24	0.2	0.27
Base capacity (MW)	330.6	273.4	181.1
Cost (M$)	79.34	54.68	48.9

Figures 5(*a*) and 5(*b*), respectively, show the exergy destructions of the heat exchange process in the MES system and the reference systems. In the MES system the thermal energy released from the chemical processes can be recovered by the power subsystem efficiently. For example, the surplus heating of syngas and flue gas of the reformer in the MSN system is used to generate the superheated steam with a temperature of 435°C and a pressure of 4 MPa (curve of A_{ea1} in Fig. 5(*b*)). In the MES system this amount of thermal energy is used to generate the superheated steam with a temperature of 510°C and a pressure of 8.38 MPa (curve of A_{ea} in Fig. 5(*a*)). Since the energy level of acceptors in the MES system is higher than that in reference systems, the exergy destruction of the heat exchange process is decreased. In the MSC system, the hot syngas from the gasifier is quenched from 1200°C to 240°C to increase the humidity of syngas and most of the thermal exergy is destructed (the area of shaded between the curves of A_{ed2} and A_{ea2} in Fig. 5(*b*)). In the MES system, the syngas produced by the dual fuel reforming is very clean with a temperature of 950°C, and the thermal energy is recovered to generate superheated steam with a pressure of 8.38 MPa. Compared to Figs. 5(*a*) and 5(*b*), the shaded area of the MES system is smaller than that of the reference systems and the exergy destruction of heat exchange in the MES is 7.48 MW (14.3%) lower than the reference systems, as shown in Table 4.

3.5 Economic Benefit of MES System. An important point emphasized here is that the syngas produced by the dual fuel reforming process is very clean. Thereby, the cleanup unit and air separation unit (ASU) are not required in the MES system. When the scale parameter is fuel thermal input (LHV), the investments of the dual fuel reformer, the conventional reformer, and the gasifier are presented in Table 5. The specific cost of conventional methane/steam reformer and catalyst is about 0.2 M$/MW, and the specific cost of gasifier, cleanup unit and ASU is about 0.27 M$/MW. The dual fuel reformer can be designed from the conventional reformer with little modification and the cost of the dual fuel reformer estimates 0.24 M$/MW, which is higher by about 20% than that of conventional methane/steam reformer. In Table 5 the fuel thermal inputs of the dual fuel reformer, the conventional reformer, and the gasifier of coal are, respectively, 330.6 MW, 273.4 MW, and 181.1 MW, and the total investments are, respectively, 79.34 M$, 54.68 M$, and 48.9 M$. The investment of the dual fuel reformer is decreased nearly by 23.4% compared to the total cost of the conventional reformer and gasifier. It must be specified that the cost estimation is valid only for a preliminary analysis.

4 Conclusions

A new kind of multifunctional energy system (MES) is proposed for more effective utilization of fossil fuels. With the same outputs of power and methanol, the new system provides a fossil fuel savings of about 12.8%. The graphical exergy analysis based on EUD reveals that the natural gas and coal are utilized synthetically by the method of dual fuel reforming. The exergy destruction of syngas generation process is decreased by about 28.5% compared with conventional methods. Based on the integration of chemical process and power plant, the unreacted syngas and thermal energy of chemical process can be utilized efficiently from the viewpoint of the operation of the whole system, and the exergy destructions of combustion process and heat exchanging process in MES system are, respectively, decreased by about 33% and 14.3% compared with the reference systems. Some processes, which are necessary in reference systems, are not required in the MES system, and the exergy destructions in these processes (2.3 percentage points of input exergy of fuel) are not included in MES system. The proposed MES system provides a new approach to utilize the coal and natural gas synthetically, which not only simplifies the system but also decreases the investment cost.

Acknowledgment

Supported by the Natural Science Fundamental of China (Grant Nos. 90210032 and 50520140517).

Nomenclature

MES = multifunctional energy system
MSC = methanol synthesis based on coal
MSN = methanol synthesis based on natural gas
CC = combined cycle
IGCC = integrated gasification combined cycle
LHV = lower heating value
TIT = turbine inlet temperature
EUD = energy-utilization diagram

References

[1] BP group., 2005, "BP Statistical Review of World Energy June 2005," Report, BP Press Centre, London.
[2] Cai, R., 1986, "Comparison Method for Comples Cycle Analysis," ASME Paper 86-JPGC-GT-6.
[3] Tsatsaronis, G., Tawfik, T., Lin, L., and Gallaspy, D. T., 1994, "Exergetic Comparison of Two KRW-Based IGCC Power Plant," J. Eng. Gas Turbines Power, **116**, pp. 291–299.
[4] Longwell, J. P., Rubin, E. S., and Wilson, J., 1995, "Coal: Energy for the Future," Prog. Energy Combust. Sci., **21**, pp. 269–360.
[5] U.S. Department of Energy and the Gasification Technologies Council, 2000, "Gasification–Worldwide Use and Acceptance," Topical Rep., USDOE, Washington, D.C.
[6] Jackson, R. G., 1989, "Polygeneration System for Power and Methanol Based on Coal Gasification," Coal Conversion, **12**, pp. 60–64.
[7] Liu, Z., and Cai, R., 2004, "Exergy Analysis of Coal-Based Polygeneration System for Power and Chemical Production," Energy, **29**, pp. 2359–2371.
[8] Kei, Y., and Leonardo, B., 2005, "Energyplexes for the 21st Century: Coal Gasification or Co-producing Hydrogen, Electricity and Liquid Fuels," Energy, **30**, pp. 2453–2473.
[9] Gao, L., 2005, "Investigation of Coal-Based Polygeneartion Systems for Production of Power and Liquid Fuel," Ph.D. thesis, Institute of Engineering Thermophysics, Chinese Academy of Science, China.
[10] Giorgio, C., Roberto, C., and Daniele, C., 1997, "Thermodynamic and Environmental Assessment of Integrated Gasification and Methanol Synthesis (IGMS) Energy Systems with CO_2 Removal," Energy Convers. Manage., **38** Suppl., pp. S179–S186.
[11] Jin, H., Ishida, M., Kobayashi, M., et al., 1997, "Exergy Evaluation of Two Current Advanced Power Plants: Supercritical Steam Turbine and Combined Cycle," J. Energy Resour. Technol., **119**, pp. 250–256.
[12] Jin, H., 1994, "Development of Thermal Power Systems Based on Graphical Exergy Analysis," Ph.D. thesis, Tokyo Institute of Technology, Tokyo.
[13] Japan Petroleum Institute, 1983, "Design of Methanol Synthesis," Tech. Report, Japan Petroleum Institute, Tokyo.
[14] Lange, J. P., 2001, "Methanol Synthesis: A Short Review of Technology Improvements," Catal. Today, **64**, pp. 3–8.
[15] Ishida, M., and Nakagawa, N., 1985, "Exergy Analysis of Pervaporation System Based on an Energy Utilization Diagram," J. Membr. Sci., **24**, pp. 271–283.
[16] Ishida, M., 1997, "Process System Synthesis and Available Information," *Proceedings of Thermodynamic Analysis and Improvement of Energy System*, Beijing, June 10–13, pp. 370–376.

A Technoeconomic Analysis of Different Options for Cogenerating Power in Hydrogen Plants Based on Natural Gas Reforming

Alessandro Corradetti

Umberto Desideri
e-mail: umberto.desideri@unipg.it

Dipartimento di Ingegneria Industriale,
Università di Perugia,
Via G. Duranti 93,
06125 Perugia, Italy

Steam methane reforming is the most common process for producing hydrogen in the world. It currently represents the most efficient and mature technology for this purpose. However, because of the high investment costs, this technology is only convenient for large sizes. Furthermore, the cooling of syngas and flue gas produce a great amount of excess steam, which is usually transferred outside the process, for heating purposes or industrial applications. The opportunity of using this additional steam to generate electric power has been studied in this paper. In particular, different power plant schemes have been analyzed, including (i) a Rankine cycle, (ii) a gas turbine simple cycle, and (iii) a gas-steam combined cycle. These configurations have been investigated with the additional feature of CO_2 *capture and sequestration. The reference plant has been modeled according to state-of-the-art of commercial hydrogen plants: it includes a prereforming reactor, two shift reactors, and a pressure swing adsorption unit for hydrogen purification. The plant has a conversion efficiency of* ~75% *and produces* 145,000 Sm^3/hr *of hydrogen (equivalent to* 435 MW *on the lower-heating-volume basis) and* 63 t/hr *of superheated steam. The proposed power plants generate, respectively,* 22 MW *(i),* 36 MW *(ii), and* 87 MW *(iii) without* CO_2 *capture. A sensitivity analysis was carried out to determine the optimum size for each configuration and to investigate the influence of some parameters, such as electricity, natural gas, and steam costs.*
[DOI: 10.1115/1.2434346]

Introduction

In the last several years, the concern with the anthropogenic greenhouse effect has increased the interest in the possibility of using hydrogen as an energy carrier for both vehicle fueling and stationary energy production. In power production, carbon capture can be accomplished with different technologies that do not necessarily include fuel decarbonization [1,2]. But in the field of transportation and small-size power generation, the easiest way to reduce greenhouse gas emission is the utilization of a decarbonized fuel, such as hydrogen.

The most widespread and mature technology for hydrogen production is steam reforming, based on the following reaction:

$$CH_4 + H_2O \leftrightarrow CO + 3H_2 \ (\Delta H_0 = 206 \text{ kJ/kmol}) \qquad (1)$$

Since it is an endothermic reaction, it is enhanced at high temperatures and typically takes place at 800–900 °C, achieving a methane conversion of up to 95%. The most common technology uses tubular reformers, in which the reacting methane and steam flow through pipes containing a Nickel-based catalyst and are heated by an external flame. A second reaction occurring simultaneously in steam methane reformer (SMR) is known as "CO-shift" because it transforms the CO into CO_2,

$$CO + H_2O \leftrightarrow CO_2 + H_2 \ (\Delta H_0 = -41 \text{ kJ/kmol}) \qquad (2)$$

The high temperature does not allow one to shift all the carbon monoxide, therefore, the reformed gas still contains a great fraction of CO. One (or two) shift reactor is generally installed after the reformer in order to minimize CO content in the gas. The final gas is very rich in CO_2, which can be captured with a suitable technology. Today, pressure swing adsorption (PSA) is commonly used for H_2 purification, instead of the amine-absorption process followed by methanation, which has traditionally been employed in the past.

Hydrogen plants based on SMR are characterized by a strong economy of scale; thus, they are the preferable choice for capacity higher than 1000–5000 Sm^3/hr [3,4], whereas electrolysis is used for smaller capacities. Hydrogen plants usually produce more steam than the amount required by the reforming process; thus, it is exported for heating purposes or industrial applications. On the other hand, electric energy is consumed by the plant, especially in the case of carbon capture, because CO_2 must be compressed and liquefied for transportation. These energy flows, together with the large size typical of the hydrogen plants, suggest that the steam can be used for electricity generation. The power production and dispatching becomes even more attractive in a hypothetical future energy scenario based on hydrogen as fuel for transportation. In this case, in fact, hydrogen facilities will be located near industrial districts and can be easily connected to the electric grid or to an electricity consumer.

Previous works have investigated the feasibility of cogenerating power in SMR-based hydrogen plants, with different technologies for the integration of the power section. Terrible et al. [5] proposed four main schemes, all without CO_2 separation: (i) a topping steam turbine, in which the steam leaving the turbine is used

Contributed by the International Gas Turbine Institute of ASME for publication in the JOURNAL OF ENGINEERING FOR GAS TURBINES AND POWER. Manuscript received June 13, 2006; final manuscript received August 10, 2006. Review conducted by Lee Langston. Paper presented at the ASME Turbo Expo 2006: Land, Sea and Air, May 8–11, 2006, Barcelona, Spain. Paper Number GT2006-90360.

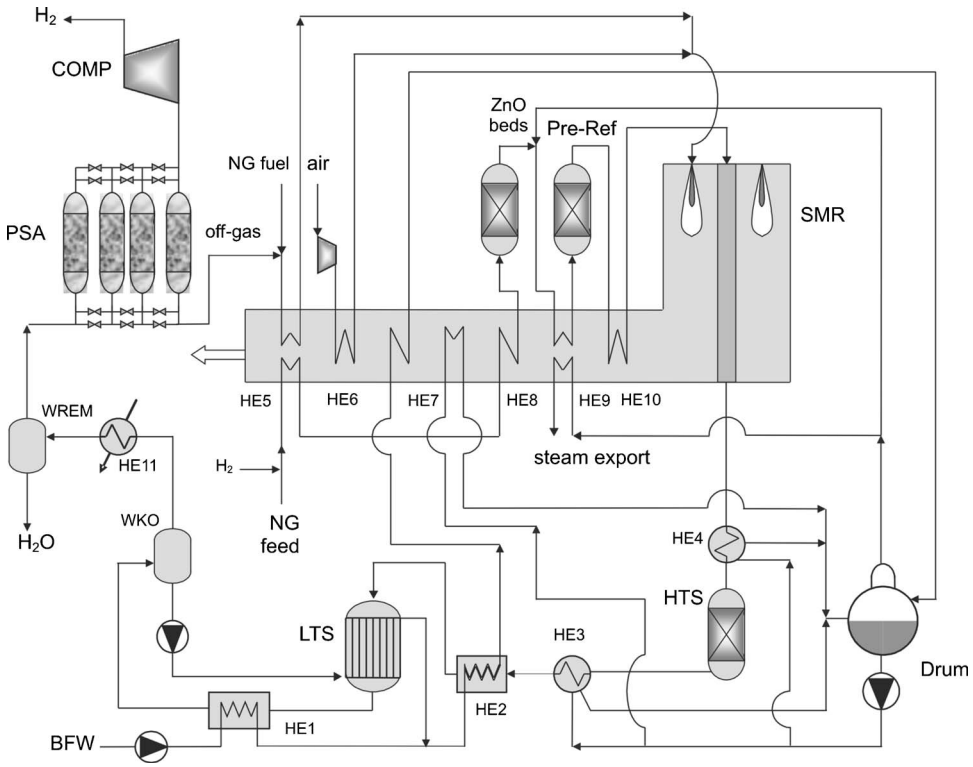

Fig. 1 Scheme of the reference hydrogen plant

for reforming; (ii) a gas turbine cycle, which uses the turbine exhaust as oxidizer in the reformer furnace; (iii) a condensing steam turbine, in which the steam for reforming is supplied by a bleeding from the turbine; and (iv) a gas turbine followed by a bottoming turbine. Consonni and Viganò [6] performed a thermodynamic and exergetic analysis of a steam cycle and combined cycle integrated with tubular reformers and auto-thermal reformers with carbon capture. In this work, the gas turbine is not used ahead of the reformer, but rather at the end of the syngas processing because it is fueled by pressure swing adsorption (PSA) off-gas. Klett et al. [7] made a technoeconomical analysis of the hydrogen plants without power generation, comparing the option of carbon capture with the standard plant with CO_2 vent.

The aim of the present paper is to perform a technoeconomic analysis of the hydrogen plants in an extensive range of possible configurations; in particular, different technologies for power production have been investigated, including a steam cycle (SC), a gas turbine cycle (GT), and a combined cycle (CC). For all the schemes, carbon capture has been compared to the standard plant with a CO_2 vent. Among the possible reforming technologies, only the tubular reactor has been chosen because it represents the most mature and widespread technology, especially when hydrogen is the primary product. In the following, the typical hydrogen production plant with no power generation will be addressed as the reference plant (REF). The hydrogen production in REF is 3.6 kg/s, equivalent to ~145,000 Sm^3/hr and 435 MW_{LHV}. This size has been fixed in order to match the oxygen request of the SMR furnace with the exhaust gas flow of an existing heavy duty 40 MW_E gas turbine. The plant can be considered as a large hydrogen facility, though the largest existing plants are in the range of 250,000–300,000 Sm^3/hr [3,4,8–10], and Haldor Topsoe [4] has recently announced the construction of the largest hydrogen production capacity in the world (600,000 Sm^3/hr). According to Contadini et al. [10], most of the existing SMR plants lie in the range of 22,000–90,000 Sm^3/hr. Therefore, the size chosen in this paper is an intermediate value between the majority of existing plants and the largest ones.

1 Description of Investigated Plants

Reference Hydrogen Plant. The reference hydrogen plant scheme is depicted in Fig. 1. The plant components have been chosen and simulated following state-of-the-art of hydrogen plants based on natural gas (NG) steam reforming. Natural gas is supposed to be available at the required pressure (27 bar), and its composition is [11] 94.4% CH_4, 3.1% C_2H_6, 0.5% C_3H_8, 0.4% C_{4+}, 0.5% CO_2, 1.1% N_2. To avoid the poisoning of the catalyst, sulfur has to be removed in the ZnO beds, which follows a hydrogenation unit. The hydrogen required to this aim is provided by recycling a small fraction of the H_2 produced. Before entering the hydrogenation and desulphurization unit, the mixture of H_2 and NG is heated up to 380°C [10] in two heat exchangers (HE5, HE8) placed in the convective section of the furnace.

After the ZnO-beds, NG is mixed with the process steam and further heated at 550°C in HE9. Hence, it enters the prereformer, an adiabatic catalytic reactor that accomplishes the reforming of the heavier hydrocarbons, thus avoiding the coking (solid carbon deposition) of the catalyst in the SMR. The gas leaves the high-temperature exchanger at 650°C and enters the reformer, which operates at 880°C and 25 bar. The hot syngas is cooled in a waste heat boiler (HE4) before entering the high-temperature shift reactor, which is adiabatic and works at 400°C. The low-temperature shift reactor is, instead, a cooled reactor operating at 200°C. It is preceded by another boiler (HE3) and the economizer HE2. Syngas is cooled down to 130°C in HE1, where boiler feed water is preheated; in the WKO, the condensed water is separated and sent to cool low-temperature shift (LTS). Syngas purification in the PSA unit requires further cooling (25°C), which is accomplished by HE11. The hydrogen recovery factor in PSA is 88%, a value typically achieved in commercial units [12]. The hydrogen produced (99.99% pure) is compressed to 60 bar for pipeline transportation. PSA off-gas is supplied to the burners of the SMR furnace; yet the heat duty of the SMR is not completely satisfied, Thus, additional natural gas is required (15% of the total). The

Table 1 Assumptions made for simulating plant performance

SYNGAS Processing		**CO_2 Compressor**	
S/C	3	Final delivery pressure (bar)	150
SMR T (°C)	880	No. of stages (intercooled)	3
NG SMR inlet T (°C)	650	Coolant T (°C)	25
Chemical equilibrium temperature approach (°C)	−10	Polytropic efficiency	0.8
SMR pressure loss (%)	3	Mechanical efficiency	0.9
SMR heat loss (%)	1.5	**H_2 Compressor**	
Pre-Ref inlet T (°C)	550	Final delivery pressure (bar)	60
Pre-Ref pressure loss (%)	3	No. of stages (Intercooled)	2
Inlet air T (°C)	15	Coolant T (°C)	25
Inlet air p (bar)	1.013	Polytropic efficiency	0.78
Furnace pressure (bar)	1.05	Mechanical efficiency	0.95
Furnace outlet temperature (°C)	930	**Gas Turbine**	
HDS inlet T (°C)	380	Specification	GE PG6591C
HTS T (°C)	400	TIT (°C)	1327
LTS T (°C)	200	Pressure ratio	19
Shift reactors pressure loss (%)	3	Airflow (kg/s)	114.7
Shift reactors chemical equilibrium T approach (°C)	+10	Coolant total mass flow (%)	15.4
PSA hydrogen recovery (%)	88	Turbine outlet T (°C)	574
PSA off-gas pressure	1.3	Net power (MW)	42.3
Pump efficiency (isentropic/mechanical)	0.8/0.95	Efficiency (%)	36.2
Fan efficiency (isentropic/mechanical)	0.8/0.95	TIT (°C)—steam injection operation	1287
Heat Exchangers		Pressure Ratio—steam injection operation	19
Heat loss (%)	0.7	Stoichiometric flame T (K)—Steam injection	2300
Gas-gas minimum ΔT (°C)	30	**Steam Turbine**	
Water-gas minimum ΔT (°C)	7–10	Turbine efficiency (Isentropic/Mechanical)	0.9/0.97
CO_2 Capture		Condenser p (bar)	0.04
Heat for solvent regeneration (MJ/t CO2)	1.0	Superheating T (°C)	550
Syngas T at ABS inlet (°C)	25	Reheating T (°C)—only in CC plants	550
Steam to stripper reboiler p (bar)	2.1	Steam pressure (bar) in SC	70
CO_2 p at stripper outlet (bar)	1.8	Steam pressure (bar) in CC	110/27/3

flue gas leaves the furnace at 930°C (50°C above the gas to be reformed) and passes through the series of convective heatexchangers. The air fed to the furnace is preheated to 250°C in HE6, whereas the off-gas and the additional NG are heated to 92°C (minimum temperature difference in gas-gas HE is 30°C). The air mass flow has been determined by imposing an excess oxygen of 3–5% higher than the stoichiometric value. The flue gas leaves the convective section of the furnace at ~85°C. Steam at 27 bar is substantially produced in two waste-heat boilers, placed after the SMR (HE4) and the HTS (HE3), though in some configurations analyzed, and in particular, in the reference case, HE7 operates both as economizer and evaporator. The steam-to-carbon ratio (S/C) has been fixed at 3.0 for all the studied plants; this value is typically found in hydrogen plants based on natural gas reforming because it ensures an adequate methane conversion and low risk of carbon deposition. All the simulations have been performed using Aspen Plus® software. The main assumptions made are summarized in Table 1.

Options for Cogenerating Power. A lot of different possible power plant schemes may be integrated with the hydrogen plant described earlier. Of course, the preference of one configuration over another strongly depends on economical considerations, which are the topic of Sec. 3. A driving factor is the availability and energy requests of nearby consumers, which could be supplied either with steam or power produced by the hydrogen plant. For this reason in this paper, we focused the attention on three configurations that correspond to different needs of a possible nearby consumer: the first configuration (SC) is a Rankine cycle, which produces only power and no steam for export; the second configuration (GT) is characterized by a gas turbine for power production and steam export; the third configuration (CC) is a combined cycle, which allows the maximum power production but no steam export.

The three plants are very similar to the REF plant and, in particular, are characterized by an identical syngas circuit. The main differences concern the heat recovery section from the SMR flue gas, as illustrated in Figs. 2–4. The SC plant is characterized by the production of high-pressure steam (70 bar), which is superheated to 550°C and then expanded in a turbine. The steam necessary to the reforming process (69% of the total produced) is supplied by a bleeding at 27 bar.[1] The remaining steam is ex-

[1]Change in ST load can affect steam extraction to SMR, but off-design analysis is not an argument of the present paper.

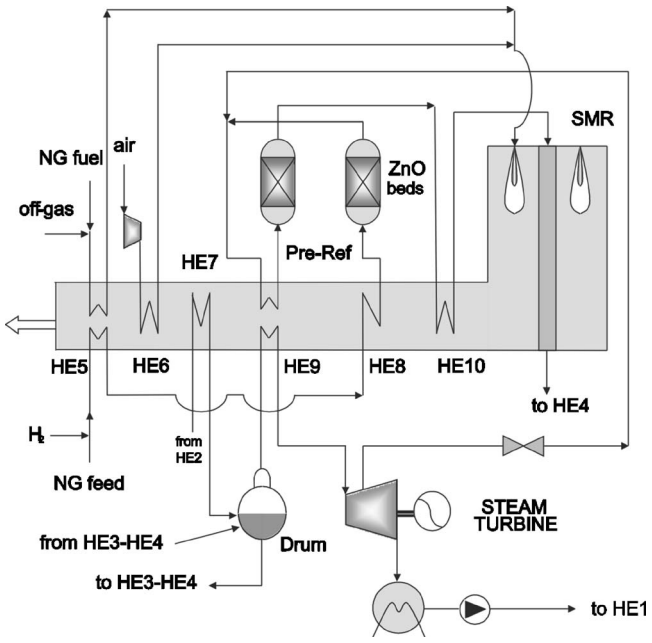

Fig. 2 Scheme of SMR in SC plant

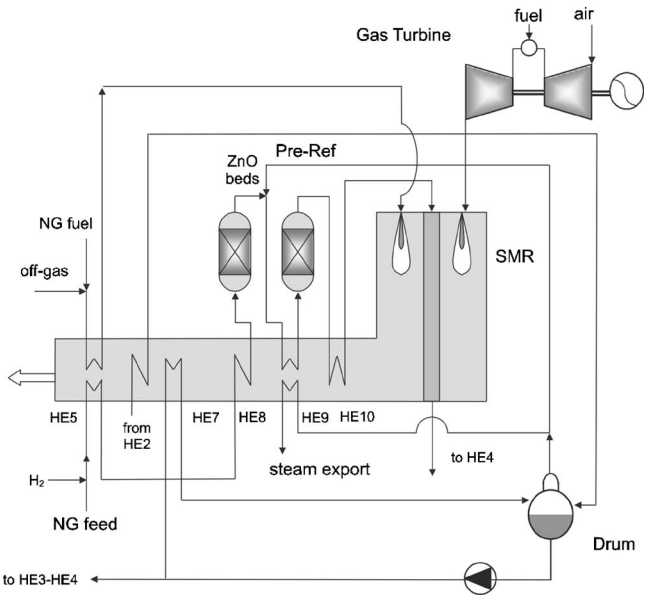

Fig. 3 Scheme of SMR in GT plant

panded to 0.04 bar, condensed and recycled back to the economizers fed by the syngas. The selected values for steam production do not represent the most advanced conditions for steam power plants (for example pressure could be increased and reheating could be introduced at 27 bar). On the other hand, these values allow the hydrogen plant to operate at conditions very similar to the reference plant. This makes the comparison between the two plants more significant. Furthermore, the results obtained are very close to the ones found by Consonni and Viganò [6] with a more advanced steam cycle. In fact the steam turbine produces 28.5 MW, equivalent approximately to the 5% of the natural gas input. Small variations in the heat recovery sections exist between this plant and the REF case: in particular the positions of HE8 and HE9 are inverted and steam production is reduced by 6%. These modifications are due essentially to the different steam pressure and to the reheating to 550°C of the process steam (see Fig. 2).

The GT configuration is characterized by a higher level of integration with the hydrogen facility than the SC; in fact, the hot gas leaving the turbine is supplied to the furnace as an oxidizer, thus decreasing the natural gas consumption in the SMR burners. The last consideration is not so obvious, as the flue gas contains a large amount of inert gas (oxygen is ~13 vol.%) and in some cases this may lead to an increasing of the fuel supplied to the burner. The gas turbine chosen in this work is a medium size (42.3 MW) heavy duty gas turbine supplied by General Electric: PG6591C [13]. This gas turbine is widely used in industrial cogeneration and process industries and is suitable for integration with SMR because of the good electrical efficiency (36%) and the high temperature of exhaust gas (574°C). The exhaust flow (117 kg/s) allows the furnace to work with the same oxygen excess as the reference case (3–5%). As previously said, the oxygen content is lower in the GT configuration; therefore, the furnace results bigger than in the reference case. However, from a thermodynamic point of view, this choice is more appropriate since the amount of the natural gas burned in the SMR is minimized in both the configurations. The heat recovery convective section is identical to the REF case, except for the air preheater, which is not necessary here. This causes an increase in the stack temperature (116°C instead of 84°C of the REF case), even if SMR fuel and

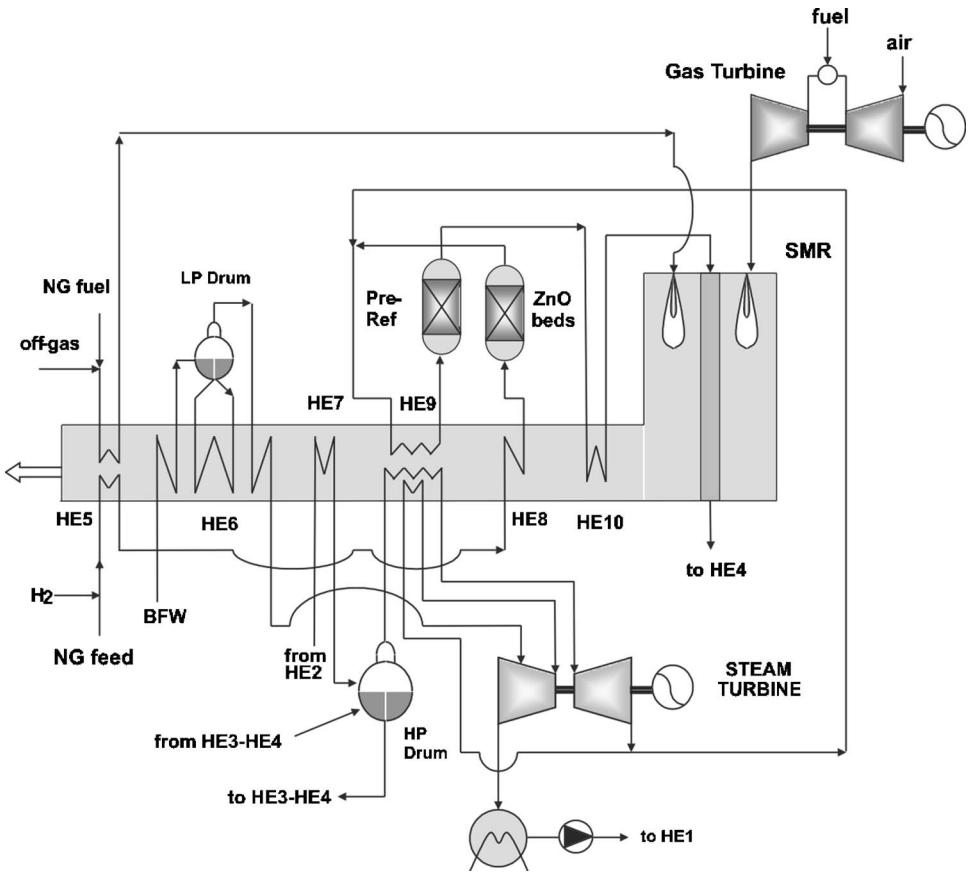

Fig. 4 Scheme of SMR in CC plant

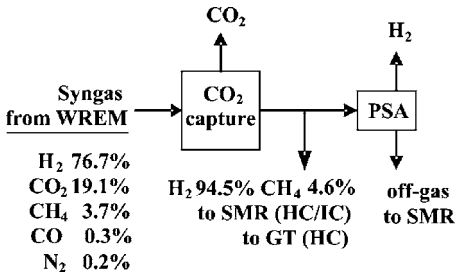

Fig. 5 Simplified scheme of the main streams and blocks and gas composition for plants with CO_2 capture

feed preheating has been raised to 127°C.

The CC plant is provided with the same gas turbine as the GT cycle, but the heat recovery section is different from the previous configuration: the steam is produced at 110 bar and, after the superheating and expansion to 27 bar, is reheated to 550°C and expanded a second time. Between HE5 and HE7, low-pressure (3 bar) steam is produced and superheated and then mixed with the steam leaving the medium pressure turbine. Therefore, the cycle can be regarded as a three pressure steam cycle, with levels at 110 bar, 27 bar, and 3 bar. Of course the bottoming section of the combined cycle takes advantage by the integration with the reformer, which realizes the supplementary firing of the turbine exhaust gas. A lot of heat is recovered for the gas preheating and the production of process steam, but the power produced by the steam cycle is much larger than in a traditional combined cycle (51.7 MW, even higher than the gas turbine power).

Plants With CO_2 Capture. CO_2 is captured by chemical absorption process based on amine solution. This is the preferable choice when CO_2 partial pressure is relatively low, as in the case of tubular reforming-based hydrogen plants. The gas is treated after cooling and condensation before entering the PSA unit (see Fig. 5). It has been assumed that 99% of CO_2 is removed in the absorber, and the heat required for solvent regeneration is 1 MJ/kg CO_2 captured [6]. This heat duty is supplied condensing a fraction of the steam produced in the boiler (REF and GT) or a bleeding from the turbine (SC and CC). The percentage of CO_2 captured in the absorber, has been kept constant at 99%, and yet for each plant, different levels of carbon removal have been investigated. This is due to the nature of the supplementary fuel burned in the SMR furnace and in gas turbine, which is either additional NG or a fraction of the produced H_2. In fact, CO_2 is removed from syngas but not from the furnace exhaust gas, since the low CO_2 concentration and low pressure make carbon capture from flue gas more expensive in terms of money and energy. Thus, burning hydrogen instead of NG in the furnace means a higher level of carbon removal. The analysis has been focused on two possible schemes for the REF and SC plant and on three configurations for GT and CC plant. Table 2 shows the acronyms used for plants with carbon capture and the kind of fuel burned.

It is worth noting that in all the plants the H_2 supplied to the gas turbine and to the reformer is not pure, but rather it is the gas leaving the absorber, which contains a hydrogen content of 94.5% (see Fig. 5). This device allows the PSA unit to treat a lower amount of gas with the same CO_2 emission at SMR stack. The burning of this hydrogen implies, however, the decrease of the plant capacity, as the same NG feed input has been assumed for all the configurations.

In the REF plant, the two schemes for carbon capture are characterized by the same excess of air (1.03–1.05 stoichiometric) in SMR furnace as the plant with CO_2 vent. This reduces the mass flow of the reformer flue gas, since in the configuration without capture SMR fuel contains 52% of CO_2, which is inert and requires more fuel (and more air) in the furnace. The decrease in airflow reduces the heat available from furnace hot gas; hence, some changes have to be made to the convective section of the reformer:

- The economizer HE7 is not present
- HE8 and HE9 positions are exchanged
- HE5 and HE6 positions are exchanged
- HE5 heats the air to a lower T (124°C for HC, 160°C for LC)
- HE6 heats the fuel and the feed gas to 280°C
- Export steam is not superheated

The production of steam is reduced by 8% with respect to the reference case. A large amount (21%) of the saturated steam produced in the drum is sent to the CO_2 plant for solvent regeneration, 72% is used for reforming, and only 7% (3.5 kg/s is exported).

In SC plants with CO_2 capture, a different methodology has been adopted for determining the mass flow of the combustion air for the furnace. Because of the absence of CO_2 in the off-gas, in fact, if the same excess air as the standard plant is used, there is no steam available for power production and there is not enough steam for solvent regeneration in the CO_2 stripper. Therefore, the air mass flow has been fixed so that the power produced matches approximately the power required by the auxiliaries and CO_2 and H_2 compressors. The resulting air mass flow is 93.8 kg/s, 20% higher than the standard SC plant. The heat recovery from reformer flue gas is identical to the standard SC plant, except for HE10, not present in the SC-HC and SC-LC.

In GT plants, the amount of oxygen in the combustion process is fixed by the turbine exhaust gas composition (O_2=13 vol%) and mass flow (117 kg/s). Therefore, GT, GT-IC, and GT-LC are characterized by the same O_2 input in the furnace but different excess of air, since off-gas composition and additional fuel are different. In particular, the oxygen amount is, respectively, 1.04, 1.22, and 1.16 for GT, GT-IC, and GT-LC. The GT-HC configuration is somewhat different with respect to the other ones. In fact, the combustion of hydrogen in the gas turbine would cause an unacceptable level of NO_x emission, since lean premix combustion with hydrogen cannot be realized at the moment [14]. Hence, steam injection has been considered for NO_x reduction. Actually, the authors have no knowledge on the possibility of syngas fueling or steam injection for NO_x reduction in the gas turbine employed (PG6591C), which is usually equipped with DLN combustors. However, in modern IGCC plants, NO_x emission control is always realized through steam/nitrogen injection or fuel saturation, also in gas turbine usually equipped with dry low NO_x (DLN) combustors. Furthermore, the aim of the present paper is to investigate the possibility of exporting power and steam; thus, steam injection and the consequent power increase has to be considered for thermodynamic and economic considerations. The steam necessary for NO_x reduction has been determined in order

Table 2 Additional fuel used in SMR in plants with CO_2 capture

	SMR additional fuel	GT fuel
REF-HC	H_2	-
REF-LC	NG	-
SC-HC	H_2	-
SC-LC	NG	-
GT-LC	NG	NG
GT-IC	H_2	NG
GT-HC	H_2	H_2
CC-LC	NG	NG
CC-IC	H_2	NG
CC-HC	H_2	H_2

to limit to 2300 K the stoichiometric flame temperature [14]. The mass flow of the required steam is equal to 4.8 times the fuel flow. The performance of the gas turbine has been determined by assuming the following conditions:

- TIT reduction of 40°C compared to the NG operation [14]
- IGV operating (same pressure ratio and reduced mass flow) to avoid compressor stall

The power produced by the gas turbine in this configuration is 48.4 MW versus 42.3 MW in the NG operation; the efficiency is 39.3% (versus 36.2%), while the TOT is 568°C (versus 574°C). Despite the TIT decrease, power production increases by 14%; this cannot be explained only by the steam injection (steam mass flow is just 6.4% of the total air inlet). Another decisive factor is the combustion of hydrogen, which produces a gas richer in steam and is thus characterized by a larger enthalpy drop across the turbine [14].

In all the GT plants with carbon capture, the heat recovery section is identical to the plant with CO_2 vent. The CC configurations are based on the same assumptions made for GT.

2 Discussion of Results

In the REF plant, the production of hydrogen is 3.6 kg/s equivalent to 435 MW_{LHV}. The natural gas consumption is 10.45 kg/s for SMR feeding and 1.45 for fuelling the furnace. The equivalent thermal input is thus 579 MW_{LHV}. The electric power consumed by the auxiliaries is 6.9 MW (~90% of which is spent in H_2 compressor). There are 17.4 kg/s of steam exported at 27 bar and 550°C; considering the enthalpy necessary to steam production and superheating, this flow corresponds to 61.0 MW_{TH}.

In order to evaluate the performance of the plant, some parameters are explained in the following:

$$\eta_H = \frac{H_2\ \text{output}[MW_{LHV}]}{\text{NG input}[MW_{LHV}]} \tag{3}$$

$$\eta_C = \frac{H_2\ \text{output}[MW_{LHV}] + H_2\ \text{to GT}[MW_{LHV}]}{\text{NG input}[MW_{LHV}] - CH_4\ \text{to GT}[MW_{LHV}]} \tag{4}$$

$$\eta_E = \frac{\text{Net electric power output [MW]}}{\text{NG input}[MW_{LHV}]} \tag{5}$$

$$\eta_G = \frac{H_2\ \text{output}[MW_{LHV}] + \text{Net electric power output}[MW] + \text{Steam Export}[MW]}{\text{NG input}[MW_{LHV}]} \tag{6}$$

The fuel efficiency η_H is the ratio between the hydrogen produced by the plant and the natural gas thermal input. The conversion efficiency η_C is the fraction of natural gas supplied to the reformer, which is actually converted to H_2; in fact, in certain configurations (i.e., GT and CC) the gas turbine can be fed either with additional natural gas or with some of the H_2 produced. Therefore, this parameter takes into account only the gas input and output relative to the hydrogen production, with no reference to the fuel supplied to the gas turbine. In the REF plant, as well as in SC, η_H and η_C are identical.

The electric efficiency η_E is the fraction of natural gas thermal input converted to power; this ratio could be negative as the numerator represents the net electric power (the power produced minus the power required by the auxiliaries). The third parameter η_G is the global efficiency, which is the sum of three different forms of energy. Thus, the value of η_G could be misleading, but is often used in technical literature and manufacturers' brochures. In the reference hydrogen plant, the net power output is negative, and it could be more appropriate considering the power for auxiliaries among the energy inputs. However in this paper, the parameters addressed before have been used for a more significant comparison to the plants cogenerating power. For REF, η_H and η_G are respectively equal to 75.2% and 84.5%. These values are similar to the ones found in technical literature (see Table 3). Both REF-LC and REF-HC have a higher conversion efficiency than REF; η_H increases, respectively, to 76.6% and 78.9% for HC and LC. This result has also been obtained by other authors [6,7], though the assumptions made here are somewhat different (for example, in [6] S/C is 3.07 in the plant with CO_2 capture and SMR temperature is 850°C). In the present paper, the increase in η_H is essentially the consequence of the lower additional fuel flow required in the furnace. As explained before, in fact, the combustion of the off-gas with a lower CO_2 content requires less fuel and less air flow.

The results concerning main thermal and mass input/output for all the studied configurations are illustrated in Table 4. It is worth noting that the conversion efficiency is always higher in LC configurations than IC or HC. This means that using NG as additional fuel in SMR furnace instead of hydrogen results in an increase of the H_2 production efficiency. The reason has to be found in the particular layout of the plant, which is provided with two waste heat boilers downstream, the SMR and the HTS. This choice is typical of syngas processing plants, where hot syngas cooling is usually coupled with steam production in order to avoid high-temperature gas-gas heat exchangers. Therefore, a great part of the thermal input of the NG entering SMR is consumed for steam production, whereas only a small fraction of the heat recovered from the furnace flue gas is used for steam production. Thus, using NG for feeding the furnace means that H_2 production is increased at the expense of a reduced steam generation.

3 Economic Analysis

Two methods have been used for evaluating the economic aspects of the systems investigated: (i) the cost of the hydrogen

Table 3 Comparison of the plant performance to values from literature

	η_H	Steam export-H_2 mass ratio	η_G	CO_2 capture (%)
REF (this study)	75.2	4.8	84.5	0
REF-LC (this study)	78.9	1.0	77.7	73.2
SC-LC (this study)	76.4	0	76.1	70.9
Uhde [9]	72.7	7.7	NA	0
Lurgi [3]	71.6	7	NA	0
Consonni Viganò [6][a]	75.7	0	78.9	0
Consonni Viganò (CO_2 capture)	78.0	0	78.0	73.6
Klett et al. [7]	75.9	5.7	NA	0
Klett et al. (CO_2 capture)	82.5	0	NA	71.0
Spath Mann [11]	75.2	NA	NA	0
Patel et al. [15] from [10]	77.9	NA	85.2	NA

[a]The values from [6] are referred to a H_2 plant, cogenerating power through a steam cycle; thus, η_G includes the contribute of electricity rather than steam export and should be compared to SC-LC.

Table 4 Performance of the investigated plants

	REF	REF HC	REF LC	SC	SC HC	SC LC	GT	GT IC	GT LC	GT HC	CC	CC IC	CC LC	CC HC
NG input-SMR feed (MW_{LHV})	**494.2**	494.2	494.2	**494.2**	494.2	494.2	**494.2**	494.2	494.2	494.2	**494.2**	494.2	494.2	494.2
NG input-SMR fuel (MW_{LHV})	**84.7**	-	57.6	**84.7**	-	75.3	**73.6**	-	51.3	-	**75.3**	-	52.1	-
NG input-GT fuel (MW_{LHV})	-	-	-	-	-	-	**116.7**	116.7	116.7	-	**116.7**	116.7	116.7	-
H_2 produced (MW_{LHV})	**435.1**	378.5	435.1	**435.1**	358.6	435.1	**435.1**	383.5	435.1	255.5	**434.9**	382.4	435.1	254.3
GT power (MW)	-	-	-	-	-	-	**42.3**	42.3	42.3	48.4	**42.3**	42.3	42.3	48.4
ST power (MW)	-	-	-	**28.5**	15.3	15.0	-	-	-	-	**51.7**	32.5	32.3	28.6
H_2 compressor (MW)	**6.1**	5.3	6.1	**6.1**	5.0	6.1	**6.1**	5.4	6.1	3.6	**6.1**	5.4	6.1	3.6
CO_2 compressor (MW)	**0.0**	8.9	8.9	**0.0**	8.9	8.9	**0.0**	8.9	8.9	8.9	**0.0**	8.9	8.9	8.9
Auxiliaries[a] (MW)	**0.8**	1.2	1.2	**1.4**	1.7	1.7	**0.5**	1.0	1.0	1.0	**1.8**	1.9	1.9	1.9
Net power (MW)	**−6.9**	−15.4	−16.2	**21.0**	−0.3	−1.7	**35.6**	27.1	26.3	35.0	**86.1**	58.6	57.7	62.7
Steam export (t/hr)	**62.7**	12.6	12.6	-	-	-	**115.9**	65.2	64.6	54.5	-	-	-	-
CO_2 emitted (kg/s)	**32.3**	5.0	8.2	**32.3**	5.0	9.2	**38.1**	11.5	14.3	5.0	**38.2**	11.5	14.4	5.0
CO_2 captured (kg/s)	-	22.6	22.6	-	22.6	22.6	-	22.6	22.6	22.6	-	22.6	22.6	22.6
CO_2 captured (%)	-	81.8	73.2	-	81.7	70.9	-	66.3	61.2	81.8	-	66.3	61.1	81.8
η_C (%)	**75.2**	76.6	78.9	**75.2**	72.6	76.4	**76.6**	77.6	79.8	76.6	**76.4**	77.4	79.6	76.7
η_H (%)	**75.2**	76.6	78.9	**75.2**	72.6	76.4	**63.6**	62.8	65.7	51.7	**63.4**	62.6	65.6	51.5
η_E (%)	**−1.2**	−3.1	−2.9	**3.6**	−0.1	−0.3	**5.2**	4.4	4.0	7.1	**12.5**	9.6	8.7	12.7
η_G (%)	**84.5**	75.4	77.7	**78.8**	72.5	76.1	**85.3**	77.6	79.2	69.5	**75.9**	72.2	74.3	64.1

[a]Power consumption for auxiliaries includes: feed-water pump, cooling water pump (assumed equal to 1% of the heat removed from condensers, compressor intercoolers [16]), amine solution pump, furnace air fan.

produced by a particular configuration has been calculated and (ii) the payback period of the additional investment for the power section has been determined. The cost of hydrogen is calculated as

$$\mathrm{CoH}[\$/\mathrm{GJ}] = \frac{\mathrm{AC}}{\mathrm{H_{2LHV}}}\left[\frac{\$/y}{GJ/y}\right] \tag{7}$$

where H_{2LHV} is the amount of hydrogen produced per year and AC is the total annual cost, given by

$$\mathrm{AC} = \mathrm{TCI_A} + \mathrm{C_{O\&M}} + \mathrm{C_{NG}} + \mathrm{CoE} - \mathrm{C_{ST}} \tag{8}$$

where TCI_A is the annual rate of the investment cost, $C_{O\&M}$ is the cost of operating and maintenance, C_{NG} is the cost of the natural gas, CoE is the cost of electric energy, and C_{ST} is the income for steam export.

The capital costs have been taken from literature and upscaled according to the power-law formula

$$\mathrm{C} = \mathrm{C_0}\left(\frac{s}{s_0}\right)^{\mathrm{f}}\mathrm{IF} \tag{9}$$

where s is the size of the equipment, C_0 and s_0 are the cost and the size of the reference equipment, f is the scale factor, and IF is the installation factor, which includes the cost for installation, BOP, general facilities, engineering, overhead, and contingencies. The values used for these parameters are shown in Table 5. Since the cost of the single component is highly variable from one author to another, the resulting total capital cost for the reference plant is compared to other values available in literature in Table 6. It is worth noting that Table 6 reports the investment cost for the plant without the hydrogen compressor because this value is more frequently used in the literature. The values found have been scaled to the size investigated in this paper with a scale factor equal to 0.67. In certain cases, however, a linear dependence between the size and the cost has been assumed, as suggested by some authors [22]. Table 6 clearly shows that there is also uncertainty concerning the capital cost of the whole hydrogen plant, though the majority is close to the mean value ($140M). The cost predicted in the present study seems to be reasonable and in line with the ones obtained in the other works. Another aspect pointed out by Table 6 is that there is a strong economy of scale for the hydrogen plant, thus the assumption of a scale factor equal to 0.67 is correct.

The annual rate of the TCI has been determined, by fixing the interest rate at 10%, the deflation rate at 2.5% and the plant lifetime at 15 years. The resulting annual capital charge rate is 15%. $C_{O\&M}$ has been set to 4% of the TCI, the plant utilization factor is

Table 5 Parameters used for capital cost estimation

Component	C_0 (10^6 US $_{2005}$)[a]	s_0	Scaling parameter	f	IF
SMR[b]	3.862	890.82	CH_4 input (MW_{LHV})	0.6[c]	2.3[c]
ΔSMR (HEs)[d]	9.951	110.57	MW_{TH}	1	1.0
Shift[e]	11.275	8.819	Mmol/hr $CO+H_2$	0.85	1.8
PSA[f]	7.455	0.294	kmol/s purge	0.74	1.0
H_2 compressor[d]	0.00269	-	\$/kWe	1	1.0
CO_2 capture[b]	13.9	44.58	kg/s CO_2	0.67	1.86
CO_2 compression[f]	14.8	13000	kW	0.67	1.0
Gas turbine[f]	30.6	67	MW_E	0.67	1.0
ST and condenser[f]	59.2	136	MW_E	0.67	1.0
Construction Interest			12% of the plant cost		

[a]A deflation of 2.5% has been applied to the reference capital cost.
[b]Lozza and Chiesa [17].
[c]Hamelinck and Faaij [18].
[d]De Lorenzo et al. [19].
[e]Williams et al. [20] in [18].
[f]Kreutz et al. [21].

Table 6 Comparison of the H_2 plant TCI with values from the literature

Source	Size	Capital Cost	S0	f	Cost scaled to present size
	tpd	10^6 $	$/GJ		10^6 $
Sjardin [22]	24.4	13.84	12.95	1	145.52
Roy [23]	48.0	41.00	19.50	0.67	144.08
Molburg, Doctor [24]	120.5	82.00	15.54	0.67	155.53
Leiby [25] in [28]	121.0	77.81	14.74	0.67	147.57
Leiby [25] in [28]	192.5	106.31	12.61	0.67	147.33
Bredesen [26] in [27]	205.1	91.80	10.22	0.67	121.94
This Study	302.4	121.05	9.14	-	120.07
Klett [6]	417.8	131.00	7.16	0.67	108.01
Foster-Wheeler [29]	607.1	265.91	10.00	0.67	170.69
Simbeck [30]	1500.0	365.00	5.56	0.67	127.81
Blok et al. [31]	2284.5	1082.65	10.82	1	148.46

90%, corresponding to 7884 operating hours. Because of the high variability of natural gas and electricity costs, it is not easy to choose an appropriate value for them. In particular NG cost, which deeply affects the final cost of hydrogen, has increased rapidly in the two last years, substantially following the trend of oil prices. Therefore, a sensitivity analysis has been performed, varying NG cost and other parameters, as described in the following section.

The reference values of NG and electricity cost have been fixed respectively at $4.7/GJ and 0.05 $/kWh, which are common for large users in the European market [32]. Steam cost has been set 10% higher than NG, i.e., equal to 5.17/GJ.[2] This assumption can be regarded as the trade-off between two opposite considerations:

- In thermal plant producing mainly steam, its cost derives from a lot of different items, among which the fuel cost is predominant. The final cost can be approximated to 1.3 times the cost of fuel [33].
- In a hydrogen plant, steam is a by-product, generated essentially by the syngas cooling. Therefore, it could be convenient to sell steam even at a cost lower than the NG theoretically necessary to its production. It is worth noting also that the quantity of steam produced is very high; thus, it could be difficult to find buyers unless a very competitive price is applied. For this reason, a sensitivity analysis has been carried out also in relation to steam cost.

The results obtained with these assumptions are shown in Table 7. The H_2 cost ($7.89/GJ) in the REF plant is relatively high if compared to other values available in literature. However, it must be considered that NG cost is usually set at $3/GJ, which is significantly lower than the actual prices in the European market. In our model, the hydrogen cost decreases to $5.9/GJ for a NG cost of $3/GJ and grows to 9.4 for NG cost of $6/GJ. These results are close to the ones obtained by Padró and Putsche [28], who found a cost of H_2, respectively, equal to 6.3 and 10.6 for a plant of an equivalent size.

It is worth noting that cogenerating power decreases the hydrogen cost in all the configurations except for the steam plant. However, small differences between the various configurations are observed. In terms of payback period, only the GT plant seems to be convenient, with a PB of approximately four years. This is due to the high cost assumed for steam, which has a strong influence on PB period as shown later.

Sensitivity Analysis. The influence of NG cost is shown in Fig. 6 for an electricity cost of $0.05/kWh and $0.06/kWh. The decrease of the hydrogen cost in SC, GT, and CC configurations is, respectively, equal to $0.14/GJ, $0.23/GJ, and $0.56/GJ, if CoE is raised to $0.06/kWh; whereas in the REF case, H_2 cost increases by $0.04/GJ. Obviously, the lines representing a particular configuration have the same slope, with the lower line corresponding to the lower CoE. Figure 6 also allows one to determine the NG cost for which a plant typology maybe convenient: for ex-

[2]In the REF plant and in all GT cycles, steam is exported at 27 bar and 550°C; thus, its enthalpy content is 3.5 GJ/t. In REF, HC and LC saturated steam at 27 bar is produced, equivalent to 2.7 GJ/t.

Table 7 Capital and annual cost of the investigated plants. The AC is relative to the base case (CoE=$0.05/kWh, NG cost =$4.7/GJ)

	REF	REF HC	REF LC	SC	SC HC	SC LC	GT	GT IC	GT LC	GT HC	CC	CC IC	CC LC	CC HC
SMR, WHB, HEs	**54.7**	51.6	51.9	**54.7**	54.1	54.0	**57.8**	55.7	55.6	56.5	**58.2**	56.1	56.1	56.9
Shift reactors, HEs	**35.7**	35.7	35.7	**35.7**	35.7	35.7	**35.7**	35.7	35.7	35.7	**35.7**	35.7	35.7	35.7
PSA unit	**16.9**	8.0	8.8	**16.9**	7.7	8.8	**16.9**	8.1	8.1	6.0	**16.9**	8.0	8.8	6.0
H_2 compressor	**16.4**	14.3	16.4	**16.4**	13.6	16.4	**16.4**	14.5	16.4	9.7	**16.4**	14.5	16.4	9.6
ST and condenser	-	-	-	**20.8**	13.7	13.5	-	-	-	-	**31.0**	22.7	22.6	20.8
GT	-	-	-	-	-	-	**22.5**	22.5	22.5	22.5	**22.5**	22.5	22.5	22.5
CO_2 capture	-	16.4	16.4	-	16.4	16.4	-	16.4	16.4	16.4	-	16.4	16.4	16.4
CO_2 compressor	-	11.5	11.5	-	11.5	11.5	-	11.5	11.5	11.5	-	11.5	11.5	11.5
Construction interests	**14.8**	16.5	16.9	**17.3**	18.3	18.8	**17.9**	19.7	19.9	19.0	**21.7**	22.5	22.8	21.5
Total Capital (million $)	**138.5**	153.9	157.6	**161.8**	170.9	175.1	**167.2**	183.9	186.0	177.1	**202.3**	209.8	212.7	200.8
TCI_A (million $/y)	**20.9**	23.2	23.8	**24.4**	25.8	26.4	**25.2**	27.7	28.0	26.7	**30.5**	31.6	32.1	30.3
$C_{O\&M}$ (million $/y)	**5.5**	6.2	6.3	**6.5**	6.8	7.0	**6.7**	7.4	7.4	7.1	**8.1**	8.4	8.5	8.0
C_{NG} (million $/y)	**77.2**	65.9	73.6	**77.2**	65.9	76.0	**90.8**	80.9	87.8	65.9	**91.0**	80.9	87.9	65.9
CoE (million $/y)	**2.7**	6.1	6.4	**–8.3**	0.1	0.7	**–14.1**	–10.7	–10.4	–13.8	**–33.9**	–23.1	–22.7	–24.7
C_{ST} (million $/y)	**–9.0**	–1.4	–1.4	**0.0**	0.0	0.0	**–16.6**	–9.3	–9.2	–7.8	**0.0**	0.0	0.0	0.0
AC (million $/y)	**97.4**	99.9	108.6	**99.8**	98.6	110.0	**92.0**	96.0	103.6	78.1	**95.6**	97.8	105.7	79.5
H_2 cost ($/$GJ_{LHV}$)	**7.89**	9.30	8.80	**8.08**	9.69	8.91	**7.45**	8.82	8.39	10.78	**7.74**	9.01	8.56	11.02
CCC ($/t CO_{2CAPT})	-	23.75	17.55		25.56	15.97		23.31	18.13	37.63		21.53	15.74	36.90
H_2 cost ($/$GJ_{LHV}$)−Ctax =20 $/t	**9.37**	9.57	9.18	**9.57**	9.97	9.33	**9.20**	9.42	9.05	11.17	**9.50**	9.61	9.22	11.41
H_2 cost ($/$GJ_{LHV}$)−Ctax =40 $/t	**10.86**	9.84	9.56	**11.05**	10.25	9.76	**10.96**	10.02	9.71	11.56	**11.26**	10.21	9.88	11.80

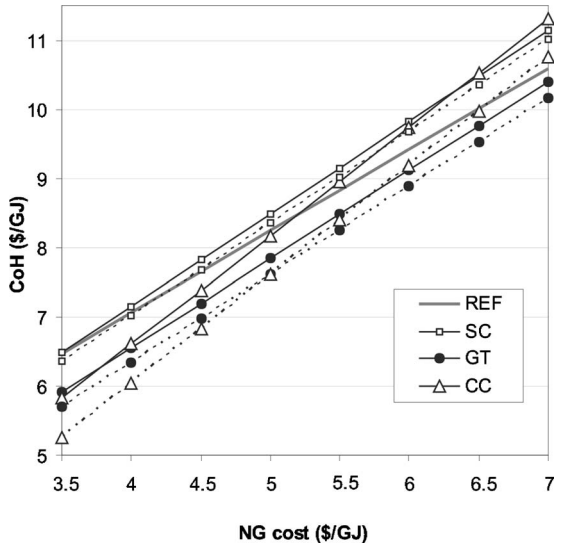

Fig. 6 CoH in function of NG cost for a CoE of $0.05/kWh (solid lines) and $0.06/kWh (dotted lines)

ample, if CoE=$0.05/kWh, the CC plant produces hydrogen at the lowest cost only for NG cost lower than $3.9/GJ. For higher NG cost, the GT becomes the most convenient. The breakeven point between these two technologies shifts to a NG cost of $5/GJ if CoE is $0.06/kWh.

However, the results of Fig. 6 are significantly affected by the cost of steam, which is assumed 10% higher than NG cost (as in the base case). This explains why GT and CC lines have different slopes even if NG consumption is the same. The influence of steam cost is shown on Fig. 7. The results are expressed in function of the cost ratio between steam and NG. The analysis has been performed with three different values of NG cost: $4.7/GJ, $5.64/GJ, and $6.58/GJ, represented respectively by solid, dotted and gray lines. In this case, electricity cost is not fixed, but rather proportional to NG cost, i.e., equal to $0.05/kWh, $0.06/kWh, and $0.07/kWh.

From Fig. 7, the following consideration can be made:

- Obviously, SC and CC are not affected by steam-NG cost ratio, as in these configurations steam is not exported.
- The assumption of an electricity cost proportional to NG cost clearly modifies the results with respect to Fig. 6. In fact, although in Fig. 6 the line representing the CC plant has the highest slope, in this case if NG cost is raised by 20%, the increase of CoH in CC configuration is the lowest ($0.92/GJ versus $1.12/GJ of SC, $1.24/GJ of GT and $1.29/GJ of REF).
- The CC is the configuration producing hydrogen at the lowest cost. GT can be convenient for steam-NG cost ratio higher than 0.9. Note that CC plant becomes even more convenient than the other configurations when increasing NG cost.

As previously said, the steam cost influences significantly the PB of the plant, since in the REF plant a high amount of steam is exported and the PB is relative to the added investment cost for power generation. For a high cost of steam (represented by solid lines in Fig. 8), only GT plant can achieve PB shorter than five years, unless the cost of electricity is raised to 0.06 (Fig. 8(*b*)), which makes competitive also the PB of CC. If the steam cost is decreased (see, for example, dotted lines representing a steam/NG cost ratio of 0.5) the PB of CC and SC is reduced and is lower than five years in a wide range. On the contrary, the PB of GT plant grows significantly.

In Fig. 9, the PB period has been determined with the assumption of a CoE proportional to NG cost. Differently from Fig. 8, in this case PB is reduced by a NG cost increase. This analysis is probably better representative of how the NG cost will influence the PB in the future. In fact, it is expectable that CoE will follow the trend of NG (and, in general, of oil price). Therefore, while Fig. 8 is useful to determine PB when CoE is given, Fig. 9 clearly demonstrates that in future the probable increasing of NG cost will favor the installation of a cogeneration plant.

Influence of Plant Capacity. Subsequently, an analysis has been carried out to investigate how the plant size affects the cost of hydrogen in the range 20–1300 MW_{LHV} equivalent hydrogen output. Essentially, only the capital cost has been varied with the capacity, according to (9) with a scale factor of 0.67. The hydrogen plant efficiency has been set constant, whereas the efficiency of the gas turbine has been varied in the range of 0.34–0.38, corresponding to a turbine power output varying between 2.1 MW and 127 MW. The results are illustrated in Figs. 10 and 11. For a high steam cost (Fig. 10), the CoH in the REF plant remains the lowest for plant capacity smaller than 600,000 Sm^3/d ($\sim$75 MW_{LHV} H_2); for a bigger capacity GT plant becomes the most convenient: this would require a gas turbine of at least 7.5 MW. CC configuration produces hydrogen at a lower cost than REF for a capacity higher than 2.1×10^6 Sm^3/d, equivalent

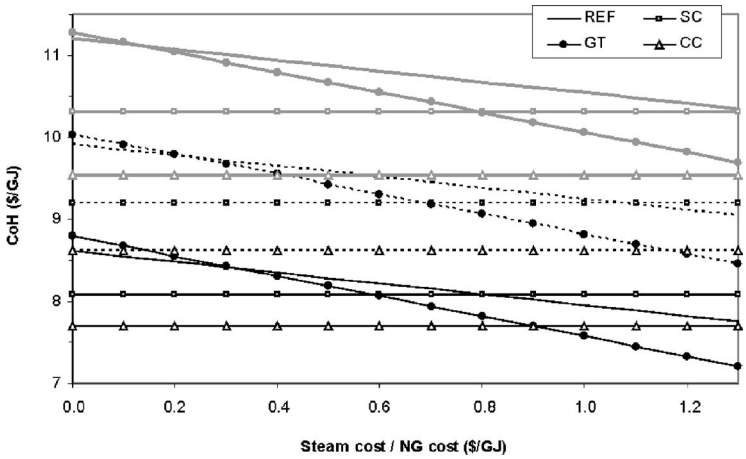

Fig. 7 CoH in function of cost ratio between steam and NG. Solid lines: NG=$4.7/GJ; CoE=$0.05/kWh and dotted lines: NG=$5.64/GJ; CoE=$0.06/kWh. Gray lines: NG=$6.58/GJ; CoE=$0.07/kWh.

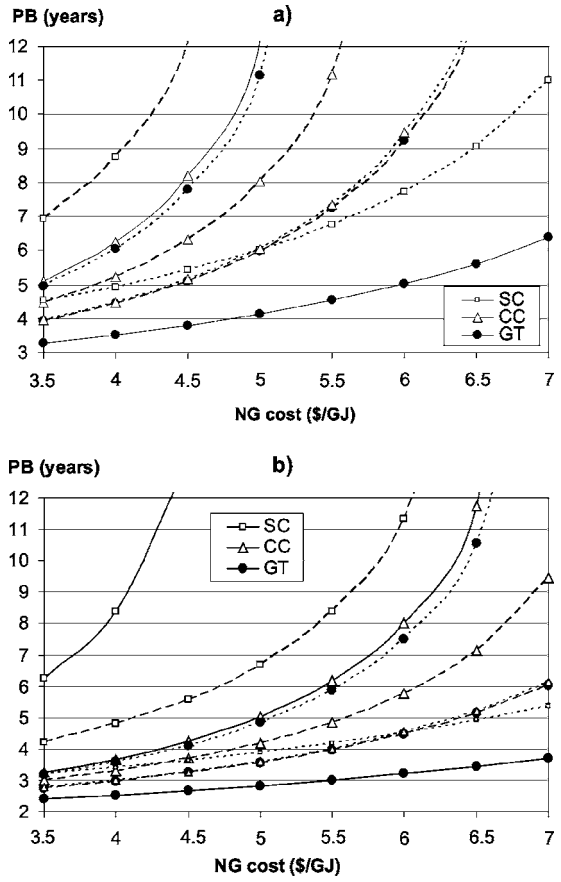

Fig. 8 PB period relative to the investment for power plant: CoE is fixed at \$0.05/kWh (*a*) and \$0.06/kWh (*b*). Steam-NG cost ratio is 1.1 (solid lines), 0.8 (dashed lines), and 0.5 (dotted lines).

to the installation of a 26 MW_E gas turbine (57 MW_E combined cycle). For a steam-NG cost ratio equal to 0.5 (see Fig. 11), the lowest CoH is obtained in REF plant for a capacity smaller than 1.1×10^6 Sm^3/d ($\sim$140 MW_{LHV} H_2) and in CC for bigger plants, thus requiring at least 30 MW_E produced in combined cycle. In this case, SC is also competitive, showing a lower CoH than REF for a capacity higher than 1.1×10^6 Sm^3/d.

The PB period relative to the investment cost for the power section is shown in Fig. 12 for two values of CoE and steam cost. The PB analysis is very significant, since the simple CoH is not

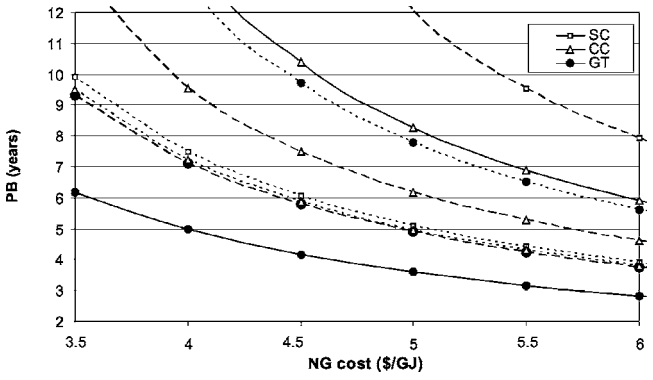

Fig. 9 PB period relative to the investment for power plant in function of NG cost: CoE=0.05/4.7×NGcost (\$/kWh); Steam-NG cost ratio is 1.1 (solid lines), 0.8 (dashed lines), and 0.5 (dotted lines)

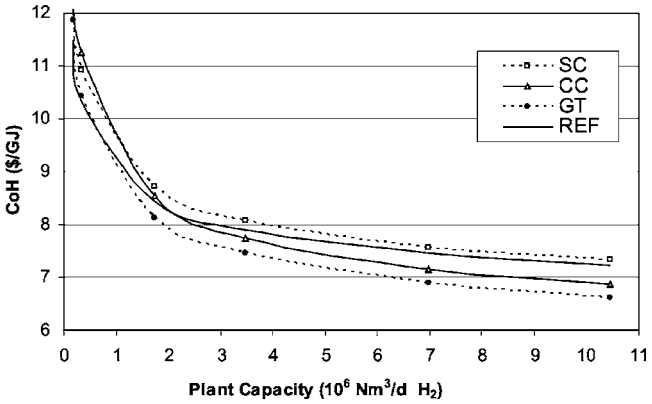

Fig. 10 Influence of plant capacity on CoH for NG cost = \$4.7/GJ, CoE= \$0.05/kWh, steam/NG cost=1.1

sufficient to evaluate the convenience of an investment. For example, if a PB of five years is considered acceptable, for a CoE of \$0.05/kWh (Fig. 12(*a*)) and steam/NG=1.1 in GT plants, this result is obtained by a plant size of approximately 2.1×10^6 Sm^3/d (corresponding to a gas turbine of 25 MW_E). This capacity is approximately equal to 3.5 times the capacity for which the CoH is lower in GT. If the CoE is raised to \$0.06/kWh, a PB of five years is obtained for a plant size of approximately 1.4×10^6 Sm^3/d (17 MW_E). CC configuration can achieve a PB of five years only for the higher CoE with a plant capacity of 3×10^6 Sm^3/d. If steam is sold at a cost equal to 0.5 times the cost of NG, the results are quite different: SC and CC show shorter PB than GT and for CoE equal to \$0.05/kWh they achieve a PB of five years both for a capacity of 4.7×10^6 Sm^3/d (equivalent to a CC of 128 MW and SC of 38 MW), which is reduced to 1.7 (CC) and 1.9 (SC) by a CoE of \$0.06/kWh (equivalent to a CC of 46 MW and SC of 16 MW).

Cost of CO_2 Capture. The main difference in the capital cost between the standard plants and the plants with carbon capture is the cost of the equipment for CO_2 removal and compression. Table 7 shows that in the plants with capture the cost for PSA system decreases (it is approximately one-half of the standard plant), as the scaling parameter used for calculation is the mole flow of the off-gas, which is significantly reduced by CO_2 absorption. In the REF plant, TCI is higher, respectively, by 11% and 14% than REF-HC and REF-LC. This result is in line with Klett et al. [7], which found an increase of 9% in the TCI. It is worth noting also that other parameters affect the final TCI, such as the

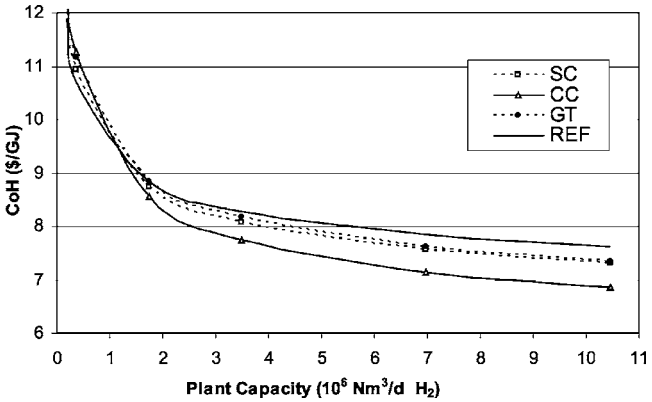

Fig. 11 Influence of plant capacity on CoH for NG cost = \$4.7/GJ, CoE= \$0.05/kWh, steam/NG cost=0.5

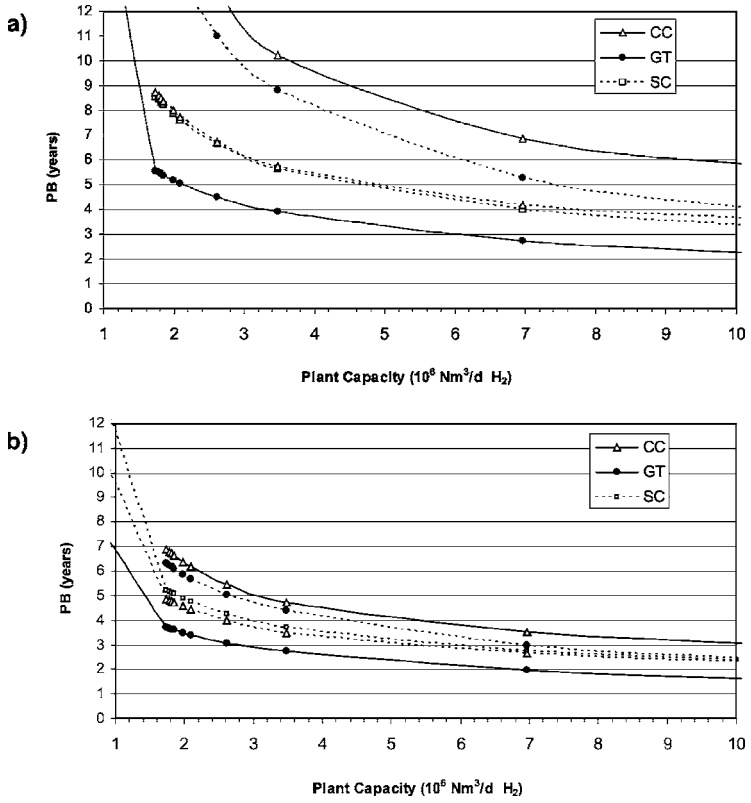

Fig. 12 Influence of plant capacity on PB for NG cost=\$4.7/GJ. Steam/NG cost=1.1 (solid lines) and 0.5 (dotted lines). (*a*) CoE =\$0.05/kWh and (*b*) CoE=\$0.06/kWh.

cost of H_2 compression, which is proportional to the amount of hydrogen produced. The cost of CO_2 capture has been determined as

$$\mathrm{CCC}[\$/\mathrm{t}] = \left[\frac{C\mathrm{oH}_{\mathrm{CAPT}} - C\mathrm{oH}}{\left(\frac{\mathrm{CO}_{2\mathrm{CAPT}}}{\mathrm{H}_{2\mathrm{LHV}}}\right)}\right]\frac{\$/\mathrm{GJ}}{t/\mathrm{GJ}} \tag{10}$$

where the subscript CAPT indicates the plant with carbon capture. Thus CCC is expressed as the ratio between the increase in the hydrogen cost due to the carbon capture and the amount of carbon dioxide captured per GJ of hydrogen produced. The results (Table 7) are particularly interesting because they show that the cost for carbon capture is very much different in relation to the configuration employed. It is evident that in all the cases the lowest hydrogen cost is obtained in the LC configuration. This is substantially due to the best conversion efficiency, which characterizes this kind of technology. Figure 13 shows how the NG cost affects the hydrogen cost in the REF plant if two different carbon taxes are applied. For a carbon tax of \$20/t CO_2 emitted, the REF plant produces hydrogen at a cost substantially higher than LC, but lower than HC. This is in agreement with the results of Table 7, in which the cost of carbon capture is 23.75 and 17.55, respectively for HC and LC: a carbon tax of \$20/t CO_2 makes attractive only the second option. However, it is worth noting that for high values of NG cost ($\sim$\$6.2/GJ), CoH is lower in REF than in LC. This is due to the steam and electricity cost, both assumed proportional to NG cost. In particular, the high steam-NG cost ratio (equal to 1.1) favors the REF plant, which exports much more steam than configurations with capture.

If carbon tax is raised to \$40/t CO_2 the cost of the H_2 in REF is 6–15% higher than in HC and 9–18% than in LC. This clearly shows the convenience of carbon capture in the plants producing only hydrogen in presence of a carbon tax. The increase in TCI ($+\$15.4\times10^6$ in HC and $+\$19.1\times10^6$ in LC compared to standard plant) is substantially recovered in a brief period if a carbon tax of \$25/CO_2 is applied, as the AC decreases by $\$16.8\times10^6$ and $\$5.8\times10^6$, respectively, for HC and LC (PB is 1 y for HC and 4.5 y for LC).

Cogeneration plants show similar results: the dependence of hydrogen cost on carbon tax is shown in Fig. 14. It is worth noting that LC configurations have the lowest cost in a wide range (for carbon tax higher than \$15/t and lower than \$90/t). On the contrary, in GT-HC and CC-HC the CCC is the highest; thus, hydrogen price in these configurations is lower than in the relative standard plant only for carbon tax higher than $\sim$\$50/t.

In plants with CO_2 capture, the PB period can be considered as the PB relative to the investment increase for CO_2 capture. Figure 15 shows the trend of PB in LC configurations in function of the carbon tax. For a Ctax equal to \$25/t, all the plants have a PB

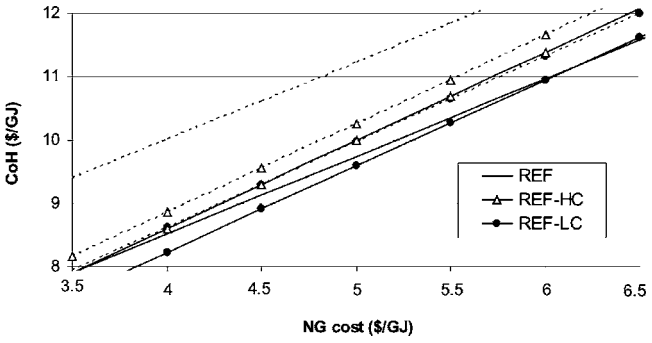

Fig. 13 Influence of NG cost on CoH in the REF plant, for a carbon tax of \$20/tCO_2 (solid lines) and \$40/tCO_2 (dotted lines)

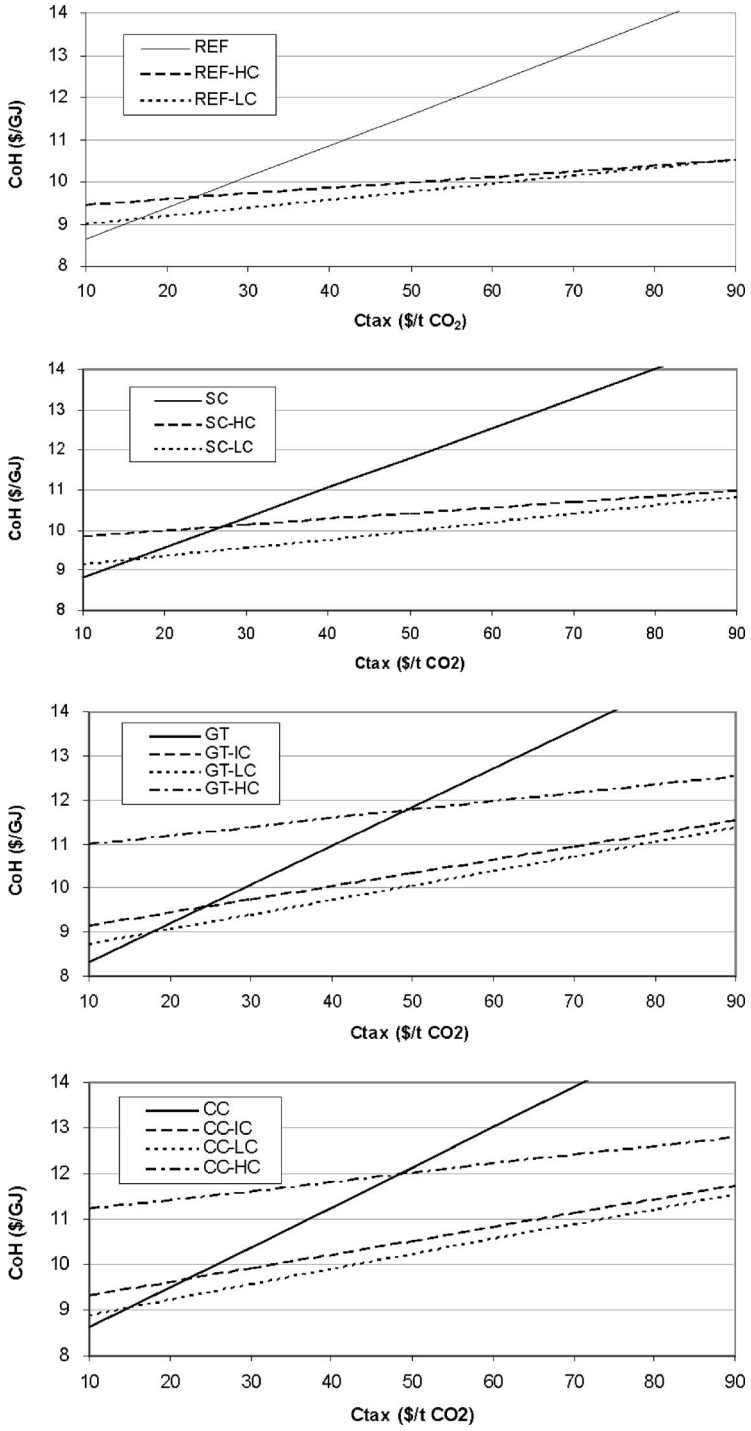

Fig. 14 Influence of Ctax on CoH (NG cost = $4.7/GJ, CoE = $0.05/kWh)

lower than five years; the PB decreases to less than two years for a Ctax of $35/t. For the analysis of the PB period in IC and HC plants, a different approach has been followed. The results illustrated in Table 7, in fact, have been obtained with the same NG input to the reformer, in order to investigate plants characterized by equipment of the same size. This causes a lower H_2 production in HC and IC configurations, while the analysis of PB period should be related to plants of the same capacity. To this aim, HC and IC plants have been scaled to the same H_2 production of the standard and LC case (equivalent to 435 MW_{LHV}). Table 8 shows the main results, which substantially are close to the ones obtained with the previous approach. Of course, the main differences concern GT-HC and CC-HC, which require a 1.7 times larger size. The trend of PB period for HC and IC as a function of the carbon tax is depicted in Fig. 16.

Conclusion

In this paper, a technoeconomic analysis has been carried out to investigate the possibility of cogenerating power and removing CO_2 in hydrogen plants based on steam methane reforming. In the reference plant, the resulting cost of hydrogen is $7.89/GJ, for a natural gas cost equal to $4.7/GJ, a cost of electricity of $0.05/kWh, and a steam cost of $5.17/GJ. For a combined cycle

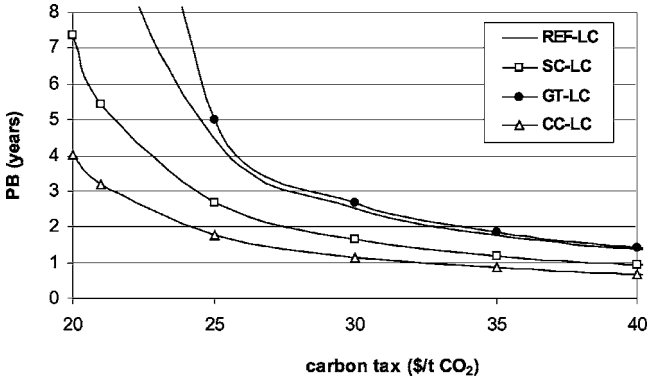

Fig. 15 Influence of Ctax on PB in LC plants (NG cost = $4.7/GJ, CoE = $0.05/kWh)

integrated plant, H_2 cost decreases to \$7.74/GJ, while the cost in gas turbine plant is \$7.45/GJ. However, the cost of hydrogen in GT plant is strongly affected by the cost of exported steam, which, instead, does not influence CC and SC. These configurations can be convenient both for a lower cost of steam or a higher cost of electricity. A plant capacity of $\sim 2.1 \times 10^6$ Sm^3/d is required to obtain a payback period relative to the investment for GT cycle lower than five years. This corresponds to the installation of a gas turbine of 25 MW_E. If the cost of steam is equal to 0.5 times the cost of natural gas and electricity is sold at \$0.06/kWh, the CC and SC show the shortest PB, equal to five years, respectively, for capacity of 1.7 (CC) and 1.9×10^6 Sm^3/d (SC) (equivalent to a CC of 46 MW_E and SC of 16 MW_E).

Table 8 Results for HC and IC with a capacity of 435 MW_{LHV}

	REF HC	SC HC	GT IC	GT HC	CC IC	CC HC
Scale factor	1.15	1.21	1.13	1.70	1.14	1.71
TCI (10^6 \$)	169.0	194.5	200.2	253.1	228.7	287.8
AC (10^6 \$/y)	113.4	117.2	107.3	123.8	109.4	125.4
CoH (\$/GJ_{LHV})	9.18	9.49	8.69	10.02	8.86	10.16
CCC (\$/t CO_{2CAPT})	21.7	22.4	21.1	29.1	18.9	27.2
CoH (\$/GJ_{LHV}) Ctax=20 \$/t	9.45	9.77	9.29	10.42	9.46	10.55
CoH (\$/GJ_{LHV}) Ctax=40 \$/t	9.71	10.05	9.89	10.81	10.06	10.94

The best option for carbon capture is fueling the SMR furnace and the gas turbine with natural gas, instead of hydrogen. This reduces the percentage of carbon captured but increases the hydrogen production and the efficiency of the plant. In this case, the cost of carbon capture has been estimated at \$16–18/t CO_2. A carbon tax of \$25/t is sufficient to reduce to acceptable values the payback period relative to the investment for carbon capture.

Acknowledgment

The software ASPEN PLUS® Version 2004.1 used in this paper is under license of Aspen Technology, Inc.

Nomenclature

AC = annual cost
BFW = boiler feed water
CC = combined cycle
CCC = cost of carbon capture
CoE = cost of electricity
CoH = cost of hydrogen
COMP = compressor
DLN = dry low NO_x
GT = gas turbine cycle
HC = high level carbon capture
HE = heat exchanger
HRSG = heat recovery steam generator
HTS = high-temperature shift
IC = intermediate level carbon capture
IGCC = integrated gasification combined cycle
IR = interest rate
LC = low level carbon capture
LHV = lower heating value
LTS = low-temperature shift
NG = natural gas
NPV = net present value
O&M = operations and maintenance
p = pressure
PSA = pressure swing adsorption
REF = reference
SC = steam cycle
ST = steam turbine
SMR = steam methane reformer
T = temperature
TCI = total cost of investment
TIT = turbine inlet temperature (first rotor)
WHB = waste heat boiler
WKO = water knock-out
WREM = water removal

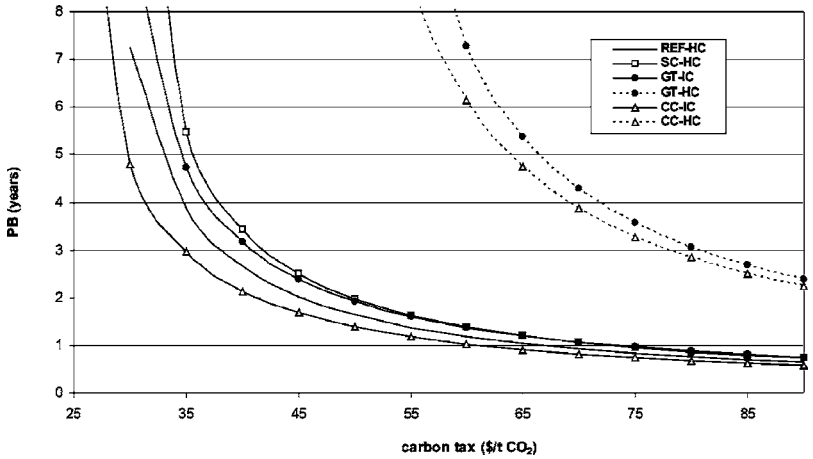

Fig. 16 Influence of Ctax on PB in HC and IC plants (NG cost = $4.7/GJ, CoE = $0.05/kWh)

References

[1] Desideri, U., and Proietti, S., 2002, "CO_2 Capture and Removal System for a Gas-Steam Combined Cycle," ASME Paper No. IMECE2002-33296.

[2] Bolland, O., and Mathieu, P., 1998, "Comparison of Two CO_2 Removal in Combined Cycle Power Plants," Energy Convers. Manage., **39**(16–18), pp. 1653–1663.

[3] Lurgi Oel Gas Chemie GmbH, "Hydrogen," newsletter available at: www.lurgi.de/lurgi-headoffice-kopie/english/nbsp/menu/media/newsletter/hydrogen.pdf

[4] Haldor Topsoe, www.haldortopsoe.com

[5] Terrible, J., Shahani, G., Gagliardi, C., Baade, W., Bredehoft, R., and Ralston, M., 1999, "Consider Using Hydrogen Plants to Cogenerate Power Needs," Hydrocarbon Process., **78**(12), pp. 45–53.

[6] Consonni, S., and Viganò, F., 2005, "Decarbonized Hydrogen and Electricity From Natural Gas," Int. J. Hydrogen Energy, **30**, pp. 701–718.

[7] Klett, M. G., White, J. S., Schoff, R. L., and Buchanan, T. L., 2002, "Hydrogen Production Facilities. Plant Performance and Cost Comparisons," U.S. DOE/NETL under Subcontract No. 990700362, Task 50802 by Parson Infrastructure and Technology Group Inc.

[8] Rostrup-Nielsen, J. R., and Rostrup-Nielsen, T., 2002, "Large-Scale Hydrogen Production," CATTECH, **6**(4), pp. 150–159.

[9] Uhde, "Hydrogen," brochure available at http://www.uhde.biz/cgi-bin/byteserver.pl/pdf/broschueren/Duengemittel/Hydrogen.pdf

[10] Contadini, J. F., Diniz, C. V., Sperling, D., and Moore, R. M., 2000, "Hydrogen Production Plants: Emissions and Thermal Efficiency Analysis," 2nd International Symposium on Technological and Environmental Topics in Transports, October 26–27, Milan.

[11] Spath, P. L., and Mann, M. K., 2001, "Life Cycle Assessment of Hydrogen Production via Natural Gas Steam Reforming," National Renewable Energy Laboratory, Technical Report No. NREL/TP-570-27637.

[12] Stocker, J., Whysall, M., and Miller, G. Q., 1998, *30 Years of PSA Technology for Hydrogen Purification*, UOP, Des Plaines, IL.

[13] *Turbomachinery International Handbook*, 2004, Business Journal Inc., Norwalk, CT, Vol. 44, No. 6, p. 79.

[14] Chiesa, P., Lozza, G., and Mazzocchi, L., 2003, "Using Hydrogen as Gas Turbine Fuel," ASME Paper No. GT-2003-38205.

[15] Patel, N. M., Davis, R. A., Eaton, N., Carlson, D. L., Kessler, F., and Khurana, V., 1994, "Across-the-Fence Hydrogen Plant Starts up at California Refinery," Oil Gas J., **92**(40), pp. 1–7.

[16] Lozza, G., and Chiesa, P., 2000, "Natural Gas Decarbonization to Reduce CO_2 Emission From Combined Cycles. Part A: Partial Oxidation," ASME Paper No. 2000-GT-0163.

[17] Lozza, G., and Chiesa, P., 2001, "Low CO_2 Emission Combined Cycles With Natural Gas Reforming, Including NO_x Suppression," ASME Paper No. 2001-GT-0561.

[18] Hamelinck, C. N., and Faaij, A. P. C., 2002, "Future Prospects for Production of Methanol and Hydrogen From Biomass," J. Power Sources, **111**, pp. 1–22.

[19] De Lorenzo, L., Kreutz, T. G., Chiesa, P., and Williams, R. H., 2005, "Carbon-Free Hydrogen and Electricity From Coal: Options for Syngas Cooling in Systems Using a Hydrogen Separation Membrane Reactor," ASME Turbo Expo 2005: Power for Land, Sea and Air, June 6–9, Reno-Tahoe, ASME Paper No. GT2005-68572.

[20] Williams, R. H., Larson, E. D., Katofsky, R. E., and Chen, J., 1995, "Methanol and Hydrogen From Biomass for Transportation, With Comparisons to Methanol and Hydrogen From Natural Gas and Coal," PU/CEES Report No. 292, Center for Energy and Environmental Studies, Princeton University, Princeton, p. 47.

[21] Kreutz, T., Williams, R., Consonni, S., and Chiesa, P., 2005, "Co-Production of Hydrogen, Electricity and CO_2 From Coal With Commercially Ready Technology. Part B: Economic Analysis," Int. J. Hydrogen Energy, **30**, pp. 769–784.

[22] Sjardin, M., 2004, "Techno-Economic Prospects of Small-Scale Membrane Reactors in a Future Hydrogen-Fuelled Tranportation Sector," Utrecht University, Copernicus Institute, Report No. NWS-I-2004-19.

[23] Roy, S., Cox, B. G., Adris, A. M., and Pruden, B. B., 1998, "Economics and Simulation of Fluidized Bed Membrane Reforming," Int. J. Hydrogen Energy, **23**(9), pp. 745–752.

[24] Molburg, J. C., and Doctor, R. D., 2003, Hydrogen From Steam-Methane Reforming With CO_2 Capture, 20th Annual International Pittsburgh Coal Conference, Sept. 15–19, Pittsburgh.

[25] Leiby, S., 1994, "Options for Refinery Hydrogen," Process Economics Program, Report No. 212, SRI International, Menlo Park, CA.

[26] Bredesen, R., and Sogge, J., 1996, "Ecological Application of Innovative Membrane Technology in the Chemical Industry," UN Seminar, Cetraro, Italy, May 1–4.

[27] Aasberg-Petersen, K., Stub Nielsen, C., and Lægsgaard Jørgensen, S., 1998, "Membrane Reforming for Hydrogen," Catal. Today, **46**, pp. 193–201.

[28] Padró, C. E. G., and Putsche, V., 1999, "Survey of the Economics of Hydrogen Technologies," National Renewable Energy Laboratory Technical Report No. NREL/TP-570-27079.

[29] Foster-Wheeler, 1996, "Decarbonisation of Fossil Fuels," IEA Greenhouse Gas R&D Programme, Report No. P H_2/2.

[30] Simbeck, D. R., 2004, "Hydrogen Costs With CO_2 Capture," 7th International Conference on Greenhouse Gas Control Technologies (GHGT-7), Vancouver, Canada, September 5–9.

[31] Blok, K., Williams, R., Katofsky, R., and Hendriks, C., 1997, "Hydrogen Production from Natural Gas, Sequestration of Recovered CO_2 in Depleted Gas Wells and Enhanced Natural Gas Recovery," Int. J. Hydrogen Energy, **22**(2/3), pp. 161–168.

[32] EU DG Energy and Transport, 2005, "Quarterly Review of European Electricity and Gas Prices," Issue 4, July.

[33] U.S. Department of Energy, Energy Efficiency and Renewable Energy, 2003, "How To Calculate the True Cost of Steam—A Best Practices Steam Technical Brief," DOE/GO-102003-1736, Sept.

Combustion Oscillation Monitoring Using Flame Ionization in a Turbulent Premixed Combustor

B. T. Chorpening
e-mail: benjamin.chorpening@netl.doe.gov

J. D. Thornton

E. D. Huckaby

National Energy Technology Laboratory,
US Department of Energy,
Morgantown, WV 26507-0880

K. J. Benson
Woodward,
Loveland, CO 80538

To achieve very low NO_x *emission levels, lean-premixed gas turbine combustors have been commercially implemented that operate near the fuel-lean flame extinction limit. Near the lean limit, however, flashback, lean blow off, and combustion dynamics have appeared as problems during operation. To help address these operational problems, a combustion control and diagnostics sensor (CCADS) for gas turbine combustors is being developed. CCADS uses the electrical properties of the flame to detect key events and monitor critical operating parameters within the combustor. Previous development efforts have shown the capability of CCADS to monitor flashback and equivalence ratio. Recent work has focused on detecting and measuring combustion instabilities. A highly instrumented atmospheric combustor has been used to measure the pressure oscillations in the combustor, the* OH *emission, and the flame ion field at the premix injector outlet and along the walls of the combustor. This instrumentation allows examination of the downstream extent of the combustion field using both the* OH *emission and the corresponding electron and ion distribution near the walls of the combustor. In most cases, the strongest pressure oscillation dominates the frequency behavior of the* OH *emission and the flame ion signals. Using this highly instrumented combustor, tests were run over a matrix of equivalence ratios from 0.6 to 0.8, with an inlet reference velocity of* 25 m/s (82 ft/s). *The acoustics of the fuel system for the combustor were tuned using an active-passive technique with an adjustable quarter-wave resonator. Although several statistics were investigated for correlation with the dynamic pressure in the combustor, the best correlation was found with the standard deviation of the guard current. The data show a monotonic relationship between the standard deviation of the guard current (the current through the flame at the premix injector outlet) and the standard deviation of the chamber pressure. Therefore, the relationship between the standard deviation of the guard current and the standard deviation of the pressure is the most promising for monitoring the dynamic pressure of the combustor using the flame ionization signal. This addition to the capabilities of CCADS would allow for dynamic pressure monitoring on commercial gas turbines without a pressure transducer.* [DOI: 10.1115/1.2431390]

Introduction

The U.S. Department of Energy (DOE) National Energy Technology Laboratory (NETL) conducts programs that support the global interest for clean power generation, such as the Turbine Program. In support of the goals of the Turbine Program, researchers at NETL are developing sensor technology for combustion monitoring and control. This sensor development is based on using the flame's electrical properties to perform real-time diagnostics and in situ monitoring of critical combustion parameters [1,2]. This paper describes ongoing research on ion and electron distribution in a lean premixed turbulent combustor, which supports this sensor development effort.

It is well known that a flame can conduct electrical current [3–6] and that the measured current conducted through the flame relates to the flame characteristics. The flame ionization detector (FID) used in gas chromatography [4,5] uses the measured current through the flame to measure very low concentrations of hydrocarbons. The reaction most often cited for providing the FID response results from the chemi-ionization of CHO^* [4,5]:

$$CH + O \rightarrow CHO^* \rightarrow CHO^+ + e^- \quad (1)$$

Application of sufficient voltage allows complete collection of the generated electrons. The number of electrons produced has been found to be proportional to the number of hydrocarbons in the sample, with modifications for specific functional groups, such as –OH. An extensive review of past research in flame ionization has been published by Fialkov [7].

In most practical combustion systems, mass flow rates are orders of magnitude higher than the flow rates in a FID. This makes complete charge collection very difficult (i.e., requiring very high electric field strength). However, a representative signal at various conditions may be obtained at relatively low electric field strengths.

To study the charged species distribution in premixed, turbulent combustion, a special combustor (Fig. 1) has been built with electrodes on the end of the premix injector center body and along the combustion chamber walls. The measuring system applies a bias to the electrodes and uses the electrons and ions in the combustion field to complete the circuit to ground (the steel walls of the combustor). The resulting current is measured from each electrode. Although this experiment does not specifically select ions or electrons as charge carriers, it is likely that electrons are the primary charge carriers due to their considerably higher mobility [8].

Contributed by IGTI for publication in the JOURNAL OF ENGINEERING FOR GAS TURBINES AND POWER. Manuscript received September 30, 2004; final manuscript received August 30, 2006. Review conducted by Lee Langston. Paper presented at the ASME Turbo Expo 2004: Land, Sea and Air (GT2004), June 14, 2004–June 17, 2004, Vienna, Austria. Paper Number GT2004-53881.

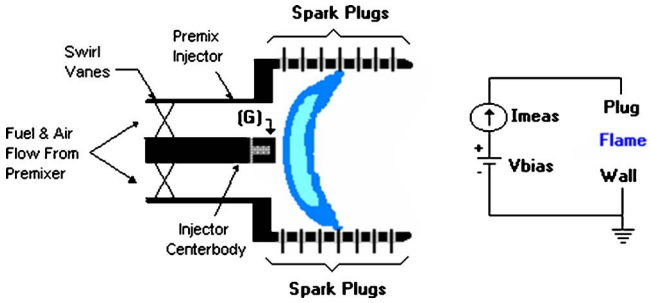

Fig. 1 Functional diagram of the experimental combustor. The flame provides a slightly conductive path between the guard electrode (G), the spark plugs, and walls of the combustor. A voltage is applied to the guard electrode and the spark plugs; the corresponding current is measured.

Apparatus

The test combustor, designated "Sparky," has an inside diameter of 78 mm (3.07 in.) and an overall length of 927 mm (36.5 in.). Details of the inlet end of the combustor are shown in Fig. 2. The guard electrode covers the last 2.5 cm (1 in.) of the premix injector center body at the combustor inlet. It is electrically isolated from the remainder of the injector by ceramic insulators around its support legs. The spark plug electrodes are spaced on 25.4 mm (1 in.) centers along the sides of the combustor, starting at the inlet end wall. During operation, the spark plug electrodes are horizontally oriented on the two sides (the top view is shown in Fig. 2). Kistler pressure transducers are located at Pc, Pn1, Pn2, and Pf to monitor the combustor pressure, two nozzle pressures, and the fuel system pressure. Four uv-grade optical fibers observe the OH emission through ports located on the top of the combustor at OH1–OH4. In these tests the OH4 probe was damaged. The light is carried through the fibers to photomultipliers, which have UG11 filters to block visible wavelengths. The inside diameter of the premixer is 26.6 mm (1.05 in.). A swirler is located at the premixer entrance shortly before fuel injection. The tip of the premixer center body has been flared to provide local flow acceleration, to encourage the flame to anchor downstream of the premixer exit.

During operation, the airflow has been varied between 9.6 and 14.4 g/s (1000–1500 ft^3/h at 60°F, 1 atm), with equivalence ratios from 0.6 to 0.8 using commercial natural gas as the fuel. A variable quarter-wave resonator has been attached to the fuel manifold to allow for acoustic tuning of the fuel injection system. This is discussed by Richards et al. [9]. In these tests, the acoustic tuner has been applied to change the magnitude and frequency of the combustion oscillations. A constant bias of +5 V has been applied to all electrodes. The current flow from each electrode is read independently through a prototype system built at NETL. Each channel is scaled independently to optimize the signal level. Only 12 current channels were available during the experiments discussed here; electrodes A1-A9, B1, B2, and the guard electrode were monitored. The analog voltages were recorded on two TEAC recorders at 6 kHz and 12 kHz. One channel on each recorder was reserved for a synchronization signal, which was used to time synchronize all the data upon processing into a digital file.

Experimental Results

Twenty individual signals were monitored at 6 kHz. Two samples of the data are shown in Figs. 3 and 4. Both show data from the combustor operating with a reference velocity (average airflow velocity in premixer) of 25 m/s (82 ft/s) and equivalence ratio of 0.7. The acoustic tuner has been adjusted to change the magnitude and frequency of the oscillations between the two cases. In the first case (Fig. 3), the primary frequency of oscillation is 193 Hz, with an rms dynamic pressure of 0.69 psi (4.8 kPa), 4.7% of the operating pressure. In the second case (Fig. 4), the primary oscillation has shifted to a frequency of 164 Hz with an rms dynamic pressure of 1.48 psi (10.2 kPa), 10.1% of the operating pressure. For simplicity, these will be referred to as the 193 Hz case and the 164 Hz case in the discussion. A simple analysis of the combustor as a tube with one end closed, filled with air at 1200 K, indicates first and third harmonic frequencies of 193 Hz and 579 Hz.

The first column of Fig. 3 shows the current carried through each electrode (in microamps) for a short segment of time. The flow through the combustor follows the plots from the bottom to the top, with the exception of electrodes B1 and B2, which are at the same downstream locations as electrodes A1 and A2 but are on the opposite side of the combustor. The second column of

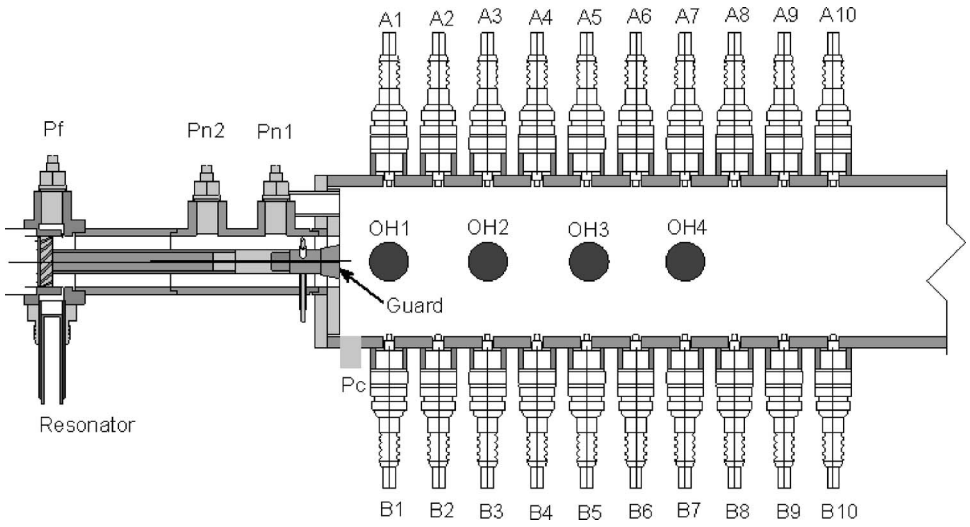

Fig. 2 Diagram of inlet end of the Sparky combustor (dimensions in inches). The spark plug electrodes are labeled A1–A10 and B1–B10, and have a 25.4 mm (1 in.) spacing. The OH^* detectors are labeled OH1–OH4, and are on a 50.8 mm (2 in.) spacing. The pressure transducers are labeled Pc (combustor), Pn1 (nozzle 1 pressure), Pn2 (nozzle 2 pressure), and Pf (fuel inlet pressure). The guard electrode is on the end of the premixer center body.

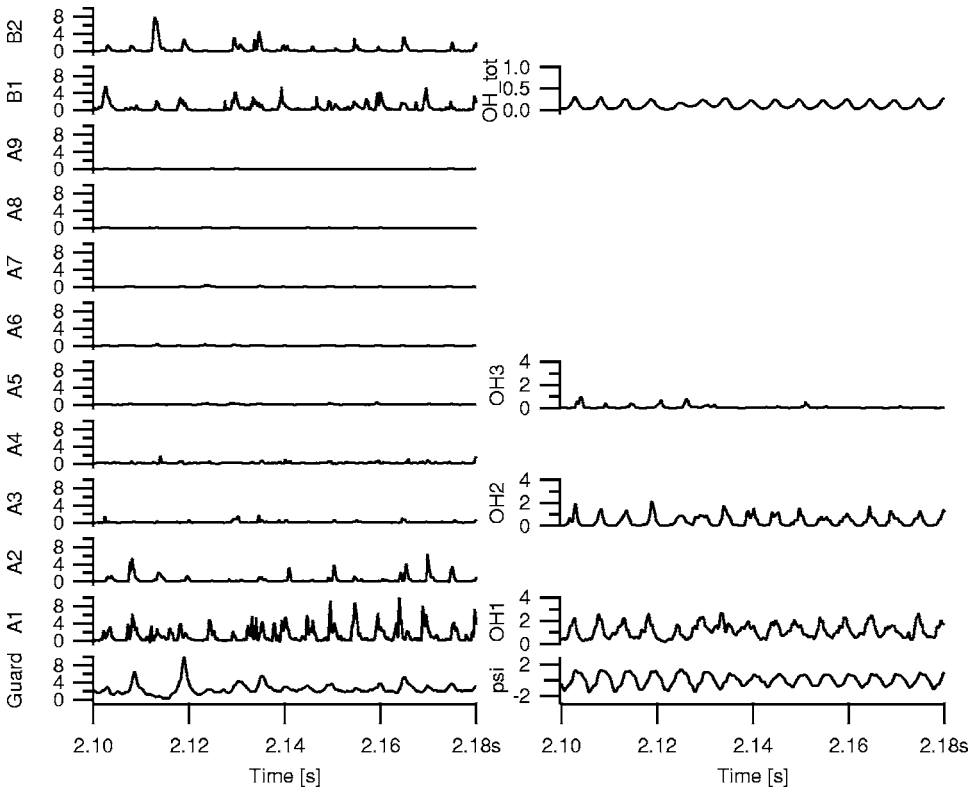

Fig. 3 Sample data from operation at a reference velocity =25 m/s with Φ=0.71. The fuel system has been tuned for smaller pressure oscillations. The electrode signals in the left column are in microamps; the OH emission signals are in arbitrary units (193 Hz case).

graphs shows the combustor chamber pressure (measured by Pc in Fig. 2 and labeled psi in Figs. 3 and 4), the signals from the OH point sensors OH1–OH3, and the OH signal from a filtered PMT looking into the combustor from the outlet (OH_tot). The OH point signal graphs have been located adjacent to the corresponding electrode graphs, based on their downstream location.

Discussion

Real-Time Data. The initial results must be seen in light of two factors. First, the potential field for each spark plug is very localized (Fig. 5). Second, the guard electrode potential field, although further reaching, is also fairly localized. This indicates that the flame position is critical to the measured current from either the centerbody or the wall electrodes.

The electronically excited OH emission in the 193 Hz case, shown in the second column of Fig. 3, indicates that the luminous zone of the flame is concentrated in the first 100 mm (4 in.) of the combustor, since the OH emission drops off considerably from the OH2 probe to the OH3 probe. In comparison, the luminous zone of the flame extends past 125 mm (5 in.) in the 164 Hz case, based on the strength of the OH3 signal. Although a small drop in equivalence ratio occurred between the two cases, which would tend to stretch out the flame, the strong increase in pressure oscillation magnitude and the reduction in frequency is more likely to have produced this extension of the luminous flame zone. The larger, slower oscillations are able to move the combustion zone further upstream and downstream in the combustor, creating the strong OH emission signal oscillations. The higher-frequency (193 Hz) case does not move the combustion zone as much, which leads to the reduced OH3 signal and the higher baseline signal at OH1.

In contrast, the current signals from the wall electrodes are stronger in the 193 Hz case than in the 164 Hz case. The 164 Hz case does show more evidence of weak current fluctuations downstream, at electrodes A6 and A7, than the 193 Hz case, which would agree with the longer flame suggested by the OH emission signals. But at locations near the premix injector exit, A1-A2, the current signals are distinctly stronger for the 193 Hz case. With the localized nature of the potential fields, this seems to indicate that the flow pattern within the combustor carries more electrons near the A1 and A2 electrodes in the 193 Hz case than in the 164 Hz case. In the 164 Hz case, the stronger guard electrode oscillations indicate the movement of the electrons back toward the tip of the injector center body, and possibly into the premixer. This flashback behavior has been observed in previous combustor testing in this facility [1]. Analysis of the system using computational fluid dynamics (CFD) with careful consideration of the fuel system acoustics is expected to add further insight into these results.

Careful examination of the time records for electrodes A1 and B1, and A2 and B2 in Fig. 3 also indicates the electron distribution is not spatially uniform across the combustor. This probably indicates the flame is either precessing or flickering at the operating condition. Both time and spatial variation of the flame is apparent on a video record taken from the exhaust end of the combustor. A pattern to the flame movement, however, cannot be discerned, possibly due to the low (30 Hz) frame rate.

Finally, both the 193 Hz and 164 Hz cases show a good correlation of the guard electrode current with the pressure signal. Both show the same dominant frequency, similar to earlier observations in high pressure testing of flame ionization sensors at NETL [10]. This dominant frequency shows up on all the current signals, as well as the OH emission signals (Fig. 6). This suggests the flame ionization sensor could be applied to monitoring combustion dynamics.

Statistical Results. A test matrix was run to investigate the link

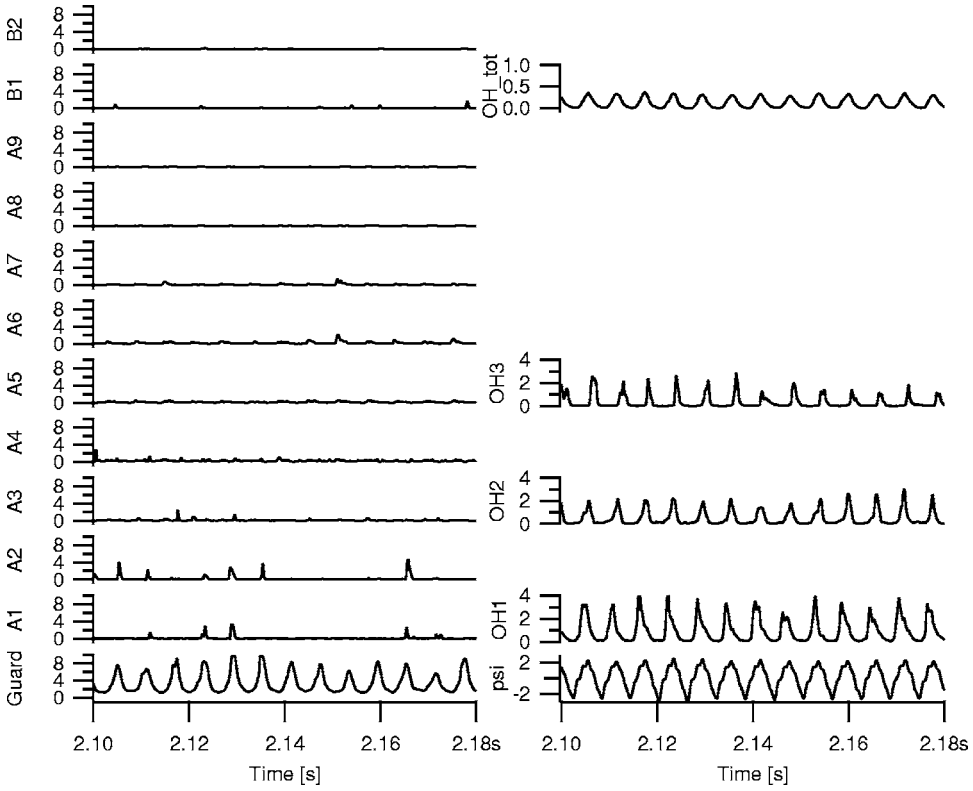

Fig. 4 Sample data from combustor with reference velocity =25 m/s, and Φ=0.69. The fuel system has been tuned to produce large pressure oscillations. The electrode signals in the left column are in microamps; the OH emission signals are in arbitrary units (164 Hz case).

between flame ionization sensor data and dynamic pressure data. This matrix is summarized in Table 1. Three statistics that were examined were the mean value of the guard current (Mean(G)), the root-mean-square value of the guard current (rms(G)), and the standard deviation of the guard current (STD(G)). The standard deviation of the chamber pressure (STD(P)) was selected as the baseline statistic since the pressure transducer is a high-speed DC transducer. Removal of the mean value in the computation of the standard deviation allows the comparison to focus on the dynamic pressure and not be misled by small offsets in the DC pressure with operating condition. In the three figures shown, the value of statistics is calculated over a four second block of time. All three

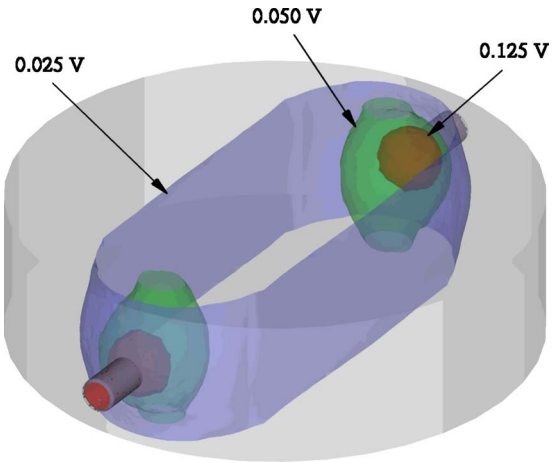

Fig. 5 Potential field at an electrode pair in the combustor without flow. The electrodes have an applied potential of 5 V. The figure shows three-dimensional potential surfaces.

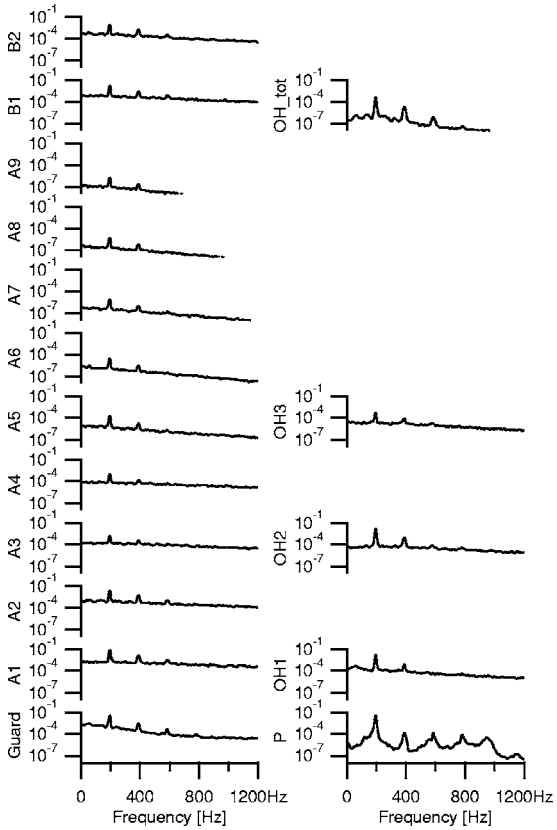

Fig. 6 Frequency spectra from real time data in the 193 Hz case. The peak magnitudes vary considerably with electrode location, but the dominant frequency is constant.

Table 1 Summary of test matrix operating conditions

Parameter	Range
Reference velocity	20–30 m/s (66–98 ft/s)
Equivalence ratio (Φ)	0.6–0.8
Dynamic pressure (rms)	(0.7–11.0 kPa) 0.1–1.6 psi

figures are based on data obtained at a reference velocity (V_{ref}), of 25 m/s (82 ft/s). Adjustment of the acoustic tuner attached to the fuel system caused variation of the magnitude of the pressure oscillations in the combustor independent of average fuel flow and reference velocity. Acoustic tuning, however, often changed the pressure oscillation frequency as well as its magnitude.

An overview of the data shows that all three statistics selected for comparison, Mean(G), rms(G), and STD(G), are functions of the equivalence ratio. This is evidenced in the comparison of the y-axes used for the three figures, with larger y-axis spans necessary for increased equivalence ratio. This trend has been observed previously [11], and logically follows from the greater number of ions and electrons generated as the equivalence ratio is increased. Blocking the data by equivalence ratio makes the link between the test statistics and the dynamic pressure more easily observed.

Focusing on the data at an equivalence ratio (Φ) of 0.6 (Fig. 7), it is obvious that the rms value of the guard current is nearly identical to the mean value in this case. Rms(G) and Mean(G) are both considerably larger signals (~10X) than the STD(G). All three statistics increase with the standard deviation of the pressure, STD(P); however, the STD(G) appears to have much less scatter than rms(G) and Mean(G) at low pressure oscillations. The scatter in rms(G) and Mean(G) may be caused by the frequency shift from 176 Hz to 182 Hz.

At an equivalence ratio of 0.6, the mean and rms values of the guard current were nearly identical. In comparison, at an equivalence ratio of 0.7 (Fig. 8), there is now a separation between rms(G) and Mean(G), which appears to increase as the magnitude of the pressure oscillations increase. The difference in signal levels between STD(G) and rms(G) is considerably reduced, to about a factor of 2. All three statistics are once again monotonic with STD(P), with low scatter. A nonlinear response appears to occur with the strongest pressure oscillations. A general decrease in dominant frequency occurs as the magnitude of the pressure oscillations increase, but no sudden jumps from a frequency change are apparent.

All three statistics behaved similarly at an equivalence ratio of 0.7. Significant differences appear between the three statistics at an equivalence ratio of 0.8, as shown in Fig. 9. At Φ=0.8, only STD(G) remains monotonic with the pressure oscillation, STD(P). The STD(G) is a factor of 2–4X smaller than rms(G); however,

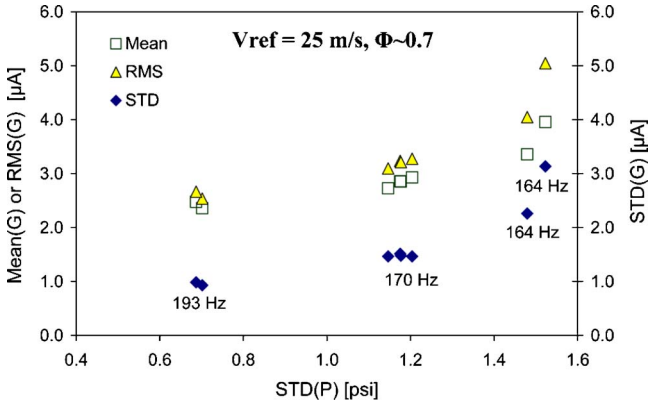

Fig. 8 Sensor statistics from Φ=0.7, V_{ref}=25 m/s

this is offset by the large fluctuations in rms(G) with STD(P). The Mean(G) follows rms(G), with varying separation between points. The rms and mean values of the guard current appear to respond strongly to the primary frequency of the pressure oscillations, which display a large shift from 563 Hz to 229 Hz (likely due to a shift in the dominant acoustic mode). The response of STD(G) to the frequency change of the pressure oscillations is much less dramatic.

Based on these results, it seems apparent that although the STD(G) is a smaller signal than rms(G), the monotonic behavior of STD(G) offers a simpler relationship with STD(P) than rms(G). This suggests that STD(G) is a superior statistic to use for sensor development.

In analyzing the data, frequency spectra were calculated for all the data. From these spectra, the strongest frequency peaks were determined. The primary frequency peak in the guard current corresponded to the primary frequency peak in the pressure in most cases, but not all, as shown in Fig. 10. When the primary frequency peaks of the pressure and guard current match, the points lie along the line with a slope of 1. Examination of the magnitude of the pressure oscillations, given by STD(P), in comparison to the frequency of the pressure oscillations shows that the match between the pressure oscillation and guard current oscillation frequencies is dependent on the magnitude of the oscillations. If the magnitude of the pressure oscillations lies below a threshold (drawn in by inspection as the dashed line), then it is too weak to dominate the guard current signal. If the pressure oscillation is strong enough (STD(P) is above the dashed line), then the pressure fluctuation dominates the guard current signal, and the strongest frequency in the guard current matches the strongest frequency in the pressure. This threshold on the frequency

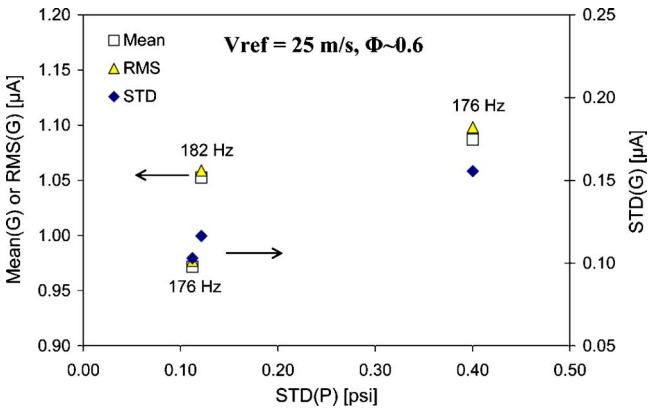

Fig. 7 Sensor statistics at Φ=0.6, V_{ref}=25 m/s

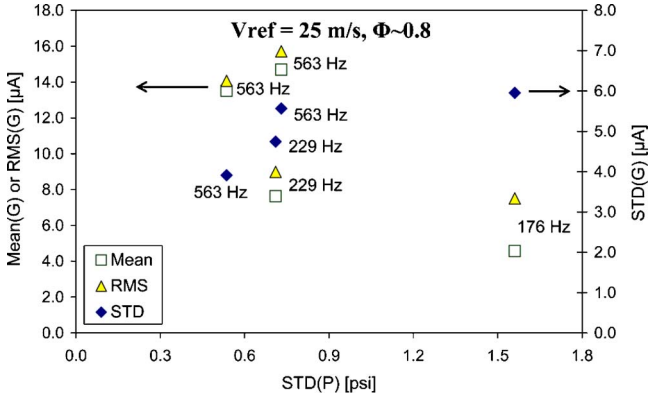

Fig. 9 Sensor statistics for Φ=0.8, V_{ref}=25 m/s. Primary oscillation frequencies of the points are indicated.

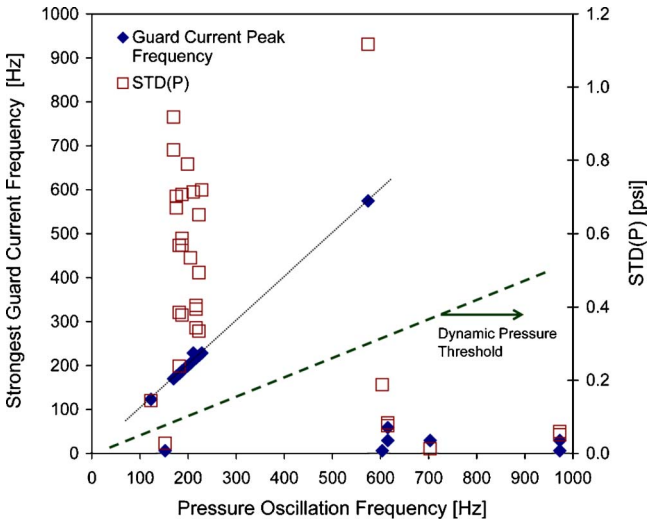

Fig. 10 Correspondence between primary pressure frequency and primary frequency in guard current oscillations

correspondence may be reduced through the application of a higher potential to the guard electrode, which would increase the strength and extent of its potential field.

Conclusions

An experimental test matrix run in a turbulent, lean premixed, atmospheric pressure combustor has shown relationships between the chamber pressure, OH emission, and flame ionization signals. Electrodes spaced on 2.5 cm (1 in.) intervals along the walls of the combustor sense local ion fields. Testing has shown that the presence of OH emission in the core of the combustor does not necessarily indicate the presence of charged species near the walls. However, an electrode covering the end of the premixer center body, called the guard electrode, maintains a signal under all observed combustion conditions.

The standard deviation of the guard electrode current has been shown to be monotonically related to the standard deviation of the chamber pressure (the dynamic pressure). Through the use of a quarter-wave resonator, the acoustics of the test combustor were tuned to modify the amplitude and the frequency of the pressure oscillations within the combustor. The mean, rms, and standard deviation of the guard electrode current are all functions of the equivalence ratio. When blocked by equivalence ratio, the standard deviation of the guard current emerges as having a monotonic relationship with the dynamic pressure. The mean and rms of the guard current do not have a monotonic relationship with the dynamic pressure, in particular at tests at $\Phi=0.8$. This appears to be related to a much stronger sensitivity to the frequency of the combustion oscillations on the magnitude of these statistics. The monotonic relationship between the standard deviation of the guard current and the dynamic pressure strongly suggests that it is possible to monitor combustion dynamics using a flame ionization sensor instead of a pressure transducer, with proper calibration.

Acknowledgment

This work was performed under the Turbine Program directed by Richard Dennis. Laboratory support of C. Utt (DOE) and Parsons Project Services (E. Robey, R. Addis, W. Fincham), and video processing by the EG&G Multimedia Department (T. Ford) is gratefully acknowledged.

Nomenclature

Φ = equivalence ratio
G = guard electrode or current to guard electrode
P = pressure
rms = root mean squared
STD = standard deviation
V_{ref} = reference velocity at combustor inlet

References

[1] Thornton, J., Richards, G. A., and Robey, E., 2000, "Detecting Flashback in Premix Combustion Systems," American Flame Research Committee International Symposium, Newport Beach, CA.
[2] Thornton, J. D., Richards, G. A., Straub, D. L., Liese, E. A., Trader, J. L., and Fasching, G. E., 2002, "Flashback Detection Sensor for Lean Premix Fuel Nozzles," U.S. Patent No. 6,429,020.
[3] Thornton, J. D., Straub, D. L., Richards, G. A., Nutter, R. S., and Robey, E., 2001, "An In-Situ Monitoring Technique for Control and Diagnostics of Natural Gas Combustion Systems," 2nd Joint Meeting of the U.S. Sections of the Combustion Institute, Oakland, CA, March 25–28.
[4] Cheng, W. K., Summers, T., and Collings, N., 1998, "The Fast-Response Flame Ionization Detector," Prog. Energy Combust. Sci., **24**, pp. 89–124.
[5] Holm, T., 1999, "Aspects of the Mechanism of the Flame Ionization Detector," J. Chromatogr., A, **842**, pp. 221–227.
[6] Calcote, H. F., 1949, "Electrical Properties of Flames: Burner Flames in Transverse Electric Fields," 3rd Symposium on Combustion, Flame, and Explosion Phenomena, pp. 245–253.
[7] Fialkov, A. B., 1997, "Investigations on Ions in Flames," Prog. Energy Combust. Sci., **23**, pp. 399–528.
[8] Bradley, D., 1986, "The Effects of Electric Fields on Combustion Processes," *Advanced Combustion Methods*, Academic Press, London, p. 340.
[9] Richards, G., Straub, D., and Robey, E., 2003, "Control of Combustion Dynamics Using Fuel System Impedance," ASME Paper No. GT2003-38521.
[10] Straub, D., Thornton, J., Chorpening, B., and Richards, G., 2002, "In-Situ Flame Ionization Measurements in Lean Premixed Natural Gas Combustion Systems," 2002 Spring Meeting of the Western States Section of the Combustion Institute, March 25–26, La Jolla.
[11] Benson, K., Thornton, J. D., Straub, D. L., Huckaby, E. D., and Richards, G. A., 2003, "Flame Ionization Sensor Integrated into Gas Turbine Fuel Nozzle," *Proc. of TURBOEXPO 2003*, June 16–19, Atlanta, ASME, New York, ASME Paper No. GT2003-38470.

Gas Turbine Combustion Technology Reducing Both Fuel-NO_x and Thermal-NO_x Emissions for Oxygen-Blown IGCC With Hot/Dry Synthetic Gas Cleanup

Takeharu Hasegawa
Central Research Institute of Electric Power Industry,
2-6-1 Nagasaka,
Yokosuka-shi,
Kanagawa-ken 240-0196, Japan
e-mail: takeharu@criepi.denken.or.jp

Takashi Tamaru
Japan Aerospace Exploration Agency,
7-44-1 Jindaiji-higashi-machi,
Chofu-shi,
Tokyo 182-8522, Japan
e-mail: tamaru@chofu.jaxa.jp

In order to improve the thermal efficiency of the oxygen-blown integrated gasification combined cycle (IGCC) and to meet stricter environmental restrictions among cost-effective options, a hot/dry synthetic gas cleanup is one of the most hopeful choices. The flame temperature of medium-Btu gasified fuel used in this system is high so that NO_x formation by nitrogen fixation results to increase significantly. Additionally, the gasified fuel contains nitrogenous compound, as ammonia, and it produces nitrogen oxides, the fuel NO_x, in the case of employing the hot/dry gas cleanup. Low NO_x combustion technology to reduce both fuel-NO_x and thermal-NO_x emissions has been required to protect the environment and ensure low cost operations for all kinds of oxygen-blown IGCC. In this paper, we have demonstrated the effectiveness of two-stage combustion and nitrogen injection techniques, and also showed engineering guidelines for the low-NO_x combustor design of oxygen-blown gasified, medium-Btu fuels. The main results obtained are as follows: (1) Based on the basic combustion tests using a small diffusion burner, we clarified that the equivalence ratio at the primary combustion zone has to be adjusted according to the fuel conditions, such as methane concentration, CO/H_2 molar ratio, and calorific values of gasified fuels in the case of the two-stage combustion method for reducing fuel-NO_x emissions. (2) From the combustion tests of the medium-Btu fueled combustor, two-stage combustion with nitrogen direct injection into the combustor results in reductions of NO_x emissions to 34 ppm (corrected at 16% O_2) or less under the gas turbine operational conditions of 25% load or higher for IGCC in the case where the gasified fuel contains 0.1% methane and 500 ppm of ammonia. Through nitrogen direct injection, the thermal efficiency of the plant improved by approximately 0.3% (absolute), compared with the case where nitrogen was premixed with gasified fuel. The CO emission concentration decreased drastically, as low as 20 ppm, or combustion efficiency was kept higher than 99.9%. The above results have shown that a two-stage combustion method with nitrogen direct injection is very effective for reducing both fuel-NO_x and thermal-NO_x emissions at once in IGCC, and it shows the bright prospects for low NO_x and stable combustion technology of medium-Btu fuel. [DOI: 10.1115/1.2432896]

Keywords: gas turbine, combustor, gasification, medium calorific fuel, ammonia, fuel-NO_x emissions, thermal-NO_x emissions, low-NO_x combustion, two-stage combustion, nitrogen direct injection

Introduction

Integrated gasification combined cycle (IGCC) is considered one of the most important systems for future coal utilization technology in power generation systems, and is being promoted throughout the world. In Japan, the government and electric power companies undertook experimental research at a 200 t/day pilot plant project [1] from 1986 to 1996. The Central Research Institute of Electric Power Industry (CRIEPI) developed an air-blown pressurized two-stage entrained-flow coal gasifier [2], a hot/dry synthetic gas cleanup system [3], 150 MW, 1573 K class [4], and 1773 K (1500°C) class gas turbine combustor technologies for low-Btu fuel [5]. Of late, the government and electric power companies are promoting a demonstration IGCC project.

Other developments concerning the IGCC system and gas turbine combustor using the oxygen-blown gasified coal fuel include: The Cool Water Coal Gasification Project [6], the flagship demonstration plant of IGCC; the Shell process (SGCP) [7] in Buggenum as the first commercial plant, which started test operation in 1994 with commercial operation from 1998; the Wabash River coal gasification repowering plant [8] in the United States, in operation since 1995; the Texaco process at the Tampa power station [9], in commercial operation since 1996; a HYCOL gasification process for the purpose of hydrogen production, which was developed in Japan [10]; and the integrated coal gasification fuel cell combined cycle (IGFC) pilot plant which consists of gasifier, fuel cell generating unit, and gas turbine, in a test operation from 2002 by the Electric Power Development Co., Ltd. in Japan. Furthermore, the diversification of fuels used for the electric power industry, such as biomass, poor quality coal, and residual oil, are

Contributed by the International Gas Turbine Institute of ASME for publication in the JOURNAL OF ENGINEERING FOR GAS TURBINES AND POWER. Manuscript received May 23, 2005; final manuscript received October 13, 2006. Review conducted by Frank Morton. Paper presented at the ASME Turbo Expo 2002: Land, Sea and Air (GT2002), Amsterdam, The Netherlands, June 3–6, 2002, Paper No. GT2002-30666.

Table 1 Typical compositions derived from the oxygen-blown gasifiers

Fuel	Coal[a]					Biomass	Heavy residue	Orimulsion
Coal type or mine	1	2	3	4	5			
Gasifier type	Fixed	Entrained				Entrained	Entrained	Entrained
Fuel feed	Dry	Dry			Slurry			
Developer	BGL[b]	Shell[c]		HYCOL	Texaco	Tampella[d]	Texaco	CRIEPI[e]
Composition								
CO	56.4%	67.8	69.5%	63.3%	40.9%	21.9%–23.1%	51.7%	43.5%
H_2	25.6%	28.8	29.2%	26.3%	29.9%	12.5%–22.4%	43.1%	42.2%
CH_4	6.6%	0.01	0.03%	0.3%	0.1%	2.2%	0.2%	0.4%
CO_2	2.8%	2.3	1.0%	1.1%	9.5%	20.7%–18.6%	3.2%	11.8%
H_2O	—[f]	(Dry base)		0.4%	12.3%	40.9%–31.5%	(Dry base)	(Dry base)
NH_2	—[f]	100	600 ppm	Unknown	Unknown	0–200 ppm	—[f]	Unknown
H_2S+COS	20 ppm	1.1	0.14%	Unknown	Unknown	0.285%–1.132%	1.6%	1.35%
Others (N_2)	8.6%	—[f]	—[f]	8.6%	7.3%	1.800%–1.048%	0.2%	0.75%
CO/H_2 mole ratio	2.2	2.1	2.4	2.4	1.4	1.0–1.8	1.2	1.0
HHV (MJ/m^3)	13.0	12.2	12.5	11.5	9.0	5.2–6.6	12.1	11.0
LHV (MJ/m^3)	12.0	11.7	11.9	10.9	8.2	4.1–5.5	11.3	10.2

[a]1=High-sulphur bituminous coal; 2=Illinois No. 5 coal; 3=Sufco mine; 4=Moura coal; 5=Moura coal.
[b]See Ref. [22].
[c]See Ref. [7].
[d]See Ref. [12].
[e]See Ref. [13].
[f]An omission.

also the most significant issues for gas turbine development in IGCC: The development of biomass-fueled gasification received considerable attention in the United States in the early 1980s [11] and the prospects for commercialization technology appear considerably improved at present [12]; Our research institute has started researching the gasification technology of orimulsion (emulsion of Orinoco tar) fuel [13]. All of the systems, which used oxygen as an oxidizer, were assumed to adopt the wet type synthetic gas cleaning system. Moreover, in almost all systems, premixing the surplus nitrogen, produced from the oxygen production unit, with a gasified fuel, increases gas turbine output and suppresses NO_x emissions. From the viewpoint of both high operating costs and initial costs of removing the NO_x in exhaust gas derived from the gas turbine system, the electric power industry aims for dry low-NO_x combustion technology that promises higher thermal efficiency and environmentally sound options. For example, electric power plants are required to comply with both gross discharge controls and concentration regulations of NO_x emissions in each local government. Many local municipalities regulations require the NO_x emissions of 10 ppm or below in the case of a gas turbine plant and there is restriction on groundwater use in industries, so dry low-NO_x, high-temperature combustion technologies that could reduce NO_x emissions 10 ppm or below are expected to be developed. Those combustion technologies could eliminate the use of denitration equipment and reduce the cost of power generation.

With respect to the research into dry low-NO_x combustion technology using medium-Btu gaseous fuel, other studies include: White et al. [14] who studied the rich-lean combustor for low and medium-Btu gaseous fuels; Döbbeling et al. [15] who studied on low NO_x combustion technology which quickly mixed fuel with air using the ABB double cone burner (called the EV burner); Döbbeling et al. [16] who studied the premixed combustion technology of medium-Btu gaseous fuel in a fundamental small burner for low NO_x emissions, because the burning velocity of medium-Btu fuel was about six times greater than conventional natural gas, a premixed combustion for low NO_x emissions was so far difficult to adopt; Cook et al. [17] who studied the effective method of returning nitrogen to the cycle, where nitrogen is injected from the head end of the combustor for NO_x control; Zanello and Tasselli [18] who studied the effects of steam content in the medium-Btu gaseous fuel on combustion characteristics; and Hasegawa et al. who studied low-NO_x combustion technology using surplus nitrogen injected from the burner [19,20] and with lean combustion of instantaneous mixing [21].

This paper will propose the dry low-NO_x combustion technology for medium-Btu gasified fuel containing ammonia, and provide useful engineering guidelines for the research and development of a gas turbine combustor using nitrogen injection technology at the burner of the combustor for fuel-NO_x and thermal-NO_x emissions control.

Description of the Oxygen-Blown IGCC System

Characteristics of the Oxygen-Blown IGCC System. In the oxygen-blown IGCC system, a large quantity of nitrogen is produced in the air separation unit. In many of the conventional systems, a part of the nitrogen is used to feed coal into the gasifier and so on, and gasified coal fuels are premixed with the rest of the nitrogen and injected into the combustor to increase electric power and to decrease thermal-NO_x emissions from the gas turbine. However, power to compress the surplus nitrogen is high in the case of premixing its nitrogen with gasified fuel. If the surplus nitrogen could be injected directly into the combustor, transmission end efficiency would increase by around 0.3%. In this paper, we will develop a combustor for an oxygen-blown type gasification system with a hot/dry synthetic gas cleanup facility, in which coal is fed into the gasifier as a water–coal slurry or with some nitrogen as a pulverized powder, and the rest of the nitrogen will be directly injected into the gas turbine combustor. The development of the combustor is intended for 1773 K (1500°C)-class (combustor-exit gas temperature is about 1773 K) gas turbines, in which gasified fuels contain ammonia not removed by the hot/dry gas cleanup. Furthermore, it is necessary to return a large quantity of nitrogen produced from the air-separation unit (as much as the fuel flow rate) to the cycle from the standpoint of recovering power for oxygen production. Basically, the flow rate of the surplus nitrogen produced in the air-separation unit is almost proportional to the fuel flow rate at any gas turbine load, and all surplus nitrogen should be effectively injected into a gas turbine combustor prior to a turbine.

Characteristics of Oxygen-Blown Gasified Fuel. The typical compositions of medium-Btu gasified fuels [7,12,13,22] produced

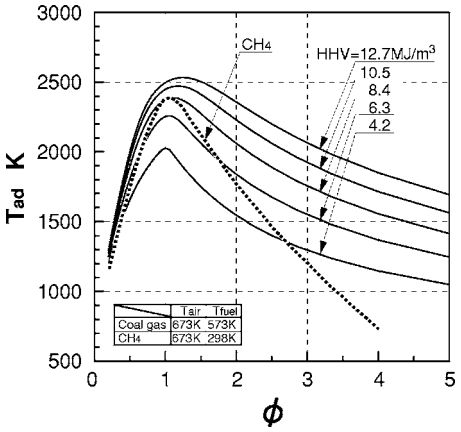

Fig. 1 Relationship between equivalence ratio and adiabatic flame temperature for various gasified fuels and CH_4

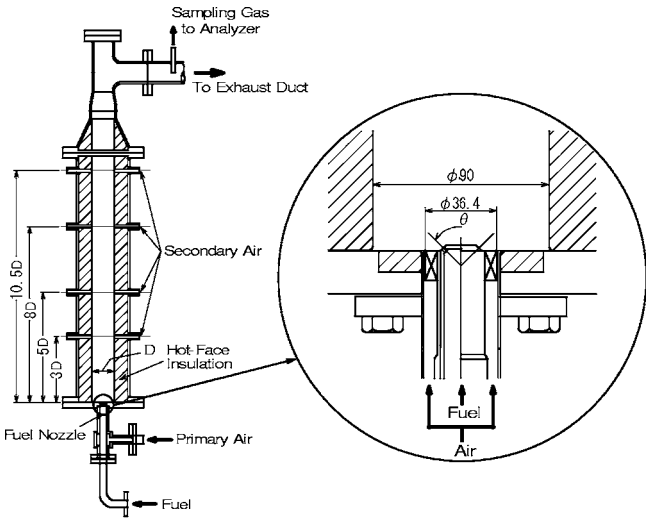

D : inner diameter of cylinder-style combustion chamber, 90mm
θ : injection angle of fuel nozzle, 90 degrees

Fig. 2 Combustor and diffusion burner of basic experimental device

in oxygen-blown gasifiers are shown in Table 1. Each gasified fuel contains carbon monoxide (CO) and hydrogen (H_2) as the main combustible components, and a small fraction of methane (CH_4). Fuel calorific values vary widely (5–13 MJ/m^3), from about 1/8 to 1/3 of natural gas, with raw materials and gasifier types. For example, a gasified fuel derived from biomass contains 30–40% steam in the fuel.

Figure 1 shows the theoretical adiabatic flame temperature of fuels which were: (1) medium-Btu fuels, with fuel high heating values (HHV) of 12.7 MJ/m^3, 10.5 MJ/m^3, 8.4 MJ/m^3, and 6.3 MJ/m^3 (at a temperature of 273 K basis) without nitrogen; (2) medium-Btu fuel blended with surplus nitrogen, or low-Btu fuel of 4.2 MJ/m^3 (HHV); and (3) methane. Calculations of flame temperature were done with a $CO-H_2$ mixture (CO/H_2 molar ratio of 2.33:1) under any condition, and the fuel calorific value was adjusted with nitrogen. In the case of gasified coal fuel, the theoretical adiabatic flame temperature rises as the fuel calorific value increases. Fuel calorific values of 4.2 MJ/m^3 and 12.7 MJ/m^3 produce maximum flame temperatures of 2050 K and 2530 K, respectively. When the fuel calorific value is 8.4 MJ/m^3 or higher, the maximum flame temperature of the medium-Btu fuel without nitrogen is about 400 K higher than that of the nitrogen-blended fuel. That is, if the medium-Btu gasified fuels which were produced in the oxygen-blown gasifiers were not premixed with the surplus nitrogen, the flame temperatures of medium-Btu fuels with fuel calorific values of 8.4–12.7 MJ/m^3 (HHV) were higher than that of high-calorie gases such as natural gas which consists mainly of methane, while the medium-Btu fuels have the calorific values as low as 1/5 of methane. Thermal-NO_x emissions are expected to increase more when burning medium-Btu fuel than burning high-calorie gas of natural gas. We intend to inject surplus nitrogen directly into higher temperature regions from the burner and to decrease thermal-NO_x emissions produced from these regions effectively.

Furthermore, gasified fuels contain ammonia when the hot/dry synthetic gas cleanup is employed. Development of low NO_x combustion technology is necessary in order to reduce fuel-NO_x emissions originating from ammonia in the fuel at the same time as reducing thermal-NO_x emissions. The new combustion technology is expected to reduce both fuel-NO_x emissions and thermal-NO_x emissions. However, the conventional premixed combustion is not applicable in the case of the gasified fuels containing H_2 component of higher burning velocity at the higher risk of backfire, and the dilution of the gasified fuels with the surplus nitrogen increase the power in the plant or the transmission end efficiency decreases. The oxygen-blown IGCCs want the next-generation technology to reduce both fuel-NO_x and thermal-NO_x emissions at once.

Design of the Combustor

Problems of the Medium-Btu Fueled Combustor. From the characteristic of medium-Btu, gasified fuel as mentioned above, it should be noted that the design of a gas turbine combustor, utilizing nitrogen supply into a combustor, should consider the following issues for an oxygen-blown IGCC with the hot/dry synthetic gas cleanup:

1. Low NO_x-emission technology: thermal-NO_x production from nitrogen fixation using nitrogen injection into the combustor, and fuel-NO_x emissions originating from ammonia using a two-stage combustion must be simultaneously restrained; and
2. Higher thermal efficiency: nitrogen injection must be tailored so as to decrease the power to compress nitrogen, which is returned into the gas turbine in order to recover a part of the power used for the air-separation unit.

Test Device and Methods for Basic Studies. Figure 2 shows an outline of the combustor and the tested burner. The combustor consists of a cylinder-style combustion chamber with an inner diameter, D, of 90 mm and a length of 1000 mm, and a primary air swirler and fuel injection nozzle. The combustion chamber is lined with heat insulating material and the casing is cooled with water. There are four sections for secondary air on the sidewalls of the combustion chamber along the direction of flow, to simulate an axial air-inlet distribution of the gas turbine combustor. In order to investigate the effect of the two-stage combustion on the fuel-NO_x and thermal-NO_x reductions, secondary air inlets at a distance from the edge of the fuel injection nozzles of $3 \times D$ are used. The diameter of the secondary air inlets at the entry to the combustor is 13 mm, and altogether 12 inlets are positioned on the perimeter of one cross section.

The tested burner consists of a fuel injection nozzle and a primary air swirler. There are 12 injection inlets with a diameter of 1.5 mm on the fuel injection nozzle with an injection angle, θ, of 90 deg. The primary air swirler has an inner diameter of 24.0 mm, an outer diameter of 36.4 mm, and 12 vanes with a swirl angle, θ_a, of 45 deg. Swirl number, S, which is calculated from the following equation, is 0.84

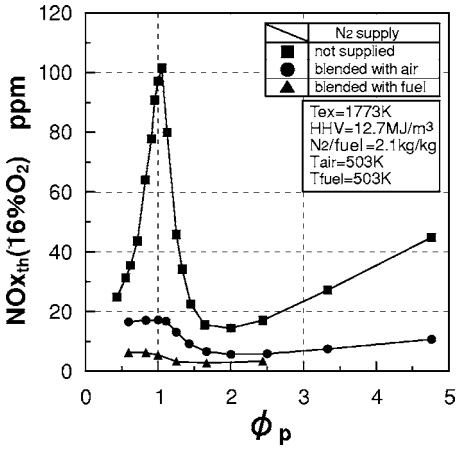

Fig. 3 Effect of nitrogen injection on thermal-NO_x emission characteristics in two-stage combustion, using a small diffusion burner

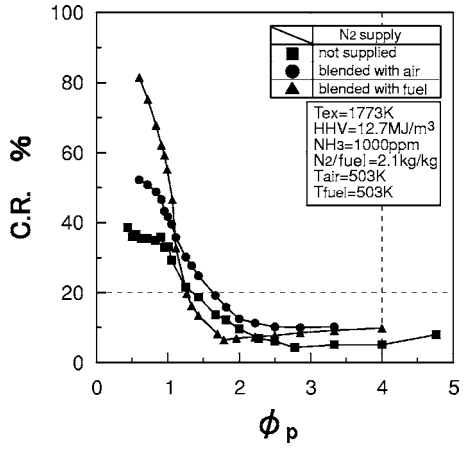

Fig. 4 Effect of nitrogen injection on the conversion rate of ammonia to NO_x in two-stage combustion, using a small diffusion burner

$$S = \frac{2}{3} \times \frac{1 - B^3}{1 - B^2} \times \tan \theta_a \tag{1}$$

where B (boss ratio of swirl vane)=0.66.

An air compressor supplies the air used for combustion. After the flow of the compressed air is adjusted to the required amount by the orifice meter and flow control valve, the air is heated to the prescribed temperature by an air heater, and then blown into the combustor. Primary air is injected into the combustor through a primary air swirler positioned around the fuel injection nozzle, and secondary air is input through air holes in the sidewalls of the combustor.

CO and H_2, which are the main combustible components of the fuel, are mixed in the prescribed proportions and fed into a cylinder to be used. The combustible components are diluted with N_2 to create the required calorific value, heated to the prescribed temperature by an electric heater, and fed through the fuel injection nozzle. The small amounts of NH_3 and CH_4 are controlled by a thermal mass flow controller, and premixed with the fuel before reaching the fuel injection nozzle.

In this study, sample gases were extracted from the exit of the combustor through a water-cooled stainless-steel probe and continuously introduced into an emissions console, which measured CO and CO_2 by a infrared analysis, NO_x by chemiluminescence analysis, O_2 by paramagnetic analysis, and hydrocarbons by a flame ionization detector. The sampling probe was located at a distance of about 1.5 m downstream from the burner. Concentrations of calibration gases for CO, CO_2, NO, O_2, and CH_4 are 270 ppm, 18%, 20 ppm for low-range NO and 180 ppm for high-range NO, 20%, and 90 ppm, respectively. Each repeatability of analyzer is between −0.5% and +0.5% of range full scale, linearity is between −1.0% and +1.0% of range full scale or between −2.0% and +2.0% of measure readings, and noise is less than 1.0% of range full scale.

Reduction of NO_x Emissions With Nitrogen Injection. To suppress thermal-NO_x production originating from nitrogen fixation, we designed the burner with nitrogen injection, based on combustion tests previously conducted using a small diffusion burner [23]. Figure 3 presents an example of the test results using a small diffusion burner, under atmospheric pressure conditions, which indicates the influence of the primary-equivalence ratio, ϕ_p, on thermal-NO_x emission characteristics in two-stage combustion for comparing three cases: (1) a fuel calorific value (HHV) of 12.7 MJ/m^3, without nitrogen injection; (2) a fuel calorific value of 12.7 MJ/m^3, where nitrogen is blended with the primary combustion air injected from the burner; and (3) a fuel blended with nitrogen of the same quantity as case (2), or low-Btu fuel of 5.1 MJ/m^3. In the tests, the fuel did not contain NH_3 and CH_4. A CO/H_2 molar ratio was set to 2.33, the combustor exit gas temperature, T_{ex}, was set to 1773 K, and the fuel injection velocity was set at a constant value of 77 m/s. The cross-sectional flow velocity of total air was 0.53 m/s at the temperature of 273 K basis in case (2). From Fig. 3, we notice that nitrogen supply, which is blended with fuel or primary air, drastically decreases thermal-NO_x emissions, and also NO_x emissions decrease with rises in ϕ_p in the case of using the two-stage combustion. That is, thermal-NO_x emissions decrease significantly by setting a fuel-rich condition when ϕ_p is 1.3 or higher in the case of nitrogen premixed with fuel, and by setting ϕ_p at 1.6 or higher in the case of nitrogen premixed with primary combustion air.

With regard to fuel-NO_x emissions on the other hand, Fig. 4 indicates the effects of nitrogen injection conditions on the conversion rate of NH_3 in the fuel to NO_x, CR, which is calculated from the following equation, in the same conditions with Fig. 3

$$\mathrm{CR} = \frac{([\mathrm{NO_x}] - [\mathrm{NO_{xth}}]) \times (\text{volume flow rate of exhaust})}{[\mathrm{NH_3}] \times (\text{volume flow rate of fuel})} \tag{2}$$

where $[NH_3]$ designates ammonia concentration in fuel.

To obtain the conversion rate of NH_3 to NO_x, CR, the concentration of thermal-NO_x, $[NO_{xth}]$, was first measured after stopping the supply of NH_3, then the concentration of total NO_x, $[NO_x]$, was measured while NH_3 was supplied, and finally fuel-NO_x was calculated by deducting the concentration of thermal NO_x from that of total NO_x. In the tests investigating fuel-NO_x emissions, 1000 ppm of NH_3 is contained in the medium-Btu fuel. In the case of a fuel blended with nitrogen, fuel was diluted, or fuel calorific value decreased to 5.1 MJ/m^3 and NH_3 concentration in the fuel decreased to 400 ppm. From Fig. 4, whether with or without nitrogen supplied, the staged combustion method effectively decreased the fuel-NO_x emissions, or CR drastically decreased as the primary equivalence ratio, ϕ_p, became higher than 1.0, which is a stoichiometric condition, and showed the minimum value at the appropriate ϕ_p. Those optimum ϕ_p become lower when the medium-Btu fuel was blended with nitrogen, while the optimum ϕ_p was not influenced in the case of nitrogen blended with the primary combustion air injected from the burner, and CR showed a tendency to become a little higher than in the other two cases. Furthermore, under lean–lean combustion conditions with a lower ϕ_p than 1.0, in the case of nitrogen premixed with medium-Btu fuel, CR becomes higher than in the case of nitrogen premixed with the primary combustion air.

From the above, it was shown that the supply method of nitro-

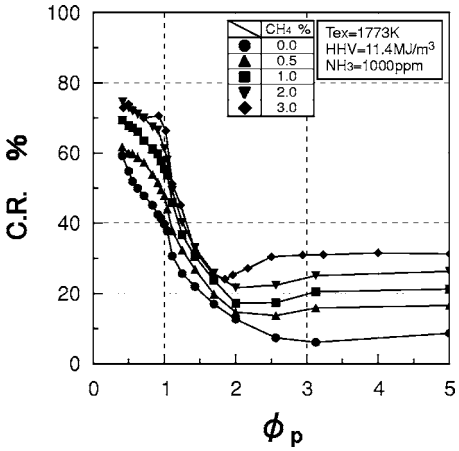

Fig. 5 Effect of CH_4 concentration in fuel on the conversion rate of NH_3 in fuel to NO_x in two-stage combustion, using a small diffusion burner

gen premixed with medium-Btu fuel possibly decreases total emissions of thermal-NO_x and fuel-NO_x, but careful attention must be paid to the homogeneity of the mixture of fuel and nitrogen, or thermal-NO_x emissions will increase. In the case of nitrogen premixed with the primary combustion air, total NO_x emissions grow slightly higher than the case of nitrogen premixed with fuel, and the power to compress nitrogen increases a little or the thermal efficiency of the plant decreases. That is, it is necessary to blend nitrogen with medium-Btu fuel evenly in the combustor, in which the lowest power to compress nitrogen is needed for nitrogen supply into the gas turbine, and not to collide the medium-Btu fuel with combustion air directly.

Optimization of Two-Stage Combustion for Fuel-NO_x Reduction. It is well known that the fuel-NO_x production mechanisms of hydrocarbon fuels such as CH_4 and nonhydrocarbon fuels such as CO and H_2, due to reaction with nitrogenous compounds in the fuel, are different [24]. Gasified fuels consist of CO and H_2 as main combustible components, but also contain thousands of ppm or a small percentage of CH_4. We therefore investigated the effects of CH_4 and CO/H_2 molar ratios in the fuel on the production characteristics of fuel NO_x caused by NH_3 in the fuel.

1. Effect of CH_4 in the Fuel. Figure 5 shows the relationship between the primary equivalence ratio, ϕ_p, in two-stage combustion, and the conversion rate of NH_3 in the fuel to NO_x, when the average temperature of combustor exit gas, T_{ex}, is set to 1773 K and fuel calorific value is 11.4 MJ/m^3, for fuel containing 1000 ppm of NH_3, CO, and H_2 of 2.33 CO/H_2 molar ratio, and with a concentration of CH_4 as a parameter.

   When the equivalence ratio at primary zone, ϕ_p, is less than 1, the NH_3 to NO_x conversion rate, CR, increases in direct proportion to the concentration of CH_4 in the fuel; and when ϕ_p is more than 1, under fuel-rich conditions in the primary combustion zone and CH_4-free fuel, CR decreases as ϕ_p increases and shows a minimum at around 3 of ϕ_p. In the case of fuel containing CH_4, an optimum ϕ_p, at which CR drops to a minimum, is varied by adjusting the concentration of CH_4. That is, the optimum ϕ_p increases as the concentration of CH_4 decreases. For example, the optimum primary-equivalence ratio in the combustor has to be adjusted at 1.7–2.4, in the case where the simulated gasified fuel used in the tests of the designed combustor contains around 3.0% CH_4.

   The effect of the CH_4 concentration on the fuel NO_x produced by NH_3 in gasified fuels was studied using the elementary reaction kinetics [23]. The nitrogen of NH_3 in the fuel has weaker bonding power than N_2. In the combustion process, NH_3 reacted with the OH, O, and H radicals and then easily decomposed into the intermediate NH_i by the following reactions

$$NH_3 + OH(O,H) \Leftrightarrow NH_2 + H_2O(OH,H_2) \quad (3)$$

$$NH_{i(i=1,2)} + OH(H) \Leftrightarrow NH_{i-1} + H_2O(H_2) \quad (4)$$

   When hydrocarbon is not contained in the fuel, NH_i is converted into N_2 by reacting with NO in the fuel-rich region. If fuel contains CH_4, HCN is produced by reactions (5) and (6) in the fuel-rich region and the HCN is oxidized to NO in the fuel-lean zone

$$CH_{i(i=1,2)} + N_2 \Leftrightarrow HCN + NH_{i\text{-}1} \quad (5)$$

$$R\text{-}CH + NH_i \Leftrightarrow HCN + R\text{-}H_i, \ (R- = \text{alkyl group}) \quad (6)$$

   Some HCN is oxidized into NO by reactions (7) and (8), and the rest is decomposed into the N radical by reaction (9). The NH radical is decomposed into the NO by reactions (10)–(12). With the rise in CH_4 concentration in gasified fuel, the HCN increases, and NO_x emissions originated from HCN in the fuel-lean secondary combustion zone increase

$$HCN + OH \Leftrightarrow CN + H_2O \quad (7)$$

$$CN + O_2 \Leftrightarrow CO + NO \quad (8)$$

$$CN + O \Leftrightarrow CO + N \quad (9)$$

$$NH + OH \Leftrightarrow N + H_2O \quad (10)$$

$$N + O_2 \Leftrightarrow NO + O \quad (11)$$

$$N + OH \Leftrightarrow NO + H \quad (12)$$

   On the other hand, some $NH_{i(i=0,1,2)}$ radicals produced by the process of reactions (3)–(5) and (10) are reacted with NO, where NO is supplied by Zel'dovich NO [25] produced by reactions (11) and (12), Prompt NO [26] produced by reactions (5) and (7)–(9), and fuel-NO originated by the terminal process of fuel-N oxidation of reaction (10), and decomposed into N_2 by reaction (13)

$$NO + NH \Leftrightarrow N_2 + OH \quad (13)$$

   That is, it is surmized that each increase in thermal-NO_x concentration and fuel NO_x affected the alternative decomposition reaction of intermediate NH radical with NO, so each of the NO_x emissions originated from the nitrogen in the air or fuel N decreased.

2. Effect of the CO/H_2 Molar Ratio in the Fuel. Figure 6 shows the relationship between the primary equivalence ratio, ϕ_p, in two-stage combustion and the conversion rate of NH_3 in the fuel to NO_x, CR, when the average temperature of combustor exit gas, T_{ex}, was set to 1773 K and fuel calorific value was 11.4 MJ/m^3, for fuel containing 1000 ppm of NH_3 and no CH_4, with the CO/H_2 molar ratio as a parameter. The optimum primary equivalence ratio, where the conversion rate of NH_3 to NO_x indicates the minimum value, increases proportionately to the CO/H_2 molar ratio in the case of medium-Btu fuel. This is due to a lower diffusion and oxidizing rate of CO than that of H_2, and so the higher the CO/H_2 molar ratio, the slower the O_2 consumption rate. Consequently, NH_3 is oxidized in the zone with a higher concentration of O_2. When the primary equivalence ratio was less than 1.0, or under the conditions of excess air, Hasegawa et al. [23] reported that the conversion rate increases proportionately to the CO/H_2 molar ratio in the case

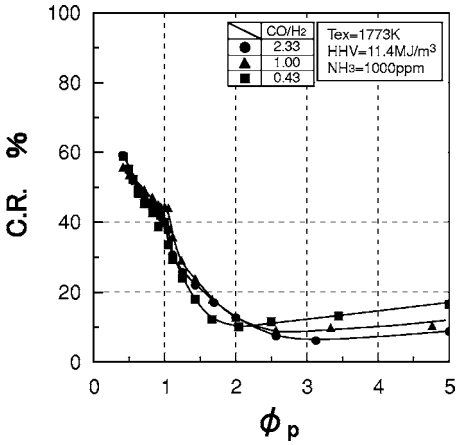

Fig. 6 Effect of CO/H_2 molar ratio on the conversion rate of NH_3 in fuel to NO_x in two-stage combustion, using a small diffusion burner

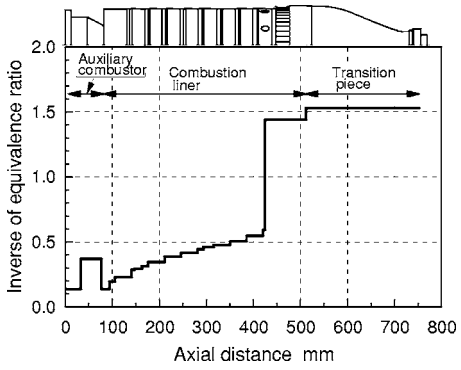

Fig. 8 Axial distribution of inverse of equivalence ratio at the rated load condition

of low-Btu fuel of 4 MJ/m^3 without CH_4. But different findings were observed in the case of medium-Btu gasified fuel.

Characteristics of Designed Combustor. Figure 7 presents the configuration and its function of a designed, medium-Btu fueled 1773 K (1500°C)-class combustor based on the above considerations. The main design concepts for the tested combustor in the present study were to secure stable combustion of medium-Btu fuel with nitrogen injection in a wide range of turn-down operations, and low NO_x combustion for reducing fuel-NO_x and thermal-NO_x emissions. In order to secure stable combustion, we installed an auxiliary combustion chamber at the entrance of the combustor and the nitrogen injection nozzles in the main swirler, which is installed at the exit of the auxiliary combustion chamber. The overall length of the combustion liner is 445 mm and the inside diameter is 175 mm.

Figure 8 illustrates the axial distribution of inverse way of equivalence ratio at the rated load condition. In order to reduce the fuel-NO_x emissions, we adopted the two-stage combustion, in which a fuel-rich combustion was carried out in the primary zone maintaining the inverse way of equivalence ratio to 1.5 (the equivalence ratio of 0.66) at the exit of the combustor and the designed combustor has the following characteristics.

1. Assurance of Flame Stabilization. The ratio of the fuel allocated to the auxiliary combustion chamber is 30% of the total amount of fuel. The fuel and air are injected into the chamber through a subswirler with a swirling angle of 30 deg. By setting the mean equivalence ratio in the auxiliary chamber at 2.4 under rated load conditions, a stable flame can be maintained in the fuel-rich combustion zone and deoxidization efficiency of NH_3 can be improved in lower load conditions. The rest of the fuel is introduced into the main-combustion zone from that surrounding the exit of the auxiliary combustion chamber.
2. Nitrogen Injection. Based on the basic experimental results, we arranged the nitrogen injection intakes between fuel and air intakes in the main swirler surrounding the primary flame from the auxiliary combustion chamber for low thermal-NO_x emissions. Nitrogen direct injection into a combustor has the effect of decreasing power to compress nitrogen. From system analysis, the thermal efficiency of the plant improves by 0.3% (absolute), compared with the case where nitrogen was premixed with gasified fuel before injection into the combustor [21]. Additionally it is possible to control the mixing of fuel, air, and nitrogen positively by way of nitrogen being injected separately into the combustor. The fuel, the combustion air, and the nitrogen from the burner are separately injected into the combustor through a swirler, (which has a 30-deg swirl angle and a 15-deg introverted angle), to collide medium-Btu fuel with air in an atmosphere where nitrogen is superior in amount to both fuel and air.
3. Fuel-NO_x/Thermal-NO_x Reduction. In order to decrease fuel-NO_x emissions, we adopted fuel-rich combustion in the primary zone and set the equivalence ratio in the primary-combustion zone to be determined based on the combustion test results using a small diffusion burner. As shown in Fig. 5, the primary equivalence ratio that minimizes the conversion rate of NH_3 to NO_x is affected by CH_4 concentration in the fuel. Because the supplied fuel contains 3% of CH_4 in the tests, the equivalence ratio in the primary-combustion zone was set around 1.9 and the equivalence ratio in the auxiliary-combustion chamber was around 2.4 to maintain the flame stabilization and to improve deoxidization of NH_3 in the fuel, simultaneously.

   These new technique that adopted the nitrogen direct injection and the two-stage combustion, caused a decrease in flame temperature in the primary combustion zone and the thermal-NO_x production near the burner was expected to be controlled and decreased just as in the case of fuel blended with nitrogen, based on the results of combustion tests using a small diffusion burner, shown in Fig. 3.

   The designed combustor was given another nitrogen injection function, in which nitrogen was bypassed to premix with the air derived from the compressor at lower load conditions, and a stable flame can be maintained in a wide range of turn-down operations. Also, because the nitrogen dilution in the fuel-rich region affected the deoxidization characteristics of NH_3, the nitrogen bypassing technique was expected to improve fuel-NO_x reduction in the cases of higher concentration of NH_3.
4. Cooling of Combustor Wall. In order to compensate for a declined cooling-air ratio associated with a surplus nitrogen injection into a gas turbine combustor, the tested combustor

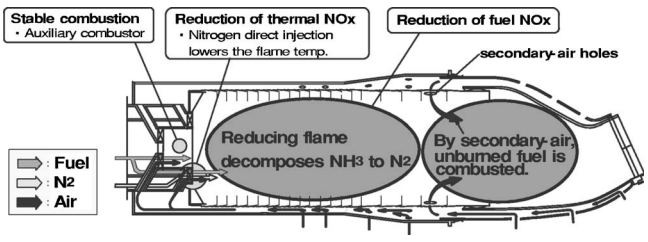

Fig. 7 Design concept of a medium-Btu fueled gas turbine combustor

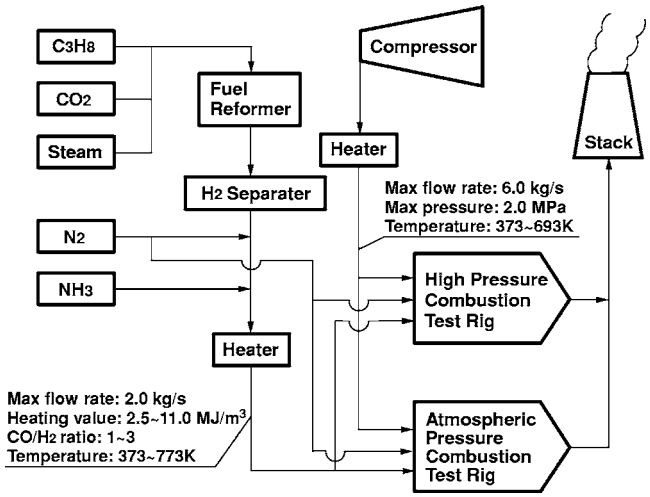

Fig. 9 Schematic diagram and specifications of experimental facility

is equipped with a dual-structure transition piece so that the cooling air in the transition piece can be recycled to cool down the combustor liner wall. The cooling air, flowing into the transition piece from the exterior wall, cools the interior wall through an impingement and convection method, and moves to the combustor liner on the upstream side. For the secondary-air inlet section where temperatures were expected to be especially high, the dual-cooling structure was employed, in which the cooling air was impinged from the air flow guide sleeve to the combustion liner. For cooling of the overall combustion liner wall, the film-cooling method was used.

Test Facilities and Test Method

Test Facilities. The schematic diagram of the test facilities is shown in Fig. 9. The raw fuel obtained by mixing CO_2 and steam with gaseous propane was decomposed to CO and H_2 inside a fuel reforming device. A hydrogen separation membrane was used to adjust the CO/H_2 molar ratio. N_2 was added to adjust the fuel calorific value to the prescribed calorie, and then simulated gases derived from gasifiers were produced.

This facility had another nitrogen supply line, by which nitrogen was directly injected into the combustor. Air provided to the combustor was pressurized to 2.0 MPa by using a four-stage centrifugal compressor. Both fuel and air were supplied to the gas turbine combustor after being heated separately with a preheater to the prescribed temperature.

The combustion test facility had two test rigs, each of which was capable of performing full-scale atmospheric pressure combustion tests of a single can for a "several" hundred MW class, multican-type combustor as well as half-scale high-pressure combustion tests, or full-scale high-pressure tests for around a 100 MW-class, multican-type combustor. Figure 10 shows a cross-sectional view of the combustor test rig under pressurized conditions. After passing through the transition piece, the exhaust gas from the combustor was introduced into the measuring section where gas components and temperatures were measured. The components of the combustion gases were analyzed by an automatic gas analyzer. After that, the gas temperature was lowered through a quenching pot, using a water spray injection system.

Combustion tests were conducted on a full-scale, single can combustor for a 100 MW-class gas turbine under high-pressurized conditions.

Table 2 shows the composition of the supplied fuel used in this paper and the typical commercial gasified fuel. As for tests, the HHV of the supplied fuel was set at 8.8 MJ/m^3 (at temperature of 273 K basis), and a $(CO+CH_4)/H_2$ molar ratio at 1.2, so the supplied gaseous fuel produced in the test facility simulated the essential features of the typical commercial gasified fuel in composition. Due to restrictions in exact adjustment of the simulated fuel composition in this test facility, we have investigated the effects of the concentrations of CH_4 and NH_3 in the supplied fuels on the combustion characteristics, and predicted the combustor's performances in the typical commercial operations. In addition, the H_2O component was represented by CO_2 and the heating value of the simulated gasified fuel was adjusted with N_2 due to restrictions of the test facility. The flow rate of surplus nitrogen produced from the air-separation unit was 0.9–1.2 times the fuel flow in the actual process. Since the density of the supplied fuel was higher than that of the commercial gasified fuel, and since the

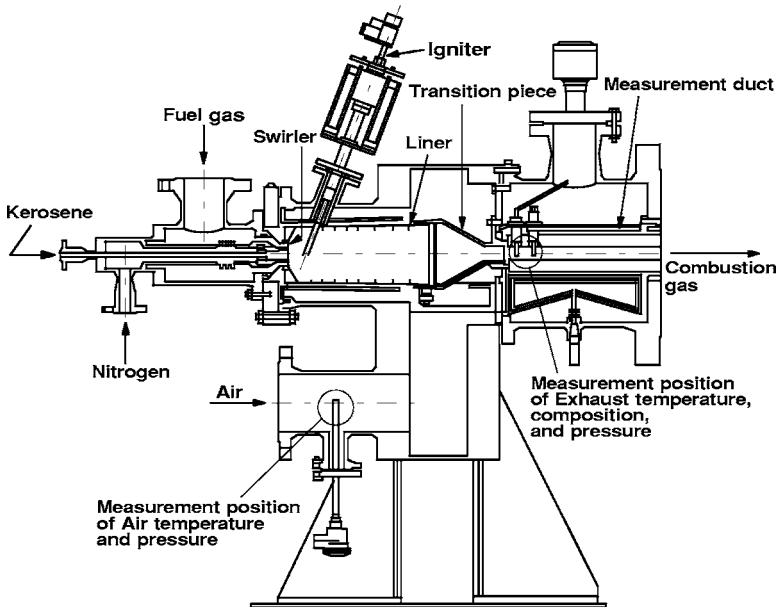

Fig. 10 Combustion test rig

Table 2 Comparison of supplied fuel in tests and typical case of commercial gasified fuel

	Supplied fuel in test	Commercial gasified fuel
Constituent		
CO	31.4%	40.9%
H_2	28.6%	29.9%
CH_4	0%–3.0%[a]	0.1%
CO_2	32.0%	9.5%
H_2O	0%	12.3%
N_2	5.0%	7.3%
NH_3	0–3000 ppm[b]	500 ppm
HHV	8.8 MJ/m^3	9.0 MJ/m^3
LHV	8.1 MJ/m^3	8.2 MJ/m^3

[a]In the case of varying CH_4 concentration in the fuel, the CO and H_2 constituents were adjusted to maintain the fuel calorific value and the CO/H_2 molar ratio constantly, and the combustor's performance of commercial gasified fueled-combustion was predicted.
[b]NH_3 concentration was different according to the gasification methods and raw materials.

temperature of supplied nitrogen was lower in the test conditions than in the actual operations, we also investigated combustor performance in the case of a 0.7 kg/kg N_2/fuel ratio, where the firing temperature of the burner exit corresponded to actual operation. Based on the reliability verification tests by the 200 t/day pilot plant, it is expected that desulfurization efficiency of developed hot/dry type synthetic gas cleanup is more than 95% and dust removal efficiency is 98%. In some cases where the gasified fuels have high concentration of chlorine depending on the gasification methods and raw materials, we might have to remove chlorine from the gasified fuel by antichlor of sodium series. Therefore, it is assumed that sulfur constituent and those of chlorine in the gasified fuels are removed thoroughly at the inlet of the gas turbine combustor and these constituents are not taken into consideration in the combustion tests.

Rated load conditions in the combustion tests are summarized in Table 3. The average temperature of combustor exit gas, T_{ex}, was 1773 K and the combustion intensity, Ic, in the combustor at the design point was 4.0×10^2 $W/(m^3\,Pa)$.

Measurement System. Exhaust gases were sampled from the exit of the combustor through water-cooled stainless-steel probes located on the centerline of a height-wise cross section of the measuring duct. The sample lines of exhaust gases were thermally insulated with heat tape to maintain the sampling system above the dew point of the exhaust gas. The exhaust gases were sampled at an area averaged points in the tail duct exit face and continuously introduced into an emission console which measured CO, CO_2, NO, NO_x, O_2, and hydrocarbons by the same methods as the test device for basic studies using the small diffusion burner. The medium-Btu simulated fuels were sampled from the fuel gas supply line at the inlet of combustor, and constituents of CO, H_2, CH_4, H_2O, CO_2, and N_2 were determined by gas chromatography.

Table 3 Standard test conditions

T_{air}:	603 K
T_{fuel}:	583 K
T_{N_2}:	333 K
N_2/fuel:	0.70 kg/kg
T_{ex}:	1773 K
ϕ_{ex}:	0.66
P:	1.2 MPa
Ic:	4.0×10^2 $W/(m^3\,Pa)$
Ur:	5.6 m/s (at 273 K basis)
$\Delta P/q$:	1.64×10^2

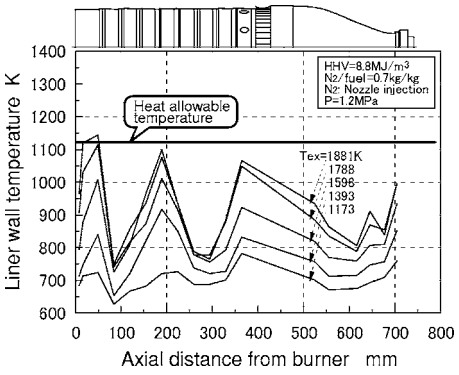

Fig. 11 Axial distributions of combustor wall temperatures using gas turbine combustor exit gas temperature as a parameter

Heating values of the simulated gaseous fuel were monitored by a calorimeter and calculated from analytical data of gas components obtained from gas chromatography.

The temperatures of the combustor liner walls were measured by 40 sheathed type-*K* thermocouples with a diameter of 1 mm attached to the liner wall with a stainless foil welding. The temperature distributions of the combustor exit gas were measured with an array of three pyrometers, each of which consisted of five type-*R* thermocouples.

Test Results and Discussion

Thermal Characteristics of the Combustor Wall. Figure 11 shows the axial distributions of the combustor wall temperatures, when the average temperature of combustor exit gas, T_{ex}, changes in proportion to the gas turbine load. As the exit gas temperature was varied, the fuel flow rate was changed to maintain the airflow rate at a constant value of 1.9 kg/s and the flow ratio of nitrogen injection over fuel (N_2/fuel) at 0.7 kg/kg. In the tests, the higher heating value of fuel was set at a constant 8.8 MJ/m^3 (at temperature of 273 K basis), the pressure in the combustor was at 1.2 MPa, and all of the nitrogen was injected from the burner. The other test conditions were pursuant to the standards shown in Table 3. Even when the combustor exit gas temperature rose to 1881 K that was a little higher than the rated temperature condition of 100% load, the combustor-wall temperature remained almost always under 1123 K (850°C) of the allowable heat resistant temperature, while the combustor-wall temperature showed a tendency to increase with a rise in the combustor exit gas temperature.

In the past tests of the previous-type combustor, we had examined the influence of the fuel temperature on the thermal characteristics of the combustor wall. When the fuel temperature was lowered by 110 K, the liner temperature in the fuel-rich, primary-combustion region decreased slightly due to the increase in the primary-equivalence ratio and the transition piece temperature was increased slightly. In other words, the fuel temperature deviation depending on the plant operational conditions was within tens of degrees of temperature and had hardly influenced the thermal characteristics of the combustor.

Emission Characteristics. We carried out research into the effects of the combustor-exit gas temperature, bypassing nitrogen flow rate, nitrogen injection flow rate, NH_3, and CH_4 concentrations in the fuel, and combustion pressure on NO_x emission characteristics.

Figure 12 shows the relationship between the average temperature of combustor-exit gas, T_{ex}, and the emission characteristics of both thermal NO_x originating from nitrogen fixation and fuel NO_x originating from NH_3 in the fuel, under the conditions that air flow rate was set and maintained at 1.9 kg/s, the nitrogen flow

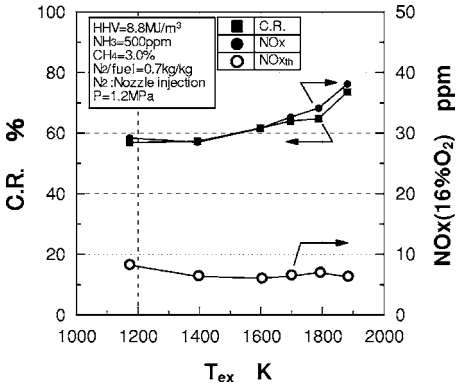

Fig. 12 Effect of combustor-exit gas temperature on NO_x emission characteristics

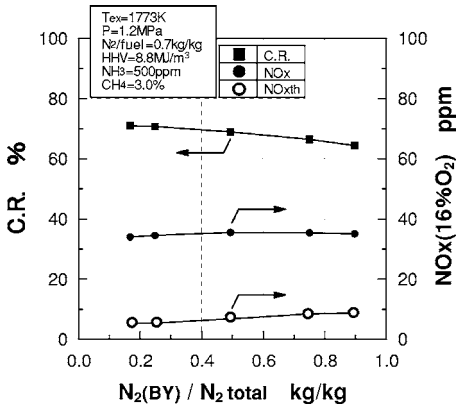

Fig. 14 Effect of bypassing nitrogen flow rate, premixed with combustion air on NO_x emission characteristics

rate of N_2/fuel was 0.7 kg/kg, the pressure inside a combustor was 1.2 MPa of slightly less than that of the practical operation at the equivalent, rated load conditions, and NH_3 and CH_4 concentration in the fuel were 500 ppm and 3.0%, respectively, just as in the case of Fig. 11. In the tests, all of the nitrogen was injected from the burner. As the average temperature of combustor-exit gas, which was equivalent to the gas turbine load condition was varied, the fuel flow rate was changed to maintain the airflow rate at a constant value of 1.9 kg/s and the flow ratio of nitrogen injection over fuel (N_2/fuel) at a constant. The other test conditions were pursuant to the standards shown in Table 3. When the average temperature of combustor-exit gas was raised to 1173 K, which corresponds to 25% of the gas turbine load or higher, the conversion rate of NH_3 in the fuel to NO_x, CR, increased gradually, while thermal-NO_x emissions were reduced as low as 10 ppm (corrected at 16% O_2). Consequently, total NO_x emissions were around 34 ppm (corrected at 16% O_2) at the rated load of 1773 K combustor-exit gas temperatures. In order to improve the thermal efficiency of the plant, it is necessary to raise the exhaust temperature of the gas turbine combustor. Even when the combustor-exit gas temperature was raised to around 1873 K, total NO_x emissions were reduced as low as 40 ppm (corrected at 16% O_2). In the case of fuel containing no ammonia, the thermal-NO_x emissions were reduced lower than 10 ppm (corrected at 16% O_2). Furthermore, not shown in Fig. 12, CO emissions were reduced as low as 20 ppm, at any gas turbine load, or combustion efficiency was kept higher than 99.9%.

Figure 13 shows the effect of the cross-sectional flow velocity of the air, Ur, on the NO_x emission characteristics at the rated

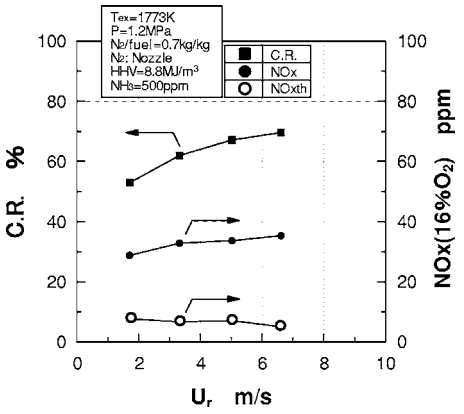

Fig. 13 Effect of sectional flow velocity of air in the combustor on NO_x emission characteristics in the case of nitrogen injection

temperature of 1773 K. In the tests, the nitrogen flow rate of N_2/fuel was set at 0.7 kg/kg, the pressure inside a combustor was at 1.2 MPa, and NH_3 and CH_4 concentrations in the fuel were 500 ppm and 3.0%, respectively, just as in the case of Fig. 12. All of the nitrogen was injected from the burner. With the rise in Ur, thermal-NO_x emissions have slightly decreased, while the conversion rate of NH_3 to fuel-NO_x tended to increase. That is, since the residence time of the combustion gas in the combustor declined with the rise in Ur, thermal-NO_x emissions decreased but maintained a low level of 10 ppm (corrected at 16% O_2) or below. On the other hand, reduction of NH_3 into N_2 in the primary combustion zone declined and fuel-NO_x emissions increased. If the residence time of the burned gases in the reduction combustion zone was increased, the fuel-NO_x emissions will be restrained more, while the thermal NO_x emissions maintain 10 ppm or below.

Nitrogen supply positions affected temperature distribution, thermal NO_x, and fuel-NO_x production in the combustor. We observed NO_x emission characteristics when a part of the nitrogen was injected into the combustor through the burner and the rest was bypassed to premix with the combustion air, which was injected from the burner-air nozzles and secondary combustion air holes. Figure 14 shows the relationship between the ratio of bypassing nitrogen flow rate over total nitrogen supply, $N_2(BY)/N_2$total, and both the conversion rate of NH_3 in the fuel to NO_x, CR, and NO_x emissions, where air flow rate was set at 1.9 kg/s, the N_2/fuel ratio was 0.7 kg/kg, the pressure was set at 1.2 MPa, and the average temperature of combustor-exit gas was maintained at 1773 K. The conversion rate of NH_3, CR, slightly decreased with rises in the $N_2(BY)/N_2$total ratio, while thermal-NO_x emissions gradually increased to 10 ppm (corrected at 16% O_2). Consequently, total NO_x emission concentration hardly changed under the condition of NH_3 500 ppm.

Nitrogen flow rate varied according to the type of gasifier and small changes occurred with each operation. We observed emission characteristics when nitrogen injection flow rate to the combustor changed. Figure 15 shows the relationship between nitrogen injection and NO_x emission characteristics, where air flow rate was set at 1.9 kg/s, pressure was set at 1.2 MPa, and the average temperature of combustor-exit gas was maintained at 1773 K. In the tests, all of the nitrogen was injected from the burner. With rises in the N_2/fuel ratio, thermal-NO_x emissions decreased, while the conversion rate, CR, increased in the lower N_2/fuel ratio and showed constant when the N_2/fuel ratio was 0.8 kg/kg or higher. As a result, total NO_x emissions decreased gradually with rises in the N_2/fuel ratio. Although not shown in Fig. 15, CO emissions were reduced as low as 20 ppm at any N_2/fuel ratio, or combustion efficiency was at around 100%.

The concentration of NH_3 in gasified fuel varies depending on the types of raw material, gasifier, and gasification conditions.

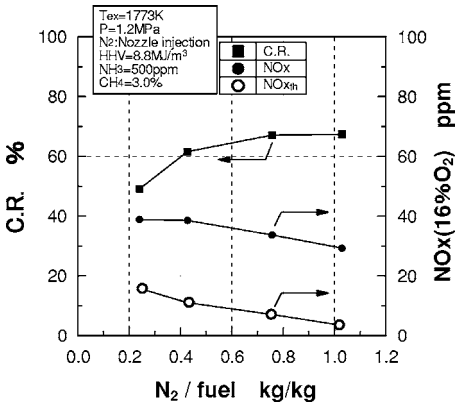

Fig. 15 Effect of nitrogen injection flow rate from the burner on NO_x emission characteristics

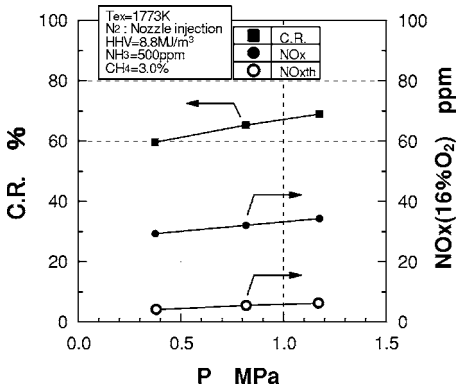

Fig. 17 Effect of pressure inside a combustor on NO_x emission characteristics

Therefore, we carried out a study of the effects of NH_3 concentrations in the fuel on NO_x emission characteristics. Figure 16 shows the relationship between NH_3 concentration in the fuel and NO_x emission characteristics when nitrogen of 0.7 kg/kg N_2/fuel ratio was injected from the burner, airflow rate was set at 1.9 kg/s, and the combustor-exit gas temperature maintained at 1773 K. With rises in NH_3 concentration, total NO_x emissions increased, while the conversion rate, CR, declined. It has been reported that higher concentration of nitrogenous compounds, in the form of NH_3 mostly, in the fuel suppresses the conversion rate of those nitrogenous compounds into NO_x [27]. Similar findings were observed in medium-Btu gasified fuel. Furthermore, when the nitrogen was bypassed and premixed with the combustion air, or NH_3 concentration in the primary combustion zone became relatively higher, the conversion rate of NH_3 to NO_x resulted in a decrease, while thermal-NO_x emissions increased slightly, as shown in Fig. 14. Consequently, the nitrogen bypassing method is expected to be effective in the case of gasified fuel contained higher concentrations of NH_3.

In combustion tests, the maximum pressure was set to 1.2 MPa of slightly less than that of the practical operation at the equivalent, rated load conditions for restrictions of the fuel supply rate. Therefore we examined the effects of pressure in the combustor on the NO_x emission characteristics. Figure 17 shows the relationship between the combustion pressure and the NO_x emissions. In the tests, all of the nitrogen was injected from the burner into the combustor, and the pressure inside a combustor was changed to maintain the residence time of the burned gas in the combustor at a constant. The conversion rate of NH_3 to NO_x slightly increased with the rise in pressure from 0.4 MPa to 1.2 MPa, and the thermal-NO_x emissions slightly increased. The pressure indexes, P_{index}, which are the inclinations of the logarithmic values of the thermal-NO_x and total-NO_x emissions against the pressure as shown by the following equation, will be shown to be 0.37 and 0.13, respectively

$$\frac{[NO_x]_2}{[NO_x]_1} = \left(\frac{P_2}{P_1}\right)^{P_{\text{index}}} \tag{14}$$

where the subscripts 1 and 2 of the NO_x emission, $[NO_x]$, and the pressure in the combustor, P, designate the respective conditions.

Regarding the effect of combustion pressure on the thermal-NO_x emissions in the gas turbine combustor using the conventional hydrocarbon fuels, it is known that the production rate of thermal-NO_x originated from the Zel'dovich NO mechanism increases nearly proportionately to the 1.5-th power of pressure (i.e., $d[NO]/dt \propto P^{1.5}$) and the thermal-NO_x emission mole fraction varies in proportion to the 0.5-th power of the combustion pressure, in theory. Actually, the number of power described above is different according to both combustion methods and configurations of the combustors. However, in the case of the medium-Btu fueled combustor with nitrogen injection, it is found that the influence of the pressure on the thermal-NO_x emissions shows a different tendency from that of the hydrocarbon fuel and lower dependence of the thermal-NO_x emissions on pressure. That is because the volume of the medium-Btu fuel was larger than that of hydrocarbon fuels, and so mixing characteristics were improved. Furthermore, the fuel-rich combustion where produced Prompt NO was employed in the first combustion zone, but the gasified fuels contained little of constituents hydrocarbons or thermal-NO_x emissions show a different tendency from the case of hydrocarbon fuels. So the thermal-NO_x emissions showed the weaker dependence on pressure.

The simulated gasified fuel produced in the test facility was slightly different from typical commercial gasified fuel in composition due to restrictions in the fuel supply rate. Therefore, we examined the effects of CH_4 concentration in the fuel. Figure 18 shows the effects of the CH_4 concentration on the NO_x emission characteristics under the conditions of pressure 1.2 MPa and estimates the NO_x emissions under the rated load conditions of the actual operations. Also, Fig. 18 shows the total-NO_x emissions in the case where the pressure in the combustor was varied maintaining the CH_4 concentration at around 3% of Fig. 17. In the tests, the residence time of the combustion gas in the combustor was set and maintained constant under the conditions where the average temperature of combustor-exit gas was set at 1773 K, the nitrogen of 0.7 kg/kg N_2/fuel ratio was injected from the burner, and NH_3 concentration in the fuel was 500 ppm. The other test conditions were pursuant to the standards shown in Table 3. In the designed combustor, the total NO_x emissions increased proportionally to

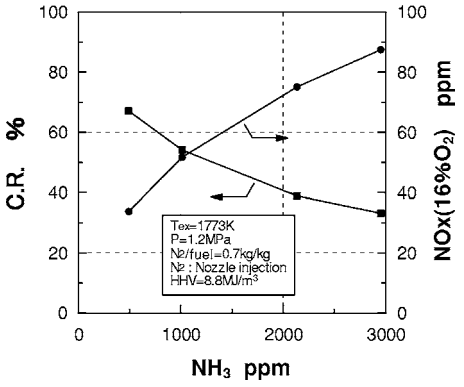

Fig. 16 Effect of ammonia concentration in fuel on NO_x emission characteristics

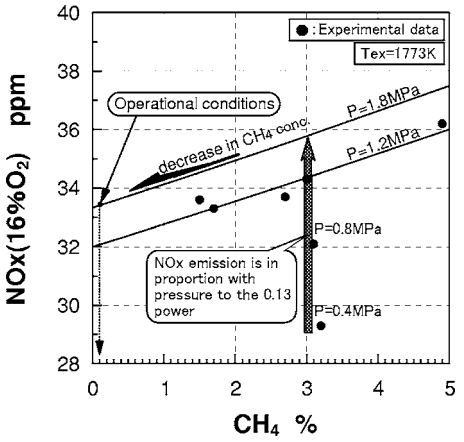

Fig. 18 Effects of methane concentration and pressure in the combustor on NO_x emission characteristics

the pressure to the power of 0.13, while the thermal-NO_x emissions were proportional to the power of 0.37 of the pressure, as shown in Fig. 17. It was found that the pressure has less influence on the fuel-NO_x emissions than on the thermal-NO_x emissions. On the other hand, the total NO_x emissions decreased with the decrease in CH_4 concentration. From these experimental results, total NO_x emissions could be estimated at around 34 ppm (corrected at 16% O_2) under the equivalent rated load conditions of medium-Btu fuel which contained 0.1% CH_4 and 500 ppm NH_3.

From the estimation method of NO_x emissions shown in Fig. 18, Fig. 19 shows the combustion emission characteristics under the simulated operational conditions of the 1773 K-class gas turbine for IGCC in the case where gasified fuel contains 0.1% CH_4 and 500 ppm NH_3. Considering the effects of CH_4 concentration and pressure as shown in Fig. 18, it will be predicted that NO_x emissions are as low as 34 ppm (corrected at 16% O_2) in the range where the gas turbine load is 25% or higher, which is the single fuel firing of gasified fuel, while the NO_x emissions tend to increase slightly with the rise in the gas turbine load.

On the other hand, we can expect that combustion efficiency is around 100% under actual operational conditions of the medium-Btu fueled gas turbine, because CO emissions tend to decrease with the rise in pressure.

From these results, it appears that two-stage combustion and nitrogen direct injection technique will sufficiently allow low NO_x emission levels in the case where the oxygen-blown IGCC employs the hot/dry synthetic gas cleanup and the IGCC system will be able to achieve the full performance benefits of this concept.

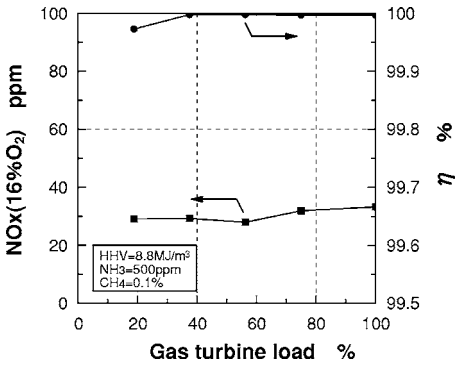

Fig. 19 Effect of the gas turbine load on combustion emission characteristics

Conclusions

Based on basic combustion test results using a small diffusion burner, we designed a combustor fitted with a suitable nitrogen injection nozzle and two-stage combustion for oxygen-blown IGCC, and demonstrated that combustor's performance under gas turbine operational conditions. Test results are summarized as follows:

1. Based on the basic combustion tests, we clarified that the equivalence ratio at the primary combustion zone has to be adjusted according to the fuel conditions, such as methane concentration and CO/H_2 molar ratio in the gasified fuels when reducing fuel-NO_x emissions through a two-stage combustion method.
2. From the combustion tests of the medium-Btu fueled combustor, two-stage combustion with nitrogen direct injection results in reductions of NO_x emissions to 34 ppm (corrected at 16% O_2) or less under gas turbine operational conditions of 25% load or higher for IGCC in the case where the gasified fuel contained 0.1% methane and 500 ppm ammonia. Through nitrogen direct injection, the thermal efficiency of the plant improved by approximately 0.3% (absolute), compared with a case where nitrogen was premixed with gasified fuel. The CO emission concentration decreased drastically, as low as 20 ppm, or combustion efficiency was kept higher than 99.9%.
3. The tested combustor has further shown that the total NO_x emissions were reduced as low as 40 ppm (corrected at 16% O_2), the thermal-NO_x emissions lower than 10 ppm (corrected at 16% O_2) in the case of fuel containing no ammonia, and the combustion efficiency higher than 99.9% even when the combustor-exit gas temperature was raised to around 1873 K for the improvement of the plant thermal efficiency.

The above results show that the two-stage combustion method with nitrogen direct injection is very effective in reducing both fuel-NO_x and thermal-NO_x emissions at once for higher thermal efficiency of gas turbine in oxygen-blown IGCCs. To keep stable supplies of energy and protect the global environment, it will be important that human beings not only use finite fossil fuel, such as oil and coal, but also reexamine unused resources and reclaim waste, and develop highly effective usage of such resources. The IGCC technologies could have the potential to use highly efficient resources not widely in use today for power generation.

Acknowledgment

The authors wish to express their appreciation to the many people who have contributed to this investigation. In testing this combustor, we received helpful support from Mr. K. Kawashima, and Y. Kousaka, (Central Research Institute of Electric Power Industry), Mr. H. Sezaki, M. Suzuki, and K. Terada, (Techno Service Corp.).

Nomenclature

- CO/H_2 = molar ratio of carbon monoxide and hydrogen in the fuel
- CR = conversion rate from ammonia to NO_x (%)
- HHV = higher heating value of the fuel at temperature of 273 K basis (MJ/m^3)
- LHV = lower heating value of the fuel at temperature of 273 K basis (MJ/m^3)
- H_{ex} = lower heating value of the unburned fuel in the exhaust gas
- H_f = lower heating value of the fuel supplied to the combustor
- Ic = combustion intensity in the combustor at temperature of 273 K basis ($W/(m^3\,Pa)$)

N_2/fuel = nitrogen over fuel supply ratio (kg/kg)
N_2total = total injection rate of nitrogen (kg/s)
N_2(BY) = flow rate of bypassing nitrogen premixed with the combustion air (kg/s)
$NO_x(16\%O_2)$ = NO_x emissions corrected at 16% oxygen in the exhaust gas (ppm)
NO_{xth} = thermal NO_x emissions
P = pressure inside the combustor (MPa)
T_{ad} = adiabatic flame temperature (K)
T_{air} = temperature of supplied air (K)
T_{ex} = average temperature of combustor exit gas (K)
T_{fuel} = temperature of supplied fuel (K)
T_{N_2} = temperature of supplied nitrogen (K)
Ur = mean velocity of cross-sectional flow of air at temperature of 273 K basis (m/s)
η = combustion efficiency $(\%)=(1-H_{ex}/H_f)\times 100\%$
ϕ = equivalence ratio
ϕ_{ex} = equivalence ratio at combustor exit
ϕ_p = equivalence ratio in the primary combustion zone
$\Delta P/q$ = total pressure loss coefficient (characteristics section is combustor-exit)

References

[1] Ichikawa, K., 1996, "Test Results of 200T/D IGCC Coal Gasification Pilot Plant," *Proceedings 8th DOE-METC/ANRE-NEDO Joint Technical Meeting on Surface Coal Gasification*, Penn State, October.

[2] Kurimura, M., Hara, S., Inumaru, J., Ashizawa, M., Ichikawa, K., and Kajitani, S., 1995, "A Study of Gasification Reactivity of Air-Blown Entrained Flow Coal Gasifier," *Proceedings 8th International Conference on Coal Science*, Oviedo, Spain, September 10–15, Elsevier Science B.V., Amsterdam, Vol. 1, pp. 563–566.

[3] Nakayama, T., Ito, S., Matsuda, H., Shirai, H., Kobayashi, M., Tanaka, T., and Ishikawa, H., 1990, "Development of Fixed-Bed Type Hot Gas Cleanup Technologies for Integrated Coal Gasification Combined Cycle Power Generation," Rep. No. EW89015, Central Research Institute of Electric Power Industry, 1-6-1 Ohtemachi, Chiyoda-ku, Tokyo 100-8126 Japan.

[4] Nakata, T., Sato, M., Ninomiya, T., Yoshine, T., and Yamada, M., 1993, "Effect of Pressure on Combustion Characteristics in LBG-Fueled 1300°C-Class Gas Turbine," ASME Paper No. 93-GT-121.

[5] Hasegawa, T., Sato, M., and Ninomiya, T., 1998, "Effect of Pressure on Emission Characteristics in LBG-Fueled 1500°C-Class Gas Turbine," Trans. ASME: J. Eng. Gas Turbines Power, **120**(3), pp. 481–487.

[6] Savelli, J. F., and Touchton, G. I., 1985, "Development of a Gas Turbine Combustion System for Medium-Btu Fuel," ASME Paper No. 85-GT-98.

[7] Bush, W. V., Baker, D. C., and Tijm, P. J. A., 1991, "Shell Coal Gasification Plant (SCGP-1) Environmental Performance Results," EPRI Interim Rep. No. GS-7397, Project 2695-1, EPRI, Palo Alto, CA.

[8] Roll, M. W., 1995, "The Construction, Startup and Operation of the Repowered Wabash River Coal Gasification Project," *Proceedings 12th Annual International Pittsburgh Coal Conference*, September 11–15, University of Pittsburgh, Pittsburgh, pp. 72–77.

[9] Jenkins, S. D., 1995, "Tampa Electric Company's Polk Power Station IGCC Project," *Proceedings 12th Annual International Pittsburgh Coal Conference*, September 11–15, University of Pittsburgh, Pittsburgh, p. 79.

[10] Ueda, T., Kida, E., Nakaya, Z., Shikata, T., Koyama, S., and Takagi, M., 1995, "Design of the HYCOL Gasifier," *Proceedings of the CSPE-JSME-ASME International Conference on Power Engineering-'95*, Shanghai, China, May, The Chinese Society of Power Engineering, Shanghai, pp. 242–247.

[11] Kelleher, E. G., 1985, "Gasification of Kraft Black Liquor and Use of the Products in Combined Cycle Cogeneration," Phase 2 Final Rep. No. DOE/CS/40341-T5, prepared by Champion International Co. for U.S. Department of Energy, Washington, D.C.

[12] Consonni, S., Larson, E. D., and Berglin, N., 1997, "Black Liquor-Gasifier/Gas Turbine Cogeneration," ASME Paper No. 97-GT-273.

[13] Ashizawa, M., Takahashi, T., Taki, M., Mori, K., Kanehira, S., and Takeno, K., 1996, "A Study on Orimulsion Gasification Technology," *Proceedings of 9th International Conference & Exhibition for the Power Generating Industries*, Orlando, FL, December 4–6, PennWell Corp. and PennEnergy, Inc., Houston, Vol. 8, pp. 235–243.

[14] White, D. J., Kubasco, A. J., LeCren, R. T., and Notardonato, J. J., 1983, "Combustion Characteristics of Hydrogen-Carbon Monoxide Based Gaseous Fuels," ASME Paper No. 83-GT-142.

[15] Döbbeling, K., Knöpfel, H. P., Polifke, W., Winkler, D., Steinbach, C., and Sattelmayer, T., 1994, "Low NO_x Premixed Combustion of MBtu Fuels Using the ABB Double Cone Burner(EV burner)," ASME Paper No. 94-GT-394.

[16] Döbbeling, K., Eroglu, A., Winkler, D., Sattelmayer, T., and Keppel, W., 1996, "Low NO_x Premixed Combustion of MBtu Fuels in a Research Burner," ASME Paper No. 96-GT-126.

[17] Cook, C. S., Corman, J. C., and Todd, D. M., 1994, "System Evaluation and LBtu Fuel Combustion Studies for IGCC Power Generation," ASME Paper No. 94-GT-366.

[18] Zanello, P., and Tasselli, A., 1996, "Gas Turbine Firing Medium-Btu Gas from Gasification Plant," ASME Paper No. 96-GT-8.

[19] Hasegawa, T., Hisamatsu, T., Katsuki, Y., Sato, M., Iwai, Y., Onoda, A., and Utsunomiya, M., 1999, "A Development of Low NO_x Combustion in Medium-Btu Fueled 1300°-Class Gas Turbine Combustor in IGCC," *Proceedings International Gas Turbine Congress 1999 Kobe*, November 14–19, Kobe, The Gas Turbine Society of Japan, Vol. 2, pp. 783–791.

[20] Hasegawa, T., Hisamatsu, T., Katsuki, Y., Sato, M., Yamada, M., Onoda, A., and Utsunomiya, M., 1998, "A Study of Low NO_x Combustion on Medium-Btu Fueled 1300°-Class Gas Turbine Combustor in IGCC," ASME Paper No. 98-GT-331.

[21] Hasegawa, T., Hisamatsu, T., Katsuki, Y., Sato, M., Koizumi, H., Hayashi, A., and Kobayashi, N., 2003, "Development of Low NO_x Combustion Technology in Medium-Btu Fueled 1300°-Class Gas Turbine Combustor in IGCC," Trans. ASME: J. Eng. Gas Turbines Power, **125**(1), pp. 1–10.

[22] Smith, L. D., 1993, "Clean Coal 5 eyes BGL Gasification at Camden," Mod. Power Syst., **13**(8), pp. 21–24.

[23] Hasegawa, T., Sato, M., and Nakata, T., 1999, "A Study of Combustion Characteristics of Gasified Coal Fuel," Trans. ASME: J. Eng. Gas Turbines Power, **123**(1), pp. 22–32.

[24] Fenimore, C. P., 1976, "Effects of Diluents and Mixing on Nitric Oxide from Fuel-Nitrogen Species in Diffusion Flames," *Proceedings 16th Symposium (International) on Combustion*, The Massachusetts Institute of Technology, Cambridge, MA, August 15–20, The Combustion Institute, Pittsburgh, PA, pp. 1065–1071.

[25] Fenimore, C. P., 1971, "Formation of Nitric Oxide in Premixed Hydrocarbon Flames," *Proceedings 13th Symposium (International) on Combustion*, The University of Utah, Salt Lake City, UT, August 23–29, The Combustion Institute, Pittsburgh, PA, pp. 373–379.

[26] Miller, J. A., and Bowman, C. T., 1989, "Mechanism and Modeling of Nitrogen Chemistry in Combustion," Prog. Energy Combust. Sci., **15**, pp. 287–338.

[27] Fenimore, C. P., 1972, "Formation of Nitric Oxide from Fuel Nitrogen in Ethylene Flames," Combust. Flame, **19**(2), pp. 289–296.

Investigation of Entropy Noise in Aero-Engine Combustors

Friedrich Bake
e-mail: friedrich.bake@dlr.de

Ulf Michel

Ingo Roehle

Department of Engine Acoustics,
Institute of Propulsion Technology,
German Aerospace Center (DLR),
Mueller-Breslau-Str. 8,
10623 Berlin, Germany

Strong evidence is presented that entropy noise is the major source of external noise in aero-engine combustion. Entropy noise is generated in the outlet nozzles of combustors. Low-frequency entropy noise, which was predicted earlier in theory and numerical simulations, was successfully detected in a generic aero-engine combustion chamber. It is shown that entropy noise dominates even in the case of thermo-acoustic resonances. In addition to this, a different noise generating mechanism was discovered that is presumably of even higher relevance to jet engines: There is strong evidence of broad band entropy noise at higher frequencies (1 to 3 kHz *in the reported tests). This unexpected effect can be explained by the interaction of small scale entropy perturbations (hot spots) with the strong pressure gradient in the outlet nozzle. The direct combustion noise of the flame zone seems to be of minor importance for the noise emission to the ambiance. The combustion experiments were supplemented by experiments with electrical heating. Two different methods for generating entropy waves were used, a pulse excitation and a sinusoidal excitation. In addition, high-frequency entropy noise was generated by steady electrical heating.* [DOI: 10.1115/1.2364193]

Introduction

Combustion noise gains importance, especially during the landing approach of modern aircraft. This observation is mainly based on the achievements in decreasing jet mixing noise and fan noise of modern aero-engines.

The total noise radiated by a combustion chamber system consists of direct and indirect combustion noise as shown in a generalized acoustic energy equation by Dowling [1]. The direct noise sources are related to the unsteady combustion process itself, e.g., to unsteady heat release. The indirect combustion noise is generated when a fluid with a nonuniform entropy distribution is accelerated in or convected through the nozzle located at the downstream end of the combustion chamber. The accelerated or decelerated hot spots radiate sound. In gas turbines, the inlet guide vanes for the first turbine stage represent a nozzle for the combustion chamber flow. The flow in this nozzle is choked in aero-engines in practically all relevant operating conditions. The underlying theory of the acoustic mechanism is described by Marble and Candel [2]. In the following, indirect combustion noise (ICN) and entropy noise (EN) are used as equivalent expressions.

Up to now, there was little direct experimental proof of the existence of entropy noise in combustion with respect to the noise emission to the ambiance, presumably because of the difficulty to separate the different noise generating processes leading to entropy and direct combustion noise. Exceptions are the work in 1976 of Bohn [3], in which entropy waves and entropy noise were generated electrically, and the experimental investigations of Muthukrishnan et al. [4], who separated the combustion noise sources via a coherence analysis.

The dispersion behavior of entropy fluctuations in a combustor flow was calculated by Sattelmayer [5]. Entropy waves are frequently studied with respect to their significance as a feedback force for combustion instabilities and thermo-acoustic oscillations; see, e.g., [6–8]. However, the contribution to the noise emission of aero-engine combustors remained unknown. With the goal to evaluate the respective ratio of direct and indirect combustion noise, a model combustor and a reference test rig were setup and acoustically investigated within the framework of a DFG research unit on combustion noise (http://www.combustion-noise.de). The results of this ongoing research work are presented in this paper.

Experimental Setup

For the experiments two different test rigs have been used. The first one, called the entropy wave generator (EWG), is a nonreactive reference test rig to investigate the sound emission of artificially induced entropy waves in an accelerated tube flow. The second one is a model combustor test rig to demonstrate the noise emission of accelerated entropy perturbations in a reactive combustor flow.

Entropy Wave Generator (EWG). The entropy wave generator is basically an accelerated tube flow with the capability of inducing entropy waves via a heating module. The idea of this setup is to optimize and test detection methods for entropy noise. Furthermore, it allows us to validate numerical (CFD + CAA) studies and to confirm theoretical considerations.

A sketch of the design is shown in Fig. 1. The flow, which is supplied by a compressed air system, is calmed in a settling chamber with a honeycomb flow straightener before it enters the tube section via a bell-mouth intake. The inner diameter of the tube is 30 mm. The heating module consists of six ring sections with ten platinum wires stretched through the each cross section. The wires have a diameter of 25 μm and a total length of about 1.2 m. In the current setup the wires can be heated with an electrical power of up to 200 W. The length of the heating module in the streamwise direction amounts to 48 mm. The tube section following the heating module is exchangeable so that three different lengths, 42.5, 92.5, and 192.5 mm, can be tested. Further downstream the flow is accelerated through the convergent part of a convergent-divergent nozzle and then decelerated in the subsonic divergent diffuser part of the nozzle. The following 1020 mm long tube section has a diameter of 40 mm and is equipped with wall-flush-mounted microphones at different axial positions for acoustic analysis. The flow leaves the test rig through an anechoic termination in order to minimize acoustic reflections into the measurement section. The maximum mass flux limited by the air supply is 18 g/s and the maximum Mach number in the nozzle throat

Contributed by the International Gas Turbine Institute (IGTI) of ASME for publication in the JOURNAL OF ENGINEERING FOR GAS TURBINES AND POWER. Manuscript received October 1, 2005; final manuscript received February 1, 2006. IGTI Review Chair: R. S. Abhari. Paper presented at the ASME Turbo Expo 2006: Land, Sea and Air (GT2006), Barcelona, Spain, May 8–11, 2006, Paper No. GT2006-90093.

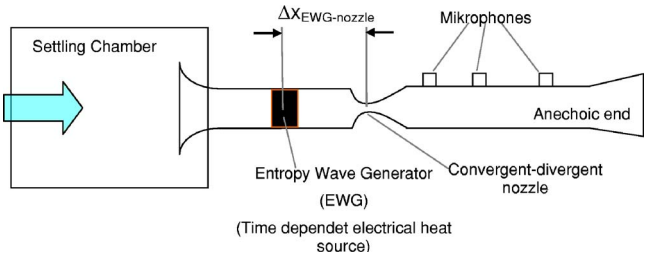

Fig. 1 Sketch of the entropy wave generator (EWG)

amounts to Ma=1 at a mass flux of about 11 g/s and a nozzle diameter of 7.5 mm. A photo of the entropy wave generator is displayed in Fig. 2.

Combustor Test Rig Setup. The combustor setup for the experimental investigation is chosen to replicate fuel-air-mixing characteristics of full scale gas turbines while still permitting analysis by experimental means. In order to simplify the acoustic analysis and the numerical approach, the system is designed axisymmetrically.

The test rig, shown in Figs. 3 and 4, consists of three sections: combustion chamber, outlet nozzle, and exhaust duct. A swirled dual air-flow nozzle is used to drive the combustion zone. Methane gas is injected as the fuel through an annular slot between the air streams.

The combustion chamber itself is made of either a fused quartz glass or a stainless steel cylinder with 100 mm inner diameter. It has a length of 113 mm and is terminated by a convergent-divergent nozzle as shown in Fig. 4. The outlet nozzle can be exchanged with nozzles of different throat diameters (7.5, 17, 20, and 30 mm) for testing the influence of the outlet Mach number on the indirect combustion noise.

The outlet nozzle is attached to an exhaust duct with the same diameter as the combustion chamber. In order to reduce the impedance jump at the exhaust outlet, an end diffuser is installed. In addition, the diffuser is perforated with holes of 2 mm diameter with increasing perforation density towards the exit. This exhaust duct termination is designed in consideration of the experimental investigations of Shenoda [9].

In order to excite the combustion process with perturbations, a piezoelectric device is installed in the fuel gas supply system to modulate the fuel mass flux dynamically. The fuel gas modulator is driven by a frequency generator.

Sound pressure measurements in combustion environments put high demands on the acoustic equipment. High temperatures of up to 2000 K and highly corrosive exhaust gases forbid the usage of normal microphone setups in the standard way. To prevent sensor destruction a probe microphone configuration like the one shown in Fig. 5 is used.

Due to the spatial separation of the measurement location at the

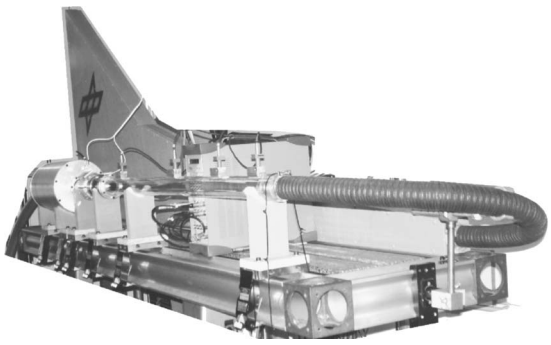

Fig. 2 Photo of the entropy wave generator (EWG)

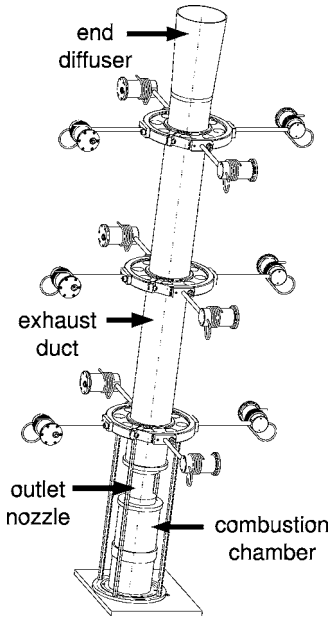

Fig. 3 Isometric view of the combustor test rig

combustion chamber wall or exhaust duct and the microphone itself, common $\frac{1}{4}$ in. microphones can be used. The connection between the exhaust duct wall and the microphone is realized by a steel tube of 2 mm inner diameter. For impedance matching and to minimize standing wave effects in the probe tube, this is extended according to the principle of the semi-infinite acoustic duct.

The microphone itself is perpendicular and flush-mounted inside the cylindrical chamber shown in Fig. 5. From the rear end, the probe tube is purged with cooling gas with a well controlled small flow rate. The purging prevents the diaphragm of the microphone from damage by corrosive combustion products. Of course, the phase shift in the collected data due to the propagation delay through the probe tube has to be corrected afterwards. Since the probe tube is finite, small reflection effects remain in the transfer function of the probe microphone. A detailed description of the calibrated transfer functions is given by Forster et al. [10].

In the current setup the combustion chamber can be equipped with up to three probe microphones at different axial positions. On the exhaust duct system 12 microphones can be installed at three axial and four circumferential positions. From the acoustic time series, the downstream and upstream propagating acoustic waves

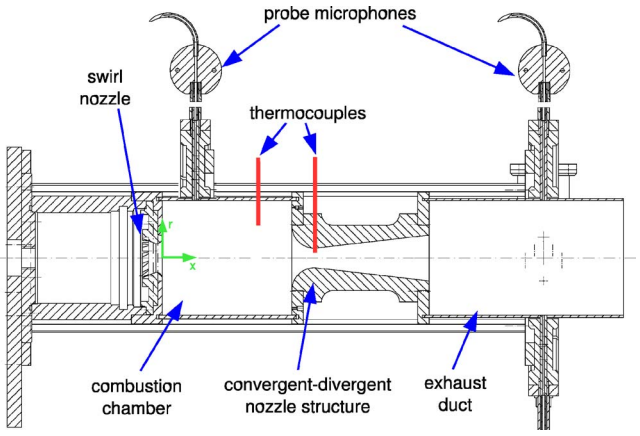

Fig. 4 Sketch of the combustion chamber setup

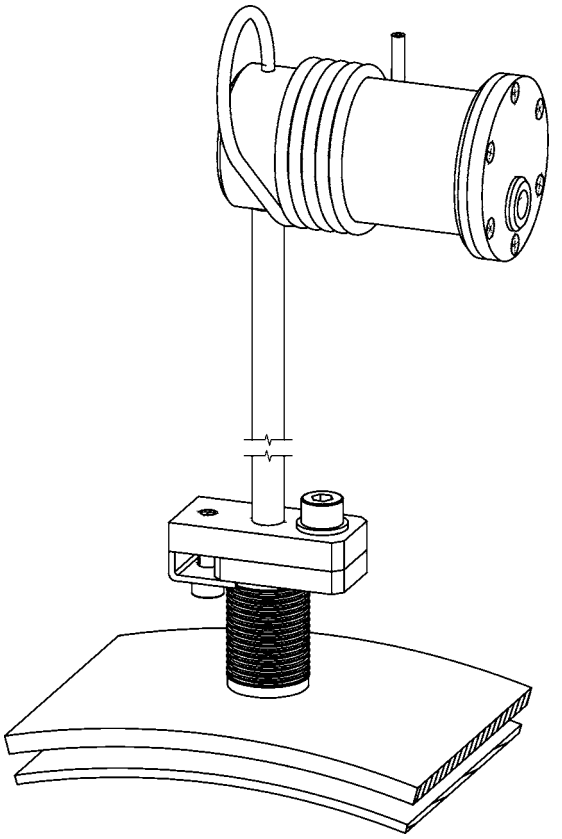

Fig. 5 Sketch of the probe microphone. The microphone is installed in the cylindrical pressure cell.

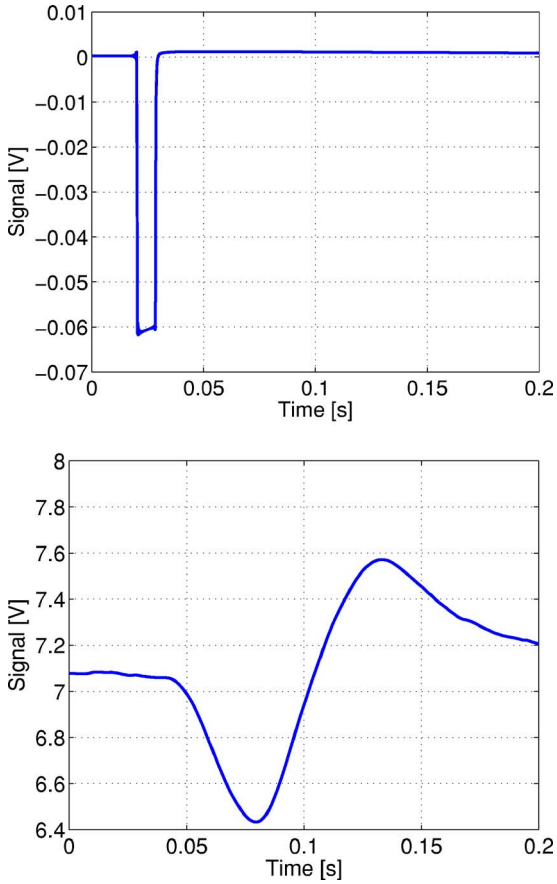

Fig. 6 Phase averaged time series of trigger (above) and thermocouple (below) signal in the pulse excitation mode

can be determined using an inhouse processing code for mode analysis [11,12]. Thus, the total sound power emitted by the combustion system can be determined. In the considered frequency range, the plane wave modes are the only propagating modes.

In order to obtain information about convecting temperature fluctuations or so-called entropy waves, bare wire thermocouples with a diameter of 25 μm are installed in the combustion chamber and in the throat of the outlet nozzle.

For validation purposes and to map the flow field topology, the flow velocity field was measured using a quartz glass combustion chamber with square cross section and a three-component laser doppler system. Results were reported in [13–15].

Tests and Results

The investigations meant to provide the evidence of entropy noise can be divided into three different approaches:

1. The time domain analysis of microphone signals in a pulse excitation mode. In the combustor setup the fuel gas supply is regulated by a piezo-electrical gas modulator. In the EWG rig the platinum wires are heated once per second, controlled by square pulses from a function generator.
2. The cross-spectral analysis of microphone signals and either thermocouple signals in the combustor rig or excitation signals in the EWG, respectively, as a reference. For this the combustor rig is operated in a self-excited oscillating mode while the EWG is heated periodically.
3. By the spectral analysis of broadband entropy noise emission in a higher frequency range.

In the following the results of these three different approaches are presented for the combustor setup and the EWG rig, respectively.

Pulse Excitation

Combustor Test Rig. In the combustor test rig the nonsinusoidal excitation was implemented using a piezoelectric fuel gas modulator. Hereby, once per second the fuel gas supply was increased for a period of about 17 ms. In the postprocessing the microphone and thermocouple signals are phase averaged in reference to the excitation trigger signal. In this setup the thermocouple signal was acquired from the throat position of the convergent–divergent nozzle. The combustor was operated at a power of 9.05 kW and an equivalence ratio of 1.25, resulting in a mean bulk velocity of $\approx$1.2 m/s in the combustion chamber. The Mach number in the combustor outlet nozzle was 0.5.

In the current work the thermocouple signals were not compensated. The associated amplitude loss is not of interest since the amplitudes are not further evaluated for the time domain and cross spectral analysis. With respect to the phase relation, it is assumed that the regarded frequency ranges are above the cutoff frequency of the probe and therefore in a nearly phase constant region in the low-pass filter behavior of the thermocouples. Since only relative phase dependencies are regarded, the absolute phase error is not relevant. However, the relative phase behavior of the thermocouples was determined using a chopped laser beam directed on the thermocouple junction and was found to be approximately constant for the here regarded frequency ranges.

Figure 6 shows the phase averaged time traces of the fuel modulator trigger input on the left and of the thermocouple signal in the outlet nozzle on the right. After a delay period of about 50 ms from the trigger pulse (t_0=0.02 s) the thermocouple indicates a distinct temperature modulation in the outlet nozzle with an amplitude of ±0.6 V corresponding to a temperature fluctuation in the order of ±50 K. The real temperature fluctuation is pre-

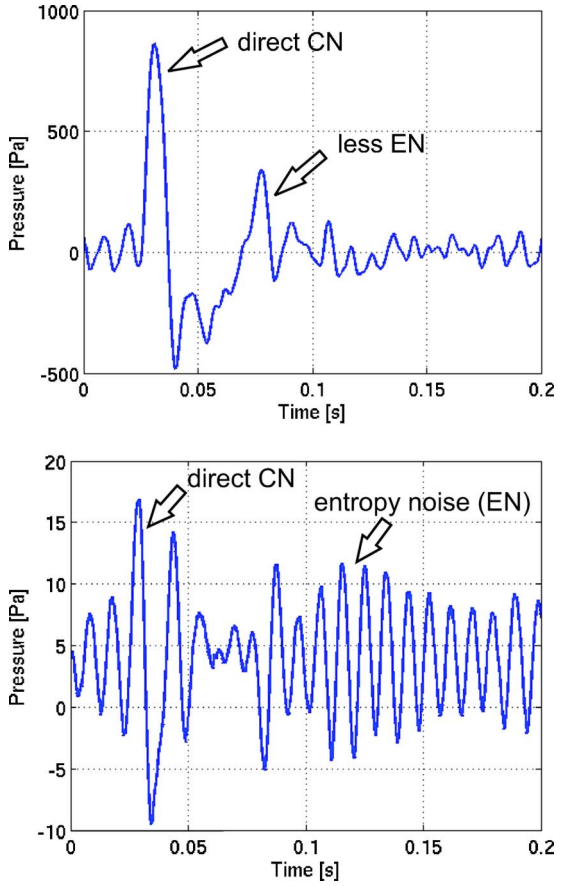

Fig. 7 Phase averaged time series of combustion chamber microphone (above) and exhaust duct microphone (below) signal in the pulse excitation mode

sumedly much higher since uncompensated thermocouple data were processed here. Thus the triggered modulation of the fuel mass flux generates a perturbation of the heat release and with it a convecting entropy wave.

The phase averaged microphone signals are displayed in Fig. 7. Both the combustion chamber (left) and the exhaust duct (right) microphone show an intense pressure pulse shortly after the fuel trigger, which corresponds to the direct flame response. The modulation in the fuel mass flux causes a fluctuation in the heat release, which generates the primary propagating sound wave. But the fluctuation in the heat release also produces a downstream convecting entropy wave, which creates in the outlet nozzle another pressure fluctuation indicated again in both microphone signals in Fig. 7. The convection time of about 50 ms fits to the mean flow velocity and the convection path in the combustion chamber from the flame to the nozzle. The effect of the two microphones in the combustion chamber and the exhaust duct being out of phase at the second pressure pulse series is also described in theory [2].

EWG. At the reference test rig the wires in the heating module of the EWG were electrically heated in the pulse excitation mode once per second with a pulse of ≈3.5 A at 77 V and a pulse duration of 10 ms. Under variation of various parameters like mean flow velocity, Mach number, and distance between heating module (EWG) and nozzle ($\Delta x_{\text{ewg-nozzle}}$), microphone signals from positions upstream and downstream of the nozzle were acquired. In the postprocessing analysis the signal traces were phase averaged using the current excitation signal as reference.

Figure 8 shows the phase averaged signals of a microphone downstream of the nozzle for different bulk velocities in the tube flow and therefore different Mach numbers in the nozzle. The

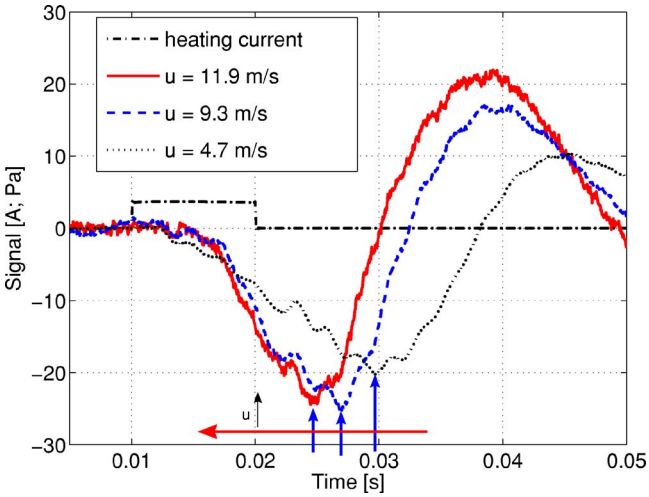

Fig. 8 Phase averaged time series of entropy-wave-generator microphone signals in the pulse excitation mode at different bulk velocities

heating current signal is also plotted in the graph as a dashed line. The entropy wave induced by the EWG generates a positive pressure pulse in the nozzle throat after a propagation delay. This pressure pulse then propagates with the speed of sound and is recorded by the microphones downstream of the nozzle. It can be seen in Fig. 8 that the increase of the bulk velocity yields a corresponding decreased time delay and an increased pressure amplitude. The maximum Mach number at this measurement series was Ma=1.

Figure 9 shows the time-domain averaged signals at different distance lengths between EWG and nozzle throat. For the measurements, tube sections with different lengths have been inserted in the test rig. Here, the bulk velocity in the tube section was 11.9 m/s and the Mach number in the nozzle Ma=1. The propagation delay of the entropy wave and the corresponding pressure pulse is equivalent to the changing propagation path between EWG and nozzle throat if the noise generating entropy waves are traveling with the mean velocity of the flow. The amplitudes of the pressure pulses decrease slightly with increasing duct length, probably due to an increased dispersion of the entropy wave.

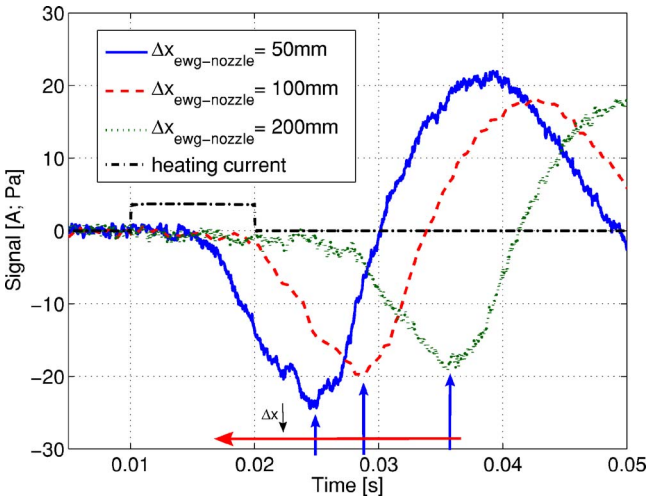

Fig. 9 Phase averaged time series of EWG microphone signals in the pulse excitation mode for different tube lengths Δx between heating module (EWG) and nozzle

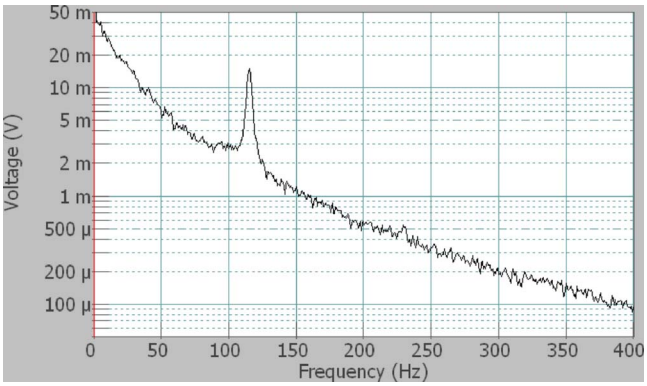

Fig. 10 Power spectrum of the thermocouple signal in the combustion chamber in a self-oscillating mode

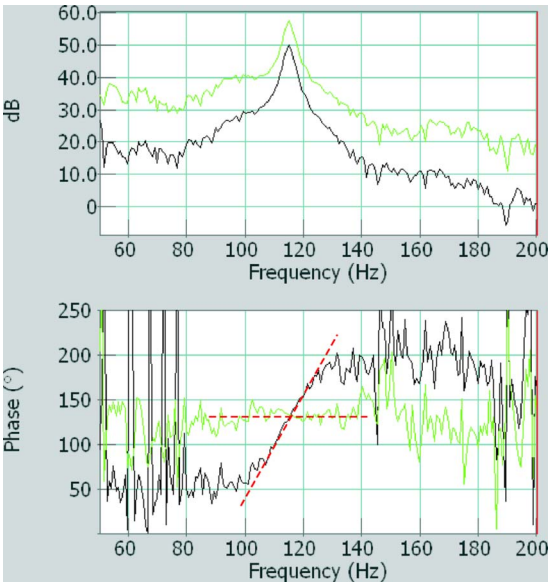

Fig. 11 Cross spectra between thermocouple and combustion chamber microphone (gray) and the exhaust duct microphone (black) at a self-oscillating mode

Sinusoidal Excitation

Combustor Test Rig. In general, to determine the propagation speed of traveling perturbations measured by certain sensors at different positions, the phase relationships between the signals of these sensors have to be analyzed. First the cross spectrum between the two sensors has to be calculated. Then the phase relation in a frequency range of strong coherence between these two sensors has to be considered. A phase relation that is linear with frequency stands for a propagating perturbation, whereby the slope of the phase relation is antiproportional to the propagation speed. Thus, at constant propagation, path perturbations propagating with the speed of sound result in a much flatter phase line than perturbations traveling with flow velocity.

The combustion chamber setup was hereby operated in a resonant self-oscillating mode at a power of 8.35 kW and an equivalence ratio of 1.25. Signals from a thermocouple in the combustion chamber as well as microphone signals of the combustion chamber and the exhaust duct were acquired. The outlet nozzle diameter used was 7.5 mm, which yields an outlet Mach number of Ma≈0.47. The mean bulk velocity in the combustion chamber was ≈1.03 m/s.

Figure 10 shows the power spectrum of the thermocouple in the combustion chamber at $x=85$ mm and $r=25$ mm with a clear peak at 115 Hz, which is also found in the acoustic signals. This indicates the convection of hot spots with the resonance frequency of the system. To extract the phase relationship the cross spectral density function is evaluated between the thermocouple and the microphones in the combustion chamber and the exhaust duct, respectively. Figure 11 displays the zoomed cross spectra for the above-mentioned self-oscillating resonance case.

Considering plane propagation modes the slope in a phase-frequency diagram is inversely proportional to the corresponding propagation speed. The difference between the curves of the two cross spectra in Fig. 11 is obvious. While the phase between the thermocouple and the combustion chamber microphone (gray) shows a negligible slope, the phase relation between the thermocouple and the exhaust microphone (black) indicates a much steeper slope related to a distinctly lower propagation velocity. Regarding a propagation distance between the thermocouple and the convergent-divergent nozzle of 52.5 mm, the phase relation results in a propagation velocity of approximately 3 m/s, which matches the mean flow velocity in this region. In comparison the speed of sound in the combustion chamber is as high as 900 m/s. Thus, the temperature or entropy perturbation is convected with flow velocity from the primary combustion zone passing the thermocouple and accelerated in the outlet nozzle, where the entropy noise generation takes place. The latter is detected by the exhaust duct microphone. In contrast, the phase-frequency relationship between the thermocouple and the combustion chamber microphone (gray) shows a phase that is almost independent of frequency, which indicates high propagation speeds.

EWG. At the EWG test rig a cross spectral analysis was conducted of measurements in a sweep excitation mode. Hereby, the EWG module was heated with a slow sweep over a certain frequency range. Since in this frequency range the microphone signals downstream of the nozzle indicate a strong coherence with the excitation signal and also exhibit a linear phase relation, the slope of this phase relation could be evaluated to provide the propagation velocity of the perturbations.

Figure 12 shows the phase plot of the cross spectra between heating current and microphone signals downstream of the nozzle for an excitation sweep from about 85 to 145 Hz. The different traces correspond to different tube lengths between EWG and nozzle throat. The longest path distance ($\Delta x_{\text{ewg-nozzle}}=200$ mm) results in the steepest phase line due to the same propagation velocity.

From this phase relation the propagation velocity can be quantified as shown in Table 1. Here, the second column displays the

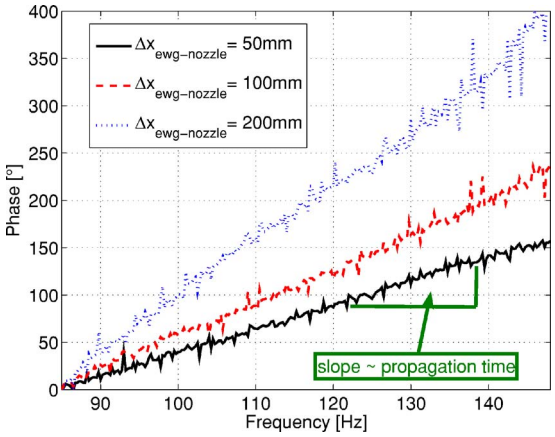

Fig. 12 Phase relation of cross spectra between heating current and microphone signals downstream of nozzle for different tube length between heating module (EWG) and nozzle

Table 1 Propagation velocities of entropy waves calculated from phase relation in comparison with bulk velocity of the flow for different tube lengths Δx between heating module (EWG) and nozzle

Distance $\Delta x_{\text{ewg-nozzle}}$ (mm)	Time delay (ms)	Propagation velocity (m/s)	Bulk velocity (m/s)
50	6.9	11.7	11.9
100	9.9	13.6	11.9
200	18.1	12.8	11.8

time delays resulting from the slope of the phase relation at different tube lengths (column 1). Considering the acoustic propagation time of the generated entropy noise, the traveling speed of the entropy waves can determined in column 3. These phase velocities give a good agreement compared to the bulk velocity of the flow (column 4). However, it has to be considered that the tube flow features a certain flow profile, where the bulk velocity, calculated from the mass flux, the tube cross section, and the mean density, is only a spatial mean value.

Broadband High-Frequency Noise

Combustor Test Rig. Further measurements in the combustion test rig indicate another probable entropy related noise generation mechanism. Hereby, the microphone signals of the combustion chamber and the exhaust duct are compared.

Figure 13 displays the corresponding power spectra in a frequency range up to 5 kHz. It demonstrates the increased sound pressure level of the exhaust duct microphone (gray line) over the combustion chamber microphone (black line) in the frequency range between 1.4 and 3.3 kHz. The unsteady combustion process seems to create small scale entropy perturbations, which generate high-frequency broadband noise when accelerated through the combustion chamber outlet nozzle. A possible jet noise contribution in the exhaust duct yields much lower sound pressure levels due to the low mean flow velocity ($\approx$2 m/s). Thus, jet noise cannot be the reason for this elevated sound pressure level. Above 3.5 kHz the spectrum of the combustion chamber microphone shows the appearance of higher acoustic modes, which are cut off in the nozzle and cannot be observed in the exhaust duct. Since these higher order cut-on standing waves do not emit acoustic power, the dominating effect of broadband entropy noise in the exhaust duct system exists for all frequencies above 1.1 kHz. The operation conditions of this section were the same as in the previous one about the sinusoidal excitation.

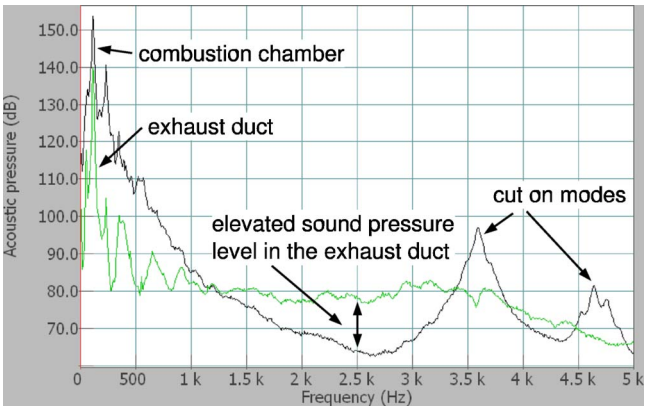

Fig. 13 Power spectra of combustion chamber and exhaust duct microphones up to 5 kHz

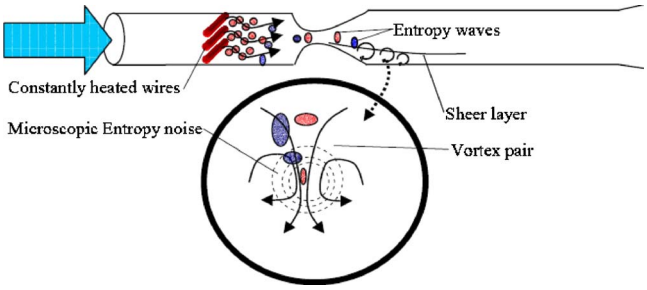

Fig. 14 Sketch of noise generation by small scale entropy perturbations in the entropy wave generator at constant heating

EWG. In order to study broadband entropy related noise sources the EWG heating module was heated continuously in order to generate hot streaks in the wake of each wire. Since the distance between the heating module and the nozzle is comparatively small an equalization of these nonuniform temperature distributions does not occur. The authors are convinced that the strong acceleration of these temperature streaks and nonuniformities through the nozzle generates broadband entropy noise at higher frequencies. A sketch of this mechanism is shown in Fig. 14.

Figure 15 shows the power spectra of microphone signals downstream of the nozzle structure in the region from 500 to 3000 Hz. The dashed line shows the reference case without heating at a nozzle Mach number of 0.35. The peaks in the spectrum are resonance frequencies of the flow system. The solid curve displays the power spectrum with constant heating of all six wire sections. It is obvious that the sound pressure level is elevated in the heated case over almost the total frequency range. Especially in regions with lower background noise, the augmentation of the total noise level by entropy noise amounts up to 7 dB in sound pressure level.

For a detailed quantification of the noise increase and its dependency on the nozzle Mach number the frequency band power of the microphone signals between 1 and 4.5 kHz has been calculated at different Mach numbers for the nonheated and the permanently heated case, respectively. As a result, Fig. 16 shows a strong nonlinear increase in frequency band power difference with the Mach number. This observation supports the theory of Marbel and Candel [2], where a strong increase of entropy noise with the

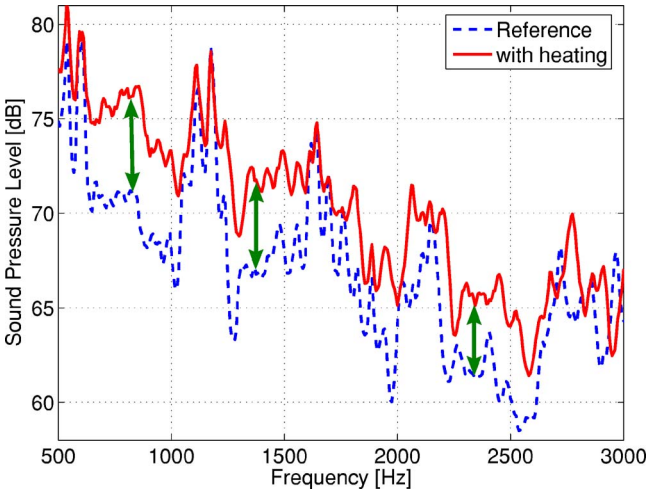

Fig. 15 Power spectrum of EWG microphone downstream of the nozzle with and without constant heating at nozzle Mach number 0.35

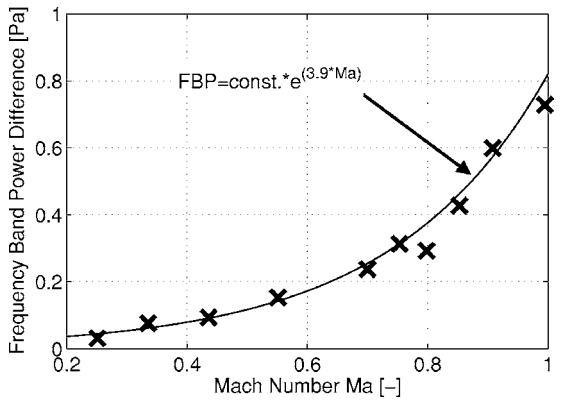

Fig. 16 Increase of frequency band power (1–4.5 kHz) between nonheating and constant heating for changing nozzle Mach numbers

nozzle Mach number was predicted. In Fig. 16 the measured results can be fitted by an exponential function, which underlines the strong Mach number dependence.

Conclusion

Entropy noise is generated when convecting entropy perturbations are accelerated through a nozzle at high Mach numbers. It was shown that entropy noise is the dominant source for the pressure fluctuations in the exhaust duct of a generic combustion chamber. The same conclusions can be drawn from experiments in a reference test rig (EWG) in which the entropy waves were generated by electrical heating.

Three different excitation schemes were applied in the electrically heated reference test rig. The results in a constant heating mode show the generation of broadband entropy noise at higher frequencies due to a spatially nonuniform distribution of the temperature in the wakes of the heating wires. The entropy noise is shown to increase in amplitude with increasing flow Mach number as predicted theoretically.

The same effects including the high-frequency broadband entropy noise in a well audible range between 1 and 3.5 kHz were found in the combustion test rig. It was shown that even at operating conditions with self-excited thermoacoustic oscillations, the emitted sound power of the combustion system is related to entropy noise effects. So far, the nozzle outlet Mach number in the combustion rig reached only $\mathrm{Ma} \approx 0.5$. Since the combustor outlet of aero-engines is choked in all relevant operation conditions, and since the effect of entropy noise is expected to increase strongly with Mach number as shown in the reference experiment (EWG), it can be concluded that entropy noise will be even higher in real jet engines.

In aero-engines it can be assumed that additional entropy noise is generated in each turbine stage when the flow with nonuniform entropy passes the stages.

Considering the achievements in fan and jet noise reduction, the entropy noise mechanism requires further research activities, especially with respect to the design of future aero-engine combustors to yield a more uniform temperature distribution in the outlet of the combustor.

Acknowledgment

The authors gratefully acknowledge the financial support by the German Research Foundation (DFG) through the Research Unit FOR 486 "Combustion Noise". We also would like to thank Sirko Niedworok for setting up and conducting the measurements at the "Entropy-Wave-Generator." Thanks go to Professor Oliver Paschereit (TU Berlin) for his support of this work.

References

[1] Dowling, A. P., 1996, "Acoustics of Unstable Flows," in *Theoretical and Applied Mechanics*, T. Tatsumi, E. Watanabe, and T. Kambe, eds., Elsevier, Amsterdam, pp. 171–186.
[2] Marble, F. E., and Candel, S. M., 1977, "Acoustic Disturbances From Gas Non-uniformities Convected Through a Nozzle," J. Sound Vib., **55**(2), pp. 225–243.
[3] Bohn, M. S., 1976, "Noise Produced by the Interaction of Acoustic Waves and Entropy Waves With High-Speed Nozzle Flows," Ph.D. thesis, California Institute of Technology, Pasadena, CA.
[4] Muthukrishnan, M., Strahle, W. C., and Neale, D. H., 1978, "Separation of Hydrodynamic, Entropy, and Combustion Noise in a Gas Turbine Combustor," AIAA J., **16**(4), pp. 320–327.
[5] Sattelmayer, T., 2000, "Influence of the Combustor Aerodynamics on Combustion Instabilities From Equivalence Ratio Fluctuations," ASME Paper No. 2000-GT-0082.
[6] Polifke, W., Paschereit, C. O., and Döbbeling, K., 2001, "Constructive and Destructive Interference of Acoustic and Entropy Waves in a Premixed Combustor With a Choked Exit," Int. J. Acoust. Vib., **6**(3), pp. 135–146.
[7] Eckstein, J., Freitag, E., Hirsch, C., and Sattelmayer, T., 2004, "Experimental Study on the Role of Entropy Waves in Low-Frequency Oscillations for a Diffusion Burner," ASME Paper No. GT2004-54163.
[8] Eckstein, J., 2004, "On the Mechanisms of Combustion Driven Low-Frequency Oscillations in Aero-engines," dissertation, Technische Universität München, München, Germany.
[9] Shenoda, F. B., 1973, "Reflexionsarme Abschlüsse für durchströmte Kanäle," dissertation, Technische Universität Berlin.
[10] Forster, S. F., Roehle, I., and Michel, U., 2004, "Optimierung der passiven und aktiven Dämpfung von thermoakustischen Schwingungen," Abschlussbericht 4.4.2C, Deutsches Zentrum für Luft-und Raumfahrt, DLR, Berlin Charlottenburg. AG Turbo II-Verbundprojekt für ein CO2-armes Kraftwerk.
[11] Maier, R., Zillmann, J., Roure, A., Winninger, M., Enghardt, L., Tapken, U., Neise, W., Antoine, H., and Bouty, E., 2001, "Active Control of Fan Tone Noise From Aircraft Engines," 7th AIAA/CEAS Aeroacoustics Conference, Paper No. 2001-2220.
[12] Enghardt, L., Zhang, Y., and Neise, W., 1999, "Experimental Verification of a Radial Mode Analysis Technique Using Wall-Flush Mounted Sensors," J. Acoust. Soc. Am., **105**, p. 1186.
[13] Flemming, F., Olbricht, C., Wegner, B., Sadiki, A., Janicka, J., Bake, F., Michel, U., Lehmann, B., and Röhle, I., 2005, "Analysis of Unsteady Motion with Respect to Noise Sources in a Gas Turbine Combustor: Isothermal Flow Case," Flow, Turbul. Combust., **75**(1–4), pp. 3–27.
[14] Duan, X. R., Weigand, P., Meier, W., Keck, O., Stricker, W., Aigner, M., and Lehmann, B., 2004, "Experimental Investigations and Laser Based Validation Measurements in a Gas Turbine Model Combustor," Prog. Comput. Fluid Dyn., **4**, pp. 175–182.
[15] Duan, X. R., Meier, W., Weigand, P., and Lehmann, B., 2005, "Phase-Resolved Laser Raman Scattering and Laser Doppler Velocimetry Applied to Periodic Instabilities in a Gas Turbine Model Combustor," Appl. Phys. B, **80**, pp. 389–396.

Numerical Simulations of Isothermal Flow in a Swirl Burner

M. García-Villalba
Institute for Hydromechanics,
University of Karlsruhe,
Karlsruhe, 76128 Germany

J. Fröhlich
Institute for Technical Chemistry and Polymer Chemistry,
University of Karlsruhe,
Karlsruhe, 76128 Germany

W. Rodi
Institute for Hydromechanics,
University of Karlsruhe,
Karlsruhe, 76128 Germany

In this paper, the non-reacting flow in a swirl burner is studied using large eddy simulation. The configuration consists of two unconfined coannular jets at a Reynolds number of 81,500. The flow is characterized by a Swirl number of 0.93. Two cases are studied in the paper differing with respect to the axial location of the inner pilot jet. It was observed in a companion experiment (Bender and Büchner, 2005, Proc. 12 Int. Cong. Sound and Vibration, Lisbon, Portugal) that when the inner jet is retracted the flow oscillations are considerably amplified. This is also found in the present simulations. Large-scale coherent structures rotating at a constant rate are observed when the inner jet is retracted. The rotation of the structures leads to vigorous oscillations in the velocity and pressure time signals recorded at selected points in the flow. In addition, the mean velocities, the turbulent fluctuations, and the frequency of the oscillations are in good agreement with the experiments. A conditional averaging procedure is used to perform a detailed analysis of the physics leading to the low-frequency oscillations. [DOI: 10.1115/1.2364198]

Introduction

In recent years, there has been increased demand for gas turbines that operate in a lean premixed mode of combustion in an effort to meet stringent emission goals. Highly turbulent swirl-stabilized flames are often used in this context. However, swirling flows are prone to flow instabilities, which can trigger combustion oscillations and cause damage to the device. Lean premixed burners in modern gas turbines often make use of a richer pilot flame, which is typically introduced near the symmetry axis.

In order to prevent the appearance of undesired flow instabilities, it is necessary to understand the underlying physical phenomena. Several mechanisms have been identified in the literature as potential triggers of combustion instabilities. There is, however, no consensus about the real importance of each of them. Lieuwen et al. [1] suggested that heat-release oscillations excited by fluctuations in the composition of the reactive mixture entering the combustion zone are the dominant mechanism responsible for the instabilities observed in the combustor. Other authors [2,3] favor the in-phase formation and combustion of large-scale coherent vortical structures. In premixed combustors, these large-scale structures play an important role in combustion and heat-release processes by controlling the mixing between the fresh mixture and hot combustion products [4].

The formation of large-scale coherent structures is a fundamental fluid-dynamical problem, which must be understood also in the absence of combustion. Large eddy simulation (LES) is a particularly suitable approach for studying this problem. It allows the treatment of high-Reynolds-number flows and at the same time the explicit computation of these structures. If properly conducted, LES should have only limited sensitivity to modelling assumptions. In the context of swirling flows, LES was first applied by Pierce and Moin [5]. Wang et al. [6] performed LES of swirling flow in a dump combustor and studied the influence of the level of swirl on the mean flow and on turbulent fluctuations. LES has also been used in combination with other techniques like acoustic analysis; for example, Roux et al. [7] studied the interaction between coherent structures and acoustic modes and found important differences between iso-thermal and reactive cases.

In the present paper LES is used to study the iso-thermal flow in a swirl burner at two different configurations. The analysis of the results focuses on the strength and sensitivity of flow instabilities generating large-scale coherent structures. In [8,9] the present authors performed LES of an unconfined annular swirling jet. Instabilities leading to large-scale coherent structures were detected and identified to be responsible for the oscillations observed in the corresponding experiment.

Preliminary results for the configurations considered below were reported in [10]. These simulations were repeated thereafter with an improved inlet condition. Furthermore, the analysis presented below goes into substantially more detail, e.g., by determination of conditional averages.

Physical and Numerical Modeling

Experimental Configuration. In [11] a co-annular swirl burner was developed that allows the change of geometrical features over a wide range. The burner, depicted in Fig. 1, is composed of two co-annular jets, a central pilot jet and a concentrically aligned main jet, whose swirl can be adjusted individually. In the experimental conditions considered here, a radial swirler was used for generating the swirl in the main jet. For the central pilot jet, an axial swirler was used to generate a co-rotating flow.

A large number of experiments were performed with this burner in several configurations including isothermal and reactive cases [11,12]. For the isothermal flow without external forcing, it was observed that axial retraction of the central jet into the duct leads to an increased amplitude of flow oscillations reflected by audible noise. In order to investigate this phenomenon by means of LES, two cases were selected. In the first case the inner jet is not retracted, i.e., both jets exit at the same position. In the second case, the pilot jet is retracted by 40 mm. This retraction of the pilot jet generates a double expansion for the main jet (see Fig. 2).

In both cases the co-annular jets issue into an ambient of the same fluid, which is at rest in the experiment. The outer radius of the main jet, $R=55$ mm, is used as the reference length. The reference velocity is the bulk velocity of the main jet $U_b=22.1$ m/s and the reference time is $t_b=R/U_b$. The inner radius of the main jet is $0.63R$. For the pilot jet the inner radius is $0.27R$ and the outer radius is $0.51R$. The mass flux of the pilot jet is 10% of the total mass flow. The Reynolds number based on the bulk velocity of the main jet U_b and R is $\mathrm{Re}=81{,}000$. The swirl number is defined as

Contributed by the International Gas Turbine Institute (IGTI) of ASME for publication in the JOURNAL OF ENGINEERING FOR GAS TURBINES AND POWER. Manuscript received October 1, 2005; final manuscript received February 1, 2006. IGTI Review Chair: R. S. Abhari. Paper presented at the ASME Turbo Expo 2006: Land, Sea and Air (GT2006), Barcelona, Spain, May 8–11, 2006, Paper No. GT2006-90764.

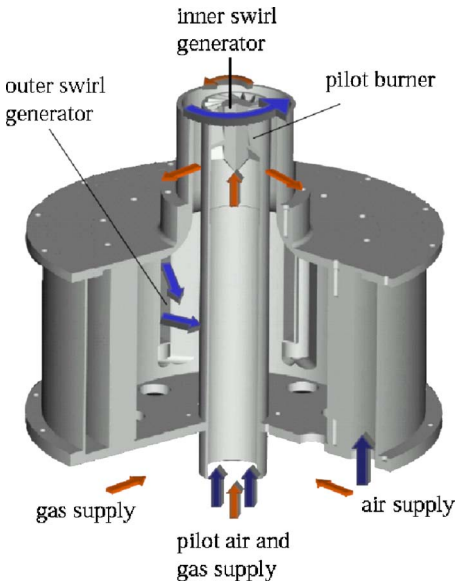

Fig. 1 Sketch of the burner (taken from [11])

$$S = \frac{\int_0^R \rho \langle u_x \rangle \langle u_\theta \rangle r^2 \, dr}{R \int_0^R \rho \langle u_x \rangle^2 r \, dr} \tag{1}$$

where $\langle u_x \rangle$ and $\langle u_\theta \rangle$ are the mean axial and azimuthal velocities, respectively. Its value at the burner exit is $S=0.93$.

As mentioned above, two cases have been considered, one without retraction of the pilot jet, i.e., $x_{\text{pilot}}=0$. In the second one the retraction is $x_{\text{pilot}}=-0.73R$. LDA measurements are available for both cases [11]. In particular, radial profiles of mean and RMS velocities are available at four axial stations in the near field of the burner. Only for the case with retraction, power spectra of velocity fluctuations were also measured.

Numerical Setup. The simulations were performed with the in-house code LESOCC2 [13], which is a successor of the code LESOCC [14]. It solves the incompressible Navier-Stokes equations on curvilinear block-structured grids. A collocated finite-volume discretization with second-order central schemes for convection and diffusion terms is employed. Temporal discretization is performed with a three-stage Runge-Kutta scheme solving the pressure-correction equation in the last stage only. The Rhie and Chow momentum interpolation [15] is applied to avoid pressure-velocity decoupling. The dynamic Smagorinsky subgrid-scale model [16] was used in the simulations. The model parameter was determined using an explicit three-dimensional box filter of width equal to twice the mesh size. The eddy viscosity was clipped to avoid negative values and was smoothed by temporal relaxation [17].

The computational domain extends $32R$ downstream of the burner exit located at $x/R=0$ and $12R$ in radial direction. It also covers part of the inlet ducts (Fig. 2). The block-structured mesh consists of about 8.5 million cells with 160 cells in azimuthal direction. The grid is stretched in both the axial and radial directions to allow for concentration of points close to the nozzle and the inlet duct walls. The stretching factor is everywhere less than 5%.

The specification of the inflow conditions for both jets requires a strong idealization. For the main jet, the way the swirl is introduced is not so critical because the swirler is located upstream, far away from the region of interest. Therefore, the flow is prescribed at the circumferential inflow boundary located at the beginning of the inlet duct (see Fig. 2). At this position steady top-hat profiles for the radial and azimuthal velocity components are imposed. This procedure was validated in [9]. The swirler of the pilot jet, on the other hand, is located directly at the jet outlet (Fig. 1). A numerical representation of this swirler would be very demanding because of the large number of blades and was therefore not considered in the present investigation. Instead, the inflow conditions for the pilot jet were obtained by performing simultaneously a separate, streamwise periodic LES of developed swirling flow in an annular pipe (see Fig. 2) using body forces to generate co-rotating swirl with $S_{\text{pilot}}=2$ as described in [18], where S_{pilot} is the swirl number of the pilot jet only. Recall that S_{pilot} has little impact on the swirl number of the entire flow due to the small mass flux of this stream. No-slip conditions were applied at solid walls. The fluid entrained by the jet is fed in by a mild co-flow of 5% of U_b. By using different values of the co-flow velocity it was shown in [19] that the flow development is not sensitive to this conditions. Free-slip conditions were applied at the open lateral boundary. A convective outflow condition was used at the exit boundary.

In both cases simulated, the same boundary conditions were employed. Figure 2 displays a zoom of the inflow region for $x_{\text{pilot}}=-0.73R$. In the case $x_{\text{pilot}}=0$, not shown here, the inflow region differs because the wall separating main and pilot jet and the cylindrical center body reach until $x=0$, with the inflow plane for the pilot jet still located at the same position $x/R=-0.73$. This is illustrated in Fig. 3.

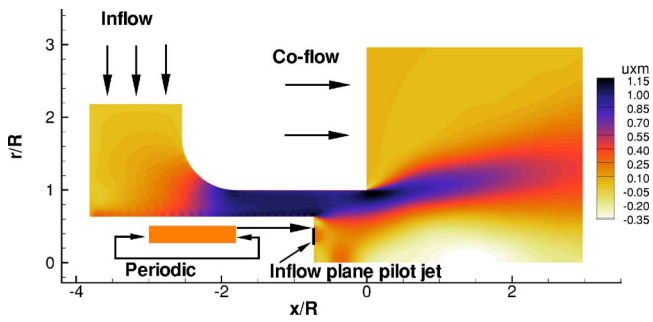

Fig. 2 Numerical setup and boundary conditions. Color represents mean axial velocity.

Average Flow

After discarding initial transients, statistics were collected for $100t_b$, which is long enough to obtain converged values in the near field of the burner. The averaging was performed in time and also along the azimuthal direction. Only resolved fluctuations are accounted for. It was checked, however, that the modelled subgrid-scale contributions are negligible [19].

Streamlines. Figure 3 shows the two-dimensional streamlines of the average flow in an axial plane for both cases. It is well known that at this high level of swirl a recirculation zone forms in the central region of the flow [20]. This phenomenon is related to the presence of a low pressure region on the symmetry axis. The influence of the retraction of the inner jet is remarkable. For $x_{\text{pilot}}=0$ the recirculation forms immediately behind the cylindrical center body and the length of the recirculation zone is about $9R$. In the case $x_{\text{pilot}}=-0.73R$ the length of the recirculation zone is only about $5R$. The two streams mix before the final expansion and the recirculation is detached from the burner. The maximum width of the recirculation bubble is about $0.8R$ in both cases and it is attained at $x/R=1.2$ for $x_{\text{pilot}}=0$ and at $x/R=1.5$ for $x_{\text{pilot}}=-0.73R$. Far downstream of the jet exit, for $x/R \geq 6$, the mean flow is not fully converged in the vicinity of the symmetry axis, as indicated by the wavy streamlines. The reason is that at this po-

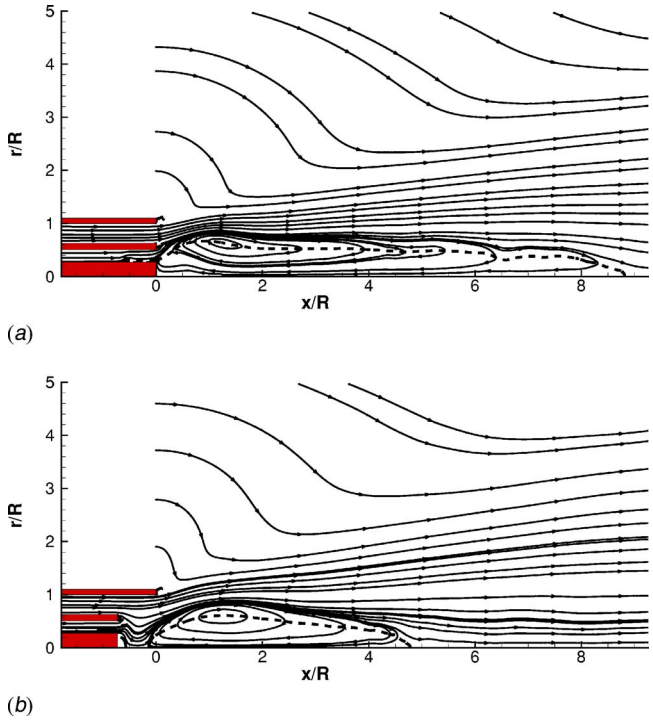

Fig. 3 Streamlines of the average flow in an axial plane (*a*) $x_{pilot}=0$ and (*b*) $x_{pilot}=-0.73R$

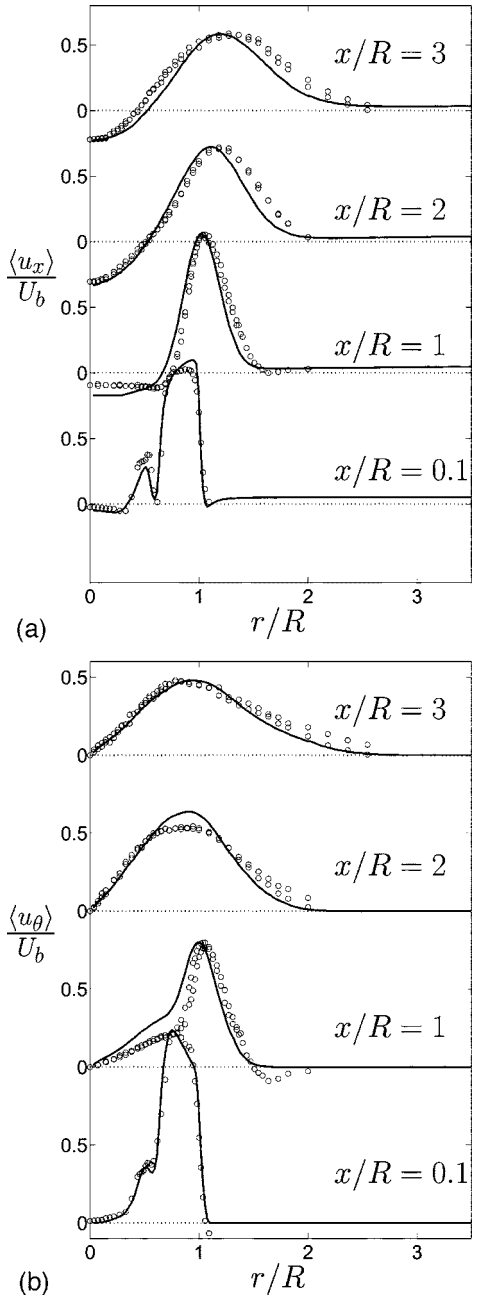

Fig. 4 Radial profiles of mean velocity $x_{pilot}=0$. (*a*) Axial velocity. (*b*) Tangential velocity. Symbols, experiments [11]. Lines, LES.

sition the motions are slower and substantially longer averaging times would be necessary to obtain a fully converged mean flow.

Mean and RMS Velocity Profiles. A comparison of simulations with experiments is reported in Figs. 4–7, showing radial profiles of mean velocity and turbulent fluctuations at several axial stations for both cases.

The agreement with the experimental data is in general good for the mean flow. The case $x_{pilot}=0$ is well reproduced in the simulation (Fig. 4), which is noteworthy in spite of the strong idealization in setting up the inflow conditions for the pilot jet. The limited strength of the pilot jet can be appreciated by the mean axial and tangential velocity at $x/R=0.1$. In the case $x_{pilot}=-0.73R$ (Fig. 5), a discrepancy is evident at $x/R=0.1$; the backflow is overpredicted in the simulation. This implies that the recirculation zone in Fig. 3(*b*) does not correspond exactly to the experimental one, which was measured to be slightly further downstream. Nevertheless, other characteristics are very well predicted so that this simulation is still close to the experiment. For example, the spreading of the jet is in good agreement with the experiment and so are the turbulent fluctuations of axial and tangential velocity (Fig. 7). The agreement is also good for the turbulent fluctuations in the case $x_{pilot}=0$ (Fig. 6).

Some features are common in both cases. Apart from the presence of a recirculation zone, two complex shear layers subject to curvature effects are present in the flow. The inner shear layer is formed between the main jet and the recirculation zone. The outer shear layer is formed between the main jet and the surrounding co-flow. In the case $x_{pilot}=0$, the turbulent fluctuations generated in these layers are clearly visible up to $x/R=1$ in the profiles of RMS fluctuations by corresponding peaks (Fig. 6). In the case $x_{pilot}=-0.73R$ this feature is only observed in the profile of the axial fluctuations very close to the jet exit 7(*a*). Note also that the level of fluctuations at $x/R=0.1$ is much higher for $x_{pilot}=-0.73R$. In that case the maximum RMS is about $0.5U_b$ while in the case $x_{pilot}=0$ it does not reach $0.3U_b$. Further downstream at $x/R=3$ this difference has vanished and in both cases the maximum RMS fluctuation is close to $0.3U_b$, although the radial spreading of the profiles is larger in the case $x_{pilot}=-0.73R$.

Fluctuating Kinetic Energy. To conclude the description of the average flow, Fig. 8 displays contours of the fluctuating kinetic energy, using the same scale for both cases. It is obvious that the retraction of the pilot jet leads to a large increase in the level of the fluctuating energy. In the case $x_{pilot}=0$ the fluctuating kinetic energy is concentrated in the two shear layers mentioned above and the maximum level is $k_{max}/U_b^2 \sim 0.14$. In the case $x_{pilot}=-0.73R$ the kinetic energy is concentrated in three regions, just behind the inner part of the burner, at the beginning of the recirculation bubble (compare Figs. 8(*b*) and 3(*b*)), and in the region of the inner shear layer. As evidenced by the RMS profile of tangential velocity fluctuations (Fig. 7 at $x/R=0.1$ (and radial fluctua-

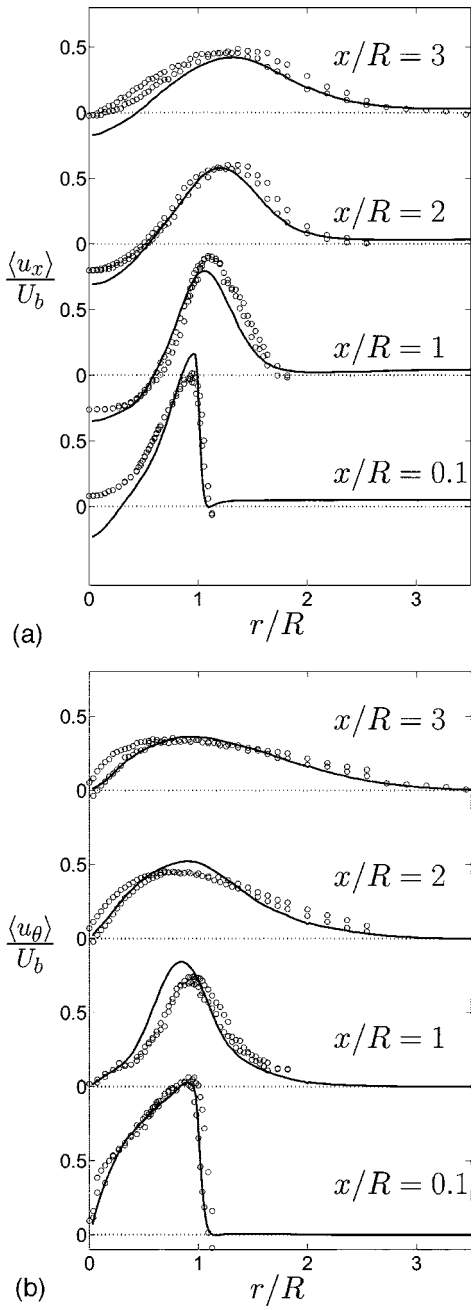

Fig. 5 Radial profiles of mean velocity $x_{pilot}=-0.73R$. (*a*) Axial velocity. (*b*) Tangential velocity. Symbols, experiments [11]. Lines, LES.

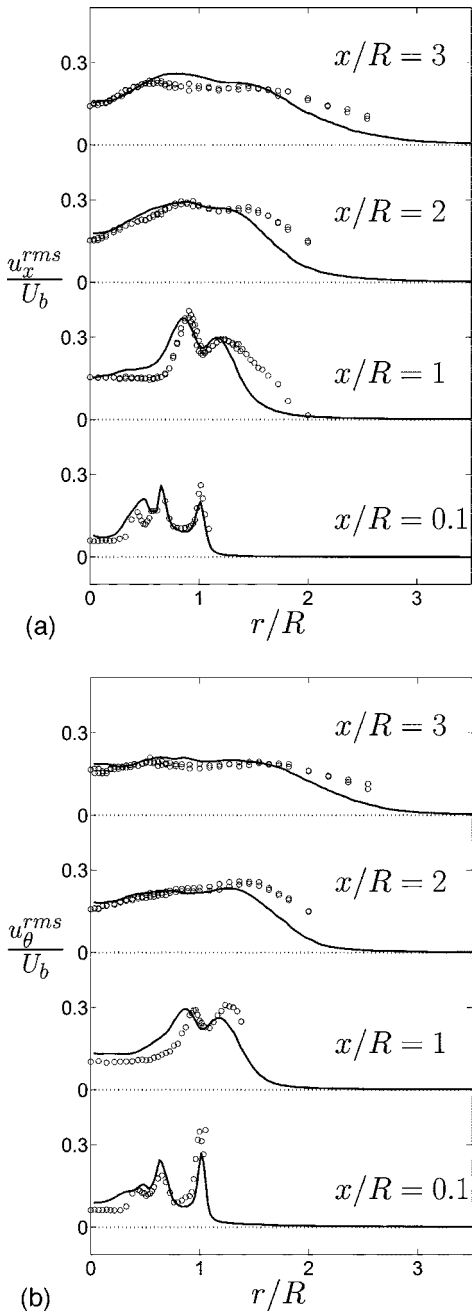

Fig. 6 Radial profiles of RMS velocity $x_{pilot}=0$. (*a*) Axial velocity. (*b*) Tangential velocity. Symbols, experiments [11]. Lines, LES.

tions, not shown here), showing a pronounced local maximum at the symmetry axis), these two components (radial and tangential) contribute mainly to the concentration of kinetic energy at the beginning of the recirculation zone. The features observed here will be discussed below in connection with the vortical structures present in the respective flows.

Instantaneous Flow and Spectra

Coherent Structures. For a swirling annular jet, large-scale coherent structures were identified and their evolution and interaction described in [8,9]. It was shown that two families of structures appear, an inner one oriented quasi-streamwise and located in the inner shear layer formed by the jet on its boundary with the recirculation zone (the so-called precessing vortex cores [20]), and an outer one oriented at a larger angle to the axis and situated in the outer shear layer formed on the boundary with the surrounding co-flow. Figure 9 shows iso-surfaces of pressure fluctuations p'' for both cases visualizing the coherent structures of the flow. Pressure fluctuations are more suitable for the visualization of coherent structures than the commonly used instantaneous pressure [21] because iso-surfaces of the latter are influenced by the spatially variable average pressure field, which is unrelated to instantaneous structures. Figures 9(*a*) and 9(*c*) display two different levels of p'' for the case $x_{pilot}=0$, namely $p''=-0.3$ and $p''=-0.15$, respectively. Figures 9(*b*) and 9(*d*) show the level $p''=-0.3$ at two different instants in time for the case $x_{pilot}=-0.73$. The color of the structures is given by the radial gradient of mean axial velocity. In the inner shear layer $\partial\langle u_x \rangle/\partial r > 0$ and the iso-surface

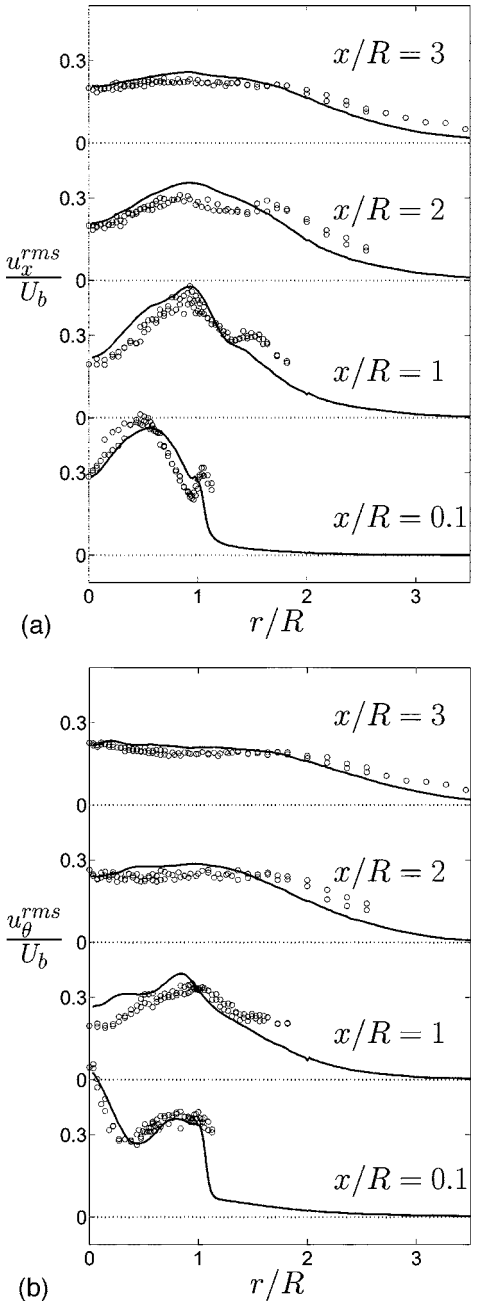

Fig. 7 Radial profiles of RMS velocity $x_{pilot}=-0.73R$. (*a*) Axial velocity. (*b*) Tangential velocity. Symbols, experiments [11]. Lines, LES.

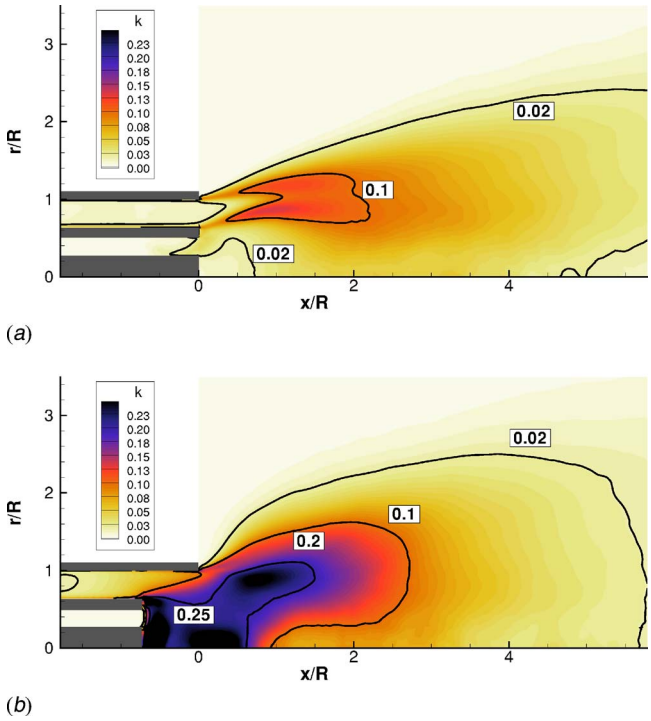

Fig. 8 Fluctuating kinetic energy: (*a*) $x_{pilot}=0$ and (*b*) $x_{pilot}=-0.73R$

is light colored. In the outer shear layer $\partial\langle u_x\rangle/\partial r<0$ and the isosurface is dark colored.

Pronounced large-scale coherent structures are observed in the case of the retracted pilot jet (Figs. 9(*b*) and 9(*d*)). As in the case without inner jet [9], two structures can be observed in these pictures. Animations have shown that the rotation of the inner structure around the symmetry axis is very regular. At some instances, however, the inner structure branches lead to two arms as shown in Fig. 9(*d*). The leading one, in the direction of the rotation, is faster than the second one and takes over in terms of strength. The one behind disappears at the exit in less than half a rotation period and in the downstream field during another half period. In the case without retraction, $x_{pilot}=0$, the structures are substantially smaller and more irregular. In fact, if one compares the same level of pressure fluctuations $p''=-0.3$, hardly any structure is visible in the flow (Fig. 9(*a*)). Increasing the pressure level to $p''=-0.15$, small structures are visible, which exhibit small coherence. At this point it should be recalled that the same flow with just the pilot jet blocked shows substantial coherent structures, similar to the ones for $x_{pilot}=-0.73R$ but somewhat weaker and less organized [8]. In the case $x_{pilot}=0$, hence, the pilot jet destroys the large-scale structures. When the pilot jet is retracted to $x_{pilot}=-0.73R$ this is not observed. The cylindrical tube enclosing the main jet prevents the recirculation bubble from moving upstream to the central bluff body containing the exit of the pilot jet. This holds for the mean flow (Fig. 3(*b*)) as well as for the conditionally averaged flow discussed later. The pilot jet therefore only "hits" the upstream front of the recirculation bubble but cannot penetrate into the inner shear layer where it would be able to impact on the coherent structures. The different coherent structures observed in both cases explain the different levels of fluctuating kinetic energy encountered close to the burner exit in Fig. 8. In a theoretical study [22], Juniper and Candel performed a stability analysis for the case of co-annular jets without swirl. They showed how stability is reduced if the inner stream mixes with the outer one before the exit plane of the outer tube, the same trend as reported here. It would be interesting to perform a similar stability analysis for cases with swirl.

Spectra. In the experiment [11], time signals of velocity have been recorded at several radial positions close to the burner exit at $x/R=0.1$ for the case $x_{pilot}=-0.73R$. The case $x_{pilot}=0$ was not measured because in preliminary tests no instability was observed. During the simulation velocity and pressure signals were recorded at the same positions for a duration of $80t_b$. Furthermore, signals were recorded for each of these x and r positions at 12 different angular locations over which additional averaging was performed. On the symmetry axis no angular averaging is possible and only one signal was recorded, and at $r/R=0.1$ and $r/R=0.18$ only four angular signals were recorded with the particular grid used. The spectra were obtained splitting each signal in three overlapping segments of length $40t_b$ multiplying it by a Hanning window, and averaging over the segments.

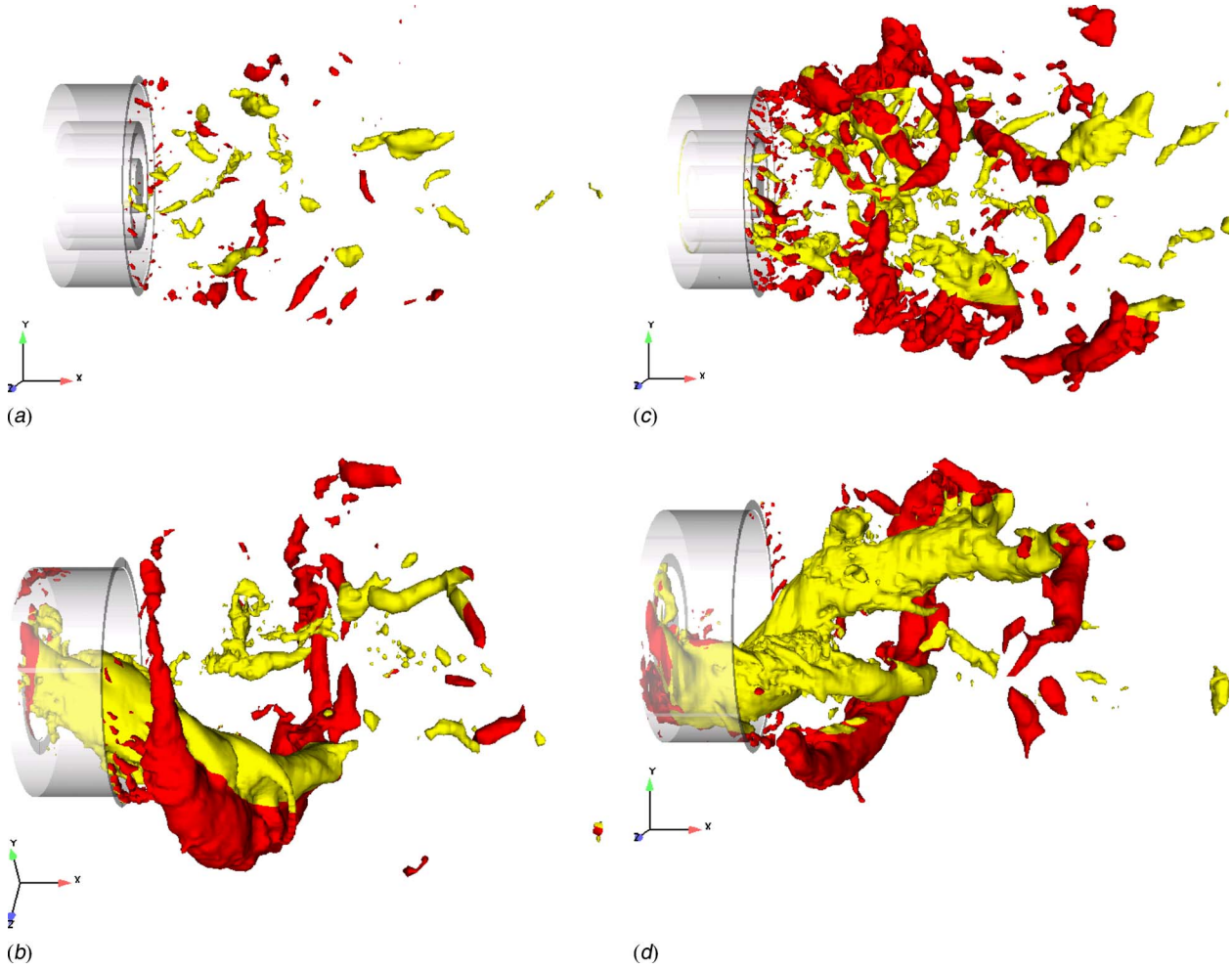

Fig. 9 Coherent structures visualized using an iso-surface of pressure fluctuations. Left, $x_{pilot}=0$. Right, $x_{pilot}=-0.73R$. (*a*, *b*, *d*) $p-\langle p\rangle=-0.3$. (*c*) $p-\langle p\rangle=-0.15$. Color as explained in the text.

The difference between the time signals of both cases is evident from Fig. 10. In the case $x_{pilot}=0$ (Fig. 10(*a*)), the signal exhibits the typical irregularity of a turbulent signal. Figure 10(*b*), on the other hand, shows that in the case $x_{pilot}=-0.73R$ a flow instability has developed that causes a regular oscillation of the signal with large amplitude. The low-frequency oscillations of this signal produce a pronounced peak in the power spectrum of the axial velocity fluctuations (Fig. 11). The frequency of the principal peak is $f_{peak}=0.25U_b/R$, which in dimensional units corresponds to a value of $f_{peak}=102$ Hz. The amplitude of the peak is very large, covering almost two decades in logarithmic scale. The total fluctuating energy is substantially larger than for the case $x_{pilot}=0$, reflected by the larger integral under this curve. This is in line with the fluctuating kinetic energy contours of Fig. 8 and the RMS values of Figs. 6 and 7. In the case $x_{pilot}=0$, no pronounced peak is observed, which confirms the preliminary experimental tests in which no flow instability was detected. The smaller peak, which appears in the case $x_{pilot}=0$ at a frequency $0.16U_b/R$, cannot be related to the small coherent structures observed in Fig. 9(*c*) because these structures have a shorter time scale, which would correspond to higher frequencies. This finding deserves further investigation.

A comparison of the spectrum from the LES for $x_{pilot}=-0.73R$ and the corresponding experimental spectrum in Fig. 11 serves to further validate the simulations. The agreement for both frequency and amplitude of the dominant peak is remarkable. Also the second harmonic is well predicted in the simulations.

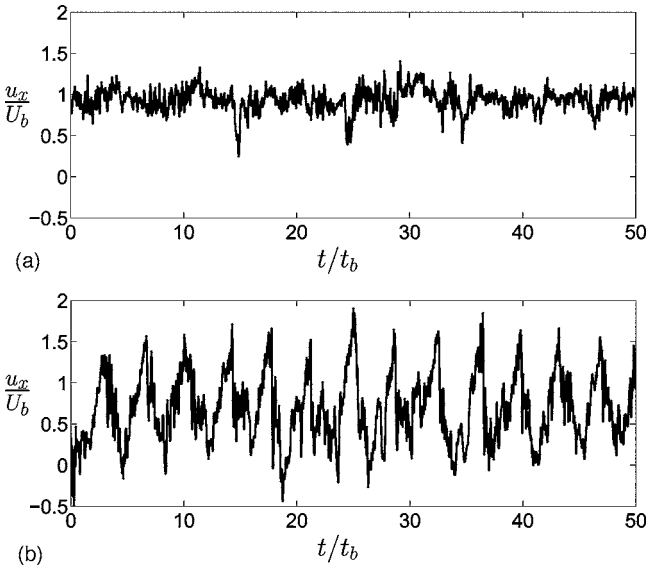

Fig. 10 Time signal of axial velocity at $x/R=0.1$, $r/R=0.73$ recorded during the simulations. (*a*) $x_{pilot}=0$. (*b*) $x_{pilot}=-0.73R$.

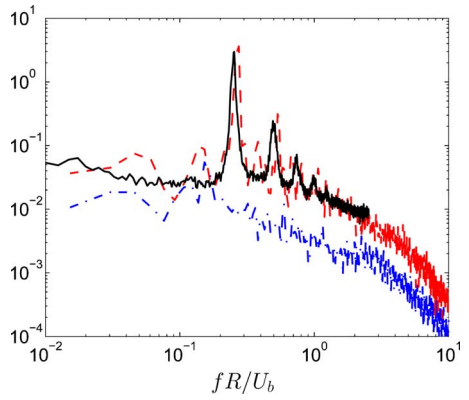

Fig. 11 Power spectrum of axial velocity fluctuations at $x/R=0.1$, $r/R=0.73$. Solid line, experiment [11] $x_{pilot}=-0.73R$. Dashed line, simulation $x_{pilot}=-0.73R$. Dash-dotted line, simulation $x_{pilot}=0$.

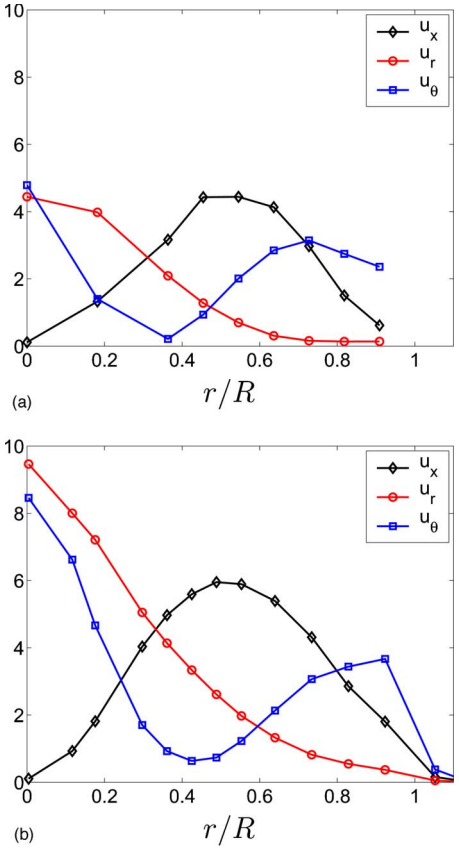

Fig. 12 Amplitude of the power spectrum at the fundamental frequency f_{peak} at $x/R=0.1$ as a function of r/R for case $x_{pilot}=-0.73R$. (*a*) Experiment [11]. (*b*) Simulation.

The amplitude of the power spectrum at the peak frequency is now considered. It is quite a sensitive quantity, much more than the peak frequency itself. Figure 12 shows this amplitude at the fundamental frequency f_{peak} as a function of the radial position. The shapes of the curves are different for the three velocity components. The simulation reproduces quite well the trends of the experiment. Only for $r/R<0.2$ the simulation overpredicts the amplitudes. In that region the impact of azimuthal averaging is small (even nonexistent at the axis) so that this could have an effect. In [9] similar plots were reported for an annular jet. It was shown there that an important issue is the location of the minimum for the amplitude of tangential velocity fluctuations. This minimum indicates the mean radial location of the center of the inner structure. Therefore, it is noteworthy that the minimum is well reproduced in the simulation.

Conditionally Averaged Flow

It has been shown in the previous sections that large-scale structures rotating around the symmetry axis are present in the flow in the case $x_{pilot}=-0.73R$. Due to the high level of turbulence, the vortical structures are highly irregular as evidenced by the difference between Figs. 9(*b*) and 9(*d*). The pronounced peak in the power spectrum, Fig. 11, indicates that the rotation of the structure is very regular and allows the calculation of conditional averages. The purpose of the latter is to remove the irregularity induced by the turbulent motions. The method, which is described in the following section, consists basically in defining a coordinate system $y-z$ with origin at the symmetry axis, which rotates with the structure, and performing the averaging procedure in this rotating coordinate system. Note that it is not possible to perform this kind of analysis for the case $x_{pilot}=0$ due to a lack of a regular frequency of oscillation (Fig. 11).

Procedure. In order to investigate the main characteristics of the coherent structures, 140 instantaneous three-dimensional fields have been recorded. They are separated in time by $0.8t_b$, so that in each period of rotation of the structure five fields have been recorded. The time span covered by the fields is $112t_b$. If the oscillations are truly periodic, the definition of the axes which rotate with the structure is straightforward, with a fixed angle of rotation in a fixed time. In the present case, however, the motion of the structure is only quasi-periodic and therefore the method has to be more elaborate. The center of the structure has to be determined for each instantaneous field and a subsequent rotation of the field is performed, such that the center of the vortex is always on the y axis. This is equivalent to defining a coordinate system $y-z$ that rotates with the structure.

The method is illustrated in Fig. 13 and proceeds as follows. The radial location of the dominant inner structures in the transverse plane $x/R=0.1$ is known from Fig. 12 (minimum of u_θ). In the present case $r/R=0.35$ is used. The center of the vortex is identified as the local minimum of the pressure fluctuations at that position. In the present case the coherent structure is very regular and the detection is simple. In other cases [9], up to three of these coherent structures can coexist at certain instants and in that case the dominant one is selected. Then, the full three-dimensional field is rotated by an angle α (Fig. 13), so that each field has the structure at the same location and standard averaging is performed. Midgley et al. [23] used a similar method to analyze two-dimensional data from experiments on fuel injectors. Here, however, three-dimensional fields are available. Note that this procedure is fundamentally different from phase averaging. There is no external trigger or internal frequency that would suggest dividing the rotation period into several phases, reducing therefore the number of samples in each phase. Instead, all angles are statistically equivalent due to the cylindrical symmetry of the problem.

Results. In the following, conditionally averaged quantities are indicated with an upper index c. Figure 14(*a*) shows an isosurface of pressure fluctuations, $p^c-\langle p\rangle=-0.1$ visualizing the coherent structures of the flow using the same style as Figs. 9(*b*) and 9(*d*). It is clear that, using this procedure the large-scale coherent structures have been substantially smoothed. The criterion that has been used to obtain the conditional averages involves only the inner structure. Nevertheless, the outer structure does not disappear with the conditional averaging but appears at the same angular position, demonstrating its link to the inner structure. In fact, the outer structure is triggered by the inner one as demonstrated by different studies of similar flows [8,9]. In [9] this issue was investigated for a pure annular jet with weaker coherent struc-

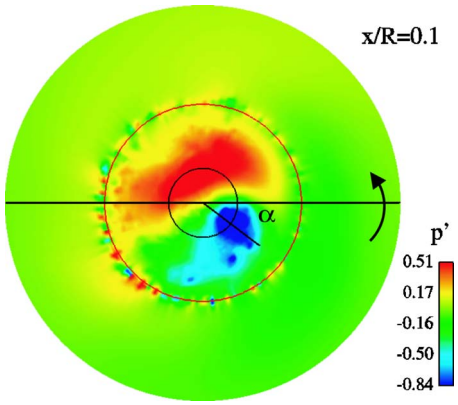

Fig. 13 Illustration of the conditional average procedure. Color according to $p-\langle p\rangle$. The black circle indicates the points where the minimum of the pressure is looked for. The other circle (further outward) indicates the outer radius of the burner.

tures. Determining the correlation between u_x'' and p'', it was found for that case that strong positive u_x'' values correlate with negative p'', i.e., the inner vortex structure, and, in fact, advance these in the sense of rotation. The same behavior is obvious in the present case from the conditional average. The surface of positive u_x^c fluctuations in Fig. 14(*b*) advances the negative p^c fluctuations of the inner structure in Fig. 14(*a*). When plotting all three iso-surfaces in a single graph it is even more visible that the downstream end of the positive u_x^c-fluctuation surface winds along the connection line between the inner and the outer vortex structure of Fig. 14(*a*). This feeds the outer structure, turning in the clockwise sense around its own axis in the view of Fig. 14(*a*). Negative fluctuations of u_x^c, represented by in Fig. 14(*b*), occur at the opposite side of the jet and seem not related to a continuously present rotating large-scale coherent structure.

Figures 15 and 16 show two-dimensional cuts of the conditionally averaged flow. Pseudo-streamlines of this flow field projected onto two planes are displayed. In Fig. 15 the pseudo-streamlines are based on (u_r^c, u_θ^c) and in Fig. 16 on (u_x^c, u_r^c). The color represents p^c and the thick line indicates the contour line $u_x^c=0$. The latter shows that the recirculation region is displaced off the symmetry axis in Fig. 15. The pressure minimum generated by the inner vortex structure is well visible in the $y-z$ plane together with the vortex motion surrounding it. The pressure minimum is off the axis at $r/R=0.35$ (a posteriori justifying the choice of this radius for the conditioning) and by definition at the y axis. The pseudo-streamlines spiral around a different point closer to the axis. The view in Fig. 15 is in the downstream direction and rotation of the flow and the structures is in the counter-clockwise direction. The recirculation region hence lags behind the inner structure by about 130 deg.

The inner and outer structures of Fig. 14 are also visible in Fig. 16. The inner structure shows up through the pressure minimum around $x/R=0$ and $z>0$. The outer structure is reflected by the recirculation regions and the spiralling or bending streamlines at the top and the bottom of the figure. From the pseudo-streamlines for $x\sim 0$ in this figure it is also clear that the inner structure is correlated with high forward axial velocity, for $z>0$, while the low axial velocity is located in the opposite side for $z<0$. This is indicated also by the asymmetry of the recirculation region (see also Fig. 17).

The previous information is contained in a more quantitative way in Fig. 17, which shows mean and conditional averaged profiles of pressure and velocity. In Fig. 17(*a*), the strength of the pressure minimum related to the center of the structure is visible by comparison to the mean pressure. Note also in Fig. 17(*b*) that the conditionally averaged axial velocity u_x^c at $y=0$, hence in the

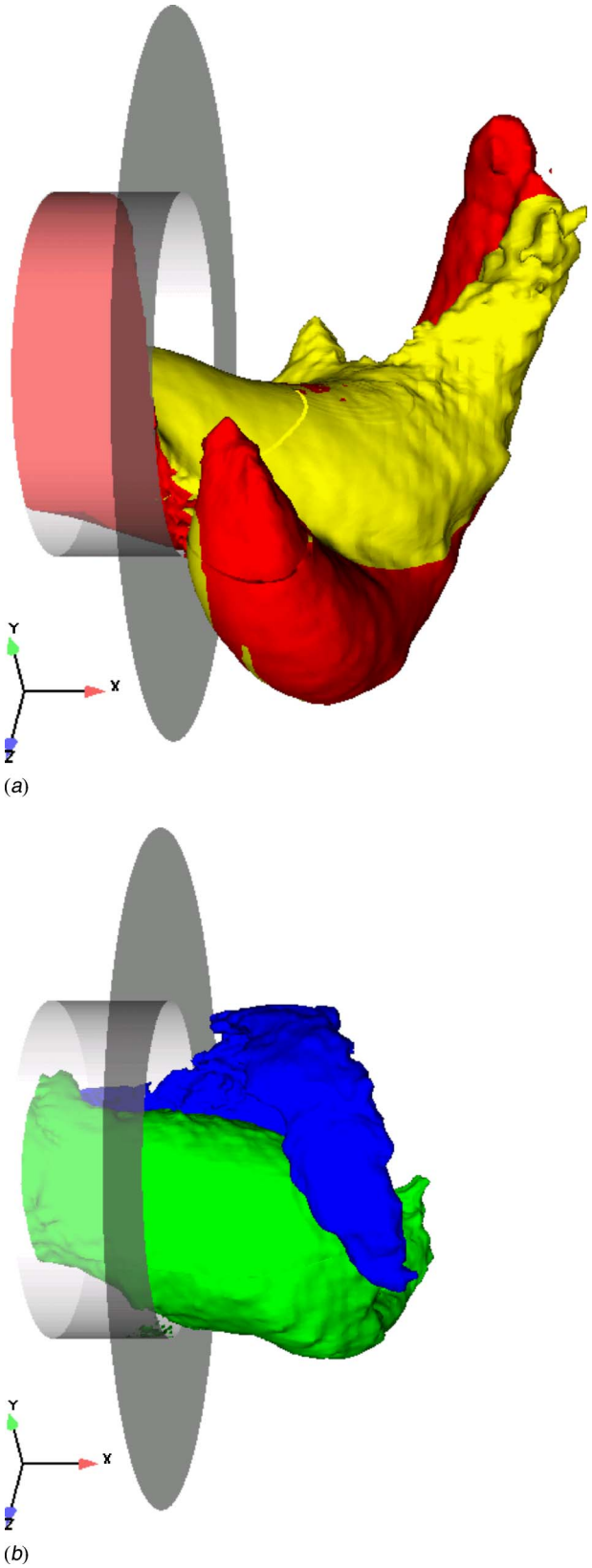

Fig. 14 Coherent structures obtained using the conditional average flow field. (*a*) Iso-surface $p^c-\langle p\rangle=-0.1$. Color as in Fig. 9. (*b*) Iso-surfaces $u_x^c-\langle u_x\rangle=0.3$ and $u_x^c-\langle u_x\rangle=0.3$.

inner structure, is higher than the mean axial velocity. The recirculation zone, as expected from the two-dimensional plots, is displaced towards the opposite side. In Fig. 17(*c*), the radial position

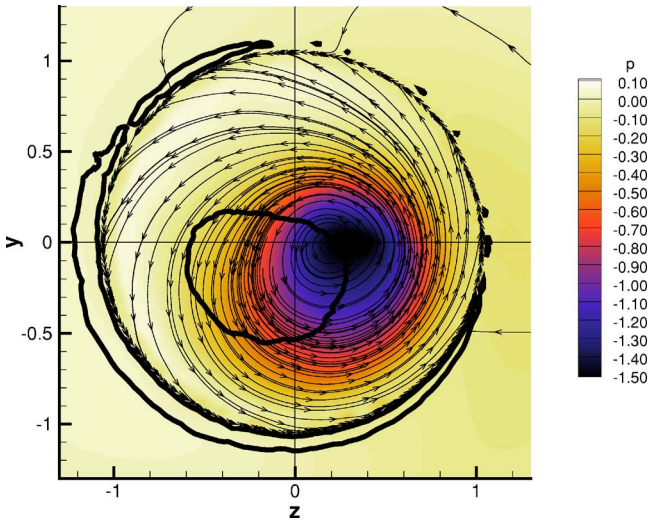

Fig. 15 Two-dimensional cut through the plane $x/R=0.1$ of the conditional-averaged flow. Color is given by p^c. Pseudo-streamlines calculated using u_r^c and u_θ^c. Thick black line $u_x^c=0$.

at which the conditionally averaged tangential velocity u_θ^c at $y=0$ equals the mean velocity roughly corresponds to the minimum of the pressure. This is also expected because at the center of the structure the fluctuations of the tangential velocity component have to vanish, as discussed in [9].

Finally, Fig. 18 shows the same plane as Fig. 15 but the color and streamlines are given by the equivalent Reynolds-decomposed quantities, i.e., color by $p^c-\langle p\rangle$ and streamlines by $(u_r^c-\langle u_r\rangle, u_\theta^c-\langle u_\theta\rangle)$. The thick line again represents $u_x^c=0$. In this figure the region of low pressure fluctuations corresponds to the inner structure of Fig. 14(*a*). Note that it forms outside the boundary of the recirculation zone.

Yazdabadi et al. [24] performed phase-averaged measurements in a cyclone dust separator and obtained similar plots as Fig. 15. Their conclusion was that the reverse flow zone displaces the central vortex core to create the precessing vortex core. The reverse flow zone would then provide feedback for the precessing vortex core and precess around the central axis behind the precessing vortex core. In the present case, Figs. 14(*a*) and 18 suggest an alternative explanation, although perhaps compatible with the previous one: The inner structure (precessing vortex core) is formed as an instability of the shear layer (Kelvin-Helmholtz instability). It is therefore formed on the boundary of the recirculation zone (Fig. 18) and advected by the mean flow. This structure then constrains the motion of the recirculation zone, which is displaced off the symmetry axis and precesses behind the structure.

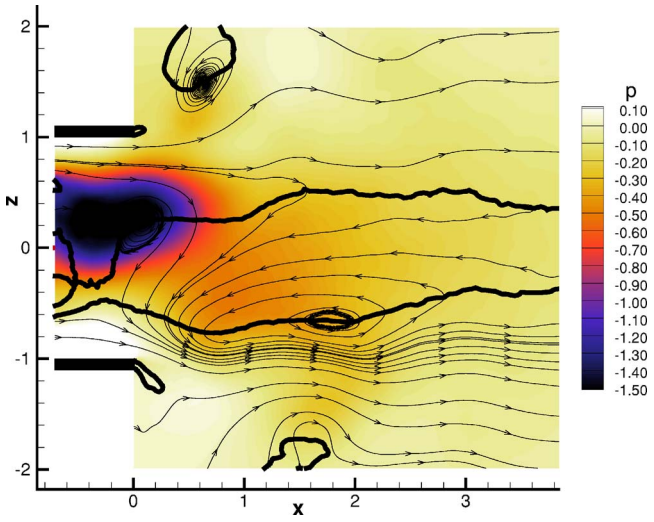

Fig. 16 Two-dimensional cut through the plane $y/R=0$ of the conditional-averaged flow. Color is given by p^c. Pseudo-streamlines calculated using u_x^c and u_r^c. Thick black line $u_x^c=0$.

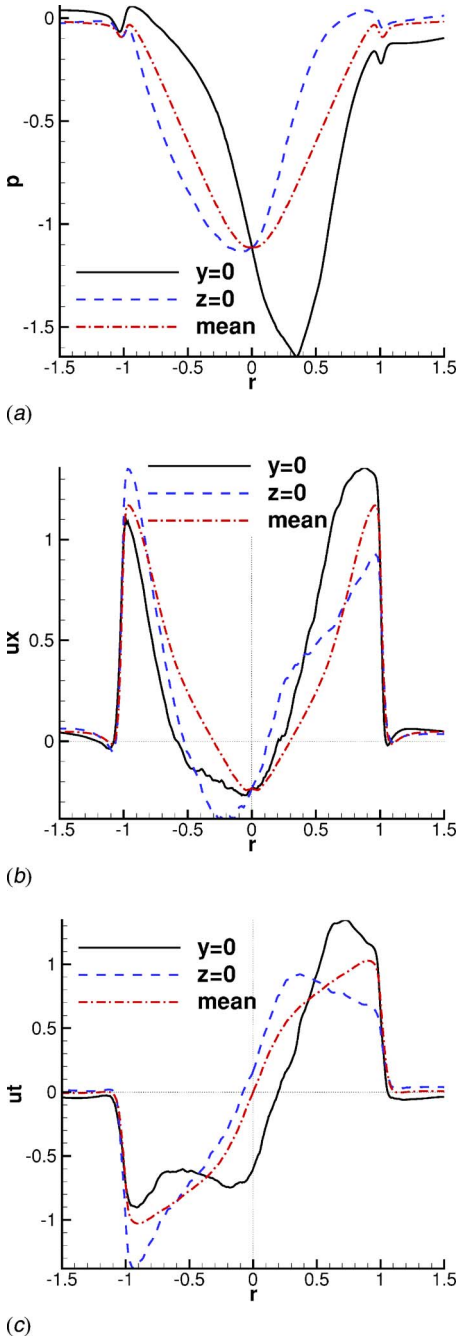

Fig. 17 Conditional-averaged velocity profiles at $x/R=0.1$. (*a*) Pressure. (*b*) Axial velocity. (*c*) Tangential velocity.

Conclusions

Large-eddy simulations of incompressible flow in a swirl burner have been reported. The influence of geometrical features of the burner has been investigated by comparison of two cases with a different exit position of the inner jet. The simulations have

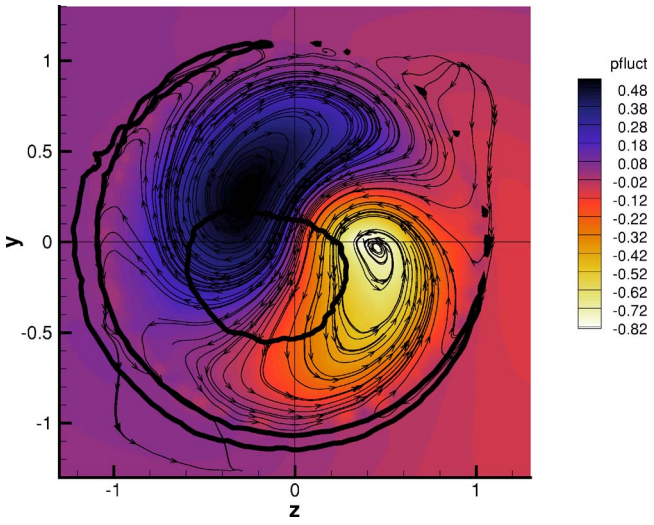

Fig. 18 Two-dimensional cut through the plane $x/R=0.1$ of the conditional-averaged flow. Color is given by $p^c-\langle p\rangle$. Pseudo-streamlines calculated using $u_r^c-\langle u_r\rangle$ and $u_\theta^c-\langle u_\theta\rangle$. Thick black line $u_x^c=0$.

been validated by comparison with corresponding experiments and very good agreement was obtained for mean flow, turbulent fluctuations, and the frequency of oscillation. The simulations have confirmed that the retraction of the pilot jet leads to the generation of enhanced flow instabilities. The related large-scale coherent structures have been identified and analyzed by using instantaneous plots, spectra, and conditional averages. The latter provides a precise picture of the characteristics of the large-scale coherent structures by removing the irregularity associated with the turbulent motions. These structures are relevant to the mixing of heat and species in the near field of the burner, and the technique can presumably be applied to the reactive case as well.

Acknowledgment

This work was funded by the German Research Foundation (DFG) through project A6 in the Collaborative Research Centre SFB-606 at the University of Karlsruhe. The authors are grateful to Dr. H. Büchner and O. Petsch for providing the experimental data. The calculations were carried out on the HP XC6000 Cluster of the University of Karlsruhe Computer Centre.

Nomenclature

f_{peak} = fundamental frequency of oscillation
k = fluctuating kinetic energy
p = modified pressure
R = outer radius of the main jet
Re = Reynolds number
RMS = root mean square
S = swirl number
t_b = characteristic time based on R and U_b
U_b = bulk velocity of the main jet
u_x = axial velocity component
u_r = radial velocity component
u_θ = tangential velocity component
x,r,θ = cylindrical coordinates (axial, radial, tangential)
x,y,z = Cartesian coordinates
x_{pilot} = axial location of the pilot jet exit
α = angle used in the conditional-average technique
$\langle\phi\rangle$ = mean value of the quantity ϕ
ϕ^c = conditional average of the quantity ϕ
ϕ'' = instantaneous fluctuation of the quantity ϕ, $\phi''=\phi-\langle\phi\rangle$
ρ = density

References

[1] Lieuwen, T., Torres, H., Johnson, C., and Zinn, B. T., 2001, "A Mechanism of Combustion Instability in Lean Premixed Gas Turbine Combustors," ASME J. Eng. Gas Turbines Power, **123**, pp. 182–189.
[2] Paschereit, C. O., Gutmark, E., and Weisenstein, W., 2000, "Excitation of Thermoacoustic Instabilities by Interaction of Acoustics and Unstable Swirling Flow," AIAA J., **38**, pp. 1025–1034.
[3] Külsheimer, C., and Büchner, H., 2002, "Combustion Dynamics of Turbulent Swirling Flames," Combust. Flame, **131**, pp. 70–84.
[4] Coats, C. M., 1996, "Coherent Structures in Combustion," Prog. Energy Combust. Sci., **22**, pp. 427–509.
[5] Pierce, C. D., and Moin, P., 1998, "Large Eddy Simulation of a Confined Coaxial Jet With Swirl and Heat Release," AIAA Paper No. 98-2892.
[6] Wang, P., Bai, X. S., Wessman, M., and Klingmann, J., 2004, "Large Eddy Simulation and Experimental Studies of a Confined Turbulent Swirling Flow," Phys. Fluids, **16**(9), pp. 3306–3324.
[7] Roux, S., Lartigue, G., Poinsot, T., Meier, U., and Bérat, C., 2005, "Studies of Mean and Unsteady Flow in a Swirled Combustor Using Experiments, Acoustic Analysis, and Large Eddy Simulations," Combust. Flame, **141**, pp. 40–54.
[8] García-Villalba, M., and Fröhlich, J., 2005, "On the Sensitivity of a Free Annular Swirling Jet to the Level of Swirl and a Pilot Jet," *Engineering Turbulence Modelling and Experiments 6*, W. Rodi and M. Mulas, eds., Elsevier, Amsterdam, pp. 845–854.
[9] García-Villalba, M., Fröhlich, J., and Rodi, W., 2006, "Identification and Analysis of Coherent Structures in the Near Field of a Turbulent Unconfined Annular Swirling Jet Using Large Eddy Simulation," Phys. Fluids, **18**, p. 055103.
[10] García-Villalba, M., Fröhlich, J., Rodi, W., Petsch, O., and Büchner, H., 2005, "Large Eddy Simulation of Flow Instabilities in Co-annular Swirling Jets, *Proc. 6th Direct and Large Eddy Simulation Workshop*, Poitiers, France.
[11] Bender, C., and Büchner, H., 2005, "Noise Emissions from a Premixed Swirl Combustor, *Proc. 12th Int. Cong. Sound and Vibration*, Lisbon, Portugal.
[12] Habisreuther, P., Bender, C., Petsch, O., Büchner, H., and Bockhorn, H., 2005, "Prediction of Pressure Oscillations in a Premixed Swirl Combustor Flow and Comparison to Measurements," *Engineering Turbulence Modelling and Experiments 6*, W. Rodi and M. Mulas, eds., Elsevier, Amsterdam.
[13] Hinterberger, C., 2004, "Dreidimensionale und tiefengemittelte Large-Eddy-Simulation von Flachwasserströmungen," Ph.D. thesis, University of Karlsruhe, Karlsruhe, Germany.
[14] Breuer, M., and Rodi, W., 1996, "Large Eddy Simulation of Complex Turbulent Flows of Practical Interest," *Flow Simulation With High Performance Computers II, Vol. 52 of Notes on Numerical Fluid Mechanics*, E. H. Hirschel, ed., Vieweg, Braunschweig, pp. 258–274.
[15] Rhie, C. M., and Chow, W. L., 1983, "Numerical Study of the Turbulent Flow Past an Airfoil With Trailing Edge Separation," AIAA J., **21**(11), pp. 1061–1068.
[16] Germano, M., Piomelli, U., Moin, P., and Cabot, W. H., 1991, "A Dynamic Subgrid-Scale Eddy Viscosity Model," Phys. Fluids A, **3**, pp. 1760–1765.
[17] Breuer, M., and Rodi, W., 1994, "Large Eddy Simulation of Turbulent Flow Through a Straight Square Duct and a 180° Bend," *Fluid Mechanics and Its Applications*, Vol. 26, P. R. Voke, R. Kleiser, and J. P. Chollet, eds., Kluwer Academic, Dordrecht.
[18] Pierce, C. D., and Moin, P., 1998, "Method for Generating Equilibrium Swirling Inflow Conditions," AIAA J., **36**(7), pp. 1325–1327.
[19] García-Villalba, M., 2006, "Large Eddy Simulation of Turbulent Swirling Jets," Ph.D. thesis, University of Karlsruhe.
[20] Gupta, A. K., Lilley, D. G., and Syred, N., 1984, *Swirl Flows*, Abacus.
[21] Fröhlich, J., Mellen, C. P., Rodi, W., Temmerman, L., and Leschziner, M. A., 2005, "Highly Resolved Large-Eddy Simulation of Separated Flow in a Channel With Streamwise Periodic Constrictions," J. Fluid Mech., **526**, pp. 19–66.
[22] Juniper, M. P., and Candel, S. M., 2003, "The Stability of Ducted Compound Flows and Consequences for the Geometry of Coaxial Injectors," J. Fluid Mech., **482**, pp. 257–269.
[23] Midgley, K., Spencer, A., and McGuirk, J. J., 2005, "Unsteady Flow Structures in Radial Swirled Fed Fuel Injectors," ASME J. Dyn. Syst., Meas., Control, **127**, pp. 755–764.
[24] Yazdabadi, P., Griffiths, A. J., and Syred, N., 1994, "Characterization of the PVC Phenomena in the Exhaust of a Cyclone Dust Separator," Exp. Fluids, **17**, pp. 84–95.

Fabio Ciampoli

John W. Chew

Fluids Research Centre,
School of Engineering,
University of Surrey,
Guildford, Surrey GU2 7XH, UK

Shahrokh Shahpar

Elisabeth Willocq

Rolls-Royce plc,
PO Box 31,
Derby DE24 8BJ, UK

Automatic Optimization of Preswirl Nozzle Design

The objective of the research described here is to develop and demonstrate use of automatic design methods for preswirl nozzles. Performance of preswirled cooling air delivery systems depends critically on the design of these nozzles which is subject to manufacturing and stress constraints. The best solution may be a compromise between cost and performance. Here it is shown that automatic optimization using computational fluid dynamics (CFD) to evaluate nozzle performance can be useful in design. A parametric geometric model of a nozzle with appropriate constraints is first defined and the CFD meshing and solution are then automated. The mesh generation is found to be the most delicate task in the whole process. Direct hill climbing (DHC) and response surface model (RSM) optimization methods have been evaluated. For the test case considered, significant nozzle performance improvements were obtained using both methods, but the RSM model was preferred. [DOI: 10.1115/1.2364194]

1 Introduction

As is shown by the ideal Joule (or Brayton) cycle, gas turbine efficiency increases with pressure ratio. For a fixed turbine inlet temperature the maximum specific work output occurs at an optimal pressure ratio. As turbine temperature increases, so does optimal specific work and pressure ratio. These basic thermodynamic results show that turbine entry temperature is crucial to engine performance, and explain the importance of heat transfer in turbine design.

Internal and film cooling of high pressure turbine blades is commonly used in aeroengines, allowing considerably higher turbine gas temperatures than would otherwise be the case. The blade cooling air is taken from the compressor and bypasses the combustor, before being taken on-board the turbine rotor. Obviously, the cooling air must be at high enough pressure to ensure positive flow and better cooling is achieved with lower air temperatures. Less obviously, in considering blade heat transfer, it is appropriate to use the relative total temperature of the cooling air, and this depends on the details of how the air is delivered to the rotor.

While complete cooling system design involves a complex trade-off between different requirements, the possible advantage of using a preswirled cooling air delivery system may be illustrated using basic thermodynamic theory. Defining the swirl ratio (SR) as $v_\phi/\Omega r$, where v_ϕ is the tangential velocity of the air and Ωr is the rotor speed, the absolute and relative total air temperatures are related as follows

$$\frac{T_{\text{abs}} - T_{\text{rel}}}{\Omega^2 r^2/2C_p} = 2\text{SR} - 1 \tag{1}$$

Here C_p is specific heat of air at constant pressure. This equation is obtained directly from the definitions of T_{abs} and T_{rel} and shows that increasing the swirl of the air (without increasing T_{abs}) leads to a reduction in the total temperature relative to the rotor.

The desired increase in swirl velocity may be achieved using stationary preswirl nozzles. This does require a loss of pressure, but no work is done in the stationary frame so T_{abs} is unchanged (provided there is no heat transfer). Now suppose that a cooling air delivery pressure of p_{ref} is required, and that this air may be taken from any point of an ideal, isentropic compressor with zero swirl. In this compressor it is assumed that the absolute total temperature is T_{ref} at the point where the pressure is p_{ref}. Assuming isentropic flow throughout and ideal preswirl system behavior, it may then be shown that the preswirled delivery relative total air temperature is given by

$$\frac{T_{\text{rel}}}{T_{\text{ref}}} = 1 + \frac{\Omega^2 r^2}{2C_p T_{\text{ref}}}(1 - 2\text{SR} + \text{SR}^2) \tag{2}$$

This equation indicates that T_{rel} has a minimum value (equal to T_{ref}) when the swirl ratio is unity. At this condition the cooling air must be taken from the compressor at a high enough pressure to support the flow through the preswirl nozzles. This idealized example is a gross simplification of engine conditions, but does illustrate that preswirling can be advantageous.

In what appears to be the earliest published work on preswirl systems Meierhofer and Franklin [1] recognized that pre-swirl nozzle effectiveness is one of the main components of the effectiveness of the whole delivery system. More recent research, for example Refs. [2–6], has confirmed many of Meierhofer and Franklin's findings and has presented more detailed information on various aspects of preswirl system flow and heat transfer. While Meierhofer and Franklin characterized the whole preswirl system behavior through a velocity effectiveness for the nozzle, Chew et al.'s [5] elementary analysis separated the nozzle and delivery chamber effects. The present study considers nozzle performance in isolation from other parts of the system. There is evidence to support the assumption that the nozzle flow is only weakly affected by the flow in the chamber provided, for example, there is sufficient spacing between the nozzle exit and the rotor. For example, Dittman et al. [2] concluded that the presence of the rotor had little effect on the preswirl nozzle discharge coefficients for their experimental conditions. There is further evidence [2,6], relevant to the present study, that CFD models of isolated nozzles can give good estimates of in situ nozzle behavior.

The objective of the work described here is to develop and demonstrate use of automatic design methods for preswirl nozzles. Nozzle design is important to the performance of the cooling system, but is subject to cost, manufacturing, and stress constraints. Ideally, the nozzle should operate isentropically ejecting flow uniformly in the tangential direction, thus maximising use of the available pressure drop. In addition, manufacturing costs and (for aeroengines) weight should be minimised and the

Contributed by the International Gas Turbine Institute (IGTI) of ASME for publication in the JOURNAL OF ENGINEERING FOR GAS TURBINES AND POWER. Manuscript October 1, 2005; final manuscript received October 1, 2005. IGTI Review Chair R. S. Abhari. Paper presented at the ASME Turbo Expo 2006: Land, Sea and Air (GT2006), Barcelona, Spain, May 8–11, 2006, Paper No. GT2006-90249.

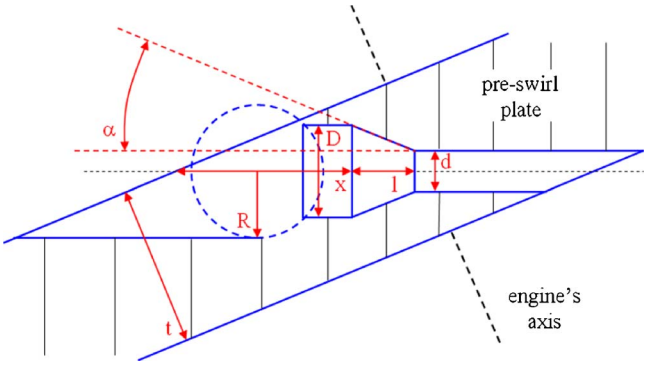

Fig. 1 Parametric representation of nozzle

design must accommodate other constraints, such as axial movements and stress limits. It is recognized that the case study presented does not include all design possibilities or constraints, but it does quantify benefits of aerodynamic optimization and demonstrates how automatic design methods and CFD can be used within the wider design process.

In the next section the nozzle geometry used in this case study is described and its parametric model presented. Parameter limitations and constraints are also introduced. Meshing and CFD modeling are then discussed in Secs. 3 and 4. The optimization techniques used are explained in Sec. 5, with results presented in Sec. 6, and the main conclusions summarized in Sec. 7.

2 The Parametric Geometry

The nozzle design used in this study is shown in Fig. 1, and is based on an aeroengine example. The preswirl angle (to the engine tangential) is 15 deg, the thickness of the preswirl plate is t, d is the downstream nozzle diameter, D is the upstream nozzle diameter, l is the chamfer length, α is the chamfer angle, R is the radius of a spherical drilling on the upstream face, and x is nozzle axial distance of the chamfered section from the upstream face of the plate.

This nozzle geometry may be completely defined by five independent parameters. These parameters were chosen to be t, d, l, α, and x. The radius of the spherical drilling at the inlet R, whose presence is imposed by manufacturing constraints, is a dependent parameter, and is set to be 0.6 mm larger than the upstream nozzle diameter D. D is itself a dependent parameter and can be obtained from d, l, and α. Table 1 shows the baseline design values for the design parameters and the range of values allowed in the optimization process.

Five geometrical constraints were imposed during the optimization process. Some of these were required to preserve the functionality of the preswirl system (type 1). Others were imposed in order to automate the mesh generation which is described in the next section (type 2). Figure 2 illustrates the constraints.

Constraints 1 and 2 are type 2 and arise from the requirement for the upstream face of the plate (A) to intersect the spherical drilling (B) between positions $A_{\min}$ and $A_{\max}$. These two limits translate to two algebraic constraints.

Constraint 3 is also type 2. The length f is required to be greater than a small positive value ε, in order for the geometry to remain similar, as required in the meshing approach adopted.

Constraint 4 is type 1. To avoid intersection of the preswirl plate downstream face with the chamfer volume the length m must be bigger than $m_{\min}$.

Constraint 5 is type 1. To avoid intersection of the preswirl plate downstream face with the spherical drilling the length g must be bigger than $g_{\min}$.

Table 1 Optimization design parameters

Parameter	Description	Base line value	Min	Max
t	Preswirl plate thickness	13 mm	10	20
d	Downstream nozzle diameter	7.2 mm	6.7	12
l	Chamfer length	0.8 mm	0.8	15
α	Chamfer angle	45 deg	5	60
x	Chamfer distance from inlet	23 mm	21	28

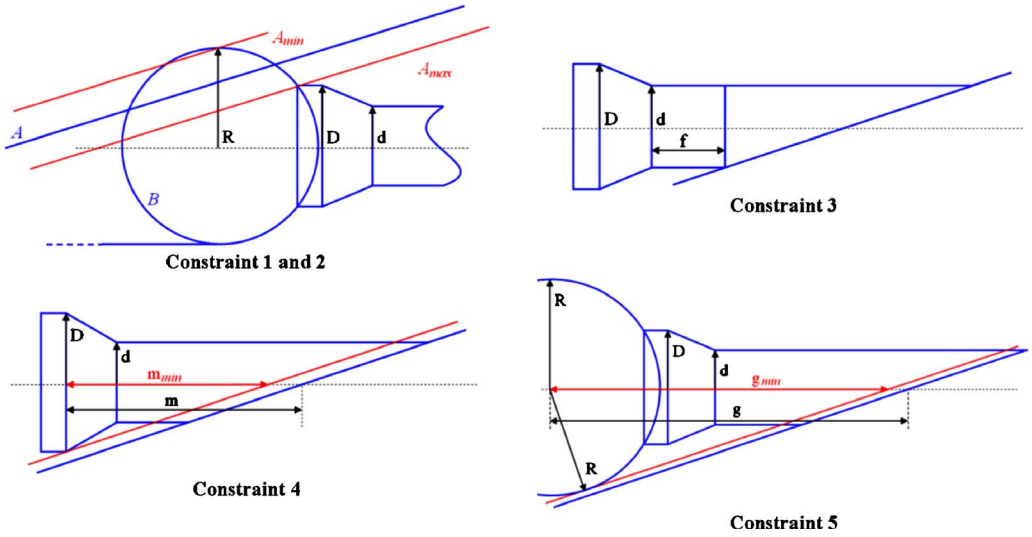

Fig. 2 Geometric constraints

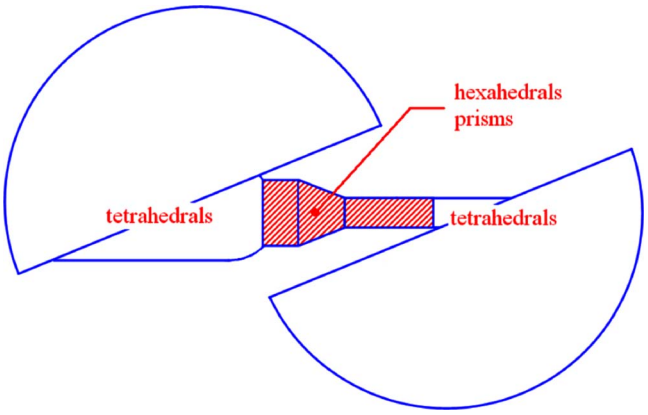

Fig. 3 CFD domain and meshing strategy

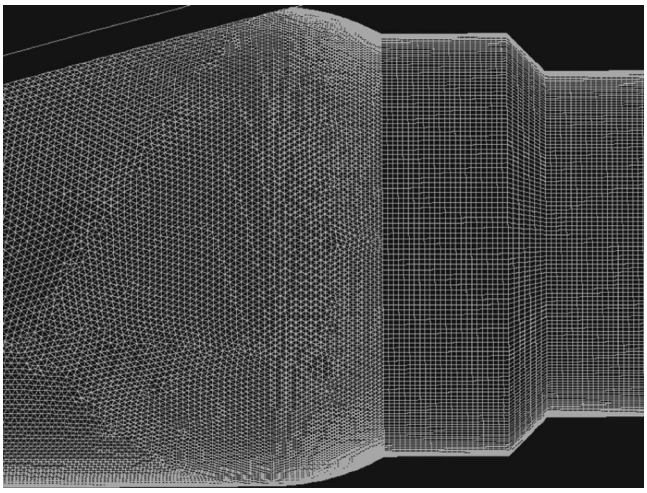

Fig. 4 View of mesh for base line geometry

3 Meshing Strategy

Generation of the mesh and its automation is considered the most delicate task in the present work. As in every CFD simulation, mesh quality largely determines the quality of the results obtained.

Figure 3 shows a section of the computational domain used. This includes the nozzle and two hemispherical volumes around the inlet and outlet. The computational effort has been reduced by taking advantage of the symmetrical nature of the domain and boundary conditions. The journal file facility in the commercial mesh generator GAMBIT [7] was used to automate the meshing process. This involved writing a *C* code to generate a journal file when the values of the five independent parameters are input. The file is then fed into GAMBIT which in turn generates the mesh. A sixth optional parameter allows for adjustment of the mesh size.

As suggested by Bret [8], the geometry of the parametric model in the journal file has been defined using basic elements in order to avoid errors in the mesh generation due to numbering ambiguities. The meshing strategy is indicated in Fig. 3. To allow the mesh to fit such a complex geometry, especially where the nozzle intersects the preswirl plate (at a sharp angle of 15 deg), tetrahedral cells have been used in a large portion of the domain. This portion consists of the external hemispheres, the zones where the nozzle intersects the plate and the spherical drilling. The use of tetrahedral cells ensures success in generating the mesh for the whole range of variation of the parameters. Hexahedral cells have been used to mesh the boundary layer in the nozzle core, and prisms have been used away from the boundary layer in this core region.

The size of the mesh is very sensitive to the values of the design parameters. The number of nodes in the mesh ranges from as low as 0.4 million to as many as 2 million nodes. The reason for such a large difference in the mesh size is that the mesh density and its variation within the domain have been defined by imposing the node spacing along the edges of the domain, and not by imposing a fixed number of nodes. In this way it has been possible to keep the mesh smooth, without distorted cells or discontinuities in cell size, but the number of nodes has been highly variable. Figure 4 shows a close-up view of the mesh at the nozzle inlet for the baseline configuration.

Once a mesh has been generated it is fed to the Rolls-Royce developed packages JM52 and JM56 to generate input files for the HYDRA [9] CFD code. JM52 translates the mesh to a HYDRA compatible format, sets up the boundary conditions, and generates the initial flow field. JM56 produces weights for the mesh and generates higher mesh levels for multigridding.

Some limitations of the meshing procedure have been noted. The use of GAMBIT as a parametric mesh generator requires the geometry of the nozzle to remain self-similar. For example, the upstream face of the preswirl plate must always intersect the nozzle through the spherical drilling. Also, the meshing algorithm may fail if some precautions are not taken in the journal file generation process. This is why the type 2 constraints described in Sec. 2 were introduced.

Sometimes the execution of JM56 failed to generate the coarser meshes required for multigrid convergence acceleration, and sometimes the execution of HYDRA failed, even if JM56 did not. This was attributed to high distortion of the coarser grid levels. These issues may be avoided by reducing the number of multigrid levels used, but this imposes a severe limitation in terms of computational effort required to obtain a converged solution.

4 The CFD Model

Nozzle performance was calculated using the HYDRA [9] CFD code on a distributed memory computer cluster. This general aerodynamic code has been used for numerous turbomachinery applications, and for the results presented here applies a density based, preconditioned, time marching algorithm to a finite volume discretization on unstructured meshes. The numerical scheme is second order for smooth flow using characteristic based artificial viscosity. Multigrid acceleration is available, and the code also supports parallel computing.

The $k-\varepsilon$ turbulence model with wall functions has been used, with the meshing parameters set so as to ensure nondimensional near-wall mesh spacing in the range $30<y^+<60$. Conventional no-slip boundary conditions were applied at walls. The curved surfaces of the hemispheres indicated in Fig. 3 were defined as inlet and outlet boundaries. Total pressure and temperature were set to 4.385×10^5 Pa and 300 K at the inlet, and static pressure was set to 3.021×10^5 Pa at the outlet.

For use in the optimization procedure it was important to ensure that CFD results were not significantly mesh dependent and that the solution was computationally efficient. Some preliminary tests were therefore conducted at the base line conditions in order to guide the choice of solution parameters to be used in the optimization calculations.

As mentioned earlier, the mesh specification software accepts one parameter which defines the mesh density. Varying this parameter it has been possible to assess the mesh dependency of the baseline design case. Figure 5 shows the value of the objective function (mass flow weighted average axial velocity at nozzle outlet) plotted against the number of nodes in the mesh. The value of the mesh density parameter for the two largest meshes is, respectively, 0.6 (298,323 nodes) and 0.5 (476,219 nodes). The mass-averaged velocity is respectively 203.18 and 205.59 m/s, the corresponding variation is 1.19%, a reasonable value to ensure

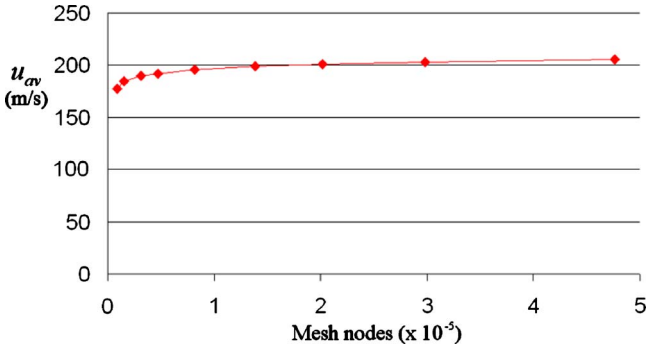

Fig. 5 Mesh dependency for the base line condition

the present work is not unduly mesh dependent. The mesh density parameter for the optimization process has been set at 0.5.

While CFD calculations are sometimes run for a fixed number of iterations, a convergence criterion has been adopted here. The HYDRA runs have been stopped when satisfactory solution residual levels were reached. This criterion should ensure a good quality of the solution for the whole range of the parameters involved. Figure 6 shows the value of the objective function plotted against the residuals level reached by the simulation in base line design conditions. A value of 10^{-12} for the residuals level has been deemed satisfactory and selected for use in the optimization process.

The use of the multigrid technique helps in significantly reducing the computational time required for any single HYDRA run. Figure 7 shows the speed gain for the base line design; the simulation time necessary to reach a value of the residuals of 10^{-10} is plotted against the number of multigrid levels used. The number of multigrid levels was initially set at 4 in the optimization studies. As mentioned above, some problems were encountered for

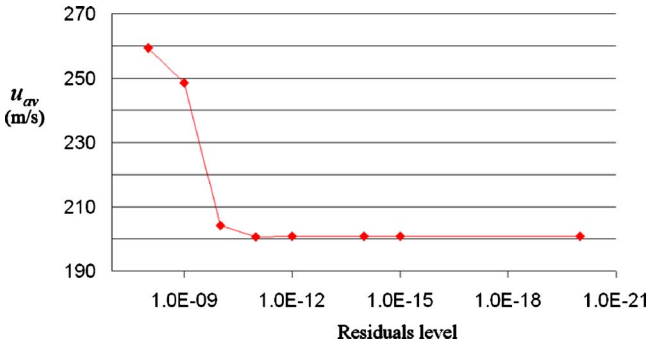

Fig. 6 Influence of convergence criterion

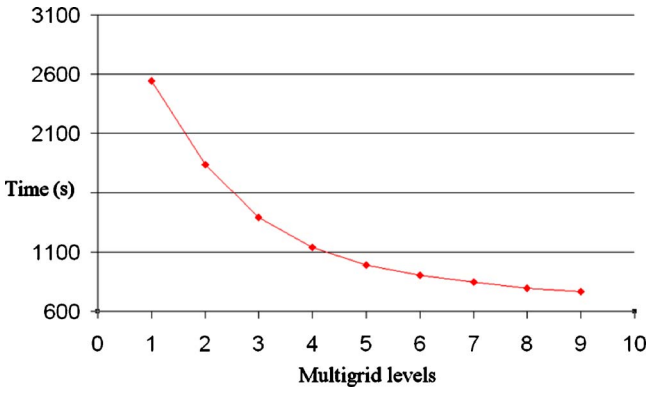

Fig. 7 Influence of the number of multigrid levels on computing time

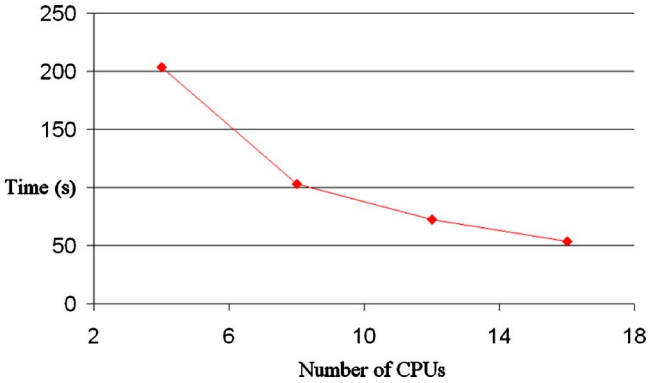

Fig. 8 Influence of the number of processors used on the compute time

other geometries. Nevertheless, these results show that multigrid methods potentially offer large savings.

Figure 8 shows results of tests concerning the parallel efficiency of the CFD code. The computation time has been plotted against the number of CPUs used (each node on the cluster has 2 CPUs). The speed gain from 4 to 8 CPUs is almost ideal, with the computation time almost halved by using double the number of CPUs. Further increasing the number of CPUs, there is still a reduction of the computation time but the gain is lower. For overall efficiency of use of the computational resource, the number of CPUs used for the optimization process was set at 8.

5 Optimization Techniques

The automatic optimization process has been driven by the Rolls-Royce developed software package SOFT [10–12]. SOFT is actually a collection of optimization tools which also allows optimization loops to be setup using external codes to evaluate constraints and objective functions. The present work has basically made use of two different optimization strategies; dynamic hill climbing and response surface model. These are described in the following subsections.

The objective set for the optimization was to maximize the mass flow weighted average axial velocity at the outlet of the nozzle. Here axial is relative to the nozzle's axis (rather than the engine axis).

5.1 Dynamic Hill Climbing. DHC is a direct optimization technique using real CFD computed objective function values at each step of the optimization process. Starting from an initial design SOFT, through an iterative process, can manage the direct optimization by running CFD, evaluating the objective function, and defining an updated design until a satisfying optimum has been reached. The whole process is summarized in Fig. 9. As shown in the top section of this figure, the optimization process is entirely managed by SOFT, which reads the CFD computed objective function and produces a new set of design parameters at each iteration until the optimum condition has been reached.

The simulation step is expanded in the bottom section of Fig. 9. This shows how the constraints described in Sec. 2 were handled. Usually constraints are implemented in an optimization process by penalizing the objective function when violation occurs. In the case considered here, it is not possible to run a CFD simulation if the constraints are violated. Hence, it was not possible to use the constraint handling procedures in SOFT. A secondary execution manager (EXECMANAGER in Fig. 9) was introduced in the optimization loop. This code checked the constraints and decided whether to run CFD or feed SOFT with a dummy poor objective function (190 m/s) to keep the solution away from the constraint violation design space.

The main limitation found using the DHC method was problems in handling unsuccessful CFD runs. The "solution" to this

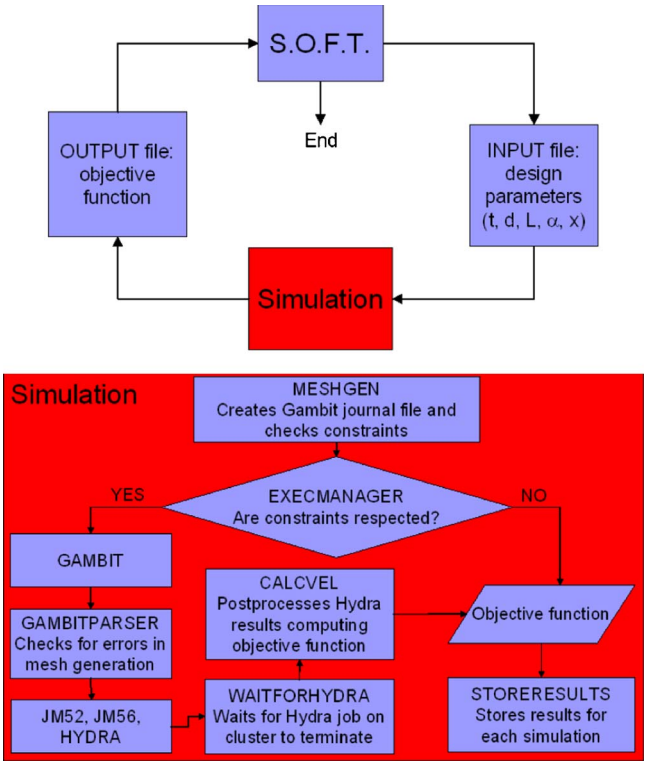

Fig. 9 DHC method

issue was to use the postprocessing code (CALCVEL) to assess whether the CFD run had been correctly completed or not and pass a mildly penalized objective function (200 m/s) back to SOFT in the event of a failure. The danger with this method is that the optimization procedure may be misled.

5.2 Response Surface Model. The RSM method is based on an approximate approach. A model of the design space is built based on a number of experiments, and the search for the optimum is executed on the approximate model. The main steps of this method, as applied here, are summarized below.

- A number of experiments (CFD simulations) are run to determine the objective function and the constraint values for a sample population spread in the design space.
- An approximate RSM-linear radial basis functions (RBF) model is built based on the results of the experiments.
- The optimum of the approximate model is determined using one of the optimization algorithms available in SOFT (DHC, simulated annealing, genetic algorithm, etc.).
- The approximate optimum objective function is checked against the value of the objective function calculated by running CFD at the same conditions. If the check is not satisfactory, the CFD run is added to the population and a new RSM-linear RBF model is built (returning to the previous point). This phase is called update of the model.

The RSM method is illustrated in Fig. 10. The content of the CFD box is similar to the simulation box in Fig. 9. The main difference is in the EXECMANAGER code. A new code was written to handle the RSM optimization. This is capable of reading an input file containing the parameters defining the initial population and executing in sequence all the CFD runs that are required to compile the response matrix. If any of the constraints are violated, no CFD is run and the objective function is set at a dummy value, which is 190 m/s minus the sum of the values of the violated constraints.

The main advantage the RSM method had over the DHC

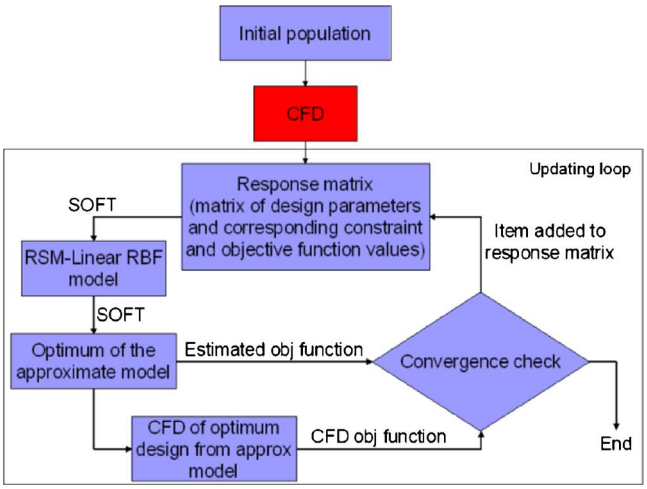

Fig. 10 RSM method

method in this study was its flexibility in handling failed CFD runs. In generating the response matrix some CFD runs failed (due to JM56 failure to generate higher level grids, HYDRA divergence, etc.). Once the first version of the response matrix was generated it was possible, with user intervention, to rerun the failed CFD runs modifying values for the parameters (number of multigrid levels, CFL number, etc.) which triggered the CFD failure. In this way all the CFD results were genuine and the optimizer was not misled. Another inherent advantage of RSM is that the response matrix can be generated by running in parallel on a given cluster, hence, this is an efficient way of obtaining a solution.

6 Results

6.1 Dynamic Hill Climbing Method Performance. Figure 11 shows a typical SOFT execution history. The dummy values fed to SOFT when one of the constraints is violated (190 m/s) and when the CFD simulation has failed (200 m/s) are apparent. The CFD failures were linked with the large variability of the geometry and use of multigrid acceleration. Most failures would not have occurred if only 1 grid and a low CFL number ($\leqslant$0.5) were used. However, these two parameters were critical in determining the computational time required, and they could not be chosen to be too "conservative."

A first DHC optimization was run starting from the base line design. The optimization process took about 10 days to converge on 8 nodes of the cluster. The optimum solution determined is

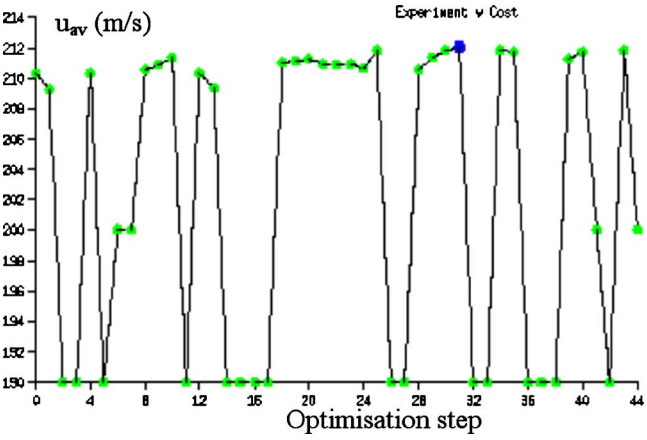

Fig. 11 Execution history of the DHC method

Table 2 Results from the DHC method

	Base line design	First DHC optimum	RSM optimum/ Second DHC optimum
t (mm)	13	11	11
d (mm)	7.2	6.7	6.7
l (mm)	0.8	1.43	7.9
α (deg)	45	46.12	10.63
x (mm)	23	24.38	21
Objective function u_{av} (m/s)	208.21	213.64	217.68
C_d	0.794	0.817	0.830
η	0.844	0.866	0.882
Deflection angle (deg)	3.77	3.65	2.91

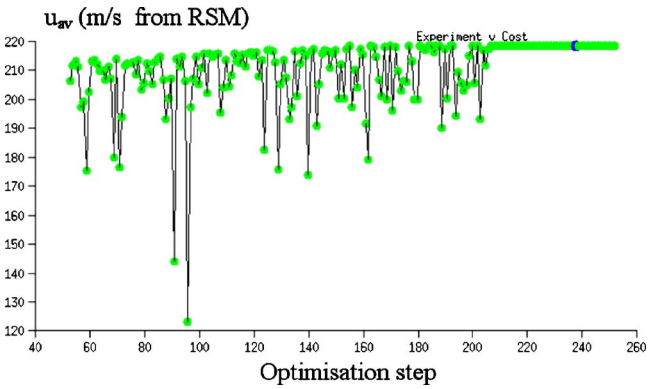

Fig. 12 Execution history of the RMS method

presented in Table 2. Theoretical considerations and experimental data (see, for example, Ref. [13]) suggest that the performance of a nozzle improves if it is converging. In the present work this suggests that the optimum chamfer length will be close to its upper limit. However, the predicted optimum geometry had a relatively small chamfer length.

A second DHC optimization was run starting from a converging nozzle design. As for the first run, some CFD runs failed, but in this case convergence was achieved after just 3 days. The objective function achieved in this case was significantly higher than in the first run, and the chamfer section was considerably longer than that given by the first run. This experience with the DHC method let to the decision to investigate further with the RSM optimization method.

6.2 Response Surface Model Performance. As previously described and illustrated in Sec. 5.2, the RSM method requires the generation of an initial population of experiments. Since no CFD is run if any of the constraints are violated, the execution of an experiment that violates any of the constraints is very fast. Moreover, the probability that a randomly selected set of parameters from the design space violates at least one of the constraints is very high. Thus it was decided to choose a large initial population in order to have a significant number of CFD results in the initial response matrix. The number of independent parameters is 5. For each parameter three values were considered (range minimum, range maximum and range middle point). The total number of experiments arising from all the possible combinations of such parameters is $3^5=243$.

It took almost 2 weeks to fill the initial response matrix. Only 28 experiments out of 243 required CFD runs. The time required for a single CFD run was highly variable. This was due to the large change in mesh size, which increased significantly with increasing preswirl plate thickness t. Four of the CFD runs failed initially. These were identified once automatic execution of all of the 243 experiments had finished, and then executed manually with fine tuning of the CFD input parameters.

Some minor improvements were made in the mesh generation script, compared to that used in Sec. 6.1. The baseline and two optimum geometries from the DHC calculations were repeated using the new meshing script, and the results were then added to the response matrix.

A further improvement was made in the treatment of constraints. The dummy value used in case of constraint violation for the objective function was 190 m/s minus the sum of the values of the violated constraints. This was introduced to improve the behavior of the optimization algorithms close to the design space boundaries.

Figure 12 shows a typical SOFT execution history for an optimization in the updating loop of Fig. 10. The simulated annealing algorithm was selected to find the optimum of the approximate RSM-linear RBF model based on the response matrix. The updating loop was stopped when the difference between the estimated objective function and the CFD computed objective function was lower than 0.1 m/s. The loop took only three steps to converge. The optimum design determined by the RSM method was almost exactly the same as the second optimum determined by the DHC method.

Considering the results from both the DHC and RSM method, the RSM method is recommended for future use as it was found less prone to corruption due to failed CFD runs. The RSM method also allows exploration of the full design space and use of all compatible pre-existing CFD results. However, it may be noted that the DHC method found the same global solution as the RSM, but with more user intervention.

6.3 Nozzle Geometry and Performance. Geometric and performance parameters for the base line and two optimum geometries given by the DHC and RSM method are summarized in Table 2. The three geometries are also shown in Fig. 13. It is immediately apparent that the second optimum is closer to a convergent nozzle design, and gives the best results for the objective function u_{av}.

Both the optimum designs determined by the DHC method are better than the base line design in terms of the objective function. There is a 2.61% gain in the objective function value between the base line design and the first DHC optimum and a 1.89% gain

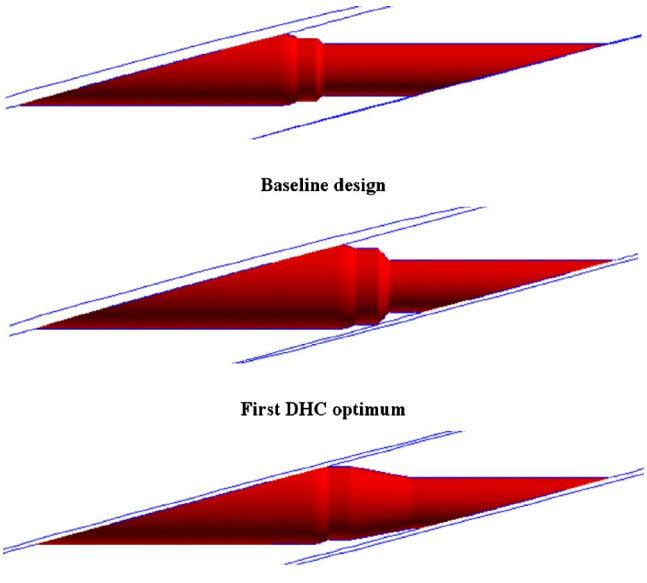

Fig. 13 Nozzle geometries

between the first and the second DHC optimum: so there is a 4.55% overall improvement. Table 1 also shows velocity effectiveness η discharge coefficient C_d, and a deflection angle for each nozzle. η is simply the ratio of u_{av} to the ideal isentropic value, so obviously follows the same trends. Discharge coefficients show a similar improving trend. The jet deflection angle represents the difference between flow angle at nozzle exit and the nozzle axis. It is positive towards the axis of the engine, and hence, the results indicate a further small improvement in performance of the optimized nozzles, pushing the overall improvement in effectiveness to about 5%.

Comparing the base line and first DHC optimum geometries, the preswirl plate thickness is reduced from 13 to 11 mm. This reduces the length of the nozzle and part of the improvement may be attributed to the reduced friction losses along the nozzle walls. There also is an increase in the upstream to downstream section area ratio from 1.23 to 1.49. The optimized downstream diameter is 6.7 mm, which is the minimum allowed. Constraint 4, which prevents intersection of chamfer volume with the downstream face of the plate, is close to be violated.

The second or global optimum has an upstream to downstream section area ratio of 1.49, and the downstream diameter is again 6.7 mm, as for the first DHC optimum. As already noted this geometry is closer to a conventional converging nozzle. Constraints 1 and 3 are close to be violated, and x (21 mm) is at its minimum allowed value. This means that the thickness of the preswirl plate (11 mm) cannot be further reduced without restricting the convergent section of the nozzle. The global optimum thus appears to be a compromise between the improvement given by the reduction of the plate thickness, the improvement given by the use of a converging nozzle, and the applied constraints.

7 Conclusions

Automatic optimization has been successfully applied to a parameterized preswirl nozzle design, including manufacturing constraints. Starting from a base line design from an aeroengine, an improved design was derived, giving a predicted 5% improvement in preswirl effectiveness. The optimized design includes an extended convergent section and reduced plate thickness. Further improvement may be possible if the constraints imposed by manufacturing and the automatic mesh generation technique could be relaxed. Although not confirmed experimentally, the results indicate the benefits of careful nozzle design, and show that optimization methods can be useful in the design process.

In this study it was found that the DHC optimization method was less robust than the RSM method combined with the simulated annealing algorithm. The DHC method was susceptible to disruption by failures of the CFD simulations, and initially got trapped in a local optimum solution. The RSM methodology is more robust and (with user intervention) can easily deal with failures of any kind in the response matrix building process.

Care was taken to ensure that the CFD solutions used in the optimization were fully converged and accurate. This involved use of fine meshes and relatively long computing times. The parametric mesh generation was found to be the greatest challenge in automating the analysis. This is obviously going to be a critical step in any applications where the handling of complex geometries is required. A second issue is the robustness and speed of the CFD solution. For example, it was shown that multigrid acceleration can reduce run times considerably, but its application was limited in the present study as it lead to a greater risk of CFD solutions failing.

Acknowledgment

The authors would like to thank Rolls-Royce plc and the Engineering and Physical Sciences Research Council for funding this work. Technical help from colleagues is also gratefully acknowledged. In particular the authors would like to thank Dr. Jerome Boudet, Dr. Nick Hills, and Dr. Timothy Scanlon, for their contributions.

Nomenclature

- A = refers to plate face position
- B = refers to spherical drilling
- C_p = constant pressure specific heat
- d = downstream nozzle diameter
- D = upstream nozzle diameter
- g = nozzle axial distance from downstream plate face to spherical drilling
- l = chamfer length
- m = nozzle axial distance from downstream plate face to chamfer
- p = pressure
- r = radial coordinate
- R = spherical drilling radius
- SR = swirl ratio
- t = preswirl plate thickness
- T = total temperature
- u_{av} = mass flow weighted axial velocity at nozzle exit
- v_ϕ = air tangential (or swirl) velocity
- x = nozzle axial distance from upstream plate face to chamfer
- y^+ = conventional nondimensional distance to wall
- α = chamfer angle
- Ω = angular velocity

Subscripts

- abs = in absolute frame of reference
- max = maximum value
- min = minimum value
- ref = reference conditions
- rel = in relative frame of reference

References

[1] Meierhofer, B., and Franklin, C. J., 1981, "An Investigation of Preswirled Cooling Airflow to a Turbine Disc by Measuring the Air Temperature in the Rotating Channels," ASME Paper No. 81-GT-132.
[2] Dittman, M., Geis, T., Schramm, V., Kim, S., and Wittig, S., 2001, "Discharge Coefficients of a Pre-Swirl System in Secondary Air Systems," ASME Paper No. 2001-GT-0122.
[3] Geis, T., Dittmann, M., and Dullenkopf, K., 2003, "Cooling Air Temperature Reduction in a Direct Transfer Preswirl System," ASME Paper No. GT2003-38231.
[4] Wilson, M., Pilbrow, R., and Owen, J. M., 1995, "Flow and Heat Transfer in a Pre-Swirl Rotor-Stator System," ASME Paper No. 95-GT-239.
[5] Chew, J. W., Hills, N. J., Khalatov, S., Scanlon, T., and Turner, A. B., 2003, "Measurement and Analysis of Flow in a Pre-Swirled Cooling Air Delivery System," ASME Paper No. GT2003-38084.
[6] Chew, J. W., Ciampoli, F., Hills, N. J., and Scanlon, T., 2005, "Pre-Swirled Cooling Air Delivery Performance," ASME Paper No. GT2005-68323.
[7] Fluent Inc. GAMBIT User's Guide, 2.0.4 ed.
[8] Bret, V., 2004, "Design Optimization of a Turbine Rotor-Stator Cavity Using CFD," TFSUTC/2004/7, 2004.
[9] Rolls-Royce plc, 2004, "The HYDRA User's Guide," version 0.03.
[10] Shahpar, S., 2000, "Smart Optimization for Turbomachinery (SOFT) System: Part 1: Introduction to the GUI (ver 1.01), Library of Optimisers and Test Suite," Dec.
[11] Rolls-Royce/EDS, 2003, "Smart Optimization For Turbomachinery (SOFT) System: GUI User Guide," Oct.
[12] Shapar, S., 2002, "SOFT: A New Design and Optimization Tool For Turbomachinery," *Evolutionary Methods for Design, Optimization and Control*, K. Ginnakoglou, et al. eds., CIMNE, Barcelona.
[13] Grey, R. E., and Wilsted, H. D., 1948, "Performance of Conical Jet Nozzles in Terms of Flow and Velocity Coefficients," NACA Technical Note 1757.

Kinetics of Jet Fuel Combustion Over Extended Conditions: Experimental and Modeling

Philippe Dagaut
C.N.R.S.,
Laboratoire de Combustion et Systèmes Réactifs,
1C, Avenue de la Recherche Scientifique,
45071 Orléans cedex 2, France

The oxidation of kerosene (Jet-A1) has been studied experimentally in a jet-stirred reactor at 1 to 40 atm *and constant residence time, over the high temperature range* 800–1300 K*, and for variable equivalence ratio* $0.5<\varphi<2$*. Concentration profiles of reactants, stable intermediates, and final products have been obtained by probe sampling followed by on-line and off-line GC analyses. The oxidation of kerosene in these conditions was modeled using a detailed kinetic reaction mechanism (209 species and 1673 reactions, most of them reversible). In the kinetic modeling, kerosene was represented by four surrogate model fuels: 100% n-decane, n-decane-n-propylbenzene* (74%/26% mole)*, n-decane-n-propylcyclohexane* (74%/26% mole)*, and n-decane-n-propylbenzene-n-propylcyclohexane* (74%/15%/11% mole)*. The three-component model fuel was the most appropriate for simulating the JSR experiments. It was also successfully used to simulate the structure of a fuel-rich premixed kerosene-oxygen-nitrogen flame and ignition delays taken from the literature.* [DOI: 10.1115/1.2364196]

1 Introduction

Kerosene (Jet A, Jet A1, JP-8, TR0) is a complex mixture of alkanes (50–65% vol.), mono- and poly-aromatics (10–20% vol.) and cycloalkanes or naphtenes (mono- and polycyclic, 20–30% vol.) widely used in aircraft engines [1]. The average chemical formula for kerosene (Jet A, Jet A-1, TR0, JP-8) differs from one source to another: $C_{12}H_{23}$ for Gracia-Salcedo et al. [2], $C_{11}H_{21}$ for Edwards and Maurice [3], $C_{11.6}H_{22}$ for Martel [4], $C_{11}H_{22}$ for Guéret [5], and $C_{11}H_{23}$ for Nguyen and Ying [6]. In this study, the adopted formula was $C_{11}H_{22}$. A better knowledge of its kinetic of combustion is of interest for (i) modeling its combustion in aviation turbine engines and (ii) for safety reasons. Actually, the first issue must be addressed through high-pressure studies whereas the second one that covers pool fires can be addressed via atmospheric pressure studies. The compounds identified in kerosene at the highest levels of concentration are *n*-alkanes. Due to the complexity of the composition of this fuel, it is necessary to use a surrogate model fuel for simulating its oxidation. Under high-pressure jet-stirred reactor (JSR) conditions, the detailed kinetic modeling of kerosene oxidation was initially performed using *n*-decane as a model fuel [7], since *n*-decane and kerosene showed very similar oxidation rates under JSR [7–9] and premixed flame conditions [10]. It was clearly shown in a previous work [7] that *n*-decane is an acceptable model fuel for kerosene oxidation under high pressure, if modeling the formation of aromatics is not a major issue since the oxidation of *n*-decane yields much less aromatics that kerosene. Therefore, more complex model fuels are necessary to model the formation of aromatics from the oxidation of kerosene [11–14]. Surrogate model fuels consisting of *n*-decane and mixtures of *n*-decane with simple aromatic hydrocarbons and cycloalkanes are tested here, mainly under JSR conditions. The detailed kinetic reaction mechanisms for the pure components of the surrogate model fuel had first to be validated before merging the subschemes to yield a kerosene kinetic reaction mechanism [15,16]. In this paper, we present new experimental results obtained for the oxidation of kerosene in a JSR at 1 atm, over a wide range of equivalence ratios (0.5 to 2), and temperatures in the range 900–1300 K. The oxidation of *n*-decane in a premixed flame is modeled, validating the kinetic scheme prior to modeling kerosene oxidation under JSR, shock-tube, and premixed flame conditions, using *n*-decane based model fuels.

2 Experimental Setup

The JSR experimental setup used here is that used earlier [7–9,15,16]. The reactor consisted of a small sphere of 4 cm diameter (30.5 cm^3) made of fused silica (to minimize wall catalytic reactions), equipped with four nozzles of 1 mm i.d. for the admission of the gases that are achieving the stirring. A nitrogen flow of 100 L/h was used to dilute the fuel. As before [7–9,15,16], all the gases were preheated before injection in order to minimize temperature gradients inside the JSR. A regulated heating wire of ca. 1.5 kW maintained the temperature of the reactor at the desired working temperature. The reactants were diluted by nitrogen ($<$50 ppm of O_2; $<$1000 ppm of Ar; $<$5 ppm of H_2) and mixed at the entrance of the injectors. High purity oxygen (99.995% pure) was used in these experiments. Kerosene Jet-A1 was sonically degassed before use. A piston pump (Isco 100DM) or a Shimadzu 10AD VP pump were used to deliver the fuel to an atomizer-vaporizer assembly maintained at 200°C. Good thermal homogeneity along the vertical axis of the reactor was observed for each experiment by thermocouple (0.1 mm Pt-Pt/Rh, 10% located inside a thin-wall silica tube) measurements (gradients of ca. 1 K/cm). The reacting mixtures were probe sampled by means of a fused-silica low pressure sonic probe. The samples (ca. 4–6 kPa) were taken at steady temperature and residence time. They were analyzed on-line by means of a GC-MS and off-line after collection and storage in 1 L Pyrex bulbs. High-vapor-pressure species and permanent gases were analyzed off-line whereas low vapor-pressure compounds were analyzed on-line. These experiments were performed at steady state, at a constant mean residence time, the reactants continually flowing in the reactor. The temperature of the gases inside the JSR was varied stepwise. A high degree of dilution was used, reducing temperature gradients in the JSR and heat release (no flame occurred in the JSR).

Gas chromatographs (GC), equipped with capillary columns (Poraplot-U, Molecular Sieve-5A, DB-5ms, DB-624, Plot

Contributed by the International Gas Turbine Institute (IGTI) of ASME for publication in the JOURNAL OF ENGINEERING FOR GAS TURBINES AND POWER. Manuscript received October 1, 2005; final manuscript received February 1, 2006. IGTI Review Chair: R. S. Abhari. Paper presented at the ASME Turbo Expo 2006: Land, Sea and Air (GT2006), Barcelona, Spain, May 8–11, 2006, Paper No. GT2006-90015.

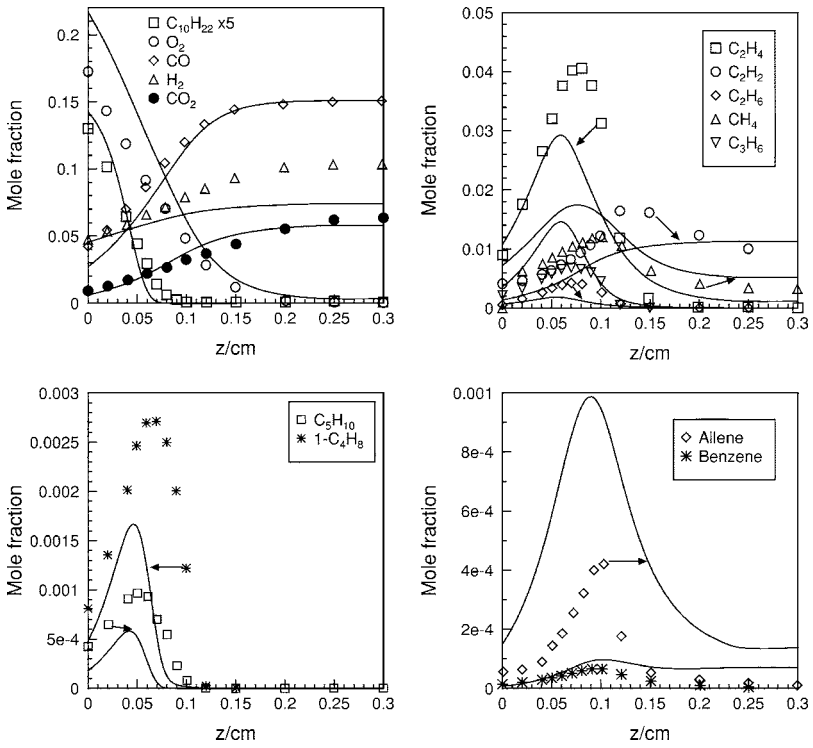

Fig. 1 The oxidation of *n*-decane under premixed flame conditions (1 atm, 0.010 740 33 g/cm^2/s, initial mole fractions were 0.0319 for *n*-decane, 0.285 714 3 for oxygen, 0.682 385 7 for nitrogen). The data of [10] (symbols) are compared to the modeling (lines).

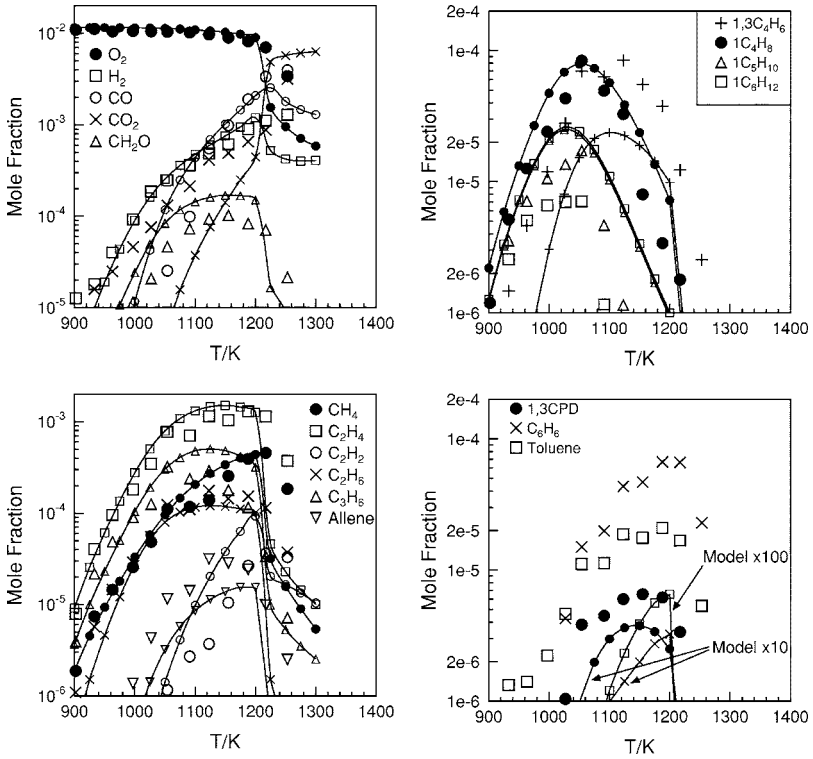

Fig. 2 The oxidation of kerosene in a JSR (700 ppmv of kerosene, 11,550 ppmv of oxygen, nitrogen diluent; 0.07 s, 1 atm). The data (large symbols) are compared to the modeling (lines and small symbols) using *n*-decane as a model fuel (770 ppmv of *n*-decane, 11,550 ppmv of oxygen).

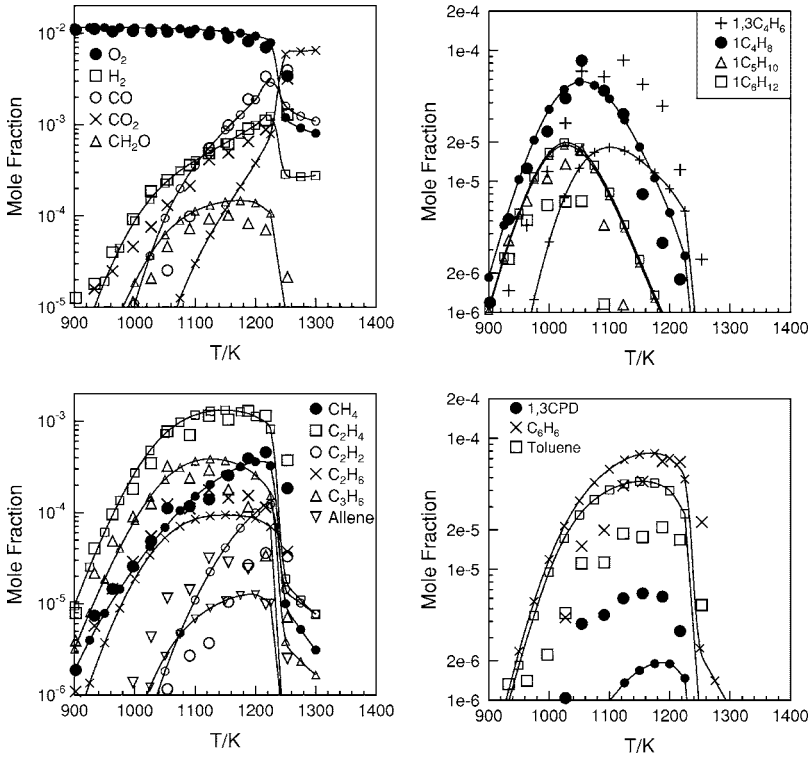

Fig. 3 The oxidation of kerosene in a JSR (700 ppmv of kerosene, 11,550 ppmv of oxygen, nitrogen diluent; 0.07 s, 1 atm). The data (large symbols) are compared to the modeling (lines and small symbols) using *n*-decane/*n*-propylbenzene as a model fuel (585 ppmv of *n*-decane, 206 ppmv of *n*-propyl-benzene, 11,550 ppmv of oxygen).

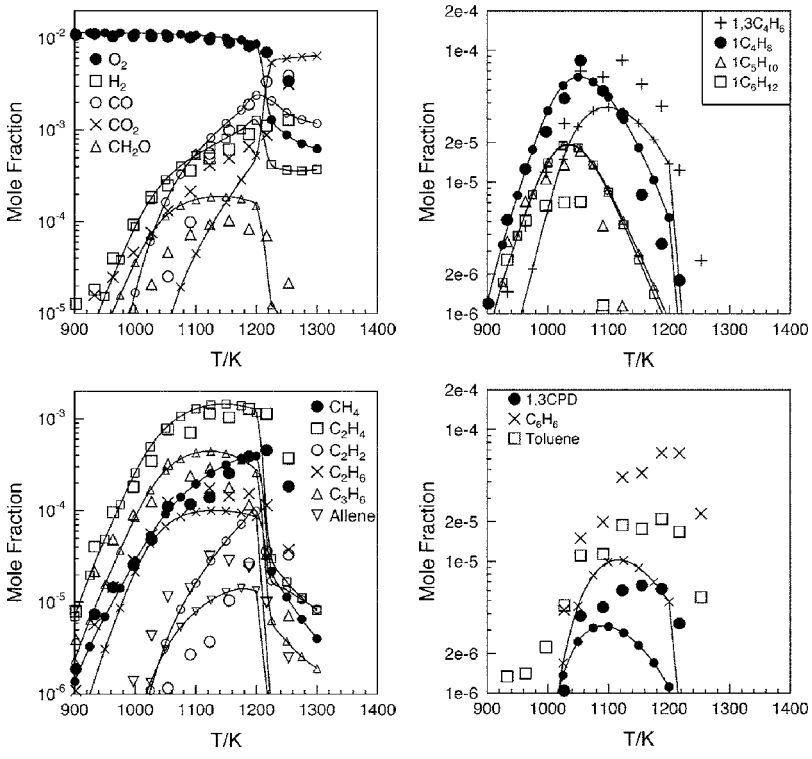

Fig. 4 The oxidation of kerosene in a JSR (700 ppmv of kerosene, 11,550 ppmv of oxygen, nitrogen diluent; 0.07 s, 1 atm). The data (large symbols) are compared to the modeling (lines and small symbols) using *n*-decane/*n*-propylcyclohexane as a model fuel (585 ppmv of *n*-decane, 206 ppmv of *n*-propylcyclohexane, 11,550 ppmv of oxygen).

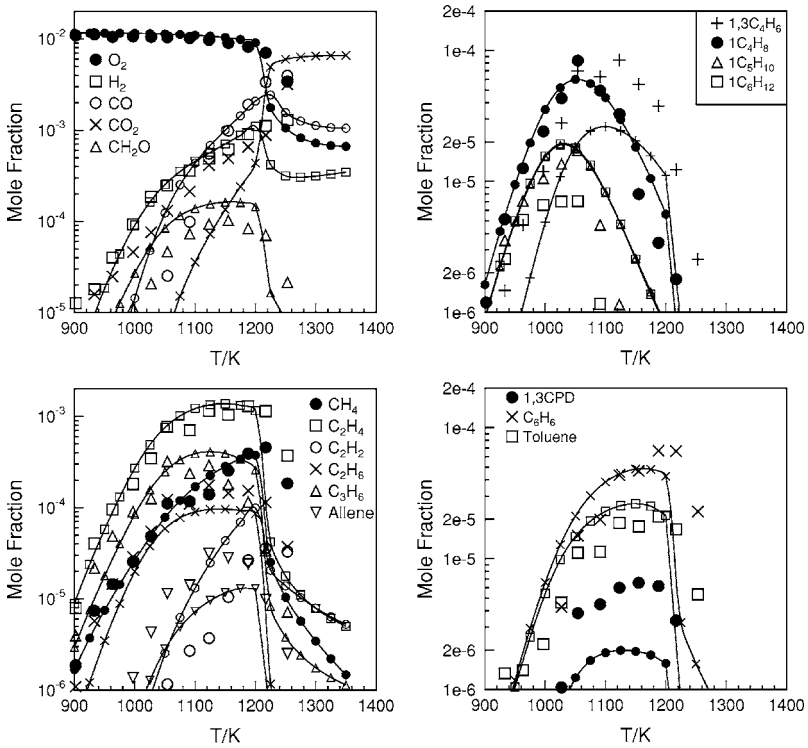

Fig. 5 The oxidation of kerosene in a JSR (700 ppmv of kerosene, 11,550 ppmv of oxygen, nitrogen diluent; 0.07 s, 1 atm). The data (large symbols) are compared to the modeling (lines and small symbols) using *n*-decane/*n*-propylbenzene/*n*-propylcyclohexane as a model fuel (585 ppmv of *n*-decane, 119 ppmv of *n*-propylbenzene, 87 ppmv of *n*-propylcyclohexane, 11,550 ppmv of oxygen).

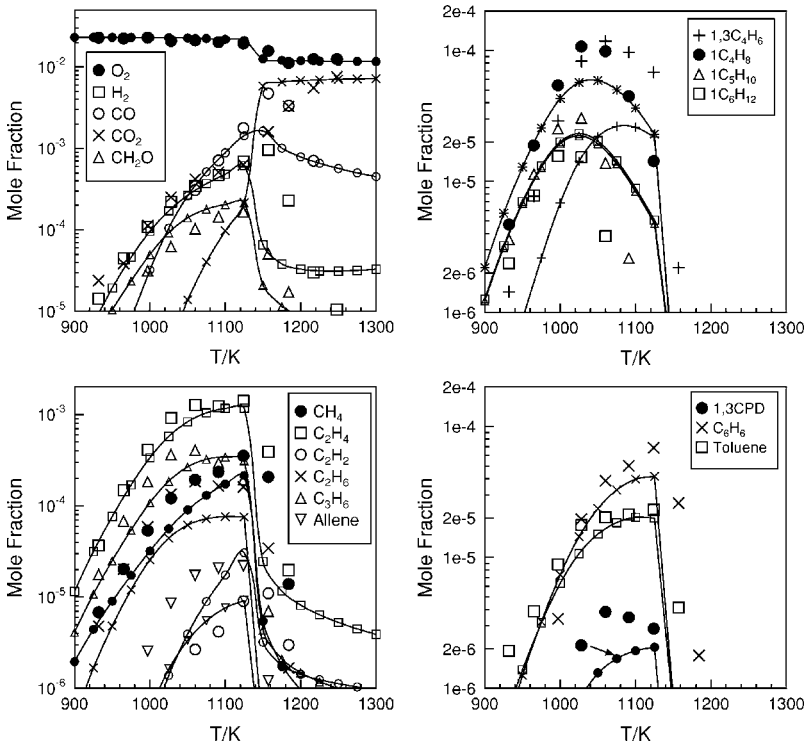

Fig. 6 The oxidation of kerosene in a JSR (700 ppmv of kerosene, 23,100 ppmv of oxygen, nitrogen diluent; 0.07 s, 1 atm). The data (large symbols) are compared to the modeling (lines and small symbols) using *n*-decane/*n*-propylbenzene/*n*-propylcyclohexane as a model fuel (585 ppmv of *n*-decane, 119 ppmv of *n*-propylbenzene, 87 ppmv of *n*-propylcyclohexane, 11,550 ppmv of oxygen).

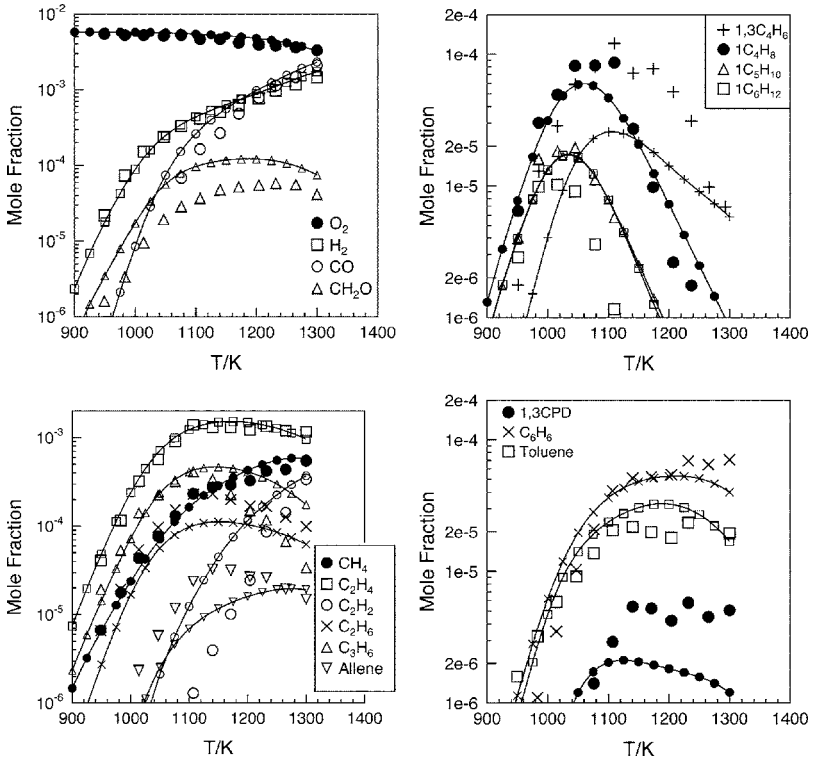

Fig. 7 The oxidation of kerosene in a JSR (700 ppmv of kerosene, 5775 ppmv of oxygen, nitrogen diluent; 0.07 s, 1 atm). The data (large symbols) are compared to the modeling (lines and small symbols) using *n*-decane/*n*-propylbenzene/*n*-propylcyclohexane as a model fuel (585 ppmv of *n*-decane, 119 ppmv of *n*-propylbenzene, 87 ppmv of *n*-propylcyclohexane, 11,550 ppmv of oxygen).

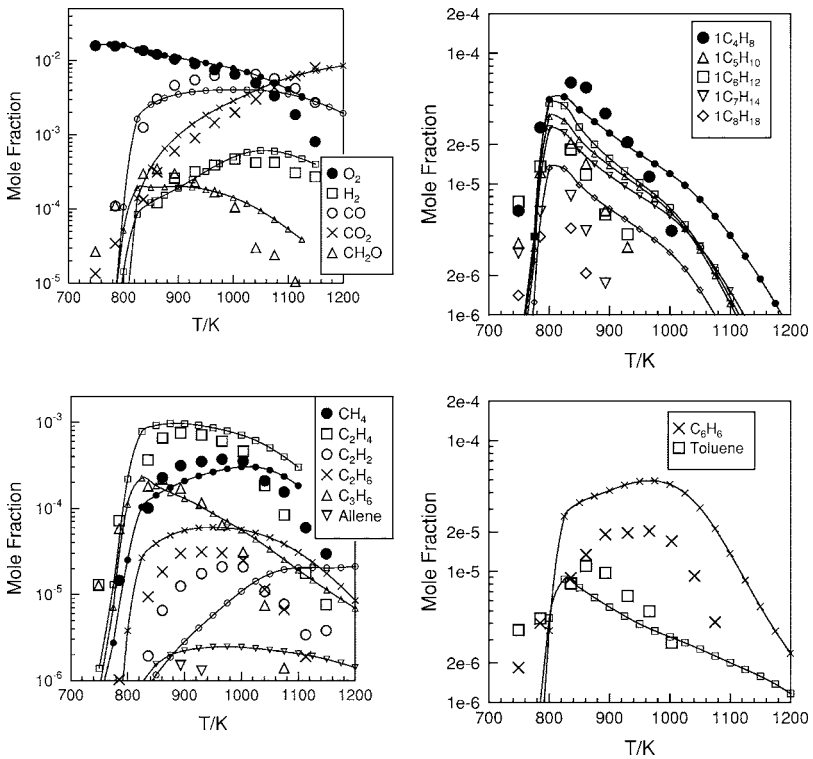

Fig. 8 Oxidation of kerosene in a JSR at 10 atm and t=0.5 s (initial conditions: 1000 ppmv of kerosene TR0, 16,500 ppmv of O_2, diluent nitrogen) [7]. Comparison between experimental results (large symbols) and modeling (small symbols and lines) using *n*-decane/*n*-propylbenzene/*n*-propylcyclohexane as a model fuel (836 ppmv of *n*-decane, 169 ppmv of *n*-propylbenzene, 124 ppmv of *n*-propylcyclohexane, 16,500 ppmv of oxygen).

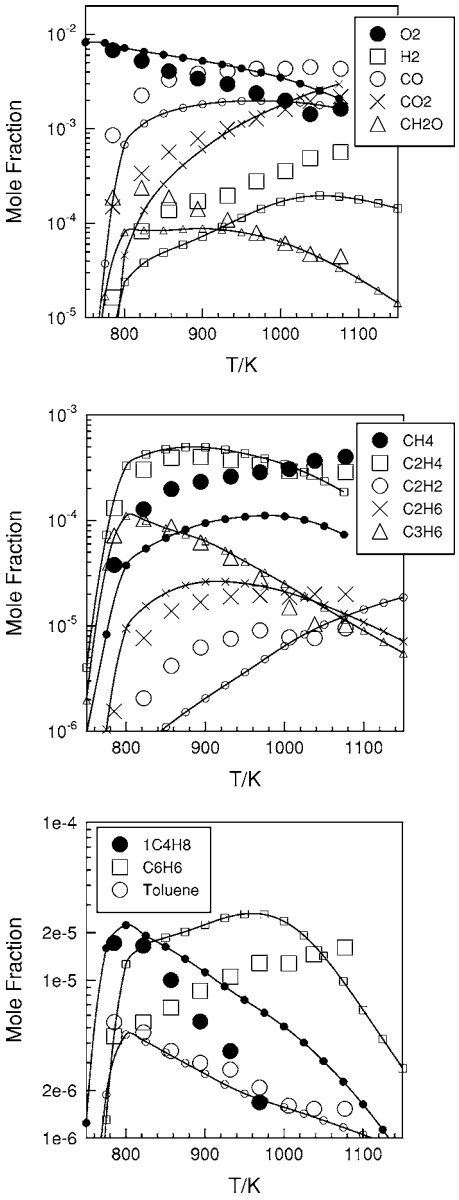

Fig. 9 Oxidation of kerosene in a JSR (500 ppmv of kerosene, 8250 ppmv of oxygen, nitrogen diluent; 1.0 s, 20 atm) [7]. The data (large symbols) are compared to the modeling (lines and small symbols) using *n*-decane/*n*-propylbenzene/*n*-propylcyclohexane as a model fuel (418 ppmv of *n*-decane, 85 ppmv of *n*-propylbenzene, 62 ppmv of *n*-propylcyclohexane, 8250 ppmv of oxygen).

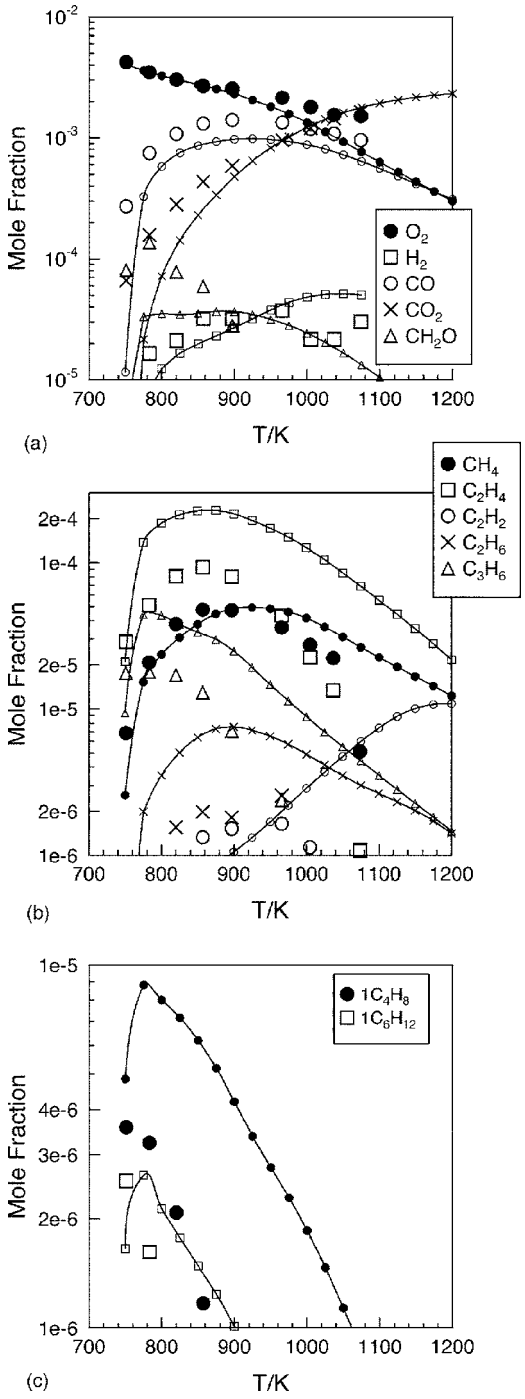

Fig. 10 Oxidation of kerosene in a JSR at 40 atm and *t*=2.0 s (initial conditions: 250 ppmv of kerosene TR0, 4125 ppmv of O_2, diluent nitrogen) [7]. Comparison between experimental results (large symbols) and modeling (small symbols and lines) using *n*-decane/*n*-propylbenzene/*n*-propylcyclohexane as a model fuel (209 ppmv of *n*-decane, 423 ppmv of *n*-propylbenzene, 31 ppmv of *n*-propylcyclohexane, 4128 ppmv of oxygen).

Al_2O_3/KCl, Carboplot-P7), TCD, and FID were used for measuring stable species. Compound identifications were made through GC/MS analyses of the samples. An ion trap detector operating in electron impact ionization mode (GC/MS Varian Saturn 2000) was used. As before [15,16], CH_2O and CO_2 were measured by FID after hydrogenation on a Ni/H_2 catalyst connected to the exit of the GC column. A good repeatability of the measurements and a good carbon balance ($100\pm10\%$) were obtained in this series of experiments.

3 Kinetic Modeling

For simulating the oxidation of *n*-decane and kerosene [10] in premixed flames, we used the Premix computer code [17]. For simulating the ignition delays of kerosene-air mixtures, we used the SENKIN code [18]. For the JSR computations, we used the PSR computer code [19], which computes species concentrations from the balance between the net rate of production of each species by chemical reactions and the difference between the input and output flow rates of species. These rates are computed from the kinetic reaction mechanism and the rate constants of the elementary reactions calculated at the experimental temperature, using the modified Arrhenius equation. The reaction mechanism

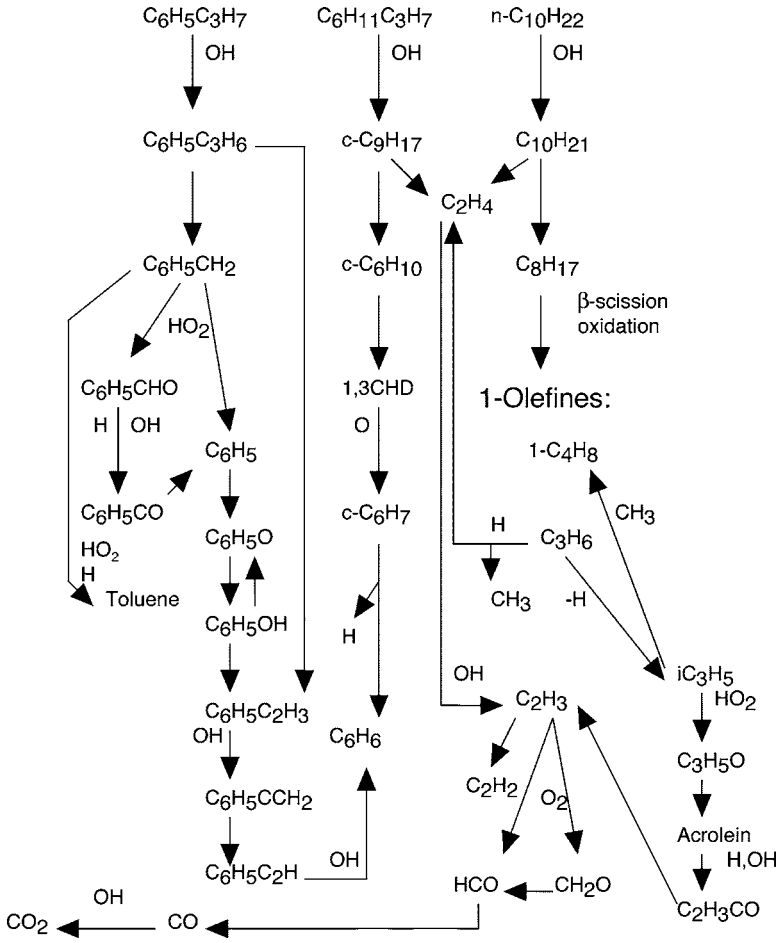

Fig. 11 Reaction paths for kerosene oxidation drawn from the modeling using the selected three-component model fuel

used in this study has a strong hierarchical structure. It is based on the comprehensive commercial fuel oxidation mechanism developed earlier [12], where the rate expressions of pressure-dependent reactions have been updated. The reaction mechanism used here consisted of 209 species and 1673 reversible reactions. This mechanism, including thermochemical data, is available from the author (dagaut@cnrs-orleans.fr). Since most of it has been presented in detail in previous papers [7,15,16], only the reaction of importance here will be described in the text. The rate constants for reverse reactions are computed from the corresponding forward rate constants and the appropriate equilibrium constants, $K_c = k_{\text{forward}}/k_{\text{reverse}}$ calculated using thermochemical data [20–22].

4 Results and Discussion

The kinetic model was tested against the atmospheric pressure *n*-decane premixed flame data of Douté et al. [10] to verify the validity of the proposed kinetic scheme for *n*-decane oxidation in flame conditions. The experimental temperature profile reported by the authors was used in the computations. The results of the comparison between the experimental data and the modeling results are presented in Fig. 1. A good agreement between the data and the modeling was observed, confirming the validity of our kinetic scheme. It is noticeable from Fig. 1 that the computed and experimental mole fraction profiles for *n*-decane, oxygen, CO, CO_2, and benzene are in very good agreement. However, the model tends to underestimate the maximum mole fractions of hydrogen, ethylene, acetylene, and ethane and to overestimate those of methane, propene, and allene (propadiene). Since we were pretty confident in this kinetic scheme, it was included as a subscheme into the kerosene kinetic reaction mechanism used in the other computations.

For the oxidation of kerosene in a JSR, the experimental results consisted of the mole fractions of the reactants, stable intermediates, and final products measured at fixed residence time, as a function of temperature. They are compared to PSR simulations in Figs. 2–7. These results confirm the already reported intermediate formation of simple olefins (mainly ethylene and propene) and methane representing the major intermediate hydrocarbons [7,8,10] formed from the oxidation of kerosene.

To test the effect of the model fuel composition on the computations, we modeled the oxidation of a stoichiometric mixture of kerosene using four different model fuels. These computational results are reported in the following paragraphs.

First, *n*-decane was used as a model fuel. As can be seen from Fig. 2, the modeling of kerosene oxidation in a JSR using this single-component model fuel yields good agreement between the data and the modeling results for most of the species but 1,3-cyclopentadiene (noted 1,3CPD), benzene, and toluene, for which the model strongly underestimates the concentration. These results confirm the already reported similitude between *n*-decane and kerosene kinetics of oxidation [7–10]. They also confirm the inclusion of nonparaffin components in the model fuel is necessary to simulate the formation of aromatics from kerosene oxidation [12].

The second model fuel tested was a *n*-decane/*n*-propylbenzene (74%/26% mole) mixture. As can be seen from Fig. 3, the modeling of kerosene oxidation in a JSR in stoichiometric conditions

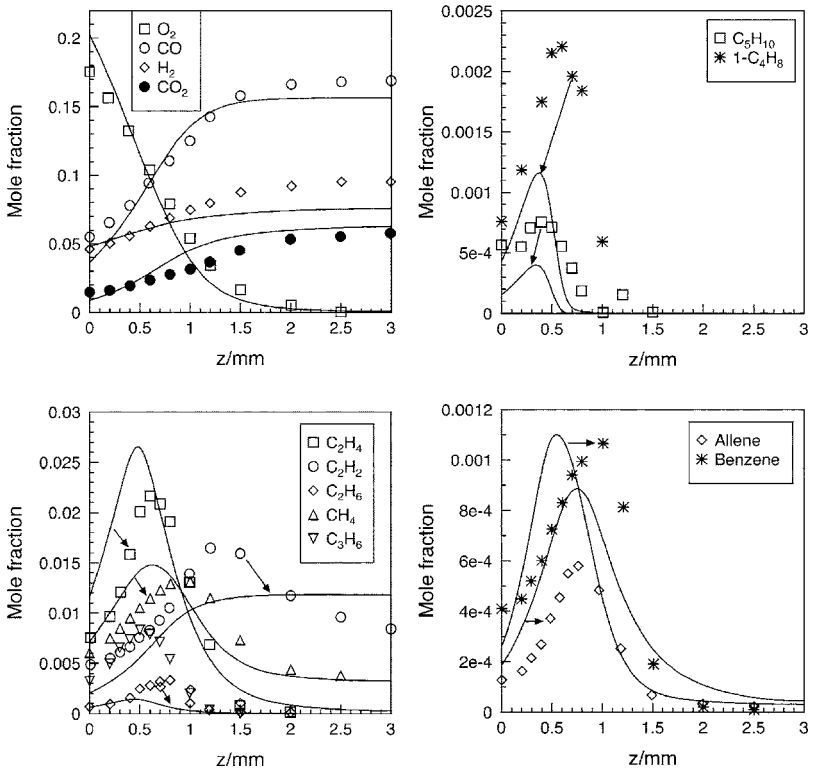

Fig. 12 The oxidation of kerosene under premixed flame conditions (1 atm, 0.010 739 794 g/cm^2/s, initial mole fractions: 0.0319 of kerosene, 0.286 43 of oxygen). The data of [10] (symbols) are compared to the modeling (lines). The initial mole fractions used in the modeling were *n*-decane, 0.024 636 85; *n*-propylbenzene, 0.004 993 912; *n*-propylcyclohexane, 0.003 662 271, oxygen, 0.286 43; nitrogen, 0.680 276 967).

using this model fuel yields good agreement between the data and the modeling for most of the species but 1,3-cyclopentadiene, benzene, and toluene. It is noticeable that the mole fractions of benzene and toluene are overestimated whereas that of 1,3-cyclopentadiene is underestimated. These results confirm the inclusion of cycloalkanes in the kerosene model fuel is necessary [12].

The third model fuel used was an *n*-decane/*n*-propylcyclohexane (74%/26 mole) mixture. As can be seen from Fig. 4, the modeling of kerosene oxidation using this model fuel yields good agreement between the data and the modeling for most of the species but benzene and toluene, which are strongly underestimated. These results were expected based on a study of the oxidation of *n*-propylcyclohexane [15] showing little formation of benzene and toluene.

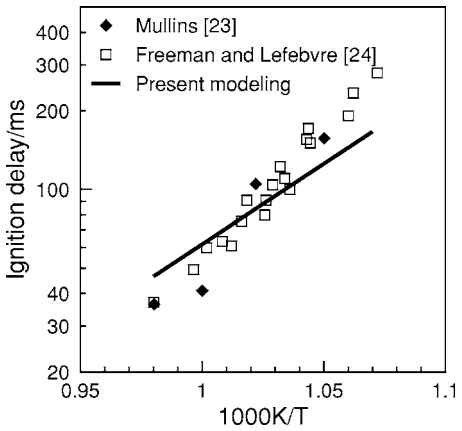

Fig. 13 Ignition delay of kerosene/air mixtures at 1 atm

Finally, a mixture *n*-decane/*n*-propylbenzene/*n*-propylcyclohexane (74%/14%/11% mole) was tested as a model fuel. This mixture was more representative of the composition of kerosene [1,12]. Figure 5 shows that the modeling of kerosene oxidation in a JSR using this model fuel yields good agreement between the data and the computational results for most of the species, including simple aromatics (benzene, toluene). Therefore, this three-component model fuel was selected for modeling the oxidation of kerosene in other experiments [7,10]. Figures 6 and 7 further demonstrate that using this three-component model fuel is convenient for modeling the oxidation of kerosene under JSR conditions at 1 atm.

The proposed model was further tested under high-pressure conditions modeling previous JSR experiments performed at 10, 20, and 40 atm [7]. In these conditions also, the presently proposed kinetic model performed well, as depicted in Figs. 8–10. We noted no major influence of the pressure on the model capabilities. More high pressure data, unavailable at present, would be necessary to further test the present scheme.

We performed a kinetic analysis of the reaction paths during the oxidation of the kerosene model fuel at 10 atm, under stoichiometric conditions (cf. Fig. 8). It indicated that the overall oxidation of the fuel is mostly driven by *n*-decane. According to the model, at 900 K, the early stages of the fuel oxidation involve the oxidation of *n*-decane, *n*-propylbenzene, and *n*-propylcyclohexane (reaction rates of respectively 8.5×10^{-8}, 1.8×10^{-8}, 1.3×10^{-8} mol/cm^3/s at 10 ms and 900 K). Hydroxyl radicals are the main species involved in the oxidation of the fuel mixture. The

oxidation of *n*-decane is responsible for the production of these radicals via a complex reaction scheme that can be summarized as follows:

$$n\text{-}C_{10}H_{22} \Rightarrow 3\text{-}C_{10}H_{21}, 4\text{-}C_{10}H_{21}, \quad \text{and} \quad 5\text{-}C_{10}H_{21}$$

$$n\text{-}C_{10}H_{22} \Rightarrow 1\text{-}C_8H_{17}, 4\text{-}C_8H_{17}, 2\text{-}C_8H_{17}, \quad \text{and} \quad 3\text{-}C_8H_{17}$$

The decyl and octyl radicals isomerize and decompose. Their decomposition yields 1-butyl and 1-propyl radicals that in turn decompose. The further reactions in turn yield OH radicals: $1\text{-}C_4H_9+M \Rightarrow C_2H_5+C_2H_4+M$; $1\text{-}C_3H_7+M \Rightarrow CH_3+C_2H_4+M$; $C_2H_5+O_2 \Rightarrow C_2H_4+HO_2$; $2HO_2 \Rightarrow H_2O_2+O_2$; $H_2O_2+M \Rightarrow OH+OH+M$; $CH_3+HO_2 \Rightarrow OH+CH_3O$. Sensitivity analyses indicated that benzene formation mostly depends on the kinetics of *n*-propylbenzene$+OH \Rightarrow C_6H_5\text{-}C_3H_6+H_2O$, benzyl$+HO_2 \Rightarrow C_6H_5\text{-}CH_2O+OH$, Styrene$+H \Rightarrow C_6H_5+C_2H_4$, $C_6H_6+O \Rightarrow C_6H_5O+H$, and $H+O_2+M \Rightarrow HO_2+M$. A schematic representation of the main reaction paths is given in Fig. 11.

The atmospheric pressure premixed flame of kerosene reported in [10] was also simulated to further test the validity of the proposed kinetic scheme using the selected three-component model fuel. The experimental temperature profile reported by the authors [10] was used in the computations. The results of the comparison between the experimental data and the kinetic computations are presented in Fig. 12. An overall good agreement between the data of [10] and the present modeling was observed, further confirming the validity of our kinetic scheme and the choice of the surrogate three-component model fuel. It is noticeable in Fig. 12 that the computed and experimental mole fraction profiles for oxygen, hydrogen, CO, CO_2, allene, and benzene are in good agreement.

Nevertheless, the proposed kinetic model tends to underestimate the maximum mole fractions of acetylene by 20%, and that of ethane by a factor of 2. Also, the proposed model tends to overestimate the maximum mole fractions of ethylene by 20%, of methane by 10%, and of propene by 30%.

The ignition delays of few kerosene-air mixtures at atmospheric pressure have been reported before [23,24]. They have been used in several previous modeling efforts where reasonable agreement between computations and data was achieved [11,13,14,25]. The present computed results shown in Fig. 13 are in line with these previous modeling results.

5 Conclusion

New experimental results were obtained for the oxidation of kerosene in a JSR at 1 atm. These data were used in conjunction with literature data consisting of (i) high-pressure JSR experiments, (ii) flame structures of *n*-decane and kerosene, and (iii) kerosene-air ignition data to validate a detailed kinetic scheme for kerosene ignition, oxidation, and combustion. Four surrogate kerosene model fuels were tested: (i) *n*-decane, (ii) *n*-decane-*n*-propylbenzene (74%-26% mole), (iii) *n*-decane-*n*-propylcyclohexane (74%-26% mole), and (iv) *n*-decane-*n*-propyl-benzene-*n*-propylcyclohexane (74%–15%–11% mole). Among these four model fuels, the *n*-decane/*n*-propyl-benzene/*n*-propylcyclohexane mixture yielded the best modeling of the JSR experiments. Further validations of the proposed kinetic scheme and surrogate model fuel are still necessary, particularly under high pressure. Such validations require new measurements unavailable at present. The use of more complex model fuels might also improve the agreement with the data as postulated for modeling diesel fuel combustion [26].

Acknowledgment

The author is grateful to Dr. M. Cathonnet for his interest in this work and to Dr. A. El Bakali, Dr. F. Lecomte, and Dr. A. Ristori for their help with the experiments.

Nomenclature

φ	=	equivalence ratio
FID	=	flame ionization detector
GC	=	gas chromatography
GC-MS	=	gas chromatography-mass spectrometry
JSR	=	jet-stirred reactor
TCD	=	thermal conductivity detector

References

[1] Dagaut, P., and Cathonnet, M., 2006, "Experimental and Kinetic Modeling Study of the Oxidation and Combustion of Kerosene," Prog. Energy Combust. Sci., **32**, pp. 48–92.

[2] Gracia-Salcedo, C. M., Brabbs, T. A., and McBride, B. J., 1988, "Experimental Verification of the Thermodynamic Properties of Jet-A Fuel," NASA Tech. Memorandum No. 101475.

[3] Edwards, T., and Maurice, L. Q., 2001, "Surrogate mixtures to Represent Complex Aviation and Rocket Fuels," J. Propul. Power, **17**, pp. 461–466.

[4] Martel, C. R., 1988, "Molecular Weight and Average Composition of JP-4, JP-5, JP-8, and Jet A," AFWAL/POSF Report, July 15.

[5] Guéret, C., 1989, "Elaboration d'un modèle cinétique pour l'oxydation du kérosène et d'hydrocarbures représentatifs," thesis, University of Orléans (in French).

[6] Nguyen, H. L., and Ying, S. J., 1990, "Critical Evaluation of Jet-A Spray Combustion Using Propane Chemical Kinetics in Gas Turbine Combustion Simulated by KIVA-II," Paper No. AIAA-90-2439, 26th Joint Propulsion Conference, July 16–18, Orlando, FL.

[7] Dagaut, P., Reuillon, M., Boettner, J.-C., and Cathonnet, M., 1994, "Kerosene Combustion at Pressures up to 40 atm: Experimental Study and Detailed Chemical Kinetic Modelling," Proc. Combust. Inst., **25**, pp. 919–926.

[8] Dagaut, P., Reuillon, M., Cathonnet, M., and Voisin, D., 1995, "High Pressure Oxidation of Normal Decane and Kerosene in Dilute Conditions From Low to High Temperature," J. Chim. Phys. Phys.-Chim. Biol., **92**, pp. 47–76.

[9] Cathonnet, M., Voisin, D., Etsouli, A., Sferdean, C., Reuillon, M., Boettner, J.-C., and Dagaut, P., 1999, "Kerosene Combustion Modelling Using Detailed and Reduced Chemical Kinetic Mechanisms," Symp. Applied Vehicle Technology Panel on Gas Turbine Engine Combustion, Emissions and Alternative Fuels, Lisbon, Portugal, Oct. 12–16, RTO Meeting Proceedings 14, pp. 1–9.

[10] Douté, C., Delfau, J.-L., Akrich, R., and Vovelle, C., 1995, "Chemical Structure of Atmospheric Pressure Premixed n-decane and Kerosene Flames," Combust. Sci. Technol., **106**, pp. 327–344.

[11] Mawid, M. A., Park, T. W., Sekar, B., and Arana, C., 2002, "Development and Validation of a Detailed JP-8 Fuel Chemistry Mechanism," AIAA Paper No. 2002-3876.

[12] Dagaut, P., 2002, "On the Kinetics of Hydrocarbons Oxidation From Natural Gas to Kerosene and Diesel Fuel," Phys. Chem. Chem. Phys., **4**, pp. 2079–2094.

[13] Mawid, M. A., Park, T. W., Sekar, B., and Arana, C., 2003, "Sensitivity of JP-8 Fuel Combustion and Ignition to Aromatic Components," AIAA Paper No. 2003-4938.

[14] Mawid, M. A., Park, T. W., Sekar, B., and Arana, C., 2004, "Importance of Surrogate JP-8/Jet-A Fuel Composition in Detailed Chemical Kinetics Development," AIAA Paper No. 2004-4207.

[15] Ristori, A., Dagaut, P., El Bakali, A., Cathonnet, M., 2001, "The Oxidation of n-Propylcyclohexane: Experimental Results and Kinetic Modeling," Combust. Sci. Technol., **65**, pp. 197–228.

[16] Dagaut, P., Ristori, A., El Bakali, A., and Cathonnet, M., 2002, "The Oxidation of n-Propylbenzene: Experimental Results and Kinetic Modeling," Fuel, **81**, pp. 173–184.

[17] Kee, R. J., Grcar, J. F., Smooke, M. D., and Miller, J. A., 1985, 'Premix: A Fortran Program for Modeling Steady Laminar One-Dimensional Premixed Flame," Sandia Report No. SAND85-8240, Sandia National Laboratories, Livermore, CA.

[18] Lutz, A. E, Kee, R. J., and Miller, J. A., 1988, "Senkin: A Fortran Program for Predicting Homogeneous Gas Phase Chemical Kinetics with Sensitivity Analysis," Sandia Report No. SAND87-8248, Sandia National Laboratories, Livermore, CA.

[19] Glarborg, P., Kee, R. J., Grcar, J. F., and Miller, J. A, 1986, "PSR: A FORTRAN Program for Modeling Well-Stirred Reactors," Sandia Report No. SAND86-8209, Sandia National Lab, Livermore, CA.

[20] Tan, Y., Dagaut, P., Cathonnet, M., and Boettner, J.-C., 1994, "Acetylene Oxidation in a JSR from 1 to 10 atm and Comprehensive Kinetic Modeling," Combust. Sci. Technol., **102**, pp. 21–55.

[21] Kee, R. J., Rupley, F. M., and Miller, J. A., 1991, "Thermodynamic Data Base," Sandia Report No. SAND87-8215, Sandia National Laboratories, Livermore, CA.

[22] Muller, C., Michel, V., Scacchi, G., and Côme, G.-M., 1995, "THERGAS: A Computer Program for the Evaluation of Thermochemical Data of Molecules and Free Radicals in the Gas Phase," J. Chim. Phys. Phys.-Chim. Biol., **92**, pp. 1154–1178.

[23] Mullins, B. P., 1953, "Studies on the Spontaneous Ignition of Fuels Injected Into a Hot Air Stream. V-Ignition Delay Measurements on Hydrocarbons," Fuel, **32**, pp. 363–379.
[24] Freeman, G., and Lefebvre, A. H., 1984, "Spontaneous Ignition Characteristics of Gaseous Hydrocarbon-Air Mixtures," Combust. Flame, **58**, pp. 153–162.
[25] Montgomery, C. J., Cannon, S. M., Mawid, M. A., and Sekar, B., 2002, "Reduced Chemical Kinetic Mechanisms for JP-8 Combustion," AIAA Paper No. 2002-0336.
[26] Mati, K., Ristori, A., Gaïl, S., Pengloan, G., and Dagaut, P., 2007, "The Oxidation of a Diesel Fuel at 1–10 atm: Experimental Study in a JSR and Detailed Chemical Kinetic Modeling," Proc. Combust. Inst., 31, 10.1016/j.proci.2006.07.073

Lean Blowout Limits and NO_x Emissions of Turbulent, Lean Premixed, Hydrogen-Enriched Methane/Air Flames at High Pressure

P. Griebel[1]
e-mail: peter.griebel@psi.ch

E. Boschek

P. Jansohn

Combustion Research,
Paul Scherrer Institut (PSI),
5232 Villigen PSI,
Switzerland

Flame stability is a crucial issue in low NO_x combustion systems operating at extremely lean conditions. Hydrogen enrichment seems to be a promising option to extend lean blowout limits (LBO) of natural gas combustion. This experimental study addresses flame stability enhancement and NO_x reduction in turbulent, high-pressure, lean premixed methane/air flames in a generic combustor capable of a wide range of operating conditions. Lean blowout limits and NO_x emissions are presented for pressures up to 14 bar, bulk velocities in the range of 32–80 m/s, two different preheating temperatures (673 K, 773 K), and a range of fuel mixtures from pure methane to 20% H_2/80% CH_4 by volume. The influence of turbulence on LBO limits is also discussed. In addition to the investigation of perfectly premixed H_2-enriched flames, LBO and NO_x are also discussed for hydrogen piloting. Experiments have revealed that a mixture of 20% hydrogen and 80% methane, by volume, can typically extend the lean blowout limit by ~10% compared to pure methane. The flame temperature at LBO is ~60 K lower resulting in the reduction of NO_x concentration by ≈35% (0.5→0.3 ppm/15% O_2). [DOI: 10.1115/1.2436568]

Keywords: lean blowout limits, NO_x emissions, hydrogen enrichment, high-pressure, lean premixed flames

Introduction

Currently, lean premixed combustion is the favored method for low-emission power generation from natural gas used in stationary gas turbines. Homogeneous mixing of the fuel and air combined with ultralean operation provide a reduction of flame temperature and are key to its success in minimizing NO_x formation. Increasing environmental concerns will lead to heavier restrictions on NO_x emissions from gas turbines prompting a need to exploit this combustion technique to its maximum potential. One of the major challenges facing designers of such combustion systems is the flame stability at these lean conditions. Since further reduction of NO_x will require even leaner mixtures, schemes for lean stability extension must be considered. Hydrogen doping is a known method of increasing LBO limits of hydrocarbon fuels and shows a great deal of promise for application to lean premixed combustors.

Several experimental results of research combustors operated at atmospheric pressure were reported in literature. Schefer [1] and Schefer et al. [2] injected hydrogen in methane/air flames in a completely premixed mode in a combustor at atmospheric pressure and for swirling flow conditions. Inlet velocities up to 100 m/s were reported. Significant lean blowout extension was observed for addition of up to 20% hydrogen by volume. Reduction of the lean stability limit of 10.4% and 16.6% are given for an inlet velocity of 20 m/s for 10% and 20% hydrogen, respectively. Emissions of CO and NO_x were measured by gas probe measurements and the flame was characterized using both planar laser induced fluorescence of the OH radical (OH-PLIF) and direct luminous photographs. Wicksall et al. [3,4] studied the effect of fuel composition for H_2/CH_4 mixtures on the velocity field in a similar setup to that used by Schefer [1]. The velocity field was characterized using particle image velocimetry (PIV), and the measurements were extended to include both velocity measurement and OH-PLIF simultaneously. Data for only pure CH_4 and a mixture of 60% CH_4 and 40% H_2 by volume are given. It was concluded that the flame and flow structures for CH_4 and H_2-enriched CH_4 flames (in air) are quite distinct. H_2-enriched flames were described as shorter and more robust. It was stressed that the location of flame stabilization was altered with hydrogen. Nguyen and Samuelson [5] conducted experiments in a swirling flow combustor at atmospheric pressure with discrete hydrogen dopant injection in premixed natural gas and air. Incoming air was not preheated and reference velocities were 5 m/s and 7.5 m/s. Ratios of hydrogen to natural gas up to 1.11% in terms of energy output were tested. From these tests, it was concluded that such a hydrogen addition scheme could significantly widen the lean stability limits of the combustor.

Characteristics of hydrogen-enriched flames in model burners (counterflow, jet-stirred reactor) were also reported in literature. Jackson et al. [6] has investigated, numerically and experimentally, the effect of hydrogen on lean premixed methane flames at atmospheric pressure using a highly strained counterflow burner. The fuel/air mixtures were preheated to 300°C and 400°C. Velocity profiles were measured using laser Doppler velocimetry (LDV). Lean extinction was measured for a range of strain rates and concentrations of hydrogen 0%, 5%, 10%, and 20% (defined by fraction of oxygen consumed by H_2). The conclusion was made that the improved lean flammability was mainly attributed

[1]Corresponding Author. Currently at the German Aerospace Center (DLR), Institute of Combustion Technology, Pfaffenwaldring 38-40, 70569 Stuttgart, Germany.

Contributed by the International Gas Turbine Institute (IGTI) of ASME for publication in the JOURNAL OF ENGINEERING FOR GAS TURBINES AND POWER. Manuscript received July 3, 2006; final manuscript received August 15, 2006. Review conducted by Dilip R. Ballal. Paper presented at the ASME Turbo Expo 2006: Land, Sea and Air (GT2006), Barcelona, Spain, May 8–11, 2006. Paper No. GT2006-90490.

to the increase in flame speed, but transport effects by way of Lewis number reduction were also cited. Similarly, Guo et al. [7] has modeled ultralean counterflow flames to investigate the effect of hydrogen on flammability limits and NO_x emission of methane/air flames. It was claimed that, because of enhancement in the rate of the NNH or N_2O intermediate, NO increases for a given equivalence ratio when H_2 is added. However, hydrogen enrichment allows combustors to operate at ultralean conditions, resulting in significant reductions of NO_x emissions. Ren et al. [8] used a single jet-wall stagnation flow burner for experiments and numerical modeling. With this configuration laminar flame speeds were measured for low strain rates as well as the values for the extinction strain rates. Axial velocities were measured using LDV, and stable species concentrations were measured by molecular beam mass spectrometry. NO_x was measured with a chemiluminescence analyzer. Mixtures of up to 8% H_2 in CH_4/air flames at atmospheric pressure were presented. It was shown that by adding up to 8% hydrogen the laminar flame speed increases on the order of 5–10%. Computations predict that this amount of hydrogen reduces the extinction limit by 7%.

Only a few high-pressure studies can be found in literature. Dagaut and Dayma [9] have studied the oxidation of hydrogen-enriched natural gas blends experimentally and numerically. The experiments were performed in a fused silica jet-stirred reactor at elevated pressures (up to 10 bar), different equivalence ratios (0.3, 0.5, 1), and with different mixtures of hydrogen and natural gas. The results showed a significant increase of the reactivity of the natural gas blend when hydrogen is added due to an increase of the OH radical concentration. Halter et al. [10] has characterized the effects of pressure and hydrogen concentration on laminar premixed flames. Measurements were performed in a spherical combustor at pressures between 0.1 MPa and 0.5 MPa, equivalence ratios of $\phi=0.7-1.2$ and hydrogen concentrations up to 20% by volume. Measurements consisted of Schlieren photography of the flame initiated by central ignition in the spherical combustor. He concludes that addition of hydrogen increases the laminar burning velocity, decreases the laminar flame thickness, and reduces the dependence of the laminar burning velocity against flame stretch. Increasing pressure has the effect of decreasing the burning velocity and also the laminar flame thickness for all mixtures. Additionally, Halter et al. [11] has extended the investigations to turbulent, lean premixed flames. Measurements were carried out in a Bunsen-type burner at pressures up to 1 MPa at a constant mean flow velocity of 2.1 m/s and for pure methane as well as mixtures of 10% and 20% hydrogen (by volume in methane) with an equivalence ratio of 1. The main focus of the work was to characterize the flame front geometry, flame surface density, and the instantaneous flame front thermal thickness. Measurements included Mie-scattering tomography and Rayleigh scattering. It was observed that the mean flame height decreases with hydrogen addition. Flame brush thickness also was seen to decrease with hydrogen addition, which was attributed to both the reduction in flame height and the decrease in laminar flame thickness. It was additionally concluded that small-scale flame front wrinkling is enhanced by hydrogen addition. This is based on the observation that there is a slight broadening of the structure size distribution. Finally, the ratio of turbulent flame speed to laminar flame speed, S_T/S_L, was said to increase with hydrogen addition due to the augmentation of flame surface density.

In spite of the quantity of current research activity involving hydrogen enrichment to lean premixed combustion, a deficit exists for experiments at gas turbine relevant conditions. More specifically, there is very little high-pressure data for turbulent, lean premixed flames available. Changes in flame characteristics at elevated pressures (flame position, flame structure, flame speeds, pollutant formation, etc.) necessitate those experiments. The goal of the present research is to experimentally investigate to what extent mixtures of hydrogen in methane, both premixed with air and piloted, can effectively improve flame stability and to quantify the impact on NO_x emissions.

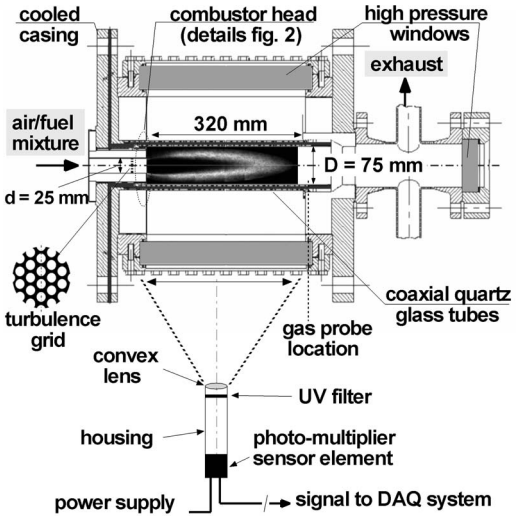

Fig. 1 High-pressure combustor with OH chemiluminescence detector

Use of large amounts of pure hydrogen for application in power generation is not considered feasible at the present time in spite of its favorable combustion characteristics. Its main drawback is a lack of a natural source and supporting infrastructure. The complexity and limitation of modern competitive hydrogen production techniques still make costs prohibitive. However, current interest in hydrogen technologies among the scientific community is driving the development of hydrogen production and distribution techniques as well as devices for onboard fuel reformation of hydrocarbon fuels. Taking these factors into account, an upper limit of 20% hydrogen in fuel mixtures by volume (7% of total thermal power) was set by the authors for experimental consideration. Fuel reformers could be designed to supply mixtures containing such amounts of hydrogen derived from the natural gas used as the main fuel source. However, for a real gas turbine application due to the limited space in the high-pressure section, the reformer should be as small as possible thereby limiting the amount of hydrogen enrichment.

Lean blowout limits and NO_x emissions were measured for premixed methane/hydrogen/air flames with a preheating temperature of 673 K and 773 K. Inlet bulk velocities were varied from 32 m/s to 80 m/s at pressures between 5 bar and 14 bar. Fuel mixtures of 0–20% hydrogen by volume in methane were tested. Additionally, LBO and NO_x were measured also for some hydrogen piloted cases.

Experimental Setup

The experiments were carried out in a generic, high-pressure combustor shown in Fig. 1. The combustor with complete optical access is specifically designed to study turbulent, lean premixed flames (Fig. 1). It is capable of operation up to a pressure of 30 bar, with a maximum airflow rate of 750 m_N^3/hr (0.3 kg/s) and flame temperatures up to 1850 K. The combustion air can be electrically preheated as high as 823 K. The combustor has a maximum thermal power of 400 kW. The cylindrical liner consists of two coaxial quartz glass tubes (inner quartz glass tube diameter $D=75$ mm), which are convectively air cooled. The combustor inlet diameter d is 25 mm. The flame is stabilized by the recirculation of hot flue gases due to the sudden expansion geometry. A hydrogen torch igniter is used to ignite the homogeneously premixed fuel/air mixture. In this study, pure methane/air

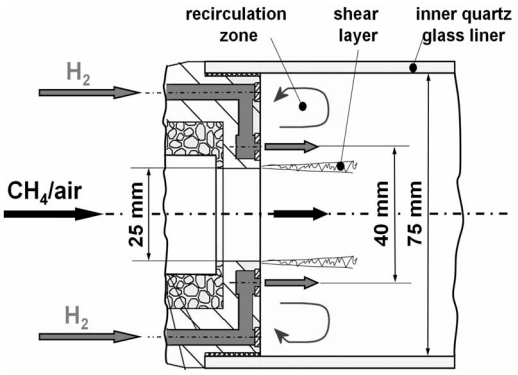

Fig. 2 Hydrogen piloting

mixtures and mixtures with H_2 enrichment up to 20% by volume of the fuel (up to 7% of total thermal power) were investigated in the premixed and piloted mode. In the piloting experiments, hydrogen was injected through 12 holes ($d_{hole}=1$ mm) each located at the radius 20 mm (see Fig.2). The high level of optical access required for nonintrusive laser diagnostics (PIV, PLIF) is provided by three large high-pressure windows.

A water-cooled gas probe located at the exit of the combustor coupled with a conventional exhaust gas analysis system was used to measure the concentration of the major species (CO, CO_2, O_2, NO_x). The NO_x detection limit was 0.1 ppm (1% of full scale). A more detailed description of the setup can be found in [12,13]. Exhaust gas temperatures were measured with a thermocouple (S-type Pt/Pt-Rh) also located at the center of the combustor exit. The measured temperatures reported here are corrected for heat losses due to radiation, convection, and conduction [14]. The corrected temperatures $T_{exhaust}$ are ~60 K higher than the measured values. Taking advantage of the optical access, a sensor was used to record the OH chemiluminescence signal at a rate of up to 1 kHz (see also Fig. 3). Because of the sensor design [15], the resulting signal is proportional to the OH chemiluminescence integrated over a significant extension of the flame.

LBO limits are determined using the combination of the measurement techniques previously mentioned. These measurements are typically carried out, starting from a stable flame at a fixed fuel-to-air ratio and then slowly decreasing the fuel flow rate in steps, keeping the other conditions constant, until LBO occurs. The exhaust gas concentrations, the exhaust gas temperature, and the OH chemiluminescence signal are simultaneously recorded. However, the temporal resolution of the exhaust gas concentration measurements is much smaller (1 Hz) than for the chemiluminescence signal. Additionally, there is a certain time delay in the response of the exhaust gas analysis system to a concentration change because of a high exhaust gas volume in pipes, pump, filters, etc. At each step, a certain period of time is allowed to elapse to verify whether the flame is stable or not (criteria: exhaust gas temperature and species concentrations are steady in time). Then, toward LBO, the flame-sensing signal begins to fluctuate heavily, and large regions of local extinctions are observed (the signal may even reach zero for short periods of time; see Fig. 3). Proximity to lean extinction is made even more evident by a rapid increase in the CO concentration indicating incomplete combustion due to local extinction events. The flame then enters a self exciting mode (fluctuations are getting stronger and stronger) in which its position, shape, and length change rapidly until LBO occurs. When the flame is completely extinguished, the exhaust gas temperature quickly decreases and the OH chemiluminescence signal becomes zero, thus defining the critical equivalence ratio ϕ_{LBO}. An example of the OH chemiluminescence time history of a lean blowout event is shown in Fig. 3. The repeatability of the measured LBO values was observed to be $<3\%$ ($\Delta\Phi \approx 0.01$). This can be attributed to inaccuracies associated with the various components of the measurement and control chain (mass flow controllers for the reactants and coolants, thermocouples, pressure transducers, exhaust gas analyzers, etc.) as well as minor variations in heat loss from the combustor, which has proven quite challenging to perfectly reproduce.

The turbulence intensity u' and the integral length scale L_T in the inlet [16] can be varied by using different turbulence grids (defined by hole diameter d_H and blockage ratio) or by mounting these grids at different axial positions within the combustor inlet section (see Fig. 1). In this study, perforated plates with hexagonally located holes ($d_H=3$ mm) of two different blockage ratios (50% and 65%) and two grid position ($x_g=10$ and $x_g=30$) were used. The nomenclature of the grids is explained in Table 1. x_g is the normalized grid position, which is defined as the axial distance from the grid position to the combustor inlet ($x=0$ mm), divided by the grid hole diameter d_H. The experimental conditions of the studied flames are presented in Table 2.

Results

Lean Blowout Limits and NO_x of Premixed Flames. In Fig. 4, lean stability limits (LBO) are shown for a pressure of 5 bar and a bulk velocity range of 32–80 m/s, with 10% and 20% H_2 enrichment and for two different inlet temperatures (673 K, 773 K). For comparison, LBO results for pure methane are also given. Stable flames are observed in the regime on the right-hand side of each curve, whereas on the left-hand side of each curve lean blowout occurs. For all fuel mixtures, increasing the bulk velocity causes the flames to extinguish at less lean conditions because of an increased flame stretch due to higher velocity gradients between the jet core and the recirculation zone. For a con-

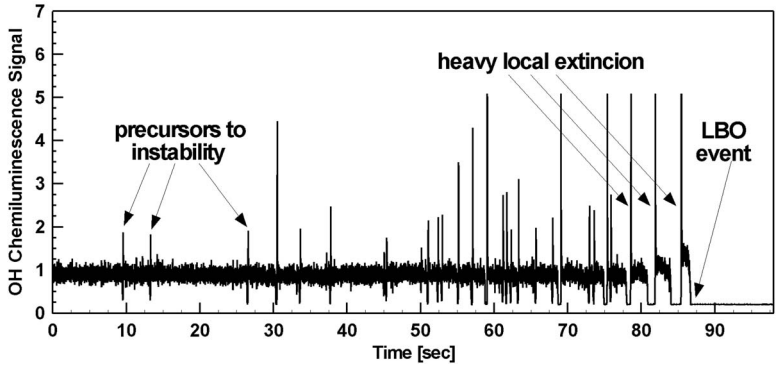

Fig. 3 Time history of the OH chemiluminescence signal during lean blowout

Table 1 Grid nomenclature and turbulent quantities at the inlet.

Grid nomenclature	Hole diameter d_H (mm)	Blockage ratio (%)	Position xg	Relative turbulence intensity at inlet u'/u_{bulk} (%)	Integral length scale at inlet L_T (mm)
g365,xg10	3	65	10	15	2.2
g350,xg30	3	50	30	5	3.1

stant preheating temperature, the slope of each curve is equal for all fuel mixtures. Adding hydrogen enhances the flame stability because of a higher OH radical concentration [9,17], which leads to a higher global reaction rate and a higher flame speed, which finally leads to lower values of the critical equivalence ratio. The laminar flame speed of premixed methane/air flames enriched with 20% H_2 by volume is ~20% higher than for pure methane/air flames [10]. For 20% hydrogen enrichment by volume, the critical equivalence ratio is 9–10% lower in comparison to pure methane. Because of a higher flame temperature for the higher preheating cases (773 K) and, subsequently, higher flame speed, the lean blowout limits are shifted to lower equivalence ratios and the slope is steeper than for the cases with a preheating temperature of 673 K. This indicates a lower sensitivity of the high-temperature flames to flame stretch because of higher flame speeds. Increasing the preheating temperature of 100 K results in a 13–18% decrease of the critical equivalence ratio, depending on the absolute value of the bulk velocity.

The dependency of LBO limits seems to be linear, which will be further elucidated in Fig. 5. This figure shows the LBO limits as a function of the hydrogen content of the fuel for two preheating temperatures (673 K, 773 K), two pressures (5 bar, 14 bar), and a bulk velocity of 40 m/s. As pointed out earlier, the critical equivalence ratio linearly depends on the hydrogen content of the fuel. In consideration of a reproducibility of the measured LBO data ($\Delta\Phi \approx 0.01$), the slope is equal for all curves (at both preheating temperatures and pressures). The high-pressure results document that the extension of the lean stability limits measured at 5 bar are also valid for real gas turbine pressures.

The influence of the turbulence characteristics on LBO limits is discussed with the help of Fig. 6, which shows the results for two different turbulence grids. The characteristic values of the turbulence intensity and the integral length scale are given in Table 1. The detailed velocity field measurements are described in [16]. In the low bulk velocity range (up to ≈50 m/s), almost no difference can be observed between the high- and low-turbulence grid. For higher bulk velocities, the critical equivalence ratios of the low-turbulence grid (g350,xg30) are slightly lower (≈3%) compared to the LBO limits of the g365,xg10 grid. This can be attributed to lower flame stretch effects due to lower turbulence intensities in the jet core associated with the grid g350,xg30. This trend is maintained in the H_2-enriched flames.

The positive impact of the discussed LBO extension on the emission characteristics of lean premixed flames due to H_2 enrichment is presented in Fig. 7, which shows the NO_x and CO emissions together with the measured exhaust gas temperatures for pure methane and 20% H_2 enrichment. The data were measured at 5 bar, 673 K, and 40 m/s. For a better illustration of the correlation of NO_x concentration and temperature, the calculated adiabatic flame temperatures are also presented. Because the differ-

Table 2 Experimental conditions

bulk velocity at inlet u_{bulk} (m/s)	32–80
inlet temperature (K)	673, 773
pressure (bar, absolute)	5–14
equivalence ratio Φ	0.33–0.57
H_2 content of fuel (vol%)	0–20

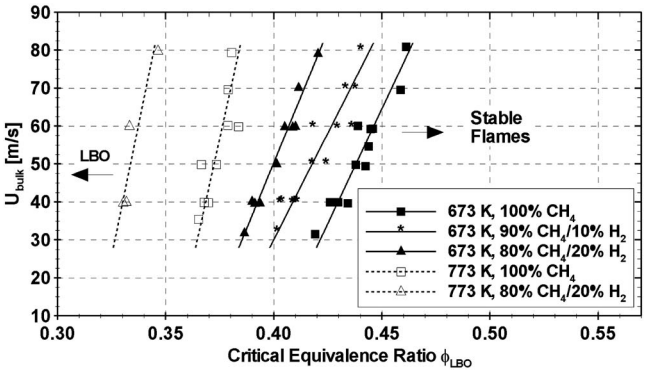

Fig. 4 LBO limits of the velocity variation for two different inlet temperatures (673 K, 773 K) and different CH_4/H_2 mixtures (5 bar, 40 m/s, grid g365,xg10)

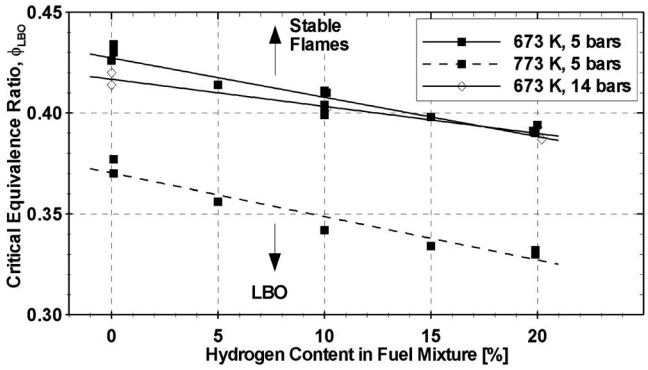

Fig. 5 Effect of H_2 enrichment on LBO limits for two different inlet temperatures (673 K, 773 K) and pressures of 5 bar and 14 bar (40 m/s, grid g365,xg10)

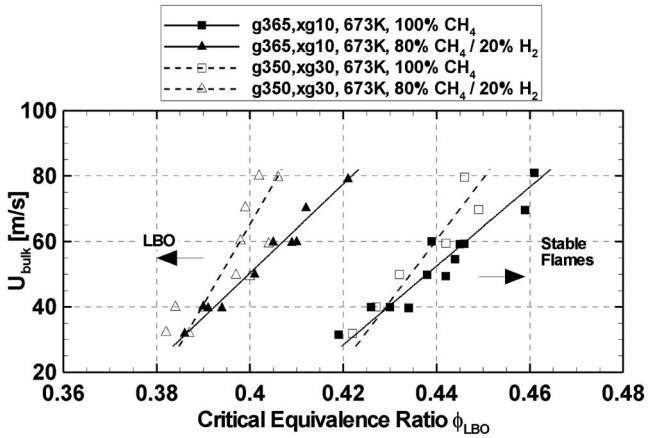

Fig. 6 Effect of turbulence intensity on LBO limits (673 K, 5 bar, grids g365,xg10 and g350,xg30)

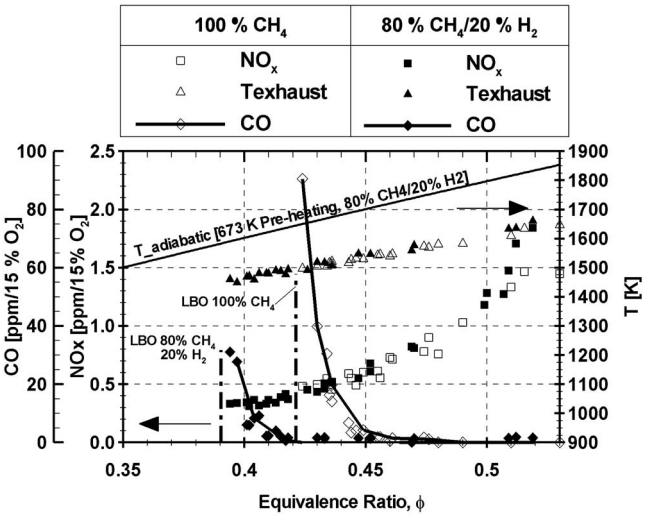

Fig. 7 Effect of LBO extension due to H_2 enrichment on NO_x, CO, and exhaust gas temperature (673 K, 5 bar, 40 m/s, grid g365,xg10)

ence between the adiabatic flame temperatures of pure methane and 20% H_2-enriched methane is very small ($\approx$10 K), only the values for 20% H_2 enrichment are shown. Because of the extension of the LBO limits for hydrogen addition, lower minimum NO_x emissions can be reached because of a lower flame temperature at lower equivalence ratios (Fig. 7). The maximum NO_x reduction is $\sim$35% compared to pure methane flames. For a constant equivalence ratio at very lean conditions ($\Phi < 0.43$), the NO_x concentrations of pure methane and methane/hydrogen flames are almost the same indicating no chemical effect of hydrogen addition on NO_x. This is not true for higher equivalence ratios ($\Phi > 0.50$). In this equivalence ratio range, the NO_x concentration of the methane/hydrogen flames is higher than for pure methane flames. This will be discussed in more detail later with the help of Fig. 8.

Except for extremely lean conditions (close to LBO), the measured CO emissions are always close to zero. Because of the low flame temperature at equivalence ratios close to LBO and a higher probability of local extinction events at these conditions, the CO concentration increases while approaching LBO. For these low temperature conditions, the residence time is not sufficient for complete oxidation of CO. The presented exhaust gas temperatures are approximately 100–150 K below the adiabatic flame

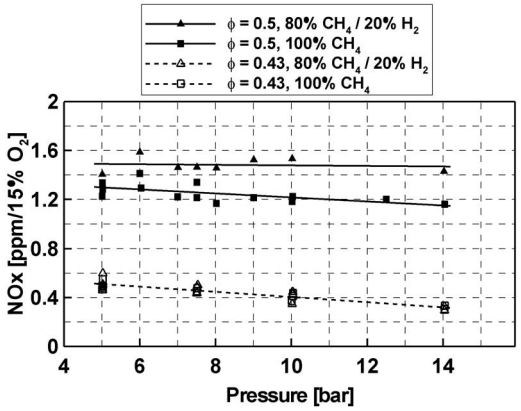

Fig. 8 Pressure influence on NO_x for pure methane and methane/hydrogen flames and two different equivalence ratios (673 K, 40 m/s, grid g365,xg10)

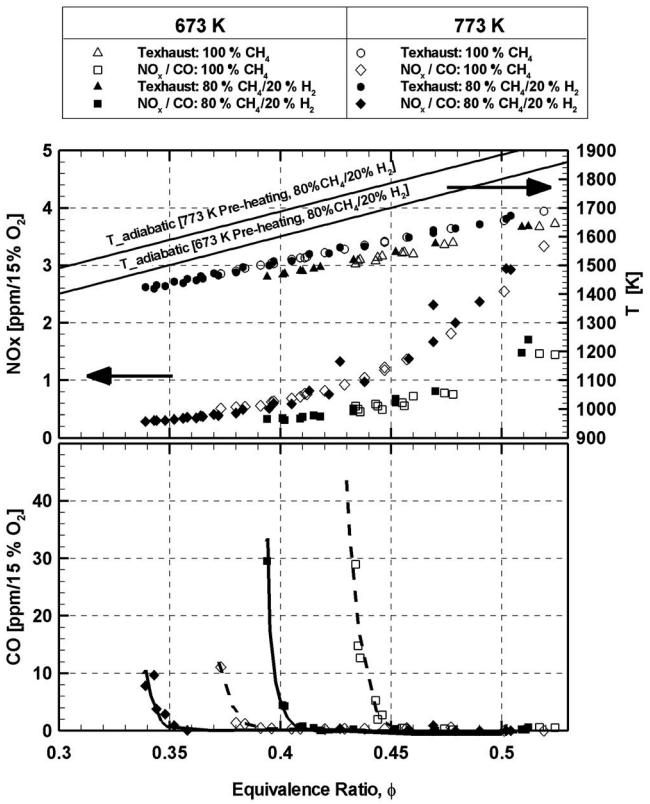

Fig. 9 Influence of preheating on NO_x, CO, and exhaust gas temperature for pure methane and methane/hydrogen flames (5 bar, 40 m/s, grid g365,xg10)

temperatures, which can be attributed to a relative combustor heat loss of $<8\%$ of the thermal power and to the measurement error of the unshielded thermocouple (S-type).

The existence of a chemical effect of H_2 enrichment on NO_x at less lean conditions is more evident in Fig. 8, in which the comparison of the NO_x concentrations for pure methane and methane/hydrogen flames at different pressures (5–14 bar) and two different equivalence ratios (0.5, 0.43), is presented.

At an equivalence ratio of $\Phi = 0.5$, the NO_x concentration is higher when H_2 is added and seems to be independent of pressure. Because of an exhaust gas temperature, which is the same for both mixtures (see Fig. 7), this can only be a chemical effect, e.g., due to a higher OH radical concentration when hydrogen is added [9], which leads to a higher thermal NO_x formation (e.g., $N+OH \rightarrow NO+H$). Another possibility would be the enhanced NO_x formation via the intermediate routes NNH and N_2O according to [7]. For pure methane/air flames at $\Phi = 0.5$, the NO_x concentration does slightly decrease with increasing pressure. This can be attributed to the well-known decrease in the radical pool concentration with increasing pressure, which lowers the thermal NO_x formation rate [18]. For the leaner equivalence ratio ($\Phi = 0.43$), the adiabatic flame temperature is well below the "Zeldovich limit" of 1800 K; therefore, the NO_x formation rate is low. This is probably the reason why a higher OH radical concentration due to H_2 enrichment does not increase the NO_x formation for such lean equivalence ratios. Therefore, the NO_x emissions of the pure methane and methane/hydrogen flames are the same (Fig. 8, $\Phi = 0.43$).

As discussed earlier, increasing the preheating temperature of the fuel/air mixture results in an extension of the LBO limit (Fig. 4). But due to a higher flame temperature, the NO_x emission is significantly increased. This can be seen in Fig. 9, which shows the NO_x concentration, the exhaust gas temperature, and the calculated adiabatic flame temperatures for a preheating temperature

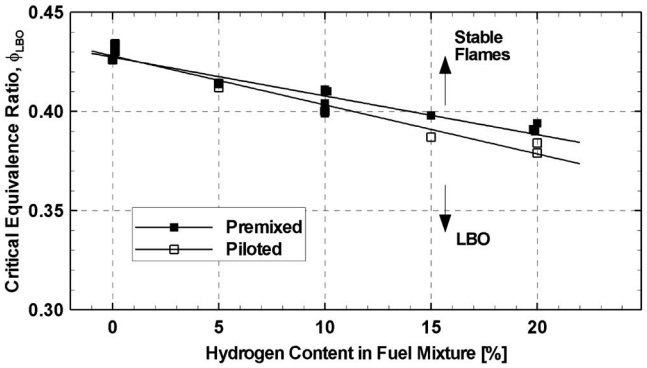

Fig. 10 Comparison of LBO limits for H_2 addition premixed versus piloting (673 K, 5 bar, 40 m/s, grid g365,xg10)

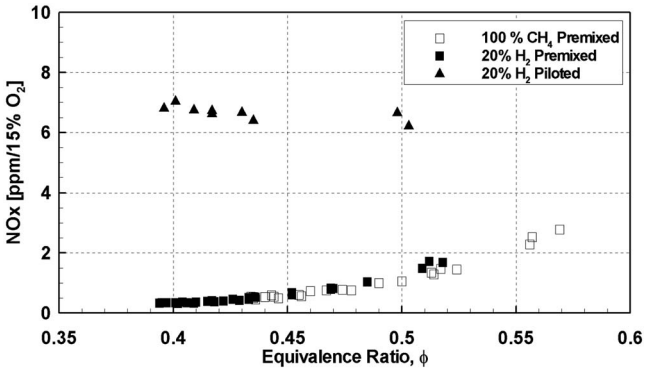

Fig. 11 Typical flame shape of premixing and H_2 piloting (673 K, 5 bar, 40 m/s, Φ=0.5, grid g365,xg10)

of 673 K and 773 K. These measurements were performed at 5 bar and 40 m/s. The strong (exponential) dependency of NO_x on temperature can be clearly seen in Fig. 9.

For a constant fuel mixture (methane or methane/hydrogen), the minimum NO_x concentration is approximately the same for 673 K and 773 K preheating temperature, but they are obtained at different equivalence ratios. Because of the LBO extension due to the higher preheating temperature of 773 K, the minimum NO_x is measured at $\Phi \approx 0.34$ for H_2 enrichment ($\Phi \approx 0.37$ for pure methane), whereas for 673 K the minimum NO_x is measured at $\Phi \approx 0.39$ for 20% H_2 enrichment ($\Phi \approx 0.43$ for pure methane). Because of the higher flame temperature ($\approx +50$ K) because of a higher preheating temperature (773 K), the maximum CO emissions are lower than for the preheating temperature of 673 K.

Lean Blowout Limits and NO_x of H_2-Piloted Flames. All LBO limits and NO_x emissions presented thus far were measured for perfectly premixed fuel air mixtures. In comparison, LBO limits and NO_x emissions for hydrogen piloting are presented in Figs. 10 and 11.

As expected, adding hydrogen via pilot jets instead of a perfectly premixed H_2 enrichment extends the LBO limits more effectively. For 20% hydrogen addition, this extension is ~3% of the LBO limit for premixed H_2 enrichment (Fig. 10). Hydrogen addition via pilot jets form high-temperature zones in a region close to the combustor head because of a less lean mixture in the vicinity of the jets and therefore create high radical concentrations, which improve the flame stability. These highly reactive high-temperature zones close to the combustor head are clearly visible in Fig. 12(*b*) in which the OH chemiluminescence signal for a typical H_2 piloted flame is shown. The OH chemiluminescence signal, which has been scaled to the same maximum in both figures, is known to be a good marker of the heat release zone [19]. The comparison of both cases (piloted and premixed) shows that for the perfectly premixed hydrogen addition a lifted jet flame is formed, whereas for the hydrogen jets an attached flame is visible (Fig. 12). Because the global equivalence ratio is the same in both cases, for the piloted case more fuel (hydrogen) is added in zones where the jets are located. This consequently causes leaner conditions in the region close to the centerline causing the higher overall flame length (dark gray zone) of the piloted flames.

These high-temperature zones with high radical concentration are the reason for the higher NO_x emissions of the piloted flames compared to H_2 premixing. In Fig. 11, the NO_x emissions for both flames are presented. In the equivalence ratio range $0.4 < \Phi < 0.5$, almost no influence of the NO_x concentration of the H_2 piloting flames on the equivalence ratio can be seen and the NO_x levels are an order of magnitude higher than for H_2 premixing. This confirms the dominating role of the high-temperature zones for NO_x formation. In the present study, the hydrogen jets were

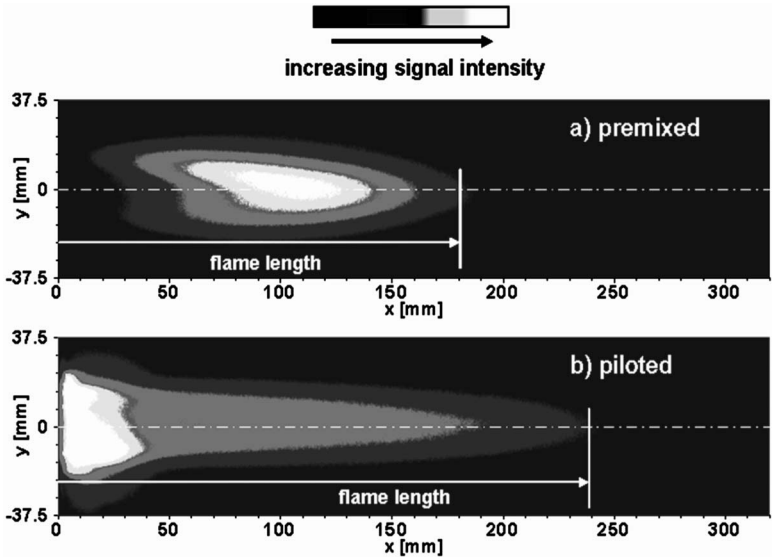

Fig. 12 Comparison of NO_x emissions for H_2 addition premixed versus piloting (OH chemiluminescence, 673 K, 5 bar, 40 m/s, grid g365,xg10)

located to mainly dope the recirculation zone. This is one of the two extreme possibilities (doping the recirculation zone or the shear layer).

It can be concluded that doping the recirculation is not the optimal solution because of high NO_x formation due to high temperatures and long residence times in the recirculation zone. Doping the shear layer seems to be a more promising option to improve the flame stability without increasing the NO_x formation too much. Previous experimental results of CH_4/air flames have shown that the flame stabilizes within the high-turbulent shear layer [13]. Therefore, doping the shear layer with hydrogen would significantly improve the flame stability. However, the consequence of doping the shear layer with H_2 on NO_x formation has to be further investigated in the future.

Conclusions

For a further optimization of the lean premixed combustion technology, hydrogen addition seems to be a promising option to enhance the flame stability and to achieve lower NO_x emissions. This stimulates the experimental investigation of lean blowout (LBO) limits and NO_x emissions for lean premixed methane/hydrogen/air flames in a generic combustor at conditions relevant to modern, low-emission, stationary gas turbines. The experiments were performed for a broad set of parameters including an inlet velocity variation from 32 m/s to 80 m/s, pressures from 5 bar to 14 bar and two preheating temperatures (673 K, 773 K). Fuel mixtures containing between 0% and 20% hydrogen in methane by volume (up to 7% of total thermal power) were investigated in the premixed and piloted mode.

The results showed that premixing of hydrogen can extend the lean stability limit significantly. Because of a higher OH radical concentration, which leads to a higher global reaction rate and a higher flame speed, the equivalence ratios, where LBO is observed, are lower with hydrogen enrichment. This extension of the LBO limit is linearly dependent on the hydrogen content of the fuel. For 20% hydrogen enrichment by volume, the critical equivalence ratio is ~10% lower in comparison to pure methane. For higher bulk velocities, decreasing the turbulence intensity in the combustor inlet results in slightly lower LBO limits compared to LBO limits of the high-turbulence grid. This can be attributed to lower flame stretch effects due to lower turbulence intensities in the jet core. A strong positive impact of the LBO extension on the emission characteristics of lean premixed flames due to H_2 enrichment was found. Because of the extension of the LBO limits for hydrogen addition, lower minimum NO_x emissions can be obtained because of a lower flame temperature at lower equivalence ratios. The maximum NO_x reduction is ~35% compared to pure methane/air flames.

Doping the recirculation zone with hydrogen with hydrogen piloting does not significantly improve the LBO limits. Furthermore, NO_x emissions are significantly higher in this case because of high-temperatures zones with high radical concentration formed in the vicinity of the hydrogen jets.

The presented results show the potential of further lowering the NO_x emissions in lean premixed combustion for stationary gas turbines if a small amount of hydrogen is added. The influences of H_2 enrichment on turbulent flame speeds and flame structure are interesting questions, which will be worked on in the future.

Acknowledgment

The authors gratefully acknowledge financial support of this research by the Swiss Federal Office of Energy (BFE). The authors would also like to thank Daniel Erne for the technical support, Florian Heiniger, and Marius Bloch for their help in the LBO and NO_x measurements, and Rolf Bombach for his help in setting up the OH chemiluminescence technique.

References

[1] Schefer, R. W., 2003, "Hydrogen Enrichment for Improved Lean Flame Stability," Int. J. Hydrogen Energy, **28**(10), pp. 1131–1141.

[2] Schefer, R. W., Wicksall, D. M., and Agrawal, A. K., 2002, "Combustion of Hydrogen-Enriched Methane in a Lean Premixed Swirl-Stabilized Burner," *Proc. of the Combustion Institute*, Pittsburgh, Vol. 29, pp. 843–851.

[3] Wicksall, D. M., Agrawal, A. K., Schefer, R. W., and Keller, J. O., 2003, "Fuel Composition Effects on the Velocity Field in a Lean Premixed Swirl-Stabilized Combustor," ASME Turbo Expo 2003 Power for Land, Sea, and Air, Atlanta.

[4] Wicksall, D. M., Agrawal, A. K., Schefer, R. W., and Keller, J. O., 2005, "The Interaction of Flame and Flow Field in a Lean Premixed Swirl-Stabilized Combustor Operated on H_2/CH_4/Air," *Proc. of the Combustion Institute*, Pittsburgh, Vol. 30, pp. 2875–2883.

[5] Nguyen, O., and Samuelsen, S., 1999, "The Effect of Discrete Pilot Hydrogen Dopant Injection on the Lean Blowout Performance of a Model Gas Turbine Combustor," The International Gas Turbine and Aeroengine Congress and Exhibition, Indianapolis.

[6] Jackson, G. S., Sai, R., Plaia, J. M., Boggs, C. M., and Kiger, K. T., 2003, "Influence of H_2 on the Response of Lean Premixed CH_4 Flames to High Strained Flows," Combust. Flame, **132**, pp. 503–511.

[7] Guo, H. S., Smallwood, G. J., Liu, F. S., Ju, Y. G., and Gülder, O. L., 2005, "The Effect of Hydrogen Addition on Flammability Limit and NO_x Emission in Ultra-Lean Counterflow CH_4/Air Premixed Flames," *Proc. of Combustion Institute*, Pittsburgh, Vol. 30, pp. 303–311.

[8] Ren, J.-Y., Qin, W., Egolfopoulos, F. N., and Tsotsis, T. T., 2001, "Brief Communication: Strain-Rate Effects on Hydrogen-Enhanced Lean Premixed Combustion," Combust. Flame, **124**, pp. 717–720.

[9] Dagaut, P., and Dayma, G., 2005, "Hydrogen-Enriched Natural Gas Blend Oxidation Under High-Pressure Conditions: Experimental and Detailed Chemical Kinetic Modeling," Int. J. Hydrogen Energy, **31**, pp. 506–515.

[10] Halter, F., Chauveau, C., Djeballi-Chaumeix, N., and Gökalp, I., 2005, "Characterization of the Effects of Pressure and Hydrogen Concentration on Laminar Burning Velocities of Methane-Hydrogen-Air Mixtures," *Proc. of Combustion Institute*, Pittsburgh, Vol. 30, pp. 201–208.

[11] Halter, F., Cohé, C., Chauveu, C., and Gökalp, I., 2005, "Characterization of the Effects of Hydrogen Addition in Lean Premixed Methane/Air Turbulent Flames at High Pressure," European Combustion Meeting (ECM2005), Louvain-la-Neuve, Belgium.

[12] Griebel, P., Bombach, R., Inauen, A., Kreutner, W., and Schären, R., 2002, "Structure and NO Emission of Turbulent High-Pressure Lean Premixed Methane/Air Flames," 6th European Conference on Industrial Furnaces and Boilers, Vol. II, INFUB.

[13] Griebel, P., Bombach, R., Inauen, A., Schären, R., Schenker, S., and Siewert, P., 2005, "Flame Characteristics and Turbulent Flame Speeds of Turbulent High-Pressure Premixed Methane/Air Flames," ASME Paper No. GT2005-68565.

[14] Struk, P., Dietrich, D., Valentine, R., and Feier, I., 2003, "Technical Memorandum: Comparisons of Gas-Phase Temperature Measurements in a Flame Using Thin-Filament Pyrometry and Thermocouples," NASA, TM-2003-212096.

[15] Boschek, E., Griebel, P., Erne, D., and Jansohn, P., 2005, "Lean Blowout Limits and NO_x Emissions of Turbulent, Lean Premixed, High Pressure CH4/H2/Air Flames, 8th International Conference on Energy for a Clean Environment - CleanAir 2005, Lisbon.

[16] Griebel, P., Bombach, R., Inauen, A., Kreutner, W., Schären, R., and Siewert, P., 2003, "Flow Field and Structure of Turbulent High-Pressure Premixed Methane/Air Flames," ASME Paper No. GT2003-38398.

[17] Warnatz, J., Maas, U., and Dibble, R. W., 2001, "*Combustion*, 3rd ed., Springer, New York, p. 299.

[18] Corr, R. A., Malte, P. C., and Marinov, N. M., 1991, "Evaluation of NO_x Mechanisms for Lean, Premixed Combustion," ASME Paper No. 91-GT-257.

[19] Lawn, C. J., 2000, "Distributions of Instantaneous Heat Release by the Cross-Correlation of Chemiluminescent Emissions," Combust. Flame, **123**(1-2), pp. 227–240.

Wei Zhang
Department of Mechanical Engineering,
Pohang University of Science and Technology,
San 31, Hyo-Ja Dong,
Pohang, 790-784, Korea

Bu Geun Paik
Maritime & Ocean Engineering Research Institute,
KORDI,
Jang-dong 171, Yuseong-gu,
Daejeon, 305-343, Korea

Young Gil Jang

Sang Joon Lee
e-mail: sjlee@postech.ac.kr

Department of Mechanical Engineering,
Pohang University of Science and Technology,
San 31, Hyo-Ja Dong,
Pohang, 790-784, Korea

Su Eon Lee

Jin Hwan Kim

Turbine/Generator Business Group,
Doosan Heavy Industries &
Construction Co., Ltd.

Particle Image Velocimetry Measurements of the Three-Dimensional Flow in an Exhaust Hood Model of a Low-Pressure Steam Turbine

The three-dimensional flow structure inside an exhaust hood model of a low-pressure steam turbine was investigated using a particle image velocimetry (PIV) velocity field measurement technique. The PIV measurements were carried out in several selected planes under design operation conditions with simulated total pressure distribution and axial velocity profile. The mean flow fields revealed a complicated vortical flow structure and the major sources of energy loss. Vortices with different scales were observed inside the exhaust hood: a strong separation vortex (SV) behind the tip of the guide vane, a longitudinal vortex (LV) at the exhaust hood top, a large-scale passage vortex (PV) evolving throughout the flow path, and an end-wall vortex (EWV) in the region adjacent to the front end-wall. Both the SV and the large-scale PV seemed to consume large amounts of kinetic energy and reduce the pressure recovery ability. The results indicate that the steam guide vane and the bearing cone should be carefully designed so as to control the vortical flow structure inside the exhaust hood. [DOI: 10.1115/1.2431387]

Keywords: exhaust hood, low-pressure steam turbine, PIV

1 Introduction

The exhaust hood of a low-pressure steam turbine transforms the kinetic energy to potential energy and guides the flow from the last stage blade (LSB) to the downstream condenser. Because of the presence of the downward condenser, the flow discharged from the LSB turns 90 deg, from the axial direction to the radial direction, inducing strong circumferential and radial pressure gradients. This phenomenon increases the total pressure loss and reduces the recovery of static pressure. In addition, the increase in static pressure along the flow passage makes the flow more susceptible to separation. A well-designed exhaust hood can diffuse the flow effectively, increasing the static pressure from the LSB to the hood exit (condenser neck flange). This pressure recovery results in lower effective back pressure, and the remaining energy can be used to produce more power. In this manner, the overall efficiency of the exhaust hood is improved [1].

It has been recognized that the complicated flow passage and interaction of various structural components make the flow inside the exhaust hood one of the most challenging problems in fluid dynamics [2]. In particular, accurate information on the velocity distribution through the flow passage is required to estimate the kinetic energy loss and aerodynamic performance of an exhaust hood. Most previous studies on exhaust hoods have been carried out by computational fluid dynamics (CFD) approaches. Tindell et al. [3] numerically simulated the flow in a low-pressure turbine exhaust hood at a typical steam power generation station. They found that approximately 15–20% pressure recovery capability was lost in the exhaust hood and speculated that a strong horseshoe vortex formed at the top of the hood model was the primary source of this loss. They also mentioned that the modified flow guide performed differently under uniform and distorted (simulated turbine discharge) inflow conditions. Liu et al. [4] investigated the flow in an exhaust hood of a typical 300/600 MW steam turbine using a multigrid and multiblock three-dimensional (3D) Navier-Stokes (N-S) solver. For both uniform and distorted inflow conditions, they found that the pressure recovery was acquired mainly by the diffuser, not by the exhaust collector. By numerical simulation of the 3D flow in the same exhaust hood model, Xu et al. [5] found that the main factor reducing the static pressure recovery was a large passage vortex (PV) of high intensity. Sloldov [6], Dejean et al. [7], and Linhart and Hoznedl [8], among others, also used 3D flow simulation to predict the performance of exhaust hoods. The CFD results outlined above have contributed to our understanding of the complex 3D flow structure in exhaust hoods and have provided information to guide the development of advanced steam turbine systems.

In contrast to the plethora of simulation studies, there have been relatively few experimental studies of the flow inside exhaust hoods, primarily due to the difficulties inherent in measuring this complicated type of flow. In addition, most experimental data reported to date were obtained using pointwise measurement techniques and, hence, provide sparse data and very limited flow information [4,9]. Therefore, more accurate and reliable

Submitted to ASME for publication in the JOURNAL OF ENGINEERING FOR GAS TURBINES AND POWER. Manuscript received April 15, 2005; final manuscript received July 30, 2006. Review conducted by Lee Langston.

experimental data on the flow inside an exhaust hood are required to elucidate the detailed flow characteristics and to validate the numerical predictions.

Recently, the particle image velocimetry (PIV) technique has been accepted as a reliable velocity field measurement method in the field of fluid mechanics. This technique is a promising method for exploring the detailed flow structure in an exhaust hood. The main objective of the present study was to investigate the complex flow structure inside an exhaust hood model of a low-pressure steam turbine by means of PIV measurements and to determine the major sources of energy loss. The results can be used to improve the flow passage design and the performance of the exhaust hood, as well as to validate numerical predictions.

2 Experimental Apparatus and Methods

2.1 Exhaust Hood Model. The longitudinal and end wall views of the exhaust hood model tested are shown in Figs. 1(*a*) and 1(*b*), and a photograph of the model is in Fig. 1(*c*). Detailed scales are marked in this figure as well. The geometric scale ratio of the tested model to the prototype was 1/4.088. The entrance of the exhaust hood is defined as the LSB exit plane, and the exit of the exhaust hood is connected to the condenser neck. The bearing cone forms the inner boundary of the annular discharge flow, and the steam guide constitutes the outer boundary. Internal flanges, support struts, and other small protrusions into the flow path were removed or simplified in the exhaust hood model. The bearing cone consists of three frustum cones having various slopes as shown in Fig. 1(*a*). This configuration of the bearing cone is usually adopted for easy manufacture, even though a single streamline cone shows more satisfactory performance. For PIV measurements, most parts of the experimental model were made of transparent acrylic material.

2.2 Experimental Conditions. Before performing the PIV measurements, the total pressure distribution and the axial velocity profile of the prototype turbine were simulated at the exhaust hood entrance by attaching several annular screens with different mesh sizes. Axial velocities at four circumferential locations were measured by crossing the vertical and horizontal center planes with a Pitot tube, to get a representative velocity at an annulus height. The mean value was assumed as the axial velocity at the entrance of the exhaust hood model, as shown in Fig. 2(*a*). Figure 2(*b*) presents the simulated total pressure distribution in the annulus. Here, P is the total pressure, P_{max} (=2000 Pa) is the maximum total pressure. The maximum inflow velocity is 63 m/s, and the corresponding Reynolds number based on the annulus height of 42 mm is about 1.7×10^5. This is greater than the critical Reynolds number above, of which the Re dependence becomes negligible. Therefore, the flow pattern measured in the exhaust hood model is expected to be comparable to that in the prototype. Since the inlet Mach number tested was ~0.2, the air compressibility of the prototype steam turbine could not be simulated in this study. It should be noted that the inflow condition has a significant effect on the flow pattern and performance of an exhaust hood. In this study, the exhaust hood model without rotating blades was tested for its design operating condition [3].

2.3 PIV Measurement. The two-frame cross-correlation PIV method was employed to measure the instantaneous velocity fields. The PIV system used in this study consists of a dual-head Nd:Yag laser, optics, a high-resolution CCD camera, and a delay generator. The Nd:Yag laser produces high-energy (125 mJ) pulses at a wavelength of 532 nm. Olive oil droplets of mean diameter ~3 μm were seeded as tracer particles. The tracer particle injection tube was installed 10 m upstream of the exhaust hood model, so as not to disturb the flow in the test section. A cylindrical lens and a spherical lens were used to form a thin laser light sheet to illuminate the measurement planes. Particle images

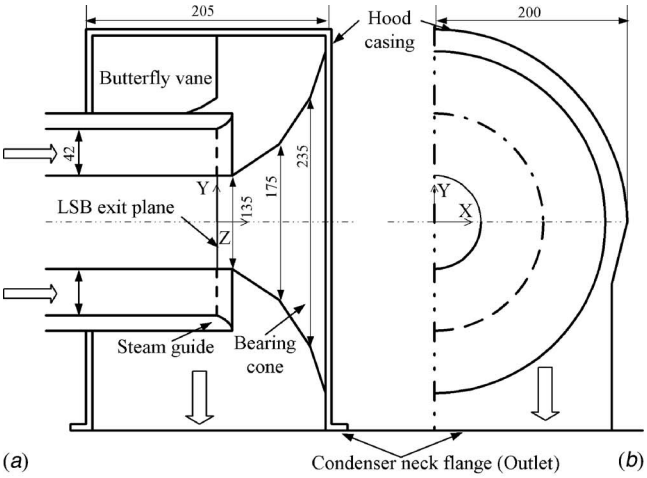

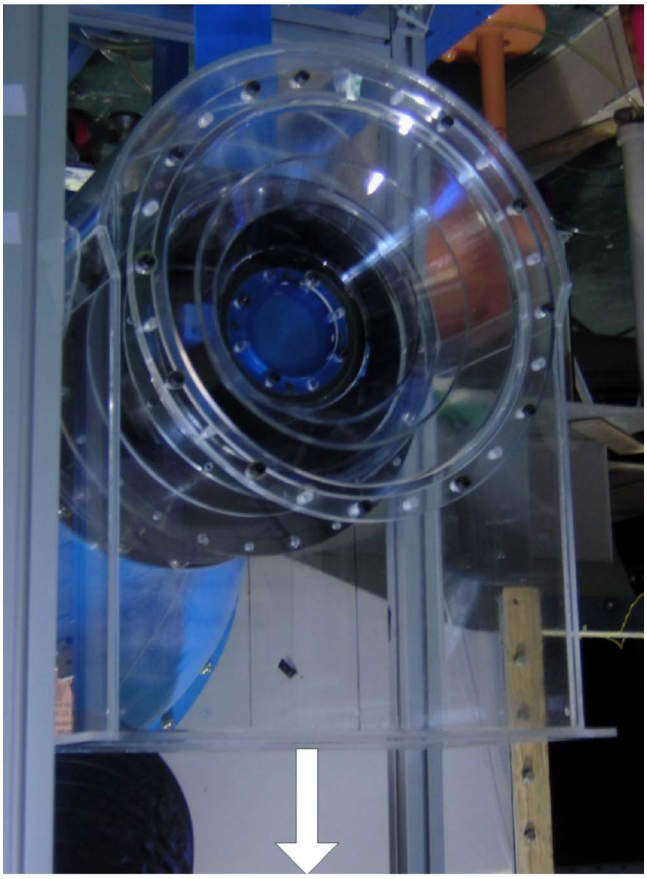

Fig. 1 Schematic diagram and photograph of the exhaust hood model tested (units in mm), (*a*) longitudinal view; (*b*) end wall view, and (*c*) photograph

were captured using a CCD camera of $2k\times2k$ pixel resolution (Kodak ES 4.0). A pulse delay generator was used to synchronize the laser and CCD camera.

Use of a transparent exhaust hood made it possible for the laser light sheet to illuminate the tracer particles in the target cross sections and for clear particle images to be captured. However, to avoid strong light scattering that occurred at the edges and boundary of the exhaust hood model, some parts of the model surfaces were painted black. The thickness of the laser light sheet was carefully adjusted to be 1–2 mm to reduce the scattering of laser light. For PIV measurements in the planes perpendicular to the

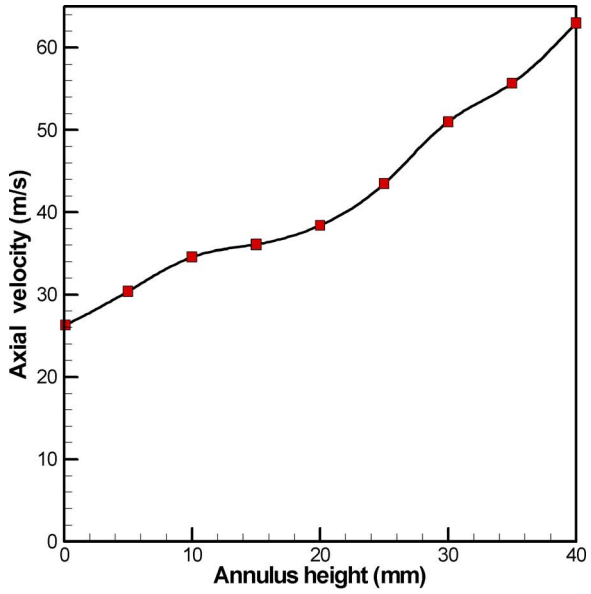

(*a*)

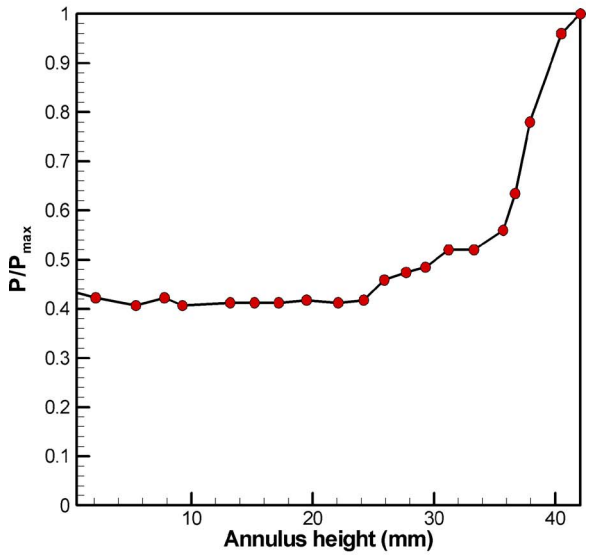

(*b*)

Fig. 2 Simulated experimental conditions in the annulus height at the entrance of the tested exhaust hood model: (*a*) axial velocity profile and (*b*) total pressure distribution (P_{max} =2000 Pa)

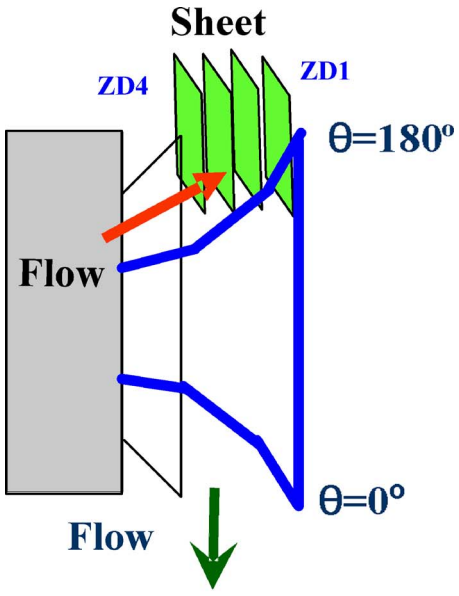

(*a*)

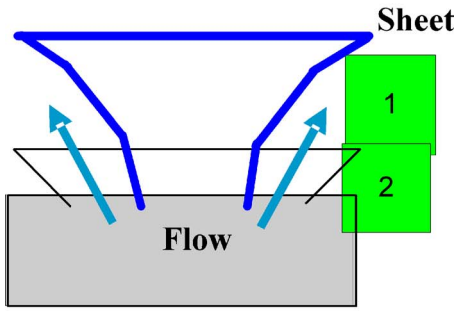

(*b*)

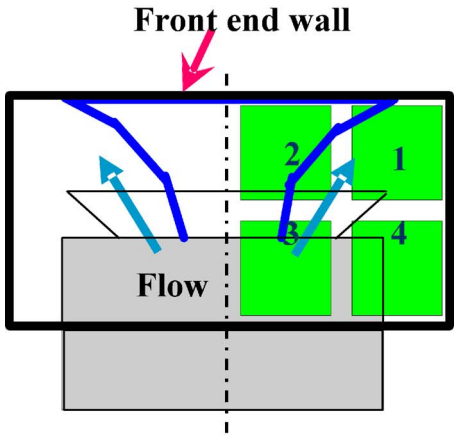

(*c*)

Fig. 3 Selected measurement planes through the flow passage of the exhaust hood model: (*a*) the vertical center plane and ZD1-ZD4 planes, (*b*) the horizontal center plane, and (*c*) the condenser neck flange

dominant flow, this thickness is sufficient to accommodate enough number of particle pairs even with strong out-of-plane motion. An additional factor degrading the image quality was attachment of the olive oil particles on the internal surface of the experimental model. To minimize this problem, the model was cleaned after a certain period of operation time, with particular care being taken to clean the test section to ensure clear particle images.

Taking into account the axisymmetric geometry of the exhaust hood model, measurements were made only in the left half of the model with respect to the vertical center plane (*Y*-*Z* plane indicated in Fig. 1(*a*)). To obtain 3D flow field information, the PIV measurements were carried out at various *X*-*Y* and *X*-*Z* planes along the flow passage. Because the size of the field of view was limited to 60×60 mm or 70×70 mm, it was impossible to simultaneously record the flow information for the entire test plane. Therefore, the entire flow field in a given plane was generated by combining several images. It should be mentioned here that combining several separated images can only be applied under steady flow conditions. For the vertical and horizontal center planes shown in Figs. 3(*a*) and 3(*b*), each was divided into two fields of view (FOVs). For the cross section of the condenser neck flange of about 175 mm×180 mm shown in Fig. 3(*c*), four FOVs were combined to cover the measurement plane. Unfortunately, some

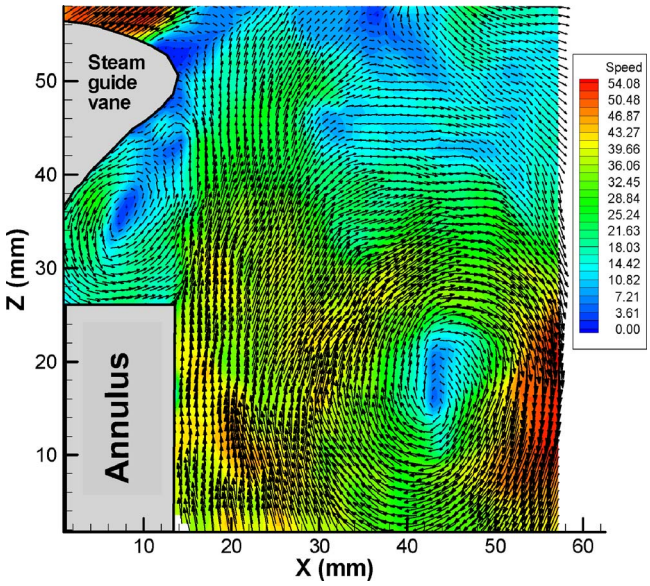

Fig. 4 Instantaneous velocity field in the horizontal center plane

gaps still remained between each FOV and the boundary, and hence, this plane could not be entirely covered. However, the velocity field obtained using the four FOVs specified above was sufficient to characterize the general flow characteristics at the condenser neck.

After capturing a series of particle images, the cross-correlation PIV algorithm was employed to extract instantaneous velocity fields using an interrogation window of 64×64 pixels with 50% overlap. The spatial resolution is ~1.8 mm. In this study, we focused on variation of large-scale vortical structure in the flow passage. The spatial resolution of these PIV measurements is reasonably sufficient to resolve the vortical flow structure. For each measurement cross section, 600 particle images were captured and then 300 instantaneous velocity fields were derived, which were subsequently ensemble-averaged to obtain the mean velocity field. Spatial distributions of turbulent statistics, such as the turbulent intensity and turbulent kinetic energy κ, were obtained by statistically averaging all the fluctuating velocity fields, derived by subtracting the mean velocity field from the instantaneous velocity fields. The turbulent kinetic energy κ was computed using the following equations:

$$\overline{w'^2} \approx \tfrac{1}{2}(\overline{u'^2} + \overline{v'^2}) \tag{1}$$

$$\kappa = \tfrac{1}{2}\rho(\overline{u'^2} + \overline{v'^2} + \overline{w'^2}) = \tfrac{3}{4}\rho(\overline{u'^2} + \overline{v'^2}) \tag{2}$$

where the contribution of the out of plane velocity component w was assumed to be the average of the measured velocity components u and v based on the assumption of isotropic turbulence. Note that, the actual turbulent kinetic energy will be somewhat different from present results in the regions of strong vortices where the isotropic assumption is not fulfilled.

3 Results and Discussion

3.1 Instantaneous Velocity Field in the Horizontal Center Plane. A typical instantaneous velocity field in the horizontal center plane is shown in Fig. 4. The main flow direction is perpendicular to the test plane, and the light sheet is coming from the right side. A large clockwise vortex is observed in the region beside the annulus. Another vortex is observed in the corner between the tip of the steam guide vane and the annulus, details of which will be discussed in the following sections. In this study, we primarily elucidated the flow structure by inspecting the spatial distributions of the mean velocity, vorticity, and turbulent kinetic energy (TKE). The following discussion examines the flow fields in the selected sections and the loss of flow energy throughout the flow passage of the exhaust hood.

3.2 Flow at the Top of the Exhaust Hood. Figure 5 shows the mean velocity field measured in the top vertical center plane (θ=180 deg) of the exhaust hood model. Two distinctly different flow regions are observed in this plane. A counterclockwise rotating vortex, as a result of flow separation arising from the "backward-facing step expansion" phenomenon, is formed in the corner between the tip of the steam guide vane and the butterfly vane. Although this vortex is restricted to the corner region, the large value of positive vorticity denotes the presence of a strong separation vortex (SV). In addition, the TKE exhibits a maximum value at the center of the vortex, indicating that a large amount of kinetic energy is consumed in this area. This type of SV has been found in previous studies [3–5], indicating that it represents a common phenomenon occurring in the steplike region behind the steam guide vane that is independent of the flow guide geometry and exhaust hood operating conditions. It can be conjectured that this vortex is one of the main causes of flow energy loss in the exhaust hood. Moreover, Xu et al. [5] and Liu et al. [4] noted the presence of a large PV and an end-wall vortex (EWV) in addition to the SV at the top of the exhaust hood. However, we did not observe these flow phenomena, likely because we used a casing of different size in the axial direction and included the butterfly vane.

On the other hand, the flow coming from the steam guide vane has a local maximum speed. As the flow approaches the bearing cone, its speed decreases gradually due to diffusion function of the flow passage. It is noticeable that a reverse flow appears in the region above the upper bearing cone, which occupies ~50% of the flow path. Prior to PIV measurements, we supplementarily measured the static pressure coefficients along the bearing cone in the vertical center plane. The static pressure rises continuously along the lower bearing cone and forms an adverse pressure gradient along the bearing cone. Because the flow with very low kinetic energy in the region near the bearing cone surface cannot resist the adverse pressure gradient acting on it, the boundary layer begins to separate. The curved shape of the bearing cone and restriction by the adjacent hood casing may facilitate formation of the reverse flow. After the boundary layer separates, the static pressure decreases to some extent in the upper bearing cone. From these results, we can see that the reverse flow hinders the recovery of the static pressure. Liu et al. [4] and Tindell et al. [3] examined the effects of different inflow conditions (including uniform and distorted flow) on the flow pattern and exhaust hood performance. They observed a separated flow over the bearing cone surface under the distorted inflow condition, while we observed a separated flow under the simulated inflow condition. The reason for this discrepancy is not clear, but it may indicate that the simulated inflow conditions of the axial velocity profile and total pressure distribution are important determinants of the flow behavior. Further work will be needed in the future to resolve this issue.

The mean flow fields in the top of the exhaust hood at several *X-Y* planes along the axial direction are shown in Figs. 6–9. Near the front end wall (ZD1), the flow moves in the opposite direction to the main flow discharging from the LSB, confirming the presence of the reverse flow along the upper bearing cone observed in Fig. 5. The streamlines are nearly uniform, without any visible vortex structure, and the variation of the speed is not so large in the ZD1 plane compared to the other planes. In the middle plane (ZD2) between the front end wall and steam guide vane, a large-scale counterclockwise rotating vortex occupies most of the flow passage. The region of uniform speed is reduced to less than half of the flow passage, and two areas with distinct flow speeds are observed. Inside the vortex structure, the minimum in the flow speed located near the top of the exhaust hood corresponds to the vortex core. The region of high flow speed is located away from the symmetric vertical center plane and the top of the exhaust

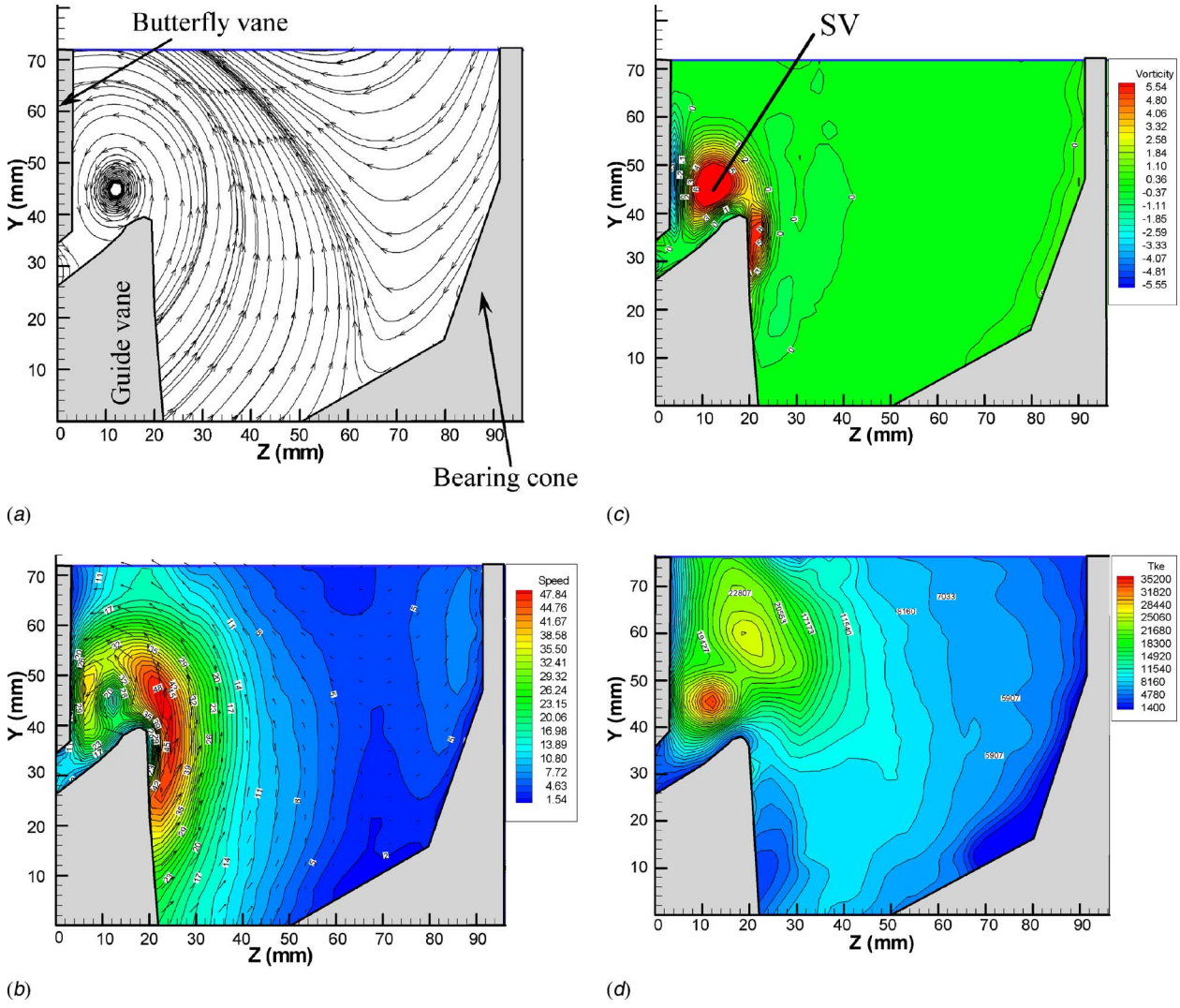

Fig. 5 Mean flow field in the top vertical center plane (θ=180 deg): (*a*) streamline distribution; (*b*) velocity magnitude contours, (*c*) vorticity contours, and (*d*) turbulent kinetic energy contours

hood. As can be seen from Figs. 8 and 9, in the ZD3 plane before the steam guide vane and ZD4 plane immediately over the steam guide vane, the general flow patterns are similar. In the ZD4 plane, the large-scale vortex dominates the flow passage, and the vortex center has migrated away from the vertical center plane (X=0) compared to that in the ZD3 plane. The trajectory of the vortex core in the region near the top of the exhaust hood between the ZD2 and ZD4 planes is well matched with the reverse flow pattern, moving downward in the opposite direction to the main flow. The vorticity shows a maximum value just in front of the guide vane. This longitudinal vortex (LV) forms from the reverse flow on the bearing cone shown in Fig. 5(*a*). The LV seems to develop into the large PV in the horizontal center plane discussed in Sec. 3.3. Even though the LV consumes less kinetic energy than the SV, its effect cannot be neglected.

From the flow field information in the vertical center plane and several X-Y planes from the end wall views at the top of the exhaust hood, we can discern two dominant vortices: a strong SV separated from the tip of the guide vane, and a large-scale LV occupying approximately half region of the flow passage. Their formation is closely related to the arrangement of the steam guide vane, the bearing cone and the butterfly vane. These two vortices seem to cause most of the momentum loss and to decrease the pressure recovery performance at the top of the exhaust hood.

3.3 Flow in the Horizontal Center Plane (θ=90 deg). Figure 10 shows the flow speed, vorticity, and TKE distribution in the horizontal center plane (θ=90 deg). The lower part of the upper-row figures and the upper part of the lower-row figures are partly overlapped at the region near the tip of steam guide vane, which appears in both sets of figures as a reference. Compared to the flow in the vertical center plane, the flow in the horizontal center plane has a more complicated structure consisting of three vortices with different scales. A jetlike high-speed flow moves along the steam guide vane and divides into two parts at a stagnation region, ~15 mm away from the tip of the guide vane. One part moves toward the front end wall of the exhaust hood and forms a medium size counterclockwise EWV. The other part forms a large-scale clockwise oval-shaped PV, expanding from the annular edge to the side wall. In addition, a small counterclockwise vortex is observed behind the tip of the guide vane, resulting from flow separation. Although the size of this SV is similar to that shown in Fig. 5, its shape is slightly different due to different boundary conditions. Furthermore, the vorticity and TKE distributions are different from those measured at the symmetric vertical center plane (θ=180 deg). For example, in the horizontal center plane (θ=90 deg) the vorticity value in the SV center is decreased to about half that in the vertical center plane, and the TKE is reduced

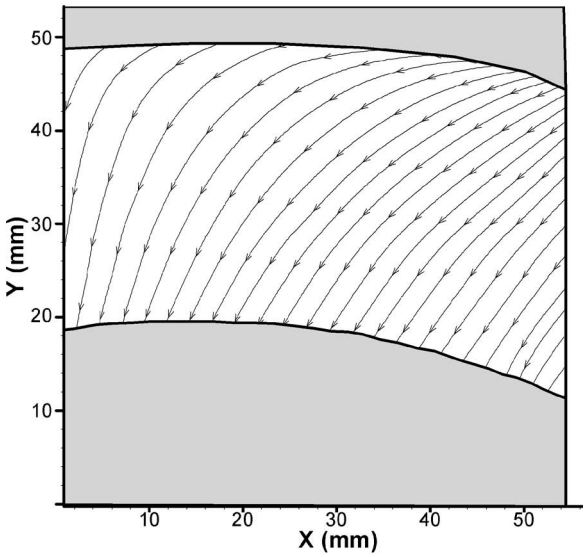

(a)

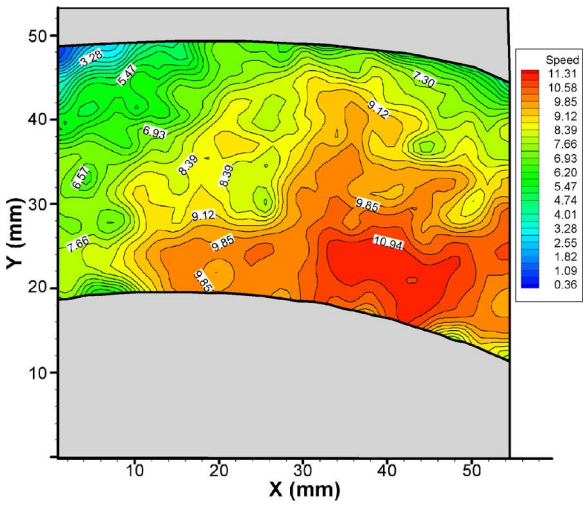

(b)

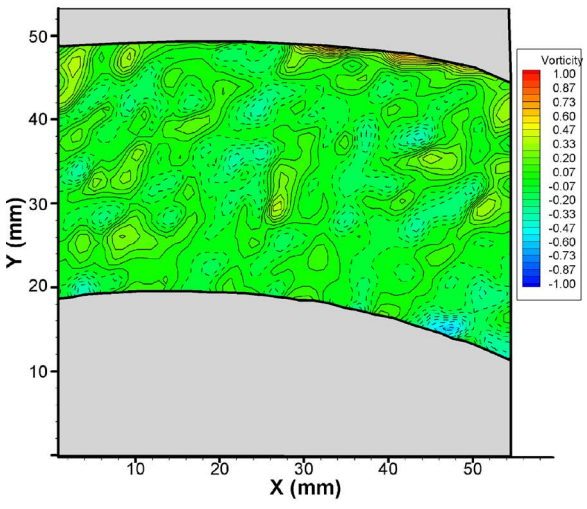

(c)

Fig. 6 Mean flow field at section ZD1 (*a*) streamline distribution, (*b*) speed magnitude contours, and (*c*) vorticity contours

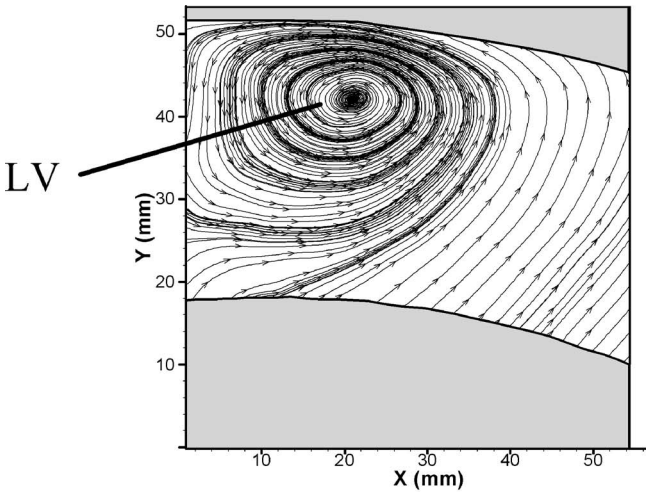

(a)

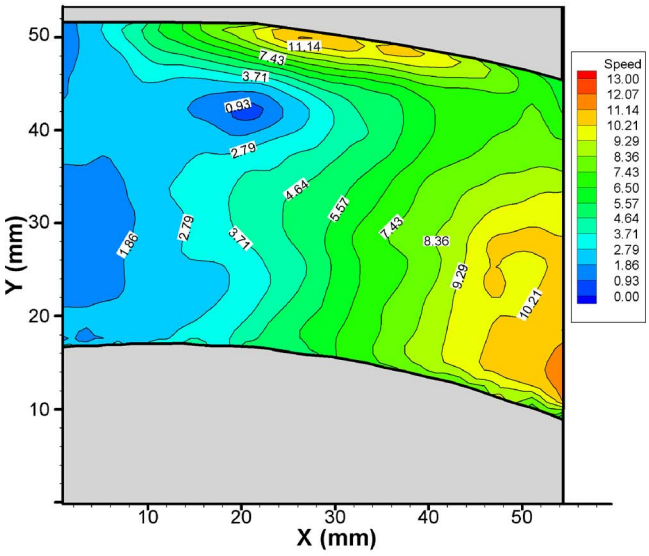

(b)

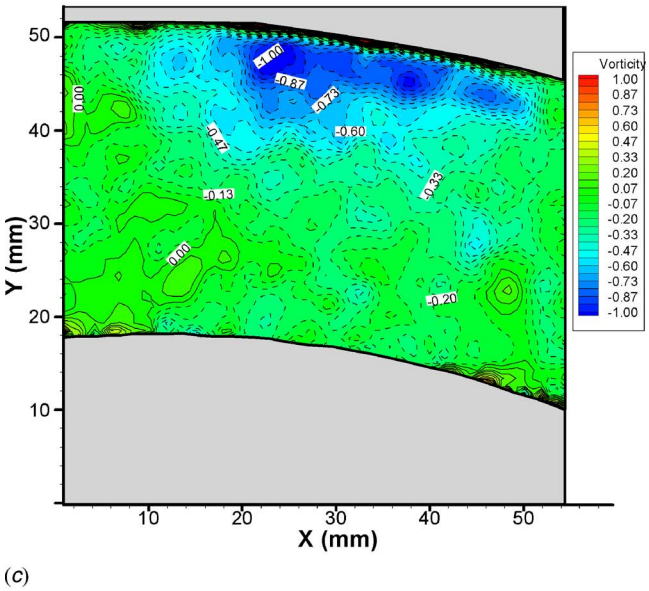

(c)

Fig. 7 Mean flow field at section ZD2: (*a*) streamline distribution, (*b*) speed magnitude contours, and (*c*) vorticity contours

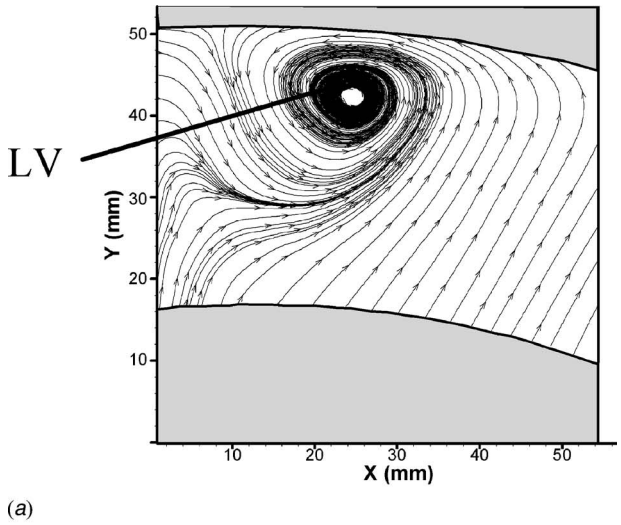

(*a*)

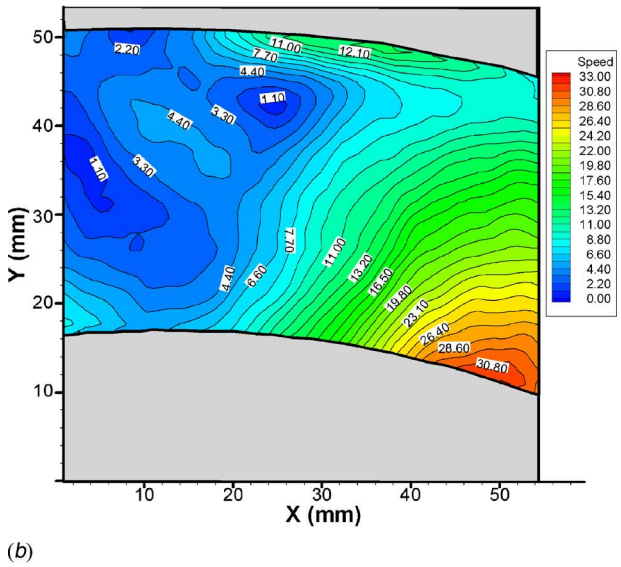

(*b*)

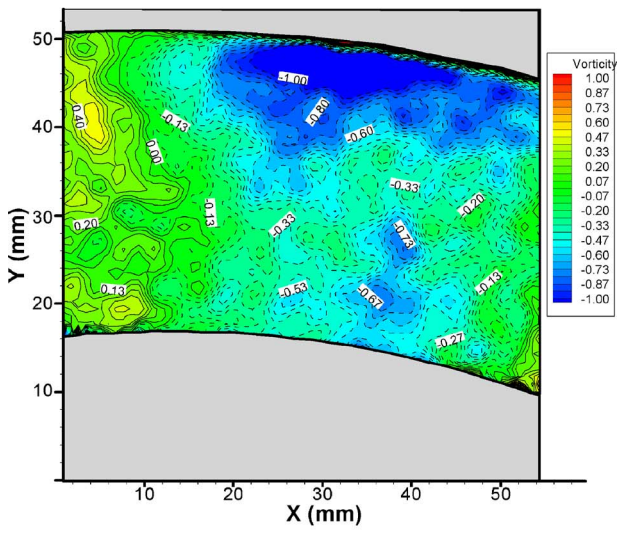

(*c*)

Fig. 8 Mean flow field at section ZD3: (*a*) streamline distribution, (*b*) speed magnitude contours, (*c*) vorticity contours

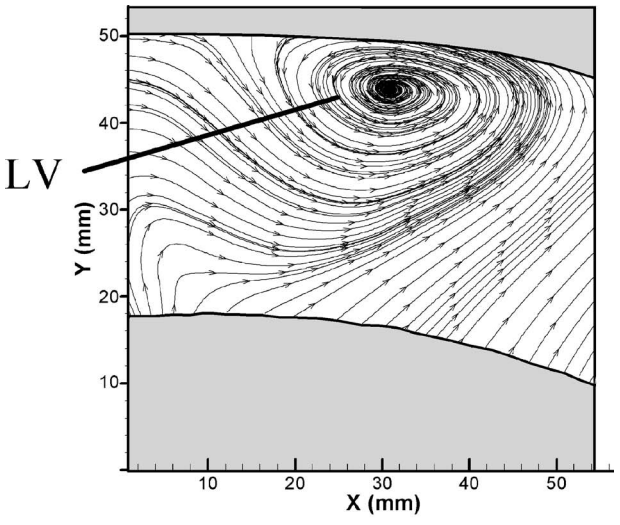

(*a*)

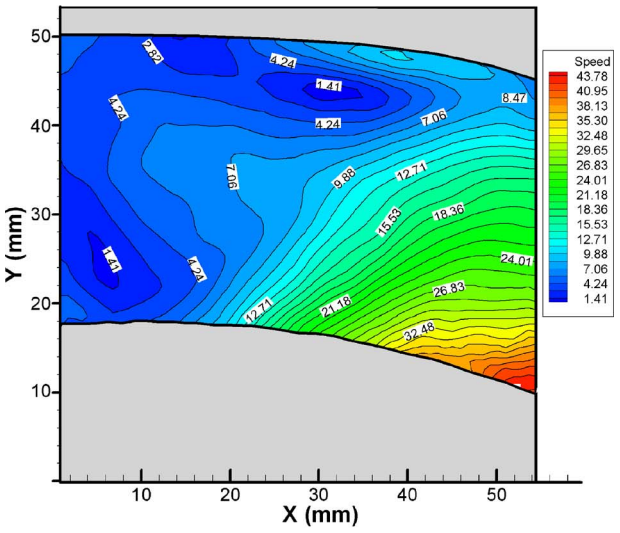

(*b*)

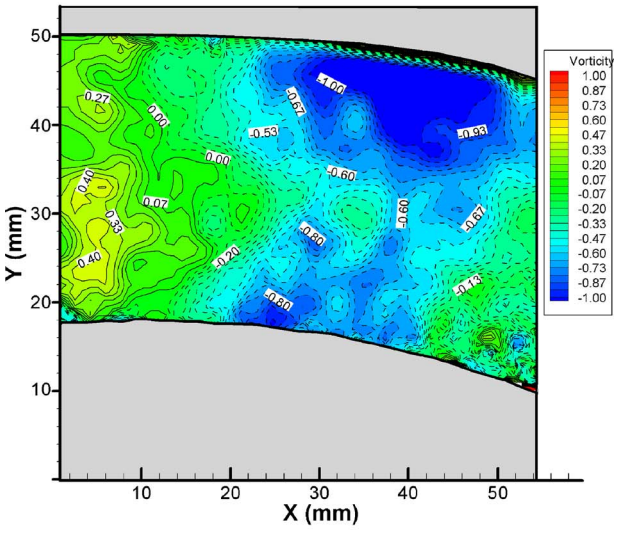

(*c*)

Fig. 9 Mean flow field at section ZD4: (*a*) streamline distribution, (*b*) speed magnitude contours, (*c*) vorticity contours

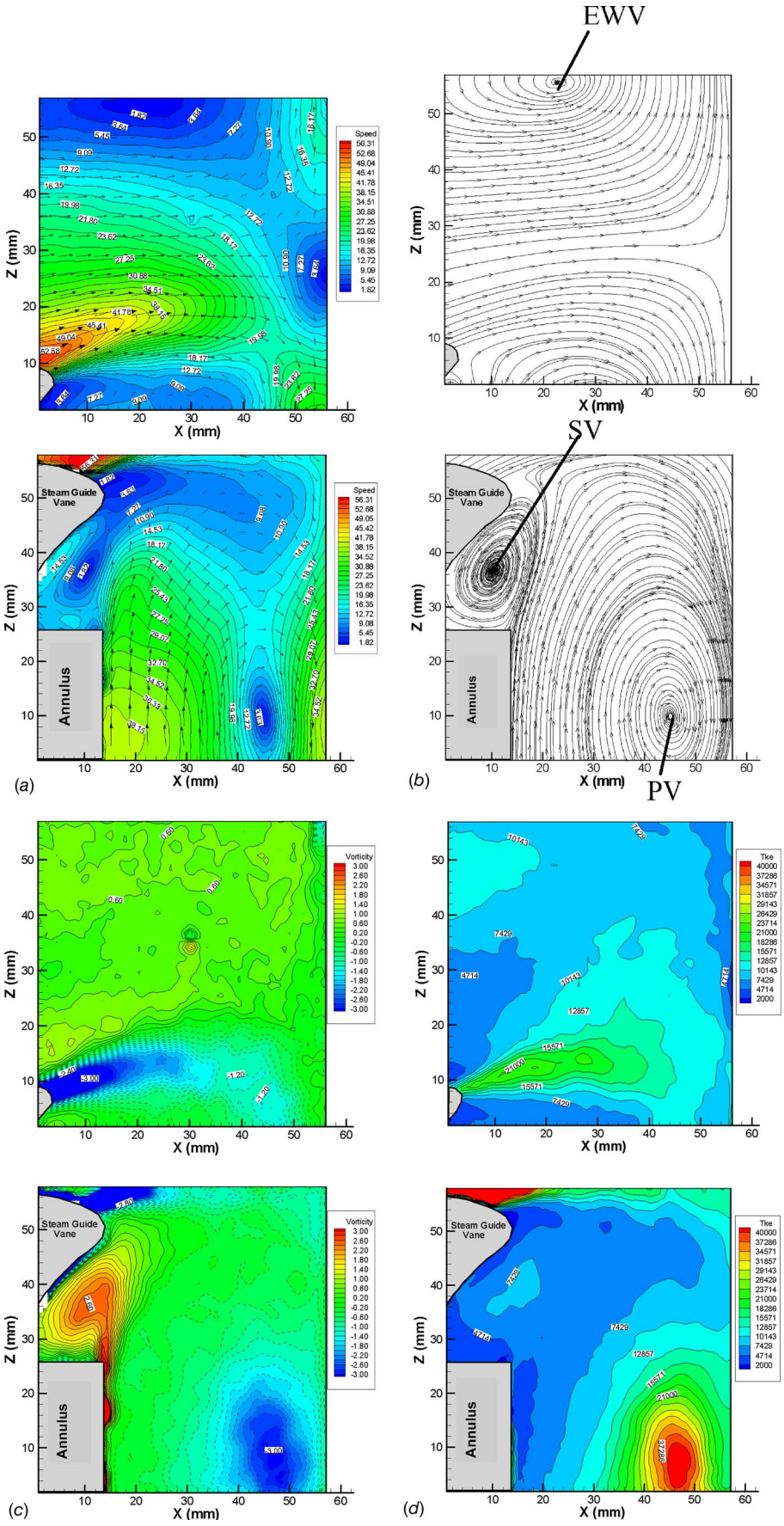

Fig. 10 Mean flow field in the horizontal center plane: (*a*) velocity magnitude contours, (*b*) streamline distribution, (*c*) vorticity contours, and (*d*) turbulent kinetic energy contours

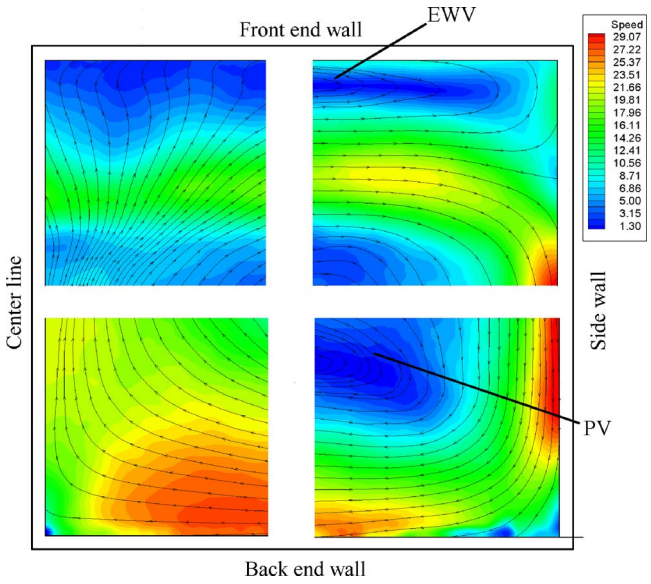

Fig. 11 Speed magnitude and streamline distribution at the condenser neck flange plane

to only ~20% of that in the vertical center plane. These results indicate that the separated vortex in the horizontal plane does not play a noticeable role in the kinetic energy loss, compared with that in the vertical center plane (θ=180 deg).

Comparing the three vortices in the horizontal center plane, we find that the EWV has the lowest positive vorticity, whereas the PV has the highest negative vorticity. The TKE has a maximum value at the core of the PV. Generally, the presence of a vortex substantially lowers the total pressure and largely consumes the flow energy. Therefore, we can conjecture that the large-scale PV consumes large amounts of kinetic energy, and that the EWV contributes less to the energy loss than the PV and the SV.

3.4 Flow in the Condenser Neck Plane. Figure 11 shows the mean velocity field measured at the plane of the condenser neck flange. Because of the small FOV for each measurement, four separate PIV results are combined to obtain the entire flow field. The streamlines clearly describe a large-scale clockwise PV occupying most of the condenser neck. It should be noted that the vortex core does not coincide with the geometric center of the condenser neck flange, but shifts toward the lower right corner between of the sidewall and the back end wall. This large PV maintains the same rotational direction as that in the horizontal center plane (θ=90 deg), indicating the consistent evolution of the PV along the flow passage. The other two relatively small vortices in the horizontal center plane are possibly combined into the PV or phased out. The large-scale PV drives low-energy fluid and pushes the main flow with a high momentum toward the surrounding area, resulting in a highly nonuniform velocity distribution at the exhaust hood outlet. The nonuniform velocity distribution is closely related to strong turbulent mixing and kinetic energy transport from the large-scale motion to the small eddy motion.

The small counterclockwise EWV formed near the front end wall seems to be similar in size to the one observed near the front end wall in the horizontal center plane (Fig. 10). It does not have any noticeable effect on the main flow. In the condenser neck plane, the PV is the main source of energy loss and plays a key role in the pressure recovery. Throughout the entire exhaust hood, the PV strongly influences the kinetic energy consumption; hence, flow separation over the bearing cone should be carefully considered in the design process.

4 Conclusions

The flow field inside an exhaust hood model has been investigated experimentally using the PIV technique, with a focus on the large vortex structure and the major sources of kinetic energy loss. Behind the tip of the steam guide vane, a strong SV is formed and maintains through almost the entire flow path of the exhaust hood. However, its vorticity decreases by half in the horizontal center plane. On the other hand, the PV originates at the exhaust hood top, evolves gradually and occupies a large area of the flow path, playing a dominant role in the flow inside the exhaust hood. In addition, near the front end wall a small counterclockwise EWV exists in the region from the horizontal center plane to the exhaust hood outlet. These vortices seem to be the major sources of kinetic energy consumption and pressure loss. Their intensities and influences vary as the flow goes downstream along the flow path. The SV and the PV seem to be closely related to the guide vane and the bearing cone, respectively. Therefore, when designing exhaust hoods, the steam guide vane and the bearing cone should be designed so as to effectively control these vortical flow structures and thus improve the hood performance.

Even though the swirling and periodic inflow conditions were not simulated, the present results on the complex 3D vortex flow structure in an exhaust hood model will provide useful data for the design of flow passage so as to improve the aerodynamic performance of the exhaust hood.

Acknowledgment

The present work was partially supported by the National Research Laboratory Program of the Ministry of Science and Technology (MOST) of Korea and SMART (330MWt) project of Doosan Heavy Industries and Construction Co., Ltd.

References

[1] Cofer, J. I., IV, 1996, "Advances in Steam Path Technology," ASME J. Eng. Gas Turbines Power, **118**, pp. 337–352.
[2] Gardzilewica, J., Swirydczuk, J., Badur, J., Karcz, M., Werner, R., and Szyrejko, C., 2003, "Methodology of CFD Computations Applied for Analyzing Flows Through Steam Turbine Exhaust Hoods," Trans. Inst. Fluid-Flow Mach., **113**, pp. 157–168.
[3] Tindell, R. H., Alston, T. M., Sarro, C. A., Stegmann, G. C., Gray, L., and Davids, J., 1996, "Computational Fluid Dynamics Analysis of a Steam Power Plant Low-Pressure Turbine Downward Exhaust Hood," ASME J. Eng. Gas Turbines Power, **118**, pp. 214–224.
[4] Liu, J. J., Cui, Y. Q., and Jiang, H. D., 2001, "Investigation of Flow in a Steam Turbine Exhaust Hood With/Without Turbine Exit Conditions Simulated," ASME Paper No. 2001-GT-0488.
[5] Xu, X., Kang, S., and Hirsch, C. H., 2001, "Numerical Simulation of the 3-D Viscous Flow in the Exhaust Casing of a Low-Pressure Steam Turbine," ASME Paper No. 2001-GT-0487.
[6] Sloldov, V. G., 1996, "Nonstationary 3-D Invisid Numerical Flow Model Through Steam Turbine Exhaust Hood," 3rd Colloquium on Process Simulation, Espoo, Finland, June 12–14, pp. 89–110.
[7] Dejean, F., Bourdonneau, L., and Duplex, J., 1997, "Three-Dimensional Coupled Flow Calculations in a Low Pressure Steam Turbine Last Stage and Exhaust Hood," 2nd European Conference on Turbomachinery—Fluid Dynamics and Thermodymics, Antwerpen, Belgium, March 5–7, pp. 21–27.
[8] Linhart, J., and Hoznedl, M., 2003, "Properties and Improvements of Flow in Steam Turbine Exhaust Hood," *Proc. of SUST Shanghai: International Conference on Energy and the Environment 2003*, Shanghai, Dec. 11–13, pp. 453–460.
[9] Angel, F., Kubiak, J., Marino, C., Marcinkowski, S., and Gardzilewicz, A., 1997, "Experimental Investigation of Exhaust Losses of a Low Pressure Steam Turbine," *Joint Power Generation Conference*, Vol. 2, ASME, New York, PWR-Vol. 32, pp. 367–372.

Application of Hot-Wire Anemometry in a Blow-Down Turbine Facility

T. Yasa

G. Paniagua

R. Dénos

Turbomachinery and Propulsion Department,
von Karman Institute for Fluid Dynamics,
Chaussée de Waterloo 72,
B1640-Rhode Saint Genèse, Belgium

In order to test HP turbine stages under engine representative conditions on a heat transfer point of view, blow-down test rigs are often used. In these rigs the evolution of gas temperature, pressure, and density is similar to a step function. Hence, the use of hot-wires, which are sensitive to flow velocity, density, and temperature, is more difficult than in an incompressible flow at constant temperature. This investigation describes how the data reduction can be performed in such an environment in order to extract the velocity. The gas temperature is measured with a thermocouple and the gas density is derived from the measurement of the total pressure thanks to an iterative procedure. Once the velocity is derived, the turbulence can be computed. The effectiveness of the method is first demonstrated in a heated jet where both pressure and temperature are varied. Tests in the turbine facility are performed at turbine inlet temperatures of 480 K. *Thus, overheat ratios up to 1.9 had to be used, leading to a very high temperature of the tungsten platinum coated wire. The aging of the probe was very fast, causing a drift in the voltage output between the successive tests. A technique is proposed to minimize the aging effect. It consists in adapting the calibration based on the resistance of the wire measured before each test. Measurements were carried out at the turbine inlet and rotor outlet. At the turbine inlet, velocity radial profiles are obtained together with measurements of the turbulence intensity. The time-averaged data is compared with pneumatic probe measurements. At the rotor exit, the time-resolved periodic velocity fluctuations are analyzed using a phase-locked average technique.* [DOI: 10.1115/1.2364191]

Introduction

Hot-wire anemometry is a well-known measurement technique to monitor flow velocities with high spatial resolution, high fidelity, and a bandwidth of several tens of kHz. Single hot-wires are extensively used to measure turbulence, concentration, and boundary layer properties. Multi-wires or rotating slanted single-wire probes (e.g., [1]) allow measuring the flow angles and the velocity components. Dual hot-wire aspirating probes, with wires operating at two different overheat ratios at a given constant Mach number, have been used to obtain time-resolved temperature and pressure [2]. Brunn [3] provides an excellent review on hot-wire anemometry.

Hot-wires have been used in turbomachinery laboratories for many years to resolve the periodic and random unsteadiness. Hot-wires are frequently used to detect the inception of stall in compressors (e.g., [4]). Smith [5] used hot wire anemometry to investigate the attenuation of a vane wake chopped by a rotor.

Regarding high-pressure turbines, hot-wire published data include detailed passage flow field traverses (e.g., [6]), rotor downstream velocity profiles (e.g., [7]), and interstage flow field (e.g., [8]). However, most of the data available in the literature was obtained at low speed, with negligible temperature variations. In high-speed high pressure turbines, unsteady velocity fluctuations have been measured with optical systems such as laser Doppler velocimeter and particle image velocimetry, which require optical access and seeding the flow. Kost et al. [9] performed turbulence measurements with a laser two-focus system and showed how the stator wakes are being cut off by the rotor blades and convected within the rotor passage. Lang et al. [10] studied the vane exit region using stereoscopic particle image velocimetry (PIV).

In the 1970's, short duration facilities were developed for high-speed turbine research to enable heat transfer measurements and reduce the cost of operation [11]. Based on the experience gained at Oxford University, the VKI compression tube facility was built [12]. In this compression tube a free-moving piston realizes a quasi-isentropic compression, driven by high-pressure air, raising simultaneously temperature and pressure. When the shutter valve is actuated, the pressurized heated air flows through the cold test section (at 290 K). The temperature, pressure, and density upstream of the turbine stage follow a steplike evolution as displayed in Fig. 1. Steady-state conditions are reached after 100 ms and are maintained typically for 200 to 400 ms. The temperature decreases by about 40 K after the initial overshot.

The large variations of flow density and temperature affect the hot-wire output voltage. Sheldrake and Ainsworth [13] presented rotor hot-wire measurements with a linear correction method to compensate for the temperature variations. The current work presents a novel methodology in which the anemometer calibration is a function of the flow density, viscosity, temperature, and the wire operation temperature of the sensor wire. This new formulation allows us to apply hot-wire anemometry in non-isothermal flows using the Nusselt correlation of Collis and Williams [14]. The methodology was first assessed in a jet where temperature was modified by comparing the hot-wire data with pneumatic probe measurements. Subsequently, tests were performed in the compression tube facility.

Elevated wire temperatures imply a rapid change of wire resistance in time, the so-called "aging" effect, resulting in a change of the wire temperature and of the velocity-voltage calibration. The effect of such resistance change may yield velocity errors up to 50% of its mean level. A post-processing procedure has been developed to minimize the error by monitoring the wire resistances prior to each test. Then, using an optimization algorithm, the calibration data are fitted to obtain the calibration constant and the

Contributed by the International Gas Turbine Institute (IGTI) of ASME for publication in the JOURNAL OF ENGINEERING FOR GAS TURBINES AND POWER. Manuscript received October 1, 2005; final manuscript received February 1, 2006. IGTI Review Chair: R. S. Abhari. Paper presented at the ASME Turbo Expo 2006: Land, Sea and Air (GT2006), Barcelona, Spain, May 8–11, 2006, Paper No. GT2006-90457.

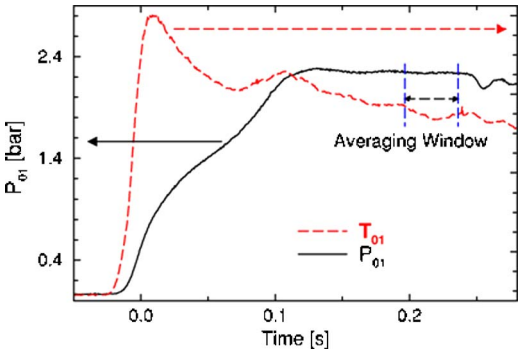

Fig. 1 Pressure and temperature evolution during a test

wire resistance for each test. Using the measured total resistance and the cable resistances, the exact wire temperature can be calculated.

Finally, measurements in the short duration turbine test rig are presented. Experiments were carried out with and without a turbulator upstream of the turbine, to investigate the effect of two boundary layer thicknesses. The measured data include radial velocity and turbulence intensity profiles. At the turbine exit plane, the time-resolved periodic velocity fluctuations are described using a phase-locked average technique.

Hot-Wire Anemometry

Description of the Instrumentation. In the present investigation the constant temperature anemometry (CTA), which offers a higher frequency response than the constant current mode, is used. The sensing element of the CTA is a 5 μm diameter platinum-coated tungsten wire. The wire is heated by Joule effect at a constant temperature thanks to an electronic conditioning unit. The wire operating temperature is adjusted through the overheat ratio (OHR), i.e., the ratio between the resistance of the wire at operating temperature and that at ambient temperature. A servo-loop rapidly adjusts the current intensity in order to keep the wire resistance constant hence the wire temperature.

Figure 2 displays the probe used in this investigation, which carries two hot-wire sensors and one thermocouple located in between the two hot-wire heads. The cutoff frequency of the current probe is about 30 kHz.

Theoretical Background. An energy balance applied on the wire implies that the heat provided to the wire by Joule effect equals that dissipated into the flow by convection $Q_{\text{Joule}} = Q_{\text{convection}}$. This balance is mathematically expressed by using the film temperature (mean temperature between the gas and wire) $T_{\text{film}} = (T_{\text{total gas}} + T_{\text{wire}})/2$.

$$\frac{E^2}{R_{\text{wire}}} = h \times S \times (T_{\text{film}} - T_{\text{wire}}) \quad \text{with} \quad h = \frac{Nu \times k_{\text{film}}}{d} \tag{1}$$

In Eq. (1), all quantities can be determined by direct measurement or calculation except the Nusselt number, which is thus an

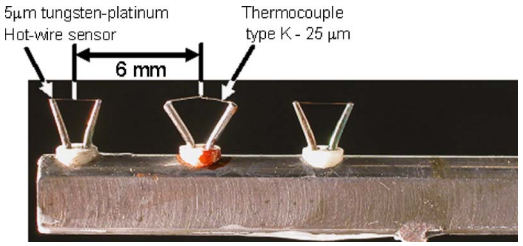

Fig. 2 Hot-wire probe manufactured at VKI

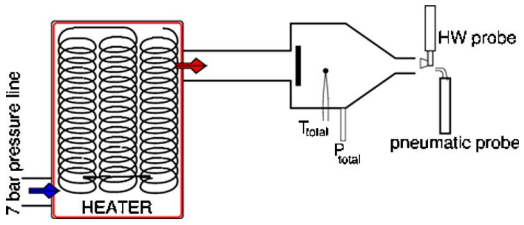

Fig. 3 Scheme of the VKI free jet calibration facility

important parameter in the calibration when the temperature of the flow is changed. At a given temperature the relationship between hot-wire voltage and fluid velocity may be modelled with a power law, such as the King's law [15]:

$$E^2 = A_{\text{King}} + B_{\text{King}} \cdot u^{n_{\text{King}}} \tag{2}$$

In Eq. (2) the calibration parameters A_{King}, B_{King}, and n_{King} can be found by performing power fittings of calibration data. A_{King} is the initial hot-wire voltage (E_0) in that is needed to heat up the wire when the flow velocity is zero, typically 1.2 V at 1.9 OHR.

The hot-wire calibration was performed in a free jet facility that allows us to perform the calibrations at several gas temperatures (see Fig. 3). The outlet diameter of the nozzle is 15 mm. The sensor wire is located 13 mm downstream of the jet exit, i.e., in the potential core. The wire axis is perpendicular to the flow direction. The flow total temperature and total pressure are measured in the settling chamber with a type-K thermocouple and a pneumatic pressure tap, respectively. The calibration procedure consists in measuring the anemometer voltage output for 20 velocities in the range 10–100 m/s for each of the four tested temperature levels. The real jet velocities were calculated using the compressible flow equations. The results of the calibration are presented in Fig. 4. When the gas temperature increases, the temperature difference between the wire temperature (about 640 K) and the flow temperature decreases, therefore less voltage difference is required in the wire for a given flow velocity.

Correction of Gas Temperature Variation. In flows with temperature variations, it is necessary to compute the wire film temperature at any given time. It is thus crucial to introduce the gas temperature into the hot-wire calibration, which is done by means of the Nusselt correlation in the energy balance (Eq. (1)). Several Nusselt correlations have been investigated by Abdel-Rahman et al. [16] for low-speed applications, where the flow velocities

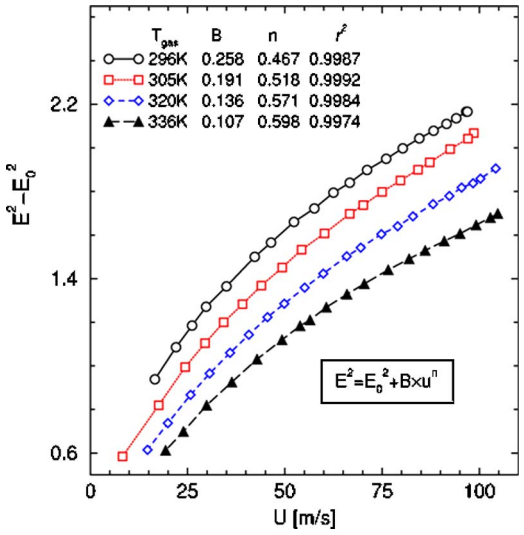

Fig. 4 Calibration results based on King's law

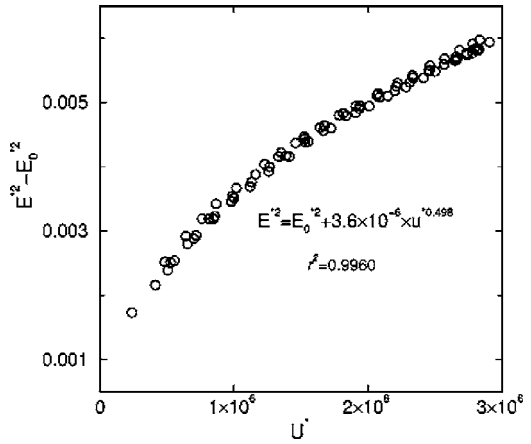

Fig. 5 Calibration results based on Collis and William's correlation

ranged between 0.83 and 8.8 m/s, and the flow temperature varied from 300 K to 370 K. Similarly, Bradbury and Castro [17] compared a set of Nusselt correlations over a wide range of wire temperatures. Both studies conclude that the best results for hot-wire anemometry are obtained with the Collis and Williams correlation [14]. Hence it is selected in the present study. The Nusselt number is defined as a function of the Reynolds number, gas temperature, and film temperature as expressed in Eq. (3).

$$Nu \times \left(\frac{T_{\text{film}}}{T_{\text{gas}}}\right)^{-0.17} = A_{\text{Collis}} + B_{\text{Collis}} \cdot \text{Re}^{n_{\text{Collis}}} \tag{3}$$

The power coefficient (n_{Collis}) is a value that depends on the wire geometry. Koch and Gartshore [18] tested several wires and found that the power law coefficient $n_{\text{Collis}}=0.45$ for a 0.5 μm tungsten-platinum wire. Combining Eqs. (1) and (3), one obtains Eq. (4), which expresses a direct relationship between the hot-wire voltage and the flow velocity at various gas temperatures. This equation can be further simplified by introducing two new variables: the generalized voltage (E^*) and the generalized velocity (u^*). The power law coefficients A, B, and n can be determined by fitting the calibration data. The flow properties are computed using the compressible flow equations, based on the measurement of the pressure and temperature of the flow.

$$\frac{E^2}{T_{\text{wire}} - T_{\text{gas}}}\left(\frac{T_{\text{film}}}{T_{\text{gas}}}\right)^{-0.17} = A + B\left(\frac{\rho_{\text{film}} \cdot u}{\mu_{\text{film}}}\right)^n \tag{4}$$

$$E^{*2} = A + B \cdot u^{*n} \tag{5}$$

The wire temperature can be accurately calculated based on the initial wire resistance and the resistivity ($\alpha_0=0.0036\ \text{K}^{-1}$ for the platinum-coated tungsten wire), as given in Eq. (6).

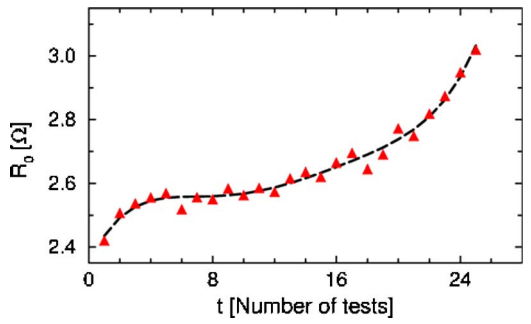

Fig. 6 Change of sensor wire resistance in consecutive tests

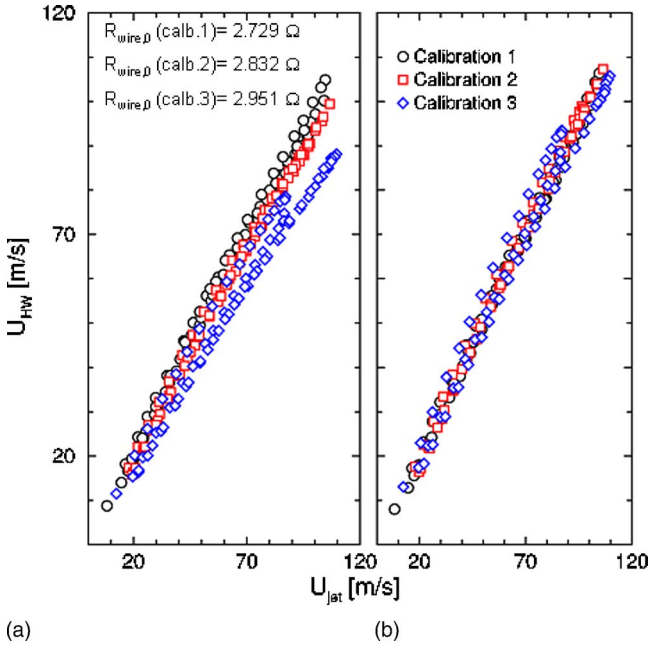

Fig. 7 Aging effect on hot-wire measurements without correction (*a*) and with correction (*b*)

$$R_{\text{wire}} = R_{\text{wire},0}[1 + \alpha_0(T_{\text{wire}} - T_0)] \tag{6}$$

However, in this study, the initial wire resistance ($R_{\text{wire},0}$) cannot be directly measured. What can be measured is the resistance of the wire plus that of the prongs and the connectors, the last two being independent from temperature. The first approximation is to consider the resistances of the prongs and connectors negligible. Neglecting the effect of the cable resistance (5 m long), one can obtain an initial guess of the wire temperature using Eq. (7), in which the $\text{OHR}=(R_{\text{wire}}+R_{\text{cable}})/(R_{\text{wire},0}+R_{\text{cable}})$:

$$R_{\text{wire}} = \text{OHR} \times R_{\text{wire},0} \tag{7}$$

Using this first guess on the R_{wire} and T_{wire} (about 550 K) an iterative procedure is used to determine the T_{wire} such that all the calibration curves displayed in Fig. 4 collapse into one curve. The optimization routine tries to maximize the correlation coefficient of the power law given by Eq. (5). Figure 5 shows that all the calibrations fit into only one power law with a relatively high correlation coefficient ($r^2=0.996$), independently of the temperature of the flow. The final value of T_{wire} in this case is 640 K.

Aging Effect Minimization. In high-temperature applications with high OHR, the wire resistance changes after each test, which in turn affects the actual wire temperature. For the measurements performed at turbine inlet, $T_{\text{gas}} \approx 480$ K, the overheat ratio was 1.9, to maximize the measurements resolution, hence this effect was important.

Figure 6 depicts the change of initial resistance after consecutive tests. In each of the tests, the hot-wire is being operated for 15 min. The resistance of the thin wire is increased by 25% in its whole life span (about 6 h).

If a constant wire resistance is used in the calibration, the procedure yields incorrect velocity values. The influence of the change of resistance on the measurements was investigated performing three consecutive calibrations such as the one displayed in Fig. 7 with an OHR=1.9; $R_{\text{wire},0}$ was 2.729, 2.832, and 2.951 Ω. Afterwards, using the calibration 1 as reference, the anemometer voltage values were converted into the velocities for all the calibrations, and the results were compared with the actual jet velocities (Fig. 7(*a*)). A significant error is observed, especially at

high velocity.

This error can be eliminated by introducing the change of wire resistance due to the aging into the data processing procedure. This is performed by including the OHR=$(R_{wire}+R_{cable})/(R_{wire,0}+R_{cable})$ in Eq. (4). The wire temperature is redefined using Eq. (8), therefore the hot-wire anemometry model can now be rewritten according to Eq. (9). This equation is solved using an optimization code in which only R_{cable}, B_{ag}, and n_{ag} are the parameters to be identified. The optimization routine starts with an initial guess of these parameters. Then, for a given velocity, the calculated voltage output is compared with the measured output signal. The iterative procedure stops when the voltage error is smaller than a certain threshold. In the case presented in Fig. 7(*a*) the results of the optimization are $R_{cable}=0.875$, $B_{ag}=7.49\times10^{-7}$, and $n_{ag}=0.48892$.

$$T_{wire} = T_0 + \frac{(\mathrm{OHR}-1)}{\alpha_0}\left(\frac{R_{cable}}{R_{wire,0}}+1\right) \tag{8}$$

$$\frac{E^2}{(\mathrm{OHR}\times R_0 - R_{cable})} = \left(A_{ag} + B_{ag}\cdot\left(\frac{\rho_{film}\cdot u}{\mu_{film}}\right)^{n_{ag}}\right) \times\left(\frac{T_{wire}+T_{gas}}{T_{gas}}\right)^{0.17}(T_{wire}-T_{gas}) \tag{9}$$

During the tests B_{ag}, n_{ag} and R_{cable} are known and, prior to each test, it is necessary to measure the $R_0=R_{wire,0}+R_{cable}$. Therefore $R_{wire,0}$ is known and T_{wire} can be calculated (Eq. (8)). Finally, using Eq. (9), the velocity can be directly derived. This method has been validated using the calibration tests presented in Fig. 7(*a*). Figure 7(*b*) shows the computed velocities when the new procedure is implemented. The difference between the calibrations has been substantially minimized.

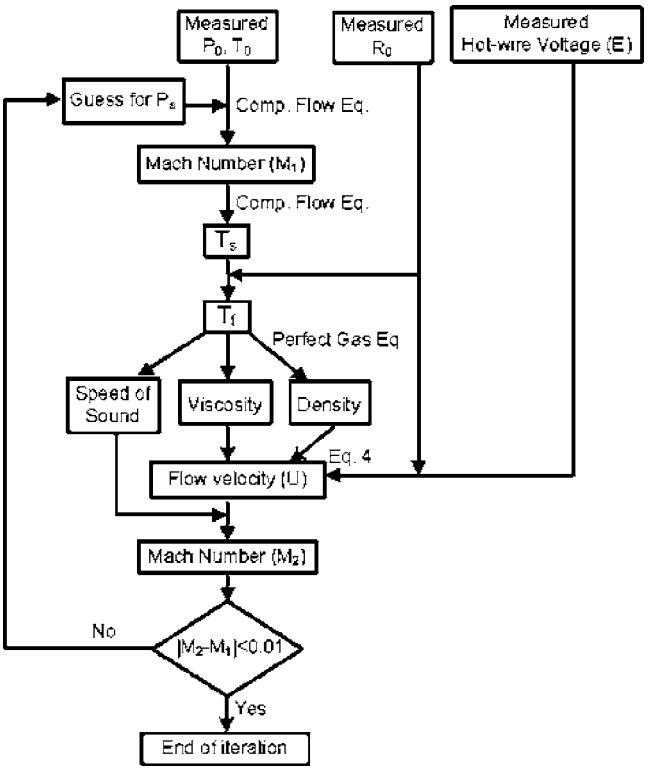

Fig. 8 Data processing methodology

Results and Discussion

Data Reduction Procedure and Validation. The data processing technique proposed to take into account temperature and density variations is outlined in Fig. 8. The direct measurements comprise the hot-wire voltage, the total pressure, the total temperature, and the initial resistance of the hot-wire anemometer (wire, prongs, and cables). The flow properties are calculated in an iterative way. A first guess is made on the static pressure. Then, Mach number, density, and viscosity are computed using the compressible flow equations under the assumption of perfect gas. Using the hot-wire voltage and the computed density and the viscosity, another value of Mach number is computed. Based on the difference between the two successive values of Mach number, the static pressure is adjusted. This procedure is repeated until the difference becomes negligible.

To validate this procedure, experiments were carried out in a free jet facility (Fig. 3), where temperature and pressure can be adjusted independently. The velocity in the jet, measured with the hot-wire, is computed in two different ways and compared with the pneumatic measurements. Figure 9 shows the change of pressure and temperature during the test (300 s duration). The so-called "*raw signal*" is the hot-wire signal processed in the conventional way, using the King's law of a calibration obtained at the mean level of temperature of the test. The "*temperature corrected*" signal was obtained using Eq. (4), since there were no problems of aging in this case. Indeed, the levels of temperature being low, an overheat ratio of 1.6 was selected. It is obvious that when the change of temperature is neglected in the data processing (raw signal) the computed velocity is very different from the pneumatic measurements, with a maximum error of 12 m/s. Thanks to the temperature correction, this error is reduced to 2.4 m/s.

Turbine Stage and Data Acquisition System. The experiments in the VKI compression tube were performed to investigate the flow field in a highly loaded high-pressure turbine stage. This rig provides full aero-engine similarity. The Mach number, Reynolds number, and temperature ratios are independently adjusted to the values encountered in actual engine operation [12]. Figure 10 displays the test section with a single HP turbine with a 43-vane stator and a 64-blade rotor. The axial distance between the stator trailing edge and the rotor leading edge is about 0.35% of $C_{s,ax}$. The inlet measurement plane (1) is located $0.33\times C_{s,ax}$ upstream of the vane, while the stage exit measurement plane (3) is located $0.5\times C_{s,ax}$ downstream of the rotor row. In some of the tests 8 mm diameter tori were located at the hub and tip end walls

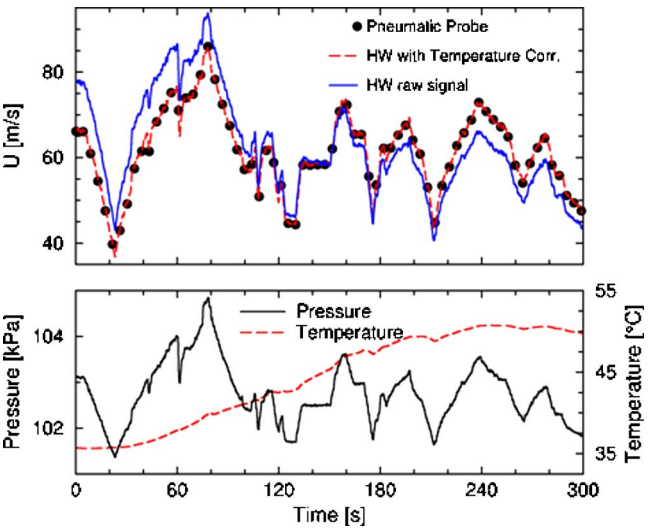

Fig. 9 Free jet velocity while the flow temperature and pressure are varying

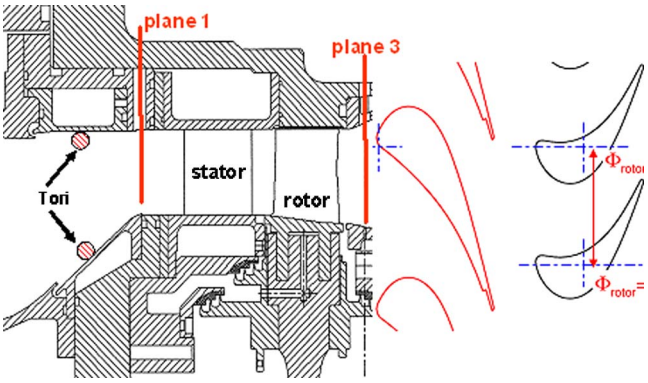

Fig. 10 Axial and blade to blade view of the turbine stage

of the inlet channel to thicken the boundary layer. The nominal conditions are $P_{01}=2.2$ bar, $T_{01}=480$ K, rotational speed 6500 rpm, and static to total pressure ratio (P_{01}/P_{s3}) 3.08.

At the turbine inlet, the hot-wire anemometer signal output is low-pass filtered at 50 kHz and sampled at 200 kHz. At the turbine exit, the signal is split into two components. The first is low-pass filtered at 750 Hz and sampled at 1.2 kHz. The second is high-pass filtered at 100 Hz and sampled at 300 kHz, with a gain of 10 to capture high-frequency components with a high resolution. Before each test, the probe is set to the desired radius. Each of the measurement points in Fig. 11 corresponds to a different test.

The flow velocity fluctuations can be decomposed into a mean velocity, periodic fluctuations, and random velocity fluctuations due to turbulence.

$$U = \bar{U} + u_{\text{periodic}} + u'_{\text{random}} \tag{10}$$

Stage Inlet Turbulence Measurements. At the turbine inlet there are no periodic velocity fluctuations. The turbulence intensity is therefore computed based on the velocity fluctuations:

$$\text{Tu}\,\% = \sqrt{\frac{\overline{u'^2}}{\bar{U}}} \quad \text{with} \quad U = \bar{U} + u' \tag{11}$$

The results are plotted in Fig. 11(*a*), using as mean velocity the local value measured by the hot-wire. Figure 11(*b*) displays the turbulence intensity using a constant mean velocity obtained from the mass flow rate. Figure 11(*b*) shows that a change of 10% in the mean flow velocity does not alter the value of turbulence intensity

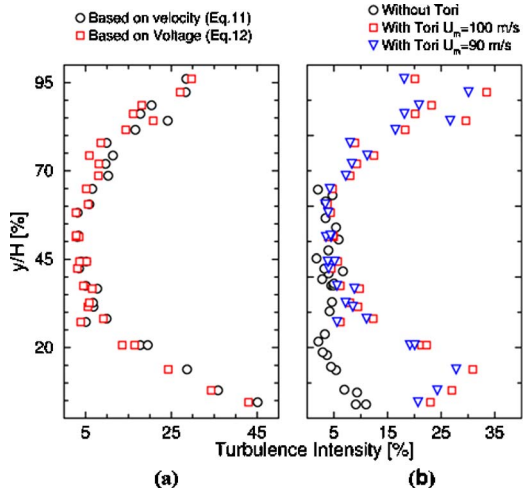

Fig. 11 Turbulence intensity profile at the turbine inlet

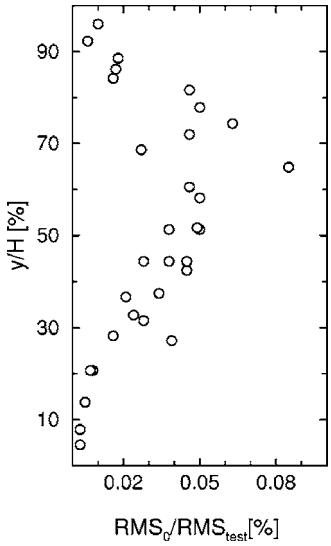

Fig. 12 Signal to noise ratio of the inlet measurements

at mid-span ~4%. Results are presented for both with and without tori. The effect of the tori, which cover 20% of the span at hub and tip, is clearly identified with regions of high turbulence intensity close to the hub and tip due to the vortex shedding.

According to the method described by Consigny [19], turbulent intensity can also be directly calculated using the output raw voltage. The flow properties are computed based on the time average temperature and pressure for a single test. The turbulence intensity can then be computed assuming a voltage-velocity relationship based on King's law. The resulting equation is rather simplified:

$$\text{Tu}(\%) = 100 \times \frac{\sqrt{\overline{u'^2}}}{\bar{u}} = 100 \times \frac{2 \times \bar{E} \times \sqrt{\overline{E'^2}}}{n \times (\bar{E}^2 - A)} \tag{12}$$

Figure 11(*a*) proves that the results of Eq. (12) are well in agreement with the results obtained using Eq. (11), in which the local value of velocity is considered at each given radius ("$\bar{U}$").

The signal to noise ratio is an important parameter to characterize turbulence measurements; electronic noise should not be considered as turbulence. In the present study, the ratio between RMS before the blow-down and during the test is presented in Fig. 12. In most of the tests, the ratio of the RMS is below 5%, which indicates that a maximum 0.2% of the turbulence intensity is originated by electronic noise. The turbulence results are little affected by temperature errors. Indeed, a change of 20 K (±10 K) in temperature implies a variation in the turbulence intensity below ±0.2%.

Stage Inlet Velocity Measurements. The measurement of the turbine inlet velocity ($T_{01}=480$ K) requires high wire temperatures (OHR=1.9). Therefore one is confronted with aging problems, and it is difficult to obtain a high accuracy in the velocity. Figure 13(*a*) shows the turbine inlet profiles of pressure and temperature. Figure 13(*b*) displays the turbine inlet velocity. In the region 60% to 70% there is a rather high error in the velocity profile. Actually, these three measurement points correspond to the last measurements done with that wire, illustrating clearly the wire aging problems.

Additionally, the effect of a temperature error on the velocity measurements has also been investigated. In a flow at 500 K, with a constant velocity of 90 m/s, an error of 10 K in temperature generates an error of about 15 m/s in the hot-wire measurement. There are three temperature probes located at the stage inlet at different peripheral directions. Measurements show that the uncer-

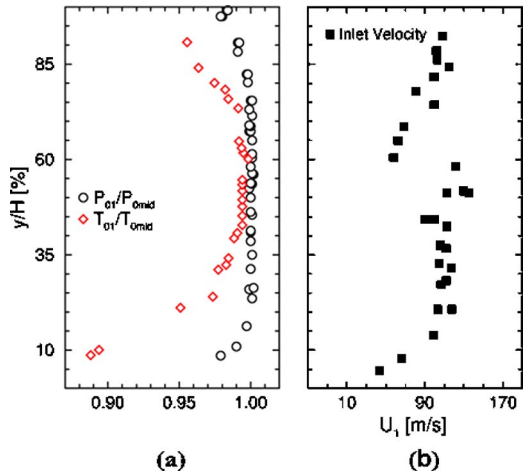

Fig. 13 Inlet pressure, temperature (*a*) and velocity distribution (*b*) along the span

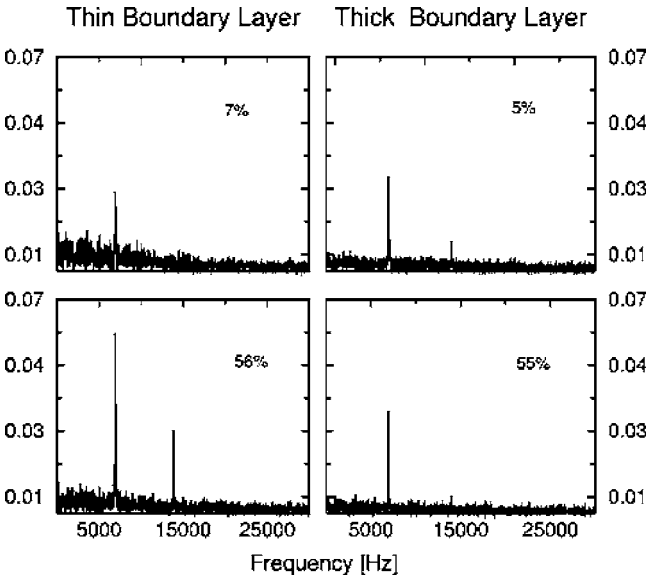

Fig. 15 FFT of the hot-wire signal downstream of the rotor

tainty of the inlet temperature can be 10 K at the mid-span.

This uncertainty is, however, much smaller than that due to aging effect. Tests were performed in a jet facility in order to investigate if the aging effect could be corrected. A correction technique was derived and was presented in a previous section. The required element to apply the correction is the resistance of the wire before the measurements. Unfortunately, this resistance was not measured before each test and it was not possible to repeat the test campaign.

Stage Outlet Time-Averaged Velocity. The time-averaged velocity distribution is calculated in a similar way to the turbine inlet measurements by time averaging during a time window of 40 ms (as displayed in Fig. 1). In Fig. 14 the results are compared with the pneumatic probe measurements by means of the Mach number distribution along the radial direction. The hot-wire results show very good agreement with the pneumatic pressure measurements. The small differences may be explained with the error of static pressure estimation during the velocity calculation. A change of 10 mbar (about ±1% of error on the static pressure) may create this small difference.

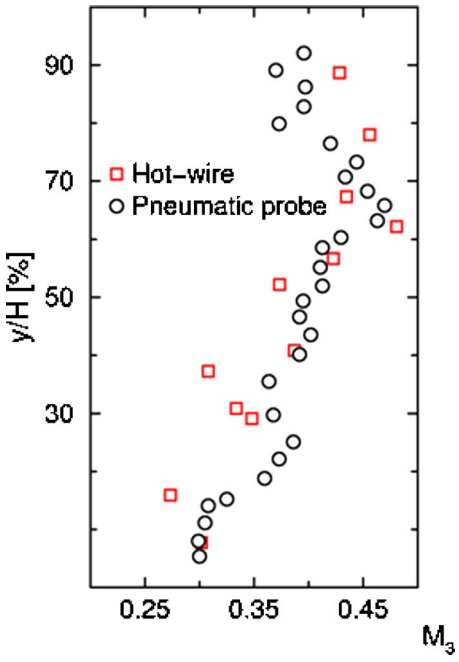

Fig. 14 Mach number distribution at the stage exit along the span-wise direction

Stage Outlet Time-Resolved Velocity. The spectrum of some selected traces for thin and thick boundary layers are reported in Fig. 15. In all cases, the fundamental frequency that corresponds to the blade passing frequency is highly visible. In some cases, a first harmonic is also seen.

At the stage exit the probe is submitted to periodic fluctuations due to the rotor blade passing events. This occurs at a rate of 6500 RPM × 64 blades = 6.9 kHz and is evidenced by Fig. 15. In order to separate the periodic component from the random contributions, a phase-locked averaging technique is applied on three rotor revolutions i.e., 192 rotor passing events. It simply consists in making the time axis of each blade passing event dimensionless between 0 and 1. The rotational speed being measured accurately, this is readily done. Then, the dimensionless axis is divided in segments. The points that fall into one segment are averaged and the RMS is computed providing thus a phase-locked averaged signal and a distribution of RMS.

The results have been plotted in Fig. 16 for two rotor pitches. In this plot, the mean value of the trace was removed and each trace is shifted among the ordinate according to its location along the span-wise direction. Rotor blade passing events can be clearly identified on both phase-locked averaged signal and RMS distributions. On the phase-locked averaged traces, a line was plotted that passes through the minimum of velocity. This should identify the center of the wake. The same line was plotted on the RMS distributions. In most cases, the velocity minimum corresponds with the peak of RMS. For the two upper traces and the lower trace, the peak of RMS does not coincide with the minimum of velocity, and the RMS variation is much larger. This can be attributed to the existence of shock waves that tends to create strong and sharp periodic discontinuities. Indeed, in the case of this turbine, the time-averaged rotor exit Mach number is 0.9. The vane exit Mach number being 1.05, the regime of the rotor is also affected by the vane traversing event and the rotor exit Mach number oscillates periodically between subsonic and transonic regime with an average exit Mach number of 0.9.

Compared to previous time-resolved total pressure measurements, the hot wire shows a much better capacity to resolve the wake. In the case of the total pressure probe, the random unsteadiness originated by electronic noise covered the velocity fluctua-

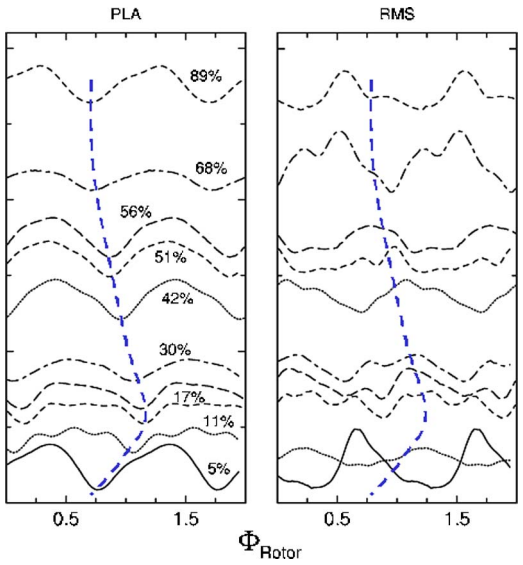

Fig. 16 Periodic component (left) and random unsteadiness (right) downstream of the rotor along the height (% span is indicated above each curve)

tions. This was due to the fact that the pressure probe had to measure the absolute total pressure, i.e., the range was approximately ten times larger than the dynamic head.

Conclusions

The hot-wire anemometry is a useful tool to determine turbulence even when the flow temperature varies. The method described here shows that the temperature and density changes can be compensated by considering flow temperature as a parameter in the calibration law. This requires an accurate estimate of the wire temperature, an accurate measurement of the gas temperature, and the computation of the density using a total pressure measurement. The method is validated in a jet facility and also in a turbine stage environment.

At turbine inlet, the technique suffers from the wire aging. Indeed, the rather high gas temperature used here required very high wire temperatures. The wire characteristics change quickly as a function of time. A method is proposed that, based on the measurements of the resistance of the wire before a test, allows finding how the calibration law is changing. Regarding the turbulence intensity, since it is computed as a ratio between the fluctuations and the mean measured values, it is much less sensitive to the problem of wire and gas temperature determination as well as aging, and reliable results are obtained.

Downstream of the stage, the temperature of the flow is much colder and allows us to operate at lower overheat ratios. The time-averaged velocity measurements are thus more accurate and compare reasonably well with the velocity distribution derived from a total pressure probe.

The periodic fluctuations of the flow due to the rotor wake and shock passage are also well resolved. A clear distribution of random unsteadiness can be observed, which was not the case using fast response total pressure probes.

Acknowledgment

Special thanks to Nicolas Billiard and Pavel Antos for their support during the preliminary investigations and the testing.

Nomenclature

A, B, n = calibration coefficients
$C_{s,ax}$ = axial stator chord
d = diameter (m)
E = hot-wire output voltage (V)
E^* = generalized hot-wire output voltage ($V/K^{0.5}$)
h = convective heat transfer coefficient (W/m^2K)
H = vane height (m)
k = thermal conductivity (W/mK)
Nu = Nusselt number ($h \times d/k$)
P = pressure (bar)
Q = heat (J)
R = resistance (Ω)
r^2 = correlation coefficient
Re = Reynolds number ($\rho \cdot u \cdot d_{wire}/\mu$)
S = surface area (m^2)
T = temperature (K)
t = time (s)
u = flow velocity (m/s)
u^* = generalized flow velocity (m^{-1})
y = span-wise direction (m)

Greek Symbols

α_0 = temperature coefficient of resistivity (K^{-1})
μ = dynamic viscosity (kg/m/s)
ρ = density (kg/m^3)
Φ = phase

Subscripts

0 = initial conditions; total conditions
1 = stage inlet
3 = stage outlet
ag = aging
s = static

Abbreviations

CTA = constant temperature anemometer
PLA = phase locked average
RMS = root mean square, $\sqrt{\Sigma_1^n (x-\bar{x})^2/n}$
OHR = overheat ratio
Tu = turbulence intensity

References

[1] Lopez Peña, F., and Arts, T., 1994, "The Rotating Slanted Hot Wire Anemometer in Practical Use," *Proceeding of the 2nd Int. Conf. On Experimental Fluid Mechanics*, Torino, Italy, July.
[2] Ng, W. F., and Epstein, A. H., 1983, "High-Frequency Temperature and Pressure Probe for Unsteady Compressible Flows," Rev. Sci. Instrum., **54**, pp. 1678–1683.
[3] Brunn, H. H., 1995, *Hot-Wire Anemometry*, Oxford University Press, New York.
[4] Day, I. J., 1993, "Stall Inception in Axial Flow Compressors," ASME J. Turbomach., **115**(1), pp. 1–9.
[5] Smith, L. H., 1966, "Wake Dispersion in Turbomachines," ASME J. Basic Eng., **88**, pp. 688–690.
[6] Hodson, H. P., 1985, "Measurements of Wake-Generated Unsteadiness in the Rotor Passages of Axial Flow Turbines," ASME J. Eng. Gas Turbines Power, **107**, pp. 467–476.
[7] Bendnarek, S., Elsner, J. W., and Drobniak, S., 1993, "Turbulence and Unsteadiness of the Flow Field in a Single Stage Cold Air Turbine," *Int. Symposium on Experimental and Computational Aero-thermodynamics of Internal Flow.*
[8] Yamamoto, A., 1991, "Instantaneous Three Dimensional Flows due to Rotor-Stator Interaction in a Low Speed Axial Flow Turbine," *Proceedings of the European Conference in Turbomachinery: "Latest Developments in a Changing Scene*," London.
[9] Kost, F., Hummel, F., and Tiedemann, M., 2000, "Investigation of the Unsteady Rotor Flow Field in a Single HP Turbine Stage," ASME Paper No. 2000-GT-432.
[10] Lang, H., Mørck, T., and Woisetschläger, J., 2002, "Stereoscopic Particle Image Velocimetry in a Transonic Turbine Stage," Exp. Fluids, **32**, pp. 700–709.
[11] Schultz, D. L., Jones, T. V., Oldfield, M. L. G., and Daniels, L. C., 1977, "A New Transient Cascade Facility for the Measurements of Heat Transfer Rates," *AGARD Symposium on "High Temperature Problems in Gas Turbines*," AGARD CP 299. Paper No. 3, Ankara, Turkey.
[12] Sieverding, C. H., and Arts, T., 1992, "The VKI Compression Tube Annular Cascade Facility," ASME Paper No. 92-GT-336.
[13] Sheldrake, C. D., and Ainsworth, R. W., 1996, "Rotating Hot-Wire Measurements in a Model Turbine Stage," *13th Symposium Measuring Techniques for*

Transonic and Supersonic Flow in Cascades and Turbomachines, ETH Zurich, Paper No. 21.
[14] Collis, D. C., and Williams, M. J., 1959, "Two Dimensional Convection From Heated Wires at Low Reynolds Numbers," J. Fluid Mech., **16**, pp. 357–384.
[15] King, L. V., 1914, "On the Convection of Heat from Small Cylinders in a Stream of Fluid. Determination of Convective Constants of Small Platinum Wires with Application to Hot-wire Anemometry," Philos. Trans. R. Soc. London, Ser. A, **214**, pp. 373–432.
[16] Abdel Rahman, A., Tropea, C., Slawson, P., and Strong, A., 1987, "On Temperature Compensation in Hot-Wire Anemometry," J. Phys. E, **20**, pp. 315–319.
[17] Bradbury, L. J.S., and Castro, I. P., 1972, "Some Comments on Heat Transfer Laws for Fine Wires," J. Fluid Mech., **51**, pp. 487–495.
[18] Koch, F. A., and Gartshore, I. S., 1972, "Temperature Effect on the Hot-Wire Anemometer Calibration," J. Phys. E, **5**, pp. 58–61.
[19] Consigny, H., 1980, "Etude expérimentale et théorique des échanges thermiques convectifs a la surface des aubes de turbines," Ph.D. thesis, Brussels, Belgium.

Design and Off-Design Characteristics of the Alternative Recuperated Gas Turbine Cycle With Divided Turbine Expansion

Sung Hoon Hwang

Soo Hyoung Yoon

Tong Seop Kim[1]
Associate Professor
e-mail: kts@inha.ac.kr

Department of Mechanical Engineering,
Inha University,
253 Yonghyun-Dong,
Nam-Gu, Incheon 402-751, Korea

In order to fully address the characteristics of the alternative recuperated cycle with divided turbine expansion, both design and off-design analyses have been performed. Two types of mechanical design are assumed: two shaft and single shaft. In particular, optimal pressure ratio division between the high- and low-pressure turbines is evaluated for the single-shaft configuration. It is predicted that the alternative recuperated cycle hardly exhibits sensible design efficiency advantage over the conventional recuperated cycle for moderate turbine inlet conditions and with usual component performances. An advantage of the alternative cycle with single-shaft design is that thermal efficiency is less sensitive to compressor pressure ratio compared to other configurations, and we can also have flexibility in the turbine division without much efficiency loss. The part load analyses have been carried out with the aid of realistic component maps and models for off-design operation. In addition to the general fuel only control, a variable speed control is assumed as the part load operating strategy of the single-shaft configuration. Obvious advantage with the alternative cycle is observed in the variable speed operation of the single-shaft design. With this strategy, the part load efficiency of the alternative cycle is far superior to the conventional cycle. Almost constant efficiency is predicted for a wide power range. [DOI: 10.1115/1.2364195]

Introduction

Recently, there has been increasing attention given to recuperated cycle gas turbines due to their great potential for various applications. A representative recuperated cycle gas turbine is the micro gas turbine. Thermal efficiencies of commercial micro gas turbines adopting recuperators are around 30% and endeavors are still being made to develop more efficient and power-upgraded versions. Thermal efficiency over 40% is the current goal of micro gas turbine developers [1]. The commercialization of recuperated gas turbines is also being attempted in small- to midsize industrial applications. Thermal efficiency between 35 and 40 % has been obtained recently in the power range of several megawatts [2,3]. Thus, the future development effort for the recuperated gas turbine will be increased further.

In addition to the practical development of the conventional recuperated cycle, an alternative concept has been suggested recently in several references. In the alternative cycle, the turbine expansion process is divided into two parts and the recuperator locates between them. Figure 1 compares, schematically, the temperature-entropy diagrams of the conventional cycle and the alternative cycle. First, recent theoretical analysis can be found in the studies of mid-1990s. Facchini [4] suggested the cycle and analyzed the design performance. Facchini and Sguanci [5] carried out the off-design performance analysis. Their main result was that regeneration is possible even at high pressure ratios, and thus, conventional gas turbines of high pressure ratio can be converted into the cycle to increase the efficiency. The two-shaft (aeroderivative) gas turbines were recommended for the conversion since the mechanical separation of the two shafts seems suitable for the insertion of the recuperator. Very recently, more analysis results have been reported for the same cycle. Cardu and Baica [6] analyzed the design performance of the cycle and concluded that the alternative cycle is better than the conventional cycle. However, their result is not general because their study was limited to the ideal cycle. Dellenback [7] also suggested the same cycle and carried out design performance analysis and a couple of parametric analyses. His conclusion is that the new cycle is optimized at a higher pressure ratio than the conventional regenerative cycle with a high maximum efficiency. However, the results are still not very reliable, especially quantitatively, because his calculation was based on constant thermodynamic properties. Elmegaard and Qvale [8] conducted more practical analyses based on variable properties and concluded that the alternative cycle is advantageous in a rather limited range of the design parameters.

Even though some aspects of the alternative cycle have been examined recently, as in the studies mentioned above, the idea of the divided expansion was originally described briefly in a literature [9] prior to those papers. In the literature, it is stated that the ideal cycle with the divided expansion is more efficient than the ideal conventional cycle for all pressure ratio conditions. However, most of the previous analyses, which adopted assumptions close to reality, have generally concluded that the divided expansion does not always provide better efficiency than the conventional cycle. Accordingly, a systematic summary on the alternative cycle, which provides a general and complete view on its design performance characteristics, is required.

Besides design performance, attention must also be paid to the off-design performance of gas turbines, since they usually operate at part load conditions for a considerable part of their lifetimes. Regardless of gas turbine configurations, performance generally degrades with a reduction in power. Accordingly, consideration must be given to the task of enhancing the part load performance to improve overall fuel economy. Therefore, in order to fully ad-

[1]Corresponding author.

Contributed by the International Gas Turbine Institute (IGTI) of ASME for publication in the JOURNAL OF ENGINEERING FOR GAS TURBINES AND POWER. Manuscript received October 1, 2005; final manuscript received February 1, 2006. IGTI Review Chair: R. S. Abhari. Paper presented at the ASME Turbo Expo 2006: Land, Sea and Air (GT2006), Barcelona, Spain, May 8–11, 2006, Paper No. GT2006-91311.

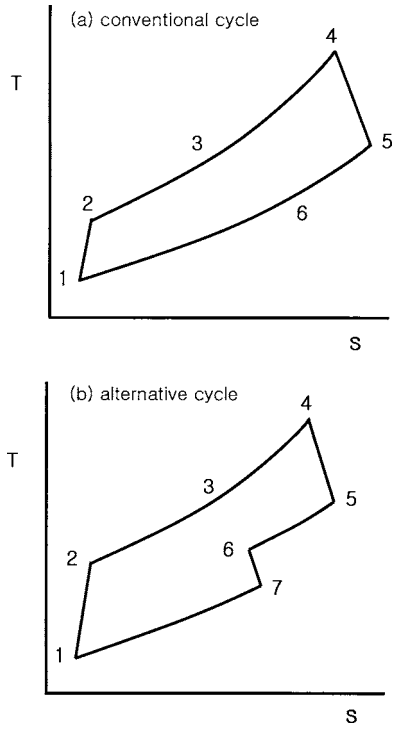

Fig. 1 Temperature–entropy diagrams of conventional and alternative recuperated cycles: (*a*) conventional cycle and (*b*) alternative cycle

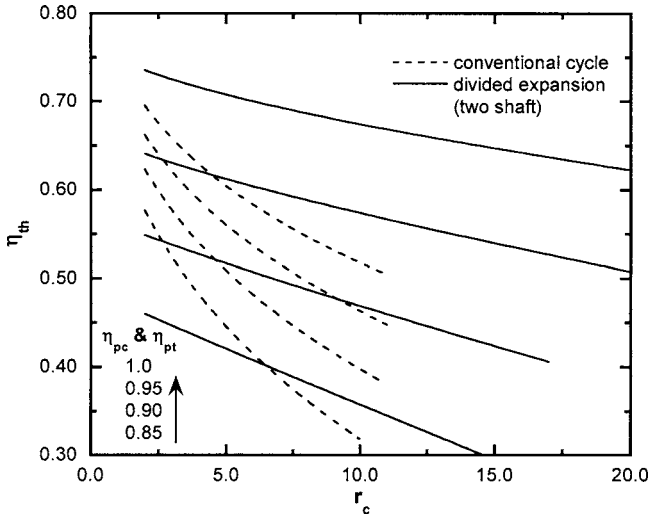

Fig. 2 Effect of compressor and turbine efficiencies on thermal efficiency (working medium: air, t=4, recuperator effectiveness=1.0)

dress the characteristics of the alternative cycle, the off-design (part load) performance should also be evaluated and compared to that of the conventional cycle.

This study aims to perform both the design and off-design analyses of the alternative recuperated cycle with divided turbine expansion as completion of the fundamentals of the cycle and to summarize cons and pros in various aspects, providing integrated information about this cycle. This paper consists of three parts. First, the fundamental characteristics of the cycle is examined with a focus on the influence of the component performance on the cycle performance. Second, various design options of the cycle including gas turbine configurations are investigated with practical assumptions. Last, part load analysis of the cycle is conducted and its performance is compared to that of the conventional cycle.

Fundamental Characteristics of the Cycle

Prior to the main analysis, the fundamental thermodynamic characteristics of the alternative cycle needs to be addressed. The thermodynamic beginning point should be the ideal cycle. The assumption of reversible components and constant properties enables analytical expressions for the thermal efficiencies of not only the conventional regenerative cycle but also the alternative cycle. They can be easily derived as follows:

$$\eta_{th} = 1 - \frac{c}{t}: \text{ conventional regenerative cycle} \tag{1}$$

$$\eta_{th} = 1 - \frac{c}{te_{\text{lpt}}} = 1 - \frac{e_{\text{hpt}}}{t}: \text{ divided expansion} \tag{2}$$

where

$$t = \frac{T_4}{T_1}, \quad e_{\text{hpt}} = \left(\frac{P_4}{P_5}\right)^{(k-1)/k}, \quad e_{lpt} = \left(\frac{P_6}{P_7}\right)^{(k-1)/k}$$

$$\text{and} \quad c = \left(\frac{P_2}{P_1}\right)^{(k-1)/k} = e_{\text{hpt}}e_{\text{lpt}}$$

Since the temperature ratio e_{hpt} and e_{lpt} are always greater than 1 but less than c, the alternative cycle exhibits higher thermal efficiency than the conventional cycle for all pressure ratios. This is the same as what was found in the literature [6,9] and an advantageous feature of the cycle. However, it does not seem always true for realistic cycles, judging from the results of others [7,8]. The gap between these two opposite observations should be explained. For this purpose, simple cycle calculations are made with varying irreversibilities of the compressor and the turbine as well as the incompleteness of the heat transfer at the recuperator. A closed-cycle gas turbine operating with air is assumed in this section. Of course, varying air properties with temperature is used. A more practical analysis based on realistic properties will be made in the following sections. The effects of the compressor and turbine efficiencies and the regenerator effectiveness are separately treated. The mechanically simple way of realizing the divided expansion is to adopt a two-shaft configuration with a free turbine. Thus, analysis is performed for the two-shaft system.

As pointed above, the divided expansion leads to higher efficiency for all pressure ratios if the cycles are ideal. Its superiority becomes manifested as the pressure ratio increases. Of course, at a very low pressure ratio, two cycles approaches Carnot cycle efficiency, with T_4 and T_1 as the heat source and the heat rejection temperatures. Assuming constant properties, the maximum pressure ratio that allows the recuperator ($T_2=T_5$) can be derived as follows:

$$\text{Conventional cycle:} \quad c^2 = t \tag{3}$$

$$\text{Divided expansion:} \quad ce_{\text{hpt}} = t \tag{4}$$

Therefore, the maximum possible pressure ratio of divided expansion is higher than that of the conventional cycle. This can be confirmed in Fig. 2 even with variable properties. Figure 2 illustrates the effects of efficiencies of the compressor and the turbine on the thermal efficiency of both cycles for the case of t=4. The recuperator effectiveness is assumed 100% in order to see only the effects of turbomachinery efficiency. The ideal alternative cycle is superior to the ideal conventional cycle. But, the alternative cycle is more influenced by the reduction of the component efficiencies as clearly shown in Fig. 2. Hence, with reduction in the turbomachinery efficiencies, the thermal efficiency of the alternative cycle

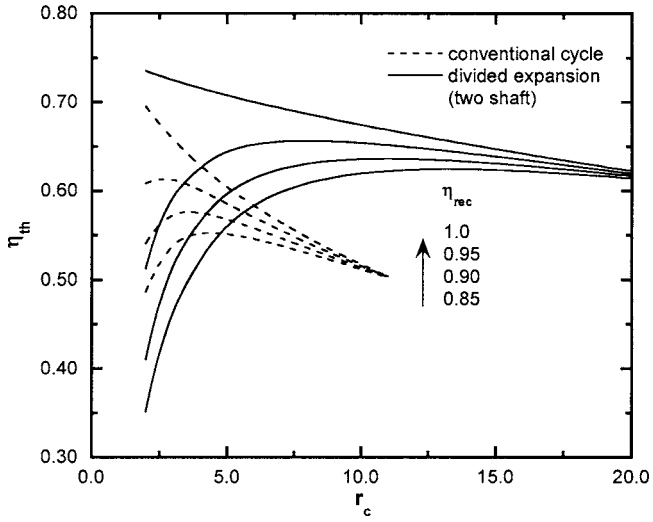

Fig. 3 Effect of recuperator effectiveness on thermal efficiency (working medium: air, t=4, compressor and turbine efficiency=1.0)

becomes lower than the conventional cycle efficiency starting from the low pressure ratio range. This range of inferior performance extends as the component efficiency reduces further. Figure 3 shows the effect of the recuperator effectiveness. In this case, a reversible compressor and turbine are assumed. The incomplete heat exchange at the recuperator causes more severe efficiency reduction of the alternative cycle at the lower compressor pressure ratio conditions. However, the maximum efficiency of the alternative is higher than that of the conventional cycle for all recuperator effectiveness values. Figure 4 shows the combined effects of Figs. 2 and 3. With the practical recuperator effectiveness, the maximum efficiency of the divided expansion can be higher than that of the conventional cycle only when the compressor and turbine efficiencies are very high.

The conclusion from this fundamental examination is that if component irreversibilities are very small, the alternative cycle with divided expansion is superior to the conventional cycle in terms of the cycle efficiency. The alternative cycle is more influenced by the reduction of the component efficiencies. Only with very high component efficiencies, which are not usually obtainable in practical gas turbines, the maximum efficiency of the alternative cycle is higher than that of the conventional cycle. Otherwise, the alternative cycle can be hardly superior to the conventional cycle.

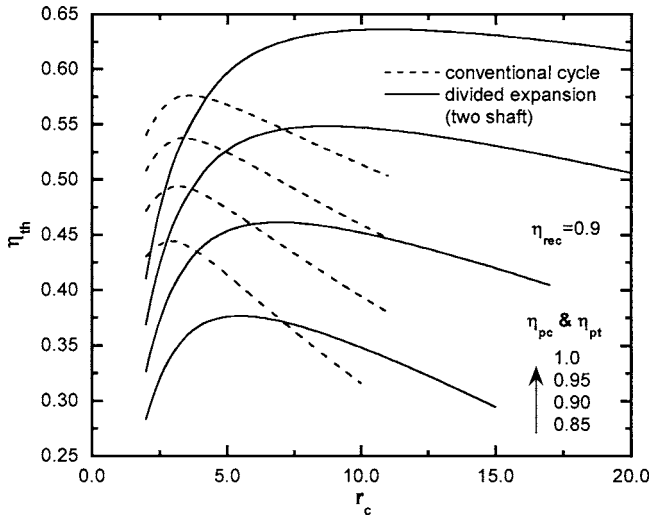

Fig. 4 Combined effects of compressor and turbine efficiencies and recuperator effectiveness on thermal efficiency (working medium: air, t=4, η_{reg}=0.9)

Practical Design Considerations

In this section, results of more practical analyses will be presented. Realistic cycle analyses with practical properties are made. For the conventional recuperated cycle, the single-shaft configuration is applied. Since there is no need to adopt only the two-shaft configuration for the alternative cycle, the single-shaft configuration is also considered. With the single-shaft design, the intermediate pressure (P_5) can be chosen arbitrarily and may be optimized to produce the maximum thermal efficiency of the cycle.

Power and efficiency of the alternative cycle are expressed as follows:

$$\text{Two shaft:} \quad \dot{m}_g \cdot (h_4 - h_5) = \dot{m}_a \cdot \frac{(h_2 - h_1)}{\eta_m}$$

$$\dot{W}_{\text{net}} = \dot{m}_g \cdot (h_6 - h_7) \cdot \eta_m \cdot \eta_{\text{gen}} \tag{5}$$

$$\text{Single shaft:} \quad \dot{W}_{\text{net}} = \left[\dot{m}_g \cdot \{(h_4 - h_5) + (h_6 - h_7)\} - \dot{m}_a \cdot \frac{(h_2 - h_1)}{\eta_m} \right] \cdot \eta_{\text{gen}} \tag{6}$$

$$\text{Thermal efficiency:} \quad \eta_{th} = \frac{\dot{W}_{\text{net}}}{\dot{m}_f \cdot LHV_f} \tag{7}$$

Analysis has been made in the turbine inlet temperature (T_4) range from 1100 to 1500 K. Since the primary concern of the recuperated cycle is midsize to small gas turbines, the following polytropic efficiencies of the compressor and the turbine [10] for those class gas turbines are used. The effect of the pressure ratio on the design efficiency of the turbomachinery is included

$$\eta_{pc} = 1 - \left[0.15 + \frac{(r_c - 1)}{90} \right] \tag{8}$$

$$\eta_{pt} = 1 - \left[0.10 + \frac{(r_t - 1)}{180} \right] \tag{9}$$

The temperature effectiveness of the recuperator is defined as follows:

$$\eta_{\text{rec}} = \frac{T_3 - T_2}{T_5 - T_2} \tag{10}$$

Turbine cooling is not considered because the high turbine inlet temperatures is assumed to be satisfied by the advanced materials [1]. Ambient condition is 101.3 kPa and 288.15 K. The assumed recuperator effectiveness is 0.85. Pressure losses of 1–4% are assumed at every flow element, such as inlet and outlet ducts, recuperator, and combustor. Mechanical and generator efficiencies of 98 and 93 % are assumed.

Comparisons of thermal efficiency and specific power between the conventional cycle and the alternative cycle are shown in Figs. 5 and 6, respectively. The qualitative efficiency trends of the conventional cycle and the two-shaft alternative cycle are similar to those of Fig. 4. At a low turbine inlet temperature, the alternative cycle is inferior to the conventional cycle. As the turbine inlet temperature increases, the gap between the two cycles in terms of the maximum efficiency becomes smaller. In general, the specific power of the alternative cycle is also smaller. In the two-shaft alternative cycle, the compressor pressure ratio corresponding to the maximum efficiency point is more than two times higher than the conventional cycle.

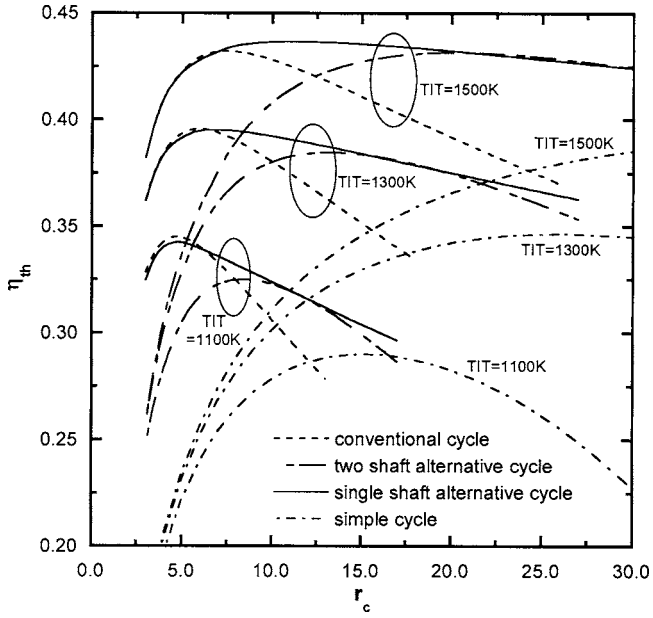

Fig. 5 Thermal efficiency versus compressor pressure ratio

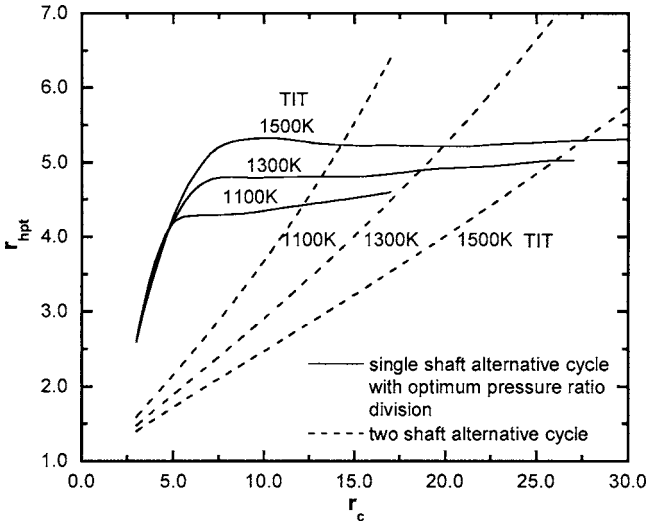

Fig. 7 Optimal pressure ratio of the high-pressure turbine

By designing with the single-shaft arrangement, more even efficiency distribution can be obtained in the middle pressure ratio range. The single-shaft results are based on the optimal division of the two turbine sections. Up to the compressor pressure ratio corresponding to the maximum efficiency of the conventional cycle, the alternative cycle is meaningless; that is, the optimal efficiency is obtained by the conventional cycle (no work contribution of the low-pressure turbine). Over this critical pressure ratio, the optimum pressure ratio division of the two turbine sections exists. Thermal efficiency of this optimized single-shaft arrangement is even higher than that of the conventional recuperated cycle at all high compressor pressure ratios. The results indicate that the optimization of the expansion ratios of the two turbine sections in the single-shaft configuration makes it possible to obtain a smooth extension of the thermal efficiency of the conventional cycle up to very high compressor pressure ratios. Even with very high pressure ratios, the alternative cycle configuration is more efficient than the simple cycle as shown in Fig. 5. The specific power of the optimized single-shaft arrangement is still smaller than that of the conventional cycle, but higher than that of the two-shaft arrangement up to nearly the maximum efficiency point of the two-shaft case.

Figure 7 illustrates the variation in the pressure ratio of the high-pressure turbine. The curves of the single-shaft alternative cycle are those for the optimized divisions, which lead to the results of Figs. 5 and 6. For comparison, results for the two-shaft configuration are also shown. In case of the two-shaft configuration, the pressure ratio of the high-pressure turbine should increase with increasing compressor pressure ratio because of the increase of the compressor work. If we can divide the turbine pressure ratios arbitrarily, maintaining the recuperator inlet temperature (the exit temperature of the high-pressure turbine) high is beneficial in view of the inherent characteristics of the recuperated cycle. However, too high a temperature requires reduction of the work of the high-pressure turbine, which means a negative effect on the power. In the single-shaft case, these two countereffects result in the optimal pressure ratio division between the two turbine sections. Figure 8 illustrates the dependence of the thermal efficiency on the pressure ratio of the high-pressure turbine. The optimized pressure ratio of the high-pressure turbine increases up

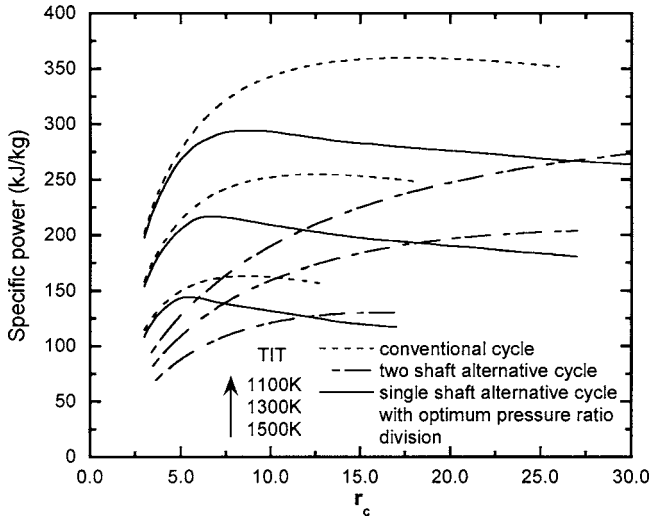

Fig. 6 Specific power versus compressor pressure ratio

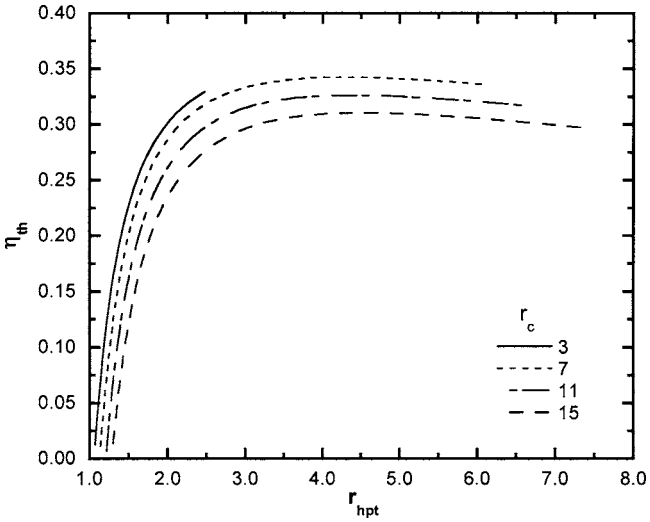

Fig. 8 Examples of dependence of thermal efficiency of the single shaft on the pressure ratio setting of the high-pressure turbine (TIT=1100 K)

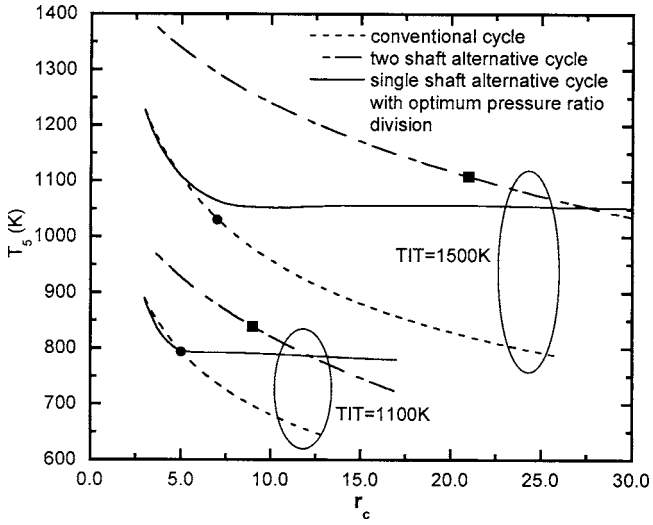

Fig. 9 Recuperator inlet temperature

to a certain compressor pressure ratio. Until then, the conventional recuperated cycle is the optimized solution (no need to divide the turbine). Over this compressor pressure ratio, there exists an optimal pressure ratio division that produces a maximum efficiency. The exact optimum pressure ratio of the high-pressure turbine remains almost constant regardless of the total pressure ratio, producing the results of Fig. 7. However, the thermal efficiency is not very sensitive to the selection of the pressure ratio division around the optimal point, as clearly shown in Fig. 8. This may provide a flexibility in the selection of the position of the turbine separation when converting an existing single-shaft gas turbine adopting a multistage turbine (with already fixed-stage pressure ratios) into the recuperated cycle version.

A critical factor in designing the recuperated gas turbine is the recuperator inlet temperature. It plays an important role in the aspect of performance as mentioned above, but it should also conform to the design technology, such as material capability of the recuperator. The limitation on this recuperator inlet gas temperature is as severe as that on the turbine inlet temperature [1]. The variations in the recuperator inlet temperature of the three configurations are shown in Fig. 9 for two turbine inlet temperatures. The increase of the compressor pressure ratio naturally leads to the lower recuperator inlet temperature (T_5) for the conventional and two-shaft alternative cycles. T_5 of the optimized single-shaft alternative cycle decreases in the initial range but maintains almost constant for sufficiently high pressure ratios due to the nearly constant pressure ratio of the high-pressure turbine in Fig. 7. The maximum efficiency points are marked for the conventional and two-shaft alternative cycles. At the maximum efficiency conditions, the two-shaft design requires 50–100 °C higher recuperator inlet temperature in comparison to the conventional cycle. However, the single-shaft design may result in a comparable recuperator inlet temperature to the conventional case.

The conclusion from this design analysis is that even though the two-shaft design of the alternative cycle seems feasible in the aspect of mechanical design simplicity, its efficiency cannot exceed the conventional cycle efficiency and, furthermore, the specific power is considerably smaller when designed at the maximum efficiency point. Thus, the two-shaft configuration can be applied only to very limited usages, such as modification of existing high pressure ratio aeroderivative engines into the recuperated cycle version focusing on the efficiency upgrade despite the power reduction. The single-shaft design with optimal division of the turbine pressure ratios provides a rather wide design range of compressor pressure ratio with only moderate efficiency loss (or even higher efficiency) in comparison to the conventional cycle. Moreover, it alleviates the reduction of the specific power and can be designed with a recuperator inlet temperature equivalent to the conventional cycle. Therefore, from the thermodynamics point of view, the single-shaft design is more advantageous in realizing the alternative cycle with divided turbine expansion.

Part Load Performance

Operation Strategies and Modeling. Diverse part load operation strategies are analyzed comparatively among different design options, such as the single-shaft conventional cycle and single- and two-shaft alternative cycles.

The simplest way of controlling the gas turbine in response to load change is to modulate the fuel supply. This method can be called fuel-only control. However, other possibilities also need to be considered for the recuperated cycle. In view of thermodynamic performance, the most important process in the regenerative gas turbine is the exhaust heat recovery process at the recuperator. Therefore, full utilization of the heat recovery effect during the part load operation is essential. For this purpose, it is very advantageous to keep the recuperator inlet temperature as high as possible by modulating the airflow rate as well. This variable airflow control improves the part load efficiency drastically for cycles involving heat recovery, such as combined cycle, cogeneration system, and recuperated cycle [11,12]. In realizing this airflow reduction in the single-shaft engine, two methods can be used. The first is to use the variable inlet guide vane of the compressor, and the second is to change the shaft speed. Ideally, the two methods can provide similar level of part load efficiency, but the usual reduction of the compressor efficiency accompanied by the variable guide vane control causes rather smaller efficiency gain and, moreover, the airflow reduction capacity is limited [12]. Gas turbines designed with a free turbine (two-shaft configuration) operate with varying compressor speeds. Thus, they have the intrinsic advantage of high heat recovery capacity since the turbine exhaust temperature is higher due to reduced mass flow at part load conditions [11,12].

In this study, focus is given to the gas turbines for electricity generation. In the fuel-only control, the speed of the shaft connected to the generator should be kept constant. The variable speed operation of the single-shaft configuration is usually applied to small gas turbines. In those cases, the gas turbine shaft drive a high-speed alternator. Then, a digital power controller (AC-DC-AC inverter) converts the varying high frequency into a constant low frequency [13]. The technology has been limited to small gas turbines, such as micro gas turbines up to 200 kW. Recently, however, the high-speed alternator has also begun to find its applications in MW class recuperated cycle gas turbines [3]. Considering that the current development effort for recuperated cycle gas turbines has been focused on up to several MWs, the benefit of using the variable speed strategy will be more manifested in the future.

In this study, both the fuel-only control and the variable speed control are applied to each of the conventional single-shaft cycle and the alternative single-shaft cycle. In addition, the part load operation for the two-shaft design of the alternative cycle is simulated. In the variable speed operation of the single-shaft configuration, the control target is to keep a constant recuperator inlet temperature (T_5) in order to maximize the heat recovery effect. This temperature corresponds to the turbine exit temperature for the conventional cycle and the high-pressure turbine exit temperature for the alternative cycle. Consequently, we have five cases to simulate as summarized in Table 1.

For comparison, design points are selected at the same turbine inlet temperature of 1100 K. The design point of the conventional cycle is the pressure ratio of maximum thermal efficiency. The same principle is applied to the two-shaft alternative cycle. The design pressure ratio of the single-shaft alternative cycle is also given equivalent to that of the two-shaft case. Moreover, the pres-

Table 1 Selected design points for part load analysis

Cycle configuration	Operating strategy	Temperature control
Single shaft conventional cycle	Fuel only control	-
	Variable speed control	Constant T_5
Single shaft alternative cycle	Fuel only control	-
	Variable speed control	Constant T_5
Two shaft alternative cycle	Fuel only control	-

sure ratio division inside the turbine is also set equivalent to that of the two-shaft case. The design points are summarized as follows:

- Turbine inlet temperature: 1100 K
- Design pressure ratio; conventional cycle: 4.3
- Design pressure ratio, alternative cycles: 10.0

The off-design characteristics of the compressor is represented by the performance map. Figure 10 illustrates an example of the compressor map used in this study. The turbine characteristics is described by the Stodola ellipse equation [14] as follows:

$$\frac{\dot{m}_{\text{in}}\sqrt{T_{\text{in}}}/P_{\text{in}}}{(\dot{m}_{\text{in}}\sqrt{T_{\text{in}}}/P_{\text{in}})_d} = \frac{\sqrt{1-(P_{\text{out}}/P_{\text{in}})^2}}{\sqrt{1-(P_{\text{out}}/P_{\text{in}})_d^2}} \tag{11}$$

A counterflow recuperator is assumed. Variation in the effectiveness is modeled using the mass flow rate as the main parameter. The following semi-theoretical correction of the overall heat transfer coefficient can be used for this purpose

$$\frac{U}{U_d} = \left(\frac{\dot{m}}{\dot{m}_d}\right)^z \tag{12}$$

This relation may not be very appropriate for the range of very low relative mass flow where longitudinal heat conduction may affect the effectiveness. However, since the lowest mass flow rate in case of the variable speed operation of this study is ~30% of the design value, application of the relation is assumed to be effective for the whole operating range. With the exponent $z<1.0$, the effectiveness increases with mass flow reduction. The exponent is set at 0.3 based on the examination on the performance variation of practical compact recuperators [12]. The part load analysis has been performed with the aid of process analysis software [15].

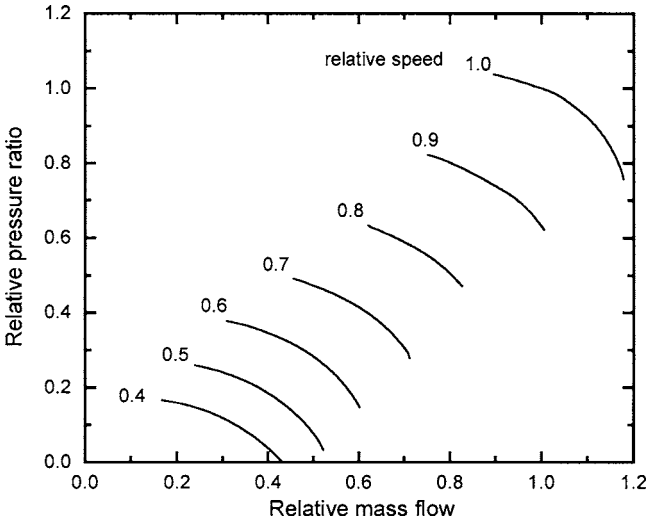

Fig. 10 Example of the compressor map

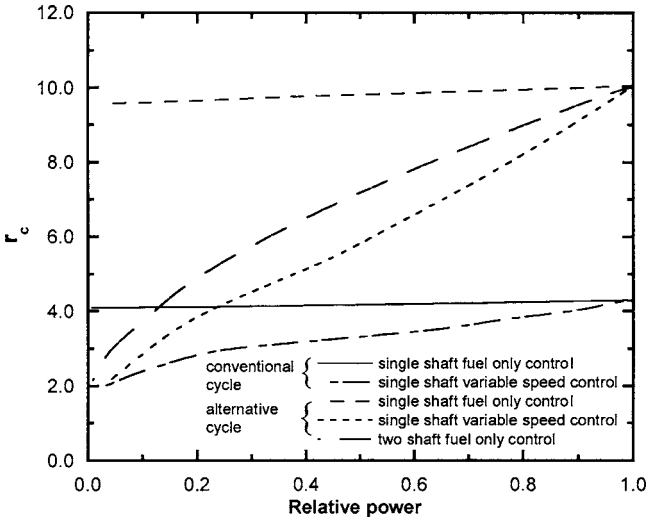

Fig. 11 Variation in the compressor pressure ratio for the part load operation

Results

A single-shaft gas turbine under the fuel-only control operates at a fixed speed. On the contrary, in the gas turbine under the variable speed control, the shaft speed decreases, and thus the airflow rate decreases with power reduction. The high-pressure shaft of the two-shaft gas turbine also reduces its speed for power reduction. As a result, the compressor pressure ratio of the operations involving speed variation changes much during the part load operation, whereas the fuel-only control requires moderate pressure ratio change. This result is shown in Fig. 11. The single-shaft configuration of the alternative cycle requires greater change in the compressor pressure ratio than the two-shaft configuration.

Variations in the hot side temperatures during the part load operation are shown in Figs. 12 and 13 for the conventional cycle and the alternative cycle, respectively. In the single-shaft design, the variable speed control enables far higher recuperator inlet temperature (constant T_5 in this study). The turbine inlet temperature

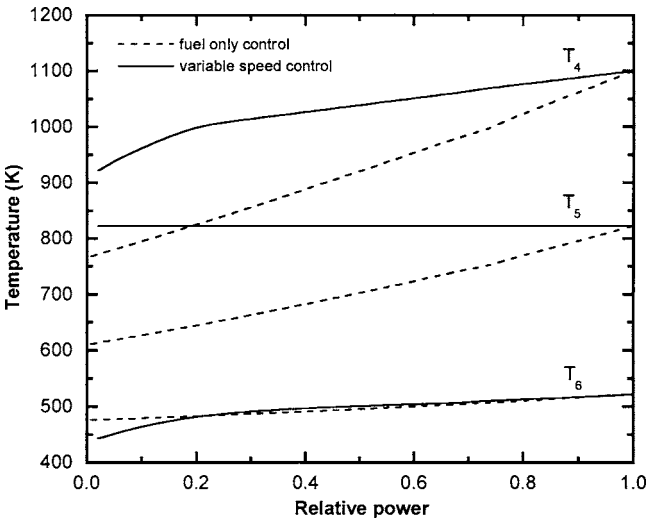

Fig. 12 Variations in the hot side temperatures for the part load operation of the conventional cycle

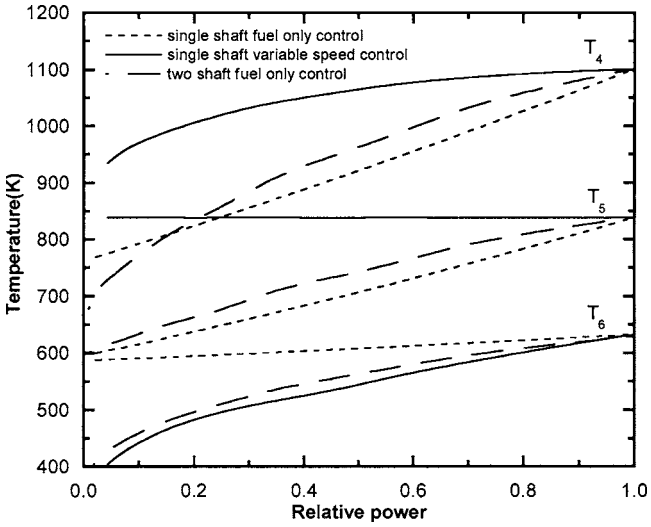

Fig. 13 Variations in the hot side temperatures for the part load operation of the alternative cycle

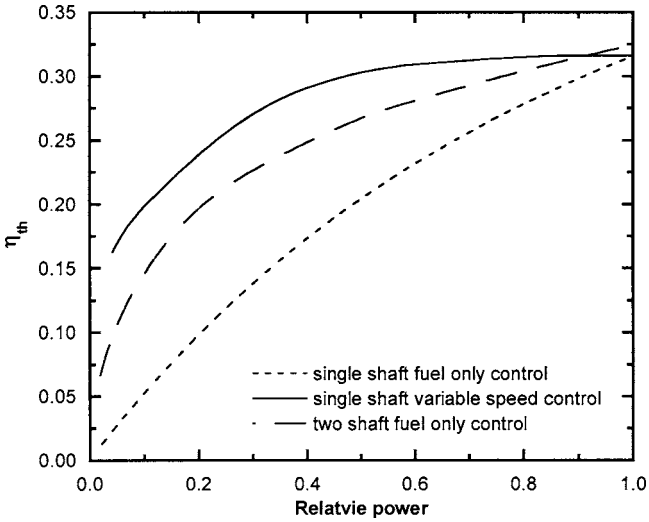

Fig. 15 Variation in part load efficiency of the alternative cycle

is also higher in the variable speed operation. Moreover, the relatively lower compressor pressure ratio, thus the lower recuperator inlet air temperature of the variable speed operation provides much larger temperature change inside the recuperator (for example, T_5-T_6). This explanation is effective for both the conventional and alternative cycle with variable speed operation. However, this is more manifested in case of the alternative cycle (more rapid increase of the temperature difference at the recuperator with power reduction). The two-shaft configuration of the alternative cycle provides larger recuperator temperature difference than the single-shaft conventional cycle with fuel-only control. However, it is not comparable to that of the variable speed control of the single shaft.

Figure 14 shows the resulting thermal efficiencies of the two operating methods of the single-shaft conventional cycle. In the conventional cycle, the variable speed operation provides far enhanced part load efficiency over the simple fuel only control. This is due to the greater temperature difference at the recuperator (better utilization of the heat recovery effect in the regenerative cycle) as pointed out in Fig. 12. Therefore, the variable speed operation should be the primary choice for better fuel economy of

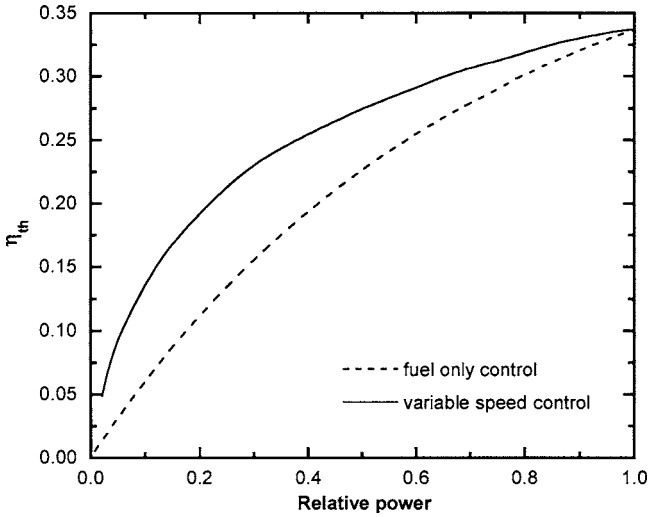

Fig. 14 Variation in part load efficiency of the conventional cycle

the recuperated cycle gas turbines. Figure 15 shows the thermal efficiencies of the three cases of the alternative cycle. The single-shaft gas turbine adopting the fuel-only control exhibits nearly the same part load efficiency as the conventional cycle counterpart. Therefore, no special performance difference exists when controlling the gas turbines only with the fuel. Maintaining a higher recuperator inlet temperature by adopting variable speed operation again improves the part load efficiency. A very important observation is that the degree of the improvement is far greater than in the conventional cycle case. This is closely related to the fact that the heat recovery effect in the recuperator is even greater in the alternative cycle, as mentioned previously. The part load efficiency remains almost at the design value for a very wide power range. Therefore, despite the slightly lower design efficiency, the overall fuel economy must be better than that of the conventional cycle. The two-shaft configuration also shows better part load efficiency than the fuel-only control of the single-shaft configuration. But, the variable speed operation of the single shaft provides even better performance than the two-shaft configuration.

Although not treated in this study, the operation with the variable inlet guide vane for the single-shaft engine and the operation with the variable nozzle area of the free turbine for the two-shaft engine may also improve the part load efficiency of the alternative cycle because they have been proved to be effective for the conventional regenerative cycle [12]. However, since their airflow modulation capacity is rather limited and the efficiencies of the compressor and turbine degrade due to the geometry variation, their part load efficiency is expected to be lower than or, at most, comparable to that of the variable speed operation of the single-shaft configuration.

Conclusion

This study has examined various aspects of the alternative recuperated cycle with divided turbine expansion from the fundamental design characteristics to the part load performance. From the results of this study, the following conclusions are obtained.

1. The alternative cycle is more influenced by the component efficiencies. Only with very high component efficiencies, the maximum cycle efficiency of the alternative cycle is higher than that of the conventional cycle. Otherwise, it is comparable to or less than that of the conventional cycle.

2. Two-shaft design of the alternative cycle requires too high compressor pressure ratio for its efficiency to be comparable to the conventional cycle. On the contrary, the single-shaft design provides a rather wide range of compressor design pressure ratio. Furthermore, the thermal efficiency is not sensitive to the pressure

ratio division in the two turbine sections, which provides good design flexibility. Therefore, from the thermodynamics point of view, the single-shaft design is more advantageous in realizing the alternative cycle with divided turbine expansion.

3. The variable speed control of the single-shaft configuration should be the primary operation strategy because it keeps a higher recuperator inlet temperature, and thus enhances much the part load efficiency in comparison to the fuel-only control. Its usefulness is more manifested in the alternative cycle. Consequently, by designing with a single-shaft configuration and operating with variable shaft-speed, the alternative cycle provides far better part load efficiency than the conventional cycle.

Acknowledgment

This work was supported by Inha University Research Grant.

Nomenclature

- $1-7$ = state in the gas turbine
- c = temperature ratio of the compressor
- e = temperature ratio of the turbine
- h = specific enthalpy (kJ/kg)
- k = specific heat ratio
- LHV = lower heating value (kJ/kg)
- $\dot{m}$ = mass flow rate (kg/s)
- P = pressure (kPa)
- r = pressure ratio
- T = temperature (K)
- t = temperature ratio
- TIT = turbine inlet temperature (K)
- U = overall heat transfer coefficient (kW/m^2K)
- $\dot{W}$ = power (kW)
- z = exponent

Greek

- η_{gen} = generator efficiency
- η_m = mechanical efficiency
- η_{pc} = compressor polytropic efficiency
- η_{pt} = turbine polytropic efficiency
- η_{rec} = recuperaqtor effectiveness
- η_{th} = thermal efficiency

Subscripts

- a = air
- c = compressor
- d = design
- f = fuel
- g = gas
- hpt = high pressure turbine
- in = inlet
- lpt = low pressure turbine
- out = outlet
- t = turbine

References

[1] McDonald, C. F., and Rogers, C., 2005, "Ceramic Recuperator and Turbine—The Key to Achieving a 40 Percent Efficient Microturbine," ASME Paper No. GT2005-68644.
[2] Farmer, R., ed., 2003, "4.6-MW Recuperated Genset is Ready for Its Commercial Debut," Gas Turbine World, **33**(5), pp. 24–25.
[3] Farmer, R., 2004, "Recuperated Marine Gas Turbine is Rated 1800 kW and 38% Efficiency," Gas Turbine World, **35**(3), pp. 32–35.
[4] Facchini, B., 1993, "New Prospects for the Use of Regeneration in Gas Turbine Cycles," *Proc. of ASME Cogen-Turbo*, ASME, New York, IGTI-Vol. 8, pp. 263–269.
[5] Facchini, B., and Sguanci, S., 1994, "RE Cycle: A System for Good Off-Design Performance," *Proc. of ASME Cogen-Turbo*, ASME, New York, IGTI-Vol. 9, pp. 169–175.
[6] Cardu, M., and Baica, M., 2002, "Gas Turbine Installations With Divided Expansion," Energy Convers. Manage., **43**, pp. 1747–1756.
[7] Dellenback, P. A., 2002, "Improved Gas Turbine Efficiency Through Alternative Regenerator Configuration," ASME Paper No. GT-2002-30133.
[8] Elmegaard, B., and Qvale, B., 2004, "Regenerative Gas Turbines With Divided Expansion," ASME Paper No. GT2004-54225.
[9] Cohen, H., Rogers, G. F. C., and Saravanamuttoo, H. I. H., 1972, *Gas Turbine Theory*, 2nd ed., Longman, London, p. 317.
[10] Wilson, D. G., 1984, *The Design of High-Efficiency Turbomachinery and Gas Turbines*, MIT Press, Cambridge, Ch. 3.
[11] Kim, J. H., Kim, T. S., Sohn, J. L., and Ro, S. T., 2003, "Comparative Analysis of Off-Design Performance Characteristics of Single and Two Shaft Industrial Gas Turbines," ASME J. Eng. Gas Turbines Power, **125**, pp. 954–960.
[12] Kim, T. S., and Hwang, S. H., 2006, "Part Load Performance Analysis of Recuperated Gas Turbines Considering Engine Configuration and Operation Strategy," Energy, **31**, pp. 260–277.
[13] Rodgers, C., Watts, J., Thoren, D., Nichols, K., and Brent, R., 2001, Microturbines, *Distributed Generation*, Borbely, A. M., and Kreider, J. F., eds., CRC Press, Boca Raton, FL, pp. 119–150.
[14] Dixon, S. L., 1978, *Fluid Mechanics, Thermodynamics of Turbomachinery*, 3rd ed., Pergamon Press, New York.
[15] Aspen Technology, Inc., 2004, HYSYS ver. 3.2.

Genetic Algorithm Optimization for Primary Surfaces Recuperator of Microturbine

Wang Qiuwang[1]
e-mail: wangqw@mail.xjtu.edu.cn

Liang Hongxia

Xie Gongnan

Zeng Min

Luo Laiqin

Feng ZhenPing

State Key Laboratory of Multiphase Flow
in Power Engineering,
Xi'an Jiaotong University,
Xi'an, Shaanxi 710049, P.R. China

In recent years, the genetic algorithm (GA) technique has gotten much attention in solving real-world problems. This technique has a strong ability for global searching and optimization based on various objectives for their optimal parameters. The technique may be applied to complicated heat exchangers and is particularly useful for new types. It is important to optimize the heat exchanger, for minimum volume/weight, to save fabrication cost or for improved effectiveness to save energy consumption, under the requirement of allowable pressure drop; simultaneously it is mandatory to optimize geometry parameters of heating plate from technical and economic standpoints. In this paper, GA is used to optimize the cross wavy primary surface (CWPS) and cross corrugated primary surface (CCPS) geometry characteristic of recuperator in a 100 kW *microturbine, in order to get more compactness and minimum volume and weight. Two kinds of fitness assignment methods are considered. Furthermore, GA parameters are set optimally to yield smoother and faster fitness convergence. The comparison shows the superiority of GA and confirms its potential to solve the objective problem. When the rectangular recuperator core size and corrugated geometries are evaluated, in the CWPS the weight of the recuperator decreases by 12% or more; the coefficient of compactness increases by up to 19%, with an increase of total pressure drop by 0.84% compared to the original design data; and the total pressure drop versus the operating pressure is controlled to be less than 3%. In the CCPS area compactness is increased to 70% of the initial data by decreasing pitch and relatively high height of the passage, the weight decreases by 17–36%, depending on the inclination angle* (θ). *Comparatively the CCPS shows superior performance for use in compact recuperators in the future. The GA technique chooses from a variety of geometry characters, optimizes them and picks out the one which provides the closest fit to the recuperator for microturbine.*
[DOI: 10.1115/1.2436550]

Keywords: genetic algorithms, cross wavy primary surface, cross corrugated primary surface, optimization, recuperator, microturbine

Introduction

Microturbine technology and deployment were initially welcomed with enthusiasm by the scientific community and industry. However, the actual applications of these machines have recently required new design in order to ensure better competitiveness and profitability in a deregulated energy distribution market. The specific capital cost is still high, and operational availability and flexibility need to be further improved to match the customers' needs in terms of an efficient, low cost, and durable supply of heat, cooling, and power.

It has been clearly demonstrated that an exhaust heat recovery recuperator is mandatory to achieve electrical efficiency of 30% or higher for microturbine engines, which is possible for a cycle pressure ratio of about 4:1. The cycle airflow is a function of the power requirement. To increase the efficiency and reduce the CO_2 emission, it is mandatory to develop a more efficient thermodynamic cycle. From a technical point of view, such a gas–air recuperator must achieve high effectiveness, good reliability, compact size, light weight, structural integrity, be leak tight, and have minimal pressure drops. From a thermoeconomic perspective, since the recuperator represents up to 30% of the total capital cost of a microturbine package, it needs to be optimized by taking into account both technical and economic considerations.

The major technological constraint for the development of the microturbine is the production weight of the unit. A microturbine unit fitted with a recuperator, with an efficiency of 90%, can achieve high electrical efficiency. Certainly, the recuperator weight optimization is one of the main challenges in microturbine engine research: a good and cost-effective design could make the difference between acceptability and rejection. Increasing the effectiveness is straightforward but results in a dramatic increase in recuperator size and weight, again aggravating the weight situation. Compact heat exchangers have been extensively studied in the open literature [1–5]. The heat transfer and flow resistance characteristics of several primary surfaces are well reported by Utriainen and Sundén [6,7]. It is obvious that different shapes and geometry of heat transfer surfaces strongly affect the heat transfer rate and flow resistance of the recuperator core, but there has been little research and optimization on the recuperator with geometry parameters of other shapes. To improve the heat transfer and pressure loss characteristics of the cross wavy primary surface (CWPS) and cross corrugated primary surface (CCPS), proper genetic algorithm (GA) tools, which could provide the optimized design, from both the technical and economic perspectives, are extremely helpful for achieving this target.

This paper presents the GA approach for the optimization of microturbine recuperators from technical and economic standpoints. With regard to the sizing procedure, a special optimization

[1]Corresponding author.
Contributed by the International Gas Turbine Institute of ASME for publication in the JOURNAL OF ENGINEERING FOR GAS TURBINES AND POWER. Manuscript received June 16, 2006; final manuscript received July 3, 2006. Review conducted by Dilip R. Ballal. Paper presented at the ASME Turbo Expo 2006: Land, Sea and Air, Barcelona, Spain, May 8–11, 2006. Paper No. GT2006-90366.

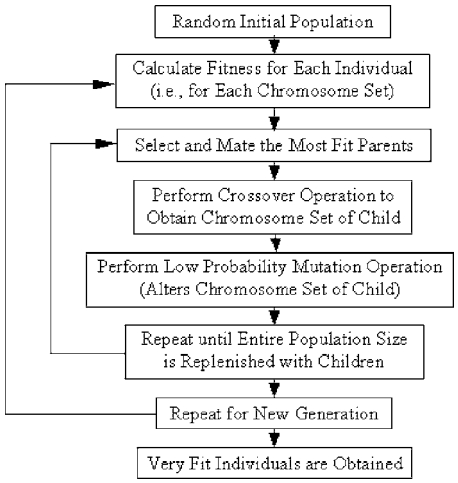

Fig. 1 Flow diagram for genetic algorithm

procedure of the recuperator matrix has been developed [8], which takes into account several targets in a single multi-objective function: the compactness, the pressure drops, and the expected weight of the device. The present work is to optimize CWPS and CCPS geometry parameters for recuperator in 100 kW microturbine under counter-cross-flow conditions. The comparison between original design results and optimum results is made in order to determine their own contribution to the total heat transfer performance and to provide important information needed for the optimization of designing CWPS and CCPS recuperators.

Algorithm Description

Because of the compactness and initial weights, it is important to determine the best possible design, under the available given constraints (areas compactness and/or weight, etc). To improve this procedure an actual optimization algorithm has been implemented in Refs. [9,10].

A brief description of the GA technique will be presented as follows. The main theory behind GA is closely related to the evolution theory of Darwin: survival of the fittest (= the optimal solution). The standard GA uses a population (i.e., a group of possible solutions) of individuals (i.e., parameter sets) that is represented in a binary format. Each parameter is encoded in a binary string. The strings for the separate parameters are then grouped into one long string. The individuals are randomly determined from the search space. An initial population of size is created from a random selection of the parameters in the parameter space. Each parameter set represents the individual's chromosomes. Each of the individuals is assigned a fitness based on how well each individual's chromosomes allow it to perform in its environment. There are then three operations that occur in GA to create the next generation: selection, crossover, and mutation. The "fitness" of the solutions (i.e., the result of the variable that is to be optimized) is determined subsequently from the fitness function, which is evaluated by survival of the fittest. The individual with the maximum fitness within the population has the highest chance to return in the next generation. This new generation is calculated and the process is repeated until the given number of generations is reached or until convergence has been obtained. To assist the visualization of GA procedure, a logic flow diagram is presented in Fig. 1.

This algorithm differs from the general optimization algorithms and search procedures as follows:

1. It uses a coded parameter set instead of the parameters that are to be optimized;
2. The optimal value is searched for within a group of possible solutions as opposed to searching on a one-by-one basis;
3. The algorithm uses the result of the function that is to be optimized as opposed to a derivative or additional information on the problem; and
4. It uses probabilistic rules to generate new solutions instead of deterministic rules.

By giving the above differences of GA compared to the more standard optimization algorithms, GA is preferred for application in discrete optimization problems, such as the optimization of various surfaces heat exchangers systems.

Model Description

In a CWPS recuperator the metal plates are closely stacked in a frame so that the orientation of the corrugation between adjacent plates is nonaligned, and this configuration enhances heat transfer by providing a large effective surface area and generating a complex flow structure in the patterns between the plates. Corrugations also strengthen the plates and give a high structural stability due to the multitude of contact points. Passive enhancement techniques may be used to reduce the physical size of the recuperator core, in the passive techniques secondary flow structures could often generate. The secondary gas and air flow structures in heat exchangers disturb the insulation of near wall layers and thus improve the thermal properties of the duct. This type of heat transfer surface offers heat transfer enhancement by accompanying an acceptable increase of the pressure losses.

The core is the key component of the recuperator, and it occupies the majority volume and weight of recuperator. Header, cover plate and connection tube etc. are auxiliary functions of sealing, connection, and assembly, thus, in this paper only the design of the recuperator core is considered. Taking recuperator weight into account, the core configuration weight is multiplied by coefficient of correction (setting to be 1.25 hereafter).

In the GA method, correlations of heat transfer and pressure drop are necessary to obtain optimal results. Analytical, numerical, optimum, and experimental results for laminar flow heat transfer in complex geometries are essential for the design and operation of compact heat exchangers [11–16]. Since the numerical and optimum investigations of fluid flow and heat transfer in corrugated channels have significant advantages over the experiment, the variation of geometric parameters by numerical simulation is much easier and less costly than by experimental investigations. Furthermore, numerical and optimum results may give detailed information of flow structure, which is difficult to supply by the experiments.

In this paper, the CWPS recuperator for a 100 kW microtubine is used as the optimized model shown in Fig. 2(*a*). The upper and lower plates of a generic couple share the same basic geometry. This CWPS recuperator has a lot of design geometry parameters. It is characterized by corrugation plate geometry parameters as follows: pitch P, internal height H, wavelength λ, internal height a, air side circle radius r, and gas side circle radius R. In the present study, the thickness of the plate is fixed as 0.1 mm, which could be commercially available. Ultimately parameters of P, H, λ, a, r, R are acted optimization variables.

On the other hand, for CCPS (see Fig. 2(*b*)) the primary determinants are the corrugation inclination angle θ, wavelength P, internal height H, radius of the circular plate R, and profile of waviness. These geometrical parameters influence the heat transfer rate, pressure drop, and recuperator core dimensions such as length $B1$, width $B2$, and height $B3$ (Fig. 2(*c*)). Generally, both heat transfer coefficients and friction losses increase with θ of chevron plates. Based on the correlations of Nusselt number and friction factor from Utriainen and Sundén [17] and the modified

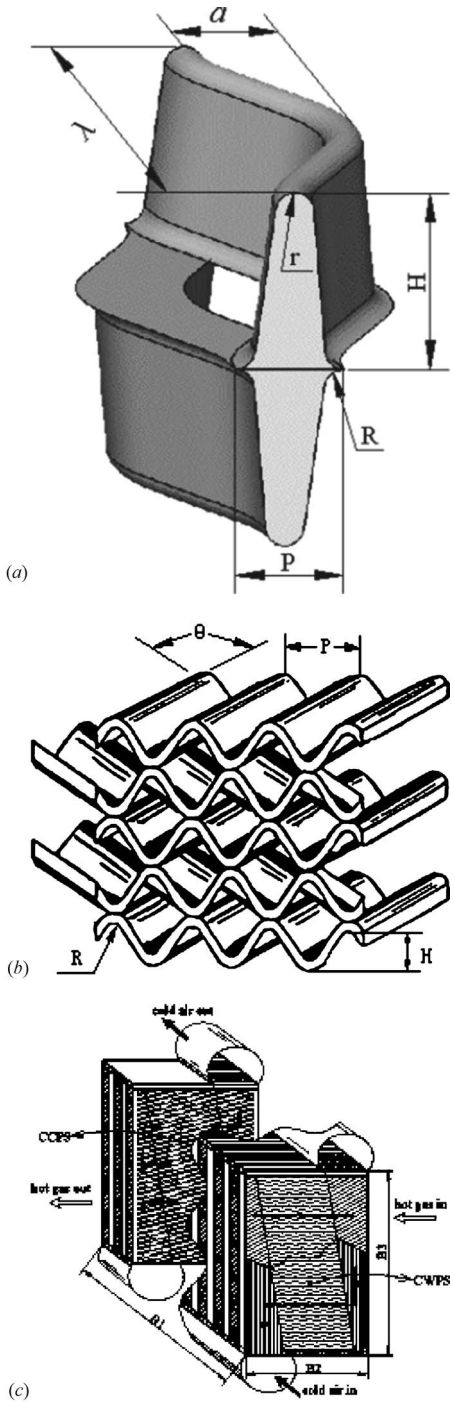

Fig. 2 Model description: (*a*) CWPS geometry parameters; (*b*) CCPS geometry parameters; and (*c*) recuperator matrix

experimental results from Ref. [14], surface geometry variables such as P, H, R were optimized for the fixed values of $\theta = 45$ deg, 60 deg, or 75 deg, respectively.

The total pressure drop is inserted as a target parameter rather than the pressure drop of one side. In fact, thermodynamic calculations show that the cycle performance does not significantly change if the total pressure drops of gas and air sides are kept constant [18]. When the recuperator design must be optimized for a particular application, different targets can be pursued as priorities, such as the best compactness, the minimum weight, and the

Table 1 Description of recuperator key design parameters

Power	(kW)	100
Air flow rate	(kg/s)	0.998
Gas flow rate	(kg/s)	1.014
Pressure ratio	(—)	3.8
Effectiveness	(%)	90
Air inlet temperature	(K)	463
Gas inlet temperature	(K)	927
Gas outlet temperature	(K)	873
Δp_{tot}	(%)	3

control of total pressure drop. In the microturbine field, one of the most important aspects is, certainly, the total weight.

In the present study, the CWPS variables are subject to: 1.4 mm $\leq P \leq$ 3.6 mm, 1.8 mm $\leq H \leq$ 3.5 mm, 2.8 mm $\leq \lambda \leq$ 9.6 mm, and 1.0 mm $\leq a \leq$ 1.4 mm. The others are influenced by the above four variables because they are not independent. The CCPS variables are subject to: 2.8 mm $\leq P \leq$ 5.0 mm, 0.6 mm $\leq H \leq$ 1.4 mm, and 0.32 mm $\leq R \leq$ 0.60 mm. Tournament selection, uniform crossover, and one-point mutation are selected. Sizes of population and maximum evolution generation are set to be 50 and 100, respectively. Probabilities of crossover and mutation are set to be 0.5 and 0.02, respectively. The key characteristics of both heat exchangers are summarized in Table 1.

The implement of optimal design consists of two procedures: one is a GA routine that includes the process of selection/crossover/mutation; the other is the rating (RAT) routine that evaluates performance of CWPS and CCPS. The FORTRAN code has been used for considering the rating problem after decoding individuals to real geometrical sizes. The flow chart of the RAT routine is presented in Fig. 3. It should be noted that the original data in Tables 2 and 3 are also obtained by the RAT procedure.

Results and Discussion

The thermal–hydraulic performance of the heat exchanger is strongly influenced by the surface-corrugation geometry of the plates employed in them. The enhanced heat transfer is directly related to these features, which provide increased effective heat transfer area, disruption, and reattachment of boundary layers, swirl or vortex flow generation, and small hydraulic diameter flow channels. Generally, both heat transfer coefficients and friction losses increase with higher a and lower λ (see Fig. 2(*a*)). As expected, the Reynolds number and the friction factor f are significantly influenced by λ/a, i.e., they increase with decreasing

Begin
Input: □ Dimensions of unit cell.
□ Total heat (Q) transferred in the recuperator matrix, calculated with help of data in table 1, calculate the parameter of property.
Calculate hydraulic diameter D_h and flow area of cell at inlet A_c.
While (Condition of termination is dissatisfied) **do**
Begin
Step 1. Choose the total flow area at inlet A_f.
Step 2. Calculate Re number, Nu number and f factor, using correlations in [3][18].
Step 3. Calculate heat transfer coefficients h for both sides and the overall heat transfer coefficient.
Step 4. Calculate heat transfer area A_{ht}, Coefficient of compactness Sv and weight W.
Step 5. Calculate the total pressure drop Δp_{tot}, if the Δp_{tot} is greater than 3%, then go back to step 1 and adjust the A_f.
End
End

Fig. 3 Flow chart of RAT routine

Table 2 Comparison of the original data and optimized results (CWPS) (G1—fitness=exp(−W); GA2—fitness=Sv/W)

	Geometry parameters									Performance		
CWPS	P (mm)	H (mm)	λ (mm)	a (mm)	r (mm)	R (mm)	$B1$ (m)	$B2$ (m)	$B3$ (m)	Δp_{tot} ($\times 10^2$)	S_v (m^2/m^3)	W (kg)
Original data	1.8	2.3	4.8	1.3	0.35	0.55	0.75	0.28	0.49	2.04	1845	116.73
GA1	1.4	1.8	4.99	1.39	0.24	0.45	0.7	0.26	0.49	2.87	2074	100.46
GA2	1.4	1.8	4.82	1.39	0.25	0.45	0.73	0.25	0.48	2.88	2191	103.1

λ/a. Small λ/a indicates a small volume of the recuperator core. Deeper corrugations (lower P/H) not only increase the effective surface area, but also promote the swirl mixing.

There are many ways to assign the fitness value. In the present study, two different fitness functions were used to calculate the fitness values based on the above results.

Minimum Weight ("GA1"). The conventional genetic algorithm determines global maximum value in search spaces. The objective of the present prediction, however, is to minimize weight of recuperator. Thus a fitness function should be given as follows:

$$\text{fitness} = F \cdot \exp(-W) \tag{1}$$

where W is the weight; and F is the stepwise factor defined by

$$F = \begin{cases} 1, & \Delta p_{-\text{tot}} < 3\% \\ 0, & \Delta p_{-\text{tot}} \geqslant 3\% \end{cases} \tag{2}$$

$\Delta p_{-\text{tot}}$ is the total pressure drop in both sides. It should be noted that the maximum value of fitness indicates the minimum weight. The evolution process of CWPS for minimum weight is the shown in Fig. 4(*a*). At the beginning of the evolution process (about less than 50 generations), the differences between every individual are relatively large, which leads to the individuals with low fitness being eliminated and individuals with higher fitness being saved. After certain generation, the variation of fitness for minimum weight is small, and finally levels off to a fixed value.

Minimum Weight and Maximum Compactness ("GA2"). The coefficient of compactness (S_v) sometimes can be used as an objective of optimum design for heat exchangers. The coefficient of compactness is defined as

$$S_v = A_{\text{ht}}/V \tag{3}$$

where A_{ht} is the heat transfer surface area of recuperator and V is the internal volume. In the present study, we consider both the compactness of recuperator and its weight as the objective function. Thus a fitness function should be given as follows:

$$\text{fitness} = F \cdot \frac{S_v}{W} \tag{4}$$

Thus compactness and weight are well fit together. In CWPS the evolution process for minimum weight and maximum compactness is shown in Fig. 4(*b*). At the beginning of the evolution process (approximately less than 100 generations), the differences between every individual are relatively large, which leads to the individuals with low fitness being eliminated and individuals with higher fitness being saved. After certain generation (approximately larger than 500 generations), the variation of fitness for minimum weight is small, and finally levels off to a fixed value.

The comparison between the original data and the optimized results are listed in Table 2. The following conclusions can be found: by both kinds of fitness assignment methods (GA1,GA2), when H and $B1$ decrease, R and r decrease in configuration. The gas side radius R is larger than the air side, because the mass flow rate has been kept constant (that is, there is almost the same mass flow rate for the gas and air streams), and the gas will occupy a greater volume flow rate at the hot gas side with lower pressure. Therefore, in order to decrease the gas side pressure drop, a larger flow area of the gas side is necessary. On the other hand, by the GA1 method, the weight decreases by 14%, the coefficient of compactness increases by 12%, and total pressure drop increases by 40% in performance; while by the GA2 method, the weight reduces by 12%, the coefficient of compactness increases by 19%, and total pressure drop increases by 0.84% in performance. The total pressure drop, $\Delta p_{-\text{tot}}$ is less than 3%. By GA2, maximum S_v/W may be obtained, and the comprehensive performance of configuration is surprisingly good.

GA optimized results for CCPS are shown in Fig. 5. The minimum weights are plotted in Figs. 5(*a*), 5(*c*), and 5(*e*) obtained by GA1. The minimum weight and maximum compactness are shown in Figs. 5(*b*), 5(*d*), and 5(*f*) obtained by GA2 for CCPS of 45 deg, 60 deg, and 75 deg, respectively. In Table 3 the original data and optimized results are compared. The optimal parameters for CCPS perform very well, and the area compactness is increased to 70% from the original data by decreasing pitch from

Table 3 Comparison of the original data and optimized results (CCPS) (GA1—fitness=exp(−W); GA2—fitness=Sv/W)

		Geometry parameters						Performance		
θ (deg)	CCPS	P (mm)	H (mm)	R (mm)	$B1$ (m)	$B2$ (m)	$B3$ (m)	$\Delta p_{-\text{tot}}$ ($\times 10^2$)	S_v (m^2/m^3)	W (kg)
45	Original data	3.48	0.87	0.45	0.58	0.21	0.46	3.39	1308	62.16
	GA1	2.8	0.6	0.32	0.75	0.13	0.42	2.989	2258	43.40
	GA2	2.8	0.6	0.32	0.61	0.13	0.52	2.994	2258	43.38
60	Original data	3.48	0.87	0.45	0.82	0.16	0.42	3.166	1308	52.58
	GA1	2.8	0.6	0.32	0.9	0.10	0.43	2.987	2258	34.88
	GA2	2.8	0.6	0.32	0.75	0.12	0.52	2.996	2258	34.69
75	Original data	3.48	0.87	0.45	0.86	0.12	0.46	3.373	1308	36.73
	GA1	2.8	0.6	0.32	0.82	0.07	0.55	2.995	2258	23.76
	GA2	2.8	0.6	0.32	0.8	0.07	0.57	2.938	2258	23.82

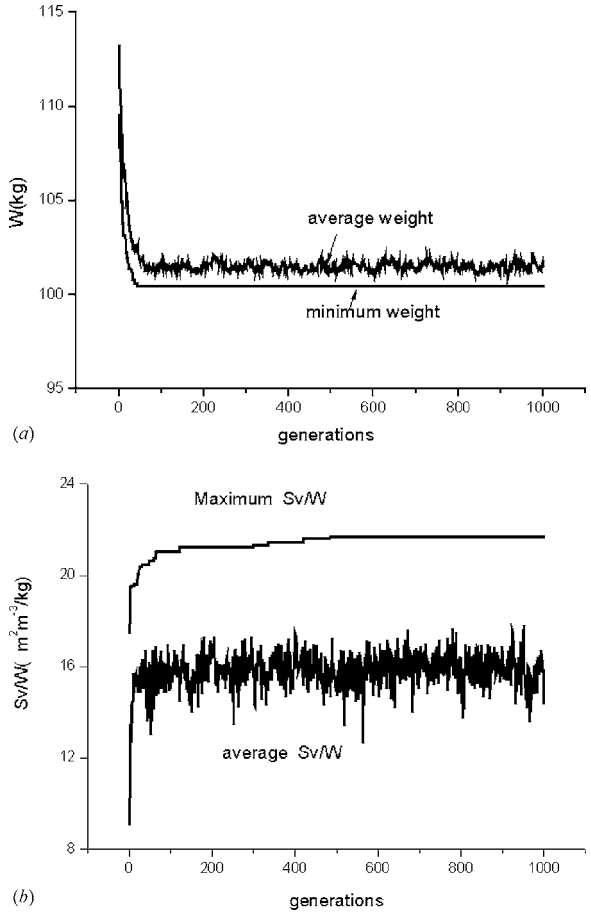

Fig. 4 Evolution process for CWPS: (*a*) by GA1 (for minimum weight); and (*b*) by GA2 (for minimum weight and maximum compactness)

3.48 mm to 2.8 mm and relatively high height of the passage from 0.87 mm to 0.6 mm, respectively. For two kinds of fitness assignment methods (GA1, GA2), the weight decreases from 17% to 36% for three different inclination angles θ, and total pressure drop decreases slightly in performance. The inclination angle between the plate corrugations is a major parameter in the thermo–hydraulic performance of CCPS. This is because a change in θ affects the basic flow structure which is the primary factor influencing the pressure drop and heat transfer rate. It is evident from the foregoing report [16], apart from flow and fluid property parameters, that Nu and f are significantly influenced by θ. The deeper corrugations increase the effective surface area and promote the swirl mixing. The large angle (θ) between the corrugations gives both smaller size and weight, and because the thermal performance enhances and the friction factors increase, the width ($B2$) of the matrix must be shorten to meet pressure drop requirements. Small pitch and high height can obtain superior performance, but smaller dimension is restricted by the metal material tractability, which shows the importance of achieving a fabrication method that gives small passage dimensions.

The performance of CCPS is compared to CWPS. CCPS has smaller weight than CWPS, the weight of CCPS is lower than CWPS by 45% or more, and optimized CCPS obtains higher area compactness. Both CWPS and CCPS show superior performance but CCPS should be the first choice for further studies for the recuperator of the microturbine if the difficulty of manufacturing this kind of surface is not taken into account. The CCPS is obtained by using a folding process, pressing, or stamping, but these are difficult because of the very small pitch and relatively high height of the passage, and cracking of the surface may also occur. The major disadvantage is that two different plates have to be fabricated, which means more work for manufacturing during the design stage.

Conclusions

In this paper, the implementation of GA as a useful support tool for optimization of CWPS and CCPS recuperators is described. As GA uses a random technique, it is possible that the global optimum is found within the optimization. Some results of the optimization of CWPS and CCPS recuperators are given.

Different objective optimizations were successfully performed in order to assess the reliability of the results. The results clearly show the superiority of primary surface recuperators for microturbine applications, since they are able to combine high heat exchange effectiveness with compact volumes and minimum weights. In the present study, the CWPS recuperator is shown to be able to decrease the volume and the material weight by 12% or more; while simultaneously the coefficient of compactness increases by 19% and total pressure drop increases by only 0.84%, and the total pressure drop is less than 3%. The CCPS area compactness is increased to 70% more than the initial data by decreasing pitch and the relatively high height of the passage, the weight decreases by 17–36%, depending on inclination angle θ. The CCPS shows superior performance for use in compact recuperators in the future, and this in turn implies an even higher potential for cost reduction due to the simpler and cheaper production process.

Acknowledgment

This work was supported by the National High Technology R&D Project of China (Grant No. 2002AA503020) and Program for New Century Excellent Talents in University of China (Grant No. NCET-04-0938). The authors wish to gratefully acknowledge Professor Hiroyuki Ozoe, the foreign export of Xi'an Jiaotong University, for his contribution to the present work.

Nomenclature

A = internal height corrugation in flow direction (mm)
A_c = Flow area of cell at inlet (m^2)
A_f = total flow area at inlet (m^2)
A_{ht} = heat transfer surface area (m^2)
$B1$ = length of recuperator core (m)
$B2$ = width of recuperator core (m)
$B3$ = height of recuperator core (m)
D_h = hydraulic diameter (m)
f = Fanning friction factor
H = heat transfer coefficient ($W\ m^{-2}\ K^{-1}$)
H = internal height (mm)
Nu = Nusselt number
P = pitch (mm)
p = static pressure (Pa)
R = radius of circle in gas side of the plate (mm)
r = radius of circle in air side of the plate (mm)
Re = Reynolds number
S_v = coefficient of compactness, ratio of heat transfer surface/internal volume ($m^2\ m^{-3}$)
V = internal volume (m^3)
W = weight (kg)

Greek

θ = inclination angle between corrugations (deg)
λ = wavelength (mm)
$\Delta p_{\_tot}$ = total pressure drop over recuperator, $=\Delta p_{\_air}/p_{\_air}+\Delta p_{\_gas}/p_{\_gas}$

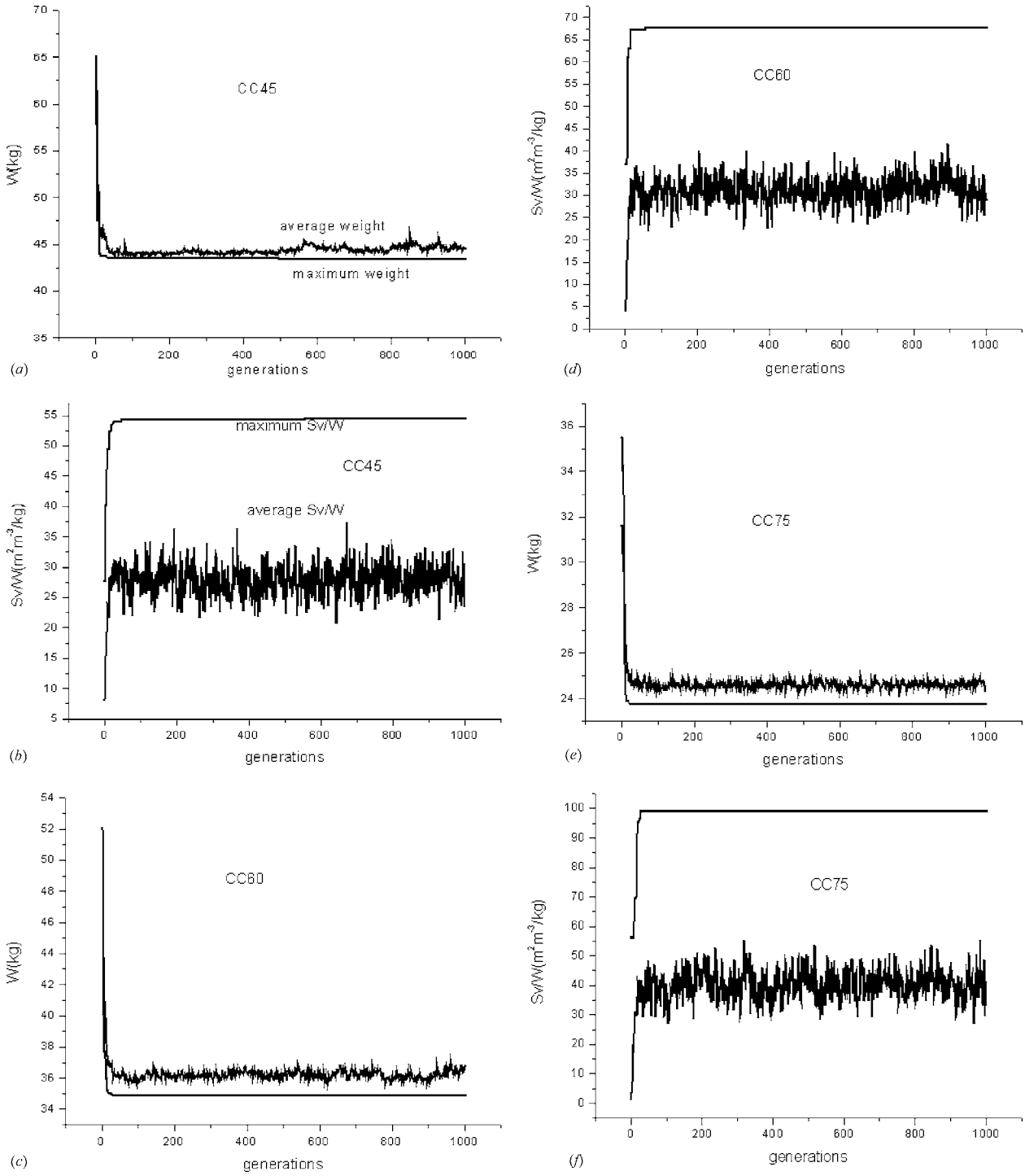

Fig. 5 Evolution process for CCPS: (*a*), (*c*), (*e*) by GA1; and (*b*), (*d*), (*f*) by GA2

References

[1] McDonald, C. F., 2000, "Low-Cost Compact Primary Surface Recuperator Concept for Microturbines," Appl. Therm. Eng., **20**, pp. 471–497.

[2] Blomerius, H., Höisken, C., and Mitra, N. K., 1999, "Numerical Investigation of Flow Field and Heat Transfer in Cross-Corrugated Ducts," ASME J. Heat Transfer, **121**, pp. 314–321.

[3] Liang, H. X., Wang, Q. W., Luo, L. Q., Feng, Z. P., and Chen, Z. Q., 2005, "Experimental and Numerical Investigation of Heat Transfer Performance of a Cross-Wavy Surface for Microtubine Recuperator," *Proceedings 5th International Symposium on Multiphase Flow, Heat Mass Transfer and Energy Conversion*, Xi'an, China, July. 3–6.

[4] Ciofalo, M., Piazza, I. D., and Stasiek, J. A., 2000, "Investigation of Flow and Heat Transfer in Corrugated-Undulated Plate Heat Exchanger," Heat Mass Transfer, **36**, pp. 449–462.

[5] Amano, R. S., 1985, "A Numerical Study of Laminar and Turbulent Heat Transfer in a Periodically Corrugated Wall Channel," ASME J. Heat Transfer, **107**, pp. 564–569.

[6] Utriainen, E. and Sundén, B., 2002, "Evaluation of the Cross Corrugated and Some Other Candidate Heat Transfer Surfaces for Microturbine Recuperators," ASME J. Heat Transfer, **124**, pp. 550–560.

[7] Utriainen, E., 2001, "Investigation of Some Heat Transfer Surfaces for Gas Turbine Recuperators," Ph.D. thesis, Division of Heat Transfer, Department of Heat and Power Engineering, Lund Institute of Technology, Lund, Sweden.

[8] Traverso, A., and Massardo, A. F., 2005, "Optimal Design of Compact Recuperators for Microturbine Application," Appl. Therm. Eng., **25**, pp. 2054–2071.

[9] Cool, T., Stevens, A., and Adderley, C. I., 1999, "Heat Exchanger Optimization Using Genetic Algorithms," *Proceedings 6th UK National Conference on*

Heat Transfer, Heriot-Watt University, Edinburgh, Sep. 15–16.
[10] Gen, M., and Cheng, R. W., 2000, *Genetic Algorithms and Engineering Optimization*, Wiley, New York.
[11] Mehrabian, M. A., and Poulter, R., 2000, "Hydrodynamics and Thermal Characteristics of Corrugated Channels: Computational Approach," Appl. Math. Model., **24**, pp. 343–364.
[12] Ciofalo, M., Stasiek, J., and Collins, M. W., 1996, "Investigation of Flow and Heat Transfer in Corrugated Passages-II. Numerical Simulations," Int. J. Heat Mass Transfer, **39**(1), pp. 165–192.
[13] Blomerius, H., and Mitra, N. K., 2000, "Numerical Investigation of Convective Heat Transfer and Pressure Drop in Wavy Ducts," Numer. Heat Transfer, Part A, **37**, pp. 37–54.
[14] Wang, Q. W., Liang, H. X., Luo, L. Q., Wang, J. W., Huang, Z. P., Feng, Z. P., and Chen, Z. Q., 2005, "Experimental Investigation on Heat Transfer and Pressure Drop in a Microturbine Recuperator with Cross-Wavy Primary Surface Channels," ASME Paper No. 2005-GT-68255.
[15] Rush, T. A., Newell, T. A., and Jacobi, A. M., 1999, "An Experimental Study of Flow and Heat Transfer in Sinusoidal Wavy Passages," Int. J. Heat Mass Transfer, **42**, pp. 1541–1553.
[16] Utriainen, E., and Sundén, B., 2002, "A Numerical Investigation of Primary Surface Rounded Cross Wavy Ducts," Heat Mass Transfer, **38**, pp. 537–542.
[17] Utriainen, E., and Sundén, B., 2001, "Comparison of Some Heat Transfer Surfaces for Small Gas Turbine Recuperators," ASME Paper No. 2001-GT-0474.
[18] Liang, H. X., Wang, Q. W., Luo, L. Q., and Feng, Z. P., 2005, "Numerical Simulation of Gas Flow and Heat Transfer in Cross-Wavy Primary Surface Channel for Microtubine Recuperators," ASME Paper No. 2005-GT-68292.

R. K. Bhargava
22515 Holly Lake Drive,
Katy, TX 77450

C. B. Meher-Homji

M. A. Chaker

Bechtel Corporation,
3000 Post Oak Boulevard,
Houston, TX 77056

M. Bianchi

F. Melino

A. Peretto

University of Bologna,
DIEM, Facolta di Ingegneria,
Viale Risorgimento 2,
Bologna 40136, Italy

S. Ingistov
Watson Cogeneration Co./BP,
11850 S. Wilmington Avenue,
P. O. Box 6203,
Carson, CA 90749

Gas Turbine Fogging Technology: A State-of-the-Art Review—Part I: Inlet Evaporative Fogging—Analytical and Experimental Aspects

Ambient temperature strongly influences gas turbine power output causing a reduction of around 0.50% to 0.90% for every 1°C of temperature rise. There is also a significant increase in the gas turbine heat rate as the ambient temperature rises, resulting in an increased operating cost. As the increase in power demand is usually coincident with high ambient temperature, power augmentation during the hot part of the day becomes important for independent power producers, cogenerators, and electric utilities. Evaporative and overspray fogging are simple, proven, and cost effective approaches for recovering lost gas turbine performance. A comprehensive review of the current understanding of the analytical, experimental, and practical aspects including climatic and psychrometric aspects of high-pressure inlet evaporative fogging technology is provided. A discussion of analytical and experimental results relating to droplets dynamics, factors affecting droplets size, and inlet duct configuration effects on inlet evaporative fogging is covered in this paper. Characteristics of commonly used fogging nozzles are also described and experimental findings presented. [DOI: 10.1115/1.2364003]

Keywords: evaporative fogging, power augmentation, droplets dynamics, fogging nozzle design

Introduction

In the rapidly deregulating power generation market worldwide, the structure of power supply agreements and the dynamics of an open market imply higher financial gains for power generated during high demand periods (such as summer months). Global power generation is expected to grow annually by approximately 3% in the next 20 years resulting in additional power generation of approximately 7500 TWh (terrawatt hours) using various fuel sources [1]. There are incentives to overcome the inherent loss of turbine power output during periods of high ambient temperature. On several heavy-duty industrial gas turbines, power output drops of around 15%–20% (compared to ISO conditions) can be experienced at an ambient temperature of 35°C (95°F), coupled with a heat rate increase of about 5%. Aeroderivative gas turbines exhibit an even greater sensitivity to changes in ambient temperature. The effect of ambient temperature change on power output and heat rate for an industrial (GE Frame-7) and an aeroderivative gas turbine (GE LM-6000) is shown in Fig. 1 [2]. This figure clearly shows higher sensitivity to ambient temperature for the aeroderivative gas turbine. An approach to counter the loss in power output associated with high ambient temperature is to cool the inlet air. While there are several inlet cooling technologies available, inlet fogging (evaporative and overspray) has seen large-scale applications over the past few years because of the advantage of its low first cost compared to the other techniques, such as media evaporative cooling and inlet chilling.

In recent years, several combined cycle plants utilizing advanced technology gas turbines as well as simple cycle peaking power units have adopted fogging for power augmentation. It is estimated that there are over 1000 gas turbines that currently use inlet fogging or overspray worldwide.

Part I of this three-part paper provides description of high pressure inlet evaporative fogging technology covering climatic and psychrometric aspects, the use of Equivalent Cooling Degree Hours (ECDH), droplets thermodynamics, heat and mass transfer considerations pertaining to inlet fogging, nozzle types and their characteristics, nozzle locations and orientation, and effects of gas turbine inlet duct system configurations. Part II [3] of this paper covers theoretical and experimental aspects pertaining to overspray fogging (also known as wet compression, high fogging, fog intercooling, supersaturation). This technique has been adopted by several major gas turbine manufacturers over the past few years. Part III [4] of this paper covers practical considerations and operational and maintenance issues, including results of field experiences related to inlet fogging and overspray. Part III also covers a review on the status of development in the area of fogging by major gas turbine manufacturers.

A comprehensive discussion of the theory and application of fogging technology was presented by Meher-Homji and Mee [5]. Tawney et al. [6] evaluated several options for power augmentation for combined cycle power plants and reported that inlet fogging resulted in a minimal impact on EPC (Engineering, Procurement and Construction) cost and was the only option that provided a small improvement in the heat rate. The highest return on equity was obtained by combining inlet fogging and supplemental firing of the heat recovery steam generator (HRSG). Jones and Jacobs [7] have recently presented an informative and detailed study of options available for enhancing combined cycle performance.

Contributed by the International Gas Turbine Institute (IGTI) of ASME for publication in the JOURNAL OF ENGINEERING FOR GAS TURBINES AND POWER. Manuscript received October 1, 2005; final manuscript received February 1, 2006. IGTI Review Chair: R. S. Abhari. Paper presented at the ASME Turbo Expo 2006: Land, Sea, and Air, Barcelona, Spain, May 8–11 2006, Paper No. GT2005-68336.

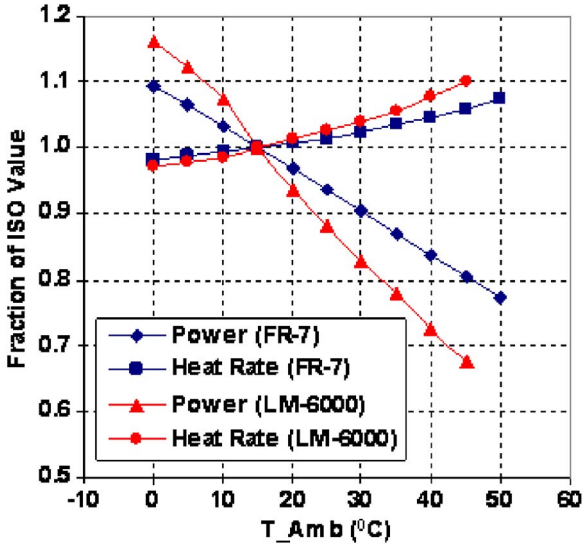

Fig. 1 Effect of ambient temperature on the performance of gas turbines [2]

Their study included an economic assessment of performance enhancement alternatives by considering a combined cycle plant consisting of two GE PG7241(FA) gas turbines, two unfired three pressure-levels HRSGs, and one GE D11 reheat condensing steam turbine with a wet cooling tower. Among the various alternatives examined, inlet fogging was found to be the least sensitive to variations in the economic parameters considered due to its insignificant impact on nonpeak plant performance and its low initial investment.

Bhargava et al. [8] have shown that while the effect of fogging on the overall cycle efficiency of combined cycles is generally small, inlet fogging results in a significant improvement in the heat rate for simple cycle gas turbines. The power boost for different classifications of gas turbines for changes in ambient temperature is shown in Fig. 2. A higher power boost is achievable with aeroderivative and older (traditional) industrial gas turbines compared to advanced technology gas turbines. Newer industrial gas turbines, referenced in Fig. 2, are those machines that were implemented with advanced technologies, such as a firing temperature higher than 1260°C (2300°F).

High Pressure Inlet Fogging

Fogging is a method of inlet cooling wherein demineralized water is converted into fine fog droplets by means of specially designed atomizing nozzles operating at pressures between 35 to 207 barg (approximately, 500 to 3000 psig). As the fog evaporates in the intake duct, it cools the air. This technique can achieve close to 100% evaporative cooling effectiveness in terms of attaining the wet-bulb temperature at the compressor inlet under design conditions.

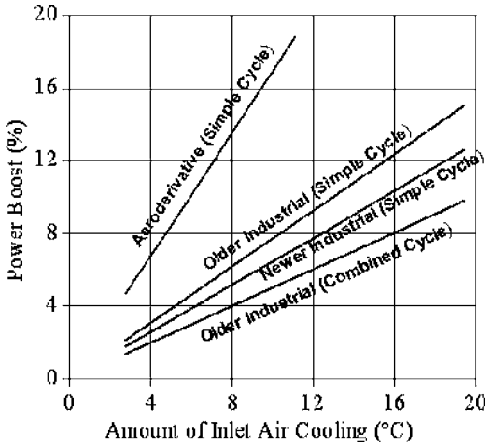

Fig. 2 Power boost versus amount of inlet air cooling [10]

The evaporative cooling effectiveness or efficiency is defined as

$$E = \frac{\text{DBT} - \text{CIT}}{\text{DBT} - \text{WBT}} \quad (1)$$

A typical high pressure fogging system consists of a series of high pressure reciprocating pumps providing demineralized water to an array of fogging nozzles located downstream of the inlet air filter elements. High pressure water is required as the droplet size is proportional, to a limit, to the (applied pressure)^a, where, value of exponent "a" varies between −0.5 and −0.1, depending on the nozzle type, nozzle geometry, liquid characteristics, and droplet diameter definition [9]. The fog nozzles create a large number of small droplets of varying size (<50 microns in diameter), which evaporate as they flow through the gas turbine intake system. A large gas turbine can have an array of several hundred nozzles. Demineralized water is necessary to minimize the potential for compressor blade fouling and hot gas path corrosion that can result from minerals naturally present in untreated water.

Climatic and Psychrometric Aspects of Inlet Fogging

The main obstacle faced by gas turbine users who wish to evaluate benefits of the fogging approach is the unavailability of easy-to-use climatic data. The obstacle comprises of two factors:

(1) Operators cannot easily locate the appropriate weather data for their site. Much of the available data at a plant site may be based on *average* data points with no representation of the values of *coincident* dry- and wet-bulb temperatures. This type of data is invaluable when evaluating any evaporative cooling solution.
(2) Even when some appropriate data is available, additional data processing is essential before any meaningful estimate can be made of cooling potential.

Modeling of Climatic Data. There are numerous problems when modeling climatic data, several of which derive from the concept of "averaging" of data. The averaging of data can underestimate the cooling potential because the highest relative humidity conditions, in practice, are never coincident with high dry-bulb temperatures. Relative humidity has a marked systematic diurnal variation opposite to the temperature. The moisture-holding capacity of air depends on its temperature, with warmer air being capable of holding more moisture than the cooler air. The relative humidity is typically high during the cool morning and evening hours and low during the hot afternoon hours. Actual data taken from a "hot and humid" site offshore of the United Arab Emirates, shown in Fig. 3, clearly indicates the spread between the dry-bulb and wet-bulb temperatures, which determines the evaporative cooling potential. Detailed climatic studies using the concept of ECDH of several hundred sites within the U.S. and around the world have been analyzed by Chaker et al. [10,11]. These studies indicated that there is a considerable amount of evaporative cooling potential available throughout the world, even in very humid locations, that would not be traditionally considered as candidate sites for evaporative cooling. There are many fog systems currently in use in the Southeast Asia, the Far East, and other hot and humid locations around the world.

Concept of Equivalent Cooling Degree Hours. The term equivalent cooling degree hours (ECDH), defined as the amount of evaporative cooling available in terms of degree hours, is an important approach in evaluating the effectiveness of fogging. The ECDH is the Wet-Bulb Depression (WBD) multiplied by the number of hours that this WBD occurs. The WBD is the difference

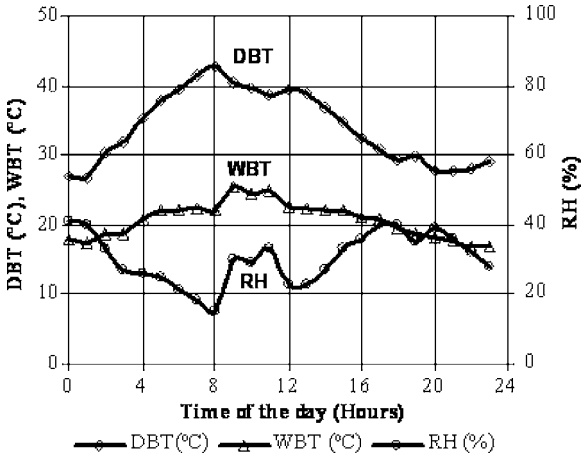

Fig. 3 Variations of site ambient condition in a day [11]

between the Dry-Bulb Temperature (DBT) and the Wet-Bulb Temperature (WBT). WBT is calculated from measured DBT and RH or Dew Point Temperature (DPT). The conversion may be done using an empirical equation or commercially available computer programs. Useful conversion equations may be found in the ASHRAE fundamental handbook [12].

The ECDH concept is important when using a fogging system to cool the air down to the wet-bulb temperature. However, icing formation at the compressor bellmouth becomes an issue when using fogging (or overspray). Consequently, the ECDH calculations should take into account the number of hours during the year that the system can operate without posing an icing risk. The value of the static temperature depression, which occurs at the compressor bellmouth because of airflow acceleration, depends on the gas turbine type and consequently the appropriate value of minimum wet-bulb temperature (MWBT) needs to be applied.

The static temperature depression can be calculated using the following equation: $\Delta T = V^2/2C_p$, where V is the airflow velocity at compressor bellmouth inlet and C_p is the constant pressure specific heat of air and can be taken equal to 1004 J/kg K.

For some gas turbines such as aeroderivative and some advanced technology gas turbines, the airflow velocity at the compressor bellmouth may reach 175 m/s, leading to a static temperature depression of 15°C. Table 1 summarizes the number of ECDH as well as the corresponding number of hours that the MWBT is above 7.2°C (45°F) for representative locations worldwide. The ECDH number can be used to calculate the power boost in kWh (power boost = ECDH number expressed in °C h multiplied by the expected boost of kW/°C). On the other hand, looking at the number of hours that are available in a year for a MWBT of 7.2°C one can see the advantage of using overspray while avoiding the icing risk at the compressor bellmouth. Consequently, from the table, we can see that, in Bombay, India, overspray may be used for 8754 h out of the 8760 yearly hours without icing risk, while this number is reduced to 6277 h for Shanghai, China. Of course, the number of operating hours with overspray is reduced when using a gas turbine with higher airflow velocities at the compressor bellmouth, which leads to higher MWBT values (15°C for example, as it is the case with aeroderivative gas turbines).

Two types of sources of weather data are available: the first one is commercial and can be obtained from the National Climatic Data Center (NCDC) or other sources that publish climatic data on compact disks. The second is data collected directly from sites. If the second source of data is used, it is very important to ensure that coincident ambient data is recorded.

As can be seen in Table 1, even locations commonly considered "humid" such as Miami, FL, Belem, Brazil, Bangkok, Thailand, and Bombay, India, have times in a year when evaporative cooling can be applied. If additional power boost is required, overspray may have to be considered. In locations considered "dry," such as Bakersfield, CA, Shanghai, China, and Sevilla, Spain significant cooling potential exists, and if needed, over-spray may be used on a limited basis.

Psychrometrics of Inlet Fogging. A psychrometric chart shown in Fig. 4 is used to illustrate a method to estimate the amount of cooling water required for a gas turbine with airflow capacity of 200 kg/s. The following ambient conditions are used: 35°C (96°F) DBT, 43% RH. First, find the ambient condition on the psychrometric chart (Start Point ❶ in Fig. 4). The moisture content at this condition is 15.1 gr of H_2O/kg of dry air. Assume that the air is cooled to the ambient wet bulb condition (100% RH as the ending condition). Proceed left up the constant wet-bulb temperature line until saturation is achieved (finish Point ❷ in Fig. 4). The moisture content corresponding to this condition is 19.6 gr of H_2O/kg of dry air. Therefore, the amount of moisture to be added to the air stream to achieve the wet-bulb temperature (WBT) is 4.5 gr of H_2O/kg of dry air. Thus, the theoretical amount of water required to cool 200 kg/s air by 10.5°C is 5.4 li/min.

Behavior and Dynamics of Fog Droplets

The reason for injecting water droplets is to increase the relative humidity of the airflow by evaporation of the droplets, which in turn leads to a decrease in the air temperature resulting in an increase in the air mass flow rate due to increased air density. While this may intuitively seem to be a simple matter, there are several interacting factors that define the success and efficiency of this evaporation process.

A complete understanding of the atomization process is critical for the analysis of the droplets size distribution produced by a fog

Table 1 ECDH(°C h) and number of hours (MWBT>7.2°C)

Location		Jan	Feb	Mar	Apr	May	Jun	Jul	Aug	Sep	Oct	Nov	Dec	Ann
Thailand,	ECDH	3580	3103	3316	3347	2939	2770	2813	2768	2301	2425	2971	3617	35951
Bangkok	Hours	744	672	744	720	740	720	704	744	720	744	8722		
USA (FL),	ECDH	1969	2044	2577	2783	2892	2277	2462	2399	2135	2209	2028	1973	27749
Miami,	Hours	723	656	736	719	742	720	744	708	685	744	720	725	8623
Brazil,	ECDH	1239	957	1057	1057	1385	1715	1871	1960	1906	1911	1859	1625	18543
Belem,	Hours	744	672	744	720	744	720	744	718	714	744	720	744	8727
Bombay,	ECDH	4195	4125	4225	3305	3268	2257	1526	1506	1750	3108	4185	4398	37848
India,	Hours	744	673	744	720	742	719	743	743	720	744	720	744	8754
China,	ECDH	263	383	930	1695	2058	1624	1855	1926	1901	2019	1472	669	16794
Shanghai,	Hours	67	92	316	652	742	720	743	739	723	734	530	219	6277
USA (CA),	ECDH	2064	3386	4906	7657	10873	13138	14442	13565	11235	8860	4459	2227	96812
Bakers Field,	Hours	357	486	629	675	734	720	744	738	709	724	544	323	7382
Spain,	ECDH	1272	1463	2528	2812	3684	4460	5879	5653	4589	3103	1893	1298	38633
Sevilla,	Hours	449	491	646	684	739	720	744	744	720	738	638	535	7850

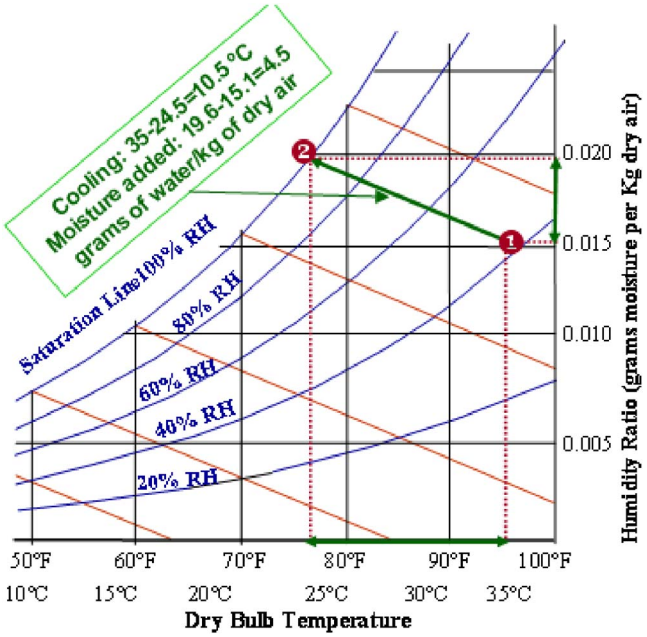

Fig. 4 Psychrometrics of inlet fogging

Fig. 5 (*a*) Swirl nozzle (*b*) impaction pin nozzle; plume characteristics at operating pressure of 138 barg (2000 psig): (*c*) swirl jet nozzle and (*d*) impaction pin nozzle [16]

nozzle. Droplet mean size, size distribution patterns and penetration of the droplets in the plume for a given cone angle, are important parameters. Many variables (such as the properties of the water, the geometries of the nozzle, and consequently the spray angle, pressure applied on the liquid and the air flow velocity) can significantly influence the results of the fogging process.

The accuracy and approach used for droplets size measurement is critical for gas turbine fogging applications. Different techniques exist to measure droplets size, including (1) a light scattering technique and (2) imaging with a high speed video camera. Light scattering techniques utilize two approaches: The first technique is a spatial technique (utilizing Malvern Spraytec equipment), which allows the sampling of a large number of droplets in a given volume. This technique is more appropriate when sampling is done in a high-density spray and with a small distance between the measurement position and the droplet sizing system detectors. The second approach is a temporal technique utilizing a Phase Doppler Particle Analyzer (PDPA). The PDPA samples and counts individual droplet passing through the sampling volume. This technique is more appropriate when sampling is done in a low-density spray and where there is a relatively large distance between the measurement position and the droplet sizing system detectors. Further details on droplets size measurement techniques are provided by Le Coz [13].

In a typical evaporative fogging system, droplets travel at the velocity of airflow and typically spend around one to two seconds between the inlet air filter and the compressor inlet. It is important that the size of the droplets is small enough for evaporation to take place in the short residence time available. If the size of droplets is too large, then the droplets would not fully evaporate, resulting in an undersaturated condition. Therefore, to attain wet-bulb temperature at the compressor inlet, a larger quantity of water (than required for saturation) would have to be injected. The combination of a larger quantity of water coupled with larger droplets sizes may lead to erosion of the compressor blades. Thus, a small size of the droplets injected with airflow in the gas turbine inlet air duct is critical.

Even small differences in the size of droplets has significant implications. For example, consider two situations with droplets diameters of 20 and 30 microns, respectively. Compared to the smaller and more desirable droplets of 20 microns, the larger (30 microns) size droplets will have (1) 3 to 4 times the mass and force of impact (higher erosion potential); (2) 33% lower surface area/unit volume (lower evaporation efficiency, since evaporation occurs at the droplets' air interface); (3) a two times faster fall rate (higher water drain amount). A discussion of the important parameters in evaluating a fogging nozzle's atomizing performance is presented by Mahapatra and Gilstrap [14].

Nozzle Types. There are two types of nozzles commonly employed in the industry, as shown in Fig. 5. The *swirl jet design nozzle* (see Figs. 5(*a*) and 5(*c*)) is one in which high pressure water is tangentially forced into a swirl chamber and then discharged through a cylindrical hole concentric to the swirl chamber. The discharged water is in the form of an axisymmetric thin conical sheet that forms ligaments and small droplets. The *impaction pin nozzle* (see Figs. 5(*b*) and 5(*d*)) utilizes high-pressure water forced with high velocity through a smooth orifice that hits an impaction pin, located above the jet. This results in the formation of a thin sheet of water in a conical shape [15]. As the water leaves the orifice, the water sheet becomes unstable and disintegrates into small thread ligaments and subsequently into billions of small size droplets. Air assisted nozzles have also been used on a limited basis for inlet fogging though swirl and impaction pin designs are the most prevalent.

Based on the recent comprehensive experimental study to evaluate comparative performance of the two types of nozzles at varying operating pressures (20.7 to 207 barg, or 300 to 3000 psig) and an airflow velocity of 15.2 m/s (50 ft/s), some interesting results were obtained [16]. Droplets sizes obtained with an impaction pin nozzle were found to be significantly lower, even with higher flow rates than a comparative swirl jet nozzle. Smaller droplets sizes are associated with a higher value of the Weber number, where the Weber number is defined as the ratio of

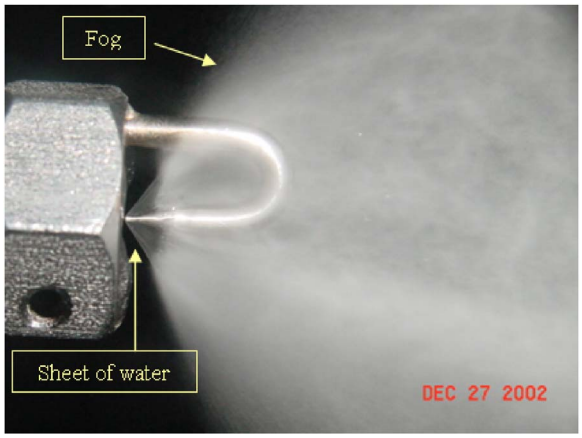

Fig. 6 Close-up picture of nozzle spray plumes operating at 138 barg [15]

aerodynamic and surface tension forces. With impaction pin nozzle designs, the Weber number effect results in a higher secondary breakup of the larger size droplets. A more detailed discussion on the secondary breakup of liquid droplets can be found in the work of Pitch and Erdman [17]. A visual examination of the plumes for the two nozzle types shows a straight edge of the cone for swirl jet nozzle, which indicates high momentum and consequently larger size droplets (Fig. 5(*c*)).

Schick and Knasiak [18] conducted an experimental investigation to understand characteristics of the two types of nozzles and examined differences in various parameters of interests, including, spray angle, flow rate, volume flux, median volume diameter, Sauter mean diameter, average flow velocity, and root-mean-square flow velocity. Their study indicated a wider spray pattern and slow velocity field, which are indicative of better mixing, with a swirl nozzle compared to the impaction pin nozzle. It is important to note, however, that evaporation efficiency is influenced more by the droplets size than the mixing effect. This study, like many others, agrees that the impaction pin nozzle provides lower size droplets than the swirl nozzle design.

Close-up, and high-speed photographs of the nozzle spray plumes (see Fig. 6) were taken in order to better understand plume formation and an atomization process for an impaction pin nozzle. A properly designed impaction pin nozzle splits the water jet when it impinges on the sharp tip of the pin, and a thin conical shaped sheet of water is formed. The water sheet thins as it expands and then breaks apart into small size droplets. Breakup occurs when the aerodynamic forces, which result from turbulence caused by the extremely high velocity of the sheet, overcome the surface tension of the water.

Heat and Mass Transfer of Droplets—Analytical Model. In an effort to understand the behavior of fog droplets emanating from a nozzle or set of nozzles, results of a simplified analytical model of heat and mass transfer for an individual droplet were recently presented showing transient behavior of a droplet and its interaction to the surrounding air conditions as it reaches saturation within a limited volume [16]. Transient behaviors of 20 μm and 50 μm droplets under the same starting ambient air conditions (30°C and 20% RH) with an active radius (RA) of 81 are shown in Figs. 7(*a*) and 7(*b*), respectively. Whereas, Figs. 7(*c*) and 7(*d*) show transient behavior of 20 μm and 50 μm droplets under the starting ambient conditions of 30°C and 60% RH with a RA of 108, respectively. Note that the active radius of the droplet, RA, defines the volume around the droplet for which saturation conditions are being calculated. A longer evaporation time for larger size droplets is quite evident. The results presented in Fig. 7 also show how droplet size reduces as the evaporation process progresses. A further examination of the effects of change in the values of RH and RA showed a reduced evaporation rate with increased values of RH and RA. This simplified model concurs with the findings in the field [15].

The effect of water temperature on droplet evaporation, within the range of water temperature used in gas turbine inlet air fogging systems, is negligible. Due to the tiny size of droplets after atomization, the temperature of droplets will converge in few milliseconds to the wet-bulb temperature, regardless of the original water temperature (within the range used).

The above discussion of heat and mass transfer effects is for a single droplet. However, in the real world there exists a mixture of droplets sizes with some droplets larger than 30 microns. In such a situation, smaller droplets will evaporate first, increasing the local relative humidity and making it even more difficult for the larger droplets to evaporate, thus posing a bigger risk for blade erosion should they be ingested into the compressor.

Factors Affecting Droplet Size—Experimental Results. Factors that determine droplets size include: (a) airflow velocity during the droplets size measurement; (b) position of measurement (viz., at the center, or edge of the plume); (c) ambient conditions around the droplet; (d) water characteristics—the difference in liquid characteristics (density, viscosity, and surface tension) due to the presence of foreign matter, and the ambient conditions may also account for some differences in droplets size distribution. The variations of droplets size as a function of airflow velocity and position of measurement, including different definitions of droplet size at an ambient condition of 30°C and 40% RH for an impaction pin nozzle, are shown in Fig. 8. Similar trends have been observed for a swirl type nozzle [15].

Effects of Operating Pressure and Position of Measurement in the Plume on the Droplet Size. As can be seen in Figs. 9 and 10, the droplets size decrease with an increase in operating pressure. This observed decrease in droplet size is quantitatively more at a low operating pressure up to 138 barg and becomes insignificant when the operating pressures increase from 138 to 207 barg. It can also be seen that the droplets size in the center of the plume is smaller (by 2 to 8 microns) than at its edge. This is due to the fact that as the droplets leave the tip of the nozzles at high velocity, the induced airflow creates a draught toward the center of the plume. This draught carries the smallest droplets to the center of the plume. It is important to note from Figs. 9 and 10 that the droplets sizes are consistently smaller for an impaction pin nozzle under all operating pressures and position of measurements.

Effect of Distance of Measurement and Flow Rate on the Droplet Size. Independent of nozzle type, an increase in the water flow rate by modifying the nozzle configuration (for example, increasing the orifice size of a nozzle) and keeping the other experimental parameters constant, will lead to an increase in droplets size. This is due to the modification in parameters governing the process of atomization such as increase in the thickness of the water sheet, or due to coalescence between droplets after the atomization process. The effects of coalescence on droplets size for an impaction pin and swirl jet nozzles are shown in Figs. 11 and 12, respectively. The experiments were done by taking measurements at different distances from the nozzle tip up to 30 cm, and by saturating the air in the measurement volume in order to neutralize the effect of evaporation. This effect is shown for the two typical airflow velocities (2.5 and 12.7 m/s, which are commonly experienced in the field for evaporative and overspray systems, respectively). The data presented in Figs. 11 and 12 for airflow velocity of 2.5 m/s is based on the experimental work of Chaker

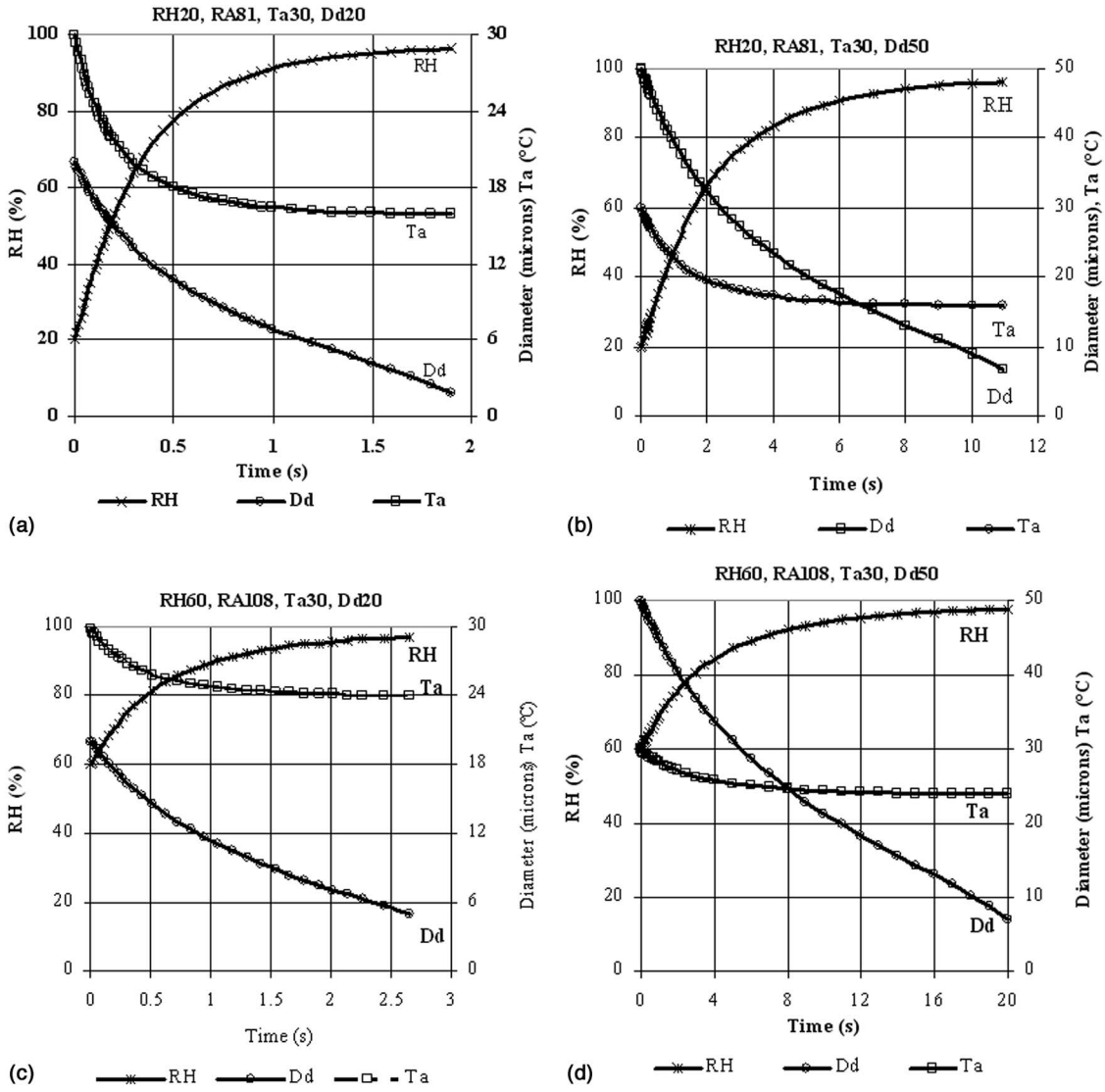

Fig. 7 (*a*) **Interaction of droplet to surrounding air condition (30°C and 20% RH)—Starting droplet size 20 microns;** (*b*) **Interaction of droplet to surrounding air condition (30°C and 20% RH)—starting droplet size 50 microns;** (*c*) **interaction of droplet to surrounding air condition (30°C and 60% RH)—starting droplet size 20 microns;** (*d*) **iinteraction of droplet to surrounding air condition (30°C and 60% RH)—starting droplet size 50 microns** [16]

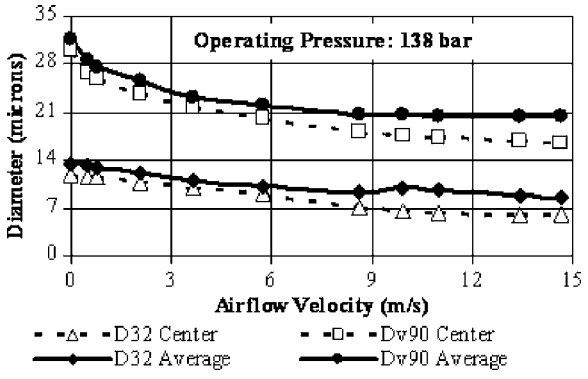

Fig. 8 Variation of droplet size as a function of airflow velocity (measurements taken at 7.6 cm from the nozzle orifice) [15]

and Kippax [19]. Dv_{90} and D_{32} droplets diameters are used to quantify the effects of coalescence.

In both figures (Figs. 11 and 12), one can see that the coalescence effect is higher at a low airflow velocity. The difference in the droplets size is small close to the nozzle exit (in the order of one micron for D_{32} and two microns for Dv_{90}) and increases with the measurement distance from the nozzle reaching 5 microns for D_{32} and 10 microns for Dv_{90}.

As shown in Fig. 11 with a water flow rate of 11.5 l/h at 207 barg for the impaction pin nozzle, the major increase in droplets size due to coalescence occurs in the first 10 cm, while in Fig. 12 with a water flow rate of 16.5 l/h at 207 barg, this increase does not seem to be attenuated, especially for Dv_{90}. Consequently, when characterizing a nozzle, it is important to measure the droplets size at a distance sufficiently far from the nozzle at which the coalescence effect is attenuated.

The coalescence effect depicted in Figs. 11 and 12 is due to the high probability of collisions between droplets in the plume cone angle, as this is a high density region. As expected, the increase in

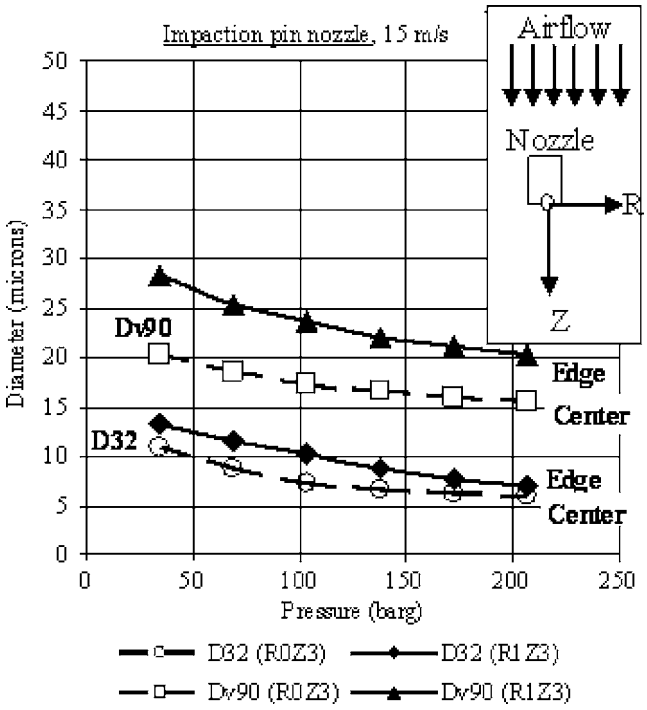

Fig. 9 Variation of droplets size in the center and at the edge of the plume as function of the applied pressure

droplet size due to coalescence is higher in Fig. 12 compared to that in Fig. 11 since the density of droplets at the plume cone angle of the swirl type nozzle is higher than that for the impaction pin nozzle.

As shown by Schick and Knasiak [18], atomization from impaction pin nozzles, in general, results in smaller droplets sizes

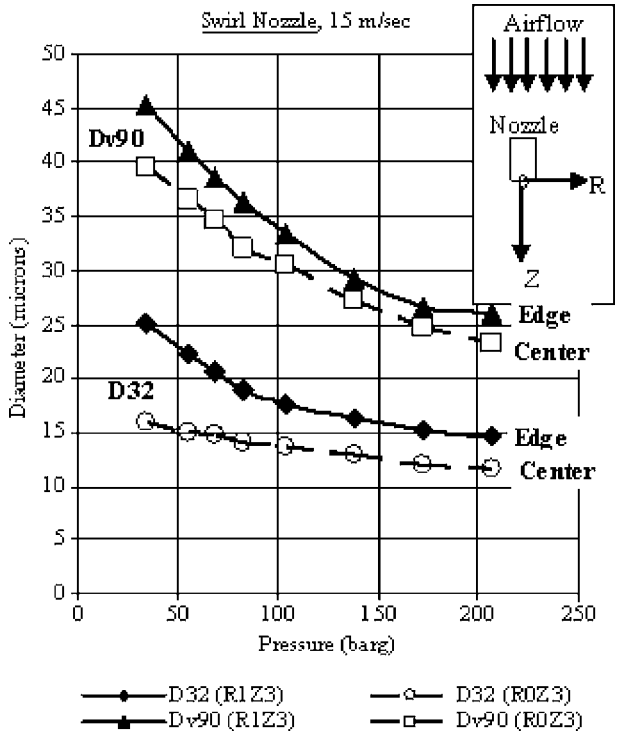

Fig. 10 Variation of droplets size in the center and at the edge of the plume as a function of the applied pressure

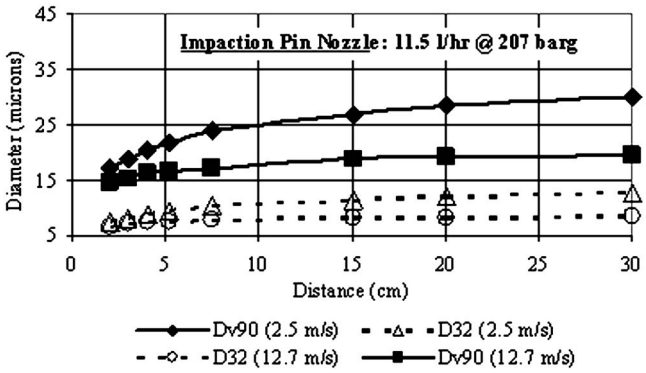

Fig. 11 Effect on droplet size of distance between the nozzle tip and the measurement position for impaction pin nozzles [19]

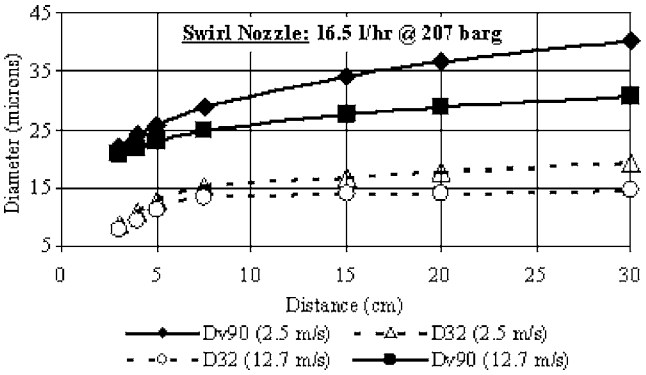

Fig. 12 Effect on droplets size of distance between the nozzle tip and the measurement position for swirl jet nozzles [19]

than atomization from swirl jet nozzles under the same experimental conditions. Because of the variance in designs of available impaction pin and swirl jet nozzles, the nozzle should be fully tested for any evaluation. As can be seen in Figs. 11 and 12, size of droplets increase with the increase of distance between the nozzle tip and the measurement position. This may be due to two effects. The first is the coalescence effect between droplets and the second is the relatively fast evaporation of smallest droplets in the spray. Close to the nozzle exit where the density of droplets is very high, the increase in droplets size is due essentially to coalescence. With an increase in distance from the nozzle, the plume expands and coalescence decreases, and the effect of evaporation of the smaller droplets on the increase in droplets size becomes more important. To quantify each effect, experimental studies on impaction pin nozzles by Chaker et al. [15] at ambient conditions and using saturated air showed that for the nozzles tested coalescence was preponderant for a distance of 20 cm from the nozzle.

Effects of Gas Turbine Inlet Configuration and Nozzle Characteristics on Fogging

Inlet Configurations. Gas turbine inlet systems come in a wide variety of configurations and shapes. Some of the complexities associated with inlet systems that have to be addressed include the following:

- multiple side entry configurations – two or three side entry configurations where the nozzle manifolds have to be arranged to ensure uniform coverage, as shown in Fig. 13;
- configurations with extremely steep curved roofs that require progressive angular changes in the nozzle angles to minimize roof wetting;

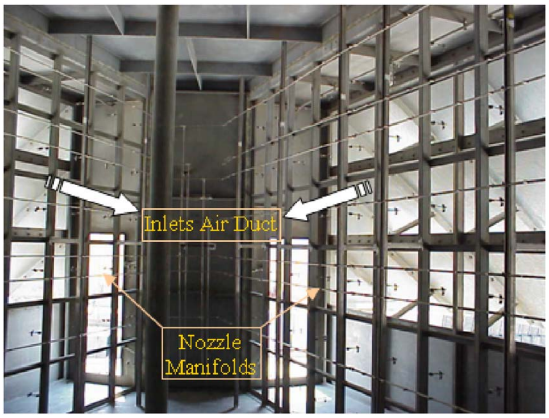

Fig. 13 V-shaped duct configuration requiring a special V-shaped fog nozzle array

Fig. 14 Nozzle array mounted in the inlet duct of Alstom GT24 gas turbine—a view looking into the intake cone (courtesy Caldwell Energy & Environmental, Inc.)

- for short duct configurations, where residence time is minimal, special patterns of the fog nozzles may have to be used to optimize the flow. In most cases, horizontal spray nozzle manifolds are used, whereas, nozzle manifolds may have to be vertically oriented (often used in filter systems with three-sided entry) to allow nozzle angular changes to be made in a vertical plane. With some extreme short duct situations, duct extensions may have to be provided to achieve an adequate evaporative residence time.
- complexities relating to unusual obstructions in the duct.

Due to the wide range of the intake duct configurations, the optimization of nozzle locations, orientation, and drain system design are often based on both modeling and experience, and in certain situations, with a systematic CFD analysis as discussed by Hoffmann [20].

Nozzle Locations. Various alternatives for locating the nozzle array/manifold are possible, namely, downstream of the inlet air filtration system and between the silencers and trash screens. The decision of where to locate the nozzle arrays depends on several factors, including installation related downtime, desire for overspray, existing inlet duct design, overall system's cost, and the fog droplets residence time. Among different available options, the nozzle manifold located upstream of the silencers and in the near vicinity of inlet air filters provides more residence time and is advantageous for evaporative fogging [21]. To avoid any possibility of foreign object damage, the nozzle manifolds must always be installed upstream of the trash screens. In certain installations involving large heavy-duty gas turbines, two nozzle manifolds may be required: one downstream of the inlet air filters for evaporative fogging and one closer to the compressor inlet for overspray (see Fig. 14).

Residence time is an important consideration that must be carefully evaluated. Typically, fog droplets attain the airflow velocity in a few milliseconds due to the large drag forces. As shown in Fig. 15, the response time for fog droplets to attain air-stream velocity is a function of their size [16].

Selecting and designing a fogging system is an art and involves CFD analysis coupled with past experience and visual observations. As shown in Fig. 16, there are, in general, three positions in the gas turbine duct where nozzle manifolds could be installed

- Zone 1: Close to the inlet filter housing after the filters where the airflow velocity is around 2.5 m/s (500 fpm) with a residence time for the droplets of approximately 1 s. This position is commonly used for evaporative fogging applications.
- Zone 2: Downstream of the silencer where the velocity is about 12.7 m/s (2500 fpm). This position is also used for evaporative fogging and for combined overspray fogging. The residence time is in the order of 0.4 s.
- Zone 3: In the duct close to the axial compressor inlet, which is the typical overspray installation, where the residence time will be of the order of 0.2 s. The velocity here would also be close to 12.7 m/s (2500 fpm).

The position of the nozzles manifold in the duct should be chosen with care considering the tradeoff between the spectrum of droplets sizes generated and residence time. Installing the fog manifold close to the inlet filter housing (zone 1), as shown in Fig. 16, where the airflow velocity is low, results in a longer residence time and, therefore, a better evaporative cooling efficiency. However, the fog spray is polydispersed and the penetration velocity of the bigger droplets emitted from the nozzle orifice is higher than the penetration velocity of the smaller ones; consequently, collision and coalescence of droplets occur.

By installing the nozzle manifold downstream of the silencer (zone 2 as shown in Fig. 16), the coalescence effect is reduced significantly due to the change in shear conditions at the nozzle, leading to increased breakup of droplets at higher flow rates and to the fast response time of the smallest droplets to the high airflow velocity. Large and small droplets are separated into different flow paths, and their collisions are greatly reduced, leading to minimization of the coalescence effect and consequently having small droplets sizes that can evaporate within the allowed residence time.

A typical impaction pin nozzle that produces a Dv_{90} of 25 microns at the lower airflow velocity near the air-filter house will produce a Dv_{90} of around 19 microns in the higher airflow veloc-

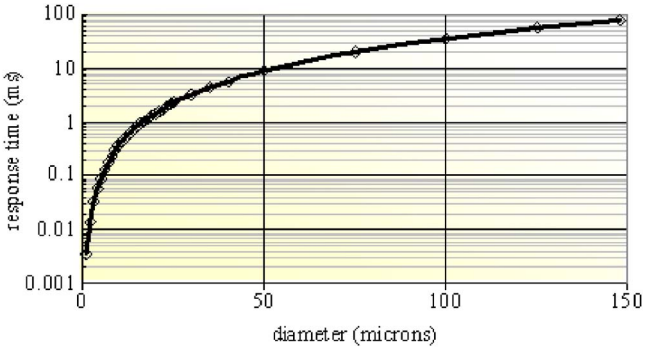

Fig. 15 Response time of droplets to attain airstream velocity as a function of droplet size [16]

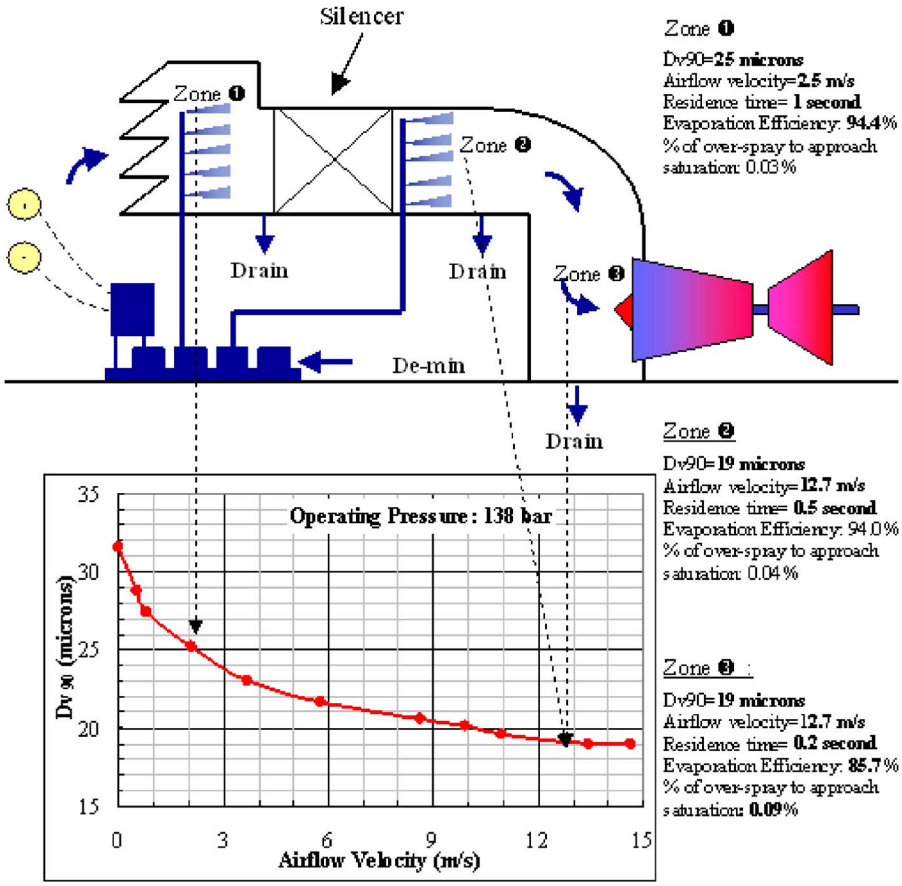

Fig. 16 Optimization of nozzle manifold position based on droplets size as a function of airflow velocity, and evaporation efficiency as a function of residence time

ity that exists downstream of the silencer. By installing the nozzles manifold downstream of the silencer, the residence time of the droplets in the duct is also reduced, typically from 1 to just 0.4 s.

Considering the above presented discussion, the position of the nozzle manifold in the duct should be chosen by taking into account the tradeoff of droplets size and residence time in the duct. Since all the droplets are small enough to rapidly attain the velocity of the airflow, the effect of the water flow velocity itself on the evaporation rate for droplets with sizes as small as the size atomized from the impaction pin nozzles is negligible. A more careful analysis should be done when using nozzles that generate larger size droplets in order to protect gas turbine components and to achieve the expected cooling system efficiency.

Nozzle Orientation and Fog Distribution. The fundamental reason for evaluating nozzle orientation and fog distribution is to obtain uniform droplets distribution in the intake duct. The value of the nozzle orientation angle chosen depends on factors such as airflow velocity, distance between nozzle arrays, operating pressure, duct wall and roof shape constraints, and duct geometry.

Several studies have been done by CFD modeling and then empirically verified using wind tunnel tests to visually see and optimize the nozzle layouts. The nozzle flow angle may vary between 0 deg (coflow; see Fig. 17(*a*)) and 90 deg (perpendicular to the flow; see Fig. 17(*b*)). The 90 deg orientation can be used when the plume does not interact with the duct walls or other nozzle arrays. At 90 deg orientation of fog nozzles, the increased angle provides a marginally longer residence time and slightly better mixing as compared to the coflow position. Furthermore, at 90 deg, the relative velocity between the droplets and the airflow is slightly higher than the coflow position. When the nozzle manifold is installed in a high airflow velocity zone (For example, downstream of the silencer), the Weber number may become sufficiently large to initiate a secondary breakup of the biggest droplets in the spray [22].

Experimental studies have been conducted to study the effect of nozzle angle with respect to the airflow [16]. The plume diameter stays relatively constant in the axial length. This is an advantage when the distance between the nozzles is not too large, as it provides a homogeneous pattern across the duct. However, in a case of large spacing between nozzles, the 90 deg position may be advantageous because the plume diameter is much larger and consequently covers more duct volume. Care must be taken that the airflow does not blow the fog back onto the manifold tube, where it can coalesce and form larger droplets. This can be a problem near the air filter house, where airflow is not always axial to the inlet duct.

Droplet to droplet coalescence will most probably not occur in the region where the plumes intersect, as at this location, the density of the droplets is much less than at a point close to the nozzle efflux. Droplet to droplet coalescence and the resulting formation of larger droplets can be significantly higher close to the orifice, where population of droplets is very dense and different sized droplets are moving at different velocities. Coalescence stops within 30 cm (1 ft) from the orifice for most inlet fogging nozzles.

It is important to understand the velocity and pressure profiles of the airflow in the intake duct and recognize that certain areas will have accelerated flow and decreasing pressure due to duct bends. Nozzles have to be specially oriented to accommodate these airflow patterns.

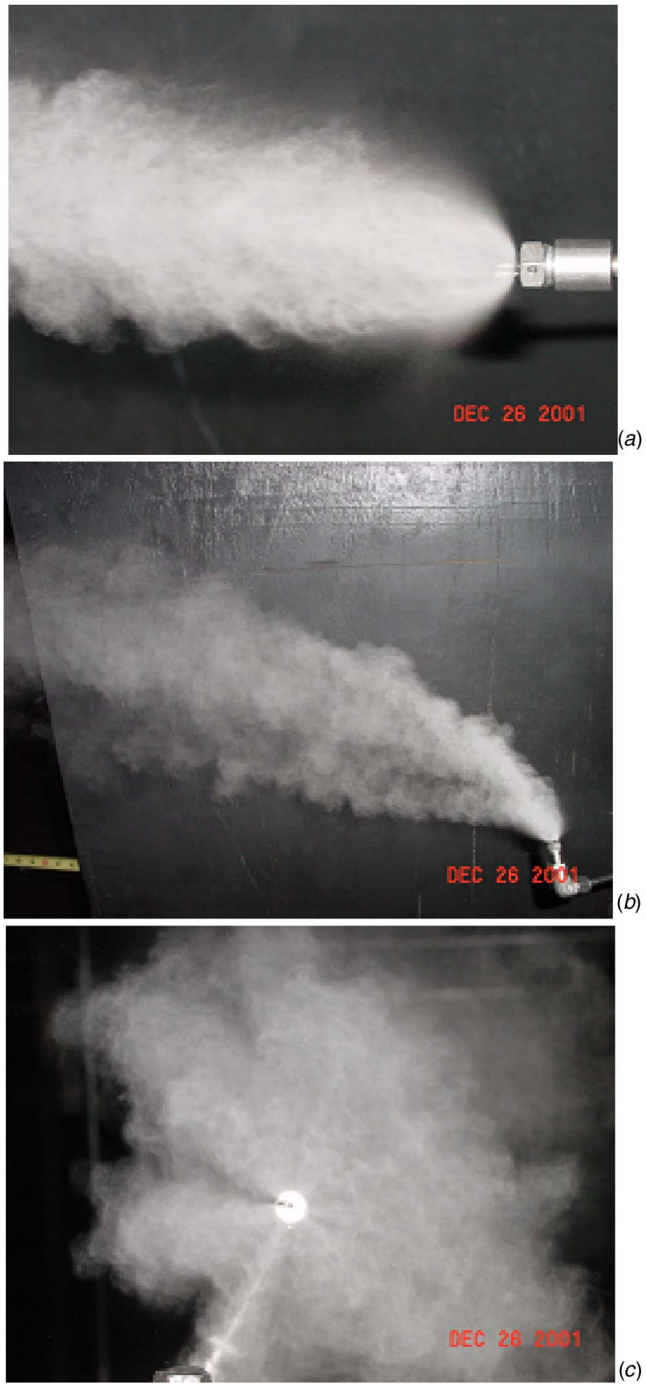

Fig. 17 (*a*), (*b*), and (*c*) Plume shape with nozzle orientation of a fog nozzle in the wind tunnel; airflow velocity is 4 m/s (800 ft/min), Operating pressure is 138 barg (2000 psig): (*a*) Co–flow; (*b*) 90 deg; (*c*) counter-flow

Number of Nozzles and Nozzle Pattern. The number of nozzles should be appropriate to provide uniform fogging in the gas turbine inlet duct. There is a tradeoff between the nozzle flow rate, number of nozzles, and associated airflow pressure drop. Having a smaller number of higher flow rate nozzles can result in a larger separation of plumes and less homogeneity in the fog distribution. Furthermore, nozzles with a high flow rate capacity often produce larger size droplets. In addition, fewer nozzles will worsen the compressor inlet temperature distribution during the part-load operating condition.

To give a feel for a typical number of nozzles, a total of 1120 nozzles were used in an installation consisting of a heavy-duty GE 7FA gas turbine [21]. The nozzle pattern itself should be such as to cover the maximum inlet duct area to avoid supersaturation in certain regions and undersaturation and coalescence in the others. Trewin [23] has discussed practical issues related to nozzle locations such as to maximize reduction in the average temperature and to minimize variations of local temperatures at the compressor inlet due to fogging effects.

Concluding Remarks

The inlet evaporative fogging of gas turbines has become a popular power augmentation technique due to its low first cost and simplicity. In this paper we have provided a comprehensive overview of the evaporative fogging technology covering climatic aspects, nozzle characteristics, and droplets dynamics in the gas turbine intake duct system. Practical considerations relating to the placement of fog nozzles in the intake duct system have been covered and experimental data reviewed. A treatment of overspray is provided in Part II of this paper, and Part III covers practical considerations and operational experiences.

Acknowledgment

Opinions stated herein are the personal opinions of the authors and may not necessarily reflect opinions or positions of their respective corporations/organizations.

Nomenclature

C_p = constant pressure specific heat ($J\,kg^{-1}\,°C^{-1}$)
CIT = compressor inlet temperature (°C)
DBT = dry-bulb temperature (°C)
DPT = dew point temperature (°C)
D_d = droplet diameter (micrometer)
Dv_{90} = droplet size number (micrometer)
D_{32} = Sauter mean diameter (micrometer)
E = evaporative cooling efficiency (effectiveness)
ΔT = static temperature depression (°C)
ECDH = equivalent cooling degrees hours (°C h)
HR = heat rate (kJ/kWh)
MWBT = minimum wet-bulb temperature (°C)
RA = active radius of the droplet (micrometer)
RH = relative humidity (%)
T = temperature (°C)
T_a = ambient temperature (°C)
T_Amb = ambient temperature (°C)
V = airflow velocity ($m\,s^{-1}$)
WBT = wet-bulb temperature (°C)
WBD = wet-bulb depression (DBT- coincident WBT) (°C)

Acronyms

HRSG = heat recovery steam generator
PDPA = phase doppler particle analyzer
TWh = terrawatt hours

References

[1] Bhargava, R. K., 2003, "Global Energy Resources, Power Generation and Gas Turbine Market - Recent Trends," *Proceedings of the International Conference on Power Engineering*, Nov. 9–13, Kobe, Japan.
[2] Bhargava, R., and Meher-Homji, C. B., 2005, "Parametric Analysis of Existing Gas Turbines with Inlet Evaporative and Overspray Fogging," ASME J. Eng. Gas Turbines Power, **127**, pp. 145-158.
[3] Bhargava, R. K., Meher-Homji, C. B., Chaker, M. A., Bianchi, M., Melino, F., Peretto, A., and Ingistov, S., 2007, "Gas Turbine Fogging Technology: A State-of-the-Art Review—Part II: Overspray Fogging—Analytical and Experimental Aspects," ASME J. Eng. Gas Turbines Power, **129**, pp. 454–460.
[4] Bhargava, R. K., Meher-Homji, C. B., Chaker, M. A., Bianchi, M., Melino, F., Peretto, A., and Ingistov, S., 2007, "Gas Turbine Fogging Technology: A State-of-the-Art Review—Part III: Practical Considerations and Operational Experience," ASME J. Eng. Gas Turbines Power, **129**, pp. 461–472.
[5] Meher-Homji, C. B., and Mee, T. R., III, 1999, "Gas Turbine Power Augmen-

tation by Fogging of Inlet Air," *Proceedings of the 28th Turbomachinery Symposium*, Houston, TX.
[6] Tawney, R., Pearson, C., and Brown, M., 2001, "Options to Maximize Power Output for Merchant Plants in Combined Cycle Applications," ASME Paper No. 2001-GT-0409.
[7] Jones, C., and Jacobs, J. A., 2000, "Economic and Technical Considerations for Combined-Cycle Performance-Enhancement Options," GE Power Systems, GER-4200.
[8] Bhargava, R., Bianchi, M., Melino, F., and Peretto, A., 2003, "Parametric Analysis of Combined Cycles Equipped With Inlet Fogging," ASME Paper No. GT-2003-38187.
[9] Lefebvre, A. H., 1989, *Atomization and Spray*, Taylor & Francis, New York, Chap. 6.
[10] Chaker, M., Meher-Homji, C. B., Mee, T. R., III, and Nicolson, A., 2001, "Inlet Fogging of Gas Turbine Engines—Detailed Climatic Analysis of Gas Turbine Evaporative Cooling Potential," ASME Paper No. 2001-GT-526.
[11] Chaker, M., and Meher-Homji, C. B., 2002, "Inlet Fogging of Gas Turbine Engines—Climatic Analysis of Gas Turbine Evaporative Cooling Potential of International Locations," ASME Paper No. 2002-GT-30559.
[12] Parsons, R., 2001, *ASHRAE Handbook-Fundamentals*, ASHRAE, Atlanta, Chap. 6, Psychrometrics.
[13] Le Coz, J. F., 1998, "Comparison of Different Drop Sizing Techniques on Direct Injection Gasoline Sprays," 9th *International Symposium on Application of Laser Techniques to Fluid Mechanics*, Lisbon, July 13–16.
[14] Mahapatra, S., and Gilstrap, J. K., 2003, "Gas Turbine Inlet Air Cooling: Determination of Parameters to Evaluate Fogging Nozzle's Atomizing Performance," International Joint Power Generation Conference, Paper No. IJPGC2003-40124.
[15] Chaker, M. A., Meher-Homji, C. B., and Mee, T., III, 2003, "Inlet Fogging of Gas Turbine Engines—Experimental and Analytical Investigations on Impaction Pin Fog Nozzle Behavior," ASME Paper No. GT2003-38801.
[16] Chaker, M., Meher-Homji, C. B., and Mee, T. R., III, 2002, "Inlet Fogging of Gas Turbine Engines—Part A: Fog Droplet Thermodynamics, Heat Transfer and Practical Considerations; Part B: Fog Droplet Sizing Analysis, Nozzle Types, Measurement and Testing; Part C: Fog Behavior in Inlet Ducts, CFD Analysis and Wind Tunnel Experiments," ASME Papers No. 2002-GT-30562, No. 30563, and No. 30564.
[17] Pitch, M., and Erdman, C. A., 1987, "The Use of Breakup Time Data and Velocity History Data to Predict the Maximum Size of Stable Fragments for Acceleration-Induced Breakup of Liquid Drops," Int. J. Multiphase Flow, **13**, pp. 741–757.
[18] Schick, R. J., and Knasiak, K. F., 2000, "Spray Characterization For Wet Compression Gas Cooling Applications," *8th International Conference on Liquid Atomization and Spray Systems*, Pasadena, CA, July.
[19] Chaker, M., and Kippax, P., 2004, "Towards a Protocol For the Analysis of the High Fogging Process Using Laser Diffraction Technology," Power Eng., Jan., p. 49.
[20] Hoffmann, J., 2002, "Inlet Air Cooling Performance and Operation," CEPSI, Paper No. T1-A-39, Fukuoka, Japan.
[21] Meher-Homji, C. B., and Mee, T. R., III, 2000, "Inlet Fogging of Gas Turbine Engines—Part B: Practical Considerations, Control and O&M Aspects," ASME Paper No. 2000-GT-308.
[22] Savic, S., Mitsis, G., Haertel, C., Khaidarov, S., and Pfeiffer, P., 2002, "Spray Interaction and Droplet Coalescence in Turbulent Air-Flow—An Experimental Study with Application to Gas Turbine High Fogging," ILASS Europe, Zaragoza, Spain, 9–11 September.
[23] Trewin, R. R., 2002, "Inlet-temperature Suppression of Inlet Air for Gas-Turbine Compressors by Evaporative Cooling of Water Spray," ASME Paper No. GT-2002-30658.

R. K. Bhargava
22515 Holly Lake Drive,
Katy, TX 77450

C. B. Meher-Homji

M. A. Chaker

Bechtel Corporation,
3000 Post Oak Boulevard,
Houston, TX 77056

M. Bianchi

F. Melino

A. Peretto

University of Bologna,
DIEM, Facolta di Ingegneria,
Viale Risorgimento 2,
Bologna 40136, Italy

S. Ingistov
Watson Cogeneration Co./BP,
11850 S. Wilmington Avenue,
P. O. Box 6203,
Carson, CA 90749

Gas Turbine Fogging Technology: A State-of-the-Art Review—Part II: Overspray Fogging—Analytical and Experimental Aspects

The strong influence of ambient temperature on the output and heat rate on a gas turbine has popularized the application of inlet fogging and overspray for power augmentation. One of the main advantages of overspray fogging is that it enhances power output as a result of decrease in compression work associated with the continuous evaporation of water within the compressor due to fog intercooling. A comprehensive review on the current understanding of the analytical and experimental aspects of overspray fogging technology as applied to gas turbines is presented in this paper.
[DOI: 10.1115/1.2364004]

Keywords: power augmentation, overspray, high fogging, wet compression, compressor performance

Introduction

Ambient temperature strongly influences gas turbine performance with power output dropping by approximately 0.50–0.90% for every 1 °C of temperature rise. There is also a significant increase in the gas turbine heat rate as the ambient temperature rises, resulting in an increased operating cost. As the increase in power demand often coincides with high ambient temperatures, evaporative fogging has become a popular approach for cooling of the inlet air during the hot part of the day when the coincident relative humidity is typically low. Theoretical and experimental aspects relating to inlet evaporative fogging have been covered in Part I [1] of this three-part paper.

Evaporative fogging, however, tends to become ineffective as the relative humidity increases resulting in a low temperature depression. In situations such as these, overspray fogging where a deliberate introduction of fine fog droplets into the axial flow compressor provides an intercooling effect reducing compressor work and providing significant power augmentation and heat rate reduction. Several major gas turbine original equipment manufacturers (OEMs) offer overspray technology for their gas turbines and have active research programs underway in this area. The main objective of this paper is to provide a comprehensive review of the work accomplished as of this date in the area of overspray fogging and discuss both theoretical and practical issues that must be considered during the design and implementation of overspray systems. Additional practical considerations and operational experiences with inlet fogging systems have been presented in Part III [2] of this paper. In addition to discussing current status of research and development efforts in the subject area, a list of unresolved issues and future needs is also presented in this paper.

Overspray Fogging

Overspray fogging (also referred to as high fogging, wet compression, and fog intercooling) is derived by the deliberate introduction of fog droplets into an axial flow compressor of a gas turbine. The compressor of a gas turbine consumes a considerable amount of the gross work produced by the gas turbine (two-thirds or more for older machines) as is evident from Fig. 1 which shows compressor work input ratio (W_C) for a wide range of old and new technology turbines. Whereas, the compressor work input ratio is defined as the compressor work divided by the total work produced by the turbine. One of the main advantages of overspray fogging is that it enhances power output as a result of decrease in compression work associated with the continuous evaporation of water within the compressor. Other factors which contribute to power augmentation are: (1) increased flow rate through the turbine and (2) increase in specific heat capacity of the fluid mixture flowing through the turbine. For most applications, the amount of overspray is in the range of 0.5–1% of the air mass flow rate of the gas turbine.

Nozzle Location for Overspray Fogging. It is commonly accepted that overspray fogging nozzles should be located relatively close to the axial compressor inlet to prevent large size droplets accumulated on the duct walls from entering in the compressor and causing damage to the blades. In most commercial applications, the nozzle array is located in the downflow section of the duct downstream of silencer prior to the compressor inlet bell

Contributed by the International Gas Turbine Institute (IGTI) of ASME for publication in the JOURNAL OF ENGINEERING FOR GAS TURBINES AND POWER. Manuscript received October 1, 2005; final manuscript received February 1, 2006. IGTI Review Chair: R. S. Abhari. Paper presented at the ASME Turbo Expo 2006: Land, Sea, and Air, Barcelona, Spain, May 8–11 2006, Paper No. GT2005-68337.

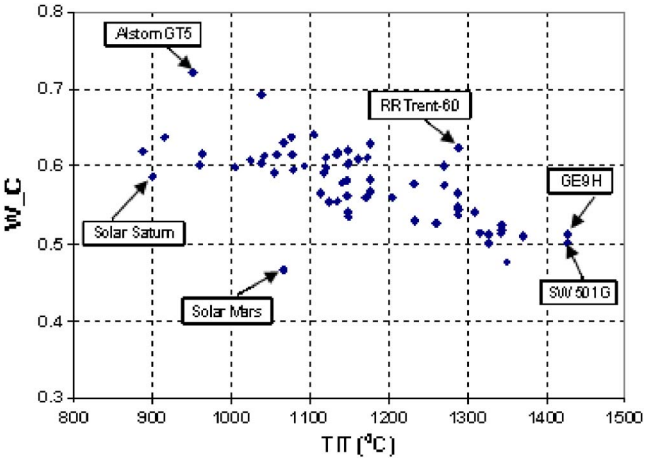

Fig. 1 Compressor work input ratio (W_C) versus turbine inlet temperature (TIT) for existing gas turbines (ambient conditions: 40 °C and 40% RH)

mouth or intake cone in case of cold-end drive machines. Further details relating to the placement of fog nozzles are presented in Part I [1] of this paper.

The concept of overspray (wet compression) is as old as development of propulsion gas turbines as is evident from the work of Kleinschmidt in the late 1940s [3]. Kleinschmidt noted that wet compression was more effective in improving gas turbine cycle performance than with traditional compressor intercooling (using an external intercooler). The reason for this, he argued, was that the heat removed from the air was returned to the working fluid in the form of steam. For a given value of turbine inlet temperature, Kleinschmidt's analysis further showed that the wet compression not only increased cycle efficiency for a given pressure ratio but also increased the cycle pressure ratio at which maximum efficiency occurred. There is a lot of analytical and experimental work reported on overspray fogging in the literature [3–18], particularly, in the last five to six years.

Early work on wet compression was focused on the use of water injection for thrust augmentation of aircraft engines. In the early 1950s, a detailed procedure for estimating thrust augmentation of a turbojet engine with the help of a psychrometric chart and Mollier diagram was presented by Wilcox and Trout [4]. The analytical study of Wilcox and Trout showed the impact of factors such as altitude, flight Mach number, and atmospheric temperature on the thrust boost associated with water injection. Beede et al. [5] experimentally examined the effects of water injection on the performance of a double-entry centrifugal compressor. Their study showed increase in total pressure ratio with an increased amount of injected water.

In the early 1960s, Hill [6] presented a systematic aerothermodynamic analysis procedure for evaluating the effects of water injection on the performance characteristics of an axial compressor and found good agreement with experimental results on medium- and high-pressure ratio compressors of turboshaft engines. For a given value of an evaporation parameter defined as $(w\lambda/\theta)$, Hill noted that the amount of work reduction due to water injection was not affected by the compressor pressure ratio. Moreover, stage work distribution was affected by the evaporation inside the compressor such that initial stages were found unloaded. He further noted that the process of mixing and evaporation depends more on the geometry and rotational speed of the compressor than on the initial droplet sizes and their distribution. It is highly likely that this conclusion could be due to the limited understanding of heat transfer effects, droplet measurement techniques available at the time, and factors relating to the state of fogging technology in the early 1960s. However, as will be presented in the later part of this paper, recent studies [1,7,8,10,11] clearly show the importance of droplet size on the evaporation process both upstream and within the compressor.

A thermodynamic analysis procedure for wet compression, similar to the above discussed work of Hill, but including a discussion on droplet size, evaporation rate, evaporation time, and the breakup of water droplets was recently presented by Zheng et al. [7]. As shown by Zheng et al., pressure and temperature for the wet compression process are related by the thermodynamic relation given below

$$\frac{p}{p1} = \left(\frac{T}{T1}\right)^{m/m-1} \tag{1}$$

where

$$\frac{m}{m-1} = \frac{\gamma}{\gamma-1} + \frac{L}{R}\frac{dw}{dT} - \frac{1}{\gamma-1}\frac{n-\gamma}{n-1} \tag{2}$$

And for isentropic wet compression

$$\frac{k}{k-1} = \frac{\gamma}{\gamma-1} + \frac{L}{R}\frac{dw}{dT} \tag{3}$$

The compressor work with wet compression can be calculated using Eq. (4) given below [7]

$$W_c = (h_{a2} - h_{a1}) + (w_2 h_{w2} - w_1 h_{w1}) - \Delta f h_{f1} \tag{4}$$

In Eqs. (1)–(3), m and k represent the polytropic and isentropic exponents, respectively, for wet compression process, and n and γ represent polytropic and isentropic exponents, respectively, for dry compression process. Variables L, R, and dw/dT represent latent heat of vaporization, gas constant, and evaporation rate, respectively. Subscripts 1 and 2 refer to compressor's inlet and discharge conditions, respectively. Subscripts a, w, and f refer to air, steam (water vapor), and water, respectively.

The thermodynamic analysis by Zheng et al. [7] showed that the polytropic index of actual wet compression is lower than the dry air compression process which results in reduced compressor work, compressor discharge temperature, and increased compression efficiency with wet compression. For given values of compression ratio and evaporation rate, it can be shown that the compressor discharge temperature becomes less than even that for an isentropic dry compression process (see Fig. 2(*a*)). The legends *t2di*, *t2d*, *t2wi*, and *t2w* in Fig. 2(*a*) represent compressor discharge temperature corresponding to dry-isentropic, dry, wet-isentropic, and actual wet compression processes, respectively. It was further shown that wet compression was more effective at high values of compressor pressure ratio and that, for a given value of pressure ratio and evaporation rate, compression work can be lower than that required for the isentropic dry air compression as is evident from Fig. 2(*b*). The legends *wdi*, *wd*, *wwi*, and *ww* in Fig. 2(*b*) represent compression work corresponding to dry-isentropic, dry, wet-isentropic, and actual wet compression processes, respectively. While lacking a detailed explanation, Zheng et al. noted that better evaporation could be achieved with smaller droplets diameter.

A detailed analytical and experimental investigation of overspray using a 115 MW gas turbine (Hitachi Frame 9E) by Utamura et al. [8] showed a 10% gain in power output and a 3% increase in thermal efficiency with 1% overspray. Their simplified model of droplets evaporation showed incomplete evaporation inside the 17-stage compressor for size of droplets larger than 30 μm. However, complete evaporation could be attained within the compressor for size of droplets lower than 20 μm. A new parameter, termed incremental efficiency, as a measure of wet compression effectiveness and defined as the ratio of incremental power to additional fuel consumption, was introduced and found to be 10% higher than the thermal efficiency for the dry case and independent of spray rate.

A linearized one-dimensional analysis of compressor off-design

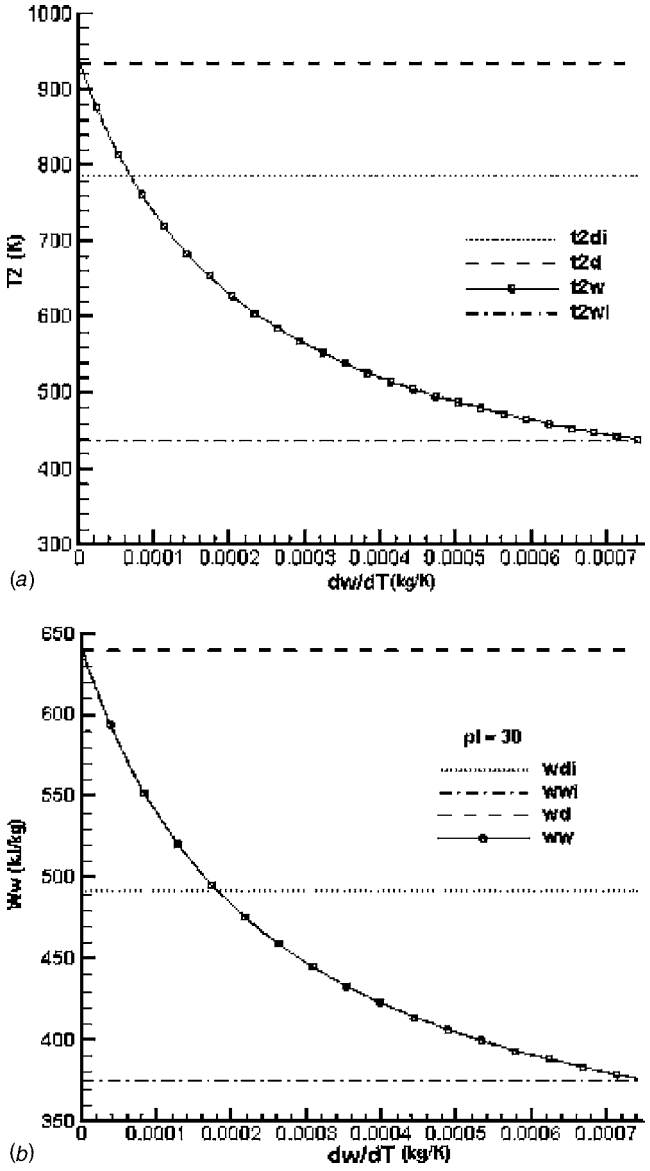

Fig. 2 (*a*) Effect of evaporation rate on compressor exit temperature for wet compression process at a pressure ratio of 30 (see Ref. [7]) and (*b*) effect of evaporation rate on compression work for wet compression process at a pressure ratio of 30 (see Ref. [7])

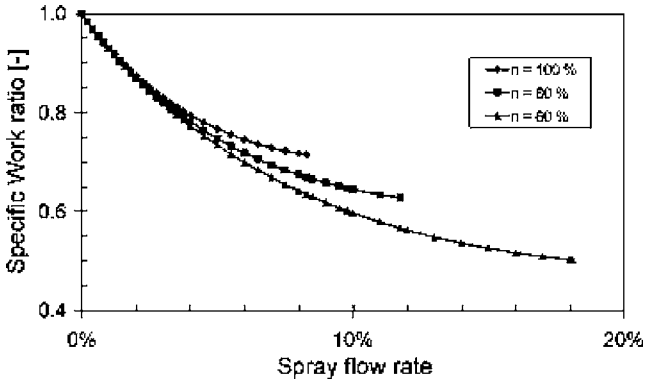

Fig. 3 Effects of spray flow rate and polytropic efficiency (denoted by "*n*" in the legend) on specific work ratio for pressure ratio of 30 (see Ref. [10])

performance, with simplifying assumptions that the gas constant, polytropic efficiency, and blade speed remain constant through compressor in presence of overspray, was presented by Horlock [9]. The values of constant pressure specific heat and polytropic exponent were assumed to have a first order change due to evaporation within the compressor. Also, the droplet temperature was assumed not to change through compressor while estimating the evaporation rate which implies neglecting the effect of convective heat transfer from droplets and overestimating evaporation length for a given droplet size.

A detailed study using two analytical models for overspray fogging, considering the effects of compression rate, droplet size, and polytropic efficiency on overall compressor performance, was recently presented by Haertel and Pfeiffer [10]. In the first model (termed ideal model), the air-liquid mixture was assumed to be in a thermodynamic equilibrium through the compression process. This implies that the droplets are very small and that the compression rate does not affect thermodynamic changes. In the second model (called droplet model), the limitations of the ideal model were addressed. Their analysis showed that the maximum spray flow rate, which corresponds to complete saturation at the compressor discharge for a given pressure ratio, depends on the pressure ratio and polytropic efficiency and its value is higher for a compressor with lower efficiency. The results further show that difference in specific work reduction due to polytropic efficiency change is insignificant for spray flow rates less than 2% (see Fig. 3). It is possible that the negligible effect of polytropic efficiency for spray flow rate less than 2% is due to the fact that stage mismatching and associated aerodynamic losses are not significant.

The effects of droplet size on compressor work ratio with a compression rate of 870 bars/s (or pressure ratio of 30) for polytropic efficiency values of 100% and 80%, based on the droplet model of Haertel and Pfeiffer are shown in Figs. 4(*a*) and 4(*b*), respectively. It is evident that an increased specific work reduction due to overspray fogging, for a given spray flow rate and droplet size, can be achieved for a compressor with lower efficiency. Because of the fact that the models proposed by Haertel and Pfeiffer did not consider effects of stage mismatching with high fogging, there exists a possibility of overestimation of the reduction in compressor specific work and discharge temperature drop.

A method combining droplet evaporation and mean-line compressor performance to examine the effects of wet compression on stage-by-stage performance was presented by White and Meacock [11]. An evaluation of overall compressor performance characteristics showed characteristics progressively moving to a higher flow and pressure ratio with increasing water injection rate. The increase in mass flow due to wet compression is due to the water injected and also the cooling caused by an evaporation effect and is therefore higher than the additional amount of injected water. Furthermore, their analysis indicated a decrease in aerodynamic efficiency as the injection rate increased which was mainly attributed to off-design operation of all the stages as seen in Fig. 5 which shows stage-by-stage normalized flow coefficient. Their study clearly shows the unloading (increased flow coefficient compared to the design value) of early stages and overloading (decrease in flow coefficient) of later stages of a compressor.

Sexton and Sexton [12] conducted a parametric study on the effects of evaporative and overspray fogging including stage-by-stage performance on a 16-stage 19.8 pressure ratio compressor. Their diffusion-controlled evaporation model assumes that each droplet of water would be rapidly entrained in the air stream and attains air velocity implying neglect of convective heat and mass transfer effects. Their study shows higher performance gains for combined effects of inlet evaporative and overspray fogging in comparison to if the water is injected directly into the compressor bell mouth.

Recently, a detailed thermodynamic analysis on the effects of

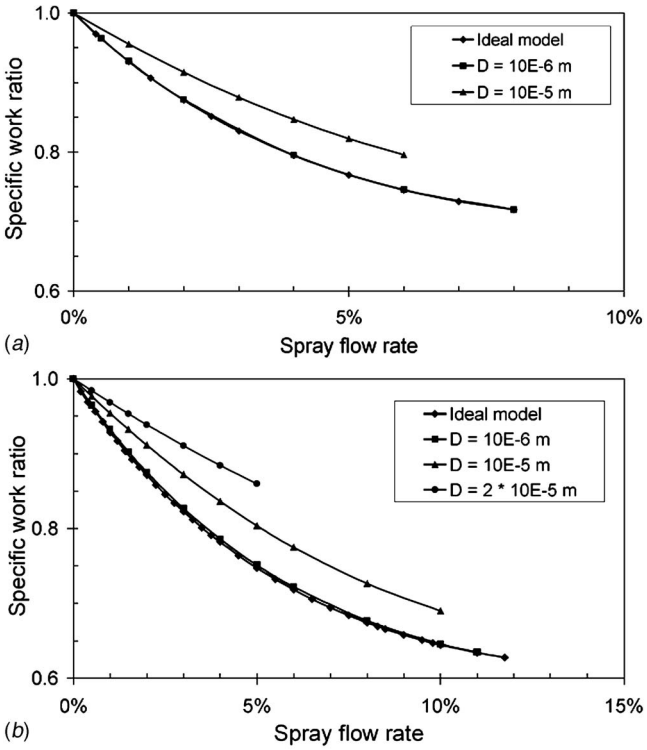

Fig. 4 (*a*) Effect of droplet size on specific work ratio (compression rate 870 bars/s and polytropic efficiency 100%); (*b*) effect of droplet size on specific work ratio (compression rate 870 bars/s and polytropic efficiency 80%) (see Ref. [10])

wet compression in a regenerative cycle gas turbine was presented by Zheng et al. [13]. For a given value of compression pressure ratio and turbine inlet temperature, specific power of a regenerative gas turbine with wet compression almost doubles compared to a simple cycle gas turbine. Also the cycle efficiency of a regenerative cycle with wet compression can be competitive with any advanced combined cycle system.

Jolly [15] presented results of field experiences with overspray on three gas turbines: GE Frame 6B, Siemen-Westinghouse W501D5A, and Alstom GT-24. It was shown that an advanced technology GT-24 requires relatively less water per unit power

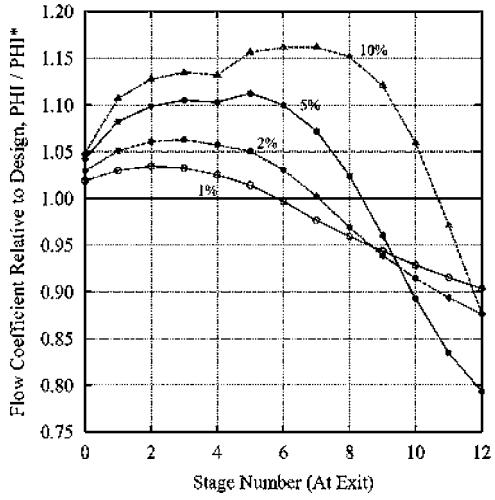

Fig. 5 Stage flow coefficient relative to their design value—effect of wet compression with 5 μm droplets (see Ref. [11])

gain compared to the other machines discussed. The field data show a power boost in the amount of 5.64% for 1% overspray. Jolly also noted that the payback period for a wet compression system is less than half that of an inlet chiller system.

Li and Zheng [17,18] recently presented compressor stability analysis in presence of wet compression and noted that in addition to improving gas turbine performance, water injection stabilizes aerodynamic instabilities in the compressor.

Another approach to wet compression, by using inter-stage water injection, has also been examined [19,20]. Arsen'ev and Berkovich [19] compared overall performance considering cases of water injection in different stages including upstream of a compressor and for a compressor modified for water injection effects. Their study showed that water injection effects are improved if water is injected within the compressor. The presented results suggested an optimum compressor stage for water injection, as for the configuration studied the performance improvement was higher with water injected at the third stage.

Recently, Bagnoli et al. [21] investigated the effects of interstage injection on the performance of a GE Frame 7EA gas turbine using aerothermodynamic modeling. In addition to estimating the overall gas turbine performance changes achievable with the interstage injection approach, the study presented impact of interstage injection on stage-by-stage compressor performance characteristics of the selected gas turbine. This study showed, similar to the work of White and Meacock [11], that various stages in a compressor operate at off-design conditions and the first few stages are unloaded and later stages are overloaded. An increased amount of water injection results in the operating point moving closer to the surge line in the 17th stage (see Fig. 6), for the modeled machine, suggesting that one has to be cautious in selecting the water amount in case of both interstage injection and overspray fogging.

Analytical studies on the effect of droplets on the blade surface reveal requirements for very small size (1–5 μm) droplets [22]. The use of swirl-flash technology, where pressurized hot water is sprayed through a swirl nozzle, has demonstrated achieving droplets of 2.2 μm in the laboratory. Swirl-Flash technology has been applied on a number of gas turbines including a GE Frame 6, Siemens V94.2, and an ABB 9D [22–24]. By using swirl nozzles fed by high temperature pressurized water, droplets roughly ten times smaller in diameter and a thousand times smaller in volume and weight than the droplets from a normal swirl spray could be achieved as reported by Liere et al. [24]. It was also shown that approximately 14% power boost could be obtained for an ABB 9D gas turbine with 2% overspray injection rate. Compared to inlet evaporative fogging, overspray has an advantage as it allows the air to reach saturation in ambient conditions with high relative humidity and low dry-bulb temperature due to the large quantity of small size droplets in the spray which results in faster evaporation.

In case droplets are not evaporated in the allowed time, they may flow through the compressor and boost the power while evaporating in the compressor. However, in order to maximize the benefit of a fogging system, it is important to get as close as possible to saturation at the compressor bell mouth. As an example, the power boost achievable for a given ambient condition (which requires 0.5% of water injection to achieve saturation at the compressor inlet) under different amount of injected water for selected gas turbines is shown in Fig. 7. It is evident from Fig. 7 that the power boost due to fog injected to saturate the air is higher than the power boost due to overspray. For example, for the ABB GT8C, the power boost up to the saturation point is 2.5% for each 1% of water sprayed into the airflow. Whereas, the power boost for GT8C is reduced to 1.25% for each 1% of injected water with overspray.

Figure 8 shows the progressive boost in power with increase in the amount of water sprayed with the inlet airflow for given am-

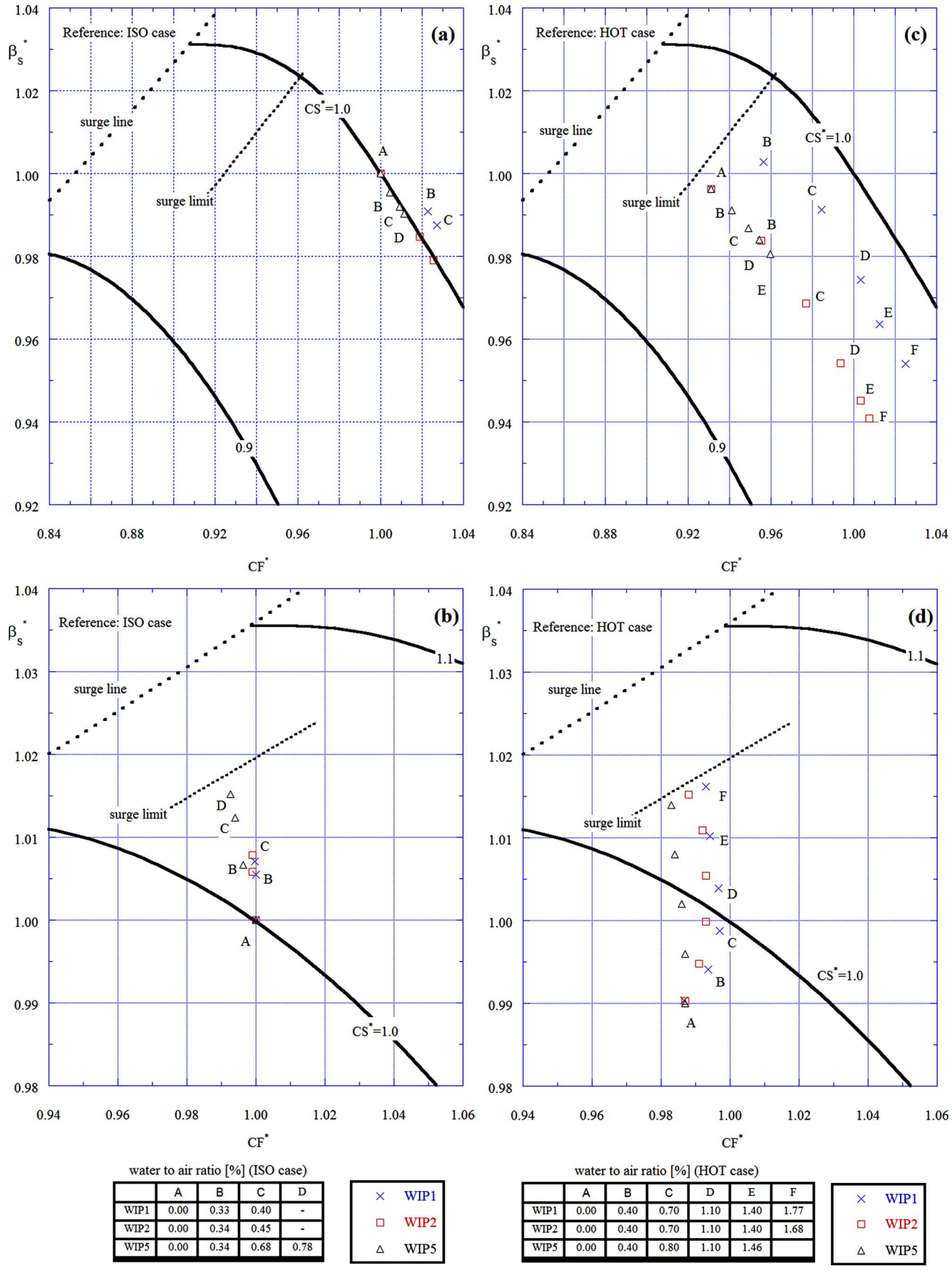

	A	B	C	D
WIP1	0.00	0.33	0.40	-
WIP2	0.00	0.34	0.45	-
WIP5	0.00	0.34	0.68	0.78

	A	B	C	D	E	F
WIP1	0.00	0.40	0.70	1.10	1.40	1.77
WIP2	0.00	0.40	0.70	1.10	1.40	1.68
WIP5	0.00	0.40	0.80	1.10	1.46	

Fig. 6 (*a*) **First stage performance maps and operating points with water injection (reference: ISO case);** (*b*) **seventeenth stage performance maps and operating points with water injection (reference: ISO case);** (*c*) **first stage performance maps and operating points with water injection (reference: HOT case);** (*d*) **seventeenth stage performance maps and operating points with water injection (reference: HOT case) (see Ref. [21])**

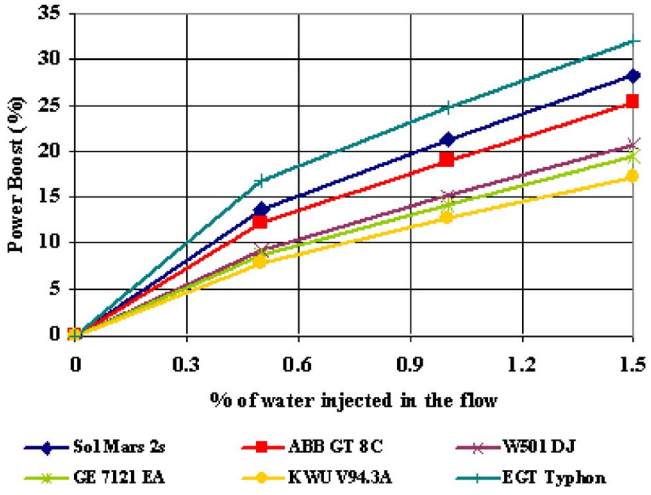

Fig. 7 Power boost due to water sprayed in the airflow DBT =37.8 °C (100 °F), WBT=26.1 °C (79 °F)

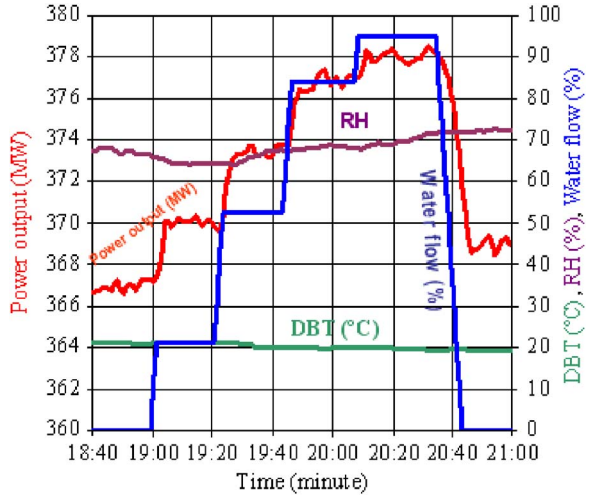

Fig. 8 Experimental power boost due to water sprayed with the airflow in an advanced industrial gas turbine inlet air duct

bient psychrometric conditions. The figure shows the step changes in power output as the injected water flow is stepped up by the activation of additional fog stages.

Ongoing Areas of Research

Issues that need to be researched in the area of overspray fogging are common to the areas mentioned in part III of this paper. Specific issues relating to overspray include:

- study of the interaction of water injection quantity and the surge margin of the machine—this should be evaluated under both new and deteriorated compressor conditions
- innovative thermodynamic cycles utilizing overspray
- special control systems to provide power during underfrequency operation
- nozzle testing protocols and standardization
- special control issues relating to multispool gas turbines

Concluding Remarks

Overspray fogging is being applied to both new and existing gas turbines with most OEMs working on ongoing implementation programs at this time. Several existing gas turbines users utilize overspray as a means for augmenting power. This paper has provided a review on the current understanding of analytical and experimental aspects of overspray fogging technology including some practical issues that are of importance. In general, most machines operate with an overspray level not exceeding 2% of the air mass flow but the limiting amount of injected water is machine specific. There are several engineering issues that have to be addressed prior to the implementation of overspray including issues relating to compressor inlet temperature profile distortion, transient effects, and reduction in the compressor's operating surge margin. Particular care should be taken of cooling air flows issues as the compressor loading will change with overpsray which could result in modified cooling flows due to a modified pressure profile through the compressor. Several practical aspects relating to these issues are covered in part III of this paper.

Nomenclature

CF^*	=	corrected flow normalized to the design value
CS^*	=	corrected speed normalized to the design value
dw/dT	=	evaporation rate (kg/K)
D	=	droplet diameter (μm)
DBT	=	dry-bulb temperature (°C)
n	=	compressor polytropic efficiency
PHI	=	flow coefficient ($=V_x/U$)
PHI^*	=	design flow coefficient
pi	=	compressor pressure ratio
RH	=	relative humidity (%)
RA	=	active radius of the droplet
$t2d$	=	compressor discharge temperature-dry (K)
$t2di$	=	isentropic compressor discharge temperature-dry (K)
$t2w$	=	compressor discharge temperature-wet (K)
$t2wi$	=	isentropic compressor discharge temperature (K)
$T2$	=	compressor discharge temperature (K)
TIT	=	turbine inlet temperature (°C)
U	=	blade velocity (m/s)
V_x	=	axial flow velocity (m/s)
w	=	vapor to air mass ratio
wd	=	compressor work-dry (kJ/kg)
wdi	=	isentropic compressor work-dry (kJ/kg)
ww	=	compressor work-wet (kJ/kg)
wwi	=	isentropic compressor work-wet (kJ/kg)
WBT	=	wet bulb temperature (°C)
W_C	=	compressor work input ratio
WIP	=	water injection point
β_s^*	=	pressure ratio normalized to the design value
λ	=	ratio of latent heat of coolant to latent heat of water
θ	=	ratio of temperature to standard day temperature

References

[1] Bhargava, R. K., Meher-Homji, C. B., Chaker, M. A., Bianchi, M., Melino, F., Peretto, A., and Ingistov, S., 2007, "Gas Turbine Fogging Technology: A State-of-the-Art Review—Part I: Inlet Evaporative Fogging—Analytical and Experimental Aspects," ASME J. Eng. Gas Turbines Power, **129**, pp. 443–453.

[2] Bhargava, R. K., Meher-Homji, C. B., Chaker, M. A., Bianchi, M., Melino, F., Peretto, A., and Ingistov, S., 2007, "Gas Turbine Fogging Technology: A State-of-the-Art Review—Part III: Practical Considerations and Operational Experience," ASME J. Eng. Gas Turbines Power, **129**, pp. 461–472.

[3] Kleinschmidt, R. V., 1947, "Value of Wet Compression in Gas-Turbine Cycles," Mech. Eng. (Am. Soc. Mech. Eng.), **69**(2), pp. 115–116.

[4] Wilcox, E. C., and Trout, A. M., 1951, "Analysis of Thrust Augmentation of Turbojet Engines by Water Injection at Compressor Inlet Including Charts for Calculating Compression Processes With Water Injection," NACA Report No. 1006.

[5] Beede, W. L., Hamrick, J. T., and Withee, J. R., 1951, "Evaluation of Centrifugal Compressor Performance With Water Injection," NACA RM-E51E21.

[6] Hill, P. G., 1963, "Aerodynamic and Thermodynamic Effects of Coolant Injection on Axial Compressors," Aeronaut. Q., **13**, pp. 331–348.

[7] Zheng, Q., Sun, Y., Li, S., and Wang, Y., 2002, "Thermodynamic Analyses on Wet Compression Process in the Compressor of Gas Turbine," ASME Paper No. GT-2002-30590.

[8] Utamura, M., Kuwahara, T., Murata, H., and Horii, N., 1999, "Effects of

Intensive Evaporative Cooling on Performance Characteristics of Land-Based Gas Turbine," Joint Power Generation Conference, PWR-Vol. 34.
[9] Horlock, J. H., 2001, "Compressor Performance With Water Injection," ASME Paper No. 2001-GT-0343.
[10] Haertel, C., and Pfeiffer, P., 2003, "Model Analysis of High-Fogging Effects on the Work of Compression," ASME Paper No. GT2003-38117.
[11] White, A. J., and Meacock, A. J., 2003, "An Evaluation of the Effects of Water Injection on Compressor Performance," ASME Paper No. GT2003-38237.
[12] Sexton, W. R., and Sexton, M. R., 2003, "The Effects of Wet Compression on Gas Turbine Engine Operating Performance," ASME Paper No. GT2003-38045.
[13] Zheng, Q., Li, M., and Sun, Y., 2003, "Thermodynamic Performance of Wet Compression and Regenerative (WCR) Gas Turbine," ASME Paper No. GT2003-38517.
[14] Yan, J., Ji, X., and Jonsson, M., 2003, "Thermodynamic Property Models for the Simulation of Advanced Wet Cycles," ASME Paper No. GT2003-38298.
[15] Jolly, S., 2003, "Performance Enhancement of GT 24 With Wet Compression," Power-Gen International, Dec. 9–11, Las Vegas, NV.
[16] Utamura, M., Takehara, I., Horii, N., and Kuwahara, T., 1997, "A New Gas Turbine Cycle for Economical Power Boosting," ASME Paper No. 97-AA-142.
[17] Li, M., and Zheng, Q., 2004, "Wet Compression System Stability Analysis: Part I—Wet Compression Moore Greitzer Transient Model," ASME Paper No. GT2004-54018.
[18] Li, M., and Zheng, Q., 2004, "Wet Compression System Stability Analysis: Part II—Simulations and Bifurcation Analysis," ASME Paper No. GT2004-54020.
[19] Arsen'ev, L. V., and Berkovich, A. L., 1996, "The Parameters of Gas-Turbine Units With Water Injected Into the Compressor," Therm. Eng., **43**(6), pp. 461–465.
[20] Ingistov, S., 2001, "Interstage Injection System for Heavy Duty Industrial Gas Turbine Model 7EA," ASME Paper No. 2001-GT-407.
[21] Bagnoli, M., Bianchi, M., Melino, F., Peretto, A., Spina, P. R., Bhargava, R., and Ingistov, S., "A Parametric Study of Interstage Injection on GE Frame 7EA Gas Turbine," ASME Paper No. GT2004-53042.
[22] van Liere, J., and Laagland, G. H. M., 1998, "The TOPHAT Project—Swirl Flash Technology to Reduce Maintenance Costs," KEMA Report No. 00376-KPG/SUP 98-1382.
[23] van Liere, J., and Meijer, C. G., "Power Augmentation and NO_x Reduction of Gas Turbines by SwirlFlash Overspray Injection," Alpha Power Systems Publication.
[24] van Liere, J., Laagland, G. H. M., and Meijer, C. G., "Retrofit of Gas Turbines by SwirlFlash Overspray," Alpha Power Systems Publication.

R. K. Bhargava
22515 Holly Lake Drive,
Katy, TX 77450

C. B. Meher-Homji

M. A. Chaker

Bechtel Corporation,
3000 Post Oak Boulevard,
Houston, TX 77056

M. Bianchi

F. Melino

A. Peretto

University of Bologna,
DIEM, Facolta di Ingegneria,
Viale Risorgimento 2,
Bologna 40136, Italy

S. Ingistov
Watson Cogeneration Co./BP,
11850 S. Wilmington Avenue,
P. O. Box 6203,
Carson, CA 90749

Gas Turbine Fogging Technology: A State-of-the-Art Review—Part III: Practical Considerations and Operational Experience

The strong influence of ambient temperature on the output and heat rate of a gas turbine has popularized the application of inlet fogging and overspray for power augmentation. In this paper we focus on practical considerations for the implementation of the fogging technology such as water quality requirements, foreign object damage, gas turbine inlet icing, intake duct design, changes in compressor performance characteristics, and blade coating distress problems. It also provides a checklist for users and project developers to facilitate the design and implementation of fogging systems. In addition, in this paper we cover operational experience and review the work pursued by gas turbine OEMs in the field of fogging technology. A list of unresolved issues and ongoing research related to the fogging technology is also provided. [DOI: 10.1115/1.2364005]

Keywords: power augmentation, evaporative fogging, overspray, wet-compression, high fogging

Introduction

While there are several gas turbine inlet-cooling technologies available, high-pressure inlet fogging (evaporative and overspray) has in the past decade seen large-scale application. Inlet fogging has been applied on a wide range of new and old gas turbines from units as small as 5 MW to advanced technology gas turbines rated at 250 MW and higher. While the underlying principle of inlet fogging is simple, there are several practical issues that need careful attention. A comprehensive review on the current understanding of analytical and experimental aspects of the high-pressure inlet evaporative fogging technology and overspray fogging for gas turbine applications has been covered in Part I [1] and Part II [2], respectively, of this three-part paper. A comprehensive overview of fogging technology was provided in 1999 by Meher-Homji and Mee [3], summarizing some design and implementation considerations. Chaker et al. [4] provided, in 2002, the first detailed theoretical and experimental treatment on the subject including practical aspects based on over 400 fogging applications.

In addition to a good understanding of droplet generation, their dynamic behavior and selection and sizing of appropriate nozzles, it is equally critical to have a thorough understanding of fog system design and implementation requirements. Our main objective in this paper is to cover several practical issues relating to fogging system design, installation, and operation. To give a complete picture of the fogging technology, a brief summary of the fog related work pursued by major gas turbine manufacturers including results of some field experiences are also covered.

High-Pressure Inlet Fogging

Inlet fogging is a method of inlet air cooling where demineralized water is converted into fog droplets by means of specially designed atomizing nozzles operating at a high pressure of 69 to 207 barg (approximately 1000 to 3000 psig). The fog provides cooling when it evaporates in the inlet air duct of a gas turbine and can attain close to 100% evaporative cooling efficiency, as discussed in Part I of this paper. Overspray (also called wet compression, high fogging, or fog intercooling) refers to a situation where some water is deliberately allowed to enter the compressor to provide an intercooling effect.

A typical high-pressure fogging system consists of series of reciprocating pumps providing demineralized water at high pressure to an array of fogging nozzles located downstream of the inlet air filter elements. More details on the commonly used nozzle locations and their influence on evaporative efficiency are presented in Part I of this paper. An array of over 600 fogging nozzles, installed upstream of the silencer, in a 80 MW class heavy-duty industrial gas turbine is shown in Fig. 1.

There are several types of nozzles (as covered in Part I of this paper) used by different manufacturers of fogging equipment that utilize different principles to obtain a very fine fog. A close-up view of a typical nozzle array, consisting of impaction pin design nozzles, installed in an inlet duct of a gas turbine, is shown in Fig. 2. The orientation and angle of nozzles (see Fig. 2) need to be optimized in order to minimize duct wetting and optimize fog distribution, details of which are discussed in Part I of this paper.

Contributed by the International Gas Turbine Institute (IGTI) of ASME for publication in the JOURNAL OF ENGINEERING FOR GAS TURBINES AND POWER. Manuscript received October 1, 2005; final manuscript received February 1, 2006. IGTI Review Chair: R. S. Abhari. Paper presented at the ASME Turbo Expo 2006: Land, Sea, and Air, Barcelona, Spain, May 8–11 2006, Paper No. GT2005-69144.

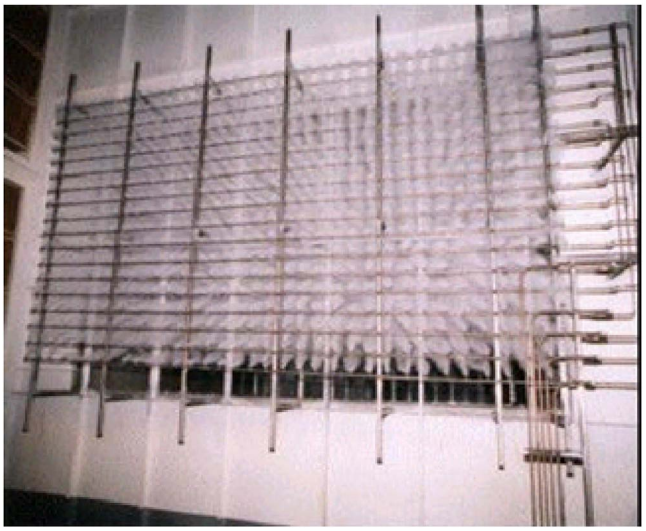

Fig. 1 Fog nozzle manifold in a 80 MW class heavy-duty gas turbine

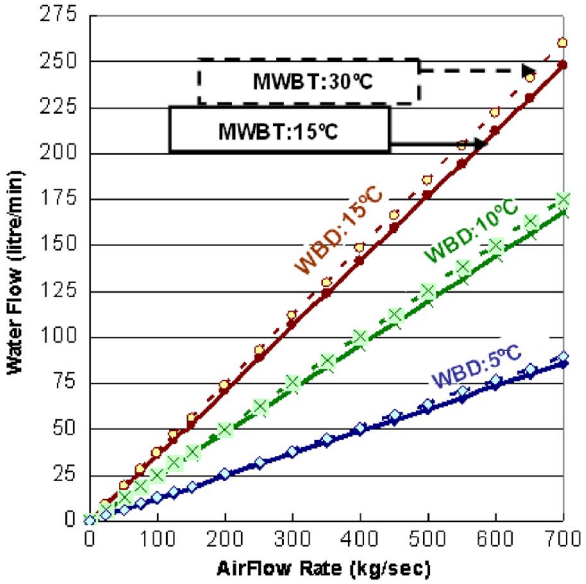

Fig. 3 A simple chart to estimate water flow requirements for varying gas turbine airflow rates and temperature depressions ranging from 5°C to 15°C (applicable for evaporative fogging only)

For a fog system to be safe and effective for the gas turbine, a proper estimation of the quantity of water required and its quality must be known, which is briefly discussed later.

Water Flow and Water Quality Requirements. The amount of water flow required for an evaporative fogging system is a strong function of the climatic design conditions and the temperature depression that can be attained. An illustration describing the procedure to calculate the required amount of water needed under given ambient psychrometric conditions is provided in Part I of this paper. Figure 3 provides a simple method to obtain a rough estimate of the water quantity required for an evaporative fogging. The quantity of water in saturated air increases with the increase of air temperature. Figure 3 shows the required amount of water to cool the air to the Minimum Wet Bulb Temperature (MWBT) of 15°C (solid lines) and 30°C (dashed lines) for a series of Wet Bulb Depressions (WBD) between 5°C and 15°C. This figure shows that for a given amount of airflow rate and WBD value, cooling the air to a high value of MWBT requires a larger quantity of fog water.

Water Quality Requirements. General water quality requirements for fogging applications are provided in Table 1. If the water quality is not up to these specifications, there can be considerable distress due to compressor fouling or hot section corrosion. While the values given in this table provide general guidelines, it is best that the gas turbine OEM's on-line water wash specification be followed. Demineralized quality water is generally acceptable for inlet fogging. It is imperative, however, that only stainless steel piping and fittings be used to transport water supply to the fogging skid.

Fig. 2 Typical high pressure nozzles in an intake duct [4]

Practical Considerations

There are several practical engineering considerations that need to be addressed during the design of inlet fogging systems and are discussed next.

Foreign Object Damage (FOD). As the nozzle manifolds are mounted in the air stream, care must be taken to avoid any chance of foreign object damage resulting from the nozzles or nozzle array components themselves. Normally for evaporative fogging, nozzles are located in a low velocity area after the inlet air filtration system. Extensive safety wiring of nozzles and an analysis of the fog nozzle array for airflow-induced vibration should be done to ensure that the structure is strong and cannot break. For example, the use of safety wires on nozzles can be clearly seen in Fig. 2. In the case of overspray applications, the fog nozzles are typically located much closer to the inlet bell-mouth of the gas turbine, usually in the vertical duct section leading to the inlet cone of the gas turbine axial compressor. Experience has shown that with careful engineering, FOD issues can be easily avoided. Some of the engineering considerations for proper nozzle array design including the evaluation of flow-induced vibration have been provided by Chaker et al. ([4], Part C).

Gas Turbine Inlet Icing. The fog control system should be designed to automatically terminate fogging whenever there is any chance of inlet icing due to the static temperature depression that occurs in the bell-mouth due to acceleration of the inlet air to

Table 1 General water quality requirements

Water quality indicator	Value
Water *p*H	6.5–7.5
Total solids (dissolved and undisolved)	5 ppm
Total alkali metals and other metals that promote hot corrosion	0.5 ppm
Conductivity	0.5-1 micro-mho/cm

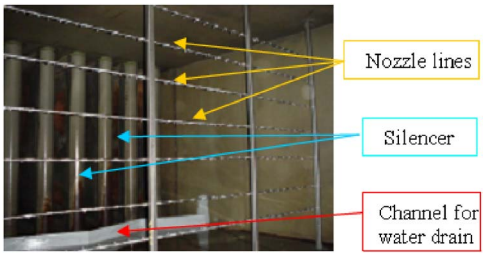

Fig. 4 Special channel system for water drain [4]

Mach number of about 0.5 for heavy duty gas turbines and 0.8 for aeroderivative machines. Several fog systems are designed to deactivate at a MWBT value of 15°C, though 12.8°C can be easily set as a minimum temperature. Several OEMs recommend a combination of relative humidity and temperature at which anti-icing measures are turned on. With fogging applications where the ending relative humidity is close to 100%, temperatures as low as 10°C can be utilized. However, to be on the conservative side, temperatures of 12.8°C are typically used as a low minimum when situations warrant it.

Duct Drainage. This is an important subject matter and there are a lot of practical issues involved. Drains should be strategically located both near the silencers and also in the intake bell-mouth region. These should be carefully designed as continuous drains and the number of drains should be determined based on experience, configuration of the duct, and obstructions that might result in water collection. Special shaped channel sections may be located on the floor and duct sections to channel water collected to the drains. One such channel is shown in Fig. 4. Appropriate sealing systems must be used to prevent the flow of ambient air into the duct. In the case where *p*-trap type seals are used, it is imperative that water be supplied to these seals to ensure that they do not run dry due to evaporation that will allow the ingress of air.

Drain flow should be monitored and logged as a function of ambient conditions and the number of fog stages in operation. This can be done simply by measuring the flow for a duration of 5 min and then calculating the drain flow rate as a percent of the overall water flow.

Special considerations are required for bell-mouth floor drains. At times, the pooling of water in localized segments can be ingested into the compressor as it is pulled forward away from the continuous drains. Figure 5 shows the proximity of the floor to the inlet of a large gas turbine. In such cases, a special arrangement may have to be made to prevent the pooling of water.

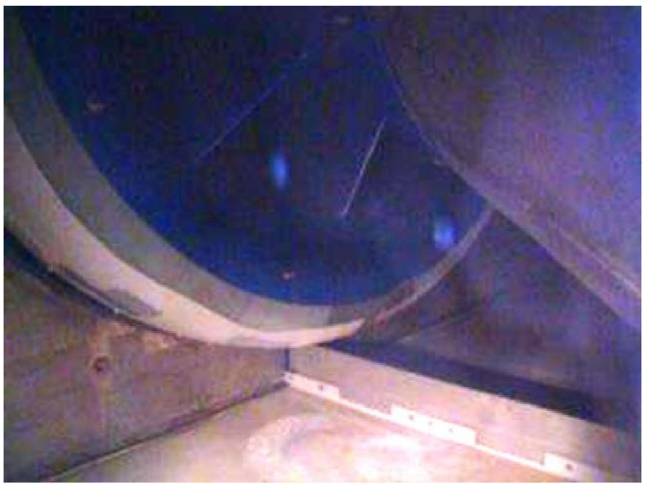

Fig. 5 Proximity of the floor to the compressor inlet can at time cause vortex ingestion of pooled water [4]

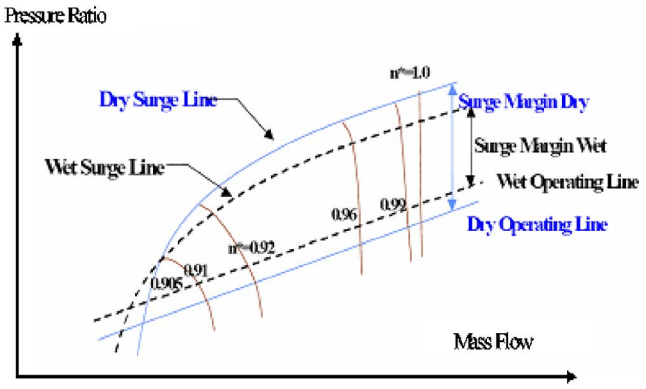

Fig. 6 A schematic showing movement of engine operating line with respect to the surge line [5]

Compressor Surge. This operational condition is of greater concern on systems that are implemented with overspray (or fog intercooling). In most cases, the extent of the overspray is a little over the amount that is allowed for compressor on-line water washing. The effect of overspray is to cause the operating points on the compressor map to move toward the surge line. Also, with overspray, there is a movement of the engine operating line and surge line as schematically presented by Lecheler and Hoffmann [5] and shown in Fig. 6. Normally, on-line water wash rates are themselves in the range of 0.4% to 0.5% of the airflow rate on most heavy-duty gas turbines. Even with evaporative fogging, compressor inlet temperature distortion and its rate of change has to be considered carefully in the design of the fogging system and the control system. The issue of the surge margin must be evaluated for each specific engine type. The evaluation should also look at factors that would impact the surge margin, including the blade surface condition and the presence of compressor fouling.

Compressor Intake Temperature Uniformity. Axial compressors have stringent intake temperature and pressure uniformity criteria. Issues relate to blading vibration that can be induced due to extensive compressor intake temperature and pressure distortions. Details of blading issues are discussed by Meher-Homji [6]. Fogging systems are designed in multiple stages and each stage has nozzle manifolds distributed within the inlet duct to provide a relatively uniform compressor intake temperature. This is an important consideration, as the susceptibility of the compressor to stall or surge could be affected by severe compressor intake temperature distortion. There are also criteria relating to rapid changes in the inlet temperature, but fogging systems cannot exceed these criteria, even in the event of an emergency shutdown of the fogging system due to the residual time and water flow in the system that never results in instantaneous shock temperature changes.

The location of gas turbine compressor inlet temperature (CIT) sensors, typically do not provide a means to evaluate temperature distortion. In several engines with complicated ducts, considerable temperature and pressure distortions exist even without fogging, and it is not uncommon to find the temperature difference of the CIT sensors of 2°C. In some gas turbines, the CIT sensors may be located in the intake duct in a location that is starved of flow. These sorts of natural distortions can be made more evident by inlet fogging. It is a good idea to map the compressor inlet temperature sensor readings with different ambient conditions and operating parameters and the number of fog stages in operation. This can form a useful baseline for an analysis of deviations in compressor inlet temperature due to a fogging application.

A common problem faced is that as the CIT sensors become

wet, they tend to read lower temperatures than the bulk inlet temperature. To avoid this problem, special shielded CIT sensors should be used.

Intake Duct Considerations. There are several issues relating to the intake duct itself that need to be considered while implementing a fogging system. On retrofit applications, it may not be possible to have "ideal" conditions and hence careful compromises are needed. For example, it may be impossible to obtain a length of duct with no obstructions and there may be items such as bleed heating pipes [often present for machines with a dry low NO_x (DLN) combustion system] where airflow is bled for controlling the combustor conditions under certain operating regimes. Furthermore, some gas turbines utilize trash screens and these will act as agglomerators causing larger droplets to form. In the intake bell-mouth region of cold-end drive gas turbines that have intake cones, cone wetting may occur and some water may progress toward the compressor. However, due to the Weber number effect, the higher velocities often result in droplet shattering, [5], and consequently the extent of the problem is minimized. The fog system supplier should be knowledgeable of these practical considerations and design their system to minimize such problems. Much of the choice of selecting and designing a fog system is an art and involves CFD (computational fluid dynamic) analysis coupled with past experience and visual observations. In some extreme cases of short ducts, duct extensions may have to be provided to achieve adequate residence time for evaporation to occur.

Axial Compressor Fouling. It is important to distinguish between the problems of natural climatic fog and the fog generated by the fogging system. High natural humidity and climatic fog that often occur during the night and early morning hours can a cause a gas turbine to trip due to high inlet air filter differential pressure and sometimes the heavily fouled filters tend to unload and leach contaminants through the filter, causing compressor fouling. However, if the air filtration system is appropriately designed and working well, the increased humidity caused by the fogging system does not inherently increase fouling. Fouling is a situation that is so site specific that it is very difficult to predict the behavior. At times, if the No. 1 bearing in a gas turbine is leaking oil, then this may combine with the high humidity (caused by inlet fogging) to create some compressor fouling. An important issue is to wash the silencers thoroughly to avoid dirt that has been accumulated here being washed into the compressor by the fogging system during startup. This is particularly important when a fogging system is being retrofitted on an older machine. On retrofit applications, it may be necessary to perform several crank washes before the problem resolves. More details on compressor fouling may be found in Meher-Homji [7] and Meher-Homji et al. [8].

Compressor Blade Erosion. In evaporative fogging systems the control system can be adjusted to maintain a margin between the compressor inlet temperature and the wet-bulb temperature, thus ensuring (in theory) that no water enters the compressor. Yet, it is possible that some droplets do enter the compressor. For a relatively small size (less than 15–20 microns) droplets, CFD studies have shown that the droplets will tend to follow the airstream. There is an issue of larger water particles forming on the trash screen and inlet cone of the gas turbine, but with proper design and drainage approaches this can be minimized. It is important to note that the operational experience shows that overspray systems have not resulted in excessive erosion problems, and several OEMs are offering this technology currently. Operational results, presented in Figs. 7 and 8, show no sign of blade erosion in the presence of overspray application [9,10].

Corrosion in the Inlet Duct

The use of demineralized water can deteriorate inlet ducts that are already in a deteriorated state—the increased humidity is clearly a corrosion factor. With proper maintenance and painting, this problem can be mitigated. The use of stainless steel (316L) as the duct material is gaining popularity. Despite the fact that the equipment first cost is a little higher, the life cycle costs are significantly lower. It is important to note that ducts often operate in a distressed condition, such as seen in Fig. 9. It is important that such problems are addressed and corrected prior to the implementation of a fogging system. Careful consideration should be given to special paint systems or the use of stainless steel liners where appropriate.

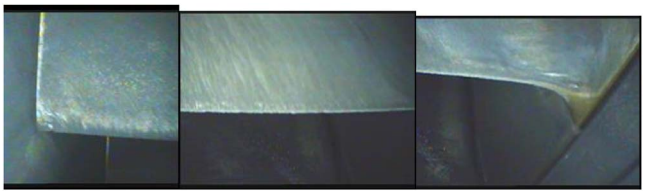

Fig. 7 Level of erosion on compressor blades of GE Frame 6B gas turbine with wet compression: First stage blade tip (left); First stage blade mid-height (Center); and First stage blade hub (Right) (Courtesy Caldwell Energy and Environmental, Inc.)

Compressor Blading and Coating Distress. Some gas turbines that have undergone overspray have experienced coating distress in the first few stages of the axial flow compressor. In most cases, this can be minimized by careful location of fogging nozzles, the avoidance of excessive water accumulation on ducts and inlet cones, and by several other proprietary approaches. Corrosive ambient conditions such as chlorides or even trace contents of hydrochloric acids will cause acidity and hence coating damage. Airborne contaminants in even the parts/billion (ppb) range can often create very acidic environments for the gas turbine axial blading. This is an issue that must be resolved by proper inlet air filtration, especially in aggressive industrial environments. The

Fig. 8 Blade condition of first stage compressor blades of ALSTOM advanced heavy duty industrial gas turbine GT24 (Courtesy Caldwell Energy & Environmental, Inc.)

Fig. 9 A view of a corroded floor of intake duct [4]

use of appropriate coatings does help protect in this area. In overspray cases, the situation should be examined on a case-by-case basis, evaluating the available blading material and coating technologies. Haskell [11] has described the criticality of ambient air quality.

Factors that can cause blading and coating distress include the following:

- excessive or improper use of overspray
- improper orientation of fog nozzles
- lack of drains or inappropriately located drains
- corrosive ambient conditions that will cause acidity and hence coating damage.

In some cases, if some blade leading edge coating distress already exists prior to fogging then this might progress with fogging due to the reasons mentioned above.

Off-Frequency Operation of Gas Turbines. This is an important consideration for countries where the grid operates under off-frequency conditions. When under-frequency operation occurs, the airflow rate drops considerably and there is a possibility for some gas turbines to operate much closer to rotating stall conditions in the early stages when the under-frequency operation is coupled with high ambient temperatures. This sort of operation must be carefully considered during the design of the fogging system. The change in power output for a large heavy-duty gas turbine operating under-frequency is shown in Fig. 10.

In the case of overspray, the aerodynamic loading through the compressor stages is modified, and so the minimum corrected compressor speed needs to be determined. As it occurs, some gas turbine models actually will modulate the inlet guide vanes at under-frequency operation at high ambient temperatures. Often, in power plants, guarantees have to be met even with under-frequency operation, and overspray may be used to mitigate this effect.

Electrostatic Buildup and Bearing Distress With Overspray. Similar to the electrostatic charges that occur in the low-pressure section of a steam turbine where condensed particles induce an electrostatic charge, machines that are operated with wet compression need to have superior shaft grounding brush systems utilized. Several installations have used Sohre Turbomachinery grounding

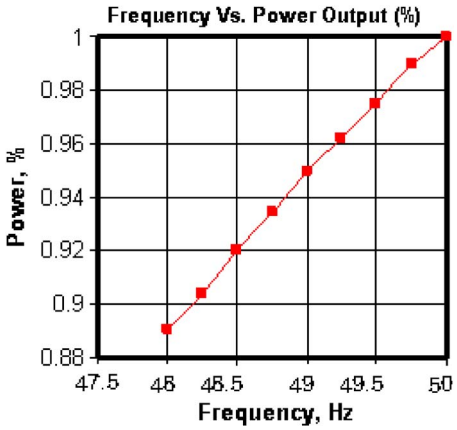

Fig. 10 Under-frequency operation of gas turbine and its effect on output (Design frequency 50 Hz)

brush systems very successfully. An installation of such a brush is shown in Fig. 11 [12]. The area of electrostatic grounding has been covered in great detail by Sohre [13].

Multispool Gas Turbines for Mechanical Drive or Power Generation Service. In the case of multispool gas turbine such as commonly found in mechanical drive service, the changes in the gas generator speed result in modified airflow through the machine. It is important, therefore, that this be taken into account during the fogging system design to ensure that the injected water is appropriate with respect to the gas turbine airflow. If two-shaft gas turbines are used for power generation applications, as is commonly done in the case of aeroderivative gas turbines, the same considerations should apply.

Considerations Relating to Engine Cooling Air Flow With Overspray. A detailed study on the overall engine and compressor performance using fixed and variable design Secondary Air System (SAS) with overspray effects has been recently reported by Cataldi et al. [14] and clearly shows impact of SAS system on the pressure distribution (see Fig. 12).

The variable SAS system implies relative cooling air mass flows to various components (such as combustor, turbine hot parts, etc.) is constant. Whereas, in the case of a fixed SAS system, the cooling air flow is influenced by the injected water. The annotations ex. 1, ex. 2, and ex. 3, in Fig. 12 represent bleed air

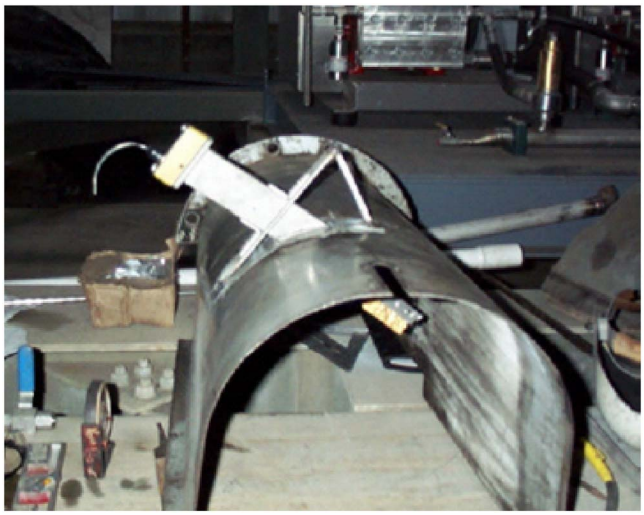

Fig. 11 Special grounding brush utilized for overspray applications

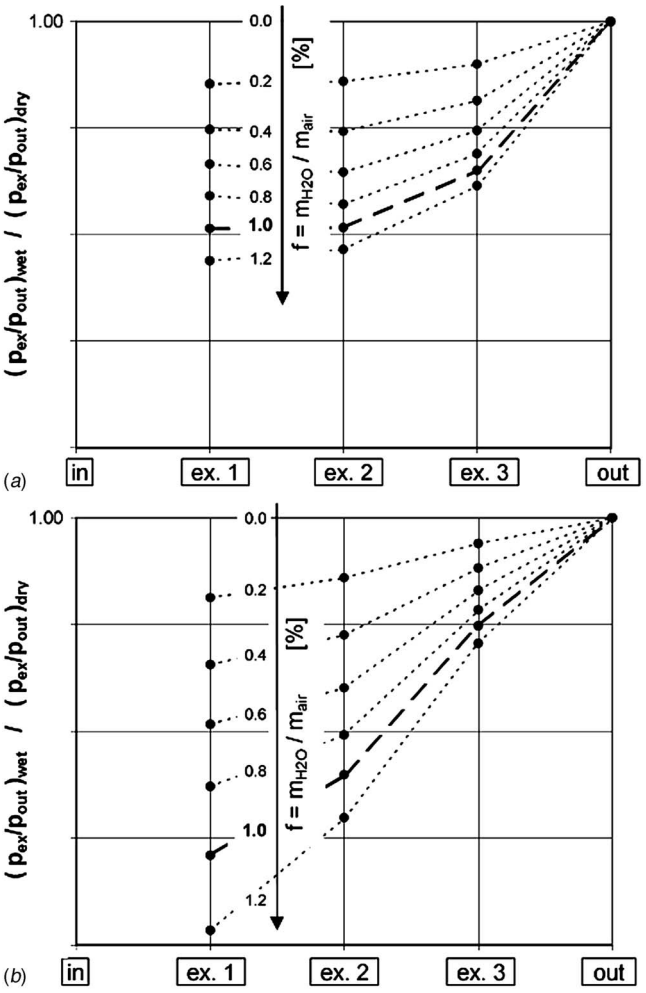

Fig. 12 Pressure variation along compressor showing pressure buildup in the rear stages for a different amount of overspray: Top—Variable SAS system; and bottom—fixed SAS system [14]

locations, whereas, "in" and "out" represent the compressor's inlet and outlet sections, respectively. Pressure ratio at various locations inside the compressor is normalized with its value for the dry case (no fogging). It was evident that for an engine designed for dry operation, the amount of water injected is limited due to changes in the secondary air flow, compressor load redistribution, and change in the surge margin. With overspray, the temperature and pressure distributions within the compressor stages change and in some cases adjustments to the bleed air orifices may be required.

The stage-by-stage change in pressure buildup with and without overspray in a compressor is shown in Fig. 13 [5]. The abscissa in Fig. 13 represents axial position in the compressor. Whereas the ordinate in Fig. 13 shows the relative change in pressure buildup and effect on the buildup with increasing amounts of overspray. The increase in the unloading of the early stages as overspray is increased is also evident in Fig. 13.

Practical Considerations for Fog System Design and Implementation

Some important practical considerations to be made, in the form of a checklist, in the implementation of any fogging system are provided below:

- Check vendors design calculations with regards to water flow requirements, off design conditions, and evaluate the design under different climatic conditions.
- Ensure that the fogging system vendor is provided with detailed sketches and photos of the inlet system. Full details including air takeoff for cooling of auxiliary systems (such as an electrical system cabin) should be provided as appropriate measures may have to be taken to avoid moisture entry into these areas.
- Evaluate amount of overspray required and ensure that the compressor can accommodate this. The surge margin should be evaluated. Check effects of overspray on the cooling air flows.
- If overspray is being considered, review generator and lube oil cooler capability.
- Insist on the use of all stainless steel piping.
- In the event of a problem, does the design permit rapid isolation so that gas turbine operation can proceed without the fogging system?

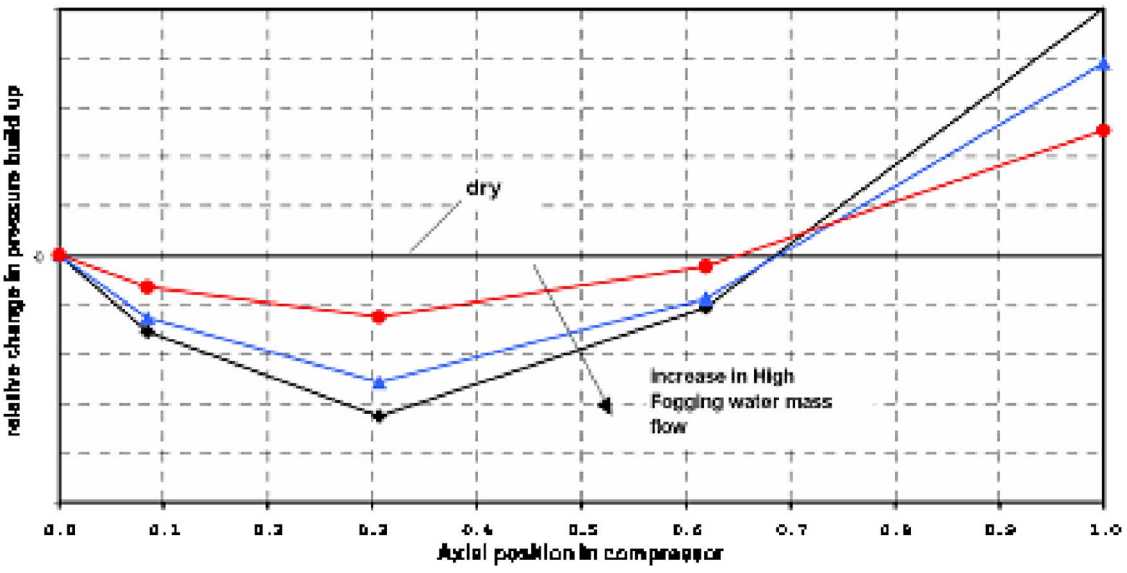

Fig. 13 Change in pressure build with overspray up in a compressor [5]

Fig. 14 View of intake from viewing window installed in a plenum [4]

- Optimize the location of the fogging manifold with respect to air filters and inlet system.
- Check that sequential fogging capability (cooling stages) is adequate to meet power demand profile and its turndown profile.
- Check design features to avoid potential FOD.
- Check the rigidity of the manifolds to avoid flow-induced vibration due to gas turbine airflow. Vendor calculations should be reviewed.
- Review vendors proposed manifold design for structural rigidity and strength.
- Review the proper tie-in of the programmable logic controller (PLC) of the fog system skid with the plant data control system (DCS).
- Ensure that there is a tradeoff between the pressure drop and the evaporation efficiency. An excessive number of nozzle manifolds with a high obstruction ratio may lead to a large pressure drop, while a very low number of nozzles with high water flow rates will lead to larger droplets sizes, poor mixing between the airflow and the droplets, and consequently lower evaporation efficiency, the higher amount of drained water, and potential risk to gas turbine components.
- Evaluate proposed installation of nozzle manifold in the duct for maintainability and accessibility.
- Ensure that appropriate drain lines will be installed in the inlet duct system.
- Galvanized material should not be used downstream of the fog manifolds.
- Installation of the weather sensor can be at skid location if this is representative of inlet conditions to the gas turbine. Ensure that there is no secondary effect (e.g., close proximity to an air cooled heat exchanger or a source of radiant heat) causing wrong measurement of ambient conditions.
- Demineralized water supply lines must be thoroughly flushed to ensure that no dirt has accumulated during installation. Supply lines must be of stainless steel construction.
- Thoroughly wash the inlet duct and silencers. Dirt in the inlet duct system can be washed by the fog into the compressor causing axial compressor fouling creating performance deterioration or compressor damage. This is of special importance on retrofit applications.
- Consider the installation of a viewing window at the compressor bell-mouth. Lighting arrangement should also be made to enable a view, as shown in Fig. 14.

Activities of Gas Turbine Manufacturers With Inlet Fogging and Overspray

The efforts pursued by major manufacturers in using inlet and overspray fogging is briefly summarized below and identifies the importance of this technology in the gas turbine industry.

General Electric. A different approach to high pressure fogging, called Sprint (Spray intercooled turbine) has been implemented by GE for gas turbines with a multispool compressor such as LM6000 [15]. In this approach, a power boost is achieved by fog spraying water, atomized with eighth-stage bleed air from the high-pressure compressor, at both low-pressure and high-pressure compressor inlet plenums. Power boosts of 12% at ISO and 30% or more at ambient temperature of 32°C (90°F) compared to the LM6000-PC gas turbine are reported. According to the latest available data, more than 260 LM6000 Sprint systems have been installed since June 1998 when the first two units went into commercial operation. With Sprint on, GE recommends 16 000 h and 50 000 h of service for HP and LP compressor blades, respectively. A cutaway of a SPRINT engine showing injection into the HP compressor is shown in Fig. 15 [16].

Siemens-Westinghouse. Wet compression technology jointly developed by Siemens-Westinghouse and Dow Chemical Company, demonstrated in 1995 on a W501A gas turbine, has been implemented on a number of W501-series gas turbines [17]. In one of the peaking applications using a W501D5A gas turbine, wet compression combined with a conventional evaporative cooler resulted in a greater than 20% power boost and a heat rate reduction of 1.5% to 3% at ambient conditions of 38°C and 14% relative humidity. In addition, W501D5A and W501D5 gas turbines equipped with a standard combustor have shown a reduction in NO_X emissions by 20% to 40% with wet compression.

Siemens-Westinghouse has also done some research work relating to testing and evaluation of fogging system effectiveness, as reported recently by Willems and Ritland [18]. This work includes the use of nine CIT probes that have special arrangements for shielding so that they accurately reflect the dry bulb temperature at the compressor inlet.

Rolls-Royce. A detailed analytical and experimental program including a CFD analysis to evaluate wet compression technology (called IFB-inlet fog boosting) in combination with other options such as fog intercooling, inlet chilling, and fog intercooling plus inlet chilling was initiated by Rolls-Royce in 1998, as reported by Walsh et al. [19]. In addition, characteristics of two main types of nozzles were examined using water and air for atomization process. Impaction pin type nozzles showed a smaller size droplets distribution compared to swirl nozzles, as also discussed in Part I of this paper based on the extensive experimental work of Mustapha et al. [4].

Alstom. Alstom has done extensive studies in fogging and overspray since 2000 on a range of their gas turbines. Alstom's term for overspray is "High Fogging." High fogging has been implemented on Alstom GT8C2 and a GT26 engine at their test facilities in Birr, Switzerland. According to Hoffman and Mckay [20] as of 2004, ten fogging systems had been supplied by Alstom ($1\times$GT8, $3\times$GT13, and $6\times$GT26) and five "High fogging" systems have been supplied ($1\times$GT8, $1\times$GT24, and $3\times$GT26). A map defined by ALSTOM [21] indicating temperature and relative humidity where fogging and high fogging are permitted for Alstom's machines is shown in Fig. 16. In Fig. 16, lines A, B, and C represent the icing limit (a low ambient temperature condition), the temperature distortion limit (for overspray condition) and the fogging efficiency limit (at high relative humidity), respectively. Also, the regions with combinations of various inlet cooling technologies are included in Fig. 16.

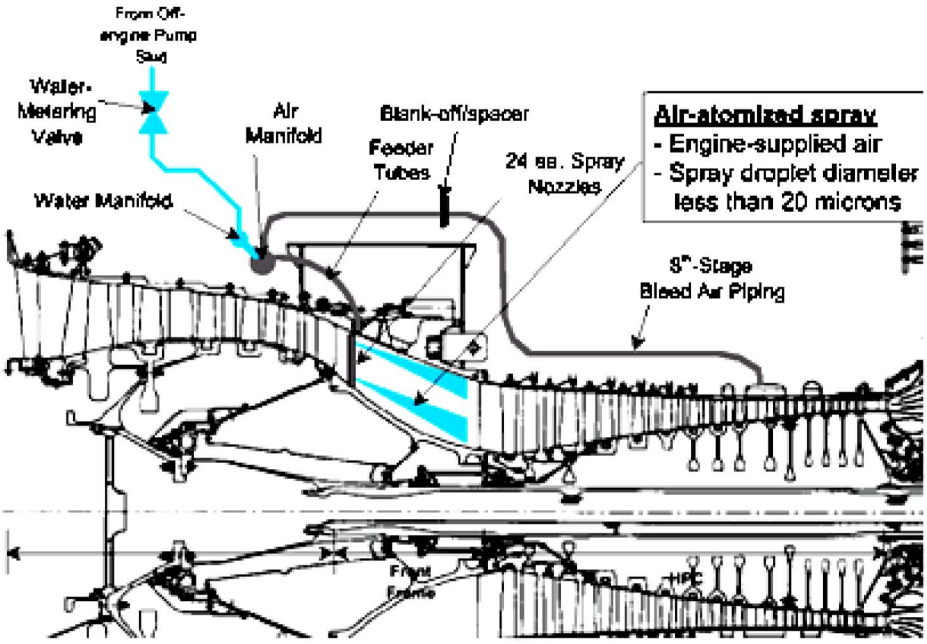

Fig. 15 Representation of a SPRINT LM6000 engine showing water injection between the LP and HP compressor [16]

Inlet Fogging—Field Experience and User Perspectives

In general, the field experience with inlet fogging has been quite positive, as evidenced by a number of gas turbines (over 1000 gas turbines worldwide) fitted with fogging equipment in recent years. A partial list of gas turbine models operating in the field with inlet fogging systems installed by third-party vendors (see Table 2) clearly shows inlet fogging implementation on gas turbines from all the major gas turbine manufacturers worldwide.

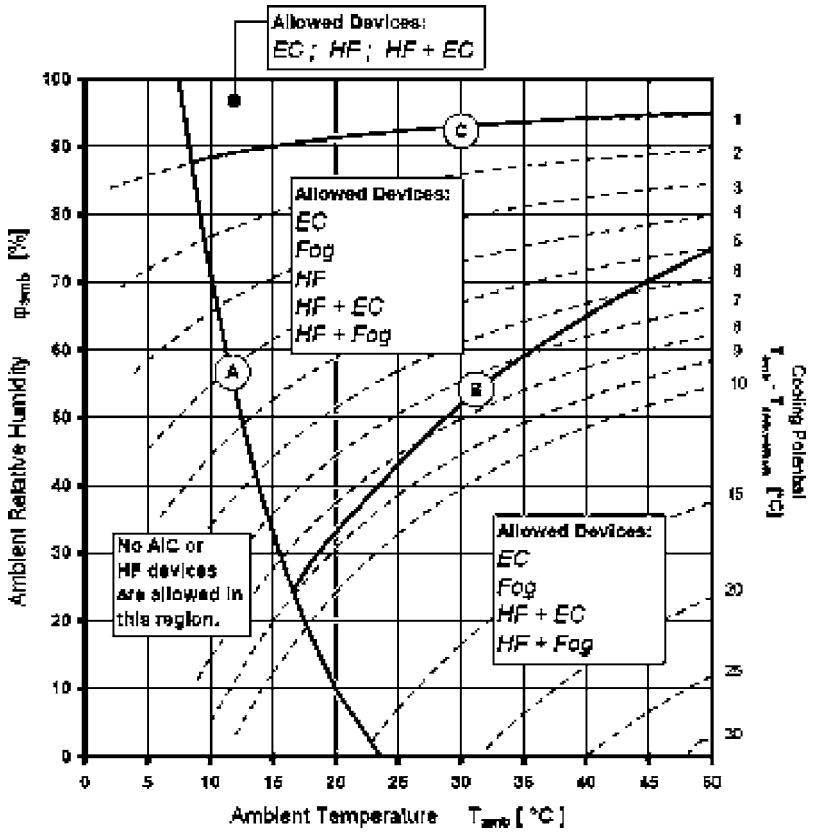

Fig. 16 Map defined by ALSTOM indicating temperature and relative humidity where fogging and high fogging is permitted [21]

Table 2 A partial list of gas turbines with third-party furnished fog systems

Gas turbine manufacturer	Gas turbine model	Number of units with fogging
Alstom	GT26, 13D2, 13E, 13E2, GT-11N, GT-10B, Tornado, 9D, GT24	26
General Electric–Frame 5	5271, 5361, 5371, MS5001, 5001P	62
General Electric–Frame 6	6001, 6531B, 6541, 6541B, 6551B, 6561B, 6F, 6101FA	59
General Electric–Frame 7	7001, 7001E, 7001B, 7001C, 7121EA, 7061EC, 7191F, 7121FA, 7221FA, 7231FA, 7241FA, 7661, 7821	347
General Electric Frame 9	9161E, 0171E, 9FA++	18
General Electric–Aeroderivatives and others	LM2500, LM5000, LM6000, LM6000PD, LM2500PE PGT10	28
Mitsubishi	M701-F, M501G, MF111AB, MW-701D	6
Pratt & Whitney	FT4, FT4 TwinPac, GG4/FT4, FT4-A5, FT8 TwinPac, GG4A9 Twin,TP4-2C1	51
Rolls-Royce	501KB7, AVON, SK30, RB211	7
Solar Turbines	Mars, Mars 100, Centaur 50, Taurus 60, Taurus 70	10
Siemens-Westinghouse	V64.3, V64.3A, V84.2, V94.2, V94.3	30
Siemens-Westinghouse	W191G, W251B11, W251E, W501AA, W501B4, WH E4-2, W501 D5A, W501F	38

It must be noted that both inlet evaporative and overspray fogging have been implemented on the gas turbines operating in wide ranging applications (base-load, peaking, simple cycle, cogeneration, combined cycles, and mechanical drive). Furthermore, Table 2 does not include gas turbines, where fogging systems have been provided by gas turbine OEMs.

A brief description on few field installations including results from a comprehensive experimental study by an OEM is given below.

Inlet Evaporative Fogging on 80 MW Class Heavy-Duty Industrial Gas Turbine in a Cogeneration Facility. A snap-shot of 8 h of operation showing changes in key performance parameters, for a 80 MW class industrial gas turbine with and without inlet evaporative fogging, is shown in Fig. 17. With inlet evaporative fogging in operation, an average power boost of approximately 2.5–3 MW can be seen. Also a decrease in the compressor discharge temperature and associated decrease in compressor dis-

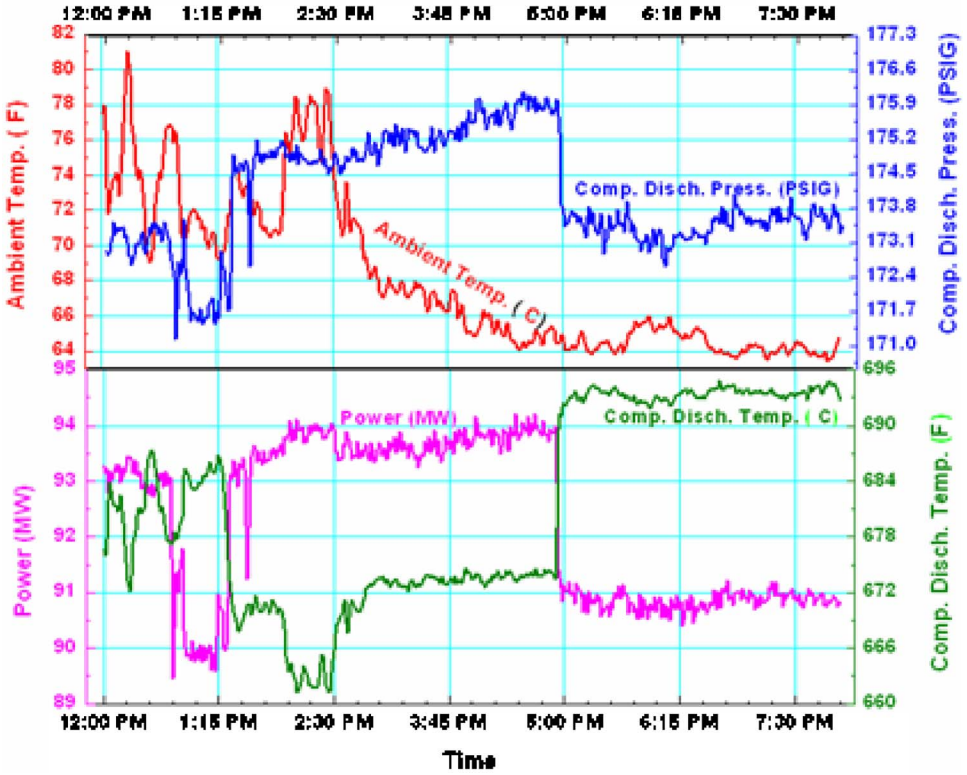

Fig. 17 Effects of inlet evaporative fogging on a 80 MW class heavy-duty industrial gas turbine

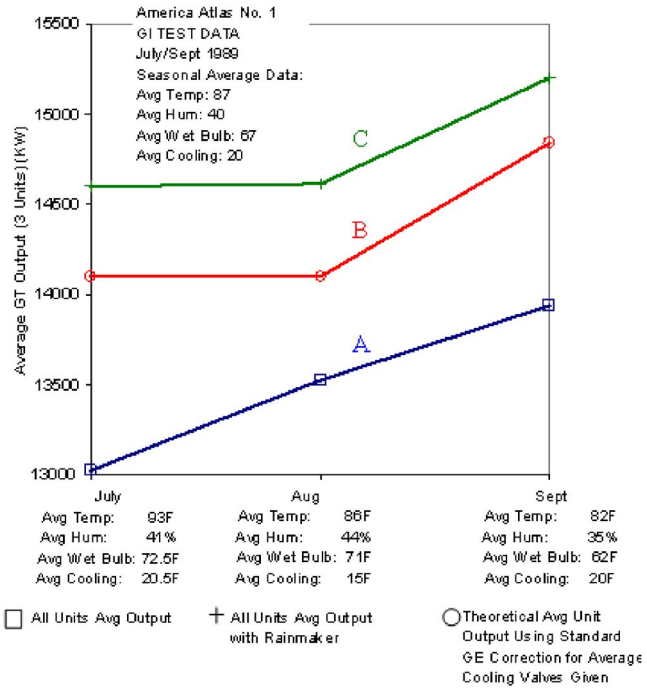

Fig. 18 The first application of overspray on Frame 5 gas turbines (reproduced from the work of Nolan and Twombly [23])

charge pressure with inlet evaporative fogging effects can also be observed in Fig. 17. As the fogging system is brought off-line (at around 5 PM), the gas turbine attains its dry rating power. The presented data was taken recently after a major overhaul and upgrade (change in firing temperature) of the machine. Details on the installed fogging system and initial test data are reported by Ingistov [22].

Application of Inlet Fogging Overspray to a Frame 5 Cogeneration Installation. The first application of wet compression or overspray was on the three Frame 5 gas turbines (with an air mass flow rate capacity of 161 lb/s) operating in a cogeneration service, and was reported by Nolan and Twombly [23]. This facility is located in Rifle, Colorado, which has long hot and dry summers. The facility examined traditional evaporative cooling approaches but chose to use a fogging system owing to its low initial cost. The system utilized 540 nozzles that allowed a total flow of 15 gpm at 600 psi pressure supplied by three reciprocating pumps.

Wet-bulb temperatures could be effectively attained (i.e., 100% evaporative effectiveness) throughout the temperature range of 70°F to 100°F. Figure 18 shows the average gas turbine output over the July to September time frame. In this figure, the lower curve (A) shows average output for all three units without fogging employed. Curve (B) in the middle shows the predicted output from the gas turbine manufacturer's curves with average wet bulb temperatures attained, i.e., with 100% evaporative cooler effectiveness. The uppermost curve (C) was the actual curve of these engines. The difference between curves B and C was due to an overspray effect. As reported by Nolan and Twombly [23], an economic analysis of this system indicated a payback period of 3.2 months.

KeySpan Corp Power Generation Plants. According to recently reported case studies, in the Second Quarter 2004 issue of Combined Cycle Journal, KeySpan Corp of Brooklyn, New York is operating 50 gas turbines (FT4s, GE Frame 5s, and GE Frame 7s) with overspray that provides an aggregate power boost of 100 MW from all machines, including a NO_x emissions reduction of 15% [24]. It was further reported that no significant damage to

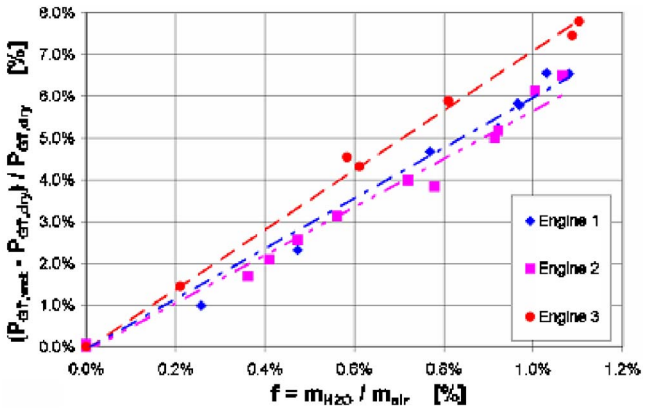

Fig. 19 Experimental test results on GT24/GT26 gas turbines by ALSTOM [14]

compressor blades, attributed directly to wet compression, has been experienced with over three years of operation.

Testing of Four GT24/GT26 Gas Turbines With Overspray by ALSTOM. At ALSTOM, tests were conducted on four GT24/GT26 series heavy-duty industrial gas turbines (reheat cycle) to evaluate performance of overspray fogging. The test results, shown for three engines in Fig. 19, revealed a linear power boost up to an injection rate of 1.2% suggesting a minor impact on compressor performance. This experimental study also showed that a power boost of approximately 7.1% with 1% of overspray can be achieved for GT24/GT26 engines.

GE Frame 6B Gas Turbine at Cardinal Cogeneration Facility. Field tests on GE Frame 6B, installed at the Cardinal cogeneration facility using overspray fogging, were conducted in April 2002 [10]. The spray nozzles, installed downstream of silencers in the inlet duct, had a total water flow rate of 22.6 gpm (an overspray of 1% of airflow). Gas turbine performance with and without overspray fogging is summarized in Table 3. The test data shows that approximately 9% power boost for 1% overspray was achieved. A drop in a compressor discharge temperature of approximately 50°F was noted with an exhaust gas temperature reduction of approximately 12°F.

Issues relating to overspray are totally different compared to traditional evaporative fogging. If overspray rates are limited to 0.5%–1%, then the potential for blade damage in the compressor is very small, provided the system is designed and operated properly. For overspray rates higher than 1%, careful consideration should be given to the compressor aerodynamics and surge characteristics. There are also potential issues relating to the generation of electrostatic charges, which might call for the use of special electric grounding brushes. The effects of overspray fogging on compressor casing temperature and dynamic pressure in the combustor through field measurements on a GE Frame-6B gas

Table 3 Field performance results on GE Frame 6B gas turbine with overspray [10]

Item	Without overspray	With overspray
Ambient dry bulb	58°F	59°F
Ambient wet bulb	52°F	52°F
Compressor Inlet air temperature	57.9°F	52°F
Compressor discharge temperature	663.5°F	614°F
Compressor discharge pressure	153 psia	158 psia
Fuel flow	6.1 lb/s	6.6 lb/sec
Turbine inlet temperature	2023.4°F	2023.6°F
Turbine exhaust temperature	1029.5°F	1017.9°F
Turbine power output	35 333 kW	38 579 kW

turbine in the cogeneration application were recently reported by Jolly [10]. In this application, two nozzle manifolds, one downstream of the inlet filters and another downstream of the silencers, were installed. While for this installation no unusual distribution in the compressor casing temperature was noted, however, high values of dynamic pressure in the dry low NO_x combustion system were reported with 1% overspray fogging.

Testing of 80 MW Class Heavy-Duty Gas Turbine. A hybrid inlet cooling system consisting of a traditional evaporative cooling system combined with inlet fogging having fog nozzles installed upstream of silencers experienced fouling in the compressor because the accumulation of dirt over years of operation of the gas turbine was washed into the compressor [22]. The compressor fouling problem was alleviated by relocating the nozzle manifold downstream of the silencer.

Inlet Fogging Applied at a 650 MW Combined Cycle Power Plant. A large scale inlet fogging system applied to three V94.2 gas turbines operating in a combined cycle plant has been recently reported by Gajjar et al. [25,26]. This application covers an interesting approach, where inlet fogging can help recover power loss when under-frequency operation occurs. These papers cover useful commissioning, operational, and maintenance experiences. These fog systems have been in operation for a period of approximately five years.

Each gas turbine has a total of 16 manifolds with spray nozzles, with a design capability of 14°C of wet-bulb inlet depression. A major benefit of the system was under-frequency operation at high ambient temperatures where deloading of the gas turbine could be avoided by lowering the compressor inlet temperature. In order to observe fog behavior at the gas turbine intake a special viewing window was installed near the bell-mouth and another viewing window was installed at the fog nozzle location in the clean air plenum downstream of the filters. The use of the viewing windows allowed the optimization of nozzle locations.

Tests on Three SWPC W501FD Gas Turbines. Willems and Ritland [18] have reported on several practical aspects derived from tests conducted on three 185 MW W501FD gas turbines. Their paper points out the importance of using shielded thermocouples for measuring the compressor inlet temperature. The traditional evaporative effectiveness relationship is defined below,

$$E = \frac{\mathrm{DBT} - \mathrm{CIT}}{\mathrm{DBT} - \mathrm{WBT}}$$

The above relationship of evaporative effectiveness cannot be used unless the CIT value is accurate and does not report on an artificially lower temperature due to the temperature sensor being wet. Their work also discusses an injection control system to avoid evaporation to saturation to ensure that no overspray occurs. They also stated that due to temperature stratification effects, multiple (nine were used by them) inlet temperature sensors should be utilized to accurately measure the bulk compressor inlet air temperature.

Ongoing Research and Unresolved Issues

There are several issues of importance either being researched today or need further study. These include the following:

- Testing the protocol for fog droplets sizing, which clearly defines the system for measurements, measurement locations, flow conditions, data analysis procedures, and representative droplets diameters. This is important in specifying fogging nozzle ensuring that comparative testing was consistent.
- A better understanding of practical issues relating to droplet wetting within inlet ducts.
- Special design of duct water removal methods.
- Developments of new fog nozzles with a lower value of Dv_{90} droplet size than currently achievable.
- Proper understanding of airflow within the inlet duct to optimize the distribution of fog nozzles in order to avoid underfogged and overfogged areas.
- Improved droplet evaporation models that allow for an accurate prediction of the size of unevaporated droplets, which may enter the compressor.
- Understanding of the performance of evaporative fogging systems under off-design conditions
- Fog system performance testing protocols
- Understanding compressor performance characteristics in the presence of inlet evaporative and overspray fogging using CFD analysis and its verification with experimental data

Concluding Remarks

Inlet and overspray fogging technology has become increasingly popular in the gas turbine market, with fogging systems being offered by both OEMs and third-party suppliers. This paper along with Part I and Part II has covered the state-of-the-art of inlet fogging technology. In this paper we have focused on some of the practical issues relating to design and implementation of inlet fogging and overspray systems. Several practical insights have been provided along with areas of concern and areas that need further study. The success of evaporative fogging and overspray systems will depend on the effectiveness with which practical aspects discussed here are addressed and considered during the design and implementation of proposed fogging systems.

Acknowledgment

Opinions stated herein are the personal opinions of the authors and may not necessarily reflect opinions or positions of their respective corporations/organizations.

Nomenclature

E = evaporative effectiveness
f = water mass fraction (m_{H2O}/m_{air})
M_{air} = air mass flow rate (kg/s)
M_{water} = water flow rate (liters/min)
m = mass flow rate (kg/s)
P = power (kW)
p = pressure (bars)
RH, φ = relative humidity (%)
T = temperature (°C)
WBD = wet bulb depression (°C)

Acronyms

AIC = air inlet cooling
CFD = computational fluid dynamics
CIT = compressor inlet temperature
DBT = dry-bulb temperature
EC = evaporative cooling
FOD = foreign object damage
HF = high fogging
MWBT = minimum wet bulb temperature
OEM = original equipment manufacturer
SAS = secondary air system
WBT = wet-bulb temperature

Subscripts

air = air
amb = ambient
dry = dry (no water injection) operation
ex = compressor air extraction
GT = gas turbine
H_2O = water
out = compressor outlet
wet = overspray operation

References

[1] Bhargava, R. K., Meher-Homji, C. B., Chaker, M. A., Bianchi, M., Melino, F., Peretto, A., and Ingistov, S., 2007, "Gas Turbine Fogging Technology: A State-of-the-Art Review—Part I: Inlet Evaporative Fogging—Analytical and Experimental Aspects," ASME J. Eng. Gas Turbines Power, **129**, pp. 443–453.

[2] Bhargava, R. K., Meher-Homji, C. B., Chaker, M. A., Bianchi, M., Melino, F., Peretto, A., and Ingistov, S., 2007, "Gas Turbine Fogging Technology: A State-of-the-Art Review—Part II: Overspray Fogging—Analytical and Experimental Aspects," ASME J. Eng. Gas Turbines Power, **129**, pp. 454–460.

[3] Meher-Homji, C. B., and Mee, T. R., III, 1999, "Gas Turbine Power Augmentation by Fogging of Inlet Air," *Proceedings of the 28th Turbomachinery Symposium*, Houston, TX, September.

[4] Chaker, M., Meher-Homji, C. B., and Mee, T. R. III, 2002, "Inlet Fogging of Gas Turbine Engines-Part A: Fog Droplet Thermodynamics, Heat Transfer and Practical Considerations; Part B: Fog Droplet Sizing Analysis, Nozzle Types, Measurement and Testing; Part C: Fog Behavior in Inlet Ducts, CFD Analysis and Wind Tunnel Experiments," ASME Papers No. 2002-GT-30562, No. 30563, and No. 30564.

[5] Lecheler, S., and Hoffmann, J., 2003, "The Power of Water in Gas Turbines-ALSTOM's Experience with Air Inlet Cooling," Power-Gen Latin America, Nov.

[6] Meher-Homji, C. B., 1995, "Blading Vibration and Failures in Gas Turbines-Part A: Blading Dynamics and the Operating Environment;" Part B: Compressor and Turbine Airfoil Distress;" Part C: Detection and Troubleshooting;" Part D: Case Studies," ASME Papers No. 95-GT-418, No. 95-GT-419, No. 95-GT-420, and No. 95-GT-421.

[7] Meher-Homji, C. B., 1992, "Gas Turbine Axial Compressor Fouling-A Unified Treatment of its Effects, Detection & Control," Int. J. Turbo Jet Engines, **9** pp. 311–334.

[8] Meher-Homji, C. B., Chaker, M., and Motiwalla, H., 2001, "Gas Turbine Performance Deterioration," *Proceedings of the 30th Turbomachinery Symposium, Turbomachinery Laboratory*, Texas A&M University, Houston, 17–20 September.

[9] Jolly, S., 2003, "Performance Enhancement of GT 24 with Wet Compression," Power Gen International, 9–11 Dec., Las Vegas, NV.

[10] Jolly, S., 2002, "Wet Compression—A Powerful Means of Enhancing Combustion Turbine Capacity," Power-Gen International, Orlando Florida, 10–12 December.

[11] Haskell, R. W., 1989, "Gas Turbine Compressor Operating Environment and Material Evaluation," ASME Paper No. 89-GT-42.

[12] Jolly, S. (personal communication).

[13] Sohre, J. S., 1980, "Shaft Currents Can Destroy Turbomachinery," Power, Mar., pp. 96–100.

[14] Cataldi, G., Guntner, H., Matz, C., McKay, T., Hoffmann, J., Nemet, A., Lecheler, S., and Braun, J., 2004, "Influence of High Fogging Systems on Gas Turbine Engine Operation and Performance," ASME Paper No. GT2004-53788.

[15] Badeer, G. H., 2000, "GE Aeroderivative Gas Turbines—Design and Operating Features," GE Power Systems, GER 3695E.

[16] Jones, C., and Jacobs, J. A., 2000, "Economics and Technical Considerations for Combined-Cycle Performance-Enhancement Options," GE Power Systems, GER-4200.

[17] Smith, E., 2000, "Wet Compression: Gas Turbine Power Output Enhancement for Peak-Load Demand," Power Journal International, pp. 29–32.

[18] Willems, D. E., and Ritland, P. D., 2003, "A Pragmatic Approach to Evaluation of Inlet Fogging System Effectiveness," International Joint Power Generation Conference, Atlanta, Georgia, 16–19 June, Paper No. IJPGC 2003-40075.

[19] Walsh, P. P., Mathieson, D., Bicknell, G., and Matthews, K., 2000, "Inlet Fog Boost Technology Acquisition Programme," Power-Gen Europe.

[20] Hoffman, J., and McKay, T., 2004, "Customer Benefits of Air Inlet Cooling and ALFog Fogging and High Fogging," Power-Gen Far East, October.

[21] Lecheler, S., Florjancic, S., and Cataldi, G., 2004, "Fogging and High Fogging: ALSTOM's Experience and Customer Benefits," Power-Gen Europe.

[22] Ingistov, S., 2000, "Fog System Performance in Power Augmentation of Heavy Duty Power Generating Gas Turbines Model 7EA," ASME Paper No. 2000-GT-305.

[23] Nolan, J. P., and Twombly, V. J., 1990, "Gas Turbine Performance Improvement Direct Mixing Evaporative Cooling System," ASME Paper No. 90-GT-368.

[24] Combined Cycle Journal, 2004, "Wet Compression," Second Quarter.

[25] Gajjar, H., Chaker, M., Dighe, A., and Meher-Homji, C. B., 2003, "Inlet Fogging For a 655 MW Combined Cycle Power Plant — Design, Implementation and Operating Experience," ASME Paper No. GT2003-38757.

[26] Gajjar, H., Modi, A., Bathija, D., and Jain, S., 2002, "Gas Turbine Inlet Air Cooling: GPEC's Experience," 11th V94.2 User's Meeting, Vadodara, India, October.

Key Parameters for the Performance of Impaction-Pin Nozzles Used in Inlet Fogging of Gas Turbine Engines

Mustapha A. Chaker
Gas Turbine Division,
Mee Industries Inc.,
Monrovia, CA 91016

The application of inlet air fogging to gas turbine engines for power augmentation has become common practice, with more than 1000 installations worldwide, including a large number of advanced gas turbines. In this paper an experimental investigation and empirical analysis of key operating parameters on the performance of impaction pin nozzles will be investigated. To date, no such correlation is available for impaction pin nozzles, which are currently used in about 75% of this type of applications. The correlations are developed from a series of experiments conducted in a wind tunnel equipped with the Malvern Spraytec droplet size measurement system. The conducted analysis covered a wide range of the relevant parameters. Mainly, the water flow rate from the nozzle orifice was (0.00126 to 0.00063 l s^{-1}: 0.02 gpm to 0.1 gpm), the operating pressure was (34.5 to 204.1 bars: 500 to 3000 psi), the airflow velocity was (1.5 to 15.2 m s^{-1}: 295 to 3000 fpm), the distance between the nozzle orifice and the location of measurement was (0.0127 to 0.508 m: 0.5 to 20 in.). Other parameters such as the plume spray cone angle and the surrounding ambient psychrometric conditions, which may affect the droplet size for impaction pin nozzles, is also discussed. [DOI: 10.1115/1.2364006]

Introduction and Background

The gas turbine output is significantly impacted by the temperature of the ambient air, with the power output dropping by 0.54% to 0.90% for every 1 °C (1.8 °F) rise in ambient temperature. One approach to overcome the loss of gas turbine power output during periods of high ambient temperature (high demand period) is to cool the inlet air. While there are several inlet air cooling technologies available, high pressure inlet fogging has become increasingly popular over the past decade due to its low cost and its effective power augmentation.

A direct evaporation effect is derived by using fog droplets generated by high-pressure pumps and atomizing nozzles installed in the inlet duct downstream of the inlet air filters. The fog evaporates in the inlet duct and cools the air down to the wet bulb temperature.

A review of the basic principles of fogging technology can be found in Chaker et al. [1–4], Meher-Homji and Mee [5,6], and Bhargava et al. [7]. Early papers on fog intercooling and wet compression started to appear in the late 1940s and include Hill [8], and Utamura et al. [9].

There are two types of nozzles commonly used in inlet fogging systems: impaction pin nozzles and swirl jet nozzles. In both types, the difference in the nozzles' configurations may lead to differences in the atomization process and, consequently, in droplet sizes. It is therefore important to provide all details regarding the nozzles under test. In this paper we study the behavior of impaction pin nozzles designed and implemented by Mee Industries in various gas turbine inlet fogging applications, as shown in Fig. 1.

Due to the use of swirl nozzles in some applications such as the atomization of fuel in gas turbine combustors, there are a number of studies characterizing this type of nozzle and summarized by Lefebvre [10]. His work includes a number of empirical formulas regarding the parameters that influence the size of the droplet from this type of nozzle.

Several papers have been published to measure the droplet size from impaction pin nozzles [11,12]. However, to our knowledge, no paper exists in the open literature that provides empirical relations of droplet size as a function of critical parameters affecting it. These equations are very useful in showing the importance of each parameter and gives the users a tool in order to estimate rapidly the droplet size based on the value of the applied experimental parameters. In this paper we make a systematic study and analysis of the different parameters that influence the droplet size and provides an empirical correlation between the droplet size and each of these parameters.

Experimental Setup

In order to measure the droplets' size in conditions similar to those found in gas turbine inlet ducts, a variable speed wind tunnel was built, as shown in Fig. 2.

A brief description of the wind tunnel is given below and more information regarding its configuration and instrumentation may be found in Chaker [1,3].

Fog is generated in the wind tunnel by forcing high-pressure, filtered, and deionized water through the small orifice nozzles. In the experimental setup, a variable-speed-drive, positive-displacement, ceramic-plunger pump is used to generate water pressures up to 207 bars (3000 psi).

The wind tunnel is equipped with a high-speed data acquisition system, which consists of a DAS 1200 board with up to 16 input channels and 2 output channels. Daisy Lab software was used to manage the data acquisition. The DAS 1200 monitors:

- temperature and relative humidity of the air in several locations
- air velocities
- water flow

Contributed by the International Gas Turbine Institute (IGTI) of ASME for publication in the JOURNAL OF ENGINEERING FOR GAS TURBINES AND POWER. Manuscript received October 1, 2005; final manuscript received February 1, 2006. IGTI Review Chair: R. S. Abhari. Paper presented at the ASME Turbo Expo 2006: Land, Sea, and Air, Barcelona, Spain, May 8–11 2006, Paper No. GT2005-68346.

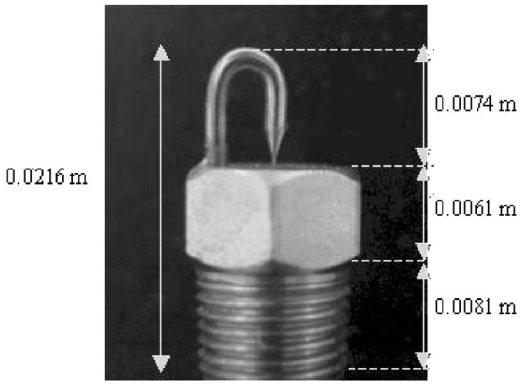

Fig. 1 Impaction pin nozzle

The position of the sensors in the duct is shown in Fig. 2 and Fig. 3.

Droplet size measurements, at different locations in the spray plume and for different airflow velocities, and operating pressures were done with nozzles located in the constricted section of the duct, where the highest airflow velocities are attainable. Measurements were taken at different locations in the spray plume using a Malvern Spraytec RTS5114 laser particle analyzer, as shown in Fig. 3. The Malvern system is based on a laser diffraction technique [13,14]. This is a spatial sampling system; consequently it allows the sampling of a large number of droplets instantaneously with a frequency up to 2500 Hz.

A nozzle manifold, installed at the inlet of the duct, was turned off when measurements were taken at ambient conditions. For measurements with a saturated airflow, these nozzles were turned on, Fig. 4, and a fog droplet filter was used, as shown in Fig. 3, to remove any unevaporated droplets. Droplet size measurement location is shown in Fig. 5.

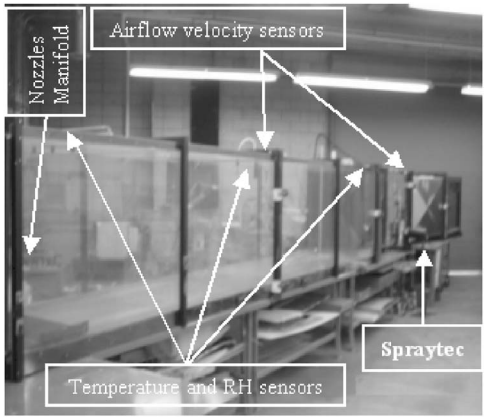

Fig. 2 11 m long 25 m s^{-1} velocity wind tunnel

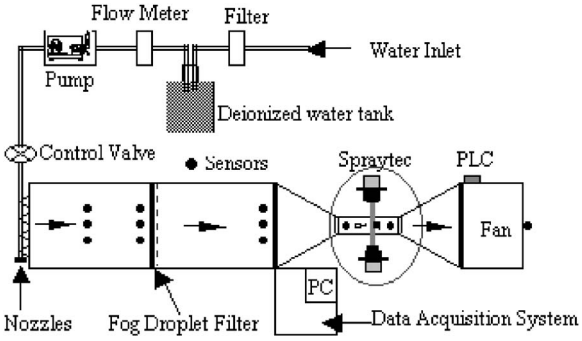

Fig. 3 Wind tunnel experimental setup

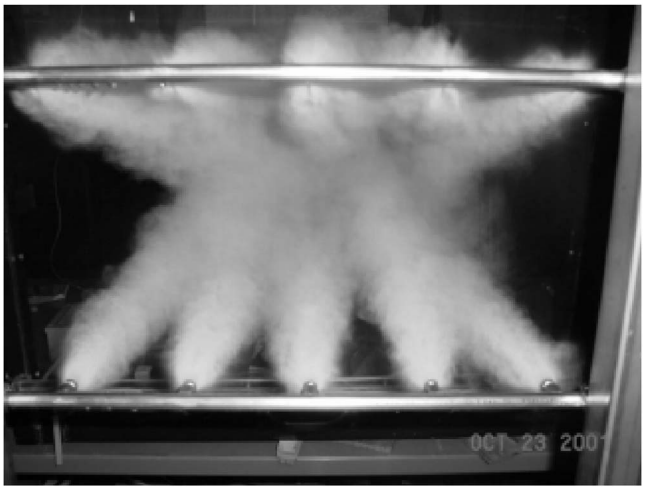

Fig. 4 Fog nozzles manifold

Experimental Results

The Spraytec unit outputs a value for concentration volume (CV). The results from each measurement position are based on the relative mass flow of water at that particular position and use the concentration volume value as a weighing coefficient. This technique mitigated errors that would have resulted from the fact that droplets in the center of the spray plume tend to be much smaller than droplets at the edges of the plume, while mass flow is much greater at the edges.

The most important variables that affect the water droplet size produced by impaction pin nozzles are as follows: the water supply pressure, the airflow velocity in which the water is atomized, the flow rate of the water from each nozzle, and the distance between the measurement position and the nozzle's orifice. Other parameters, namely the plume cone angle and consequently the width of the plume, as well as the ambient psychrometric conditions, have less impact on droplet size. Their influence will be analyzed in later sections.

Two characteristic diameters, employed in the gas turbine inlet air fogging industry, were used to study the droplets size: the first is the Sauter mean diameter (SMD) or D_{32}, which gives a droplet diameter that represents the ratio of volume to surface area of all the drops in the spray plume and, consequently, is important in showing the evaporation rate that occurs at the droplet-air interface. The second is DV90, which is a droplet diameter where 90% of the volume of water in the fog is made up of drops with diam-

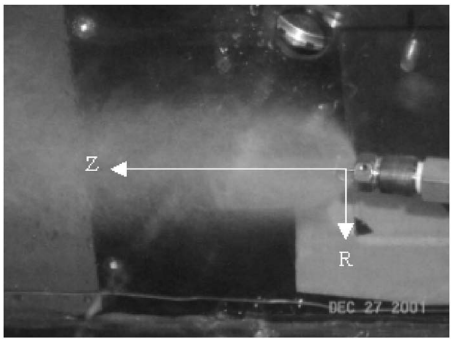

Fig. 5 Droplet size measurement in the wind tunnel

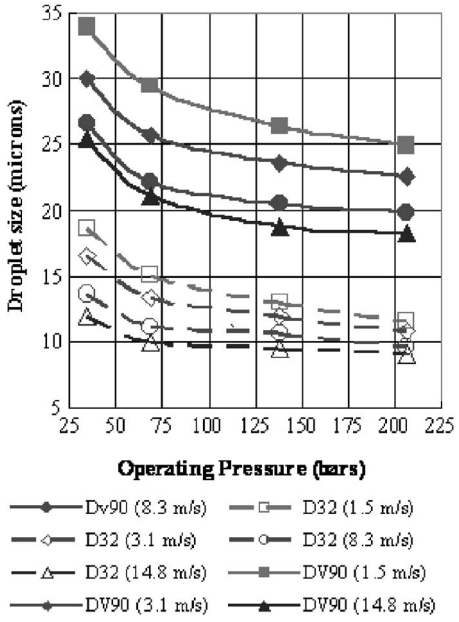

Fig. 6 Variation of droplet size as a function of the operating pressure and the location of the measurement in the spray plume. The distance between the nozzle orifice and the measurement position is 0.075 m.

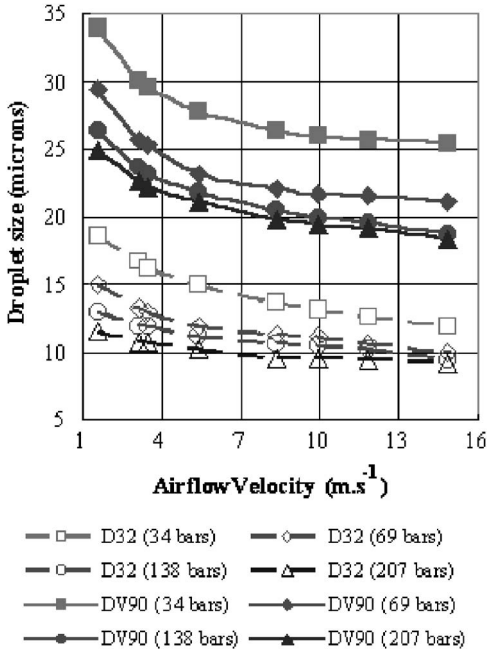

Fig. 7 Variation of the droplets size as function of the airflow velocity, at 30°C and 40% RH. The distance between the nozzle orifice and the measurement position is 0.075 m.

eters smaller than or equal to the given diameter. A small DV90 diameter indicates that a very small volume of larger droplets is produced. That minimizes any potential erosion effects on compressor components should these droplets be carried over into the compressor.

Either D_{32} or DV90 may be written as function of the abovecited most important parameters following the equation

$$\text{Diameter} = \kappa \frac{\dot{m}_w^{\mu} D^{\delta}}{\Delta P_w^{\pi} V_a^{\varpi}} \tag{1}$$

Where k is a constant of proportionality, $\dot{m}_w$ is the water flow rate in liters per second, D is the distance between the nozzle orifice and the measurement position (m), ΔP_w is the differential pressure applied on the liquid (bar), and V_a is the airflow velocity (m s^{-1}). μ, δ, π, and ω are power constants.

Effect of Applied Pressure. Figure 6 shows the effect of the operating pressure on the droplet size for different airflow velocities (from 1.5 to 15.2 m s^{-1}). It shows that as the operating pressure increases droplet size decreases. This decrease is important when the water is under an increasing operating pressure from 34.5 to 138 bar (a nozzle is typically operated at 138 bar in gas turbine inlet air fogging), however, becomes insignificant when the operating pressure increases from 138 to 207 bar.

The variation of DV90 and D_{32} as function of the applied pressure follows the empirical formulas:

$$\text{DV}_{90} \propto \Delta P^{-0.16} \tag{2}$$

$$\text{D}_{32} \propto \Delta P^{-0.23} \tag{3}$$

From Fig. 6, we can also see that the droplet size decreases when we increase the airflow velocity. Figure 7 shows this variation at different operating pressures.

Effect of Airflow Velocity. The airflow velocity was varied from 0.46 to 15.24 m s^{-1}. As can be seen in Fig. 7, a decrease in droplet size occurs as the airflow velocity increases. This decrease is important between 0.46 and 5 m s^{-1}, which is the typical airflow velocity at the location of nozzle manifolds installed in gas turbine inlet ducts upstream of the silencer. For the other nozzle manifolds position, downstream of the silencer with an airflow velocity varying between 10 and 20 m s^{-1}, depending on the gas turbine inlet duct configurations, the decrease in droplet size is much smaller and eventually levels out.

In still air, and close to the nozzle orifice where the density of the droplets is high, a coalescence phenomenon may occur due to the high probability of collision between droplets of different sizes, and therefore different penetration velocities [4].

In high-velocity air streams, the coalescence effect is greatly diminished as the airflow acts to separate droplets of different sizes, thus reducing the potential for collision.

Measurements made at ambient conditions, where fast evaporation of smallest droplets occurs, and at saturated air conditions, where no droplet evaporation occurs, exhibit no difference in size increase due to this coalescence phenomenon.

The variation of DV90 and D_{32} as function of airflow velocity follows the empirical formulas:

$$\text{DV}_{90} \propto V_a^{-0.14} \tag{4}$$

$$\text{D}_{32} \propto V_a^{-0.11} \tag{5}$$

Effect of the Measurement Distance. By increasing the distance between the nozzle's orifice and the measurement position, an increase in droplet size may occur for two reasons: The first is due to the coalescence and the second is due to the fast evaporation of the smallest droplets.

Figure 8 shows the effect of the measurement distance between the nozzle orifice and the position of measurement on the droplet sizes. The upper two lines on the chart show the DV90 diameters, while the lower two lines show the D_{32} diameters. In studying these curves, one can see that the dashed lines (which represent the droplet size under nonsaturated conditions), start to separate away from the solid lines (which represent the droplet size under dry air conditions), as the fog moves away from the nozzle orifice. That separation shows the very small effect of evaporation.

In order to experimentally quantify the effect of rapid small droplet evaporation, measurements were taken at two airflow velocities, 3 and 13 m s^{-1} (590 and 2560 fpm), and for two sets of

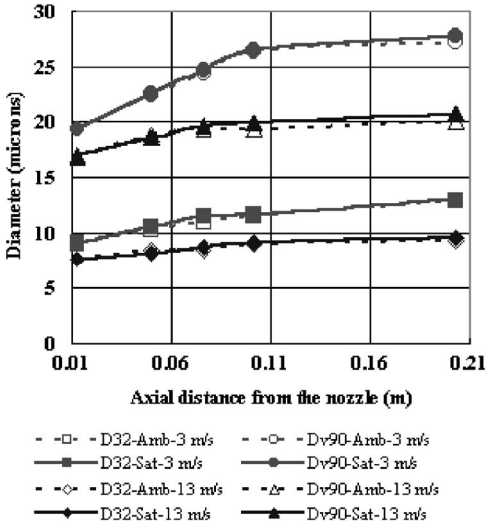

Fig. 8 Effect of ambient humidity on droplet size at different axial distances from the nozzle at 38 bars (2000 psi) pressure

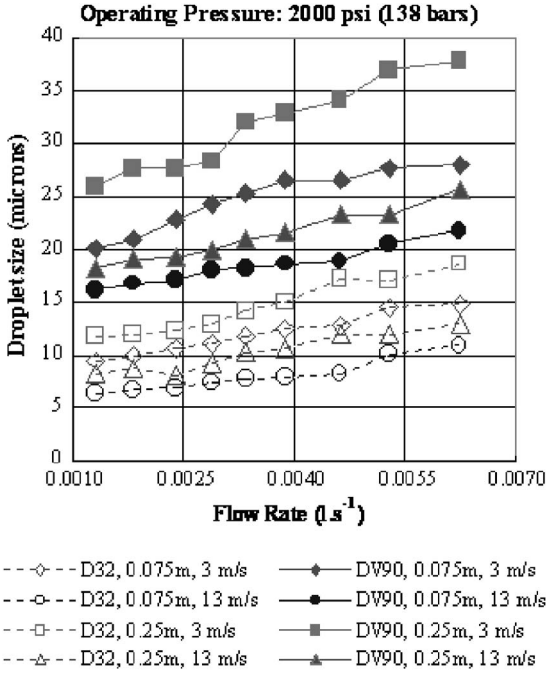

Fig. 9 Effect of flow rate on droplet size

air conditions: 30°C (86°F) with 40% RH represented by dashed lines and defined as ambient in the chart, and 20°C (68°F) with close to 100% RH represented by the solid lines and defined as saturated.

The results of the experiments (Fig. 8) show that the effect due to coalescence is much higher than that due to evaporation for the given distances of measurement. Figure 8 shows also the effect of the airflow velocity on the reduction of the coalescence effect. At 13 m s^{-1} (the blue lines) the coalescence leads to an increase of DV90 of 4 microns, whereas for an airflow velocity of 3 m s^{-1} (the green lines) the increase is 8 microns due to higher coalescence. The difference in droplet size increases also with increasing distance of measurement. D_{32} behaves similarly to DV90.

The variation of DV90 and D_{32} as function of the distance between the nozzle orifice and the measurement position follows the empirical formulas:

$$DV_{90} \propto D^{0.14} \tag{6}$$

$$D_{32} \propto D^{0.13} \tag{7}$$

Effect of Flow Rate on Droplet Size. Figure 9 shows the effect of the flow rate on the droplet size for different airflow velocities and distances from the nozzles' orifice.

It confirms that within our range of flow rate, the droplet size decreases when airflow velocity increases, and the droplet size decreases when the distance the distance between the measurement position and the nozzles' orifice decreases.

The variation of the droplet size and the flow rate may be correlated as follows:

$$DV_{90} \propto \dot{m}_w^{0.23} \tag{8}$$

$$D_{32} \propto \dot{m}_w^{0.31} \tag{9}$$

Effect of the Plume Cone Angle. The major reason for the droplets' coalescence within the plume is due to the high density of droplets close to the nozzle orifice. The collision between droplets in this region leads, in general, to their coalescence or bouncing because of a low Weber number [2]. By increasing the cone angle of the plume (by modifying the configuration of the nozzle) and consequently its width, the density of the droplets in the dense area decreases.

Two nozzles that operate at the same experimental conditions were tested (Fig. 10) at 0.2 m from the nozzle orifices and for an airflow velocity of 0.2 m s^{-1}. The first one had an initial plume width (at this distance) of 0.17 m (red plain circle), and the second had an initial plume width of 0.13 m (red empty circle).

As can be seen in Fig. 10, with the increase of airflow velocity, the plume width decreases from 0.17 to 0.1 m for the largest plume, and from 0.13 to 0.09 m for the smallest plume. At an airflow velocity of 0.2 m s^{-1}, D_{32} (blue lines) for both plumes has the same value while DV_{90} (green lines) for the smallest plume has around 7 microns more than the one for the largest plume (the size is around twice in volume). With the increase in airflow velocity, D_{32} decreases approximately in the same way for both plumes, while the decrease in DV_{90} is less important for the smallest plume. The DV_{90} of both plumes decrease to around 20 mi-

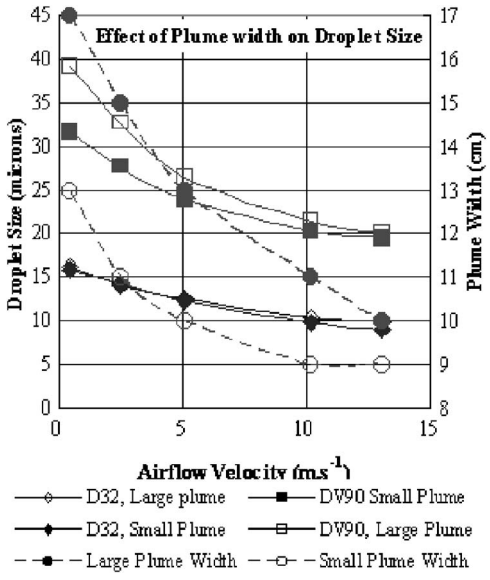

Fig. 10 Effect of plume width on droplet size as a function of airflow velocity

crons at an airflow velocity of 13 m s^{-1}.

More experiments have to done to incorporate the effect of the plume size in the empirical formula given later.

Discussion and Conclusion

The combination of the experiments described above leads to the development of new empirical correlations between the Sauter mean diameter (D_{32}) and DV_{90} and the different parameters of influence, within the range of experimental values specified above. These empirical equations are:

$$DV_{90} \propto \dot{m}_w^{0.23} D^{0.14} \Delta P^{-0.16} V_a^{-0.14} \tag{10}$$

$$D_{32} \propto \dot{m}_w^{0.31} D^{0.13} \Delta P^{-0.23} V_a^{11} \tag{11}$$

While the results of these empirical correlations give values close to the measured ones, more experiments need to be conducted to incorporate the effect of other parameters and to increase the precision and the range of the experimental values.

In this paper we provide new tools that may be used by gas turbine inlet air fogging users to estimate the droplet size from impaction pin type nozzles.

Nomenclature

CV = concentration volume (ppm)
D = distance between the nozzle orifice and the measurement location (m)
DAS = data acquisition system
DV_{90} = droplet size number (μm)
K = constant of proportionality
$\dot{m}$ = water flow (l s^{-1})
P = operating pressure (bar)
SMD (or D_{32}) = Sauter mean diameter (μm)
T = temperature (°C)
Va = airflow velocity (m s^{-1})
ΔP = differential pressure applied

Subscripts

W = water
a = air
μ, δ, π, ω = power constants

References

[1] Chaker, M., Meher-Homji, C. B., and Mee, T. R., III, 2002, "Inlet Fogging of Gas Turbine Engines—Part A: Fog Droplet Thermodynamics, Heat Transfer and Practical Considerations," ASME Papers No. 2002-GT-30562, 30563, and 30564.

[2] Chaker, M., Meher-Homji, C. B., and Mee, T. R., III, 2002, "Inlet Fogging of Gas Turbine Engines—Part B: Fog Droplet Sizing Analysis, Nozzle Types, Measurement and Testing," ASME Papers No. 2002-GT-30562, 30563, and 30564.

[3] Chaker, M., Meher-Homji, C. B., and Mee, T. R., III, 2002, "Inlet Fogging of Gas Turbine Engines—Part C: Fog Behavior in Inlet Ducts, CFD Analysis and Wind Tunnel Experiments," ASME Papers No. 2002-GT-30562, 30563, and 30564.

[4] Chaker, M. A., Meher-Homji, C. B., and Mee, T., III, 2003, "Inlet Fogging of Gas Turbine Engines—Experimental and Analytical Investigations on Impaction Pin Fog Nozzle Behavior," ASME Paper No. GT2003-38801.

[5] Meher-Homji, C. B., and Mee, T. R., 1999, "Gas Turbine Power Augmentation by Fogging of Inlet Air," *Proceedings of the 28th Turbomachinery Symposium*, Houston, TX, September.

[6] Meher-Homji, C. B., and Mee, T. R., III, 2000, "Inlet Fogging of Gas Turbine Engines—Part B: Practical Considerations, Control and O&M Aspects," ASME Turbo Expo 2000, Munich May 2000. ASME Paper No. 2000-GT-0308.

[7] Bhargava, R., Bianchi, M., Melino, F., Peretto, A. Meher-Homji, C. B. and Chaker, M. A., 2003, "Inlet Fogging for Gas Turbine Power Augmentation, a State of the Art Review," *Proceedings of the International Conference on Power Engineering—03(ICOPE-03)*, 9–13, November 2003, Kobe, Japan

[8] Hill, P. G., 1963, "Aerodynamic and Thermodynamic Effects of Coolant Ingestion on Axial Flow Compressor," Aeronaut. Q., pp. 333–348.

[9] Utamura, M., Kuwahara, T., Murata, H. Horii, N., 1999, "Effects of Intensive Evaporative Cooling on Performance Characteristics of Land-Based Gas Turbine," *Proceedings of the ASME International Joint Power Generation Conference*.

[10] Lefebvre, A. H., 1989, *Atomization and Spray*, Taylor & Francis, New York.

[11] Chaker, M., 2001, "Effect of Airflow Velocity on Droplet Size for Gas Turbine Fogging Nozzles," *ILASS Americas, 13th Annual Conference on Liquid Atomization and Spray Systems*, Madison, WI, May.

[12] Savic, S., Mitsis, G., Hartel, C., Khaidarov, P., and Pfeiffer, P., 2002, "Spray Interaction and Droplet Coalescence in Turbulent Air-Flow—An Experimental Study with Application to Gas Turbine High Fogging," ILASS Europe, Zaragoza, Spain, September 9.

[13] Harvill, T. L., and Holve, D. J., 1998, "Size Distribution Measurements Under Conditions of Multiple Scattering With Application to Sprays," Ilass, Sacramento, CA.

[14] Ward-Smith, R. S., Wedd, M. W., Jones, R. M., and Higgs, D. M. J., 1998, "A Novel Measurement Technique For Determining Continuous Particle Size Distributions of Concentrated Sprays," Ilass Europe, July 6–8, Manchester, England.

Comparative Performance Analysis of Internal and External Reforming of Methanol in SOFC-MGT Hybrid Power Plants

Daniele Cocco
e-mail: cocco@dimeca.unica.it

Vittorio Tola

Department of Mechanical Engineering,
University of Cagliari,
Piazza D'armi, 09123 Cagliari, Italy

SOFC-MGT hybrid power plants are a very attractive near term option, as they achieve efficiencies of over 60% even for small power outputs (200–400 kW). *The SOFC hybrid systems currently developed are fuelled with natural gas, which is reformed inside the same stack at about* 800–900°C. *However, the use of alternative fuels with a lower reforming temperature can lead to enhanced performance of the hybrid power plant. This paper reports a comparative performance analysis of SOFC-MGT power plants fuelled by methane and methanol. Since the reforming temperature of methanol* (250–300°C) *is significantly lower than that of methane* (700–900°C), *for the methanol fuelled plant both internal and external reforming have been examined. The performance analysis has been carried out by considering different values for the most important operating parameters of the fuel cell. The comparative analysis has demonstrated that simply replacing methane with methanol in SOFC-MGT power plants with internal reforming slightly reduces the efficiency. However, the use of methanol in SOFC-MGT power plants with external reforming enhances efficiency significantly (by about 4 percentage points). The use of methanol with external fuel reforming raises efficiency of the stack thanks to the improved heat management and to the higher hydrogen partial pressure at the anode inlet.* [DOI: 10.1115/1.2364009]

Keywords: SOFC, fuel cell, micro gas turbine, methanol reforming

Introduction

Fuel cells currently appear to be one of the most promising technologies for advanced energy systems, mainly because of their very high conversion efficiency and extremely low pollutant emissions. Depending on fuel cell type and operating conditions, conversion efficiencies of most fuel cells range between 35% and 55% [1]. Moreover, higher efficiencies can be achieved by hybrid configurations where the fuel cell is integrated with a bottoming power generation system. For thermodynamic reasons, the best performance of these hybrid cycles are achieved using high temperature fuel cells, such as molten carbonate fuel cells (MCFC) and solid oxide fuel cells (SOFC), which have operating temperature of around 600–700°C and 800–1000°C, respectively. In particular, since the operating temperature of SOFC stacks is very similar to the turbine inlet temperature of latest generation micro gas turbines (MGT), the combustion chamber of the MGT unit can be replaced by the SOFC stack. These hybrid SOFC-MGT power plants are a very attractive near-term option as they can allow to achieve efficiencies of over 60–65%, even for small power outputs (200–400 kW) [2–8].

The SOFC systems currently developed are fuelled with natural gas (composed mainly of methane), which needs to be reformed to produce the hydrogen required by the electrochemical reactions of the fuel cell. Since the operating temperature of the SOFC stack well matches the reforming temperature of methane (700–900°C), the reforming section of the hybrid SOFC-MGT power plants is usually integrated into the fuel cell stack itself, supplying directly the heat required by the endothermic reforming reactions.

On the other hand, many current R&D projects are focusing the attention on alternative fuels for distributed power generation, including methanol, di-methyl-ether (DME), and ethanol. These fuels can be produced from a wide range of primary fuels (natural gas, coal, biomass, etc.), can be easily handled and can be fed to a variety of energy conversion systems (fuel cells, gas turbines, internal combustion engines) yielding high efficiency and low pollutant emissions [9–16].

Moreover, when used in SOFC hybrid systems most of these alternative fuels can allow improvement of the energy management of the power plant, due to their low reforming temperature (for example, methanol reforms at about 250–300°C, whereas DME reforms at about 300–400°C). In this case, the fuel reforming process can be even carried out outside the SOFC stack, thus enhancing the recovery of the low temperature waste heat of the MGT. Moreover, external reforming can also increase the partial pressure of the hydrogen at the anode inlet, thus improving stack efficiency.

In this paper, a comparative performance assessment of SOFC-MGT plants fuelled by natural gas and methanol has been carried out. In particular, the paper first compares the performance of methane and methanol fuelled SOFC-MGT hybrid systems with internal reforming. Then, the use of methanol in SOFC-MGT hybrid systems with internal and external reforming has been also compared.

SOFC Modeling

The performance of the hybrid SOFC-MGT power plants considered here has been evaluated by means of the ASPEN PLUS™ simulation software, version 12.1 [17]. In particular, the ASPEN model library, which includes many standard components used by

Contributed by the International Gas Turbine Institute (IGTI) of ASME for publication in the JOURNAL OF ENGINEERING FOR GAS TURBINES AND POWER. Paper presented at the ASME Turbo Expo 2006, Barcelona, Spain, May 8–11 2006, Paper No. GT2006-90762. Manuscript received October 1, 2005; final manuscript received February 1, 2006. IGTI Review Chair: R. S. Abhari.

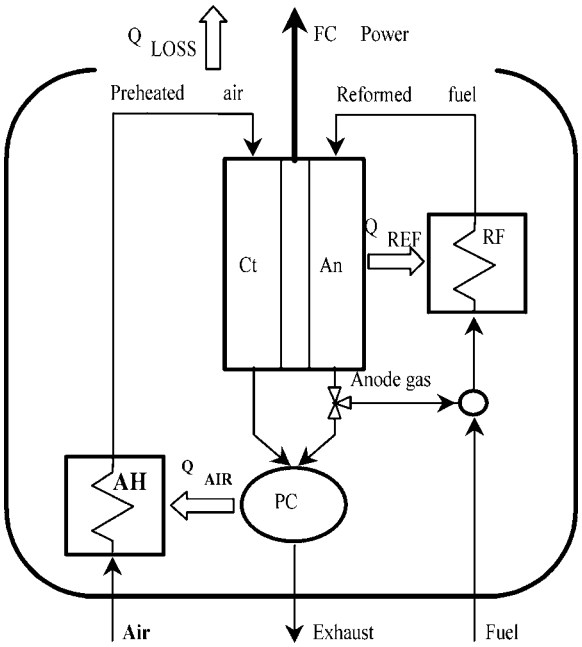

Fig. 1 Conceptual scheme of the SOFC stack

energy conversion systems (heat exchangers, pumps, turbines, reactors, etc.), has been integrated with a dedicated fuel cell model. The model simulates fuel cell performance by solving mass and energy balances, for given values of the main operating parameters.

The fuel cell model has been developed referring to the Siemens-Westinghouse tubular SOFC unit, essentially because data are readily available from published sources. However, the model can easily be modified to simulate different types of fuel cells. Figure 1 shows the conceptual scheme of the internally reformed SOFC stack considered here. The fuel (methane or vaporized methanol) is mixed with part of the anode exhaust gas (which contains water produced by hydrogen oxidation) to supply the steam required by the subsequent reforming process. The fuel/steam mixture flows through the reforming section (RF), where the endothermic fuel reforming reactions take place. Obviously, the reforming section is not required by the SOFC systems integrated with an external reforming section.

As known, the methane reforming process is based on the following steam reforming reaction:

$$CH_4 + H_2O = CO + 3H_2 - 206.3 \text{ kJ/mol} \tag{1}$$

As shown by Eq. (1), the minimum steam-to-carbon molar ratio (SCR) required to achieve complete methane reforming process is 1. However, the methane reforming reaction is always coupled with the CO-shift reaction,

$$CO + H_2O = CO_2 + H_2 + 41.4 \text{ kJ/mol} \tag{2}$$

which consumes additional steam, so that the stoichiometric SCR value required to achieve maximum hydrogen production (4 moles of H_2 per mole of CH_4) is 2.

Unlike methane, methanol can also be reformed without steam through the following thermal decomposition reaction:

$$CH_3OH = CO + 2H_2 - 90.8 \text{ kJ/mol} \tag{3}$$

However, if steam is added to the methanol, the latter reaction is coupled with the previous CO-shift conversion reaction. For this reason, the stoichiometric SCR for attaining maximum hydrogen production (3 moles of H_2 per mole of CH_3OH) is 1.

In the fuel cell model considered here, reformed gas composition has been evaluated through reactions (1) and (2) for methane and (3) and (2) for methanol, under the assumption of thermodynamic equilibrium, calculated at the SOFC operating temperature. The reformed fuel gas (composed essentially of H_2, CO, CO_2, and H_2O) flows through the fuel cell anode, where the hydrogen reacts with the oxygen ions coming from the cathode. The only electrochemical anode reaction considered here is H_2 oxidation owing to its higher reaction rate with respect to the CO oxidation. However, even the CO partakes indirectly in the anode electrochemical reactions, as it is converted to H_2 by means of the CO shift conversion reaction [2]. Therefore, the overall anode reactions are represented by the following two equations:

$$H_2 + \tfrac{1}{2}O_2 = H_2O \tag{4}$$

$$CO + H_2O = CO_2 + H_2 \tag{5}$$

Anode and cathode exhaust gases are mixed together and fed to the postcombustor (PC) to complete fuel conversion. As Fig. 1 shows, a suitable portion of the heat produced by the fuel cell stack and postcombustor is directly recovered by the air preheater (AH) and by the fuel reforming section (RF). Stack heat losses (Q_{LOSS}) are evaluated as a predetermined fraction of fuel cell energy input.

The solution of the overall mass and energy balances of the fuel cell requires the evaluation of both the voltage and the current produced by the stack. As known, fuel cell efficiency depends on its voltage, whereas power output is related to the voltage, current density, and active area,

$$P_{\text{FC}} = V \cdot I = V \cdot J \cdot A \tag{6}$$

where V denotes the voltage, I is the current, J is the current density, and A is the active area. Common voltage values for tubular SOFC stacks range from 0.5 to 0.8 V, whereas current density range usually falls between 100 and 500 mA/cm^2 [1,2]. On the other hand, the current produced by the fuel cell is closely related to the hydrogen molar flow n_{H_2} consumed by the anode reactions,

$$I = (n_{H_2})_{\text{Consumed}} \cdot 2 \cdot F \tag{7}$$

where F is Faraday's constant (96,439 C/mol).

For given stack voltage and power, Eqs. (4)–(7) are used to calculate hydrogen and oxygen consumption. Since hydrogen from the fuel and oxygen from the air are not completely consumed by the electrochemical reactions, the mass flows of fuel and air can be determined from the fuel and air utilization factors. In particular, the fuel utilization factor U_F is defined here as the ratio of the mass flow of hydrogen consumed by the anode reactions to that of hydrogen and CO fed to the anode (i.e., H_2 and CO contained in the reformed fuel gas),

$$U_F = \frac{(m_{H_2})_{\text{Consumed}}}{(m_{H_2} + m_{CO})_{\text{Anode inlet}}} \tag{8}$$

Similarly, the air utilization factor U_A is the ratio between the mass flow of oxygen consumed by the cathode reactions and the mass flow of oxygen fed to the cathode,

$$U_A = \frac{(m_{O_2})_{\text{Consumed}}}{(m_{O_2})_{\text{Cathode inlet}}} \tag{9}$$

U_F commonly ranges between 60% and 90%, U_A from 15% to 30%. Composition and mass flows of the different streams are then calculated using the above equations for a predetermined power produced by the fuel cell. Solving the overall energy balance gives the temperature of the stack exhaust gas. On the other hand, solving the overall energy balance also gives the air mass flow required for a desired flue gas temperature.

Overall performance of the SOFC stack is given by the net AC power and by the net conversion efficiency, i.e., the ratio between net power and chemical energy of the fuel,

$$\eta_{FC} = \frac{P_{FC,AC}}{m_F \cdot LHV_F} = \frac{V \cdot I}{m_F \cdot LHV_F} \cdot \eta_{DC/AC} \quad (10)$$

where m_F and LHV_F are the mass flow and lower heating value of the fuel at the stack inlet, and $\eta_{DC/AC}$ is the DC/AC conversion efficiency. Since the power is proportional to the mass flow of fuel consumed by the electrochemical reactions, SOFC efficiency linearly depends on cell voltage, for given values of the other operating parameters.

As known, actual voltage V depends on fuel cell type and on the main operating parameters (current density, operating pressure and temperature, oxidant and fuel composition, air and fuel utilization factors, etc.). For the purpose of the present study, the correlation between voltage and the different operating parameters has been evaluated with reference to published data. In particular, input data to the model include voltage produced by the fuel cell for a reference set of the main operating parameters (current density, pressure, temperature, fuel and oxidant composition, fuel and air utilization factors). The actual voltage is then calculated for the actual set of operating parameters, using the published correlations [1].

As is well known the voltage produced by a fuel cell decreases as current density increases. For a tubular SOFC, the voltage variation ΔV_J (mV) produced by an increase in current density J (mA/cm^2) with respect to the reference value, can be determined by means of the following equation:

$$\Delta V_J = -0.73 \cdot (J - J_{ref}) \text{ for } 50 \leq J \leq 400 \ \frac{mA}{cm^2} \quad (11)$$

Increasing SOFC stack operating temperature and pressure yields higher voltages. Variation in voltage versus temperature T and pressure p has been evaluated using the equations

$$\Delta V_T = 0.008 \cdot (T - T_{ref}) \cdot J \text{ for } 900 \leq T \leq 1050\,^\circ C \quad (12)$$

$$\Delta V_p = 59 \cdot \log_{10}\left(\frac{p}{p_{ref}}\right) \text{for } 1 \leq p \leq 10 \text{ atm} \quad (13)$$

Fuel composition and fuel utilization factor both affect fuel cell voltage as they produce variations in hydrogen and water partial pressures at the anode with respect to the reference values. The following correlation has been considered here for evaluating this influence,

$$\Delta V_F = 172 \cdot \log_{10} \frac{(p_{H_2}/p_{H_2O})}{(p_{H_2}/p_{H_2O})_{ref}} \text{ for } 0.9 \leq \frac{p_{H_2}}{p_{H_2O}} \leq 6.9 \quad (14)$$

where p_{H_2} and p_{H_2O} are the average hydrogen and water partial pressures at the anode side of the stack.

Similarly, the influence of air composition and utilization factor has been evaluated using the following equation:

$$\Delta V_A = 92 \cdot \log_{10} \frac{(p_{O_2})}{(p_{O_2})_{ref}} \text{ for } 0.16 \leq \frac{p_{O_2}}{p} \leq 0.20 \quad (15)$$

where p_{O_2} is the average oxygen partial pressure at the cathode side of the stack. The actual voltage of the SOFC can be determined by summing the voltage variations calculated using Eqs. (11)–(15) and the reference voltage. Table 1 shows the reference set of fuel cell operating parameters [2].

Starting from the previous equations, Fig. 2 shows the voltage and power density of a tubular SOFC versus current density for different operating pressures, while Fig. 3 shows voltage and power density versus fuel utilization factor for different operating temperatures. Figure 2 shows that the choice of the best current density leads to a compromise between high voltage (i.e., high efficiency) and high power density (i.e., low active area and then low stack cost). Obviously it should be noted that, according to Eq. (11), Fig. 2 is accurate only for current densities lower than 400 mA/cm^2. For given values of the other parameters, SOFC performance improves with increasing stack pressure and temperature, as well as with decreasing fuel utilization factor.

On the other hand, the influence of air utilization factor on SOFC stack performance is of minor importance, as an increase in U_A from 15% to 40% only reduces voltage by about 5 mV.

Table 1 Reference set of the SOFC operating parameters

Cell voltage, V_{ref}	0.59 V
Current density, J_{ref}	300 mA/cm^2
Operating cell temperature, T_{ref}	900 °C
Operating cell pressure, p_{ref}	1 atm
Fuel utilization factor, $U_{F,ref}$	85%
Air utilization factor, $U_{A,ref}$	25%
Fuel composition at the anode inlet	89% H_2, 11% H_2O, vol.
Air composition	21% O_2, 79% N_2, vol.

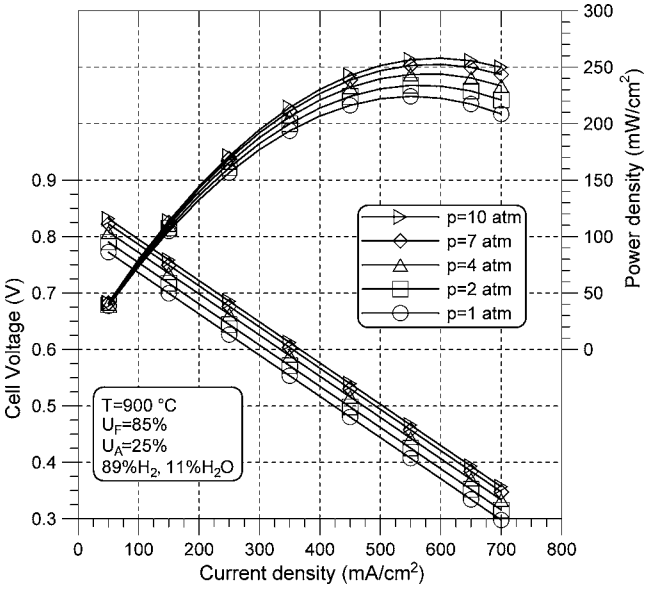

Fig. 2 Cell voltage and power density versus current density and cell operating pressure

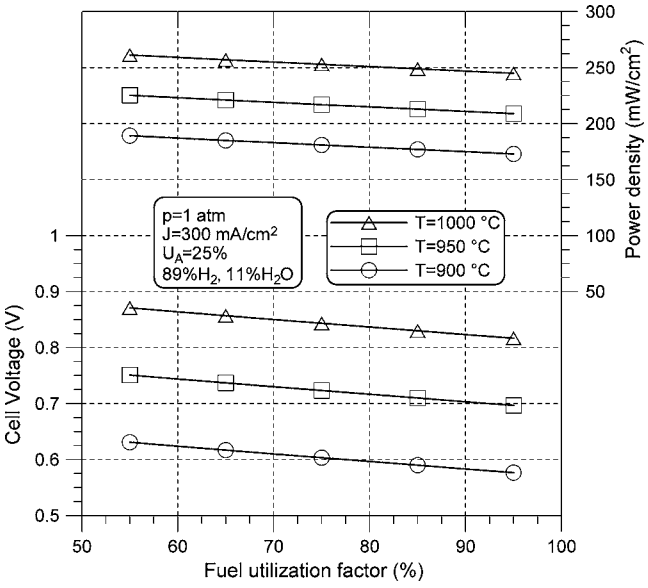

Fig. 3 Cell voltage and power density versus fuel utilization factor and cell operating temperature

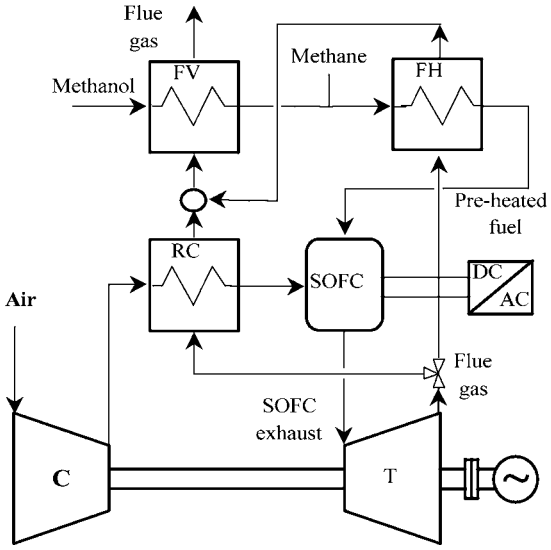

Fig. 4 Configuration of the SOFC-MGT power plant with internal reforming

SOFC-MGT Plant Configurations

A comparative performance assessment of SOFC-MGT power plants fueled with natural gas (here assumed to be composed of pure methane) and methanol has been carried out for the plant configuration in Fig. 4. Also, methanol has been considered for the plant configuration shown in Fig. 5.

In particular, Fig. 4 refers to the hybrid SOFC-MGT plant with internal reforming. This configuration is similar to the recently proposed hybrid SOFC-MGT plants and is based on an internally reformed SOFC stack integrated with a recuperated micro-gas turbine [3–6]. The air is first pressurized by the compressor (*C*), then heated in the recuperator (RC) before being supplied to the SOFC stack. After expansion through the turbine (*T*), the main portion of the SOFC exhaust gas is cooled in the recuperator, whereas the remainder is cooled in the fuel heat exchanger (FH) for preheating the fuel. For a given preheated fuel temperature (taken here as 300°C), the mass flow of exhaust gas required by the FH is calculated by assuming its minimum exit temperature (120°C for methane and 250°C for methanol). Similarly, the temperature of air exiting the recuperator is then calculated by assuming its minimum temperature difference (50°C). When methane is used as a primary fuel, it enters the FH at ambient temperature (25°C). On the other hand, when methanol is used the heat from the two flue gas streams exiting the RC and FH (both at about 250°C) can be used to vaporize the liquid methanol, thus recovering the low temperature exhaust heat. For this reason, the two streams are mixed and fed to the fuel vaporizer (FV), where the methanol is preheated and vaporized. Therefore, the SOFC-MGT power plant includes the fuel vaporizer (dotted lines of Fig. 4) only if the primary fuel is methanol, and the latter enters the FH at about 110°C (that is its vaporization temperature at the fuel inlet pressure).

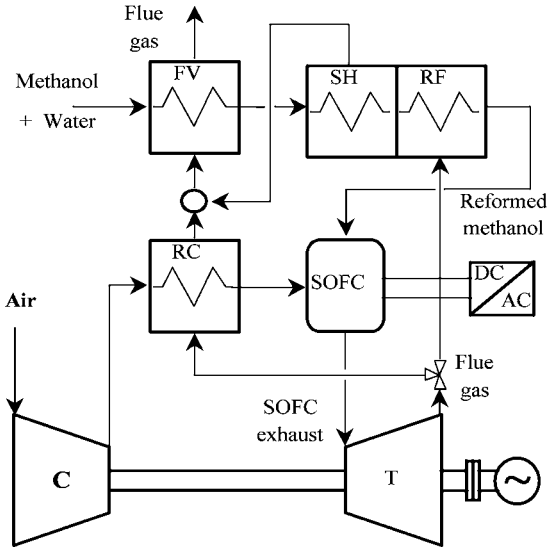

Fig. 5 Configuration of the SOFC-MGT power plant with external methanol reforming

Table 2 Main operating parameters of the SOFC-MGT plant

SOFC	
Fuel composition	100% CH_4 or 100% CH_3OH
Fuel LHV	50 MJ/kg CH_4, 19.9 MJ/kg CH_3OH
SOFC fuel inlet temperature	300°C
Stack operating temperature	900°C
Current density	300 mA/cm^2
Pressure drop (% of inlet pressure)	4.0%
Heat losses (% of fuel energy input)	3.0%
DC/AC conversion efficiency	95%
MGT	
Air mass flow	1 kg/s
Compressor inlet pressure drop	1.0%
Pressure ratio	4
Turbine inlet temperature	950°C
Compressor isentropic efficiency	81.0%
Turbine isentropic efficiency	84.0%
Minimum RC temperature difference	50°C
Minimum FH exit temperature	120°C
RC pressure drop (air side)	3.0%
FH and RC (gas side) pressure drop	5.0%
SH and RF (gas side) pressure drop	5%
FV pressure drop (gas side)	1.5%
Generator efficiency (including auxil.)	91%

Figure 5 shows the configuration considered here for the SOFC-MGT hybrid power plant with external methanol reforming. The hybrid configuration of Fig. 5 is very similar to that shown in Fig. 4. However, in this case, the fuel vaporizer is fed by the methanol/water mixture, whereas the FH heat exchanger of Fig. 4 has been replaced by the external steam reforming section. The latter comprises the catalytic steam reforming section (RF) and the superheating section (SH) of the methanol/steam mixture produced by the FV. The temperature of the reformed fuel is assumed to be the same as the preheated fuel of the hybrid plant with internal reforming (300°C). Moreover, the mass flow of exhaust gas required by the methanol reforming section has been calculated assuming the minimum temperature difference inside the RF (50°C).

Comparative Performance Assessment of Methane and Methanol Fueled SOFC-MGT Plants With Internal Reforming

The comparative performance assessment of the methane and methanol fueled SOFC-MGT power plants has been carried out for an air mass flow rate of 1 kg/s at the compressor inlet (i.e., a 140 kW-class MGT). Pressure ratio and turbine inlet temperature (TIT) of the MGT were kept constant during the analysis. Table 2 shows the main operating parameters considered in the analysis of the hybrid SOFC-MGT plant.

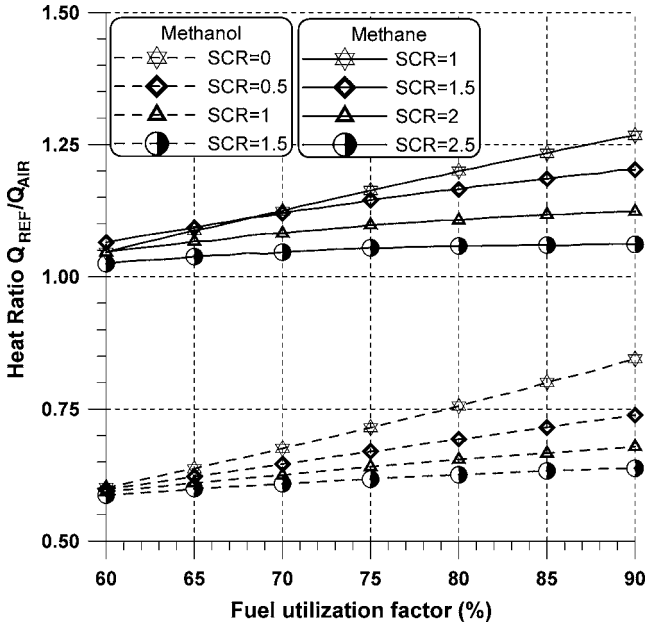

Fig. 6 Heat ratio Q_{REF}/Q_{AIR} for the internally reformed SOFC stack fuelled with methane and methanol versus U_F and SCR

As can be seen from Eqs. (1)–(3), methane reforming is more endothermic than methanol reforming. In particular, for the stoichiometric SCR values (2 for methane and 1 for methanol), the reforming heat of methane is about 20.6% of its LHV, whereas that of methanol is only 7.7% of its LHV. For this reason, to keep constant the stack and turbine inlet temperatures of the SOFC-MGT plant, with methanol more heat must be removed by the air. Figure 6 reports the ratio between the heat required by the reforming reactions and the heat removed by the air (Q_{REF} and Q_{AIR} of Fig. 1, respectively) as a function of U_F and SCR. The use of methanol instead of methane significantly reduces the heat ratio Q_{REF}/Q_{AIR}; moreover, the latter heat ratio also decreases with increasing values of SCR and decreasing values of U_F.

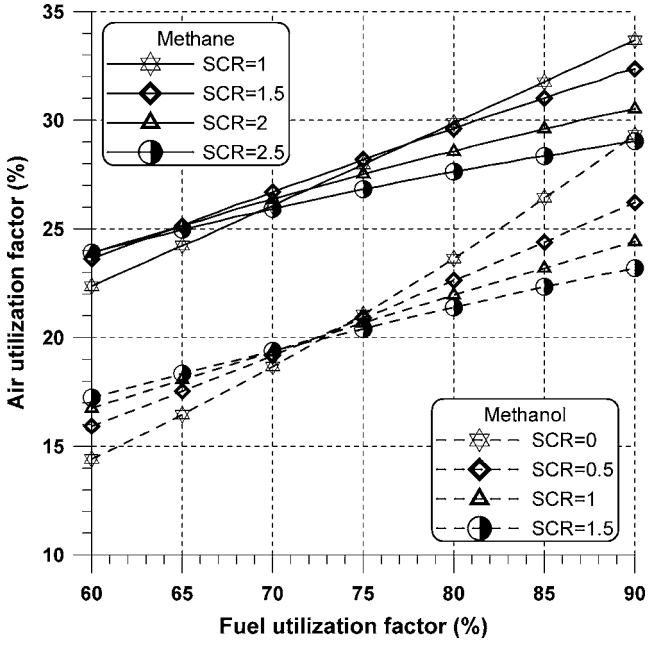

Fig. 7 Air utilization factor of the internally reformed SOFC stack fuelled with methane and methanol versus U_F and SCR

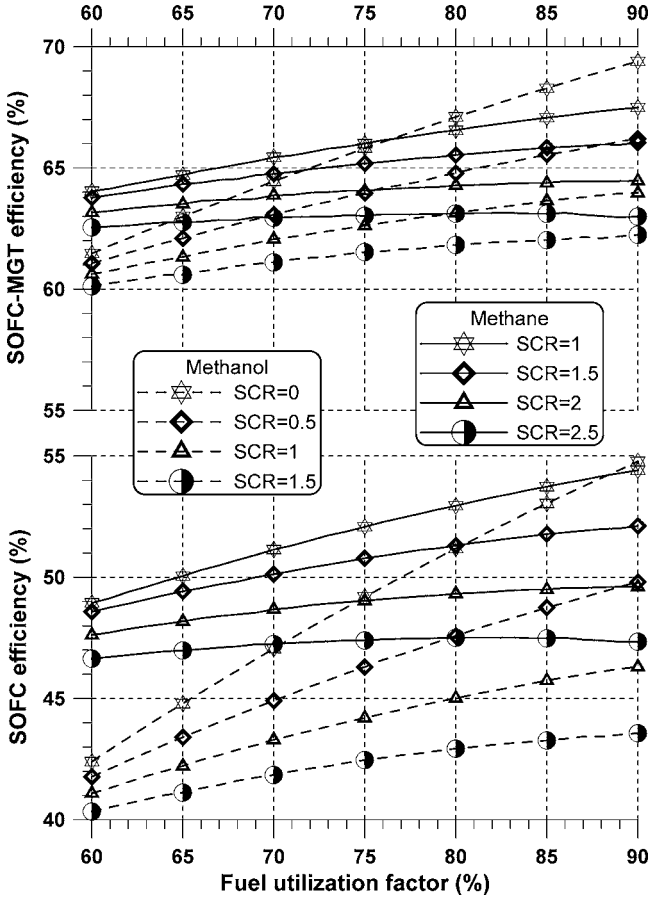

Fig. 8 Efficiencies of the internally reformed SOFC stack and the SOFC-MGT plant versus U_F and SCR

The increase of the air cooling requirements of the SOFC stack fuelled by methanol significantly reduces the air utilization factor U_A. Figure 7 gives the air utilization factor for the methane and methanol fuelled SOFC stack as a function of U_F and SCR. Figure 7 shows that U_A decreases from 24 to 32% (methane fuelled SOFC stack) to 16 to 26% (methanol fuelled SOFC stack), depending on both U_F and SCR. Moreover, for a given active area of the stack, being constant the current density (300 mA/cm^2), the decrease of U_A increases the air mass flow, as shown by Eqs. (6)–(9). Since the comparative performance analysis has been carried out for a fixed air mass flow rate (1 kg/s), the increase of the air cooling requirements significantly reduces the active area, and then the power output of the SOFC stack.

Figures 8 and 9 show efficiency and power output of the methane and methanol fuelled hybrid SOFC-MGT plant, versus fuel utilization factor U_F, for given steam-to-carbon molar ratios. The lower part of the same figures show efficiency and power output of the stack as a function of the same parameters. The figures indicate that for both fuels, an increase in U_F improves efficiency and power output of the stack, especially at lower SCRs. On the contrary, an increase in SCR results in lower stack efficiency and power output. The same trend has been observed for the overall SOFC-MGT performance.

As known, high values of SCR reduce the performance of the stack due to the hydrogen dilution produced by the increase of the anode exhaust gas recirculation. Figure 10 reports the ratio between the average partial pressures of hydrogen and steam at the anode of the stack. Figure 10 shows that the aforementioned partial pressure ratio decreases with SCR and with U_F; whereas, it does not show any significant variation when methane is substituted by methanol, by using equivalent SCRs (as 1.0 for methanol

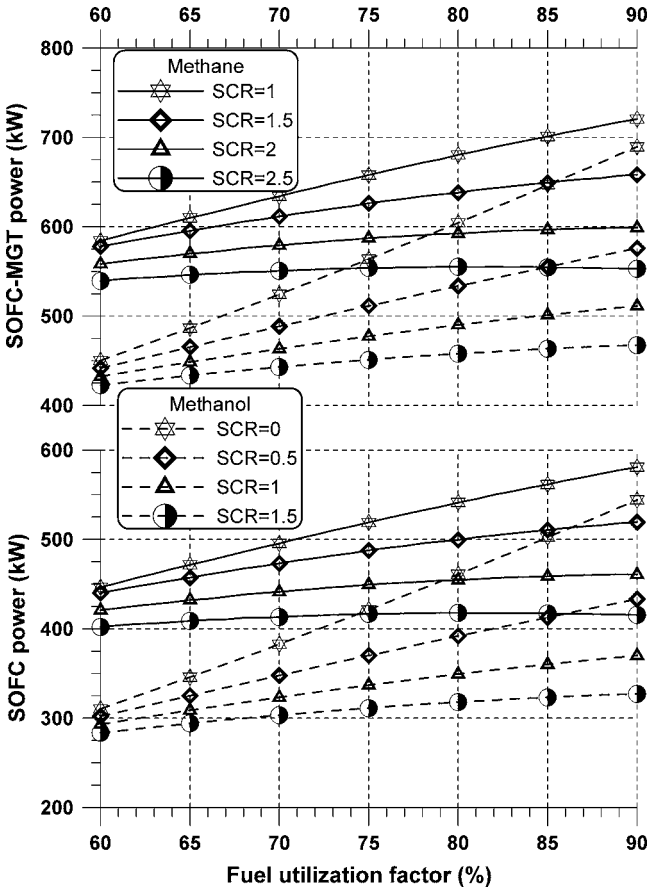

Fig. 9 Power outputs of the internally reformed SOFC stack and the SOFC-MGT plant versus U_F and SCR

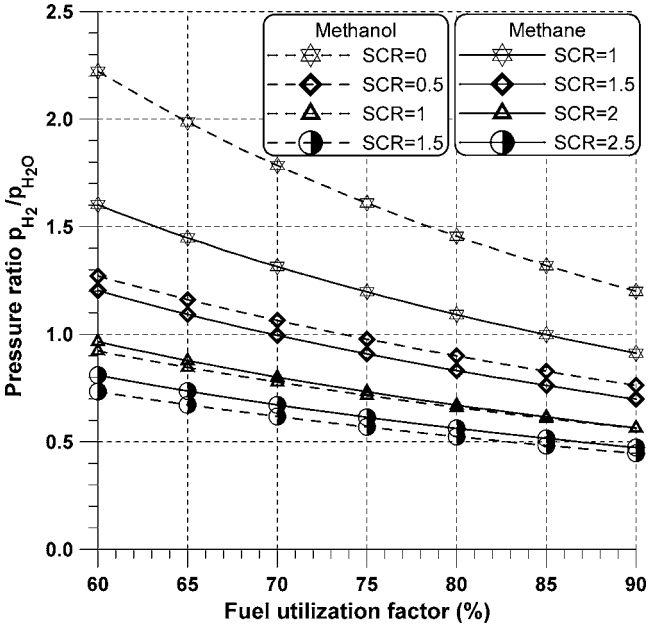

Fig. 10 Ratio of the average partial pressures of H_2 and H_2O versus U_F and SCR

and 2.0 for methane). However, SCRs that are too small are also to be avoided as they can lead to carbon formation during the fuel reforming process. So practical SCRs range between 1.5–2.0 for methane and 0.5–1.0 for methanol. On the other hand, the U_F range for tubular SOFC stacks usually falls between 75% and 85%.

Similarly to Fig. 10, Fig. 11 shows the voltage of the stack versus U_F and SCR, for both methane and methanol. As expected, for given values of p, T, and J, the cell voltage and the ratio between the partial pressures of H_2 and H_2O show almost the same behavior. Figure 11 shows that for equivalent SCRs, and in particular for the stoichiometric values, the SOFC stack fuelled by methane and methanol exhibit almost the same voltage. Being here constant the current density (300 mA/cm^2), the power density shows the same behavior of the voltage.

For the same stoichiometric conditions, Figs. 8 and 9 show that the SOFC-MGT power plants fuelled by methane exhibit higher efficiencies, as well as higher power outputs. For example, with U_F=85% and SCR equal to 1.0 for methanol and 2.0 for methane, the efficiency of the SOFC-MGT plant is about 64.4% for methane and 63.6% for methanol. Moreover, the use of methane increases power output by about 20% (597 kW versus 501 kW), mainly due to the higher active area of the stack. Figure 8 also reveals that the use of methanol in internally reformed SOFC-MGT power plants could give a significant efficiency gain only with SCR=0 (simple thermal decomposition process) and for the highest values of U_F.

Analysis of the lower part of Figs. 8 and 9 reveals that replacing methane with methanol negatively affects SOFC stack performance, as the latter always results in a reduction in both stack efficiency and power output. The inferior performance of the methanol fuelled stack is associated mainly with the different heat management inside the stack. On the other hand, Fig. 12 shows that the different heat management leads to a decrease of the power ratio P_{SOFC}/P_{MGT}; for equivalent SCRs (SCR=2 for methane and SCR=1 for methanol) and U_F in the range 75–85%, the power ratio is about 3.2–3.3 for methane and about 2.4–2.6 for methanol.

In spite of the substantially inferior stack performance, the use of methanol improves exhaust heat recovery thanks to the fuel vaporizer (FV), which preheats and vaporizes the methanol using the low temperature exhaust gas from the recuperator (RC) and the fuel preheater (FH).

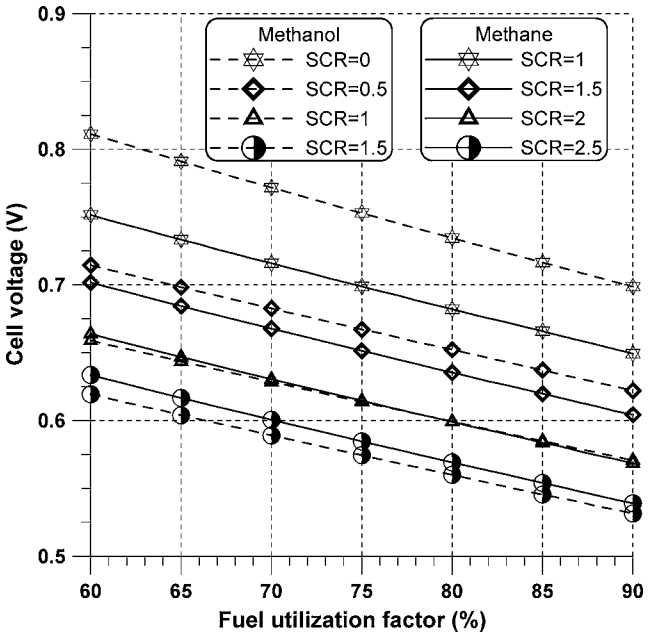

Fig. 11 Voltage of the internally reformed SOFC stack versus U_F and SCR

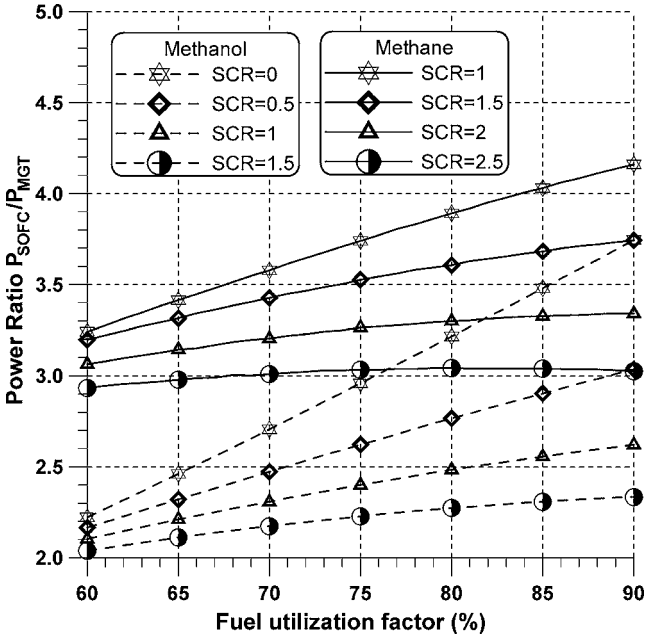

Fig. 12 Power ratio P_{SOFC}/P_{MGT} for the internally reformed hybrid SOFC-MGT plant versus U_F and SCR

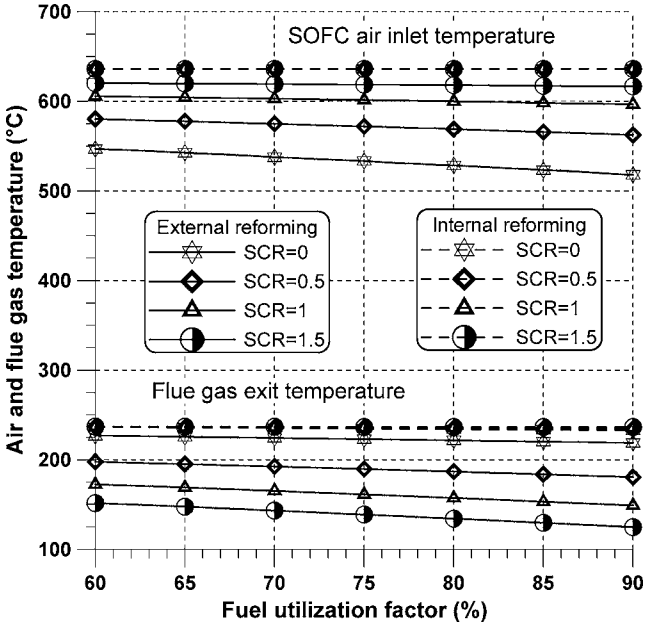

Fig. 13 SOFC air inlet temperature and flue gas exit temperature of the internally and externally reformed hybrid plant fuelled with methanol versus U_F and SCR

By recovering the exhaust heat, the final temperature of the final flue gas is reduced from 270°C (methane fuelled SOFC-MGT power plant) to 235°C, thus enhancing efficiency of the hybrid power plant.

Comparative Performance Assessment of Internal Versus External Methanol Reforming

The analysis of the hybrid SOFC-MGT power plants described above has essentially demonstrated that methane leads to a slightly higher efficiency and to a remarkably higher power output. However, methanol has a substantially lower reforming temperature than methane, and can become a more attractive proposition when externally reformed.

In particular, the performance of an externally reformed methanol fuelled SOFC-MGT plant (Fig. 5) has been compared with the hybrid plant that used internal reforming (Fig. 4), again referring to the operating parameters given in Table 2. The main difference introduced by the external reforming process is the increase in the low temperature heat recovered through the FV and the different heat management of the SOFC stack due to the absence of the internal reformer.

In the case of external reforming, the SOFC stack is directly fed by the reformed fuel gas, so the heat produced by the electrochemical and combustion reactions must be completely removed by the air. However, external methanol reforming also requires that a greater portion of the flue gas exiting the turbine must be sent to the reforming section, with a corresponding lower heat load available for the recuperator and consequently a lower air temperature at the stack inlet.

Figure 13 shows that the air temperature is about 636°C for the hybrid plant with internal reforming (according to the recuperator minimum temperature difference of 50°C), whereas for the external reforming it ranges from 550°C to 620°C (according to the reformer minimum temperature difference of 50°C). Besides, the higher air temperatures are related to the higher SCRs. Overall, as Fig. 14 shows, external reforming leads to a lower air utilization factor, even if U_A decreases significantly only for the lower values of U_F.

Figures 15 and 16 show the efficiency and power output of the methanol-fuelled hybrid SOFC-MGT power plant with internal and external reforming, versus U_F and SCR. The lower part of the figures also shows the efficiency and power output of the SOFC stack as a function of the same parameters. For given values of U_F and SCR, the shift from internal to external methanol reforming enhances SOFC stack efficiency significantly, especially at the higher U_F and SCRs. In fact, for external reforming process, anode gas recirculation is not required, thus no hydrogen dilution takes place at the anode inlet, resulting in higher cell voltage. What is more, during the external reforming process the CO shift reaction, Eq. (2), reaches equilibrium conditions at a lower temperature (300°C instead of 900°C). Since this reaction is favored at low temperatures, the hydrogen content of the reformed fuel

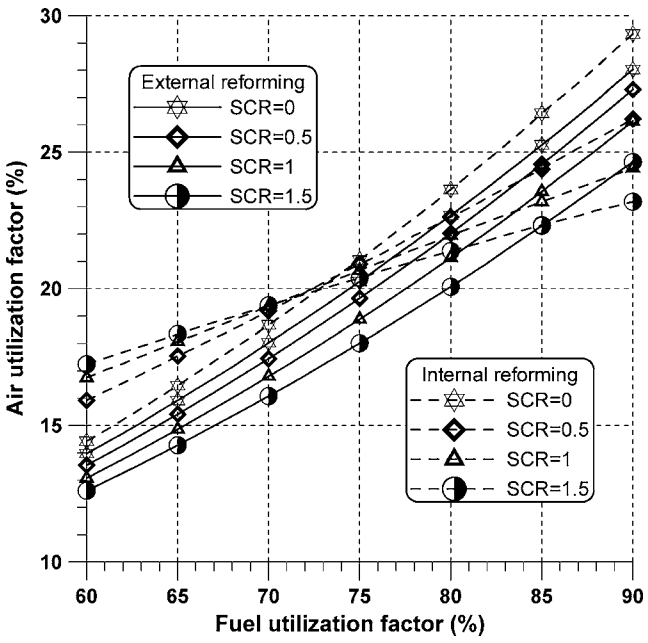

Fig. 14 Air utilization factor of the internally and externally reformed SOFC stack fuelled with methanol versus U_F and SCR

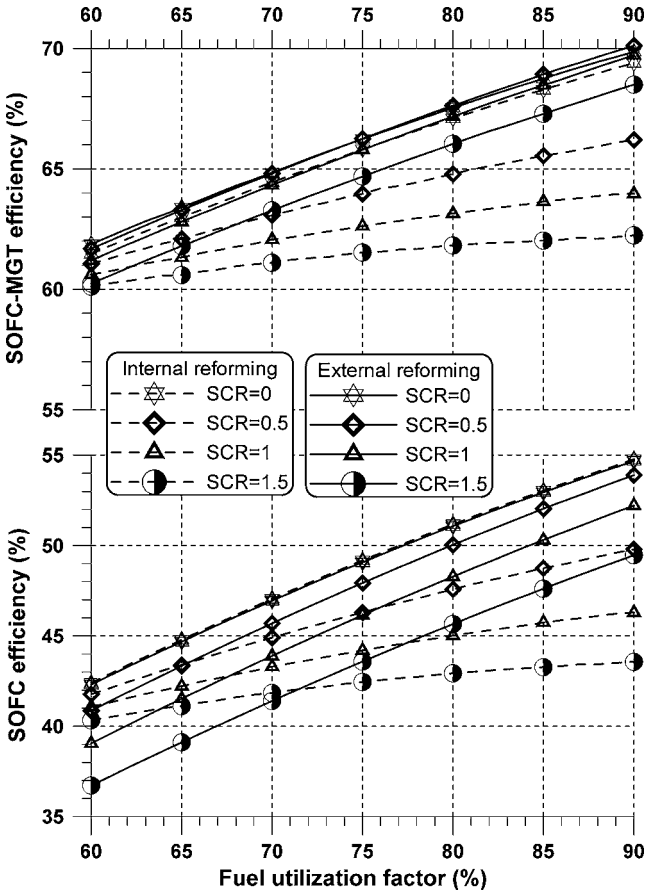

Fig. 15 Efficiencies of the SOFC stack and the SOFC-MGT plant versus U_F and SCR, using internal and external methanol reforming

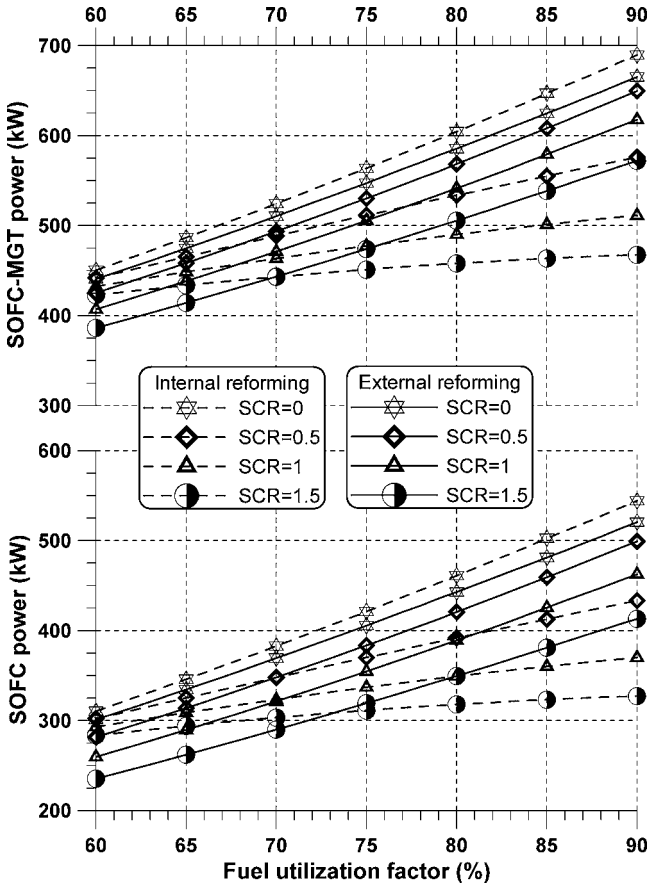

Fig. 16 Power outputs of the SOFC stack and the SOFC-MGT plant versus U_F and SCR, using internal and external methanol reforming

gas produced by the external reforming process is very high (about 65–70%). On the other hand, the absence of a suitable catalyst inhibits the reverse CO shift reaction when the temperature rises from the stack inlet to the anode inlet [18]. According to this, Fig. 17 reports the ratio between the average partial pressures of hydrogen and steam at the anode of the stack. Figure 17 shows that the shift from internal to external reforming significantly increases the aforementioned partial pressure ratio. Similarly to Fig. 17, Fig. 18 shows the cell voltage as a function of the same parameters. In particular, for $U_F=85\%$ and SCR=1, the partial pressure ratio is about 0.6 in the case of internal reforming and 1.1 in the case of external reforming; the corresponding values of the cell voltage are 0.585 V and 0.68 V.

As can be seen from Fig. 15, corresponding stack efficiencies are 45.7% and 50.3%. Moreover, Fig. 15 also shows that, for a given U_F, maximum efficiency of the hybrid SOFC-MGT plant is achieved for SCR=0.5, even if the difference between SCR=0.5 and SCR=1 is only minor (less than 0.4 percentage points).

On the whole, the improvements in SOFC stack performance and the better exhaust heat recovery achieved with the external reforming, produces significant efficiency and power output gains for the hybrid SOFC-MGT power plant. Moreover, the increase of the fuel mass flow leads to a higher mass flow of the SOFC exhausts and then to a higher MGT power output.

Table 3 compares the main performance of the three hybrid plants considered here for $U_F=85\%$. The efficiency of the hybrid plant is about 68.5% for the externally reformed methanol and 63–64% for the plants with internal reforming of methanol and methane. Moreover, the external reforming process also increases power output by about 16% (from 501 kW to 579 kW), giving a

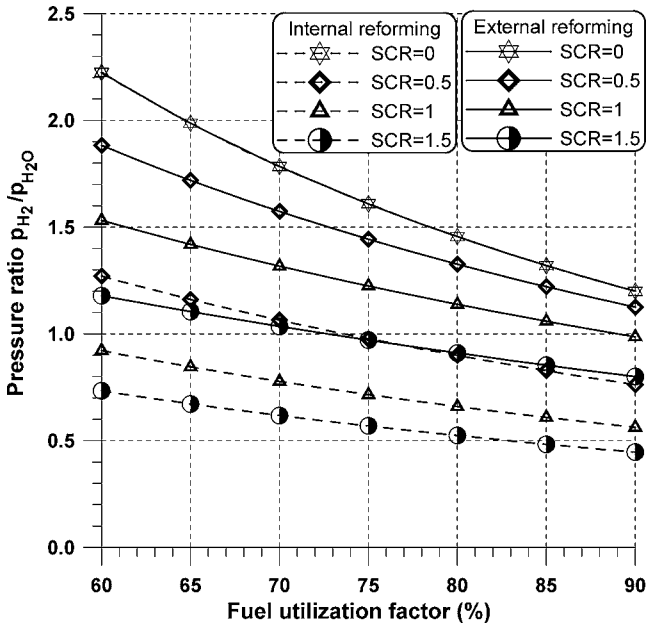

Fig. 17 Partial pressures ratio of H_2 and H_2O versus U_F and SCR, using internal and external methanol reforming

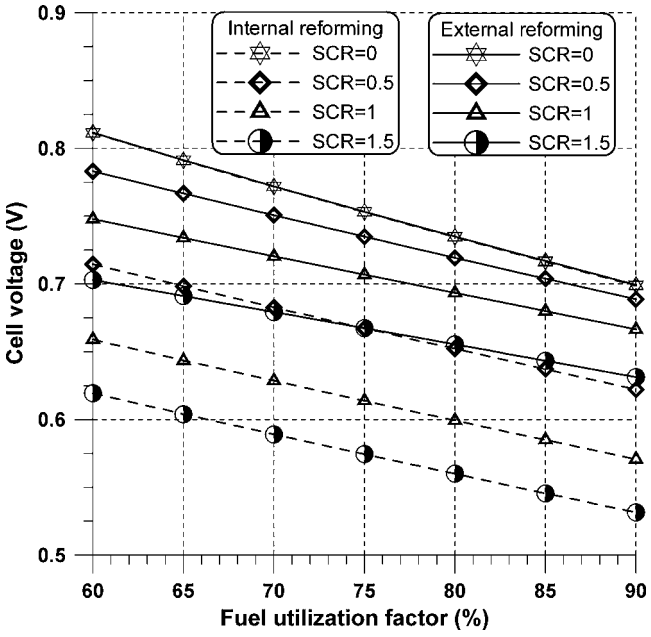

Fig. 18 Voltage of the SOFC stack versus U_F and SCR, using internal and external methanol reforming

final power output similar to that achieved for the methane fuelled SOFC-MGT plant (597 kW). Owing to the lower SOFC cooling requirements, the external reforming process leads to a slight increase in the fuel cell area.

Conclusions

The performance assessment carried out in this paper has demonstrated that methanol can be a very attractive fuel for SOFC-MGT power plants, especially when reformed externally.

Simply replacing methane with methanol in SOFC-MGT power plants with internal reforming yields only a small efficiency decrease, though power output decreases by about 16%. However, the low reforming temperature of methanol (about 250–300°C) enhances the efficiency of the hybrid plant. In fact, the reformer can be sited outside the SOFC stack, improving low temperature exhaust heat recovery. Moreover, SOFC stack performance is also enhanced by external methanol reforming, since a higher hydrogen partial pressure is attained at the anode inlet, and correspondingly higher cell voltage. Thus, using methanol in SOFC-MGT power plants with external reforming improves efficiency significantly, giving power outputs similar to methane.

It should be observed that the present study is based on the assumption of a constant current density (300 mA/cm^2). Obviously, the result would be different if the voltage and current density values were assumed to maximize the power density and then to minimize the active area.

The performance of hybrid SOFC-MGT power plants could also be enhanced using other fuels with low reforming temperatures, such as ethanol and DME. Clearly, a more in-depth comparative performance analysis of differently fuelled power generation systems entails an energy, environmental, and economic assessment of the entire energy chain from the primary fuel up to the electricity generated.

Table 3 Main performances of the SOFC-MGT plant

	SOFC Int. Ref.	SOFC Int. Ref.	SOFC Ext. Ref.
Fuel	CH_4	CH_3OH	CH_3OH
Air mass flow	1 kg/s	1 kg/s	1 kg/s
Fuel mass flow	0.0185 kg/s	0.0396 kg/s	0.0425 kg/s
Compressed air temp.	202.0°C	202.0°C	202.0°C
SCR	2	1	1
SOFC air inlet temp.	633.5°C	636.7°C	598.9°C
SOFC fuel inlet temp.	300.0°C	300.0°C	300.0°C
SOFC exit temp.	950°C	950°C	950°C
Turbine exit temp.	683.5°C	686.7°C	689.0°C
RC exit temp.	273.8°C	282.0°C	252.0°C
FH (RF) gas exit temp.	120.0°C	252.0°C	350.0°C
FV gas exit temp.		235.7°C	153.1°C
RC flue gas mass flow	0.997 kg/s	1.012 kg/s	0.837 kg/s
FH flue gas mass flow	0.021 kg/s	0.028 kg/s	0.230 kg/s
Fuel utilization factor	85%	85%	85%
Air utilization factor	29.6%	23.2%	23.6%
Cell voltage	0.584 V	0.585 V	0.680 V
Fuel cell area	275.85 m^2	216.06 m^2	219.5 m^2
SOFC power density	175 mW/cm^2	175 mW/cm^2	204 mW/cm^2
SOFC power output	458.8 kW	360.2 kW	425.5 kW
MGT power output	137.9 kW	141.2 kW	153.6 kW
SOFC-MGT power	596.7 kW	501.2 kW	579.1 kW
SOFC efficiency	49.5%	45.7%	50.3%
SOFC-MGT effic.	64.4%	63.6%	68.5%

Acknowledgment

This work has been carried out in the framework of the research project "Sviluppo di tecnologie per la produzione ed il trattamento del syngas da carbone mirato all'ottenimento e all'utilizzo di vettori energetici di alta valenza ambientale e dell'idrogeno in particolare," funded by the Italian Ministry for Education, Universities and Research (MIUR) through the Dlgs. 297/99.

Nomenclature

A = Fuel cell active area
F = Faraday's constant
I = current
J = current density
m = mass flow rate
n = molar flow rate
p = pressure
P = power
T = temperature
U_A = air utilization factor
U_F = fuel utilization factor
V = voltage
η = efficiency

Acronyms

LHV = lower heating value
MCFC = molten carbonate fuel cell
MGT = micro gas turbine
SCR = steam-to-carbon ratio
SOFC = solid oxide fuel cell

References

[1] U.S. DOE, 2004, *Fuel Cell Handbook*, 7th ed., DOE/NETL, Morgantown, WV.
[2] Singhal, S. C., and Kendall, K., 2003, *High Temperature Solid Oxide Fuel Cells. Fundamentals, Design and Applications*, Elsevier, New York.
[3] Massardo, A. F., McDonald, C. F., and Korakianitis, T., 2002, "Microturbine/Fuel Cell Coupling for High-Efficiency Electrical Power Generations," J. Eng. Gas Turbines Power, **124**, pp. 110–116.
[4] Vejo, S. E., Shockling, L. A., Dederer, J. T., Gillett, J. E., and Lundberg, W. L., 2002, "Tubular Solid Oxide Fuel Cell/Gas Turbine Hybrid Cycle Power Systems: Status," J. Eng. Gas Turbines Power, **124**, pp. 845–849.
[5] Rao, A. D., and Samuelsen, G. S., 2002, "Analysis Strategies for Tubular Solid Oxide Fuel Cell Based Hybrid Systems," J. Eng. Gas Turbines Power, **124**, pp. 503–509.
[6] Campanari, S., 2004, "Parametric Analysis of Small Scale Recuperated SOFC/Gas Turbine Cycles," ASME Paper No. GT2004–53933.
[7] Yang, W. J., Kim, T. S., Kim, J. H., Sohn, J. J., and Ro, S. T., 2005, "Comparative Performance Assessment of Pressurized Solid Oxide Fuel Cell/Gas

Turbine Hybrid Systems Considering Various Design Options," ASME Paper No. GT2005-68533.
[8] Litzinger, K. P., Vejo, S. E., Shockling, L. A., and Lundberg, W. L., 2005, "Comparative Evaluation of SOFC/Gas Turbine Hybrid System Options," ASME Paper No. GT2005-68909.
[9] Vasudeva, K., Mitra, N., Umasankar, P., and Dhingra, S. C., 1996, "Steam Reforming of Ethanol for Hydrogen Production: Thermodynamic Analysis," Int. J. Hydrogen Energy, **21**(1), pp. 13–18.
[10] Carapellucci, R., Risalvato, V., Bruno, C., and Cau, G., 1996, "Performances and Emissions of CRGT Power Generation Systems With Reformed Methanol," 31st Intersociety Energy Conversion Engineering Conference, Washington, D. C., August 11–16.
[11] Adachi, Y., Komoto, M., Watanabe, I., Ohno, Y., and Fujimoto, K., 2000, "Effective Utilization of Remote Coal Through DimethylEther Synthesis," Fuel, **79**, pp. 229–234.
[12] Jones, G. R., Holm-Larsen, H., Romani, D., and Sills, R. A., 2001, "DME for Power Generation Fuel: Supplying India's Southern Region," Proceedings of the PETROTECH 2001 Conference, New Delhi, India, January 23–25.
[13] Basu, A., and Wainwright, J. M., 2001, "DME as Power Generation Fuel: Performance in Gas Turbines," Proceedings of the PETROTECH 2001 Conference, New Delhi, India, January 23–25, 2001.
[14] Joensen, F., and Rostroup-Nielsen, J. R., 2002, "Conversion of Hydrocarbons and Alcohols for Fuel Cells," J. Power Sources, **105**, pp. 195–201.
[15] Cau, G., Cocco, D., and Tola, V., 2002, "Methanol From Coal: Prospect for Ultra-Low Emissions Gas Turbine Plants," International Conference on Clean Coal Technologies for Our Future, Chia Laguna, Italy, October 21–23.
[16] Cocco, G., and Tola, D., 2004, "Comparative Performance Assessment of CRGT Power Plants Fuelled by Hydrogen Energy Carriers," ASME Paper No. GT2004–53883.
[17] AspenPlus.11.1, 2002, Aspen Technology Inc., Cambridge.
[18] Bustamante, F., Enick, R. M., Cugini, A. V., Killmeyer, R. P., Howard, B. H., Rothenberger, K. S., Ciocco, M. V., Morreale, B. D., Chattopadhyay, S., and Shi, S., 2004, "High-Temperature Kinetics of the Homogeneous Reverse Water-Gas Shift Reaction," AIChE J., **50**(5), pp. 1028–1041.

Nonlinear Rotordynamics of Automotive Turbochargers: Predictions and Comparisons to Test Data

Luis San Andrés
e-mail: lsanandres@mengr.tamu.edu

Juan Carlos Rivadeneira

Mechanical Engineering Department,
Texas A&M University,
College Station, TX 77843

Murali Chinta
Honeywell Turbo Technologies,
Torrance, CA 90505

Kostandin Gjika
Honeywell Turbo Technologies,
88155 Thaon les Vosges, France

Gerry LaRue
Honeywell Turbo Technologies,
Torrance, CA 90905

Passenger vehicle turbochargers (TCs) offer increased engine power and efficiency in an ever-competitive marketplace. Turbochargers operate at high rotational speeds and use engine oil to lubricate fluid-film-bearing supports (radial and axial). However, TCs are prone to large amplitudes of subsynchronous shaft motion over wide ranges of their operating speed. Linear rotordynamic tools cannot predict the amplitudes and multiple frequency shaft motions. A comprehensive nonlinear rotordynamics model coupled to a complete fluid-film-bearing model solves in real time the dynamics of automotive turbochargers. The computational design tool predicts the limit cycle response for several inner and outer film clearances and operating conditions including rotor speed and lubricant feed pressure. Substantial savings in product development and prototype testing are the benefits of the present development. The paper presents predictions of the linear and nonlinear shaft motion of an automotive turbocharger supported on a semi-floating ring bearing. The shaft motion predictions are compared to measurements of shaft motion at the compressor nose for speeds up to 240 krpm*, and for lubricant inlet pressure of* 4 bar *at* 150°C. *Linear and nonlinear rotordynamic models reproduce very well the test data for synchronous response to imbalance. The nonlinear results show two subsynchronous whirl frequencies whose large magnitudes agree well with the measurements. A large side load predicted for this turbocharger must be considered for accurate prediction of the rotordynamic response.* [DOI: 10.1115/1.2204630]

Introduction

Most commercial automotive turbochargers incorporate engine oil lubricated floating ring bearings (FRBs) due to their low cost and reduced power losses [1,2]. Passenger vehicles TCs are more compact units that implement semi-floating ring bearings (SFRBs) with integral thrust bearings. FRBs comprise two fluid films in series with the ring spinning at a fraction of shaft speed. SFRBs are similar, except that the floating ring is pinned to prevent its rotation; thus, the outer film acts as a squeeze film damper. In [3], turbochargers supported on SFRBs have shown less power loss (~28%) than those utilizing FRBs with identical clearances, thus making more power available to drive the compressor or a lower requirement from the turbine, resulting in lower back pressure on the engine.

Persistent subsynchronous motions are present in rotor-bearing systems with a fully floating ring design, albeit reaching limit cycles that enable their continuous operation [2,4,5]. The lubricated bearings with inner and outer films acting in series are the source of the rotordynamic instabilities [6–8]. The dynamic response of lubricated TCs is thus highly nonlinear. The amplitudes and frequency content of the sub synchronous motions cannot be predicted using conventional linear rotordynamics tools [9–11]. More often, however, simple linear rotor-bearing models predict instability regions over wide operating speed ranges; while test measurements demonstrate stable performance due to a number of effects not accounted in the simple analysis. The uncertainty in actual rotor imbalance levels as well as thermal effects affecting the lubricant viscosity and actual film clearances are a few notable factors (see, for example, [2,4]). Due to the lack of accurate and efficient predictive tools, turbocharger rotordynamic design followed, until recently, costly test stand iteration [12,13].

The demand for maximum turbocharger speed and variable geometry technology continues to increase, thus requiring the development of lighter materials with higher strengths. Bearing systems in automotive turbochargers currently perform under extreme operating conditions with attendance to stringent environmental considerations. Present applications use low viscosity (light) lubricants delivered at high operating temperatures (up to 150°C) and with reduced feed pressures [14]. In 2000, a prominent turbomachinery manufacturer along with a university research laboratory initiated an ambitious research program to develop physical models and fast computational programs to reliably predict the nonlinear rotordynamic performance of passenger and commercial vehicle turbochargers. The ultimate goal is to deliver an experimentally validated design tool that accounts for the actual operating conditions in turbochargers, including accurate modeling of the forced response of the fluid film bearings and full integration with a comprehensive rotordynamics response program. Substantial savings in product development and prototype testing are the major expected benefits.

Within the scope of the project outlined above, Naranjo et al. [15] introduced the rudiments of FRB analysis along with experimental validation in a low speed test rotor. Later, Holt et al. [16–18] present a complete nonlinear rotordynamics model and comprehensive measurements of casing acceleration in a high speed TC unit supported on FRBs. The experiments show the effects of increasing lubricant inlet pressure and temperature on the complex TC dynamic response for shaft speeds to 100 krpm. The nonlinear rotor model incorporating the FRB reaction forces in the numerical integration of the rotor equations of motion predicts the limit cycle amplitudes with two fundamental subsynchronous whirl frequencies. The predictions, validated by the test data,

Contributed by the International Gas Turbine Institute (IGTI) of ASME for publication in the JOURNAL OF ENGINEERING FOR GAS TURBINES AND POWER. Manuscript received August 25, 2005; final manuscript received September 28, 2005. IGTI Review Chair: K. C. Hall. Paper presented at the ASME Turbo Expo 2005: Land, Sea, and Air, Reno, NV, June 6–9, 2005, Paper No. GT2005-68177.

evidence two (unstable) whirl ratios at approximately one-half ring speed and one-half ring speed plus one-half journal speed. The transient nonlinear responses reveal the importance of rotor imbalance in suppressing the subsynchronous instabilities at large rotor speeds as also observed in the experiments.

Kerth and San Andrés [19] present the flow model for prediction of FRB forced response—linear and nonlinear. This model incorporates a lumped parameter thermal energy balance for estimation of the lubricant viscosity and thermal growth of the rotor, bearing and floating ring. The FRB model, fully integrated into the nonlinear rotordynamics computational program, predicts the floating ring speed, journal and ring eccentricities, power loss, and the inner and outer films' rotordynamic force coefficients as a function of the load applied at a given rotor speed. Knowledge of the actual load conditions—static and dynamic—and the changes in operating clearance and effective lubricant viscosity are of utmost importance to estimate accurately the dynamic forced response of turbochargers. In [19], predictions for the exit lubricant temperature, power losses, and floating ring speeds agree well with measurements obtained in an automotive turbocharger test rig.

References [18,19] include extensive literature reviews of the prior art in turbocharger dynamics analysis and modeling of FRBs, along with test programs attempting to validate model predictions. Analyses based on linearized bearing force coefficients have been, for the most part, unsuccessful since the actual nonlinear TC response, i.e., limit cycle amplitudes and subsynchronous frequencies, cannot be predicted. Nonetheless, linearized analyses for simple rotor-bearing systems (e.g., [5–8]), do offer insight into the intricate response of turbochargers, rich in subsynchronous motions. The present computational development, based on the time-marching numerical integration of the rotor-bearing nonlinear equations of motion, continues earlier work given in [10,11]. The computer program, emulating a virtual laboratory for evaluation of rotor-bearing systems dynamic performance, is relatively fast due to the significant advances in high processing computer technology. The application to semi-floating rotor-bearing system of a passenger car turbocharger shows good correlation between predicted and measured steady-state shaft motions. The predictive tool can be used to design high performance products with faster product development cycle times and increased product reliability.

Test Turbocharger and Measurements

Figure 1 depicts a photograph of the test turbocharger rotor and its semi-floating ring bearing (SFRB) support. The small rotor is comprised of a long and thin shaft with one end welded to the turbine wheel. The other shaft end is threaded for installation of the compressor wheel, pushing the thrust collar towards the shaft shoulder. The turbine and compressor are made of high structural

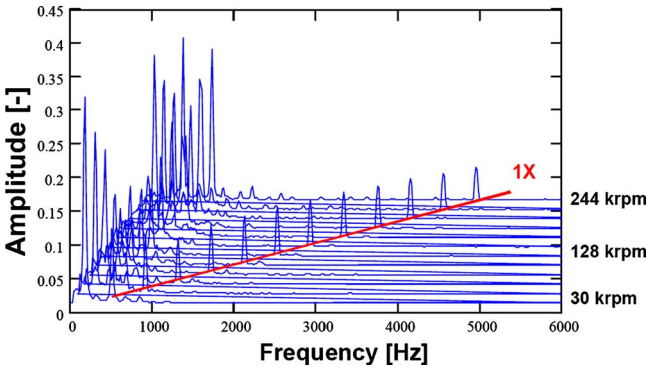

Fig. 2 Waterfall of turbocharger measured shaft displacement versus frequency. Shaft speed ranges from 29.7 krpm to 243.8 krpm. 4 bar (150°C) oil feed pressure. Vertical eddy current sensor (compressor side).

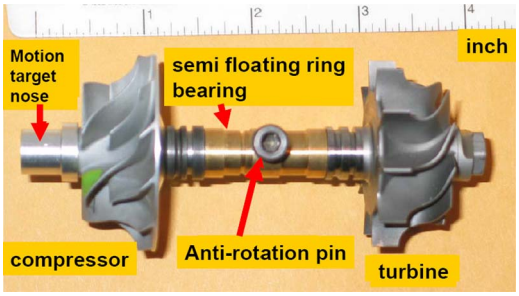

Fig. 1 Photograph of automotive turbocharger supported on semi-floating ring bearings

strength and lightweight materials (low inertia). For the experiments, the rotor was modified to include an aluminum sleeve at the compressor nose for measurement of shaft motions.

The semi-floating ring is a thick and long structural element made of a common material. The rotor and SFRB when installed in its casing give rise to an outer film and an inner film on both the compressor and turbine sides. A feed port on the casing supplies lubricant into the middle plane of the floating ring. On the other side, a pin locking the ring prevents its rotation. The inner diameter of the ring, at the location of the inner film land, is machined to form a four-pad bearing with deep axial grooves. The outer film bearing is a plain cylindrical geometry. Pressurized lubricant flowing from the feed port lubricates the ends of the fluid film lands, inner and outer.

Experiments recording the TC shaft motions were conducted with a commercial lubricant (5 W-30) supplied at a nominal inlet temperature of 150°C and feed pressures ranging from 1 to 4 bar. The lubricant has a nominal viscosity of 2.76 cPoise at the supply condition. The low lubricant viscosity and high supply temperature responds to severe environmental constraints required in modern passenger vehicle.

Calibrated imbalances (~0.1 gram mm) were inserted at the nose and back face of the turbine and compressor wheels and at the same angular location (in-phase). The imbalance distribution used denotes a most severe condition, as per the manufacturer considerations. In the experiments, a hot gas drove the turbine to a top speed of 243 krpm (4.0 kHz). Upon achieving a steady-state condition, the shaft motions at incremental rotor speeds were collected using a dynamic signal analyzer and a digital oscilloscope displaying the shaft orbital motions of the shaft at the compressor end. Fast Fourier transform (FFT) collected data has a maximum span of 6.4 kHz with frequency increments of 16 Hz (400 lines).

Figure 2 shows a waterfall of the recorded shaft vertical displacement for a 4 bar lubricant feed pressure as the rotor ramps up from 29.7 to 243.6 krpm. In the graph, the horizontal axis displays the frequency content of shaft motion, while the vertical axis denotes the amplitude of shaft motion. The shaft displacements are shown in dimensionless form, relative to the physical limit at the location of measurement. The continuous line denotes the synchronous frequency components. The test results show the dominance of subsynchronous frequency motions over the whole shaft speed range, 29.7 to 243 krpm. The shaft synchronous amplitude peaks at the lowest rotor speed and decreases slowly as the rotor speed increases. However, the shaft subsynchronous motions are of large amplitude with significant changes over the test speed range. A filter analysis of the collected data produces the components of synchronous and subsynchronous shaft motions. A discussion of the test results is given below, along with the numerical predictions.

Turbocharger Rotor and Semi-floating Ring Bearing

Figure 3 displays the finite element structural models for the rotor and semi-floating ring bearing, each represented by 45 and 4

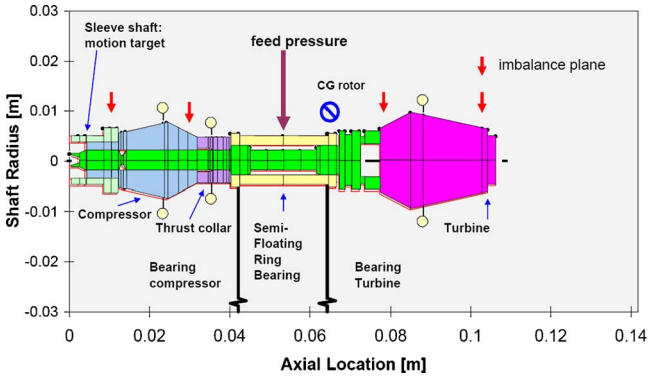

Fig. 3 Structural FE model of turbocharger rotor and semi-floating ring bearing. Location of mass imbalance planes noted.

elements, respectively. Inertia properties of the turbine, compressor, and thrust collar are included at the appropriate locations. Rap tests with the TC rotor hung from wires allow measuring its free-free mode natural frequencies and mode shapes. Two miniature piezoelectric, accelerometers, each 1 g in weight, were affixed on the rotor; one reference transducer remained at the turbine end, while the other roamed along the test rotor.

Figure 4 shows the measured and predicted free-free mode shapes. The first two natural frequencies recorded equal 1.07 and 4.77 kHz (±120 Hz), and the predicted values are 1.046 and 4.98 kHz, respectively. The agreement between predictions and measurements, both for natural frequencies and mode shapes, is excellent; thus lending validity to the structural rotor model developed. Note that rotor material properties at ambient conditions were used for the predictions.

Holt et al. [17,18] describe the integration of a rotordynamics computational program [20] to the thin film fluid flow model for prediction of the reaction loads in fully floating and semi-floating ring bearings. The rotordynamics finite element (FE) program, based on the component-synthesis method [21], predicts the linear stability (damped eigenvalues) and synchronous response of a rotor supported on bearings represented by linearized stiffness and damping force coefficients. The program, which also includes simple models for typical nonlinear mechanical elements, features a time transient numerical solution procedure for prediction of rotor responses to applied loads including shock and maneuver and initial conditions (blade simulations, for example).

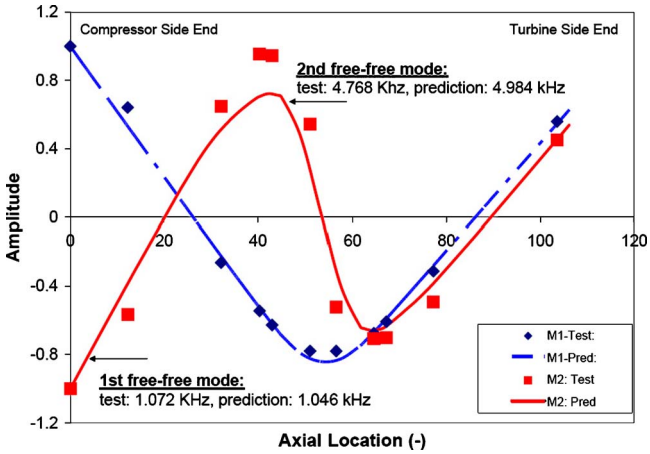

Fig. 4 Free-free mode shapes for turbocharger rotor—predictions and measurements at room temperature

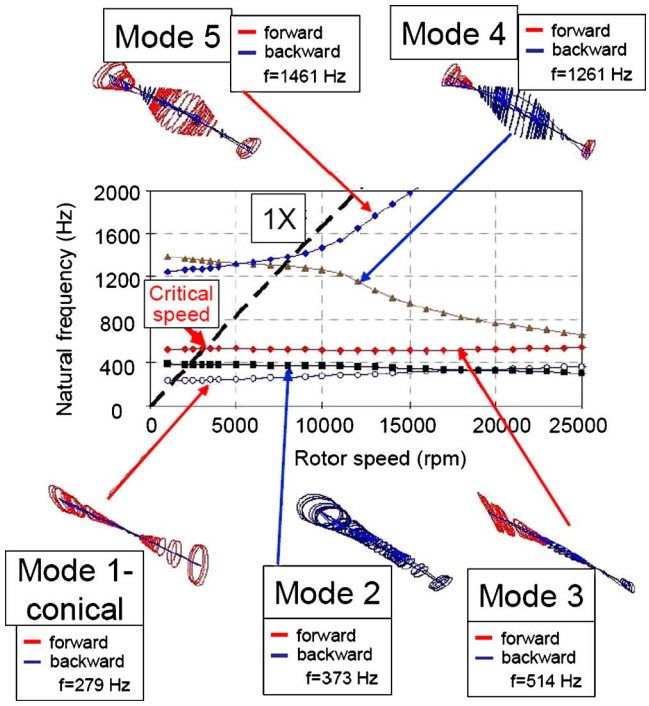

Fig. 5 Predicted damped natural frequencies versus shaft speed for test turbo charger rotor. Damped natural modes shown for shaft speed=100 krpm.

Kerth and San Andrés [19] detail the FE analysis of the laminar flow (Reynolds) equations for each fluid film along with a lumped parameter thermal model. The computational model for a (semi-) floating ring bearing predicts its forced performance as a function of the bearing geometry, applied load, shaft speed and lubricant properties, including shear thinning effects. The model does account for the temperature raise within each film, inner and outer, affecting the lubricant viscosity and operating clearances at each shaft speed.

The prediction of the nonlinear transient response of the TC rotor supported on the semi-floating ring bearings requires

(a) estimation of the static loads acting on each bearing;
(b) calculation of the equilibrium conditions for each film, namely, static eccentricity and attitude angle of journal and ring, temperature rise, and operating clearances and effective viscosities for both films in series;
(c) calculation of stiffness and damping force coefficients for the inner and outer films at the equilibrium position;
(d) integration of the actual SFRB operating conditions and side load into the rotordynamics program for prediction of system eigenvalues (damped natural frequencies and mode shapes) and the linear or nonlinear response due to a prescribed imbalance distribution.

Natural Frequencies and Associated Mode Shapes

Figure 5 depicts a map of the predicted damped natural frequencies versus shaft speed. The linear analysis relies on the specification of the stiffness and damping force coefficients for the inner and outer films at the turbine and compressor bearings. The graph also displays the rotor mode shapes at a shaft speed of 100 krpm. The rotor-bearing system critical speeds are noted on the intersection of the synchronous line (1*X*) with each of the natural frequencies. The lowest natural frequency (~200 Hz) corresponds with a rigid body conical (planar) mode shape. The other natural modes show increasing degrees of rotor bending, with

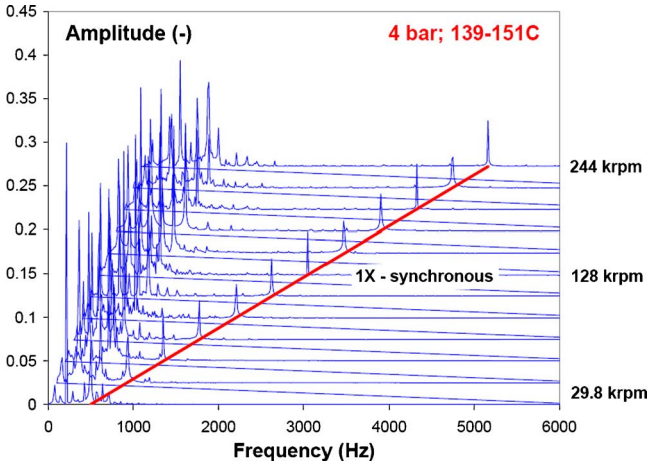

Fig. 6 Waterfall of predicted nonlinear (vertical) shaft motions at compressor end. Rotor range speed 29.7 to 244 krpm. 4 bar lubricant feed pressure. Amplitude refractive to maximum physical limit.

large motions at the compressor end, except for backward whirl mode 4. All modes are well damped (i.e., absence of instabilities) at all shaft speeds. The test data, on the other hand, show subsynchronous whirl motions over the whole speed range, thus demonstrating the limited applicability of the linear eigenvalue analysis.

Predictions of Shaft Motion and Comparisons to Test Data

The numerical integration of the nonlinear equations of motion for the rotor-SFRB system was conducted for the same test shaft speeds, 29.7 krpm (0.5 kHz) to 243 krpm (4.05 kHz), and lasting a sufficiently "long time" to warrant the prediction of a steady-state motion condition. A time step fixed at 78 μs renders a maximum frequency span equal to 6.4 kHz, similar to the signal analyzer setting recording the experiments. In most cases, the total time for integration of the governing equations lasts ~3/4 s, with only the "s-s" portion being analyzed giving a lowest frequency step of 6.25 Hz (2048 data points). In the measurements, a 16 Hz frequency step was used.

Post-processing mathematical software allows the comprehensive analysis of the nonlinear time response predictions to determine the amplitude and frequency content of the shaft motion over pre-selected time spans. FFTs are calculated with a sampling frequency of the same order as in the experiments, namely 12.5 Hz (1024 data points).

Figure 6 displays a waterfall graph of the predicted steady-state shaft motions at the compressor nose. The amplitudes are dimensionless relative to the physical limit of shaft displacement at the measurement plane. Note that, as with the experimental measurements, the predictions show persistent subsynchronous motions over the entire shaft speed range. Synchronous amplitude (1*X*) motions are but a small fraction of the total shaft motion at the compressor end. Figure 7 compares, at shaft speeds equal to 127 and 205 krpm, the FFTs of shaft motion acquired from the test data and the ones derived from the predicted nonlinear response. There is good agreement on the amplitudes of synchronous motion as well as on the location of the subsynchronous frequencies.

The waterfalls of shaft motion shown in Figs. 2 and 6 for tests and predictions, respectively, reveal a complex rotor response rich in subsynchronous activity. The test data and FFT predictions are filtered to capture the amplitude and frequency of the peak responses, including the synchronous components. The threshold amplitude for the analysis is 4% of the physical limit.

Figure 8 shows the total amplitude of shaft motion at the compressor end versus speed for both the test data and the nonlinear

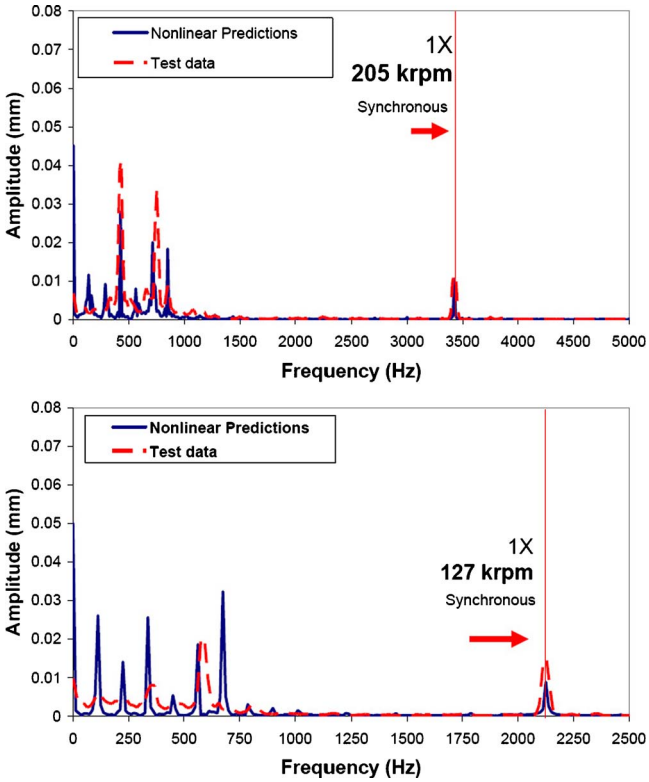

Fig. 7 FFTs of shaft motion at compressor end for rotor speeds equal to 127 krpm (bottom) and 205 krpm (top). Comparison of nonlinear predictions to test data. Note amplitudes at subsynchronous frequencies.

predictions. The size of the limit cycle orbit defines the total motion. The numerical data is analyzed over a time span that captures motions with a minimum frequency equal to 50 Hz. In general, the nonlinear predictions correlate very well with the test data at low and high shaft speeds. Predicted total motions are larger than test amplitudes in the speed range from 70 to 166 krpm, although well below the physical limit. An explanation of the differences follows later.

Figure 9 depicts the experimental and predicted amplitudes of synchronous (1*X*) motions versus shaft speed. The predictions shown are linear and nonlinear, with the nonlinear denoting the motion amplitudes synchronous with shaft speed as extracted

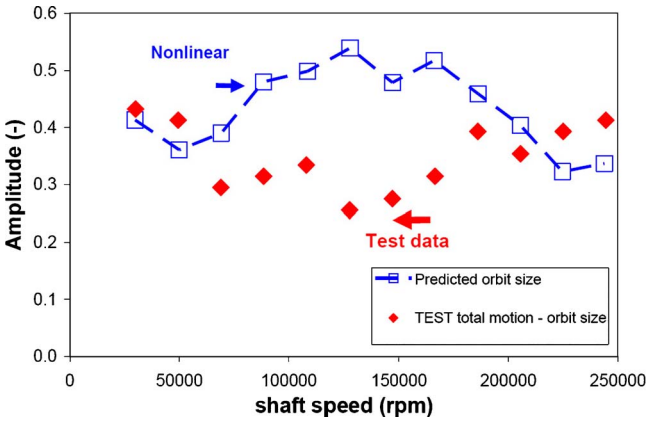

Fig. 8 Amplitudes of total motion at compressor end versus shaft speed. Comparisons between test data and nonlinear predictions. Oil feed pressure=4 bar (150°C).

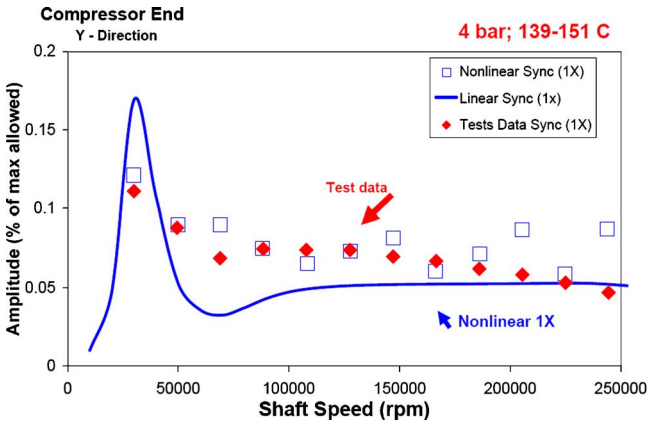

Fig. 9 Amplitudes of synchronous shaft motion versus shaft speed. Comparisons between test data and linear and nonlinear predictions. Oil feed pressure=4 bar (150°C).

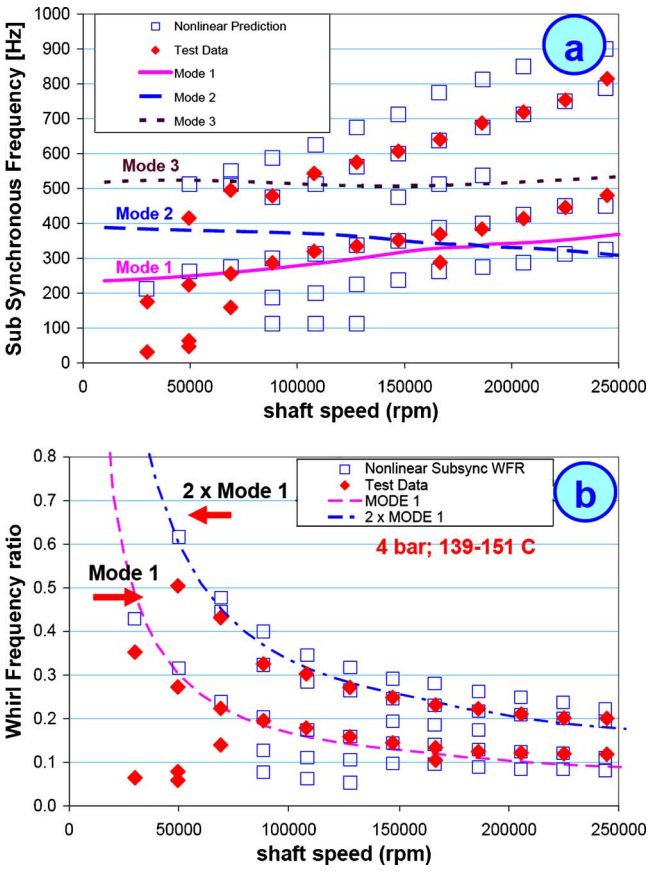

Fig. 10 (*a*) Whirl frequency of subsynchronous motions and (*b*) whirl frequency ratios versus shaft speed. Comparisons between nonlinear predictions and test data. Lines represent damped natural frequencies (linear analysis). Oil feed pressure=4 bar (150°C).

from the FFTs of the transient time response. The linear predictions, on the other hand, show the response to imbalance obtained with the (linearized) SFRB stiffness and damping coefficients for the inner and outer films. Recall that these force coefficients are calculated from small-amplitude perturbations of the journal and floating ring at their static equilibrium position. The rotordynamics software calculates the linear imbalance response very rapidly, while the nonlinear predictions need more computational time to be completed.

The nonlinear (synchronous response) predictions agree very well with the test data over the entire speed range. The linear response, on the other hand, predicts larger amplitudes at a lightly damped critical speed at 30.8 krpm (514 Hz) that represents rotor mode 3, i.e., the one with the compressor end "ringing" (see Fig. 5). Above the critical speed, the amplitudes of synchronous motion steadily decrease as the rotor operates well above any natural frequency. The rationale for the discrepancies between the measured data and nonlinear predictions are ascribed to the uncertainty in the (used) imbalance masses and their exact location in the rotor model. It is important to note that the linear analysis could be used effectively to predict the synchronous rotor response, in spite of the apparent nonlinearities.

In the analysis, a whirl frequency ratio (WFR) relates a whirl frequency to the shaft angular frequency (synchronous speed). Figure 10 depicts the frequency and WFR of the subsynchronous motions versus shaft speed in the top and bottom graphs, respectively. The test data shows two main subsynchronous frequencies that increase as the shaft speed raises. At the lowest shaft speeds, the whirl frequencies appear to coincide with the first two natural frequencies (modes 1 and 2). The nonlinear predictions for subsynchronous whirl frequencies agree very well with the measurements, albeit showing a third (unstable) higher subsynchronous frequency not evident in the tests. The WFRs decay steadily as the shaft speed increases; most notably, the second test whirl frequency is approximately two times the lowest WFR. The results demonstrate that the unstable shaft motions refer to excitations of the conical mode and its harmonics. The whirl frequencies tracking the shaft speed are particular to the operation of the nonrotating outer films (SFRB) acting as uncentralized squeeze film dampers.

Figures 11(*a*)–11(*c*) shows the amplitude of subsynchronous motions versus shaft speed (top graph) and whirl subsynchronous frequency (bottom graph). The continuous lines shown in the figures are hand-drawn and attempt to evidence characteristic trends mainly from the test data. The graphs display the intricacy of the test results and predictions. At a particular shaft speed, one or more subsynchronous amplitudes of motion are apparent. Conversely, subsynchronous amplitudes may also occur at more than one shaft speed. The results depicted intend to evidence trends of importance, for example persistent motions at a particular low frequency. The experiments and predictions indicate the largest motion occur at the lowest test rotor speed (29.7 krpm) with a frequency of ~200 Hz (WFR=0.35–0.43) coinciding with the (self-) excitation of the rotor conical mode. As the shaft speed increases to 127 krpm, the predicted and test derived amplitudes decrease steadily. For higher shaft speeds, there is a notable increase in subsynchronous motions with the test data showing larger amplitudes at the top shaft speed.

Figure 11(*b*) depicts the experimental amplitudes of subsynchronous motion to be confined in a narrow frequency range—200 to 800 Hz—which spans the first three natural modes of vibration (see Fig. 5). The hand-drawn continuous lines intend to show trends for the test data. For example, the largest amplitudes appear to correspond with the lowest mode of natural vibration and its 2nd harmonic (~200 Hz and 400 Hz) and decreasing in magnitude as the whirl frequency increases. The nonlinear predictions show similar trends, except for the appearance of the third whirl frequency in the range from 600 to 900 Hz.

Closure

Turbochargers are used in passenger vehicles to increase the overall efficiency and reduce emissions of internal combustion engines. Presently, automotive turbochargers operate at higher shaft speeds to increase their boosting power while using much lighter lubricants. Turbochargers using lubricated fluid film bearing show shaft motions with one or more subsynchronous fre-

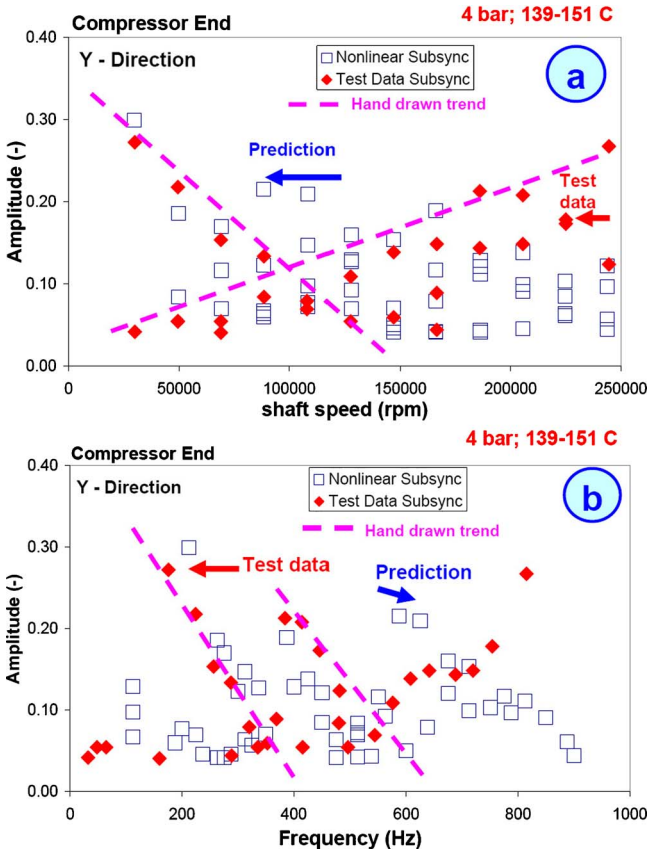

Fig. 11 Amplitudes of subsynchronous motions versus (*a*) shaft speed and (*b*) whirl frequency. Comparisons between nonlinear predictions and test data. Oil feed pressure=4 bar.

quencies, typically of large amplitude, and leading to limit cycle performance. Linear rotor dynamics analyses cannot reproduce the actual limit cycle motions.

In spite of the complexity of the measured and predicted rotor responses, i.e., rich in subsynchronous frequencies and amplitudes, the nonlinear results from the comprehensive predictive model replicate most of the trends, including amplitudes of limit cycle motion and subsynchronous whirl frequencies. The nonlinear predictions are in good agreement with the test data, thus validating the comprehensive computational model developed.

The usefulness of the predictive tool developed, however, can best be appreciated by performing an analysis of the myriad of other calculated variables that become available upon completion of the program execution. The current program delivers shaft motions at any station in the rotor, including the bearings, as well as the transmitted forces to the casing. Trends in shaft static motions, whirl orbits, lubricant exit temperatures, etc. are easily graphed for ready analysis. Even digital video clips of transient shaft motion can be generated automatically. The computational design tool effectively aids to design better turbocharger products with increased reliability and in less development time. Future publications will continue to detail further predictions and comparisons to test data.

Acknowledgment

The support of Honeywell Turbo Technologies is gratefully acknowledged, in particular for preparing the turbocharger test bed and collecting the comprehensive experimental results. Graduate student J.C.R. thanks Honeywell's engineering staff for their guidance and insight.

References

[1] Hill, H. C., 1958, "Slipper Bearings and Vibration Control in Small Gas Turbines," Trans. ASME, **80**, pp. 1756–1764.
[2] Trippett, R. J., and Li, D. F., 1983, "High-Speed Floating-Ring Bearing Test and Analysis," ASLE Trans., **27**(1), pp. 73–81.
[3] Macinnes, H., and Johnston, A., 1982, "Comparison of Power Loss Between Full Floating and Semi-Floating Turbocharger Bearings," *Proceedings of IMechE Conference on Turbocharging and Turbochargers*, London, Paper C46/82, pp. 157–164.
[4] Tatara, A., 1970, "An Experimental Study of the Stabilizing Effect of Floating-Bush Journal Bearings," Bull. JSME, **13**(61), pp. 859–863.
[5] Holmes, R., Brennan, M. J., and Gottrand, B., 2004, "Vibration of an Automotive Turbocharger–A Case Study," *Proceedings of the 8th International Conference in Vibrations and Rotating Machinery*, IMechE Wales, UK, Paper C623/011/2004, pp. 445–455.
[6] Tanaka, M., and Hori, Y., 1972, "Stability Characteristics of Floating Bush Bearings," Trans. ASME, **94**, pp. 248–259.
[7] Tanaka, M., 1996, "A Theoretical Analysis of Stability Characteristics of High Speed Floating Bush Bearings," *Proceedings of the 6th International Conference on Vibrations in Rotating Machinery*, IMechE Conference Transaction 1996-6, London, Paper C500/087/96, pp. 133–142.
[8] Tanaka, M., 2002, "A Parametric Study of the Stability of High-Speed Floating Bush Journal Bearings," *Proceedings of the 6th IFToMM International Conference on Rotor Dynamics*, Sydney, Australia, 2, pp. 549–555.
[9] Rohde, S. M., and Ezzat, H. A., 1980, "Analysis of Dynamically Loaded Floating-Ring Bearings for Automotive Applications," ASME J. Lubr. Technol., **102**, pp. 271–277.
[10] Li, C. H., and Rohde, S. M., 1981, "On the Steady State and Dynamic Performance Characteristics of Floating Ring Bearings," ASME J. Lubr. Technol., **103**, pp. 389–397.
[11] Li, C., 1982, "Dynamics of Rotor Bearing Systems Supported by Floating ring Bearings," ASME J. Lubr. Technol., **104**, pp. 469–477.
[12] Sahay, S. N., and Thouvenin, D., 1993, "Turbocharger Noise, Generating Mechanisms and Control," Noise, **93**, pp. 269–277.
[13] Sahay, S. N., and LaRue, G., 1996, "Turbocharger Rotordynamic Instability and Control," *Proceedings of the 8th Workshop on Instability in Rotating Machinery*, Texas A&M University, College Station, TX, pp. 1–11.
[14] Gjika, K., 2003, "Turbocharger Bearing Systems Technology," Garrett Booster Magazine, March, pp. 6–11.
[15] Naranjo, J., Holt, C., and San Andrés, L., 2001, "Dynamic Response of a Rotor Supported in a Floating Ring Bearing," *Proceedings of the 1st International Conference in Rotordynamics of Machinery*, ISCORMA1, Lake Tahoe, NV, Paper 2005.
[16] Holt, C., San Andrés, L., Sahay, S., Tang, P., LaRue, G., and Gjika, K., 2003, "Test Response of a Turbocharger Supported on Floating Ring Bearings–Part I: Assessment of Subsynchronous Motions," *Proceedings of the 19th Biennial Conference on Mechanical Vibration and Noise*, Chicago, IL, ASME Paper DETC 2003/VIB-48418.
[17] Holt, C., San Andrés, L., Sahay, S., Tang, P., LaRue, G., and Gjika, K., 2003, "Test Response of a Turbocharger Supported on Floating Ring Bearings–Part II: Comparisons to Nonlinear Rotordynamic Predictions," ASME Paper No. DETC 2003/VIB-48419.
[18] Holt, C., San Andrés, L., Sahay, S., Tang, P., LaRue, G., and Gjika, K., 2005, "Test Response and Nonlinear Analysis of a Turbocharger Supported on Floating Ring Bearings," ASME J. Vibr. Acoust., **127**, pp. 1–9.
[19] Kerth, J., and San Andrés, L., 2004, "Thermal Effects on the Performance of Floating Ring Bearings for Turbochargers," Proc. Inst. Mech. Eng., Part J: J. Eng. Tribol., **218**(5), pp. 437–450.
[20] XLTRC^2 Rotordynamics Software Suite v. 2, 2002, Turbomachinery Laboratory, Texas A&M University, College Station, TX.
[21] Nelson, H., and Meacham, W., 1981, "Transient Analysis of Rotor-Bearing System Using Component Mode Synthesis," ASME Paper No. 81-G7-10.

Structural Stiffness, Dry Friction Coefficient, and Equivalent Viscous Damping in a Bump-Type Foil Gas Bearing

Dario Rubio
Bechtel Corporation,
3000 Post Oak Boulevard,
Houston, TX 77056
e-mail: drubio@bechtel.com

Luis San Andres
Mast-Childs Professor, Fellow ASME
Mechanical Engineering Department,
Texas A&M University,
College Station, TX 77843-3123

High performance oil-free turbomachinery implements gas foil bearings (FBs) to improve mechanical efficiency in compact units. FB design, however, is still largely empirical due to its mechanical complexity. The paper provides test results for the structural parameters in a bump-type foil bearing. The stiffness and damping (Coulomb or viscous type) coefficients characterize the bearing compliant structure. The test bearing, 38.1 mm *in diameter and length, consists of a thin top foil supported on bump-foil strips. A prior investigation identified the stiffness due to static loads. Presently, the test FB is mounted on a non-rotating stiff shaft and a shaker exerts single frequency loads on the bearing. The dynamic tests are conducted at shaft surface temperatures from* 25 to 75 °C. *Time and frequency domain methods are implemented to determine the FB parameters from the recorded periodic load and bearing motions. Both methods deliver identical parameters. The dry friction coefficient ranges from 0.05 to 0.20, increasing as the amplitude of load increases. The recorded motions evidence a resonance at the system natural frequency, i.e., null damping. The test derived equivalent viscous damping is inversely proportional to the motion amplitude and excitation frequency. The characteristic stick-slip of dry friction is dominant at small amplitude dynamic loads leading to a hardening effect (stiffening) of the FB structure. The operating temperature produces shaft growth generating a bearing preload. However, the temperature does not significantly affect the identified FB parameters, albeit the experimental range was too small considering the bearings intended use in industry.* [DOI: 10.1115/1.2360602]

Introduction

Foil bearings (FBs) are made of one or more compliant surfaces of corrugated metal and one or more layers of top foil surfaces. The compliant surface, providing structural stiffness, comes in several configurations such as bump type (see Fig. 1), leaf type and tape type, among others. FBs operate with nominal film thicknesses larger than those found in a geometrically identical rigid surface bearing, for example, since the hydrodynamic film pressure generated by rotor spinning "pushes" the FB compliant surface [1,2].

FBs enable high speed operation and large load capacity; in particular for third generation configurations [3]. The underlying compliant structure provides a tunable structural stiffness source [4–7], and Coulomb-type damping arises due to the relative motion between the bumps and the top foil, and between the bumps and the bearing support wall [8,9], see the inset in Fig. 1.

Coulomb damping (dry friction) is a source of energy dissipation that arises when two surfaces slide against each other. Unlike a viscous damping force, a Coulomb-type force does not depend on the magnitude of the relative velocity, but acts to oppose the surfaces' motion. In its simplest form the dry friction force is $F_{\text{dry}}=\mu N\,\text{sgn}(\dot{x})$ if $(\dot{x})\neq 0$, where, μ is the dry friction coefficient, N is the normal force to the contact area, and $\text{sgn}(\dot{x})=1$ for $\dot{x}>0$, $\text{sgn}(\dot{x})=-1$ for $\dot{x}<0$.

The performance of a FB relies heavily on the compliant structural elements. With proper selection of foil and bump materials and the engineered design of their geometry, desired bearing stiffness, damping (friction) forces can be achieved. Heshmat and Ku [10] present an experimental procedure to identify the structural stiffness and equivalent viscous damping coefficient by exciting, with two electromagnetic shakers, a non-rotating shaft supported on FBs. Structure force coefficients, determined from a force equilibrium on the FB housing, indicate that the direct stiffness and equivalent viscous damping decrease with increasing *dynamic* load amplitudes. Similarly, Ku [11] carried out a test program to characterize the structural dynamic force coefficients of corrugated bump strips of various configurations. A fixed static load with superimposed dynamic loads of small amplitude act on a top foil supported by a six-bump strip. The structural stiffness derives from the slope of the dynamic load versus deflection curves. The test dynamic stiffness decreases with the amplitude of motion and increases with the static load. Empirical dry friction coefficients for various surface coatings on the top foil are estimated indirectly from matching the test structural stiffness to stiffness predictions [4] obtained using ad hoc values of the friction coefficient. The dynamic structural stiffness best correlates with theoretical values when selecting dry friction coefficients ranging from 0.4 to 0.6, depending on the surface coating.

Recently, Salehi et al. [12] performed dynamic force tests on corrugated metal sheets (bump foil strips) affixed within an arcuate surface. An equivalent viscous damping coefficient and a dry friction force are extracted from the resulting hysteresis loops of force versus displacement for various test conditions in frequency and dynamic load amplitudes. In addition, bump foil stiffness and viscous damping coefficients are identified from the complex mechanical impedance formulation using a single degree of freedom model. The authors advance a parametric (dimensionless) relationship between frictional damping and test conditions of load (W), amplitude of motion (X), and frequency (f). Based on the

Contributed by the International Gas Turbine Institute (IGTI) of ASME for publication in the JOURNAL OF ENGINEERING FOR GAS TURBINES AND POWER. Manuscript received October 1, 2005; final manuscript received February 1, 2006. IGTI Review Chair: D. R. Ballal. Paper presented at the ASME Turbo Expo 2005: Land, Sea, and Air, Reno, NV, June 6–9 2005, Paper No. GT2005-68384.

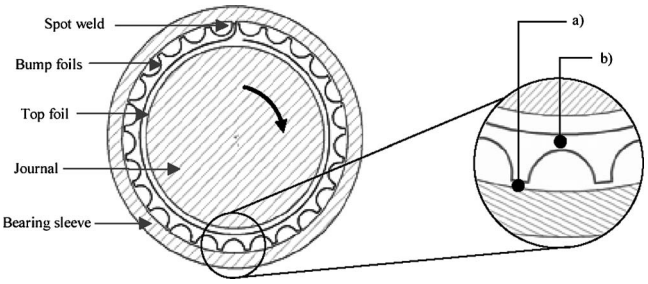

Fig. 1 Schematic representation of a bump-type foil bearing. (*a*) Contact in relative motion between top foil and bump foil; (*b*) contact in relative motion between bumps and bearing sleeve.

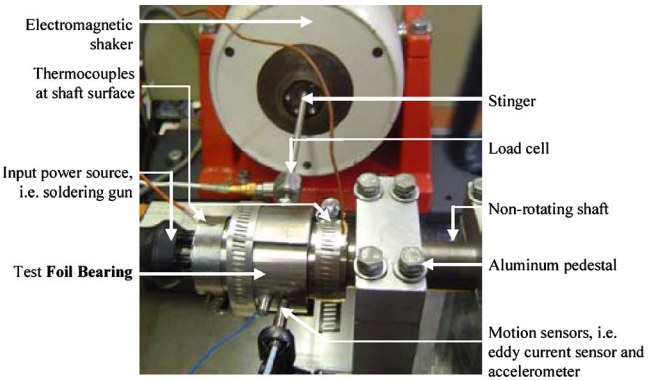

Fig. 2 Test setup for dynamic load experiments

experimental results, the equivalent viscous damping coefficient decreases with increasing frequencies, $C_{eq} \propto 1/f$, and amplitude of motions, $C_{eq} \propto 1/X$, while increasing with the magnitude of dynamic load, $C_{eq} \propto W$. The experimental results also aid to advance a parametric relationship for the dry friction coefficient (μ). Test values of the dry friction coefficient range from 0.1 to 0.4 for excitation frequencies from ~0 to ~600 Hz.

The present work aims to continue developing experimental and analytical tools to predict the structural dynamic characteristics of bump-type foil bearings. This paper offers an insight into the Coulomb frictional damping mechanism of bump-type FBs due to single frequency loads of varying magnitudes. The work contributes towards the identification of the structural characteristics of bump-type foil bearings.

Test Foil Bearing

Figure 1 shows a schematic view of the test FB and Table 1 lists the bearing dimensions and physical parameters. The bump-type FB is a "second generation" configuration [3], consisting of five arcuate bump strips, each with five bumps, affixed to the bearing circumference. Each strip is welded at one end and free at the other. Five aligned bump strips extend over the bearing axial length. The top foil, coated with Teflon of thickness 25.4 μm, consists of a thin metal sheet welded to the bearing sleeve at one end (spot weld) and free at the other end.

Experimental Setup

Figure 2 displays a photograph of the test setup for the dynamic force experiments. The experimental setup consists of two aluminum pedestals supporting a non-rotating steel shaft. The shaft nominal diameter is 38.10 mm [1.500 in.] and is 88.9 mm [3.50 in.] long. The shaft surface is polished with no coating applied on it. A slender stinger connects the test foil bearing to an electromagnetic shaker. In general, for each test condition, the excitation frequency (f) varies from 400 to 20 Hz. A piezoelectric load cell measures the dynamic force delivered by the shaker. This force transducer is attached to the stinger end facing the bearing housing. An eddy current sensor (ECS) records the resulting bearing dynamic displacement. The displacement transducer is installed opposite to the point of external load application. In addition, the FB acceleration is measured by one piezoelectric accelerometer located at the same position as the ECS.

Table 1 Nominal dimensions and material parameters of test bump foil bearing

Dimensions and parameters		Values	
Inner diameter, mm [in.]	D	38.17	[1.5048]
Outer diameter, mm [in.]	D_o	50.80	[2.00]
Axial length, mm [in.]	L	38.10	[1.50]
Clearance,[a] mm [in.]	C_{nom}	0.0355	[0.0014]
Number of bumps	N_B	25 (circumference)	
Bump pitch, mm [in.]	P	4.572	[0.18]
Bump length, mm [in.]	$2l_o$	4.064	[0.16]
Foil thickness, mm [in.]	t_f	0.102	[0.004]
Bump height, mm [in.]	h	0.381	[0.015]
Foil Poisson's ratio	ν	0.29	
Modulus of elasticity, GPa [Ksi]	E	213.7	[31,000]
Bearing mass, kg (lb)	M_B	0.40	[0.88]

[a]Nominal clearance for a 38.1 m [1.5 in.] diameter journal

Table 2 Test conditions for shaker experiments

Test conditions	Test values
Frequency range [Hz]	400–20
Frequency step [Hz]	20
Dynamic load amplitudes [N]	4, 8, 12, 16, and 20
Test temperatures [°C]	25° (Room), 50° and 75°
Temperature gradient [°C/cm]	~0.4

A soldering gun, press fitted into a concentric hole in the shaft end, heats the shaft and raises its temperature. In general, 15 W of power supplied to the soldering gun produces a temperature of 50°C at the shaft surface, while 30 W renders temperatures near 75°C.[1] Two type T thermocouples measure the shaft surface temperature at two sides of the test bearing. A small steady temperature gradient shows the shaft surface has a nearly uniform temperature, see Table 2. Surface temperature is also recorded at the soldering gun and foil bearing outer ring in order to calculate the actual shaft and foil bearing thermal expansions, see Appendix A for details.

In the tests, the displacement and acceleration signals pass through a signal conditioner into an eight-channel data acquisition (DAQ) board. The signal conditioner biases the dc offset level from the eddy current sensor and modifies the signal gains. The instrumentation also includes oscilloscopes, monitoring the measured variables, and a digital signal analyzer, serving also as a storage device.

Experimental Procedure

Once a steady-state temperature on the shaft surface is achieved, the electromagnetic shaker forces a dynamic load into the test FB. For each test condition, see Table 2, four signals are recorded, i.e., frequency generator signal (used as the trigger level), dynamic load, displacement, and acceleration. The acceleration transducer is only utilized for experiments at room temperature due to attachment looseness at the higher temperatures.

[1]The authors recognize that the temperature ranges tested are well below those expected in actual applications for gas turbines.

Table 3 Shaft and bearing temperatures and predicted thermal expansion and preload, *r*

Test parameters	Input power		
	0 W	15 W	30 W
Measured soldering gun surface temperature, T_1, °C	28.2	76.6	135.0
Measured shaft surface temperature 1, T_2, °C	28.2	54.4	76.9
Measured shaft surface temperature 2, T_2, °C	28.2	52.6	74.5
Estimated FB ring inner surface temperature, T_3, °C	⋯	37.2	40.0
Measured FB outer surface temperature, T_4, °C	28.2	32.2	36.4
Measured radial shaft expansion, δ_1, μm	⋯	3.17	6.25
Predicted radial shaft expansion, μm	⋯	3.92	6.85
Measured radial (outer) FB expansion, δ_3, μm	⋯	0.63	1.27
Predicted FB expansion (inwards-outwards), δ_B, μm	⋯	0.90	1.44
Calculated FB expansion (inwards), $\delta_2=\delta_B-\delta_3$, μm	⋯	0.27	0.17
Estimated FB radial preload, $r=\delta_1+\delta_2$, [μm]	⋯	3.44	6.42
FB preload in percentage of clearance, r/C_{nom} [%]	0	~9	~18

The five load amplitudes are referred herein as load levels 1 through 5; load level 1 is the one with lowest amplitude. In recording the test data, "steady-state" conditions need be ensured to reduce the influence of initial conditions, unsteady thermal gradients, etc.

The foil and journal expand as the test temperature increases, thus creating a mechanical preload (r) that reduces the nominal (cold) clearance in the foil bearing. A simple analysis for thermally induced expansions based on measurements of the shaft and bearing surface temperatures renders a good estimate for the preload (r). Appendix A details the thermal expansion analysis, and Table 3 shows the temperature measurements and calculated preload (r).

Model of Test Foil Bearing

The FB is modeled as a single degree of freedom (SDOF) lumped mass system excited by a dynamic load, $F(t)$, provided by the shaker, i.e. $M\ddot{x}=F(t)-F_B$. The bearing reaction, F_B, force comprises an elastic restoring force associated with its structural stiffness and a (dissipative energy) force due to dry friction between the contact surfaces, $F_B=Kx+F_{\text{dry}}\,\text{sgn}(\dot{x})$.

In the analysis of the test data, an equivalent viscous damping coefficient *or* a friction force are estimated from the energy dissipated over one period of FB motion. The FB structure stiffness, on the other hand, is identified from a frequency domain analysis of the bearing mechanical impedance.

The work performed by the external driving force over a period of FB motion is

$$W=\oint F(t)\dot{x}(t)dt=-\pi F_o X\sin(\theta) \tag{1}$$

where F_o is the magnitude of the dynamic applied load, X is the amplitude of the FB displacement, and θ is the phase angle lag between the response (x) and the force excitation (F).

Over one period of motion, the energy dissipated from viscous damping forces (E_V) and the energy dissipated by a dry friction (E_C) mechanism are

$$E_V=\oint C_{eq}\dot{x}\cdot dx \tag{2}$$

and

$$E_C=\oint F_{\text{dry}}\,\text{sgn}(\dot{x})\cdot dx \tag{3}$$

respectively. Above, C_{eq} denotes an equivalent viscous damping coefficient and F_{dry} is the dry friction force.

Each distinct energy dissipation mechanism must equal the work exerted by the driving force. Thus, the viscous damping coefficient and dry friction force are [13]

$$C_{eq}=\frac{W}{\oint[\dot{x}(t)]^2dt}=\frac{-F_o\sin\theta}{\omega X} \tag{4}$$

and

$$F_{\text{dry}}=\frac{W}{\oint\dot{x}(t)\text{sgn}(\dot{x})dt}=\frac{-F_o\pi\sin\theta}{4} \tag{5}$$

where ω is the excitation frequency. Note that Eqs. (4) and (5) follow from $x(t)=Xe^{i(\omega t+\theta)}$. The experimental results do show that the FB motion is mainly synchronous with the excitation frequency.

A crude estimation of the dry friction coefficient follows from the ratio between the frictional force and the amplitude of dynamic load, i.e.

$$\mu=\frac{F_{\text{dry}}}{F_o}=-\frac{\pi}{4}\sin\theta\leqslant\frac{\pi}{4} \tag{6}$$

The angle (θ) denotes the lag between the FB motion response and the force excitation. In the tests, for frequencies near the system natural frequency, the phase angle approaches to 90 deg, thus leading to an unrealistic dry friction coefficient bounded by $\pi/4$. This shortage in the assumed physical model is apparent in the test results, as shown later.

The identification of the FB structural stiffness is conducted in the frequency domain. For single frequency motions, the SDOF complex mechanical impedance is

$$(K-M\cdot\omega^2)+\mathbf{i}C_{eq}\omega=\frac{\mathbf{F}_{(\omega)}}{\mathbf{X}_{(\omega)}} \tag{7}$$

where K and M are the structural stiffness and system mass. $\mathbf{F}_{(\boldsymbol{\omega})}$ and $\mathbf{X}_{(\boldsymbol{\omega})}$ are the force and FB displacement as functions of frequency. The FB dynamic structural stiffness ($K-M\omega^2$) follows from the real part of the mechanical impedance, i.e., $\text{Re}(\mathbf{F}/\mathbf{X})$. The imaginary part of the mechanical impedance leads to the equivalent viscous damping coefficient, C_{eq}, identical in magnitude to the one derived from Eq. (4).

The energy dissipation mechanism in bump foil bearings may also be characterized as structural-type damping. In this case, the complex structural stiffness is $K(1+\mathbf{i}\gamma)$, where γ, the structural loss factor, is easily estimated as

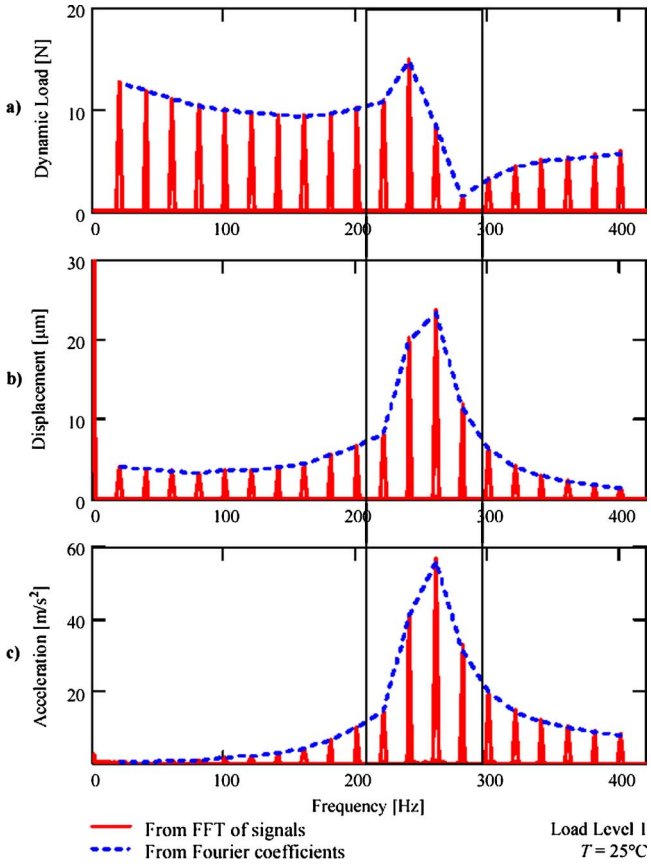

Fig. 3 Foil bearing single-frequency force excitation and dynamic responses from identified Fourier coefficients and from fast Fourier transfer of dynamic time signals. (*a*) Dynamic load amplitude, (*b*) foil bearing displacement, and (*c*) foil bearing acceleration. Load level 1 (nominal 4 N and 400 Hz), and *T* =25°C.

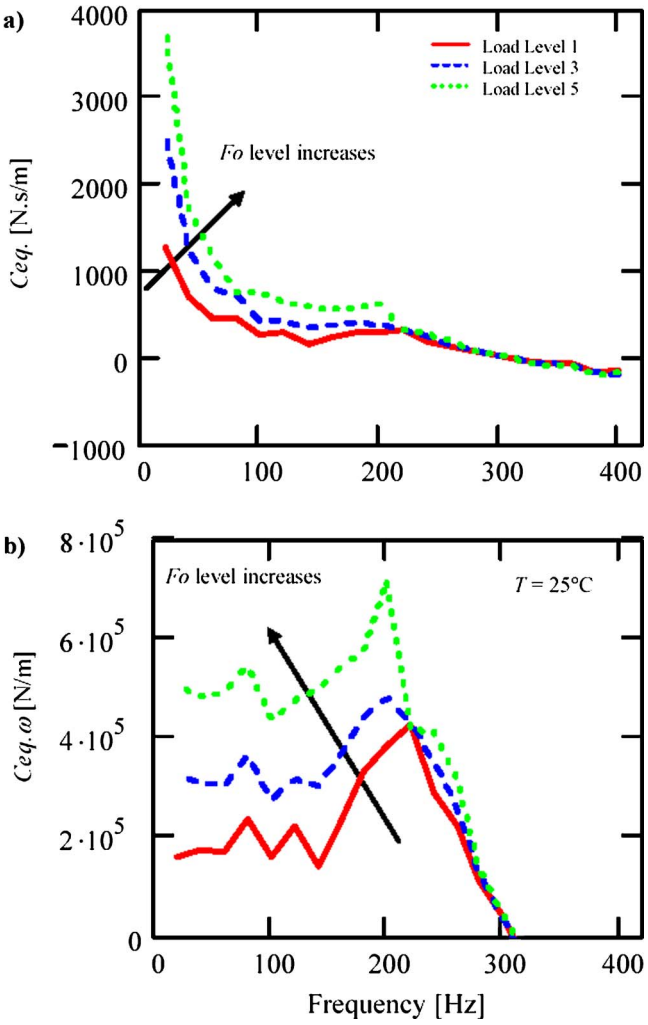

Fig. 4 Identified FB equivalent viscous damping coefficient versus frequency for three load levels. Test at room temperature=25°C. (*a*) C_{eq}, (*b*) C_{eq}.

$$\gamma = \frac{C_{eq}\omega}{K} \tag{8}$$

Experimental Results and Discussion

Figure 3 presents the test dynamic load and FB displacement and acceleration for excitation frequencies ranging from 20 to 400 Hz. The results shown correspond to the fundamental Fast Fourier coefficients of the time signals for load level 1 (nominal 4 N at 400 Hz). Similar results are obtained for other load levels in terms of displacement, acceleration, and load behavior throughout the selected frequency range. For the range of frequencies tested, 0–200 Hz, the foil bearing and its sleeve are *rigid* as verified experimentally.

The amplitude of applied load could not be held constant for tests at a fixed frequency, since the experimental results evidence a vibration resonance at approximately 260 Hz. Note that around the system natural frequency, small dynamic load amplitudes produce quite large FB displacements; thus demonstrating the FB lacks *viscous* damping when excited at its natural frequency. This phenomenon is typical of mechanical systems with dry-friction dissipation mechanism. It is important to note that in the vicinity of the natural frequency the analysis will identify inaccurately the dry-friction coefficient since the phase angle (θ) is ~90 deg.

The equivalent *viscous* damping coefficient or the dry friction force characterizing the FB are determined from the energy dissipation=work approach. Figure 4 shows the estimated viscous damping C_{eq} for three load levels and at room temperature. Figure 4(*a*) demonstrates C_{eq} has a strong dependency on frequency, in particular at low frequencies where dry friction effects are most significant. Figure 4(*b*) depicts the product ($C_{eq.}\omega=\gamma k$), i.e., imaginary part of mechanical impedance, which demonstrates a clear bounded region at low frequencies where Coulomb or dry friction forces are most effective.

As expected, the test results show that increasing the load magnitude leads to larger foil bearing displacement amplitudes. In a SDOF linear mechanical system, the estimated viscous damping coefficient should be constant, even when varying the dynamic load amplitude.[2] Presently in the test FB, however, an increase in the amplitude of dynamic load leads to significant changes in the identified viscous damping at excitation frequencies below the system natural frequency, see Fig. 4. Most importantly, at the natural frequency and above, the viscous damping in the FB is quite small (even negative). This feature is certainly undesirable for forced excitations driving the system into resonance.

Figure 5 shows that the test temperature, inducing a small bearing preload due to the shaft and bearing thermal expansions, has

[2]In a linear mechanical system, an increase in the excitation force, *nF*, leads to a proportional increase in the system response, *nX*, where *n* is a constant. The system is characterized by material parameters not determined by the motion or system state.

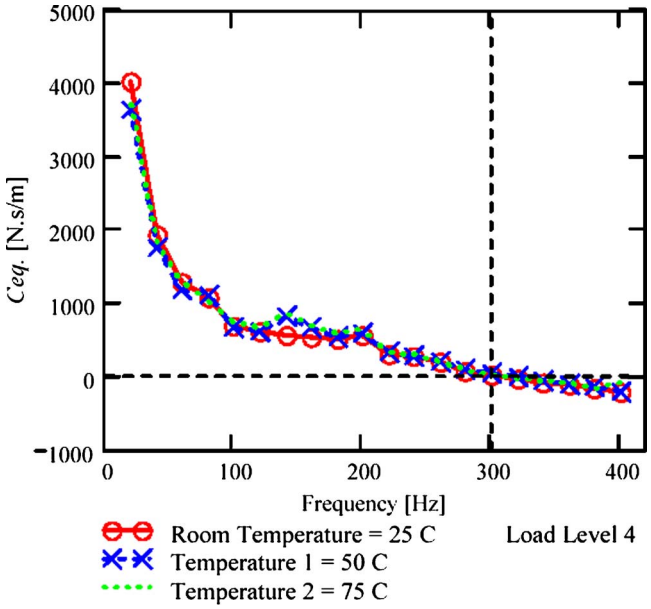

Fig. 5 Equivalent viscous damping coefficient versus frequency for three test temperatures. Load level 4 (nominal 12 N at 400 Hz).

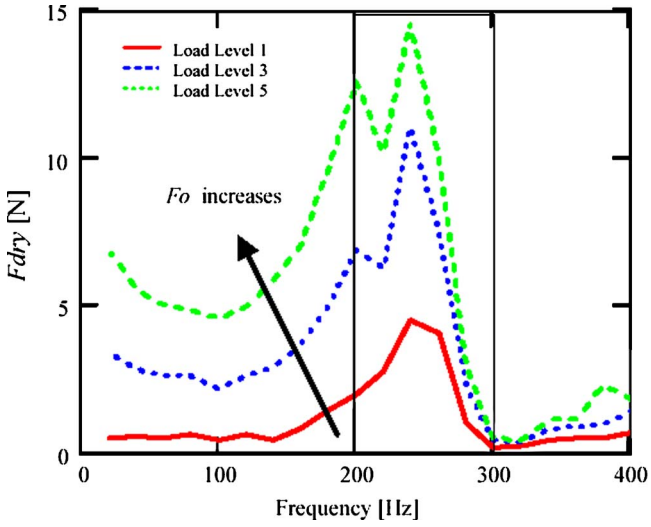

Fig. 7 Dynamic load level 3 (nominal 12 N at 400 Hz) and estimated dry-friction force versus frequency for test at T=25°C

an indiscernible effect on the estimated viscous damping coefficients for load level 4 (nominal 12 N at 400 Hz). Similar results are obtained for other load levels.

Figure 6 shows the identified dry friction force versus frequency for the experiments conducted at room temperature. F_{dry} increases with the amplitude of dynamic load in the frequency range from 0 to ~200 Hz. In this frequency range, the measurements show a nearly invariant phase angle (θ), further evidencing F_{dry} is uniform, as seen in Fig. 7, for tests at room temperature and load level 3.

For force excitations around the system natural frequency, however, the identified friction force augments at a steep rate. At the natural frequency the motion phase angle (θ) is −90 deg, thus rendering the peculiar and unrealistic value $F_{\text{dry}}=F_o\pi/4$. This shortcoming is an intrinsic feature of the physical model that equates work to dissipated energy over a full period of motion.

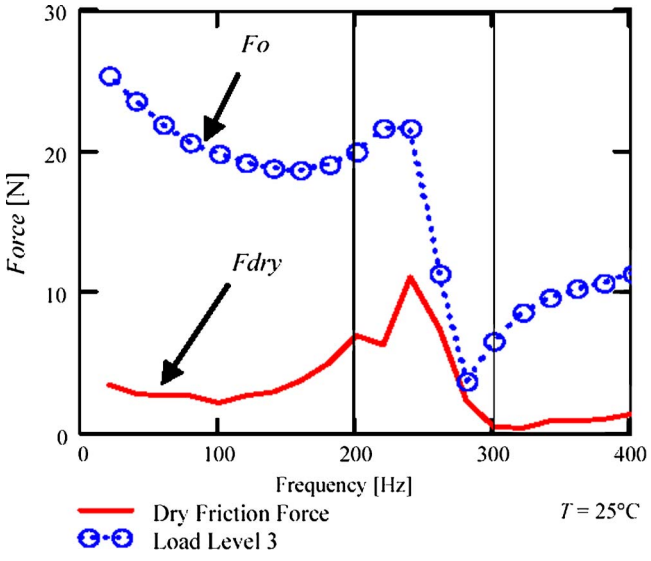

Fig. 6 Estimated dry-friction force versus frequency for three load levels. Tests at room temperature=25°C.

Figure 8 presents the derived dry friction coefficient, $\mu=F_{\text{dry}}/F_o$ versus frequency for measurements at room temperature and three increasing load levels. The unusually large values of μ, bounded by $\pi/4$, at frequencies near resonance are not to be considered. Figure 8(b) shows the estimated dry friction coefficient over the frequency range of interest, i.e., below the natural frequency. Test results of dry friction coefficient (μ) range from 0.05 to 0.2 for increasing amplitudes of dynamic load. When increasing the test temperature, the dry friction coefficient shows no significant variations in the frequency range 0–150 Hz.

The frequency domain analysis of the test data (force and displacement) determines the complex mechanical impedance for identification of parameters in a linear system. In all tests, the real part of the mechanical impedance reproduces exactly the relationship $\text{Re}(\mathbf{F}/\mathbf{X})=K-M\ \omega^2$, as seen in Fig. 9 for three load levels and tests at room temperature. A simple curve fit follows to identify the FB structural stiffness (K) and system mass (M). Table 4 lists the identified parameters for increasing loads and three temperatures. The goodness of the curve fit, i.e., correlation coefficient (r^2), is at least 97.3% in all test cases.

The identified mass (M) is ~1 kg, larger than the actual test bearing mass (0.4 kg). At the natural frequency, ~260 Hz, the two columns holding the shaft and test bearing also vibrate, and thus the identification procedure delivers a system modal mass that accounts for the support motions.

Figure 10 shows the identified structural stiffness versus the amplitude of dynamic load (at 20 Hz) for the three test temperatures. The FB structural stiffness (K) decreases as the amplitude of load increases. The rate of decrement appears similar, irrespective of the test temperature. Heshmat and Ku [10] and Ku [11] present similar findings.

The structure "hardening" effect as the load amplitude decreases is due to dry friction effects that are most apparent for small amplitude loads where stick-slip between the sliding surfaces (bumps and bearing housing) most likely occurs.

Figure 10 also includes the predicted static stiffness for the test FB based on an analysis given in [7].

As the temperature increases, the FB structure stiffness (K) does decrease though not significantly (maximum 11% drop from values at room temperature). Thus, the bearing preloads induced by shaft thermal expansion have a small effect on the system stiffness. The FB structural stiffness ranges from 3.25 MN/m (~19 lb/mil) to 2.30 MN/m (~13 lb/mil) as the amplitude of

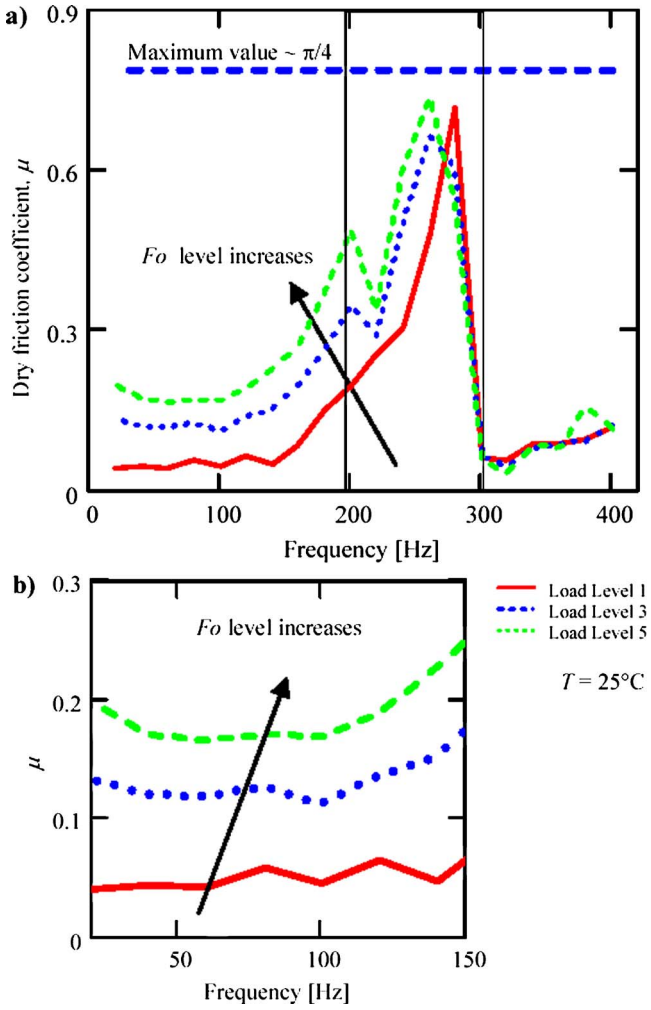

Fig. 8 Estimated fry friction coefficient versus frequency for three load levels. Tests at room temperature ~25°C. (*a*) Over entire frequency range, (*b*) for constant phase angle (θ), i.e., f <150 Hz.

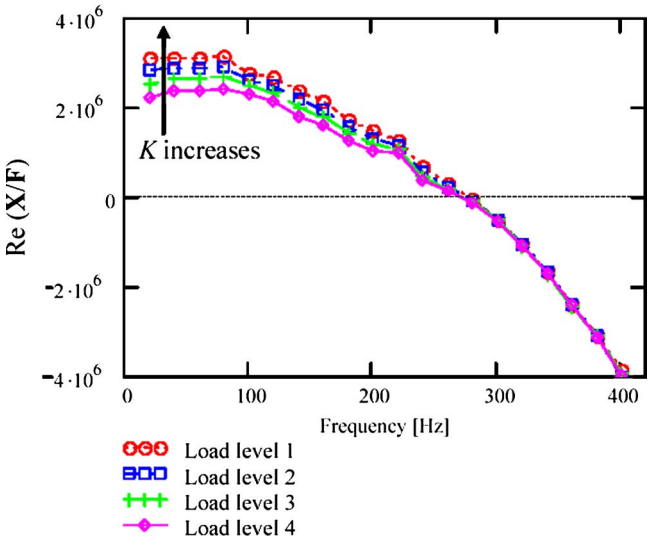

Fig. 9 Real part of test system impedance versus frequency for three load levels and T=25°C

Table 4 FB structure stiffness and system mass derived from frequency domain analysis

Temperature [°C]	F_o at 20 Hz [N]	Structure stiffness, K [MN/m]	System mass, M [kg]
20	13	3.25	1.10
	19	3.04	1.06
	25	2.83	1.02
	32	2.60	0.97
	35	2.54	0.97
50	11	3.16	1.07
	17	2.97	1.04
	22	2.75	0.99
	28	2.53	0.95
	31	2.48	0.95
75	11	3.09	1.05
	17	2.88	1.01
	22	2.60	0.96
	27	2.34	0.91
	30	2.28	0.91

load increases. In addition, the recorded maximum FB displacements are about 18 μm (~0.7 mil) at the lowest test frequency, ~20 Hz. Thus, the presently identified stiffnesses, estimated from dynamic load tests, can be correlated with FB static stiffnesses measured earlier, see [7]. Figure 10(*b*) depicts predictions of FB structure stiffness as a function of the static load and considering various dry friction coefficients. The box in the figure denotes the range of loads applied in the dynamic force tests. Predictions based on μ ranging from 0.05 to 0.35 agree best with the presently identified test stiffness (K), as depicted in Fig. 10(*a*).

In addition, the analysis of the test data also determines the structural damping loss factor, γ, shown in Fig. 11 for three load levels and at room temperature. The test γ increases with the amplitude of dynamic load; and importantly enough, it is approximately constant for excitation frequencies below 150 Hz. The identified loss factor for the test FB ranges from 0.06 to 0.20. Ku [11] reports γ=0.2–0.6 for foil-bump strips attached at one end and free at the other.

Table 5 lists a summary of the average dry friction coefficient (μ) and loss factor (γ) in the frequency range 20–140 Hz. The standard deviations noted for each parameter are small, thus indicating the dry-friction coefficient or the structural loss factor is indeed independent of frequency.

Appendix B details the general uncertainty analysis conducted on each identified parameter. The precision uncertainty, determined as a function of excitation frequency, is well below 10% for most test conditions.

Conclusions

The paper presents experimentally identified structural stiffness and dry-friction coefficient in a bump-type foil bearing. An electromagnetic shaker excites the test foil bearing, installed on a rigid non-rotating shaft, under various conditions of dynamic load, excitation frequency, and temperature.

Test results show that the excitation frequency significantly affects the FB equivalent viscous damping coefficient. At low frequencies (<50 Hz), the viscous damping reaches peak magnitudes of ~4 kN s/m (23 lb s/in.); while for large excitation frequencies (>100 Hz), damping decreases by two orders of magnitude. For excitation frequencies below ~200 Hz, the viscous damping coefficient increases as the load amplitude increases, indicating a non-linear behavior with the FB amplitude of motion. The limited range of test temperatures does not affect the identified damping coefficient.

In the frequency range of reliable parameter identification, i.e., from 0 to 150 Hz, the dry friction coefficient for the test foil bearing is nearly constant, albeit increasing in magnitude as the am-

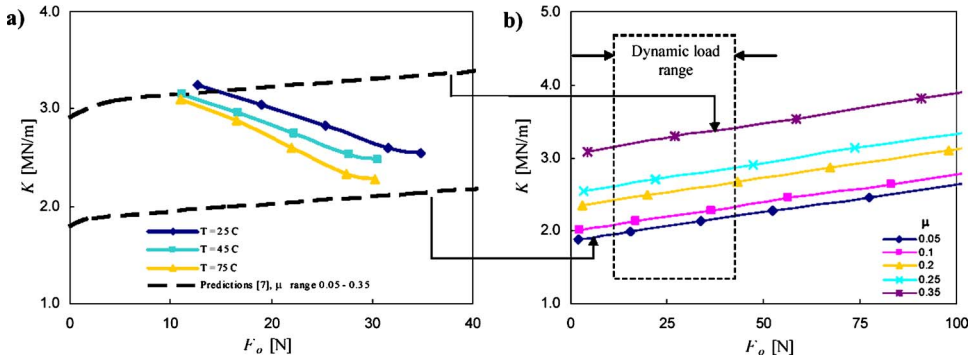

Fig. 10 (*a*) **Identified structural stiffness versus amplitude of dynamic load at 20 Hz. Three test temperatures:** (*b*) **Predictions of FB static load stiffness for various friction coefficients (μ=0.05–0.35) and preload of 6.4 μm.**

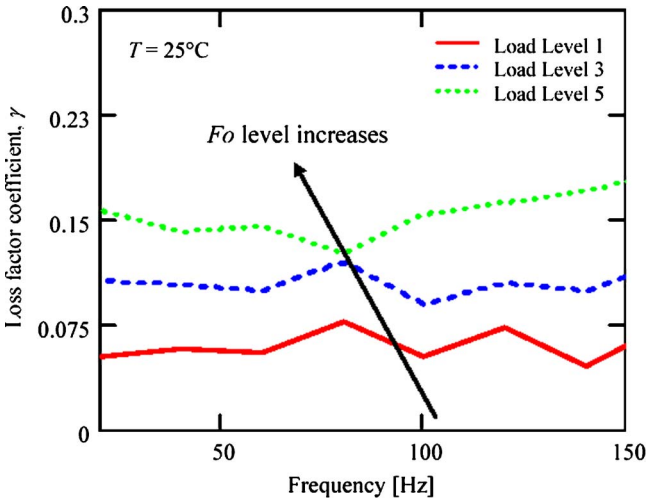

Fig. 11 Identified structural damping loss factor versus frequency for three load levels and at T=25°C

plitude of dynamic load increases. In general, the dry friction coefficient ranges from 0.05 to 0.2 for load amplitudes from 4 to 20 N. A structural damping loss factor is also derived from the test results. This loss factor, ranging from 0.05 to 0.23 as the load amplitude increases, is also quite uniform for frequencies below 150 Hz.

The identified FB structure stiffness is not frequency dependent but, due to dry friction effects, it evidences a hardening effect as the amplitude of dynamic load decreases. The identified structural stiffnesses are in agreement with predictions of static stiffness when accounting for a bearing preload of 6.4 μm.

Most importantly, the dynamic load experiments show excitation of a system natural frequency at ~260 Hz. The amplitudes of motion at this frequency are rather large even though the magnitude of the dynamic load is at its lowest. Thus, the experiments show a true resonance of the test system with the FB providing little damping at this frequency. This behavior is typical in systems characterized by dry-friction effects.

Future Work

Presently, a test rig comprised of a lightweight rotor supported on air foil bearings is in operation. Imbalance response experiments are being performed to assess the complete set of rotordynamic force coefficients for the test foil bearings. Future publications will continue to advance knowledge gained with this novel bearing technology.

Table 5 Frequency averaged dry friction and loss factor coefficients for test FB. Frequency range 20–140 Hz.

Temperature [°C]	F_o at 20 Hz [N]	μ	Standard deviation, μ	γ	Standard deviation, γ
20	12.7	**0.05**	0.008	**0.06**	0.009
	19.1	**0.09**	0.009	**0.11**	0.008
	25.4	**0.14**	0.013	**0.15**	0.009
	31.6	**0.18**	0.017	**0.19**	0.012
	34.8	**0.20**	0.021	**0.19**	0.016
50	11.1	**0.05**	0.017	**0.06**	0.014
	16.7	**0.09**	0.010	**0.10**	0.007
	22.2	**0.12**	0.013	**0.14**	0.009
	27.7	**0.17**	0.017	**0.18**	0.017
	30.5	**0.18**	0.020	**0.17**	0.013
75	11.1	**0.05**	0.009	**0.05**	0.007
	16.6	**0.09**	0.008	**0.10**	0.008
	22.0	**0.14**	0.010	**0.16**	0.009
	27.5	**0.19**	0.014	**0.21**	0.009
	30.3	**0.20**	0.020	**0.20**	0.019

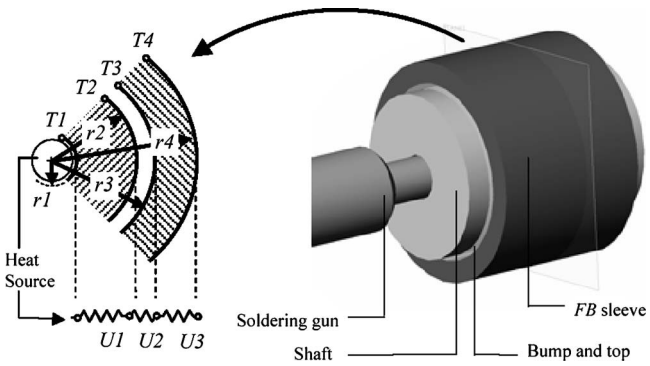

Fig. 12 Limped parameter thermal model for shaft and foil bearing system

Acknowledgment

This material is based upon work supported by the National Science Foundation under Grant No. 0322925. The authors also acknowledge the support of the TAMU Turbomachinery Research Consortium (TRC). Thanks to Foster Miller Technologies for providing the test foil bearings.

Nomenclature

C_{eq} = FB equivalent viscous damping (N s/m)
C_{nom} = FB nominal clearance (mm)
D = FB inner diameter (mm)
D_o = FB outer diameter, including sleeve (mm)
E = modulus of elasticity of foil material (GPa)
E_C = energy dissipated from Coulomb damping (J)
E_V = energy dissipated from viscous damping (J)
f = excitation frequency (Hz)
F_{dry} = estimated dry friction force (N)
F_o = amplitude of dynamic load (N)
F_B = FB reaction force (N)
h = foil bump height (mm)
i = $\sqrt{-1}$, imaginary unit
K = dynamic structural stiffness (N/m)
k_B = FB thermal conductivity (W/m°K)
k_S = shaft thermal conductivity (W/m°K)
L = FB axial length (mm)
l_o = half length of one bump (mm)
M = test system mass (kg)
M_B = FB mass (kg)
N_B = number of bumps
p = bump pitch (mm)
r = preload (μm)
t = time (s)
t_f = foil thickness (mm)
T_1, T_2 = soldering gun and shaft surface temperatures (°C)
T_3, T_4 = bearing inner and outer surface temperatures (°C)
t_f = foil thickness (mm)
W = work by external dynamic load (J)
$x(t)$ = FB displacement (m)
X = FB displacement amplitude (m)
δ_1, δ_2 = shaft radial and FB inwards thermal expansion (μm)
δ_3, δ_B = FB outwards and total ($\delta_2+\delta_3$) thermal expansion (μm)
γ = structural damping loss factor
μ = dry friction coefficient
θ = phase angle (rad)
υ = Poisson's ratio
ω = excitation frequency (rad/s)

Appendix A: Thermal Expansion Model

Figure 12 shows a schematic view of the lumped parameter model for the test shaft and foil bearing. The model assumes heat flows along the radial direction only, i.e., no heat conduction along the axial direction. K-type thermocouples measure the surface temperature at the soldering gun (T_1), shaft surface (T_2), and bearing outer surface (T_4). The temperature at the inner wall (T_3) of the foil bearing is estimated from a thermal conductivity analysis assuming radial heat flow only. While performing the experiments, the shaft and foil bearing outer surface expansions are recorded with eddy current sensors.

The thermal resistance of the test shaft and the bearing shell, U_1 and U_3, respectively, depend on the material thermal conductivity and their physical dimensions, i.e., $U_{1,3} \sim 0.06$, 0.08°C/W. At steady state thermal conditions, the heat flow rate q, i.e., 15 or 30 W, from the shaft into the bearing is

$$q = \frac{T_2 - T_4}{U_2 + U_3} \tag{A1}$$

The equivalent thermal resistance coefficient for the top and bump foils, U_2, is then obtained for a given input power and the corresponding FB outer surface temperature, T_4. The procedure leads to $U_2 \sim 1.19$°C/W. Estimation for the temperature at the foil surface (T_3) follows from

$$q = \frac{T_2 - T_3}{U_2} \rightarrow T_3 = T_2 - q \cdot U_2 \tag{A2}$$

The derived shaft and bearing thermal expansions are given by the well-known formula

$$\delta = \frac{D}{2}\bar{\alpha}\Delta T \tag{A3}$$

where $\bar{\alpha}_l$ is the material thermal expansion coefficient, ΔT is a temperature difference, and D is the nominal diameter at the reference temperature (room condition). The thermal expansion coefficients for AISI 4140 steel (shaft) and stainless steel (sleeve) are 10.4 μm/m°C and 12 μm/m°C, respectively.

Table 3 in the main text lists the measured temperatures and shaft surface expansions, and predictions for the bearing inward expansion. The bearing preload (r) induced by thermal expansion of the shaft and bearing is

$$r = \delta_1 + \delta_2 \tag{A4}$$

Preloads equal to 9% and 18% of the nominal FB clearance are calculated. The thermally induced preloads should have an affect on the FB stiffness and dry friction coefficient.

Appendix B: Uncertainty Analysis

An uncertainty analysis applied to the experimental results determines how the uncertainties in the individual measurements (force and displacements) propagate into the identified parameters, namely equivalent viscous damping, dry friction forces, and structural stiffness, among others.

In general, the precision uncertainty (U_r) of an experimental result (r), a function of J variables X_i, is given by [14]:

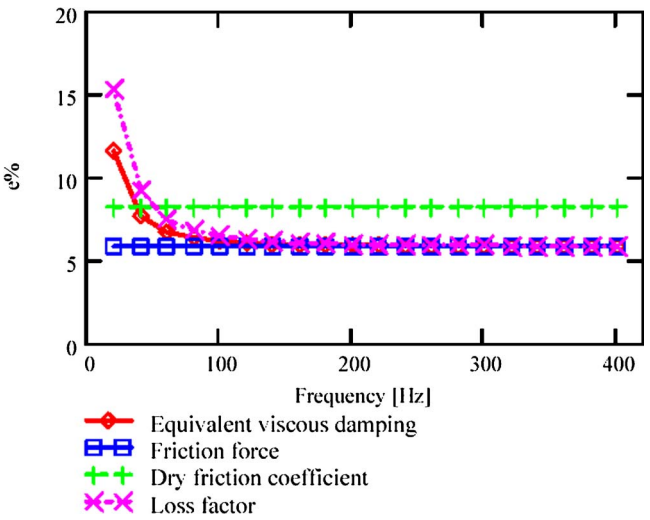

Fig. 13 Percent precision uncertainty for identified bearing parameters versus frequency. Load level 4, room temperature tests.

$$U_r = \left\{ \left[\left(\frac{\partial r}{\partial X_1} \right) \cdot U_{X_1} \right]^2 + \left[\left(\frac{\partial r}{\partial X_2} \right) \cdot U_{X_2} \right]^2 + \ldots + \left[\left(\frac{\partial r}{\partial X_j} \right) \cdot U_{X_i} \right]^2 \right\}^{1/2} \quad \text{(B1)}$$

where U_{X_i} are the uncertainties in the measured variables X_i.

The resulting precision uncertainty expressions for each identified parameter are omitted for brevity. Figure 13 shows the resulting uncertainty in percentile form, i.e.

$$\varepsilon\,\% = \frac{U_r}{r} \cdot 100 \quad \text{(B2)}$$

versus frequency. The results shown correspond to load level 4 and room temperature. Similar uncertainty values were found for other load levels.

For most test frequencies, the identified bearing structural parameters are within 10% of uncertainty. The precision uncertainty of the sensors is very small ($\sim$1% or less of recorded signal), and therefore, the derived uncertainty for the estimated parameters is also small ($<$10%, typically). The largest uncertainty occurs at low frequencies ($\sim$20 Hz) where the uncertainty in frequency recording is ±2 Hz.

References

[1] Heshmat, H., Walowit, J., and Pinkus, O., 1983, "Analysis of Gas-Lubricated Compliant Journal Bearings," ASME J. Lubr. Technol., **105**(4), pp. 647–655.

[2] Peng, J.-P, and Carpino, M., 1993, "Calculation of Stiffness and Damping Coefficient for Elastically Supported Gas Foil Bearings," ASME J. Tribol., **115**(1), pp. 20–27.

[3] Dellacorte, C., and Valco, M., 2000, "Load Capacity Estimation of Foil Air Bearings for Oil-Free Turbomachinery Applications," STLE Tribol. Trans., **43**(4), pp. 795–801.

[4] Ku, C.-P, and Heshmat, H., 1992, "Compliant Foil Bearing Structural Stiffness Analysis Part I: Theoretical Model—Including Strip and Variable Bump Foil Geometry," ASME J. Tribol., **114**(2), pp. 394–400.

[5] Ku, C.-P, and Heshmat, H., 1993, "Compliant Foil Bearing Structural Stiffness Analysis Part II: Experimental Investigation," ASME J. Tribol., **113**(3), pp. 364–369.

[6] Iordanoff, I., 1999, "Analysis of an Aerodynamic Compliant Foil Thrust Bearing: Method for a Rapid Design," ASME J. Tribol., **121**, pp. 816–822.

[7] Rubio, D., and San Andrés, L., 2004, "Bump-Type Foil Bearing Structural Stiffness: Experiments and Predictions," ASME Paper No. GT 2004-53611.

[8] Ku, C.-P, and Heshmat, H., 1994, "Structural Stiffness and Coulomb Damping in Compliant Foil Journal Bearing: Theoretical Considerations," STLE Tribol. Trans., **37**(3), pp. 525–533.

[9] Ku, C.-P, and Heshmat, H., 1994, "Structural Stiffness and Coulomb Damping in Compliant Foil Journal Bearing: Parametric Studies," STLE Tribol. Trans., **37**(3), pp. 455–462.

[10] Heshmat, H., and Ku, C.-P., 1994, "Structural Damping of Self-Acting Compliant Foil Journal Bearings," ASME J. Tribol., **116**(1), pp. 76–82.

[11] Ku, C-P., 1993, "An Experimental and Theoretical Study of the Dynamic Structural Stiffness in Compliant Foil Journal Bearings," *Vibration of Mechanical Systems and the History of Mechanical Design*, ASME, New York, DE-Vol. 63, pp. 83–88.

[12] Salehi, M., Heshmat, H., and Walton, J., 2003, "On the Frictional Damping Characterization of Compliant Bump Foils" ASME J. Tribol., **125**, pp. 804–813.

[13] Ginsberg, J., *Mechanical and Structural Vibrations*, Wiley, New York, pp. 137–139.

[14] Coleman, H., and Steele, W., 1985, *Experimentation and Uncertainty Analysis for Engineers*, Wiley-Interscience, New York, pp. 33–35.

Experimental Contribution to High-Precision Characterization of Magnetic Forces in Active Magnetic Bearings

Klaus Kjølhede
e-mail: kk@mek.dtu.dk

Ilmar F. Santos
e-mail: ifs@mek.dtu.dk

Department of Mechanical Engineering,
Section of Solid Mechanics,
Technical University of Denmark,
DK-2800, Kgs.
Lyngby, Denmark

Parameter identification procedures and model validation are major steps toward intelligent machines supported by active magnetic bearings (AMB). The ability of measuring the electromagnetic bearing forces, or deriving them from measuring the magnetic flux, strongly contributes to the model validation and leads to novel approaches in identifying crucial rotor parameters. This is the main focus of this paper, where an intelligent AMB is being developed with the aim of aiding the accurate identification of damping and stiffness coefficients of active lubricated journal bearings. The main contribution of the work is the characterization of magnetic forces by using two different experimental approaches. Such approaches are investigated and described in detail. A special test rig is designed where the four pole AMB is able to generate forces up to 1900 N. *The high-precision characterization of the magnetic forces is conducted using different experimental tests: (i) by using hall sensors mounted directly on the poles (precise measurements of the magnetic flux) and by an auxiliary system, composed of strain gages and flexible beams attached to the rotor, (ii) by measuring the input current and bearing gap variations, monitoring the bearing input signals. Advantages and drawbacks of the different methodologies are critically discussed. The linearity ranges are experimentally determined and the characterization of magnetic forces with a high accuracy of* $<1\%$ *is achieved (percent error is normalized with respect to the instantaneous measured force obtained from the strain gauges signals).* [DOI: 10.1115/1.2434345]

Introduction

One of the most attractive features of mechatronics is its ability to render products "smart." Such a smart machine makes use of the built-in active control to incorporate additional or higher performance functions. Thus, the machine may acquire higher precision and the ability for self-diagnosis and self-calibration. It can give a prognosis about its future ability to function in a satisfactory way, or about its remaining lifetime, and possibly, it can suggest a correction measure, a therapy, or even induce it itself. It is the mechatronic structure of the machine, the built-in control, its sensors, processors, actuators, and above all, its software, which enables these novel features. This is a way to design machines and products with higher performance, less maintenance costs, longer lifetime, and an enhanced customer attraction. For rotating turbomachinery, active magnetic bearings (AMB) is becoming an essential components for introducing the concept of smart machine [1,2].

An increasing number of industrial turbomachines are already built with AMB, but the potential of the AMB has not yet been fully exploited. AMBs have been used as a simple bearing and not as an integrated identification and diagnosis tool. To fully exploit AMBs, one must think of them as both an actuator and a bearing, capable not only of supporting the rotating shaft but also of exciting the shaft with predefined signals. This unique feature facilitates measurements of input-output (displacements and forces) relations and not only measurements of the system response.

The measurement of the output signals (displacements) is already integrated in AMBs as a part of the control loop to stabilize the system when AMBs are used as simple bearings, and the precision of the output measurement have reached a sufficient level when utilized eddy current probes [3].

The measurement of the input signals (forces) is still subjected to research, and different methods have been proposed [3–9]. Generally, the different force measurements in AMBs can be divided into three main groups: (i) measurement of coil currents and rotor displacements (*i-s*-method, reluctance network model) [3], (ii) direct measurement of the magnetic flux density B with Hall sensors [3], and (iii) by measuring reaction forces using load cells or fiberoptic strain gages [6,7]. The three groups have different advantages and drawbacks, but when it comes to accuracies, the Hall sensor method and the fiberoptic strain gage method have shown the most promising results [3].

In this paper, the high-precision characterization of magnetic forces in a radial AMB is investigated. The AMB has integrated Hall sensors, and the high-precision calibration is described in detail. In the characterization of magnetic forces two different approaches have been discussed earlier: (i) calibration outside the application where AMBs are intended to be used [8] and (ii) calibration directly in the application (in the field) [5,9]. Earlier calibration procedures involving Hall sensors have been conducted "in the field". Nevertheless, the calibration procedure described in this paper belongs to the first group since the AMB is mounted in a test rig specifically designed for calibration purpose.

A different Hall sensor-mounting principle is also proposed that does not require enlargement of the air gap. Earlier mounting principles are based on attaching the Hall sensor directly to the pole surface resulting in an unintended enlargement of the air gap and due to this a decrease of load capacity of the bearing. The mounting principle described in this paper involves attaching the Hall sensor in an especially postmanufactured slot at the pole surface. The principle is described in detail, and advantages and drawbacks are critically discussed. Details on how to use the

Contributed by the International Gas Turbine Institute of ASME for publication in the JOURNAL OF ENGINEERING FOR GAS TURBINES AND POWER. Manuscript received June 13, 2006; final manuscript received August 1, 2006. Review conducted by Lee Langston. Paper presented at the ASME Turbo Expo 2006: Land, Sea and Air, Barcelona, Spain, May 8–May 11, 2006. Paper No. GT2006-90658.

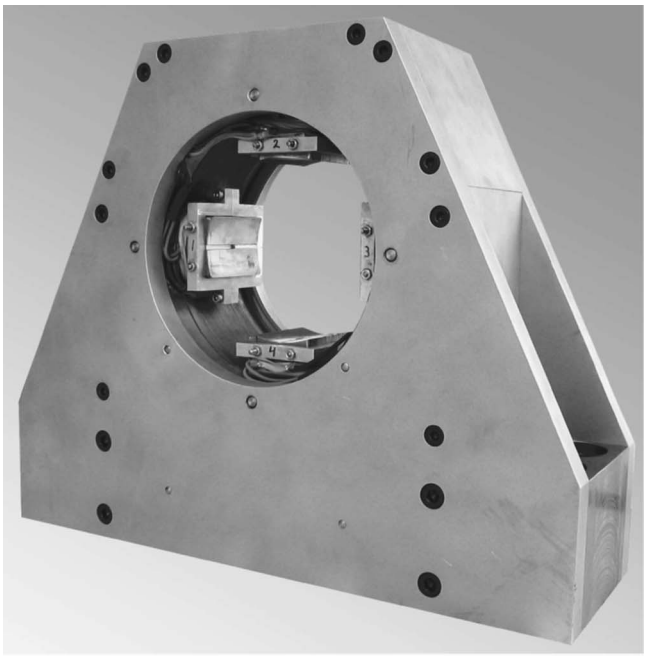

(*a*)

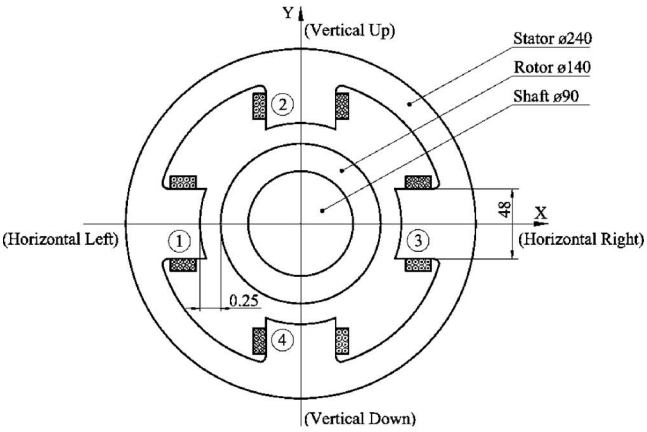

(*b*)

Fig. 1 (*a*) Active magnetic bearing (AMB) and (*b*) Schematic view; Stator, rotor, shaft and gap dimensions in millimeters

AMB to identify damping and stiffness coefficients in active lubricated bearings is elucidated in the last section of this paper.

Test Facilities and Calibration Procedures

The AMB used in the experimental setup is a four-pole radial bearing with a rotor diameter of 140 mm and a shaft diameter of 90 mm. Figure 1(*a*) shows a picture of the AMB, and Fig. 1(*b*) is a schematic view with the main dimensions and main directions. The stator and rotor are built as a stack of lamination sheets. Each sheet has a thickness of 0.5 mm, and the stator as well as rotor are composed of 140 lamination sheets. The surfaces of the lamination sheets have been oxidized to prevent any electrical contact between the sheets. The nominal radial air gap (g_0) between the rotor outer diameter and the stator legs is 0.25 mm and the AMB was designed for a load capacity of 1900 N [10].

The bearing has a flux-splitting coil configuration and is operated in differential mode [11], where one magnet is driven with the sum of bias current i_0 and control current i_x, and the other one with the difference. The operating point of the AMB is determined by the bias current, and the AMB was originally designed for a bias current of 8 A. In practice, the AMB can be operated with a bias current up to 10 A and to investigate the influence of the bias current the experiments are carried out for bias currents of 6 A, 8 A, and 10 A. The maximum bearing force is reached if for one coil the resulting current is equal to zero.

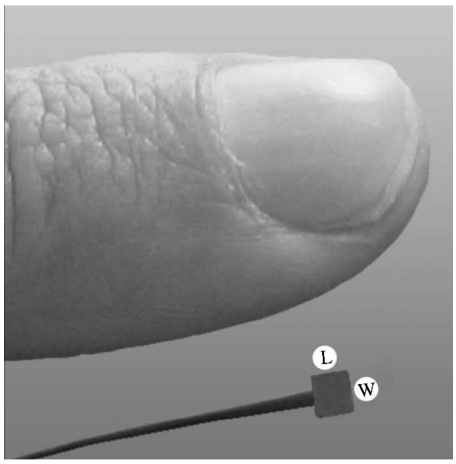

(*a*)

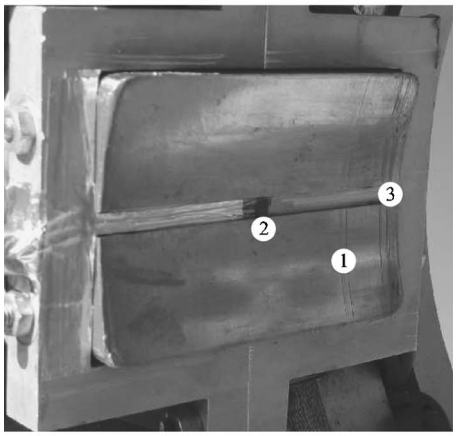

(*b*)

Fig. 2 (*a*) Hall sensor dimensions: 2×3×0.6 mm (L×W×H) and (*b*) Hall sensor mounted in slot in the pole surface: 1, Pole surface: 2, Hall sensor: 3, Slot (Dimensions: 3.3×0.7 mm (W×D))

In each of the four poles, a Hall sensor is integrated making it possible to measure the magnetic flux density B locally at the place where the sensor is mounted. The flux field is not uniform over the cross section and will be dependent on the coil current and the air gap. These local measurements of the flux densities are calibrated with an external force transducer and serves as a reference for determining the magnetic bearing forces.

The Hall sensors are mounted in an especially postmanufactured slot at the pole surface in such a way that the sensors are located just below the pole surface. Figure 2(*a*) shows the actual Hall sensor with its main geometric dimensions, and Fig. 2(*b*) shows a close-up of one pole with the Hall sensor mounted in the slot. While manufacturing the slots, no special action was taken to prevent smearing of the lamination sheets. The depth and the width of the slot are 0.7 mm and 3.3 mm, respectively, and the advantages of this special kind of mounting are as follows:

- Because the Hall sensor is located below the main pole surface, no enlargement of the air gap is necessary. Slots in the magnetic poles contribute to a reduction of the net area of the pole. Nevertheless, the area reduction is very small, once

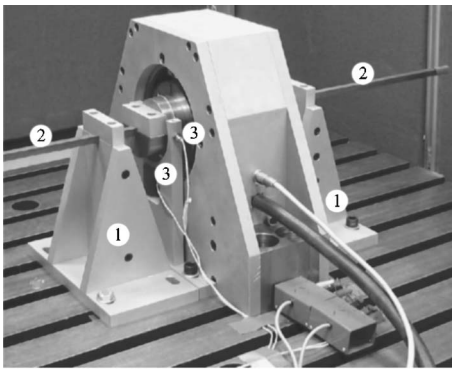

(*a*)

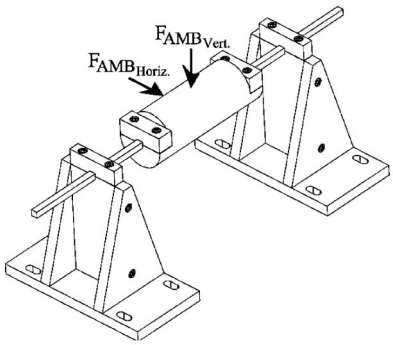

(*b*)

Fig. 3 (*a*) Experimental setup: 1, Support; 2, Flexible beam; 3, Eddy current sensor and (*b*) schematic view of the experimental setup without the magnetic bearing

such sensors can be extremely small. In Fig. 2(*b*), the relation between slot area and pole area is $A_{slot}/A_{pole}=0.07$ and the relation between slot depth and gap is $d/g_0=2.8$. Later in the paper, the load capacity as a function of A_{slot}/A_{pole} and d/g_0 is carefully investigated.

- The fragile Hall sensor is well protected in the slot. Such a design solution avoids its damage in case of contact between the pole surface and the rotor, for example, during mounting or dismounting the AMB.

The main disadvantages of such a design solution are as follows:

- The postmanufacturing of the slot is complicated and can lead to eddy current problems due to smearing of the laminations; however, if the slot is considered from the beginning of the AMB design process, its manufacturing will not be complicated. It can be achieved by laser cutting or punching of the laminated steel sections of the stator, and no smearing of the laminations will occur.
- The Hall sensor measures the magnetic flux at the slot surface and not the flux at the main pole surface. Thus, the flux measurement cannot directly be used for force calculations, and calibration procedures have to be developed.

For calibrating the Hall sensors, the AMB is mounted in a experimental setup especially designed for this purpose. Figure 3(*a*) shows the complete setup, and Fig. 3(*b*) is a schematic view. The setup is composed of the AMB with integrated Hall sensors, a shaft suspended in two flexible beams, and two rigid supports. The two beams are identical and have a square cross section with dimensions of 12×12 mm (height$\times$width). The length of the beams is also identical but can be adjusted between 20 and 200 mm. Thus, it is possible to alter the stiffness of the beams.

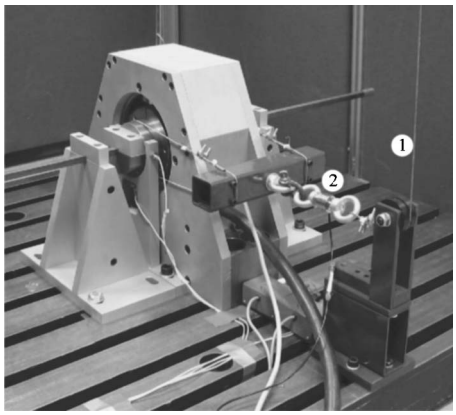

Fig. 4 Horizontal external force: 1, Wire for external force; 2, force transducer

Both beams have clamped-clamped similar boundary conditions. The rotor is centered in the air gap and the stiffness of the beams are adjusted so that when a force of ~1900 N (theoretical maximum force) is applied to the shaft, the rotor will move ~0.06 mm (24% of the air gap).

To one of the beams strain gages are attached, it allows measurement of deformations in both horizontal and vertical directions. It is assumed that all deflections are due to deformations of the beams. The assumption is reasonable because the shafts diameter is 90 mm and the square section of the beam is 12×12 mm.

A total of four eddy current sensors contactlessly measures the position of the rotor in the air gap. Two eddy current sensors measure the vertical displacement; they are mounted on each side of the AMB, making it possible also to detect nonsymmetric rotor displacement around the bearing middle plane. The other two eddy current probes measure displacement in the horizontal direction.

An external force can be applied to the shaft in both the horizontal and vertical directions. The external force is applied moment free to the shaft, and a force transducer measures the size of the force. The force transducer is able to measure 10 kN with a maximum uncertainty of ±5 N. Such an uncertainty is so negligible that it will be completely disregarded during error analyses in this paper. Figures 4–6 show how the force is applied in both horizontal and vertical directions.

The calibration procedure of the AMB is conducted in two steps. The first step is calibrating the strain gages, and the second is calibrating the Hall sensors by using the calibrated strain gages.

The strain gages are calibrated by applying an external force to the shaft in each of the four main axes—two horizontal (left and right) and two vertical (up and down), according to Fig. 1(*b*). At this step of the calibration process the AMB is turned off; thus, the shaft and rotor can move freely in the air gap. Measurements from the force transducer, strain gages, and eddy current probes are all recorded simultaneously while the external force is applied to the shaft and gradually increased. When the external force reaches ~1900 N (the maximum theoretical bearing force), the force is gradually decreased again. The measurements from the force transducer, strain gages, and eddy current sensors are still recorded, allowing one to detect any hysteresis errors. The experiment is carefully repeated, taking into consideration stick-slip phenomena at the boundaries of the beam at low loading ($<$400 N). It means that values below 400 N will be disregarded.

The second step of the calibration procedure involves the four Hall sensors. The AMB is turned on, and the bias current of 8 A is applied to each of the four coils. The control current is increased stepwise to the top coil by using a step of 0.25 A every 3 s. Consequently, the current through the bottom coil decreases equivalently (differential driving mode). At each step the measure-

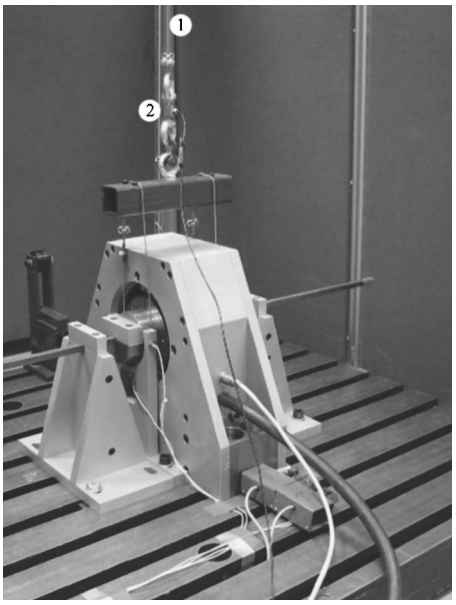

Fig. 5 Vertical up external force: 1, Wire for external force; 2, force transducer

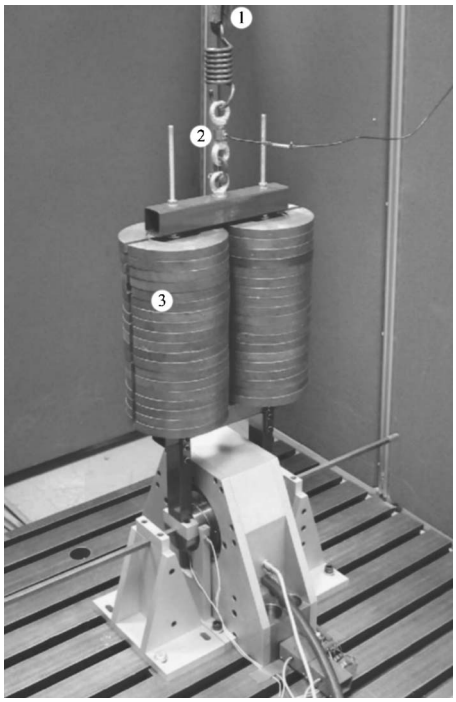

Fig. 6 Vertical down external force: 1, Wire for external force; 2, force transducer; 3, payload

ments from the Hall sensors, strain gages, eddy current sensors and the current through each coils are recorded. When the control current reaches a maximum of 8 A (consequently a total current of 16 A through the top coil and 0 A through the bottom coil), the control current is decreased stepwise again by using a step of 0.25 A every 3 s until the control current reaches zero. Measurements from the different sensors and transducers are still recorded, allowing one to detect any hysteresis errors.

Because the strain gages have been carefully calibrated in the first step, it is possible to relate the flux measurements of the Hall sensors to the actual applied magnetic force. Thus, the four Hall sensors provide information about the actual net magnetic field in the air gap of the AMB and the strain gages provide information about the force applied to the shaft, both in horizontal and vertical directions.

Mathematical Modeling

In general, the magnetic force can be computed from

$$\bar{\mathbf{F}}_{\mathrm{AMB}} = \frac{A_{\mathrm{pole}}}{2\mu_0} \sum_k \bar{\mathbf{B}}^2_{\mathrm{pole}_k} \tag{1}$$

assuming a uniform flux density in every flux-carrying cross section and no flux fringing at the tip of the poles. In Eq. (1), A_{pole} stands for the cross section of the poles carrying the flux densities B_{pole_k}. Where B_{pole_k} are the fluxes at the different magnetic poles k. μ_0 means the magnetic permeability of vacuum. Hence, the entire force of the radial bearing results from the sum of the individual forces of each pole.

In the four-pole AMB illustrated in Fig. 1, the force components in both horizontal and vertical direction can be computed from

$$F_{\mathrm{horz}} = \frac{A_{\mathrm{pole}}}{2\mu_0}(B^2_{\mathrm{pole}_1} - B^2_{\mathrm{pole}_3}) \tag{2}$$

$$F_{\mathrm{vert}} = \frac{A_{\mathrm{pole}}}{2\mu_0}(B^2_{\mathrm{pole}_2} - B^2_{\mathrm{pole}_4}) \tag{3}$$

Hall Sensor Method. The first method for determining the magnetic bearing forces is the direct measurement of the flux density by means of Hall sensors at each pole. The Hall sensor measures the flux density at the slot surface and not at the main pole surface, and due to this, a scaling factor is necessary before the measurement can be used together with Eqs. (2) and (3). The scaling factor is introduced as a geometric correction factor to the actual flux measurement. Thus, the model for the Hall sensor takes the form

$$B_{\mathrm{pole}_k} = \frac{V_{H_k}}{K_{\mathrm{HOC}_k} I_{C_k}} \mathrm{Geo}_k \tag{4}$$

In Eq. (4), index k refers to the different magnetic poles, V_H is the output voltage from the Hall sensor, K_{HOC} is the open circuit product sensitivity constant, and I_C is the control current through the Hall sensor. The factor Geo is a geometric correction factor that, takes into account that the Hall sensor is mounted in a slot. Moreover, such an empirical factor accounts also for nonuniform flux densities, saturation in core material, flux fringing at the tip of the poles among others, and not only for slot geometry.

The correction factor is sensitive to the actual slot geometry and mounting of the Hall sensor. Such a correction factor can be identified by means of experiments and a least-squares method in the following way:

$$F_{\mathrm{vert}} = \frac{A_{\mathrm{pole}}}{2\mu_0}\left[\left(\frac{V_{H_2}}{K_{HOC_2} I_{C_2}}\right)^2 \mathrm{Geo}_2^2 - \left(\frac{V_{H_4}}{K_{\mathrm{HOC}_4} I_{C_4}}\right)^2 \mathrm{Geo}_4^2\right] \tag{5}$$

$$\frac{A_{\text{pole}}}{2\mu_0}\begin{bmatrix} V_{H_{2,1}}^2 & V_{H_{4,1}}^2 \\ V_{H_{2,2}}^2 & V_{H_{4,2}}^2 \\ V_{H_{2,3}}^2 & V_{H_{4,3}}^2 \\ \vdots & \vdots \\ \vdots & \vdots \\ V_{H_{2,n}}^2 & V_{H_{4,n}}^2 \end{bmatrix}\begin{bmatrix} \dfrac{1}{(K_{\text{HOC}_2}I_{C_2})^2} & 0 \\ 0 & \dfrac{-1}{(K_{\text{HOC}_4}I_{C_4})^2} \end{bmatrix}\begin{bmatrix} \text{Geo}_2^2 \\ \text{Geo}_4^2 \end{bmatrix} = \begin{bmatrix} F_{\text{vert},1} \\ F_{\text{vert},2} \\ F_{\text{vert},3} \\ \vdots \\ \vdots \\ F_{\text{vert},n} \end{bmatrix} \tag{6}$$

Reluctance Network Method. A second force measurement method is also investigated and is based on a reluctance network model. In a reluctance network model, the bearing is modeled as a multinode network of variable reluctances resulting in a magnetic network that can be computed in an analog way to the electric networks [12]. The equivalent reluctance network model of the four-pole magnetic bearing is shown in Fig. 7.

The different reluctances in the network describe the air gaps, pole legs, and iron paths of the stator and rotor, and they all depend on the length, the cross-sectional area, and the material constant of the flux carrying material. To compute the fluxes in the network, a total of 12 algebraic equations is needed. If it is assumed that no flux fringing and no flux leakage occurs and the flux density is uniform in every flux carrying cross section, this computation can be done in a two- step procedure that parallels electrical circuit theory. First, summing the magnetomotances around each independent closed loop (equivalent to Kirchhoff's voltage law), give equations similar to

$$B_2\frac{g_2(y)}{\mu_0} + B_2\frac{l_2}{\mu_0\mu_r} + B_7\frac{l_7}{\mu_0\mu_r} + B_1\frac{g_1(x)}{\mu_0} + B_1\frac{l_1}{\mu_0\mu_r} + B_9\frac{l_9}{\mu_0\mu_r} = -N_2I_2 - N_1I_1 \tag{7}$$

The second step is to develop nodal equations using conservation of flux where flux paths intersect (equivalent to Kirchhoff's current law) giving equations similar to

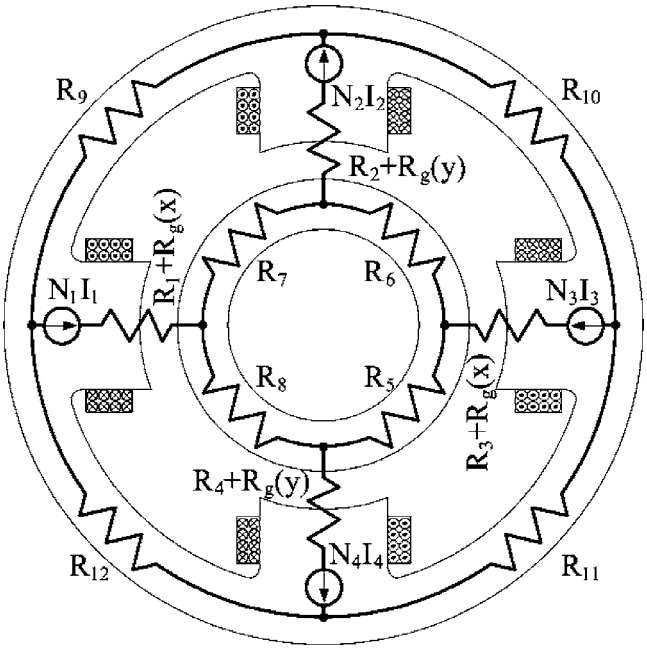

Fig. 7 Reluctance network model

$$B_9A_9 + B_{12}A_{12} - B_1A_1 = 0 \tag{8}$$

Setting up both the loop and nodal equations in matrix form gives

$$\bar{\mathbf{R}}(x,y)\bar{\mathbf{B}} = \bar{\mathbf{N}}\bar{\mathbf{I}}(i_x,i_y,i_0) \tag{9}$$

The linear set of Eqs. (9) can easily be solved for the fluxes in the air gaps (and other fluxes), and the forces can be computed using Eq. (1) taking into account the orientation of the poles.

Theoretical and Experimental Results

(a) Influence of the Slot on the Load Capacity. Figure 8 shows a finite element solution of the magnetic flux density subjected to the Hall sensor mounted in the slot. The computation is done using the finite element program from Meeker [13]. Such magnetic field is diffuse and not very homogeneous, due to the geometry of the slot. It introduces some difficulties while accurately predicting the theoretical output of the Hall sensor.

Figure 9 shows the results of the numerical investigation concerning the slot geometry and the load capacity. The length of the slot is constant and equal to the length of the pole (70 mm). Its width and depth are varied. The bearing load capacity F is normalized to the maximum load capacity, i.e., $F_{\max}$ is obtained in the absence of the slot. The slot area A_{slot} is normalized to the pole area A_{pole}, and the depth of the slot d is normalized to the nominal air gap g_0. The computation is done using the finite element program from Meeker [13].

The calculations have shown that the influence of the slot geometry, shown in Fig. 2(*b*), on the load capacity is below 2%. Such a claim can be experimentally verified by comparing the max load capacity of the bearing with and without the slot [10].

(b) Calibration of Strain Gages. Figure 10 shows the results of the calibration of strain gages for one main direction and serves as a reference between the strain gages and the external force measured by using the force transducer. The results plotted in Fig. 10 are from a complete force cycle that is starting at 0 N gradually increased to 1900 N and then again gradually decreased to 0 N.

The residual error between the force predicted from the linear strain gage model ($y=ax+b$) and the actual force measured from the force transducer is analyzed and the mean error is 0.03% with a standard deviation of 0.24%. Error percentage is normalized with respect to the instantaneous measured force reading from the force transducer, i.e. percent error$=(F_{\text{meas}}-F_{\text{model}})/F_{\text{meas}}$.

As the results from Fig. 10 shows the hysteresis error in the strain gage model is minimal and will be neglected throughout the rest of the paper. The experiment is repeated for the three remaining main directions giving a total of four calibration figures similar to Fig. 10.

(c) Magnetic Forces From Hall Sensor. Two different methods of force measurement have been investigated: (i) direct measurement of the magnetic flux at the bearing poles using slot mounted Hall sensors with empirically determined correction factors and (ii) a variable reluctance network using measurements of the current input signals and rotor position. The geometric correction factors are empirical factors, which account for slot geometry,

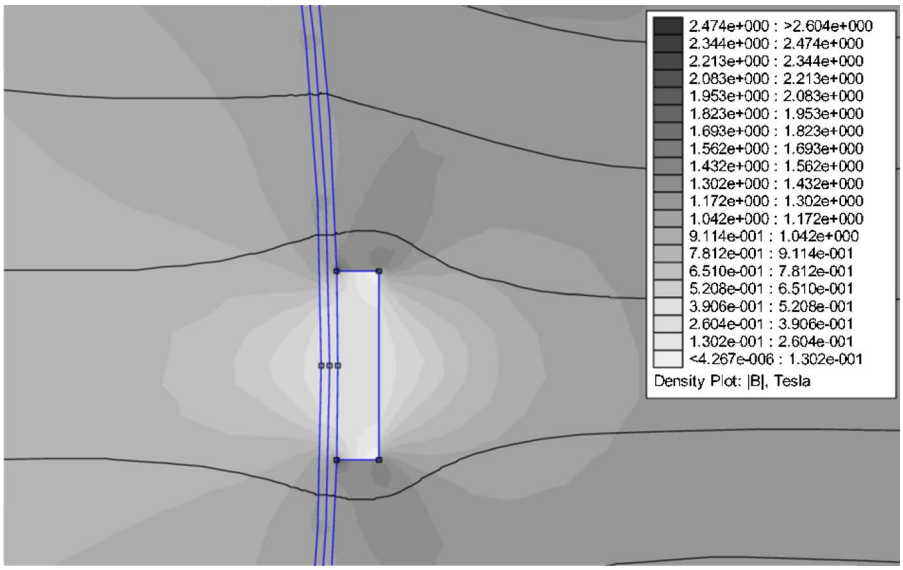

Fig. 8 Visualization of the magnetic field density around the Hall sensor and slot cross section—numerical investigation

nonuniform flux density, saturation in core material, and flux fringing at the tip of the poles. They are identified by using a least-squares method, as explained in the previous section, and presented in Table 1. Such factors are related to magnetic forces in both vertical coils. The correction factors from Table 1 are used together with Eq. (5), and the actual flux measurement to compute the magnetic force.

Figure 11 shows a plot of the experimentally measured force versus the calculated force in the vertical up direction with a bias current of 8 A (i_0), and varying the control current (i_y) from 0 A to 8 A to 0 A (that is 100% of the bearing force). The experiment is carried out numerous times. Because of stick-slip in the boundary conditions, it is not possible to get accurate results at low forces (below 400 N). Such phenomena were observed during the first step of the procedure, calibrating the strain gages, as well as during the second step, characterization of magnetic forces.

The percent error between the calculated force predicted by the flux measurement model and the measured force is analyzed and has a mean of 0.03% and a standard deviation of 0.79%. It is worthy to mention again that the error percentage is normalized

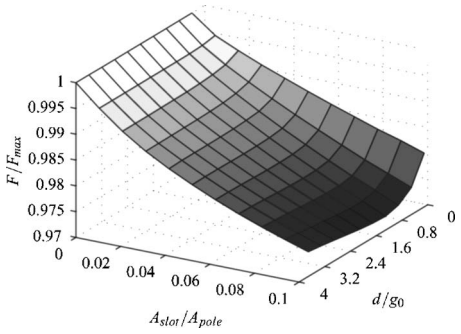

Fig. 9 Reduction of bearing load capacity as a function of area ratio A_{slot}/A_{pole} and slot depth and gap ratio d/g_0

Table 1 Geometric correction factors identified experimentally by means of least-squares method

	Vertical Up		Vertical Down	
	Geo_2^2	Geo_4^2	Geo_2^2	Geo_4^2
Bias 6 A	4.96	1.82	5.31	2.11
Bias 8 A	5.34	2.77	5.42	2.72
Bias 10 A	6.46	4.11	5.69	3.46

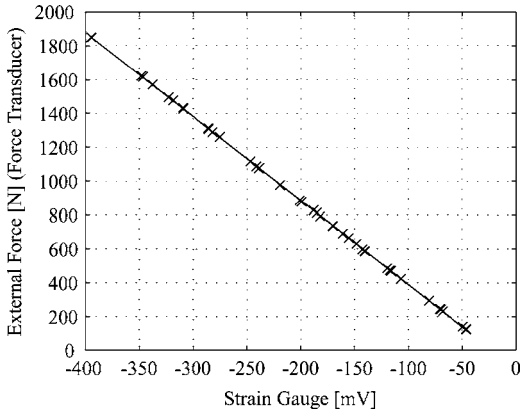

Fig. 10 Strain gage versus external force

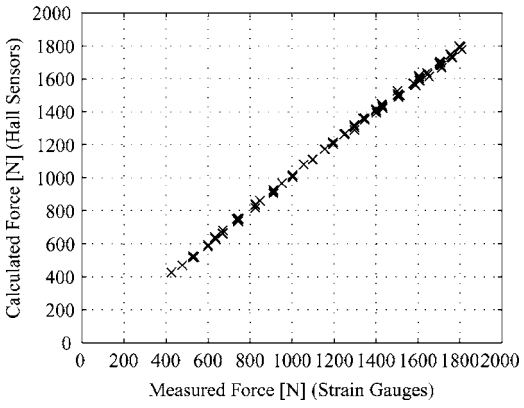

Fig. 11 Experimentally versus calculated force - Hall sensor

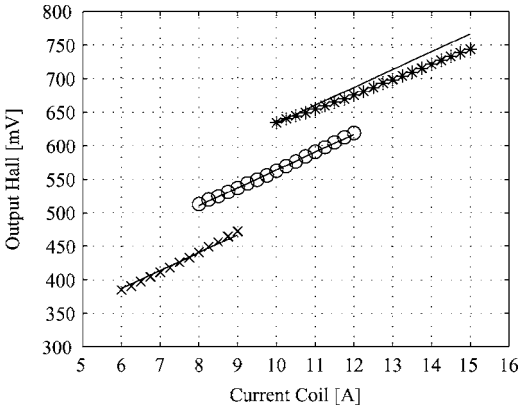

Fig. 12 Behavior of Hall sensor: Solid line, theoretical; ×, bias 6 A (experimental), ○, bias 8 A, (experimental), ⋆, bias 10 A (experimental)

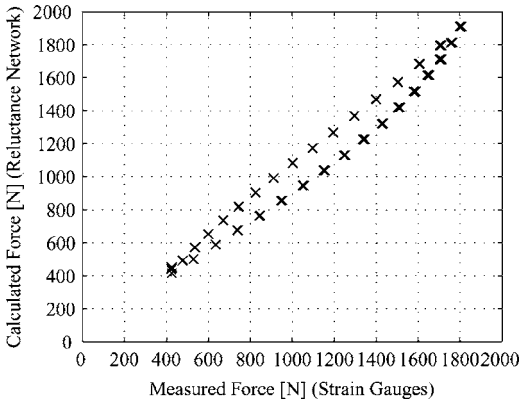

Fig. 13 Experimentally versus calculated force—reluctance network

with respect to the instantaneous measured forces, obtained from the strain gage signals. In the analyzed dataset, the maximum force error is ~1.8%.

In theory, a Hall sensor shall relate the flux to the output voltage in a linear way, and if hysteresis in the core material is negligible, it also allows one to establish a linear relation between the coil current and the output voltage. It means that a change in bias current would result in an offset of the output voltage. Figure 12 shows the theoretical behavior of a Hall sensor in an AMB with a flux-splitting coil configuration.

If the coil configuration had been such that flux splitting was not used, the lines would have no offset. Because the bearing uses flux splitting, the current through coil 1, for example, influences the flux in poles 2 and 4, even though the current is held constant in these coils, adding an offset to the Hall sensor output voltage. When the rotor is centered, these offsets cancel out because the bias current will produce equal forces on opposing poles.

The experimental behavior of the magnetic flux measured by using the Hall sensor is shown in Fig. 12. For bias current of 6 A and 8 A, good agrement between theory and experiments was found. Residual errors of the order of 1% are achieved. Nevertheless, for bias current of 10 A, Fig. 12 illustrates some deviation from the theoretical flux. The deviation is due to model error, i.e., the model is taking into account neither saturation nor other nonlinearities in the core material. Because the geometric (or correction) factors are empirically determined, the model error can be significantly reduced by identifying a set of correction factors, each set related to a bias current and each identified by using a least-squares method and the force measurements from the strain gages. Table 1 shows the sets of correction factors associated to three different values of bias current.

Two Hall sensors have different correction factors, as can be seen in Table 1. An explanation for this difference may be attributed to a combination of different uncertainties that all influence the correction factors. The uncertainties are mainly due to inaccuracies in the manufacturing of the slots and differences in the actual mounting position of the Hall sensors. Nevertheless, small differences in sensor constants, such as the open-circuit product sensitivity (K_{HOC}) and the control current (I_C), will influence the correction factors.

(d) Magnetic Forces From Reluctance Network. The same experimental data are used together with the reluctance network, Eq. (9), to calculate the force. Inputs for the network are control currents (i_x, i_y), bias current (i_0), and rotor position (x, y). Figure 13 shows the behavior of the measured force versus the calculated force using the reluctance network. The bias current is 8 A (i_0), and the control current (i_y) is varied from 0 A to 8 A to 0 A. Because of stick-slip in the boundary conditions, it is not possible to get accurate results at low forces (below 400 N).

The percent error between the calculated force predicted by the reluctance network and the measured force date is analyzed; and it has a mean of −0.59% and a standard deviation of 7.14% The error percentage is normalized with respect to the instantaneous measured force reading from the strain gages.

It is clear that the reluctance network suffers from the unmodeled nonlinearities of the magnetic material; hence, hysteresis has a significant influence on the accuracy. The network could be extended to consider nonlinear material behavior as described in, e.g., [14,15], and it would probably improve the accuracy. In the analyzed dataset, the maximum force error is ~10%.

(e) Comparison: Hall Sensor Versus Reluctance Network. In Table 2, the two force measurement methods are summarized and compared for the vertical direction and for different bias currents. It is possible to conclude that measurement of the magnetic flux density leads to the most accurate results.

Conclusions and Future Aspects

Two different methods of force measurement in a radial active magnetic bearing have been investigated and compared. The two

Table 2 Errors: vertical up and vertical down

	Vertical up				Vertical down			
	Hall sensors		Reluctance network		Hall sensors		Reluctance network	
	Average error (%)	Standard deviation (%)	Average error (%)	Standard deviation (%)	Average error (%)	Standard deviation (%)	Average error (%)	Standard deviation (%)
Bias 6 A	−0.02	0.57	−0.62	3.98	−0.11	0.93	−0.68	4.05
Bias 8 A	−0.03	0.79	−0.59	7.14	−0.06	0.88	−0.58	6.89
Bias 10 A	−0.02	1.04	−0.15	8.04	−0.23	1.22	−0.30	7.66

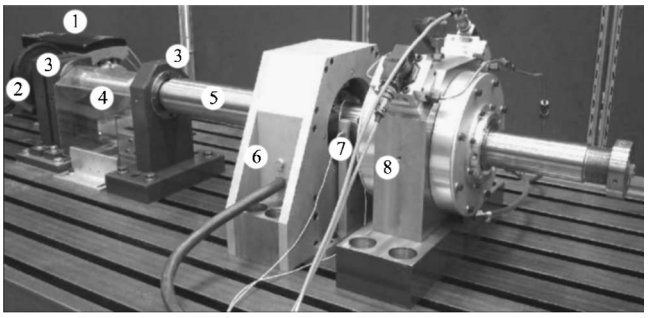

(*a*)

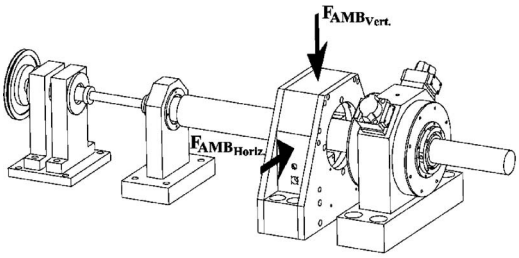

(*b*)

Fig. 14 (a) AMB and ALB test rig: 1, Motor; 2, belt drive; 3, ball bearings; 4, coupling; 5, shaft; 6, AMB; 7, eddy current sensor; 8, ALB; and (b) schematic view of the test rig

methods are based on a reluctance network and on the direct measurement of the magnetic flux density at all poles by using Hall sensors.

A novel Hall sensor mounting method has been presented that does not require enlargement of the air gap. As a result of the novel mounting method, a set of geometric correction factors are introduced and identified. The correction factors take into account uncertainties associated with each individual Hall sensor, saturation in core material among others.

The direct measurement of the flux using Hall sensors shows the most accurate results with errors of the order of 1%. This high accuracy is mainly assured due to the relative small bearing gap variations, i.e., variations up to 24% of the bearing gap.

Fig. 14 illustrates by means of a photograph and a schematic drawing how the calibrated AMB will be used to identify damping and stiffness coefficients of active lubricated bearings. Oil film coefficients in such a type of active bearings are strongly dependent on the control gains as well as servovalve dynamics. It means that such oil film coefficients are strongly frequency dependent [16,17]. Figure 14(*a*) shows the test rig composed of a long shaft supported by three bearings: a ball bearing at one of its extremity (on the left-hand side), by the investigated AMB in the middle, and by an active lubricated bearing at the shaft extremity (on the right-hand side). The AMB will be used as a calibrated shaker, and the shaft displacement inside of the gap will not exceed 24% of the bearing gap. The main advantage of the technique is the application of high accurate force (with $<1\%$ error) without contact between shaker and shaft, i.e., without introducing additional damping nor hanging inertia.

Nomenclature

A_i = cross sectional area of ith section
A_{pole} = pole cross-sectional area
A_{slot} = slot cross-sectional area
$\bar{\mathbf{B}}$ = magnetic flux density matrix
B_i = magnetic flux density in ith segment
B_{pole_k} = magnetic flux density in kth pole
$\bar{\mathbf{F}}_{\text{AMB}}$ = force vector
F_{horz} = force in horizontal direction
F_{vert} = force in vertical direction
Geo_k = geometric correction factor for kth Hall sensor
$\bar{\mathbf{I}}$ = coil current vector
I = coil current
I_{C_k} = control current for kth Hall sensor
K_{HOC_k} = open circuit product sensitivity for kth Hall sensor
$\bar{\mathbf{N}}$ = coil turn matrix
N = coil turn
$\bar{\mathbf{R}}$ = reluctance matrix
R = reluctance
V_{H_k} = output voltage of kth Hall sensor
g_k = distance between rotor and kth pole
i_0 = bias current
i_x = control current for horizontal direction
i_y = control current for vertical direction
l_i = length of ith segment
x = rotor eccentricity in horizontal direction
y = rotor eccentricity in vertical direction
μ_0 = permeability of free space
μ_r = relative permeability

References

[1] Nordmann, R., Aenis, M., Knopf, E., and Straburger, S., 2000, "Active Magnetic Bearings, a Step Towards Smart Rotating Machinery," 7th International Conference on Vibrations in Rotating Machinery (IMechE), Nottingham, Sept. 11–14.

[2] Schweitzer, G., 1998, "Magnetic Bearings as a Componet of Smart Rotating Machinery," 5th International Conference on Rotor Dynamics, Darmstadt, Sept. 7–10.

[3] Aenis, M., and Nordmann, R., 1999, "A Precise Force Measurement in Magnetic Bearings for Diagnosis Purposes," 5th International Symposium on Magnetic Suspension Technology, Santa Barbara.

[4] Knight, J. D., Xia, Z., and McCaul, E., 1992, "Determination of Forces in a Magnetic Bearing Actuator: Numerical Computation With Comparison to Experiment," ASME J. Tribol., **114**, pp. 796–801.

[5] Marshall, J. T., Kasarda, M. E.F., and Imlach, J., 2003, "A Multipoint Measurement Technique for the Enhancement of Force Measurement With Active Magnetic Bearings," ASME J. Eng. Gas Turbines Power, **125**, pp. 90–94.

[6] Traxler, A., and Schweitzer, G., 1984, "Measurement of the Force Characteristics of a Contactless Electromagnetic Rotor Bearing," *Symposium on Measurement and Estimation Proceedings*, International Measurement Confederation (IMEKO), Bressanone, Italy, pp. 187–192.

[7] Zutavern, Z. S., and Childs, D. W., 2005 "Fiber-Optic Strain Gauges Calibration And Dynamic Flexibility Transfer Function Identification in Magnetic Bearings," ASME Turbo Expo, Nevada, June 6–9.

[8] Fittro, R. L., Baun, D. O., Maslen, E. H., and Allaire, P. E., 1997, "Calibration of an 8-pole Planer Radial Magnetic Actuator," ASME Paper No. 97-GT-018.

[9] Knopf, E., and Nordmann, R., 1998, "Active Magnetic Bearings for the Identification of Dynamic Characteristics of Turbulent Journal Bearing," 5th International Conference on Rotor Dynamics, Darmstadt, Sept. 7–10.

[10] Andersen, S. B., 2003, "Konstruktion og Eksperimentelle Undersøgelser af et Aktivt Radial Magnetisk Leje til Styring af Rotorsvingninger," Master thesis, Technical University of Denmark-MEK.

[11] Schweitzer, G., Bleuler, H., and Traxler, A., 2003, "Active Magnetic Bearings - Basics, Properties and Applications of Active Magnetic Bearings," Authors reprint, Zurich.

[12] Sadiku, M. N. O., 2001, *Elements of Electromagnetics*, 3 ed., Oxford University Press, London.

[13] Meeker, D. C., "Finite Element Method Magnetics," Version 3.4.0 (21Dec2004 Build), http://femm.foster-miller.net

[14] Meeker, D. C, Maslen, E. H., and Noh, M. D., 1995, "A Wide Bandwidth Model for the Electrical Impedance of Magnetic Bearings," 3rd International Symposium on Magnetic Suspension Technology, Tallahasee, Dec.

[15] Springer, H., Schlager, G., and Platter, T., 1998, "A Nonlinear Simulation Model for Active Magnetic Bearings Actuators," 6th International Symposium on Magnetic Bearings, Massachusetts Institute of Technology, Cambridge, MA.

[16] Santos, I. F., and Scalabrin, A., 2003, "Control System Design for Active Lubrication With Theoretical and Experimental Examples," ASME J. Eng. Gas Turbines Power, **125**(1), 75–80.

[17] Santos, I. F., Nicoletti, R., and Scalabrin, A., 2004, "Feasibility of Applying Active Lubrication to Reduce Vibration in Industrial Compressors," ASME J. Eng. Gas Turbines Power," **126**(4), pp. 888–894.

Dynamic Behavior of Spherical Friction Dampers and Its Implication to Damper Contact Stiffness

K-H. Koh
e-mail: kkoh@andrew.cmu.edu

J. H. Griffin

Mechanical Engineering Department,
Carnegie Mellon University,
5000 Forbes Avenue,
Pittsburgh, PA 15213

A model that predicts the quasi-static behavior of a friction damper that has spherical contacts was developed using Mindlin's theory. The model was integrated into a dynamic analysis that predicts the vibratory response of frictionally damped blades. The analytical approach was corroborated through a set of benchmark experiments using a blades/damper test fixture. There was good agreement between the theoretical predictions of amplitude and the values that were measured experimentally over a wide range of test conditions. It is concluded that it is possible to predict the vibratory response of frictionally damped vibrating systems using continuum mechanics, provided that the contact geometry is clearly defined and the local nonlinear contact is correctly taken into account. [DOI: 10.1115/1.2436547]

1 Introduction

Friction dampers are used in gas turbine engines to increase energy dissipation and reduce vibratory response. The dampers are pieces of metal that fit between the blades and that are held in place by centrifugal force. A significant amount of research has been reported in the literature on friction damping of turbine blades. A review paper by Griffin [1] summarizes the research prior to 1990. Examples of research since 1990 are the papers by the researchers at Ohio State [2–4], Carnegie Mellon [5,6], Imperial College [7], Penn State [8,9], Csaba [10], Sextro et al. [11], and Szwedowicz [12]. This problem is a difficult one for the following reasons: three-dimensional motion across the friction interface, the effects of variable normal load (especially in the context of wedge-type dampers), modeling the dynamic behavior of the damper as an independent body, and modeling microslip. In this regard, of particular note is the progress made by the researchers at Ohio State University [13,14], at Imperial College [15–17], and at the University of Hannover [18–21]. An additional issue that has been raised by engineers in industry who design friction dampers is how to accurately predict the damper's stiffness.

Experts from Rolls Royce, GE Aircraft Engines, Pratt & Whitney, and Siemens Westinghouse attended a workshop on contact mechanics and friction damping sponsored by the U.S. Department of Defense in 2001. The unanimous view expressed by the industrial representatives was that the friction damping codes that they used tended to over predict damper performance unless the models were "calibrated" by experimental data from component tests—typically spin-pit tests [22]. In particular, they agreed that in order to get the computer codes to match the actual amplitude reductions seen in the component test data, it was necessary to significantly reduce the damper's stiffness from what would be calculated using a standard finite-element analysis of the damper. The purpose of the research reported here is to try to gain a better understanding of why this may be the case. In this context, it is necessary to look in more detail at recent research on friction dampers reported in the literature and focus on how they deal with stiffness.

There are two recent papers that report experimental studies on under-platform dampers. The behavior of wedge dampers is investigated in the paper by Sanliturk et al. [7]. Their experiments were of two types. In the first, the damper is separately tested in a special fixture to measure its hysteresis curves. The curves are fitted with an array of macroslip elements in order to have an analytical friction model that represents the damper's behavior. In a separate set of experiments, a wedge damper is secured between two vibrating blades, and the dynamic response of the system is measured over a range of frequencies and normal loads. The analytical damper friction model is then used in a nonlinear vibration analysis to predict the behavior of the vibration experiments. In order to do this, the analytical damper model was generalized to take into account variable normal load effects that occur in the vibration experiment. The agreement between the experimental data and predictions was moderately good. However, for some normal loads the peak amplitudes were off by factors of two to four and an empirical correction factor for damper rolling was developed to improve the correlations. More importantly, from the perspective of this paper, the damper stiffness used in the model was measured directly from the hysteresis tests and not analytically computed. As a result, this paper does not address the issue of whether or not it is possible to accurately predict damper stiffness.

From the perspective of predicting damper stiffness, a more relevant study is the one reported by Panning et al. [19]. In this case, the vibration test is essentially the same as Ref. [7] except that the damper is a cylindrical pin damper. The damper is modeled as a separate rigid body that is connected to the blade through a grid of contact elements that takes into account the static load distribution from Hertzian contact. Since the damper is modeled as a rigid body, the only damper flexibility is from the friction contact elements. The paper states that "the contact model is based on a discretization of the contact surfaces into several point contact elements. It includes the elasticity of the contacting surfaces in tangential as well as in normal direction, perpendicular to the contact plane." "The developed model includes roughness that causes a nonlinear dependency between the tangential and normal stiffnesses and the relative displacement in normal direction." Later in the paper, it states that the "tangential and normal stiff-

Contributed by the International Gas Turbine Institute of ASME for publication in the JOURNAL OF ENGINEERING FOR GAS TURBINES AND POWER. Manuscript received June 14, 2006; final manuscript received July 6, 2006. Review conducted by Dilip R. Ballal. Paper presented at the ASME Turbo Expo 2002: Land, Sea and Air, Barcelona, Spain, May 8–11, 2006, Paper No. GT2006-90102.

nesses can be estimated by means of a finite-element model of the blade platforms and the friction damper." From the paper it is not clear how the finite element calculated stiffness and the surface roughness induced flexibility are combined to produce the net values of stiffness that is used in the model. (It is clear, however, that it can be very large, i.e., the stiffness can go to zero because of surface roughness.) As that may be, when predictions from the analytical model are compared with the experimental data, the resulting agreement is very good. Panning et al. compare the frequency response predicted by their model with their experimental data for five different normal loads. The agreement is excellent for all but the highest normal load. From this result, one would tend to conclude that Panning, et al. had found the missing factor in the damper stiffness calculations, i.e., the additional compliance of a surface layer caused by surface roughness effects. The calculation of the flexibility caused by surface roughness is explained in more detail by Sextro in Refs. [23,24].

This result, if correct, is important for two reasons. According to engineers that design dampers [22], the missing factor in the damper stiffness calculation had a major effect, i.e., the flexibility from the unknown source was a dominant factor in determining the damper's performance. Practically this means that if Panning et al. are correct, then the compliance of the surface layer must be a dominant source of flexibility in the damper. If this is the case, then one has to reconsider the validity of any interface stress calculation that neglects the compliance caused by the roughness of the surface layer. This would, in general, have important implications to contact mechanics, and, more specifically, to the methods that are now being used to calculate contact stresses in dovetails and fir tree attachments [25] and that do not include this effect. Thus, it is important to verify the conclusion of Panning et al. that the compliance of a thin surface layer is an important factor in modeling friction dampers and, more generally, in modeling interface mechanics.

The contact geometry of the cylindrical, pin damper in contact with a flat surface as tested by Panning et al. is similar to that of a sphere in contact with a flat surface. They are both Hertzian contact problems in which the contact area depends on the magnitude of the applied load. O'Connor and Johnson [26] experimentally studied the effect of surface asperities on the tangential compliance of a smooth steel ball in contact with a rough flat surface. Johnson in his book on contact mechanics [27] summarizes his key result as follows. "An experimental study of a hard steel smooth sphere, pressed into contact with a rough flat by a constant normal force showed that the compliance under the action of a superimposed tangential force, given by Eq. (7.24), was affected very little by the roughness of the surface." Equation (7.24) referred to by Johnson was derived for a smooth sphere in contact with a smooth flat and was derived from elasticity theory and included no surface roughness effects. He goes on to explain why. "In the central region of the contact area, as Fig. 7.7 shows, the tangential traction is a minimum while the normal pressure is a maximum. The real contact area in this region will be high and, in consequence, the compliance of the asperities will be small. Since the tangential traction is also small in that region, the contribution of the asperity deformation to the bulk compliance is negligible." It seems logical that this reasoning would also apply to the cylindrical contact geometry used in the Panning et al. study. If so, then the flexibility attributed to surface roughness would have to be caused by a different mechanism not taken into account in their approach.

One source of additional compliance that is not mentioned in the paper by Panning et al. is the highly localized strain concentration that occurs because of Hertzian contact. It is important to emphasize that this effect can be calculated using simple elasticity theory of the nominal contact geometries (a smooth cylindrical damper on a smooth flat blade platform) and does not take into account surface roughness or asperities. The strain concentration is very large because the forces in the contact region are spread over a very small area, a contact patch of radius a. In the case of Hertzian contact of a sphere on a flat surface, the strains and displacements are so highly localized that it is possible to determine closed form expressions for normal and tangential stiffnesses due to the local strain concentration that are nonlinear functions of the applied load [27]. They are

$$k_N = \left(\frac{2G}{1-\nu}\right)\left[\frac{3NR(1-\nu)}{4G}\right]^{1/3} \tag{1}$$

$$k_T = \left(\frac{4G}{2-\nu}\right)\left[\frac{3NR(1-\nu)}{4G}\right]^{1/3} \tag{2}$$

where G is the shear modulus; N is the applied load; R is radius of sphere; and ν is Poisson's ratio. No such closed form expressions exist for stiffnesses in the case of cylindrical contact. The reason for this is that in two-dimensional elasticity theory, the internal displacements caused by a load applied on the surface of a half-space do not die off in the same manner as they do in three-dimensional elasticity. Let r be the distance from the applied load, in three dimensional elasticity the displacements are of order $1/r$ as $r \to \infty$, i.e., they go to zero and a unique stiffness due to highly localized strain concentrations exists. However, for two dimensional elasticity the displacements are of order $\ln(r)$ as $r \to \infty$, i.e., they do not go to zero and, while the strains tend to be highly localized, the effective stiffness depends on the full geometry of the part under consideration and how it is constrained at its other boundaries. Practically, this means that the contact stiffness of any part modeled using two dimensional elasticity has to be calculated using a numerical method, typically finite-elements. So, what are the characteristics of a finite-element model that will correctly compute the contact stiffness using plane strain or plane stress elements, and why would it be difficult for someone to correctly compute them?

The authors of the work reported here have had experience in calculating the effect of the local strain concentration on the stiffness of a damper modeled with two-dimensional elasticity theory. There are two primary considerations in getting a good answer. The first is that contact loads have to be applied over the correct length surface. Practically, this means the length of the contact surface is calculated from Hertz's theory for a cylinder, i.e., $a = [3NR(1-\nu)/4G]^{1/3}$, where a is half the length of contact [27]. Second, the finite-element mesh directly under the contact region needs to be small relative to the contact length, a. In general, it was found that in order to get converged values of stiffness the mesh size in the contact region had to be about one order of magnitude smaller than a.

It is worth noting that you cannot correctly calculate the stiffness of a damper by applying two opposite and equal forces at only two nodes. If you did this then the answer from your finite-element analysis would depend on the size of the finite element mesh. In the limit as the mesh size goes to zero, you would find that the displacements increase without bounds and that the stiffness would go to zero. The reason is that the two point constraints represent the loading as two line loads and, as the mesh gets smaller, the finite-element solution picks up the logarithmic singularities in displacements that occur directly under the line loads. The point is that to determine contact stiffness it is absolutely essential to apply the loads over the correct length and to have a local mesh that is small compared with this size scale. This is not a procedure that is commonly used by industry, nor was it mentioned as an issue in the paper by Panning et al.

The research presented in this paper focuses on the effect of the highly localized strain concentration and how it affects the stiffness of the damper and its effectiveness in reducing vibratory response. The issue is whether the resulting theory correctly predicts the experimentally measured values of damper stiffness as well as the dynamic response of a frictionally damped turbine blade system without including a stiffness reduction factor for

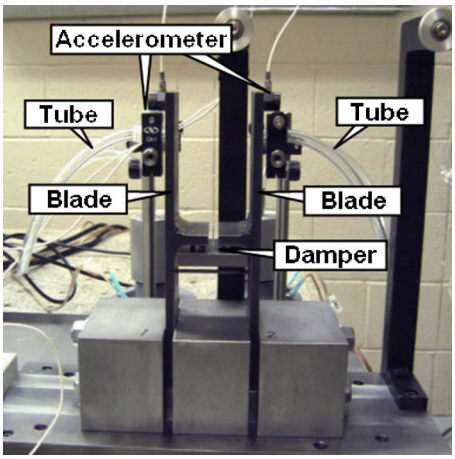

Fig. 1 Test apparatus used for vibration measurements

surface roughness. If it does, then the need for including a stiffness reduction factor because of the roughness of the surface will need to be further investigated in order to establish when it is, in fact, important and should be taken into account.

In order to examine this issue in the simplest possible context, the experiments reported here were designed to remove as many uncertainties as possible. For example, the experiments use spherical dampers, i.e., dampers in which the friction contact occurs between spherical and flat surfaces. This means that the contact locations are well known. The damper used in the vibration experiments had three hemispheres that contacted the blades (Figs. 1 and 2) so that the distribution of normal loads could be determined statically. The regions on the blades in contact with the damper were horizontal so that dynamic variations in normal load were not important and would not add unnecessary complications to the calculations. The goal was to provide an experimental benchmark in which the important factors that affect the performance of the damper where as well known as possible.

In order to provide a benchmark, the frequency response experiments reported here were performed for a range of excitation levels as well as normal loads, i.e., the excitation forces vary by about a factor of 20 and the normal loads vary by about a factor of ten. Since damper performance changes with excitation level as well as normal load, it is critical to experimentally establish the effect of each. In addition, the experiments were repeated to assess scatter. In total, the results of about 200 frequency response measurements are reported in this paper. In contrast, the earlier studies reported only one set of results for only one excitation level.

Finally, a damper that has spherical contacts was chosen for another reason. Unlike damper geometries such as cylindrical dampers or cottage roof dampers, spherical dampers have closed form elasticity solutions that characterize their behavior. The solutions take into account the nonlinear contact behavior, the local strain concentration, and microslip at the friction interface. As a result, it is relatively easy to take these factors into account and see if it is really necessary to also include surface roughness effects.

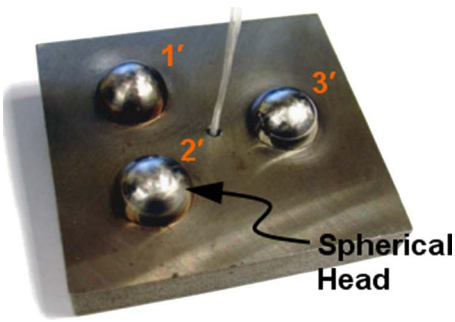

Fig. 2 Damper specimen for a vibration test

Table 1 Stiffness comparison between experiments and Mindlin's theory

Dynamic condition (Hz)	Radius (m)	Normal load (N)	k_{Exp} (N/m)	$k_{Mindlin}$ (N/m)
Dynamic (50)	0.0127	69	31.6×10^6 $^{+11.6\%}_{-7.9\%}$	31.7×10^6
Quasi-static (0.1)	0.027	8,900	327×10^6 $^{+5.0\%}_{-8.2\%}$	345×10^6
Quasi-static (0.1)	0.127	17,800	401×10^6 $^{+9.1\%}_{-4.7\%}$	435×10^6

In order to put the current research in context, it is first necessary to summarize the results of an earlier study by the authors [28] on spherical dampers. That paper reported the results of quasi-static and dynamic experiments that directly measured the properties of a spherical surface in contact with a flat surface. This entailed measuring the shear force across the friction interface as well as the relative displacement across the interface. The hysteresis curves were then processed to determine the stiffness of the dampers under various normal loads as well as the effective nonlinear stiffness and damping of the spherical contact as a function of amplitude; see Refs. [28,29] for details. The stiffnesses were determined by measuring the initial slope of the hysteresis curves and were compared with those predicted by elasticity theory, Eq. (2), without including any surface roughness effects. The results are shown here in Table 1. It is worth noting that the tangential stiffness of the damper was quite well predicted by elasticity theory for radii of curvature that varied by a factor of ten and for excitation frequencies and normal loads that varied by two orders of magnitude. In effect these results confirmed those reported by O'Connor and Johnson [26] that said that surface roughness had a negligible effect on the compliance.

Also in the paper on spherical dampers, the authors processed the experimental hysteresis curves to determine the effective nonlinear damping and stiffness of the contact. Mindlin derived a closed form solution for the hysteresis curves for a tangential load applied to spherical contact in Ref. [30] that takes into account microslip as well as gross slip of the interface. Mindlin's hysteresis curves were processed in the same manner as the experimental data to determine theoretical values of nonlinear damping and stiffness for spherical contact. A comparison of the theoretical results with the experimental results is shown in Fig. 3. Basically, Mindlin's elasticity solution of the nonlinear contact problem does a very good job of predicting the experimental data over a wide range of normal loads, frequencies, radii, and amplitudes. Furthermore, Mindlin's theory indicated that a unique set of nondimensionalized nonlinear stiffness and damping curves exist that capture the local behavior of the contact—this is the way the results are presented in Fig. 3. It is clear from the results that the experimental data does, in fact, confirm the nondimensionalization as predicted by Mindlin's use of elasticity theory.

Consequently, the results presented in Ref. [28] indicate that elasticity theory that properly takes into account the local strain concentration and microslip should be able to predict the damper's stiffness and performance without having to include an additional compliance due to surface roughness. The purpose of the research reported in this paper is to demonstrate that this is, in fact, the case.

2 Experiment

The goal of the experiments reported here is to develop a set of benchmark data that characterize the vibratory response of the blade, friction damper system shown in Fig. 1. This was done by

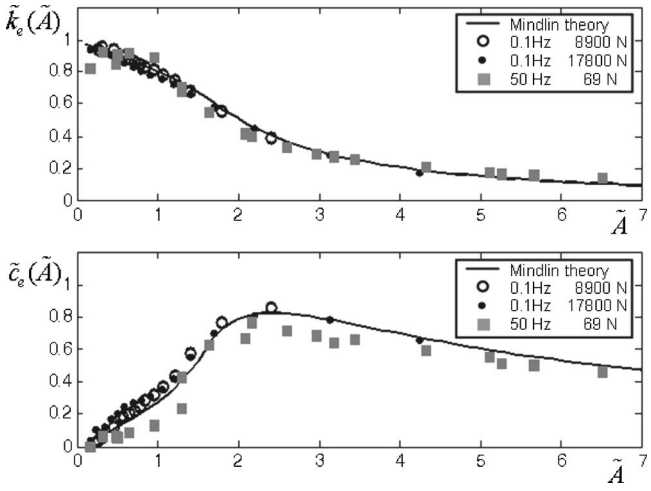

Fig. 3 Comparison between experiments and Mindlin's prediction

measuring the damper's peak amplitude and peak frequency for a range of normal loads and excitation levels. Curves of peak amplitude as a function of excitation force for fixed contact load are known as damper performance curves [5,31] and are one way of quantifying the damper's effectiveness. The results of these measurements will be compared with predictions based on Mindlin's theory in Sec. 3.

2.1 Experimental Configuration. Figure 1 shows the test fixture used in the experiments. The fixture is similar to the one used by Sanliturk et al. [7] and by Panning et al. [19]. The fixture is composed of two blades with a friction damper in between. The friction damper works as an under-platform damper when it makes contact with two horizontally protruding parts of each blade. A pulley assembly applies a force on the damper that results in normal loads on the friction interfaces. A line is attached at the friction damper's center of mass that goes over a pulley and has a dead weight hanging at the other end that consists of a "dish" and weights that are changed from one set of experiments to the next.

Each blade was excited by a speaker using a tube fitting (Fig. 1). The two blades were excited in the anti-symmetric mode in which the blade tips move toward and then away from each other. The anti-symmetric mode was chosen since it causes the maximum motion across the friction damper and provides a good test of the theory. The blades' vibratory responses were recorded using accelerometers at the blade tips that were oriented in opposite directions. As a result, the real-time average value of the two accelerometer signals then directly measures the relative motion between the blades. A thin pin under the damper was welded onto both blades to increase the frequency in the first anti-symmetric mode in order to prevent interaction between the symmetric and anti-symmetric modes during the tests.

The damper specimen shown in Fig. 2 is a blade-to-blade under-platform damper. Since its three spherical heads make contact with a flat surface, Mindlin analysis can be used to characterize its behavior. The three spheres are analogous to the three legs of a stool. They all stay in contact, and the contact forces can be easily calculated from a static analysis.

2.2 Excitation Force Calibration. Frictionally damped systems are nonlinear. As a result, it is important to know the magnitude of the force exciting the system. The speaker excitation system used in this test was calibrated from tests on the system without the friction damper. By measuring the inherent damping

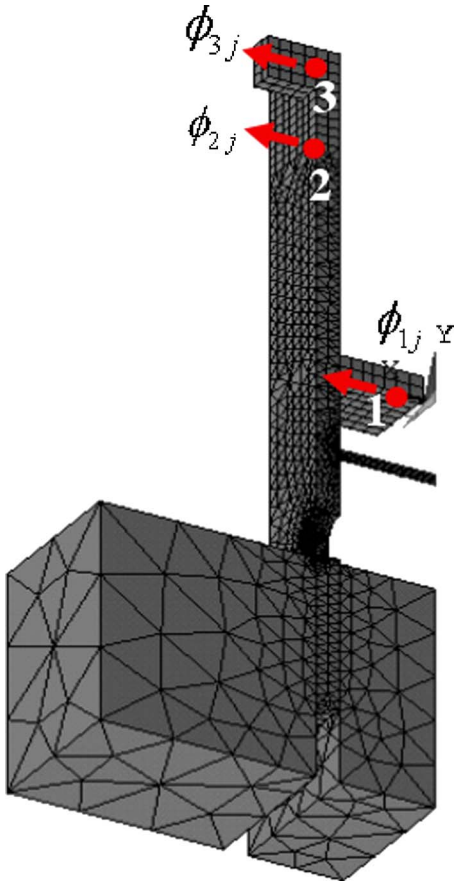

Fig. 4 A quarter model of FEM

in the system and using a finite element model of the blade[1] (Fig. 4), the force generated by the speaker system could be determined as a function of the voltage from the signal generator. The results, shown in Fig. 5, indicate that the amplifiers gradually become saturated and limit the forces to those used in the experiment. As a result, the excitation force could be varied from 0.0031 N to 0.058 N. Thus, the magnitude of the excitation force could be varied by an order of magnitude in the experiments which provides a reasonable set of benchmark experiments.

2.3 Measurement: Damper Performance Curve. A damper performance curve characterizes how well the damper works over a range of excitation forces. It is measured as follows. The normal load and the magnitude of the excitation force are held constant. The frequency of the excitation force is varied in order to measure the frequency response of the blade. The maximum amplitude of the blade (peak amplitude) as well as the frequency at which it occurs (the peak frequency) is inferred from the frequency response. The measurements are repeated over a range of excitation forces. The damper performance curve is a plot of the peak amplitude as a function of the excitation force. The damper performance curves were measured for four different values of damper load corresponding to a contact force W equal to 0.44 N, 0.89 N, 1.78 N, and 3.56 N. In addition, plots of peak frequencies were also determined as a function of the magnitude of the excitation

[1]Note that the displacements at only three points are relevant in this study, points 1, 2, and 3, i.e., the point where the damper contacts the blade, the point where the blade is excited, and the point where the accelerometer is attached. The damper contacts the blade at two points on one side and a single point on the other. Because of the geometry and the types of modes that participate in the response, it was found that all three points have essentially the same modal deflections. As a result, a single value of modal deflection could be used to represent their response.

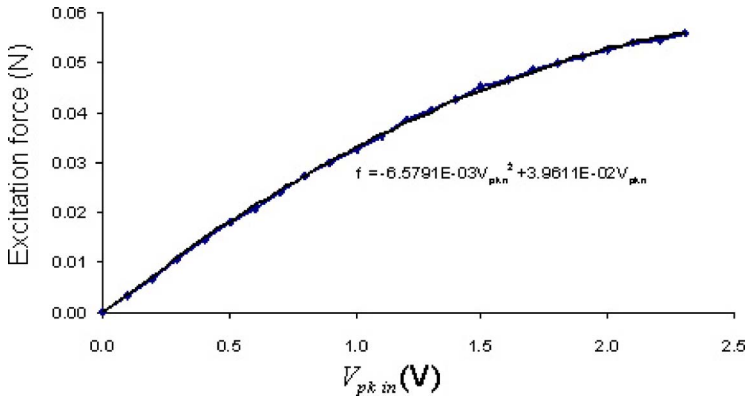

Fig. 5 Peak voltage input versus excitation force graph

force for the four normal loads. The results of the measurements will be shown in Sec. 4 where they will be compared with the predictions.

3 Analysis

The analysis presented here involves three ideas. The first is that the nonlinear forces are periodic and can be approximated by the lowest frequency terms in their Fourier series expansion, i.e., the nonlinear equations will be solved using the harmonic balance (HB) method. This is a very standard approach and is used in most of the papers referenced here. The second is that the complete friction damper (including the contact points with the blade platforms) can be replaced with a single equivalent nonlinear element. This idea uses the concept that the damper can be represented in terms of complex spring elements, see Sanliturk et al. [7]. The third is that dynamic response of the linear portions of the test apparatus can be characterized by using receptances [13,14,32–37]. The process results in a system of nonlinear algebraic equations that are solved numerically. This is described in more detail in the following subsections.

3.1 Harmonic Balance. The fundamental terms in a Fourier series expansion of the nonlinear force include a part that is in phase with the motion and a part that is out of phase. The in-phase part can be thought of as the equivalent stiffness, and the out-of-phase part as the equivalent damping. As a result, the nonlinear force on each spherical contact can be related to the motion across the contact in terms of an equivalent stiffness and damping. In the case of spherical contact, unique expressions for these quantities can be derived from Mindlin's theory [28]. The dimensionless nonlinear stiffness and damping are plotted in Fig. 3 as a function of dimensionless amplitude. Analytic expressions for the two curves were obtained by fitting a fourth-order Padé rational function approximation to the results (see the Appendix). The following subsection describes how this result was applied to the actual damper that has multiple contact points.

3.2 Incorporating Nonlinear Damper Elements. Equivalent friction forces can be applied separately to each contact surface, assuming that the contact joint itself behaves like a spring and damper acting in parallel (Fig. 6). The spring provides a force that is in phase with the displacement, while the damper provides a force that is 90 deg out of phase with the displacement. Therefore, the contact joint can be treated as a spring that has the complex stiffness

$$k_c = k + ic\omega \tag{3}$$

Figure 7(*a*) shows one of the friction dampers used in the testing. In effect, the two spherical contacts on the left are like two complex springs in parallel. The body of the damper has an equivalent linear stiffness that acts like a spring in series. Finally, the spherical contact on the right acts like a complex spring in series. This leads to the equivalent complex spring system shown in Fig. 7(*b*). The two contact joints acting in parallel on the left each have a complex stiffness k_{c1}. There is an equivalent linear spring k_L that represents the bulk stiffness of the material in the middle. There is another contact joint on the right that has a different contact stiffness k_{c2} because it has a different normal load. Figure 7(*c*) shows three spring elements that act as springs in series through which the force $2f_1$ is transmitted.

By breaking the damper system down in this manner, it is possible to calculate an equivalent complex stiffness for the damper system. Since some of the elements are nonlinear, it is necessary to implement the process numerically. The procedure is the following: First, a value of displacement across the first contact region on the left, x_1, is assumed. From Mindlin's theory the relationship between the force f_1 and the displacement x_1 is known, so k_{c1} is calculated and f_1 is known. Second, this result is multiplied by 2 to define the force acting on the joint on the right. Since

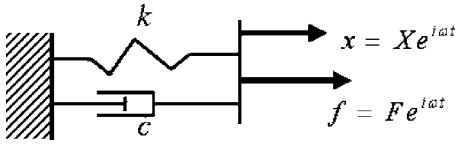

Fig. 6 Spring and damper in parallel

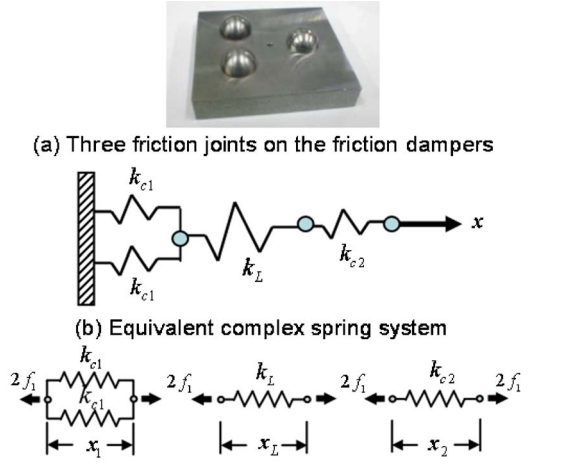

Fig. 7 Friction joints replaced with equivalent nonlinear elements

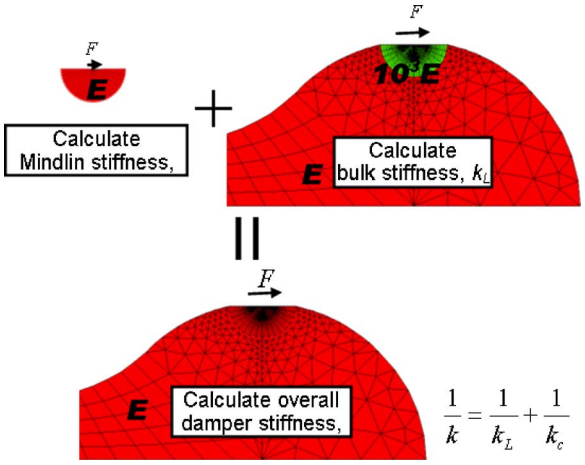

Fig. 8 Application of springs-in-series concept

the relationship between force and displacement in the joint on the right is known, the displacement in the joint on the right can then be determined. Once the displacement in the joint on the right is known, its complex stiffness can be calculated. Because the springs act in series, the equivalent stiffness for the whole joint can be calculated as

$$\frac{1}{k_{\text{equiv}}} = \frac{1}{2k_{c1}} + \frac{1}{k_L} + \frac{1}{k_{c2}} \tag{4}$$

Next, the displacements x_1, x_L, and x_2 are added to determine the total displacement across the joint, z. Consequently, the equivalent complex stiffness can be calculated as a function of total displacement, z.

The linear stiffness of the bulk material was calculated using a static finite-element analysis. A special approach was required here, due to the fact that high strain concentration at the contact points affects the stiffness and this effect has already been taken into account by using Mindlin's theory and the complex stiffnesses k_{c1} and k_{c2} to represent the contacts. The approach used was based on the springs-in-series concept described in Fig. 7. Because Mindlin's theory takes into account the deformation in the high-strain region surrounding the contacts, it was eliminated by using a much higher elastic modulus in these regions. This was done by setting the elastic modulus 1000 times higher in small hemispherical regions surrounding the contact points (Fig. 8). The radii of the spheres were taken to be ten times the contact radius as calculated from Hertz theory. This practically eliminates the local deformation since it is known that more than 90% of the strain energy is contained within this region [27]. The bulk linear stiffness k_L was then calculated using the resulting finite element model. Its value was at least an order of magnitude larger than the nonlinear stiffnesses of the joints. As a result, it had little effect on the predicted behavior of the friction damper. Thus, nearly all of the deformation in the damper was caused by the high strain concentrations directly under the contact points that were captured by Mindlin's elasticity analysis and incorporated in the complex stiffnesses k_{c1} and k_{c2}.

The values of equivalent stiffness and damping that were calculated for the complete damper system are shown in Fig. 9 as functions of z. Figure 9(a) shows the stiffness and damping when the total load on the damper W equals 0.44 N and Fig. 9(b) shows the results for 3.56 N. Because the majority of the damper's flexibility is caused by local deformation in the contact regions, its stiffness and damping are determined from Mindlin's theory and are proportional to the cube root of the vertical load W on the

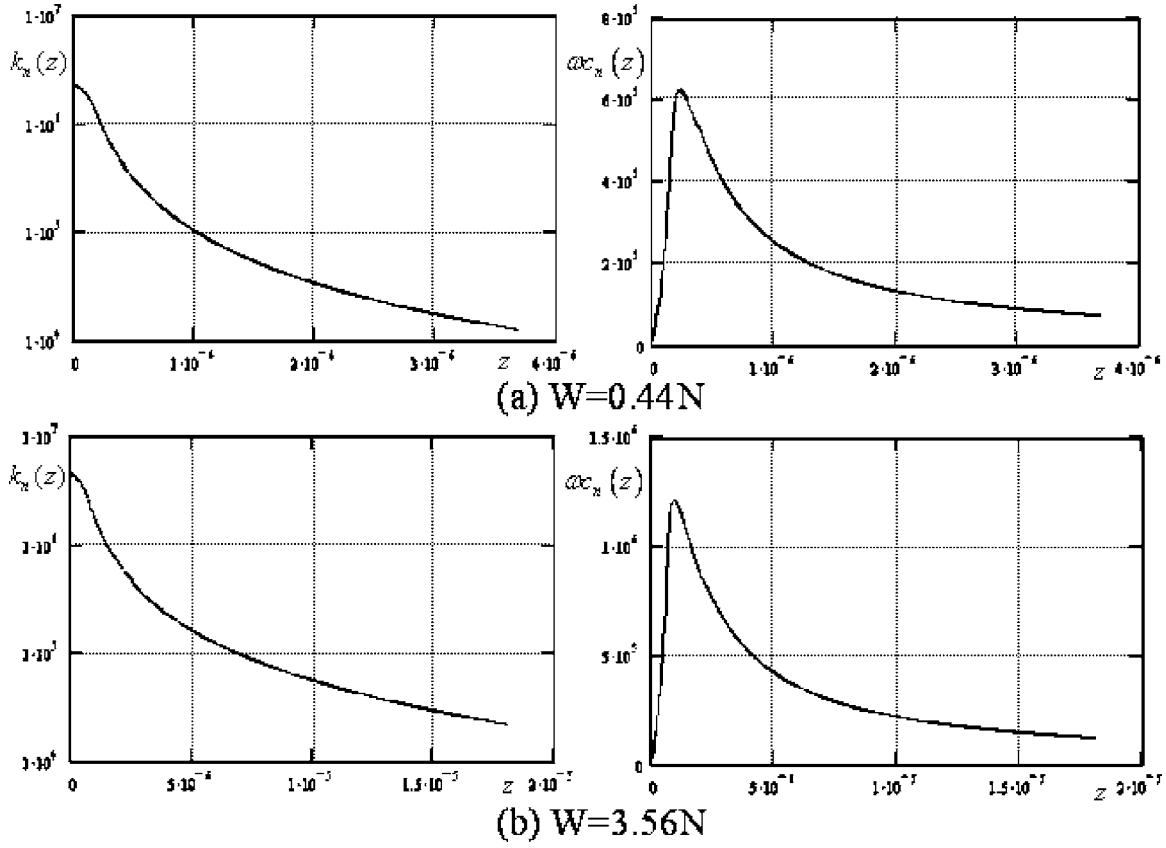

Fig. 9 Combined effective stiffness and damping through all joints

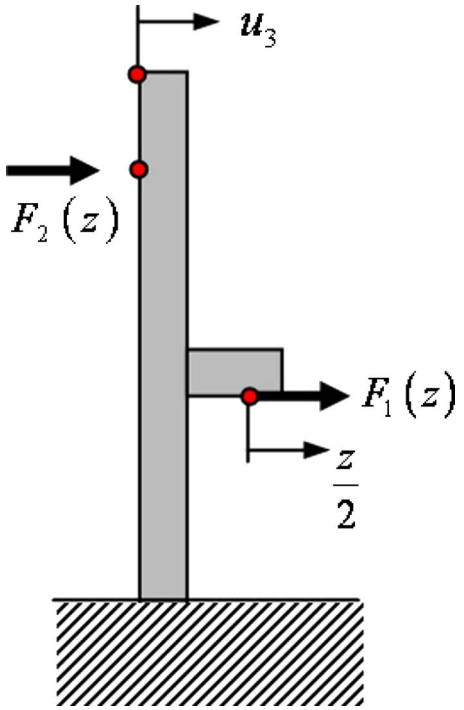

Fig. 10 One blade with external forces

damper. Thus, the equivalent stiffness and damping are predicted to be twice as large when W equals 3.56 N, Fig. 9(b), than they are when W equals 0.44 N (Fig. 9(a)). In addition, the horizontal axes also roughly scale by a factor of two as indicated by the points at which maximum damping occur in the two curves. The fact that the theory predicts very different behavior in these two cases indicates that the experiments should provide an interesting test of the theory.

3.3 Receptance Formulation and Numerical Solution. To complete the formulation, receptances [13,14,32,33] were used to represent the remaining parts of the test apparatus. To understand the approach used here, consider the schematic of the blade shown in Fig. 10. In the figure, F_1 represents the force from the friction damper and F_2 the acoustic force from the speaker. The displacements in the blade are similar to that of a beam in its first bending mode. As a result, the deflections in the platform are essentially uniform along the width of the blade. Consequently, the two friction forces from the two different spherical contact points on the left side of the damper can be replaced with an equivalent force acting at a single point that is twice as large. From the information in Fig. 9, the friction force F_1 is a known function of the relative motion across the damper, z. In addition, it will be shown that the external force F_2 can also be determined if z is known. Thus, both forces are designated as functions of the relative motion across the blade platforms, z.

The procedure for determining $F_2(z)$ and the motion at the blade tip $u_3(z)$ is the following. First, the motion z and frequency of excitation ω are assumed, so that force F_1 can be calculated from the information in Fig. 9 as

$$F_1(z) = -z[k_n(z) + i\omega c_n(z)] \tag{5}$$

The displacement z can be expressed in terms of the applied forces by using receptances R_{ij} where the i subscript indicates the point where the displacement is calculated and the j subscript indicates the point at which the force is applied

$$\frac{z}{2} = F_1 R_{11} + F_2 R_{12} \tag{6}$$

The receptances of the test apparatus without the damper were calculated in the standard manner [13,14] by summing ten finite element modes[2] and using the value of inherent damping that was measured in the excitation force calibration experiment (see Sec. 2.2). The displacement is equal to $z/2$ since z represents the total displacement across the damper and only half of it comes from the blade on the left.

If it is assumed that z is known, then $F_1(z)$ is calculated from Eq. (5) and $F_2(z)$ from Eq. (6), i.e.

$$F_2(z) = \frac{z/2 - F_1 R_{11}}{R_{12}} \tag{7}$$

Once F_1 and F_2 are determined, u_3 may also be calculated using receptances

$$u_3 = F_1 R_{31} + F_2 R_{32} \tag{8}$$

Since u_3 and F_2 are both known, the motion at the blade tip, u_3, is now known as a function of F_2 and ω

$$u_3 = u_3(F_2, \omega) \tag{9}$$

This approach was implemented in the following manner. For a fixed value of ω, it was assumed that z incrementally took on a series of values from 0 to z_{max}. For a given value of z, the nonlinear stiffness and damping terms were determined from the information in Fig. 9; consequently, F_1 could be calculated from Eq. (5). Because ω was known, the receptances in Eqs. (7) and (8) could be calculated. Since z and F_1 were now known, Eq. (7) could be used to calculate the external force F_2. Equation (8) was then used to calculate the displacement at the accelerometer u_3. This process was repeated for all the values of z between 0 and z_{max}. At the end of the process, the values of z were eliminated and the values of F_2 and u_3 stored as a table. The displacement $u_3(F_2)$ was calculated by interpolating values in the table. This process was repeated over the range of frequencies tested in the experiments to define $u_3(F_2, \omega)$. In the computations, z was assumed to be a real number; as a result, both u_3 and F_2 were complex numbers. Physically, the important information is the magnitude of the external force F_2, the magnitude of the displacement at the accelerometer location u_3, and the phase of u_3 relative to F_2 (the absolute phase of the input force F_2 is irrelevant when calculating harmonic response). All three of these quantities could be determined from the complex values of F_2 and u_3 computed using the approach just described. Since F_2 and ω are known in the experiments, the amplitudes measured in the experiments could be compared with those predicted from Eq. (9). The procedure described in this section was implemented numerically using MATHCAD.

4 Results and Comparison

Figures 11 and 12 show comparisons of experimentally measured damper performance curves with those predicted using the analytical approach described in the previous section. Three different experiments were performed in order to assess the scatter in the experimental results. The second set of experimental results was measured approximately 2 weeks after the first set of tests using the same physical damper. The experiments were then repeated with a different damper of the same type. In general the experimental scatter was acceptable.

The analytical prediction of the damper's performance curve was completely determined analytically except for a single value of coefficient of friction that was chosen to best match the analytical predictions to the measured data. The value of coefficient

[2]Appropriate boundary conditions were applied to the finite element model shown in Fig. 4 so that only anti-symmetric modes were generated for use in the receptance calculation, i.e., modes in which the tips of the blades move in opposite directions.

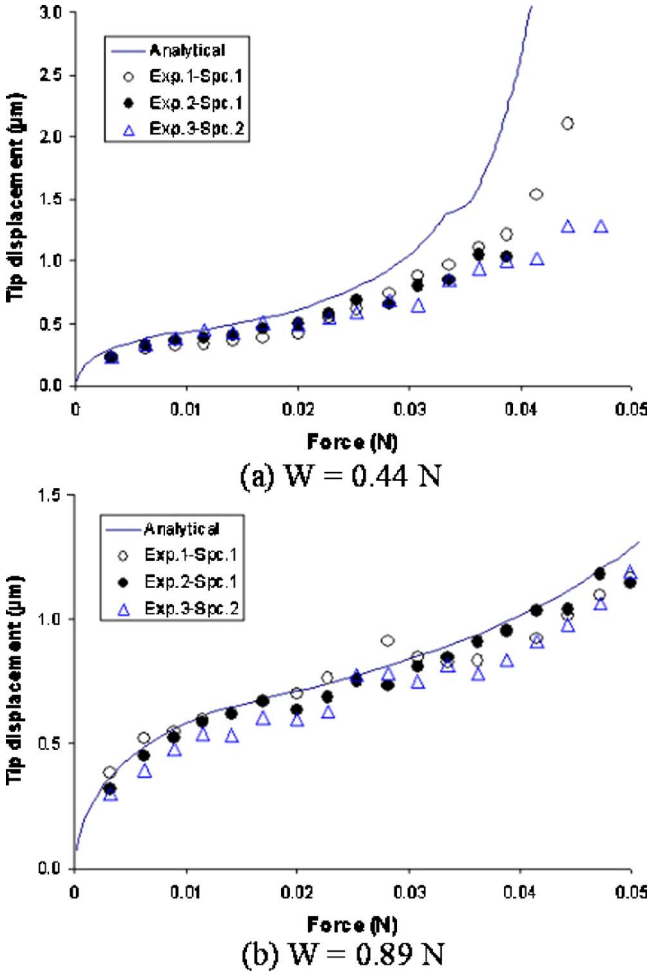

Fig. 11 Amplitude comparison for 0.44 N and 0.89 N

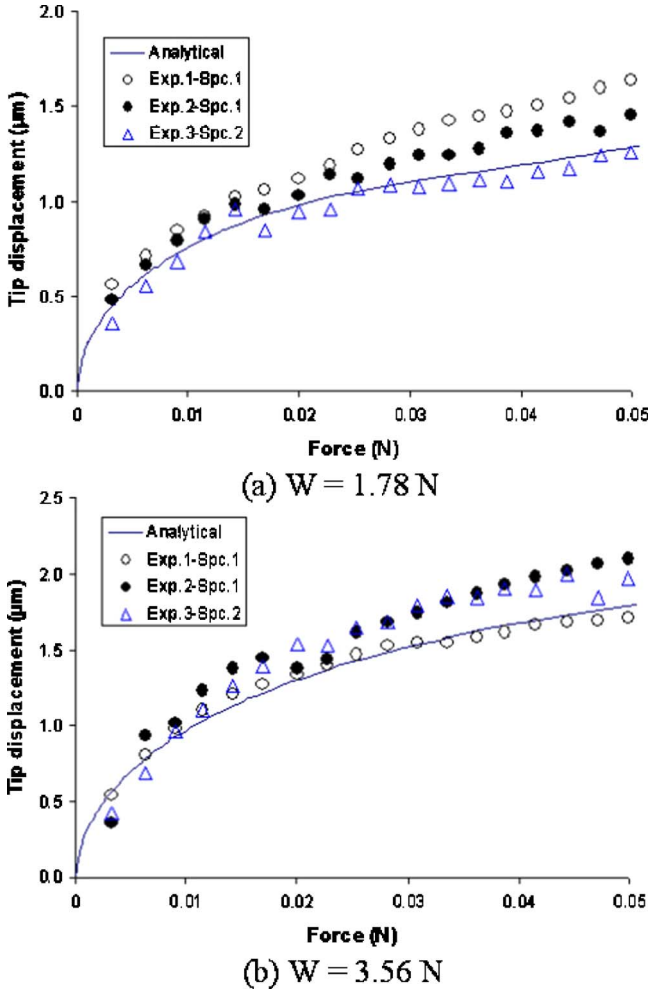

Fig. 12 Amplitude comparison for 1.78 N and 3.56 N

of friction used was 0.75, which was a value comparable to those seen in the quasi-static tests discussed in [28] and also reported in the literature [38,39].

As shown in Fig. 11(*a*), the agreement for *W* equal 0.44 N is good at low force levels, but not as good as at higher excitation levels. A possible explanation of this is the role played by the damper's own weight. The damper's weight of approximately 2.22 N is balanced by the weight of the support disk. When *W* equals to 0.44 N, the net force is only 20% of the damper's weight. When the net force is small, it is easier to have errors in the net force and it is also easy for the damper to loose contact at one of the friction interfaces. One indication that this might be the case is that during the tests for *W* equal to 0.44 N there was an audible rattling noise at high force levels. Since rattle would produce an additional source of energy dissipation that is not modeled by the theory, it would be expected that at higher levels of excitation the experimental amplitude would be less than those predicted by the theory, as is indeed the case. The rattling noise did not occur in the tests with higher normal loads. Thus, they should provide a better assessment of the theory.

For the case of *W* equal to 0.89 N, Fig. 11(*b*) indicates reasonably good agreement between the theory and the experiment over the entire range of excitation forces. Reasonable agreement is also obtained for 1.78 N, Fig. 12(*a*), even though there was more scatter in the experimental results. The agreement for *W* equal to 3.56 N is also reasonably good, see Fig. 12(*b*). In general, the predictions matched the experimental results reasonably well for a range of 14:1 in excitation force and for a range of 8:1 in normal load.

The peak frequency of the damper also was measured as a function of the excitation force for the four different normal loads. The experimental results are compared with those predicted by the theory in Figs. 13 and 14. As the figures demonstrate, the frequency of peak response varied from 300 Hz to about 250 Hz. The theory indicates that for higher damper loads and lower excitation forces the damper does not slip as much and that it has a higher effective stiffness (Fig. 9). This is consistent with the behavior seen in Figs. 13 and 14.

Finally, to get a better sense of how well the theory predicts the experimental results, some frequency response predictions and measurements are shown in Fig. 15 for a damper load *W* equal to 0.89 N. The results shown were chosen to cover a broad range of excitation force. The frequency response shown in Fig. 15(*a*) corresponds to the second lowest force used in the experiments an the agreement is reasonably good. Figure 15(*d*) shows a comparison when the excitation force is about ten times higher and the agreement is still quite good. Considering the fact that the harmonic balance method keeps only the fundamental terms in the Fourier series expansion of the nonlinear forces and consequently tends to smooth the frequency response curves, the theory fairly accurately captured the frequency response of the system as measured in the experiments.

In summary, all the input parameters to the theory were either measured or calculated, except for a single value of coefficient of friction that was chosen to best fit the data. In general there was

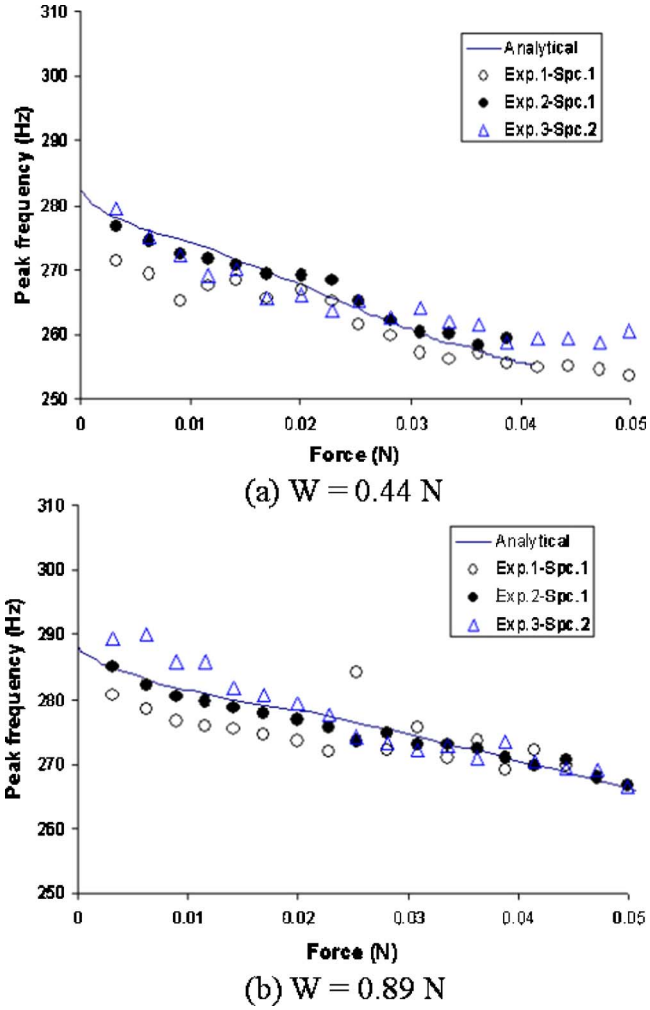

Fig. 13 Peak frequency comparison for 0.44 N and 0.899 N

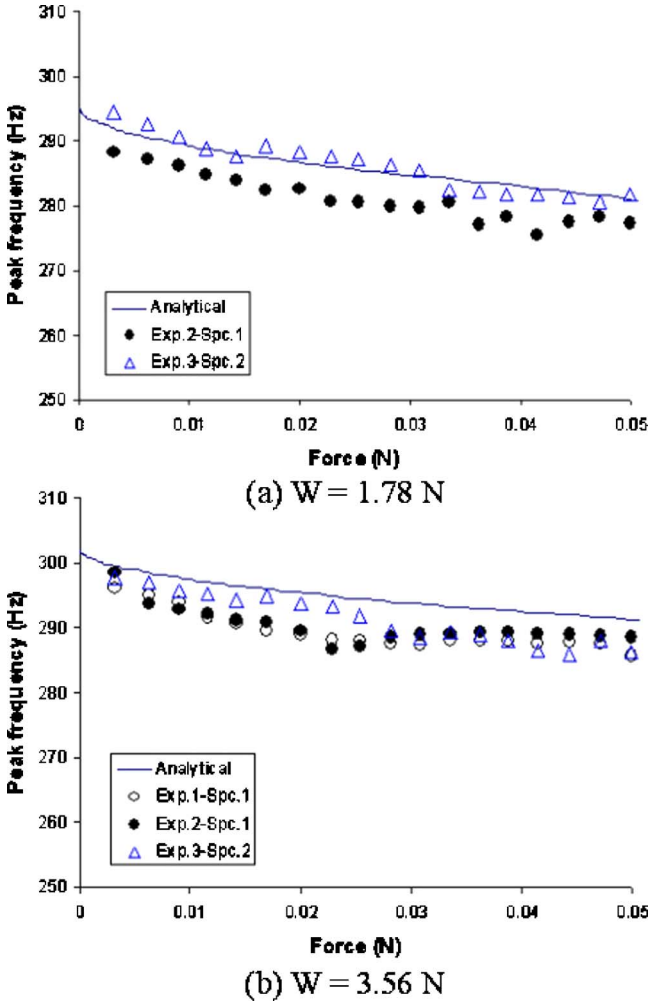

Fig. 14 Peak frequency comparison for 1.78 N and 3.56 N

reasonably good agreement between the vibratory response predicted by the theory and those measured in the experiments over a wide range of test conditions.

5 Conclusions

A set of benchmark experiments were conducted to measure the vibratory response of frictionally damped blades. In addition, an analytical approach was developed to predict the system's vibratory response. It was found that the performance of the damper could be predicted quite well using elasticity theory and contact mechanics—a result that has several implications.

One of the implications is that the effective stiffness of the spherical damper was significantly reduced because of very large local strain concentrations in the contact region that can be predicted by elasticity theory provided the local contact mechanics are correctly taken into account. Because of the local strain concentrations, the stiffness of the damper was a factor of 15–30 times smaller than the "bulk" stiffness of the damper that would be calculated if the local strain concentration were not taken into account. This may explain, at least qualitatively, why engineers in industry reported difficulties in correctly predicting the damper's stiffness [22,40].

The second implication is that the results of the vibration tests indicated that surface roughness does not significantly change the compliance of the friction interface. These results are consistent with the quasi-static tests reported in Ref. [28] and also those reported by O'Connor and Johnson in Ref. [26]. This is especially interesting since the normal loads are very light in the experiments reported here, and from Ref. [19] one would expect surface roughness effects to be even more important under these test conditions. Consequently, it is necessary to further examine the results reported by Panning et al. in Ref. [19]. They use a surface roughness correction factor for stiffness that reduces the stiffness to zero as the contact loads are reduced. This correction factor has a very similar behavior to that caused by the strain concentration reported here, see Eq. (2). The authors of the work reported here performed quasi-static tests on cylindrical dampers that have contact geometries similar to the pin dampers tested by Panning et al. The quasi-static tests were essentially the same as the ones reported for spherical dampers in Ref. [28] and discussed in the Sec. 1 of this paper. In this case, the stiffnesses of the cylindrical specimens were computed using a finite element analysis that took the nonlinear, Hertzian type contact into account. The experimentally measured values of damper stiffness agreed quite well with the values computed using finite elements and elasticity theory—without including surface roughness effects. Consequently, based on the experience reported in this paper, it would seem likely that the dynamic response of a cylindrical damper could also be predicted quite well without having to introduce a surface roughness stiffness reduction factor, provided sufficient care was taken in analyzing the local contact mechanics.[3]

Last, the results reported here may have a broader implication

[3]This might mean using an extremely small mesh in the finite element model or possibly using a substructuring technique to capture the local contact behavior.

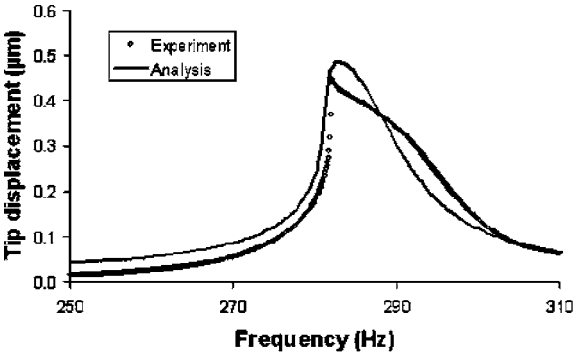

(a) Force=0.006 N

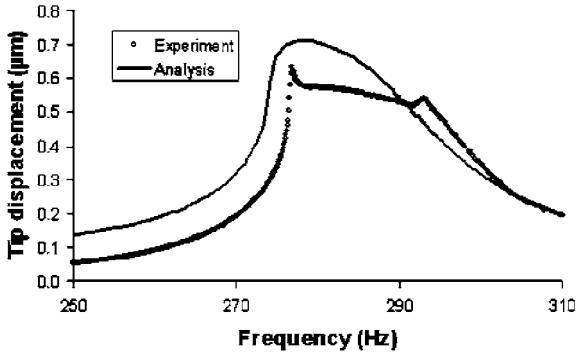

(b) Force=0.020 N

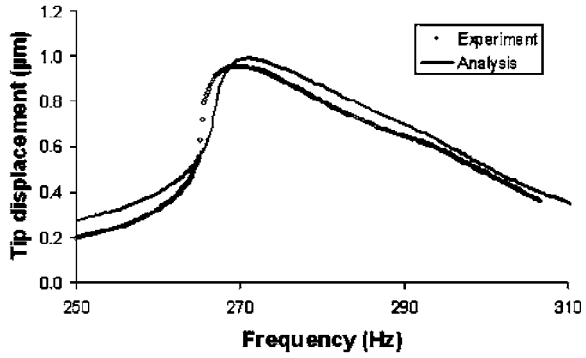

(c) Force=0.039 N

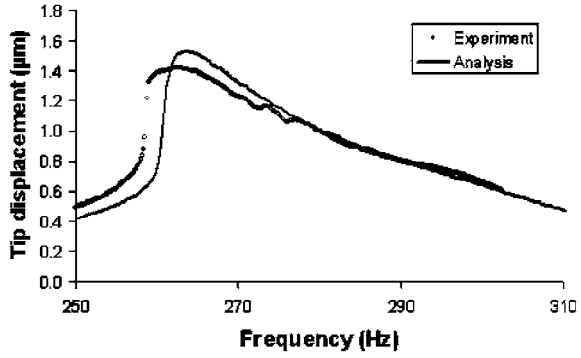

(d) Force=0.056 N

Fig. 15 Amplitude comparison between experiment and analysis for 0.89 N normal load

to other damper geometries. It is possible that similar very high local strain concentrations also occur in other damper geometries and that they may also significantly reduce the damper's effective stiffness. For example, the blade's platform may tend to preferentially load the corner of a wedge shaped damper during part of the vibration cycle. The corner loading could result in very similar local strain concentrations to those discussed here. The problem is far more complicated than that considered in this paper because the loading in a wedge damper is more difficult to define (the contacting surfaces may not be parallel and can change significantly because of the motions of the blades). This means that solving the wedge damper problem may require a broader, interdisciplinary approach in which local contact mechanics analyses are efficiently integrated with nonlinear dynamics.

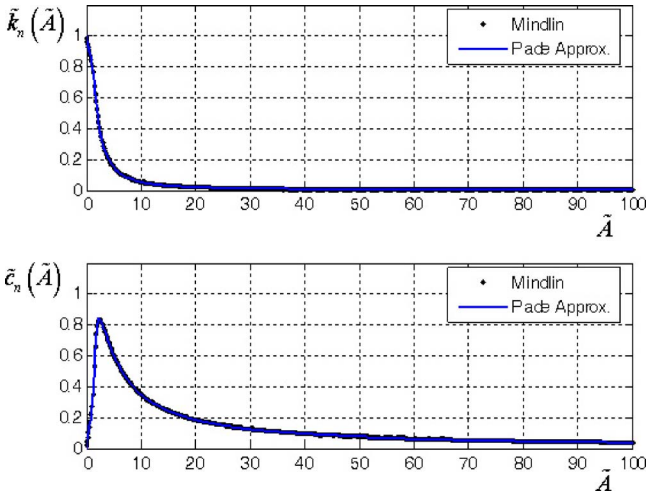

Fig. 16 Padé rational function approximation

Acknowledgment

This research was primarily supported by NAVAIR, Contract No. N00421-01-1-0001, under the direction of Mr. Mark Klein and was partially funded by AFOSR. The authors would like to acknowledge the stimulating discussions and suggestions provided by Dr. Daniel J. Segalman of Sandia National Laboratories.

Appendix: Padé Approximation of the Dimensionless Nonlinear Stiffness and Damping

A fourth order Padé rational function approximation was used to fit the numerically generated dimensionless nonlinear effective stiffness and damping curves for the case of a sphere in contact with a flat surface, Fig. 16. The dimensionless amplitude in the fit varied from 0 to 100. The Levenberg-Marquardt method was used for fitting the two curves. R-square values of 0.999994 and 0.999903 were obtained, respectively,

$$\tilde{k}_n(\tilde{A}) = \frac{a_1 + a_2\tilde{A} + a_3\tilde{A}^2 + a_4\tilde{A}^3 + a_5\tilde{A}^4}{a_6 + a_7\tilde{A} + a_8\tilde{A}^2 + a_9\tilde{A}^3 + a_{10}\tilde{A}^4} \tag{A1}$$

Table 2 Coefficients of $\tilde{A}$ in Eqs. (A1) and (A2)

$a_1=3.7583$	$b_1=-0.3351$
$a_2=-3.2563$	$b_2=14.4012$
$a_3=1.1010$	$b_3=-16.4449$
$a_4=0.0876$	$b_4=7.2881$
$a_5=-0.0004$	$b_5=0.0043$
$a_6=3.7619$	$b_6=45.6078$
$a_7=-2.7470$	$b_7=-41.0664$
$a_8=1.2190$	$b_8=15.8831$
$a_9=-0.4873$	$b_9=-3.9152$
$a_{10}=0.3349$	$b_{10}=1.9080$

$$\tilde{c}_n(\tilde{A}) = \frac{b_1 + b_2\tilde{A} + b_3\tilde{A}^2 + b_4\tilde{A}^3 + b_5\tilde{A}^4}{b_6 + b_7\tilde{A} + b_8\tilde{A}^2 + b_9\tilde{A}^3 + b_{10}\tilde{A}^4} \quad \text{(A2)}$$

where a_n and b_n $(n=1,2,\ldots 10)$ are listed in Table 2. The dimensionless amplitude $\tilde{A}=Ak_T/\mu N$ where A is the physical amplitude of the motion across the spherical contact, μ is the coefficient of friction, N is the normal load, and k_T is the stiffness caused by the high local strain concentration given by equation (2). The dimensionless stiffness k_n is equal to the effective nonlinear stiffness of the contact divided by k_T and the dimensionless damping $\tilde{c}_n$ is equal to $\pi c_n \omega/k_T$ where c_n is the effective nonlinear damping constant of the contact and ω is the frequency of the motion in radians/sec.

References

[1] Griffin, J. H., 1990, "A Review of Friction Damping of Turbine Blade Vibration," Int. J. Turbo Jet Engines, **7**, pp. 297–307.

[2] Yang, B.-D., 1996, "Contact Kinematics of Friction Interfaces and Applications to the Prediction of Resonant Response of Frictionally Constrained Turbine Blades (Damping)," Ph.D. thesis, The Ohio University, Columbus, OH.

[3] Yang, B. D., and Menq, C. H., 1997, "Modeling of Friction Contact and Its Application to the Design of Shroud Contact (96-GT-472)," J. Eng. Gas Turbines Power, **119**(4), pp. 958–963.

[4] Yang, B. D., and Menq, C. H., 1998, "Characterization of Contact Kinematics and Application to the Design of Wedge Dampers in Turbomachinery Blading: Part 1—Stick-Slip Contact Kinematics (97-GT-19)," J. Eng. Gas Turbines Power, **120**(2), pp. 410–417.

[5] Griffin, J. H., Wu, W. T., and El-Aini, Y., 1998, "Friction Damping of Hollow Airfoils: Part I—Theoretical Development (96-GT-109)," J. Eng. Gas Turbines Power, **120**(1), pp. 120–125.

[6] Griffin, J. H., and Menq, C. H., 1991, "Friction Damping of Circular Motion and Its Implications to Vibration Control," ASME J. Vibr. Acoust., **113**, pp. 225–229.

[7] Sanliturk, K. Y., Ewins, D. J., and Stanbridge, A. B., 2001, "Underplatform Dampers for Turbine Blades: Theoretical Modeling, Analysis, and Comparison With Experimental Data," J. Eng. Gas Turbines Power, **123**(4), pp. 919–929.

[8] Cha, D., and Sinha, A., 1999, "Statistics of Response of a Mistuned Bladed Disk Assembly Subjected to White Noise and Narrow Band Excitation," J. Eng. Gas Turbines Power, **121**(4), pp. 710–718.

[9] Cha, D., and Sinha, A., 2003, "Computation of the Optimal Normal Load of a Friction Damper Under Different Types of Excitation," J. Eng. Gas Turbines Power, **125**(4), pp. 1042–1048.

[10] Csaba, G., 1999, "Modelling of a Microslip Friction Damper Subjected to Translation and Rotation," ASME Paper No. 99-GT-149.

[11] Sextro, W., Popp, K., and Wolter, I., 1997, "Improved Reliability of Bladed Disks Due to Friction Dampers," ASME Paper No. 97-GT-189.

[12] Szwedowicz, J., Ravindra, B., Kissel, M., and Kellerer, R., 2001, "Estimation of Contact Stiffness and Its Role in The Design of a Friction Damper," ASME Paper No. GT2001-0290.

[13] Chen, J. J., and Menq, C. H., 2001, "Periodic Response of Blades Having Three-Dimensional Nonlinear Shroud Constraints," J. Eng. Gas Turbines Power, **123**(4), pp. 901–909.

[14] Chen, J. J., Yang, B. D., and Menq, C. H., 2000, "Periodic Forced Response of Structures Having Three-Dimensional Frictional Constraints," J. Sound Vib., **229**(4), pp. 775–792.

[15] Petrov, E. P., 2004, "Method for Direct Parametric Analysis of Nonlinear Forced Response of Bladed Disks With Friction Contact Interfaces," ASME J. Turbomach., **126**(4), pp. 654–662.

[16] Petrov, E. P., and Ewins, D. J., 2004, "Generic Friction Models for Time-Domain Vibration Analysis of Bladed Disks," ASME J. Turbomach., **126**(1), pp. 184–192.

[17] Petrov, E. P., and Ewins, D. J., 2003, "Analytical Formulation of Friction Interface Elements for Analysis of Nonlinear Multi-Harmonic Vibrations of Bladed Disks," ASME J. Turbomach., **125**(2), pp. 364–371.

[18] Panning, L., Popp, K., Sextro, W., Gotting, F., Kayser, A., and Wolter, I., 2004, "Asymmetrical Underplatform Dampers in Gas Turbine Bladings: Theory and Application," ASME Paper No. GT2004-53316.

[19] Panning, L., Sextro, W., and Popp, K., 2000, "Optimization of Interblade Friction Damper Design," ASME Paper No. 2000-GT-0541.

[20] Panning, L., Sextro, W., and Popp, K., 2002, "Optimization of the Contact Geometry Between Turbine Blades and Underplatform Dampers With Respect to Friction Damping," ASME Paper No. 2002-GT-30429.

[21] Panning, L., Sextro, W., and Popp, K., 2003, "Spatial Dynamics of Tuned and Mistuned Bladed Disks with Cylindrical and Wedge-Shaped Friction Dampers," Int. J. Rotating Mach., **9**(3), pp. 219–228.

[22] Ewins, D. J., and Griffin, J. H., 2001, "Workshop on the Modeling, Analysis, and Measurement of Friction Constraints in Gas Turbine Components," Final Rep. submitted to USAF, AFRL, AFOSR/NA, Award Number: F49620-01-1-0325.

[23] Sextro, W., 1999, "Forced Vibration of Elastic Structures With Friction Contacts," ASME Paper No. DETC99/VIB-8180.

[24] Sextro, W., 2000, "The Calculation of the Forced Response of Shrouded Blades with Friction Contacts and Its Experimental Verification," ASME Paper No. 2000-GT-0540.

[25] Sinclair, G. B., and Cormier, N. G., 2000, "Contact Stresses in Dovetail Attachments: Physical Modeling," ASME Paper No. 2000-GT-356.

[26] O'Connor, J. J., and Johnson, K. L., 1963, "The Role of Surface Asperities in Transmitting Tangential Forces Between Metals," Wear, **6**, pp. 118–139.

[27] Johnson, K. L., 1985, *Contact Mechanics*, Cambridge University Press, Cambridge, UK.

[28] Koh, K. H., Griffin, J. H., Filippi, S., and Akay, A., 2005, "Characterization of Turbine Blade Friction Dampers," ASME J. Eng. Gas Turbines Power, **127**(4), pp. 856–862.

[29] Filippi, S., Akay, A., and Gola, M. M., 2004, "Measurement of Tangential Contact Hysteresis During Microslip," J. Tribol., **126**(3), pp. 482–489.

[30] Mindlin, R. D., Mason, W. P., Osmer, T. F., and Deresiewicz, H., 1952, "Effects of an Oscillating Tangential Force on the Contact Surfaces of Elastic Spheres," *Proceedings of 1st U. S. National Congress of Applied Mechanics*, pp. 203–208.

[31] Cameron, T. M., Griffin, J. H., Kielb, R. E., and Hoosac, T. M., 1990, "An Integrated Approach for Friction Damper Design," ASME J. Vibr. Acoust., **112**, pp. 175–182.

[32] Menq, C. H., Chidamparam, P., and Griffin, J. H., 1991, "Friction Damping of Two-Dimensional Motion and Its Application in Vibration Control," J. Sound Vib., **144**, pp. 427–447.

[33] Menq, C. H., and Griffin, J. H., 1985, "A Comparison of Transient and Steady State Finite Element Analyses of the Forced Response of a Frictionally Damped Beam," ASME J. Vibr. Acoust., **107**, pp. 19–25.

[34] Ren, Y., and Beards, C. F., 1994, "A New Receptance-Based Perturbative Multi-Harmonic Balance Method for the Calculation of the Steady State Response of Non-Linear Systems," J. Sound Vib., **172**(5), pp. 593–604.

[35] Bonello, P., Brennan, M. J., and Holmes, R., 2004, "A Study of the Nonlinear Interaction Between an Eccentric Squeeze Film Damper and an Unbalanced Flexible Rotor," J. Eng. Gas Turbines Power, **126**(4), pp. 855–866.

[36] Budak, E., and Nevzat Ozguven, H., 1993, "Iterative Receptance Method for Determining Harmonic Response of Structures With Symmetrical Non-Linearities," Mech. Syst. Signal Process., **7**(1), pp. 75–88.

[37] Ren, Y., 1994, "Two Condensation Algorithms for the Receptance-Based Perturbative Multi-Harmonic Balance Method," J. Sound Vib., **170**(5), pp. 683–689.

[38] Grigoriev, I. S., and Meilikhov, E. Z., 1997, *Handbook of Physical Quantities*, CRC, Boca Raton, FL, pp. 145–146.

[39] Sullivan, J. F., 1988, *Technical Physics*, Wiley, New York, p. 204.

[40] Griffin, J. H., 1980, "Friction Damping of Resonant Stresses in Gas Turbine Engine Airfoils," J. Eng. Power, **102**, pp. 329–333.

Test Results and Analytical Predictions for Rotor Drop Testing of an Active Magnetic Bearing Expander/Generator

Lawrence Hawkins
e-mail: larry@calnetix.com

Alexei Filatov

Shamim Imani

Calnetix, Inc.,
Cerritos, CA 90703

Darren Prosser
Air Products,
Allentown, PA 18195

A cryogenic gas expander system that incorporates a high-performance, high-speed permanent magnet, direct-drive generator and low loss magnetic bearings is described. Flow loop testing to 30,000 rpm *was completed at the system manufacturer's facility in January 2005, and field installation is scheduled for October 2005. As part of the system testing, the rotor was dropped onto the backup bearings multiple times at an intermediate speed and at* 30,000 rpm*. Orbit and time-history data from a full speed drop and spin down are presented and discussed in detail. A transient, nonlinear rotordynamic analysis simulation model was developed for the machine to provide insight into the dynamic behavior. The model includes the dead band clearance, the flexible backup bearing support, and hard stop. Model predictions are discussed relative to the test data.*
[DOI: 10.1115/1.2436549]

Keywords: magnetic bearing, backup bearing, auxiliary bearing

Introduction

A direct drive expander/generator on active magnetic bearings (AMBs) has recently been developed which has the high-speed expansion turbine directly mounted onto the generator shaft. Expanders have been used for some time to provide refrigeration in industrial air separation plants. When the shaft energy is greater than 100 kW, economics have allowed energy recovery by driving a 50–60 Hz generator through a gearbox. The new system eliminates gearbox, maintenance, and support systems and allows economic energy recovery down to 10 kW. Furthermore, by incorporating AMBs, the system becomes a completely oil-free system that reduces the risk of accidental contamination of the process. The expander/generator module is shown in Fig. 1 with the nominal 114 mm (4.5 in.) expander wheel used for the initial prototype application. Up to 110 kW of refrigeration power will be consumed by the prototype expander which will be placed into service in an air separation plant in Europe. The expander/generator utilizes a permanent magnet (PM) generator and magnetic bearings contained within a high-pressure-capable housing. The generator has a conventional tooth type stator together with a two pole, high-strength steel sleeved rotor assembly. This arrangement is configured for minimum rotor losses and the cold temperatures the rotor may see in the cryogenic expansion process. The expander/generator rotor is supported by two PM bias, radial AMBs, and an anisotropic (load capacity in one direction is larger than the other direction), electromagnetic (EM) bias axial AMB. A duplex pair of angular contact backup bearings is located on each end of the machine.

The overall system design of the generator module, including the control system, and rotordynamics were discussed in Ref. 1. The design of the magnetic bearing actuators was described in Ref. 2. A necessary component of a magnetic bearing system for turbomachinery rotors is an auxiliary or backup bearing system. Backup bearings are typically ball bearings, but bushings are also sometimes used in low-cost, lightweight machines. The backup bearings provide support for the rotating assembly when the magnetic bearing system is deactivated. Also, in the event of a failure of some component of the magnetic bearings or in the event of an overload of the magnetic bearings, the backup bearings provide rotor support. In normal operation, the backup bearings are not active as they will have a small radial clearance to the rotating assembly. This clearance is typically less than one-half of the magnetic bearing air gap. The backup bearings in this machine, duplex pairs of angular contact ball bearings, are supported in resilient mounts with a hard stop to limit radial deflection.

A typical certification test for a backup bearing system is to intentionally deactivate the magnetic bearings at operating speed, causing the rotor to drop onto the backup bearings and spin down to rest. There is a substantial body of work in the open literature that investigates the dynamics of AMB rotors in backup bearings. Kirk [3] presented a detailed nonlinear analysis for a rotor dropped into backup bearings. Hawkins [4] developed a rotordynamic simulation that included a nonlinear magnetic bearing saturation model as well nonlinear backup bearing clearance effects to analyze shock response in a magnetic bearing system. Cuesta [5] presented an analysis that included a kinematic impact model and compared the predictions to test data on a small test rig. Keogh [6] has been studying control schemes that improve magnetic bearing performance during auxiliary bearing contact due to temporary overload. Several authors have described full five axis drop tests for test rigs or for machines intended for industrial service. Kirk [7] and Swanson [8] have presented numerous test results and analysis from a full scale, AMB rotor drop test stand. Schmeid and Pradetto [9] presented drop test results for a 8.9 kN (1 t) compressor rotor. Caprio [10] presented results for drop testing on a large, vertical energy storage flywheel. However, all of these drop tests are for machines considerably heavier and slower than the expander/generator described here, and all but Ref. 10 are for EM bias magnetic bearings. The backup system for the new expander/generator was tested by completing ten full drops and spin downs from 23,000 rpm and ten full drops and spin downs from 30,000 rpm. Position orbit data and time–history data from one of the full speed drops are presented here. A nonlinear simulation analysis was developed to help interpret the results and to

Contributed by the International Gas Turbine Institute of ASME for publication in the JOURNAL OF ENGINEERING FOR GAS TURBINES AND POWER. Manuscript received June 15, 2006; final manuscript received September 14, 2006. Review conducted by Lee Langston. Paper presented at the ASME Turbo Expo 2006: Land, Sea and Air, Barcelona, Spain, May 8–11, 2006, Paper No. GT2006-90283.

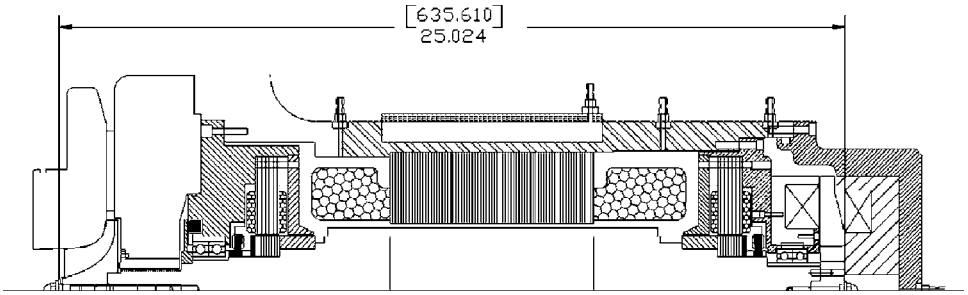

Fig. 1 Crosssection of expander generator with nominal 114 mm (4.5 in) wheel

estimate the loads reacted by the backup bearings. The results of this analysis are discussed relative to the test data.

Backup Bearing Design

The backup bearing system for the expander generator consists of two pairs of duplex, face-to-face, angular contact ball bearings. The bearing pair on the expander end of the machine provides backup in both thrust and radial directions (Fig. 2). Both bearing pairs had a light preload, factory set by grinding the inner and outer race end faces to achieve a precise offset which results in a preload when the bearing pair is locked together. The key parameters for the backup bearing design are summarized in Table 1. The bearings are hybrid ceramic, with conventional SAE 52100 steel races and SiN3 balls. Brass landing sleeves on the rotor provide a nonsparking touchdown surface on the shaft, a requirement for some of the potential applications of the generator/expander unit. The radial backup bearing clearance is nominally 0.09 mm (0.0035 in.). The clearance is atypically small, 17.5% of magnetic air gap, to accommodate clearance requirements of the expander wheel. Both backup bearing pairs are mounted in a resilient mount which reduces the support stiffness to 1.3E7 N/m (75,000 lbf/in.). Compliance in the machined metal mount is achieved using tangential spring arms that have a slip fit into the housing. The mount is intended to serve several purposes: (1) reduce the synchronous reaction forces during a critical speed traverse (by lowering the forward natural frequency); (2) reduce the impact force during a drop down event; and (3) reduce the whirl frequency (by lowering the lowest support natural frequency).

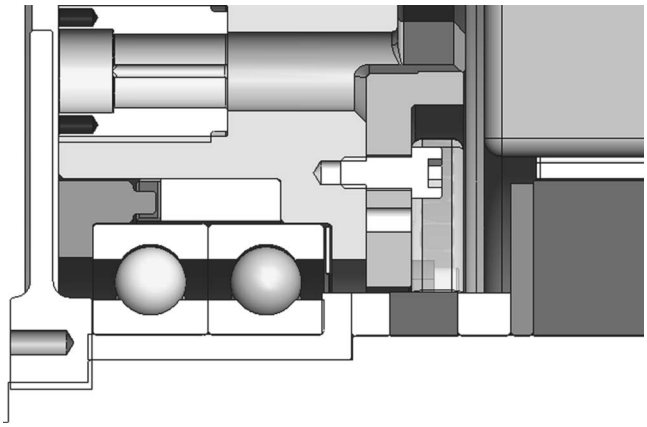

Fig. 2 Crosssection showing radial/thrust backup bearing

Table 1 Rotor and backup bearing parameters

Nominal spin speed, rpm	30,000
Rotor mass, kg (lbm)	29.0 (63.9)
Polar inertia kg m^2 (lbm $in.^2$)	0.039 (133)
Transverse inertia kg m^2 (lbm $in.^2$)	0.718 (2448)
Distance from expander end backup bearing to CG mm (in.)	251 (9.90)
Backup bearing span, mm (in.)	472 (18.59 in.)
AMB passive negative stiffness, each bearing, N/m (lbf/in.)	1.93E6 (11,000)
Bearing bore, mm	55
Expander end	45
Nonexpander end	
Bearing preload, N (lbf)	315 (71)
Expander end	230 (52)
Nonexpander end	
Backup bearing radial clearance, mm (in.)	0.09 (0.0035)
Resilient mount stiffness, Nm (lbf/in.)	1.3E7 (75,000)
Hard stop radial clearance, mm (in.)	0.127 (0.005)
Rotor sleeve material	Lead bronze

The resilient mount also contributes light friction damping through slipping at the interfaces of the mount and the housing. The requirements listed above drive the design toward low stiffness values; however, the lower bound on stiffness is set by the maximum radial displacement allowed by critical clearances in the machine. In particular, peak deflection during the drop or impact transient must be considered as well as the static sag on the backup bearings. This is particularly important in turbomachinery where it is desired to keep design clearances between the impeller and shroud as small as possible.

In this machine, the allowable travel on the resilient mount is restricted to a minimum of 0.038 mm (0.0015 in.) radial. Beyond that, the resilient mount is bypassed by contact between the bearing outer race and the housing, resulting in the much stiffer support stiffness of the duplex bearing pair in series with the housing. A design choice was made to set the minimum stiffness for the resilient mount by limiting the static sag to half of the minimum travel, or 0.019 mm (0.00075 in.). This sets a lower bound on stiffness of 7900 N/mm (45,000 lbf/in.) at each end of the machine for the 29 kg (64 lbf) rotor. The support stiffness from the mount is somewhat asymmetric, having the same stiffness in orthogonal axes, but a softer value inbetween. The influence of equivalent backup bearing stiffness on the critical speeds is shown by the undamped critical speed map in Fig. 3. The analysis includes constant values for the permanent magnet bias negative stiffness at the magnetic bearing actuator locations. With the target mount stiffness of 1.3E7 N/m, the lowest rigid body critical speed is 8000 rpm (133 Hz).

Backup Bearing Rotor Drop Testing

The backup system was tested by completing ten full drops and spin downs from 23,000 rpm and ten full drops and spin downs from 30,000 rpm (full speed). All of the drop transients are of short duration, because the system control is configured to brake the rotor quickly to rest in the event of an alarm condition. This is done by closing the inlet slam valve to the expander, thus remov-

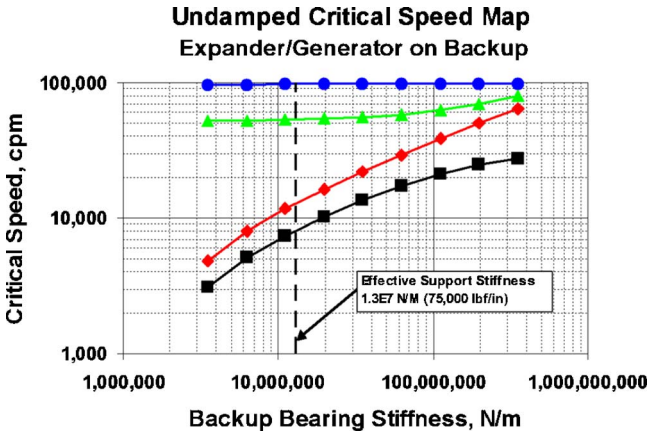

Fig. 3 Undamped critical speed map for the rotor supported at the backup bearings

ing the driving source. The generator is then loaded with a resistor bank located in the control cabinet which pulls the machine speed from 30,000 rpm to rest in about 10 s.

The position data from one of the 30,000 rpm drops is shown in Figs. 4–6. The data was collected by the logging feature of the magnetic bearing controller. This feature automatically writes position sensor and current command data to synchronous RAM when triggered by a delevitation or an alarm condition. The position sensors are between the magnetic bearings and backup bearings and provide a good estimate of the relative shaft/housing motion at the backup bearings. The radial bearing (and sensor) axes are oriented at 45 deg to the vertical to share gravity load between the two bearing axes. The configuration of the data acquisition, which was set up to accommodate a wide range of needs during commissioning, allowed a data set length of 6 s at a 1750 Hz sample rate. Although this sample rate is somewhat marginal for recording synchronous motion, it provides excellent fidelity for the largely rigid body motions during the rotor drop.

Figure 4 shows the radial displacement amplitude at the expander end bearing and the spin speed versus time. Considering the radial position data, the delevitation event occurs at about 1.28 s (there is a 1.28 s pretrigger on the data acquisition). The speed drops slightly due to the added drag from the backup bearings and then recovers. The slam valve closes at about 2.5 s, removing the driving source and allowing the generator to pull the speed down to zero. The delay between the drop and the shutdown occurs because the drive enable (alarm) signal from the magnetic bearing has a 1.0 s delay to avoid nuisance trips. The 6 s record length setting for the internal data acquisition allowed data recording only down to 16,000 rpm.

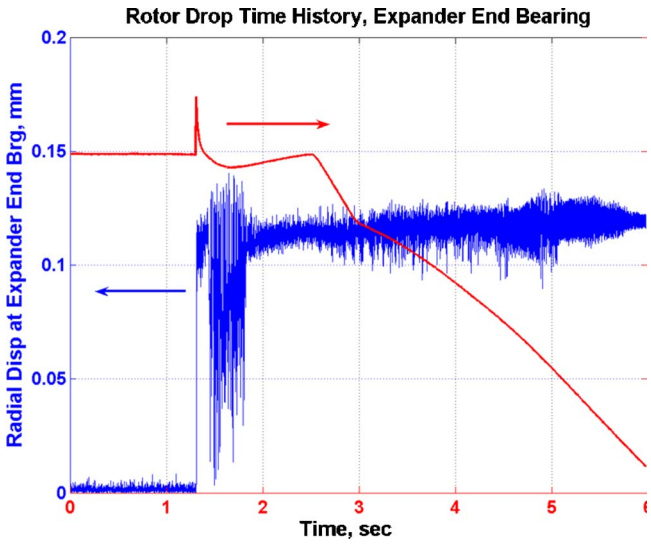

Fig. 4 Displacement and speed versus time during rotor drop and spin down

Orbit plots for three different time slices are shown in Fig. 5. The positive coordinate axes are 45 deg to either side of the vertical. The time slice from 1.28 s to 1.43 s, (Fig. 5(*a*)), shows the drop transient. After hitting the backup bearing, the rotor bounces several times while remaining in roughly the same spot on the bearing. The bearing inner race should be spinning up toward the rotor speed during this period. Just after 1.43 s the rotor goes into a whirl for about 0.4 s as shown in the time slice from 1.43 s to 1.83 s (Fig. 5(*b*)). This whirl motion is somewhat elliptical due to the asymmetry of the resilient mount. The rotor then settles down to a rocking oscillation at the bottom of the backup bearing for the remainder of the time record (1.83–6 s shown in Fig. 5(*c*)). In several other drop tests (data not shown), the rotor took on a rocking motion at the bottom of the bearing just after the initial drop, followed by the same short duration circular whirl observed in Fig. 5(*b*).

Expanded time histories from the orthogonal x and y position sensors are shown in Fig. 6. The rotor spin vector is along the positive z coordinate so for forward circular whirl, x would lead y by 90 deg. Figure 6(*a*) shows the time–history data from 1.28 s to 1.43 s. From this perspective it can be seen that the rotor bounces at about 125 Hz after it hits the backup bearing. Figure 6(*b*) shows the time slice from 1.4 s to 1.6 s when the rotor is executing a roughly circular whirl around the backup bearing clearance space. The whirl is forward whirl as the x signal leads the y signal. Forward whirl observations have been reported by numerous authors [5,8–10]. The x signal clearly has a longer period on the positive half cycles compared to the negative half cycles. This probably happens because in the negative direction, the combined static weight and dynamic load compress the resilient mount to the hard (stiff) stop. In the positive direction, the spring is not fully compressed and the rotor spends part of the cycle in the clearance space. A Fourier transform of the signal during the full whirl shows the dominant frequency is 82 Hz, with a much smaller 110 Hz component.

Figure 6(*c*) shows a time slice from 3.2 s to 3.9 s during the spin down when the rotor was rocking at the bottom of the backup bearing. In this time slice the rocking frequency is initially 50 Hz and then switches to about 110 Hz around 3.7–4.0 s when the rotor speed is near 24,000–22,000 rpm. At lower speeds, the rotor seemed to switch back and forth periodically between and 50 Hz and 110 Hz. The 50 Hz motion can be explained by assuming that the rolling element bearings allow the rotor rigid body to effectively slip along the arc of the backup bearing inner race. This is the motion of a simple pendulum which for a small rocking angle has a natural frequency, f_n of

$$f_n = \sqrt{\frac{g}{r}}\frac{1}{2\pi}\text{Hz} \tag{1}$$

where g is the gravitational constant (9.81 m/s^2), and r is the radius of the rocking motion. Given that the effective rocking radius, the backup bearing clearance plus static deflection, is about 0.11 mm (0.0042 in.), Eq. (1) predicts a natural frequency of 48 Hz, very close to the measured value. It is possible that the 110 Hz motion is due to a rocking mode with the two ends of the rotor out of phase, however, the data show a phase difference of less than 45 deg between the two ends of the rotor throughout the spin down. It is more likely that the 110 Hz is a transient response of the lowest rigid body mode of the rotor on the resilient mounts.

After completion of testing, the bearings were disassembled and inspected and found to be in reusable condition. There was no evidence of Brinell damage that would have indicated excessive

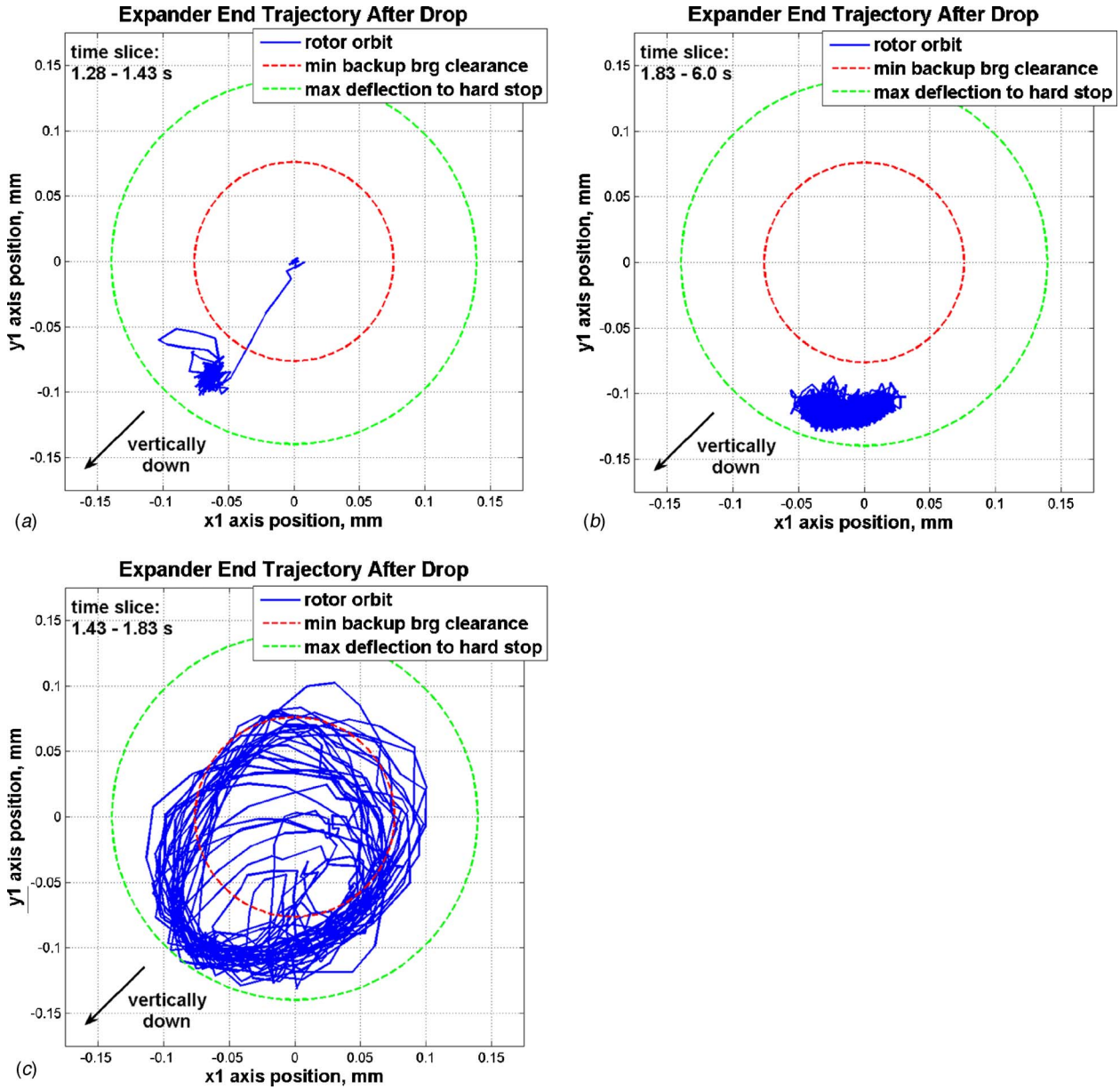

Fig. 5 Displacement orbit at expander end during rotor drop and spin down: (*a*) 1.28–1.43 sec; (*b*) 1.43–1.83 sec; and (*c*) 1.83–6.0 sec

impact loading. The measured hardness values for the races were within factory specification of 58.5–61 Rockwell C, indicating that the races temperatures remained well below the 204°C (400°F) annealing threshold. There was evidence of minor slipping on the races of the inboard bearing of the expander end pair. This bearing can be unloaded during a touchdown if the thrust load is high enough. Higher preload could prevent this but was traded off against margin for thermal growth in the design.

Nonlinear Rotor Drop Simulation

A nonlinear, simulation model for the rotor/housing/backup bearing system was developed to investigate several aspects of the data and the design, and to determine: (1) the bearing loads during the whirling and rocking phases of the motion, and (2) the influence of rotor balance quality on the rocking and whirling motions. The simulation was performed using an analysis tool previously described [4]. In this analysis, the rotordynamic equations of motion for a coupled rotor/casing system represented in second-order form are

$$[M]\{\ddot{\mathbf{q}}\} + [C]\{\dot{\mathbf{q}}\} + [K]\{\mathbf{q}\} = \{\mathbf{f}\} \tag{2}$$

where M, C, K, represent the mass, damping, and stiffness matrices for a coupled rotor housing system, and $\mathbf{q}$ is a vector of physical displacements. Nonlinear and time dependent forces are applied as part of the external force vector, $\mathbf{f}$. Equation (2) is integrated through time using the Newmark-β algorithm. This formulation allows simulation modeling of backup bearings with large clearance, friction during inner race spinup, bearing mount flexibility, and a hard stop to limit radial displacement on the mount. This approach has been used extensively by the author to model rotor drop events onto backup bearings.

A weakness of the simulation tool is that it does not currently have a sophisticated impact contact model; therefore it cannot be

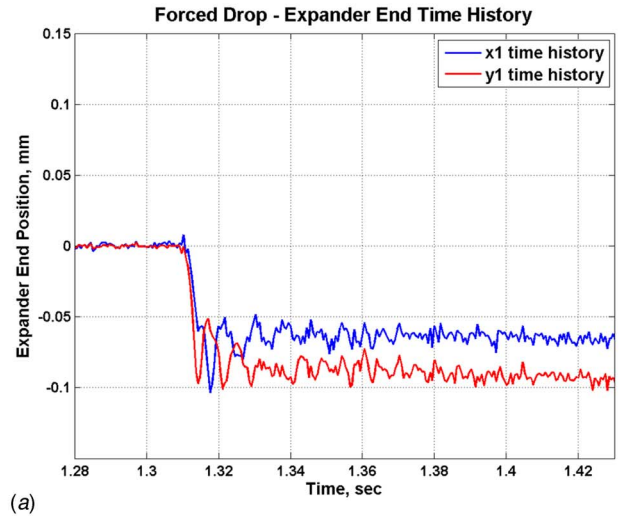

(*a*)

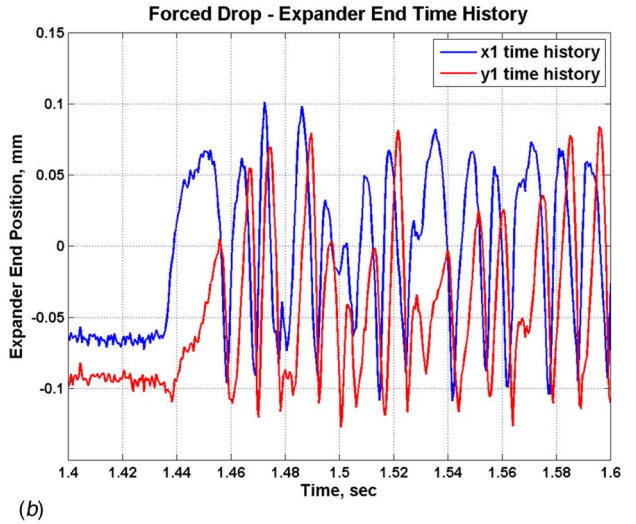

(*b*)

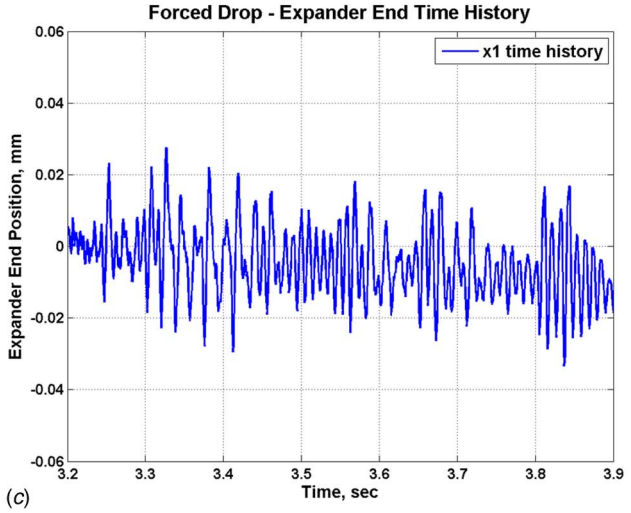

(*c*)

Fig. 6 Displacement time history at expander end: (*a*) 1.28–1.43 sec; (*b*) 1.4–1.6 sec; (*c*) 3.2–3.9 sec

used to make accurate estimates of loads and dynamics just after impact. Therefore, the focus of the simulations reported here is on other aspects of the backup bearing drop. This is not to minimize the importance of the drop transient as drop impact loads can be large enough to cause Brinnell damage and early failure, particularly in machines with hard mounted backup bearings. Resiliently mounting the backup bearings, as in the expander/generator studied here, will reduce the impact loads. As mentioned above, the post-test inspection of the bearings showed no impact damage.

The system model that was created included the flexible rotor model, an axisymmetric housing model that provides a good approximation of the total mass and mass distribution of the housing, a backup bearing model, and the magnetic bearing. The housing was connected to ground at the impeller end mounting flange using vertical and horizontal shear and moment springs. The spring values were selected so that the lowest measured natural frequencies (85 Hz horizontal and 195 Hz vertical) were predicted. The nominal bearing model includes a 0.09 mm (0.0035 in.) radial clearance space, a linear stiffness of 1.3E7 N/m (75,000 lbf/in.), and no tangential friction between the bearing inner race and the shaft. A hard stop in parallel with the resilient mount has a radial clearance space of 0.127 mm (0.005 in.) and stiffness of 8.8E7 N/m (500,000 lbf/in.). The magnetic bearings were included in the model for preliminary runs to establish initial conditions for the drop analysis. Those initial conditions are used for all of the simulation runs reported here, but the magnetic bearing control force is zeroed at the beginning of the run, so the rotor drop occurs at time zero ($t=0$ s) for all reported results. The magnetic bearing actuators used in this machine have a permanent magnet bias so the passive radial negative stiffness of 1.9E6 N/m (11,000 lbf/in.) per bearing remains in the model at the magnetic bearing actuator locations even after the drop. The nominal unbalance was 12.7 gm mm (0.5 gm in.) at the impeller and 25.4 gm mm (1.0 gm in.) at the axial magnetic bearing disk. The static weight of the rotor (285 N/63.9 ibf) and housing (6681 N/1498 ibf) are applied as separate distributed loads calculated by multiplying the mass matrix by the gravitational acceleration constant. Gravity acts in the negative y direction in the model.

Figures 7–10 show predicted results for rotor drop simulations at a spin speed of 30,000 rpm. The presented results are all for the expander end touchdown bearing. The displacement orbit during and after the drop for the nominal model is given in Fig. 7(*a*). The rotor bounces a number of times and then settles into a rocking motion covering about 110 deg at the bottom of the bearing. This behavior is a reasonable simulation of the actual rotor motion in its rocking phase (see Fig. 5(*c*)). The Fourier transform of this motion in Fig. 7(*b*) shows that the motion is mostly at 45 Hz, with much smaller response at 90 Hz and the 500 Hz spin frequency. The 45 Hz motion is in good agreement with the measured data and the fundamental pendulum calculation in Eq. (1). The bearing load magnitude and phase, Fig. 7(*c*), show that the load has a number of impact peaks up to 1784 N (400 lbf), but is generally below 446 N (100 lbf). The rms value of the load is 415 N (93 lbf). This predicted load is shared between the duplex bearing pair, and is carried largely by the resilient mount, with the hard stop coming into play intermittently.

In order to investigate the loads in a whirling condition, additional unbalance was added to the rotor model in several steps. Other authors [5,7] have suggested that the tendency to full whirl should increase as the unbalance force approaches the rotor weight. The unbalance values used and the subsequent ratio of unbalance to the rotor weight at 30,000 rpm are given in Table 2, where G=rotor weight (285 N). The unbalance force is a vector sum of the two applied unbalances. Unbalance is applied at the impeller and thrust disk because those two components were balanced as components and installed on the balanced generator rotor. The nominal unbalance, Case 1, reflects the estimated unbalance based on operation on the magnetic bearings. The additional unbalance for Cases 2–4 was added to the thrust disk because this component is significantly heavier than the impeller and would produce the largest unbalance from relocation error.

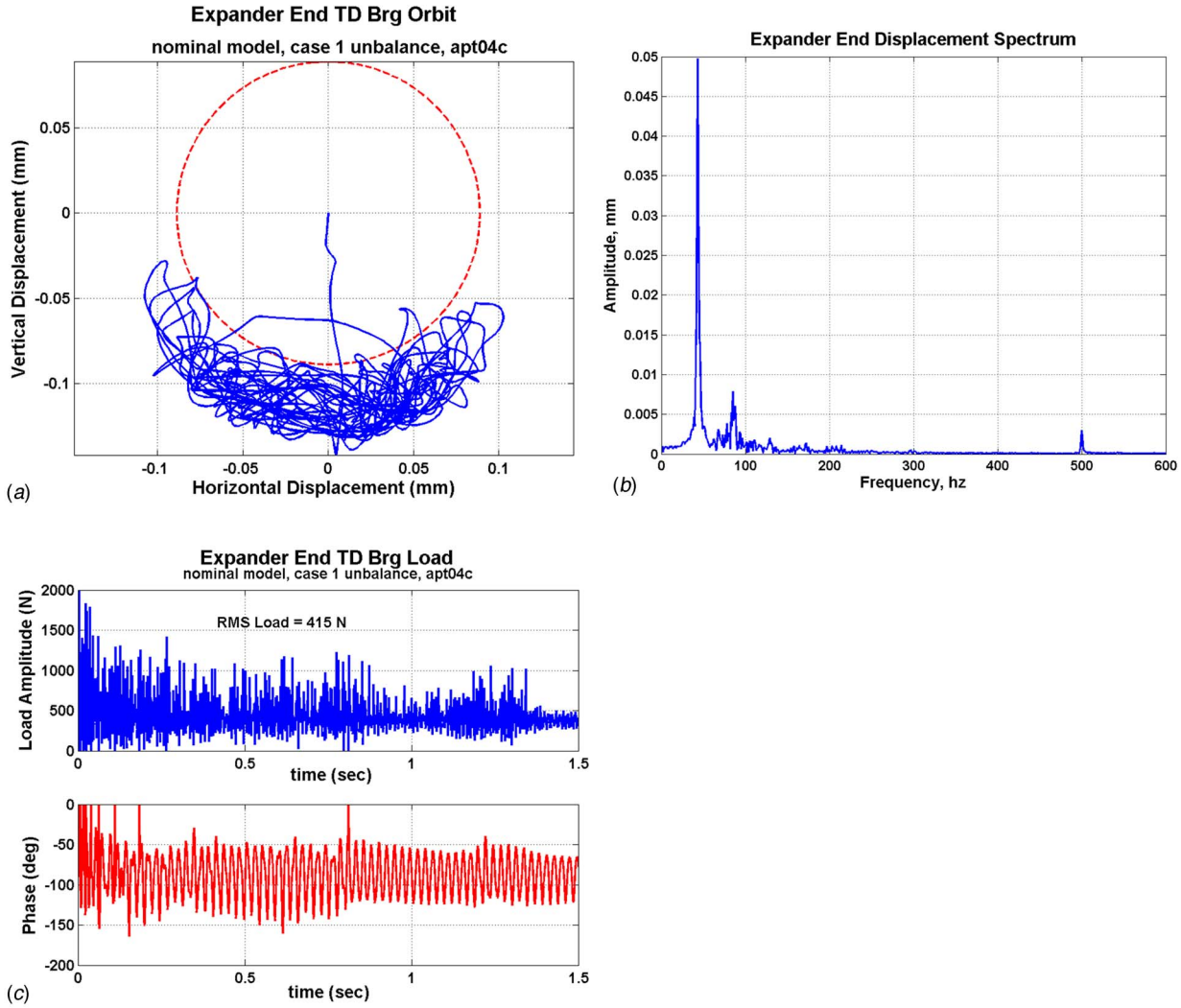

Fig. 7 Predicted drop response for nominal model: (*a*) orbit at expander end; (*b*) Fourier transform of *x* axis; and (*c*) expander end backup brg load mag and phase

Figure 8 shows the predicted displacement orbit for unbalance Case 2. The rotor still rocks at the bottom of the bearing, but the rocking motion now approaches a 180 deg arc. The rocking frequency is still dominated by 45 Hz, but there is also a significant component at 90 Hz. The predicted orbit for unbalance Case 3, (Fig. 9), shows the rotor bouncing in and out of the clearance space, occasionally executing full whirl cycles. The dominant frequency is 125 Hz which is approximately the expected lowest rigid body mode on the resilient mount. The result for the largest analyzed unbalance, Case 4, is shown in Fig. 10. The predicted whirl orbit predominately circles the clearance space, with occasional excursions into the clearance space. The dominant frequency is 130 Hz and there is a substantial component at the 500 Hz spin frequency. These results certainly indicate that increasing the level of unbalance pushes the rotor from a rocking orbit to a full orbit. To predict the threshold of whirl, additional unbalance cases were run where the unbalance was progressively increased from the Case 2 value. An unbalance level of 1.95 G was required before the simulation began predicting full whirl. The predicted whirl threshold so much greater than 1.0 G must be partly due to the permanent magnet negative stiffness. With the rotor at the bottom of the backup bearing the additional downward force from the negative stiffness is slightly greater than the rotor weight (1.2 G). In a simulation using the Case 2 unbalance with no negative stiffness, a larger angle rocking motion was predicted compared to Fig. 8, but full whirl still was not predicted. Additional factors are: (1) that most of the unbalance is applied at the end of the rotor, at the thrust disk, instead of at the centerofgravity; and (2) relative proximity of the spin frequency to system natural frequencies should impact the onset of the whirl condition.

The loads predicted for the different unbalance cases are summarized in Table 3. The rms load certainly increases as the rotor approaches full whirl, but this would happen with these changes in balance quality even without the large clearance space. Even with the worst balance case analyzed, the predicted loads are not unreasonable for the duplex pair of backup bearings. However, a correlation of the observed synchronous orbit on magnetic bearings with the rotordynamic model suggests that it is unlikely that the balance quality relative to the backup bearing journals is any worse than the milder Case 2 unbalance. Additional simulations show that for the Case 3 and Case 4 unbalance, the full whirl should be sustained down to about 5000 rpm. So it is not clear what causes the rotor to execute a brief forward whirl sometime after the initial drop followed by a return to a rocking motion. In some simulation runs, a coefficient of friction of 0.1 was included at the inner race/shaft contact point to try to produce whirl at a lower unbalance level, but there was not a substantial change in the result. Two other factors that might affect the whirl behavior

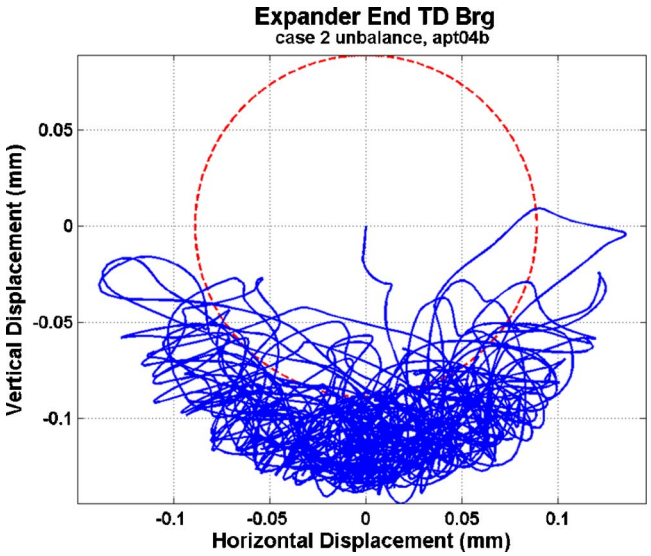

Fig. 8 Predicted displacement orbit for unbalanced Case 2

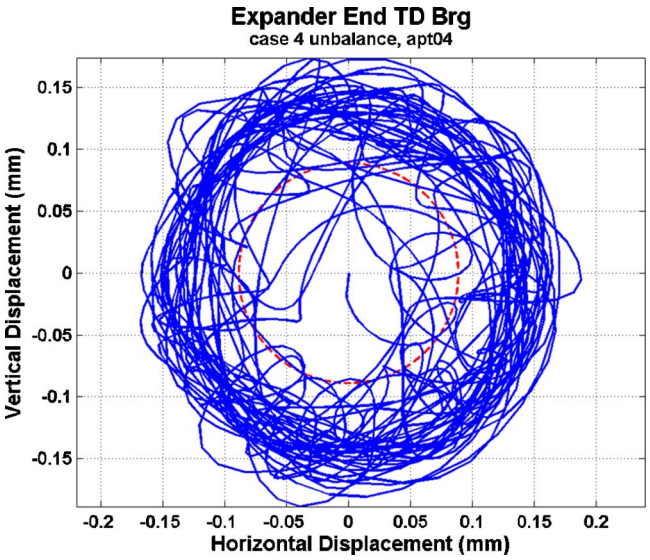

Fig. 10 Predicted displacement orbit for unbalanced Case 4

that may not be well characterized in the simulation are support stiffness asymmetry and damping or other energy dissipation factors.

Conclusions

Backup bearing rotor drop testing was successfully conducted for an AMB supported expander/generator. The test results were presented and discussed. Results from a nonlinear simulation of the drops were presented and discussed as follows:

1. The measurements show a brief period of forward whirl, shortly after touchdown, followed by a rocking motion at the bottom of the backup bearings during the spin down.
2. The simulation analysis shows that as the unbalance level increases, the expected rotor motion in the backup bearings should transition from a rocking motion to full whirl. This doesn't seem to explain the brief full whirl of the rotor in this machine, since the simulation predicts that full whirl motion should be sustained down to 5,000 rpm, whereas the data show only a brief whirl period. Weaknesses in characterizing unbalance distribution, stiffness asymmetry, and energy dissipation factors in the simulation model may be at fault.
3. The simulation predicts that the bearing reaction loads do not go up in a marked way after transition from rocking to full whirl, other than that implied by the increased unbalance.
4. The measured rocking frequency of 50 Hz is correctly predicted by assuming the rocking motion is the motion of simple pendulum. The nonlinear simulation also predicts the same rocking frequency for a well balanced rotor.

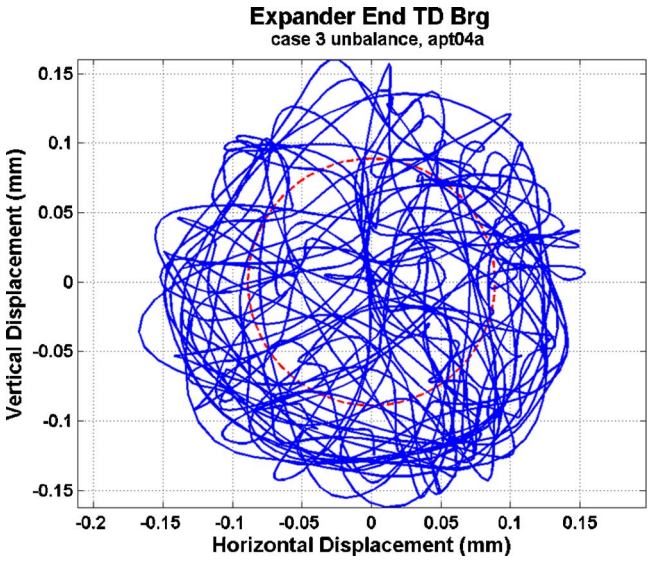

Fig. 9 Predicted displacement orbit for unbalanced Case 3

Table 2 Unbalance cases

	Unbalance (gm mm)		
Case	Impeller (0 deg)	Thrust disk (90 deg)	*G* @ 30 krpm
1	12.7	25.4	0.98
2	12.7	50.8	1.81
3	12.7	127.0	4.42
4	12.7	254.0	8.81

Table 3 Predicted loads for different unbalance cases

Case	RMS load *N* (lbf)	Peak load *N* (lbf)
1	415 (93)	1784 (400)
2	455 (102)	2230 (500)
3	1227 (275)	6690 (1500)
4	2163 (485)	9812 (2200)

References

[1] Hawkins, L., Imani, S., Prosser, D., and Johnston, M., 2004, "Design and Shop Testing of a 165 kW Cryogenic Expander/Generator on Magnetic Bearings," *Proc. 9th International Symposium on Magnetic Bearings*, Lexington, KY, August 3–6, Paper 60.

[2] Filatov, A., McMullen, P., Hawkins, L., and Blumber, E., 2004, "Magnetic Bearing Actuator Design for a Gas Expander Generator," *Proc. 9th Interna-*

tional Symposium on Magnetic Bearings, Lexington, KY, August 3–6, Paper 81.
[3] Kirk, R. G., Raju, K. V. S., and Ramesh, K., 1997, "Modeling of AMB Turbomachinery for Transient Analysis," *Proc. MAG 97*, Alexandria, VA, August 21–22, pp. 139–153.
[4] Hawkins, L. A., 1997, "Shock Analysis for a Homopolar, Permanent Magnet Bias Magnetic Bearing System," ASME Paper No. 97-GT-230.
[5] Cuesta, E. N., Montbrun, N. I., Rastelli, V., and Diaz, S. E., 2005, "Simple Model for a Magnetic Bearing System Operating on the Auxiliary Bearing" ASME Paper No. GT-2005–69013.
[6] Keogh, P., Cole, M., Sahinkaya, N., and Burrows, C., 2002, "On the Control of Synchronous Vibration in Rotor/Magnetic Bearing Systems Involving Auxiliary Bearing Contact," ASME Paper No. GT-2002–30292.
[7] Kirk, R. G., Swanson, E. E., Kavarana, F. H., Wang, X., and Keesee, J., 1994, "Rotor Drop Test Stand for AMB Rotating Machinery, Part I: Description of Test Stand and Initial Results," *Proc. 4th International Symposium on Magnetic Bearings*, ETH Zurich, August 23–26, pp. 207–212.
[8] Swanson, E. E., Kirk, R. G., and Wang, J., 1995, "AMB Rotor Drop Initial Transient on Ball and Solid Bearings," *Proc. MAG 95*, Alexandria, VA, August 10–11, pp. 207–216.
[9] Schmied, J., and Pradetto, J. C., 1992, "Behavior of a One Ton Rotor Being Dropped Into Auxiliary Bearings," *Proc. 3rd International Symposium on Magnetic Bearings*, Alexandria, VA, July 29–31, pp. 145–156.
[10] Caprio, M. T., Murphy, B. T., and Herbst, J. D., 2004, "Spin Commissioning and Drop Tests of a 130 kW-hr Composite Flywheel," Proc. 9th International Symposium on Magnetic Bearings, Lexington, KY, Paper 65.

Experimental Investigation of Mode Shape Sensitivity of an Oscillating Low-Pressure Turbine Cascade at Design and Off-Design Conditions

Damian M. Vogt
e-mail: damian.vogt@energy.kth.se

Torsten H. Fransson

Chairs of Heat and Power Technology,
Royal Institute of Technology,
S-100 44 Stockholm, Sweden

The effect of negative incidence operation on mode shape sensitivity of an oscillating low-pressure turbine rotor blade row has been studied experimentally. An annular sector cascade has been employed in which the middle blade has been made oscillating in controlled three-dimensional rigid-body modes. Unsteady blade surface pressure data were acquired at midspan on the oscillating blade and two pairs of nonoscillating neighbor blades and reduced to aeroelastic stability data. The test program covered variations in reduced frequency, flow velocity, and inflow incidence; at each operating point, a set of three orthogonal modes was tested such as to allow for generation of stability plots by mode recombination. At nominal incidence, it has been found that increasing reduced frequency has a stabilizing effect on all modes. The analysis of mode shape sensitivity yielded that the most stable modes are of bending type with axial to chordwise character, whereas high sensitivity has been found for torsion-dominated modes. Negative incidence operation caused the flow to separate on the fore pressure side. This separation was found to have a destabilizing effect on bending modes of chordwise character, whereas an increase in stability could be noted for bending modes of edgewise character. Variations of stability parameter with inflow incidence have hereby found being largely linear within the range of conditions tested. For torsion-dominated modes, the influence on aeroelastic stability was close to neutral. [DOI: 10.1115/1.2436567]

Introduction

The designing and maintaining of flutter-free gas turbine engines remains one of the paramount challenges for engine manufacturers. Flutter denotes a self-excited and self-sustained instability phenomenon that might lead to structural failure in a short period of time unless properly damped. To predict eventual occurrences of flutter during engine operation, it is necessary to accurately assess the unsteady aerodynamics during flutter and its mutual effects on the structure. The recent advances in computational fluid dynamics now allow predicting unsteady aerodynamics of vibrating turbomachine components at a high degree of detailing and in a reasonable amount of time. Unless validated, reliable application of the existing tools can, however, not be guaranteed. Despite the experimental efforts made during the last several decades, a need for detailed validation data that are acquired on realistic geometries and at design and off-design conditions is expressed throughout the aeroelastic research community.

Commonly, turbomachine flutter test data are acquired in simplified setups, e.g., cascades, featuring measurement of unsteady blade surface pressure during controlled blade oscillation. Such tests are either performed with all the blades oscillating in a traveling wave mode and the unsteady blade surface pressure measured on one blade (traveling wave mode approach) or with only one blade oscillated while the unsteady blade surface pressure is measured on the oscillating blade and a number of neighbor blades (influence coefficient approach). Assuming small disturbances and linear superposition of the unsteady flow, these two approaches are theoretically equivalent as elucidated below.

One of the most complete compilations of flutter tests has been given by [1], including data from both compressor and turbine cascades of annular as well as linear shape and at two-dimensional (2D) blade oscillation. Data have thereby been acquired using both traveling wave mode and influence coefficient approaches and thus represents one of the few conclusive studies made on the validation of the influence coefficient technique. It has been found that the two approaches correlate well for small oscillation amplitudes. Similar studies have been presented by [2–4] employing linear cascades of compressor blades leading to equivalent findings. Reference [5] has, for the first time, addressed the influence of varying spanwise bending amplitude on the unsteady aerodynamics using a linear cascade that comprised solely the oscillating blade itself. The oscillated blade was thereby hinged at the hub and actuated in a chordwise bending mode. The study yielded that the normalized local response was of heavily nonlinear character, featuring relatively higher amplitude at hub than at tip. The effect of incidence and separated flow in turbine cascades has among others been addressed by [6] on a linear cascade of low-pressure (LP) blades with one blade undergoing torsion oscillation. It has thereby been found that the overall effect of separated flow on aeroelastic stability was of a stabilizing character for the investigated mode.

In that perspective, the present study has been conceived to investigate the unsteady aerodynamics during flutter in a simplified but, to a large degree, realistic turbomachine environment. A typical nonproprietary low-pressure turbine rotor blade profile of three-dimensional (3D) twisted shape has been employed. The profile is operated in a nonrotating frame of reference and as blade row only (i.e., cascade test) without adjacent blade rows. To introduce realistic three-dimensional flow features, a blade with an

Contributed by the International Gas Turbine Institute of ASME for publication in the JOURNAL OF ENGINEERING FOR GAS TURBINES AND POWER. Manuscript received June 20, 2006; final manuscript received August 7, 2006. Review conducted by Lee Langston. Paper presented at the ASME Turbo Expo 2006: Land, Sea and Air (GT2006), Barcelona, Spain, May 8–11, 2006. Paper No. GT2006-91196.

aspect ratio of around 2 has been chosen. The blade is included in a test section of annular shape and at a nominal tip clearance of 1% span. The circumferential extent of the cascade has been shortened to a sector of seven free-standing blades in order to match the present test module to an existing and continuously operating air supply system. One of the blades could be made oscillating in two rigid-body bending modes and one torsion mode spanning an orthogonal mode space. The bending modes were characterized by linearly increasing amplitude from hub to tip to assimilate realistic low-order blade modes. Inflow incidence could be varied continuously from nominal to negative incidence, which allowed studying the aeroelastic behavior at off-design conditions.

The work put forward herein represents the first complete set of midspan data acquired for three orthogonal modes and in an annular setup with the blade oscillated at spanwise varying bending amplitude. By studying three orthogonal modes at design and off-design conditions, a platform has been provided for assessing mode shape stability and its dependency on inflow incidence.

Influence Coefficient Approach

The tests have been performed using an influence coefficient approach with a single blade oscillating. Commonly, flutter in turbomachine blade rows is described by a traveling wave mode approach assuming that all the blades are oscillating in the same mode and at the same amplitude and frequency [7,8]. Reference [9] has shown that this assumption represents the least stable condition and therefore tends to be overconservative. Considering a blade row of N blades the traveling wave mode response contains contributions from all the blades, which superimpose linearly at a certain interblade phase angle, such as

$$\hat{c}^{m,\sigma}_{p_{A,\mathrm{TWM}}}(x,y,z) = \sum_{n=-(N/2)}^{n=+(N/2)} \hat{c}^{n,m}_{p_{A,\mathrm{IC}}}(x,y,z)e^{-i\sigma n} \tag{1}$$

In the above equation $\hat{c}^{m,\sigma}_{p_{A,\mathrm{TWM}}}(x,y,z)$ is the complex pressure coefficient at point (x,y,z), acting on blade m, with the cascade oscillating in traveling wave mode and at interblade phase angle σ and $\hat{c}^{n,m}_{p_{A,\mathrm{IC}}}(x,y,z)$ is the complex pressure coefficient of the vibrating blade n, acting on the nonvibrating reference blade m at point (x,y,z). Blade indices are herein ascending in the direction of the suction side and descending in the direction of the pressure side, respectively. The coefficients on the left-hand side of Eq. (1) are describing the traveling wave mode domain, whereas the ones on the right-hand side are describing the influence coefficient domain.

The complex pressure coefficient yields from the unsteady pressure amplitude represented as complex number and normalized by the reference dynamic head, as well as the oscillation amplitude as

$$\hat{c}_p = \frac{\hat{p}}{Ap_{\mathrm{dyn,ref}}} \tag{2}$$

For the analysis of unsteady blade surface pressure, the angular amplitude of the blade oscillation in degrees has been applied, whereas for the composition of the stability maps the unsteady pressure coefficient has been normalized on a per-millimeter and per-radian basis for bending and torsion modes, respectively. The reference dynamic head $p_{\mathrm{dyn,ref}}=p_{0,in}-p_{s,in}$ is based on upstream conditions and has been measured at 20% axial chord upstream of the cascade. The phase is defined such that it is positive when the pressure response is leading the blade motion.

By analyzing Eq. (1) in more detail, it can be recognized that the contribution from the oscillating blade on itself ($n=0$) enters the superposition as constant value, whereas the contribution of blade pair ±1 ($n=1, n=-1$) leads to a sinusoidal variation of the traveling wave mode pressure coefficient over interblade phase angle. Any higher blade pair (±2, ±3, etc.) is leading to its respective higher harmonic variation, i.e., the ±2 blade pair enters the traveling wave mode superposition with $e^{\pm i2\sigma}$ and thus gives a second harmonic contribution. Usually, the influence decays rapidly away from the oscillating blade and gets small after blade pair ±1 as shown below. The curve has therefore a particular sinusoidal shape, which leads to the denotation of S-curve.

To obtain aeroelastic stability data from distributions of the complex pressure coefficient integration of infinitesimal force components in the three orthogonal directions (axial, circumferential, torsion) as given below is performed along the blade arc

$$d\hat{f}_\xi = \hat{c}_{p,A}\cdot\vec{n}_\xi\cdot ds$$

$$d\hat{f}_\eta = \hat{c}_{p,A}\cdot\vec{n}_\eta\cdot ds$$

$$d\hat{m}_\zeta = (\vec{r}\times\hat{c}_{p,A})\cdot\vec{e}_{\zeta_\perp}\cdot ds \tag{3}$$

Considering all investigated orthogonal modes, the integration yields a force matrix

$$[\hat{F}] = \begin{bmatrix} f_{\xi\xi} & f_{\xi\eta} & f_{\xi\zeta} \\ f_{\eta\xi} & f_{\eta\eta} & f_{\eta\zeta} \\ f_{\zeta\xi} & f_{\zeta\eta} & f_{\zeta\zeta} \end{bmatrix} \tag{4}$$

wherein the first index refers to the mode causing the force and the second to the direction in which the force is acting. The diagonal terms thus represent forces done by the unsteady response on the mode causing the response. The off-diagonal terms reflect forces done by the response on the other modes. For an arbitrary mode, the aeroelastic force is a combination of the orthogonal forces given by

$$\hat{F}_i = \{\hat{h}_i\}^T[\hat{F}]\{\hat{h}_i\} \tag{5}$$

where $\{\hat{h}_i\}=\{\hat{h}_\xi,\hat{h}_\eta,\hat{a}_\zeta\}$ denotes a mode shape vector. The aeroelastic stability is yielding from integrating the force over one oscillation cycle as

$$W_{\mathrm{cycle}} = \int_T \hat{F}_i\cdot\hat{h}_i e^{i\omega t}dt \tag{6}$$

The definition of the work is such that a positive value indicates energy transfer from the fluid to the structure, i.e., a situation of instability. After solving Eq. (6), it is apparent that only the imaginary part enters the work per cycle. In accordance with [10], a stability parameter Ξ is used that represents the normalized negative work per cycle given by

$$\Xi = \frac{-W_i}{\pi h_i} = -\,\mathrm{Im}(f_i) \tag{7}$$

During the analysis of mode shape sensitivity at various flow conditions, so-called stability maps are employed that are based on representing any mode by a fictional 2D torsion mode as, for example, applied by [11].

Description of Test Case

Figure 1 depicts profile sections of the low-pressure (LP) turbine profile used in the study at three spanwise heights. The profile features a real chord of 50 mm at midspan and an aspect ratio (span/chord) of 1.94 at a radius ratio of 1.25. The blade is assembled in an annular cascade with cylindrical hub and casing contours at a pitch/chord ratio of 0.68 at midspan and a tip clearance of 1% span. The passage shape included in Fig. 1 reveals that the throat location is gradually being shifted from 75% axial chord at hub toward the fore part of the blade close to tip.

The blade is nominally operated at high subsonic outflow Mach number of $M_2=0.8$. In the present tests, the outflow Mach numbers has been varied form low subsonic ($M_2=0.4$) over medium subsonic ($M_2=0.6$) to high subsonic ($M_2=0.8$). Nominal inflow to the cascade was at −26 deg yielding 87 deg in turning. In addition to nominal inflow, two negative incidence off-design cases have been tested. The reduced frequency has been varied during the

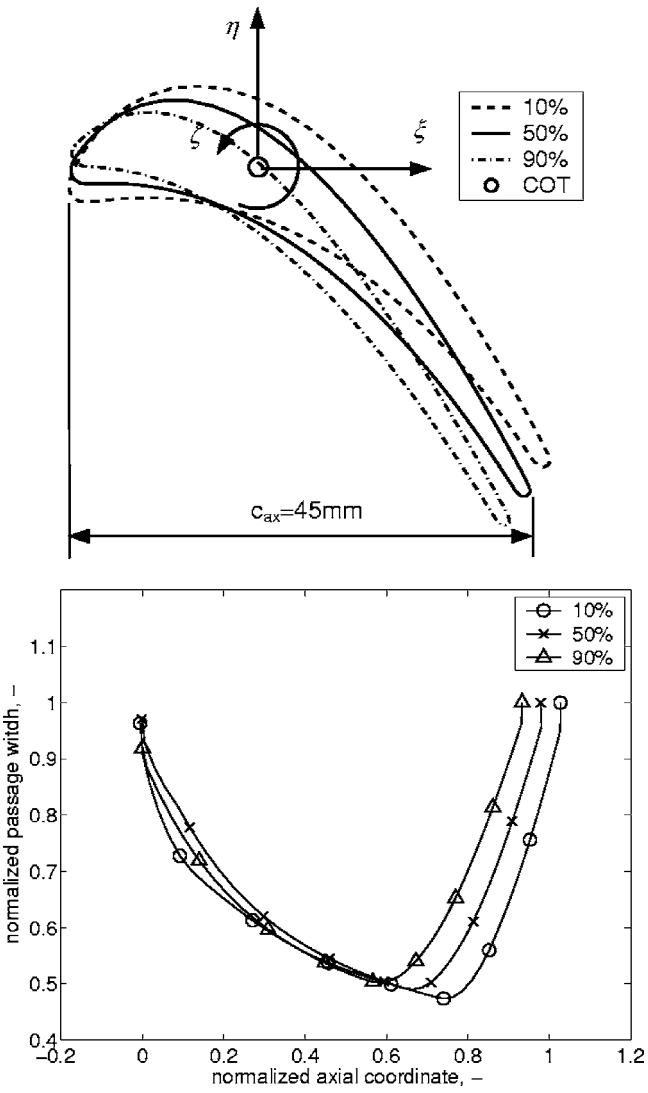

Fig. 1 Test object; top: profile sections and modes tested, bottom: passage shape

tests by controlling the blade oscillation frequency. The reduced frequency is here based on full chord and defined as follows:

$$k = \frac{2\pi fc}{u} \tag{8}$$

where f denotes the oscillation frequency in Hertz, c the real chord at midspan, and u the absolute outflow velocity. At low subsonic outflow, the maximum reduced frequency tested was $k = 0.5$. The modes tested were an axial bending mode, a circumferential bending mode, and a torsion mode, as indicated in Fig. 1. These modes thereby spanned an orthogonal mode space. The center of torsion was placed at 40% axial chord. The motion of the blade was of rigid-body type and was achieved by pivoting the blade at a short distance underneath the hub. This setup yielded linearly, increasing bending amplitude from hub to tip, which is here referred to as three-dimensional bending mode.

Description of Test Setup

The tests have been performed in a continuous working full-scale test facility located at the Royal Institute of Technology in Sweden [12,13]. Figure 2 shows the facility and a schematic representation of the test module. Pressurized air is provided by a 1 MW screw compressor at a maximum mass flow rate of

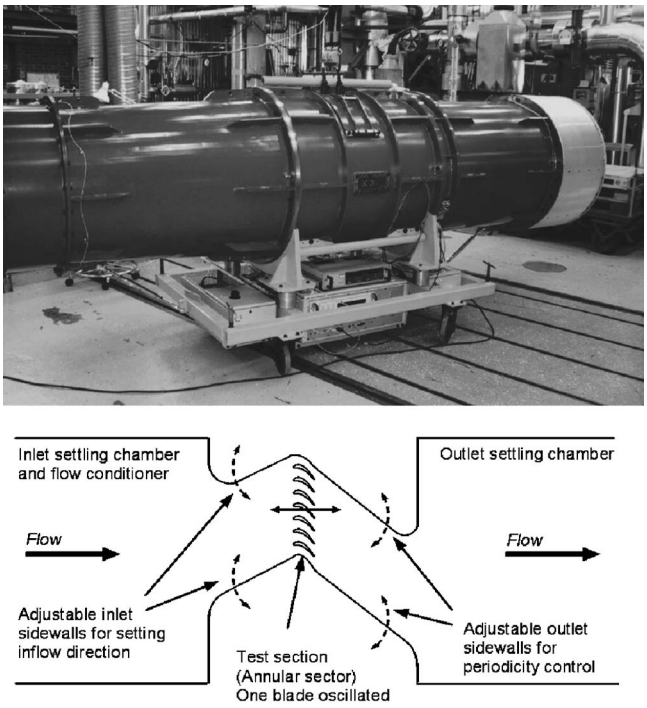

Fig. 2 Test facility and sketch of test module

4.75 kg/s and conditioned to a total inlet temperature of 303 K for all tested operating points. The facility comprised a flow settling and conditioning chamber and a variable annular sector inlet duct to the cascade to set the inflow angle continuously. The variability of the duct was achieved by means of purpose-built flexible sidewalls that provided sealed guidance of the flow at any arbitrary inflow angle.

The test section consisted of a cascade of seven free-standing blades with either sidewall being shaped as suction and pressure side of the employed profile. At the outlet of the cascade, the flow was discharging through a variable annular sector outlet duct that was used to tune flow periodicity in the cascade. The tests were run with the facility discharging to ambient through an outlet silencer. One of the blades has been made oscillating in the above-described modes. The employed blade actuation mechanism was of mechanical type, featuring two co-rotating circular cams. By placing the actuator underneath the hub, intruding parts into the flow passage could be avoided. The transition between the oscillating blade and the hub was made from a flexible material that was molded onto the blade's lower end as well as onto the hub. Eventual leakage flows could thereby be avoided completely.

The test facility has been equipped with steady-state measurement locations on the blades, hub, and tip in order to describe the mean flow field as well as to provide reference values for data normalization. In addition, probe traverses have been performed 20% axial chord upstream and 20% axial chord downstream of the cascade using a four-hole wedge probe that has been calibrated in Mach number ($M = 0.1, \ldots, 0.9$), yaw angle and pitch angle (both ±20 deg). Steady pressure measurements have been performed using a multichannel PSI8400 system with 100 kPa scanners and a SOLARTRON barometer at a combined accuracy of ±50 Pa.

The unsteady blade surface pressure has been measured by means of fast-response pressure transducers (KULITE XCQ-062 and LQ-080), which were in a recessed manner off the blades. A set of instrumented oscillating and nonoscillating blades was used for the present tests that differed slightly in spatial resolution of the measurement locations as shown in Fig. 3. The positions indicated are referenced by a normalized arcwise coordinate that originates at the leading edge and spans the suction side of the

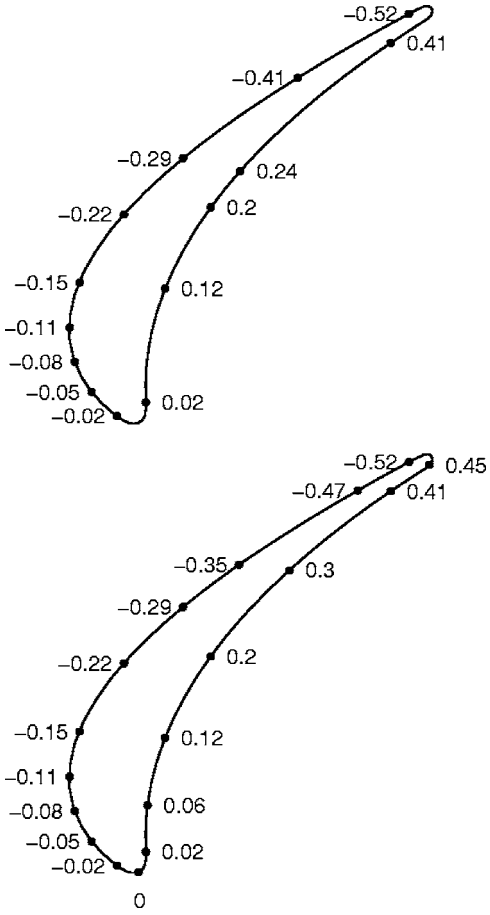

Fig. 3 Distribution of unsteady pressure measurement locations on the oscillating (top) and nonoscillating blades (bottom)

blade in the negative direction and the pressure side in the positive direction, respectively. The normalization basis of this coordinate is the total arc length of the blade profile at the regarded section.

The method of recessed-mounted pressure transducers has been chosen to allow reusing transducers for several measurement points by means of fast connecting devices. The entire unsteady pressure measurement setup has been calibrated statically and dynamically using an in-house built dynamic calibration system as described in [14], allowing one to keep the final uncertainty for unsteady pressure measurements down to ±130 Pa. The unsteady pressure has been referenced to the blade motion using inductive trigger devices, comprised in the actuator, that have been calibrated with respect to blade motion using a pointwise laser vibrometer (LMI Selcom) applied on the oscillating blade. Calibration of the setup yielded accuracy in unsteady pressure phase with respect to blade motion of ±5 deg. Furthermore, it has been verified that the blade did not deform flexibly during the present tests. Unsteady data have been recorded using a 32 channel digital high-speed data acquisition system (Kayser-Threde KT8000) featuring individually programmable preamplifiers, signal filtering, and 15-bit AD-converters. Data were sampled at 20 kHz over, typically, 200 periods and thereafter ensemble-averaged as given by

$$\tilde{p}_{EA}(x,t) = \frac{1}{N}\sum_{n=0}^{N} p(x,t_0+nT) \tag{9}$$

The unsteady pressure data was thereafter reduced to a complex number, assuming harmonic response, and finally normalized by the inlet dynamic head and the oscillation amplitude, as given in Eq. (2).

Table 1 Operating conditions of nominal incidence cases

Value	Units	Low	Medium	High
T_{01}	K	303	303	303
p_{01}	kPa	112.3	128.4	160.6
p_1	kPa	109.2	123.6	151.1
P_2	kPa	102.9	105.8	107.5
α_1	deg	−23.9	−21.1	−22.8
α_2	deg	56.8	57.4	57.1
M_1	-	0.21	0.28	0.30
M_2	-	0.37	0.62	0.71
$k_{\max}$	-	0.5	0.4	0.3

Steady-state and unsteady performance of the facility have been verified prior to acquisition of the presented data. It has been found that the facility featured approximately ±5% nonperiodicity in outlet flow field and less than ±5% nonperiodicity in blade loading for the tested conditions over the cascade extent covered. Repetitivity was determined to be <1%. The dynamic performance has been addressed by investigating the acoustic resonant behavior of the facility and eventual presence of pressure reflections from the sidewalls. A resonance was initially present when discharging the flow to an existing exhaust system; this resonance could be completely avoided by discharging the flow to ambient, and consequently, this setup was used for the present tests. Pressure reflections from lateral sidewalls have found being negligible, whereas the unsteady blade-to-blade periodicity was determined to be approximately within ±5% [13].

Three velocity levels have been tested ranging from low subsonic (M_2=0.4, "low"[1]) over medium subsonic (M_2=0.6, "medium") to high subsonic (M_2=0.8, "high"). In addition, the inflow incidence has been varied from nominal ($a1$=−26 deg, "nom") to negative incidence (α_1=0 deg, "off1") and to high negative incidence (α_1=14 deg, "off2"). The purpose of testing negative incidence cases was to force the flow to separate on the fore pressure side and to allow studying of the influence of flow separation on the aeroelastic stability of the cascade. An overview of nominal incidence flow conditions is contained in Table 1, including averaged measured values from the up- and downstream flow field traverses.[2] At each operating point, a set of three orthogonal modes have been tested as were axial bending ("axial"), circumferential bending ("circ"), and torsion ("tors"). The reduced frequency was thereby varied in steps of 0.1 starting from k=0.1, by controlling the blade oscillation frequency up to a maximum frequency that depended on flow velocity. The values of maximum tested reduced frequency are included in Table 1.

Experimental Results and Discussion

Steady Flow Results. Flow field traverse data and blade loading data are employed to describe the underlying flow physics. Figure 4 shows circumferentially area-averaged values of static and total pressure coefficient at 20% axial chord downstream of the cascade for the low subsonic case. The distributions reveal a radial gradient in static pressure that is due to the annular shape of the test setup roughly equaling the inlet dynamic head (Δc_p =1.08). The respective values for the medium and high subsonic cases are Δc_p=1.51 and Δc_p=1.73. Furthermore, a deficit in total pressure coefficient toward the casing can be recognized that is due to losses associated with the tip leakage flow. This deficit is similar in strength and extent for the higher-velocity cases. The Mach number distribution and secondary flow vectors included in

[1]The values indicated in the parentheses indicate the operating parameter and the abbreviation used hereafter.

[2]Note that the actual outlet Mach numbers (as from flow field averages) were not exactly set to M=0.4, 0.6, and 0.8, respectively. This was kept consistent throughout the tests.

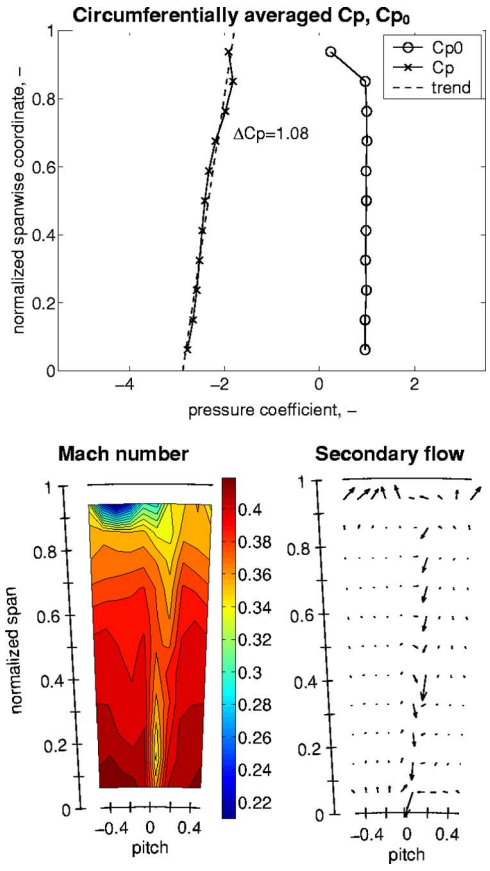

Fig. 4 Outlet flow traverse data for low subsonic operating point

Fig. 4 reveal the prevalent flow structure; again, a radial gradient in flow velocity increasing toward the hub can be recognized due to the annular shape of the setup. The wake located around pitch=0 is characterized by a strong velocity deficit as well as a distinct downwash seen in the secondary flow vector plot. Furthermore, a strong tip vortex is observed close to the casing and on the suction side edge of the wake.

Steady blade loading data for the three velocity levels at nominal incidence are included in Fig. 5. Data are plotted against the normalized arcwise distance as introduced above with the negative values spanning the suction side and the positive values on the pressure side. The leading edge is located at the origin. A distinct suction peak is observed for all velocity levels at arc=

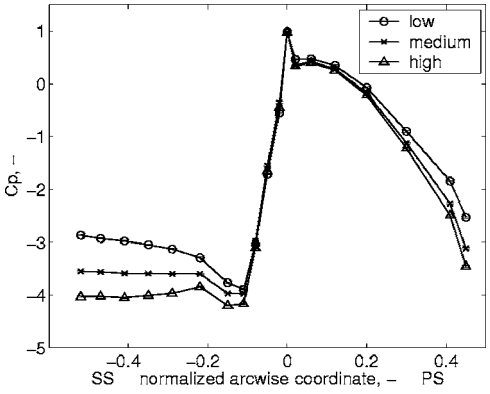

Fig. 5 Blade loading data at midspan for the three velocity levels at nominal incidence

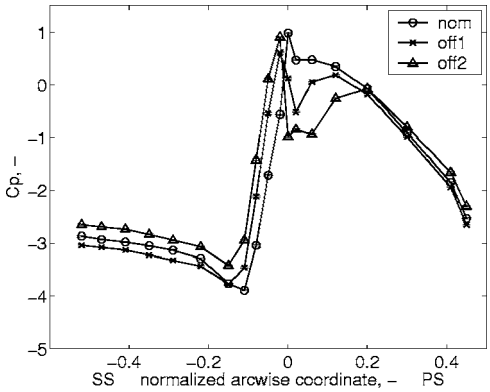

Fig. 6 Blade loading data at midspan for the three incidence cases at low subsonic flow velocity

−0.11 followed by a slight deceleration toward the aft suction side; the strength of this deceleration decreases from low subsonic to high subsonic. From surface flow visualization tests using a mixture of silicone oil and titanium oxide, it has been recognized that flow transition coincides with the observed suction peak. Furthermore, the steady loading curves reveal an increase in outlet dynamic head with increasing flow velocity. On the pressure side, the loading shows little change with flow velocity apart from the aforementioned increase in outlet dynamic head.

Figure 6 depicts steady blade loading data for the three incidence cases at low subsonic flow velocity. A region of reduced pressure coefficient becomes apparent on the fore pressure side that grows in strength and extent as incidence increases. From surface flow visualization, it has been recognized that the local decrease in pressure coefficient is due a region of separated flow. The extent of the separated flow region is monotonically increasing with increasing negative incidence; at the high negative incidence case, the region extends to arc=0.2 or 44% of the pressure side starting from the leading edge. Additionally, negative off-design operation is causing the leading-edge stagnation point to move onto the fore suction side. The magnitude of the suction peak is thereby decreasing as well as slightly being moved downstream. These observations are indications for the increasing unloading of the profile with negative incidence off-design operation.

Unsteady Pressure Data. The focus is first put on the effects of blade mode shape on the unsteady response and then led over to effects of flow velocity and reduced frequency. Data are thereby presented bladewise with the normalized unsteady pressure amplitude being plotted in the respective top window and the phase being included in the bottom window. Note that the phase has been plotted in the range ±180 deg and therefore might be subject to 360 deg jumps at either limit without any physical significance. In each plot, the respective blade index is contained in the top left corner of the amplitude window. The aforementioned error margins in C_p amplitude and phase are marked with error bars at the data points.

Unsteady blade loading data at axial bending mode are contained in Fig. 7 for blades +1 through −1 and in Fig. 8 for blades +2 and −2. The major part of the unsteady response is observed on blades 0 and −1, i.e., the oscillating blade and the pressure-side neighbor. On these blades, a peak in response amplitude is apparent on the suction side at arc=−0.11, while the phase around this peak is fairly constant. On the suction side of the oscillating blade, the unsteady pressure is largely in phase with the blade motion, i.e., the pressure increases instantaneously on movement of the blade in a positive axial direction, whereas it is 180 deg out of phase on the suction side of blade −1. On the pressure side of blade 0, the response is of constant though moderate magnitude

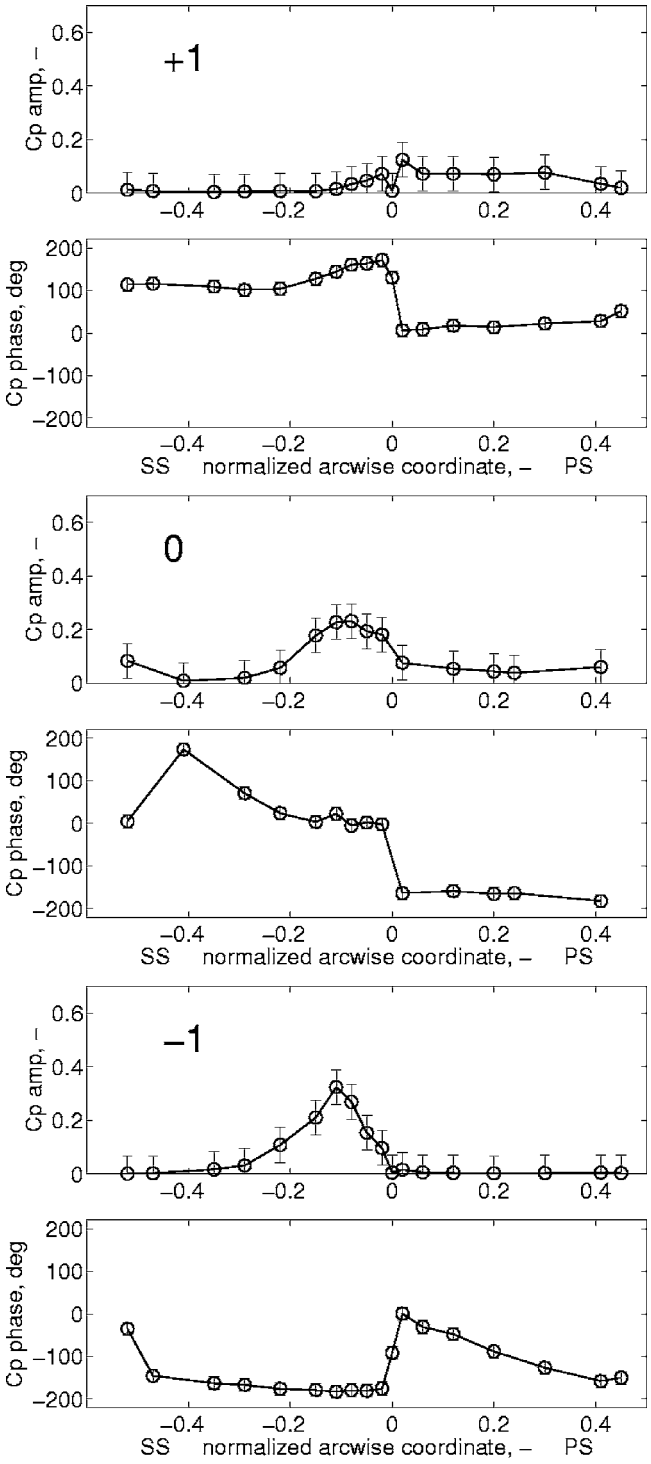

Fig. 7 Unsteady blade loading data at midspan on blades +1, 0, and −1; axial bending, low subsonic, nominal inflow, k=0.1

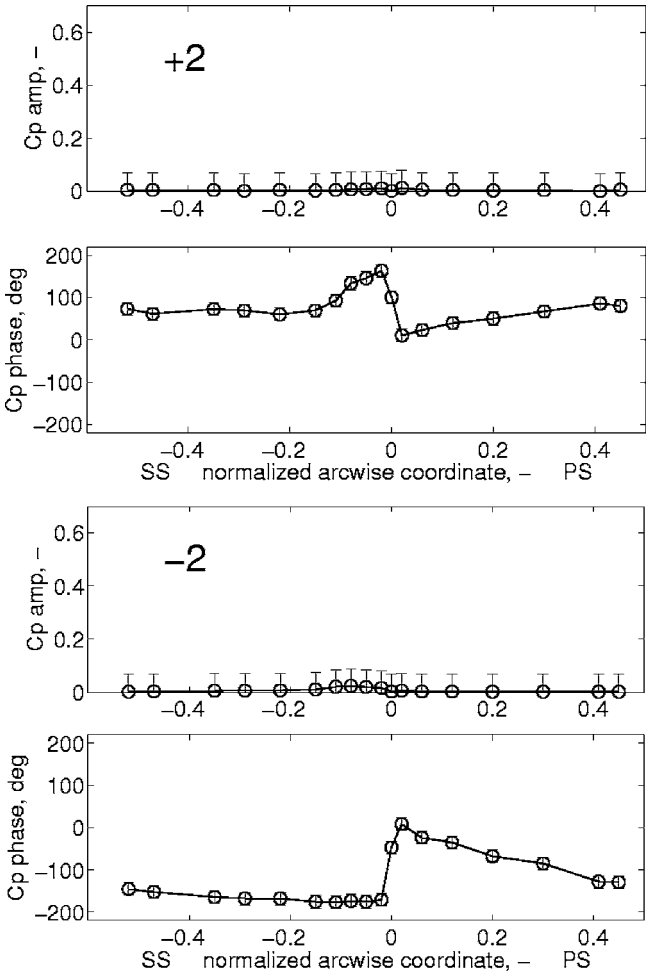

Fig. 8 Unsteady blade loading data at midspan on blades +2 and −2; axial bending, low subsonic, nominal inflow, k=0.1

lying around 180 deg out of phase to the blade motion. On blade +1, the major part of the response is observed on the pressure side, which is as well in-phase with the blade motion. On blades +2 and −2, the measured unsteady pressure amplitude is within measurement accuracy on both suction and pressure side. A general note shall be made at this position that the measured phase might become noisy in regions of low response magnitude; the effect thereof on final stability data is however negligible.

Next, response data at circumferential bending mode are presented in Fig. 9 for blades +1 through −1. Data on blades +2 and −2 are not included here because the response has been found negligible. Again, it is observed that the major part of response is present on blades 0 and −1, although the overall absolute level is considerably smaller than at axial bending mode. The response is again showing a peak on the suction side at arc=−0.11 decreasing monotonically toward the leading and trailing edge. On the pressure side of blade +1, a limited region of relevant response is measured around arc=0.3 with the rest of the blade lying within measurement accuracy. The suction side of blade 0 shows again in-phase behavior while the response on the suction side of blade −1 lies out of phase. This observation agrees with the one made above from axial bending mode data.

Finally torsion mode data are included in Fig. 10 on blades −1 through +1. The major response is observed on the suction side of blade −1, while blade 0 features a relatively lower response again peaking on the suction side at arc=−0.11. Blade +1 features increasing response magnitude from leading to trailing edge, which for this mode is showing relevant magnitude even on the suction side. It is assumed that this is due to oscillation of the wake shed from blade 0 as the oscillating blade is undergoing torsional movement. The direct opposite surfaces (pressure side blade +1 and suction side blade 0, pressure side blade 0 and suction side blade −1) are relatively in phase to each other as well as in and out of phase to the blade motion, respectively.

The above observations indicate a characteristic behavior that is common for all investigated modes; the highest response magnitudes are present on the suction side, whereas the direct opposite surfaces tend to be in phase with each other. As observed from

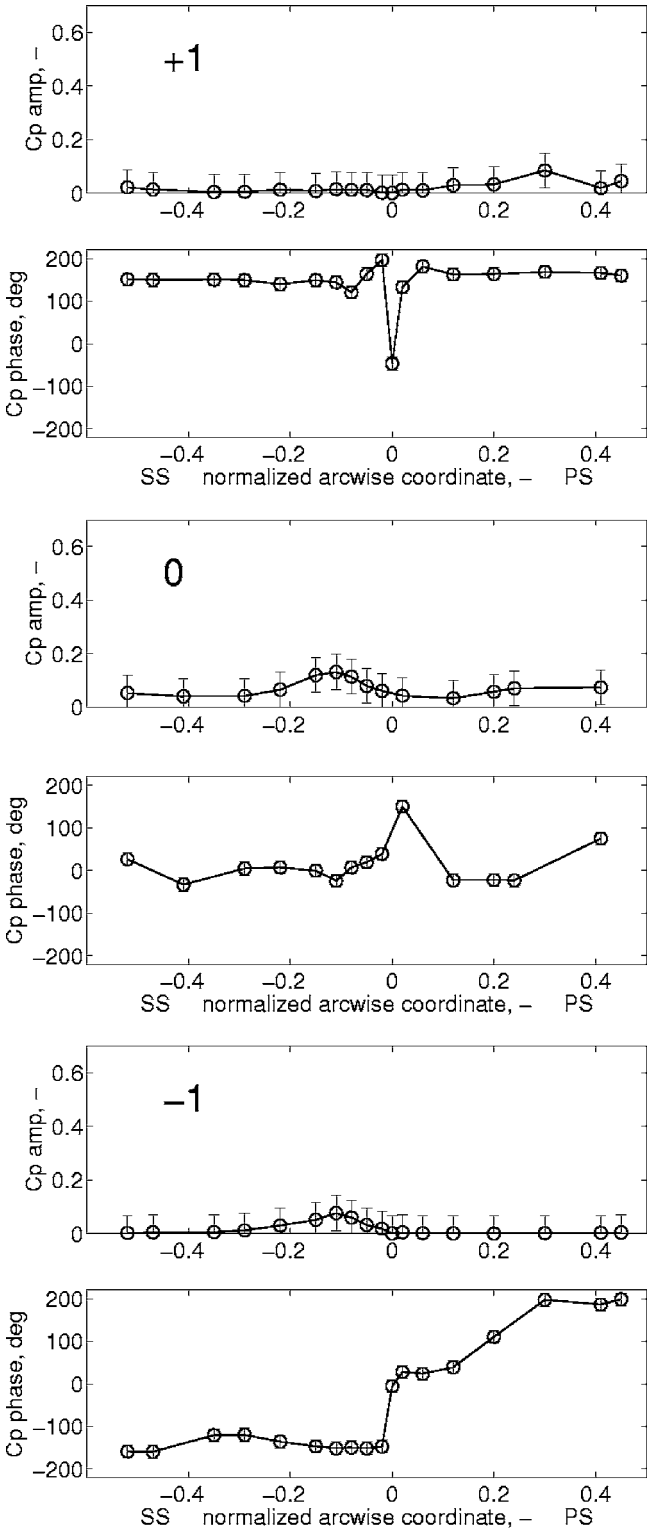

Fig. 9 Unsteady blade loading data at midspan on blades +1, 0 and −1; circumferential bending, low subsonic, nominal inflow, *k*=0.1

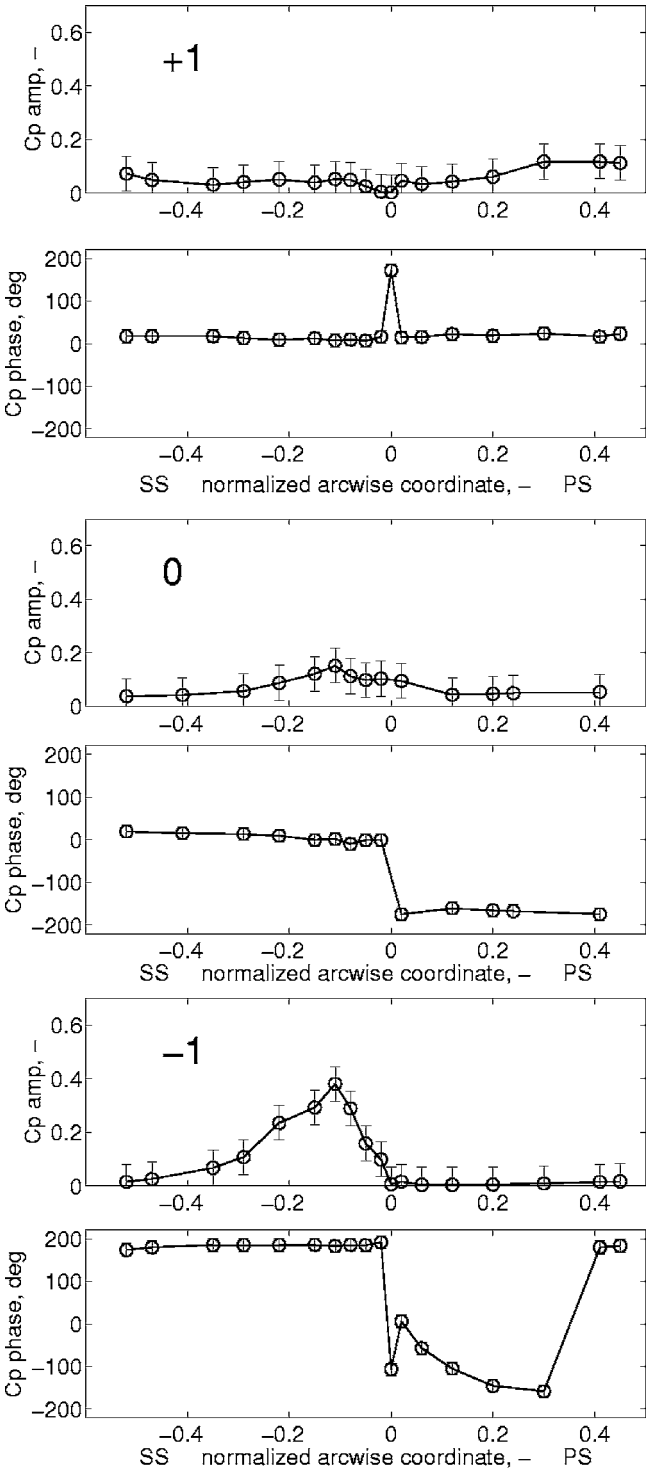

Fig. 10 Unsteady blade loading data at midspan on blades +1, 0 and −1; torsion, low subsonic, nominal inflow, *k*=0.1

steady loading, occurrences of high steady c_p and large c_p gradient changes (i.e., second derivatives) represent a situation where small perturbations can lead to high amplitudes in unsteady pressure. This becomes primarily apparent for the observed unsteady response peak on the suction side at arc=−0.11, which coincides with steady peak suction. The in-phase behavior of direct opposite surfaces (i.e., suction side of blade 0 and pressure side of blade +1, suction side of blade −1 and pressure side of blade 0) suggests that the instantaneous passage flow around the oscillating blade tends to have a dominant influence. The passage flow, in turn, is resulting from the instantaneous passage shape during oscillation, which is primarily affected by the passage throat; on closing of the throat, the pressure in the passage is increased due to higher blockage leading to an in-phase situation. Opening of the throat,

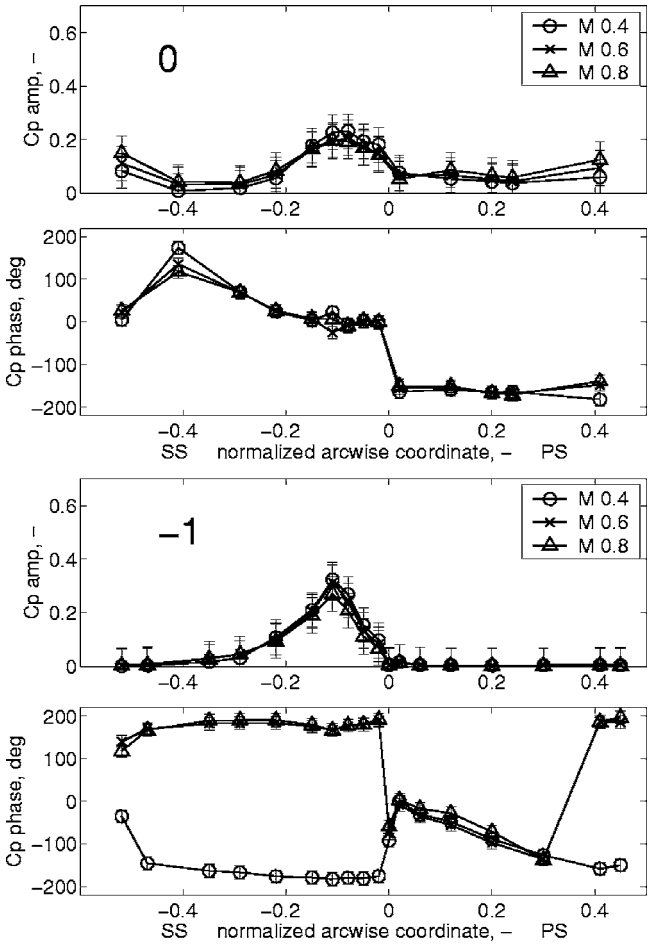

Fig. 11 Effect of flow velocity on unsteady blade loading data at midspan on blades 0 and −1; axial bending, nominal inflow, $k=0.1$

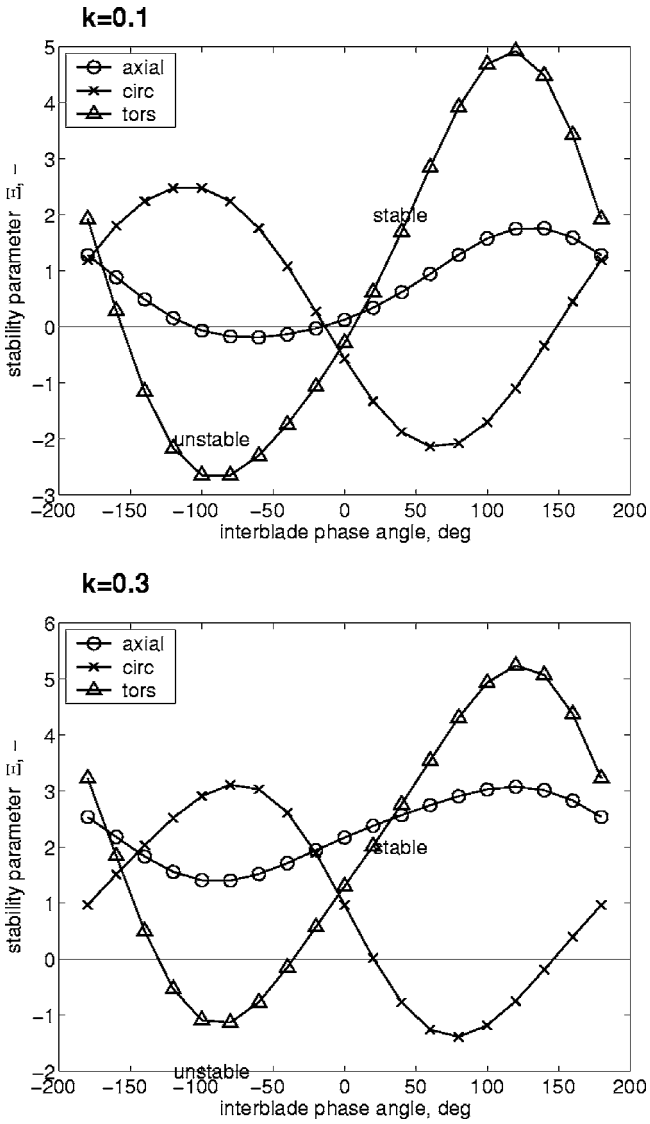

Fig. 12 Variation of traveling wave mode stability versus interblade phase angle at $k=0.1$ (top) and $k=0.3$ (bottom); low subsonic, nominal inflow

consequently, leads to a decrease in blockage and, thus, a decrease in pressure. This phenomenon becomes quite visible, for example, at torsion mode on the aforementioned blade sides.

The effect of flow velocity on the unsteady blade loading is addressed in Fig. 11 for the axial bending mode on blades 0 and −1, i.e., the blades featuring the major response magnitudes. The data suggest a moderate increase in normalized response magnitude with increasing flow velocity on the oscillating blade. The response phase is thereby largely constant, apart from a region around arc=−0.4 on the suction side, which is located right downstream of the throat. On blade −1 little change in response magnitude is noted in both magnitude and phase. These observations indicate that, from an overall view, the response magnitudes scale fairly well with the inlet dynamic head, suggesting that the absolute unsteady pressure level increases accordingly with increasing flow velocity. These observations are similarly valid for the other two modes.

Stability Data at Nominal Incidence. The set of unsteady blade surface pressure data of the investigated modes has been reduced to blade-specific influence coefficients. These influence coefficients have been superimposed to traveling wave mode data as elucidated above in order to assess the aeroelastic stability versus interblade phase angle. Results at low subsonic speed and two reduced frequencies are included in Fig. 12. The characteristic S-shape of the curves is apparent, suggesting a dominant influence from the ±1 pair and subordinate influence from the ±2 pair. This influence is however greater than the influence from the oscillating blade itself (i.e., the direct influence apparent as mean offset) leading to the stability becoming negative in a certain range of interblade phase angles. Unless any kinetic constraints are applied on the blades (e.g., part- or full-span shrouds, sectoring), it has to be assumed that flutter will establish at the least stable traveling wave mode. From that perspective, the present blade row would have to be considered unstable in all modes at $k=0.1$ at the depicted operating condition. With an increase in reduced frequency from $k=0.1$ to $k=0.3$, it is noted that the stability tends to be increased for all three modes, which is largely due to an increasingly stabilizing behavior from blade 0. At axial bending mode, the direct influence overweighs the coupling influences from blade pairs ±1 and ±2, leading to the blade row being stable for the entire range of interblade phase angles. For the other two modes, the range of unstable interblade phase angles has been reduced although negative values still occur.

The mode shape sensitivity of the blade row operated at nominal inflow is addressed in Fig. 13 for low and high subsonic flow conditions. The figure includes mode shape stability plots displaying the minimum stability for the entire range of interblade phase angle (−180 deg to +180 deg) for various modes. Regions of positive stability have been shaded. Any mode is represented by the reference blade (highlighted bold in the maps) oscillating around a

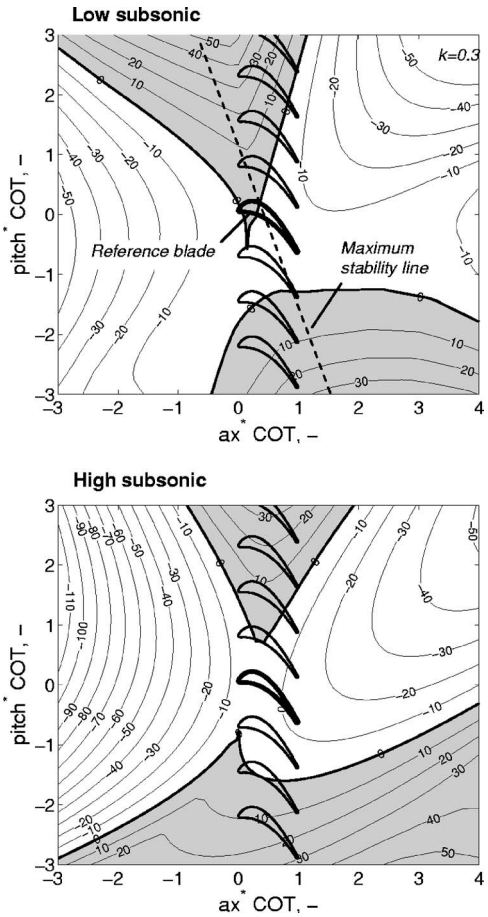

Fig. 13 Stability plot at low subsonic and high subsonic Mach number, nominal inflow, shaded areas mark stable regions, and values display stability parameters

fictional center of torsion. Torsion-dominated modes thus feature a center of torsion close to the reference blade, whereas bending dominated modes are represented by a center of torsion that is located several chord lengths away from the reference blade. For the present discussions, a standard extract-sized three axial chord lengths in any direction away from the reference blade has been found suitable to discuss mode shape sensitivity.

At both flow velocity levels, two stable regions are identified that are distributed around the reference blade and roughly aligned in cascade circumferential direction. This suggests that bending modes of axial character tend to be stable, whereas bending modes of circumferential character tend to have negative stability. Focusing on the region close to the reference blade, i.e., torsion-dominated modes, it is recognized that the stable areas change in extent and location as flow velocity increases. This indicates that the effect of flow velocity increases with respect to aeroelastic stability is heavily dependent on the torsion axis location, suggesting great mode shape sensitivity for torsion-dominated modes.

Tying up with the observations made above during the discussion of the unsteady blade surface data the stability maps reveal that the most stable modes are agglomerated around a line that is passing through the reference blade and slightly inclined away from circumferential direction, as indicated in Fig. 13. Similar findings have been documented by [15] for different turbine blade row geometries. Indeed, modes that are located on this line act efficiently on the passage throats adjacent to the reference blade. As elucidated above, changes in passage throat were found to affect the respective opposite blade surfaces in such a way that the unsteady pressure is largely in phase with the motion on one side of the oscillating blade and out of phase on the other. For the cases depicted in Fig. 13, it is thus concluded that the response phase is such that it acts stabilizing at axial bending mode, whereas it leads to a destabilization at circumferential bending.

Stability Data at Negative Incidence. On the background of the aeroelastic response phenomenon at nominal inflow conditions, the focus is now drawn toward the impact of off-design operation on aeroelastic stability and mode shape sensitivity. The axial bending mode has, for this purpose, been selected as an object of discussion for addressing the impacts on unsteady blade loading and blade influence coefficients before addressing the impact on mode shape sensitivity.

The unsteady response at axial bending mode, depicted in Fig. 14, indicates that substantial differences in response magnitude becomes apparent on the fore pressure side of blades 0 and +1, whereas the response phase shows only moderate variations. To conclude from steady loading data, these differences occur in the region of separated flow and can therefore directly be linked to the underlying structure of the mean flow field. On blade 0, an influence is also detected on a limited region on the fore suction side between leading edge and response peak at arc=−0.11. On blade −1, the response is little affected by off-design operation apart from a limited impact on the fore pressure side at high negative incidence operation. On the suction side, a small increase in response magnitude is observed around response peak that is attributed to larger gradients in steady loading as apparent from steady data.

The effect of flow incidence on traveling wave mode stability is included in Fig. 15. It is noted that the overall level of stability is decreased with increasing negative incidence, however, not beyond the stable range. Furthermore, it is observed that this influence is nonuniformly present over the range of interblade phase angles, whereas stability is affected very little in a range of IBPA=−50 deg to IBPA=0 deg. It shows increasing influence outside this range. The location of minimum stability is thereby shifted monotonically from around IBPA=−70 deg at nominal inflow over IBPA=−100 deg at off-design 1 to IBPA=−140 deg at off-design 2.

These changes shall be discussed further by addressing blade influence coefficients. Figure 16 shows the influence coefficients for blade 0 (direct influence), ±1 pair and ±2 pair (coupling influences) versus reduced frequency and inflow incidence. From the dependency of reduced frequency, it is noted that the direct influence stands for the major increase in total stability as reduced frequency is increased. It is also observed that the influence from the higher neighbor pair ±2 is around one order of magnitude smaller than the influence from the direct neighbors. Both coupling influences feature only moderate increase with reduced frequency resulting in the overall traveling wave mode stability becoming stable as reduced frequency is increased. This change in stability occurs between $k=0.1$ and $k=0.2$ for the depicted mode. The dependency from operating point reveals that all regarded influence coefficients tend to become more unstable with increasing negative incidence. Because the sum of the coupling influences is smaller than the direct influence, the setup will, nevertheless, be stable in the traveling wave mode domain. The above observation stands in agreement with the S-curves depicted in Fig. 15.

Finally, attention is drawn to the effect of off-design operation on mode shape sensitivity. For this purpose the incremental changes in stability rather than the absolute stability itself are plotted in Fig. 17. As a reference, the stability map at low subsonic flow velocity included in Fig. 13 is adapted. The incremental changes thus reveal how the stability is being affected by a change from nominal to either of the two off-design conditions; regions in which stability is affected positively have been shaded. The amount of change in stability is included by contour lines that readily could be overlaid to the stability values indicated in the reference stability map in order to achieve total stability at off-

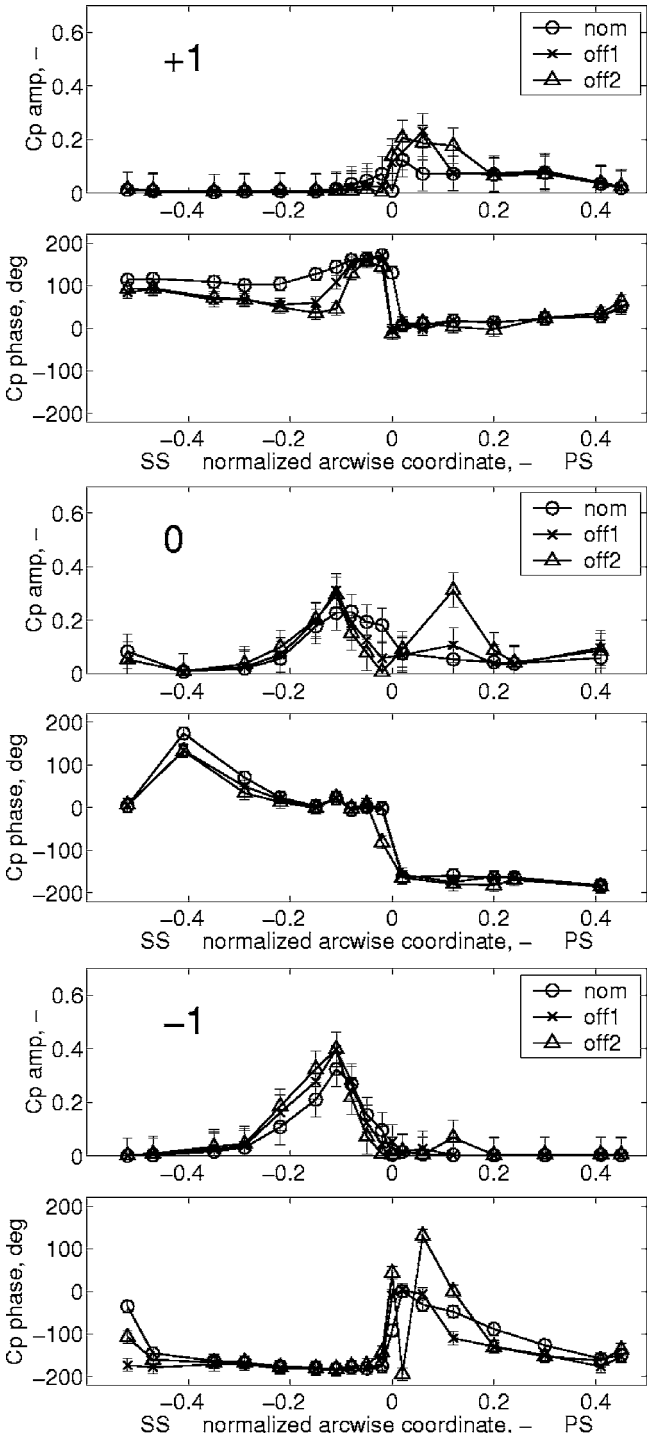

Fig. 14 Effect of inflow incidence on unsteady blade loading data at midspan on blades +1, 0 and −1; axial bending, low subsonic, $k=0.1$

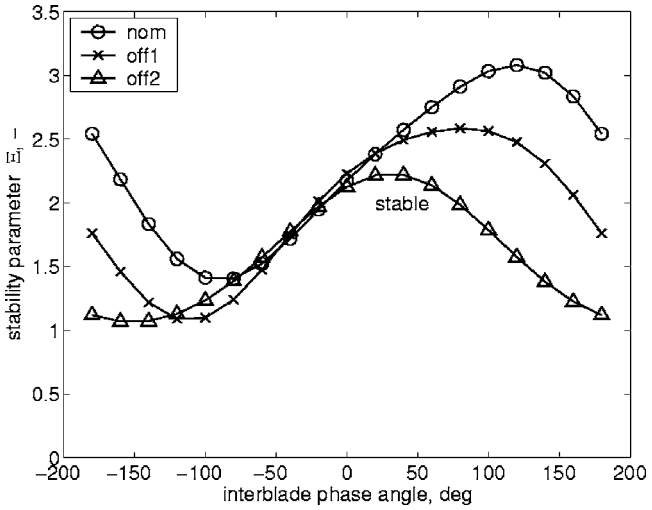

Fig. 15 Effect of flow incidence on traveling wave mode stability, axial bending, low subsonic, $k=0.3$

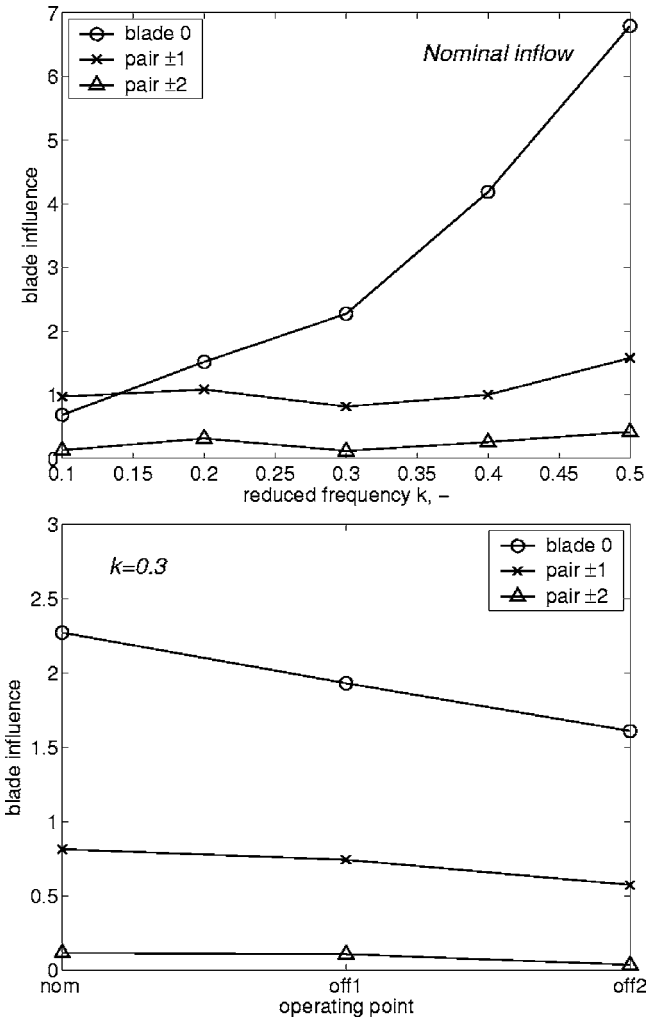

Fig. 16 Effect of reduced frequency (top) and flow incidence (bottom) on blade influence coefficients; axial bending; low subsonic

design operation. At first sight, it becomes apparent that the two incremental maps look qualitatively similar but the magnitude of stability change is greater with increased negative incidence. This observation suggests that the increase in off-design incidence affects the stability in a fairly linear way over the range of conditions tested; trends in stability behavior that are observed on change of incidence to off-design 1 are rather augmented than inverted when continuing to off-design 2. The region of maximum stability at nominal conditions that has been aligned slightly away from the cascade circumferential experiences a destabilization at

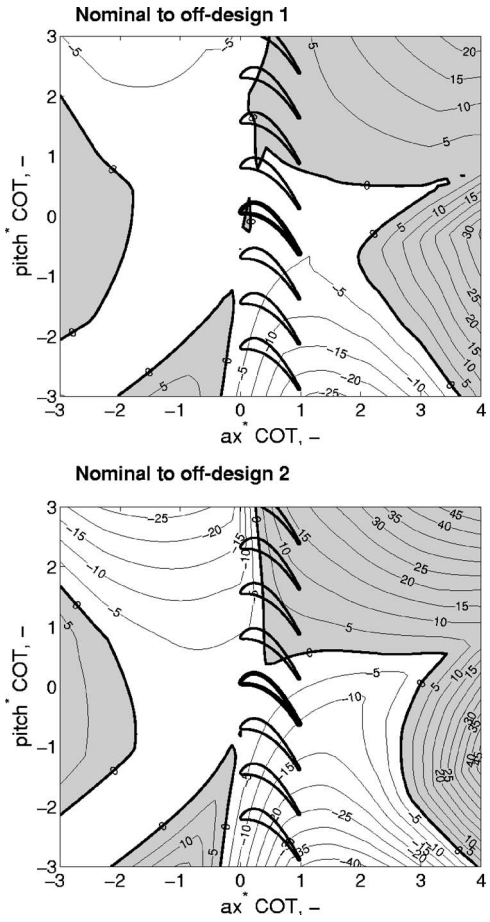

Fig. 17 Incremental change in stability with inflow incidence; low subsonic, $k=0.3$; shaded areas mark stabilizing change

off-design operation while the torsion-dominated modes close to the reference blade are only marginally affected. On the other hand, modes that are of bending type of circumferential to edgewise character experience a stabilization as incidence changes from nominal to negative. The force realization in the regions of changed unsteady response properties, i.e., the fore pressure side, on these modes is seen as the key driver for this behavior.

Conclusions

The results of an experimental study have been presented that aimed at investigating mode shape sensitivity of a typical low-pressure (LP) turbine rotor blade row during controlled blade oscillation at design and off-design conditions. Unsteady blade surface pressure data have been acquired on five blades at midspan in an annular sector cascade with the center blade made to oscillate at controlled rigid-body modes. Data have been reduced to influence coefficients and combined to traveling wave mode results employing linear superposition. The present work represents the first complete set of midspan data acquired for three orthogonal modes and in an annular setup with the blade oscillated at spanwise varying bending amplitude.

Analysis of the local unsteady pressure during blade oscillation yielded that the major response is found on the oscillating blade and its direct neighbors. Furthermore, the distributions reveal dominant behavior of the instantaneous passage shape around the oscillating blade, which, in turn, is affected by the instantaneous passage throat. It has been found that an increase in flow velocity from low subsonic to high subsonic only leads to minor changes in unsteady response, whereas an increase in reduced frequency is showing a clear trend toward increased stability. Mode shape sensitivity has been addressed by means of stability maps revealing that the most stable modes are of bending type with axial to chordwise character. Torsion-dominated modes, on the other hand, feature high mode shape sensitivity, as small changes in torsion axis location might have a major influence on aeroelastic stability.

By operating the cascade at negative incidence, the flow on the fore pressure side was forced to separate. The separation was found to have a destabilizing influence for the axial bending mode, whereas stability was increased for bending modes of circumferential to edgewise character. These effects were observed in both direct and coupling influence coefficients but were of subordinate strength compared to the stabilizing effect with increase in reduced frequency. Torsion-dominated modes are neutrally affected by negative incidence operation. The reported effects of negative incidence operation have been found to be fairly linear with increase in off-design operation within the range of conditions tested.

Acknowledgment

The present study has been promoted within the Swedish Gas Turbine Center (GTC) and the EU-funded project DAIGTS (Contract No. ENK5-CT2000-00065). The authors would like to acknowledge this financial support as well as the support from the Royal Institute of Technology, Sweden.

Nomenclature

A = blade oscillation amplitude, deg
c = blade chord
c_p = static pressure coefficient, $c_p=(p-p_{s,\mathrm{ref}})/(p_{0,\mathrm{ref}}-p_{s,\mathrm{ref}})$
$\hat{c}_{p,A}$ = normalized unsteady pressure coefficient (complex), per-degree basis for 3D consideration, per millimeter (bending) and per radian (torsion), respectively, for 2D consideration (stability plots)
df = infinitesimal force component
f = frequency
$\hat{F}$ = force, force vector
$\hat{h}$ = modal vector
i = imaginary unit, $i=\sqrt{-1}$
M = Mach number
n,m = blade indices, period number
$\vec{n}$ = normal vector to surface element
N = number of blades
p = pressure
$\hat{p}$ = unsteady pressure amplitude (complex)
$\tilde{p}$ = unsteady pressure (time domain)
$\vec{r}$ = distance from center of torsion to force realization point
u = flow velocity
W_{cycle} = work per cycle
x,y,z = Cartesian coordinates
σ = interblade phase angle
Ξ = stability parameter

Subscripts

0 = total
ax = axial
dyn = dynamic
IC = influence coefficient
in = inlet, -20% c_{ax}
ref = reference
s = static
TWM = traveling wave mode
ζ = torsion direction
η = circumferential bending direction
θ = circumferential component

ξ = axial bending direction

Acronyms

COT = center of torsion
IBPA = interblade phase angle

References

[1] Bölcs, A., and Fransson, T. H., 1986, "Aeroelasticity in Turbomachines—Comparison of Theoretical and Experimental Results," *Communication du Laboratoire de Thermique Appliqué et de Turbomachines*, EPFL, Lausanne, Vol. 13.

[2] Carta, F. O., 1983, "Unsteady Gapwise Periodicity of Oscillating Cascaded Airfoils," ASME J. Eng. Power, **105**, pp. 565–574.

[3] Buffum, D. H., and Fleeter, S., 1990, "Oscillating Cascade Aerodynamics by an Experimental Influence Coefficient Technique," J. Propul. Power, **6**, pp. 612–620.

[4] Buffum, D. H., Capece, V. R., King, A. J., and El-Aini, Y. M., 1998, "Oscillating Cascade Aerodynamics at Large Mean Incidence," ASME J. Turbomach., **120**, pp. 122–130.

[5] Bell, D. L., and He, L., 2000, "Three-Dimensional Unsteady Flow for an Oscillating Turbine Blade and the Influence of Tip Leakage," ASME J. Turbomach., **122**, pp. 93–101.

[6] He, L., 1996, "Unsteady Flow in Oscillating Turbine Cascade; Part 1: Linear Cascade Experiment," ASME Paper No. 96-GT-374.

[7] Crawley, E. F., 1988, "Aeroelastic Formulation for Tuned and Mistuned Rotors," *AGARD Manual on Aeroelasticity in Axial-Flow Turbomachines* (Vol. 2, Structural Dynamics and Aeroelasticity), M. F. Platzer and F. O. Carta, eds., AGARD, Neuilly sur Seine, France, AGARD-AG-298, pp. 19-1–19-24.

[8] Hanamura, Y., Tanaka, H., and Yamaguchi, Y., 1980, "A Simplified Method to Measure Unsteady Forces Acting on the Vibrating Blades in Cascade," Bull. JSME, **23**(18), pp. 880–887.

[9] Nowinski, M., and Panovsky, J., 2000, "Flutter Mechanisms in Low Pressure Turbine Blades," ASME J. Eng. Gas Turbines Power, **122**, January, pp. 82–88.

[10] Verdon, J. M., 1987, "Linearized Unsteady Aerodynamic Theory," *AGARD Manual on Aeroelasticity in Axial-Flow Turbomachines* (Vol. 1, Unsteady Turbomachinery Aerodynamics), M. F. Platzer and F. O. Carta, eds., AGARD, Neuilly sur Seine, France, AGARD-AG-298, pp. 2-1–2-31.

[11] Kielb, R., Barter, J., Chernysheva, O., and Fransson, T., 2003, "Flutter of Low-Pressure Turbine Blades With Cyclic Symmetric Modes—A Preliminary Design Method," ASME Paper No. GT2003-38694.

[12] Vogt, D. M., and Fransson, T. H., 2002, "A New Turbine Cascade for Aeromechanical Testing," 16th Symposium on Measuring Techniques in Transonic and Supersonic Flows in Cascades and Turbomachines, Cambridge, UK.

[13] Vogt, D. M., 2005, "Experimental Investigation of Three-Dimensional Mechanisms in Low-Pressure Turbine Flutter," Ph.D. thesis, Royal Institute of Technology, Stockholm.

[14] Vogt, D. M., and Fransson, T. H., 2004, "A Technique for Using Recessed-Mounted Pressure Transducers to Measure Unsteady Pressure," 17th Symposium on Measuring Techniques in Transonic and Supersonic Flows in Cascades and Turbomachines, Stockholm.

[15] Tchernycheva, O., Fransson, T. H., Kielb, R. E., and Barter, J., 2001, "Comparative Analysis of Blade Mode Shape Influence on Flutter of Two-Dimensional Turbine Blades," ISABE Paper No. ISABE-2001-1243.

Lifetime Prediction of Components Including Initiation Phase

Michael Besel

Angelika Brueckner-Foit
e-mail: a.brueckner-foit@uni-kassel.de

Institute for Materials Engineering,
Kassel University,
Kassel D-34109, Germany

The lifetime distribution of a component subjected to fatigue loading is calculated using a micromechanics model for crack initiation and a fracture mechanics model for crack growth. These models are implemented in a computer code which uses the local stress field obtained in a finite-element analysis as input data. Elemental failure probabilities are defined which allow us to identify critical regions and are independent of mesh refinement. An example is given to illustrate the capabilities of the code. Special emphasis is put on the effect of the initiation phase on the lifetime distribution.
[DOI: 10.1115/1.2436569]

Introduction

Lifetime prediction of components subjected to fatigue loading is based on suitable models for crack initiation and crack growth. In the crack growth phase fracture mechanics models work very well as long as there is no extensive plastic deformation and the cracks are not too small. This is typically the case if the material in question contains second phase particles which have sizes exceeding the average grain diameter. The probability of failure at a given number of load cycles is then equal to the probability that at least one crack has reached its critical size. In principle, the calculation of this probability is straightforward and can be performed by a suitable postprocessor, if the stress distribution in the component is determined in a finite-element analysis. However, efficient and "foolproof" numerical procedures have to be employed in order to make sure that the result is not dependent on the finite-element mesh or the skills of the user. Examples of such postprocessors are the lifetime of cracked components (LOCC) code which has been developed recently by University of Kassel and the Darwin code developed by SWRI [1]. The initiation phase is much more difficult to deal with within the framework of a reliability analysis. The most straightforward way is to introduce an initiation rate and to simulate the fact that some cracks will not start to grow at startup, but some time later. However, this procedure neglects the fact that the initiation phase is dominated by the microstructure and that small cracks may be stopped at microstructural barriers [2]. As a substantial part of the component's lifetime may be spent in the initiation phase it is worthwhile to look for more advanced models which will provide a more realistic description of the initiation phase. A good candidate is the Tanaka–Mura model [3] which relates the number of cycles to crack initiation to the grain size and the resolved shear stress in the crack plane. A reliability model based on the Tanaka–Mura model was proposed by Tryon and Cruse [4]. A similar approach is used in this paper. An example is given which illustrates the influence of the initiation phase on the lifetime distribution.

Crack Initiation and Crack Growth

This section presents the basic models for crack initiation and crack growth which are applied for the calculation of the failure probability of a component under fatigue loading. The symbols used are defined in the Nomenclature.

Contributed by the International Gas Turbine Institute of ASME for publication in the JOURNAL OF ENGINEERING FOR GAS TURBINES AND POWER. Manuscript received July 5, 2006; final manuscript received August 5, 2006. Review conducted by Dilip R. Ballal. Paper presented at the ASME Turbo Expo 2006: Land, Sea and Air (GT2006), Barcelona, Spain, May 8–11, 2006. Paper No. GT2006-90710.

Three different scenarios of crack initiation under fatigue loading are given in literature.

1. Cracks may be initiated from small inclusions for two different reasons. Debonding of the inclusion may lead to crack initiation in the matrix or cracks in the inclusions which remain attached to the matrix may extend into the matrix. In addition a combination of these two mechanisms is possible;
2. Under fatigue loading and microplastic deformation cracks may be initiated by dislocation pileup at microstructural barriers; and
3. A combination of these two mechanisms.

In Case 1 there is virtually no initiation time [5] and the initiation phase can be neglected. In the second case, an initiation rate can be derived from the Tanaka–Mura relation which allows to estimate the number of cycles to crack initiation N_i inside a grain

$$N_i = \frac{8G \cdot W_c}{\pi(1-\nu) \cdot D \cdot (\Delta\tau_{\text{res}} - 2\tau_c)^2} \tag{1}$$

Here G is the shear modulus; ν is Poisson's ratio; D is the length of slip line; $\Delta\tau_{\text{res}}$ is the range of the resolved shear stress; τ_c is the critical shear stress; and W_c is the fracture energy per unit area. The parameters G, τ_c, and W_c are material constants and can be found in the literature; and N_i denotes the number of cycles to crack initiation in the specific slip band. The length of the slip band D can be assumed to be equal to the grain size. Upon initiation a microcrack is formed with an initial length $2c_i = D$.

Microcracks may extend irregularly if their size is of the same order of magnitude as the distance between microstructural barriers. The classical model for intermittent crack growth was proposed by Navarro and de los Rios [6]. This model is completely deterministic for a given grain structure. This implies that once the spatial distribution of the grains is given, the number of cycles to failure of a specific microcrack can be calculated directly. Lifetime predictions can be based on these simulations and the Tanaka–Mura model for crack initiation [7].

Even though models of intermittent crack growth are appealing from a theoretical point of view, their usability in reliability analyses of real components is very limited, as it is not possible to simulate the microstructure of a real component. Therefore it is more realistic to assume that the microstructure is taken into consideration in the initiation phase and to use a continuous fracture mechanics model to analyze the crack extension phase. If small crack growth should play a role, statistical fudging factors can be used to get conservative estimates of its effect.

If a microcrack is initiated, it is assumed to be of semi-elliptical shape and with a depth a_i. After initiation, the microcrack behaves

like a macroscopic semi-elliptical surface crack. This implies that crack growth and failure can be analyzed in terms of the corresponding stress intensity factors. Assuming a Paris-type crack growth law leads to the following expressions:

$$\frac{da}{dN} = C(\Delta K_{\text{depth}})^m \quad \text{(depth direction)} \tag{2a}$$

$$\frac{dc}{dN} = C(\Delta K_{\text{surface}})^m \quad \text{(length direction)} \tag{2b}$$

with

$$\Delta K_{\text{depth}} = \frac{1.12\Delta\sigma\sqrt{\pi a}}{\Psi}$$

$$\Delta K_{\text{surface}} = \frac{1.12\Delta\sigma\sqrt{\pi a}}{\Psi}\left(\frac{a}{c}\right)^{1/2}$$

$$\Psi = \left[1 + 1.464\left(\frac{a}{c}\right)^{1.65}\right]^{1/2} \quad \text{for } \frac{a}{c} \leqslant 1$$

where a is the crack depth; $2c$ is the crack length; C and m are material parameters; and $\Delta\sigma$ is the stress range given by the solution of a finite-element analysis. This system of equations for crack growth can be solved numerically. Dividing Eq. (2*a*) by Eq. (2*b*) and solving the corresponding differential equation yields a simple relation for the aspect ratio a/c

$$\left(\frac{c}{a}\right)^{(m+2)/2} = 1 - \left(\frac{a_i}{a}\right)^{(m+2)/2} \cdot \left[1 - \left(\frac{a}{c}\right)_i^{(m+2)/(-2)}\right] \tag{3}$$

where a_i and c_i are the depth and half length of the initial crack, respectively. An important observation is that the actual value of the aspect ratio a/c depends only on the initial values of crack depth and the initial aspect ratio $a_i/c_i=(a/c)_i$ and on the final value of the crack size and not explicitly on the number of load cycles or the stress amplitude. This implies that system of differential equations can be reduced to an ordinary differential equation which can be solved by separating variables.

The number of cycles to failure is related to the critical crack size via the failure criterion

$$\max(K_{\text{depth}}, K_{\text{surface}}) \geqslant K_{Ic} \tag{4}$$

with K_{depth} and K_{surface} as in Eqs. (2) with the stress range $\Delta\sigma$ replaced by the maximum stress. Inserting Eq. (3) into the failure criterion yields a unique relation between the initial values of the crack depth and of the aspect ratio and the critical value of the crack depth a_c.

As a result of Eqs. (2)–(4), and if the crack initiation phase is neglected (i.e., $N_i=0$), the relation between the lifetime and the corresponding critical initial crack depth $a_{c,i}$ (i.e., the crack with an initial depth value which just reaches the critical value at time $N_f=N_g$) in a given stress field can be summarized as follows

$$N_g = \int_{a_{c,i}}^{a_c} \frac{\left[1 + 1.464\left(\frac{a}{c}\right)^{1.65}\right]^{m/2}}{C \cdot (\Delta\sigma)^m \cdot (\sqrt{\pi a})^m \cdot 1.12^m} da \tag{5}$$

with the critical crack depth a_c.

Equation (5) can be easily generalized to include crack initiation. If a crack of depth $a_{c,i}=1/2(a/c)_i D$ is initiated after N_i load cycles where D and N_i are related by the Tanaka–Mura criterion, Eq. (1), then the crack extension phase is reduced to $N_g=N_f-N_i$ load cycles for a design life of N_f. Hence Eq. (5) is modified to

$$N_f - N_i = \int_{a_{c,i}}^{a_c} \frac{\left[1 + 1.464\left(\frac{a}{c}\right)^{1.65}\right]^{m/2}}{C \cdot (\Delta\sigma)^m \cdot (\sqrt{\pi a})^m \cdot 1.12^m} da \tag{6}$$

The local stress value is contained in the stress range $\Delta\sigma = \sigma_{\max}(1-R)$, in terms of the maximum normal stress $\sigma_{\max}$ in the critical crack size a_c via the failure criterion Eq. (4), and in the number of cycles to crack initiation N_i in terms of the resolved shear stress τ_{res}. According to Ref. [4], the following relation holds

$$\tau_{\text{res}} = \frac{2}{\sqrt{3}}\sigma_{\text{von Mises}} \tag{7}$$

Consequently, the value of $a_{c,i}$ is uniquely determined by Eq. (6) for each point in a structure if the stress field is available, e.g., from a finite-element analysis.

Probabilistic Model

A crack initiated at load cycle N_i with depth a_i will extend under cyclic loading until it reaches a critical size a_c. The probability that the crack size after N load cycles $a(N)$ exceeds a_c, is called the local failure probability $P(a(N)>a_c)$ and depends on the nature and the parameters of the crack growth law, Eq. (6), the initial crack size a_i, the initiation time N_i, and the local stress field σ_{ij} which may also depend on the cycle number.

For a specific area A_{el} with its local stress distribution a normalized local failure probability is determined by

$$Q_{1,\text{el}} = \frac{1}{A_{\text{el}}}\int_{A_{\text{el}}} P(a(N) > a_c) dA_{\text{el}} \tag{8}$$

This quantity is independent of the size of A_{el} as can be easily seen by inserting a constant stress field into Eq. (8). $Q_{1,\text{el}}$ is the conditional probability that failure has occurred at or before load cycle N provided there is exactly one crack (natural flaw with $N_i=0$ or fractured grain with initiation time N_i) in the area under consideration.

If the total area A_{total} is divided into subareas A_{el} as in a FE mesh, the corresponding conditional failure probabilities are related by

$$Q_{1,\text{total}} = \frac{1}{A_{\text{total}}}\sum_{A_{\text{el}}} A_{\text{el}} \cdot Q_{1,\text{el}} \tag{9}$$

In general, the component under consideration may contain a random number of flaws, i.e., defects, and/or highly stressed grains from which cracks can be initiated within design life. The actual number of flaws is a Poisson distributed random variable if the material is homogeneous and the number of flaws is low. This assumption leads to the following expression for the failure probability

$$P_f = 1 - \exp(-M_{\text{total}} \cdot Q_{1,\text{total}}) \tag{10}$$

where M_{total} is the average number of crack initiation sites in the component.

If the lifetime N_f is specified as the design life, then Eq. (6) yields a unique relation between the crack depths $a_{c,i}$ and a_c. This is very useful in a probabilistic analysis for two reasons:

1. The couple system of differential equations, Eqs. (2*a*) and (2*b*), is replaced by a simple nonlinear integral. This greatly improves the numerical convergence; and
2. There is a unique relation between the critical crack size at the end of the design life and the initial crack size which grows into a_c during the lifetime of the component. This is very useful in a probabilistic analysis as the local failure

probability, i.e., the probability that a crack initiated at a given site has exceeded its critical size after N load cycles, can now be rewritten as

$$P(a(N) > a_c) = P(a_i > a_{c,i}) \tag{11}$$

Hence it is not necessary to update the crack depth distribution, but all calculations can be performed with the initial crack depth distribution function. This is very convenient if the aspect ratio is also a random variable, because the instantaneous values of a and a/c are coupled through Eq. (3) and, consequently, depth and aspect ratio are not independent random variables.

Once the critical initial crack depth $a_{c,i}$ is known, the local probability for a given area A_{el} to contain a crack with depth longer than $a_{c,i}$ can be calculated using Eqs. (8) and (11). In the simplest case, all material parameters are constant and a fixed value is selected for the initial value of the aspect ratio $(a/c)_i$ (e.g., $(a/c)_i = 1$ for a globular grain structure or a material containing spherical inclusions). This implies that the probability in Eq. (11) can be written down in closed form

$$P(a(N) > a_c) = [1 - F_{a_i}(a_i = a_{c,i})] \tag{12a}$$

where $F_{a_i}(\cdot)$ is the statistical distribution of the initial value of the crack depth if initiation can be neglected. If the initiation phase plays an important role (see Eqs. (1) and (6), then we have

$$P(a(N) > a_c) = \left\{ 1 - F_D\left(D = 2\left(\frac{c}{a}\right)_i a_{c,i} \right) \right\} \tag{12b}$$

where $F_D(\cdot)$ is the statistical distribution of the grain size.

More complex probabilistic models can be built up by including the effect of the random variables $Y_1, Y_2, \ldots, Y_n$ in the expression for the local failure probability

$$P(a(N) > a_c) = \int \cdots \int \left\{ 1 - F_D\left(D = 2\left(\frac{c}{a}\right)_i a_{c,i} \right) \right\} \cdot f_{Y_1}(y_1) \cdot \cdots \cdot f_{Y_n}(y_n) dy_1 \ldots dy_n \tag{13}$$

with crack initiation taken into account. The quantities $f_{Y_k}(\cdot)$ denote the probability density functions of the random variables $Y_k, k = 1, \ldots, n$. The integrals in Eq. (13) can be solved by numerical integration or by Monte Carlo simulation and will be omitted in the following in order to simplify the notation.

LOCC Computer Code

The LOCC code is currently being developed at Kassel University. It calculates the failure probability of a component after an arbitrary user-defined number of load cycles. The lifetime distribution can be obtained by varying the value of the design life N_f. The stress field can vary in a very general way throughout the component and is assumed to be determined by a finite-element analysis. The initial flaw size is assumed to be random with a user-defined probability distribution function. If all other random variables (denoted as $y_1, \ldots, y_n$ in Eq. (13)) are kept constant, the local failure probability $P(a(N) > a_c)$ can be determined without additional Monte Carlo simulation using the relations developed in the previous section. A more elaborate probabilistic model, e.g., one which contains random material parameters will require additional Monte Carlo simulations which can be performed outside the LOCC code using a commercial simulation software.

The conditional local failure probability given in Eq. (8) is calculated for each element of a finite-element mesh by numerical integration. One possibility to quantify the contribution of each element to the total failure is the local risk of fracture which is defined as [8]

$$P(\text{fatal crack in element}) = \frac{Q_{1,\mathrm{el}} \cdot A_{\mathrm{el}}}{Q_{1,\mathrm{total}} \cdot A_{\mathrm{total}}} \tag{14}$$

with $Q_{1,\mathrm{total}}$ given in Eq. (9) as the integral over the total surface area of the component.

This quantity is the conditional failure probability that the element in question contains the fatal crack under the condition that no other element is critical. The local risk of fracture approaches the conditional probability density function for very small elements and is therefore a well-defined stochastic quantity. However, the interpretation of the numerical values of the local risk of fracture is less straightforward than the conditional failure probabilities given by the LOCC code.

Calculation of the Critical Crack Depth. The critical crack depths $a_{c,i}$ and a_c are calculated from Eqs. (2)–(7) assuming that the initial aspect ratio $(a/c)_i$ is known. The integral is replaced by a Gaussian integration sum. A system of two nonlinear equations is obtained and solved by a Newton based algorithm using line search and backtracking for (nearly) global convergence. The routine calling this Newton solver calculates "good" values as starting points for the following iterative solution process. With the simplification $a/c = 1$ Eqs. (4) and (5) are used to calculate this "good" values

$$a_{c,\ \mathrm{Start}} = \left(\frac{K_{Ic} \cdot \psi}{1.12 \cdot \Delta\sigma \cdot \sqrt{\pi}} \right)^2 \tag{15a}$$

$$a_{c,i,\ \mathrm{Start}} = \left[a_{c,\ \mathrm{Start}}^{1-m/2} - N_f \cdot C \cdot \frac{2-m}{2} \cdot (1.12 \cdot \Delta\sigma)^m \cdot \left(\frac{\psi}{\pi} \right)^{-m/2} \right]^{1/1-m/2} \tag{15b}$$

A check for physical consistency is performed. If the solver fails for numerical reasons, it is recalled with improved starting points. Thus the crack depths $a_{c,i}$ and a_c can be calculated for realistic problems.

Flaw Size Distribution. The probability of containing (or initiating) an initial crack of the critical depth $a_{c,i}$ (or deeper) is calculated for each surface area of a finite element using Eqs. (8) and (12*a*) or (12*b*).

Various probability distribution functions for $F_{a_i}(\cdot)$ and $F_D(\cdot)$ are contained in the code. Thus the LOCC code can be applied to various materials with specific defect structures. At present four of these functions are implemented: the exponential distribution, the lognormal distribution, the Weibull distribution, and the Gumbel distribution. If initiation is taken into account, the initial flaw size distribution is equal to the grain size distribution $F_D(\cdot)$. It is common practice to use a lognormal distribution in this case.

Numerical Integration. In general it is not possible to solve Eq. (8) analytically for a given element, and Gaussian sums are used to determine the integrals. This is a straightforward procedure for the number of cycles to crack initiation, which is needed for calculating the critical crack depth, but rather involved for the integration over the surface area of an element. The integration limits of the integral have to be transformed to -1 and 1 in order to use a Gaussian sum. The following expression is obtained for a finite element of arbitrary shape and order

$$Q_{1,\mathrm{el}} = \frac{1}{A_{\mathrm{el}}} \cdot \int_{A_{\mathrm{el}}} [1 - F_{a_i}(a_i = a_{c,i})] dA_{\mathrm{el}} \approx \frac{1}{A_{\mathrm{el}}} \cdot \sum_{j=1}^{L} h_j(\vec{x}_j) \cdot G(\vec{x}_j) \cdot T(\vec{v}, \vec{x}_j) \tag{16}$$

with

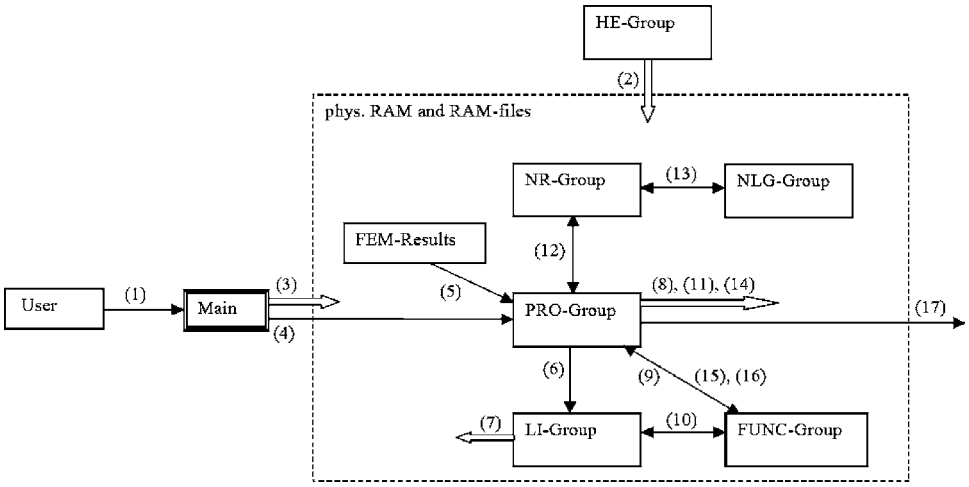

Fig. 1 General flow chart of the computer code

$$G(\vec{x}_j) = 1 - F_{a_i}(a_i = a_{c,i}(\vec{x}_j))$$

$\vec{v}$ is vector of the coordinates of all nodes of the element area; and $\vec{x}_j = \{\xi_j, \eta_j, \zeta_j\}$ the vector of the coordinates of the Gauss integration points. $T(\vec{v}, \vec{x}_j)$ denotes the transformation factor which represents the transformation between the $\vec{x}_j$ in the area A_{el} of the finite element and the Gauss area $(\xi_G, \eta_G \in [-1, 1])$.

The quantity $G(x_j)$ is calculated for each Gauss integration point of the surface area using the (element) nodal stress output of a finite-element analysis program (e.g., ABAQUS). Up to three transformations are needed to calculate the transformation factor $T = T(\vec{v}, \vec{x}_j)$ which transforms the integration limits of the integral Eq. (8) to the Gauss area.

Structure of the LOCC Code and Flow Chart. The LOCC code consists of one main function, three headers and 46 procedures, functions, and libraries. The code has a modular structure with well-defined interfaces which allow modifications. The shortest function contains ten lines, the longest one more than 600 lines. The different parts of the computer code are arranged in seven groups. These groups are briefly presented.

1. Group "main": one member, main code to run the program;
2. Group "FUNC": seven members, small functions used by several parts of the program;
3. Group "HE": three members, headers for general declarations and include directives;
4. Group "LI": ten members, procedures, functions, declarations, and definitions depending on the finite elements type used in the FE analysis;
5. Group "NLG": three members, containing the nonlinear equation system and the used Gauss points and weights;
6. Group "NR": six members, procedures; of the Newton-based routines; and
7. Group "PRO": twenty members, procedures for the calculations and general data-manipulation.

Figure 1 shows the flow chart of the interaction of these group members during the calculations. Only the general group names are used in order to facilitate understanding of the general structure of the computer code.

The numbers in Fig. 1 denote the following steps:

1. User input or parameter selection: file name with the finite element method (FEM)-results of the stress calculation, design life, parameters of the material for the crack growth law, distribution function for the depth of the initial cracks and their parameters, and parameter for the failure probability function.
2. Global variables are declared. The parameters of the Newton-based numerical solver are also defined.
3. The input data of Step 1 are defined as global variables.
4. The main starts to call all procedures one after another.
5. The element type is read from the FEM results.
6. The libraries are called with the element type as input data.
7. The properties of the element type are published as global variables.
8. The FEM results are rearranged in new RAM files containing stress tensors at the nodes, element definitions, element type, node definitions, and nodal coordinates in the local system.

9–11. The procedures are called: 9 to determine, calculate 10, and save the following data in RAM files, step 11: neighbors of each element, surface elements, nodal stress of these surface elements, integration points for the surface areas, stress at these integration points using step 10 for transformations and shape functions, stress for the crack growth at the integration points, size of the surface areas, and corresponding transformation factors.

12–14. The numerical solver is called to calculate the critical depth of the initial cracks that leads to failure after the specified number of lifecycles. For each integration point of the surface areas the critical crack depths are calculated. The results are saved in a RAM file.

15. At each integration point the probability $P(a_i > a_{c,i})$, Eq. (12), is calculated. If there is no initiation (e.g., if the von Mises stress is too low for crack initiation), $P(a_i > a_{c,i})$ is set to zero.

16. The results of step 15 and the corresponding transformation factors are used to calculate the local failure probability according to the integral given in Eq. (16). This calculation is performed for each surface area. The results are used to calculate the total failure probability according to Eq. (10).

17. The conditional failure probability of each element, Eq. (8), and the total failure probability, Eq. (10), are stored in output files.

Example

The crack sensitive part of a transmission case was selected to study the effect of crack initiation and growth under fatigue loading. The two-dimensional model (plane stress) and the boundary conditions used are shown in Fig. 2. The material data are taken from literature and are supposed to be valid for conventional steel. The input data are summarized in Table 1. A cyclic load with constant amplitude is applied in the axial direction. The simulation is supposed to capture the situation in a lab test, i.e., the failure probabilities range from 0 to 1 and are much higher than those used in probabilistic design.

Some details of the FE model and of the PC system on which the calculations were performed are given in Table 2.

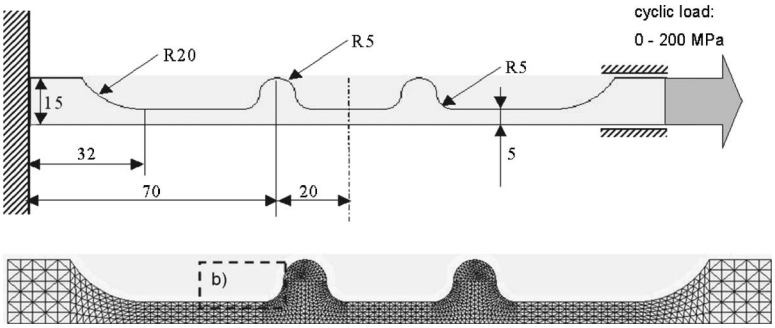

Fig. 2 Transmission case, boundary conditions, and FE mesh

The run time needed does not depend on the value of the failure probability as no Monte Carlo simulations are needed. Similar investigations with notched tensile bars are on the way.

The values given in the literature for the quantity W_c differ by several orders of magnitude. Therefore, three different cases are considered here as follows:

Table 1 Input data

Shear modulus G (GPa)	81
Specific fracture energy W_C (kJ/m^2)	0, 2, 20
Critical shear stress τ_c (MPa)	108
Poisson's ratio ν (-)	0.3
Crack growth parameter C (m, MPa, load cycle)	10^{-12}
Crack growth exponent m	3.5
Fracture toughness K_{IC} (MPa $\sqrt{}$(m))	80
Initial value of the aspect ratio $(a/c)_i$	2/3
Mean value of grain/defect size (10^{-6} m)	52
Variance of grain/defect size (10^{-12} m^2)	383

Table 2 Calculation details

Surface elements	322
Surface nodes	570
CPU: Pentium 4	2.53 GHz
RAM	1.00 GB
OS	Windows XP Professional 2002
Calculation time for 1 run	approx. 3 min

1. $W_c=0$, no crack initiation phase, all cracks start to grow at the very first load cycle. This case relates to materials that contain defects before applying the load (e.g., resulting from casting, forging, etc.).
2. $W_c=2$ kJ/m^2: Almost all cracks will initiate after a few hundred load cycles, i.e., most of the lifetime will be spent in the crack growth phase.
3. $W_c=20$ kJ/m^2: This value was estimated from the macroscopic fracture toughness and the energy release rate. The number of cycles to crack initiation is comparable to the number of cycles spent in the crack growth phase.

In Fig. 3 the conditional failure probabilities $Q_{1,el}$ are given for each element. Only part (*b*) (see Fig. 2) of the structure is shown for a more detailed presentation of results. The elemental failure probability decreases smoothly from the maximum value of 83.4% along the surface, even though the finite-element mesh contains elements of different sizes (see Fig. 3). The kinks in the contours (and the subsurface probabilities with values greater than 0) are related to the fact that nodal values were transferred to the graphics postprocessor. Figure 3 was obtained for $W_c=0$, i.e., a crack initiation phase was not taken into account. A plot for any of the other two cases would give a very similar picture.

Figure 4 shows the conditional failure probability of the most critical element as a function of the number of load cycles.

The effect of the initiation phase leads to a small shift in the lifetime distribution to higher lifetimes. However, this effect is not dramatic in contrast to the general statement that most of the lifetime is spent in the crack initiation phase. It has to be kept in mind, however, that this statement is made on the basis of a technical crack which has a depth of about 0.5–1 mm, i.e., is ten times deeper than the microcracks considered here. Moreover, cracks start to grow immediately after initiation. A threshold value to account for the retardation at the first microstructural barrier will be taken into account in future investigations.

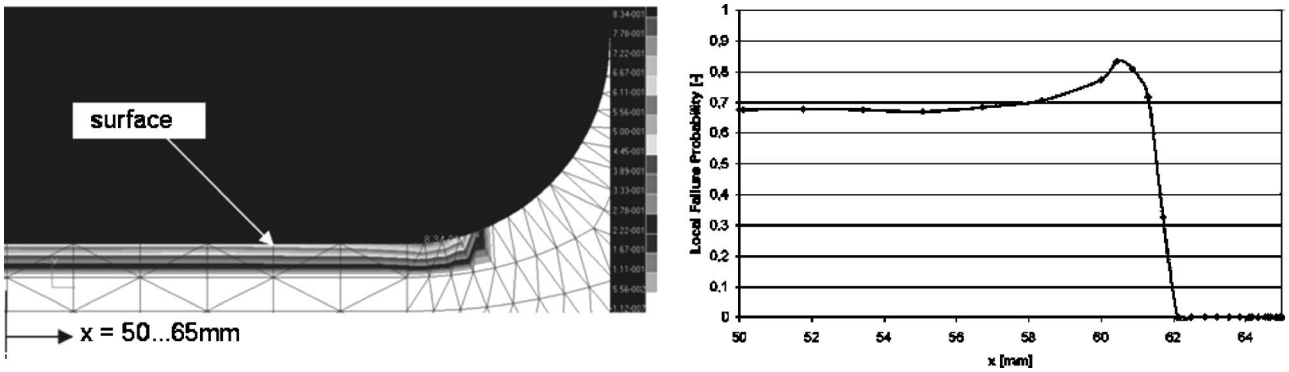

Fig. 3 Transmission case (detail *b*, see Fig. 2), elemental failure probabilities for N=600,000 and W_C=0

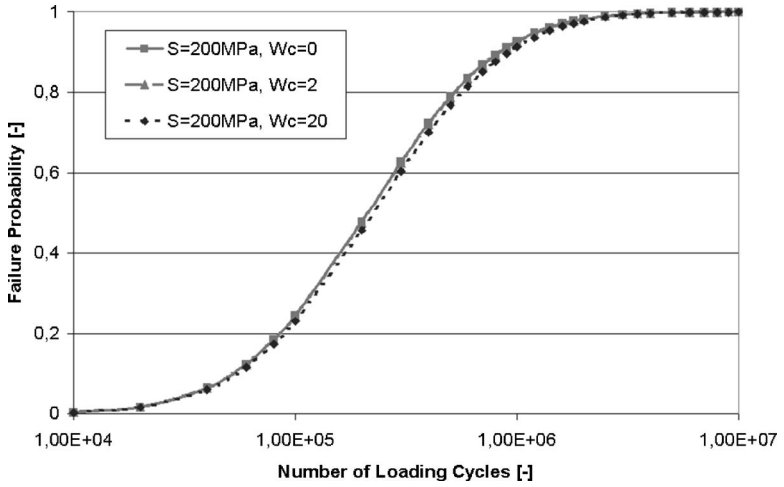

Fig. 4 Maximum local failure probability for different loading cycles and a maximum stress *S*=200 MPa

It is indeed true that the simulation shows that most of the lifetime is spent until a macroscopic value of the crack size is reached in agreement with common knowledge.

An additional explanation for the small effect of the initiation phase (Fig. 4) is given with the nature of Eqs. (1), (6), and (7). According to Eqs. (1) and (7) the number of cycles for crack initiation is inversely proportional on the squared difference of the von Mises stress and the critical shear stress. High values of the von Mises stress cause short crack initiation phases, i.e., the influence of the crack initiation phase increases for $2/\sqrt{3}\cdot\Delta\sigma_{\text{von Mises}}\rightarrow 2\tau_c$. Figure 5 shows this effect for a maximum stress $S=160$ MPa.

In comparison to Fig. 4, Fig. 5 shows that a lower stress leads to a longer lifetime and that at the same time the influence of the crack initiation phase increases as mentioned above.

Conclusions

The LOCC code is a post-processor for a commercial finite-element code and calculates local and global failure probabilities at a user-defined number of load cycles. The lifetime distribution is obtained by varying the number of load cycles. The initiation phase is included in addition to the crack growth phase. The results obtained depend on the mesh size only in terms of the stress field. Numerical convergence and stability are very good. Hence the code can be used as lifetime tool in a toolbox for probabilistic design.

Acknowledgment

Part of this work was supported by the European Union under Contract No. NNE5/2001/375 Nanorotor.

Nomenclature

$a, 2c, a_i$ = crack depth, crack length, initial crack depth
$a_c, a_{c,i}$ = critical crack depth, critical initial crack depth
C, m = parameters of the Paris law
D = grain diameter
G = shear modulus
K_{Ic} = fracture toughness
N_f = (design) lifetime of the component
N_g = number of cycles in the crack growth phase
N_i = number of cycles to crack initiation
R = stress ratio
W_c = fracture energy per unit area
$\Delta\tau_{\text{res}}$ = range of the local resolved shear stress
$\Delta\sigma$ = range of the local normal stress (Mode I)

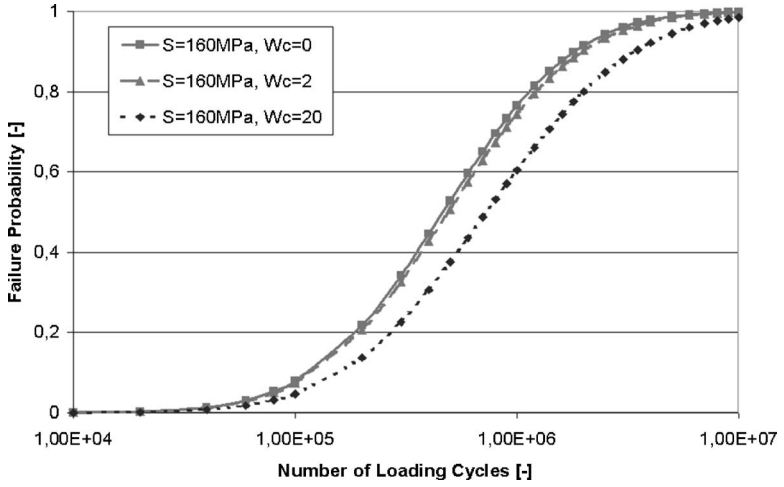

Fig. 5 Maximum local failure probability for different loading cycles and a maximum stress *S*=160 MPa

ν = Poisson's ratio
τ_c = critical shear stress

Symbols for the Probabilistic Model

$F_{a_i}(\cdot)$ = distribution of the initial crack depth
$F_D(\cdot)$ = distribution of the grain size
P_f = probability of failure of a component containing an arbitrary number of flaws
$Q_{1,\mathrm{el}}$ = conditional probability of failure provided that area A_{el} contains 1 flaw
$Q_{1,\mathrm{total}}$ = conditional probability of failure based on $Q_{1,\mathrm{el}}$ for an area A_{total} which is divided into several subareas A_{el}

References

[1] McClung, R. C. et al., 1999, "Development of a Probabilistic Design System for Gas Turbine Rotor Integrity," *Proceeding's Fatigue '99 The 7th International Fatigue Conference*, Beijing, China, June 8–12, pp. 2655–2660.

[2] Miller, K., 1982, "The Short Crack Problem," Fatigue Eng. Mater. Struct., **5**, pp. 223–232.

[3] Tanaka, K., and Mura, T., 1981, "A Dislocation Model for Fatigue Crack Initiation," ASME J. Appl. Mech., **48**, pp. 97–103.

[4] Tryon, R. G., and Cruse, T. A., 1998, "A Reliability-Based Model to Predict Scatter in Fatigue Crack Nucleation Life," Fatigue Fract. Eng. Mater. Struct., **21**, pp. 257–267.

[5] Fischmeister, H., Quadfasel, U., Banhardt, V., Brückner-Foit, A., Jäckels, H., Eßlinger, P., and König G., 1990, "Towards a Probabilistic Lifetime for Turbine Disks," Z. Metallkd., **81**, pp. 707–714.

[6] Navarro, A., and de los Rios, E., 1986, *The Behaviour of Short Fatigue Cracks*, European Group of Fracture, London.

[7] Ahmadi, A., and Zenner, H., 2005, "Simulation of Microcrack Growth for Different Load Sequences and Comparison With Experimental Results," Int. J. Fatigue, **27**, pp. 853–861.

[8] Brückner-Foit, A., Heger, A., and Munz, D., 1994, "Effect of Proof Testing on the Failure Probability of Multiaxially Loaded Ceramic Components," *Life Prediction Methods and Data for Ceramic Materials, ASTM STP 1201*, C. R. Brinkman and S. F. Duffy, eds., American Society for Testing and Materials, Philadelphia, pp. 346–359.

Transient Rotor/Active Magnetic Bearing Control Using Sampled Wavelet Coefficients

Iain S. Cade
e-mail: i.s.cade@bath.ac.uk

Patrick S. Keogh

M. Necip Sahinkaya

Department of Mechanical Engineering,
University of Bath,
Bath BA2 7AY, UK

A novel method for transient rotor/active magnetic bearing control using sampled wavelet coefficients is proposed. Control currents are formulated in the wavelet transform domain, prior to signal reconstruction. The wavelet based controller is designed from target transient responses due to step changes in wavelet coefficients of applied forces. Transient system dynamics are embedded in the controller and evaluated from on-line system identification. Experimental validation is undertaken using a flexible rotor/active magnetic bearing system. Mass loss tests were performed at two critical speeds corresponding to near sudden changes in unbalance that are capable of exciting rotor dynamic modes in a transient manner. The controller is shown to suppress the transient responses within a finite settling time. [DOI: 10.1115/1.2436570]

1 Introduction

Rotor/magnetic bearing systems may experience disturbances giving rise to transient rotor vibration. Unbalance changes, flow induced forces, base acceleration, sensor malfunctions and other component failures leading to loop signal perturbations are example disturbances. Traditional controllers aimed at cancellation of steady-state vibration may not offer the desired levels of control during transient periods.

Many different control strategies have been devised to control rotor/magnetic bearing systems during both steady state and transient forcing conditions. Optimal control strategies such as H_∞ and μ synthesis have been developed. Keogh et al. [1] present an H_∞ control method for transient vibration attenuation. It is important for such optimal controller design to have an accurate model of the system. Nonami and Ito [2] use μ-synthesis to formulate a more accurate representation of plant perturbations and errors in order to achieve improved controller performance. However, optimally designed controllers are limited in their performance due to the compromise between a high system order and computational efficiency for real-time implementation.

Burrows and Sahinkaya [3,4] use an open-loop technique to eliminate steady synchronous vibration. Knospe et al. [5–7] present adaptive open-loop updating of currents on a cyclic basis in order to remove synchronous vibration components. An adaptive open-loop controller is simulated by Shafai et al. [8] to solve the problem of sudden variation in rotor unbalance. These techniques can be extended to consider multiple frequency components to provide more general rotor control. Zimmerman et al. [9] use the Fourier components of the system disturbance in order to provide control within a finite time. Cole et al. [10] use a multilevel approach involving multiple frequencies, while transient control using sampled Fourier harmonics has been considered by Keogh et al. [11].

One of the main drawbacks of using Fourier based techniques for control is the delay incurred in evaluation of the Fourier coefficients. More recently, wavelet based methods of harmonic analysis have been used to study rotor vibrations to overcome transient averaging during Fourier analysis [12–14]. Furthermore, Fourier harmonics do not provide the most efficient representation of a transient vibration signal. Wavelet analysis, based around a localised oscillatory basis function, offers improved time–frequency resolution and its transient nature may provide an improved representation of the transient response. Chancey and Flowers [12] use wavelet analysis to extract transient patterns from measured rotor vibration signals. However, the literature describing wavelet based control strategies is limited. This paper therefore focuses on the use of the wavelet transform to provide a method of control for a flexible rotor/active magnetic bearing system when multiple frequency components are present in the system transient response. A method of transient rotor control is presented, which is formulated in the wavelet coefficient domain and designed around a prespecified target transient response. It is envisaged that magnetic bearing equipped rotors operating in motion induced environments or during transient fault conditions would benefit from the application of the wavelet based controller.

2 Wavelet Analysis and Filter Banks

2.1 Introduction to Wavelet Analysis. Wavelet analysis is a well established signal processing technique and accordingly there is much literature on the subject. For completeness a brief overview is presented here. More detailed explanations are given in Refs. [15,16]. Wavelet analysis provides a multiresolution time–frequency decomposition of a signal. This is achieved by integrating a signal with an appropriate mother wavelet, ψ, at different dilations, a, and translations, b, where ψ has zero mean, i.e., it must be oscillatory. Many of the problems associated with Fourier analysis such as fixed resolution and windowing are overcome by use of wavelet analysis. The wavelet transform of a function $f(t)$ is defined as

$$c(a,b) = |a|^{-1/2} \int_{-\infty}^{\infty} f(t)\psi\left(\frac{t-b}{a}\right)dt \tag{1}$$

2.2 Wavelet Analysis and Filter Banks. In a discrete sampled system the wavelet coefficients, $c(a,b)$, can be evaluated on a discrete grid where a and b are assigned regularly spaced values: $a=ma_0$ and $b=nb_0$, where m and n are integer values. This can be formulated using filter banks. References [15,16] show that a discrete time signal can be transformed into its wavelet coefficients, $c(a,b)$, by being passed through high-pass and low-pass filters in parallel and downsampled by a factor of 2. The output signals are referred to as the approximate and detail coefficients, respectively. The approximate coefficients correspond to the

Contributed by the International Gas Turbine Institute of ASME for publication in the JOURNAL OF ENGINEERING FOR GAS TURBINES AND POWER. Manuscript received July 5, 2006; final manuscript received July 14, 2006. Review conducted by Dilip R. Ballal. Paper presented at the ASME Turbo Expo 2006: Land, Sea and Air (GT2006), Barcelona, Spain, May 8–11, 2006, Paper No. GT2006-90212.

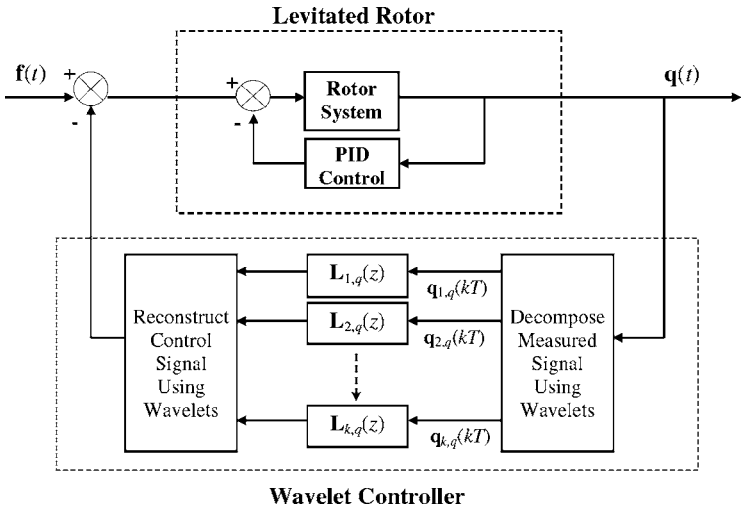

Fig. 1 Block diagram showing feedback control structure in the wavelet coefficient domain

wavelet coefficients, $c(a,b)$. Different wavelets are specified by filters having different impulse responses. Successive wavelet decompositions can be obtained by repeating the filtering and downsampling. The discrete output, $\mathbf{y}'(k)$, from a multilevel filter bank can be expressed as a vector of wavelet coefficients of the form

$$\mathbf{y}'(k) = [y_1(2k), y_2(4k), \ldots y_i(2^i k), y_i(2^i k + 1)]^T \tag{2}$$

where the subscript, i, indicates the octave number. The sample time at any given subband, i, is scaled by 2^i since it is downsampled by 2 in each channel. This is called *Dyadic sampling*. Perfect signal reconstruction can be achieved through successive upsampling, filtering with reconstruction filters, and summation of the coefficients associated with the detail signal.

3 Rotor Dynamics

A discretized flexible rotor model with N degrees of freedom can be described in terms of the vector of rotational and lateral displacements at each node, $\mathbf{x}(t)$. Denoting the vector of disturbance forces acting on the rotor as $\mathbf{f}(t)$ and any control force vector as $\mathbf{u}(t)$, the dynamics of the rotor, operating at a rotational speed Ω, can be derived from

$$\mathbf{M}\ddot{\mathbf{x}} + (\Omega\mathbf{G} + \mathbf{C})\dot{\mathbf{x}} + \mathbf{K}\mathbf{x} = \mathbf{B}_f\mathbf{f} + \mathbf{B}_u\mathbf{u} \tag{3}$$

where $\mathbf{M}$, $\mathbf{C}$, $\mathbf{K}$, and $\mathbf{G}$ are the mass, damping, stiffness, and gyroscopic matrices, respectively. $\mathbf{B}_f$ and $\mathbf{B}_u$ are distribution matrices, which map the dimensions of $\mathbf{f}$ and $\mathbf{u}$ to that of $\mathbf{x}$. This can be transformed into a first order problem without control ($\mathbf{u}(t) = \mathbf{0}$) as

$$\dot{\mathbf{q}} = \mathbf{A}\mathbf{q} + \mathbf{B}\mathbf{f}, \quad \mathbf{q} = \begin{bmatrix} \mathbf{x} \\ \dot{\mathbf{x}} \end{bmatrix} \tag{4}$$

$$\mathbf{A} = \begin{bmatrix} \mathbf{0} & \mathbf{I} \\ -\mathbf{M}^{-1}\mathbf{K} & -\mathbf{M}^{-1}(\Omega\mathbf{G} + \mathbf{C}) \end{bmatrix}, \quad \mathbf{B} = \begin{bmatrix} \mathbf{0} \\ \mathbf{M}^{-1} \end{bmatrix} \tag{5}$$

where $\mathbf{q}$ denotes the state vector. The system characteristics may be derived from the eigenvalue problem.

$$\mathbf{A}\mathbf{V} = \mathbf{V}\Lambda \tag{6}$$

The transformation $\mathbf{q} = \mathbf{V}\rho$ implies that

$$\dot{\rho}(t) = \Lambda\rho(t) + \mathbf{V}^{-1}\mathbf{B}\mathbf{f}(t) \tag{7}$$

The response of a specific mode, l, can be isolated by taking a single row of Eq. (7):

$$\dot{\rho}_l(t) = \lambda_l\rho_l(t) + (\mathbf{V}^{-1}\mathbf{B})_l\mathbf{f}(t) \tag{8}$$

where λ_l indicates the eigenvalue of mode l, and $(\mathbf{V}^{-1}\mathbf{B})_l$ corresponds to the lth row of $\mathbf{V}^{-1}\mathbf{B}$. Taking the Laplace transform of Eq. (8), as indicated by $\bar{\cdot}$, gives

$$s\bar{\rho}_l(s) = \lambda_l\bar{\rho}_l(s) + (\mathbf{V}^{-1}\mathbf{B})_l\bar{\mathbf{f}}(s) \tag{9}$$

The response of the system can be evaluated by superposing the individual modal contributions

$$\bar{\mathbf{q}}(s) = \sum_{l=1}^{2N} \frac{\mathbf{V}_l(\mathbf{V}^{-1}\mathbf{B})_l}{s - \lambda_l}\bar{\mathbf{f}}(s) \tag{10}$$

where $\mathbf{V}_l$ is the lth modal (column) vector.

4 Wavelet Coefficient Behavior

The proposed method of transient control is based around the wavelet decomposition of the rotor vibration, $\mathbf{q}(t)$. The controller will act in the wavelet coefficient domain with the objective of minimizing wavelet coefficients derived from measurement signals. The time dependent control signal will then be generated from the reconstruction of wavelet control coefficients (Fig. 1). The manner in which the wavelet coefficients are related needs to be assessed.

4.1 Multilevel Wavelet Representation of Rotor Vibration and Disturbance Force. Using the discrete wavelet transform it is possible to represent a signal over a limited time period T by

$$\mathbf{q}(t) = \mathbf{q}_1^0 + \sum_{p=0}^{\infty}\sum_{q=0}^{2^p-1} \mathbf{q}_{p,q}(T)\psi(2^p t - q), \quad 0 \leqslant t < T \tag{11}$$

where $\mathbf{q}_1^0$ is the average value of the signal. Separating the states into components of the signal over successive periods:

$$\mathbf{q}(t)=\begin{cases}\mathbf{q}_1^0+\sum_{p=0}^{\infty}\sum_{q=0}^{2^p-1}\mathbf{q}_{p,q}(T)\psi(2^pt-q) & 0\leqslant t<T\\ \mathbf{q}_2^0+\sum_{p=0}^{\infty}\sum_{q=0}^{2^p-1}\mathbf{q}_{p,q}(2T)\psi(2^pt-q) & T\leqslant t<2T\\ \vdots & \vdots\\ \mathbf{q}_k^0+\sum_{p=0}^{\infty}\sum_{q=0}^{2^p-1}\mathbf{q}_{p,q}(kT)\psi(2^pt-q) & (k-1)T\leqslant t<kT\\ \vdots & \vdots\end{cases} \tag{12}$$

A similar expression can be written to represent the input disturbances on the system

$$\mathbf{f}(t)=\begin{cases}\mathbf{f}_1^0+\sum_{a=0}^{\infty}\sum_{b=0}^{2^a-1}\mathbf{f}_{a,b}(T)\psi(2^at-b) & 0\leqslant t<T\\ \mathbf{f}_2^0+\sum_{a=0}^{\infty}\sum_{b=0}^{2^a-1}\mathbf{f}_{a,b}(2T)\psi(2^at-b) & T\leqslant t<2T\\ \vdots & \vdots\\ \mathbf{f}_k^0+\sum_{a=0}^{\infty}\sum_{b=0}^{2^a-1}\mathbf{f}_{a,b}(kT)\psi(2^at-b) & (k-1)T\leqslant t<kT\\ \vdots & \vdots\end{cases} \tag{13}$$

The wavelet coefficients of the system states and the input disturbance vectors are given by

$$\mathbf{q}_{p,q}(kT)=|p|^{-1/2}\int_{kT-q/2^p}^{kT}\mathbf{q}(t)\psi(2^pt-q)dt$$

$$\mathbf{f}_{a,b}(kT)=|a|^{-1/2}\int_{kT-b/2^a}^{kT}\mathbf{f}(t)\psi(2^at-b)dt \tag{14}$$

These decompositions offer a multiresolution approach and in order to design an effective controller it is desirable to understand how the input disturbance coefficients, $\mathbf{f}_{a,b}(kT)$, affect the system dynamics. Taking the Laplace transform of the input disturbance vector

$$\bar{\mathbf{f}}(s)=\sum_{k=1}^{\infty}\int_{(k-1)T}^{kT}\left[\mathbf{f}_k^0+\sum_{a=0}^{\infty}\sum_{b=0}^{2^a-1}\mathbf{f}_{a,b}(kT)\psi(2^at-b)\right]e^{-st}dt \tag{15}$$

In order to evaluate Eq. (15) the wavelet must now be specified. Under mass loss conditions the input disturbance can be considered as a step change in rotor unbalance. Hence, the Haar wavelet, with its step like characteristics, is a convenient choice. It also offers maximum resolution in time and frequency and takes the minimum time to evaluate using filters. The Haar wavelet is

$$\psi(t)=\begin{cases}1 & 0\leqslant t<1/2\\ -1 & 1/2\leqslant t<1\\ 0 & \text{otherwise}\end{cases} \tag{16}$$

Specific to the Haar wavelet, Eq. (15) becomes

$$\bar{\mathbf{f}}(s)=\sum_{k=1}^{\infty}\left[\frac{-\mathbf{f}_k^0e_1(s,kT)}{s}+\sum_{a=0}^{\infty}\sum_{b=0}^{2^a-1}\mathbf{f}_{a,b}(kT)\frac{e_2(s,kT,b)}{s}\right] \tag{17}$$

where

$$e_1(s,k,T)=e^{-skT}-e^{-s(k-1)T}$$

$$e_2(s,k,T,a,b)=2e^{-s[(k-1)T+2^{-b/2}-2^a]}-e^{-s[(k-1)T+2^{-b}-2^a]}-e^{-s[(k-1)T-2^a]} \tag{18}$$

From the modal expansion of the system response (Eq. (10)) the input wavelet coefficients dictate that

$$\bar{\mathbf{q}}(s)=\sum_{k=1}^{\infty}\sum_{l=1}^{2N}\frac{\mathbf{V}_l(\mathbf{V}^{-1}\mathbf{B})_l}{s(s-\lambda_l)}\left[-\mathbf{f}_k^0e_1(s,k,T)+\sum_{a=0}^{\infty}\sum_{b=0}^{2^a-1}\mathbf{f}_{a,b}(kT)e_2(s,k,T,a,b)\right] \tag{19}$$

Poles exist at $s=0$ and $s=\lambda_l$. The exponential terms in Eqs. (18) and (19) give rise to delays in the time domain. The dynamic response of the system is derived from the inverse Laplace transform

$$\mathbf{q}(t)=\sum_{k=1}^{\infty}\sum_{l=1}^{2N}\frac{\mathbf{V}_l(\mathbf{V}^{-1}\mathbf{B})_l}{\lambda_l}\left[-\mathbf{f}_k^0e^{\lambda_lt}u_1(t,\lambda_l,k,T)+\sum_{a=0}^{\infty}\sum_{b=0}^{2^a-1}\mathbf{f}_{a,b}(kT)e^{\lambda_lt}u_2(t,\lambda_l,k,T,a,b)\right] \tag{20}$$

where

$$u_1(t,\lambda_l,k,T)=H(t-kT)e^{-\lambda_lkT}-H(t-(k-1)T)e^{-\lambda_l(k-1)T}$$

$$\begin{aligned}u_2(t,\lambda_l,k,T,a,b)=&H(t-(k-1)T-2^a)(e^{-\lambda_l((k-1)T-2^a)}-1)\\&+H(t-(k-1)T+2^b-2^a)(e^{-\lambda_l((k-1)T+2^b-2^a)}-1)\\&-2H(t-(k-1)T+2^{b/2}-2^a)\\&\times(e^{-\lambda_l((k-1)T+2^{b/2}-2^a)}-1)\end{aligned} \tag{21}$$

and $H(t)$ is the Heaviside step function. From Eq. (20) the relation between wavelet coefficients of the system states can be evaluated as function of the wavelet coefficients of the input disturbance. Defining

$$g_1(m,T,\lambda_l,k,T,p,q)=|p|^{-1/2}\int_{(m-1)T}^{mT}u_1(t,\lambda_l,k,T)e^{\lambda_lt}\psi(2^pt-q)dt$$

$$g_2(m,T,\lambda_l,k,T,a,b,p,q)=|p|^{-1/2}\int_{(m-1)T}^{mT}u_2(t,\lambda_l,k,T,a,b)e^{\lambda_lt}\psi(2^pt-q)dt \tag{22}$$

Eq. (20) can be transformed in to the wavelet coefficient domain as

$$\mathbf{q}_{p,q}(mT)=\sum_{k=1}^{m-1}\sum_{l=1}^{2N}\frac{\mathbf{V}_l(\mathbf{V}^{-1}\mathbf{B})_l}{\lambda_l}\left[-\mathbf{f}_k^0g_1(m,T,\lambda_l,k,T,p,q)+\sum_{a=0}^{\infty}\sum_{b=0}^{2^a-1}\mathbf{f}_{a,b}(kT)g_2(m,T,\lambda_l,k,T,a,b,p,q)\right] \tag{23}$$

However, since $\mathbf{q}_{p,q}(mT)$ is evaluated as a summation over $1\leqslant k\leqslant m-1$, Eqs. (22) reduce to

$$g_1(m,T,\lambda_l,k,T,b,p) = \frac{|p|^{-1/2}}{\lambda_l} e_1(-\lambda_l,k,T)$$

$$g_2(m,T,\lambda_l,k,T,a,b,p,q) = \frac{|p|^{-1/2}}{\lambda_l} e_2(-\lambda_l,k,T,a,b)e_2(\lambda_l,m,T,p,q) \tag{24}$$

Thus

$$\mathbf{q}_{p,q}(mT) = -\sum_{k=1}^{m-1}\sum_{l=1}^{2N} |p|^{-1/2}\frac{\mathbf{V}_l(\mathbf{V}^{-1}\mathbf{B})_l}{\lambda_l^2}\left[\mathbf{f}_k^0 e_1(-\lambda_l,k,T) - \sum_{a=0}^{\infty}\sum_{b=0}^{2^a-1}\mathbf{f}_{a,b}(kT)e_2(-\lambda_l,k,T,a,b)e_2(\lambda_l,m,T,p,q)\right] \tag{25}$$

The response of the system at the next time step can be obtained by replacing mT with $(m+1)T$. Evaluating the difference between time steps as $\mathbf{q}_{p,q}((m+1)T) - \mathbf{q}_{p,q}(mT)$ gives

$$\mathbf{q}_{p,q}((m+1)T) - \mathbf{q}_{p,q}(mT) = -\sum_{l=1}^{2N}\frac{\mathbf{V}_l(\mathbf{V}^{-1}\mathbf{B})_l}{\lambda_l^2}|p|^{-1/2}\left[(\mathbf{f}_m^0 e_1(-\lambda_l,m,T) - \mathbf{f}_{m-1}^0 e_1(-\lambda_l,(m-1),T)) - \sum_{a=0}^{\infty}\sum_{b=0}^{2^a-1}(\mathbf{f}_{a,b}(mT) \times e_2(-\lambda_l,k,T,a,b)e_2(\lambda_l,m,T,p,q) - \mathbf{f}_{a,b}((m-1),T)e_2(-\lambda_l,k,T,a,b)e_2(\lambda_l,(m-1)T,p,q))\right] \tag{26}$$

Equation (26) contains two main terms. The first, involving $\mathbf{f}_m^0$ and $\mathbf{f}_{m-1}^0$, describes a change in the average value of the forcing between two periods. For a periodic signal $\mathbf{f}_{m-1}^0 = \mathbf{f}_m^0 = \mathbf{f}_0^0$, where $\mathbf{f}_0^0$ represents the constant force acting on the system. The second term, involving $\mathbf{f}_{a,b}(mT)$ and $\mathbf{f}_{a,b}((m-1)T)$, corresponds to forcing by a wavelet at a given dilation and translation. Since Eq. (26) represents sampled time signal data, it can be converted into the Z-transform domain. Using the standard notation

$$\mathbf{q}_{p,q}(mT) \to \mathbf{Q}_{p,q}(z)$$

$$\mathbf{f}_{a,b}(mT) \to \mathbf{F}_{a,b}(z) \tag{27}$$

after some work, Eq. (26) yields

$$\mathbf{Q}_{p,q}(z) = \mathbf{G}_{p,q}^0\mathbf{f}_0^0 - \sum_{a=0}^{\infty}\sum_{b=0}^{2^a-1}\mathbf{G}_{p,q,a,b}(z)\mathbf{F}_{a,b}(z) \tag{28}$$

Here

$$\mathbf{G}_{p,q,a,b}(z) = \sum_{l=1}^{2N}\frac{\gamma_{p,q,a,b}e^{-2\lambda_l T}\mathbf{V}_l(\mathbf{V}^{-1}\mathbf{B})_l}{\lambda_l^2}\left(\frac{z-1}{z-e^{2\lambda_l T}}\right) \tag{29}$$

$$\gamma_{p,q,a,b} = |p|^{-1/2}(2e^{2^a-2^{-b/2}} - e^{2^a-2^{-b}} - e^{2^a}) \times (2e^{-2^p+2^{-q/2}} - e^{-2^p+2^{-q}} - e^{-2^p}) \tag{30}$$

and for periodic forcing

$$\mathbf{G}_{p,q}^0 = \sum_{l=1}^{2N}|p|^{-1/2}\frac{\mathbf{V}_l(\mathbf{V}^{-1}\mathbf{B})_l}{\lambda_l^2} \tag{31}$$

5 Discrete Control

Controller design is to be based on a control force evaluated from single or multiple wavelet coefficients. Assuming that an orthogonal wavelet (e.g., Haar) is used to decompose the measured signals and reconstruct the control signal, each control wavelet coefficient can be evaluated using a different set of control parameters. The closed loop response of a given wavelet coefficient can be evaluated by replacing $\mathbf{F}_{a,b}(z)$ by $\mathbf{F}_{a,b}(z) + \mathbf{B}_u\mathbf{U}_{a,b}(z)$ in Eq. (28). The control force wavelet coefficients, $\mathbf{U}_{p,q}(z)$, are now specified by

$$\mathbf{U}_{p,q}(z) = -\mathbf{L}_{p,q}(z)\mathbf{Q}_{p,q}^{(m)}(z) \tag{32}$$

where $\mathbf{L}_{p,q}(z)$ represents the controller operating on wavelet coefficients at level p. The matrix $\mathbf{B}_m$ is used to extract the measurement states from the system state vector as $\mathbf{Q}_{p,q}^{(m)}(z) = \mathbf{B}_m\mathbf{Q}_{p,q}(z)$. The closed loop response of the system satisfies

$$[\mathbf{I} - \mathbf{G}_{p,q,p,q}(z)\mathbf{B}_u\mathbf{L}_{p,q}(z)]\mathbf{Q}_{p,q}^{(m)}(z) = \mathbf{G}_{p,q}^0\mathbf{f}_0^0 - \sum_{a=0}^{\infty}\sum_{b=0}^{2^a-1}\mathbf{G}_{p,q,a,b}(z)\mathbf{F}_{a,b}(z) \tag{33}$$

The controller objective is to minimize the transient response of the measured states at a given level of wavelet decomposition, p. The controller is also required to provide optimal steady state performance. In order to achieve this the controller is designed around a desired closed loop transient response due to a step change in the wavelet coefficients of an input disturbance:

$$\text{Step input: } \mathbf{F}_{p,q}(z) = \frac{1}{z-1}\mathbf{B}_u$$

$$\text{Desired output: } \mathbf{Q}_{p,q}^{(m)}(z) = \alpha_{p,q}(z)\mathbf{G}_{p,q,p,q}(z)\mathbf{B}_u \tag{34}$$

The least squares solution of Eq. (33) for a controller with the specified transient response of Eq. (34) is

$$\mathbf{L}_{p,q}(z) = [\mathbf{G}_{p,q,p,q}(z)\mathbf{B}_u]^*\left[\frac{1}{\alpha_{p,q}(z)(z-1)} - 1\right] \tag{35}$$

where * denotes the pseudo-matrix inverse.

It is noted that closed loop instability could result from the application of the controller specified in Eq. (35), for example, due to residuals arising from the least squares solution. An assessment of closed loop stability could be made at this stage if a system modeling approach is adopted. A controller could also be derived from a model based on system identification and assessed using on-line testing to determine acceptable operating boundaries. The latter approach overcomes certain issues relating to modeling uncertainty and for this reason is selected for this paper.

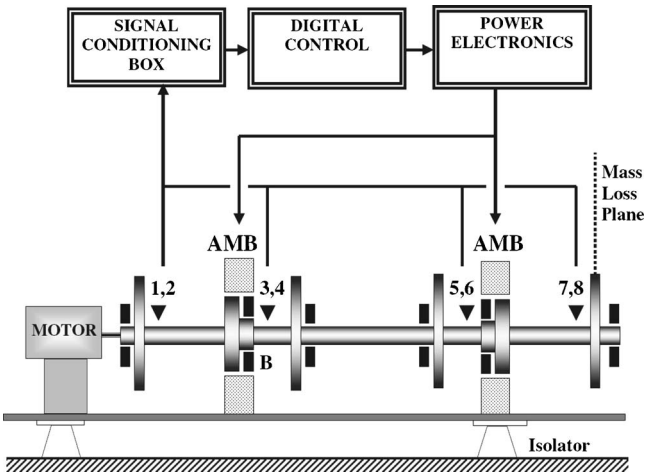

Fig. 2 Experimental flexible rotor/ active magnetic bearing facility. Sensors measuring displacement relative to base motion are shown as 1-8. Experimental mass loss plane is also shown.

6 Variations of Transient Response Characteristic

The control action is dictated by the specified transient response characteristic. Exponential decay of the wavelet coefficients can be achieved by setting $\alpha_{p,q}(z)$ to

$$\alpha_{p,q}(z) = \frac{w_{p,q}}{z - v_{p,q}} \tag{36}$$

where $0 \leqslant w_{p,q} < 1$ and $0 \leqslant v_{p,q} < 1$. However, any other decay characteristic can also be specified. Expressing the desired transient response characteristic as a series

$$\alpha_{p,q}(z) = \sum_{k=1}^{\infty} \frac{c_k}{z^k} \tag{37}$$

then c_k is the desired transient response after the kth time step.

7 System Identification for Controller Design

From Eq. (28), the transient response of the system is determined by knowledge of $\mathbf{G}_{p,q,a,b}(z)$. In principle, Eq. (29) may be evaluated from system modeling. However, this may lead to uncertainties due to discretization errors. An alternative method is to identify $\mathbf{G}_{p,q,a,b}(z)$ using direct measurement. The rotor response due to a step input in the wavelet coefficients at a level a, applied through the magnetic bearings, can be measured. Gain matrices, $\mathbf{A}^{(k)}_{p,q,a,b}$, can then be identified to represent the transfer function of the system at a given time step and level p:

$$\mathbf{G}_{p,q,a,b}(z) = \sum_{k=1}^{\infty} \frac{\mathbf{A}^{(k)}_{p,q,a,b}}{z^k} \tag{38}$$

The pseudo-inverse transfer function can then be expressed as

$$[\mathbf{G}_{p,q,a,b}(z)\mathbf{B}_u]^* = \sum_{k=1}^{\infty} \frac{\mathbf{B}^{(k)}_{p,q,a,b}}{z^k} \tag{39}$$

where the $\mathbf{B}^{(k)}_{p,q,a,b}$ are derived from sets of linear equations.

8 Experimental Validation

8.1 Flexible Rotor/Active Magnetic Bearing Facility. Controller performance was evaluated experimentally on a flexible rotor/active magnetic bearing facility (Fig. 2). The rotor consists of a 2 m long shaft of mass 50 kg upon which four moveable 10 kg disks are positioned. The shaft and disks are 50 mm and 250 mm in diameter, respectively. The rotor is supported by two radial active magnetic bearings. Each eight-pole magnetic bearing is capable of providing radial forces of 1700 N before rolloff occurs at 100 Hz. These form two orthogonal opposing coil pairs and are positioned at ±45 deg to the vertical to maximize static load. Auxiliary rolling element bearings are positioned inside the magnetic bearings to prevent rotor contact with the lamination stacks. Rotor displacements are measured using eight eddy current transducers arranged in four orthogonal pairs and positioned at ±45 deg to the vertical. Initial rotor control is achieved using proportional-integral-derivative (PID) control with the four transducers local to the magnetic bearings. The PID controller was designed to provide sufficient control forces to ensure rotor stability. The wavelet coefficient controller was configured with a parallel feedback structure (Fig. 1).

Table 1 Measurement parameter terminology

Parameter	Description
$x^{(i)}$	Displacement measured by sensor i
$x^{(i)}_{1,1}$	Wavelet coefficient ($p=1$, $q=1$) of displacement measured by sensor i
$u^{(j)}$	Magnetic bearing force in the jth control axis
$u^{(j)}_{1,1}$	Wavelet coefficient ($p=1$, $q=1$) of force in the jth control axis
$b(k)$	Element (1,1) of matrix $\mathbf{B}^{(k)}_{1,1,1,1}$ (see Eq. (39))

8.2 Experimental Procedure and Results. The experimentally derived parameters to be presented are specified in Table 1. The system was identified from measurement of the wavelet coefficients with a pseudo-frequency matching the rotational frequency. Control wavelet coefficients were set at the same level such that $a=p=1$. Figure 3(*a*) shows the measured response at sensor 1 due to a step wavelet disturbance applied through control axis 1. The inverse transfer function has been identified and truncated after 10 and 5 time steps (Figs. 3(*b*) and 3(*c*)). The fifth-order version was selected to allow for real time controller implementation. The controller evaluation time required there to be a three cycle delay in control action.

Variation of the parameters $w_{1,1}$ and $v_{1,1}$ was used to create controllers with different target transient responses. From observations of the rotor displacements, controllers were classified un-

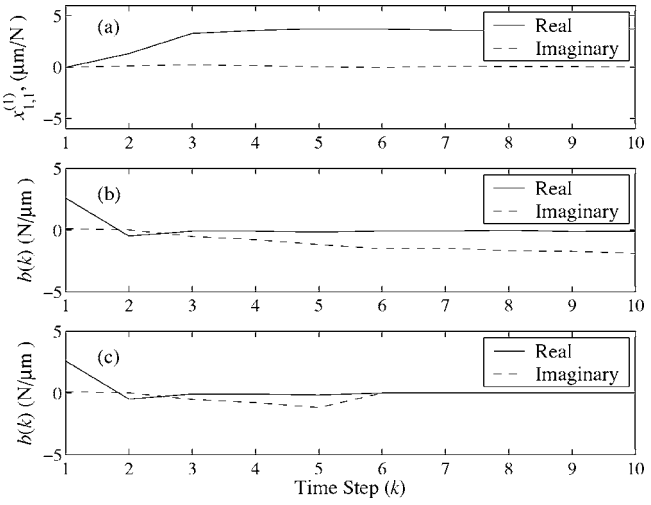

Fig. 3 System identification at sensor 1 due to wavelet harmonic forcing in control axis 1 at rotational speed of 11 Hz: (*a*) measured synchronous harmonic wavelet coefficients; (*b*) tenth-order inverse transfer function; and (*c*) fifth-order inverse transfer function.

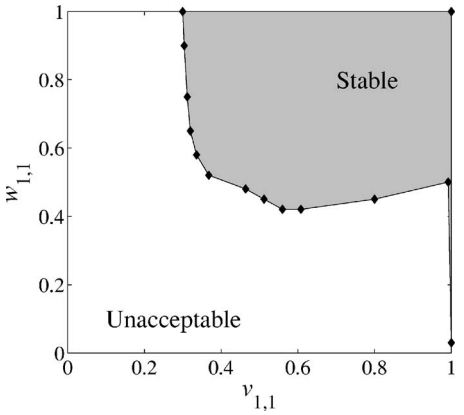

Fig. 4 Acceptable performance diagram for a prescribed transient exponential decay at a rotational speed of 11 Hz

acceptable if the vibration exceeded a specified limit of 0.5 mm in any control plane. A systematic experimental search of the stability limit yielded the boundary shown in Fig. 4 for a controller designed to operate at 11 Hz. The same procedure was used to identify a limit on the maximum linear decay rate per time step for controllers operating at 11 Hz. This was found to be 0.3 per time step.

Mass-loss experiments were performed at the nondriven end disk (Fig. 2) at the first two critical speeds: 11 Hz and 18 Hz. Mass loss was initiated by a blade mechanism using a tied on mass from an initial indeterminate state of unbalance. The effective unbalance loss was 430 g cm. The wavelet coefficient controller was configured to give an exponential decay as prescribed by Eq. (36) where $w_{1,1}=0.7$ and $v_{1,1}=0.7$. Figure 5 shows the mass-loss response of the rotor at a rotational frequency of 11 Hz at the nondriven end disk and at the driven end active magnetic bearing for uncontrolled and controlled cases. The corresponding wavelet coefficients are presented at each sampled step for the controlled case. The controller is shown to suppress the transient responses within a finite settling time. Figure 6 shows both the wavelet control force and the total control force at each magnetic bearing. The mass loss response at a rotational frequency of 18 Hz is presented in Fig. 7 for $w_{1,1}=v_{1,1}=0.7$. Variation of the prescribed transient response is shown in Fig. 8 for $w_{1,1}=v_{1,1}=0.5$

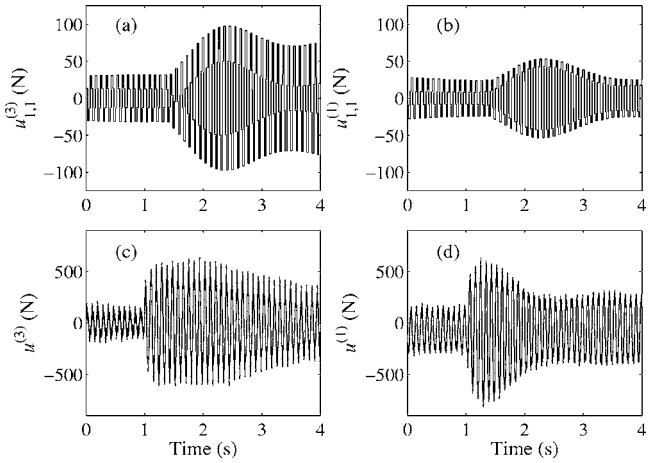

Fig. 6 (*a*) and (*b*) show the wavelet control forces at nondriven end and driven end active magnetic bearing at a rotational speed of 11 Hz; and (*c*) and (*d*) show the total control force

(faster exponential decay), $w_{1,1}=v_{1,1}=0.9$ (slower exponential decay), and a linear decay rate of 0.2 per time step. These results demonstrate how the transient rotor response can be directly influenced by the selected target setting of Eq. (34). Moreover, the wavelet coefficient variations provide strong correlations to the boundary envelopes of the directly measured rotor vibratory signals. The potential for transient control in the wavelet coefficient domain has thus been shown to be highly positive.

Limitations in the level of possible transient control relate to stability issues in the closed loop, which are caused primarily by the control evaluation delays. For ultra high speed rotors, processor limitations could result in increased delays and hence degrade closed loop stability. Measurement noise could also contribute to reduced controller performance and stability margins. However, the on-line testing procedure presented could, in principle, be used to determine a more conservative acceptable performance diagram for the controller.

9 Conclusions

A novel method of transient rotor/ active magnetic bearing control using sampled wavelet harmonics has been proposed. Control

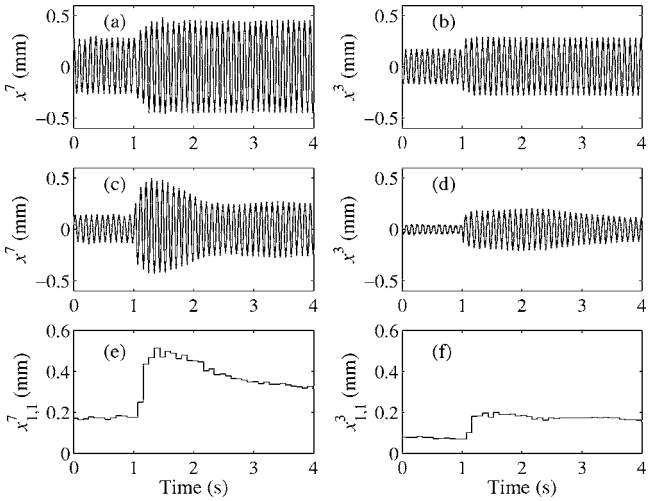

Fig. 5 Measured mass loss response at the nondriven end and driven end AMB at a rotational speed of 11 Hz: (*a*),(*b*) show uncontrolled response and (*c*),(*d*) show controlled response. Wavelet coefficients are shown in (*e*),(*f*).

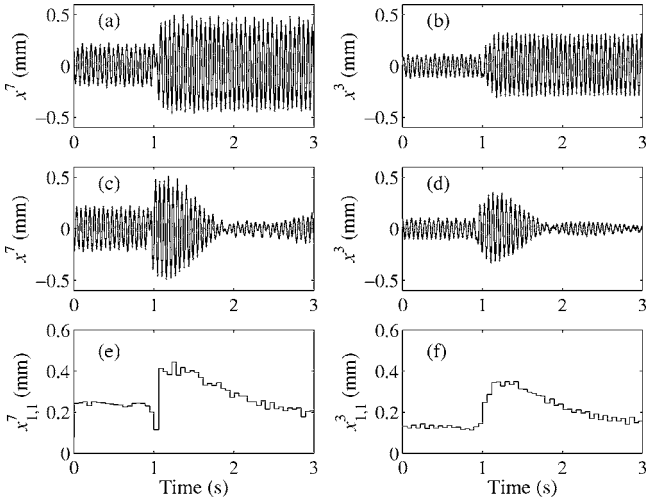

Fig. 7 Measured mass loss response at the nondriven end and driven end AMB at a rotational speed of 18 Hz: (*a*),(*b*) show uncontrolled response and (*c*),(*d*) show controlled response. Wavelet coefficients are shown in (*e*),(*f*).

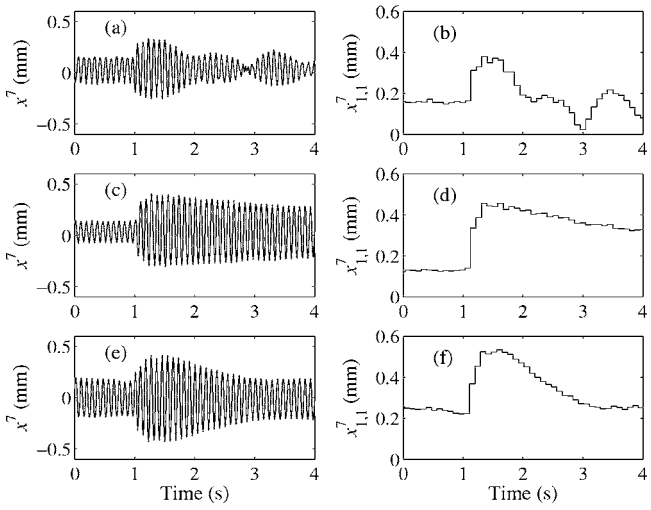

Fig. 8 Measured mass loss response and wavelet coefficients at the nondriven end at a rotational speed of 11 Hz: (*a*) and (*b*) correspond to a fast exponential decay rate; (*c*) and (*d*) correspond to a slow exponential decay rate; and (*e*) and (*f*) show a prescribed linear decay.

currents were formulated in the wavelet coefficient domain in order to attenuate the measured transient rotor vibration. The wavelet based controller was designed from a target transient response due to step changes in wavelet coefficients of input disturbances. Transient system dynamics were embedded in the controller and derived from on-line system identification.

Experimental validation was performed on a flexible rotor/ active magnetic bearing facility. Mass loss experiments were undertaken at the first two critical rotor speeds. The controller suppressed the transient responses within a finite settling time. Variation of the prescribed transient responses are shown to allow shaping of the rotor vibratory signals. Stability criteria for linear and exponentially decaying wavelet controllers are identified. This method offers potential for an improved control strategy utilizing multiple wavelet levels. Optimizing the computational efficiency to minimize control evaluation delays would improve stability margins and performance.

Acknowledgment

The authors gratefully acknowledge the funding support of the Engineering and Physical Sciences Research Council through Grant No. GR/R45277/01.

References

[1] Keogh, P. S., Mu, C., and Burrows, C. R., 1995, "Optimised Design of Vibration Controllers for Steady State and Transient Excitation of Flexible Rotors," Proc. Inst. Mech. Eng., Part C: J. Mech. Eng. Sci. **209**(3), pp. 155–168.

[2] Nonami, K., and Ito, T., 1994, "μ-Synthesis of Flexible Rotor Magnetic Bearing Systems," *Proc. of 4th International Symposium on Magnetic Bearings*, p. 73–78.

[3] Burrows, C. R., and Sahinkaya, M. N., 1983, "Vibration Control of Multi-Mode Rotor-Bearing Systems," *Proceedings of the Royal Society, London*, 386(1790), pp. 77–94.

[4] Burrows, C. R., Sahinkaya, M. N., and Clements, S., 1989, "Active Vibration Control of Flexible Rotors: An Experimental and Theoretical Study," *Proceedings of the Royal Society, London*, 422(1862), pp. 123–146.

[5] Knospe, C. R., Hope, R. W., Fedigan, S. J., and Williams, R. D., 1995, "Experiments in the Control of Unbalance Response Using Magnetic Bearings," Mechatronics, **5**(4), pp. 385–400.

[6] Knospe, C. R., Fedigan, S. J., Hope, R. W., and Williams, R. D., 1997, "A Multitasking DSP Implementation of Adaptive Magnetic Bearing Control," IEEE Trans. Control Syst. Technol., **5**(2), pp. 230–238.

[7] Knospe, C. R., Tamer, S. M., and Lindlau, J., 1997, "New Results in Adaptive Vibration Control," *Proc., 1997 Industrial Conference and Exhibition on Magnetic Bearings*, pp. 209–219.

[8] Shafai, B., Beale, S., LaRocca, P., and Cussons, E., 1994, "Magnetic Bearing Control Systems and Adaptive Forced Balancing," IEEE Control Syst. Mag., **14**(2), pp. 4–13.

[9] Zimmerman, D. C., Inman, D. J., and Juang, J. N., 1991, "Vibration Suppression Using a Constrained Rate-Feedback-Threshold Strategy," ASME J. Vibr. Acoust., **113**(3), pp. 345–353.

[10] Cole, M. O. T., Keogh, P. S., and Burrows, C. R., 2002, "Control of Multifrequency Rotor Vibration Components," Proc. Inst. Mech. Eng., Part C: J. Mech. Eng. Sci., **216**(2), pp. 165–177.

[11] Keogh, P. S., Cole, M. O. T., and Burrows, C. R., 2002, "Multi-State Transient Rotor Vibration Control Using Sampled Harmonics," ASME J. Vibr. Acoust., **124**(2), pp. 186–197.

[12] Chancey, V. C., and Flowers, G. T., 2001, "Identification of Transient Vibration Characteristics Using Absolute Harmonic Wavelet Coefficients," J. Vib. Control, **7**(8), pp. 1175–1193.

[13] Newland, D. E., 1994, "Wavelet Analysis of Vibration, Part 1: Theory," ASME J. Vibr. Acoust., **116**(4), pp. 409–416.

[14] Newland, D. E., 1994, "Wavelet Analysis of Vibration, Part 2: Wavelet Maps," ASME J. Vibr. Acoust., **116**(4), pp. 417–425.

[15] Strang, G., and Nguyen, T., 1996, *Wavelets and Filter Banks*, Wellsey-Cambridge Press.

[16] Vetterli, M., and Kovačević, 1995, *Wavelets and Subband Coding*, Prentice-Hall, Englewood Cliffs, NJ.

Experimental Investigation of Flow Phenomena of a Single Fuel Jet in Cross-Flow During Highly Preheated Air Combustion Conditions

Magnus Mörtberg

Wlodzimierz Blasiak

Department of Mechanical Engineering,
The Combustion Laboratory,
University of Maryland,
College Park, MD 20742
and Department of Materials Science
and Engineering,
Division of Energy and Furnace Technology,
Royal Institute of Technology (KTH),
S10044, Stockholm, Sweden

Ashwani K. Gupta[1]

Department of Mechanical Engineering,
The Combustion Laboratory,
University of Maryland,
College Park, MD 20742
e-mail: akgupta@eng.umd.edu

Particle image velocimetry and a spectroscopy technique has been used to obtain information on the flow dynamics and flame thermal signatures of a fuel jet injected into a cross-flow of normal temperature and very high-temperature combustion air. Flame fluctuations were obtained using a high-speed camera and then performing fast Fourier transform on the signal. High-temperature air combustion has been demonstrated to provide significant energy savings, higher heat flux, and reduction of pollution and equipment size of industrial furnaces. The dynamics of flow associated with high temperature combustion air conditions (for mean velocity, axial strain rate and vorticity) has been obtained in two-dimensional using propane and methane as the fuels. The data have been compared with normal temperature combustion air case, including the nonburning case. A specially designed experimental test furnace facility was used to provide well-controlled conditions and allowed air preheats to 1100°C *using regenerative burners. Four different experimental cases have been examined. The momentum flux ratio between the burning and nonburning conditions was kept constant to provide comparison between cases. The results provide the role of high-temperature combustion air on the dynamics of the flow, turbulence, and mixing under nonburning and combustion conditions. The data provide the direct role of combustion on flow dynamics, turbulence, and flame fluctuations. High-temperature combustion air at low-oxygen concentration showed larger flame volume with less fluctuation than normal or high-temperature normal air cases. High-temperature combustion air technology prolongs mixing in the combustion zone to enhance the flame volume, reduce flame fluctuations, and to provide uniform flow and thermal characteristics. This information assists in model validation and model development for new applications and technology development using high-temperature air combustion principles.* [DOI: 10.1115/1.2436558]

Keywords: high temperature air combustion, flow dynamics, energy conservation, pollution reduction

Introduction

During the past decade the use of highly preheated and oxygen deficient combustion air as the oxidizer using regenerative combustion systems has grown strong interest for industrial and power systems. This combustion method offers significant energy savings (up to about 60%), reduced emissions of NO_x, CO_2 to the environment (about 30%), reduced size of the equipment for same process throughput (about 25%), and enhanced and uniform thermal field in the combustion zone [1–3]. Far more uniform thermal field and higher and uniform heat flux distribution in the combustion zone helps to achieve better quality of product from the thermal process. The method has been shown to provide wider adoption in the industrial furnaces due to demonstrated evidence of significant energy savings and reduced pollution in a range of industrial furnaces [2,3].

One of the distinctive features of high-temperature air combustion (HiTAC) is the noticeable change in flame properties as the air-preheat temperature increases and oxygen concentration in the combustion air decreases [1,3]. As reported by many different researchers, one of the main characteristics is the increase in the flame volume with high-temperature combustion air. Gupta [1] reported an increase in the flame size and volume with increase in temperature and decrease in oxygen concentration of the combustion air. These results have also been reported by several other authors, e.g., experimental observations by Blasiak et al. [4] and numerical investigations by Yang and Blasiak [5]. Mortberg et al. [6] studied flow dynamics of fuel jets under high-temperature conditions for low calorific value fuels and normal gaseous fuels and noted significant differences of the jet behavior under high-temperature conditions for the different fuels examined and a strong influence of the temperature and oxygen concentration. Fuel chemical properties have significant influence on the flow and combustion characteristics under HiTAC conditions [7].

Under high-temperature and low-oxygen concentration of the combustion air a green color flame has been produced with hydrocarbon fuels. This green color flame has not been observed with hydrocarbon fuels using normal combustion air. Other flame colors have also been observed using other types of oxidative environments. This change of flame color provides capability to alter and control flame signatures and heat flux distribution in the combustion zone. Hasegawa et al. [2] and Tsuji et al. [3] studied

[1]Corresponding author.

Contributed by the Fuels and Combustion Technologics Division of ASME for publication in the JOURNAL OF ENGINEERING FOR GAS TURBINES AND POWER. Manuscript received October 22, 2004; final manuscript received May 28, 2006. Review conducted by Kenneth Mark Bryden.

the flame thermal characteristics of a basic flame and measured considerably lower temperature gradients for flames with increasing preheat temperature and decreasing O_2 concentration of the oxidizer in a small-scale test stand, which suggested significantly different flame properties under HiTAC conditions as compared to normal temperature air case. The flame volume was significantly enhanced to fill the entire combustion chamber volume with much higher heat flux as compared to the normal combustion air case [2,3]. In some cases the flame was observed to be colorless [1] and this mode of combustion is now referred to as flameless oxidation [3,6]. To date no data have been reported on the flow dynamics associated with high-temperature air combustion conditions. This is because the technology is relatively new and the diagnostics used to examine the flowfield in combustion has only recently been developed [8]. Laser velocimetry can be used but it is very time consuming and the data obtained are time mean in property so that it is not easy to determine the higher order of turbulence that is required for newer models to validate high-temperature air combustion conditions.

The jet in cross-flow is an important flow configuration and has many different industrial applications due to very fast mixing between the reactants. It has been shown in the case of combustion that a jet in cross-flow provides an efficient mixing and combustion as compared to coflow jets. In combustion a fuel jet injected into a cross-flow results in complex fluid dynamic phenomena due to the complex interaction between the fuel jet and cross-flow.

The particle image velocimetry (PIV) diagnostics provides detailed information on the entire flow field quickly as compared to other laser diagnostic methods. Until recently it was not possible to use PIV diagnostics in combustion studies due to high background radiation from flame which provided poor quality of the images. The use of narrow band filters placed in front of the cameras or seeding the flow with fluorescence particles to eliminate the background radiation provided unacceptable results. Gupta et al. [8] recently developed the technique so that flow field measurements can be successfully obtained in flames with high background radiation.

The jet in cross-flow is an important flow configuration and has many different industrial applications due to very fast mixing between the reactants. For the case of combustion, it has been shown that a jet in cross-flow provides an efficient mixing and combustion as compared to co-flow jets. However, during combustion a fuel jet injected into a cross-flow results in complex fluid dynamic phenomena due to the complex interaction between the fuel jet and cross-flow.

A number of different studies on jets in cross-flow have been carried out by several different researchers [9,10]. Donghee and Mungal [11] investigated flow fields and the distribution of CH in flames using co-flow and cross-flow jet arrangement. Stabilization mechanism of jet diffusion flames is given in Ref. [12].

The normal practice has been to use the information for the normal combustion case when calculating the flow dynamics associated with combustion using high-temperature air [5]. In the present study the effect of various gas jets on the flow, mixing, and thermal characteristics has been obtained in a jet in cross-flow arrangement. A basic understanding of the complex flow phenomena associated with the HiTAC conditions results in a better foundation for further development of the technique. These experiments also help to validate and develop the model of combustion for such technologically important conditions for which no such data exists in the literature. The data help to further control the more desired features of the flame and to assist in wider applications than the existing applications to furnaces and low-grade fuels.

In this paper we report results from an experimental investigation on the flow field associated with the nonburning and burning fuel jet in a cross-flow of combustion air (at normal and high temperature) using methane and propane as the fuels. Propane and methane are among the two most important gaseous fuels used in industries in Europe and the USA, The combustion air used is at very high temperature, in excess of 1173 K, and simulates the conditions present in HiTAC conditions for furnaces and other applications using high-temperature air combustion principles. Thermal behavior of the flames is also reported.

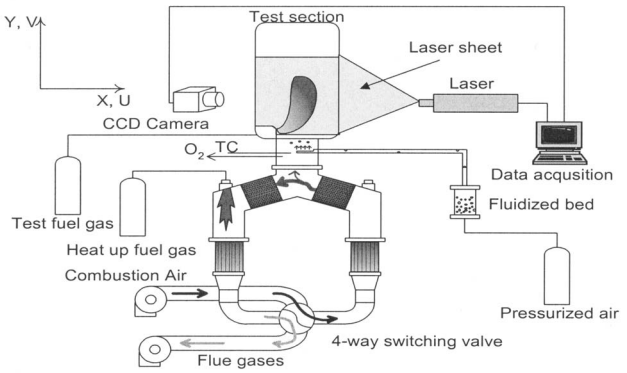

Fig. 1 A schematic diagram of the experimental high-temperature air combustion test facility

Experimental Facility and Investigative Methodology

A schematic diagram of the high temperature air combustion test facility used in the experimental investigation is shown in Fig. 1. The facility consists of two burners, firing in two different furnace Sections A and B of the facility. The furnace sections are equipped with ceramic honeycomb regenerators for thermal storage of the heat before the exhaust gases are vented to the environment. Thus almost all the thermal energy is extracted from the exhaust gases before their discharge to the atmosphere.

The facility generates a continuous flow of highly preheated (in excess of 1200 K) air in the test section by passing the air (of any composition) through ceramic honeycombs. The air at ambient temperature is preheated during its passage through the thermal storage honeycomb bed. The ceramic honeycombs are heated by alternate firing of the burner in left and right section of the test facility. The temperature of the preheated air in the test section can be selected in the range between 1073 K and 1373 K. A fuel jet is introduced in the test section normal to the preheated airflow, via a nozzle of 1 mm in diameter, to form a jet in cross-flow. The temperature of the fuel jet was 298 K while that for the combustion air in the cross flow was either 298 K or 1173 K. The jet in cross-flow allowed easy control of the fuel temperature to room temperature. The dimensions of the test section were 200 mm $\times$ 260 mm (in the X and Y directions, respectively). The test section was equipped with quartz glass windows to allow optical observation of the flame. The oxygen concentration and gas temperature were measured shortly before the flow entered the test section. The flow rate of the cross-flow was also monitored. Gupta [1] provides detailed information on the facility.

A two-dimensional (2D) PIV system was used to determine the flow dynamics associated with the combustion of commercial grade propane at different air preheat temperatures and oxygen concentration in the combustion air. A control module was used to operate the camera for image acquisition. A Solo PIV Nd: YAG laser was used as the light source for illuminating the test section. Gupta et al. [8] provide details on the development of the system used in combustion studies that may also have high background flame radiation or flame luminosity. A charge-coupled device (CCD) camera with an active pixel array of 1360×1024 was used. The camera was equipped with mechanical shutters and a narrow band-pass filter (0.87 nm) at center wavelength of 532 nm to allow maximum signal transmission and minimum background

Table 1 The experimental test matrix

Oxidizer preheat temperature	Fuel jet	Fuel jet flowrate (L/h)	Fuel jet velocity, U_0 (m/s)	Air cross flow flowrate (m^3/h)	N_2 cross flow flowrate (m^3/h)	Oxygen concentration (%)	Cross flow velocity, V_0 (m/s)	Momentum flux ratio, r^2	Patrick number, λ^2
298 Nonburning	C_3H_8	42	14.9	16.0	0.0	21.0	0.9	392	0.0026
298 Burning	C_3H_8	42	14.9	16.0	0.0	21.0	0.9	392	0.0026
1173 Burning	C_3H_8	25	8.8	3.8	12.2	5.0	0.9	392	0.0025
298 Nonburning	CH_4	70	24.8	16.0	0.0	21.0	0.9	409	0.0025
298 Burning	CH_4	70	24.8	16.0	0.0	21.0	0.9	409	0.0025
1173 burning	CH_4	42	14.9	3.8	12.2	5.0	0.9	416	0.0024

radiation. This alleviated entrance of stray flame radiation onto the camera detector to provide very high signal to noise ratio.

In order to trace motion of the flow, submicron sized, hollow glass spheres (glass microballoons) were introduced into the airflow using a fluidized bed. The glass spheres seeded to the flow were so chosen to allow for their thermal characteristics and their ability to follow the fluid motion at several hundred Hz of frequency fluctuations. The dispersion of small size glass spheres uniformly into the flow is a challenge so that care must be exercised to seed the tracer particles via a fluidized bed into the flow. The fuel jet was not seeded with any submicron size tracer particles due to the very small size (1 mm) of the fuel jet orifice. This precluded information on the very near region immediately downstream of the fuel jet exit since no particles are present in the fuel jet and no particles are entrained from the seeded air flow. However, immediately downstream jet features could be captured.

A thin laser sheet beam was used to illuminate the seeded particles in the flow. In the investigated area the laser sheet thickness was 2 mm. The laser sheet thickness also add some generic error to the PIV results in the near region of the fuel jet orifice, as the fuel jet initially is of 1 mm diameter, and the thickness of the laser sheet was 2 mm. In the experiments the laser frequency was set at 5 Hz, which was also synchronized with the camera frequency to alleviate background radiation from flame. The particles present in the flow scattered the incident laser sheet light. The camera, placed normal to the laser sheet beam, was used to detect the image of the particles in the flow. Two images acquired were the first initial position of the submicron size seeded particle and second image position of the particle after a known time interval. The measured area in the test section was 114.0×90.0 mm $(X*Y)$ (Fig. 1). When a large number of image pairs had been acquired, the images were processed with software in order to determine the mean motion of the flow field as well as the associated turbulence characteristics. Data acquisitions were conducted from an average of 400 image pairs of the flow field, from which mean and turbulence characteristics of the flow were determined.

Optical spectroscopy technique was used to determine the flame thermal signatures including flame fluctuations.

The measurements were carried out under both nonburning and burning conditions using normal air and HiTAC conditions (having high-temperature and low-oxygen concentration combustion air). The measurements were performed with several gas jet flows. The momentum flux ratio between the gas jet and cross-flow was maintained constant when examining different gaseous fuel jets and cross-flows, thus providing similarity in mixing between the fuel and air for different test conditions. The operating and experimental conditions are summarized in Table 1.

Results and Discussion

Data for a large number of different configurations were collected, although only a limited number of results are presented here. The collected data provide important insight on the flow dynamics, turbulence, and strain rates associated with the jet in cross-flow under high-temperature air combustion conditions. This type of data provides critical information on the dynamics of the flow and mixing associated with the flow under nonburning and burning conditions. The data also aid in computer model validation and model development as the conventional models have provided a lack of accurate flow and combustion prediction of the HiTAC flow behavior [5]. Validation of the flow model without the presence of complex chemistry represents an important step for such flows. In the present study the gas jet was quantified by: (a) the jet Reynolds number and (b) the momentum ratio between the fuel jet flow and cross-flow.

The intent of the collected data is to provide an understanding of the complex flowfield associated with high-temperature combustion air conditions. The data can also be used to compare results from numerical simulations, thus aiding in model validation and model development. The Reynolds number was varied here between 1400 and 4500. The momentum ratio, p_r, between the jet and cross-flow was calculated from

$$p_r = \frac{p_f}{p_c} = \frac{\rho_j \cdot U_0^2}{\rho_c \cdot V_0^2} \tag{1}$$

where U_0 and V_0 represent the fuel jet velocity and cross-flow velocity, respectively. This momentum ratio is of prime importance for characterizing the jet in cross-flow. In addition, velocity ratio between the gas jet and cross-flow is also important. The velocity ratio, λ, or also denoted as Patrick number was calculated as

$$\lambda^2 = \frac{\rho_c}{\rho_j} \cdot \frac{V_0^2}{U_0^2} \tag{2}$$

From the acquired data for a number of different cases, mean and turbulence characteristics, as well as the vorticity and axial strain were calculated. The vorticity is defined as the curl of the velocity vector

$$\Omega_z = \nabla \times \mathbf{u} = \frac{1}{2}\left(\frac{du}{dy} - \frac{dv}{dx}\right) \tag{3}$$

And the axial strain in the direction of the combustion air flow is given by

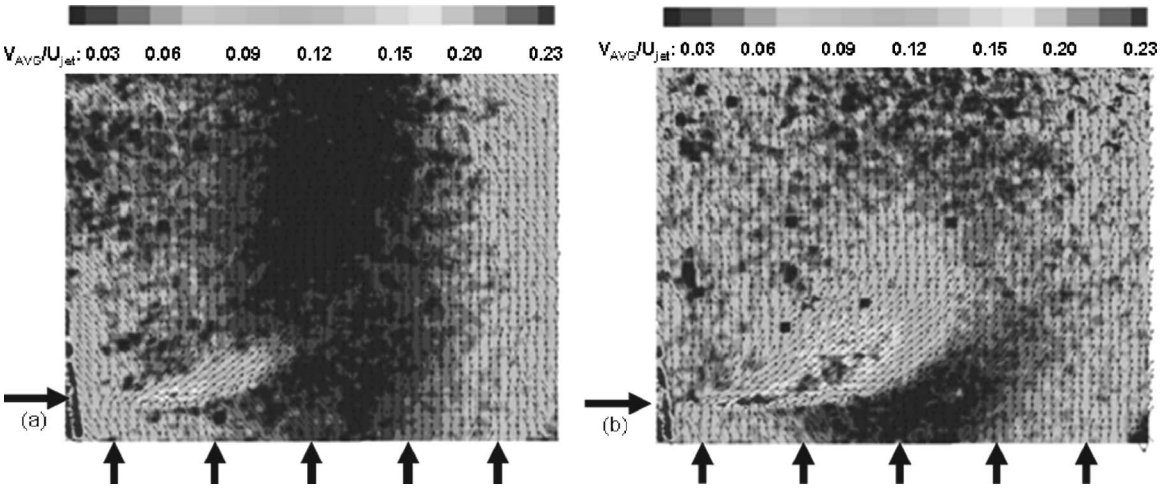

Fig. 2 Average velocity, normalized by jet exit velocity at (*a*): 298 K, 21% O_2 combustion air, nonburning, fuel jet=42.0 L/h C_3H_8 (left diagram); and (*b*) 298 K, 21% O_2 combustion air, burning fuel jet=42.0 L/h C_3H_8 (right diagram)

$$S_y = \frac{dv}{dy} \tag{4}$$

The flow field results for the nonburning and burning cases using propane and methane as the fuels are shown in Figs. 2–7. The vector length provides information on the total velocity in the plots (i.e., the resultant velocity component of axial and radial velocity). The direction of the vector gives information on direction of the flow field. The gray scale coded information in the bar above the flow field image gives information on the velocity magnitude of the particular component.

The most common sources of error in the PIV results that should be considered are particle lag and image-processing errors. The sampling frequency for the PIV system was 5 Hz and the camera was able to expose two consecutive images within 5 μs. The most common sources of error in the PIV results that should be considered can be divided into the generic error originating from the experiment itself, such as, particle lag and image-processing errors. The sampling frequency for the PIV system was 5 Hz and the camera was able to expose two consecutive images within 5 μs. PIV methods measure the Lagrangian velocities of the particles, and therefore are based upon the assumption that the particles follow the surrounding fluid motion. The use of hollow glass microspheres allowed particles to follow much higher frequency fluctuations than its solid spheres counterpart. The mean diameter of the hollow glass spheres was 5 μm. Since the glass spheres have some inertia in the motion when they are following the fluid flow, some error might appear due to particle lag. This error must be considered. According to the analysis of Raffel et al. [13] the relaxation time, or particle lag of a particle to a step change in the fluid velocity, is given as

$$\tau_S = d_p^2 \frac{\rho_p}{18 \cdot \mu} \tag{5}$$

The relaxation time is calculated to be approximately 0.15 μs assuming a particle size d_p of 5 μm, a particle density ρ_p of 2500 kg/m^3, and temperature of the flame about 1500 K, and allowing μ to be the kinematic viscosity of the fluid. This is of the same magnitude as the smallest time scale of the jet, which should be estimated by η/U_{J0} where η is the Kolmogorov scale, defined by

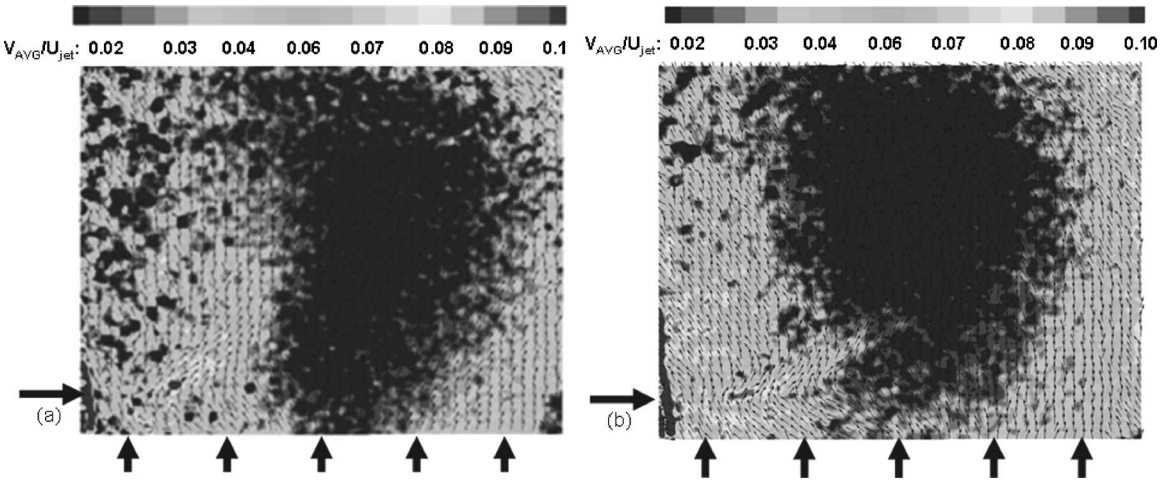

Fig. 3 Average velocity normalized by jet exit velocity at: (*a*) 298 K, 21% O_2 combustion air, nonburning, fuel jet=70.0 L/h CH_4 (left diagram); and (*b*) 298 K, 21% O_2 combustion air, burning, fuel jet=70.0 L/h CH_4 (right diagram)

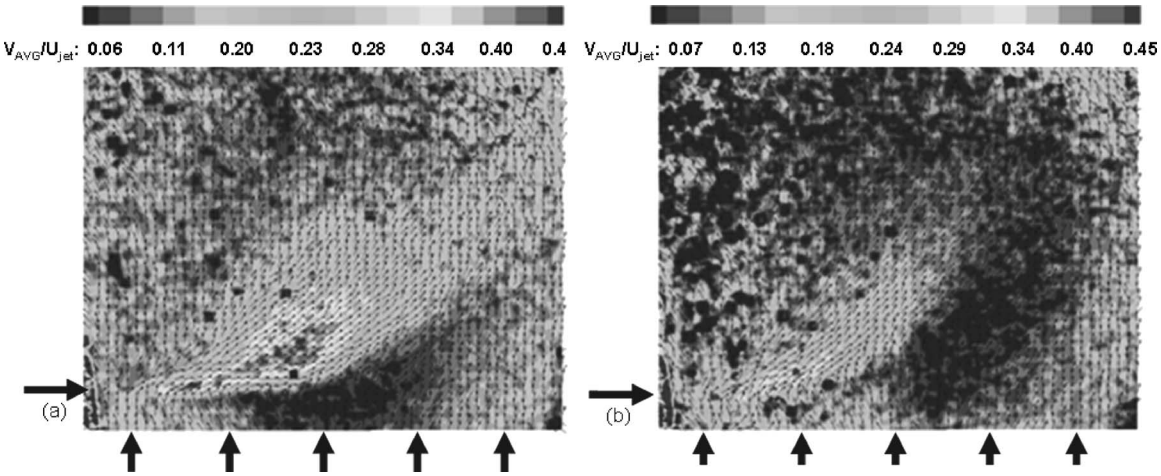

Fig. 4 Average velocity normalized by jet exit velocity at: (*a*) 1173 K, 5%O_2 combustion air, burning, fuel jet =25.0 L/h C_3H_8 (left diagram); and (*b*) 1173 K, 5%O_2 combustion air, burning, fuel jet=42.0 L/h CH_4 (right diagram)

$$\eta = \left(\frac{\upsilon^3 \cdot \delta}{U_{J0}^3} \right)^{1/4} \tag{6}$$

where $U_{J,0}$ is the centerline velocity near the nozzle. This gives the smallest time scale of the jet, η/U_{J0} of about 0.3 μs. However, the smallest characteristic time scale of the experimental system used was 0.6 μs. This was obtained from δ_r/U_{J0}, where δ_r is the spatial resolution of the experimental system ($\delta_r \sim 1.1$ mm). Therefore, the error from the particle lag is not significant for the current experimental conditions.

Not considered in the error estimation is the fact that the surface of the particles can terminate or initiate reactions and induce additional radiative loss from the flame, which has not been accounted for.

Figures 2 and 3, show the mean flow velocity and direction for the nonburning and burning cases using propane and methane as the fuel at 21% oxygen concentration in air. The fuel jet causes strong impingement into the cross-flow for high-temperature air case with the same momentum between nonburning and burning cases. For the normal air temperature case the jet deflects gradually into the cross-flow with a smoother trajectory. However, for the high-temperature case the jet has a much larger velocity distribution in a small well-defined region, before its deflection. The more well-defined region of higher velocity indicates a reduced dissipation rate of the fuel jet momentum. This suggests greater dependency of the combustion air temperature and properties on the jet mixing and to provide a large influence on the scale of the impingement of the jet, which depends on the physical properties of the fluids. The properties of the fluids change with the preheated temperature, thus the momentum flux ratio was kept constant where the influence of the changed parameters could easily be distinguished. Further downstream the velocity distribution is smaller where most of the combustion occurs. The results showed that combustion decreases the degree of turbulence in the region where the jet deflects into the cross-flow. Overall the turbulence levels for the high-temperature case are low compared to the normal air case. These results shows the high-temperature air combustion results in a less turbulent mixing, which depends on the longer mixing times required for complete combustion due to the low-oxygen concentration of the cross-flow. A very small local region of higher turbulence can be seen in the zone of high vorticity and axial strain. This region provides local mixing of the

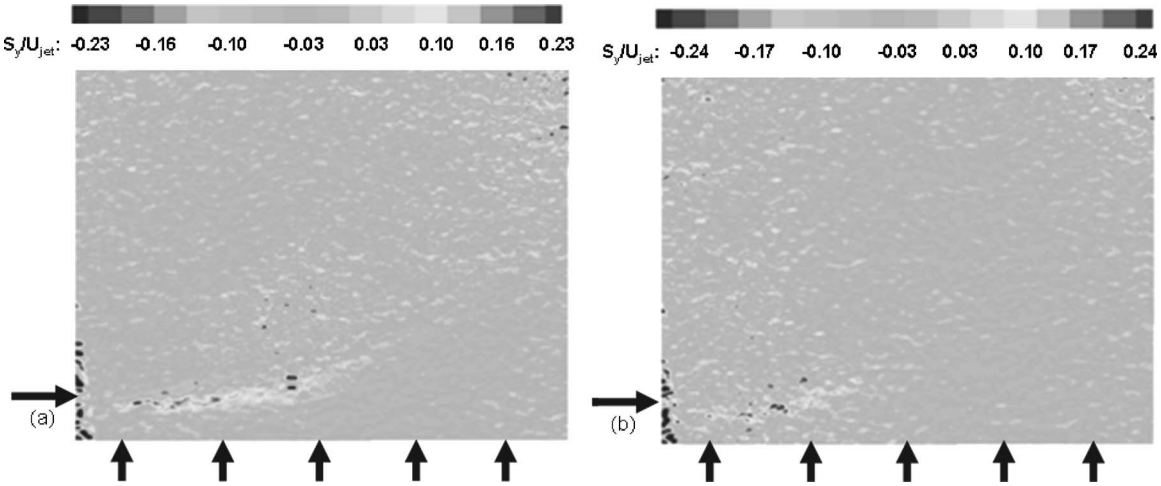

Fig. 5 Average velocity normalized by jet exit velocity at: (*a*) 1173 K, 5%O_2 combustion air, burning, fuel jet =25.0 L/h C_3H_8 (left diagram); and (*b*) 1173 K, 5%O_2 combustion air, burning, fuel jet=42.0 L/h CH_4 (right diagram)

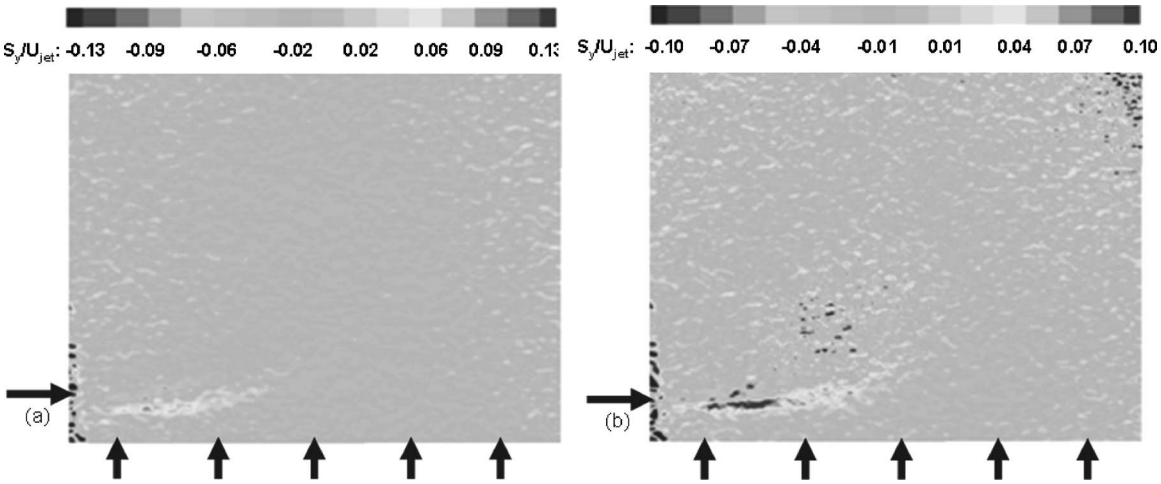

Fig. 6 Axial strain rate distribution normalized by jet exit velocity at: (*a*) 298 K, 21%O_2 combustion air, nonburning, fuel jet=42.0 L/h C_3H_8 (left diagram); and (*b*) 298 K, 21%O_2 combustion air, burning fuel jet=42.0 L/h C_3H_8 (right diagram)

fuel jet with the cross-flow. This information provides a direct role of combustion on the flow dynamics associated with normal and high-temperature combustion air conditions.

The corresponding mean velocity with propane and methane as the fuel for the normal and high air preheats temperature case is shown in Figs. 4 and 5. Similar dependency can be seen for the methane jet case, but not as pronounced as for the propane jet case. Furthermore, it also indicates the dependency of the fuel jet properties, such as the fuel jet density. The average velocity plots for the propane and methane case, respectively, show an increase of jet spread for the high-temperature air conditions. The greater spreading of the jet with high-temperature conditions is more pronounced and noticeable with propane as the fuel than for the low-temperature case. This indicates a delayed mixing for the high-temperature case. This also explains the longer flame length and larger flame volume observed with high-temperature air cases. Other experiments [15–17] show an increased ignition delay time with reduced oxygen concentration, and a reduced ignition delay time with increasing preheat temperature of the oxidizer.

The axial strain rate, given in Eq. (4) is plotted in Figs. 6 and 7 for the propane fuel jet case and in Figs. 8 and 9 for the methane fuel jet case at 21% oxygen concentration in air. The axial strain rate can be explained as acceleration or deceleration of the flow in the axial direction. This indicates that the zones of positive axial strain have a somewhat higher local pressure, and the zones with negative axial strain indicate zones of lower local pressure, which also suggests that when there are larger differences in the axial strain above and below the entraining jet, it will rapidly deflect into the cross-flow. The figures reveal a much larger and a more well-defined zones of both positive and negative axial strain below and above the jet trajectory, respectively, for the high-temperature air cases. In contrast the radial strain case was found to be lower for the high-temperature than the normal temperature case. This then suggests delayed mixing for the high-temperature case in the main flow domain. One can also notice that for the case of normal air temperature the axial strain levels are lower, but the regions are somewhat larger in size. This implies stronger entrainment of the air to provide enhanced mixing of the jet for the normal air case. Larger flame volume results from the increased penetration of the fuel jet into the air flow with higher radial strain rates to cause expansion of the fuel jet over a larger volume. This then explains why one obtains a larger flame volume with high-temperature air combustion process.

The above observations are also confirmed from the stronger

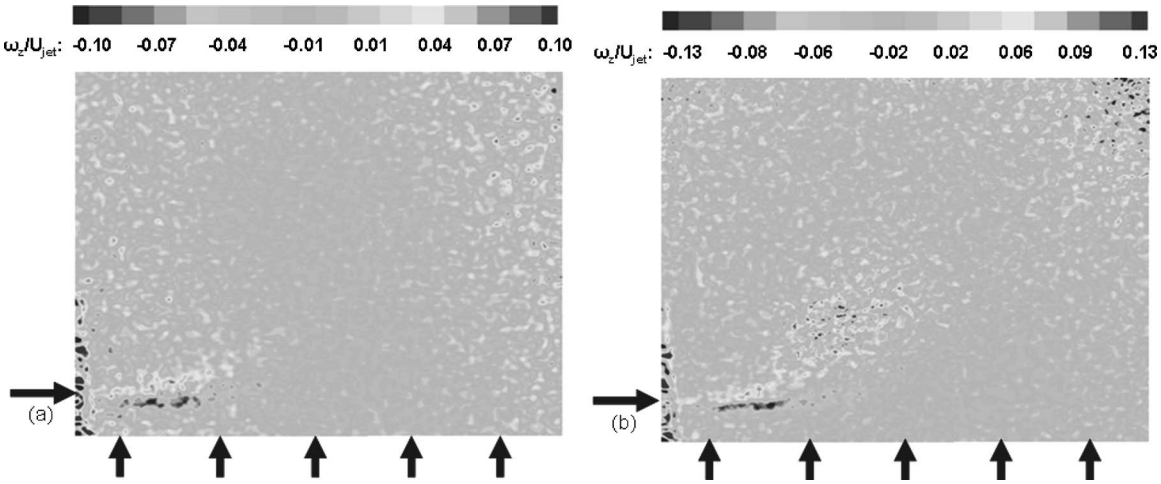

Fig. 7 Vorticity distribution normalized by jet exit velocity at: (*a*) 298 K, 21%O_2 combustion air, nonburning, fuel jet=42.0 L/h C_3H_8 (left diagram); and (*b*) 298 K, 21%O_2 combustion air, burning fuel jet=42.0 L/h C_3H_8 (right diagram)

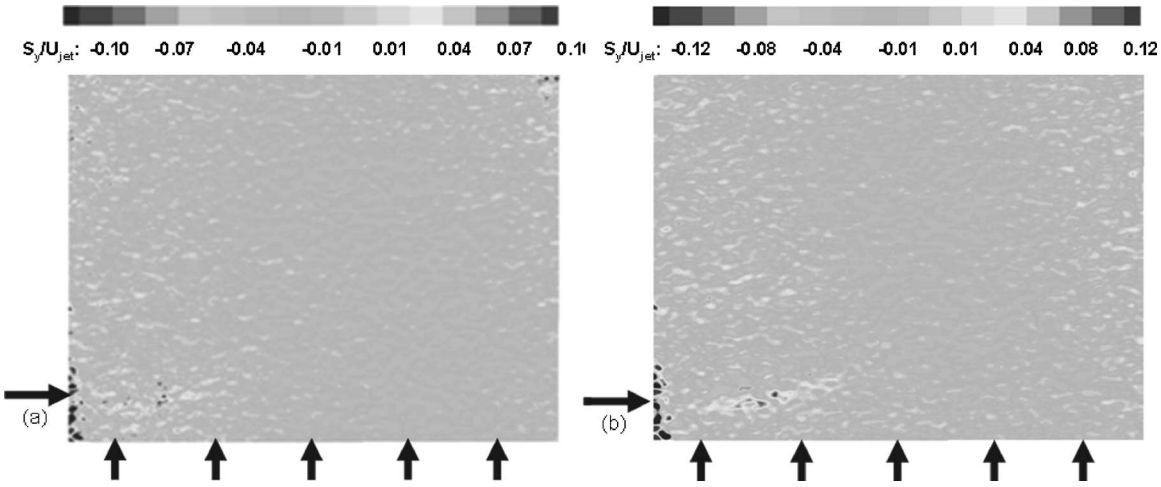

Fig. 8 Axial strain rate distribution normalized by jet exit velocity at: (*a*) 298 K, 21%O_2 combustion air, nonburning, fuel jet=70.0 L/h CH_4 (left diagram); and (*b*) 298 K, 21%O_2 combustion air, burning, fuel jet=70.0 L/h CH_4 (right diagram)

vorticity observed for the normal temperature and high-temperature air cases as shown in Figs. 7, 9, and 10 for the propane and methane fuel jet case. The figures reveals higher vorticity for the high-temperature combustion case. They also show two well-defined regions of vorticity that are in connection with the jet trajectory. There is a region of negative rotation above the fuel jet and a region of positive rotation under the fuel jet. These results reveal that a larger region of mixing takes place around the propane fuel jet for the nonburning propane case as compared to the high-temperature air case. The magnitude of the rotation is much greater for the high-temperature air case, than for the normal air cross-flow case. The entrainment can also be seen as the flows are either accelerated or decelerated. A strong entrainment of the surrounding fluid can be seen in the high-temperature combustion case as compared to the normal jet case, which results in much less entrainment. Also one can expect a larger rotation around the fuel jet due to the vortex formation that results from the higher velocity of the entraining fuel jet. The methane fuel jet case showed trends similar to the propane case.

High-speed camera and fast Fourier transform (FFT) analysis was used to examine the thermal characteristics of the propane fuel jet using normal temperature, high temperature, and high-temperature and low-oxygen concentration combustion air. This provided information on the flame fluctuations. The definition of flame fluctuations and the experimental procedure are described in more detail in Ref. [14]. The results are shown in Fig. 11. Highest flame fluctuations were found with the normal air case and the least for high-temperature air combustion conditions [14]. These results clearly show and support the findings using PIV diagnostics, which showed delayed mixing and lower turbulence with high-temperature air combustion conditions. They also show lower fluctuations of the flame with high-temperature air combustion conditions than normal air or the high-temperature case.

Conclusions

The flow field associated with the normal and high-temperature air combustion has been acquired for the first time to provide information on mean and rms flow velocity, vorticity, and strain associated with the flow. A 2D PIV diagnostics and optical spectroscopy was used to determine the flow and thermal characteristics of the flow in a jet in cross-flow arrangement under nonburning and burning conditions using propane and methane as the

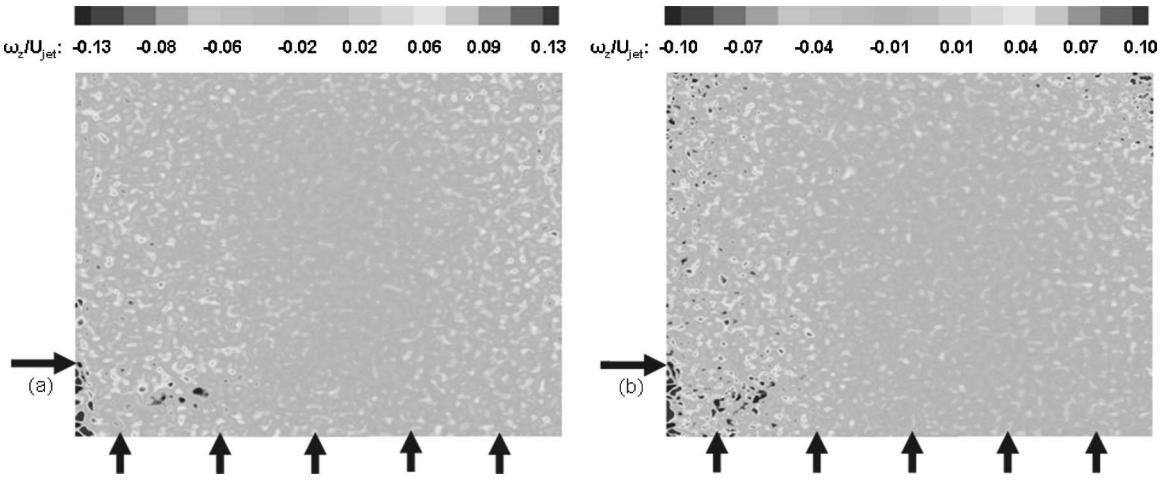

Fig. 9 Vorticity distribution normalized by jet exit velocity at: (*a*) 298 K, 21%O_2 combustion air, nonburning, fuel jet=70.0 L/h CH_4 (left diagram); and (*b*) 298 K, 21%O_2 combustion air, burning, fuel jet=70.0 L/ CH_4 (right diagram)

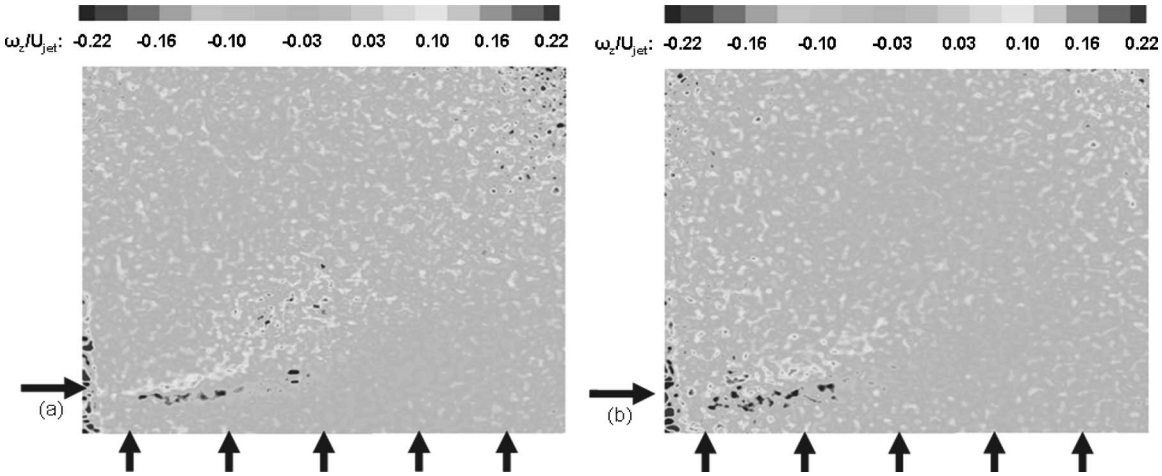

Fig. 10 Vorticity distribution normalized by jet exit velocity at: (*a*) 1173 K, 5%O_2 combustion air, burning, fuel jet=25.0 L/h C_3H_8 (left diagram); and (*b*) 1173 K, 5%O_2 combustion air, burning, fuel jet=42.0 L/h CH_4 (right diagram)

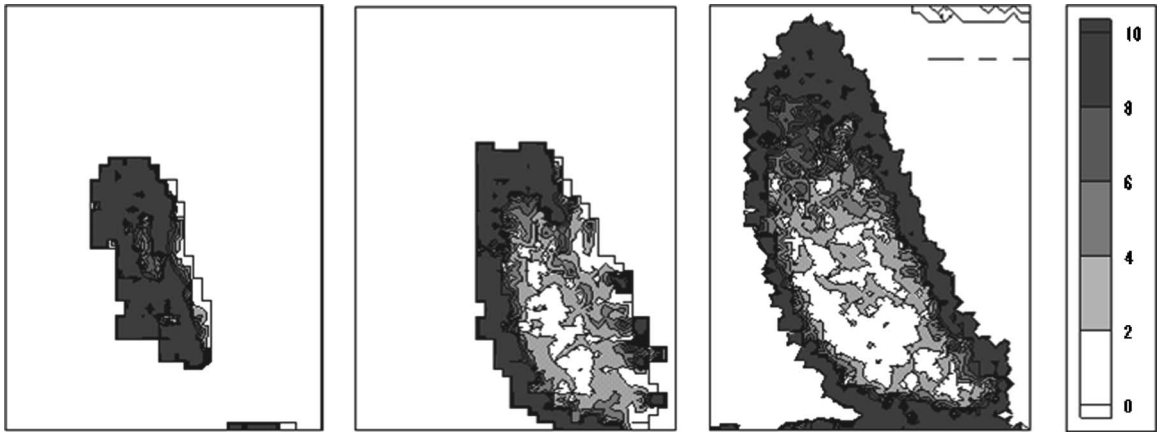

Fig. 11 Flame fluctuations with: (*a*) normal temperature air, (*b*) high-temperature air; and (*c*) high-temperature and low-oxygen concentration air [14]

fuels. The temperature of the air was very high to simulate the flow dynamic behavior of flames with high-temperature combustion air conditions.

The fuel jet penetration and expansion was found to be stronger for the high-temperature air combustion case. Furthermore, the turbulence levels around the fuel jet were found to decrease with the combustion. The results also suggest delayed mixing as compared to the nonburning jet at normal temperature conditions. The axial strain was higher for the high-temperature case and lower for the normal-temperature case.

The flame fluctuations were found to be smaller in the flame (occupied over a larger flame volume) with high-temperature air combustion conditions than for the normals temperature case. The data provide detailed insights into the flow characteristics and it is expected that this detailed data will assist in model validation and model development of high-temperature air combustion systems.

Acknowledgment

The research was partially supported by NSF and NASA and is much appreciated. This work was carried out at the Combustion Laboratory, University of Maryland. The support provided by SGC, Swedish Gas Technological Centre, and Jernkontoret, the Swedish steel producers association to one of the authors (M.M.) during his extensive stay at the University of Maryland is gratefully acknowledged. The experimental facility was designed and built by NFK, Japan and is gratefully acknowledged.

References

[1] Gupta, A. K., 2002, "Flame Characteristics and Challenges with High Temperature Air Combustion," 2nd International Symposium on High Temperature Air Combustion and Applications, Taipei, Taiwan, May 16–18.

[2] Hasegawa, T., Mochida, S., and Gupta, A. K., 2002, "Development of Advanced Industrial Furnace using Highly Preheated Air Combustion," J. Propul. Power, **18**(2), pp. 233–239.

[3] Tsuji, H., Gupta, A. K., Hasegawa, T., Katsuki, K., Katsuki, M., and Morita, M., 2003, *High Temperature Air Combustion: From Energy Conservation to Pollution Reduction*, CRC Press, Boca Raton, FL.

[4] Blasiak, W., Szewczyk, D., and Dobski, T., 2001, "Influence of N_2 Addition on Combustion of Single Jet of Methane in Highly Preheated Air," *Proceedings of International Joint Power Generation Conference, New Orleans, June*, JPGC2001/FACT-19048.

[5] Yang, W., and Blasiak, W., 2001, "Numerical Study of Fuel Temperature Influence on Single Gas Jet Combustion in Highly Preheated and Oxygen Depleted Air," *Proceedings 3rd International Symposium on Advanced Energy Conversion Systems and Related Technologies*, Nagoya, Japan, December 15–17.

[6] Mortberg, M., Blasiak, W., and Gupta, A. K., 2004, "Combustion of Low Calorific Fuels in High Temperature Oxygen Deficient Environment," *Proceedings of the 23rd International Conference on Incineration and Thermal Treatment Technologies*, Phoenix, AZ.

[7] Weber, R., Orsino, S., Verlaan, A., and Lallemant, N., 2000, "Combustion of Natural Gas with High Temperature Air and Large Quantities of Flue Gas,"

Proceedings of the 28th Symposium (International) on Combustion, The Combustion Institute, Pittsburgh, PA, p. 1315.
[8] Gupta, A. K., Linck, M., and Archer, S., 2004, "A New Method to Measure Flowfield in Luminous Spray Flames," J. Propul. Power, **20**(2), pp. 1217–122.
[9] Broadwell, J. E., and Breidenthal, R. E., 1984, "Structure and Mixing of a Transverse Jet in Incompressible Flow," Combust. Flame, **114**, pp. 319–335.
[10] Choudhuri, A. R., and Gollahalli, S. R., 2000, "Effects of Ambient Pressure and Burner Scaling on the Flame Geometry and Structure of Hydrogen Jet Flames in Cross-flow," Int. J. Hydrogen Energy, **25**, pp. 1107–1118.
[11] Donghee, H., and Mungal, M. G, 2003, "Simultaneous Measurements of Velocity and CH Distribution. Part II: Deflected Jet Flames," Combust. Flame, **133**, pp. 1–17.
[12] Gordon, M., and Soria, J., 2002, "PIV Measurements of a Zero-net-mass-flux Jet in Cross Flow," Exp. Fluids, **33**, pp. 863–872.
[13] Raffel, M., Willert, C., and Kompenhans, J., 1998, *Particle Image Velocimery*, Springer, Berlin, p. 14.
[14] Konishi, N., Kitagawa, K., Arai, N., and Gupta, A. K., 2002, "Two-Dimensional Spectroscopic Analysis of Spontaneous Emission from a Flame using Highly Preheated Air Combustion" J. Propul. Power, **18**(1), pp. 199–204.
[15] Mortberg, M., Blasiak, W., and Gupta, A. K., 2006, "Combustion of Low Calorific Fuels in High Temperature Oxygen Deficient Environment," Combust. Sci. Technol., **18**, pp. 1345–1372.
[16] Mortberg, M., Blasiak, W., and Gupta, A. K., 2005, "Flow Phenomena of Normal and Low Calorific Value Fuels in High Temperature Air Combustion Conditions," Ind. Heat., **42**(1), pp. 45–54 (in Japanese).
[17] Gupta, A. K., 2004, "Thermal Characteristics of Gaseous Fuel Flames Using High Temperature Air," ASME J. Eng. Gas Turbines Power, **126**(1) pp. 9–19.

Prediction of Sorbent Performance in a Circulating Fluidized Bed Boiler Based on Petrographic Properties

Peter L. Rozelle

Sarma V. Pisupati[1]
e-mail: spisupati@psu.edu

Alan W. Scaroni

Department of Energy and Geo-Environmental Engineering,
The Pennsylvania State University,
110 Hosler Building,
University Park, PA 16802

A method for prediction of sorbent consumption is presented here and has been developed based on plant operating data for a boiler in which several limestone and dolostone products were tested under similar firing conditions. The method considers the characteristic partitioning of calcium and sulfur between the flyash and bottom ash stream for the boiler, the feed particle size distribution of the sorbent, and petrographic properties of the sorbents. The predictions of sorbent usage were compared to plant operating data for five sorbents, of two distinct petrographic types. The plant operating data used featured full load operation. The five sorbents tested were all from Pennsylvania, and each contained greater than 40 wt. *% CaO. In four of the five cases, the predicted sorbent usage was within* 10 wt. *% of the average full load sorbent usage by the boiler.*
[DOI: 10.1115/1.2431388]

Introduction

Power plants equipped with circulating fluidized bed (CFB) boilers commonly add limestone sorbents to the process for emissions control. The required expenditure for purchasing sorbent in the operation of a circulating fluidized bed boiler is often a significant item in a plant's operating budget. This requirement is a function of sorbent usage by the boiler and the cost of the sorbent delivered to the boiler. Although the latter may be readily estimated, predicting the former is a challenge. The availability of such a means would be of benefit for CFB power plants, which have several available sources of sorbent, the goal being to minimize plant compliance costs.

Research activities into the phenomena surrounding sorbent performance in the CFB boiler process can be of significant value in the commercial arena, if a means can be developed for prediction of sorbent usage by a given plant. Ideally, this would be based on fuel sulfur content and firing requirements, and one or more analytical techniques commonly applied to limestone products.

Improved prediction of sorbent requirements can ensure minimized compliance costs for CFB power plants, notably where several competitive suppliers of sorbent are available. This improvement can also assist in minimizing risks associated with CFB power projects under development, improving the accuracy in predicting sorbent usage. This can ultimately improve the competitiveness of the technology.

Based on analytical techniques applied to sorbents, as well as to boiler test results, a method for the prediction of sorbent performance has been developed and is presented here. This method is based on the attrition behavior of the sorbent and predicted sulfation levels of the ash streams.

Background

The behavior of sorbent particles in the fluidized bed combustion process is the subject of a significant body of literature. This body includes laboratory studies of reaction kinetics involving calcination [1] and sulfation [2], the reduction of calcium sulfate by reducing gases [3], and the effects of particle size and sorbent chemical characteristics [4,5].

In spite of the large existent set of research results available, correlations of sorbent analytical results with sorbent consumption in commercial boiler operations have remained elusive [5]. Two constraints have restricted the applicability of research results in predicting sorbent performance:

1. The wide variety of sorbent properties, which may influence sulfur capture performance,
2. The range of conditions encountered by sorbent particles in the CFB boiler process, the limitations of plant data acquisition systems in monitoring these conditions, and most notably, how sorbent performance test data are interpreted with respect to these limitations.

Among the suite of sorbent properties that have been examined, the utility of sorbent petrographic analyses in predicting sorbent attrition behavior has been demonstrated [6,7]. In turn, attrition behavior has been linked to sorbent consumption in boiler tests [8], through analysis of calcium and sulfur partitioning between the ash streams.

The current work quantifies sorbent requirements in terms of a petrographically described grain size. Predicted sorbent requirement, based on this quantification is compared to boiler test data using several sorbents.

Sorbent Grain Size and Attrition. Grain size is a characteristic feature of a limestone product that is commonly described by a petrographic analysis. Petrographic analyses were carried out as part of the previously mentioned sorbent test program. Based on these analyses, the sorbents were classified by the scheme of [9]. Previously published [5] boiler tests with sorbents in two distinct petrographic categories are relevant here:

1. Sorbents that were classified as micrites, with a characteristic grain size in the 4 μm range. These will be referred to as micritic sorbents.
2. Sorbents that could not be classified according to the Folk scheme [5], and exhibited a sparry grain size, in the range of 30 μm. These will be referred to as sparry sorbents.

[1]Corresponding author.
Submitted to ASME for publication in the JOURNAL OF ENGINEERING FOR GAS TURBINES AND POWER. Manuscript received July 26, 2005; final manuscript received August 8, 2006. Review conducted by Kenneth Mark Bryden.

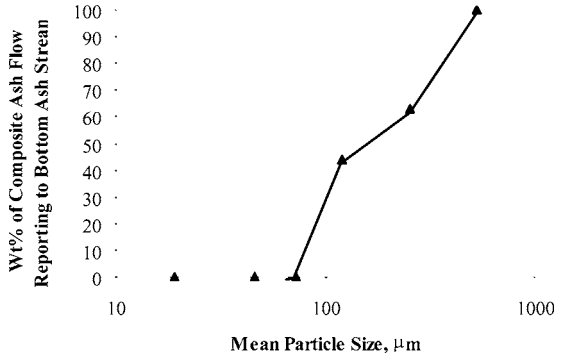

Fig. 1 CFB boiler ash stream partition curve

Sorbents in these two categories have been found to exhibit differences in attrition behavior in both boiler operation and laboratory test systems [6,8]. Sparry sorbents in both systems were found to exhibit significantly more attrition than micritic sorbents.

Calcium Material Balances and Measurement of Sorbent Attrition. CFB boiler system typically classifies solids into two ash streams: flyash and bottom ash. This classification can be described using a *partition curve*, as seen in Fig. 1. The partition function, which is described by the curve, relates to the particle size distribution of the composite ash flow from the boiler as follows:

$$F_{ba} = \sum_{x=1}^{nx} k_d(x) M_{ca,x} F_{ca} \tag{1}$$

The composite ash flow in terms of the flyash and bottom ash flows is

$$F_{ba} + F_{fa} = F_{ca} \tag{2}$$

The measurement of individual ash stream flow rates, as well as the particle size distribution of each ash stream, allows for the reconstitution of a composite ash flow rate, as seen in Eq. (2). Comparisons of the bottom ash and composite ash flow rates for each particle size interval then allows for the development of the partition function, $k_d(x)$. The direct measurement of the ash stream flow rates is generally difficult in a commercial CFB boiler. An expedient method for calculating these flow rates, from solids input rates and the solution of simultaneous material balances, is provided elsewhere [7].

Sorbent attrition may be described in several ways. Here, the primary interest is the partitioning of sorbent particles to the ash streams, which will be affected by: (i) the partition function of the boiler, (ii) the particle size distribution of the as-fed sorbent, and (iii) the fraction of sorbent, initially coarse enough to be removed with the bottom ash that is removed with the flyash. The third item is a measure of sorbent attrition that can be gleaned directly from a calcium material balance and will be referred to here as the *attrition coefficient*. It is defined as the mass of calcium in the sorbent that is initially coarse enough to report to the bottom ash stream but is removed with the flyash stream. The attrition coefficient for species i can be described as follows:

$$K_{i,a} = 1 - \left(\frac{M_{i,ba}}{M_{i,kd}} \right) \tag{3}$$

For a perfect separation of solids into the two ash streams, a single limiting size could be considered to define $M_{I,kd}$, such as a classification cut size (i.e., the point where $k_d(x)$ is 0.5). All feed solids coarser than this size could be considered as the fraction initially coarse enough to report to the bottom ash stream. However, as seen in Fig. 1, the partition function does not behave in this fashion, rather it exhibits a continuous decrease in $k_d(x)$ with decreasing particle size.

The solids initially coarse enough to report to the bottom ash stream are related to the partition function and the particle size distribution of the feed solids of species i as follows:

$$M_{i,kd} = \sum_{x=1}^{nx} k_d(x) M_{is,x} \tag{4}$$

Development of the attrition coefficient for sorbent particles, on a weight basis, is complicated by the weight changes to which the sorbent particles are subject due to chemical reactions. However, the species that remains in the solid sorbent particles is calcium, and the required measurements for Eq. (3) may be affected using calcium material balances. Calcium in ash sample is commonly reported as CaO, and CaO material balances are used here, although it is acknowledged that the calcium reported by the CaO analyses represents both CaO and $CaSO_4$.

Also complicating the use of Eq. (3) is the condition where the presence of CaO in the ash streams, derived from fuel ash, is significant. Fuels with low sulfur contents and high ash contents can be expected to present this challenge. Equation (3) can be rewritten to separate the CaO derived from fuel and sorbent, removed with the bottom ash stream, as follows:

$$K_{s,a} = 1 - \left(\frac{F_{\mathrm{Ca},ba} - F_{\mathrm{Ca},ba,f}}{F_s M_{s,kd} \mathrm{Ca}_s} \right) \tag{3'}$$

Development of a sorbent attrition index through the use of Eq. (3′) requires knowledge of the fraction of the CaO removed with the bottom ash that is derived from the fuel ash. This quantity is not readily obtained from boiler ash samples. Where the input of CaO to the boiler with the fuel is small compared to that of the sorbent, it may be ignored, and Eq. (3′) becomes

$$K_{s,a} = 1 - \left(\frac{F_{\mathrm{Ca},ba}}{F_s M_{s,kd} \mathrm{Ca}_s} \right) \tag{3''}$$

The test results reported here, from testing of a range of sorbents in a boiler fired by a low sulfur content, high ash content fuel, cannot assume a small fuel contribution to the bottom ash stream. However, the sorbents were used under similar conditions with the same fuel. As such, variations in fuel CaO partitioning between the ash streams are neglected, and rather than an attrition coefficient, CaO material balances will be used to develop relative attrition indices, $I_{s,a}$, as follows:

$$I_{s,a} = 1 - \left(\frac{F_{\mathrm{Ca},ba}}{F_s M_{s,kd} \mathrm{Ca}_s} \right) \tag{5}$$

The (experimentally measured) fraction of the CaO in the composite ash stream partitioned to the bottom ash is β_{Ca}. If it is assumed that the partitioning behavior of the sorbent particles, between the ash streams, is that measured from a boiler CaO balance, and the contribution of fuel CaO to the bottom ash stream is neglected, the result is

$$\beta_{\mathrm{Ca}} = \frac{F_{\mathrm{Ca},ba}}{F_s \mathrm{Ca}_s} \tag{6}$$

This allows the use of a simpler form of Eq. (5),

$$I_{s,a} = 1 - \left(\frac{\beta_{\mathrm{Ca}}}{M_{s,kd}} \right) \tag{5'}$$

The attrition index is a relative measure of sorbent attrition, useful for examining differences in attrition behavior among sorbents tested under similar conditions. Results presented subsequently use the attrition index rather than the attrition coefficient, reflecting uncertainties regarding the fuel ash contribution to the overall CaO balance of the system.

Sulfation Levels of the Two Ash Streams. The ability to predict the partitioning of sorbent particles between the ash streams

may result in a means of predicting sorbent usage requirements, if the sulfation levels of the two ash streams can be predicted. A means of predicting the sulfation levels of the two ash streams may include one or more of the laboratory tests for which research results have been reported. In the case of the results presented here, boiler test results simplified the means for prediction of the ash stream sulfation levels.

These results yielded two trends of interest [5,7,8]:

1. Flyash sulfation levels among the sorbent tests using higher CaO (40+ wt. %) sorbents were between 4.5:1 and 5.5:1 (Molar Ca:S).
2. Minimal sulfur was removed from the system with the bottom ash.

These trends, while unique to the boiler system investigated, provide an expedient means to predict the ash stream sulfation levels. Notably, the majority of the sulfur was removed from the system with the flyash (71–86 wt. % [8]), and the sulfation levels found for this ash stream were within a relatively narrow range.

As such, average sulfation levels for the ash streams, from the boiler test results, are used here and presented in the results and discussion section. It must be noted, however, that the trends in ash stream sulfation levels shown here are unique to this boiler. For the prediction method demonstrated here to have broad applicability, other means of predicting ash stream sulfation levels, preferably using laboratory techniques, are required.

Development of a Model for Predicting Sorbent Consumption. If the sorbent attrition properties are estimated using a coefficient or index as outlined in Eqs. (3) and (5), then the partitioning of sorbent CaO between the ash streams can be predicted. Using predicted ash stream sulfation levels (as evidenced by Ca:S molar ratios), then sorbent consumption may be predicted, using the following expressions:

- The weight fraction of the sorbent CaO that will report to the bottom ash stream, ϕ_{ba} can be expressed by

$$\phi_{ba} = \frac{F_s \mathrm{Ca}_s (1 - I_{s,a}) \sum_{x=1}^{nx} k_d(x) M_{s,x}}{F_s \mathrm{Ca}_s} \tag{7}$$

  which reduces to

$$\phi_{ba} = (1 - I_{s,a}) \sum_{x=1}^{nx} k_d(x) M_{s,x} \tag{7'}$$

- Similarly, the weight fraction of the sorbent CaO reporting to the flyash stream is

$$\phi_{fa} = 1 - \phi_{ba} = 1 - (1 - I_{s,a}) \sum_{x=1}^{nx} k_d(x) M_{s,x} \tag{8}$$

The presence of CaO, derived from the fuel, complicates the assessment of the sulfation levels of sorbent particles removed with the ash streams. The molar calcium to sulfur ratios of the sorbent particles removed with the bottom ash and flyash streams are R_{ba} and R_{fa}, respectively. Where the input of CaO to the system with the fuel is small compared to that with the sorbent, these ratios may be assumed to be those calculated directly from chemical analyses of the ash streams. Where the CaO input with the fuel cannot be ignored, some assumptions will be required in deriving these quantities from ash stream analyses.

The molar flow rates of sorbent CaO partitioned to the bottom ash $m_{\mathrm{Ca},ba}$, and flyash, $m_{\mathrm{Ca},ba}$, relate to the sorbent feed as follows:

$$m_{ca,ba} = \frac{F_s \mathrm{Ca}_s \phi_{ba}}{\mathrm{MW}_{\mathrm{CaO}}} \tag{9}$$

$$m_{ca,fa} = \frac{F_s \mathrm{Ca}_s \phi_{fa}}{\mathrm{MW}_{\mathrm{CaO}}} \tag{10}$$

The molar flow rates of sulfur removed from the system with the bottom ash ($m_{s,ba}$) and flyash ($m_{s,fa}$) relate to the molar flow rates of CaO partitioned to the ash streams and the molar Ca:S ratios of the sorbent particles in the ash streams as such,

$$m_{s,ba} = \frac{m_{ca,ba}}{R_{ba}} \tag{11}$$

$$m_{s,fa} = \frac{m_{ca,fa}}{R_{fa}} \tag{12}$$

The total molar sulfur removal rate with the ash streams is the sum of the rates for the two streams. They are combined as follows:

$$m_s = m_{s,ba} + m_{c,fa} = \frac{F_s \mathrm{Ca}_s \phi_{ba}}{\mathrm{MW}_{\mathrm{CaO}} R_{ba}} + \frac{F_s \mathrm{Ca}_s \phi_{fa}}{\mathrm{MW}_{\mathrm{CaO}} R_{fa}} \tag{13}$$

or

$$m_s = m_{s,ba} + m_{c,fa} = \left[\frac{\phi_{ba}}{R_{ba}} + \frac{\phi_{fa}}{R_{fa}} \right] \frac{F_s \mathrm{Ca}_s}{\mathrm{MW}_{\mathrm{CaO}}} \tag{13'}$$

The molar Ca:S ratio of the sorbent particles in the composite ash stream is

$$R_{cs} = \frac{F_s \mathrm{Ca}_s}{\mathrm{MW}_{\mathrm{CaO}}} \frac{1}{m_s} = \frac{1}{\left(\frac{\phi_{ba}}{R_{ba}} + \frac{\phi_{fa}}{R_{fa}} \right)} \tag{14}$$

The sulfur capture coefficient σ is the fraction of the fuel sulfur that is removed with the composite ash stream, in this case 90 wt. % as mandated by the plant air quality permit. The molar ratio of sorbent calcium to fuel sulfur, as fed the boiler, relates to the molar Ca:S ratio in the composite ash stream as follows:

$$R_{\mathrm{feed}} = \frac{R_{ca}}{\sigma} \tag{15}$$

Substituting Eq. (15) into Eq. (14) yields an expression that relates sulfur and sorbent feed rates,

$$R_{\mathrm{feed}} = \frac{1}{\sigma \left(\frac{\phi_{ba}}{R_{ba}} + \frac{\phi_{fa}}{R_{fa}} \right)} \tag{16}$$

The relationship in Eq. (16) can be used to express a predicted sorbent requirement based on the following:

1. The partitioning of the sorbent calcium between the ash streams (based on sorbent sizing, the partition function, and attrition behavior)
2. The molar Ca:S ratios characteristic of the sorbent particles in the two ash streams
3. The feed rate of sulfur to the system

Equation (16) may also be rewritten in terms of predicted sorbent feed requirement F_s',

$$F_s' = \frac{F_f S_f}{\sigma \left(\frac{\phi_{ba}}{R_{ba}} + \frac{\phi_{fa}}{R_{fa}} \right)} \frac{\mathrm{MW}_{\mathrm{CaO}}}{\mathrm{MW}_s} \frac{1}{\mathrm{Ca}_s} \tag{16'}$$

The use of Eq. (16) requires knowledge of the sorbent CaO partitioning between the ash streams. This, in turn, requires sorbent sizing, knowledge of attrition behavior, and the boiler partition function.

Also required are the sulfation levels of the sorbent particles in the two ash streams. Levels found to be characteristic of the system are used here. For other systems, laboratory tests to predict

Table 1 Chemical analyses of sorbents examined

Sorbent	1	2	3	4	11
Wt. % CaO	55.7	55.2	51.9	49.5	42.8
Wt. % MgO	0.41	0.54	0.46	2.86	6.45
Wt. % Fe_2O_3	0.07	0.05	1.41	0.30	0.61
Wt. % SiO_2	0.69	0.74	3.18	3.57	6.65
Wt. % Al_2O_3	0.31	0.35	0.25	0.45	1.47
Wt. % LOI*	43.4	43.2	42.0	42.1	40.4
Grain size	Micrite	Spar	Micrite	Micrite	Spar

Table 3 Operating parameters for the boiler used for sorbent tests

Main Steam Flow, kg/s	34.1
Steam Pressure, MPa	10
Steam Temperature, K	783
Fuel Wt. % Ash[a]	63.5
Fuel Wt. % S[a]	0.28
Fuel Wt. % CaO[a]	0.53
Fuel HHV, Mj/kg[a]	5.8
Plant net generation capacity, MWe	30

[a]As-received basis

these sulfation levels, notably fluid bed sulfation tests for prediction of bottom ash sulfation levels may be useful for this purpose.

Experimental

The experimental data are based on results from the testing of 20 sorbents in a commercial CFB boiler, and more detailed discussions of the test program and its results appear elsewhere [5,10]. Chemical analyses of the sorbents of specific interest are shown in Table 1. The numbers assigned to the sorbents are those used in the original test results report [5]. These chemical analyses are used to perform CaO balances around the sorbent and bottom ash streams, which are used to estimate the attrition behavior of the sorbents.

Also shown are the characteristic grain sizes, as determined through petrographic analyses. Three of the sorbents (1, 3, and 4) exhibited the micritic grain size, while the other two (2 and 11) exhibited the sparry grain size.

Particle size distributions of the sorbents, as fed to the boiler, are shown in Table 2, and the operating parameters of the boiler used for the testing are shown in Table 3. Under full load conditions, the boiler typically required 50,000 kg/hr fuel, with a corresponding CaO input rate of 260 kg/hr. The sorbent feed rates ranged from 2000 to 4000 kg/hr, corresponding to CaO feed rates ranging from 1000 to 2000 kg/hr.

Fuel and sorbent feed rates were measured by the plant distributed control system (DCS), with readings available every 15 min. Ash stream flow rates were measured by solution of simultaneous material balances, using ash stream chemical analyses, and a previously presented method [8].

The data selection, both for material balances and measurements of sorbent feed rate, was based on the previously presented methodology [8]. Data for a time interval were not considered unless each individual DCS load reading over the interval varied by $<5\%$ of the mean for the interval.

A more detailed description of the selection of plant DCS data for the performance of material balances appears elsewhere [10], as well as an expanded discussion of the use of simultaneous material balances for the calcultion of flyash and bottom ash flow rates from a CFB boiler. Calculated ash stream flow rates, along with particle size distributions of flyash and bottom ash samples, were used to develop the boiler partition function, using Eqs. (1) and (2). Attrition behavior of each class of sorbent was quantified using particle size distributions of the sorbents, characterization of the boiler classification, or partition function, and the flow rate of calcium oxide with the bottom ash.

Results and Discussion

Boiler Partition Function. The boiler partition function was calculated using Eqs. (1) and (2). From this function, linear interpolations were used to calculate the individual partition function values at mean particle sizes representing the intervals for which the sorbent size analyses were available. These values are shown in Table 4.

Development of Sorbent Attrition Indices. The attrition indices were developed from boiler tests of sorbents 2 and 4, representing each of the two characteristic grain sizes. The particle size distributions of the two sorbents, along with the values for the partition function for the corresponding size intervals, are shown in Table 5. The attrition indices were calculated using Eqs. (4) and (5′). There is an order of magnitude difference between the calculated attrition indices. The attrition index for the sparry sorbent (2) is 0.71, while that for the micritic sorbent (4) is 0.07. Experimental work on the attrition rates of these sorbents, conducted in a laboratory fluid bed reactor, and based on CaO balances, found the same order of magnitude difference between the sorbents [10]. The attrition index for sparry stones will be assumed to be 0.71. That for micritic stones will be assumed to be 0.07.

Sulfation Levels of Boiler Ash Streams. The sulfation levels of ash streams from tests of sorbents 2, 4, and 11 have been previously presented [8]. Of the 12 sorbents, with >40.0 wt. % CaO, chemical analyses of the flyash and bottom ash streams were available for seven of the tests [5]. These data are presented in Table 6.

Several trends are of interest. The first is the relatively uniform flyash properties, ranging from 6.1 to 7.5 wt. % CaO, 0.72 to 0.97 wt. % S, and 4.5 to 5.5 molar Ca:S. The second is the differences in CaO contents in the bottom ash between the micritic sorbents and the sparry sorbents. The sorbent 7 test results featured a sorbent that was ground finer than the other sorbents. The balance of the data in Table 6 are for sorbents ground under identical machinery settings in the sorbent preparation plant. Within that data subset, the micritic sorbents produced bottom ash

Table 2 Particle size distributions of sorbents tested in the boiler

Particle size (μm)			Sorbent (wt. % direct)				
Passing	Retained	Mean	1	2	3	4	11
4000	2360	3180	3	3	5	4	3
2360	1000	1680	16	14	18	14	18
1000	707	853	15	8	16	17	12
707	180	443	14	3	13	14	9
180	149	164	7	3	7	8	6
149	75	112	10	7	9	9	10
75	0	38	35	62	32	34	42

Table 4 Interpolated values of the boiler partition function

Mean particle size (μm)	Fraction of size interval reporting to bottom ash stream
3180	1
1680	1
853	1
443	0.85
164	0.06
112	0
38	0

Table 5 Calculation of attrition indices

Mean particle size, μm	2	4	$k_d(x)$
3180	3	4	1
1680	14	14	1
853	8	17	1
443	3	14	0.85
164	3	8	0.06
112	7	9	0
38	62	34	0
$M_{s,kd}$	28	47	
β_{Ca} [8]	8	44	
$I_{s,kd}$ (from Eq. (5′))	0.71	0.07	
Sorbent type	Sparry	Micritic	

ranging in CaO content from 3.40 to 4.22 wt. %, while the corresponding figures for the sparry sorbents were 0.52 and 1.00 wt. % CaO.

These data are the result of differences in attrition behavior and, hence, CaO partitioning behavior resulting from the differences in grain structure among the sorbents. The third trend of interest, as discussed previously [8], is the relatively poor sulfation level found in each bottom ash product, as compared to the corresponding flyash product.

Assumptions Regarding Ash Stream Sulfation Levels. The average molar Ca:S ratio found among the flyash samples was 5.0. Previously published data showed that 71–86 wt. % of the sulfur fed to the boiler was removed with the flyash, 10 wt. % left the boiler with the flue gas as SO_2, and 4–9 wt. % was removed with the bottom ash. The actual fraction of the CaO removed with each ash stream, that was derived from fuel ash, was unkown. However, it was assumed that in each case 75 wt. % of the CaO in the flyash was derived from the sorbent particles, and that a mean value of the sulfation level of the sorbent particles in this stream, R_{fa}, is expressed by a molar Ca:S of 3.8. The mean Ca:S ratio of the bottom ash streams found in Table 6 is 12, which will be used as the value of R_{ba}.

Table 7 shows the values of ϕ_{ba}, ϕ_{fa}, R_{ba}, and R_{fa} used in Eq. (16), along with the resultant values of the required sorbent feed rates for compliance, expressed as molar Ca:S ratios. The values of ϕ were calculated using Eqs. (7′) and (8), using partition data shown in Table 4, the particle size distributions found in Table 2 and attrition indices for sorbent of the two petrographic types.

The method in Eq. (16) predicts feed requirements for the micritic sorbents, with feed Ca:S ratios in the range of 6.0. The predicted values for the sparry sorbents are in the range of 4.5.

Comparison of Predicted and Measured Sorbent Consumption Rates. There are two means by which predicted values of sorbent consumption can be compared to measured values. The first is to compare sets of individual DCS readings to predicted values. This comparison appears in Fig. 2. Here, it is apparent that even when the data sets are screened for constancy of boiler operation, significant variations in sorbent consumption were encountered. However, a trend is apparent between predicted and measured values.

A second method of evaluation uses average sorbent consumption values. This method may be more commonly applied, an example being averaging sorbent consumption over the time span of a boiler performance test. However, as was discussed previously, constancy of load over the time span in question is expected to have an effect on mean sorbent consumption for the span. Average consumption for each of the five sorbent tests is compared to the corresponding prediction in Table 8. The mean values were calculated from only DCS data sets that met the criterion for constant load (each load reading varying by $<5\%$ of the mean for the time span). The trend between predicted and measured values is

Table 6 Flyash and bottom ash chemical analyses for a range of boiler tests

	Bottom ash			Flyash				
Sorbent test	Wt. % CaO	Wt. % S	Molar Ca:S	Wt. % CaO	Wt. % S	Molar Ca:S	Sorbent Wt. % CaO	Grain size[a]
1	4.22	0.13	18.3	7.31	0.76	5.5	55.7	Micrite
2	0.52	0.04	8.5	7.43	0.97	4.5	55.2	Spar
3	3.40	0.20	9.7	6.90	0.72	5.5	51.9	Micrite
4	3.73	0.14	14.9	6.92	0.76	5.2	49.5	Micrite
6	3.70	0.11	19.2	6.80	0.82	4.7	46.7	Micrite
7[b]	1.16	0.11	6.1	6.19	0.78	4.5	46.0	Micrite
11	1.00	0.06	9.5	7.00	0.86	4.6	42.8	Spar

[a]More detailed descriptions from petrographic analyses are found in Morrison [5]
[b]Test data for sorbent 7 reflect a finer as-fed size consistency, as the sorbent grinding plant was operated differently as compared to the preparation of the other sorbents

Table 7 Predicted molar Ca:S values of sorbent consumption by the boiler

Sorbent	1	2	3	4	11
ϕ_{ba}	0.43	0.08	0.44	0.46	0.12
ϕ_{fa}	0.57	0.92	0.56	0.53	0.88
R_{ba}	12.3	12.3	12.3	12.3	12.3
R_{fa}	3.8	3.8	3.8	3.8	3.8
R_{feed}	5.9	4.4	6.0	6.1	4.5

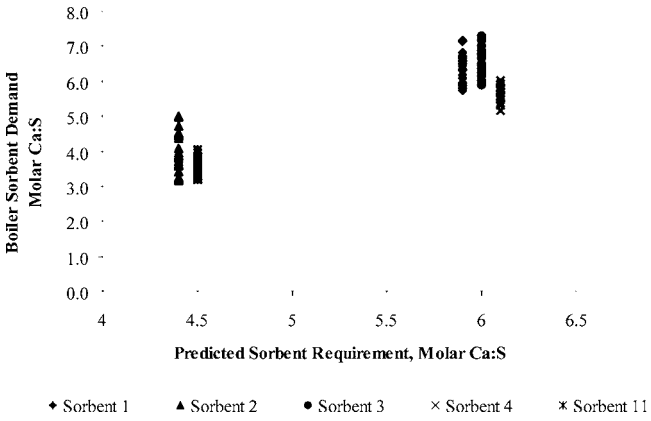

Fig. 2 Comparison of predicted sorbent requirement with measured sorbent requirements (individual DCS readings)

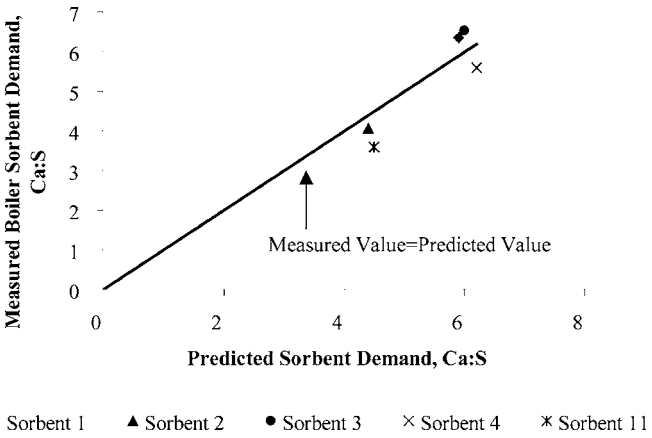

Fig. 3 Comparison of predicted sorbent requirement with measured sorbent requirements (mean values)

illustrated in Fig. 3.

These predicted values show reasonable agreement with the measured values. Excepting the case of sorbent 11 (20%), the measured values vary from the predicted values by $<10\%$.

Utility of Method. This method offers the potential to predict the sorbent consumption requirements of a CFB boiler based on a boiler performance parameter (the partition function), sorbent properties (attrition characteristics, particle size distribution), and sulfation levels of the sorbent particles in the ash streams. The application of attrition behavior and the boiler partition function to the particle size distribution of the sorbent is straightforward. In the case of the tests described here, the flyash stream accounted for the majority of the sulfur fed to the boiler and sulfation levels for this stream were found to be in a relatively narrow range across the range of sorbent tests. This simplified the estimation of the sulfation levels of the sorbent particles in the ash streams. This boiler system was, however, somewhat unique due to the low sulfur content and high ash content of the fuel. Application of this method to other fuel types, notably those with lower ash and higher sulfur contents, will likely require a closer examination of the predicted sulfation levels of the sorbent particles in the ash streams. Prediction of sulfation levels of sorbent particles partitioned to the two ash streams will likely require the inclusion of additional analytical techniques for sulfation testing. The differences, notably particle size, between the ash streams suggests that no single sulfation test method (i.e., fluid bed reactor, thermogravimetric analysis) can be expected to predict the sulfation levels of sorbent particles in both ash streams.

Conclusions

A method has been presented for the prediction of sorbent requirements of a CFB boiler based on a sorbent property (grain size), boiler operating parameters, and predicted sulfation levels of sorbent particle partitioned to the boiler ash streams. The sorbent sulfation levels were based on averages that were determined across a range of tests where several sorbents were tested under similar conditions in a CFB boiler.

Based on experimental results from the boiler tests, an attrition index was assigned to five sorbents, based on their grain sizes as determined by petrographic analyses. The boiler partition function was determined from particle size analyses and calculated flow rates for the boiler ash streams.

Data from the boiler DCS were used for comparison of actual sorbent feed rates required to maintain the required sulfur capture levels, and those predicted for the sorbents using the method developed here. The only test data used were for extended periods of operation, where each 15 min DCS reading for boiler load varied by $<5\%$ from the mean for the span. Of the five sorbents examined, measured sorbent demand by the boiler agreed to within 10% of the predicted demand.

The method presented here, along with the test data, suggests the following:

1. No single analytical test procedure can be used to reliably predict sorbent consumption by a CFB boiler.
2. Grain size, as measured by a petrographic analysis, should be considered when evaluating the suitability of a limestone for sorbent use by a CFB power project.
3. Particle size distributions of sorbents and, to a lesser extent, attrition properties are considered to be important parameters governing sorbent performance. The parameters are important within the context of the boiler partition function and should be taken into account in any method used to predict sorbent performance.

Table 8 Comparison of predicted and mean measured values for boiler sorbent demand (measured as molar Ca:S)

Sorbent	1	2	3	4	11
Predicted sorbent demand	5.9	4.4	6.0	6.1	4.5
Measured sorbent demand	6.3	4.1	6.5	5.6	3.6

Nomenclature

Ca_s = fractional CaO content of the sorbent
F_{ba} = flow rate of bottom ash from the system, kg/s
F_{ca} = flow rate of the reconstituted composite ash stream, kg/s
$F_{Ca,ba}$ = flow rate of CaO with the bottom ash stream, kg/s
$F_{Ca,ba,f}$ = flow rate of CaO with the bottom ash stream, derived from the fuel ash, kg/s
F_f = feed rate of fuel to the system, kg/s
F_{fa} = flow rate of bottom ash from the system, kg/s
F_s = feed rate of sorbent to the system, kg/s
F'_s = predicted sorbent feed rate required to achieve air quality compliance, kg/s
$I_{s,a}$ = sorbent attrition index
$k_d(x)$ = boiler partition function
$K_{i,a}$ = attrition coefficient of species i
$K_{s,a}$ = attrition coefficient of the sorbent
$m_{Ca,ba}$ = molar flow rate of sorbent CaO partitioned to the bottom ash, mole/s
$m_{Ca,fa}$ = molar flow rate of sorbent CaO partitioned to the flyash, mole/s

$M_{ca,x}$ = mass fraction of the reconstituted composite ash stream within size interval x

$M_{i,ba}$ = mass fraction of particles of species i that reports to the bottom ash stream

$M_{i,kd}$ = mass fraction of particles of species i initially coarse enough to report to the bottom ash stream

$M_{i,x}$ = mass fraction of particles of species i within size interval x

$m_{s,ba}$ = molar flow rate of sulfur removed from the system with the bottom ash stream, mole/s

$m_{s,fa}$ = molar flow rate of sulfur removed from the system with the flyash stream, mole/s

$\mathrm{MW}_{\mathrm{CaO}}$ = molar weight of CaO

$\mathrm{MW}_{\mathrm{sulfur}}$ = molar weight of sulfur

nx = number of particle size intervals in a particle size analysis

R_{ba} = molar Ca:S ratio of the sorbent particles removed from the system with the bottom ash stream

R_{cs} = molar Ca:S ratio of sorbent particles in composite ash stream

R_{fa} = molar Ca:S ratio of the sorbent particles removed from the system with the flyash stream

R_{feed} = predicted molar ratio of sorbent calcium to fuel sulfur required to achieve air quality compliance

S_f = fractional sulfur content of the fuel

x = particle size interval

$\beta\mathrm{Ca}$ = fraction of the total CaO feed to the system that is partitioned to the bottom ash

ϕ_{ba} = fraction of the sorbent CaO that is partitioned to the bottom ash stream

ϕf_a = fraction of the sorbent CaO that is partitioned to the flyash

σ = fraction of the feed sulfur that is removed with the composite ash stream (sulfur capture coefficient)

References

[1] Romans, D. E., 1997, "Sorbent Performance in Fluidized-Bed Combustors: The Effect of Calcination on the Sulfation Rate and Calcium Utilization," Ph.D. thesis, Materials Science and Engineering, Pennsylvania State University, 279.

[2] Simons, G. A., and Garman, A. R., 1986, "Small Pore Closure and the Deactivation of the Limestone Sulfation Reaction," AIChE J., **32**(9), pp. 1491–1499.

[3] Ghardashkani, S., Lungstrom, E., and Lindqvist, O., 1989, "Release of Sulfur Dioxide From Calcium Sulfate Under Reducing Conditions,"Tenth International (ASME) Conference on Fluidized Bed Combustion, San Francisco.

[4] Haji-Sulaiman, M. Z., and Scaroni, A. W., 1991, "The Calcination and Sulfation Behavior of Sorbents in Fluidized Bed Combustion," Fuel, **70**, pp. 169–176.

[5] Morrison, J., Romans, D. E., Liu, Y., Naiyi, H., Pisupati, S. V., Miller, B. G., Miller, S. F., and Scaroni, A. W., 1994, *Evaluation of Limestones and Dolostones for Use as Sorbents in Atmospheric Pressure Circulating Fluidized-Bed Combustors*, The Pennsylvania State University for Pennsylvania Energy Development Authority, Harrisburg, PA, p. 124.

[6] Liu, Y., and Scaroni, A. W., 1996, "The Attrition Behavior of Sorbents in Fluidized Bed Combustion: Effect of Grain Structure and Physical Strength," *Proc. of 13th Annual Pittsbugh Coal Conference*, University of Pittsburgh, Pittsburgh, pp. 43–48.

[7] Rozelle, P. L., Pisupati, S. V., and Scaroni, A. W., 2000, "The Measurement of Flyash and Bottom Ash Flow Rates From a Circulating Fluidized Bed Boiler by Simultaneous Solution of Material Balances." Environ. Prog., **19**(3), pp. 175–182.

[8] Rozelle, P. L., Pisupati, S. V., Morrison, J. L., and Scaroni, A. W., 1999, "The Partioning of Calcium and Sulfur Between Bottom Ash and Flyash in a Commercial CFB Boiler," *Proc. of 15th International Conference on Fluidized Bed Combustion*, Savannah, ASME, New York, CD Rom Paper No. 99-0134.

[9] Folk, R. L., 1962, *Spectral Subdivision of Limestone Types*, American Association of Petroleum Geologists, Tulsa, OK, Vol. AAPG Memoir 1, pp. 62–84.

[10] Rozelle, P. L., 2000, "The Effect of Fuel and Sorbent Properties on Their Partitioning Between the Flyash and Bottom Ash Streams in Fluidized Bed Combustion," Ph. D. thesis, Fuel Science, The Pennsylvania State University, 217.

Experimental Investigations on a Hydrogen-Diesel Dual Fuel Engine at Different Compression Ratios

M. Masood
Associate Professor
e-mail: masoodtayyab@yahoo.com

S. N. Mehdi
Professor
e-mail: nawazishmehdi@yahoo.co.in

Mechanical Engineering Department,
M. J. College of Engineering and Technology,
Hyderabad-34, India

P. Ram Reddy
Professor
Jawaharlal Technological University,
Hyderabad-73, India

An experimental investigation was carried out on a computer interfaced single cylinder variable compression ratio, compression ignition engine to optimize the performance characteristics and to find the useful higher compression ratio (UHCR) with hydrogen-diesel dual fuel mode. Experimentations were conducted on five different compression ratios and the performance characteristics were calculated. The effect of blending on NO_x, HC, CO, *and particulate matter were measured and reported. The rate of heat release and speed of combustion with increase in compression ratio with simultaneous increase in hydrogen substitution were measured. Intake temperature of air was increased and for three different temperatures, the effect of increase in temperature of air-hydrogen mixture on* NO_x *were studied and found that there was a sharp increase in the* NO_x *value as the inlet temperature was increased from 65 to* 85°C. [DOI: 10.1115/1.2227418]

Introduction

As the world finds itself in the midst of a universal energy shortage, compounded by a parallel need to reduce pollutants of all kinds, we must take an increasingly serious look at novel sources of abundant energy, and methods for their best utilization. Hydrogen, with its remarkable combustion properties in the conventional internal combustion engine, appears to be proving itself as the best transportation fuel of the future if it can be produced economically. Importantly, it can be used in existing internal combustion engines, yielding unprecedented efficiencies and extremely low levels of exhaust pollution [1]. Hydrogen has, for years, been recognized for its extremely high energy potential. But because of inherent difficulties in handling hydrogen in its gaseous form, technology has, over the past two decades, emphasized the utilization of hydrogen in its liquid form.

Hydrogen can be used advantageously in internal combustion engines as an additive to a hydrocarbon fuel. Hydrogen can be used in conjunction with compact liquid fuels such as gasoline; alcohol or diesel provided each is stored separately.

As with hydrogen, the drawback of lean operation with hydrocarbon fuels is a reduced power output. Lean operation of hydrocarbon engines has additional drawbacks. Lean mixtures are hard to ignite, despite the mixture being above the low fire (point) limit of the fuel. This result in misfire, which increases un-burned hydrocarbon emissions, reduces performance and wastes fuel.

Mixing hydrogen with other hydrocarbon fuels reduces all of these drawbacks. Hydrogen's low ignition energy limit and high burning speed makes the hydrogen/hydrocarbon mixture easier to ignite, reducing misfire and thereby improving emissions, performance, and fuel economy. Regarding power output, hydrogen augments the mixture's energy density at lean mixtures by increasing the hydrogen-to-carbon ratio, and thereby improves torque at wide-open throttle conditions.

Most research in dual fuel engine has concentrated on defining the extent of dual fueling and its effect on emissions and performance [1,2]. Natural gas in combination with diesel was tried and found to be very effective in NO_x reduction but engine operation can suffer from high hydrocarbons (HC) emissions and poor performance, especially at high loads [3,4]. The auto ignition of methane was studied experimentally to obtain ignition delay data as a function of engine cylinder pressure and temperature by Sandia National Laboratory [5,6].

Karim et al. [7,8] and Gunea et al. [9], concluded that at low outputs, much of the primary gaseous fuel remain unburned leading to high hydrocarbon (HC) and CO emissions which is mainly due to very lean operation and a weak ignition source. At high loads a large amount of gaseous fuel admission results in uncontrolled reaction rates near the pilot spray causing rough engine operation.

Experimental investigation on a LPG—diesel dual fuel engine by Poonia et al. [10,11] revealed that at low loads, the brake thermal efficiency is always lower than diesel values but is better at high loads. Also, at low outputs increasing the pilot quantity and intake temperature improves the thermal efficiency. The HC and CO emissions were found to increase in the dual fuel mode.

Daisho et al. [12] showed that emission characteristics and brake thermal efficiency of a dual engine using natural gas can be improved by reciprocating exhaust gas, increased brake thermal efficiency with increase intake temperature is also reported.

In the present study experiments were conducted on a hydrogen-diesel dual fuel engine under constant speed, variable compression ratios, and variable load conditions. The amount of primary fuel, i.e., diesel admitted was varied and hydrogen was substituted at each load. The objective was to determine in detail the performance, emissions, and combustion characteristics of the engine.

Experimental Setup and Experimentation

The engine used in the present study was a Kirloskar AV-1, single cylinder direct injection, water-cooled diesel engine with the specifications given in Table 1. Diesel injected with a nozzle hole size of 0.15 mm and simultaneous provision of compressed natural gas injector (to inject hydrogen directly in to the cylinder) is also provided. The engine was coupled to a dc dynamometer and all the experiments were carried out at a constant speed of 1400 rpm. The engine was modified and provision was provided to vary the compression ratio from 14.5 to 24.5. The intake tem-

Contributed by the Internal Combustion Engine Division of ASME for publication in the JOURNAL OF ENGINEERING FOR GAS TURBINES AND POWER. Manuscript received February 3, 2005; final manuscript received March 19, 2006. Review conducted by D. Assanis.

Table 1 Engine specifications

Type	Four-stroke, single cylinder, Compression ignition engine With Variable compression ratio
Make	Kirloskar AV-1
Rated Power	3.7 KW, 1500 RPM
Bore and Stroke	85 mm×110 mm
Compression Ratio	16.5: 1, variable from 14.3 to 24.5
Cylinder Capacity	624. cc
Dynamometer	Electrical-ac Alternator
Cylinder Pressure	Piezo sensor, Range: 2000 psi
Orifice Diam.	0.15 mm
Fuel	Diesel, Hydrogen
Hydrogen Injection	By CNG injector and by Induction method

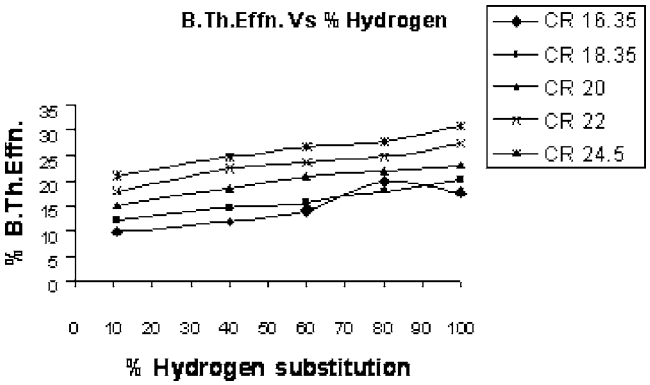

Fig. 1 Effect of hydrogen substitution on brake thermal efficiency

perature and pressure were chosen to give stable and knock free engine operation. Crank-angle-resolved in-cylinder pressure and the diesel injection pressure were measured. A computer interfaced piezoelectric sensor, of range 145 bar was used to note the in cylinder pressure. Pressure signals were obtained at one-degree crank angle intervals using a digital data acquisition system. The average pressure data from 100 consecutive cycles were used for calculating combustion parameters. Special software was used to obtain combustion parameters. Intake, cylinder head and exhaust gas temperatures were measured with *k*-type thermocouples. The valve lift was detected with a gap sensor in the injector. On the shaft projection, a reference indicator was provided to mark the top dead center (TDC), which was detected by a proximity sensor. The hydrogen gas was injected into the cylinder and a thermal mass flow controller controlled its flow rate. The hydrogen cylinder pressure was reduced before injecting into the cylinder. The airflow rate was measured using a laminar flow element. The engine speed was maintained constant by controlling the hydrogen gas mass flow rate. Engine exhaust emissions were also measured using an advanced AVL five-gas analyzer. Load was varied ranging from 20% to 100% of full load. The injection was set at 20 deg BTDC for both hydrogen and diesel. At each load the amount of hydrogen was varied. The maximum amount of hydrogen supplied was limited by unstable operation at low outputs and by rough engine running due to knock at high out puts. When the hydrogen supply was increased, the diesel injection was automatically decreased by the governor mechanism of the engine to maintain the speed constant; details are given in Table 2. The experimentation was repeated by varying the compression ratios. The tests were carried out for the compression ratios of 16.35, 18.35, 20, 22, and 24.5 and each time all the parameters were noted down in the way as explained above. To study the effect of inlet temperature on NO_x, the intake temperatures of air were varied carefully to avoid the risk of precombustion of hydrogen in the intake manifold for one compression ratio of 24.5. The inlet temperature was measured after mixing in the inlet manifold. Three temperatures 65, 75, and 85°C were choiced to study the NO_x.

Results and Discussion

Significant results were obtained at various percentage substitution of hydrogen at different compression ratios. The percentage of hydrogen substitution varied continuously from 20% to 100% of full load, and this substitution was different at different compression ratios for the same load.

Brake Thermal Efficiency. The brake thermal efficiency was calculated for various loads varying from 20% to 100% of full load for various compression ratios. However, they are plotted only for 100% load at various compression ratios to study the effect of substitution by varying the compression ratio. Hydrogen percentage was varied from 10% to 100%. As shown in Fig. 1, the brake thermal efficiency is increasing with the increasing percentage of hydrogen and it is maximum with 100% hydrogen. For all the compression ratios it was found that in the beginning with low percentage of hydrogen and with low outputs, the value of brake thermal efficiency is low. As the compression ratio increases, it results in closer contact between the molecules of fuel and oxygen reducing the time of reaction. The increase in compression temperatures as well as decrease in minimum auto ignition temperature decreases the delay period. At low outputs (like 20% of full load), the brake thermal efficiency reduces as the energy derived from hydrogen increases. At this condition the diesel injected is low in quantity and introduction of hydrogen further reduces it. Thus the ignition centers formed by the injected diesel reduces as the hydrogen is introduced at low outputs. Hence poor ignition of gaseous fuel results in low efficiency. However, at higher outputs, the efficiency increases due increase in combustion and the inducted mixture is reasonably rich to burn. For CR 24.5, when the hydrogen substitution was varied from 10% to 90%, the percentage change in brake thermal efficiency was around 31.8% of the initial values. For CR 18.35, this percentage change of thermal

Table 2 Diesel and hydrogen substitutions at different compression ratios at different loads

Compression ratio (CR)	Amount of diesel (kg/h)					Amount of hydrogen (Kg/h)				
	16.35	18.335	20	22	24.5	16.35	18.35	20	22	24.5
% **Load**										
20	0.85	0.956	0.9	0.87	0.92	0.096	0.108	0.13	0.102	0.084
40	0.665	0.728	0.85	0.75	0.82	0.108	0.114	0.14	0.108	0.087
60	0.51	0.624	0.71	0.61	0.65	0.114	0.114	0.12	0.114	0.09
80	0.413	0.493	0.56	0.51	0.54	0.132	0.138	0.13	0.117	0.093
100	0.32	0.45	0.47	0.36	0.45	0.138	0.15	0.15	0.12	0.096

Table 3 Result analysis

	Hydrogen substitution range		Compression ratio					Effect of Change in CR on properties %	Remarks
	From	To	16.35	18.35	20	22	24.5	16.35 to 24.5	
% Change in Brake thermal efficiency	10%	90%	23	29	28	30	31.85	27	Increased
% CO Emissions	10%	90%	75	66	73	88	95	21	Reduced
% NO_x Emissions	10%	90%	25	27	35	37	38	38	Increased
% Particulate Matter	10%	90%	82	92.7	93.3	94	98	16	Reduced
HC Emissions	10%	90%	77	82.57	88	90	93.63	17	Reduced
Peak pressures	10%	90%	19	24	26	30	33	42	Increased

efficiency was around 29%. The percentage change in brake thermal efficiency when the compression ratio was changed from CR16.35 to CR 24.5 was around 27% for 90% hydrogen substitution, for details Table 3 can be seen. One more observation, which can be made from Fig. 1, is that it has the highest value of brake thermal efficiency for a higher compression ratio, which predicts that hydrogen could be, better used at higher compression ratios.

HC Emissions. The HC emission is shown in Fig. 2, for only 100% load, at various percentages of hydrogen varying from 10% to 100% at different compression ratios. As shown the HC decreases with the increasing percentage of substitution of hydrogen and becomes approximately zero at 100% hydrogen. Even at 10% hydrogen, since the applied load is 100%, HC percentage is very low. This is because the combustion is complete under these conditions due to sufficient quantity and higher gas temperatures in the cylinder. It was also observed that at higher compression ratio of 24.5, these emissions are the lowest even at 10% hydrogen. This is because at higher compression ratios, the compressed air temperatures are higher which promotes faster and complete combustions. With the variation of percentage substitution of hydrogen from 10% to 90%, the percentage reduction in the HC value is 93.63%, for CR 24.5, and for CR 18.35; the percentage reduction is 82.57%. The effect of compression ratio when changed from 16.35 to 24.5 for the same change in percentage substitution is reduction of HC by 17%.

CO Emissions. As shown in Fig. 3, The CO value continuously decreases with the increase in the percentage substitution of hydrogen for all compression ratios and for 100% load. The obvious reason being, increase of hydrogen percentage (which does not contain any carbon in it at 100%), complete combustion and higher inside temperatures, and for the other percentages of hydrogen the amount of diesel present in it is also getting burned completely and leaving only a few traces of CO. Both HC and CO is very low at higher percentages of hydrogen. It is evident that best diesel substitutions at low loads can be decided on the level of HC and CO emissions that can be permitted. As the percentage hydrogen substitution is varied from 10% to 90%, the value CO is reduced by 95% for CR 24.5 and 66.67% for CR 18.35. Only with 10% hydrogen substitution, as the compression ratio is varied from CR18.35 to CR 24.5, the percentage reduction in CO is 21%, Table 3 gives further details.

NO_x Emissions. In Fig. 4, the effect of hydrogen substitution can be seen on NO_x. Though the over all range of NO_x is low but it is observed that as the percentage of hydrogen increases the NO_x level was also increasing. It was found to be higher with higher compression ratios and higher percentages of hydrogen substitutions. It is high with a compression ratio of 24.5. The reason is, as the operating temperatures are high for higher compression ratios and with higher hydrogen percentage substitutions. At higher loads increased hydrogen leads to rapid combustion and this rises NO_x level due to rise in the flame propagation rate in hydrogen-air mixture. Thus at high loads the concentration of NO_x (that can be) tolerated can be used to fix the hydrogen sub-

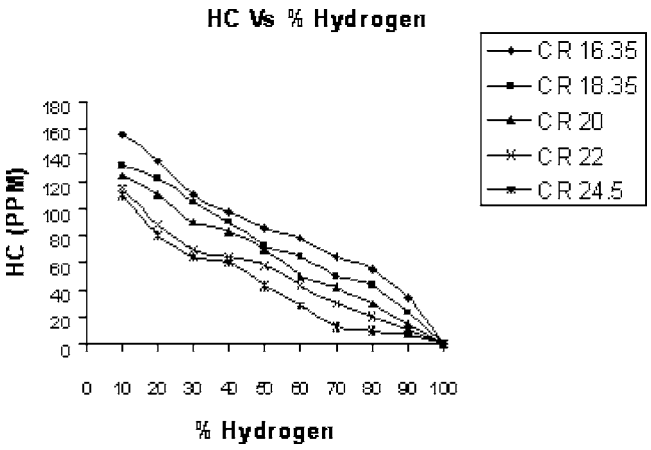

Fig. 2 Effect of hydrogen substitution on HC

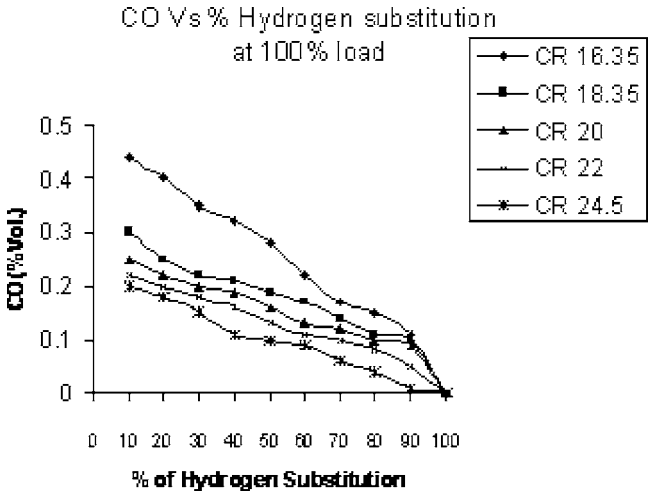

Fig. 3 Effect of hydrogen substitution on CO

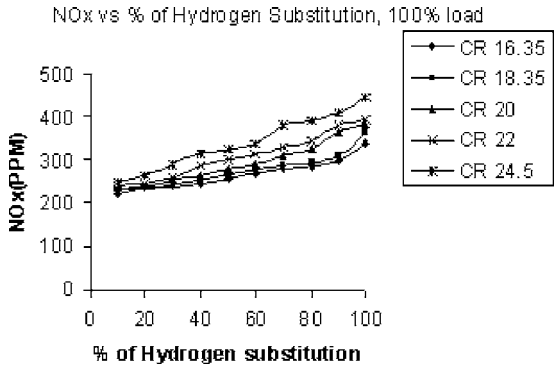

Fig. 4 Effect of hydrogen substitution on NO_x

stitution. As the percentage of hydrogen substitution was varied from 10% to 90%, it was found that the NO_x increased by 38% for CR 24.5 and at 100% load, and for CR 18.35, this increase was 27%. The high heating value of hydrogen is one of the reasons for the high operating temperatures. As the compression ratio was increased from CR16.35 to CR 24.5, for 90% hydrogen substitution, the value of NO_x was increased by 38%, which is the effect of higher compression ratios. The inlet temperatures could control the value of NO_x.

Particulate Matter. As shown in the Fig. 5, the particulate matter shows a drastic drop as the percentage of hydrogen increases. It is shown only for two compression ratios of 18.35 and 22. Though the value of particulate matter will be affected by the method of measurement, however, it is very clear that it falls down drastically with increase in hydrogen substitution. This is because the amount of diesel is decreasing and also because of higher temperatures as hydrogen percentage is increasing. It was observed that for CR 18.35, as the percentage substitution of hydrogen was varied from 10% to 90%, the particulate matter was reduced by 92.7%, and for CR 22 this reduction was 82.6%. When CR was changed from 16.35 to 24.5, the percentage change in PM was 16% (Table 3 for details).

Combustion Parameters.

Pressure Crank Angle Diagram. Figure 6 shows the pressure crank angle diagram at 100% load and 80% hydrogen. The figure shows that the cylinder pressure is maximum at a compression ratio of 24.5. When compared to pure diesel (see Fig. 7 for details), the rise of pressure per degree of crank angle is more in dual mode. This is because of the high flammability of hydrogen and rapid combustion. Similarly with 50% hydrogen and 80% load, and with 80% hydrogen and 80% load, it was noted that for higher compression ratios the pressures increase with the increase in the percentage of hydrogen. In case of low loads, the combustion duration increases. This is due to the reduced combustion rate

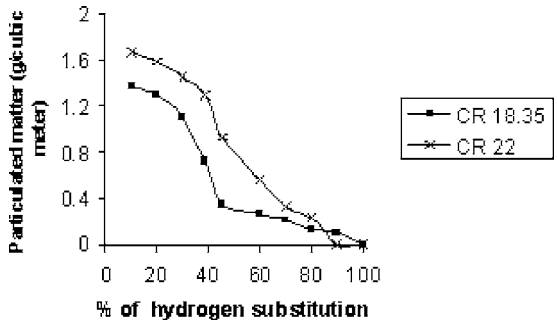

Fig. 5 Effect of hydrogen substitution on PM

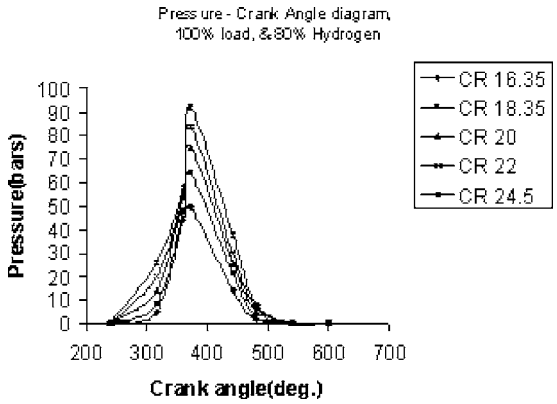

Fig. 6 Pressure-crank angle diagram at 80% hydrogen substitution

of the primary fuel air mixture as a result of the reduction in the ignition centers. As the percentage of hydrogen is increased, the rate of pressure rise per crank angle is simultaneously increased (Fig. 8 for details). Hydrogen has high flame speed at stoichiometric ratios. Under these conditions, the hydrogen flame speed is nearly an order of magnitude higher (faster) than that of gasoline. This means that hydrogen engines can more closely approach the thermodynamically ideal engine cycle. At leaner mixtures, how-

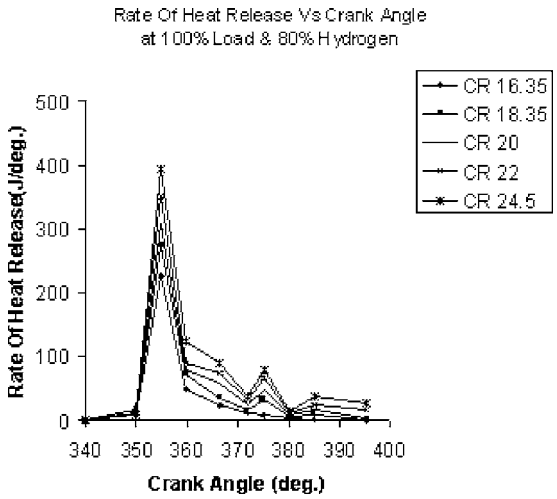

Fig. 7 Heat release rate at 80% hydrogen substitution

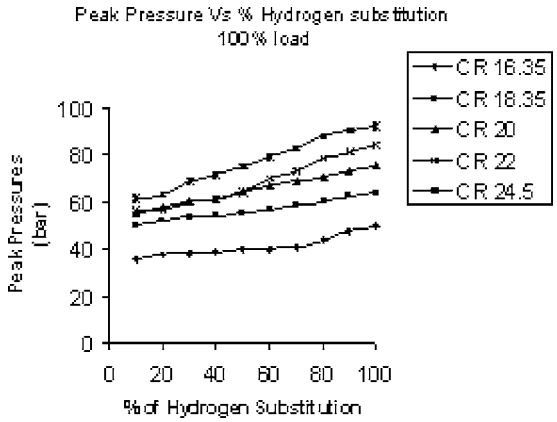

Fig. 8 Peak pressures at different compression ratios and at various % H_2 substitution

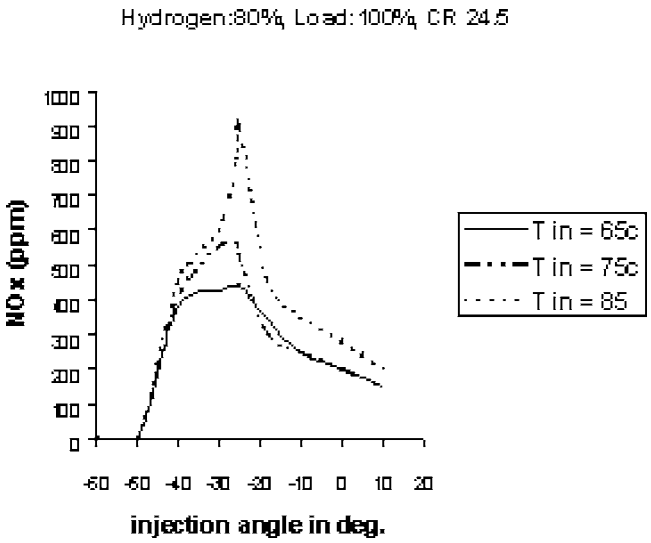

Fig. 9 Effect of inlet temperature on NO_x at different injection angles

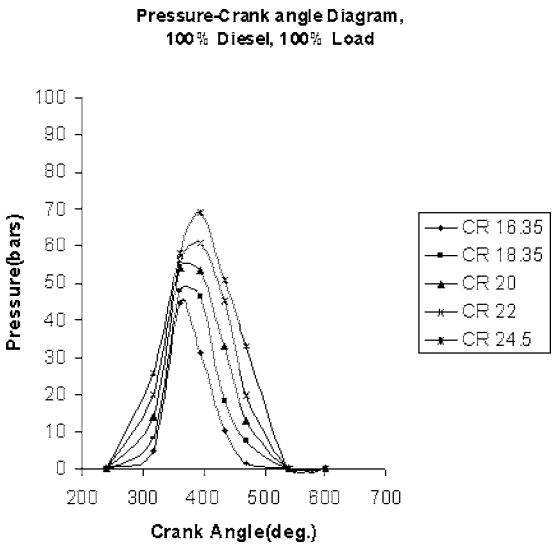

Fig. 10 Pressure-crank angle diagram with diesel as fuel and at different compression ratios

ever, the flame velocity decreases significantly.

It was also noted that for the lower percentages of hydrogen and more percentages of diesel the pressure rise is lower at lower percentages of loads. This is due to the reduced combustion rate of the primary fuel air mixture as a result of reduction in ignition centers. For the lower compression ratios and lower loads, the pressure rise is further low for the said reasons.

The Rate of Heat Release. As shown in Fig. 9, the rate of heat release per degree of crank angle for the different compression ratios (see Table 4). There are two main stages in the dual fuel mode like in diesel mode. The first is mainly the combustion of diesel and the hydrogen entrained in the diesel spray, while the second is mainly due to the combustion of hydrogen by flame propagation from the ignition centers formed by the diesel spray. The peak heat release rate, that is, the peak combustion is considerably low in the dual fuel mode as compared to the diesel mode at low outputs. This is the reason for the reduced brake thermal efficiency and rate of pressure rise as compared to diesel at low outputs. The second stage is stronger than the diesel mode as most of heat release occurs by the combustion of hydrogen by flame propagation. The rate of heat release increases with hydrogen substitution at high outputs. As the hydrogen percentage increases, the substitution tends to richer hydrogen-air mixtures. This sets the rapid combustion rates, which tends to increase the pressure rapidly in the dual fuel mode. The flame is set with diesel injection in the first phase and in the second phase the combustion of hydrogen takes place by the flame propagation formed by the diesel spray. The rate of heat release is higher in dual fuel because of combined burning of two fuels. This is one of the reasons for higher thermal efficiency in dual fuel mode at high outputs [13]. At higher compression ratios the flame speed or the rate of combustion is higher when compared to lower compression ratios, which can be seen by comparing the rate of heat release at different compression ratios in Fig. 9. It was noted that the percentage change in pressure, when the hydrogen substitution was varied from 50% to 80%, for the same compression ratio of CR 24.5, was 13% and it was 15%, for CR 18.35, for the same percentage change in hydrogen substitution. The percentage change in the rate of heat release, when the hydrogen substitution was varied from 50% to 80%, for CR 24.5 was 17%, and this percentage change was 20% for CR 18.35. It can be seen that as the percentage hydrogen is increased, both the pressure rise and rate of heat release has increased. As shown, as the compression ratio is increased, the heat release rate and pressure rise has also increased.

Peak Pressures. As shown in Fig. 8, the peak pressures obtained with various substitutions of hydrogen starting from 10% to 100% at 100% load for different compression ratios. It is evident that peak pressures are higher for higher percentage substitution and higher compression ratios at high outputs. In dual fuel mode, there is a drop in the maximum rate of pressure rise in the case of low outputs, that is, 20% and 40% output. This is due to the weakening of the ignition source, as a result of the reduction in the primary fuel. The maximum rate of pressure rise increases with hydrogen substitution at high outputs. Further, an increase in

Table 4 In cylinder pressures at various percentages of diesel and hydrogen substitutions at 100% load

Fuel Percentages		Cylinder Pressures				
% D	%H 2	16.35	18.35	20	22	24.5
90	10	36	50.5	55	56	62
80	20	38	52	58	57	69
60	40	38	53	60	60	71
50	50	39	54	61	61	75
40	60	40	55.5	64	64	79
30	70	40.5	57	67	70	83
20	80	41	58.5	70	73	88
10	90	44	60	73	78	90
0	100	48	64	75	81	92

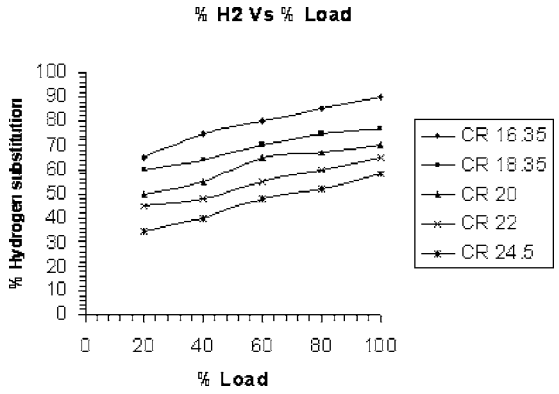

Fig. 11 % hydrogen substitution at different loads

the hydrogen substitution leads to a relatively richer hydrogen-air mixture. Rise in the hydrogen admission rate also leads to more of this fuel being entrained within the diesel spray and a rapid initial combustion phase. These are the reasons for the increase in the maximum rate of pressure in the dual fuel mode. The high rate of pressure rise leads to knock at high outputs and this limits the amount of hydrogen substitution that can be substituted at these conditions.

It was noted that for CR 24.5, when the percentage substitution was varied from 10% to 90% of hydrogen, the percentage pressure rise was 33%. For CR 18.35, this difference for the same percentage substitutions is 24%; this again, shows the effect of compression ratio on the pressure rise. The reason is the same as explained in the case of rate of heat release. Another thing, which could be noted, is that in the case of 90% hydrogen substitution, percentage rise in pressure from CR 16.35 to CR 24.5 is around

Table 5 Initial conditions for NO_x analysis

Inlet temperatures	65, 75, 85°C
Compression ratio	24.5
Angle of injection For Diesel	Varied between 40 deg BTDC to 5 deg ATDC
Load	100%
% Hydrogen	80%
Angle injection for Hydrogen	20 deg BDTC, constant for all percentages of fuel

42%. This is a measure of reduction in the delay period (both physical and chemical delay), with the increase in compression ratio in dual fuel condition.

Effect of Increased Intake Temperature on NO_x. Figure 10 shows the effect of temperature on NO_x at 80% hydrogen substitution, compression ratio 24.5% and 100% load and for three different intake temperatures of 65, 75, and 85°C. As expected, increased intake temperature resulted in higher NO_x and faster burning rates. Higher intake temperatures results in faster fuel combustion and shorter combustion durations, which has negative impact on the NO_x. There is a sharp increase in NO_x from 400 to 900 ppm when the temperature is increased from 65 to 85°C. The higher intake temperatures have most of the heat released close to TDC. Similarly for other percentages of hydrogen substitution, a similar trend was observed for different compression ratios.

Effect of Injection Timings on NO_x. When the injection angle was advanced from near TDC, NO_x increased and had the maximum value near 23 deg BTDC, which can be seen from Fig. 10. When the injection angle was further advanced, NO_x value decreased. This is because; there is no high temperature area due to

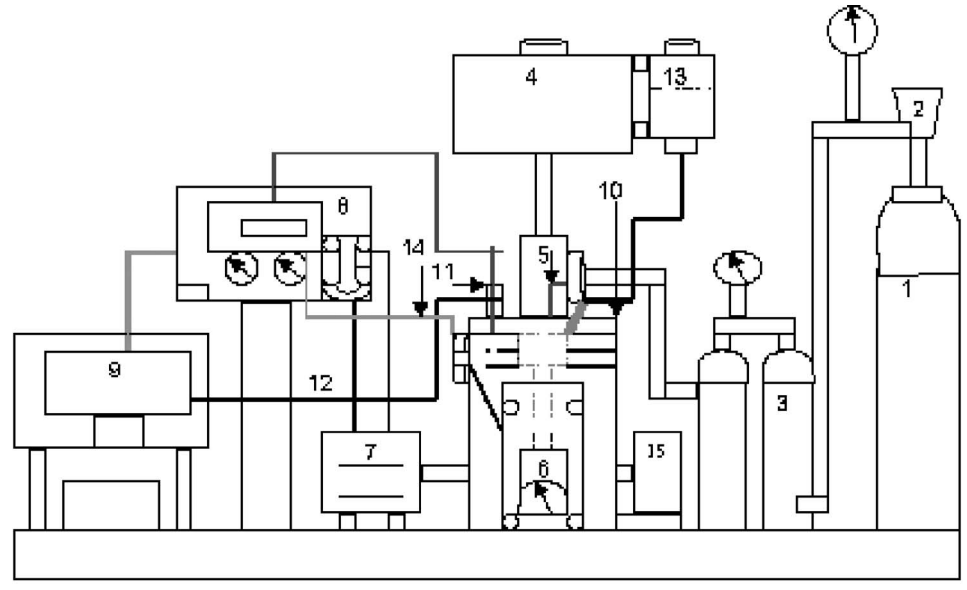

Fig. 12 Schematic representation of the experimental setup

well mixing of hydrogen, air, and diesel. Diesel, which is around 20% in the present case, as 80% is hydrogen substitution. Minimum NO_x can be observed if injected at 18 deg BTDC as shown in Fig. 10 hydrocarbons are exhausted because the combustion of diesel is incomplete (see Figs. 11 and 12).

Conclusions

The following conclusions can be drawn based on the experimental results and discussions (see Table 5).

- The brake thermal efficiency is increasing with the increased percentage of hydrogen and it is maximum with 100% hydrogen. For all the compression ratios it is found that in the beginning with low percentage of hydrogen and with low outputs, its value is low;
- hydrogen performed better at high compression ratios;
- the HC decreases drastically with the increasing percentage substitution of hydrogen and becomes zero at 100% hydrogen;
- the CO value continuously decreases with the increase in the percentage substitution of hydrogen for all compression ratios for 100% load;
- it is observed that as the percentage of hydrogen increases the NO_x level is also increasing. It is found to be higher with higher compression ratios and a higher percentage of hydrogen substitution;
- the particulate matter shows a drastic drop as the percentage of hydrogen increases;
- the cylinder pressure is maximum at the compression ratio of 24.5. When compared to diesel the rise of pressure per degree of crank angle is more. For the lower percentages of hydrogen and more percentages of diesel the pressure rise is lower at lower percentages of loads;
- the rate of heat release increases with hydrogen substitution at high outputs;
- peak pressures for the all the compression ratios were obtained at maximum hydrogen substitutions and at high outputs;
- increased intake temperature resulted in higher NO_x and faster burning rates. The rate of heat release and peak rate of heat release is advanced closer to TDC;
- there is a sharp increase in NO_x from 400 to 900 ppm when the temperature is increased from 65 to 85°C.

Acknowledgment

The authors sincerely acknowledge "*The All India Council for Technical Education" (AICTE)*, New Delhi, India for the Financial support in carrying out this research work.

References

[1] Yashuhiro, Kou, T., Yuki, Shigeki, N., Ryoji, K., and Takeshi, S., 1995, "Controlling Combustion and Exhaust Emissions in a Direct-Injection Diesel Engine Dual Fueled With Natural Gas," Paper No. SAE 952436.

[2] Karim, G. A., Liu, T., and Jones, W., 1993, "Exhaust Emissions From Dual Fuel Engines at Light Loads," Paper No. SAE 932822.

[3] Abd-Alla, G. H., Soliman, H. A., Badr, O. A., and Abd-Rabbo, M. F., 2000, Energy Convers. Manage., **41**, pp. 559–572.

[4] Singh, S., 2002, "The Effect of Fuel Injection Timing and Pilot Quantity on the Pollutant Emissions From a Pilot Ignited Natural Gas Engine," Masters thesis, The University of Alabama.

[5] Fraser, R. A., Siebers, D. L., and Edwards, C. F., 2003, "Auto-ignition of Methane and Natural Gas in a Simulated Diesel Environment," Paper No. SAE 2003-01-0755.

[6] Naber, J. D., Siebers, D. L., Caton, J. A., Westbrook, C. K., and Di Julio, S. S., 1994, "Natural Gas Auto Ignition under Diesel Condition: Experiments and Chemical Kinetics Modeling," Paper No. SAE 942034.

[7] Karim, G. A., 1983, "The Dual Fuel Engine of the Compression Ignition Type—Prospects, Problems and Solutions—A Review," Paper No. SAE 831073.

[8] Karim, G. A., Jones, W., and Rain, R. R., 1989, "An Examination of Ignition Delay Period in Dual Fuel Engines," Paper No. SAE 892140.

[9] Gunea, C., Razavi, M. R. M., and Karim, G. A., 1998, "The Effect of Pilot Fuel Quantity on Dual Fuel Engine Ignition Delay," Paper No. SAE 982453.

[10] Poonia, P. M., Ramesh, A., and Gaur, R. R., 1999, "Experimental Investigation of the Factors Effecting the Performance of a LPG-Diesel Dual Fuel Engine," SAE Journal of Fuels and Lubricants, Paper No. SAE 99-01-1123.

[11] Poonia, P. M., Ramesh, A., and Gaur, R. R., 1998, "The Effect of Air Temperature and Pilot Fuel Quantity on the Combustion Characteristics of a LPG-Diesel Dual Fuel Engine," Paper No. SAE 982455.

[12] Daisho, Y. et al., 1995, "Controlling Combustion and Exhaust Emissions in a Direct Injection Diesel Engine Dual—Fueled with Natural Gas," Paper No. SAE 952436.

[13] Ganesan, V., and Rames, A., 2002, "Experimental Investigation on LPG-Diesel Dual Engine," J. Inst. Eng. (India), Part AG, **83**, pp. 105–111.

G. P. McTaggart-Cowan[1]
e-mail: g.mctaggart-cowan@lboro.ac.uk

H. L. Jones

S. N. Rogak

W. K. Bushe

P. G. Hill

Department of Mechanical Engineering,
University of British Columbia,
2054-6250 Applied Science Lane,
Vancouver, B.C., V6T 1Z4, Canada

S. R. Munshi
Westport Innovations, Inc.,
1691 W. 75th Avenue,
Vancouver, B.C., V6P 6P2, Canada

The Effects of High-Pressure Injection on a Compression–Ignition, Direct Injection of Natural Gas Engine

This study investigated the effects of injection pressure on the performance and emissions of a pilot-ignited, late-cycle direct-injected natural gas fueled heavy-duty engine. The experiments, conducted on a single-cylinder engine, covered a wide range of engine speeds, loads, and exhaust gas recirculation fractions. The injection pressure was varied at each operating condition while all other parameters were held constant. At high loads, increasing the injection pressure substantially reduced particulate matter and CO *emissions, with small increases in* NO_x *and no significant effect on hydrocarbon emissions or fuel consumption. At low loads, injection pressure had no significant impact on either emissions or performance. At high loads, higher injection pressures consistently reduced both the number density and the size of particles in the exhaust stream. Injection pressure had reduced effects at increased engine speeds.* [DOI: 10.1115/1.2432894]

Keywords: alternative fuels, natural gas, direct injection, diesel pilot ignition, injection pressure

Introduction

Diesel engines, while efficient and reliable, emit significant quantities of oxides of nitrogen (NO_x) and fine particulate matter (PM). NO_x is a key component in the formation of photochemical smog [1], while PM emissions have been linked to increased cardiovascular mortality rates, impaired lung development in children, and a host of other health impacts [2,3]. As a result, environmental regulatory bodies have legislated substantial reductions in PM and NO_x emissions from heavy-duty on-road diesel engines in the 2007–2010 timeframe [4].

Techniques for diesel engines to meet the upcoming emissions regulations include exhaust gas recirculation (EGR), pulsed injections, increased injection pressures, and post-exhaust aftertreatment. Shifting from diesel fuel to natural gas can also achieve substantial emissions reductions [5,6]. One option currently under development is to retain the late-cycle direct-injection process, but to replace the bulk of the diesel fuel with direct-injected natural gas; a diesel pilot injection is retained to initiate the combustion. This technique reduces NO_x and PM emissions with no penalty in efficiency [5]. One option to achieve further PM emission reductions from natural-gas direct injection engines is, as for diesel engines, to increase the injection pressure. The current work studies the effects of injection pressure over the widest accessible range of engine operating conditions, investigates the primary factors by which injection pressure influences harmful emissions, and identifies its role in changing PM size distributions.

Injection Pressure Effects

Numerous studies report the effects of increasing the injection pressure on diesel engine performance and emissions. In general, higher injection pressures significantly reduce PM emissions; this is often attributed to improved atomization and enhanced air entrainment, resulting in a leaner mixture in the spray core and hence lower soot formation [7–9]. Conversely, in-cylinder studies suggest that soot formation is actually enhanced by the more rapid evaporation of the fuel, but that improved mixing also increases soot oxidation rates, resulting in a net reduction in the engine-out soot [10,11]. Higher injection pressures reduce the size of the emitted particles, with significant reductions in the number of accumulation-mode particles (particle aerodynamic diameter, $D_p > 50$ nm). However, at some midload conditions, nucleation-mode ($D_p < 50$ nm) particle numbers increase substantially [9]. The effects of injection pressure on particle size distributions decrease at higher engine speeds [12].

Injection pressure also affects NO_x emissions, with some researchers demonstrating increases by as much as a factor of three at some operating conditions [8,11]. Other studies suggest that at high EGR fractions, NO_x is relatively insensitive to injection pressure [13]. One confounding effect in most studies is that the timing of the injection process is fixed: hence, as increased injection pressures often reduce the ignition delay, the combustion occurs earlier in the cycle. Thus, the effects of injection pressure cannot be decoupled from those of combustion timing, a factor which strongly influences NO_x emissions [14].

The primary effect of increasing the injection pressure on the diesel ignition process is to reduce the physical delay (the time required for the droplets to evaporate and mix to a combustible stoichiometry). Chemical effects, relating to the break-up of long-chain hydrocarbons and the formation of radicals in the precombustion reactions, are typically not as significantly affected by injection pressure [8,11,15].

Direct Injection of Natural Gas Combustion

For a pilot-ignited, direct-injected natural gas engine, increasing injection pressure will likely influence the pilot combustion similarly to that of a diesel engine. Specifically, the atomized liquid spray must evaporate, during which it entrains air, a process which is sensitive to injection pressure. Conversely, for the burning gaseous jet, there will be little air entrainment into the core of the jet, and the effect of injection pressure will most likely be substantially less. Furthermore, the fraction of the fuel that burns

[1]Corresponding author.

Contributed by the Internal Combustion Engine Division of ASME for publication in the JOURNAL OF ENGINEERING FOR GAS TURBINES AND POWER. Manuscript received September 28, 2005; final manuscript received September 28, 2006. Review conducted by Margaret Wooldridge.

Table 1 Research engine and injector specifications

Engine	Single cylinder four-stroke
Fueling	Direct injection natural gas with diesel pilot
Displacement	2.5 L
Compression ratio	19:1
Bore/Stroke/Connecting rod length	137/169/261 mm
Injector	Westport Innovations Inc. dual-fuel concentric needle prototype
Injection control	Separate diesel and CNG solenoids
Injector holes	Seven pilot, nine gas
Injection angle	18 deg below firedeck

in a purely non-premixed combustion event may be very different from that of an equivalent diesel combustion process. These and other fundamental physical and chemical differences between a liquid diesel spray and an underexpanded gaseous jet could well lead to substantially different influences of injection pressure on combustion performance and emissions.

The fundamental impacts of injection pressure on gaseous jets under engine-like conditions have been studied by Rubas et al. [16] and Hill and Ouellette [17]. Increasing the injection pressure increases the jet penetration, but proportional to only the $\frac{1}{4}$ power of density (that is, doubling the density of the jet will only increase the penetration by 20%) [17]. Increased injection pressures will also tend to increase the turbulent motion inside the combustion chamber. Studies of an auto-igniting natural gas jet indicate that, similar to diesels, higher injection pressures reduce ignition delay times by enhancing mixing [18].

In conjunction with other combustion modifications, increasing the injection pressure can improve the performance of direct-injection natural gas engines [5,19]. These previous studies did not attempt to identify systematically the influence of injection pressure independent of other parameters. Preliminary studies show that at a midspeed, midload operating condition, increasing the injection pressure reduces PM emissions with little effect on other engine performance measures [20]. However, the effects of injection pressure may vary substantially with in-cylinder conditions; as a result, assessment of these effects over the full engine operating range is required.

Experimental Apparatus

This study used a Cummins ISX series heavy-duty six-cylinder, four-stroke, direct-injection diesel engine modified to operate on only one cylinder. The operating combustion chamber geometry was unmodified from that of the stock diesel engine. The engine was equipped with a Westport Innovations Inc. prototype fuelling system. In this system, the auto-ignition of a small quantity of diesel pilot fuel, injected into the combustion chamber shortly before the natural gas (typically, 5–15 deg crank angle (CA) before top-dead center), initiates the combustion. The burning diesel then ignites the natural gas. The natural gas used in these tests contained predominantly methane ($CH_4 \sim 96$ mol %) with small amounts of ethane ($C_2H_6 \sim 2$ mol %) as well as N_2, CO_2, and propane (all <0.5 mol %). The pilot fuel was low-sulfur (<500 ppm) road grade diesel that met Canadian General Standards Board specification CAN/CGSB-3.520.

The SCRE facility has previously been described and characterized [21]. The base (six-cylinder) engine has a rated power of 300 kW and a rated torque of 1966 N m, with a maximum speed of 1800 rpm. Table 1 provides specific details of the modified single-cylinder engine. An independent compressor with dryer and filters supplies clean, dry (dew point $-40\,^{\circ}C$) combustion air. The exhaust line pressure is maintained approximately 10 kPa above the intake pressure to drive exhaust gas through a high-pressure EGR system equipped with an EGR cooler.

The fueling system provides natural gas and diesel to the engine's internal common fuel rails at pressures up to 31 MPa. Pressures in the fuel rail are controlled to within 0.1 MPa and the measured amplitude of fluctuation in the rails is less than 3%. The dual-fuel injector uses concentric needles, with separate solenoids to control the timing and duration of the diesel and natural gas injection processes. This allows independent control of the fuel flow, combustion timing, and injection pressure.

A coriolis type flowmeter measures the natural gas flow, while a gravimetric system measures the liquid pilot flow. A subsonic venturi measures the supply rate of fresh air to the engine. A flush-mounted water-cooled piezo-electric pressure transducer measures cylinder pressure, while an optical shaft encoder ($\frac{1}{2}$ deg CA resolution) provides the corresponding CA. A raw emissions bench, equipped with infrared analyzers (CO_2, CO, CH_4), a flame ionization detector (HC), and a chemiluminescent analyzer (NO_x) measures the gaseous emissions. A second infrared analyzer measures the CO_2 concentration in the intake stream, from which the EGR fraction is determined.

Particulate Measurements. Particulate measurements are carried out using a microdilution system where dry nitrogen is used to dilute a sample drawn from the exhaust stream at volume ratios of $\sim$15:1 (further information is provided in Jones et al. [22]). The dilution ratio is calculated from measurements of the CO_2 concentration in the raw exhaust and in the diluted stream. A tapered element oscillating microbalance (TEOM) (Rupprecht and Patashnick Model 1105) measures total particulate mass, including solid carbon and condensed volatile species. Previous work shows that the TEOM is sensitive to sample humidity and filter face temperature [23,24]. By maintaining high filter face temperatures ($50\pm2\,^{\circ}C$), a constant dilution ratio, and sufficient stabilization time, the effects of water content on the TEOM are minimised. The TEOM measurements correlate strongly with gravimetric filter samples (probability of association using chi-squared analysis $>99.9\%$) [25].

A TSI Model 3936 scanning mobility particle sizer (SMPS) provides particle size distributions. The SMPS is composed of a differential mobility analyzer (DMA) (TSI Model 3085) and a condensation particle counter (CPC) (TSI Model 3022A). The fundamental operation of the DMA is described elsewhere [26]. The unit used in this work measures particles between 5 nm and 160 nm in mobility diameter; an impactor with a cut diameter of 615 nm excludes significantly larger particles. To avoid saturating the CPC, a filtered recirculation system provides secondary dilution of the sample fed to the SMPS at a volume ratio of 14:1.

Experimental Parameters. Due to the SCRE's high internal friction, brake-performance parameters (which are often negative) are not representative of the in-cylinder conditions. As a result, the engine's operation is represented on the basis of the gross-indicated power—the integral of the in-cylinder pressure versus volume curve over the compression and power strokes only, as defined in Heywood [27]. This parameter is also used to normalize the emissions and fuel consumption. The indicated power, normalized by engine speed and displaced volume, provides the gross-indicated mean effective pressure (GIMEP), which is representative of the load. The gross-indicated specific fuel consumption (GISFC) represents the total fuel mass flow, with the natural gas component included as an energy-equivalent mass of diesel. Differentiating the in-cylinder pressure trace estimates the net heat-release rate (HRR), the rate of energy release from the combustion processes less wall heat transfer and crevice flow losses. By integrating the HRR up to a given crank angle and normalizing by the total energy released over the full cycle, the fraction of the energy released up to that point can be determined. The midpoint of this curve (50% of the integrated heat release—50% IHR) defines the combustion timing.

Other parameters relevant for control of the single-cylinder en-

Table 2 Engine operating condition definitions

ID	Speed (rpm)	GIMEP (bar)	Load (% of max.)	ϕ	Y_{intO2}	P_{inj} (MPA)	Pilot (%)
1	800	3	10	0.3	0.23,0.19	21,30	11
2	800	8.5	40	0.45	0.23,0.19	21,30	6
3	800	13.5	70	0.6	0.23,0.19	21,30	3
4	1200	8.5	40	0.45	0.23,0.19	21,30	6
5	1200	13.5	70	0.6	0.23,0.19	21,30	3
6	1500	13.5	70	0.6	0.23,0.19	21,30	3

gine include the oxygen-based equivalence ratio (ϕ=ratio of actual to stoichiometric fuel/oxidizer ratio) and the intake oxygen mass fraction (Y_{intO2}-the dilution of the charge), which is 0.23 for undiluted air and decreases with increasing dilution (increasing EGR). Defining ϕ, Y_{intO2}, 50%IHR, GIMEP, and engine speed fully constrains the engine's operating condition. A comprehensive discussion of appropriate operating condition definitions for an EGR-equipped nonstoichiometric engine is available in the literature [28].

Experimental Methodology. This study investigated the effects of injection pressure over the full range of engine operating conditions accessible to the single-cylinder test facility (Table 2). Parameters held constant included the combustion timing (50% IHR at 10 deg after top-dead-center (ATDC)), the separation time between pilot and gas injections (1.0 ms), and the pilot quantity (5 mg/injection). The constant pilot quantity resulted in a change in the pilot fraction (on an energy basis) from 11% at low load to 3% at high load. The selected combustion timing provided a reasonable tradeoff between NO_x emissions and efficiency based on previous results, and is similar to the timings used in conventional multicylinder engines [20]. Statistical assessment of the results used an analysis of variance (ANOVA), whose main role was to identify which of the principal effects and interactions were significant.

To facilitate the statistical analysis, the test plan was based on a completely randomized full-factorial experimental design, with two replications per test point. This resulted in eight data points per operating condition and a total test matrix of 48 points. To avoid high-order interactions between engine speed and load, two separate ANOVAs were executed, one for the three conditions where load was constant (3, 5, and 6) and one where speed was constant (1, 2, and 3). Thus, these analyses will identify the effect of speed and load (both in combination with injection pressure and EGR) independently. In carrying out the analysis, an α level of 0.05 (a 1 in 20 chance of identifying a significant effect when one is not present) was used. Further details on the model development can be found elsewhere [25]; for further information on statistical analysis and design of experiments, the reader is referred to one of a number of excellent textbooks on the subject (e.g., Ref. [29]).

A further test set was carried out at the peak-torque condition (point No. 5 in Table 2), at both intake oxygen mass fractions. For this case, the injection pressure was varied over a wider range (four values, from 18 MPa to 30 MPa) to provide improved experimental resolution. Tests were conducted with both diluted (EGR) and fresh charge; for the diluted case, the combustion timing was retarded (from 10 deg to 17.5 deg ATDC) to investigate the effect of injection pressure on the late-stage combustion process.

Results

Previous work indicates that the various engine operating condition parameters interact significantly and in a nonlinear fashion [28]. Therefore, any analysis that includes multiple operating condition parameters will routinely exhibit third-order and higher interactions, making statistical interpretation of the results difficult. In this work, the primary interest in the effects of operating condition is how they relate to the influence of variations in injection pressure. As a result, the effects of injection pressure are analyzed as a function of speed and load independently. The ANOVA results indicate which effects are statistically significant; graphical presentation of the results provides further information on the directions and magnitudes of the identified influences.

Statistical Results. Table 3 shows the ANOVA results for the effect of injection pressure at various loads (at constant speed); significant associations, defined as a P value of <0.05 (the probability of the factor not having a significant effect on the measured parameter being less than 5%) are shown in bold font. The results indicate that for most emissions, load interacts significantly with both the injection pressure and the intake oxygen mass fraction. (Recall that an interaction term indicates that the response of the dependent variable to one independent variable varies for different levels of a second independent variable: i.e., if dependent variable C responds differently to a change in parameter A at different levels of parameter B, then there is an interaction effect between A and B on C.) If the results include significant second-order interaction terms, the lower-order terms (main effects) may not be

Table 3 Effects of injection pressure ANOVA at 800 rpm

		P value					
Term	DOF[b]	GISFC	CO	NO_x	HC	PM	Comb. dur.
Load	2	**0**	**0**	**0.008**	**0**	**0**	**0**
Y_{intO2}	1	0.159	**0**	**0**	**0**	**0**	**0.049**
P_{inj}	1	0.863	**0**	**0.002**	0.064	**0**	**0**
Load[a] Y_{intO2}	2	0.062	**0**	**0.002**	**0**	**0**	**0**
Load[a] P_{inj}	2	0.17	**0**	0.033	0.134	**0**	0.135
Y_{intO2}[a] P_{inj}	1	0.24	0.091	0.066	0.3	0.062	0.055
Load[a] Y_{intO2}[a] P_{inj}	2	0.346	0.332	0.746	0.933	**0.021**	0.49
Experimental error	23						

[a]Interaction between parameters.
[b]DOF (degrees of freedom): the number of unconstrained variables used in calculating the parameter effects.

Table 4 Effects of injection pressure ANOVA at 13.5 bar GIMEP

Term	DOF	*P* value					
		GISFC	CO	NO_x	HC	PM	Comb. fur.
Speed	2	**0**	**0**	**0**	**0**	**0.031**	**0**
Y_{intO2}	1	**0.041**	**0**	**0**	**0**	**0**	**0.001**
P_{inj}	1	0.766	**0.004**	0.845	0.382	**0.043**	**0**
Speed[a] Y_{intO2}	2	0.143	**0.027**	**0.001**	**0**	0.228	0.972
Speed[a] P_{inj}	2	0.172	**0**	0.253	**0.011**	0.08	**0.002**
Y_{intO2}[a] P_{inj}	1	0.073	0.169	0.84	0.398	0.49	0.204
Speed[a] Y_{intO2}[a] P_{inj}	2	0.693	**0.019**	0.344	**0.003**	0.252	0.067
Experimental error	23						

[a]Interaction between parameters.

accurately represented by the ANOVA [29].

Salient results from the ANOVA at fixed speed include that the GISFC is independent of injection pressure. The CO and NO_x emissions display significant second-order interactions between injection pressure and load, indicating that the influence of injection pressure varies with load. The HC emissions (>95% unburned CH_4) show no interactions with injection pressure, suggesting that the effects of injection pressure on HC emissions do not vary significantly with either load or intake dilution. The PM emissions show a third-order interaction between load, injection pressure, and intake oxygen mass fraction; this suggests that the effects of injection pressure vary with the levels of both load and intake dilution.

Table 4 shows the results of the ANOVA conducted for the three speeds at high load. Important effects identified include that injection pressure does not have a consistent influence on either the GISFC or the NO_x emissions at high load. The effects of injection pressure on combustion duration vary with speed, while the effects on CO and HC emissions vary with both engine speed and intake dilution. The PM emissions depend on injection pressure, speed, and intake dilution independently (main effects); there are no significant interactions. This indicates that at high load, the effects of injection pressure on PM are consistent and statistically significant at all the conditions evaluated. In general, the ANOVA results demonstrate that the influences of injection pressure tend to depend on the engine's speed and load, but not as frequently on the intake dilution level. The presence of second-order interactions limits the evaluation of the significance of the main effects. To develop further insight into the effects of injection pressure requires graphical interpretation.

Effects of Operating Condition. As shown in the preceding statistical analyses, the influence of injection pressure on emissions depends strongly on operating condition. The results are presented graphically (Figs. 1–5) with each dependent parameter plotted individually; each plot includes all six speed/load operating conditions. For a given operating condition, the individual bars represent the low and high injection pressure cases, with and without intake dilution (EGR). The values shown are averages of the two values collected for each test point. Table 5 provides a tabular representation of the results, including the pressure ratio between the injection pressure and the peak cylinder pressure (P_{inj}/P_{cylmax}) for each condition. This pressure differential indicates that for the low-load cases, the pressure ratio is as much as five times greater than the cylinder pressure; however, at the high-speed, high-load, low injection pressure condition, the injection pressure is only 30% higher than the peak cylinder pressure. As will be discussed later, this has a substantial influence on the effects of injection pressure at different operating conditions.

Figure 1 demonstrates the statistically insignificant effect of injection pressure on GISFC. Of the other parameters, load has the largest influence on GISFC, with optimum efficiency at the mid-load cases. The influence of injection pressure on NO_x emissions (at constant 50%IHR timing, Fig. 2) varies in a statistically sig-

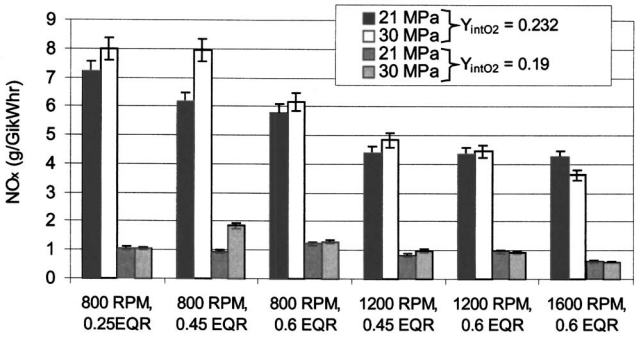

Fig. 2 Injection pressure and operating condition influences on NO_x emissions (g/GikWhr)

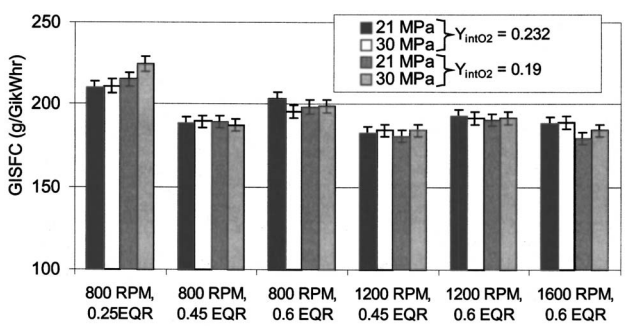

Fig. 1 Injection pressure and operating condition influences on GISFC (g/GikWhr)

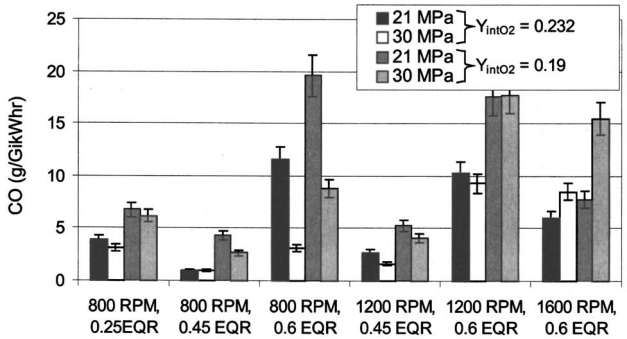

Fig. 3 Injection pressure and operating condition influences on CO emissions (g/GikWhr)

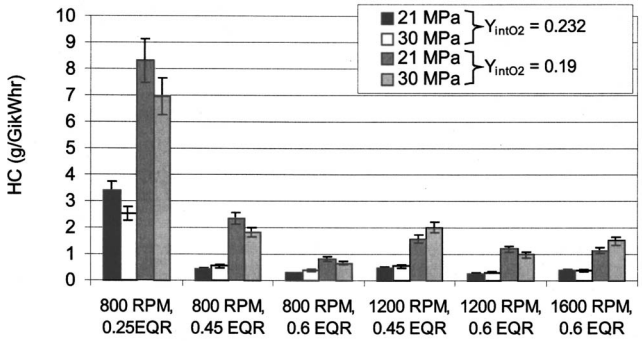

Fig. 4 Injection pressure and operating condition influences on HC emissions (g/GikWhr)

nificant manner (Tables 3 and 4) with operating condition. Higher injection pressures appear to increase NO_x without intake dilution (except at 1600 rpm); however, as Table 4 showed, this result was not consistent or statistically significant over the range of engine speeds investigated. With intake dilution (EGR), the NO_x results show no consistent dependence on injection pressure; only at the midload (0.45ϕ, at both 800 and 1200 rpm) do higher injection pressures significantly increase NO_x emissions. The particularly large increase at 800 rpm was due to test condition repeatability, where both low-injection pressure cases had, by chance, intake oxygen mass fractions of approximately 0.185, compared to 0.191 for the high injection pressure cases. The extreme sensitivity of

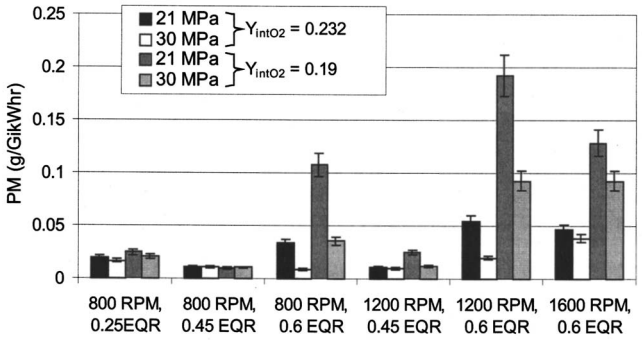

Fig. 5 Injection pressure and operating condition influences on PM emissions (g/GikWhr)

NO_x to intake dilution has previously been demonstrated [28]. This was the only condition where the difference in intake oxygen concentration was greater than 0.003; as a result, this effect should not have influenced the accuracy of the results at any of the other conditions.

The statistical results (Tables 3 and 4) indicate that the effects of injection pressure on CO emissions vary significantly with operating condition (speed, load, and intake dilution). Figure 3 demonstrates these complex interactions; in general, the CO emissions are greatest at the highest loads, while intake dilution doubles the CO emissions at almost all the operating conditions. At low speed (and midspeed midload) higher injection pressures tend to reduce CO emissions. However, at high load at intermediate speed, the CO emissions are relatively unchanged by higher injection pressure, while at high speed the CO emissions are significantly increased. This nonlinear behavior of CO with injection pressure may be due to the competing influences of enhanced mixing and increased turbulent shear stresses as the injection pressure increases, as will be discussed later.

Similar to the CO emissions response, the effects of injection pressure on HC emissions (Fig. 4), vary with operating condition. At all the conditions, the HC emissions are primarily methane, indicating that unburned gaseous fuel is the principal source of this pollutant. Hydrocarbon emissions are, on a power-specific basis, highest at low load. This may be at least partially a result of unburned fuel from fixed-volume sources such as the nozzle sac; the amount of fuel which is retained during the combustion event, and is then released late in the combustion cycle, will be essentially constant on a per-cycle basis, leading to higher power-specific emissions at low-power levels. Other factors, including increased turbulent strain leading to more local extinction events may also be contributing to the HC emissions. The variability in the HC emissions with operating condition demonstrates the complex interactions between these various potential mechanisms. At all the operating conditions, the effects of injection pressure on HC emissions were secondary to the influences of operating condition and intake dilution.

Injection pressure has a strong and relatively consistent influence on PM emissions, as shown in Fig. 5. The PM emissions are also affected by intake dilution and load, as demonstrated in Table 3. At low and midload, PM emissions are relatively insensitive to intake dilution or injection pressure. At high load, increasing the injection pressure reduces PM emissions by a factor of almost three both with and without intake dilution. In general, at low-load PM emissions are relatively low, and increases in intake dilution do not substantially increase them. PM emissions at these loads

Table 5 Summary of data from operating condition tests

Operating condition		800 rpm 2.5 bar		800 rpm 8.5 bar		800 rpm 13.5 bar		1200 rpm 8.5 bar		1200 rpm 13.5 bar		1600 rpm 13.5 bar	
Parameter	P_{inj} Y_{intO2}	21	30	21	30	21	30	21	30	21	30	21	30
GISFC	0.23	210	210	188	189	203	196	183	184	193	192	189	189
(g/GikWhr)	0.19	215	224	189	187	199	199	181	184	191	191	180	184
NO_x	0.23	7.2	8	6.2	7.9	5.8	6.1	4.4	4.8	4.3	4.4	4.3	3.6
(g/GikWhr)	0.19	1.1	1.1	0.94	1.9	1.2	1.3	0.83	1	0.96	0.93	0.62	0.6
CO	0.23	3.9	3.1	0.96	0.97	11.6	3.1	2.7	1.6	10.3	9.3	6	8.5
(g/GikWhr)	0.19	6.7	6.2	4.2	2.6	19.6	8.8	5.3	4.1	17.6	17.7	7.8	15.5
HC	0.23	3.4	2.5	0.43	0.55	0.3	0.4	0.46	0.55	0.28	0.32	0.38	0.4
(g/GikWhr)	0.19	8.3	6.9	2.34	1.82	0.82	0.67	1.58	2.01	1.2	0.98	1.14	1.5
PM*100	0.23	2	1.7	1.1	1.1	3.4	0.84	1.1	1	5.4	2	4.6	3.8
(g/GikWhr)	0.19	2.5	2.1	1	1	10.8	3.5	2.5	1.2	19.2	9.3	12.9	9.3
Comb. Dur.	0.23	5	4.7	15.5	11	24.5	19.8	24.3	22.3	31	27.3	38	31.8
(°C A)	0.19	8	7	11.5	10	22.3	18	22	18	28.5	25.3	38.5	27.3
P_{inj}/P_{max}	0.23	3.3	4.8	2.1	2.7	1.5	2.2	2.1	3	1.5	2.2	1.5	2.1
	0.19	2.8	3.9	1.8	2.4	1.4	1.9	1.9	2.7	1.4	2	1.3	1.9

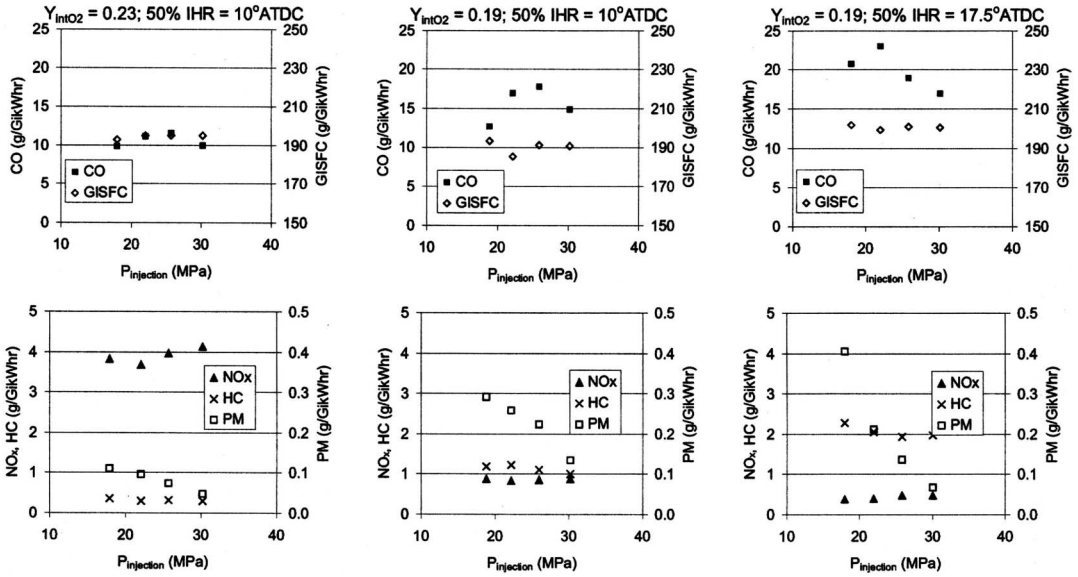

Fig. 6 Effect of injection pressure at a single operating condition (1200 rpm, 13.5 bar GIMEP, ϕ 0.6)

have previously been attributed to volatiles originating from the lubricating oil or the diesel pilot [22]. At higher load conditions and with intake dilution, the carbonaceous component of the PM, which originates mainly from the natural gas, is significantly greater. This suggests that increases in the injection pressure are significantly reducing PM formation in the natural gas flame. Differentiating the effects of increased in-cylinder turbulence due to the higher injection pressure from the effects on the gas jet dynamics is an area of ongoing research.

Injection Pressure Details. In the preceding section, a range of operating conditions was investigated at only two injection pressures (21 and 30 MPa). As such, any nonlinear effects of injection pressure would not have been identified. As discussed previously, a more detailed study was also carried out at the midspeed high-load operating condition (test condition No. 5 in Table 2). In conducting the tests, variations in the operating condition were minimized by restricting the randomization of the tests. Due to this restriction, the results were not statistically analyzable.

In general, the trends in emissions and performance for the three conditions, shown in Fig. 6, are comparable to those in the earlier tests. For all three cases, increased injection pressure reduces PM emissions in a generally linear manner; in all cases, the reduction between the lowest and highest pressures is approximately 50%. Increased injection pressure results in a relatively small increase in NO_x and a correspondingly small reduction in HC. There is no consistent trend in GISFC with injection pressure. The CO emissions, however, respond in a nonlinear manner to injection pressure; at all three conditions, CO is maximized between 22 and 26 MPa injection pressure. This may explain the varying influence of injection pressure on CO emissions (Fig. 3), as at different operating conditions the location of the peak CO emissions levels varies substantially. At 1600 rpm, the peak may be shifted toward higher injection pressures, resulting in the observed increase between 21 and 30 MPa. This is most likely due to changes in in-cylinder turbulence intensity, as well as the increased overall combustion duration (in degrees CA) for the higher speed condition.

Although the nonrandomness of the test plan means that comparisons between operating conditions are not reliable, it would appear that in general the trends in emissions and performance are consistent at the different conditions. This indicates that the effects of injection pressure, at this high-load condition, are relatively independent of intake dilution and combustion timing. However, the specific levels of the emissions vary substantially between the operating conditions tested.

In-Cylinder Performance. Higher injection pressures reduce the combustion duration (from 5% to 95% of the integrated HRR) (Fig. 7). The fact that the rate at which the fuel is introduced into the combustion chamber has a significant impact on the combustion duration indicates that the overall duration of the combustion process is at least partially controlled by the mixing rate. As such, any method which increases the injection rate will tend to reduce the combustion duration.

The in-cylinder pressure trace and HRR provide further insight into the combustion event; Fig. 8 shows these for the low-load, low-speed condition (Table 2, point No. 1). At this condition, both with and without dilution, the influence of injection pressure is relatively minor. The greatest difference is a shorter delay between diesel start-of-combustion (first peak on the HRR plot around 0 deg CA for all conditions) and the main combustion event. This shorter delay (approximately 1 deg CA in both cases) may contribute to the observed reductions in HC emissions. Higher injection pressures slightly increase the peak HRR in both cases; this results in a slightly shorter overall combustion. Figure 9 shows a similar set of plots for the midspeed, high-load condition. Increasing the injection pressure substantially increases the combustion

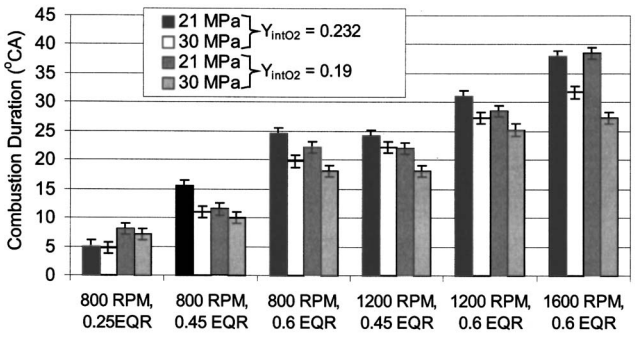

Fig. 7 Injection pressure and operating condition influences on combustion duration (degree CA)

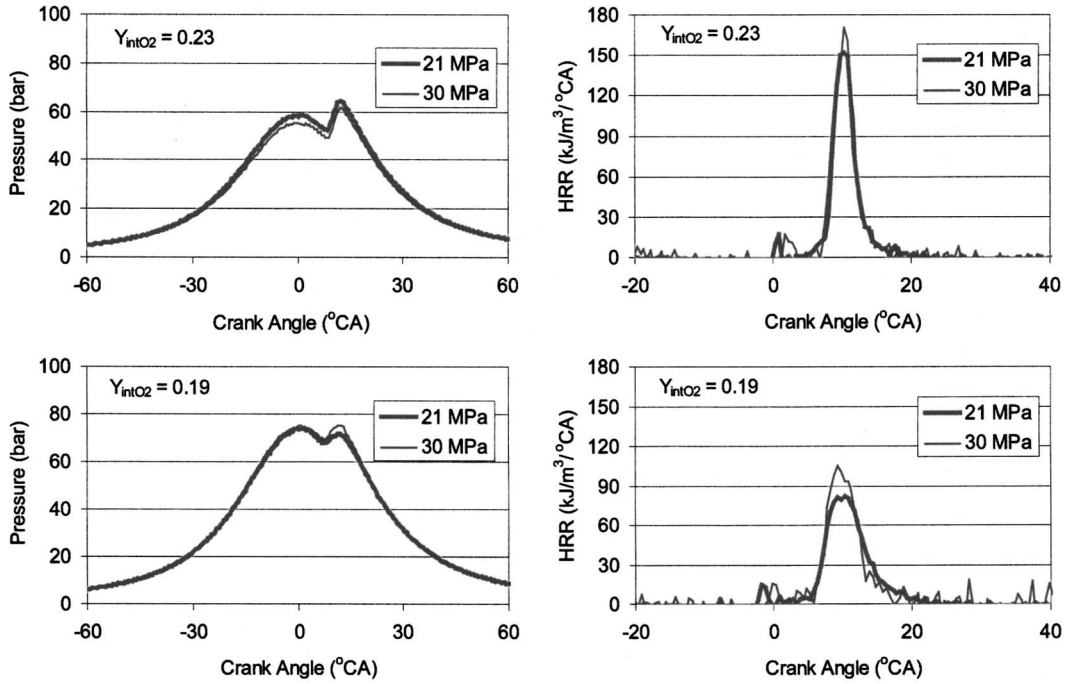

Fig. 8 Effect of injection pressure on cylinder pressure (left) and heat-release rate (right) at 800 rpm, 3 bar GIMEP, ϕ 0.25

rate, with and without intake dilution. The main-fuel combustion starts significantly (approximately 2 deg CA) earlier for the lower injection pressure, but the late-phase combustion processes (after 15 deg CA) are virtually indistinguishable. These effects are due to the more rapid injection of fuel, resulting in a greater fraction of the fuel having mixed to a combustible level before ignition occurs. The fact that the effects of injection pressure are more significant at high load is due to the relatively small differential pressure between the fuel rail and the combustion chamber (Table 5). The increase in injection pressure has a relatively larger effect than it does at low load, where the differential pressure is already very high.

Effect on Particle Size Distributions. The particle size distri-

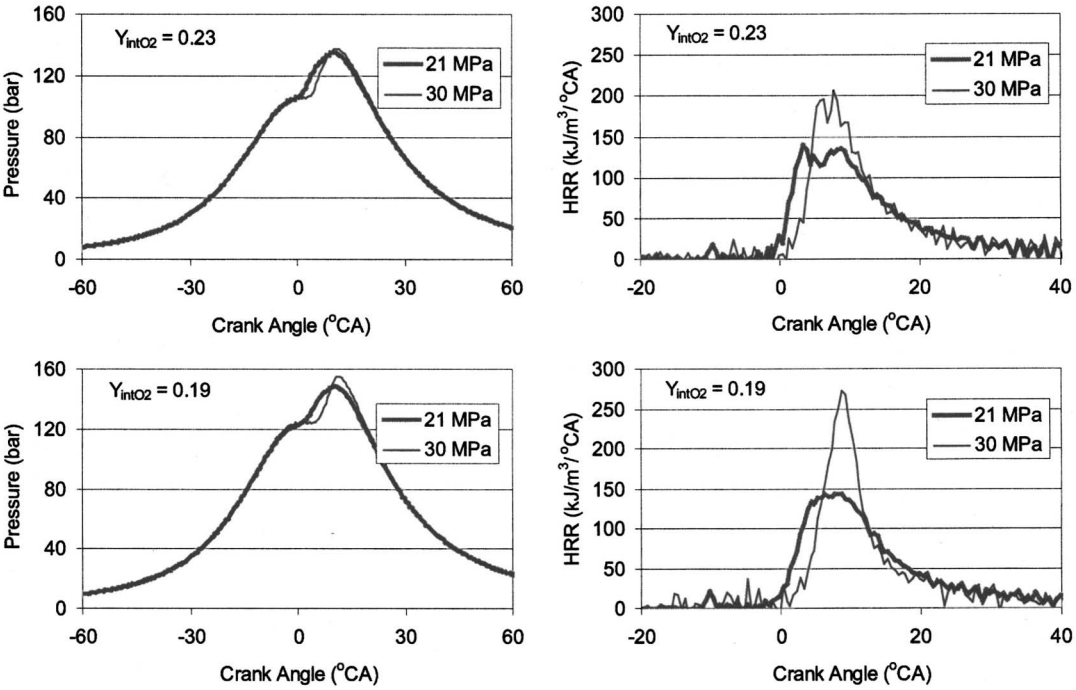

Fig. 9 Effect of injection pressure on cylinder pressure (left) and heat-release rate (right) at 1200 rpm, 13.5 bar GIMEP, ϕ 0.6

butions at the low-speed, low-load condition are shown in Fig. 10. (Note that the distributions are adjusted for dilution ratio, such that they represent the number concentration per unit volume of raw exhaust.) Both with and without intake dilution, the injection pressure has very little influence on the number distribution. In both cases, there is a discernable "nucleation mode" ($D_p < 50$ nm) peak, although with intake dilution, the "accumulation mode" ($D_p > 50$ nm) peak is larger. For diesel engines, the nucleation mode particles are thought to be primarily condensed liquid droplets, comprised of sulfuric acid, water, and volatile hydrocarbons that have nucleated in the exhaust stream [30]. Diesel-engine researchers report that the mode of the nucleation peak occurs at particle diameters of approximately 10 nm [31], which is similar to the mode of the peak shown in Fig. 10. This suggests that the bulk of the particulate emissions at this condition are composed of volatile species which are unaffected by changes in injection pressure.

Increasing the load at the same speed (point No. 3 in Table 2) significantly affects the particle size distribution (Fig. 11), with a unimodal distribution with no indication of a nucleation-mode peak. This suggests that engine-out particles are making a greater contribution to the total emissions, as these particles tend to be larger due to longer residence times and higher concentrations in the predilution exhaust system; this results in greater particulate agglomeration. At the same time, any volatiles in the exhaust will tend to condense onto these particles rather than forming new nucleation mode particles. Higher injection pressures reduce both the number and the mode diameter of these particles, both with and without EGR. The number concentration of particles less than ~25 nm in mobility diameter is as much as an order of magnitude lower at higher injection pressures. The fact that the particles are both smaller and fewer in number suggests that the higher injection pressure is leaving less time for particulate inception to occur. This is consistent with higher fuel-air mixing rates, resulting in a shorter residence time for the particle precursors to nucleate in the high-temperature fuel-rich region of the combustion zone.

The size distributions for the high-speed, high-load case (Fig. 12, point No. 6 in Table 2) indicate a relatively small effect of injection pressure, compared to lower speed conditions. This coincides with the relatively smaller influence on total PM mass shown in Fig. 5, and agrees with results from diesel-fueled engine research [12]. This provides further evidence that the injection pressure is having less of an effect on improving the turbulent mixing process at higher speeds.

Discussion

In general, the effects of injection pressure on the natural gas combustion system are qualitatively similar to those observed in diesel engines, including reduced ignition delay times, reduced particulate matter emissions, and higher NO_x emissions (without intake dilution). Conversely, some diesel engine results suggest that significant increases in total particle number occur with higher injection pressures at certain conditions; no such results are observed with natural gas combustion. There are most likely other significant differences between natural gas and diesel combustion. However, without conducting identical tests on the same engine with diesel fueling, it is not possible to provide more than broad generalities on the apparent similarities in the influence of injection pressure on the two different combustion systems.

The results show that the injection pressure has a significant influence on emissions, but little impact on efficiency, of a pilot-ignited direct-injection of natural gas engine. The effect varies with engine speed and load due to changes in the in-cylinder conditions. At low speed, the in-cylinder turbulence will be at its lowest levels, while as the speed increases, in-cylinder turbulence induced by charge induction and piston motion increases. As such, the effects of higher injection pressures enhancing in-cylinder turbulence could be most significant at low speed; as speed increases, the relative importance of the charge-induced motion becomes larger. This is the most likely explanation for the significant variations in the effects of injection pressure on CO and NO_x as a function of speed. Furthermore, the increased turbulence induced by higher injection pressures appears to be more significant at high load (where the reduction in PM is very substantial) than at lower loads. The most likely reason for this is that the 21 MPa injection pressure is already substantially higher than the in-cylinder pressure at low load (as demonstrated by the differential pressure in Table 5); this provides sufficient turbulence for the combustion to complete rapidly. Hence, turbulent mixing does not appear to be the limiting factor for the combustion event at low-load conditions, with and without EGR, at constant oxygen equivalence ratio. From the particulate size distributions, it appears that at low-load conditions nucleation of volatile hydrocarbons or sulphates is a significant contributor to the PM loading.

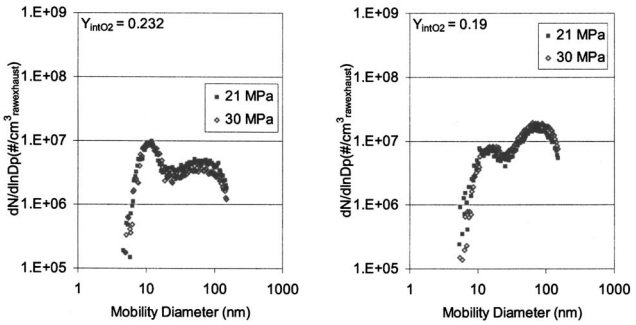

Fig. 10 Effect of injection pressure on particle size distributions, at 800 rpm, 3 bar GIMEP, ϕ 0.25

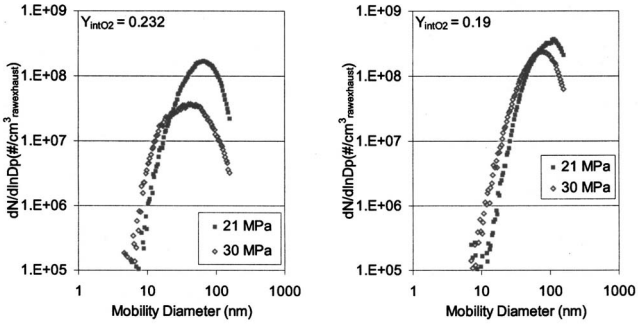

Fig. 11 Effect of injection pressure on particle size distributions, at 800 rpm, 13.5 bar GIMEP, ϕ 0.6

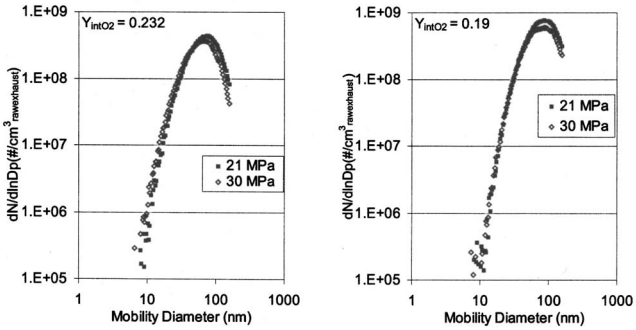

Fig. 12 Effect of injection pressure on particle size distributions, at 1600 rpm, 13.5 bar GIMEP, ϕ 0.6

The fact that injection pressure does not influence the size distribution suggests that it also has little influence on volatile emissions.

At higher loads, the effect of injection pressure is more significant, as the in-cylinder pressure is higher; this results in a larger relative change in the fuel-combustion chamber differential pressure over the same range of injection pressures. The higher injection pressure tends to increase the density gradient between the underexpanded gas jet and the combustion chamber while also increasing the kinetic energy of the jet. This has a substantial influence on the combustion process, primarily through enhanced turbulence in the combustion chamber. Enhanced fuel-jet turbulence may also be leading to reduced soot formation (as there is less time in the high-temperature fuel-rich zone) as well as enhancing soot oxidation in the later stages of combustion. This effect is more significant with intake dilution, where the in-cylinder pressure is higher, the combustion duration is longer, and PM levels are higher. Offsetting these influences at the higher speeds are the increases in the in-cylinder turbulence due to the more rapid piston motion and the longer injection duration (relative to the piston motion; the absolute time for injection is relatively unchanged).

Conclusions

1. At high loads, higher injection pressures substantially reduce both mass and number of PM emissions. At low load, post-exhaust nucleation mode particles dominate the PM loading; the mass and number of these particles are independent of injection pressure. The effects of injection pressure on PM become less significant as in-cylinder turbulence increases with engine speed.
2. The combustion process at all operating conditions is restricted by the rate at which the fuel and oxidizer are mixing. Increasing the injection pressure increases both the mass flux of fuel into the combustion chamber and the in-cylinder turbulence, resulting in enhanced mixing, reducing the combustion duration and increasing the peak combustion intensities.
3. The injection pressure has a significant impact on emissions but little influence on fuel consumption. The nature of the influence depends strongly on operating condition parameters including engine speed, load/equivalence ratio, and intake oxygen mass fraction. Significant high-order interactions between operating condition parameters indicate that most of the emissions are a result of multiple competing influences, the relative importance of which varies substantially with operating condition.
4. At low and moderate speeds, CO emissions are reduced with higher injection pressures. At the highest engine speed, CO emissions are increased, possibly due to changes in the relative contributions of cylinder and gaseous-jet induced turbulence to the combustion process. The effects of injection pressure on HC emissions are inconsistent and insignificant compared to the effects of operating condition and intake dilution.
5. At higher in-cylinder pressures (high load), the differential pressure between the injected fuel and the cylinder is lower; hence increasing the injection pressure has a greater influence on the combustion process. With high differential pressures, the flow through the nozzle is choked, resulting in less sensitivity to in-cylinder conditions.
6. Without EGR, NO_x emissions are slightly increased with higher injection pressures due to more rapid and more intense combustion. With EGR, the effects of injection pressure on NO_x are not significant; differences due to variability in the intake dilution level dominate the observed variations in the NO_x emissions.

Acknowledgment

The authors would like to acknowledge the invaluable technical assistance of Westport Innovations Inc. and the staff at the University of British Columbia, and in particular Mr. Robert Parry. Financial support was generously provided by Westport Innovations and NSERC Canada.

References

[1] Seinfeld, J. H., and Pandis, S. N., 1996, *Atmospheric Chemistry and Physics: From Air Pollution to Climate Change*, Wiley, New York.
[2] Pope, C. A. III, Burnett, R. T., Thurston, G. D., et al., 2004, "Cardiovascular Mortality and Long-Term Exposure to Particulate Air Pollution: Epidemiological Evidence of General Pathophysiological Pathways of Disease," Circulation, **109**, pp. 2671–2677.
[3] Gauderman, W. J., Avol, E., Gilliland, F., et al., 2004, "The Effect of Air Pollution on Lung Development from 10 to 18 Years of Age," New England Journal of Medicine, **351**(11), pp. 1057–1067.
[4] Code of Federal Regulations (CFR) 40 Parts 69, 80, and 86, 2001, Control of Air Pollution from New Motor Vehicles: Heavy Duty Engine and Vehicle Standards and Highway Diesel Fuel Sulfur Control Requirements; Final Rule; US Federal Register, Vol. 66(12), pp. 5002–5050.
[5] Harrington, J., Munshi, S., Nedelcu, C., Ouellette, P., Thomson, J., and Whitfield, S., 2002, "Direct Injection of Natural Gas in a Heavy-Duty Diesel Engine," SAE Tech. Pap. Ser. 2002-01-1630.
[6] Kamel, M., Lyford-Pike, E., Frailey, M., et al., 2002, "An Emissions and Performance Comparison of the Natural Gas Cummins Westport Inc. C-Gas Plus Versus Diesel in Heavy-Duty Trucks," SAE Tech. Pap. Ser. 2002-01-2737.
[7] Dodge, L., Simescu, S., Neely, G., Maymar, M., Dickey, D., and Savonen, C., 2002, "Effect of Small Holes and High Injection Pressures on Diesel Engine Combustion," SAE Tech. Pap. Ser. 2002-01-0494.
[8] Benajes, J., Molina, S., Garci, J., and Novella, R., 2004, "Influence of Boost Pressure and Injection Pressure on Combustion Process and Exhaust Emissions in a HD Diesel Engine," SAE Trans., **113**, pp. 834–845.
[9] Bertola, A., Schubiger, R., Kasper, A., Matter, U., Forss, A. M., Mohr, M., Boulouchos, K., and Lutz, T. 2001, "Characterization of Diesel Particulate Emissions in Heavy-Duty DI Diesel Engines with Common Rail Fuel Injection - Influence of Injection Parameters and Fuel Composition," SAE Trans., **110**.
[10] Morgan, R. E., Gold, M., Laguitton, O., Crua, C., and Heikal, M., 2003, "Characterisation of the Soot Formation Processes in a High Pressure Combusting Diesel Fuel Spray," SAE Trans., **113**, pp. 2086–2094.
[11] Rente, T., Gjirja, S., and Denbratt, I., 2004, "Experimental Investigation of the Effect of Needle Opening (NOP) Pressure on Combustion and Emissions Formation in a Heavy Duty DI Diesel Engine," SAE Trans., **112**, pp. 1692–1711.
[12] Pagan, J. 1999, "Study of Particle Size Distributions Emitted by a Diesel Engine," SAE Trans., **108**.
[13] Singh, I., Zhong, L., Lai, M., Henein, N., and Bryzik, W., 2003, "Effect of Nozzle hole Geometry on a HSDI Diesel Engine-Out Emissions," SAE Trans., **112**, pp. 957–977.
[14] Yu, R. C., and Shahed, S. M., 1981, "Effects of Injection Timing and Exhaust Gas Recirculation on Emissions from a D.I. Diesel Engine," SAE Trans., **90**.
[15] Kobori, S., Kamimoto, T., and Aradi, A., 1999, "A Study of Ignition Delay of Diesel Fuel Sprays," Int. J. Engine Res., **1**(1), pp. 29–39.
[16] Rubas, P. J., Paul, M., Martin, G., Coverdill, R., Lucht, R., Peters, J., and DelVecchio, K., 1998, "Methane Jet Penetration in a Direct-Injection Natural Gas Engine," SAE Trans., **107**.
[17] Hill, P. G., and Ouellette, P., 1999, "Transient Turbulent Gaseous Fuel Jets for Diesel Engines," ASME J. Fluids Eng., **121**, pp. 93–101.
[18] Sullivan, G. S., Huang, J., Wang, T. X., Bushe, W. K., and Rogak, S. N., 2005, "Emissions Variability in Gaseous Fuel Direct Injection Compression Ignition Combustion," SAE Trans., **114**, pp. 780–789.
[19] Goudie, D., Dunn, M., Munshi, S. R., Lyford-Pike, E., Wright, J., Duggal, V., and Frailey, M., 2004, "Development of a Compression Ignition Heavy Duty Pilot-Ignited Natural Gas Fuelled Engine for Low NOx Emissions," SAE Tech. Pap. Ser. 2004-01-2954.
[20] McTaggart-Cowan, G. P., Bushe, W. K., Rogak, S. N., Hill, P. G., and Munshi, S. R., 2003, "Injection Parameter Effects on a Direct Injected, Pilot Ignited, Heavy Duty Natural Gas Engine with EGR," SAE Trans., **112**, pp. 2103–2109.
[21] McTaggart-Cowan, G. P., Bushe, W. K., Hill, P. G., and Munshi, S. R. 2003, "A Supercharged Heavy-Duty Diesel Single-Cylinder Research Engine for High-Pressure Direct Injection of Natural Gas," Int. J. Engine Res., **4**(4), pp. 315–330.
[22] Jones, H. L., McTaggart-Cowan, G. P., Rogak, S. N., Bushe, W. K., Munshi, S. R., and Bucholtz, B., 2005, "Source Apportionment of Particulate Matter from a Diesel Pilot-Ignited Natural-Gas Fuelled Heavy-Duty DI Engine," SAE Trans., **114**, pp. 944–954.
[23] Gilbert, M. S., and Clark, N. N., 2001, "Measurement of Particulate Matter From Diesel Engine Exhaust Using a Tapered Element Oscillating Microbalance," Int. J. Engine Res., **2**(4), pp. 277–287.
[24] Okrent, D. A., 1998, "Optimization of a Third-Generation TEOM Monitor for Measuring Diesel Particulate in Real Time," SAE Tech. Pap. Ser. 980409.
[25] McTaggart-Cowan, G. P., 2006, "Pollutant Formation in a Gaseous-Fuelled,

Direct Injection Engine," Ph.D. dissertation, The University of British Columbia.
[26] Knutson, E. O., and Whitby, K. T., 1975, "Aerosol Classification by Electric Mobility: Apparatus, Theory, and Applications," J. Aerosol Sci., **6**, pp. 443–451.
[27] Heywood, J. B., 1988, *Internal Combustion Engine Fundamentals*, McGraw-Hill, New York.
[28] McTaggart-Cowan, G. P., Bushe, W. K., Rogak, S. N., Hill, P. G., and Munshi, S. R., 2004, "The Effects of Varying EGR Test Conditions on a Direct Injection of Natural Gas Heavy-Duty Engine With High EGR Levels," SAE Tech. Pap. Ser. 2004-01-2955.
[29] Hicks, C. R., and Turner, K. V., 1999, *Fundamental Concepts in the Design of Experiments*, 5th ed., Oxford University Press, Oxford, UK.
[30] Khalek, I. A., Kittelson, D. B., and Brear, F., 2000, "Nanoparticle Growth During Dilution and Cooling of Diesel Exhaust: Experimental Investigation and Theoretical Assessment," SAE Tech. Pap. Ser. 2000-01-0515.
[31] Abdul-Khalek, I., Kittelson, D., and Brear, F., 1999, "The Influence of Dilution Conditions on Diesel Exhaust Particle Size Distribution Measurements," SAE Trans., **108**.

Prediction of Peak Cylinder Pressure Variations Over Varying Inlet Air Condition of Compression-Ignition Engine

Gong Chen
Department of Mechanical Engineering,
Gannon University,
Erie, PA 16541

Peak cylinder pressure (p_{max}) of a compression-ignition engine can be affected by the engine inlet air condition, such as its inlet air temperature (T_i) and pressure (p_i). The variation of peak cylinder pressure due to varying inlet air temperature or pressure is analytically studied. A model is developed and simplified, and thus the variations of p_{max} can be predicted along with varying inlet air temperature or pressure. The analysis and prediction indicate that cylinder active compression ratio (CR) and intake air boost ratio (p_{m0}/p_{i0}) play relatively significant roles in affecting the variation of p_{max} over inlet air temperature and pressure, and the pressure variation is proportional to CR^k and ratio p_{m0}/p_{i0}. Comparison between the predicted results using the simplified model and those from engine experiments shows a close agreement in both the trend and magnitude. The investigation and prediction also include modeling the variation in p_{max} due to varying the cylinder TDC clearance volume (V_c). The simplified model is presented and shows that the change in p_{max} versus varying V_c also depends on the cylinder compression ratio. It is indicated that for a certain change in the clearance volume, a higher compression-ratio configuration would produce a greater change in p_{max} than a lower one does, especially as the rest of the engine design and operating parameters remain unchanged.
[DOI: 10.1115/1.2431389]

Introduction

Peak cylinder pressure (p_{max}), indicated on a general curve of cylinder pressure versus crank angle position in Fig. 1, is one of the primary in-cylinder combustion parameters affecting not only the output performances, but also the level of mechanical loading on the power subassembly components of a compression-ignition engine. Consider medium and low-speed compression-ignition engines, which are widely used for marine, power generation, and diesel-electric locomotive applications, and usually operate continuously at their respective rated speed and full load conditions. Then, p_{max} of a full-load operation of an engine of this type is usually set close to but not exceeding a specified allowable maximum at a standard inlet air condition, as described by Hsu and Chen [1] and Chen et al. [2]. The inlet air condition under consideration in this work mainly include inlet air temperature (T_i) and inlet air pressure (p_i). The inlet air herewith refers to the air either entering directly the intake manifolds of a naturally aspirated engine or entering the turbocharger compressor of a turbocharged engine.

The general outputs and performance of a compression-ignition engine are influenced by inlet air temperature and pressure, such as described by Spence and William [3]. It is also understood that as the engine inlet air T_i or p_i or both changes, p_{max} will vary to be higher or lower, depending on the direction of the inlet air condition changing, as discussed by Chen et al. [4] for varying T_i and by Chen and Hsu [5] for varying p_i. Thus, it is needed, in designing and operating an engine of this type, to understand and evaluate quantitatively the variation of p_{max} due to changing the inlet air condition parameters. A simple analytical model and prediction can be beneficial and can provide preliminary and useful indications of the variation in p_{max} before any engine experimental measurements or engine in-cylinder cycle simulations become available and convenient. The development of such a simple model and prediction for the variation of p_{max} versus T_i and p_i of a compression-ignition engine is focused in this paper. The analysis and modeling also include the investigation of the variation in p_{max} due to varying the cylinder clearance volume (V_c) when the piston is located at the top dead center (TDC).

Model and Prediction of p_{max} Variation

The peak pressure p_{max} of a compression-ignition engine is composed of intake manifold air pressure (p_m) and two pressure rises from p_m: the pressure rise due to the cylinder gas compression/expansion without combustion and the pressure rise due to the combustion heat added to the cylinder content, which also undergoes compression/expansion thereafter toward p_{max}, as graphically illustrated in Fig. 1. Then, the variation (Δp_{max}) of p_{max} over the inlet air parameters T_i and p_i is studied based on a simple air-standard cycle analysis treating the cylinder content as an ideal gas, such as the air-standard cycle described in [6] by Heywood. Consider that using an extended air cycle analysis, Hsu [7,8] evaluated the instant pressure rise due to the amount of combustion heat added into the cylinder content at an arbitrary crank-angle position. Thus, the determination of the total pressure rise toward p_{max} during the engine cycle is developed, as described in the Appendix. With the derivation in more detail given in the Appendix, peak pressure p_{max}, which occurs at crank-angle position θ_{pmax} and cylinder volume V_{pmax}, is written as

$$p_{max} = p_m CR^k \left(\frac{V_c}{V_{p\,max}}\right)^k + \frac{RQ}{c_v V_c}\left(\frac{V_c}{V_{p\,max}}\right)^k \left(\frac{V_\theta}{V_c}\right)^{k-1}_{Ave} \frac{\Delta\theta_{p\,max}}{\Delta\theta}$$

$$= p_m CR^k \left(\frac{V_c}{V_{p\,max}}\right)^k + \frac{RQ}{c_v V_c}\eta_p \quad \text{MPa} \tag{1}$$

where CR is cylinder active compression ratio, V_c the cylinder

Contributed by the Internal Combustion Division of ASME for publication in the JOURNAL OF ENGINEERING FOR GAS TURBINES AND POWER. Manuscript received September 30, 2005; final manuscript received August 15, 2006. Review conducted by Margaret Wooldridge.

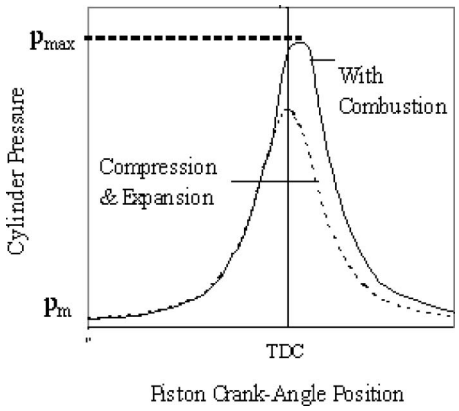

Fig. 1 Illustration of peak cylinder pressure

TDC volume, k a cycle-averaged cylinder process polytropic index, R the gas constant, c_v the constant-volume specific heat of the cylinder content, Q the amount of combustion heat added into the cylinder content per cycle, and η_p is a ratio factor of the actual pressure rise of $p_{\max}$ due to combustion heat to the rise of $p_{\max}$ if the combustion heat Q per cycle is added into the cylinder content at TDC.

Then, η_p in Eq. (1) is either greater or smaller than unity, depending on the crank-angle position of the combustion duration, as finite durations of fuel injection and combustion always take place in a real engine. Again, the first term on the right-hand side of Eq. (1) indicates the pressure rise due to the cylinder content solely under compression/expansion, and the second term is the pressure rise due to the heat of combustion added prior to $p_{\max}$, which occurs at $V_{p\max}$.

It may reasonably be assumed for a compression-ignition diesel engine that the variation in the combustion heat release behavior is less significant than the variation in the compression/expansion of the cylinder content as solely inlet air temperature T_i or pressure p_i varies with fuel injection/combustion timing remaining unchanged. Then, the variation of $p_{\max}$ versus varying T_i and p_i can be obtained as an approximate function of compression ratio CR, variation of p_m, and position of $p_{\max}$ over T_i and p_i as

$$dp_{\max} \approx \mathrm{CR}^k \left(\frac{V_c}{V_{p\,\max}} \right)^k \left(\frac{\partial p_m}{\partial T_i} dT_i + \frac{\partial p_m}{\partial p_i} dp_i \right) \tag{2}$$

Intake manifold air pressure p_m of a compression-ignition engine varies as inlet air temperature T_i or pressure p_i changes. Although the variation is straightforward to be understood and can be easily determined for a naturally aspirated engine when T_i or p_i changes, the determination of the variation for a turbocharged engine is more complex due to the turbocharger operational responses to engine input conditions, such as described, in general, by Watson and Janota [9], and mentioned for medium speed diesel engine by Geist and Holtbecker [10]. For the sake of modeling and determination of a change in p_m due to varying T_i or p_i with intake manifold air temperature T_m remaining unchanged, the relation between p_m and the parameters of T_i and p_i in this work for a turbocharged engine are expressed using the form as follows:

$$\frac{p_m}{p_{m0}} = \left(\frac{T_i}{T_{i0}} \right)^{-n} \left(\frac{p_i}{p_{i0}} \right)^m \tag{3}$$

where n and m are exponential coefficients that describe the effects of T_i and p_i on p_m, and the subscription 0 simply refers to a standard reference condition of p_m, T_i, and p_i. It is apparent that $m=1$ and $n=0$ for a naturally aspirated engine. For a turbocharged and intercooled engine when T_m remaining constant in a general case, the values of n and m are both greater than zero and generally less than unity due to the effect of the turbocharger operational responses to varying T_i or p_i on manifold air pressure p_m. For example, when T_i is higher or p_i is lower, the density of the charge air entering the turbocompressor will be lower, but the turbocharger will be driven to become faster due to the increased exhaust energy content and vice versa.

The actual values of the exponential coefficients m and n may vary between different designs/configurations of engines or turbochargers. The values of m and n can be quantitatively determined for a particular engine, analytically or experimentally as its engine and turbocharger configuration is specified. For example, the coefficient n was determined in an experimental work to be 0.8 for a medium-speed turbocharged diesel engine, as described by Chen [11] and this value of the coefficient n is also used later in the work of this paper. The value of m is determined and verified using the experimental data for a particular diesel engine later in this paper. Then, substitute Eq. (3) into Eq. (2) for p_m, consider that T_i and p_i vary independently of each other from reference T_{i0} and p_{i0}, respectively, and Eq. (2) becomes

$$dp_{\max} \approx \mathrm{CR}^k \left(\frac{V_c}{V_{p\,\max}} \right)^k \times \left[-np_{m0} \frac{T_{i0}^n}{T_i^{n+1}} dT_i + m \left(\frac{p_{m0}}{p_{i0}} \right) \times \left(\frac{p_i}{p_{i0}} \right)^{m-1} dp_i \right] \tag{4}$$

Furthermore, integrating Eq. (4) over T_i and p_i results in the variation of $p_{\max}$, which is at T_i, p_i, and p_m, from $p_{\max 0}$, which is at T_{i0}, p_{i0}, and p_{m0}, as follows:

$$p_{\max} - p_{\max\,0} = \Delta p_{\max} = p_{m0} \mathrm{CR}^k \left(\frac{V_c}{V_{p\,\max}} \right)^k \times \left\{ \left[\left(\frac{T_i}{T_{i0}} \right)^{-n} - 1 \right] + \left[\left(\frac{p_i}{p_{i0}} \right)^m - 1 \right] \right\} \tag{5}$$

It is understood that $p_{\max}$ occurs at a position usually after but close to TDC in a practical compression-ignition engine, depending on the crank-angle location of the fuel injection and burning duration. Then Eq. (5) may be simplified to

$$\Delta p_{\max} = p_{m0} \mathrm{CR}^k \left\{ \left[\left(\frac{T_i}{T_{i0}} \right)^{-n} - 1 \right] + \left[\left(\frac{p_i}{p_{i0}} \right)^m - 1 \right] \right\} \quad \mathrm{MPa} \tag{6}$$

Thus, with p_{m0} and CR specified for a particular engine, $\Delta p_{\max}$ versus T_i or p_i can be determined using the model equation (Eq. (5)) or the simplified model (Eq. (6)). Recognizing that the value of the cycle-averaged polytropic index k may also vary between different engine designs/configurations, where the cylinder content heat transfer to the cylinder walls may change [7], the index needs to be evaluated and determined once a particular engine is specified and studied.

Variation of $p_{\max}$ Over Inlet Air T_i

The variation of $p_{\max}$, due to varying T_i only, is herewith investigated. For varying T_i only, Eqs. (5) and (6) become

$$\Delta p_{\max} = p_{m0} \mathrm{CR}^k \left(\frac{V_c}{V_{p\,\max}} \right)^k \left[\left(\frac{T_i}{T_{i0}} \right)^{-n} - 1 \right] \tag{7}$$

and

$$\Delta p_{\max} \approx p_{m0} \mathrm{CR}^k \left[\left(\frac{T_i}{T_{i0}} \right)^{-n} - 1 \right] \tag{8}$$

Results of $\Delta p_{\max}$ versus T_i predicted using both Eq. (7) as a model and Eq. (8) as a further-simplified model for an assumed engine sample with its relevant parameters specified are plotted in Fig. 2. Without knowing the location of $p_{\max}$ ($V_{p\max}$), the simplified model Eq. (8) is able to closely predict a change in $p_{\max}$ due to varying T_i, about 10% over those from using the model equation (Eq. (7)), as shown in Fig. 2.

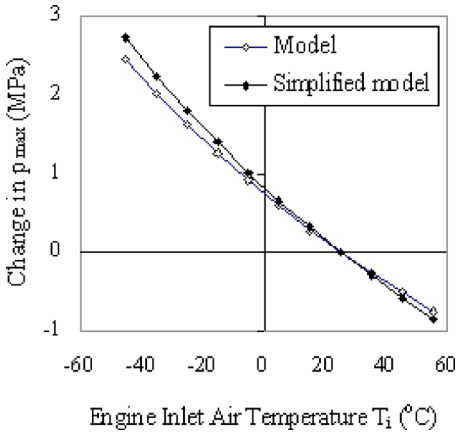

Fig. 2 Comparison of predicted Δp_{max} between using model and simplified model (k=1.32, n=0.8, CR=15, p_{m0}=0.32 MPa)

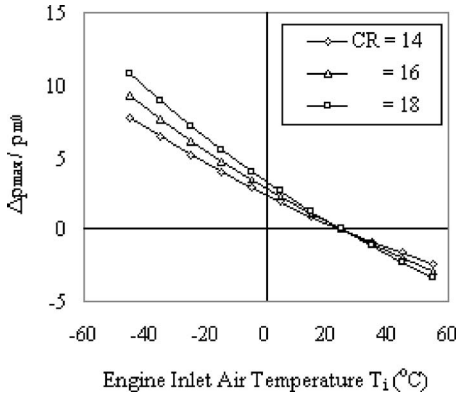

Fig. 4 Predicted $\Delta p_{max}/p_{m0}$ versus inlet air temperature at various compression ratio (k=1.32, n=0.8)

The rate of variation of p_{max} over T_i is obtained by rearranging and simplifying Eq. (4) as

$$\frac{dp_{max}/p_{m0}}{dT_i/T_{i0}} \approx -n\mathrm{CR}^k\left(\frac{T_i}{T_{i0}}\right)^{-(n+1)} \tag{9}$$

The dimensionless term $(dp_{max}/p_{m0})/(dT_i/T_{i0})$ is evaluated and plotted versus T_i at various CR, as shown in Fig. 3, where T_{i0} =25°C is used. As a result of the determination using the model of prediction, the term of $\Delta p_{max}/p_{m0}$ is plotted versus T_i at various CR in Fig. 4. It is indicated that the magnitude of Δp_{max} due to varying T_i increases as CR increases, and the rate of Δp_{max} varies as T_i moves away from its baseline condition T_{i0}.

Figure 5 shows the predicted results of Δp_{max} affected by the baseline intake air boost ratio p_{m0}/p_{i0} as T_i changes from its baseline condition T_{i0}. As indicated in Fig. 5, the effect of changing T_i on varying p_{max} is stronger when the air boost ratio p_{m0}/p_{i0} becomes bigger.

Then, comparing the rates of variation of p_{max} versus T_i for two different compression ratios to the same baseline conditions, using Eq. (9), gives

$$\frac{dp_{max\,1}}{dp_{max\,2}} = \left(\frac{\mathrm{CR}_1}{\mathrm{CR}_2}\right)^k \tag{10}$$

which indicates that the p_{max} variation versus T_i is proportional to CR^k. Thus, the variation of p_{max} corresponding to varying T_i of a higher-CR engine configuration is greater than that of a lower-CR configuration. Starting from an identical p_{max} at a standard T_i, the engine under a higher compression ratio will result in a larger p_{max} than that under a lower compression ratio as T_i becomes lower, vice versa, as displayed in Fig. 4.

Experimental results of the engine-average change in p_{max} from testing a medium-speed diesel engine are used in this work to verify and validate the model and prediction for Δp_{max} versus T_i. The engine tested was a 16-cylinder GE-7FDL four-stroke diesel engine with its general specifications described in [2]. It was turbocharged and intercooled, and was able to deliver a full brake power of 3356 kW at the rated speed of 1050 RPM. The experimental results of the average change in p_{max} from testing the engine are presented in Fig. 6 versus its inlet air temperature T_i and compression ratio CR. The predicted results of Δp_{max} versus T_i using the simplified model for the engine are also plotted in Fig. 6 for comparison. In the prediction, k=1.32 as used by Hsu [7] and n=0.8 as derived by Chen [11] are rationally used. It can be seen from Fig. 6 that the analytical prediction agrees closely with the engine experimental results in both the trends and the magnitudes of p_{max} variation.

Variation of p_{max} Over Inlet Air p_i

The variation of peak cylinder pressure, due to solely varying inlet air pressure p_i, is then studied and predicted by using the simplified model for p_{max} variation. For varying p_i only, Eqs. (4) and (6) can be simplified as

$$\frac{dp_{max}}{dp_i} \approx m\mathrm{CR}^k\left(\frac{p_{m0}}{p_{i0}}\right)\left(\frac{p_i}{p_{i0}}\right)^{m-1} \tag{11}$$

and

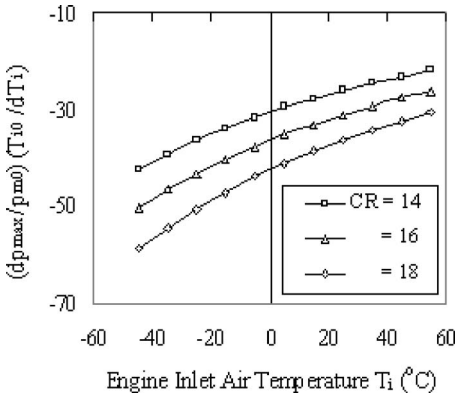

Fig. 3 Predicted p_{max}-variation rate over inlet air temperature at various compression ratio (k=1.32, n=0.8)

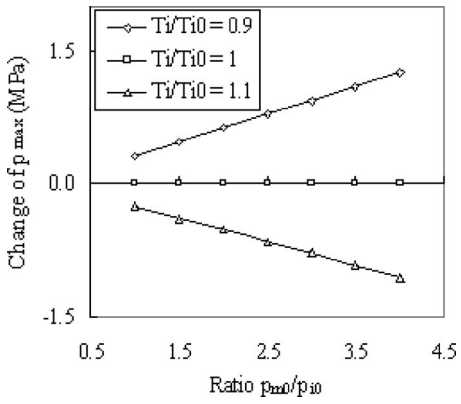

Fig. 5 Predicted change in p_{max} versus intake air boost ratio at various inlet air temperature (k=1.32, n=0.8, CR=15)

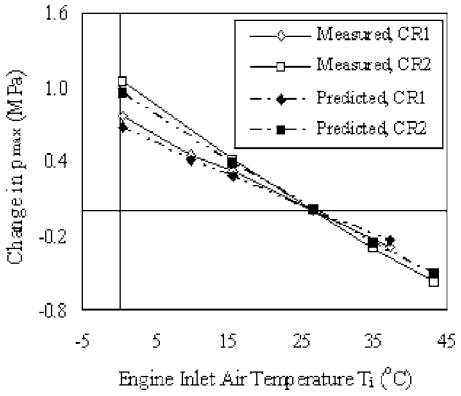

Fig. 6 Predicted and measured change in p_{max} versus inlet air temperature of engine

$$\Delta p_{\max} \approx p_{m0}\mathrm{CR}^{k}\left[\left(\frac{p_i}{p_{i0}}\right)^{m} - 1\right] \text{ MPa} \tag{12}$$

The dimensionless term $dp_{\max}/dp_i$ in Eq. (11) as the rate of variation in $p_{\max}$ over varying p_i, is evaluated and plotted versus p_i at various compression ratio CR, as shown in Fig. 7, where p_{i0} =0.1 MPa is used. As a result of the determination, $\Delta p_{\max}$ based on Eq. (12) is calculated and plotted versus p_i at various CR in Fig. 8 for p_{m0}=0.32 MPa used. It is indicated in Fig. 8 that the magnitude of $\Delta p_{\max}$ due to varying p_i also increases as CR increases, and the rate of $\Delta p_{\max}$ intends to vary as p_i moves away from its baseline condition p_{i0}.

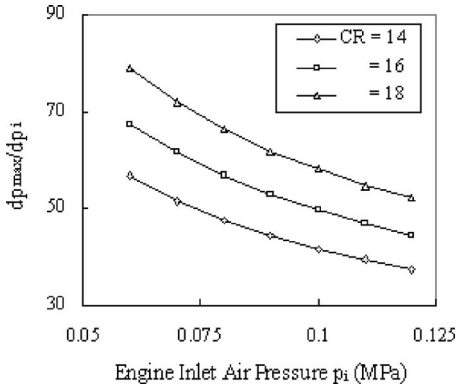

Fig. 7 Predicted rate of variation of p_{max} over inlet air pressure at various compression ratio (k=1.32, m=0.4, p_{m0}/p_{i0}=3.2)

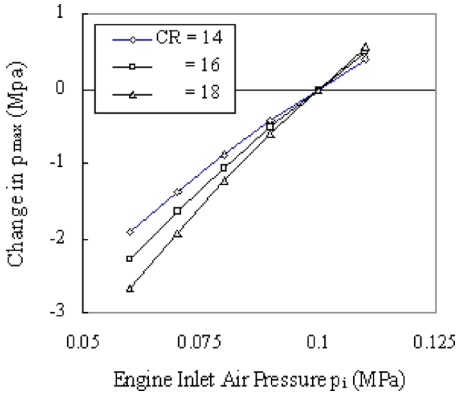

Fig. 8 Predicted change in p_{max} versus inlet air pressure at various compression ratio (k=1.32, m=0.4, p_{m0}/p_{i0}=3.2)

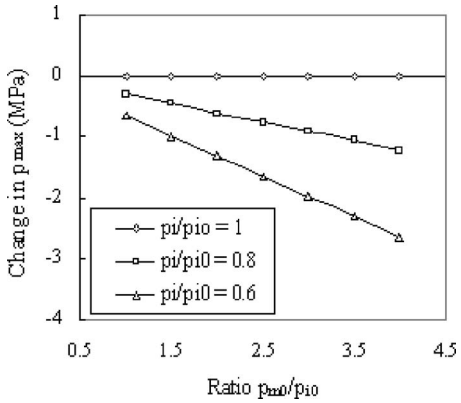

Fig. 9 Predicted change in p_{max} over air boost ratio and inlet air pressure (k=1.32, m=0.4, CR=15)

Figure 9 shows the predicted results of $\Delta p_{\max}$ affected by the baseline intake air boost ratio p_{m0}/p_{i0} as p_i changes from its baseline condition p_{i0}=0.1 MPa used. As indicated in Fig. 9, the effect of changing p_i on varying $p_{\max}$ is also stronger when the air boost ratio p_{m0}/p_{i0} becomes larger.

Comparing the rates of variation of $p_{\max}$ versus p_i between two different compression ratios with identical baseline conditions, using Eq. (11), gives an expression the same as Eq. (10) as

$$\frac{dp_{\max 1}}{dp_{\max 2}} = \left(\frac{\mathrm{CR}_1}{\mathrm{CR}_2}\right)^{k} \tag{10'}$$

which indicates that the variation of $p_{\max}$ versus p_i is proportional to CR_k. Thus, the variation of $p_{\max}$ due to varying p_i of a higher-CR engine configuration is greater than that of a lower-CR configuration. Starting from an identical $p_{\max}$ at a standard p_i, the engine under a higher compression ratio will also result in a larger $p_{\max}$ than that under a lower one as p_i becomes higher, vice versa, as displayed in Fig. 8.

Experimental results of testing a medium-speed single-cylinder research diesel engine are used to verify the model and prediction of $\Delta p_{\max}$ versus varying p_i, and presented in Fig. 10. The tested engine was a single-cylinder version of the GE-7FDL series engine, with the general setup of the engine and testing system given in [2,12,13]. In testing the engine for the effect of p_i on $p_{\max}$, the inlet air pressure was simulated by adjusting intake manifold air pressure and cylinder exhaust pressure. Two different levels of p_i shown in Fig. 10 were achieved and are available for the comparison in this study. The predicted results of $\Delta p_{\max}$ versus p_i using the simplified model of prediction for the two points are also

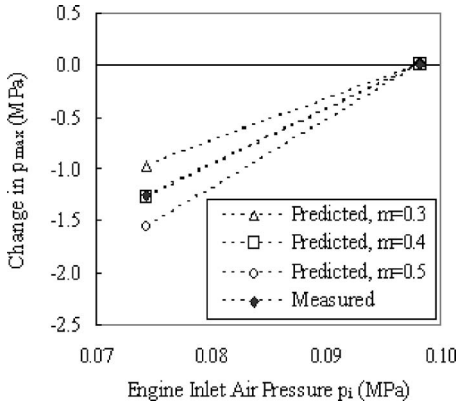

Fig. 10 Predicted and measured change in p_{max} versus inlet air pressure of engine

plotted in Fig. 10 for comparison. In the prediction, $k=1.32$ is used. It was attempted to use three different values of the coefficient m in the prediction for the engine tested. It can be seen from Fig. 10 that the analytical prediction agrees closely with the engine experimental results, as $m=0.4$ is used, in both the trends and the magnitudes of $p_{\max}$ variation for this particular engine.

Variation of $p_{\max}$ Over TDC-Volume V_c

It is often of interest in design and construction of a compression-ignition engine that how a variation in the cylinder clearance volume (V_c), at which the piston is located at the top dead center (TDC), affect the peak cylinder pressure ($p_{\max}$), especially as the piston total active displacement volume (V_s) remains unchanged. The analytical investigation and simplified prediction for the effects of V_c on the cylinder compression ratio (CR), in turn on $p_{\max}$, is conducted. Since CR and V_c are related by

$$\mathrm{CR}=\frac{V_s+V_c}{V_c}=1+\frac{V_s}{V_c} \quad \text{and} \quad V_c=\frac{V_s}{\mathrm{CR}-1}\ \mathrm{m}^3 \tag{13}$$

where V_s is the piston total active displacement volume for compression, then $\Delta\mathrm{CR}$, the variability of CR, due to solely varying V_c by taking the first-order Taylor expansion of CR is

$$\frac{d\mathrm{CR}}{dV_c}=\frac{-V_s}{V_c^2}=-\frac{(\mathrm{CR}-1)^2}{V_s} \tag{14}$$

or

$$\Delta\mathrm{CR}\approx\frac{-V_s}{V_c^2}\Delta V_c=-\frac{(\mathrm{CR}-1)^2}{V_s}\Delta V_c \tag{15}$$

Thus, for an identical change (ΔV_c) in V_c, the consequent change in CR ($\Delta\mathrm{CR}$) between two different baseline compression ratios with an identical V_s can be compared as

$$\frac{\Delta\mathrm{CR}_2}{\Delta\mathrm{CR}_1}=\left(\frac{\mathrm{CR}_2-1}{\mathrm{CR}_1-1}\right)^2\approx\left(\frac{\mathrm{CR}_2}{\mathrm{CR}_1}\right)^2 \tag{16}$$

Equation (16) indicates that, with an identical variation in the clearance volume V_c, the resulted change in CR is greater in the case of a higher CR than that in the case of a smaller CR, as the displacement volume V_s remains the same. The ratio of the changes is roughly proportional to the square of the CR ratio in a compression-ignition engine where usually $1/\mathrm{CR}\ll 1$.

For obtaining a simplified approach to $\Delta p_{\max}$, it may be rationally assumed that a change of engine cylinder peak pressure ($p_{\max}$) due to varying CR is mainly contributed by the consequent effect on cylinder content compression and, thus, the effect on combustion heat release is insignificant and negligible. Thus, the variability of engine cylinder peak pressure ($p_{\max}$) due to the variation of CR affected by ΔV_c can be expressed using Eq. (A2) of the Appendix by

$$\Delta p_{\max}\approx kp_m\mathrm{CR}^{k-1}\Delta\mathrm{CR}=-kp_m\mathrm{CR}^{k-1}\frac{(\mathrm{CR}-1)^2}{V_s}\Delta V_c\ \mathrm{MPa} \tag{17}$$

or

$$\frac{\Delta p_{\max}}{p_m}=-k\mathrm{CR}^{k-1}(\mathrm{CR}-1)\frac{\Delta V_c}{V_c} \tag{18}$$

The predicted ratio $\Delta p_{\max}/p_m$ versus ratio $\Delta V_c/V_c$ with $k=1.32$ used is plotted in Fig. 11 in various baseline compression ratio cases. Then, the variability of $p_{\max}$ over ΔV_c between two different compression ratio bases with p_m and V_s remaining the same can be compared as

$$\left.\frac{\Delta p_{\max 2}}{\Delta p_{\max 1}}\right|_{\Delta V_c}=\left(\frac{\mathrm{CR}_2}{\mathrm{CR}_1}\right)^{k-1}\left(\frac{\mathrm{CR}_2-1}{\mathrm{CR}_1-1}\right)^2\approx\left(\frac{\mathrm{CR}_2}{\mathrm{CR}_1}\right)^{k+1} \tag{19}$$

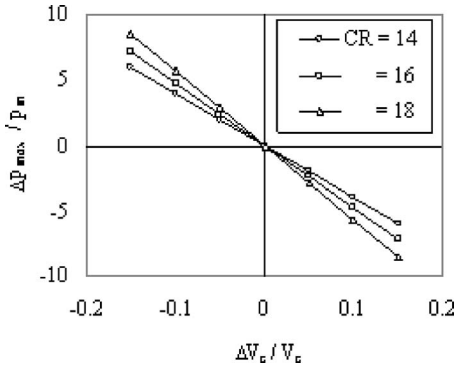

Fig. 11 Predicted variation of $p_{\max}$ over cylinder TDC volume at various compression ratio

Alternatively, the variability of $p_{\max}$ over $\Delta V_c/V_c$, which is a relative change of V_c, between two different compression ratio cases with p_m remaining fixed can be compared as

$$\left.\frac{\Delta p_{\max 2}}{\Delta p_{\max 1}}\right|_{\Delta V_c/V_c}=\left(\frac{\mathrm{CR}_2}{\mathrm{CR}_1}\right)^{k-1}\left(\frac{\mathrm{CR}_2-1}{\mathrm{CR}_1-1}\right)\approx\left(\frac{\mathrm{CR}_2}{\mathrm{CR}_1}\right)^{k} \tag{20}$$

Equations (19) and (20) indicate that, with either an identical change ΔV_c in V_c or an identical relative change $\Delta V_c/V_c$, the higher CR configuration will produce a greater change in $p_{\max}$ than the lower one does. As the intake manifold air pressure p_m and displacement volume V_s remain the same between the two, the ratio of changes in $p_{\max}$ over ΔV_c is roughly proportional to $(k+1)$ power of CR ratio, and the ratio of changes in $p_{\max}$ over $\Delta V_c/V_c$ becomes roughly proportional to the power of (k) of CR ratio for p_m fixed.

Conclusions

The investigation and analytical prediction of the variations in peak cylinder pressure due to varying the engine inlet and input conditions are conducted for compression-ignition engines. The followings are shown through the investigation.

1. The simplified model and prediction for the variation of peak cylinder pressure $p_{\max}$ due to varying engine inlet air temperature and pressure, and as well cylinder TDC clearance volume are established. Although the more-complete model for $\Delta p_{\max}$ requires knowing the crank-angle position of $p_{\max}$, the simplified model can be used to predict $\Delta p_{\max}$ versus T_i and p_i closely without the need of knowing the crank position. Comparison between the results predicted and those from the engine experiments shows close agreements in both the trends and magnitudes of the $p_{\max}$ variations as those inlet condition parameters vary.

2. In varying the engine inlet air temperature or pressure, the most significant engine design input parameters affecting the variation of $p_{\max}$ include the engine cylinder active compression ratio CR and the baseline intake air boost ratio p_{m0}/p_{i0}, as indicated by the simplified models and prediction. The variation of $p_{\max}$ is proportional to CR^k and p_{m0}/p_{i0}. Thus, the change of $p_{\max}$ in a higher CR configuration would be greater than that in a lower CR as T_i or p_i varies and the rest of the engine configuration and operation parameters remain unchanged. As indicated, the effect of changing T_i or p_i on varying $p_{\max}$ is also stronger when the air boost ratio p_{m0}/p_{i0} becomes larger.

3. It is also indicated by the simplified model and prediction that, for a change in the cylinder TDC volume V_c, a higher compression-ratio configuration of this type of engine would produce a greater change in $p_{\max}$ than a lower compression-ratio configuration. The regarded change in $p_{\max}$ versus V_c is roughly proportional to CR^{k+1} as the active displacement volume V_s and intake manifold air pressure p_m remain constant. The change ver-

sus $\Delta V_c/V_c$ is roughly proportional to CR^k. Thus, any variation in V_c would result in a change in CR and, in turn, in a corresponding variation in p_{max} for a fixed V_s.

4. The models and prediction developed in this paper are based on the general consideration of compression-ignition engine processes. Because of the similar characterizations of engine process and system configuration, the model and prediction are applicable to compression-ignition engines, in general. For a particular engine or engine configuration of this type, the analytical prediction, using appropriate values of the parameters, such as k, n, and m described and used in this work, can also provide indications of the p_{max} variations over varying the engine inlet air or input conditions.

Nomenclature

- CR = cylinder active compression ratio
- c_v = specific heat at constant volume, J/(kg K)
- k = cylinder content polytropic process index
- m = p_m-over-p_i exponential coefficient
- n = p_m-over-T_i exponential coefficient
- p_i = inlet air pressure entering turbo-compressor, MPa
- p_m = intake manifold air pressure, MPa
- p_{max} = cylinder peak firing pressure, MPa
- Q = heat of combustion, Joule
- R = gas constant, J/(kg K)
- TDC = top dead center
- T_i = inlet air temperature entering turbo-compressor, K
- V_c = volume of cylinder content at the top dead center, m^3
- V_s = piston total active displacement volume, m^3
- V_{Pmax} = volume of cylinder content at p_{max}, m^3
- η_p = ratio of pressure rises due to heat of combustion
- θ = crank angle, degree
- Δ = change in a variable parameter

Subscripts

- 0 = reference condition
- 1 = engine in configuration and condition 1
- 2 = engine in configuration and condition 2

Appendix

The analyses and derivation of the model equation for evaluating p_{max} in studying the variation of p_{max} are described in more detail as follows. Consider that the peak cylinder pressure p_{max} is composed of the intake manifold air pressure (p_m) and two pressure rises from p_m: the pressure rise p_{max_p} due to the cylinder content compression/expansion without combustion; and the pressure rise p_{max_q} due to the combustion heat added to the cylinder content, which also undergoes compression/expansion thereafter toward p_{max}. Thus p_{max}, which occurs at crank-angle position θ_{pmax} and cylinder volume V_{pmax}, can be written as

$$p_{max} = p_{max\,p} + p_{max\,q} \quad \text{MPa} \tag{A1}$$

For p_{max_p}, the cylinder content undergoes a polytropic compression/expansion from pressure p_m (which is at cylinder volume V_t) to p_{max} (which is at cylinder volume V_{pmax}). Using an air-standard cycle analysis treating the cylinder content as an ideal gas [6], p_{max_p} is derived as

$$p_{max\,p} = p_m\left(\frac{V_t}{V_{p\,max}}\right)^k = p_m\left(\frac{V_t}{V_c}\right)^k\left(\frac{V_c}{V_{p\,max}}\right)^k = p_m CR^k\left(\frac{V_c}{V_{p\,max}}\right)^k \tag{A2}$$

where CR is cylinder active compression ratio, V_t the cylinder volume at the beginning of the cylinder compression, V_c the cylinder volume at TDC, and k is a cycle-averaged value of the cylinder process polytropic index.

Regarding p_{max_q}, consider an instant amount of combustion heat (dQ) added into the cylinder content at crank-angle position θ and cylinder volume V_θ. The instant pressure rise at θ and V_θ due to dQ is then compressed/expanded continuously prior to reaching p_{max}. Based on the evaluation of the instant pressure rise due to adding a combustion heat to the cylinder content at an arbitrary crank-angle position given by Hsu [7,8], the final pressure rise due to dQ on p_{max} can be derived herewith to be

$$dp_{max\,q} = \frac{RdQ}{c_v V_\theta}\left(\frac{V_\theta}{V_{p\,max}}\right)^k = \frac{RdQ}{c_v V_c}\left(\frac{V_c}{V_{p\,max}}\right)^k\left(\frac{V_\theta}{V_c}\right)^{k-1} \tag{A3}$$

where R is the gas constant and c_v is the constant-volume specific heat of cylinder content. Integrate dp_{max_q} in Eq. (A3) with respect to θ over the duration from θ_s (which is the combustion-start crank angle) to θ_b (which is either the combustion-ending position in the case of combustion ending prior to p_{max} or the position of p_{max} at θ_{pmax} in the case of combustion ending after p_{max}). This results in the total p_{max_q} as

$$p_{max\,q} = \frac{R}{c_v V_c}\left(\frac{V_c}{V_{p\,max}}\right)^k \int_{\theta_s}^{\theta_b} \frac{dQ}{d\theta}\left(\frac{V_\theta}{V_c}\right)^{k-1} d\theta \tag{A4}$$

Thus, p_{max} of Eq. (A1) becomes

$$p_{max} = p_m CR^k\left(\frac{V_c}{V_{p\,max}}\right)^k + \frac{R}{c_v V_c}\left(\frac{V_c}{V_{p\,max}}\right)^k \int_{\theta_s}^{\theta_b} \frac{dQ}{d\theta}\left(\frac{V_\theta}{V_c}\right)^{k-1} d\theta \tag{A5}$$

To further simplify the expression, assume the combustion heat (Q) per cycle is uniformly distributed over the burning period ($\Delta\theta$), and the form of Eq. (A4) becomes

$$p_{max\,q} = \frac{RQ}{c_v V_c}\left(\frac{V_c}{V_{p\,max}}\right)^k \frac{\int_{\theta_s}^{\theta_b}\left(\frac{V_\theta}{V_c}\right)^{k-1} d\theta}{\Delta\theta} = \frac{RQ}{c_v V_c}\left(\frac{V_c}{V_{p\,max}}\right)^k \left(\frac{V_\theta}{V_c}\right)^{k-1}_{ave} \frac{\Delta\theta_{p\,max}}{\Delta\theta} \tag{A6}$$

where $(V_\theta/V_c)^{k-1}_{ave}$ is an averaged value of the term over the range of integration, and $\Delta\theta_{pmax} = \theta_b - \theta_s$. Furthermore, Eq. (A6) can be rearranged to have

$$p_{max\,q} = \frac{RQ}{c_v V_c}\eta_p \quad \text{where} \quad \eta_p = \left(\frac{V_c}{V_{p\,max}}\right)^k \left(\frac{V_\theta}{V_c}\right)^{k-1}_{ave} \frac{\Delta\theta_{p\,max}}{\Delta\theta} \tag{A7}$$

where $RQ/c_v V_c$ is simply the pressure rise for all of Q being added into the cylinder content at TDC. Thus, Eq. (A5) can be rewritten as

$$p_{max} = p_m CR^k\left(\frac{V_c}{V_{p\,max}}\right)^k + \frac{RQ}{c_v V_c}\eta_p \quad \text{MPa} \tag{A8}$$

References

[1] Hsu, B. D., and Chen, G., 2001, "Increased Compression Ratio Diesel Engine Assembly for Retarded Fuel Injection Timing," U.S. Patent No. 6,318,308, assigned to General Electric Co.

[2] Chen, G., Flynn, P. L., Gallagher, S. M., and Dillen, E. R., 2003, "Development of the Low-Emission GE-7FDL High-Power Medium-Speed Locomotive Diesel Engine," ASME J. Eng. Gas Turbines Power, **125**, pp. 505–512.

[3] Spence, P. B., and Williams, T. J., 1974, "The Influence of Ambient Temperature and Pressure on Compression-Ignition Engine Performance," Proc. Inst. Mech. Eng., **188**.

[4] Chen, G., Marsh, G. A., Till, R. H., and Valentine, P. L., 2001, "Locomotive Engine Inlet Air Apparatus and Method of Controlling Inlet Air Temperature," U.S. Patent No. 6,327,980, assigned to General Electric Co.

[5] Chen, G., and Hsu, B. D., 2000, "Reduced Emissions Elevated Altitude Speed Control for Diesel Engines," U.S. Patent No. 6,158,416, assigned to General Electric Co.
[6] Heywood, J. B., 1988, *Internal Combustion Engine Fundamentals*, McGraw-Hill, New York.
[7] Hsu, B. D., 1984, "Heat Release, Cycle Efficiency and Maximum Cylinder Pressure in Diesel Engine—The Use of an Extended Air Cycle Analysis," SAE Paper No. 841054.
[8] Hsu, B. D., 2002, *Practical Diesel Engine Combustion Analysis*, Scocity of Automotive Engineers, Warrendale, PA.
[9] Watson, N., and Janota, M. S., 1982, *Turbocharging the Internal Combustion Engine*, Wiley, New York.
[10] Geist, M., and Holtbecker, R., 1995, "Low and Medium Speed Diesel Engines, Compliance With Prospective Emission Regulations," ASME Paper No. ICE-Vol. 25–1, pp. 39–49.
[11] Chen, G., 2004, "Understanding of Intake Air Boost Parameters and Turbo-changed Diesel Engine Performance and Emissions," *Proc. of 24th CIMAC World Congress on Combustion Engine Technology*, CIMAC, Kyoto, Japan, CIMAC Paper No. 190.
[12] Hsu, B. D., and Hoffman, J. G., 1985, "The Effect of Diesel Fuel Properties on the Combustion of a Medium Speed Diesel Engine," ASME Paper No. 85-DGP-14.
[13] Hsu, B. D., 1986, "Combustion of Water-in-Diesel Emulsion in an Experimental Medium Speed Diesel Engine," SAE Paper No. 860300.

Experimental Validation of a Common-Rail Injector Model in the Whole Operation Field

Marco Coppo
e-mail: marco.coppo@polito.it

Claudio Dongiovanni
e-mail: claudio.dongiovanni@polito.it

Dipartimento di Energetica,
Politecnico di Torino,
Corso Duca degli Abruzzi 24,
10129 Torino, Italy

The present study deals with the definition of an accurate mathematical model of a production common-rail-type injector for automotive diesel engines. The mathematical model defined in a previous work was refined, accounting for a broader range of effects on injector performance, thus allowing a more strict validation of the model predictions against experimental data. The geometry of the control-valve holes, crucial in determining the actual discharge coefficient, was accurately evaluated by means of silicone molds. The moving mechanical components of the injector, such as control valve, needle, and pressure rod were modeled using the mass–spring–damper scheme. The axial deformation under pressure of needle, pressure rod, nozzle and injector body was modeled. This effect was found to also affect the control valve device operation, and was properly accounted for. The model obtained was implemented in Simulink; the ordinary differential equations were solved by means of the numerical differentiation formulas implicit scheme of second-order accuracy, while the partial differential equations were integrated using the finite-difference Lax–Friedrichs method. In order to obtain sufficient data for validating the model in its entire operation field, two separate sets of tests were carried out. In the first analysis, a constant reference pressure was imposed in the rail, and the injector energizing time was progressively increased from values relative to small pilot injections to values characteristic of large main injections. The injected volume per stroke was measured by means of a mean delivery meter (EMI) device. During the second set of tests, the injector was mounted on a flow rate meter (EVI) device so as to measure the injection law. Electric current flowing through the injector solenoid, oil pressure in the common rail, and at the injector inlet, needle, and control valve lift were also gauged and recorded. The good agreement between numerical and experimental results allowed the use of the model to gain greater insight into the mechanisms and phenomena that regulate injector behavior. The nozzle hole discharge coefficient dependence upon time and needle lift was discussed, and the trends were presented in several working conditions. The flow in the control volume holes was studied, in order to determine whether cavitation occurs or not, giving an answer to a long disputed topic. Finally, the effects of injector deformation caused by fuel pressure on performance were investigated.
[DOI: 10.1115/1.2432889]

Keywords: injection systems, common-rail, discharge coefficient

1 Introduction

The direct-injection (DI) diesel engine has widened its natural application field from heavy duty to light duty applications, replacing the spark ignition engine. This expansion has been due to its higher thermal efficiency and capability to meet the stringent emission standards imposed by regulations. The introduction of the common rail fuel injection system [1–3] certainly played an essential role in achieving the current performance of the diesel engine.

Many experimental works show the positive effects of splitting the injection process in several pilot, main, and post-injections on the reduction of noise, soot and NO_x emission [4–8]. In addition, the success of engine downsizing [9] and homogeneous charge combustion engines (HCCI) [10,11] is deeply connected with the injection system performance and injection strategy. However, the experimental optimization of the injection strategies involves lengthy campaigns, and yields results that apply only to the particular engine under investigation.

In this context, numerical analysis can significantly reduce this optimization process by properly simulating flow and combustion in the cylinder; these phenomena are deeply connected to the spray models and, thus, to the characteristics of the fuel flow at the nozzle hole outlet [12]. In turn, these can be obtained by means of an injection system model, which must be validated in a wide range of engine working points in order to obtain significant results.

Many common-rail injector models are reported in the literature [6,13–20]. One of the older common-rail injector model was presented in Ref. [13] and successively improved and employed for the analysis of the instability phenomena due to the control valve behavior [14]. An important input parameter in this model was the magnetic attraction force in the control valve dynamic model. This was calculated interpolating the experimental curve between driving current and magnetic force measured at fixed control valve position. The discharge coefficient of the feeding and discharge control volume holes were determined and the authors asserted that the discharge hole operates, with the exception of short transients, under cavitating flow conditions at every working pressure. Furthermore, the deformation of the stressed injector mechanical components were not taken into account. In Refs. [15,16,18,19] the electromagnetic attraction force was evaluated by means of a phenomenological model. The force was consid-

Contributed by the Internal Combustion Engine Division of ASME for publication in the JOURNAL OF ENGINEERING FOR GAS TURBINES AND POWER. Manuscript received January 3, 2006; final manuscript received September 22, 2006. Review conducted by Jim Cowart.

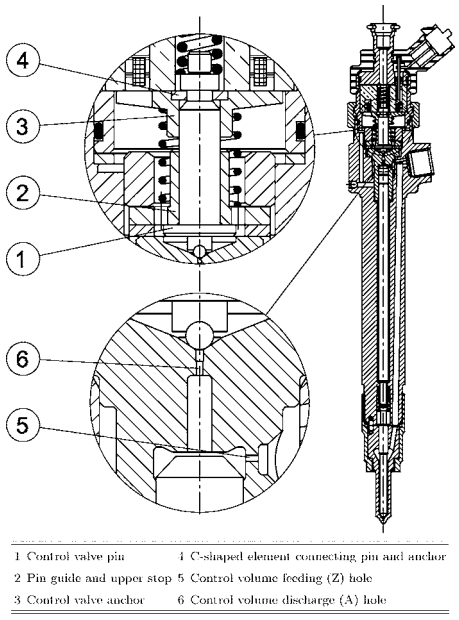

Fig. 1 The Bosch common rail injector analyzed

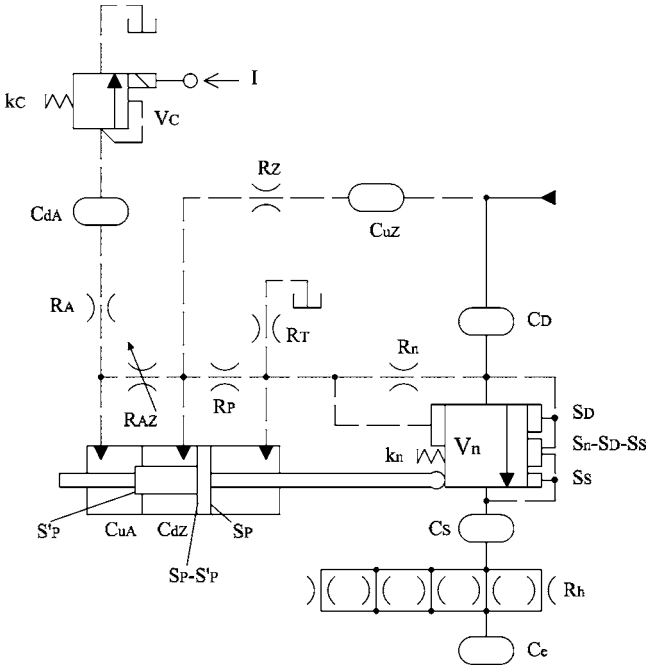

Fig. 2 Injector equivalent hydraulic circuit

ered directly proportional to the square of the magnetic flux and the proportionality constant was experimentally determined under stationary conditions. The elastic deformation of the moving injector components was considered, but the injector body was treated as a rigid body. Payri et al. [20] report a model developed in the AMESim environment, and suggest silicone molds as an interesting tool for characterising valve and nozzle hole geometry.

In a previous work [21], a model of a Bosch common rail injector used in car engines was developed, validated in a few conditions, and then used to demonstrate the effect of certain parameters on injector performance. Taking advantage of this experience, in the present work a series of improvements performed on the original model is presented. To characterize the flow through the control volume holes a model of discharge coefficient was adopted, which required the knowledge of the hole geometrical shape. This was measured by creating silicone moulds of the holes and then measuring their shape with optical techniques.

A new, dynamic model for the discharge coefficient of the nozzle holes was developed, which also included the effect of the needle tip movement on the flow in the holes.

As far as the mechanical part was concerned, the model was made more accurate by including the effects of deformation under working fuel pressure of nozzle, needle, control piston, and injector body. This also made it possible to correctly estimate the maximum needle lift, as a function of fuel pressure. An extensive validation against experimental data was carried out, showing the benefits of the modifications introduced.

2 Mathematical Model

The injector under investigation was a standard Bosch unit (Fig. 1) of the common-rail type used in car engines. It was disassembled and thoroughly analyzed, resulting in the definition of hydraulic, mechanical, and electromagnetic models. Details of this analysis can be found in Ref. [21] and are omitted here, where the main focus is posed on the improvements and modifications of the original injector model.

2.1 Hydraulic Model. Figure 2 shows the equivalent hydraulic circuit of the injector, drawn following ISO 1219 standards. The hydraulic parts of the injector were modeled with ideal components such as uniform pressure chambers and laminar or turbulent hydraulic resistances, according to a zero-dimensional modeling approach. The internal pipe connecting the injector inlet to the nozzle delivery chamber was modeled according to a one-dimensional modeling approach [21].

2.1.1 Discharge Coefficient of the Control Volume Holes. According to Bernoulli's law, the flow rate through control-volume feeding and discharge holes, nozzle holes, and in the needle-seat opening passage is proportional to the square root of the pressure drop, Δp, across the orifice, namely

$$Q = \mu A \sqrt{\frac{2\Delta p}{\rho}} \tag{1}$$

The flow model through these orifices plays a fundamental role in the simulation of the injector behavior in its whole operative field, so the evaluation of the μA factor is extremely important.

The discharge coefficient of control volume orifices A and Z was evaluated according to the model proposed in Ref. [22]. This considers four flow regimes inside the hole: laminar, turbulent, reattaching, and fully cavitating; neglecting cavitation occurrence, a preliminary estimation of the hole discharge coefficient can be obtained as follows

$$\frac{1}{\mu} = \sqrt{K_I + f\frac{l}{d} + 1} \tag{2}$$

where K_I is the inlet loss coefficient, which is a function of the hole inlet geometry [23]; l is the hole axial length; d is the hole diameter; and f is the wall friction coefficient, evaluated as

$$f = \mathrm{MAX}\left(\frac{64}{\mathrm{Re}}, 0.316\,\mathrm{Re}^{-0.25}\right) \tag{3}$$

where Re stands for the Reynolds number. The ratio between the cross-section area of the vena contracta and the geometrical hole area, μ_{vc}, can be evaluated with the relation

$$1/\mu_{vc}^2 = \begin{cases} 1/\mu_{vc_0}^2 - 11.4 r/d & r/d \leq 0.15 \\ 1 & r/d > 0.15 \end{cases} \tag{4}$$

where $\mu_{vc_0}=0.61$ [22,23] and r is the fillet radius of the hole inlet.

If cavitation occurs the potential flow theory allows the appli-

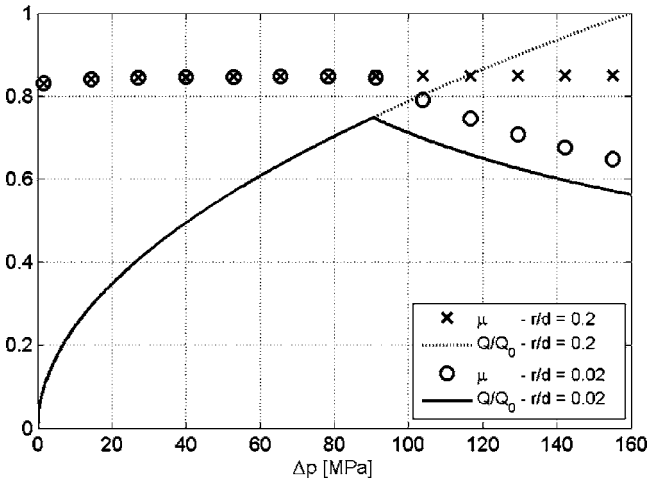

Fig. 3 Predicted flow through an orifice in presence/absence of cavitation

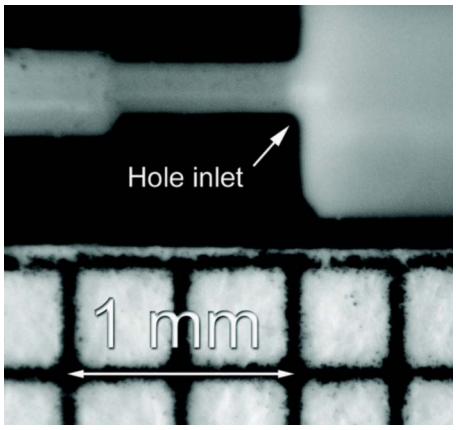

Fig. 4 Silicone mold of the control volume hole *A*

cation of the Bernoulli's equation between the upstream chamber and the vena contracta without any losses [22]. It follows that the pressure in the latter can be estimated as

$$p_{vc} = p_u - \frac{\rho_l}{2}\left(\frac{Q}{A\mu_{vc}}\right)^2 \tag{5}$$

If the pressure in the vena contracta (p_{vc}) is higher then the oil vapor pressure (p_v), cavitation does not occur and the value of the hole discharge coefficient is given by Eq. (2). Otherwise, cavitation occurs and the discharge coefficient is evaluated according to

$$\mu = \mu_{vc}\sqrt{\frac{p_u - p_v}{p_u - p_d}} \tag{6}$$

The hole inlet geometrical profile plays a crucial role in determining, or avoiding, the onset of cavitation in the flow. In turn, the occurrence of cavitation strongly affects the flow rate through the orifice, as can be seen in Fig. 3, which shows two trends of predicted normalized flow rate (Q/Q_0) in function of pressure drop (Δp) through holes with the same diameter and length, but characterized by two different values of the r/d ratio. In this figure Q_0 is the theoretical flow rate evaluated in absence of cavitation when $\Delta p = 160$ MPa. In absence of cavitation ($r/d = 0.2$), the relation between flow rate and pressure drop is monotonic while, if cavitation occurs ($r/d = 0.02$), the hole experiences a decrease in flow rate as pressure drop is further increased. This behavior agrees with experimental data reported in the literature [24].

If the control volume holes happened to cavitate in some working conditions, such behavior would reflect strongly on the injector performance. Therefore, in order to accurately model the injector functioning, it was necessary to accurately measure the geometrical profile of the control volume holes *A* and *Z*; a technique similar to that proposed in Ref. [20] was used for the purpose. Silicone molds of these holes were obtained, and their magnified image was recorded by means of a high resolution camera, as shown in Figs. 4 and 5, respectively.

This made it possible to obtain accurate measurements of the r/d and l/d ratios, as reported in Table 1. The value of K_I, in Eq. (2), is a function of r/d only [25] and, hence, easily obtainable.

Even though a reference dimension was included in the mold images, it was preferred not to measure the hole diameter directly, to avoid errors due to optical aberrations. Instead, knowing that during production a hydro-erosion process is applied to make sure that all the holes yield the same flow rate under steady flow conditions, an iterative procedure was applied to determine the hole diameter that, together with the discharge coefficient model presented above, yielded the declared flow rate. More specifically, a guess approximation of the hole diameter was chosen so as to calculate the discharge coefficient by means of Eq. (1) and with the discharge coefficient model above described; a new diameter approximation was then defined aiming to minimize the difference between the two values of discharge coefficient. The iterative process terminated when the difference between two following hole diameter approximations was lower than 1 μm.

In the control valve used in our experiments, under a pressure drop of 10 MPa, with a back pressure of 4 MPa, the holes *A* and *Z* yielded 6.5 ± 0.2 cm^3/s and 5.3 ± 0.2 cm^3/s, respectively. With these values it was possible to calculate the most probable diameter of the control volume holes, as reported in Table 1. It is worth noting that the precision with which the diameters were evaluated was higher than that of the optical technique used for evaluating the shape of the control volume holes. This resulted from the fact that K_I shows little dependence on r/d when the latter assumes values as high as those measured. As a consequence, the experimental uncertainty in the diameter estimation is mainly originated from the uncertainty given on the stationary flow rate through the orifices.

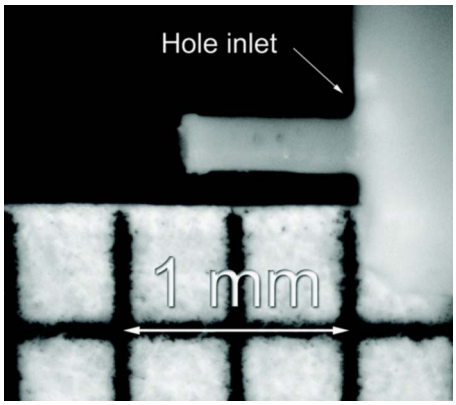

Fig. 5 Silicone mold of the control volume hole *Z*

Table 1 Characteristics of control volume holes

Hole	r/d	l/d	K_I	d (μm)
A	0.23±5%	3.4±5%	0.033	280±2%
Z	0.22±5%	2.8±5%	0.034	249±2%

2.1.2 Discharge Coefficient of the Nozzle Holes. The discharge coefficient of the needle-seat and of the nozzle holes were carefully modeled.

The needle-seat discharge coefficient was assumed as needle lift dependent according to Ref. [26] where this coefficient was experimentally evaluated after removing the nozzle tip.

The model of the discharge coefficient of the nozzle holes was designed on the base of the unsteady coefficients reported in Ref. [27]. These coefficients were experimentally evaluated for minisac nozzles in the real working conditions of a distributor pump–valve–pipe–injector type injection system taking into account the needle-seat discharge coefficient pattern which was evaluated in Ref. [26]. The pattern of nozzle hole discharge coefficient versus needle lift evidences three different phases. In the first phase, during injector opening, the moving needle tip strongly influences the efflux through the nozzle holes. In this phase, the discharge coefficient progressively increases as the needle lift does. In the second phase, when the needle is at its maximum stroke, the discharge coefficient increases in time, independently from the pressure level at the injector inlet. In the last phase, during the needle closing stroke, the discharge coefficient remains almost constant. These three phases above mentioned describe a hysteresis-like phenomenon. In order to build a model suitable for a common rail injector in its whole operation field these three phases need to be considered.

Therefore, the nozzle hole discharge coefficient was modeled as needle lift dependent by considering two limit curves: a lower limit trend (μ_h^d), which models the discharge coefficient in transient efflux conditions, and an upper limit trend (μ_h^s), which represents the steady-state value of the discharge coefficient for a given needle lift. The evolution from transient to stationary values was modeled with a first-order system dynamics.

It was experimentally observed [27,28] that the transient trend presents a first region in which the discharge coefficient increases rapidly with needle lift, following a sinusoidal-like pattern, and a second region, characterized by a linear dependence between discharge coefficient and needle lift. Thus, the following model was adopted

$$\mu_h^d(\xi) = \begin{cases} \mu_h^d(\xi_0)\sin\left(\dfrac{\pi}{2\xi_0}\xi\right) & 0 \leqslant \xi < \xi_0 \\ \dfrac{\mu_h^d(\xi_M) - \mu_h^d(\xi_0)}{\xi_M - \xi_0}(\xi - \xi_0) + \mu_h^d(\xi_0) & \xi \geqslant \xi_0 \end{cases} \tag{7}$$

where ξ is the needle-seat relative displacement; and ξ_0 is the transition value of ξ between the sinusoidal and the linear trend.

The use of the variable ξ, rather than the needle lift, x_n, emphasizes the fact that all the mechanical elements subject to fuel pressure deform, thus the real variable controlling the discharge coefficient is not the position of the needle, but rather the effective clearance between the latter and its seat in the nozzle.

The maximum needle lift, ξ_M, varies with rail pressure due to the different level of deformation that this parameter induces on the mechanical components of the injector. A linear relation was used

$$\xi_M = K_1 p_{r0} + K_2 \ (\mu\text{m}) \tag{8}$$

where p_{r_0} is the reference rail pressure, and K_1 and K_2 are experimentally evaluated constants.

Similarly, the value of ξ_0 was assumed to vary in function of the operating pressure. Thus, the following fit was used

$$\xi_0 = K_3 p_{r0} + K_4 \ (\mu\text{m}) \tag{9}$$

where K_3 and K_4 are experimentally evaluated constants.

In order to define the relation between the steady state value of the nozzle-hole discharge coefficient (μ_h^s) and the needle-seat relative displacement (ξ) the device in Fig. 6 was designed. It contains a camshaft that can impose to the needle a continuously variable lift up to 1 mm. Then, a modified injector equipped with this device was connected to the common rail injection system and installed in a Bosch measuring tube, in order to control the nozzle hole downstream pressure, and the steady flow rate was measured by means of a set of graduated burettes.

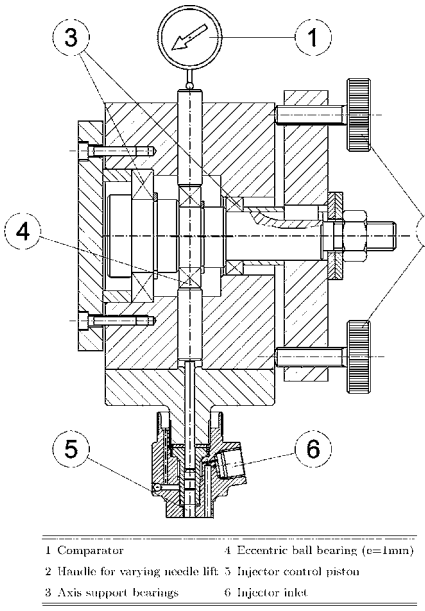

Fig. 6 Device for manually controlling the needle lift

Figure 7 shows the trends of steady-state flow rate versus needle lift at rail pressures of 10 and 20 MPa, while the back pressure in the Bosch measuring tube was kept to either ambient pressure or 4 MPa; whereas Fig. 8 shows the resulting stationary hole discharge coefficient, evaluated for the nozzle under investigation. It was not possible to impose rail pressures higher than 20 MPa during the experiments because of the limited pump displacement (0.657 cm^3/rev) and revolution speed allowed by the test rig (2500 rpm).

Despite these limitations, and taking advantage of the reduced variation of μ_h^s with operation pressure, it was possible to use the measured values to extrapolate the trends of steady-state discharge coefficient for higher pressures, thus defining the upper boundary of variation of the nozzle hole discharge coefficient values.

During the injector opening phase the unsteady effects are predominant and the sinusoidal-linear trend of the hole discharge

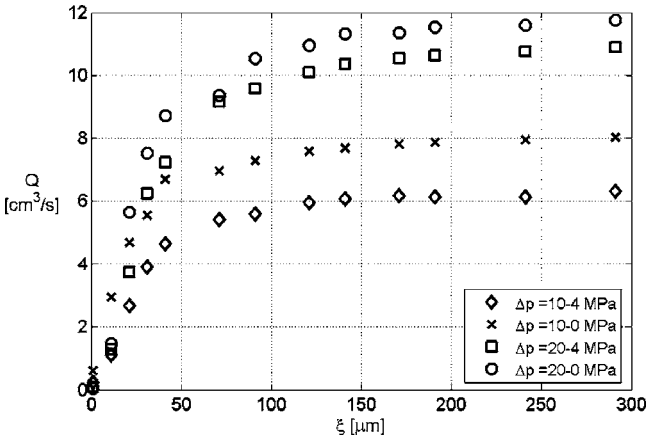

Fig. 7 Measured flow rate through nozzle as function of needle lift

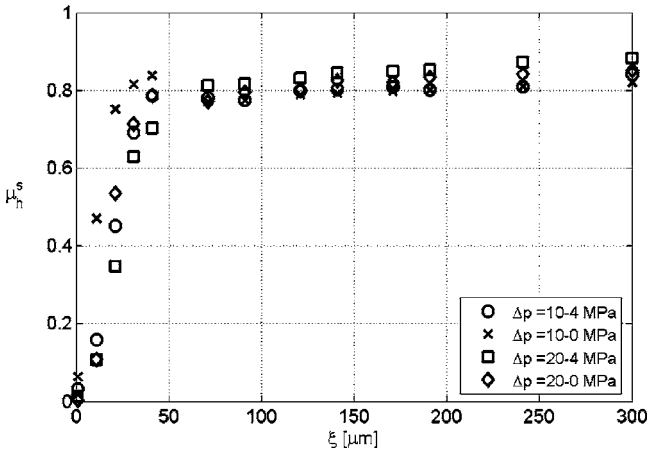

Fig. 8 Measured trends of stationary nozzle hole discharge coefficient

coefficient, Eq. (7), was considered; when the needle-seat relative displacement approaches its relative maximum value ξ_M^r, the discharge coefficient increases in time, which means that the efflux through the nozzle holes is moving to the stationary conditions. In order to describe this behavior, a transition phase between the unsteady and the stationary values of the hole discharge coefficient at this needle lift was considered. This phase was modeled as a temporal exponential curve, namely

$$\mu_h = \mu_h^d(\xi_M^r)[\mu_h^s(\xi_M^r) - \mu_h^d(\xi_M^r)]\left[1 - \exp\left(-\frac{t - t_0}{\tau}\right)\right] \quad (10)$$

where t_0 is the instant in time at which the needle-seat relative displacement approaches its maximum value ξ_M^r; $\mu_h^d(\xi_M^r)$, and $\mu_h^s(\xi_M^r)$ are the unsteady and the stationary hole discharge coefficients evaluated at this needle-seat relative displacement; and τ is the time constant of this phenomenon.

2.1.3 Flow in Long Pipes and Fluid Model. A one-dimensional modeling approach was followed in order to model the fluid flow in the pipe connecting injector and rail and in the injector internal duct that carries the fluid from the inlet to the delivery chamber. This was necessary to correctly take into account pressure waves propagation that occurs in those elements. The pipe flow conservation equations were written for a single-phase fluid. An isothermal flow was assumed in the present study and only the momentum and conservation equations were written

$$\frac{\partial \mathbf{w}}{\partial t} + A\frac{\partial \mathbf{w}}{\partial x} = \mathbf{b} \quad (11)$$

where

$$\mathbf{w} = \begin{Bmatrix} u \\ p \end{Bmatrix}, \quad A = \begin{Bmatrix} u & 1/\rho \\ \rho c^2 & u \end{Bmatrix}, \quad \mathbf{b} = \begin{Bmatrix} -4\tau/\rho d \\ 0 \end{Bmatrix}$$

and τ is the wall shear stress that was evaluated under the assumption of steady-state friction. In the present study the model works with imposed constant pressure in the common rail. Junctions were treated as minor losses and only the continuity equation was locally written.

Density, wave propagation speed and kinematic viscosity of the ISO4113 test oil had been evaluated as a function of pressure and temperature [29]. These oil properties were approximated with analytic functions of the exponential type in the range of pressures from 0.1 to 200 MPa and temperatures from 10°C to 120°C. These analytic formulas were derived from the actual value of properties, which were supplied by the oil company, by using the least-square method for nonlinear approximation functions with two independent variables.

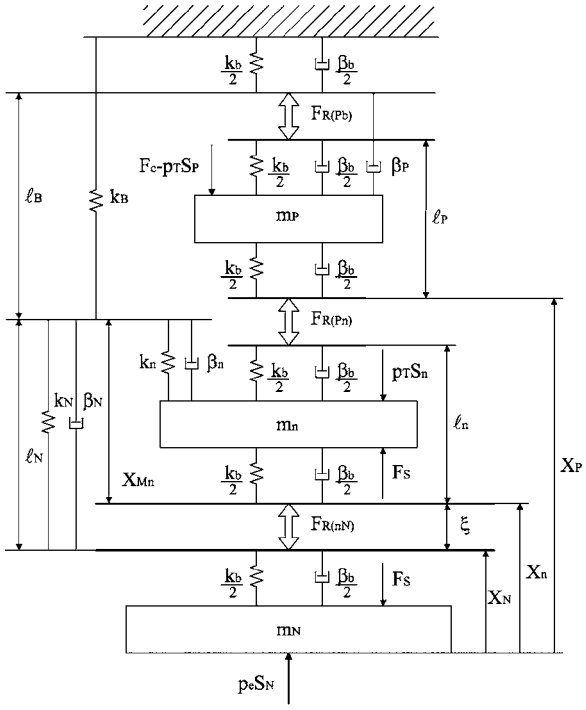

Mass (g)	Damping factor (kg/s)	Stiffness (N/mm)
$m_P = 8.0$	$\beta_P = 6.5$	$k_n = 32.6$
$m_n = 3.2$	$\beta_n = 6.1$	

Fig. 9 Mechanical model of needle, control piston, and nozzle

2.2 Mechanical Model. All mechanical devices whose position can vary during injector functioning (i.e., needle, control piston and control valve) were modeled using the conventional mass–spring–damper scheme, governed by a mechanical equilibrium equation, in which the dynamic parameters are function of element position. In order to take into account the effects of the axial deformation of nozzle and injector body, the nozzle was modeled by means a conventional mass–spring–damper scheme too, while the injector body was modeled by means of a simple spring having appropriate stiffness. Injector needle, control piston and nozzle form a three degrees of freedom mechanical system, which can be modeled as shown in Fig. 9. Three equilibrium equations are needed to describe the system motion, one for each element. With reference to Fig. 9, the dynamic equilibrium equation for control piston ($j=P$), needle ($j=n$), and nozzle ($j=N$) reads

$$m_j\frac{d^2x_j}{dt^2} + \bar{\beta}_j\frac{dx_j}{dt} + \bar{k}_j x_j + \bar{F}_{0j} = F_j \quad (j = P,n,N) \quad (12)$$

where m_j is the displacing mass; $\overline{\beta_j}$ the damping coefficient; $\bar{k}_j$ the spring stiffness; and $\bar{F}_{0_j}$ the spring preload; the bar above the symbols indicates that these coefficients are evaluated according to the relative position of the moving elements [21]; the external force F_j applied to the mass has the following meaning, with reference to Figs. 2 and 9,

$$F_j = \begin{cases} -F_c + p_T S_P + F_{R(Pn)} - F_{R(Pb)} & (j = P) \\ -p_T S_n - F_{R(Pn)} + F_S + F_{R(nN)} & (j = n) \\ -F_S + p_e S_n - F_{R(nN)} & (j = N) \end{cases} \quad (13)$$

where $F_{R(ij)}$ is the force that ith and jth element apply to each other when they are in contact

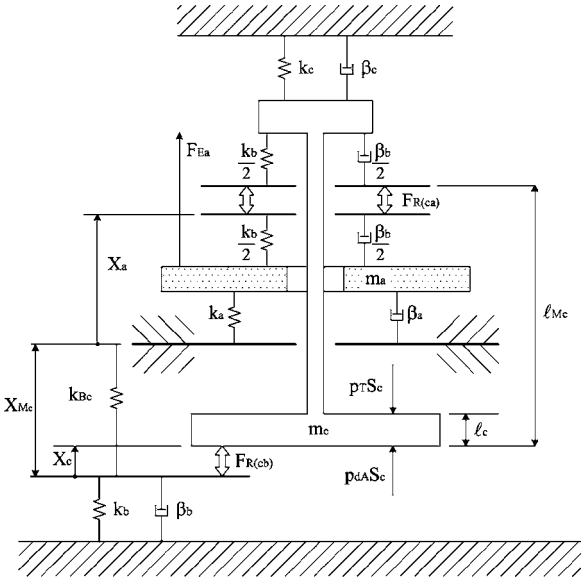

Mass (g)	Damping factor (kg/s)	Stiffness (N/mm)
$m_a = 3.2$	$\beta_a = 5.1$	$k_a = 1.7$
$m_c = 3.5$	$\beta_c = 28$	$k_c = 46$

Fig. 10 Control valve mechanical model

$$F_c = p_{uA}S'_P + p_{dZ}(S_P - S'_P) \tag{14}$$

and

$$F_S = p_S S_S + p_D S_D + [\gamma p_S + (1-\gamma)p_D](S_n - S_D - S_S) \tag{15}$$

where $\gamma=0$ indicates that the nozzle is closed while $\gamma=1$ indicates open nozzle conditions.

The control valve contains two mobile components: the pin element having mass m_c and the anchor element of mass m_a; they can be modeled with the two degrees of freedom scheme shown in Fig. 10. The two dynamic equilibrium equations were written in a similar fashion as Eq. (12) where $j=a$ indicates the anchor and $j=c$ the control pin, while the external forces F_j can be evaluated as

$$F_j = \begin{cases} F_{Ea} - F_{R(ca)} & (j=a) \\ (p_{dA} - p_T)S_c + F_{R(ca)} + F_{R(cb)} & (j=c) \end{cases} \tag{16}$$

where F_{Ea} represents the electromagnetic action that the current generates when it flows in the solenoid coil. The authors would like to stress that the anchor upper mechanical stop is indirectly imposed by the control-pin stop [1] and it is not independent as some authors claim [6,18,19]. With reference to Fig. 1, the controlpin 1, which is stopped by the element 2, stops the anchor 3 through the C-shaped element 4.

The axial deformation of each mechanical element (i.e., needle, nozzle, and control piston) was taken into account. These elements were considered only axially stressed, while the effects of the radial stress were neglected. The axial length of control piston (l_P), needle (l_n), and nozzle (l_N) was evaluated as function of the axial compressive load (F_C) in each element. Therefore, the deformed length l of these elements, which were considered formed by m parts having cross section A_j and initial length l_{0_j},was evaluated as follows

$$l = \sum_j l_{0_j}\left(1 - \frac{F_{C_j}}{EA_j}\right) \tag{17}$$

where E is Young's modulus of the considered material.

The axial deformation of the injector body was taken into account by introducing in the model the elastic elements indicated as k_B and k_{Bc} in Figs. 9 and 10. The injector body deformation cannot be theoretically calculated very easily, because one should need to take into account the effect and deformation of the constraints that fix the injector on the test rig. For this reason, in order to evaluate the elasticity coefficient of k_B and k_{Bc}, an empirical approach was followed, which consisted in obtaining a relation between the axial length of these elements and the fluid pressure inside the injector body. As direct consequence, the maximum stroke of the needle-control piston (ξ_M) and of the control valve (X_{Mc}) could be expressed as a function of the injector structural stress.

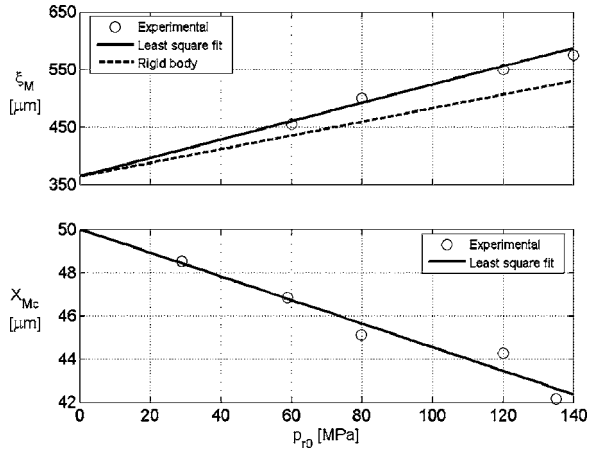

Fig. 11 Effect of injector body deformation on control piston (top) and control valve (bottom) maximum stroke

Figure 11 reports the actual maximum needle-control piston lift (circular symbols) as a function of rail pressure. At the rail pressure of 30 MPa the maximum needle-control piston lift was not reached, so no value was reported at this rail pressure. The continuous line represents the least-square fit interpolating the experimental data and the dashed line shows the maximum needle-control piston lift calculated by considering only nozzle, needle, and control-piston axial deformation. The difference between the two lines represents the effect of the injector body deformation on the maximum needle-control piston lift. This can be expressed as a function of rail pressure and can be estimated in 0.41 μm/MPa. By means of the linear fit (continuous line) reported in Fig. 11 it was possible to evaluate the parameters $K_1=1.59$ μm/MPa and $K_2=364$ μm that appear in Eq. (8).

In order to evaluate the elasticity coefficient k_{Bc}, an analogous procedure was followed, this time analyzing the maximum control-valve lift dependence upon fuel pressure, as shown in Fig. 11. It was found that the effect of injector body deformation was that of reducing the maximum control valve stroke of 0.06 μm/MPa.

2.3 Electromagnetic Model. The electromechanical actuator that drives the control valve was modeled in order to predict the attraction force that the solenoid applied on the anchor in function of the electrical current flowing into its coils. The magnetic circuit geometry of the control valve was thoroughly analyzed in order to evaluate the magnetic energy (W_m) stored in the gap. The magnetic force applied by the solenoid on the anchor (F_{Ea}) was obtained by applying the principle of energy conservation to the anchor-coil system, and evaluated as

$$F_{\mathrm{Ea}} = -\left.\frac{\partial W_m}{\partial x_a}\right|_{\Phi} = -\frac{1}{2}\left(\frac{NI}{\Re}\right)^2 \frac{d\Re}{dx_a} \tag{18}$$

where x_a is the anchor lift; NI is the ampere-turns in the exciting coil; and $\Re$ the equivalent circuit reluctance connected to the

magneto motive force generator [21].

The saturation phenomenon, which occurs to every ferromagnetic material, was taken into account by limiting the maximum magnetic flux in the materials. This implies a superior limit to the magnetic attraction force. Material hysteresis, nonlinearity, and flux leakages were neglected.

3 Numerical Algorithm

The equations obtained in the injector model development stage were implemented in Simulink, a MATLAB Toolbox designed for modeling dynamic systems. Then a numerical differentiation formulas (NDF) [30] implicit multistep scheme of second-order accuracy was used to solve the resulting system of differential equations. The choice of this scheme was dictated by the nature of the system to be solved, which showed numerical stiffness, hence requiring a specific discretization technique.

The Lax–Friedrichs finite difference scheme [31] was used to discretize the partial differential equations that describe the flow into the injector feeding pipe and injector internal main duct. The conservative scheme adopted is of the first-order accuracy and presents a minimum diffusion term when the Courant number $(c\Delta t/\Delta x)$ is chosen to be equal to one. An iterative process was chosen in order to synchronize the NDF solver, which works with a varying time increment, and the Lax–Friedrichs algorithm, which operates with constant time step, in order to maintain the Courant number as close to one as possible.

4 Injection System

The commercial injection system under investigation was of the common rail type for passenger cars. It was made up of a volumetric high-pressure pump, a pressure regulator, a fuel rail, a rail pressure sensor, four electric injectors, and connecting pipes. In the present study, only one injector was connected to the common rail in order to minimize the rail pressure oscillation and thus allowing a more precise validation of the injector model.

The high pressure pump, a three-piston Bosch unit with a displacement of 0.657 cm^3/rev., was provided with an embedded pressure regulator displaced on its delivery port. The regulator, controlled by the system electronic control unit (ECU), was responsible for maintaining the value of the oil pressure in the rail (p_r) at the desired level (p_{r_0}).

The common rail had a trapped volume of 20 cm^3 and was capable of feeding four injectors. The rail and the injector feeding pipe were 305 mm and 200 mm long, respectively.

The electric injector under investigation was a standard Bosch unit fitted with a nozzle of microsac type. It presented five cylindrical holes that had been finished with a hydroerosion process that guarantees a flow rate increase of about 10%. Hence, the nozzle was characterized by a stationary flow rate of 9.0 $cm^3/s \pm 0.17$ cm^3/s at a constant injection pressure of 10 MPa.

5 Experimental Analysis

Experimental investigation of injector performance was carried out on a test rig designed for testing both traditional and common rail type diesel fuel injection systems. Two experimental setups were defined. The first one presented a Bosch measuring tube (EVI) for the injection rate measurement. In the second experimental setup, the EVI indicator was replaced by an EMI equipment for the evaluation of the mean quantity of fuel injected per stroke. The injection system used, and the most important quantities under control during the tests, are presented in Fig. 12, where the symbol # indicates a sensor.

The oil employed during the test was compliant with ISO4113 specifications and was supplied at a temperature of $40°C \pm 1°C$ and a relative pressure of $0.08\% \pm 5\%$ MPa to the injection system. Temperature of the injector body was continuously measured so as to identify the stationary working conditions of the injection system.

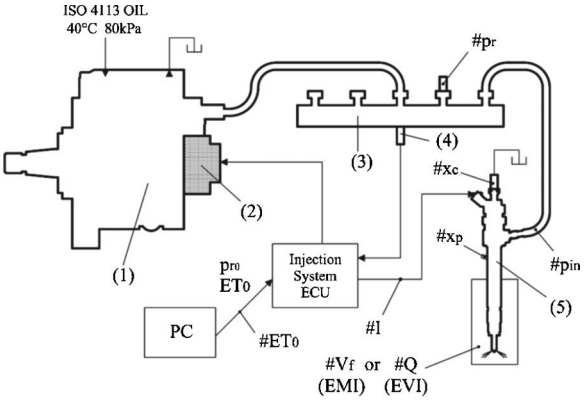

1	High pressure pump	$\#I$	Solenoid current
2	Pressure regulator	$\#V_f$	Injected volume
3	Common rail	$\#Q$	Injection flow rate
4	Rail pressure transducer	$\#p_{in}$	Pressure at injector inlet
5	Injector	$\#p_r$	Rail pressure
ET_0	Reference ET value	$\#x_P$	Control piston lift
p_{r_0}	Reference rail pressure	$\#x_c$	Control valve lift

Fig. 12 Tested injection system layout and main measured quantities

In the first test (EVI), the experiments were carried out under five different sets of boundary conditions which characterize the injector working field. The rail pressure, p_{r_0}, and the injector energizing time, ET_0, reference values, which were imposed through the injection-system test rig, were set at the values shown in Table 2.

The conditions *A*, *B*, and *C* refer to main injections, while *D* and *E* refer to pilot injections.

The second test (EMI) was carried out by fixing the rail pressure reference value p_{r_0} at 30 MPa, 60 MPa, 80 MPa, 120 MPa, and 140 MPa, while ET_0 was continuously increased up to 1000 μs.

Pressure signals were gauged by means of piezoresistive transducers (Kistler 4067). A noncontact eddy current displacement sensor ($\mu\epsilon$ S05) was employed for the measurement of the control piston lift. The gauging of the control valve lift was performed by means of an inductive transducer (AVL 423) whose magnetic core was connected to the valve body by means of an extension rod brazed to the valve head. A Hall effect transducer measured the electric current flowing into the solenoid coil, while the mean injector reflux flow rate was measured by means of a set of graduated burettes.

The mass of the injector mechanical elements, the stiffness of the springs, and the geometrical dimensions were evaluated with an uncertainty of 1% after the completion of the experimental campaign.

6 Result and Discussion

Model performance was assessed by comparing numerically obtained and experimentally measured data. The electric current signals gauged during experimentation were fed to the model, so

Table 2 EVI analysis test points

Test	*A*	*B*	*C*	*D*	*E*
p_{r0} (MPa)	135	80	30	135	80
ET_0 (μs)	780	700	670	300	300

Table 3 Values of parameters used in the discharge coefficient models

Eq. (7)		Eq. (9)		Eq.(10)
$\mu_h^d(\xi_0)$	$\mu_h^d(\xi_M)$	K_2	K_3	τ
0.75	0.85	0.28 μm/MPa	63 μm	25 μs

as to compare simulated and actual injector behavior when driven by the same input. Pressure in the common rail was imposed to be constant during the theoretical analysis. This assumption was justified by the limited fluctuation of the rail pressure, which was always lower than 6% of the nominal value, p_{r_0}, in the considered test cases. This was the result of the choice of connecting only one injector to the rail, as pressure fluctuations would have been considerably larger if all four injectors were connected and activated, thus making it difficult to evaluate the effects of every single injector operation on the system.

Every theoretical result was obtained by setting the parameters in the discharge coefficient models to the values shown in Table 3.

A first validation test was carried out by comparing the predicted and measured values of fuel volume injected per stroke, V_f, in function of the injector energisation time, ET_0, as shown in Fig. 13. Lines represent experimental data at a given reference rail pressure, while circular symbols refer to simulated results. Figure 14 shows the error evaluated as the difference between theoretical and actual injected fuel volume (V_f), which was usually lower than ±1.5 mm^3. This shows that the model was able to accurately

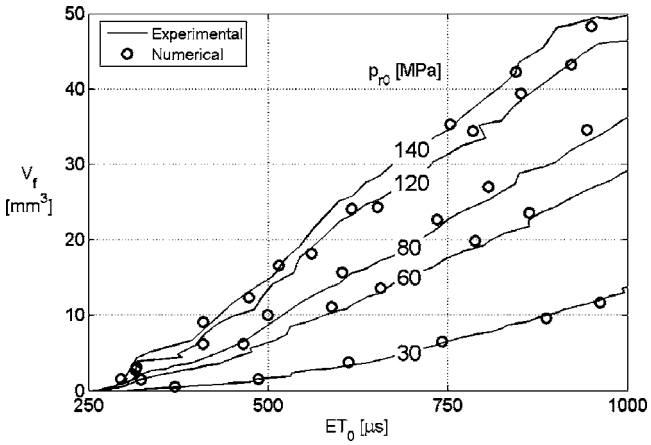

Fig. 13 Model validation—injected fuel volume per stroke

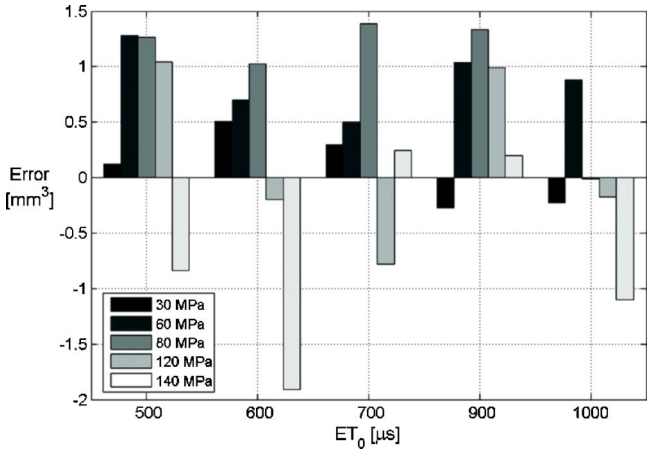

Fig. 14 Model error—injected fuel volume per stroke

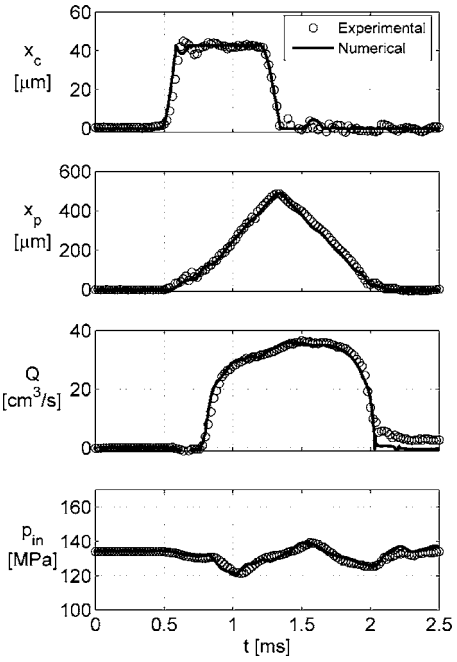

Fig. 15 Model validation—test conditions *A*

reproduce the injector behavior in its entire working field. Comparisons between experimental and numerical time histories of pressure at the injector inlet, control piston lift and control valve lift were also carried out for this test, but were not reported here for the sake of brevity.

A detailed validation of an injector model cannot be limited to the sole comparison of simulated and measured injected volume, because this quantity represents the integral of the injector internal operation. However unlikely, due to the extensive range of pressure and ET_0 values considered in the first test, it could be possible that this integral value results from a series of errors that compensate each other in the prediction of the evolution of variables that influence the calculation of the injected volume per stroke.

In order to make sure to exclude the occurrence of this possibility in our model, a second series of validation tests was performed. The evolution of key variables such as oil pressure at injector inlet (p_{in}), control valve lift (x_c), control piston-needle lift (x_P), and injected flow rate (Q) were predicted in the five conditions presented in Table 2, and compared with the relative experimental results, as shown in Figs. 15–19. The reported experimental trends were obtained as the ensemble average of the values measured during 20 consecutive injection cycles and were drawn with circular symbols. The numerical results were drawn with continuous lines.

Observing the control piston lift trends, a high scattering in the measured data was noticed during the injector opening phase. The particular type of sensor used was found to be responsible for such inaccurate readings, as the small eddy currents used to evaluate distance were affected by the large electromagnetic field generated by the large current flowing in the solenoid. Confirmation of this explanation is the evidence that, once the solenoid was de-energized, the readings became accurate again. A novel optical sensor (thus insensitive to electromagnetic disturbance) developed by the authors gave further evidence to confirm this theory, as shown in Ref. [32].

The comparisons presented in Figs. 15–19 showed good agreement between experimental and numerical results for all the test conditions. This allowed us to: (i) completely trust the model to yield accurate operation predictions of the injector and the devices

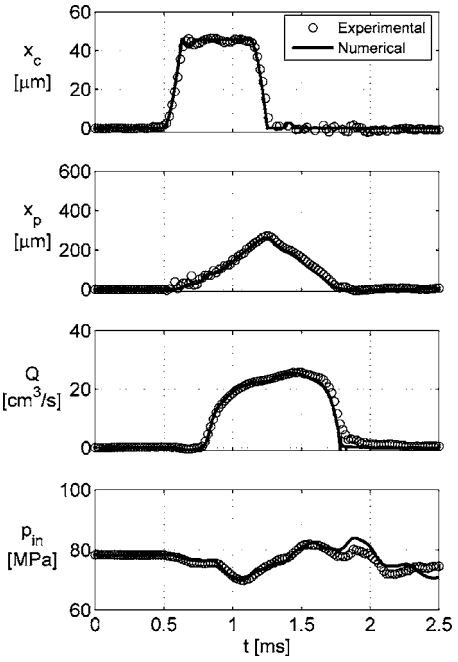

Fig. 16 Model validation—test conditions *B*

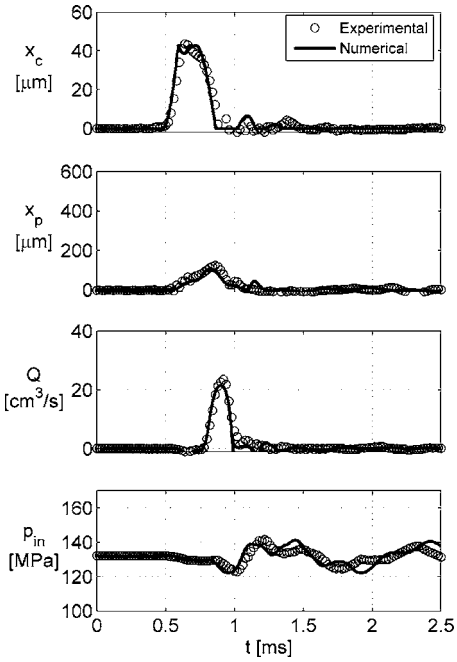

Fig. 18 Model validation—test conditions *D*

that constitute it; and (ii) implicitly validate the models of discharge coefficient and injector deformation developed in this work.

6.1 Discharge Coefficient of the Nozzle Holes. Figure 20 shows the computed nozzle hole discharge coefficient, μ_h, dependence upon needle-seat relative displacement, ξ, in accordance with the proposed model, in a wide range of operating conditions, as defined in Table 2. For completeness, the needle–seat discharge coefficient [26] is also reported is this figure.

Examining the discharge coefficient, μ_h, trends for the three main injections during the opening phase, it is interesting to note that for a given value of the needle lift, lower discharge coefficients are to be expected at higher operating pressures. This can be explained considering that the flow takes longer to develop if the pressure differential, and thus the steady-state velocity to reach, is higher.

The main injection trends also show the transition from the sinusoidal to the linear dependence of the transient discharge coefficient on needle lift.

The phase in which the needle has reached the maximum value and the discharge coefficient increases in time from unsteady to stationary values is not very evident in main injections, because the former increases enough during the opening phase to approach

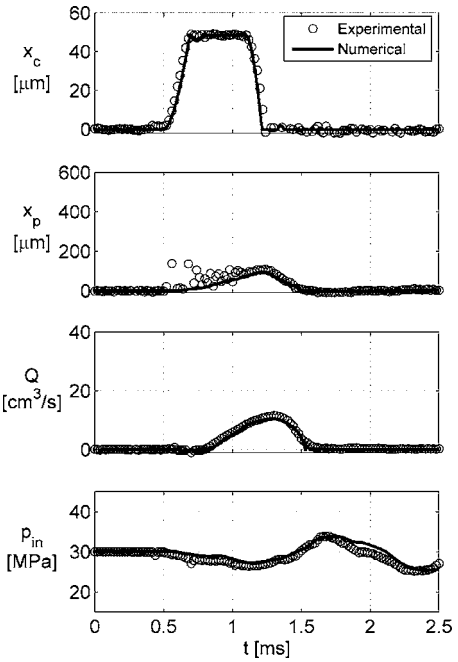

Fig. 17 Model validation—test conditions *C*

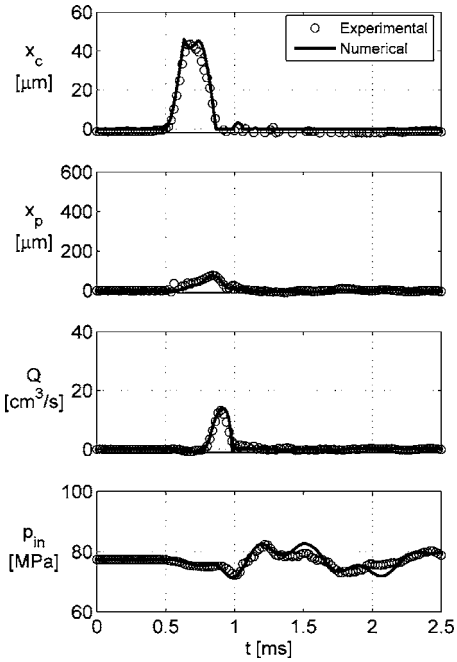

Fig. 19 Model validation—test conditions *E*

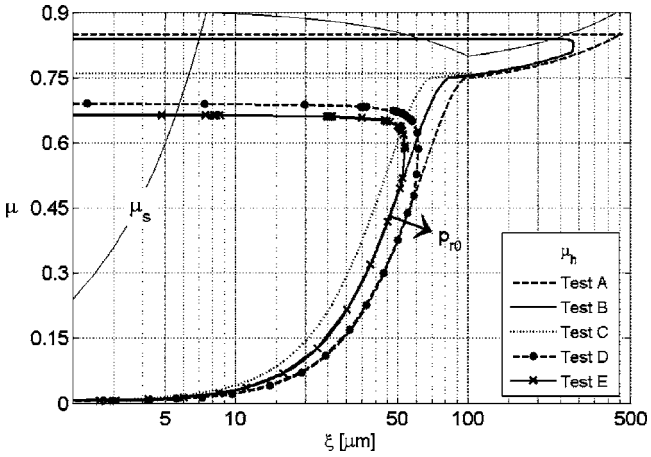

Fig. 20 Dependence of the nozzle-hole and needle-seat discharge coefficients on needle lift

the latter. This happens because the needle reaches sufficiently high lifts as to have reduced effect on the flow in the nozzle holes, and the longer injection allows time for complete flow development.

Conversely, during pilot injections (Tests *D* and *E*), the needle reaches lower maximum lifts, hence lower values of the unsteady discharge coefficient, so that the phase of transition to the stationary value lasts longer. The beginning of this transition can be easily identified by analyzing the curves marked with dots and crosses in Fig. 20. The point at which they depart from their main injection counterpart (same line style but without markers) marks the beginning of the exponential evolution in time to stationary value of discharge coefficient.

For both pilot and main injections, the nozzle hole discharge coefficient remains constant, and equal to the stationary value, during the injector closing phase, as shown by the horizontal profile of the trends in Fig. 20.

6.2 Discharge Coefficient of the Control Volume Holes. Figure 21 presents the calculated discharge coefficient and Reynolds number in the control volume holes *A* and *Z* for very low (30 MPa), medium (80 MPa), and very high (135 MPa) reference rail pressure, p_{r_0}. The discharge coefficient trends in both holes are similar, presenting a very steep rise as the flow develops, to reach very high stationary values (0.93–0.95). The Reynolds number can be directly linked to the pressure drop across the orifice, and the fact that the discharge coefficient seems to vary little in function of operative pressure drop suggests the absence of cavitation in the flow in the holes A and Z, in every possible injector working conditions. This result contrasts with what suggested by Refs. [6,14]. This discrepancy is mainly due to the fact that, in the present work, the correct inlet fillet radius to hole diameter ratio was accurately measured and was found to be relatively high (0.22–0.24), and its effect on the flow in the holes was accounted for with a suitable model.

Analyzing the trends predicted by the discharge coefficient model presented in Fig. 3, it becomes evident that the onset of cavitation causes a discontinuity in the hole behavior as, once cavitation occurs, the flow rate decreases for increasing pressure drops. As a result, it stands to reason that a large fillet was created at the inlet of the control volume holes, as this allowed the achievement of a higher degree of control over the injector, by eliminating a source of discontinuity in its behavior.

The model predictions suggest another benefit of creating a large fillet at the hole inlet. As can be noted by analyzing Fig. 21, the developed flow discharge coefficient presents only a very little dependence upon working pressure. In this way the injector designers eliminated another source of nonlinear effects on the valve dynamics, thus easing injection control.

6.2.1 Effects of Injector Body Deformation. The evaluation of the axial deformation of the injector moving elements (needle and control piston) and of the nozzle plays an important role in the simulation of the injector operation because these deformations may be significant when compared to the maximum needle lift. To demonstrate this, let us consider that when the injector under investigation was set up, the maximum needle-control piston lift was 364 μm. Applying the model developed in the first part of this work and considering the worst case scenario (operating pressure equal to the maximum allowed value, 140 MPa), we obtain deformations of approximately 106 μm for the control piston, 52 μm for the needle, and 16 μm for the nozzle. Thus, in these conditions, the maximum needle-control piston lift during operation can increase by about 50% with respect to the set up conditions.

The top graph in Fig. 22 shows the control piston lift at a rail pressure of 140 MPa generated with an ET_0 of 1230 μs, while the

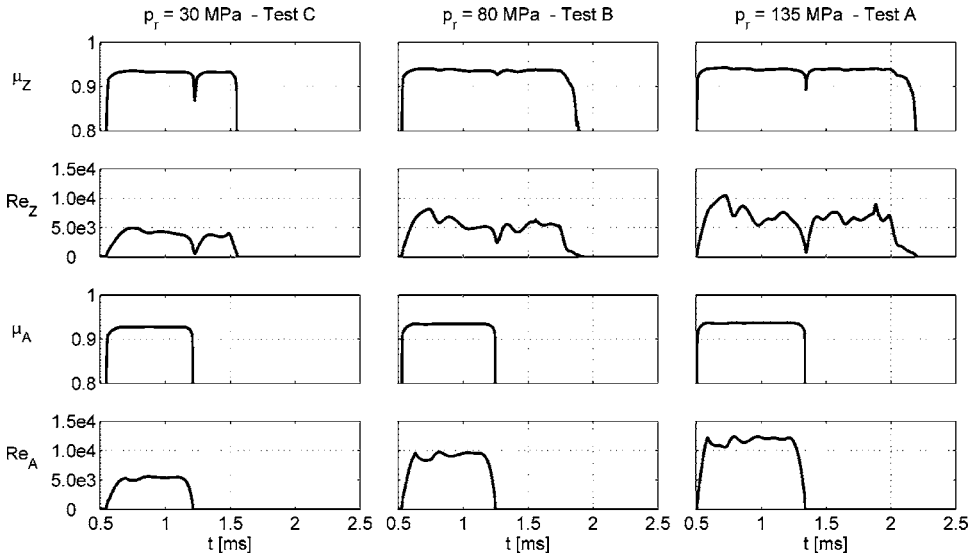

Fig. 21 Discharge coefficient and Reynolds number in the control volume holes *A* and *Z* at different rail pressure levels

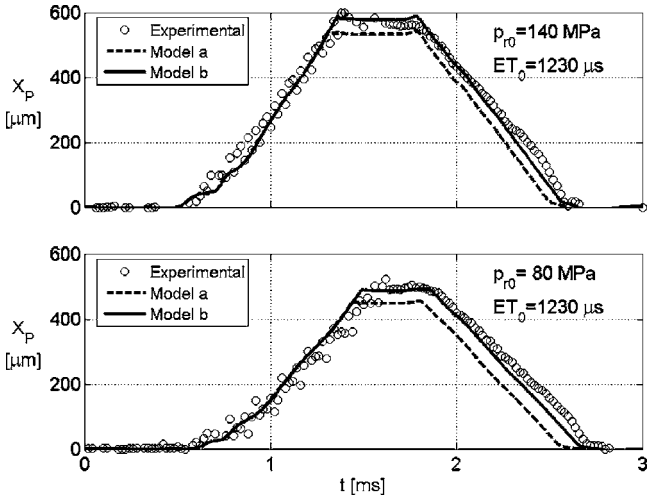

Fig. 22 Effect of injector body deformation on the maximum control piston stroke

bottom graph shows the same trend at a rail pressure of 80 MPa, and generated with the same value of ET_0. The experimental results are drawn by circular symbols, while lines refer to theoretical results. The dashed lines (Model a) show the theoretical needle-control piston lift evaluated by taking into account the axial deformation of the moving elements and nozzle, while the continuous lines (Model b) show the theoretical results evaluated by taking into account the injector body deformation too. The difference between the two models is significant, and it highlights the necessity of accounting for deformation of the entire injector body, if accurate predictions are sought.

Indeed, the maximum needle lift evaluation plays an important role in the simulation of the injector behavior in its whole operative field because it influences both the calculation of the injected flow rate (as the discharge coefficients of needle-seat and nozzle holes depend also on needle lift) and of the injector closing time, thus strongly affecting the predicted volume of fuel injected per cycle.

Considering that the deformation of the injector body also affects the maximum control valve stroke, a similar analysis was performed to evaluate its effects on injector performance. Our study showed that this parameter does not play as important a role as the maximum needle stroke, because the effective flow area of the *A* hole is smaller than the one generated by the displacement of the control valve pin, and thus it is the *A* hole that controls the efflux from the control volume to the tank.

7 Conclusions

A previously developed numerical model of a common-rail type diesel injector was refined here, with the aim of obtaining accurate predictions of injector operation in its entire application field.

The model of flow through the control volume feeding and discharge holes was further detailed, and silicone molds were used to accurately measure the shape of these holes, as it was shown to play an important role in determining the flow regime in the orifice. The diameter of the control volume holes was determined indirectly by matching the values of steady flow rate declared by the manufacturer. In this way, it was ensured that the modeled holes behaved as close as possible to the real ones.

The model of discharge coefficient of the nozzle holes was also improved. Experimental evidence had shown that flow in the nozzle holes is strongly affected by the position and movement of the needle during the injector opening phase. Hence, to reproduce this behavior, a transient discharge coefficient versus needle lift relationship was developed. It was also noted that, once the needle had reached its maximum lift during the injection, the discharge coefficient increased in time to reach the value measured at fixed needle lift in steady-state conditions, and then remained constant during the injector closing phase. A device for controlling the needle position was developed, and tests were performed with the aim of characterizing the stationary hole discharge coefficient in the function of needle position. Finally, the transition between transient and steady-state values of the discharge coefficient was modeled with a first-order system dynamics, with a time constant of 25 μs. During the injector closing phase, the discharge coefficient was kept constant.

The elasticity of needle, control piston, nozzle, and injector body was considered, thus enabling the model to take into account the variable deformation that these components show as a result of the action of fuel pressure, and its effect on injector performance. The main parameters through which deformation affects performance were identified as the maximum needle lift and the actual needle-seat relative displacement.

Experimentally measured and numerically obtained values of injected volume per stroke were compared, showing the ability of the model to reproduce with good accuracy the injector operation in its entire working field, which was explored in terms of energization time and working pressure.

Stricter validation tests were also performed in order to ensure that not only the injected quantity of fuel per cycle was correctly predicted, but also the evolutions in time of control valve and needle lift, injected flow rate, and pressure at the injector inlet were accurately estimated. This allowed us to trust model predictions of the evolution of each model variable, and thus use it for analyzing detailed aspects of injector operation, which cannot be easily, or at all, experimentally studied.

The results obtained with the model of discharge coefficient of the nozzle holes were analyzed, showing that, during the opening phase, and for the same needle position, higher operating pressures tend to result in lower values of the unsteady discharge coefficient, especially when it shows a sinusoidal dependence on needle lift. The analysis also evidenced how, during main injections, the value of the discharge coefficient at the end of the opening phase almost reaches the stationary value, so that little or no evolution time from unsteady to stationary values is registered. However, in pilot injections the unsteady value reached at relative maximum lift is lower (due to lower needle lift) and the transition phase during which the discharge coefficient increases to reach the stationary value lasts long enough to become evident.

The analysis of the discharge coefficient in the control volume holes showed how, due to an accurate hole inlet shape design, it was possible to avoid the occurrence of cavitation in the flow, and thus of discontinuities in the injector behavior. Moreover, the large radius used for the hole inlet fillet allowed us to reach very high values of discharge coefficient, which showed only a slight dependence on operating pressure, thus easing injector control by eliminating these nonlinear effects on control valve dynamics.

As far as the mechanical model was concerned, it was shown that deformation of injector components due to operating pressure can increase the maximum needle lift of about 50% of the setup value, and that this parameter plays a significant role in determining injector performance. Moreover, despite its bulkiness, the effects of injector body deformation on estimation of maximum needle lift was shown to be significant, and thus it should not be neglected. Maximum control valve lift was also affected by injector body deformation, but it was noted that this did not affect performance predictions, because at the lifts at which this effect becomes apparent, the efflux area generated between control valve pin and seat results is considerably larger than that of the *A* hole, so that the latter only controls the flow from control volume to tank.

Acknowledgment

The authors would like to thank the CRF (FIAT Research Centre) for its technical support.

Nomenclature

A = geometrical area (m^2)
C = uniform pressure chamber
c = wave propagation speed (m/s)
d = hole ‖ pipe diameter (m)
e = eccentricity (m)
E = Young's modulus (Pa)
EMI = einspritzmengenindikator—mean delivery meter
EVI = einspritzverlaufsindikator—flow rate meter
ET = injector solenoid energization time (s)
F = force (N)
f = friction factor
I = electric current (A)
K = coefficient
k = spring stiffness (N/m)
l = length (m)
m = mass (kg)
N = number of coil turns
p = pressure (Pa)
Q = flow rate (m^3/s)
r = rail ‖ fillet radius (m)
R = hydraulic resistance
Re = Reynolds number
S = surface area (m^2)
t = time (s)
u = average cross-sectional velocity of the fluid (m/s)
V = valve ‖ volume
W = energy (J)
X = distance (m)
x = displacement ‖ axial coordinate (m)
β = damping factor (kg/s)
γ = switch (0=nozzle closed,1=nozzle open)
Δ = increment ‖ drop
Φ = magnetic flux (Wb)
ξ = needle-seat relative displacement (m)
μ = contraction ‖ discharge coefficient
ρ = density (kg/m^3)
τ = wall shear stress ‖ time constant (Pa‖s)
$\mathfrak{R}$ = reluctance (H^{-1})

Subscripts

A = control-volume discharge hole
a = anchor
B = injector body
b = seat
C = compression
c = control valve
D = delivery
d = downstream
E = electromechanical
e = injection environment ‖ external
f = fuel
h = hole
l = inlet loss ‖ liquid phase
in = injector inlet
M = maximum value
m = magnetic
N = nozzle
n = needle
P = piston
R = reaction force
r = rail
S = sac
s = needle-seat
T = tank
u = upstream
v = vapor
vc = vena contracta
Z = control-volume feeding hole
0 = reference value

Superscripts

d = dynamic
r = relative
s = steady state

References

[1] Stumpp, G., and Ricco, M., 1996, "Common Rail—An Attractive Fuel Injection System for Passenger Car DI Diesel Engines," SAE Trans. No. 960870.
[2] Boehner, W., and Kumel, K., 1997, "Common Rail Injection System for Commercial Diesel Vehicles," SAE Trans. No. 970345.
[3] Schommers, J., Duvinage, F., Stotz, M., Peters, A., Ellwanger, S., Koyanagi, K., and Gildein, H., 2000, "Potential of Common Rail Injection System Passenger Car DI Diesel Engines," SAE Tech. Pap. Ser. 2000-01-0944.
[4] Badami, M., Mallamo, F., Millo, F., and Rossi, E. E., 2002, "Influence of Multiple Injection Strategies on Emissions, Combustion Noise and BSFC of a DI Common Rail Diesel Engines," SAE Tech. Pap. Ser. 2002-01-0503.
[5] Schmid, M., Leipertz, A., and Fettes, C., 2002, "Influence of Nozzle Hole Geometry, Rail Pressure and Pre-Injection on Injection, Vaporization and Combustion in a Single-Cylinder Transparent Passenger Car Common Rail Engine," SAE Tech. Pap. Ser. 2002-01-2665.
[6] Brusca, S., Giuffrida, A., Lanzafame, R., and Corcione, G. E., 2002, "Theoretical and Experimental Analysis of Diesel Sprays behavior From Multiple Injections Common Rail Systems," SAE Tech. Pap. Ser. 2002-01-2777.
[7] Park, C., Kook, S., and Bae, C., 2004, "Effects of Multiple Injections in a HSDI Diesel Engine Equipped With Common Rail Injection System," SAE Tech. Pap. Ser. 2004-01-0127.
[8] Henelin, N. A., Lai, M.-C., Singh, I. P., Zhong, L., and Han, J., 2002, "Characteristics of a Common Rail Diesel Injection System Under Pilot and Post Injection Modes," SAE Tech. Pap. Ser. 2002-010218.
[9] Beatrice, C., Belardini, P., Bertoli, C., Del Giacomo, N., and Migliaccio, M., 2003, "Downsizing of Common Rail D.I. Engines: Influence of Different Injection Strategies on Combustion Evolution," SAE Tech. Pap. Ser. 2003-01-1784.
[10] Canakci, M., and Reitz, R. D., 2004, "Effect of Optimization Criteria on Direct-Injection Homogeneous Charge Compression Ignition Gasoline Engine Performance and Emissions Using Fully Automated Experiments and Microgenetic Algorithms," J. Eng. Gas Turbines Power, **126**, pp. 167–177.
[11] Yamane, K., and Shimamoto, Y., 2002, "Combustion and Emission Characteristics of Direct-Injection Compression Ignition Engines by Means of Two-Stage Split and Early Fuel Injection," J. Eng. Gas Turbines Power, **124**, pp. 660–667.
[12] Dongiovanni, C., Negri, C., and Pisoni, D., 2003, "Macroscopic Spray Parameters in Automotive Diesel Injector Nozzles With Different Hole Shape," *Proceedings of the ASME ICED Spring Technical Conference*, Salzburg, Austria, May 11–14.
[13] Amoia, V., Ficarella, A., Laforgia, D., De Matthaeis, S., and Genco, C., 1997, "A Theoretical Code to Simulate the Behavior of an Electro-injector for Diesel Engines and Parametric Analysis," SAE Trans. No. 970349.
[14] Ficarella, A., Laforgia, D., and Landriscina, V., 1999, "Evaluation of Instability Phenomena in a Common Rail Injection System for High Speed Diesel Engines," SAE Tech. Pap. Ser. 1999-01-0192.
[15] Bianchi, G. M., Pelloni, P., and Corcione, E., 2000, "Numerical Analysis of Passenger Car HSDI Diesel Engines With the 2nd Generation of Common Rail Injection Systems: The Effect of Multiple Injections on Emissions," SAE Tech. Pap. Ser. 2001-01-1068.
[16] Bianchi, G. M., Pelloni, P., Filicori, F., and Vannini, G., 2000, "Optimization of the Solenoid Valve Behaviour in Common-Rail Injection Systems," SAE Tech. Pap. Ser. 2000-01-2042.
[17] Catalano, L. A., Tondolo, V. A., and Dadone, A., 2002, "Dynamic Rise of Pressure in the Common-Rail Fuel Injection System," SAE Tech. Pap. Ser. 2002-01-0210.
[18] Bianchi, G. M., Falfari, S., Pelloni, P., Filicori, F., and Milani, M., 2002, "A Numerical and Experimental Study Towards Possible Improvements of Common Rail Injectors," SAE Tech. Pap. Ser. 2002-01-0500.
[19] Bianchi, G. M., Falfari, S., Pelloni, P., Kong, S.-C., and Reitz, R. D., 2002, "Numerical Analysis of High-Pressure Fast-Response Common Rail Injector Dynamics," SAE Tech. Pap. Ser. 2002-01-0213.
[20] Payri, R., Climent, H., Salvador, F. J., and Favennec, A. G., 2004, "Diesel Injection System Modelling. Methodology and Application for a First-Generation Common Rail System," Proc. Inst. Mech. Eng., Part D (J. Automob. Eng.), **218**, pp. 81–91.
[21] Coppo, M., Dongiovanni, C., and Negri, C., 2004, "Numerical Analysis and Experimental Investigation of a Common Rail Type Diesel Injector," J. Eng. Gas Turbines Power, **126**, pp. 874–885.
[22] Von Kuensberg Sarre, C., Kong, S.-C., and Reitz, R. D., 1999, "Modeling the Effects of Injector Nozzle Geometry on Diesel Sprays," SAE Tech. Pap. Ser. 1999-01-0912.

[23] Nurick, W. H., 1976, "Orefice Cavitation and Its Effects on Spray Holes," J. Fluids Eng., **98**, pp. 681–689.
[24] Lefebvre, A. H., ed., 1989, *Atomization and Sprays*, Hemisphere, New York.
[25] Munson, B. R., Young, D. F., and Okiishi, T. H., eds., 1990, *Fundamentals of Fluid Mechanics*. Wiley, New York.
[26] Xu, M., Nishida, K., and Hiroyasu, H., 1992, "A Practical Calculation Method for Injection Pressure and Spray Penetration in Diesel Engines," SAE Trans. No. 920624.
[27] Catania, A. E., Dongiovanni, C., Mittica, A., Badami, M., and Lovisolo, F., 1994, "Numerical Analysis vs. Experimental Investigation of a Distribution type Diesel Fuel Injection System," J. Eng. Gas Turbines Power, **116**, pp. 814–830.
[28] Catania, A. E., Dongiovanni, C., Mittica, A., Negri, C., and Spessa, E., 1997, "Experimental Evaluation of Injector-Nozzle-Hole Unsteady Flow-Coefficients in Light Duty Diesel Injection Systems," *Proceedings of the 9th International Pacific Conference on Automotive Engineering*, Bali, Indonesia, November 16–21.
[29] Dongiovanni, C., 1997, Influence of Oil Thermodynamic Properties on the Simulation of a High Pressure Injection System by Means of a Refined Second Order Accurate Implicit Algorithm, ATA Automotive Engineering, pp. 530–541.
[30] Klopfenstein, R. W., 1971, "Numerical Differentiation Formulas for Stiff Systems of Ordinary Differential Equations," RCA Rev., **32**, pp. 447–462.
[31] LeVeque, R. J., 1994, *Numerical Methods for Conservation Laws*, Birkhuser Verlag, Berlin.
[32] Coppo, M., Dongiovanni, C., and Negri, C., 2006, "A Linear Optical Sensor for Measuring Needle Displacement in Common–Rail Diesel Injectors," Sens. Actuators, A, Paper No. 10.1016/j.sna.2006.05.038.

Enhanced Splash Models for High Pressure Diesel Spray

L. Allocca
Istituto Motori CNR,
Via Marconi, 8,
80125 Napoli, Italy
e-mail: l.allocca@im.cnr.it

L. Andreassi
e-mail: lucand@mail.mec.uniroma2.it

S. Ubertini
e-mail: stefano.ubertini@uniroma2.it

University of Rome "Tor Vergata",
Dip. di Ingegneria Meccanica,
Via del Politecnico 1-00133 Rome, Italy

*Mixture preparation is a crucial aspect for the correct operation of modern direct injection (DI) Diesel engines as it greatly influences and alters the combustion process and, therefore, the exhaust emissions. The complete comprehension of the spray impingement phenomenon is a quite complete task and a mixed numerical-experimental approach has to be considered. On the modeling side, several studies can be found in the scientific literature but only in the last years complete multidimensional modeling has been developed and applied to engine simulations. Among the models available in literature, in this paper, the models by Bai and Gosman (Bai, C., and Gosman, A. D., 1995, SAE Technical Paper No. 950283) and by Lee et al. (Lee, S., and Ryou, H., 2000, Proceedings of the Eighth International Conference on Liquid Atomization and Spray Systems, Pasadena, CA, pp. 586–593; Lee, S., Ko, G. H., Ryas, H., and Hong, K. B., 2001, KSME Int. J., **15**(7), pp. 951–961) have been selected and implemented in the KIVA-3V code. On the experimental side, the behavior of a Diesel impinging spray emerging from a common rail injection system (injection pressures of 80 and* 120 MPa*) has been analyzed. The impinging spray has been lightened by a pulsed laser sheet generated from the second harmonic of a Nd-yttrium-aluminum-garnet laser. The images have been acquired by a charge coupled device camera at different times from the start of injection. Digital image processing software has enabled to extract the characteristic parameters of the impinging spray with respect to different operating conditions. The comparison of numerical and experimental data shows that both models should be modified in order to allow a proper simulation of the splash phenomena in modern Diesel engines. Then the numerical data in terms of radial growth, height and shape of the splash cloud, as predicted by modified versions of the models are compared to the experimental ones. Differences among the models are highlighted and discussed.* [DOI: 10.1115/1.2432891]

Introduction

Diesel spray impingement onto cylinder walls is an important physical process affecting engine combustion efficiency and exhaust emissions. The deposition of liquid fuel on the walls has generally a negative effect on mixture formation and it is also the main cause of hydrocarbon emissions in small, high-speed direct injection Diesel engines [1,2]. Under cold start conditions the fuel droplets adhere to the wall, slowly vaporize, and consequently increase the unburned hydrocarbon emissions. However, at warmed-up engine conditions, the high-pressure spray impingement on the wall expands the total air-fuel volume, produces a stream of small secondary droplets, and enhances the gas entrainment in the spray, thus favoring the mixture preparation [3–5].

The spray impingement process involves three physical phases (droplet, wall, and gas in the near-wall region) and two main physical processes (wall spray development and wall film evolution) and it is influenced by parameters related to both physical and kinematic properties of the impinging droplets. In fact, the impinging spray behavior is significantly affected by the droplets velocity (related to the injection pressure and the orifice characteristics), the backpressure in the chamber and the wall and gas temperatures. Therefore, a better understanding of the interaction mechanisms, through the identification of the main parameters involved, is required in order to improve Diesel engine performance. At this time, there is definitely a lack of experimental data, of theoretical understanding of the involved thermofluid dynamic processes, and of numerical models for the spray impact phenomena.

Because of its complexity, spray impingement phenomena are difficult to be experimentally analyzed under engine operating conditions. Most of the experiments reported in the literature are carried out in simplified laboratory configurations. (i.e., on purpose built test chamber), where a high pressure spray impinges on flat plates [5–12]. Even if some of the complexities of the spray-wall interaction mechanism are removed, useful qualitative information are provided. However, particularly in the case of dense sprays (i.e., Diesel sprays), the quantitave data available from the experiments are limited by the difficulty of measuring droplet size and velocity distributions in the near-wall region.

On the other hand, computational modeling offers a promising opportunity to obtain detailed information on the spray-wall impingement and wall-film building. One of the first numerical formulations was presented by Naber and Reitz [13] who used the results of Wachters and Westerling [14] to define a droplet-wall interaction model to be linked to a multidimensional code. This model was then extended by Allocca et al. [15], who kept into account droplets atomization, by Eckause and Reitz [16], who investigated the heat transfer during impingement and by Guerrassi and Champoussin [17], who proposed the use of probability functions to calculate the secondary droplet diameters and normal velocities. Another significant study was performed by Wang and Watkins [18], who defined a new droplet-wall impingement model implemented in a two-phase CFD code. Their model could correctly predict the wall-spray radius but the height was underpredicted for all the analyzed test cases. One of the most interesting study was performed by Mundo et al. [19,20], who use empirical correlations given in the form of exponential or polynomial functions. Subsequently, Marengo et al. [21] improved this numerical model by incorporating the effects of wall film thickness on the splash regime. Based on the splash criteria defined by Mundo [19], Grover and Assanis [22] introduced a new splash model into the KIVA-3V code. Their model is based on the conservation of mass, tangential velocity, and kinetic energy and it uses specific

Contributed by the Internal Combustion Engine Division of ASME for publication in the JOURNAL OF ENGINEERING FOR GAS TURBINES AND POWER. Manuscript received April 19, 2006; final manuscript received September 4, 2006. Review conducted by Margaret Wooldridge.

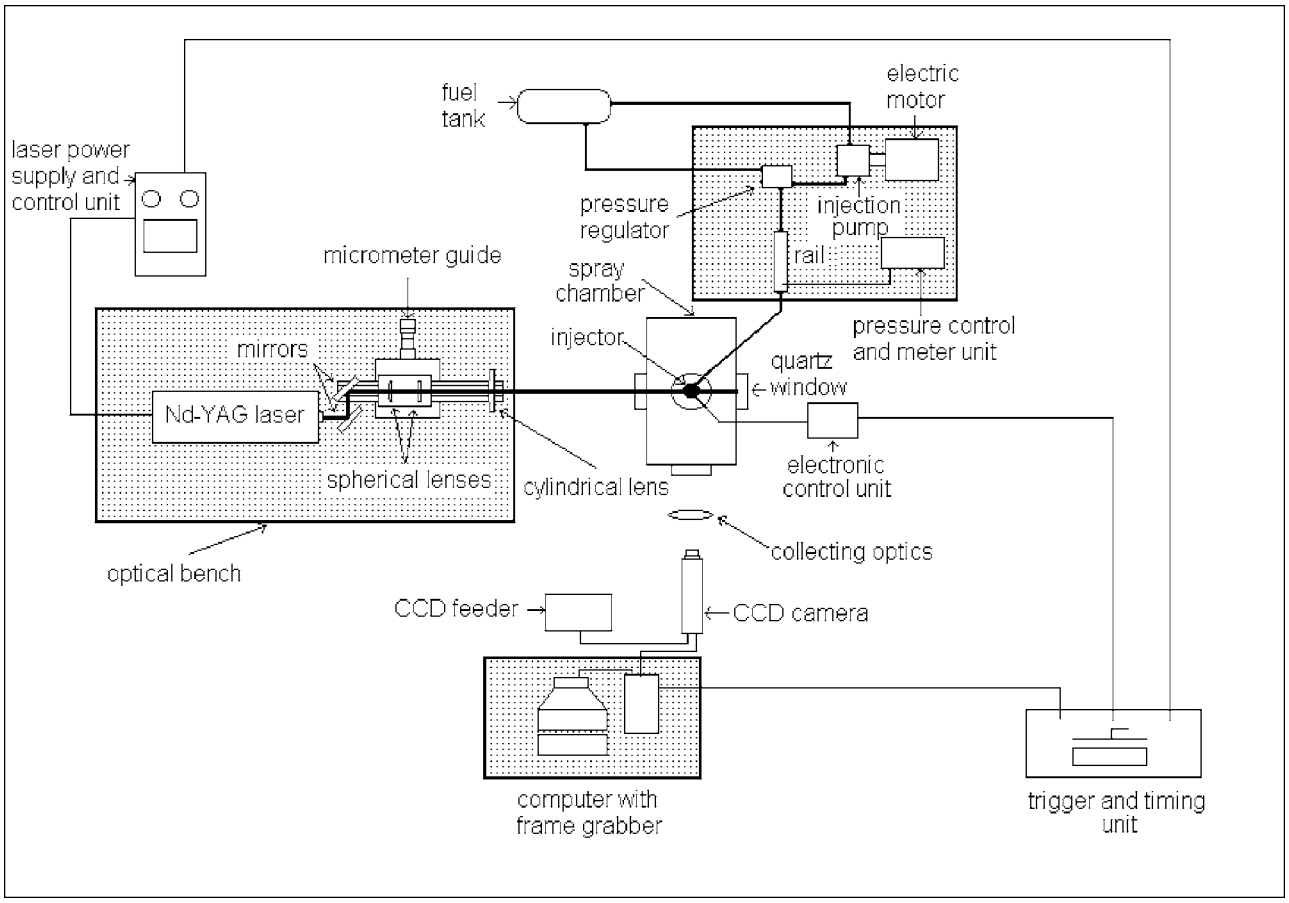

Fig. 1 Experimental apparatus

criteria to make a distinction between dry and wetted surface. Furthermore, the model incorporates a viscous dissipation effect and it distinguishes between the energy lost to viscous dissipation and to wall film formation. The submodel proposed by Stanton and Rutland [23] is always based on the experimental data of Mundo [19]. It involves the splash effect and the liquid film model and the ejection angle is uniformly determined from linear interpolation of the experimental data. Also Yarin and Weiss [24] performed a mixed experimental-numerical study on the splash phenomenon, showing that this effect corresponds to the velocity discontinuity occurring between the fluid moving outward from the splash location and slower fluid on the wall. In contrast to the study of Mundo [19], it is not observed any correlation between incident droplet size and normal velocity.

Bai and Gosman [25] developed a model that solves the conservation of energy of an impinging parcel and makes use of a number of assumptions derived from experimental data. More recently O'Rourke and Amsden [26,27] incorporated a new model in the KIVA code. In their model, the spray-wall interaction depends on the film thickness, the impinging droplet velocity component normal to the wall, the impinging drop diameter and the liquid density, viscosity and surface tension. Lee and Ryou [28] and Lee et al. [29] showed that some of the previous discussed models significantly underestimate the height of the splashed cloud. Accordingly, they suggested to include a static model of the wall film into the spray-wall interaction model. The proposed model includes three representative regimes (rebound, deposition, and splash).

In previous publications [30,31], we investigated the capabilities of some of the described numerical models to correctly represent this physical process. All these models were implemented into a modified version of the KIVA-3V code and numerical results were compared with experimental data. All the investigated models in their original formulation resulted to be inadequate to reproduce the splash phenomena under Diesel-like conditions (i.e., high impinging droplets velocity). Nevertheless, preliminary results showed that after slight modifications and a proper updating phase, the models derived from the formulation made by Bai and Gosman [25] and by Lee and Ryou [28] and Lee et al. [29] can provide a good agreement with the experimental data.

In the present paper, these numerical models are further investigated, analyzing their performance under different injection pressures and backpressures (typical small-bore Diesel engine chamber pressures during the injection phase).

The experimental tests are carried out in an on purpose built test chamber, where a high pressure spray impinges on flat plates [11,31]. The observation of the experimental splash phenomenon, allowed to identify the number of secondary droplets and the ejection angle as the critical parameters to be modified in the numerical models. Then a general enhanced formulation for both models is provided and the modified models are validated in terms of splash height and radius using experimental measurements at two different injection pressures (80 and 120 MPa) with a backpressure ranging from 0.1 to 5 MPa.

Finally, the liquid film formation and spreading are numerically investigated, as the film spreading characteristics and the fuel film thickness can provide insight into cold starting spray interactions.

Experimental Set-up and Procedures

The Diesel spray evolution and fuel-wall impingement is carried out in an optically accessible high-pressure vessel equipped

Table 1 Splash models main features

	BG	LR
Splash regime transition criterion	$We_0 > We_{crit}$ $We_{crit}=2630La^{0.183}$ for dry wall; $We_{crit}=1320La^{0.183}$	$E^2=\rho w_0 d_i/\sigma\, 1/\min(h_0/d_i,1)+\delta_{bl}/d_i > E^2_{crit}$
Ratio of the splashed mass to the incident mass	$r_m=m_s/m_i=0.2+0.6\cdot RN(0,1)$ for dry wall $r_m=0.2+0.9\cdot RN(0,1)$ for wetted wall	$r_m=0.2+0.6\cdot RN(0,1)$ for dry wall $r_m=0.2+0.9\cdot RN(0,1)$ for wetted wall.
Number and size of secondary droplets	$f(d_s)=1/d_{mean}e^{-(d_s/d_{mean})}$ $d_{mean}=d_i\left[r_m/30\cdot(We_0/We_{crit}-1\right]^{1/3}$	$n_s=0.187\cdot We_{0,n}-4.45$ $d_s=(r_m/n_s)^{1/3}d_i$
Secondary droplets velocity	$\boldsymbol{V}=C_f v_0 \boldsymbol{t}+w_s \boldsymbol{n}$ $w_{s,1}/w_{s,k}\approx \ln(d_{s,1}/d_i)/\ln(d_{s,k}/d_i)$ *for* $k=1,p$ $1/2\, m_s/p[\sum_{k=1}^{p}(w^2_{s,k})]=1/2\, m_i V_i^2+E_{I\sigma}-E_D-E_{S\sigma}$ $\phi=RN(0;2\pi)$	$We_s=(r_m/n_S)^{1/3}\,1/r_m\left[We_0-(4.5We_{0,n}\gamma^4_{max}/Re_0-12)\right]-12$ $\nu_s=0.452\cdot C_f\cdot Re^{1/8}_{0,n}\cdot w_0/\sqrt{\Psi}$ $\phi=RN(0;2\pi)$

with three large quartz windows. The volume of the bomb is 8×10^{-3} m^3 and it can be filled with nitrogen (N_2) at pressures up to 5.0 MPa.

A stainless-steel flat plate, 1.077 μm mean roughness, is used for impinging the fuel on the wall. It is located at 22 mm from the nozzle tip on an x-z-φ micrometric apparatus for positioning and tilting configurations. The plate can be heated by a 200 W electrical resistance in the range 298–773 K. The temperature is controlled by a Watlow 985 Series system (+/−1 °C) with a j-type thermocouple located at the center of the plate 0.5 mm under the impinging surface. The temperature of the gas in the vessel is measured by a thermocouple located in a non interfering location respect to the jet evolution. In this paper experimental results are reported only at a temperature of 298 K for both the plate and the gas.

The sprays are generated, in single-shot mode, by a common rail injection apparatus. Open software allows setting injection pressure, injection duration and timing via an electronic control unit. Injection pressures of 80 and 120 MPa are set with a nominal injection duration of 1.0 ms. The ISO 4113 calibration fluid is used. Its main characteristics are reported in Ref. [32]. An axial single-hole sacless nozzle injector type is used with the hole diameter and length of 0.18 and 1.0 mm, respectively.

The spray, emerging coaxially the chamber, is lightened by a pulsed laser sheet, 100 μm in thickness and 12 ns in duration, generated by a Nd-yttrium-aluminum-garnet laser operating on its second harmonic. The injector/laser/charge couple device (CCD) electronic command configuration allows carrying out planar images along the spray axis. The pictures are captured by a PULNIX TMC-6 CCD camera synchronized with the laser pulse providing images size of 768×568 pixels, 8 bit resolution.

A digital delay and pulse generator by Stanford Research System Inc. and a Tektronix TDS 684 B (1 GHz) four channel digital scope enable synchronizing, delaying, and controlling the laser/detector system with respect to TTL pulse command with a fine temporal resolution.

A schematic diagram of the experimental apparatus is reported in Fig. 1. Further details of the apparatus are reported in Refs. [9–11].

Image postprocessing is performed with a customized procedure employing both commercial and on purpose developed software in order to clean images (i.e., background noise related to light scattering of residual floating droplets and dust in the vessel, overexposures in high fuel density zones, and finely atomized nonimpacting droplets) and extract the parameters of interest (i.e., spray structure and morphology, jet cone angles, tip penetrations, and impact geometry). Each frame used for the present analysis results from an average of five synchronized frames.

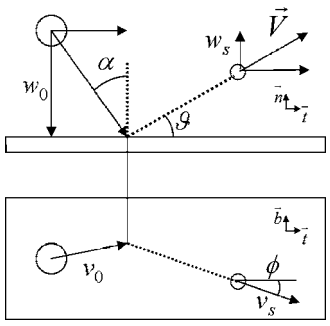

Fig. 2 Schematic diagram of impinging and splashed droplets

Spray, Splash, and Film Modeling

The main numerical code used in the present paper is a modified version of the KIVA-3V code that solves the three-dimensional equations of chemically reactive flows with sprays with a multiblock structured grid approach.

The atomization mechanism is simulated through a hybrid approach that distinguishes between a jet primary breakup, which is the atomization process that may take place inside the injector to the dense part of the spray, and a droplet secondary breakup, which describes how the parcels of liquid initially formed are transformed to a dilute spray, composed by small spherical droplets.

In the primary jet breakup phase a combined approach of turbulence, cavitation and droplet surface wave-like disturbance is used. The phenomenological flow model proposed by von Kuensberg Sarre et al. [33] is used to evaluate the flow regime inside the injector (turbulent or cavitating) and to simulate the effects of nozzle geometry on fuel injection and spray processes.

Table 2 Selected test cases

Case No.	Injectionpressure(MPa)	Backpressure (MPa)
1	80	0.1
2		1
3		3
4		5
5	120	0.1
6		1
7		3
8		5

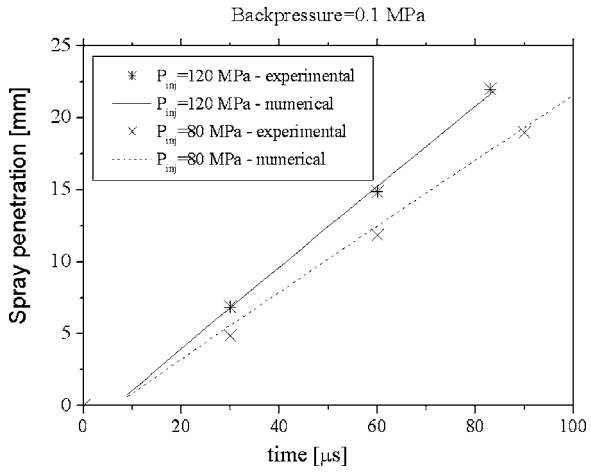

Fig. 3 Spray penetration: numerical-experimental comparison at different injection pressures

The resulting cavitation predictive submodel provides the initial conditions for the spray model in terms of initial parcels size and velocity.

The turbulent kinetic energy of the flow inside the injector nozzle and its dissipation rate are also evaluated to predict jet atomization due to turbulence as proposed by Hu and Gosman [34]. The possible cavitation effects are considered as a source of turbulent fluctuation inside the spray. The wave breakup (WB) model [35], based on a stability analysis of liquid jets, is also used to simulate primary atomization of liquid core. Each model provides a time scale of atomization. Assuming that the above mechanisms compete with each other, the time scale, which produces the fastest set-off of instability, is chosen to set-off the breakup event.

For the secondary breakup simulation, deformation and breakup of a liquid droplet by aerodynamic forces is classified through the Weber dimensionless number that defines the ratio between the inertia and the surface tension forces. A critical Weber number (We_c) fixed to 12, is the limit over which deformation leads to breakup. Depending on the intensity of the aerodynamic force, five distinct regimes are considered: vibrational, bag, chaotic, stripping, and catastrophic [36]. Each of these regimes is assumed to exist in a certain range of Weber number and for each regime a distinct secondary breakup modeling approach is used: the standard Taylor analogy breakup model [37] for the vibrational regime (slower droplets, usually at the periphery of the spray); the droplet deformation and breakup (DDB) approach [38] for the bag breakup; the WB model for the stripping regime [36]; a competition between the DDB model and the WB model for the chaotic regime; a competition between the *R-T* model [39] and the WB model for the catastrophic regime. Finally, the collision and the coalescence model of the original version of KIVA-3V is considered [37].

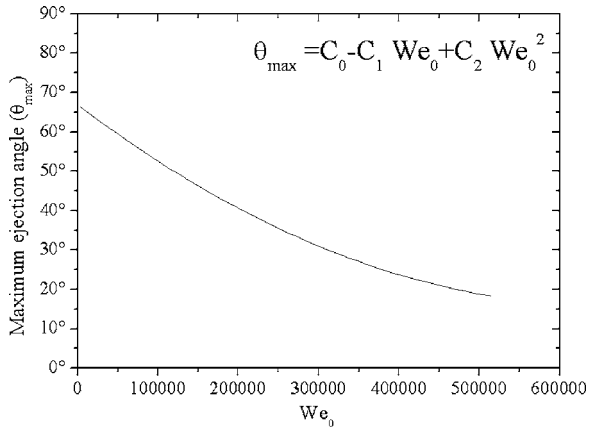

Fig. 4 Relationship between the maximum ejection angle and the impinging droplet normal Weber

Table 3 Major updates in BG model (the employed constants are C_0=66.8, C_1=1.54e-4, and C_2=1.17e-10)

	Original BG	Modified BG
Ejection angle θ	Random 5 deg$<\theta<$50 deg	Random 2 deg$<\theta<\theta_{max}$ $\theta_{max}=C_0-C_1We_0+C_2We_0^2$
Friction Coefficient C_f	0.7	0.95

A detailed description of several of the implemented submodels can be found in a previous paper [36].

Regarding the spray-wall interaction, four after-impingement regimes are considered with increasing impinging droplets Weber numbers [25]:

— stick, when the droplet forms liquid film and adheres to the surface in a nearly spherical form
— rebound, when the droplet bounces against the wall at low impact energy
— spread, when the droplet forms liquid film and, being its impact energy high enough, merges with the liquid film
— splash, when each droplet generates some secondary parcels and film

Considering that in modern small-bore Diesel engines the velocity of impinging droplets is usually very high (up to 250 m/s), due to the high injection pressures, the present analysis regards only the splash regime, which is the most frequent occurring one.

Among the models available in literature, the authors focused their attention on the works by Bai and Gosman [25] (BG model) and by Le and Ryou [28] and Lee et al. [29] (LR model), because of their performance and capability of representing the splash phenomenon, with particular emphasis on sprays with characteristics typical of modern small-bore direct injection (DI) Diesel engines [30,31]. Both models are based on mass and energy conservation laws and on empirical correlations.

The basic equations of these models are summarized in Table 1, which compares the models on the basis of:

- the splash criterion, which means the regime transition criterion used for predicting if splashing occurs.
- the ratio of the splashed mass to the incident mass. The total splashed mass is determined by means of the impinging mass. Bai and Gosman [25], Lee and Ryou [28], and Lee et al. [29] all make the hypothesis that for wetted wall the splashed mass may be even greater than the impinging mass since the secondary droplets may take some liquid out from the film.
- the secondary droplets size. The number and the size of splashed droplets are strictly related to each other by means

Table 4 Major updates in LR model (the employed constants are C_0=66.8, C_1=1.54e-4, and C_2=1.17e-10)

	Original LR	Modified LR
Ejection angle θ	from v_s (see Table 1)	random $2°<\theta<\theta_{max}$ $\theta=C_0-C_1We_0+C_2We_0^2$
Number of splashed droplets	N	$N/2$

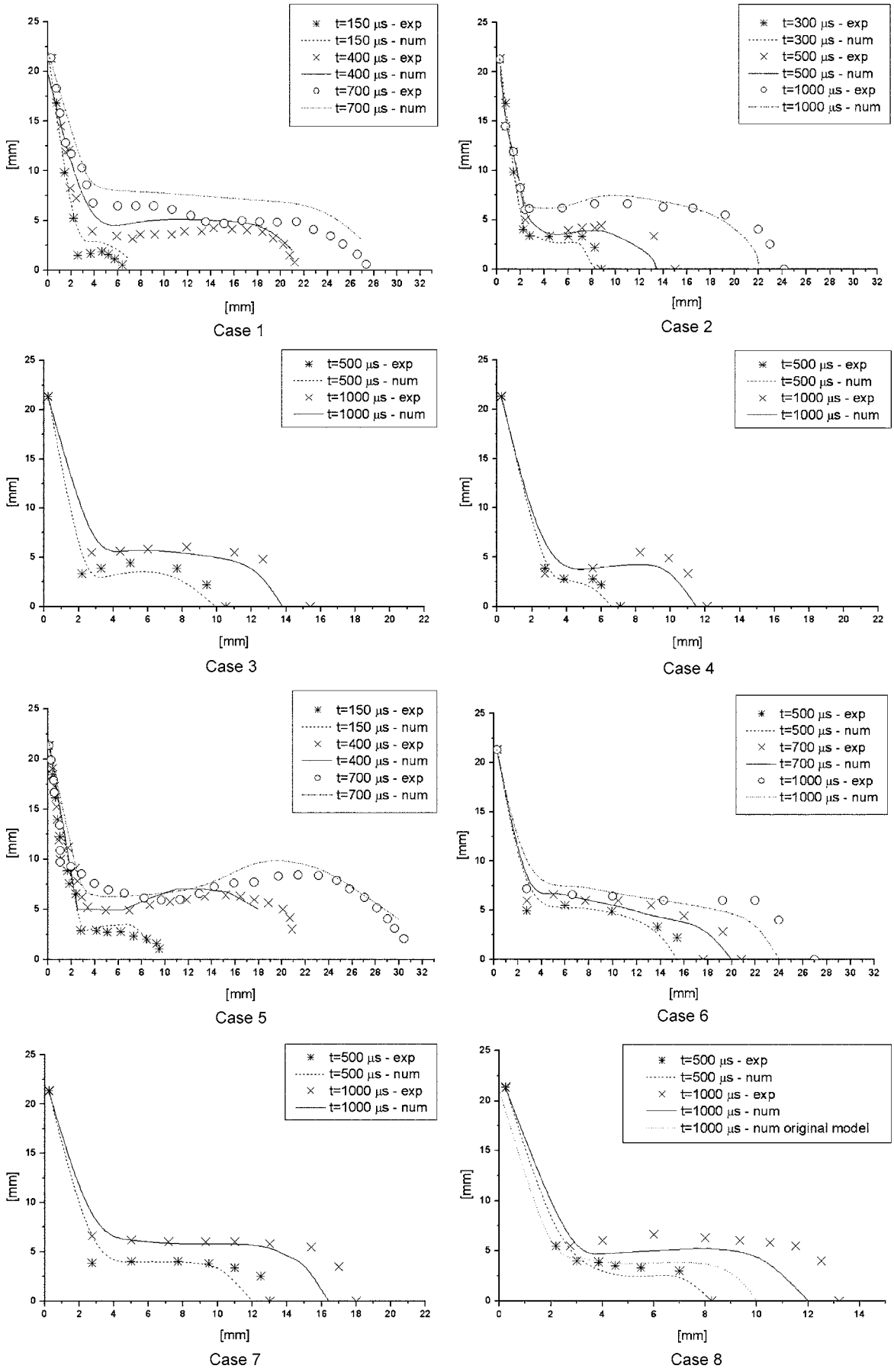

Fig. 5 Profiles of the splash cloud at different time from SOI: experimental-numerical (BG model) comparison

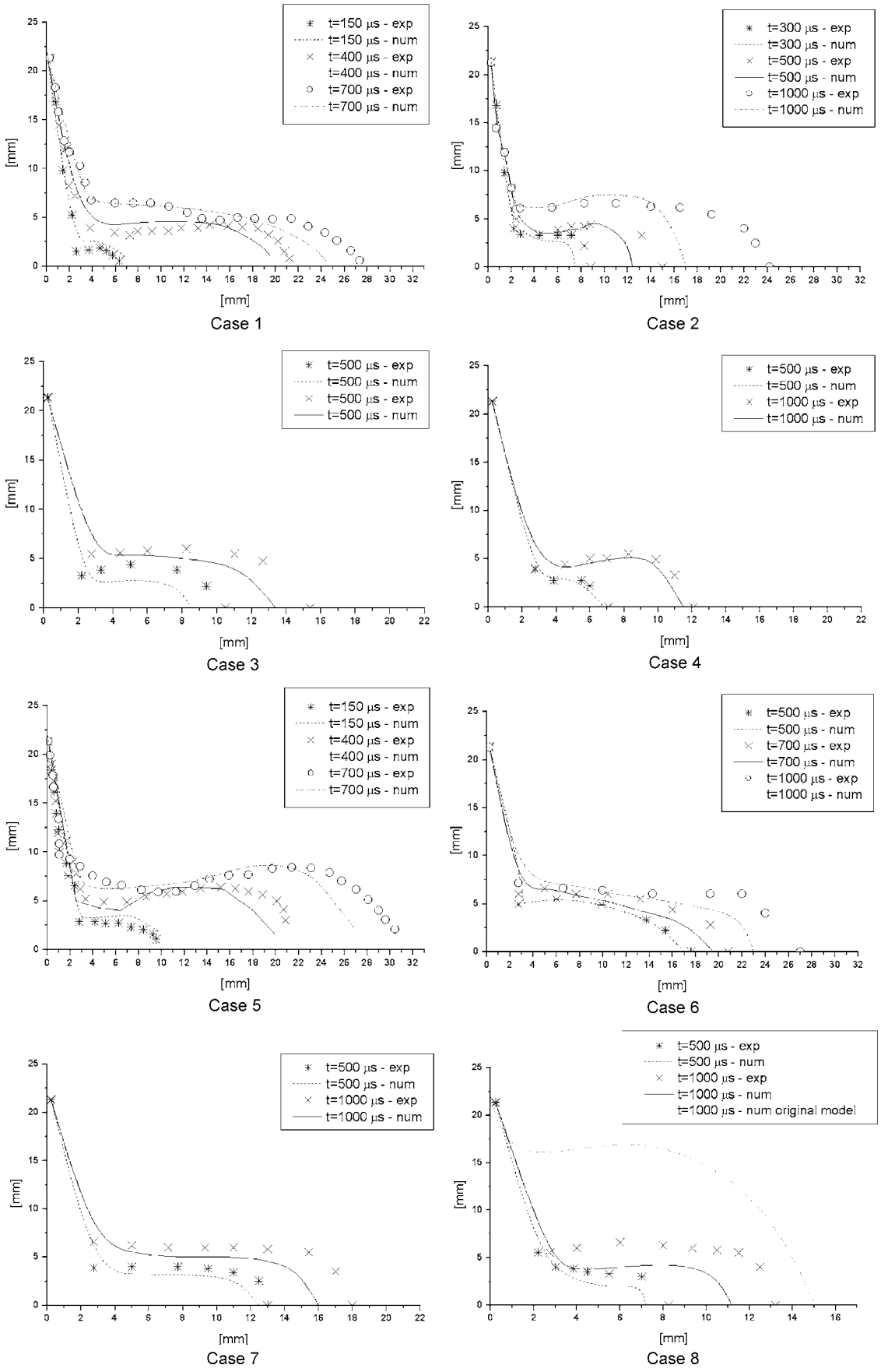

Fig. 6 Profiles of the splash cloud at different time from SOI: experimental-numerical (LR model) comparison

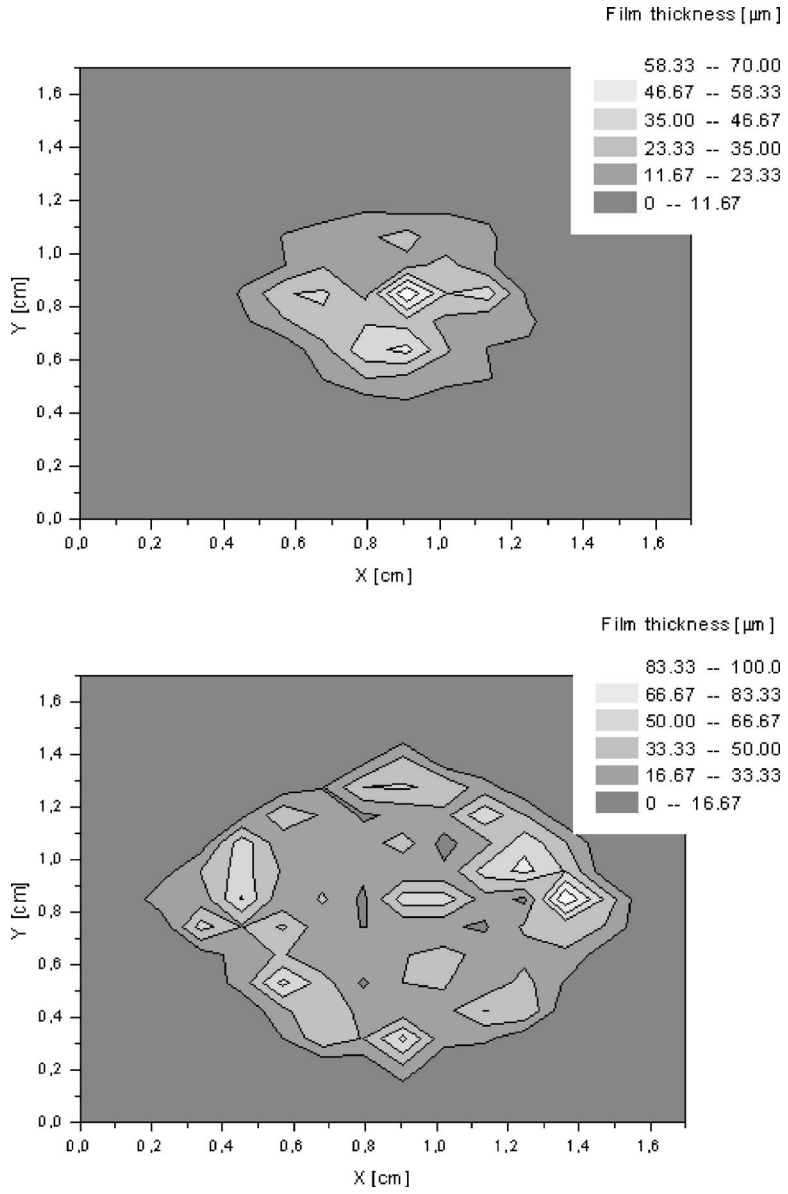

Fig. 7 Contours and thickness of wall films at 500 and 1000 μs after impingement—Case No. 4 - BG model

of the mass conservation principle. The BG model starts from the calculation of the droplets size on the basis of a prescribed distribution function, while the LR model uses an empirical formula to determine the number of splashed droplets.

- the secondary droplets velocity, which is the element that mainly characterizes the different models. Both models use the energy conservation principle with different assumptions and approximations. Figure 2 shows a schematic diagram of impinging and splashed droplets, highlighting the main kinematic parameters and the coordinate system.

A more detailed description of these features can be found in Refs. [30,31].

The wall film model derives from the research and O'Rourke and Amsden [27]. This model is able to represent the wall film dynamics keeping into account all the major physical processes affecting the liquid film including mass, momentum and energy contribution to the film due to the spray impingement, splashing effects, shear forces, heat transfer in and above the boundary layer, etc.

The major assumption of the model is that the fuel film is so thin that the film flow is laminar and that the inertial force can be neglected. This assumption stops existing close to sharp corners where an inertial separation criterion is considered.

A particle numerical model is used for the wall film for the compatibility with the spray model and for the possibility to easily calculate the film convective transport.

Numerical Results and Validation

The numerical results obtained through the BG and LR models for spray impingement were compared to the experimental data of the spray wall interaction under Diesel-like injection pressures. Two different injection pressures have been investigated (80 and 120 MPa) with a backpressure ranging from 0.1 to 5 MPa. Details

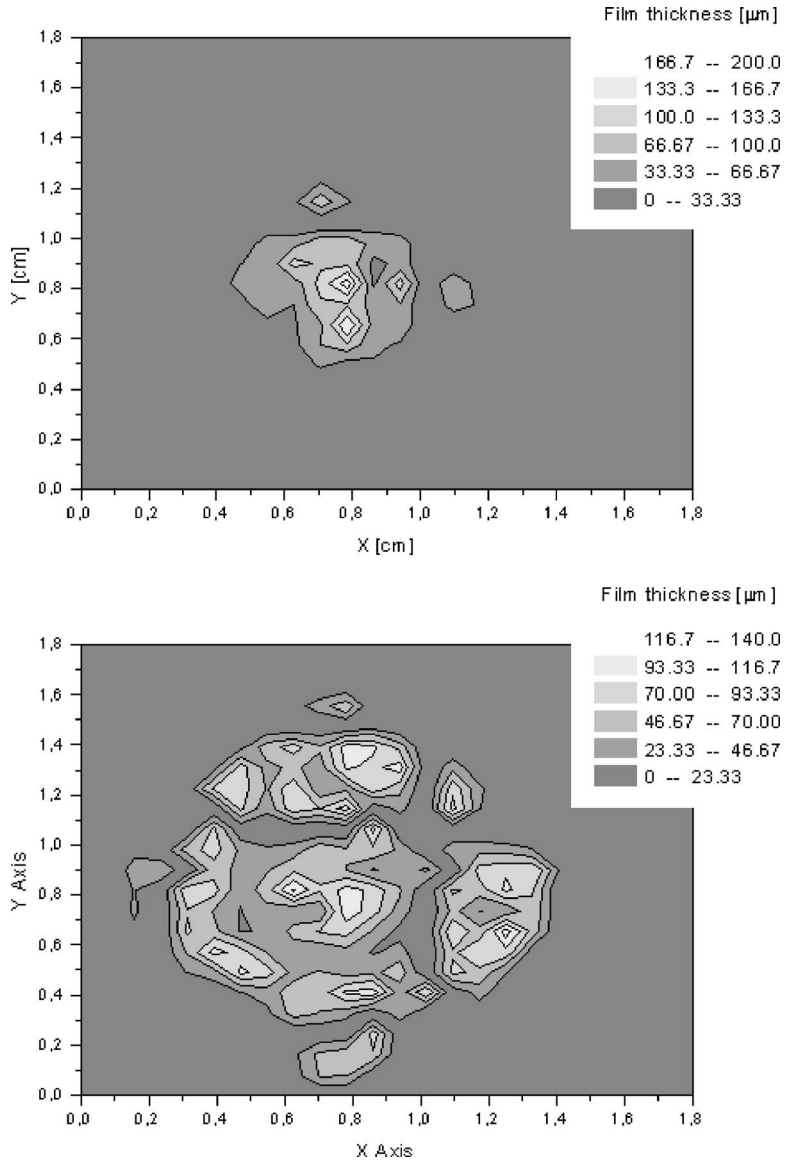

Fig. 8 Contours and thickness of wall film at 500 and 1000 μs after impingement—Case No. 4 - LR model

of the experimental-numerical tests are reported in Table 2. The computational domain used for the simulations is a $70\times70\times25$ mm^3 structured grid with a 1 mm spacing, fine enough to reduce the grid-size sensitivity of less than 1% in terms of spray penetration.

The spray initiation is based on the measured needle opening and closure times. The fuel flow rate law is made up of three parts: two for the opening and closure phases at constant slope and one part with constant fuel flow rate. A total of 10,000 sample parcels are introduced during the injection time.

Figure 3 shows the comparison between the experimental and numerical spray tip penetration with a backpressure of 0.1 MPa. A good agreement between numerical and experimental results is observed. It is worth noting that it is not possible to discriminate penetration regimes, due to the very high injection pressure and the very low backpressure.

Splash Results. The numerical data have been obtained with both BG and LR model, after a proper updating phase. In fact, the original BG model significantly underestimates the splash radial growth while the original LR one considerably overestimates splash height and underestimates the splash cloud radial growth (almost one half of the experimental one), as reported in a previous paper [31].

Comparing the experimental data and the numerical results given by the models in their original formulation, the inability of reproducing the splash phenomenon can be related to the number of secondary droplets generated by the spray-wall interaction (and then to the secondary droplets dimension) and to the tangential component of the splashed droplets velocity. In the LR model, in fact, the number of splashed droplets is a function of the Weber number by the experimental correlation reported in [13]. However, this correlation was extrapolated for a low velocity impinging spray. At high injection pressures this gives very small low-penetrating splashed droplets, thus resulting into an underprediction of the splash cloud radius. Therefore, the LR model has been modified by reducing of one half the number of splashed droplets. Moreover, in both the LR and the BG models the calculation of the tangential component of the splashed droplets velocity is based on a theoretical correlation resulting from the analysis of a low impinging velocity single droplet [24]. How-

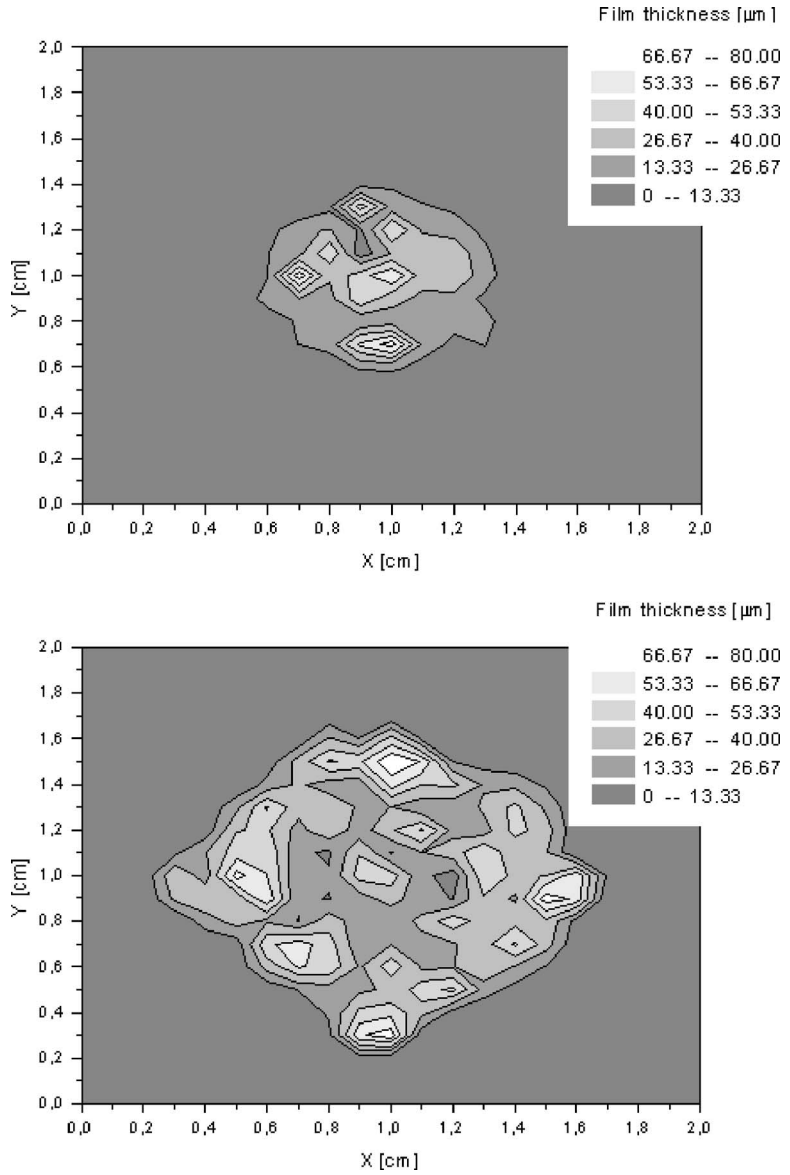

Fig. 9 Contours and thickness of wall films at 500 and 1000 μs after impingement—Case No. 8 - BG model

ever, the experimental results demonstrate that the effects of a spray droplet impacting onto a fluctuating film on a wall significantly differ from those of a single droplet impacting onto a stationary, uniform film.

Therefore, for both models, the direction of the splashed droplets velocity has been calculated by defining the ejection angle range as a function of the impinging droplet normal Weber number in order to keep into account the different operative conditions in terms of injection pressure and backpressure. Employing a relationship with the droplet normal Weber number as the variable should make the model general, as the spray characteristics before impingement are determined by multiple factors, not only injection and chamber gas pressure, but also orifice characteristics.

The employed relationship between the maximum ejection angle, θ_{max}, and We_0 is reported in the graph of Fig. 4. Moreover, in the updating phase of the BG model a friction coefficient value of 0.7 has been found. In the authors' opinion, considering that the majority of the spray is impinging on a wet wall, a high friction coefficient is more related to the fuel film, that makes the surface very smooth, than to the roughness of the plate surface. However, more experimental tests with different plate roughness would clarify this point.

Finally, regarding the number of secondary droplets in the LR model, the proposed empirical distribution produce very small droplets due to the high impinging We. Therefore, due to their insufficient inertia, the secondary droplets low penetrate in the gas chamber. Simply halving the number of secondary droplets calculated with the proposed empirical correlation has been found to produce satisfying results.

Major updates in BG and LR model are summarized in Tables 3 and 4, respectively.

These changes allow both models to reproduce with good accuracy the experimental splash cloud produced by Diesel-like high pressure sprays with different backpressures. A good agreement between numerical and experimental splash height and radial width for both models can be observed in Figs. 5 and 6 that show the spray profiles after wall impingement at different times after the state of injection (SoI) for the test cases reported in Table 2. The improvement from the original version of the models is demonstrated by the comparison of the predicted splash cloud

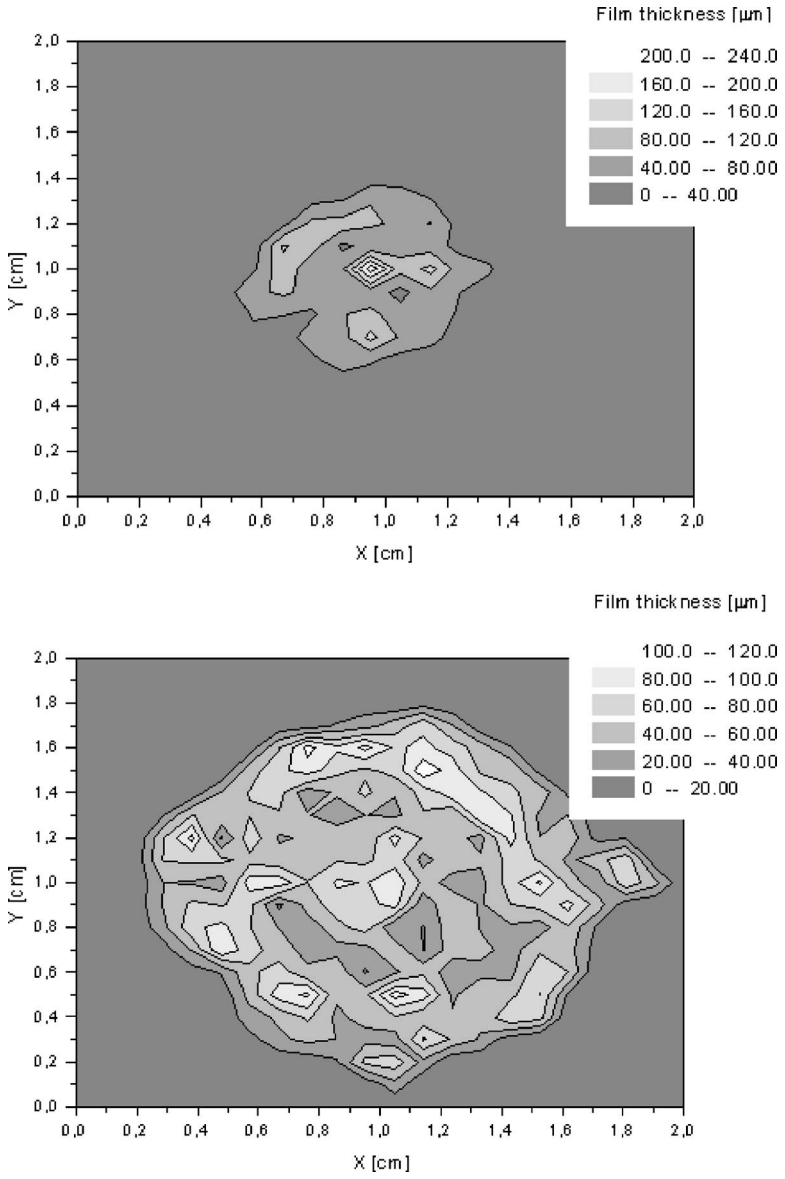

Fig. 10 Contours and thickness of wall films at 500 and 1000 μs after impingement—Case No. 8 - LR model

profiles in case No. 8 of Figs. 5 and 6.

Under almost all the defined operative conditions, the enhanced BG model gave better results than the LR one in terms of splash height, radial extension, and growth rate. In particular, the LR model underestimates almost everywhere radial growth and splash cloud thickness. This is probably related to the fact that the choice of halving the number of secondary droplets, made after an updating phase for case No. 5, does not correctly take into account the effects of the impinging droplets characteristics and of the backpressure.

Film Results. The wall film formation and thickness play a fundamental role in the spray-wall impingement phenomena. In fact, when a drop impinges on a thick film most of the drop energy is dissipated by the film itself resulting in less splashing or no splashing if the film is thick enough. Thus, a trade-off exists between spray impingement, prompting film spreading, and too much spray, causing an excessive amount of fuel in the same area in a short duration.

Figures 7 and 8 show the contours of liquid film distribution for different times with reference to case No. 4 for BG and LR models, respectively. The same characteristics are represented in Figs. 9 and 10 for BG and LR models under the operating conditions defined by case No. 8. For both models, the liquid films are propagating along with the radial direction but initially the incomplete symmetric contours can be seen. This is because the tangential velocity and the pressure sources in the film momentum are mainly affected by random postimpingement characteristics. Nevertheless, as time goes on, the film shape tends to be symmetric.

Some differences can be observed between the BG and LR models at the beginning of the spray impact on the wall. In fact, during this first phase, the LR model results are characterized by a significantly higher thickness, mainly located along the spray axis. This effect is directly connected to the different splash criterion as described in Table 1. Consequently, a considerable number of the impinging droplets tend to stick and spread along the surface. The majority of the drops momentum is transferred to the film, thus increasing the surface area of the piston bowl covered with fuel.

The film thickness profiles for both the models are reported in Figs. 11–14 under the operative conditions of the cases No. 4 and No. 8. The area around the stagnation point is immediately

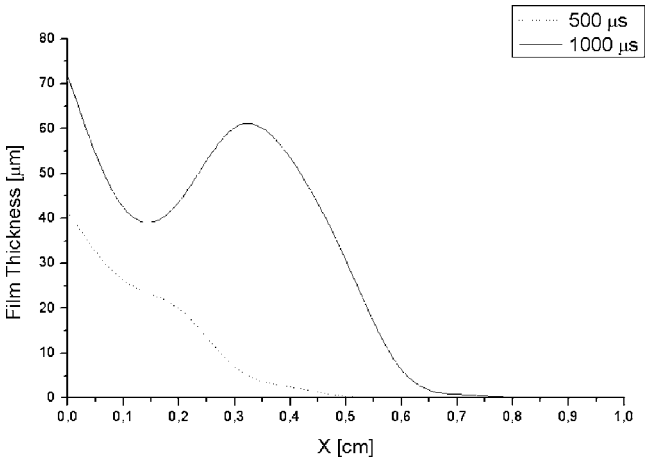

Fig. 11 Predicted film thickness distributions at different times for case No. 4 - BG model

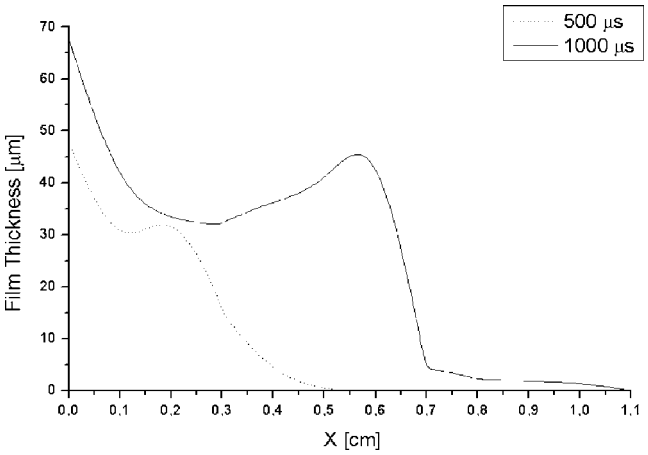

Fig. 13 Predicted film thickness distributions at different times for case No. 8 - BG model

flooded. Also in this case it is possible to observe a quite different behavior at the beginning and a substantially similar behavior in the last phase.

The predicted two peaks profile agrees with the results in Ref. [1] and is basically due to two phenomena. Initially, a liquid wall-jet is formed at the onset of impingement in this region which widens in the radial direction causing the liquid wall-jet to decelerate. Then, the film experiences the majority of the spray-film interaction in this region which results in splashing of secondary droplets thus reducing the amount of mass in film.

Conclusions

This paper presents a combined numerical and experimental analysis of high velocity diesel spray impinging on a flat wall, with the aim of developing accurate numerical models for simulating the process of spray-wall interaction in modern small-bore DI Diesel engines.

The experimental tests have been performed injecting into a 298 K temperature quiescent gaseous environment a nonevaporative fuel from a common-rail injection system. The experimental setup and the used image processing technique allowed obtaining detailed information on the shape and the structure of the impinging spray.

Regarding the numerical analysis, the authors have selected and implemented in a multidimensional code two splash models based on the conservation of mass and energy available in literature. As shown in a previous paper, at the high injection pressures typical of modern DI Diesel engines, both models, in their original version, were inadequate for correctly reproducing the splash phenomena.

In this paper we demonstrate that this inability is related to:

- the number of secondary droplets generated by the spray-wall interaction
- the tangential component of the splashed droplets velocity

Therefore, the models have been modified by reducing the number of splashed droplets and relating the ejection angle range limit to the impinging droplet Weber number, on the basis of the experimental results. The enhanced version of the model by Bai and Gosman [25] best performs in capturing the splash cloud height and radial extension, in all the time range at two different injection pressures (80 and 120 MPa) with a backpressure ranging from 0.1 to 5 MPa. This is probably related to the empirical relationship employed to evaluate the number of secondary droplets in the enhanced version of the LR model. Better results are expected relating the number of secondary droplets to the impinging droplets characteristics.

Finally, the wall liquid film distribution and thickness with the enhanced models are investigated, showing how the film formation, especially at the beginning of the spray impact on the wall, is significantly influenced by the chosen splash criterion.

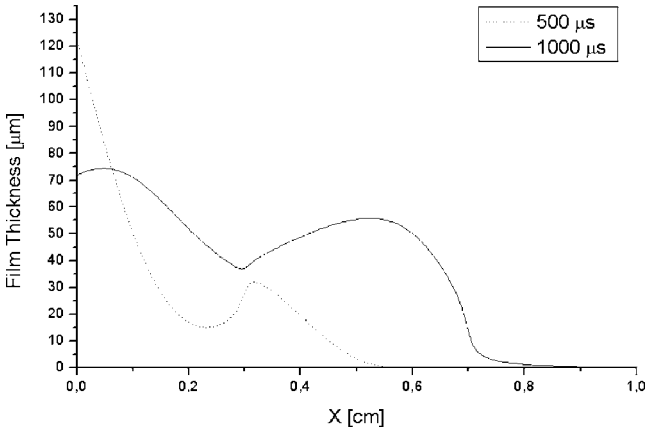

Fig. 12 Predicted film thickness distributions at different times for case No. 4 - LR model

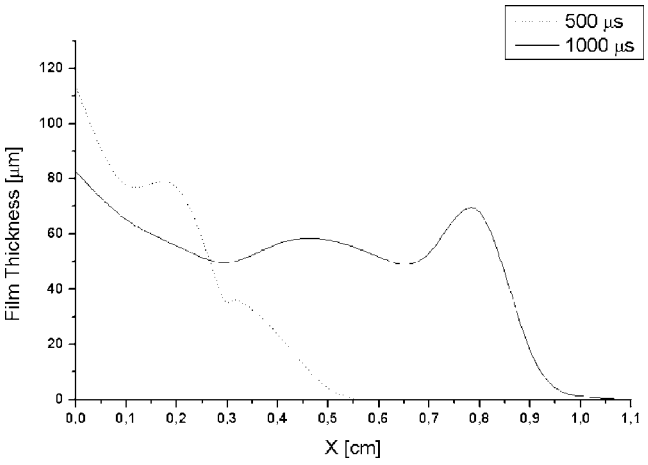

Fig. 14 Predicted film thickness distributions at different times for case No. 8 - LR model

Acknowledgment

This research is partially supported by the MIUR COFIN 2004.

Nomenclature

Dimensionless Numbers

La = Laplace number
Re = Reynolds number
We = Weber number

Vectors

$\mathbf{b}$ = $n \times t$
$\mathbf{n}$ = unit vector normal to the wall
$\mathbf{t}$ = unit vector tangent to the wall
$\mathbf{V}$ = splashed droplet velocity vector

Symbols

α = angle between the incident droplet velocity and the wall normal vector
β = value related to α
δ_{bl} = boundary layer thickness
ϕ = azimuthal angle
γ_{max} = dimensionless parameter
θ = ejection angle
ρ = fuel density
σ = fuel surface tension
Ψ = constant used to calculate the splashed droplet tangential velocity in the LR model
$C_{0,1,2}$ = model constants (relationship θ_{max} versus We_0)
C_f = friction coefficient
d_i = incident droplet diameter
d_{mean} = mean diameter related to d_i
d_s = splashed droplet diameter
E = splash impact energy
E_{crit} = critical value of E (57.7)
E_D = dissipative energy loss
$E_{I\sigma}$ = incident droplet surface energy
$E_{S\sigma}$ = splashed droplets surface energy
h_0 = film thickness
m_i = incident droplet mass
m_s = splashed droplet mass
n_s = number of splashed droplet per impinging parcel
r_m = splashed to incident mass ratio
RN = random number
v_0 = incident droplet velocity component tangential to the wall
v_s = splashed droplet velocity component tangential to the wall
We_0 = incident droplet Weber number
We_{crit} = critical Weber number
We_s = splashed droplet Weber number
w_0 = incident droplet velocity component normal to the wall
w_s = splashed droplet velocity component normal to the wall

References

[1] Hong, K., Lee, S. H., and Ryou, H. S., 2001, "Modelling of Wall Films Formed by Impinging Diesel Sprays," SAE Technical Paper No. 2001-01-3228.
[2] Gavaises, M., Theodorakakos, A., and Bergeles, G., 1996, "Modelling Wall Impaction of Diesel Sprays," Int. J. Heat Fluid Flow, **17**, pp. 130–138.
[3] Mohammadi, A., Kidoguki, Y., and Miwa, K., 2002, "High Time-Space Resolution Analysis of Droplets Behavior and Gas Entrainment into Diesel Sprays Impinging on Walls," 16th ICLASS Europe Meeting, Germany.
[4] Borthwick, F. P., and Farrel, P. V., 2002, "Fuel Injection Spray and Combustion Chamber Wall Impingement in Large Bore Diesel Engines," SAE Technical Paper No. 2002-01-0496.
[5] Katsura, N., Saito, M., Senda, J., and Fujimoto, H., 1989, "Characteristics of a Diesel Spray Impinging on a Flat Wall," SAE Technical Paper No. 890264.
[6] Saito, A., Kawamura, K., Watanabe, S., Takahashi, T., and Tuzuki, N., 1993, "Analysis of Impinging Spray Characteristics under High-Pressure Fuel Injection," Trans. Jpn. Soc. Mech. Eng., Ser. B, **59**, pp. 3290–3295.
[7] Fujimoto, H., Senda, J., Nagae, M., Hashimoto, A., Saito, M., and Katsura, N., 1990, "Characteristics of a Diesel Spray Impinging on a Flat Wall," *Proceedings of COMODIA 90 Int. Symposium on Diagnostic and Modeling of Combustion in I.C. Engines*, Kyoto, Japan, pp. 193–198.
[8] Arcoumanis, C., and Chang, J. C., 1994, "Flow and Heat Transfer Characteristics of Impinging Transient Diesel Sprays," SAE Technical Paper No. 940678.
[9] De Vita, A., Di Angelo, L., and Allocca, L., 2002, "Early Injection and Time-Resolved Evolution of a Spray for GDI Engines," ASME Fluids Engineering Division Summer Meeting, Montreal.
[10] Di Stasio, S., and Allocca, L., 2000, "Influence of the Gas Ambient Nature on Diesel Spray Properties at High Injection Pressure: Experimental Results," THIESEL 2000, Valencia, Spain.
[11] Allocca, L., De Vita, A., and Di Angelo, L., 2002, "Wall-Impingement Analysis of a Spray From a Common Rail Injection System for Diesel Engines," THIESEL 2002, Valencia, Spain.
[12] Winterbone, D. E., Yates, D. A., Clough, E., Rao, K. K., Gomes, P., and Sun, J. H., 1994, "Quantitative Analysis of Combustion in High-Speed Direct Injection Diesel Engines," COMODIA 94 July 11–14, 1994 Yokohama, Japan.
[13] Naber, J. D., and Reitz, R. D., 1988, "Modeling Engine/Spray Wall Impingement," SAE Technical Paper No. 881316.
[14] Wachters, L. H. J., and Westerling, N. A. J., 1966, "The Heat Transfer From a Hot Wall to Impinging Water Drops in the Spheroidal State," Chem. Eng. Sci., **21**, pp. 1047–1056.
[15] Allocca, L., Amato, U., Bertoli, C., and Corcione, F. E., 1990, "Comparison of Models and Experiments for Diesel Fuel Sprays," COMODIA 1990, Int. Symposium on Diagnostic and Modelling of Combustion in IC Engines, Kyoto, Japan, pp. 225–261.
[16] Eckause, J. E., and Reitz, R. D., 1995, "Modeling Heat Transfer to Impinging Fuel Sprays in Direct-Injection Engines," Atomization Sprays, **5**, pp. 213–242.
[17] Guerrassi, N., and Champoussin, J. C., 1996, "Experimental Study and Modeling of Diesel Spray/Wall Impingement," SAE Technical Paper No. 960864.
[18] Wang, D. M., and Watkins, A. P., 1993, "Numerical Modeling of Diesel Spray Impinging on Flat Walls," Int. J. Heat Fluid Flow **14**, pp. 301–312.
[19] Mundo, C., Sommerfeld, M., and Tropea, C., 1995, "Droplet-Wall Collisions: Experimental Studies of the Deformation and Breakup Process," Int. J. Multiphase Flow, **21**(2), pp. 151–173.
[20] Mundo, C., Sommerfeld, M., and Tropea, C., 1996, "Spray Wall Impingement Phenomena: Experimental Investigations and Numerical Predictions," 12th Annual Conference of ICLASS Europe, Lund, Sweden, pp. 19–21.
[21] Marengo, M., Steigleder, T., and Tropea, C., 1996, "Aufprall von Tropfen auf Flussigkeitsfilmen," Workshop uber Sprays, Erfassung von Spruhvorgangen und Techniken der Fluidzerstaubung, pp. A 3-1–A 3-8.
[22] Grover, R. O., Jr., and Assanis, D. N., 2001, "A Spray Wall Impingement Model Based Upon Conservation Priciples," Fifth International Symposium on Diagnostics and Modeling of Combustion in Internal Combustion Engines, pp. 551–559.
[23] Stanton, D. W., and Rutland, C. J., 1996, "Modelling Fuel Film Formation and Wall Interaction in Diesel Engines," SAE Technical Paper No. 960628.
[24] Yarin, A. L., and Weiss, D. A., 1995, "Impact of Drops on Solid Surfaces: Self-Similar Capillary Waves, and Splashing as a New Type of Kinematic Discontinuity," J. Fluid Mech., **283**, pp. 141–173.
[25] Bai, C., and Gosman, A. D., 1995, "Development of Methodology for Spray Impingement Simulation," SAE Technical Paper No. 950283.
[26] O'Rourke, P. J., and Amsden, A. A., 1996, "A Particle Numerical Model for Wall Film Dynamics in Port-Injected Engines," SAE Technical Paper No. 961961.
[27] O'Rourke, P. J., and Amsden, A. A., 2000. "A Spray/Wall Interaction Submodel for the KIVA-3V Wall Film Model," SAE Technical Paper No. 2000-01-0271.
[28] Lee, S., and Ryou, H., 2000, "Modeling of Spray-Wall Interactions Considering Liquid Film Formation," *Proceedings of the Eighth International Conference on Liquid Atomization and Spray Systems*, Pasadena, CA, pp. 586–593.
[29] Lee, S., Ko, G. H., Ryou, H., and Hong, K. B., 2001, "Development and Application of a New Spray Impingement Model Considering Film Formation in a Diesel Engine," KSME Int. J., **15**(7), pp. 951–961.
[30] Andreassi, L., and Ubertini, S., 2005, "Multidimensional Modeling of Spray Impingement in Modern Diesel Engines," SAE Technical Paper No. 2005-24-092.
[31] Allocca, L., Andreassi, L., and Ubertini, S., 2006. "Evaluation of Splash Models With High-Pressure Diesel Spray," SAE Technical Paper No. 2006-01-1117.
[32] International Standard (1998) ISO 4113, 2nd ed., 1998-11-15.
[33] von Kuensberg Sarre, C. K., Kong, S. C., and Reitz, R. D., 1999, "Modeling the Effects of Injector Nozzle Geometry on Diesel Sprays," SAE Technical Paper No. 1999-01-0912.
[34] Hu, K., and Gosman, A. D., 1991, "A Phenomenological Model of Diesel Spray Atomization," *Proc. of the International Conference on Multiphase Flows*, Tsukuba, Japan.
[35] Reitz, R. D., and Diwakar, R., 1987, "Structure of High Pressure Fuel Sprays," SAE Technical Paper No. 870598.
[36] Bella, G., Rocco, V., and Ubertini, S., 2002, "Combustion and Spray Simulation of a DI Turbocharged Diesel Engine," 2002 SAE Trans. J. Engines, **111**,

pp. 2549–2565.
[37] O'Rourke, P. J., and Amsden, A. A., 1987, "The Tab Method for Numerical Calculation of Spray Droplet Breakup," SAE Technical Paper No. 872089.
[38] Ibrahim, E. A., Yang, H. Q., and Przekwas, A. J., 1993, "Modeling of Spray Droplets Deformation and Breakup," J. Propul. Power, **9**, pp. 651–654.
[39] Patterson, M. A., and Reitz, R., 1998, "Modeling the Effects of Fuel Spray Characteristics on Diesel Engine Combustion and Emission," SAE Technical Paper No. 980131.

Journal of Engineering for Gas Turbines and Power

Technical Brief

Effect of Vortex Flow on Heat Transfer to Combustion Chamber Wall

A. Ghafourian
Department of Aerospace Engineering,
Sharif University of Technology,
P.O. Box 11365-9567,
Tehran, Iran
e-mail: Ghafourian@sharif.edu

M. H. Saidi[1]
School of Mechanical Engineering (CEEC),
Sharif University of Technology,
P.O. Box 11365-9567,
Tehran, Iran
e-mail: Saman@sharif.edu

S. Jahangirian
e-mail: Jahangirian@mehr.sharif.edu

M. Abarham
e-mail: Abarham@mehr.sharif.edu

Sharif University of Technology,
P.O. Box 11365-9567,
Tehran, Iran

A new experimental facility was designed, fabricated, and tested to model and study the effect of bidirectional swirl flow on the rate of heat transfer to combustion chamber walls. Reduction of this heat transfer can result in time and cost of design and fabrication methods of combustion chambers. The experimental study was performed using propane and air with oxygen as fuel and oxidizer, respectively. For similar flow rates, in cases where bidirectional flow was present, wall temperature reductions of up to 70% were observed. In cases where only some of the oxidizer was injected from the chamber end to generate the bidirectional swirl flow, the lowest wall temperature existed. This can be due to better mixing of fuel and oxidizer and absence of hot spots in the combustion core. [DOI: 10.1115/1.2431386]

[1]To whom correspondence should be addressed.

Submitted to ASME for publication in the JOURNAL OF ENGINEERING FOR GAS TURBINES AND POWER. Manuscript received August 14, 2005; final manuscript received July 28, 2006. Review conducted by Dilip R. Ballal.

Introduction

Vortex flows taking place in many combustion chambers have direct effects on boundary layers and on the rate of heat transfer between flow field and walls. Therefore, controlling the quality of vortices, the combustion efficiency can be increased and the location of energy release can be controlled. Marble [1] studied growth of diffusion flame in a vortex structure. The hot reaction zone location is strongly influenced by the flow field structure.

Chiaverini et al. [2] worked on vortex trust chambers employing an oxidizer swirl injector just upstream of the converging section of nozzle to generate a coaxial vortex flow field. They found substantial reduction in chamber wall temperature. Vyas et al. [3] derived an exact solution for the flow field of a bidirectional coaxial vortex. This study proved that the flow does not short circuit from the injection point to the exit nozzle, but rather a tendency exists for the flow to go all the way up to one end and then return through a core flow, which is referred to as a bidirectional flow.

Theoretical Background

Tangential vortices have the advantage of being nonperiodic in comparison to longitudinal vortices. Previous theoretical modeling of industrial cyclones has proven the existence of bidirectional tangential swirl flow in such chambers. A rather complete analysis of this type of flow is presented in the work of Bloor and Ingham [4]. Ignoring the small transition zone at the inlet to the chamber, the rest of the flow is assumed to be axsisymmetric. Assuming: steady, inviscid, incompressible, rotational, and nonreactive, the governing equations can be simplified as [3]

$$\frac{1}{\bar{r}}\frac{\partial(\bar{r}\bar{u}_r)}{\partial\bar{r}}+\frac{\partial(\bar{u}_z)}{\partial\bar{z}}=0 \tag{1}$$

$$\bar{u}_r\frac{\partial\bar{u}_r}{\partial\bar{r}}+\bar{u}_z\frac{\partial\bar{u}_r}{\partial\bar{z}}-\frac{\bar{u}_\theta^2}{\bar{r}}=-\frac{1}{\bar{\rho}}\frac{\partial\bar{P}}{\partial\bar{r}} \tag{2}$$

$$\bar{u}_r\frac{\partial\bar{u}_\theta}{\partial\bar{r}}+\frac{\bar{u}_\theta\bar{u}_r}{\bar{r}}=0 \tag{3}$$

$$\bar{u}_r\frac{\partial\bar{u}_z}{\partial\bar{r}}+\bar{u}_z\frac{\partial\bar{u}_z}{\partial\bar{z}}=-\frac{1}{\bar{\rho}}\frac{\partial\bar{P}}{\partial\bar{z}} \tag{4}$$

These equations can easily be solved by using the following boundary conditions:

$$\bar{r}=a,\quad \bar{z}=L,\quad \bar{u}_\theta=U$$

$$\bar{z}=0,\quad \forall\,\bar{r},\bar{u}_z=0$$

$$\bar{r}=0,\quad \forall\,\bar{z},\bar{u}_r=0$$

$$\bar{r}=a,\quad \forall\,\bar{z},\bar{u}_r=0$$

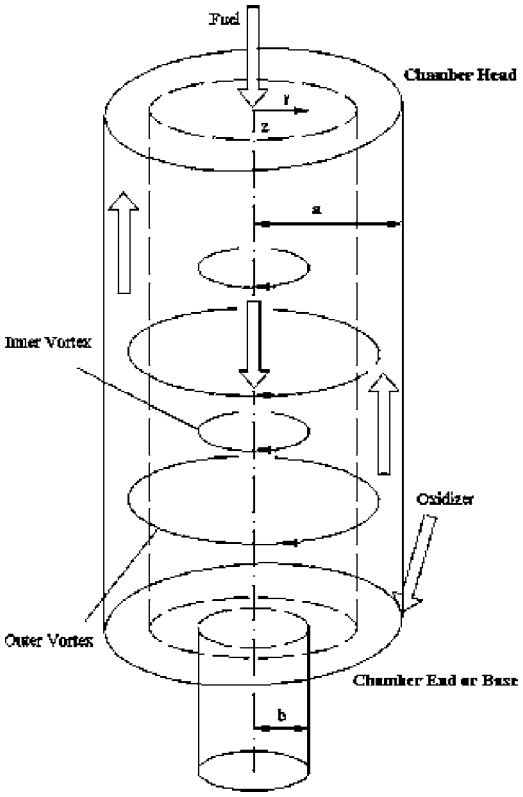

Fig. 1 Bidirectional swirl flow in a chamber

$$\bar{z} = L, \quad \bar{Q}_o = \bar{Q}_i = UA_i \tag{5}$$

From the solution of the above governing equations the axial velocity (u_z) in the combustion chamber shows the existence of a bidirectional swirl flow.

In real situations, the flow rate of oxidizer is much higher than the fuel flow rate. Therefore, if oxidizer is injected from the end of the chamber with a tangential orientation and fuel is injected from the head of the chamber, the oxidizer flow pattern dominates and the same bidirectional swirl flow will form. On the vicinity of the wall, oxidizer alone will move tangentially upward, having the ability to cool the walls. When oxidizer reaches the head, it mixes with fuel and tangentially moves downward the chamber through a core flow. Fuel and oxidizer are mixed in the core, and thus, they can react in the core only. This flow arrangement is schematically shown in Fig. 1.

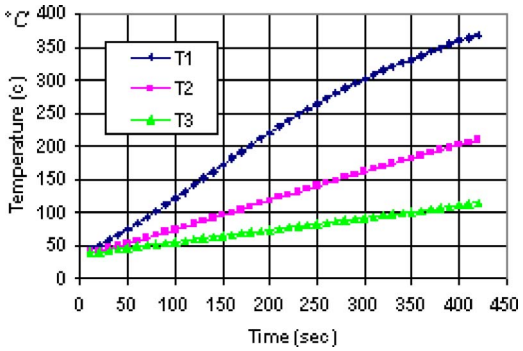

Fig. 2 Longitudinal chamber wall temperature in three positions of T_1: base, T_2: middle, T_3: head versus time, $\dot{m}_{fuel}$ =0.61 gr/s

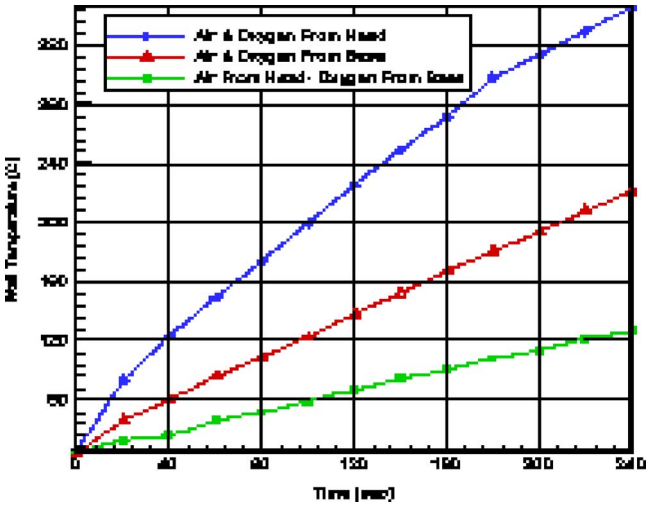

Fig. 3 Wall temperature variation (T_2) versus time for three different cases, ϕ=0.8, x=0.35, $\dot{m}_{air}$=10.4 gr/s, $\dot{m}_{oxygen}$ =2.5 gr/s, $\dot{m}_{fuel}$=1.07 gr/s

Results and Discussion

The chamber wall temperature variation with time is presented in Fig. 2. The results indicate that the chamber wall temperature at head, middle, and end increase with time.

Addition of oxygen to air increases the operating limits of the experimental facility. Usage of oxygen causes higher flow rates of fuel and oxidizer to combustion chamber. Figure 3 presents the data for the following three cases:

1. Fuel, air, and oxygen entered from the chamber head,
2. Fuel and air entered from the chamber head and oxygen from the chamber end,
3. Fuel entered from chamber head, and air and oxygen entered from the chamber end.

The flow rates for all three cases were kept constant. In the third case, the wall temperature decreased by ~36%, whereas in the second case a wall temperature decrease of ~62% was observed.

Analysis of exhaust gas composition, which is shown in Fig. 4, proved that combustion was most complete in the second case as compared to the other cases. To justify this observation, it is reasonable to assume that heat transfer from the combustion core to the chamber walls is mainly performed by radiation. Cooling of chamber walls are done by convection. Therefore, in the second case where fuel and air entered from the chamber head and oxygen from the chamber end, a better chance of mixing existed as

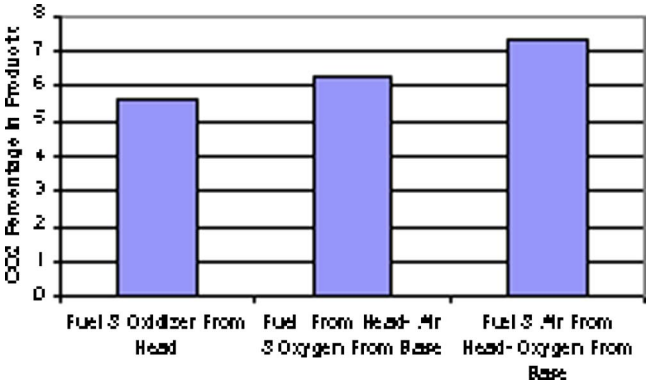

Fig. 4 CO_2 Percentage in combustion products for three different cases

compared to the third case. This resulted in a distributed combustion throughout the chamber length. This distributed combustion eliminated the possible local hot spots where, due to existence of high oxygen concentration, temperature might be very high. Since the radiation is strongly influenced by temperature, presence of hot spots can substantially increase the rate of heat transfer to the walls.

Presence of bidirectional swirl flow in a combustion chamber can effectively reduce the chamber wall temperature as experimentally measured. Injecting some of the oxidizer from the chamber end, and not all of it, results in efficient combustion and lower wall temperature.

Conclusions

Based on analytical results for the existence of bidirectional swirl flow in certain chamber geometries and flow condition and with the motivation of keeping combustion chamber walls cool, a new experimental facility was designed, fabricated, and tested. Propane and air accompanied by oxygen were used as fuel and oxidizer, respectively. In cases of existing bidirectional flow, wall temperature reductions of up to 50% were observed. In experiments where only some of the oxidizer was injected from the chamber end, to generate the bidirectional swirl flow and some of the oxidizer was injected with the fuel from the chamber head, the lowest wall temperature was observed.

Nomenclature

a = chamber radius
L = chamber length
$\bar{P}$ = chamber pressure
$\bar{Q}_o$ = outlet volumetric flow rate
$\bar{Q}_i$ = inlet volumetric flow rate
r = radial coordinate
T_{chamber} = chamber temperature
T_P = product temperature
u_r = radial velocity
u_z = axial velocity
u_θ = tangential velocity
U = inlet velocity
$\dot{V}_{\text{air}}$ = volumetric flow rate of air
$\dot{V}_{\text{oxygen}}$ = volumetric flow rate of oxygen
x = volumetric ratio of added oxygen to total air and oxygen
z = axial coordinate
β = fraction of nozzle to chamber
$\bar{\rho}$ = density
ϕ = equivalence ratio

References

[1] Marble, F. E., 1985, "Growth of a Diffusion Flame in the Field of a Vortex," *Recent Advances in the Aerospace Sciences*, in Honor of Luigi Crocco, E. Casci, ed., Plenum, New York, pp. 395–413.
[2] Chiaverini, M. J., Malecki, M. J., Knuth, W. K., and Gramer, D. J., 2003, "Vortex Thrust Chamber Testing and Analysis for O2-H2 Propulsion Application," AIAA Paper No. 2003-4473.
[3] Vyas, A. B., Majdalani, J., and Chiaverini, M. J., 2003, "The Bidirectional Vortex. Part 1: An Exact Inviscid Solution," AIAA Paper No. 2003-5052.
[4] Bloor, M. I. G., and Ingham, D. B., 1987, "The Flow in Industrial Cyclones," J. Fluid Mech., **178**, pp. 507–519.